

DTIC FILE COPY



UNIVERSITY OF MISSOURI-ROLLA



AD-A198 078

PREPRINTS FOR THE

# TENTH SYMPOSIUM ON TURBULENCE

September 22-24, 1986

DTIC  
ELECTE  
AUG 29 1988  
S D

DEPARTMENT OF CHEMICAL ENGINEERING  
ENGINEERING CONTINUING EDUCATION  
UNIVERSITY OF MISSOURI-ROLLA

**DISTRIBUTION STATEMENT A**  
Approved for public release  
Distribution Unlimited

Directed by

X B Reed, Jr.

University of Missouri-Rolla

Co-Directors

Gary K. Patterson  
University of Arizona

Jacques L. Zakin  
The Ohio State University

88 8 29 157

↓  
*This report includes the following topics*  
 TENTH SYMPOSIUM ON TURBULENCE

Sunday, September 21, 1986

7:00-10:00 p.m. Registration and Social Hour, Zeno's Motel and Steak House, Rolla, Missouri

Monday, September 22, 1986

7:30-8:30 a.m. Late Registration -- Miner Lounge, University Center-East, UMR

8:30 a.m. Symposium Opening -- Centennial Hall-West

8:35 a.m. Welcoming Remarks, Dr. Martin Jischke, Chancellor, UMR

8:45 a.m. Announcements and General Information

Monday (cont.)

COHERENCE IN TURBULENCE - Centennial Hall-West  
 Session Chairman - A.K.M.F. Hussain

Paper  
 Number

Invited Lecturers - Hassan Mahmoud Nagib, Illinois Institute of Technology, and Yann G. Guezennec, The Ohio State University, "On Coherent Large Scale Structures in Turbulent Boundary Layers and Their Suppression" 1

R. Erbeck and W. Merzkirch, Universität Essen, Republic of Germany, "Speckle Photographic Measurement of Turbulence in an Air Stream With Fluctuating Temperature" 2

N. Toy and C. Wisby, University of Surrey, Guildford, United Kingdom, "A Preliminary Investigation of Real-Time Image Analysis of a Visualized Turbulent Wake" 3

Thomas B. Francis and Joseph Katz, Purdue University, "The Study of the Flow Structure of Tip Vortices on a Hydrofoil" 4

H. Maekawa, T. Nozaki, M. Tao and S. Yamazaki, Kagoshima University, Kagoshima, Japan, "Visualized Large-Scale Motions in the Turbulent Wake Behind a Thin Symmetrical Airfoil" 5

J.T. Kegelman, McDonnell Douglas Research Laboratories, "A Flow-Visualization Technique for Examining Complex Three-Dimensional Flow Structures" 6

J.T. Kegelman and F.W. Roos, McDonnell Douglas Research Laboratories, "Spanwise Coherence of Vortical Structures in a Reattaching Turbulent Shear Layer" 7

C.C. Chu and R.E. Falco, Michigan State University, "A Vortex Ring/Viscous Wall Layer Interaction Model of the Turbulence Production Process Near Walls" 8

Stephen K. Robinson, NASA Ames Research Center, "Large-Eddy Detection in a Supersonic Turbulent Boundary Layer" 9

page 1



Quality Code  
 Available for Special  
 Dist  
 A-1

Charles G. Speziale, Georgia Institute of Technology, "On the Decomposition of Turbulent Flow Fields for the Analysis of Coherent Structures" 10

J. Swirydczuk, Polish Academy of Sciences, Gdansk, Poland, "Formation of a Concentrated Vortex Structure Induced by an Interaction of a Single Vortex with Unsteady Vortex Layer Shedding from an Airfoil" 11

NUMERICAL SIMULATION AND MODELING - Centennial Hall-West  
Session Chairman - M.M. Reischmann

Invited Lecturers - J.R. Herring, National Center for Atmospheric Research and Olivier Metais, NCAR, Advanced Program and CNRS, Grenoble, France, "Numerical and Theoretical Calculations of Stratified Turbulence" 12

V. Eswaran and S.B. Pope, Cornell University, "An Examination of Forcing in Full Turbulence Simulations" 13

P. Andre, R. Creff and J. Batina, Universite d'Orleans, Orleans, France, "A Numerical Investigation of the Turbulent Pulsating Flow in a Pipe" 14

Karam Azab and John B. McLaughlin, Clarkson University, "Numerical Simulation of the Viscous Wall Region" 15

F.F. Grinstein, Berkeley Research Associates, E.S. Oran and J.P. Boris, U.S. Naval Research Laboratory, and A.K.M.F. Hussain, University of Houston, "Numerical Study of the Mean Static Pressure Field of an Axisymmetric Free Jet" 16

L. Shtilman, City College of the City University of New York, R.B. Pelz, Rutgers University, A. Tsinober, Tel Aviv University, Tel Aviv, Israel, "Numerical Investigation of Helicity in Turbulent Flow" 17

Steven Keleti and X B Reed, Jr., University of Missouri-Rolla, "Spectral Properties of Exact Random Solutions to Burgers' Equation for Modified Thomas Initial Conditions" 18

Tuesday, September 23, 1986

STABILITY, TRANSITION AND DEVELOPMENT - Centennial Hall-West  
Session Chairman - R.J. Hansen

Invited Lecturer - W.S. Saric, Arizona State University, "Boundary Layer Transition to Turbulence: The Last Five Years" 19

F.O. Thomas and K.M. Prakash, Oklahoma State University, "An Experimental Investigation of a Global Resonance Mechanism in the Two-Dimensional Turbulent Jet" 20

Beatrice Martinet and Ronald J. Adrian, University of Illinois at Urbana-Champaign, "Rayleigh-Benard Convection: Experimental Study of the Oscillatory Instability" 21

R.W. Miksad, R.S. Solis and E.J. Powers, The University of Texas at Austin, "Experiments on the Influence of Mean Flow Unsteadiness on the Laminar-Turbulent Transition of a Wake" 22

Concurrent Sessions

NOVEL EXPERIMENTAL APPROACHES - Centennial Hall-West  
Session Chairman - W.G. Tiederman

J.P. Giovanangeli, Institut de Mecanique Statistique de la Turbulence, Marseille, France, "A New Method for Measuring in Stream Small Scale Static Pressure Fluctuations with Application to Wind-Wave Interactions" 23

Christopher Landreth and Ronald J. Adrian, University of Illinois at Urbana-Champaign, "Double Pulsed Laser Velocimeter with Directional Resolution for Complex Flows" 25

L.G. Ozimek and R.S. Azad, The University of Manitoba, Manitoba, Canada, "A Comparison of Analog and Digital Systems of Measurements of Turbulence Parameters" 27

H. Branover and S. Sukoriansky, Ben-Gurion University of the Negev, Beer-Sheva, Israel, "Flows with Strongly Anisotropic Turbulence-Dynamic and Heat Transfer Aspects" 29

Ioannis C. Lekakis, Ronald J. Adrian and Barclay G. Jones, University of Illinois at Urbana-Champaign, "Time Delay Correlations of the Reynolds-Stress Tensor in Turbulent Pipe Flow" 31

A. Tsinober, E. Kit, and M. Teitel, Tel Aviv University, Tel Aviv, Israel, "Electromagnetic Methods of Turbulence Measurements: Shortcomings and Advantages" 33

C.B. Reed, B.F. Picologlou, P.V. Dauzvardis and J.L. Bailey, Argonne National Laboratory, "Techniques for Measurement of Velocity in Liquid-Metal MHD Flows" 35

COMPLEX TURBULENT FLOWS WITH WALL EFFECTS, - Mark Twain Room  
Session Chairman - David Stock

Shiki Okamoto, Shibaura Institute of Technology, Tokyo, Japan, "Experimental Study of Mutual Interference Between Two Spheres Placed on Plane Boundary" 24

N. Toy and T.A. Fox, University of Surrey, Guildford, United Kingdom, "The Generation of Turbulence from Displaced Cross-Members in Uniform Flow" 26

Paul Dawson, Brian Lamb, Daniel Martin, and David Stock, Washington State University, "Modeling of Exhaust Fume Concentrations Near Buildings" 28

Essam Eldin Khalil, Cairo University, Cairo, Egypt, "Numerical Computations of Flow Patterns in Aluminum Reduction Cells" 30

Barry Gilbert, Grumman Corporate Research Center, "Turbulence Measurements in a Flow Generated by the Collision of Radially Flowing Wall Jets" 32

J.M.M. Barata, D.F.G. Durao and M.V. Heitor, Instituto Superior Tecnico, Lisboa, Portugal, "Experimental and Numerical Study on the Aerodynamics of Jets in Ground Effect" 34

Richard D. Gould, Warren H. Stevenson and H. Doyle Thompson, Purdue University, "Experimental and Computational Investigation of Turbulent Transport in an Axisymmetric Sudden Expansion" 36

↓  
 CONFINED TURBULENT FLOWS, - Centennial Hall-West  
 Session Chairman - Barclay J. Jones

M.M.A. Khalifa and A.C. Trupp, University of Manitoba, Manitoba, Canada, "Measurements of Fully Developed Turbulent Flow in a Trapezoidal Duct" 37

A.M. El-Kersh, Minia University, Minia, Egypt, and A.H. El-Gammal, Alexandria University, Alexandria, Egypt, "A Lag-Entrainment Method for the Prediction of a Turbulent Boundary Layer in an Annular Diffuser with Swirled Flow" 39

O. Turan, R.S. Azad, and S.Z. Kassab, " University of Manitoba, Manitoba, Canada, "Evaluation of  $k_1^{-1}$  Spectral Law in Three Wall-Bounded Flows" 41

J.C. Lai, University of New South Wales, Duntroon, Australia, and K.J. Bullock, University of Queensland, St. Lucia, Australia, "Distribution of Convection Velocities and Lifetimes of Turbulence Structures in Fully Developed Pipe Flow" 43

↓  
 FREE SHEAR TURBULENCE - Mark Twain Room  
 Session Chairman - R.J. Adrian

R.D. Mehta and J.H. Bell, Stanford University, Q. Inoue and L.S. King, NASA Ames Research Center, "Experimental and Computational Studies of Plane Mixing Layers" 38

D.F.G. Durao, M.V. Heitor and J.C.F. Pereira, Instituto Superior Tecnico, Lisboa, Portugal, "The Turbulent and Periodic Flows Behind a Squared Obstacle" 40

C.A. Thompson, N.G. Fico and F. Costa Filho, Instituto Militar De Engenharia, Rio de Janeiro, Brazil, "Circular Jets: Effects of Sinusoidal Forcing and Strouhal Number" 42

C.A. Thompson, N.G. Fico and F. Costa Filho, Instituto Militar De Engenharia, Rio de Janeiro, Brazil, "Hot-Wire Measurements on a Plane Turbulent Jet" 44

Return to Single Session

DRAG REDUCTION - Centennial Hall-West  
 Session Chairman - J.L. Zakin

Mark T. Coughran, David G. Bogard, and Choon L. Gan, University of Texas, "An Experimental Study of the Burst Structure in a LEBU-Modified Boundary Layer" 45

	<u>Paper Number</u>
B. Frings, University of Dortmund, Republic of Germany, "Heterogeneous Drag Reduction in Turbulent Pipe Flows Using Various Injection Techniques"	46
S.M. Penix and C.A. Petty, Michigan State University, "A Mechanism for Drag Reduction Based on Stress Relaxation"	47
Wednesday, September 24, 1986	
TURBULENT TRANSPORT, INCLUDING CHEMICAL REACTION - Centennial Hall-West Session Chairman - R.S. Brodkey	
Invited Lecturer - Carl H. Gibson, University of California at San Diego and Scripps Institute of Oceanography, "Turbulent Mixing by the Rate-of-Strain"	48
R.W. Claus, NASA Lewis Research Center, "Direct Numerical Simulation of a Forced, Chemically Reacting, Mixing Layer"	49
J. Picart and R. Borghi, CNRS, Mont-Saint-Aignan, France and J.P. Chollet, CNRS, Saint-Martin D'Herès, France, "Numerical Simulation of Turbulent Reactive Flows"	50
T. Lookman and P. Sullivan, University of Western Ontario, Ontario, Canada, "A Numerical Experiment on the Dilution of a Contaminant Cloud"	51
T.H. Chen, A.J. Lightman, W.J. Schmoll and P.P. Yaney, University of Dayton, "Simultaneous Two-Dimensional Velocity and Concentration Measurements in Jet Flows"	52
A. Cenedese, Università degli Studi di Roma "La Sapienza", Rome, Italy, L. Accardo and R. Milone, Centro Esperienze Idrodinamiche della Marina Militare, Rome, Italy, "Fluid-Dynamic Field Near a Propeller"	53
Rajan Menon, TSI Incorporated, "Phase-Averaged Measurements Using a 3-Component LDV System"	54
R.M. Privette, W.G. Tiederman and W.M. Phillips, Purdue University, "Cycle-to-Cycle Variation Effects on Turbulent Shear Stress Measurements in Pulsatile Flow"	55
R. Creff and P. Andre, Université d'Orléans, Orléans, France, "Experimental Study of a Periodic Reverse Current in a Pulsed Turbulent Flow"	56
H. Wu and G.K. Patterson, University of Arizona, "Distribution of Turbulence Energy Dissipation Rates in a Rushton Turbine Stirred Mixer"	57

NASA Technical Memorandum 88896

# Direct Numerical Simulations of a Temporally Evolving Mixing Layer Subject to Forcing

Russell W. Claus  
*Lewis Research Center*  
*Cleveland, Ohio*

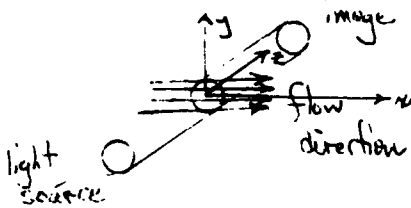
Prepared for the  
10th Symposium on Turbulence  
cosponsored by the Office of Naval Research  
and the University of Missouri—Rolla  
Rolla, Missouri, September 22-24, 1986

**NASA**

Session I

R. ERBECK AND W. MERZKIRCH, UNIVERSITÄT  
ESSEN, REPUBLIC OF GERMANY

Patterson, University of Arizona: As in single beam holography, can speckle photography focus on narrow x-y planes normal to the beam?



Merzkirch: Yes, when it is applied for measuring velocity in a flow that has been seeded with tracer particles.

In my presentation, speckle photography was applied for measuring density fluctuations in a flow without tracers. The light beam is transmitted through the flow and it integrates all the information along its path. We have shown how this information can be disintegrated in the case of isotropic turbulence. It is not possible to obtain information with a light sheet (no scatterers!).

Hussain, University of Houston: I know that speckle velocimetry is rather promising under some circumstances. Could you indicate when it is so. Also, could you please comment on its limitations, vis-a-vis other measurement techniques?

Merzkirch: Speckle velocimetry is a promising technique when the aim is to measure two velocity components in one plane simultaneously for one particular instant of time, and when the velocities are not too high. The latter limitation, probably the most severe at this time, results from intensity problems. The intensity per unit area in a laser light sheet is much lower than the intensity concentrated in the

measuring volume of a LDA. The higher the velocity, the shorter must be the light pulse generating the sheet, and the lower is the available intensity scattered from tracers in the sheet. The low sensitivity of ordinary photographic material at the wavelength emitted by a ruby laser is adding to this limitation.

It should be pointed out, that the subject of my paper is not speckle velocimetry from tracers, but measurement of density by means of a speckle method.

N. TOY AND C. WISBY, UNIVERSITY OF SURREY

Hussain, University of Houston:

Sufficiently far from the point of introduction of smoke, the smoke boundary has little to do with the local vertical flow boundary or local coherent structures. Thus, you can say little about the structure from smoke pictures. Flow visualization is extremely helpful when supplementing quantitative data but can be extremely misleading.

Toy: The limitations of smoke flow visualization have been appreciated for many years and extreme caution must be exercised when attempting to obtain quantitative information from this technique. It is proposed that a direct comparison of the considered flow case be undertaken in the future using established measurement techniques in order to appreciate more fully the correlation between the obtained statistics.

Brodkey, Ohio State University: What are the effects of velocity and scan rate on blurring?

Wisby: Standard vidicon technology causes the image to be integrated over the field acquisition time of 20 ms (ignoring blanking periods and assuming 50 Hz video rate), causing a 'blur'

phenomenon. In order to examine this effect, a snap-shot solid-state CCD camera has been employed that allows variable integration periods of between 1-20 ms while maintaining standard video output rates.

Nagib, Illinois Institute of Technology:  
How will you account for smoke and light intensity variations in the quantitative utilization of the image intensity exercises you indicated as extensions in future work?

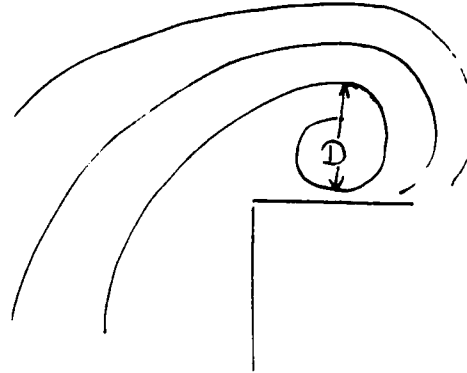
Wisby: Work is presently being undertaken to investigate the extent to which variations in injected smoke volumes and associated physical injection details can affect consequential variations in the registered light intensity distributions. As a preliminary investigation, the light intensity distributions are being interpreted on a purely relative basis with regard to individual experiments.

THOMAS B. FRANCIS AND JOSEPH KATZ,  
PURDUE UNIVERSITY

Rabi Mehta, Stanford University:  
Secondary vortices are generated near the wing surface due to the induced velocities (by the main vortex) on the sheet of opposite signed vorticity--necessary to satisfy the no-slip condition in the cross-flow plane. How do you define the vortex diameter--how is it measured from the photographs?

Katz: D is not the diameter of the core, but a characteristic vortex size. It can be defined as the diameter of the space created by the streamline (actually a projection of the streamline) that makes a complete loop. It was measured on the TV monitor's screen. Future work with injected particles will determine the core diameter, the diameter based on the traces with the highest speed. Note,

unfortunately, there is an error in the formula for D/C. The coefficient 0.9 should be replaced by 0.9/24.



H. MAEKAWA, T. NOZAKI, M. TAO AND S. YAMAZAKI, KAGOSHIMA UNIVERSITY

Hussain, University of Houston:

(a) I assume that the self-preserving region of a plane wake of a circular cylinder would not be different from the self-preserving region of an airfoil or a flat plate. If that is so, then the cylinder wake does not start with the double ring structure that Kobashi and Ichijo have recommended. How then will the structure that you recommend for a wake develop in the case of the cylinder wake?

(b) You are probably aware of the wake structure study of Hayakawa recently completed at University of Houston. The far field structure found by him in a cylinder wake is rather different from that proposed by you.

Maekawa: In the case of the turbulent wake behind an airfoil, 3-D coherent structure already exists just behind the trailing edge. I assume that they will be aligned wavy in the spanwise direction, in the case of the cylinder wake, and make the 2-dimensional vorticity concentrations that you and Dr. Hayakawa found in the self-preserving region of a cylinder wake.

J.T. KEGELMAN AND F.W. ROOS, McDONNELL  
DOUGLAS RESEARCH LABORATORIES

Hussain, University of Houston:

Comment: The apparent up and down bouncing of the mixing layer boundary as revealed by your visualization, may not indicate flapping of the mixing layer. It may be due to passage of large-scale structures connected by ribs. That is, the mixing layer thickness at the ribs is much lower than at the rolls. Furthermore, no flow facility can be built disturbance-free. Typically, facilities include resonant acoustic modes (the only way to establish that the modes are weak is to show free-stream velocity spectrum). Even when the fluctuation level is small, the energy may be concentrated in narrow bands. Only small peaks in a receptive or 'dangerous' frequency range can trigger instability. In the presence of even a small disturbance, a shear layer roll up may be organized spanwise. This organization can even be augmented due to feedback in situations such as reattaching shear layers, as you have studied. We have seen in a direct numerical simulation of mixing layers (Metcalfe, et al. 1985) that the mixing layer structures are not at all organized spanwise, contrary to the results of Browand and Troutt. In their case, the strong spanwise contortions within the large-scale structures in the plane mixing layer (established by multi-wire vorticity map data in our laboratory) are smoothed out because their data are taken not with vorticity probes, but with single wires in the potential flow outside the mixing layer. Even a slight amount of spanwise forcing introduced in the numerical simulation (which shows large-scale structures without spanwise coherence) induces spanwise coherence from the start.

P. BUCHHAVE, LDA TECH. (DANTEC)

Mehta, Stanford University: How do you deal with the apparent coincidence problem in 3-D systems and keep the probe volume down to a reasonable size (necessary for 3-D)? Do you have any 3-D (simultaneous) measurements which can be validated through comparison with theory or other measurement technique (say, a cross-wire)?

Buchhave: We use off-axis detection by combining two optical units. One acts as a transmitter of blue and receiver of green, whereas the other acts as receiver of blue and transmitter of green. The resulting measuring volume is small, s/n is improved, and particles are detected within the same measurement volume for blue and green beams.

Thompson, Military Institute of Engineering: How do you handle seeding a free jet with an L.D.A. system?

Buchhave: You have to seed the entire room.

Carl Gibson, Scripps, Inst.: Are there any advantages to using fiber optics in LDA's? What are the disadvantages?

Buchhave: Advantages are ability to access areas inaccessible to normal LDA's, easier traversing, and using an optical link from the laser to the fiber optic head, you can place the laser further away from the measurement.

CHARLES G. SPEZIALE, GEORGIA INSTITUTE  
OF TECHNOLOGY

Hansen, NRL: You make the point that the helicity is not Galilean invariant. Recent calculations of this quantity (Pelz, et al. 1985) suggest that this quantity is very small in turbulent shear flows. Would you comment further on the validity of this finding.

Speziale: In my opinion, no direct correlation can be established between the helicity density  $\underline{v} \cdot \underline{\omega}$  and turbulence activity in general turbulent shear

flows since it is not Galilean invariant. This lack of invariance allows for a situation where there can be arbitrarily different fluctuations in the helicity density for a given set of turbulence statistics (see Speziale, Quart. Appl. Math., in press, for more details). This measure of local helicity may be of some use in the analysis of homogeneous, isotropic turbulence which has a preferred reference frame (namely, the frame in which the mean velocity vanishes). However, general turbulent shear flows have no preferred reference frame (the problem of turbulent Couette flow discussed in my presentation serves as a good example of this fact), and hence the lack of Galilean invariance constitutes a serious deficiency. If a direct correlation is to be established between helicity and such turbulence activity as coherent structures and small scale intermittency, it will have to be based on some alternative measure of local helicity that is properly invariant (the coherent helicity discussed in my paper may be of some use in this regard).

Hussain, University of Houston: This is an additional response to the question by R.J. Hansen to Speziale in re helicity.

That helicity can be related to dissipation is a direct consequence of the simple identity

$$|\underline{u} \cdot \underline{\omega}|^2 + |\underline{u} \times \underline{\omega}|^2 = |\underline{u}|^2 |\underline{\omega}|^2,$$

which is equivalent to the trigonometric identity,

$$\cos^2 \theta + \sin^2 \theta = 1$$

and the fact that  $\underline{u} \times \underline{\omega}$  is the nonlinear term in the Navier-Stokes equation which is responsible for energy cascade, and thus creation of smaller scales and also dissipation. Thus, domains of high dissipation can be assumed to be different from domains of high helicity

density  $\underline{u} \cdot \underline{\omega}$ ,--a suggestion made by Moffatt and by Tsinober and Levich. However, the association of coherent structures with high helicity is based on the expectation that coherent structures are indeed long-lived. Even though most researchers believe that coherent structures have long life-times, we have long contended otherwise, i.e. their life-time is of the order of their turnover time.

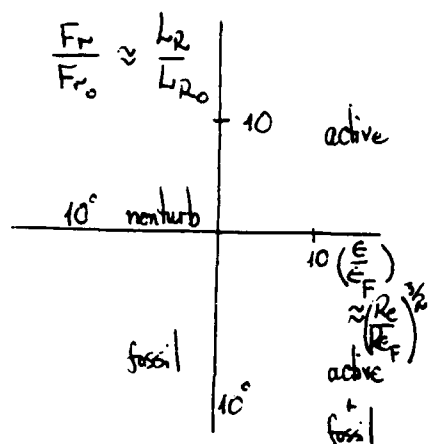
The claim of Tsinober and Levich that coherent structures are helical was countered by my stating that the spanwise roll in the plane mixing layer and the toroidal structure in the near field of an axisymmetric jet have iso helicity. They have then countered by the claim that all three-dimensional structures are helical. Clearly this is always true as it is impossible to conceive of a three-dimensional vortical structure in a flow which is helicity free.

Jack Herring, NCAR: Isn't the reason large helicity (density) may be expected to be associated with a coherent structure is that regions where it is large have (relatively) small forcing  $[\underline{u} \times (\nabla \times \underline{u})]$ , and so would last longer than regions where it is small?

Speziale: It is not strictly true that regions of low dissipation (retarded energy cascade) are associated with high helicity. In fact, only the solenoidal part of  $\underline{u} \times \underline{\omega}$  contributes to the energy cascade. Low magnitudes of the solenoidal part of  $\underline{u} \times \underline{\omega}$  can be associated with either high or low helicity. Therefore, there is no direct correlation between local helicity and the energy cascade. Consequently, arguments concerning the connection between high helicity and long-lived turbulence structures are unrigorous.

J.F. HERRING, NATIONAL CENTER FOR ATMOSPHERIC RESEARCH

Carl Gibson, Scripps, Inst.: It would be interesting to know the hydrodynamic state of the temperature field during the course of your numerical simulation using a hydrodynamic phase diagram, that is, a normalized Froude number versus normalized Reynolds' number plot (Gibson 1986 JFM).



$$\epsilon_F = 25vN^2$$

$$L_R = (\epsilon/N^3)^{1/2}$$

$$L_{R_0} = (\epsilon_0/N^3)^{1/2} \approx 1.6 L_P$$

at beginning of fossilization

$L_P$  = maximum overturn scale - Thorpe scale.

Herring: At present we have not assembled from the numerical runs all the information needed to place our experiments on your diagram. For the runs described in my talk, the Froude number ranged from 0.8 (the least stable flow) down to 0.1 (the most stable case). The value of the Reynolds' number ( $R_\lambda$ ) is about 30, but remember we apply a hyperviscosity ( $v^4$ ) to keep small scales under control. This also complicates the evaluation of  $\epsilon_F$ .

Russ Claus, NASA Lewis: The order of your time-stepping and wave number truncation can affect the stability of your results. What order accuracy is the time-stepping and what form (if any) of truncation was used. Can you comment on the effects of these parameters?

Eswaran: The time-stepping was done by a second-order Runge-Kutte scheme. The highest wave number (cut off) was  $\frac{2}{3} N k_0^{1/2}$ , where  $N$  is the number of nodes on one side of the computational cube, and  $k_0$  is the lowest non-zero wave number. The ratio of the cut off wave number to  $k_0$  will affect the spatial resolution of the grid. However, if the flow is well-resolved, this ratio should not affect the numerical stability. Although no value of the critical Courant number has been theoretically predicted for our scheme, I would expect that an increased order of the time-stepping procedure would increase the numerical stability of the computations.

Victor Goldschmidt, Purdue University: Did you vary the distribution over wave number of the forcing function? (If not, what guarantee do we have that the high wave number quantities were not dependent on the forcing parameters?)

Eswaran: No, we did not vary the distribution of the forcing function. However, the energy input rate at each wave number was usually different (as it also depended on the Fourier modes of the velocity). We intend to study the effect of forcing different numbers of nodes. I would expect that the results will not be substantially different. We varied the forcing parameters over a large range without detecting significant differences in the high wave-number quantities (at the same Reynolds' number). The results strongly

suggest that these quantities are very insensitive to the low-wave number forcing.

Jack Herring, NCAR: Could you comment on why your computed skewness decreases as  $R_\lambda$  increase.

Eswaran: The physical relevance of the skewnesses  $S_u$  and  $S_G$  are explained in Kerr (1983). We chose these quantities to give us a basis of comparison for our results with Kerr's. The results were substantially the same.

P. ANDRE, R. CREFF AND J. BATINA,  
UNIVERSITE d' ORLEANS

Jack Hansen, NRL: 1) Could you explain further the 3-order of magnitude discrepancy in your numerically concluded quasi-steady condition ( $\Omega/Re^{1.75}$ ) and that in experiments?  
2) How do your predictions of velocity profiles etc., compare with existing experiments?

Andre: 1) The first shown order of magnitude for the factor  $\Omega/Re^{1.75}$ , namely  $\Omega/Re^{1.75} < 5.6 \times 10^{-7}$ , comes from the comparison of the steady velocity profile and the unsteady velocity amplitude profile as computed with the model. If the relative difference between those two distributions does not exceed 1%, it is, a priori, proposed as a criterion that the flow may be stated as quasi-steady. An almost identical criterion was proposed by Ohmi et al. (1978).

From several experiments undertaken in boundary layer flows subjected to oscillations, it appears that the different criteria given by authors to depict the quasi-steadiness of the flow can also be expressed as quantitative values for the factor  $\Omega/Re^{1.75}$ . Unfortunately, there is a discrepancy between those different values and the one suggested from the results of the model. Therefore, it is interesting

that the same dimensionless quantity may relate the overall behavior of oscillating flows: the numerical analysis devoted to steady and unsteady (forced) quantities and experiments on turbulent intensity, shear stress, etc. in an oscillating boundary layer show that there is a range of possible values for  $\Omega/Re^{1.75}$  with which oscillating flows may not be considered as quasi-steady; in this case they may display an interaction between the natural turbulence and the forced modulation in so far as they are not quasi-steady.

2) The predictions agree, at least qualitatively, with existing experiments dealing with dynamic phenomena only (OHMI [1976]); more precisely:

i) the annular effect and the tendency of the peak amplitude position to approach the wall as the frequency increases,

ii) the phase velocity behavior along the tube radius vs the frequency

iii) the similarity of steady and unsteady velocity profiles when approaching the quasi-steadiness.

As long as the boundary conditions are the same and identical values for  $Re$  and  $\Omega$  are maintained, good agreement with experiments is expected. This was done by OHMI using, for the theoretical approach, a several region model for the eddy diffusivity instead of a mixing-length model as in the present case.

On the other hand, there are no available experimental results about the unsteady thermal fluid field in oscillating flows and this is what we will achieve in the near future.

Hussain, University of Houston: It was my understanding that a large number of studies of pulsation of turbulent boundary layers and pipe flows showed no effect of pulsation on time-average measures of the mean and rms turbulent

velocity profiles. It seems that your results suggest otherwise. Could you please explain and delineate what is new?

André: The important result brought up by MIZUSHINA (1978) is that, effectively, for a certain range of the forced modulation frequency, no change is observed on the mean velocity profile as well as on the rms turbulent velocity distribution. But, he has shown also that there exists a preferred value of the frequency for which a sort of resonance appears between the forced modulation and the bursting process; at the same time, the rms turbulence intensity profiles show important (non negligible) departures from classical rms profiles. Moreover, since MIZUSHINA's experiments, several works dealing with purely dynamic phenomena in oscillating flows and/or transport properties, have confirmed, directly or indirectly, the existence of preferred values for the frequency combined with the Reynolds' number value which may affect the normal or classical distributions [see, for instance, RAMASRIAN and TU, JFM, (1979); Binder (1985)....].

From the proposed model it appears that the same dimensionless quantity, namely  $\Omega/Re^{1.75}$ , may help to predict:

- i) the quasi-steadiness of the flow
- ii) the possible combination of  $\Omega$  and  $Re$  values leading to non-negligible, purely unsteady effects between two opposite limits: quasi-steadiness for small frequencies and large  $Re$ , or small unsteady amplitudes for large frequencies and relatively small  $Re$ .

The criteria proposed from recent experiments relative to point i) may be re-expressed as functions of  $\Omega/Re^{1.75}$ . Finally, the same quantity ( $\Omega/Re^{1.75}$ ) can help to state the amplitude (and

general behavior) of forced quantities (numerical model) and to state the interaction between oscillations and the boundary layer (experiments).

Finally, would it be not the one and only one criterion helpful in qualifying the dynamics of oscillating flows?

KARAM AZAB AND JOHN B. McLAUGHLIN,  
CLARKSON UNIVERSITY

Wm. Tiederman, Purdue University: What is the upper limit for your integrations with respect to time when you calculate average values? If the bursting period is an appropriate time-scale for the wall region, then  $T^+_{200(90)} = 18,000$ . Since your only mechanism for interaction is the mean profile, I would expect poor correspondence in calculated and measured  $\overline{uv}$  levels. Have you made this comparison?

McLaughlin: We have integrated for  $T^+ = 2000$ . We compute averages over  $x$  and  $z$  as well as time in an effort to improve statistics. We find reasonably good agreement with experiment for the Reynolds' stress and the production of turbulent kinetic energy.

C. Petty, Michigan State University:

- 1) Have you gained any insight about what terms in the Navier-Stokes equations are important in the viscous sublayer? A comparison with Sternberg's earlier hypothesis would be interesting.
- 2) Did you study the temporal structure the flow?
- 3) What was the correlation coefficient for the Reynolds' stress?

McLaughlin: 1) We haven't attempted to obtain that information, but we shall consider it.

2) We have obtained frequency spectra of the spatial Fourier components of the flow corresponding to the wavelength measured by Morrison, Bullock, and Kronauer, and we obtained good agreement with their phase velocity, based on the

frequency for which our spectrum reaches a maximum. However, the spectra were very broad.

3) We haven't computed the Reynolds' stress coefficient.

Brodkev, Ohio State University: It would seem that the cyclic b.c. is the cause of the 15% unsteady initial contribution and the final deviation. Did you use longer (or could you),  $x$  values?

McLaughlin: We haven't attempted to use larger periodicity lengths because we are currently limited by the size and speed of the minicomputer on which the calculations were performed. It should be possible to make runs with larger periodicity lengths on a supercomputer.

Hussain, University of Houston: It is worthwhile to note that while Laufer's pipe data are unquestionably reliable, there are serious doubts regarding Laufer's channel data. It seems that his flow was not fully developed at the measurement location.

F.F. GRINSTEIN, BERKELEY RESEARCH ASSOCIATES

V. Goldschmidt, Purdue University: You compare predictions of momentum flux variations at exit velocities of 200m/s to data for much lower exit velocities. Have you tried to run your model for incompressible flows?

Grinstein: Our present numerical model (involving an explicit solver) was tailored for compressible calculations. In the incompressible limit the time steps dictated by the Courant condition for numerical stability are unreasonably small from the physical point of view. Because of this, calculations at the nozzle exit velocities of the experiments were inefficient and extremely expensive at this stage, and therefore they were not attempted. We are presently testing an

implicit version of the model suitable for incompressible fluids and hope to be able to do these comparisons in the near future.

L. SHTILMAN, CITY COLLEGE OF THE CITY UNIVERSITY OF NEW YORK

R. Adrian, University of Illinois: The plots of  $P(\cos\theta)$  vs  $\theta$  look much like the result you would expect if  $\theta$  were a random variable uniformly distributed between  $(-\pi, \pi)$ . What do the results look like for  $P(\theta)$ ?

Shtilman: The peaks at  $\pm 1$  were observed for  $P(\theta)$  too, but in 3-d the measure of isotropy of the angle between velocity and vorticity is  $\cos\theta$  and not  $\theta$ . Indeed, the elementary solid angle between these vectors  $d\Omega \sim d(\cos\theta)$  unlike the 2-d case.

Speziale, Georgia Institute of Technology: You used the results of your direct simulations of isotropic turbulence, where the preferred orientation of velocity parallel to vorticity (and, hence the existence of large helicity density) are accompanied by low dissipation, to draw general conclusions. However, for a two-dimensional turbulence (which can be approached by any turbulent flow in a rapidly rotating framework sufficiently far from solid boundaries) the helicity density is small while the dissipation rate is also small due to spectral blocking. Consequently, how can you claim that there is a direct correlation between the helicity density and the dissipation?

Shtilman: Rapidly rotating fluid is not exactly two-dimensional flow and the product of vertical velocity by a very large vorticity is not small.

STEVEN KELETI AND X B REED, JR.,  
UNIVERSITY OF MISSOURI-ROLLA

Gibson, Scripps: It would be interesting to see your Kolmogoroff normalized spectra compared to universal forms for 3D turbulence.

Reed: That's a good idea. We will take a look at that.

Miksad, University of Texas: The nonlinear advective term in Burgers' equation, when transformed, yields a term where any two wave numbers which sum or difference to  $k$  can potentially transfer energy to the  $k$  wave number as time progresses. How did you handle this term? Was your procedure 'exact'?

Reed: Yes, it was an exact solution, so that spectral transfer was computed from the exact solution. No attempt was made to obtain contributions to one wave number band,  $(k, k + \Delta k)$  from other bands. Consequently, detailed comparisons with, e.g., direct-interaction calculations were not made.

Session III

F.O. THOMAS AND K.M. PRAKASH, OKLAHOMA STATE UNIVERSITY

Hussain, University of Houston: One perhaps needs to be careful about talking about potential cores which is a time-mean, and almost useless, concept when one is dealing with instantaneous flow dynamics including vortex pairing. Instantaneously, the jet core fluid remains potential for a much longer distance than is apparent from centerline time-mean data.

X B Reed, Jr., University of Missouri-

Rolla: Spectral coherence measurements are typically 'ragged'. Did you 'window' your spectral coherence measurements? If so, with which one(s) and why? If not, why?

Thomas: In our coherence measurements we employed a Hanning window. We found

that in many applications this gives good performance. The application of a simple cosine window gave results with no appreciable difference, suggesting that the results we presented are not sensitive to window choice. In order to smooth the coherence spectra we used ensemble averaging over approximately 200 samples. The coherence spectra were computed digitally with standard FFT techniques.

R.W. MIKSAD, R.S. SOLIS AND E.J. POWERS,  
THE UNIVERSITY OF TEXAS AT AUSTIN

Thomas, Oklahoma State University:

Three part question: 1) Are the bicoherence and complex digital demodulation techniques restricted to streamwise locations where the flow is 'orderly', and if so, in what respect? 2) Were the bicoherence measurements ensemble averaged? and 3) What do you consider to be sufficient frequency resolution for such measurements?

Miksad: 1) The answer is twofold. Bicoherence spectra are best suited for regions of flow where you have some randomness (turbulent or quasi-turbulent flow). When the flow is orderly, you have to do averaging over an ensemble. You are looking for a statistically meaningful phase coherence between three spectral components. The phases of three coupled modes always sum to the same value ('null out'). Just because three such null out at an instant in time, however, that does not guarantee that is the true value for all times, and an ensemble average must be carried out in order to establish the coherence between the phases. Digital complex demodulation is complementary to this and is most suited for orderly flows. Complex demodulation is equivalent to the old technique of heterodyning in radio receivers. The idea is to identify the center frequency (one must

tell the technique what to look for) and then determine variations of phase and amplitude modulation. But in a jittery flow, the carrier frequency cannot be identified very well and the technique gives a sort of 'fuzzy' output. When nonlinear 3-wave interactions occur, and one of the waves is very low frequency, then when it interacts back with high frequency modes, it produces sum and difference frequencies (side bands to carrier frequency). The side band structure in the frequency domain is the spectral signature of a wave whose amplitude and phase are modulated in the time domain. You can look at nonlinear interactions with either bicoherence techniques or demodulation techniques. When you use the latter, you are looking at behavior in the time domain, when the former, you are looking at nonlinear interactions in the frequency domain. Bicoherence thus yields useful information at virtually all stages, whereas demodulation loses its utility rapidly as jitter enters.

- 2) Yes. That's the key to whole process.
- 3) The answer is complicated. It depends on whether the dominant interaction involves the production of high frequency (sum modes) or low frequency (difference modes). If it is high frequency (producing, say, harmonics), then you don't need so great a record length. If the interaction scheme involves low frequency modes interacting with high frequency modes, then you have a problem. You must take longer records in order to resolve low frequency fluctuations; the usual limitation is then the data acquisition system. In a real flow, you have both sum and difference modes and these are the 'black art' sorts of questions of signal analysis, (J.S. Bendat and A.G.

Piersol, Random Data: Analysis and Measurement Procedures, Wiley-Interscience, 1971. A. Papoulis, Probability, Random Variables, and Stochastic Processes, 2nd edition, McGraw-Hill (1984)).

For further exposition on these matters, see R.W. Miksad, F.L. Jones, C.P. Ritz, and E.J. Powers, "The rate of nonlinear wave-wave interactions in laminar-turbulent transition" Archives of Mechanics, in press, probably Dec. '87 publication date.

#### Session IV

J.P. GIOVANANGELI, INSTITUT de MECANIQUE STATISTIQUE de la TURBULENCE

Khalifa, University of Manitoba: How do you calibrate the ring around the pitot tube.

Giovanangeli: The same way that we calibrate the hot wire.

C. LANDRETH AND R.J. ADRIAN, UNIVERSITY OF ILLINOIS AT URBANA-CHAMPAIGN

R. J. Hansen, Naval Research Laboratory: What is the difference between mean square estimation and Lumley's orthogonal decomposition? The equations look similar.

Adrian: The intent of mean square estimation is to estimate the state of the fluid around a point where the state is prescribed. Practically, the method provides a picture of the large scale structure that occurs in a volume on the order of several integral scales in dimension. It provides a means of interpreting 2-point spatial correlations in terms of vector fields. By itself, orthogonal decomposition (the Karhunen-Loève expansion) determines a set of deterministic orthogonal functions that best represent the random process in the sense of rapid convergence. The eigenfunctions do not

necessarily look like coherent structures. For example, in homogeneous turbulence, the eigenfunctions are just the set of complex exponentials. Randomness in the orthogonal decomposition is relegated to the Fourier coefficients in the expansion. Lumley extracts compact structures from the orthogonal decomposition by combining it with a shot-noise model. When this is done, the results of mean square estimation and shot-noise decomposition become not dissimilar, but still not identical. In homogeneous turbulence Lumley's characteristic eddies are more compact than the conditional eddies.

J. Herring, NCAR: Is the core region in your experiment stable, and if so, do you see oscillations where frequencies correspond to the stability?

Adrian: We did not measure the mean temperature but on the basis of other experiments, I expect that the core was stably stratified. The Brunt-Vaisala frequency would be somewhat higher than 100mHz if the temperature stratification exceeded 0.2°C/cm, so internal waves could have been present in the higher frequency range of our spectra. We see no strong peaks in this range, however.

R. Brodkey, Ohio State University: To what accuracy can you get the vorticity normal to the photographic plane?

Landreth: This is a topic of ongoing investigation. With our present system we anticipate measurement errors of between 10% and 20%.

K.R. Saripalli, McDonnell Douglas:

(a) What is the major difference between your technique and the speckle velocimetry?

(b) What are the maximum velocities for which this technique is used? And what about laser power?

Landreth: (a) The particle density is the difference. In this technique, the density used is such that particle

images do not overlap on the PLV photograph, which would result in the formation of speckle.

(b) This technique can be used up to 500 m/sec, and they used 2 1/2 J/Pulse Pulsed Ruby Laser.

L.G. OZIMEK AND R.S. AZAD, THE UNIVERSITY OF MANITOBA

Giovanangeli, Institut de Mecanique

Statistique de la Turbulence: In your analog method, how did you determine u and v? What was the turbulence intensity?

Azad: The u and v were separated by the following method:

$$u + v = s e_1, \quad (1)$$

$$u - v = s e_2, \quad (2)$$

$$u = \frac{s}{2}(e_1 + e_2), \quad (3)$$

$$v = \frac{s}{2}(e_1 - e_2). \quad (4)$$

s was determined from calibration of each wire and they were matched to give the same value of s the turbulence intensity varied from 5 to 60%

X B Reed, Jr., University of Missouri-

Rolla: 1) What was your sampling rate and how did you determine it? After your spectral measurements?

2) Your  $-\overline{u^2v}$  extrema were always greater for digital than for analog measurement. Is there a reason?

Azad: 1) Boundary layer--sampling rate-- $3 \times 10^3$  samples/sec.

Diffuser Flow--sampling rate-- $2 \times 10^4$  samples/sec.

First, the sampling rate was fixed in the boundary layer by comparing the results with other published data and then it was extrapolated to diffuser flow. The moments must agree with other results in the literature for boundary layers.

2) Experimental errors of the flow from one day to another can produce the errors that you have pointed out at extrema.

H. BRANOVER AND S. SUKORIANSKY, BEN-GURION UNIVERSITY OF THE NEGEV

C. B. Reed, Argonne National Laboratory:

What was the interaction parameter in these experiments?

Sukoriansky: Unity

A. TSINOBER, E. KIT AND M. TEITEL, TEL AVIV UNIVERSITY

Branover, Ben-Gurion University: 1) Is silver chloride coating of electrode tips to take care of all the electro-chemical effects? If yes, how long does it last and how does it deteriorate with time?

2) My second question is of a more provocative nature. You conclude for some special cases of turbulence measurements in water (electrolyte) that the method you discussed can be applied. The remaining question, though, is why should one go through all the trouble of squeezing a water flow into a gap of a magnet and other troubles, while other methods of turbulence measurement exist?

Tsinober: 1) The AgCl coating, when properly made, reduces the electro-chemical noise (offset) to the level of the noise of the electronics, which is approximately  $0.3\mu\text{V}$  ( $0 + 200$  Hz). It is stable for several days if not exposed to air.

2) Even for only the vorticity measurements, it is worth while spending several hundreds of K\$. The reason is that this method is an absolute one (and does not require any calibration). Therefore, it promises to obtain results of fundamental value for turbulence. My confidence in this presently is increased after spending a couple of months in the laboratory of Prof. J. Wallace building and calibrating g-hot wire probes. Other important advantages of the PDP method are described in the paper.

Session V

N. TOY AND T.A. FOX, UNIVERSITY OF SURREY

Sanderson, Iowa State University: Were the side forces on either the forward or trailing members measured or deduced. There is work showing that spacing of two parallel members may experience a maximum in side forces at certain spacings?

Fox: The drag forces have been calculated at the center-line of each member in the configuration and these show that maximums do occur at certain spacings. However, the side forces have not been calculated at this stage in the study. It would be useful to consider such forces in conjunction with aspects of the dynamic response of each member to changes in the member spacing.

King, NASA-Ames: Have you looked at the acoustics of this setup, particularly with regard to edgetone generation below the critical gap width.

Fox: Considerable work has been done in the past on the acoustic characteristics of two cylinders arranged in parallel when modelling power lines. In the present investigation this particular aspect has not been considered, and it is difficult to define the practical application of such a study.

P. DAWSON, R. LAMB, D. MARTIN AND D. STOCK, WASHINGTON STATE UNIVERSITY

Gilbert, Grumman: COMMENT: Your last slides show disagreement between measured and predicted concentration values at the ground along a line directly downstream of the model. However, you showed that the predicted downstream plume slants off to the left. Perhaps the results could correlate better if you used values along a line that tracks the center of the plume.

Stock: Good suggestion, we will try it. Also, we will remove the asymmetry in future computations.

R. Claus, NASA Lewis: Numerical accuracy can seriously affect your calculated results, especially in the scalar field. Your modifications to the k- $\epsilon$  turbulence model can be invalidated by numerical diffusion. Care to comment?

Stock: The k- $\epsilon$  model was compared with the vertical profile of the Leipzig data, and that calculation was used to evaluate the changes to the standard k- $\epsilon$  model. For the 1-dimensional calculation a very fine grid could be used. We did not try to use our 3-D calculation to tune the turbulence model.

R. Privette, Goodyear Aerospace Corp.: Have any calculations been performed using a less computationally intensive closure model in an effort to evaluate the ability of other methods to predict the experimental results.

Stock: We are interested in flow with recirculation zones and therefore believe that the k- $\epsilon$  model is the least computationally intensive model that should be used.

B. GILBERT, GRUMMAN CORPORATE RESEARCH CENTER

K.R. Saripalli, McDonell Douglas: How significant is the contribution of this flow to V/STOL flow field, since the important jet impingement region has been excluded. Are you aware of the recent work at McDonell-Douglas Research Laboratories on the V/STOL flow field that included the jet impingement region which reveal lower spreading rates and higher turbulence intensities.

Gilbert: We are planning further studies of the problem to include the impinging jets. By studying the problem without impinging jets, the idea is to

isolate and quantify the effects of coupling between the impinging jets and the fountain. I am not aware of the recent work at McDonell Douglas on the twin-impinging-jet-fountain flows.

R.D. GOULD, W.H. STEVENSON AND H.D. THOMPSON, PURDUE UNIVERSITY

Eswaran, Cornell University: Did you obtain the constants for the k- $\epsilon$  model from the literature or did you optimize them to fit your data?

Gould: We used the standard constants given by Pun and Spalding (1976). The reference is given in the paper.

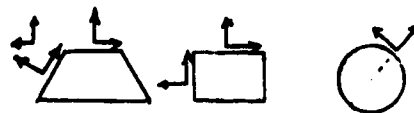
#### Session VI

M.M.A. KHALIFA AND A.C. TRUPP, UNIVERSITY OF MANITOBA

André, Université de Orleans: What are the expected effects on the pressure drop and on heat transfer due to the trapezoidal shape?

Khalifa: The Blasius and Dittus-Boelter equations hold to within about 10% if the equivalent hydraulic diameter is used.

Jones, University of Illinois: By orienting your probe geometry with respect to the fixed duct axes, the v and w components as you approach the side walls will not be directly interpretable with respect to  $\tau_w$  and thus the comparison with rectangular and circular duct data may lead to discrepancies. Can you clarify how you rationalize direct comparison of such results?



Khalifa: Only the Reynolds stresses for fluid adjacent to the top and bottom walls (and not the inclined wall) were compared to the results for square and circular ducts. For these two walls, the measurement coordinate system is aligned parallel and normal to them. For the inclined wall, the Reynolds stress components must be computed from the transformation corresponding to a  $30^\circ$  rotation of the coordinate system.

Session VII

R.D. MEHTA AND J.H. BELL, STANFORD UNIVERSITY

Adrian, University of Illinois: How were the forced oscillations imposed upon the vortices in the vortex blob calculation?

Mehta: By including a sine function on the normal ( $v$ ) velocity of the form:

$$v_p(t) = A \sin(2\pi ft)$$

Hussain, University of Houston: 1) Your simulation, which is two-dimensional, does not take into account the most crucial feature of the mixing layer, namely, longitudinal vortices or 'ribs'. Without these the central physics of the mixing layer will be missed.

2) In your numerical study with artificially induced longitudinal vortices that you plan in the future, what spanwise spacing would you use?

3) The spanwise structure in the mixing layer is not necessarily a legacy of upstream boundary layer but results from secondary or spanwise instability of the shear layer itself.

4) This instability has been studied by Lin and Corcos and by Pierrehumbert and Widnall.

5) I am concerned by the fact that your mixing layer is in free space between two rectangular jets, thus surrounded by the shear layers around the perimeter of

the two rectangular jets. I am worried about influences, even coupling, of the single-stream mixing layer all around on the two-stream mixing layer, in the mixing layer that you have studied.

6) The measurements you mention are time-average measures and thus may not reveal any coupling.

Mehta: 1) Yes, this is borne out by the results-- $\overline{(v')^2}$  (the normal Reynolds stress) is high in the computations (by a factor of ~3)--we attribute this to the lack of the three-dimensionality in the simulations which would relax this stress.

2) We hope to use experimental data (USC or Imperial College, for example) to guide us. At this moment we are only including one or two longitudinal vortices (very high computation times are the main problem).

3) I think you mean streamwise structure spacing. Nominally 2-D boundary layers always have spanwise variation in properties (e.g.,  $\delta$ ,  $c_f$ , etc..) the level and wavelength of which is determined by the flow conditioning (see Mehta and Hoffmann, Tr-66, Aero and Astro Dept., Stanford University Report, for example). It has been found (e.g. Wood, Ph.D. thesis, Imperial College) that this spanwise variation feeds into the mixing layer. It is conceivable that the longitudinal vortices, or rather their spacing, would be triggered by this.

4) Yes but I am not sure if 'real' mixing layers (in the laboratory) show any known scaling for the structures.

5) So were we. In the near-field our data seems to agree with other results and self-similar solutions--this has all been discussed in an article (latest Exp. in Fluids). We have also recently checked the measurements with a test section installed.

Stock: Good suggestion, we will try it. Also, we will remove the asymmetry in future computations.

R. Claus, NASA Lewis: Numerical accuracy can seriously affect your calculated results, especially in the scalar field. Your modifications to the k- $\epsilon$  turbulence model can be invalidated by numerical diffusion. Care to comment?

Stock: The k- $\epsilon$  model was compared with the vertical profile of the Leipzig data, and that calculation was used to evaluate the changes to the standard k- $\epsilon$  model. For the 1-dimensional calculation a very fine grid could be used. We did not try to use our 3-D calculation to tune the turbulence model.

R. Privette, Goodyear Aerospace Corp.: Have any calculations been performed using a less computationally intensive closure model in an effort to evaluate the ability of other methods to predict the experimental results.

Stock: We are interested in flow with recirculation zones and therefore believe that the k- $\epsilon$  model is the least computationally intensive model that should be used.

B. GILBERT, GRUMMAN CORPORATE RESEARCH CENTER

K.R. Saripalli, McDonell Douglas: How significant is the contribution of this flow to V/STOL flow field, since the important jet impingement region has been excluded. Are you aware of the recent work at McDonell-Douglas Research Laboratories on the V/STOL flow field that included the jet impingement region which reveal lower spreading rates and higher turbulence intensities.

Gilbert: We are planning further studies of the problem to include the impinging jets. By studying the problem without impinging jets, the idea is to

isolate and quantify the effects of coupling between the impinging jets and the fountain. I am not aware of the recent work at McDonell Douglas on the twin-impinging-jet-fountain flows.

R.D. GOULD, W.H. STEVENSON AND H.D. THOMPSON, PURDUE UNIVERSITY

Eswaran, Cornell University: Did you obtain the constants for the k- $\epsilon$  model from the literature or did you optimize them to fit your data?

Gould: We used the standard constants given by Pun and Spalding (1976). The reference is given in the paper.

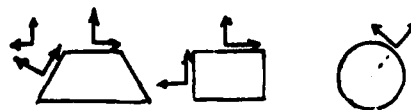
#### Session VI

M.M.A. KHALIFA AND A.C. TRUPP, UNIVERSITY OF MANITOBA

André, Université de Orleans: What are the expected effects on the pressure drop and on heat transfer due to the trapezoidal shape?

Khalifa: The Blasius and Dittus-Boelter equations hold to within about 10% if the equivalent hydraulic diameter is used.

Jones, University of Illinois: By orienting your probe geometry with respect to the fixed duct axes, the v and w components as you approach the side walls will not be directly interpretable with respect to  $\tau_w$  and thus the comparison with rectangular and circular duct data may lead to discrepancies. Can you clarify how you rationalize direct comparison of such results?



20 ppm and was well mixed before entering the test section.

Patterson, University of Arizona: Did you inject insoluble polymer threads into the wall region for comparison with your results in order to prove the hypothesis that the polymer threads alter the turbulence?

Frings: No, because we have not found an insoluble polymer which has nearly the same density as water and is not toxic (necessary because the outlet of the test pipe is connected with the sewer).

#### Session IX

C. GIBSON, UNIVERSITY OF CALIFORNIA AT SAN DIEGO AND SCIRPPS INSTITUTE OF OCEANOGRAPHY

J. Herring, NCAR: For low Pr, you seem to show  $-17/3$  spectra, even for cases (Kerr's numerical simulations) in which there is no  $-5/3$  range for the velocity field. Could you comment.

Gibson: The  $\Gamma-k^{-17/3}$  subranges observed from both the laboratory measurements and numerical simulations occupy a narrow range of wavenumbers because the spectrum is so steep, of order  $\log [Pr^{-1/4}]$  decades. The subrange widths are smaller than the inertial subranges of the velocity fields, but are displaced to higher wave numbers-- which does not seem unreasonable for a mixing process--in this case 'uniform-gradient-wrinkling'.

Hussain, University of Houston: 1) I wonder if you have looked at the implication of scalar pinch-off in the flow topology, in particular, the vorticity field. If there is a corresponding pinch off of vortex lines, this will be interesting from the point of view of helicity dynamics, in particular, creation of helicity.  
2) In Clay's measurement, was the sensor

sufficiently small with respect to the Kolmogoroff scale?

3) The  $-11/3$  roll-off at high k, which was derived for  $Pr \ll 1$ , seems also to hold for  $Pr > 1$ . Can you explain this?

Gibson: 1) I agree that this is an interesting approach, and have been able to derive equations for the kinematics of iso-ensrophy and iso-helicity surfaces and extrema, similar to those presented for iso-scalar surfaces and extrema used in my 1968 theory. They are more complex and harder to visualize, but I think worth thinking about and computing from numerical simulations.

2) The velocity sensor was an 0.1 mm conical hot film and the microbead thermistor was even smaller. The velocity sensor was spatially limited for the very high Reynolds number flow -  $Re_M = 270,000$ , but the temperature signal was limited only by electronic noise, and neither frequency response nor spatial resolution.

3) I think the numerical  $Pr > 1$  spectra hit the noise before they can show departure from the Batchelor exponential form. The laboratory and ocean temperature ( $Pr \sim 10$ ) do not show  $k^{-17/3}$  subranges.

Reed, University of Missouri-Rolla: 1) What do you see as the 'next' good question(s) in the area? Paradoxes?  
2) A phrase was missing from your presentation--passive additive--which would underline my 2nd question: Have you begun to look at mixing with source terms, such as buoyancy in liquids or modelling local turbulence in combustion, with an eye toward small scales and universality?

Gibson: 1) Does the 'gradient-pinching' mechanism work in the 3-D simulations? How do the strain-rate-mixing models interact with the vorticity field in 3-D

simulations? Why is the  $k^{-17/3}$  spectrum displaced to higher wave-numbers than the  $k^{-5/3}$  velocity spectral subrange?

2) The Batchelor (1959) spectral form should be produced even if the rate-of-strain field which mixes the microstructure is non-turbulent, as shown in my paper in J. Geoph. Res. (1982) on 'Fossil Turbulence in the Denmark Strait'.

Claus, NASA Lewis: Would you care to comment on the development of a subscale model of the scalar field that might result from this work?

Gibson: To the extent that sub-grid-scale models can be devised which exploit the new scalar mixing mechanisms and the new general spectral forms, I would certainly expect progress in developing more representative sub-grid-scale models.

Brodkey, Ohio State University: How does  $128^3$  size compare to  $k_B$  where development of numerical simulation from Clay occurs.

Gibson: The Kerr (1985) numerical simulation used a mesh size of about  $1/4 L_K$ , so for  $Pr < 1$  the Batchelor scale  $L_B = L_K Pr^{-1/2}$  will be much larger than the mesh size.

J. Hansen, NRL: In light of the limitations of 2D turbulence simulations which you have correctly noted, what level of confidence do you have that the gradient pinching mechanism identified there is a reality?

Gibson: I would be very surprised if the gradient pinching mechanism fails for 3-D simulations because there is such a straight-forward explanation for the mechanism using the expression

$$\frac{\partial \theta}{\partial t} + \mathbf{u} \cdot \nabla \theta = - \frac{D \nabla^2 \theta}{|\nabla \theta|} \nabla \theta$$
 The scalar field should follow the velocity best where  $|\nabla \theta|$  is large, in both 2-D and 3-D

R.W. CLAUS, NASA LEWIS RESEARCH CENTER

Patterson, University of Arizona: What do you expect closure modellers of chemical reactions in turbulent mixing to learn from full direct digital scalar modeling?

Claus: Direct numerical simulations can provide the early, pre-transition, information that closure models fail to represent. Hopefully, these simulations will be run at increasingly higher Reynolds' number to someday provide information for closure model development. It is currently premature to tie numerical simulations to the development of reaction closures.

A. PICART AND R. BORGHI, CNRS, MONT-SAINT-AIGNAN

Patterson, University of Arizona: Do you think that a value of 5 or any value  $> 1$  for  $\theta$  in  $W = k C_A (1 - C_A)^\theta$  is realistic enough for your further experiments?

Picart: A higher value of  $\theta$  will produce a steeper gradient in the scalar field and, so, numerical instabilities.  $\theta = 5$  is a realistic value for a premixed flame whose flame velocity is not too high. The limitation of  $\theta$  is due to the numerical code. These are limited to low Re number and, so, low Schmidt number.

J. Hansen, NRL: 1) What do you anticipate the next steps in your numerical study will be?

2) Is  $32^3$  resolution adequate for this calculation?

Picart: 1) The next steps will be a full simulation until  $C_A$  nears zero with different characteristic times  $\tau_c$  and, so, of the ratio  $\frac{\tau_c}{\tau_r}$  (which is the Damkohler number) the forcing of the turbulence field would be interesting in order to get a stationary turbulence field. Afterwards, I think it would be interesting to introduce two scalar

fields in the code in order to simulate a diffusion flame.

2)  $32^3$  is adequate for the behavior of mean statistical results. This limits the Reynolds' number, but with  $128^3$  which is the higher resolution, the Re number is not much higher.

Reed, University of Missouri-Rolla:

Have you looked at the effect of initial conditions on your results? (e.g., different initial spectra, different concentration ratios?)

Picart: Yes, I have looked, but the initial conditions have no influence on mean quantities such as the mean value, the variance, and the correlation. The shape of the scalar spectra determines the shape of the scalar P.D.F. and joint P.D.F. and the values of the length scales (scalar). The concentration ratio is not important if it is near one (i.e., far from the concentration where the reaction proceeds). The decrease of length scale is due to an initial spectrum which is not in equilibrium.

T. LOOKMAN AND P. SULLIVAN, UNIVERSITY OF WESTERN ONTARIO

J. Herring, NCAR: It would be interesting to compare your calculation to the work of H. Aref (JFM?; 84)

Sullivan: Yes. When more results are in we will certainly compare.

T.H. CHEN, A.J. LIGHTMAN, W.J. SCHMOLL AND P.P. YANEY, UNIVERSITY OF DAYTON

Reed, University of Missouri-Rolla:

COMMENTS: 1) Your 1st color slide beautifully illustrates the source of the local minimum of  $u'$  on the axis for some distance downstream.

2) The downstream development of shear flows and in particular of jets is 'moment by moment', in the sense that  $U$  first becomes self preserving, then  $u'$  and so on to higher moments. Thus, the lower moments may already start

'decaying' before the high moments have 'come up' to statistical equilibrium (similarity).

Almost all your fluctuating fields showed a more pronounced 'RHS' than 'LHS'. Was that a flow asymmetry or an artifact (perhaps optical)?

Chen: Jet flows are very sensitive to the surrounding boundary conditions. It is especially true for the low-velocity jets. The configurations of optical hardware and laser safety covers around the jet are by no means axisymmetrical. Due to this asymmetrical far field condition, the jet is slightly bent towards the 'LHS'. Consequently, the 'RHS' shows more fluctuations. However, it can be seen from the fluctuation contours that the transitional regime is fairly axisymmetrical. The asymmetry occurs further downstream and would not affect the results of our study significantly.

Gould, Purdue University: How did you separate your LDV signal from your Raman signal? Did you have to stagger the signal in time, and if you did, did this affect the velocity-concentration correlation?

Chen: The LDV and Raman systems are based on two different Argon laser wave lengths, LDV at 514.5 nm and Raman at 488 nm. The Raman signal is frequency shifted from the elastic scattering (Rayleigh) by the appropriate Raman shift. The spectrometer used to isolate the Raman signal rejects the Rayleigh component sufficiently that stray signal never exceeds 3% at the Raman frequency. As a result the Raman and LDV signal are independent and there is no induced velocity-concentration correlation.

Session X

R.M. PRIVETTE, W.G. TIEDERMAN AND W.M. PHILLIPS, PURDUE UNIVERSITY

Rajan Menon, TSI, Inc.: Since statistics are calculated on a cycle-to-cycle basis it would be good to know the amount of error (error bands)

especially for  $\overline{u'v'}$  calculations.

Tiederman: The statistics at each location were averaged over 55 cycles. Since the velocities were sampled on an equal time interval basis, the major sources of uncertainty are the finite size of the ensemble and the finite size of the window for 'filtered' data. The unfiltered data also includes an uncertainty due to cycle-to-cycle variation of the mean signal. The uncertainty of the turbulence intensities and the Reynolds' stress for the filtered data are on the order of 5%.

R. CREFF AND P. ANDRÉ, UNIVERSITÉ d'ORLEANS

Reed, University of Missouri-Rolla: A 'bullet' of parabolic shape can be used which, when moved linearly along the axis, provides for a linear variation of velocity in the steady state. How was your high frequency periodically variable-flow generator designed?

André: I am afraid of a misunderstanding about the frequency range used in the study. This is a low frequency range.

The frequencies which are obtained by means of the time varying sonic-section range between 0 and 35 Hz. The two acoustic resonance modes obtained here are equal to 9.3 Hz and 27.7 Hz, respectively.

H. WU AND G.K. PATTERSON, UNIVERSITY OF ARIZONA

Reed, University of Missouri-Rolla:

COMMENT: We are three of the half dozen odd people (pun intended) who worry about turbulence in flows not like flat plates and axisymmetric jets. It's a dirty job, but somebody's got to do it. You are to be commended for the measurement program, and for doing something to quantify the well-recognized periodicity due to the blades and to take it into account in viscous dissipation calculations that needed to be done.

Brodkey, Ohio State University:

- 1) Can you discuss the energy balance?
- 2) Have you discarded the trailing edge vortex in  $\epsilon$ , which (t.e.v.) still can be important in the mixing mechanism?

Patterson: 1) The energy was balanced for each of several regions between measurement locations in the impeller stream. Both turbulent (total including periodic) and mean kinetic energies were included. The balances were good to a few percent.

2) The periodic turbulence does not contribute to energy dissipation where it exists. When vorticity is connected downstream, where it degrades to non-periodic turbulence (real turbulence), energy dissipation results at the downstream location.

Reischman, Office of Naval Research:

What is the influence of, and have you ever changed the geometry of, the external mixing vanes (baffles)?

Patterson: So far we haven't changed the wall baffles. Their influence is to kill strong fluid rotation in the vessel as a whole and to produce large vortices near the wall.

# Direct Numerical Simulations of a Temporally Evolving Mixing Layer Subject to Forcing

*Russell W. Claus  
National Aeronautics and Space Administration  
Lewis Research Center  
Cleveland, Ohio 44135*

## Abstract

The vortical evolution of mixing layers subject to various types of forcing is numerically simulated using pseudospectral methods. The effect of harmonic forcing and random noise in the initial conditions is examined with some results compared to experimental data. Spanwise forcing is found to enhance streamwise vorticity in a nonlinear process leading to a slow, secondary growth of the shear layer. The effect of forcing on a chemical reaction is favorably compared with experimental data at low Reynolds numbers. Combining harmonic and subharmonic forcing is shown to both augment and later destroy streamwise vorticity.

## Nomenclature

$Y_0$  = radial location where  $U = (U_{-\infty} + U_{+\infty})/2$

$\lambda$  = forcing wavelength

$\theta_{0.90}$  = radial distance where the flow reaches 90 percent of  $U_{\infty}$

## Introduction

Direct numerical simulations of turbulent flows are increasingly being used to extract turbulent flow physics (e.g., refs. 1 and 2). This technique has distinct advantages over laboratory experiments. First, numerical simulations can unambiguously perform experiments where the effect of changing one single parameter can be individually studied in detail. Experimental studies, done in the laboratory, can rarely separate individual cause and effect trends. Second, numerical simulations contain all the information concerning flow dynamics. Various statistical properties can be easily extracted from the computations. Laboratory experiments usually cannot measure all important flow quantities and measurement accuracy is always a problem.

But numerical simulations are not without basic limitations as well. Although numerical simulations can sample any statistical quantity, these computations are very computer intensive, requiring on the order of several CPU hours to calculate only a few seconds of flow time. Whereas an experiment can usually be run for hours to measure various statistics, the numerical simulations have to be sampled over a much shorter time period. Another limitation of the numerical simulations is related to the range of turbulent scales which can be represented on the computational mesh. In direct numerical simulations, highly accurate (pseudospectral) numerical methods are used to solve the Navier-Stokes equations on a computational mesh. Despite the high phase and amplitude accuracy of these techniques, turbulent fluctuations both larger than

and smaller than the computational mesh cannot be resolved. The later restriction limits the simulation to a low Reynolds number flow (approximately 50 to 100 based on the Taylor microscale). When one applies the results of a low Reynolds number calculation to understand high Reynolds number turbulence, an inherent assumption is made that the large energetic scales of turbulent motion display characteristics that are Reynolds number independent. Testing of this assumption provides part of the motivation for this report.

Another motivation for this report is to examine the impact of vortical motion on mixing and chemical reactions in a planar mixing layer. The planar mixing layer is a convectively unstable type of flow in which small perturbations, either naturally occurring or induced by the flow hardware, can rapidly grow as these perturbations are convected downstream (ref. 3). This prototypical flow provides a unique opportunity to study the effect of small changes in the initial conditions of the flow and to observe how these changes alter the characteristics of a passive chemical reaction. A chemical reaction is quite sensitive to the dynamics of mixing at the smallest scales (ref. 4), and this will be examined in a comparison with experimental data.

There have been a number of previous numerical studies of mixing layers (refs. 5 thru 8). In relation to this report, the most pertinent of these is reference 5, in which the importance of large scale motions in enhancing chemical reactions is illustrated. Primarily, this study used two-dimensional numerical simulations to represent the increased interfacial area and enhanced entrainment that can result from large scale vortex rollup. However, two-dimensional simulations cannot represent the small-scale (inherently three-dimensional) structures that have been experimentally shown to occur in the mixing layer. These small-scale structures lead to a substantial increase in scalar mixing (ref. 9). The formation of these structures and the related increase in mixing is termed the "mixing transition." Before the mixing transition the flow is principally two-dimensional and laminar. After the mixing transition the flow is turbulent and three-dimensional while still retaining some of the characteristics of two-dimensionality. Previous studies have failed to observe the onset of the mixing transition because of a lack of grid refinement limiting the resolvable Reynolds number. The mixing transition occurs somewhere around a Reynolds number of 5000 (based on the local momentum thickness), whereas the simulations are typically one-fifth this level.

A new generation of supercomputers is currently becoming available which should eliminate this restriction. The first high speed processor obtained under NASA's Numerical Aerodynamic Simulation (NAS) project combines a relatively fast CPU with about 258 million words of memory. This may permit numerical simulations up to and perhaps beyond the mixing transition. This report details the initial calculations made with the NAS in a continuing study to examine various factors influencing mixing in chemically reacting, mixing layers. The effects of various types of forcing are studied and the vortical evolution of the flow is graphically illustrated. Although these calculations were made typically at low Reynolds number, they form the basis for future high Reynolds number studies.

## Computational Approach

The numerically-simulated mixing layer is conceptually represented as shown in figure 1. The orientation of typical streamwise and spanwise vorticity along with the orientation of the axes is illustrated. The mean axial velocity profile is initially set to a hyperbolic-tangent profile representative of experimental data (ref. 10). Imposed on this profile is a low level of random noise corresponding to a noise spectrum that is well resolved on the computational mesh. This provides a divergence-free, low level (typically less than one percent) of turbulence in all velocity components. To simulate spanwise forcing, harmonic and (sometimes) subharmonic perturbations are imposed in the initial conditions to generate a rapid spanwise-vortex rollup.

The time-dependent Navier-Stokes equations are solved for incompressible flow. Three scalar transport equations are solved to simulate a passive (no heat release) chemical reaction. This system of differential equations is solved explicitly by using second-order accurate time-differencing and pseudospectral approximations (Fourier series) of the spatial field as noted in reference 6. Spherical wavenumber truncation was performed by following the method described in reference 11. The flow Reynolds number was about 200 based on the initial velocity thickness, and the Damkohler number of the chemical reaction was set to 5.

The computational box size for these numerical simulations was scaled to include one complete cycle of the longest forced wavelength in the X (axial) direction. The Y direction was typically slightly more than twice this length, and the Z direction extent was typically equal to one-half the X direction length. Grid points were equally spaced along each direction. Boundary conditions in the X and Z direction were periodic. In the Y direction, no stress type boundary conditions were used; quantities such as U (axial velocity) were set to provide a zero gradient across the boundary and quantities such as V (radial velocity) were set to provide a reflection across the boundary.

As noted previously the numerical simulations reported here are for a time-evolving mixing layer. This comprises a Lagrangian description of the spatially developing mixing layer with the computational domain following the mean flow velocity. The drawback that this imposes in comparisons with experimental data is offset by the increased numerical resolution available in the Lagrangian description of the flow. The time-evolving simulation cannot represent some important features of experimental data (such as the asymmetric development of the layer) and should be looked at as more of a tool to study "idealizations" of real flows where the primary aim is to study the structure of turbulent flows.

## Results and Discussion

Numerical simulations of mixing layers subject to various types of forcing are examined here. Initially, the effect of harmonic forcing and random noise in the initial conditions is examined and some results are compared with experimental data (refs. 12-13). In the second section, the effect of combined harmonic and subharmonic forcing is illustrated. The wavelength of the harmonic forcing corresponds to the most amplified

frequency as predicted from linear stability theory (ref. 10). The subharmonic is twice this length.

### Harmonic Forcing and Random Noise

A series of numerical simulations of a mixing layer subject to harmonic forcing is compared to the experimental data of references 12 and 13. Both of these experiments employed a high degree of spanwise forcing in the entrance flow. This simplifies the specification of the initial conditions for the numerical simulation, since the high level of spanwise forcing dominates the natural random noise normally associated with high Reynolds number experimental flows. The spatially evolving shear layer is among those types of flows classified as convectively unstable; therefore, any small disturbance can rapidly grow as it is convected downstream. The highly excited harmonic forcing should grow more rapidly than the lower level random disturbances. This leads to the early part of the flow being largely two-dimensional. By taking advantage of this fact, we will examine how well a two-dimensional numerical simulation describes the velocity field of a harmonically excited shear layer.

The mean velocity half-width calculated from a two-dimensional numerical simulation (64x65 grid points) with harmonic excitation is compared to the experimental data of reference 12 in figure 2. For this comparison, data from the slow speed side of the layer is chosen as the dynamics of growth and saturation are more apparent than on the high speed side. *It should be noted that the simulation is of a time-evolving layer whereas, the experiment spatially evolves, a transformation similar to that described in reference 8 must be performed to relate the spatial and temporal information.* Once this transformation is performed the evolution of the experimental data is well simulated up to the point of saturation of the shear layer (60-80 cm). Beyond this point (> 100 cm) the slow growth of the layer is simulated poorly. Enlarging the computational domain and inputting various perturbations fails to reproduce the slow growth represented in the experimental data. The two-dimensional simulations simply exhibit vortex nutation or a change in the orientation of the axis of the rolled-up vortex with no significant increase in shear layer width. These results are similar to the findings of reference 14 where two-dimensional simulations were compared to the experimental data of Ho and Huang (ref. 15). Again the simulations fairly represented the early rollup and saturation, but failed downstream of this region. Reference 16 indicates that streamwise vorticity can be more significant beyond saturation, and these results tend to support that finding. In other words, the two-dimensional simulations fail to represent the growth of three-dimensional streamwise vorticity following saturation in the shear layer.

The Reynolds stresses at two different axial locations are compared in figure 3. The locations selected for comparison are within the region where the flow is primarily two-dimensional; hence, the comparison between simulation and experimental data is qualitatively good. The simulation does not match the peak experimental values, and the simulated profiles appear to be spread over a greater radial distance than the experimental data; however, the change in sign observed experimentally is faithfully reproduced. This correctly represents the change in the energy transfer between the

mean flow and the turbulence. When the Reynolds stresses are negative, energy is transferred from the turbulence to the mean flow causing the decrease in shear layer thickness seen in figure 2 (around 60 cm). The failure of the simulation to more closely match the experimental data profile is probably due to the difference in Reynolds number between the two flows.

The mean velocity half-width of three-dimensional simulations (32x33x32 grid points) using harmonic forcing with a low level of random noise or just random noise with no forcing is displayed in figure 4. The simulation using harmonic forcing exhibits a development similar to the two-dimensional calculations (figure 2) up to and just beyond the point of saturation. Beyond saturation the three-dimensional forced simulation displays a slow, steady growth which is in general agreement with the experimental trend. In contrast to the forced results, the mean velocity half-width of the "random noise only" simulation indicates a much slower overall growth of the shear layer.

Three-dimensional surface plots of constant vorticity are shown for the harmonic forcing simulation in figure 5. In the streamwise vorticity plots, both positive and negative vorticity levels are displayed with alternate colors indicating the change in vorticity rotation. The streamwise vorticity is weak and poorly organized at  $T=19.2$  seconds, whereas, counter-rotating vortex pairs are clearly evident in the  $T=43.2$  seconds plot. These are the mushroom-shaped structures experimentally observed by Bernal (ref. 17). In the simulation these structures evolve from the weak level of random noise included in the initial conditions. It is interesting to note that these structures do not get organized until after saturation of the harmonic wave. Apparently the orientation of the main spanwise vortex, which is involved in the change in sign of the Reynolds stresses (ref. 18) also contributes to the generation of streamwise vorticity.

Total vorticity surface plots are also shown in figure 5 for  $T=19.2$  and 43.2 seconds. Two different magnitudes of vorticity are color coded to indicate that the strongest vorticity is associated with the harmonic rollup (or spanwise vorticity). A lower level of total vorticity is also plotted to display the formation of streamwise vorticity on the spanwise structure. At much later times the spanwise vorticity grows sufficiently in strength to disrupt the spanwise structure.

Figure 6 displays the results of a high resolution calculation of the harmonically excited shear layer. In this simulation, 128x129x32 grid points are used to more fully resolve the flow field. Essentially, the dynamics of the flow are unchanged from the results noted earlier indicating that the vorticity field is sufficiently well resolved in these simulations. Also evident in the simulation is the distortion of the spanwise structure caused by the strong streamwise vorticity. The streamwise vorticity appears to gain energy at the expense of the spanwise structure.

Three-dimensional surface plots of constant vorticity for the numerical simulation with random noise only in the initial conditions are shown in figure 7. From these images it is apparent that both the spanwise structure and the streamwise vorticity take longer to evolve. Although the spanwise structure takes longer to evolve, the streamwise vorticity again does not appear until after saturation of the harmonic wave. Once it does form, the streamwise vorticity is notably weaker than the streamwise

vorticity that formed under harmonic forcing (fig. 5). Despite the fact that harmonic forcing adds no energy into the Z direction modes, the nonlinear interaction with the spanwise structure is important to the formation of the streamwise vorticity.

Forcing can also have a notable impact on scalar mixing and, thereby, on a chemical reaction. The previous two numerical simulations were repeated using much finer mesh resolution (128x129x32 in the X, Y, and Z direction respectively) to accurately simulate a passive chemical reaction. Figure 8 displays the results of these calculations compared with the experimental data of reference 13. (Here the total product versus time from the simulations is compared to the experimentally measured product thickness as defined in ref. 13. This provides a qualitatively comparable basis for examining both flows.) The effect of experimental forcing noted at low Reynolds number is qualitatively similar to the trend seen in the numerical simulations. Since the numerical simulations are for a low Reynolds number (less than 1000 based on the local momentum thickness) this qualitative agreement is expected. What seems unusual about these results is that the effect of increased mixing that should result from the formation of strong streamwise vorticity (especially in the forced simulations for times greater than 20 seconds) is not readily apparent. Purely two-dimensional simulations (with no streamwise vorticity) display very similar levels of product formation. Previous simulations have shown that the majority of the product is formed in the vortex cores (ref. 5). The braid region contributes only slightly to the total amount of product formed. Therefore, though the streamwise vorticity may increase product formation, it only does this along the braids, and does not significantly affect the total amount of product formed.

In the high Reynolds number experiment, the rapid increase in product formed for distances greater than 20 cm may be due to increased mixing resulting from smaller scale streamwise vorticity. Numerical simulations (not shown) run at a higher Reynolds number, but with no other changes in the simulation, actually produced less product than the low Reynolds number simulation primarily because of the reduction in diffusivity necessary to maintain a constant Prandtl number. This is certainly contrary to the experimental trend. It seems likely that as the Reynolds number is increased in these simulations, the initial noise spectrum will also have to be changed to add more energy at the higher wavenumbers. This would more closely replicate "real" experimental flows which have more small-scale fluctuations at the high Reynolds number. These additional small-scale fluctuations might make up for the reduced diffusivity and lead to greater product formation.

### Combined Harmonic and Subharmonic Forcing

The temporal evolution of both streamwise and total vorticity of a shear layer subject to harmonic and subharmonic forcing is displayed in figures 9, 10, and 11. At a time of 15 seconds (fig. 9), fairly coherent counter-rotating pairs of streamwise vorticity are apparent in the region between the two spanwise vorticities. Less well organized streamwise vorticity is obvious in the braid region at the limits of the X axis, resulting from the strong random noise in the initial conditions. At a time of 24 seconds (fig. 10), the two forced spanwise structures are merged together. This merging greatly reduces the area between the two structures and vortex stretching

enhances the streamwise vorticity in this region. This streamwise vorticity is rotated approximately 270 degrees between  $T=15$  and 24 seconds, whereas, the streamwise vorticity in the outer braid region is stretched to a much lesser extent. At  $T=33$  seconds the streamwise vorticity in the center of the new merged vortex core is no longer apparent in the simulation. Dissipation being proportional to the square of the vorticity, it appears that these streamwise structures are so strongly stretched that they become sensitive to the viscosity of the fluid. There exists no strong mechanism (such as a mean shear in the proper direction) to transfer energy into these structures as rapidly as it is dissipated, therefore, the vorticity in the vortex core disappears. The Reynolds number of this flow remains less than 1000 during the calculation so that the dissipation that occurs in this simulation may not occur in high Reynolds number flows. This Reynolds number effect can be a significant factor in the transition to turbulence process. As the viscosity of the fluid is reduced (as the Reynolds number increases) these small intense streamwise structures should play an increasingly more important role in turbulent mixing. The large (forced) spanwise structures will entrain fluid which will then be intensely mixed by the remnants of the streamwise vorticities as suggested by reference 19.

The subharmonic pairing process is also evident in the high resolution simulations of figure 12. In these figures the total vorticity is used to simultaneously observe both the streamwise vorticity and the forced spanwise structures. These calculations used  $128 \times 129 \times 32$  grid points to resolve the flow field and the random noise was introduced at a very low level ( $<0.1$  percent). This lower level of random noise leads to the development of much less streamwise vorticity which is readily dissipated by vortex stretching. Some streamwise vorticity is apparent at  $T=9$  seconds in the braid region, but no streamwise vorticity is evident between the large spanwise structures as they collide ( $T=18$ ) and merge ( $T=27$ ). At  $T=36$  seconds some streamwise vorticity appears to regenerate based on the rollup of the single merged vortex.

The evolution of streamwise vorticity in this flow suggests an answer to the rescaling question posed in reference 20. Experimentally it has been observed that the streamwise vorticity appears to rescale after the pairing process with fewer streamwise vortex pairs evident after pairing of the spanwise vortices. These simulations suggest that the streamwise vorticity is regenerated based on the local scale of the spanwise structure. Of course, these simulations cannot provide a definitive answer because of the limits on Reynolds number in the simulated flow, and the dissipating effect this has on the small-scale streamwise vorticity. In addition, attempting to draw definitive conclusions based on only one numerical simulation is analogous to using a single flow visualization experiment which may or may not be representative of the usual behaviour of the flow. Additional simulations are necessary to build up confidence in the noted results.

## Summary of Results

Numerical studies of a planar mixing layer subject to various types of forcing indicate

1. Low Reynolds number direct numerical simulations qualitatively represent some velocity field features of a high Reynolds number turbulent shear layer subject to harmonic forcing.

2. The effect of forcing on a chemical reaction is qualitatively similar for low Reynolds number experimental data and numerical simulations. Currently, the experimental trends seen at high Reynolds number have not been accurately simulated.

3. Streamwise vorticity is greatly enhanced by periodic spanwise forcing and can contribute (albeit weakly) to shear layer growth.

4. In low Reynolds number numerical simulations of the vortex pairing process, streamwise vorticity can be both significantly enhanced and then dissipated as the spanwise vortices merge.

## Concluding Remarks

The active control of turbulence through various types of forcing has a great potential for manipulating combustion processes. The numerical simulations displayed in this report have indicated some of the changes in vortical structure that are possible using various types of forcing. Although current simulations of chemical reactions have only compared favorably with low Reynolds number data, it seems likely that the high resolution computations, that are now possible, will overcome this limitation. The resulting increased understanding of chemically reacting flows that will evolve from these studies promises significant technological benefits for many applications.

## Acknowledgements

The author is pleased to acknowledge many useful discussions with R.W. Metcalfe (Flow Research), J.J. Riley (University of Washington), P. McMurthry (University of Washington) and G. Mungal (Stanford University). This research was performed while the author was working at the Ames Research Center and the assistance of several individuals there is gratefully acknowledged.

## References

1. Moin, P. and Kim, J., "The Structure of the Vorticity Field in Turbulent Channel Flow. Part 1. Analysis of Instantaneous Fields and Statistical Correlations," *Journal of Fluid Mechanics*, Vol. 155, June 1985, pp. 441-464.

2. Kim, J. and Moin, P., "The Structure of the Vorticity Field in Turbulent Channel Flow. Part 2. Study of Ensemble-Averaged Fields," *Journal of Fluid Mechanics*, Vol. 162, January 1986, pp. 339-364.

3. Bechert, D. W., "Excitation of Instability Waves," *Z. Flugwiss. Weltraumforsch.* 9 (1985), Heft 6.
4. Koochesfahani, M. M., "Experiments on Turbulent Mixing and Chemical Reactions in a Liquid Mixing Layer," Ph.D. Thesis, California Institute of Technology, 1984.
5. Riley, J.J., Metcalfe, R.W., Orszag, S.A., "Direct Numerical Simulations of Chemically Reacting Turbulent Mixing Layers," *Physics of Fluids*, Vol. 29, No. 2, Feb. 1986, pp. 406-422.
6. McMurthry, P.A., Jou, W.H., Riley, J.J., Metcalfe, R.W., "Direct Numerical Simulations of a Reacting Mixing Layer With Chemical Heat Release," AIAA-85-0143, January 1985.
7. Cain, A.B., Reynolds, W.C., Ferziger, J.H., "A Three-Dimensional Simulation of Transition and Early Turbulence in a Time-Developing Mixing Layer," Stanford University, Dept. of Mechanical Engr. Report TF-14, 1981.
8. Riley, J.J., Metcalfe, R.W., "Direct Numerical Simulation of a Perturbed Turbulent Mixing Layer," AIAA-80-0274, January 1980.
9. Breidenthal, R.E., "A Chemically Reacting, Turbulent Shear Layer," Ph.D. Thesis, California Institute of Technology, 1978.
10. Michalke, A., "On the Inviscid Instability of the Hyperbolic-Tangent Velocity Profile," *Journal of Fluid Mechanics*, vol. 19, 1964, pp. 543-556.
11. Patterson, G.S., Orszag, S.A., "Spectral Calculations of Isotropic Turbulence: Efficient Removal of Aliasing Interactions," *Physics of Fluids*, Vol. 14, 1971, p.2538.
12. Weisbrot, I., "A Highly Excited Turbulent Mixing Layer," M.S. Thesis, Tel-Aviv University, Dept. of Fluid Mechanics and Heat Transfer, 1984.
13. Roberts, F.A., Roshko, A., "Effects of Periodic Forcing on Mixing in Turbulent Shear Layers and Wakes," AIAA-85-0570, 1985.
14. McInville, R.M., Gatski, T.B., Hassan, H.A., "Analysis of Large Vortical Structures in Shear Layers," AIAA Journal, Vol. 23, No. 8, Aug. 1985, pp. 1165-1171.
15. Ho, C-M., Huang, L.S., "Subharmonics and Vortex Merging in Mixing Layers," *Journal of Fluid Mechanics*, Vol. 119, 1982, pp. 443-473.
16. Metcalfe, R.W., Orszag, S.A., Brachet, M.E., Menon, S., Riley, J.J., "Secondary Instability of a Temporally Growing Mixing Layer," submitted to *Journal of Fluid Mechanics*.
17. Bernal, L.P., "The Coherent Structure of Turbulent Mixing Layers I. Similarity of the Primary Vortex Structure II. Secondary Streamwise Vortex Structure," Ph.D. Thesis, California Institute of Technology, 1981.
18. Ho, C-M., Huerre, P., "Perturbed Free Shear Layers," *Annual Review of Fluid Mechanics*, 1984, pp. 365-424.

19. Ho, C-M., "Mixing Processes in Free Shear Layers," AIAA-86-0234, January 1986.

20. Roshko, A., "The Plane Mixing Layer Flow Visualization Results and Three Dimensional Effects," The Role of Coherent Structures in Modelling Turbulence and Mixing, Lecture Notes in Physics, Springer-Verlag, 1980. pp. 208-217.

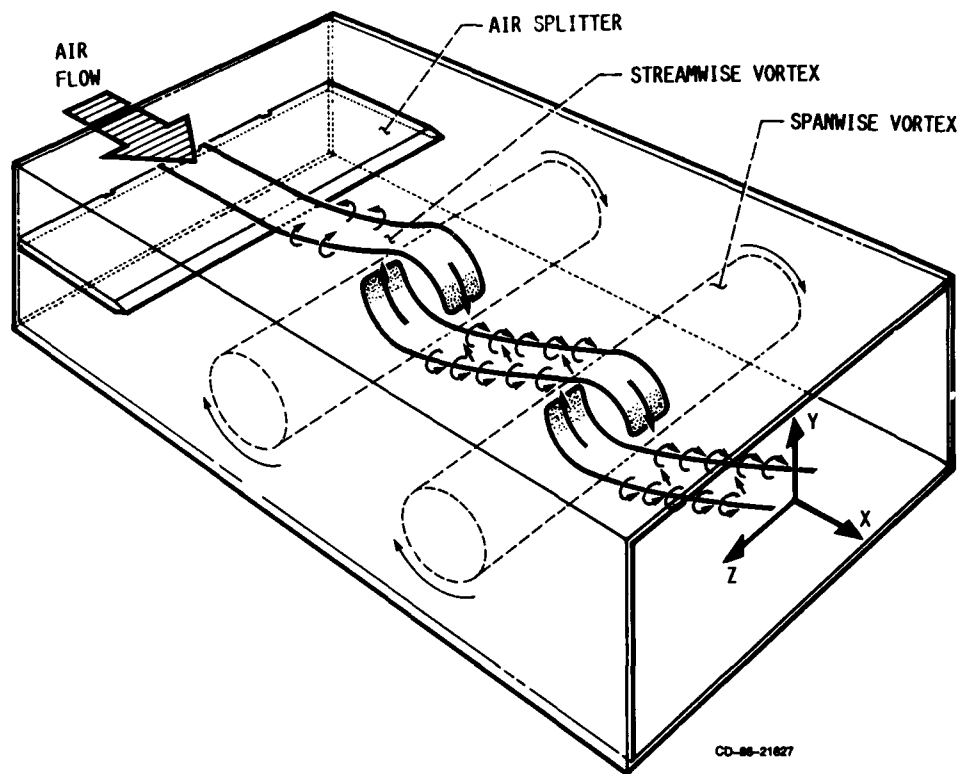


FIGURE 1. - SCHEMATIC REPRESENTATION OF THREE-DIMENSIONAL, PLANE SHEAR LAYER.

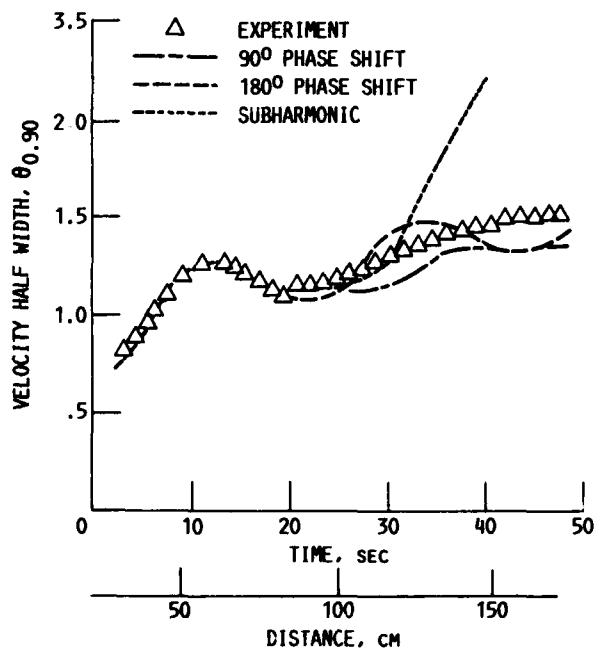


FIGURE 2. - EVOLUTION OF MEAN VELOCITY HALF-WIDTH AS FUNCTION OF TIME (FOR NUMERICAL SIMULATION) AND DISTANCE DOWNSTREAM (FOR EXPERIMENT). AT  $t = 24$  SECONDS AN ADDITIONAL PERTURBATION WAS ADDED TO SIMULATION AS NOTED.

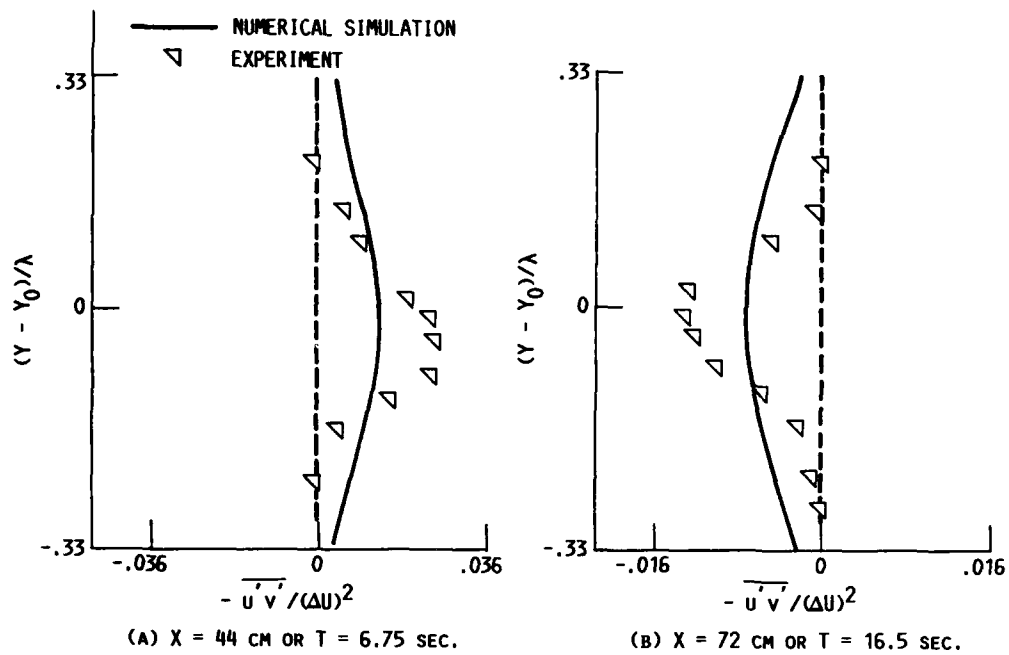


FIGURE 3.- REYNOLDS SHEAR STRESSES IN CONSTANT DENSITY SHEAR LAYER: COMPARISON BETWEEN TWO-DIMENSIONAL NUMERICAL SIMULATION AND EXPERIMENTAL DATA, REFERENCE 12.

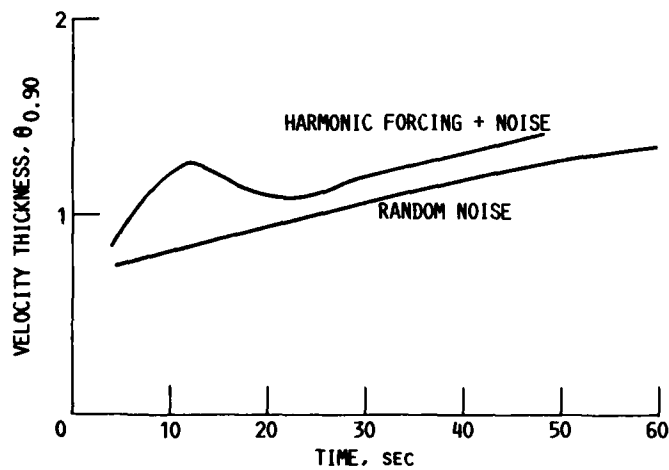


FIGURE 4. - EVOLUTION OF MEAN VELOCITY HALF-WIDTH FOR THREE-DIMENSIONAL NUMERICAL SIMULATIONS WITH AND WITHOUT HARMONIC FORCING.

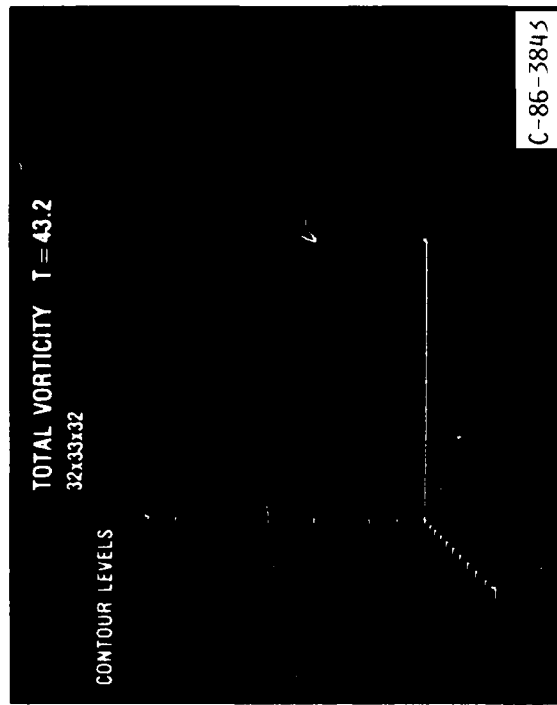
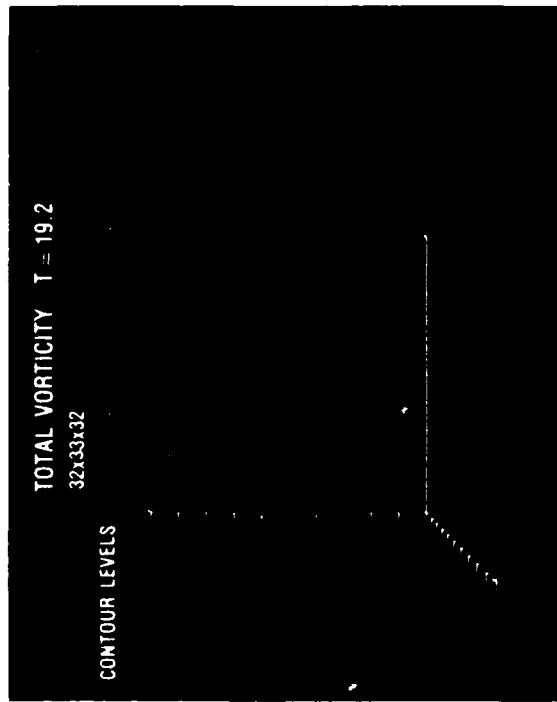
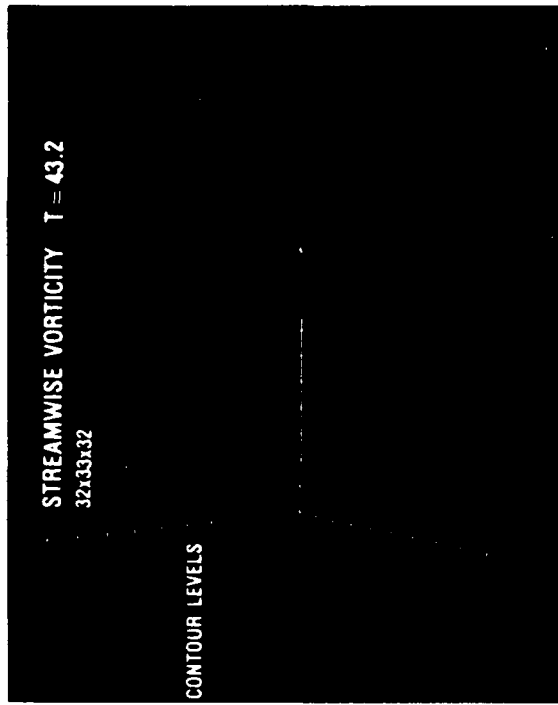
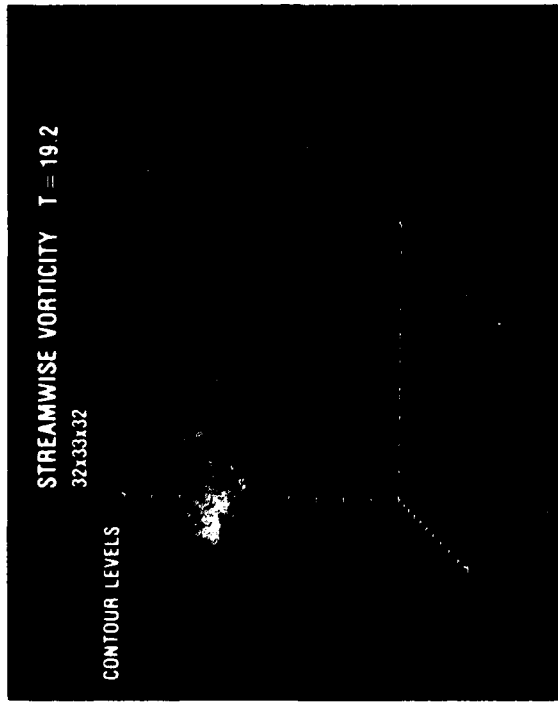


FIGURE 5. - THREE-DIMENSIONAL SURFACE PLOTS OF CONSTANT (STREAMWISE OR TOTAL) VORTICITY FOR HARMONICALLY EXCITED MIXING LAYER. CONTOURS ARE SHOWN FOR TWO DIFFERENT TIMES,  $T = 19.2$  AND  $43.2$  SECONDS.  $32 \times 33 \times 32$  GRID POINTS ARE USED IN THE X, Y, AND Z DIRECTION, RESPECTIVELY.

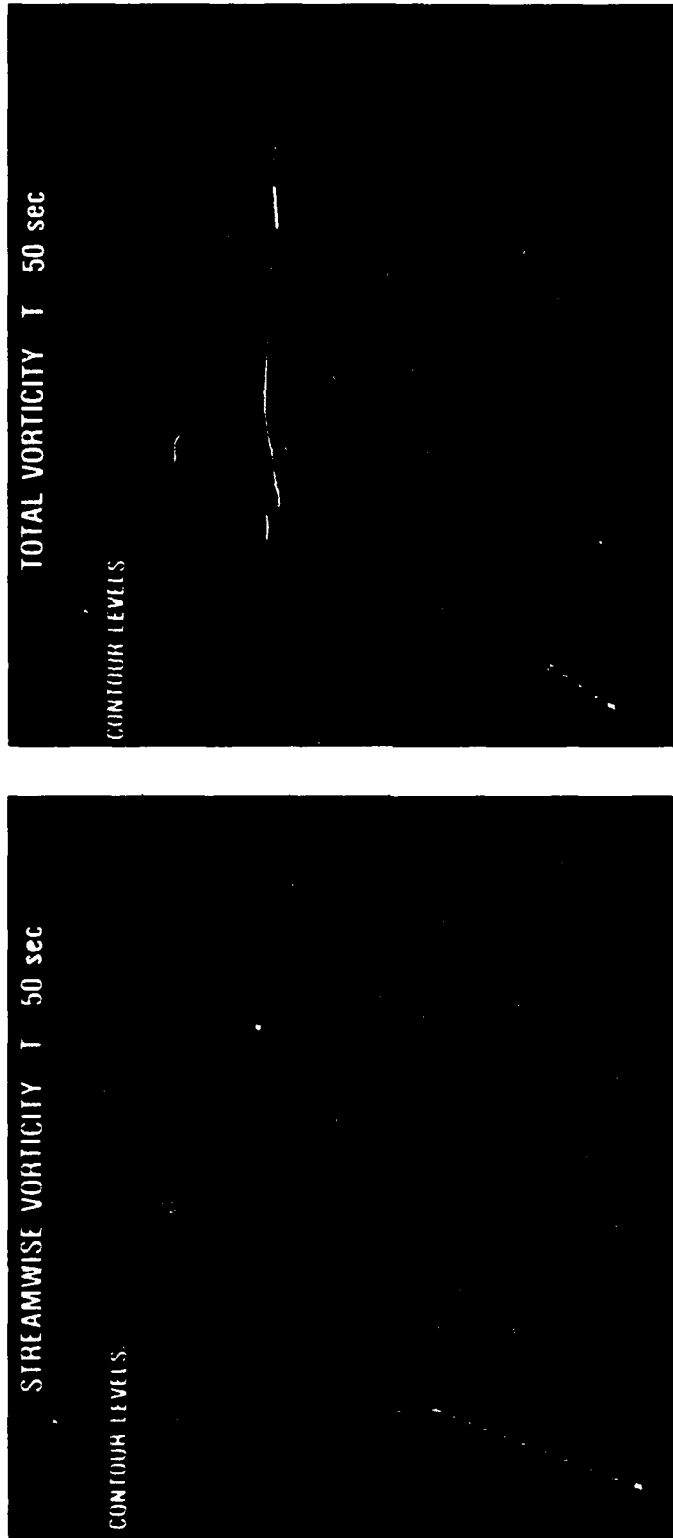


FIGURE 6. - THREE-DIMENSIONAL SURFACE PLOTS OF CONSTANT (STREAMWISE OR TOTAL) VORTICITY FOR A HARMONICALLY EXCITED MIXING LAYER NUMERICALLY SIMULATED USING 128X129X32 GRID POINTS.

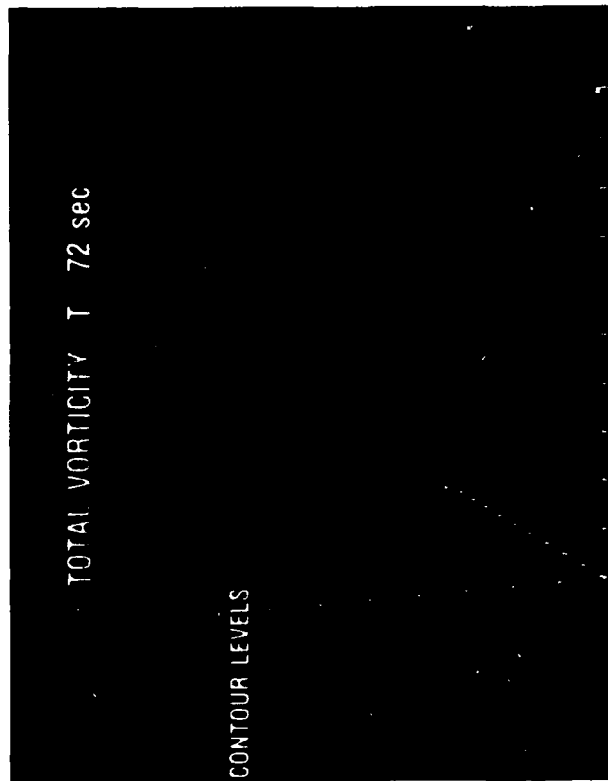
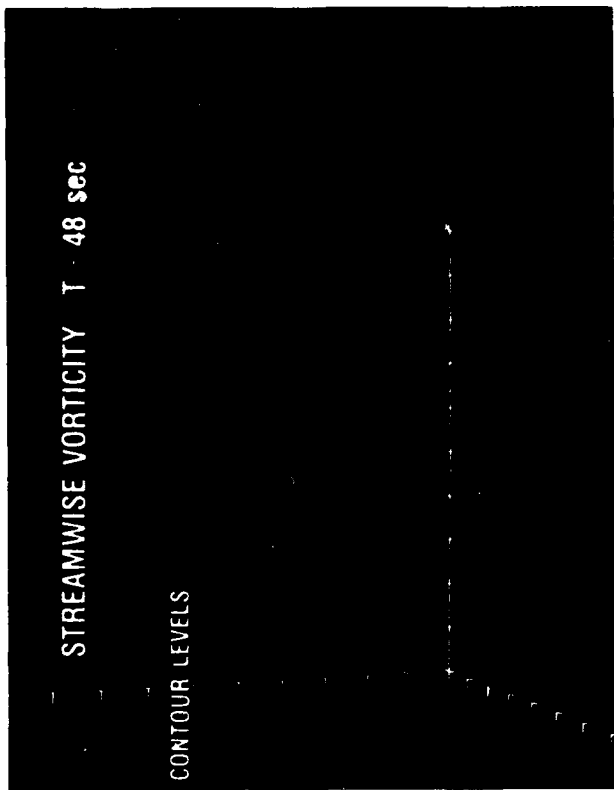
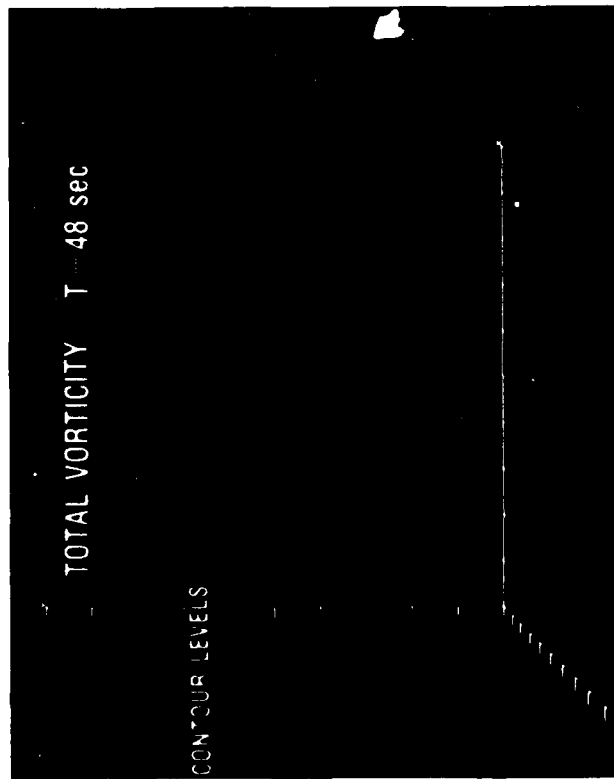
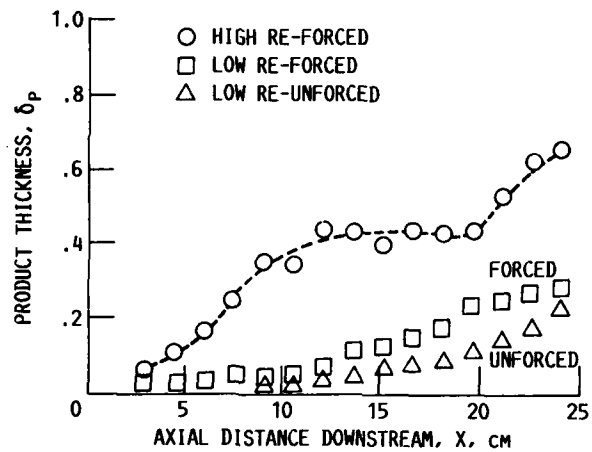
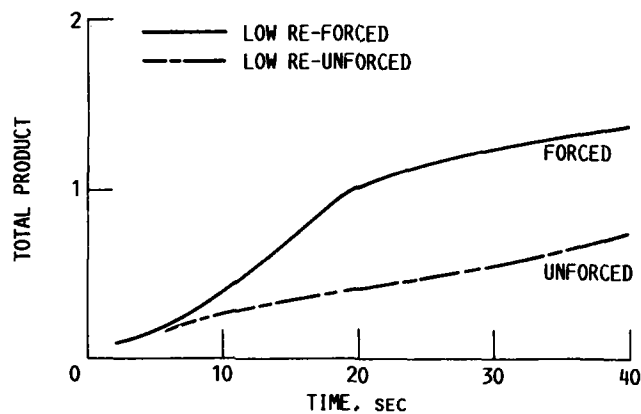


FIGURE 7. - THREE-DIMENSIONAL SURFACE PLOTS OF CONSTANT (STREAMWISE OR TOTAL) VORTICITY FOR A SHEAR LAYER PERTURBED WITH RANDOM NOISE IN THE INITIAL CONDITIONS. 32x33x32 GRID POINTS USED IN THE X, Y, AND Z DIRECTION, RESPECTIVELY.



(A) EXPERIMENTAL DATA FROM REFERENCE 13.



(B) NUMERICAL SIMULATION RESULTS.

FIGURE 8. - EXPERIMENTAL AND NUMERICALLY SIMULATED PRODUCT LEVELS IN A PASSIVE CHEMICAL REACTION.

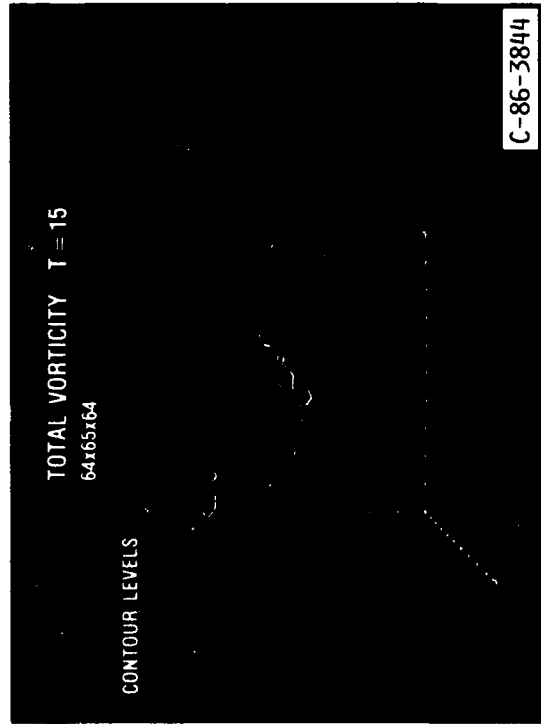
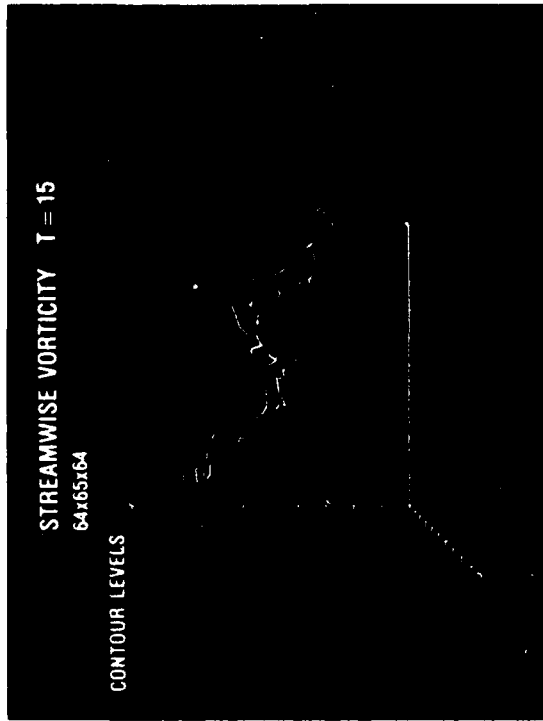
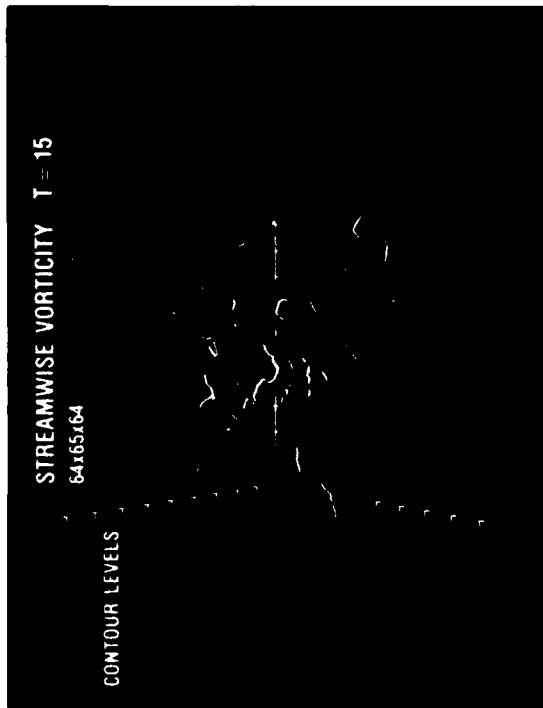


FIGURE 9. - THREE-DIMENSIONAL SURFACE PLOTS OF CONSTANT (STREAMWISE OR TOTAL) VORTICITY FOR SHEAR LAYER SUBJECT TO COMBINED HARMONIC AND SUBHARMONIC FORCING AT TIME OF 15 SECONDS. 64X65X64 GRID POINTS ARE USED IN THE X, Y, AND Z DIRECTION, RESPECTIVELY.

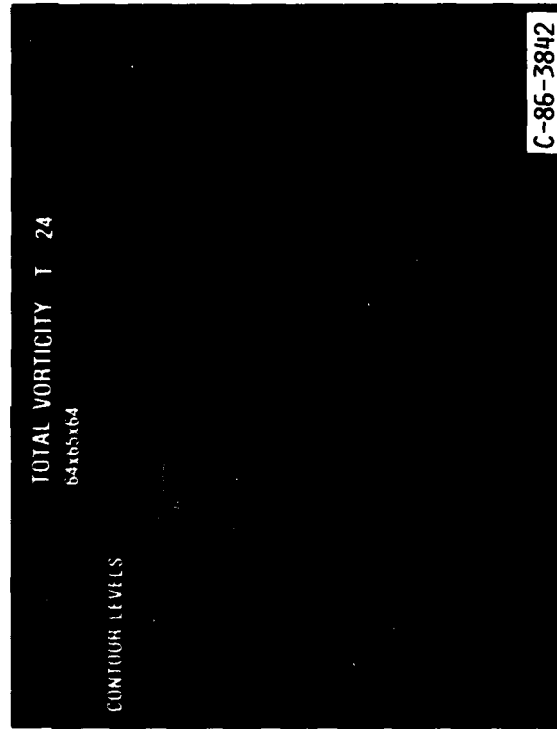
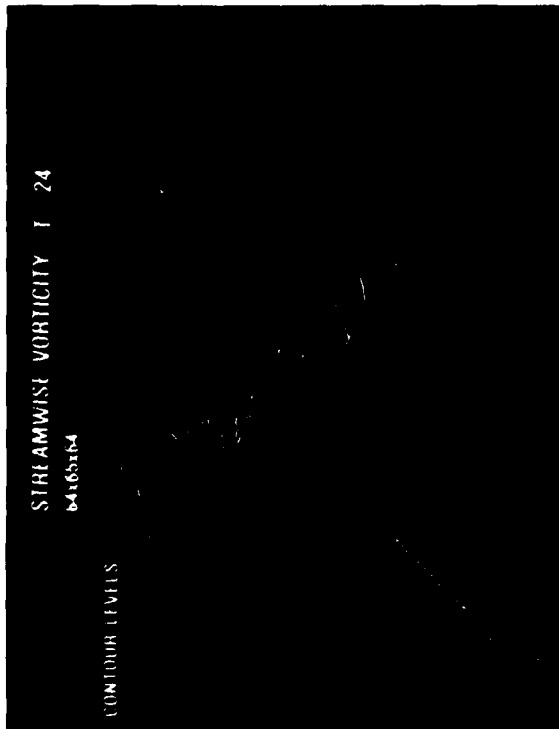
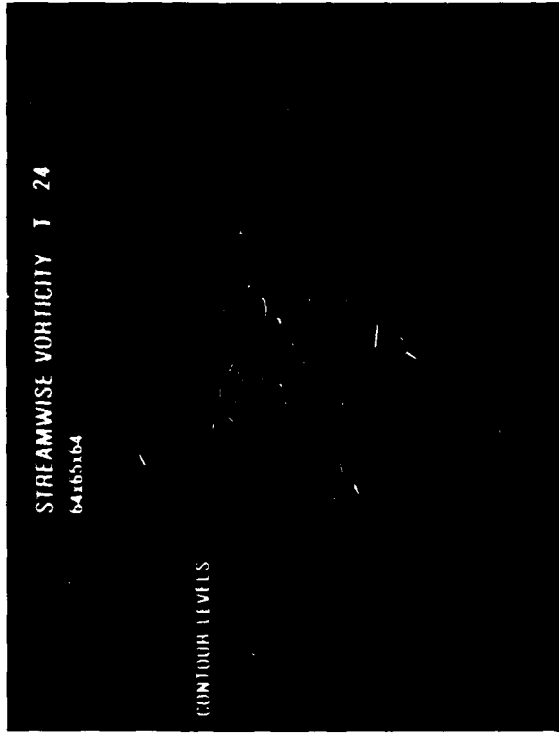


FIGURE 10. - THREE-DIMENSIONAL SURFACE PLOTS OF CONSTANT (STREAMWISE OR TOTAL) VORTICITY FOR SHEAR LAYER SUBJECT TO COMBINED HARMONIC AND SUBHARMONIC FORCING AT TIME OF 24 SECONDS. 64X65X64 GRID POINTS ARE USED IN THE X, Y, AND Z DIRECTION, RESPECTIVELY.

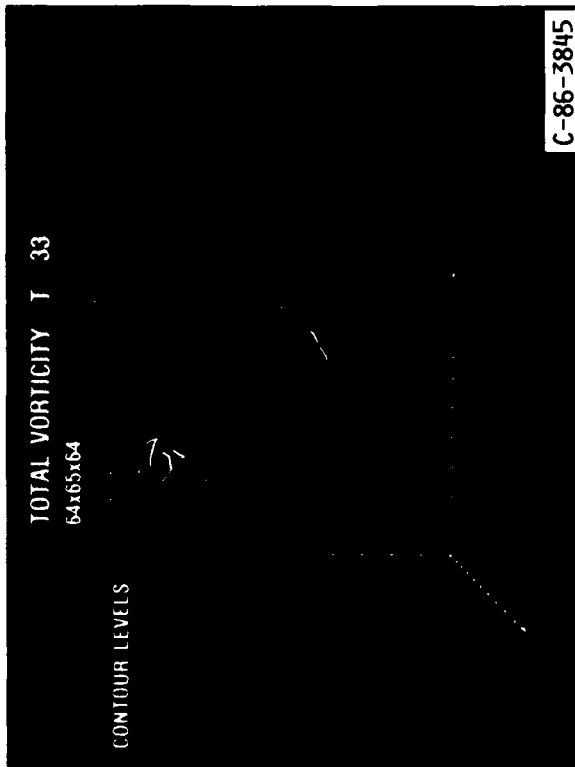
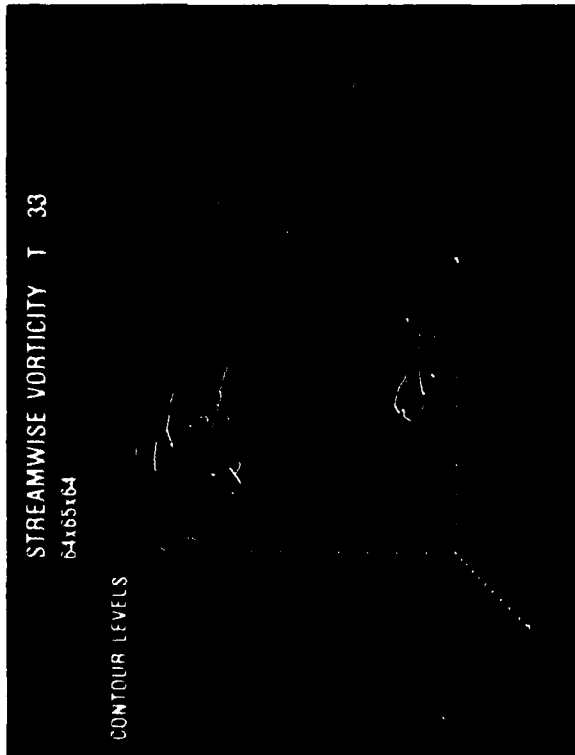


FIGURE 11. - THREE-DIMENSIONAL SURFACE PLOTS OF CONSTANT (STREAMWISE OR TOTAL) VORTICITY FOR SHEAR LAYER SUBJECT TO COMBINED HARMONIC AND SUBHARMONIC FORCING AT TIME OF 33 SECONDS. 64x65x64 GRID POINTS ARE USED IN THE X, Y, AND Z DIRECTION, RESPECTIVELY.

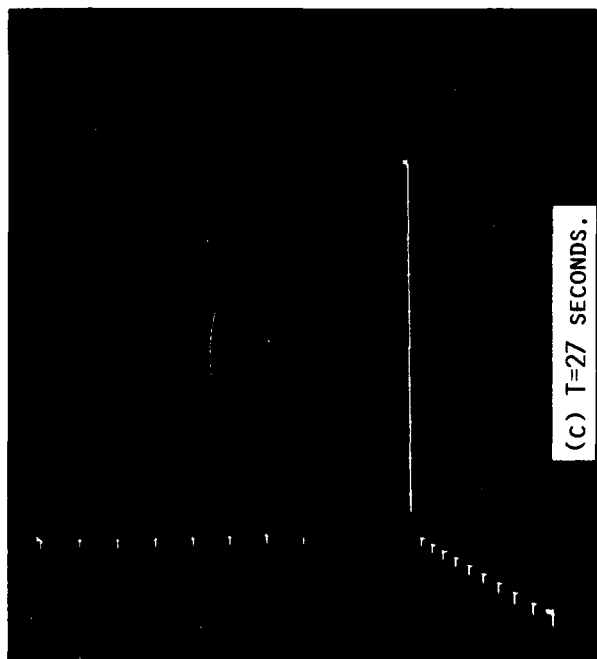
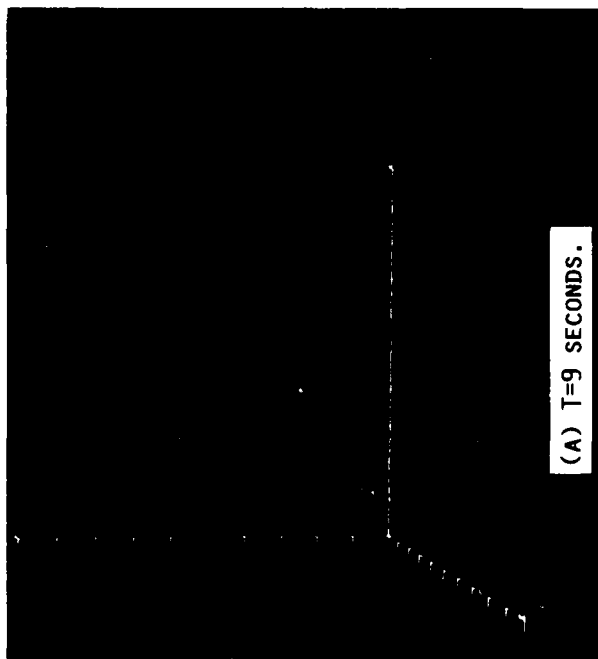
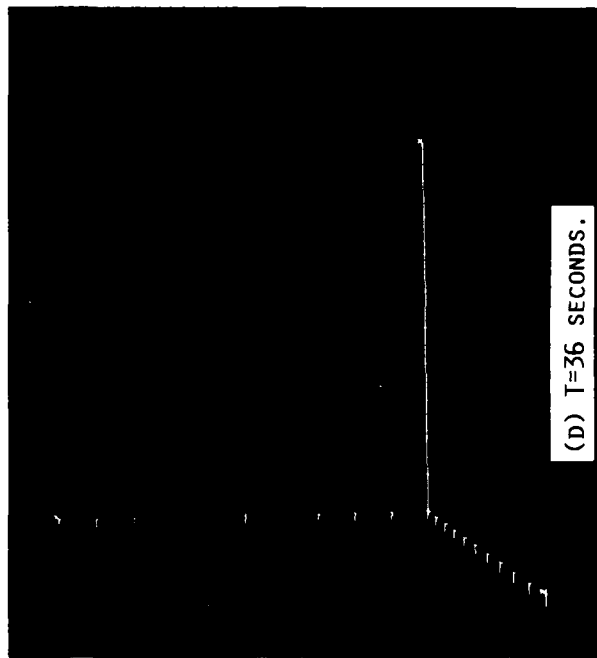
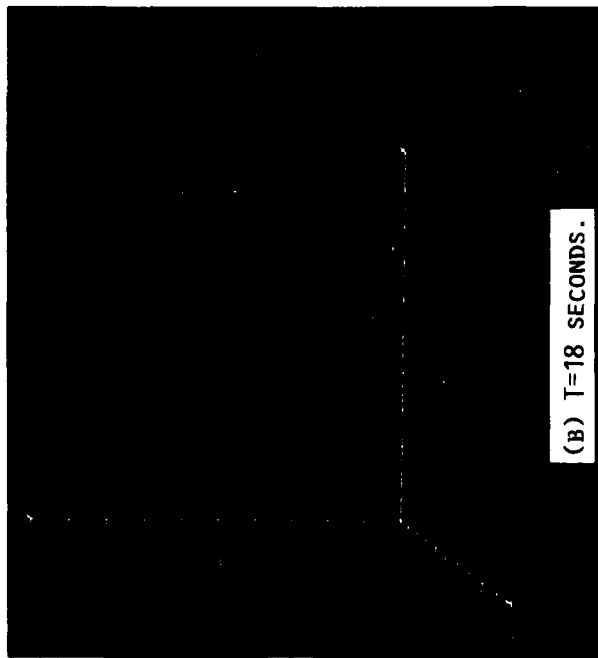


FIGURE 12. - THREE-DIMENSIONAL SURFACE PLOTS OF CONSTANT TOTAL VORTICITY AT TIMES OF 9, 18, 27, AND 36 SECONDS FOR SHEAR LAYER SUBJECT TO COMBINED HARMONIC AND SUBHARMONIC FORCING WITH VERY LOW LEVEL OF RANDOM NOISE IN THE INITIAL CONDITIONS. 128x129x32 GRID POINTS ARE USED IN THE X, Y, AND Z DIRECTION, RESPECTIVELY. CYAN = 0.15 AND MAGENTA = 0.60.

1. Report No. <b>NASA TM-88896</b>		2. Government Accession No.		3. Recipient's Catalog No.	
4. Title and Subtitle <b>Direct Numerical Simulations of a Temporally Evolving Mixing Layer Subject to Forcing</b>				5. Report Date <b>February 1987</b>	
				6. Performing Organization Code <b>505-62</b>	
7. Author(s) <b>Russell W. Claus</b>				8. Performing Organization Report No. <b>E-3313</b>	
				10. Work Unit No.	
9. Performing Organization Name and Address <b>National Aeronautics and Space Administration Lewis Research Center Cleveland, Ohio 44135</b>				11. Contract or Grant No.	
				13. Type of Report and Period Covered <b>Technical Memorandum</b>	
12. Sponsoring Agency Name and Address <b>National Aeronautics and Space Administration Washington, D.C. 20546</b>				14. Sponsoring Agency Code	
15. Supplementary Notes <b>Prepared for the 10th Symposium on Turbulence, cosponsored by the Office of Naval Research and the University of Missouri - Rolla, Rolla, Missouri, September 22-24, 1986.</b>					
16. Abstract <b>The vortical evolution of mixing layers subject to various types of forcing is numerically simulated using psuedospectral methods. The effect of harmonic forcing and random noise in the initial conditions is examined with some results compared to experimental data. Spanwise forcing is found to enhance streamwise vorticity in a nonlinear process leading to a slow, secondary growth of the shear layer. The effect of forcing on a chemical reaction is favorably compared with experimental data at low Reynolds numbers. Combining harmonic and subharmonic forcing is shown to both augment and later destroy streamwise vorticity.</b>					
17. Key Words (Suggested by Author(s)) <b>Numerical simulations Mixing layer</b>			18. Distribution Statement <b>Unclassified - unlimited STAR Category 34</b>		
19. Security Classif. (of this report) <b>Unclassified</b>		20. Security Classif. (of this page) <b>Unclassified</b>		21. No. of pages <b>21</b>	22. Price* <b>A02</b>

## ON THE STRUCTURE OF TURBULENT BOUNDARY LAYERS

Hassan M. Nagib,  
Illinois Institute of Technology,  
Chicago, Illinois, 60616

Yann G. Guezennec,  
The Ohio State University  
Columbus, Ohio, 43210

### Introduction

The structure of turbulent boundary layers has been the object of numerous studies over the past twenty years. From the wealth of available information, one realizes that they are characterized by a hierarchy of three-dimensional scales. At least, three major scales have been identified and seem to play a prominent role in the overall dynamics of the boundary layer. The following paragraphs will summarize some of their key features.

Streaks. First observed visually by Hama (1956, see Corrsin, 1957), they have been the object of numerous visual studies; e.g., Schraub and Kline (1965), Kline et al. (1967) and others. They appear to be omnipresent in the near-wall region and to have very long streamwise extent of the order of 1000 wall units. These findings have been confirmed by the measurements of Achia and Thompson (1976), Tiederman and Oldaker (1977), Hanratty (1982) and others. Blackwelder (1978) demonstrated that the streaks are formed by two elongated streamwise vortices pumping low-speed fluid away from the wall. They appear to have a quasi-periodicity in the spanwise direction of the order of 100 to 150 wall units.

Nagakawa and Nezu (1981) and Smith and Metzler (1982) studied their spanwise distribution as a function of height in the boundary layer. They found that the distributions are highly skewed towards large separations and that the average spacing between them increases linearly with increasing distance from the wall. However, they point out that the streaks are confined to a very

thin region near the wall ( $y^+ < 30$ ) and are increasingly difficult to locate farther up in the boundary layer.

In summary, these streaks are associated with pairs of counter-rotating vortices located very near the wall and confined to that region. They are omnipresent and they persist for large downstream distances and reform immediately when disturbed, i.e. they seem to represent a product of an "eigenmode" of the viscous wall region.

Bursts and Hairpins. Kline et al. (1967) first observed that occasionally a streak would

lift up, oscillate and erupt violently (bursting sequence). Kim et al. (1971) associated those bursting events with lifting and stretching hairpins that lead to high shear above the wall layer. The visual evidence of those bursts and ejections obtained by Kline et al. (1967), Kim et al. (1971), Corino and Brodkey (1969) and others points to an event which is very energetic and has a scale much larger than the streaks, but less than the outer scales. The evidence of an intermediate scale associated with the bursting motion can also be found in the measurements of Blackwelder and Kaplan (1976), Chen and Blackwelder (1978), Corke et al. (1982) and others.

The strong perturbation associated with these events extends well beyond the viscous sublayer into the logarithmic region ( $y^+ = 100-200$ ). A good indication of that is the fact that the frequency of detected events does not vary significantly up to  $y^+ = 100$  (Blackwelder and Kaplan, 1976). There is a general agreement that the ejection phase of the bursting motion contributes to a very large turbulence production over a rather short period of time. Most models of that process (Kim et al., 1971; Offen and Kline, 1974, 1975; Hinze, 1975; Smith, 1978; etc.) involve horseshoe or hairpin eddies being lifted from the wall and inducing a strong ejection of fluid between them. Recently, Moin and Kim (1986) also identified hairpin vortices associated with the ejection and sweep events in a numerical simulation of a turbulent channel flow.

Outer-Flow Structures. Blackwelder and Kovaznay (1972) showed that velocity fluctuations near the wall ( $y/\delta = 0.03$ ) remain substantially correlated through a large portion of the boundary layer. This was also confirmed by Brown and Thomas (1977) and Chen and Blackwelder (1978), who recorded the presence of large-scale structures inclined at a small angle over the wall and spanning the entire boundary layer. More recently, Kim (1985) identified large-scale disturbances associated with the VITA-detection of events near the wall in a turbulent channel flow simulation. The recent work on drag reduction by Corke et al. (1982) and others on the control and suppression of

large scales also demonstrates a clear link between the events at the wall and the large scales.

### Objectives

Many studies have attempted to meld some or all of these observations into a unified view of the boundary layer and the turbulence production cycle. In support of such an effort, many techniques have been developed to detect and count the so-called bursts or wall events during which most of the turbulence production occurs. However, it is clear that each technique focuses on a particular feature of this complex phenomenon, and hence it is hard to reconcile and link the various findings.

In this study, it is proposed to integrate the various facets of the turbulence production cycle, and systematically investigate the interrelation between the structures identified by various techniques. In addition, based on the findings of a related study (Guezennec and Nagib, 1986), a model of the turbulent boundary layer will be proposed.

### Experimental Facilities

The experiments were performed in the high-speed test section of the Mark V. Morkovin wind tunnel at I.I.T. The tunnel operates in a closed return mode and is powered by a vane-axial fan. A series of honeycomb and screens precedes a four-to-one contraction leading to the test section, allowing turbulence intensities of less than 0.1 percent for speeds up to 35 m/s.

The test section has a rectangular cross section of 0.61 m by 0.91 m and an overall length of 5.88 m. An aluminum test plate is suspended in the test section 30 cm. above the floor and levelled. The leading edge of the plate is machined to a razor-thin edge and slightly curved downwards. This nose geometry ensured that the stagnation line was always on the upper side of the plate (measurement side) and that no separation occurred. A 20 cm. section near the leading edge of the plate was covered by 24 grit sand paper and recessed in such a way that the upper surface of the sand paper substrate was flush with the other plate sections. This configuration allowed to fix the transition rather than actually tripping the boundary layer. To compensate for the growth of the boundary layers on the test plate, roof and the side walls of the test section, an adjustable flexible ceiling was set to provide a zero pressure gradient along the whole length of the plate.

All measurements were performed digitally through the course of this experiment. The analog outputs of the transducers were conditioned before digital acquisition. This signal conditioning consisted of a biasing of the DC component and subsequent amplification to use the full range of the A/D converter and ensure the maximum resolution. Thus, the actual resolution of the transducer signals was of the order of a fraction of a millivolt. In addition to this conditioning, the signals were low-pass filtered using fourth-order Butterworth analog filters. The cut-off frequency was set according to the Nyquist criterion as a function of the sampling rate. The hot-wires signals were linearized digitally and compensated to account for the small variations in the tunnel operating temperature.

Measurements were performed using a fixed V-shaped array of wall-shear sensors and a movable X-wire probe traversed in space with respect to the wall probe. Details of the geometry of the probes can be found in a report by Guezennec and Nagib (1985). In order to maximize the spatial resolution of the probes, a free-stream velocity of 11 m/s was chosen. The Reynolds number based on the momentum thickness was 4900 at the location of the wall sensors and was deemed sufficiently high to be representative of a high Reynolds number turbulent boundary layer. A series of mean velocity profiles taken at various downstream station along the plate are shown in Figure 1. The profiles follow the law of the wall with the usual constants and the boundary layer is clearly self-similar. For more details about the characteristics of the flow field, the reader is referred to Guezennec and Nagib (1985).

### Data Processing and Reduction

Several standard techniques for the detection of wall events were used in this study, involving one or more sensors. In addition, a new technique was developed to permit the non-intrusive detection of wall events. Each technique and its practical implementation will be described in the following paragraphs.

VITA Technique. Introduced originally by Blackwelder and Kaplan (1976), the Variable Interval Time Averaging (VITA) technique has been used by a large number of investigators. It relies on the short-term variance, which is defined as follows:

$$\text{var}(t, T_h) = \frac{1}{T_h} \int_{t-\frac{T_h}{2}}^{t+\frac{T_h}{2}} u^2(t) dt - \left[ \frac{1}{T_h} \int_{t-\frac{T_h}{2}}^{t+\frac{T_h}{2}} u(t) dt \right]^2$$

where  $t$  is time,  $T_h$  is the averaging time and  $u$  is the quantity to be processed (typically the streamwise velocity signal). It should be pointed out that this process acts in effect as a non-linear band-pass filter. The high frequency fluctuations are averaged over the integration time and the low frequencies do not contribute since the short-term variance is computed with respect to the local mean. The non-linearity arises from the squaring which emphasizes the large excursions from the local mean. Hence, this processing technique responds to the most energetic events which have the proper time scale. The detection of wall events is achieved by requiring the local variance to exceed a given threshold. This threshold is usually defined with respect to the long-term variance of the signal:

$$\begin{cases} I(t) = 1 & \text{if } \text{var}(t, T_h) > k\sigma_u^2 \\ I(t) = 0 & \text{otherwise} \end{cases}$$

where  $I(t)$  is the detection function,  $k$  the threshold and  $\sigma_u^2$  is the long term variance. The detection point is normally set in the center of the region where the threshold is exceeded. An alternate definition of the detection point will be

introduced later. In addition, the slope of the original signal at the point of detection is examined to further discriminate between positive and negative slope events (accelerating and decelerating events). These events will be referred to as positive VITA (Vp) and negative VITA (Vn) events for the remainder of this paper.

**Quadrant Technique.** This method was first introduced by Willmarth and Lu (1972) and has been widely used since. It relies on sorting the streamwise and normal velocity fluctuations  $u$  and  $v$  into four "quadrants" defined by the four combinations of their respective signs. In the second and fourth quadrant ( $u < 0, v > 0$  and  $u > 0, v < 0$  respectively), the Reynolds stress is negative and therefore contributes to the turbulence production. On the other hand, the first and third quadrant motions contribute to negative turbulence production. Events are detected whenever the  $(u, v)$  pair is in the correct quadrant and the absolute value of their product exceeds a given threshold ( $k'$ ). The threshold is defined with respect to the product of the r.m.s. of  $u$  and  $v$ . Throughout the rest of this paper, second and fourth quadrant events will be referred to as Q2 and Q4 events, respectively. Their detection is implemented as follows:

$$Q2: \begin{cases} I(t) = 1 & \text{if } \begin{cases} u < 0 \\ v > 0 \\ uv > k' \sigma_u \sigma_v \end{cases} \\ I(t) = 0 & \text{otherwise} \end{cases}$$

$$Q4: \begin{cases} I(t) = 1 & \text{if } \begin{cases} u > 0 \\ v < 0 \\ uv > k' \sigma_u \sigma_v \end{cases} \\ I(t) = 0 & \text{otherwise} \end{cases}$$

where  $\sigma_u$  and  $\sigma_v$  are the r.m.s of the streamwise and normal velocity fluctuations and  $k'$  is the detection threshold.

**Shear Sensor Technique.** This technique was developed in an attempt to be non-intrusive and to allow the spanwise registering or centering of the wall events over the detection probe.

Careful examination of the joint probability density function of  $u$  and  $v$  in the near wall region reveals that motions associated with a very large negative  $u$  have a very low probability of occurrence in the third quadrant. This signifies that strong second quadrant motions can be detected solely on the basis of  $u$ . The converse holds true for strong fourth quadrant motions being detectable by a very large positive  $u$ . Hence, for strong Q2 and Q4 events, the quadrant can be inferred solely by  $u$  on a statistical basis. Moreover, a strong  $u$  is most likely to be associated with a large  $v$  (and therefore turbulence production) due to the shape of the joint probability density function.

Due to the large degree of coherence of  $u$  in the vertical direction near the wall (See Corke et al., 1982, for example), this pseudo-quadrant method can be extrapolated to the wall. Strong  $u$  in the buffer region is likely to be associated with strong instantaneous streamwise shear,  $sh_x$ .

Hence, strong second quadrant events (Q2) will be associated with large negative  $sh_x$  peaks, and fourth quadrant events (Q4) will be associated with large positive  $sh_x$  peaks.

In addition, the centering of the structures over the probe can be achieved by requiring that the instantaneous spanwise component of the shear  $sh_z$ , be very small, i.e. that both shear sensors detect strong but symmetric signals. Given the spanwise spacing of the wall sensor ( $\Delta z^+ = 45$ ) and the typical spanwise wavelength associated with near wall motions ( $\lambda^+ = 100$ ), any asymmetry of the shear signals should represent a misalignment of the structure over the probe. Therefore, this centering technique provides a way to decrease the spanwise jitter of the detected structures, and to enhance the definition of the ensemble-averages. The shear sensor detection technique can be summarized as follows:

$$Q2 \begin{cases} I(t) = 1 & \text{if } \begin{cases} sh_x < k_x \sigma_{shx} ; k_x < 0 \\ sh_z < k_z \sigma_{shz} \end{cases} \\ I(t) = 0 & \text{otherwise} \end{cases}$$

$$Q4 \begin{cases} I(t) = 1 & \text{if } \begin{cases} sh_x > k_x \sigma_{shx} ; k_x > 0 \\ sh_z < k_z \sigma_{shz} \end{cases} \\ I(t) = 0 & \text{otherwise} \end{cases}$$

where  $I(t)$  is the detector function,  $sh_x$  and  $sh_z$  are the streamwise and spanwise shear fluctuations,  $\sigma_{shx}$  and  $\sigma_{shz}$  are their respective r.m.s. values and  $k_x$  and  $k_z$  are the detector thresholds.

#### Characterization of Various Classes of Wall Events

In this section, the characteristics of the classes of wall events detected by the various techniques described above will be presented. In addition, the relationship between those events will also be examined and their contribution to the turbulence production will be evaluated.

#### Characteristics of Events Detected by the VITA Technique.

It has been shown before that the VITA technique acts as a band-pass filter and selects events associated with a particular time scale related to the averaging time used. A typical signature of the velocity traces obtained for the positive VITA technique (Vp) is shown on the top of Figure 2 for a non-dimensional averaging time of 10. The ensemble averaged signatures were obtained by educting the streamwise ( $u$ ) and normal ( $v$ ) velocity components and the Reynolds stress ( $uv$ ) around the detection point. The detection point was defined in the usual manner at the mid-point of the period during which the short-time variance exceeds the prescribed threshold. After removing their mean values, the velocity signals are normalized by their r.m.s. values. The Reynolds stress is normalized by the product of the r.m.s of  $u$  and  $v$ . The time is counted from the detection

point and is non-dimensionalized by inner variables. This normalization of the signals and time will be used throughout the rest of this study. The threshold used in this figure was 1.0, but similar results have been obtained for other values.

As observed by other investigators, the streamwise velocity exhibits a deceleration followed by a very rapid acceleration and slow return to the average value. The normal velocity exhibits a positive peak (upward motion) followed by a weak and relatively broad negative peak before returning to its average value. The Reynolds stress is characterized by a strong negative peak aligned with the negative peak in the  $u$  signal, followed by a weak and broad peak after the detection point. The second Reynolds stress peak is always weaker than the first one, especially for short averaging times.

Most investigators have recognized only one Reynolds stress peak associated with VITA events. Based on the existence of a small but broad second peak after the detection of a positive VITA event, it was felt that there may be a second Reynolds stress contribution which was not brought out properly by the detection technique, because of the poor registering of individual events and the resulting smearing by the ensemble-averaging process. Hence, the definition of the detection point in the VITA technique was redefined to correspond to the location of the first  $u$ -peak following the normal VITA detection point. Using this modified technique, the same data were reprocessed. A comparison of the ensemble averaged velocities and Reynolds stress signatures of positive VITA events obtained for the normal and modified definition of the detection point is shown on the bottom of Figure 2. The detection parameters used in this case are identical to those used for the normal VITA detection above. The modified definition of the detection point clearly brings out the second Reynolds stress peak while reducing and broadening the first one. This confirms the conclusion that positive VITA events are comprised of two turbulence-producing events occurring in rapid succession, but within a range of time delays. Moreover, the normal VITA processing tends to register the detection on the negative  $u$ -peak and smears out the opposite phase sub-event.

The corresponding ensemble-averaged velocities and Reynolds stress signatures of negative VITA events ( $V_n$ ) have been also obtained as shown on the top of Figure 3. The threshold and averaging times are identical to those used for the positive VITA events. The structure of the event appears reversed, i.e. the  $u$ -signal exhibits a positive peak followed by a rapid deceleration to negative values and return to zero. The normal velocity exhibits a weak negative peak (downward motion) followed by a strong positive (upward motion) peak. The Reynolds stress exhibits two peaks, with the second one much larger than the first one.

A similar redefinition of the detection point was performed for the negative VITA event. In this case, the detection point was defined at the location of the  $u$ -peak preceding the normal VITA detection point. The ensemble-averaged signatures obtained with the modified definition of the detection point is shown in the bottom of Figure 3. This alternate definition of the detection point increases the strength of the first Reynolds stress peak while broadening and weakening the second one.

This indicates that negative VITA events are also associated with two Reynolds stress events, the first of which may not be clearly brought out by the standard VITA detection technique.

Characteristics of Events Detected by the Quadrant Technique. The ensemble-averaged velocities and Reynolds stress signatures obtained with the quadrant technique for second quadrant events (Q2) are shown on the top of Figure 4 for a threshold value  $k' = 3.0$ . The streamwise velocity exhibits a large negative peak and the normal component undergoes a large positive peak (upward motion). The Reynolds stress is characterized by a very large and narrow peak. Thus, it is clear that second quadrant events correspond to ejections, i.e. low speed fluid moving upward away from the wall, and that this type of motion contributes to very large Reynolds stresses and hence turbulence production. Unlike the VITA detected events, the Q2 events are associated with one single Reynolds stress contribution and all peaks are centered at the detection time.

The ensemble-averaged velocities and Reynolds stress signatures associated with fourth quadrant events (Q4) are shown on the bottom of Figure 4. These signatures were obtained for a threshold  $k' = 3.0$ . The streamwise velocity exhibits a broad positive peak while the normal component displays a narrow negative spike. This type of event clearly represents the sweep of high speed fluid moving towards the wall and is associated with a very large Reynolds stress. As in the Q2 case, all peaks are aligned at the detection point, although the broad streamwise velocity signature possibly indicates the passage of the large disturbance which initiates a very local downward motion.

Relation Between VITA Technique and Quadrant Technique Events. In light of the previous paragraphs, it is clear that the VITA technique and the quadrant technique do not detect the same events. Given the prominent part played by both techniques in detecting turbulence-producing wall events, efforts were made to understand the relationship between those two classes of events and their role in the turbulence production process. Close examination of VITA events reveals that each Reynolds stress peak is very similar to individual second and fourth quadrant events detected by the quadrant technique. In other words, positive VITA events appear to be composed of a Q2 event (ejection) followed by a Q4 event (sweep) in rapid succession. Conversely, negative VITA events appear to consist of a Q4 event followed by a Q2 event. To further investigate this apparent relationship, the location and strength of the Reynolds stress peaks, corresponding to second and fourth quadrant motions, and immediately preceding or following VITA events were recorded. The Reynolds-stress peaks chosen for this analysis were the closest peaks belonging to the proper quadrant, within 20 viscous time units from the VITA events. The search was performed for Reynolds-stress peaks both before and after the VITA events. For this particular analysis, an averaging time  $T_h$  of 10 and a threshold of 1.0 were used to detect VITA events.

Figure 5 (top) depicts the probability of occurrence of Q2 and Q4 peaks before and after positive VITA events ( $V_p$ ) as a function of the

absolute value of the time delay between the Reynolds-stress peaks and the VITA events. Again, this time delay has been non-dimensionalized with inner variables. The figure shows a peak centered near zero time delay for Q4 events occurring before Vp events and Q2 events occurring after Vp events. The probability of such a succession of events decreases rapidly to zero as the time delay increases. The opposite succession of events, i.e. Q2 before Vp and Q4 after Vp, is characterized by a broad probability peak centered around a delay of six to eight viscous time units. Those successions of events correspond to the sequence proposed earlier. However, the peak near zero time delay corresponding to Q4-Vp and Vp-Q2 sequences does not agree with this scenario. It should be kept in mind that all Reynolds-stress peaks are included here, regardless of their strength. Thus, a more meaningful way to judge the relative importance of each sequence is to weight the probability distributions of the delays by the strength of the peaks. This is shown in the bottom part of Figure 5. The only significant sequences are the Q2-Vp and Vp-Q4 sequences, hence confirming that a positive VITA event corresponds to a Q2 event followed by a Q4 event. It should also be noted that the distribution of time delays for the Vp-Q4 sequence is broader than for Q2-Vp, which is consistent with the smearing of the second Reynolds-stress peak (Q4) in the ensemble-averaged VITA signatures.

To confirm the significance of this result, the probability density distribution of the strength of the Reynolds-stress peaks neighboring positive VITA events is shown in Figure 6 (top). The most likely sequences (Q2-Vp and Vp-Q4) are associated with significant Reynolds stress while the Q4-Vp and Vp-Q2 sequences are weak (below 2.0). In the bottom part of the same figure, the same probability distributions have been weighted by the Reynolds stress to represent the contributions of those sequences to the overall production. This figure illustrates the overwhelming importance of the Q2-Vp and Vp-Q4 sequences and confirms that Vp events are comprised of significant Q2-Q4 sequences.

A similar analysis has been performed for the negative VITA events (Vn). The probability distributions of the various sequences are shown as a function of time delay in Figure 7. The top part of the figure represents the regular probability distribution, and the bottom part is weighted by the intensity of the Reynolds-stress peaks. This figure shows that the Q4-Vn and Vn-Q2 have the largest probability of occurrence and those sequences are most likely to exist with time delays of six to eight viscous time units. Once again, the distribution of delays between Q4 and Vn is broader than between Vn and Q2, which explains the partial smearing of the first Reynolds-stress peak in the ensemble-averaged signatures of negative VITA events. Figure 8 depicts the probability distributions of the Reynolds-stress intensity of the Q2 and Q4 events neighboring Vn events. The top part is not weighted while the bottom part is weighted by the Reynolds stress. This figure shows the importance of the Q4-Vn and Vn-Q2 sequences and confirms that negative VITA events consist of a Q4 event followed by a Q2 event.

This processing clearly demonstrates that VITA

events are made of ejection/sweep or sweep/ejection sequences in rapid succession. To completely establish the equivalence, the data base was searched for Q2 and Q4 events occurring in rapid succession. The velocity and Reynolds stress signals were ensemble-averaged about the mid-point of these sequences. Based on the results described above, a threshold ( $k'$ ) of 2.0 was used for detecting individual Q2 and Q4 events. Furthermore, a time window of 4 to 24 viscous time units was chosen to select pairs of Q2-Q4 or Q4-Q2. The choice of those values was based on the probability distributions presented earlier, and represent the most likely events in a pair. Figure 9 shows a comparison between the ensemble-averaged velocities and Reynolds-stress signatures of Q2-Q4 pairs (synthetic Vp) and true Vp. The streamwise velocity signatures are in close agreement. The normal component exhibits good qualitative agreement, but a higher amplitude is observed in the synthetic case. The Reynolds stress traces also compare very well. The minor differences in the normal velocity and Reynolds-stress traces can be attributed to a better registering of the events in the synthetic case. The time scale of the two events matches rather closely. A similar comparison between a negative VITA event and a synthetic (Q4-Q2) event is depicted in Figure 10. The agreement is particularly good. Once again, however, the first Reynolds-stress peak is better resolved in the synthetic case. Incidentally, a comparable number of VITA detections and synthetic Q2-Q4 or Q4-Q2 sequences was found.

The link between VITA events and Q2-Q4 or Q4-Q2 sequences has just been conclusively demonstrated. However, a large number of Q2 or Q4 events do not appear in rapid pairs and therefore are not associated with VITA events. In other words, only a fraction of the turbulence producing events are tagged by the VITA technique. The percentage of the Q2 and Q4 population involved in positive VITA events is shown on the top of Figure 11 as a function of their Reynolds stress intensity. This figure indicates that only a small percentage of the individual Q2 and Q4 events are interacting to form positive VITA events. A similar result is obtained for the Q4-Q2 sequences and is shown in the bottom of Figure 11.

Characteristics of Events Detected by the Shear Sensor Technique. The ensemble-averaged wall-shear signatures obtained using the shear sensor detection technique are shown in Figure 12 (top) for decelerated events, i.e. second quadrant events. This figure depicts the streamwise and spanwise wall-shear signatures obtained using thresholds of -1.9 and 0.7 in the streamwise ( $k_x$ ) and spanwise ( $k_z$ ) direction, respectively. As expected, no significant spanwise motion can be observed, hence demonstrating that the detected events are symmetric about the detecting probe at the wall, at least in the statistical sense (ensemble-averaged sense). The streamwise shear exhibits a strong single peak, very reminiscent of the streamwise velocity signature obtained with the quadrant technique for the Q2 event. More evidence about the relationship between events detected by the quadrant technique and the shear-sensor technique will be given later.

The ensemble-averaged wall-shear signatures associated with Q4 events detected by the shear-sensor technique are shown in the bottom of Figure 12. The thresholds used in this particular case were 2.5 and 0.7 for  $k_x$  and  $k_z$ , respectively.

As in the Q2 case, the spanwise wall-shear signature is virtually zero, indicative of the adequate centering of the structures at the wall. The streamwise wall-shear exhibits a strong positive peak similar to the streamwise velocity peak associated with Q4 events detected by the quadrant technique.

Relation Between Shear-Sensor Technique and Quadrant Technique Events. In order to validate the use of the wall shear sensor detection technique, a similar analysis was performed to correlate events detected at the wall to second and fourth quadrant events at  $y^+ = 55$  by an X-wire. Figure 13 gives the probability distribution of delays between Q2

events detected at  $y^+ = 55$  and those detected at the wall. The distribution is centered around zero time delay and is rather narrow. The probability distribution of Reynolds-stress intensity at  $y^+ = 55$  for Q2 events detected at the wall is shown in Figure 14. The unweighted distribution (top) exhibits a peak around 2.5. The Reynolds-stress weighted probability distribution is shown on the bottom, and clearly indicates that the shear-sensor detection technique recognizes strong second quadrant events which contribute significantly to the global turbulence production.

The same processing was performed to correlate Q4 events at  $y^+ = 55$  using an X-wire probe to Q4 events detected at the wall by the shear-sensor technique. The probability distribution of the time delays between the two events is presented in Figure 15. Once again, the distribution is centered around zero time delay and is fairly narrow, which indicates the good registration of the energetic Q4 events by the shear-sensor technique. The probability distribution of the Reynolds-stress intensity at  $y^+ = 55$  for events detected at the wall is shown in Figure 16, both unweighted (top) and Reynolds-stress weighted (bottom). This figure confirms the feasibility of detecting strong Q4 events at the wall, and that those events contribute significantly to the global turbulence production.

#### Discussion

In a related study, Guezennec and Nagib (1986) have shown that wall-detected Q2 and Q4 events are associated with large scale structures, but that their frequency of occurrence scales with inner variables. Actually, the scaling of the frequency of occurrence of individual Q2 and Q4 events has not been established yet. However, the results presented earlier clearly demonstrate that their mutual interaction is the VITA event, which implies that this interaction occurs at a frequency which scales with inner variables. The following section will attempt to resolve this apparent dichotomy and to formulate a model of the turbulent boundary layer consistent with these new results and past findings.

In the study mentioned above, the three-dimensional mapping of Q2 and Q4 wall events was performed using the non-intrusive detection scheme based on wall-shear sensors. The reader is referred to Guezennec and Nagib (1986) for a complete description of the experiment and the results. It was found that these strong wall events are associated with a pair of large-scale counter-rotating roller-like structures. These results are best summarized by looking at a composite figure showing the streamwise evolution of the vector maps of normal ( $v$ ) and spanwise ( $w$ ) velocity perturbations associated with each event. The Q4 event is depicted in this fashion in Figure 17, and the Q2 event in Figure 18. Regardless of the amount of smearing inherent to the ensemble-averaging process used to generate those maps, it is clear that the structures detected at the wall have a very large scale and cannot be characterized as wall or inner structures. Although their shape is somewhat reminiscent of the elongated streamwise vortices of Blackwelder (1978), Hatzivramidis and Hanratty (1979), Bakewell and Lumley (1967) or more recently Herzog (1985), they clearly represent a different structure which spans most of the boundary layer. Also, they represent the dominant secondary motion in that region, while being intimately related to the strongest events at the wall. These roller-like structures have a typical spanwise extent of 400 to 600 wall units, and extend up to at least  $y^+$  of 600, especially in their downstream part.

Evidence of such organized motion has been previously obtained, although in a totally different context which did not link them to the wall events. This evidence stems from the work of Blackwelder and Kovasznay (1972). A composite of their iso-correlation contours is presented in Figure 19. The top part of the figure represents a vertical cut through the space-time correlation maps of streamwise velocity ( $R_{uu}$ ) with respect to a fixed probe located near the wall at  $Y/\delta = 0.03$ . The bottom figure represents isocorrelation contours of streamwise velocity ( $R_{uu}$ ) in a horizontal plane at  $y/\delta = 0.5$ . The end view added on the bottom left corner of the figure represents the interpretation of these correlation maps in light of the roller-like structures found in this study.

This figure clearly illustrates that velocity fluctuations at the wall are strongly correlated with fluctuations over a large portion of the boundary layer. These regions of correlated motions are also inclined at a fairly small angle to the wall. The spanwise correlation map is consistent with the proposed motions depicted on the side, and that can be induced by a pair of rollers. Since those are time-averaged correlation measurements, no information can be inferred directly from them about the sense of rotation of the streamwise rollers. Given a boundary layer thickness of the order of 1000 wall units in our case (see Figure 1), the spanwise scale of the rollers found in this study is commensurate with the correlation maps of Blackwelder and Kovasznay (1972). It is very important to note that the correlation maps were not conditioned on a wall event and encompass all motions. Therefore, the agreement with the present

data indicates that the newly identified rollers are the most dominant coherent motion in the boundary layer.

The vortex line patterns of the ensemble-averaged flow field (See Guezennec and Nagib, 1986) are in reasonable qualitative agreement with those of Kim and Moin (1986). A composite of their results is shown in Figure 20 for the Q4 and Q2 events. The differences may be attributed in part to the imperfect spatial resolution in the experimental study. However, the qualitative features of the flow fields are essentially the same. In line with the numerous investigations indicating the presence of hairpins (see review above), Kim and Moin (1986) concluded from the same data that the hairpins are the predominant flow module associated with wall events. The general outline of the rollers found by Guezennec and Nagib (1986) was superimposed on their distorted sheets of vortex lines in Figure 20. It can be seen that the rollers are not inconsistent with the hairpin-shaped eddies. In fact, they can induce the deformation of vortex lines into that particular configuration. In other words, the rollers are the cause, rather than the result of the hairpin eddies. The predominant hairpin orientation found in other studies (Head and Bandyopadhyay, 1978, 1981; Perry and Chong, 1982; Moin and Kim, 1985 and others) of 45 degrees is also observed in that study. This is only representative of the tilting and reorientation of the hairpins along the principal axis of strain by the mean shear once they have been deflected in the normal direction by the rollers.

In other words, the rollers correspond to coherent regions of instantaneous secondary flows. They should not be considered as vortices in the inviscid sense, since vortex lines are threading in and out of them. This phenomenon is very reminiscent of the recent interpretation by Williams (1985) of the so-called "lambda vortex" in transitional boundary layers. He argues that the coherent structure is not a vortex tube, but a spatially coherent realignment of the vorticity vector.

It is important to recognize that the large-scale roller-like structures are only perfectly symmetric in the ensemble averages. Individual structures may have substantial asymmetries. These deviations result from the complex and random features of the superposed range of turbulent scales.

It is interesting that the presence of large scale roller-like structures can be inferred from the results of an earlier paper by Kim (1985), where the three-dimensional flow field associated with a VISA event was ensemble-averaged. The VISA events are the spatial counterparts of the temporal VITA events. A composite of his results is shown in Figure 21. The top part of the figure depicts contours of equal perturbation streamwise velocity on the centerplane of the event. The middle and bottom parts of the figure show the streamlines associated with the secondary flow in the cross-stream plane, at sections A and B, upstream and downstream of the event, respectively. The perturbation streamwise velocity contours clearly delineate the succession of two very large inclined structures, one on each side of the detection point. Each of those structures is very similar to

those obtained for the Q4 and Q2 event on centerline (See Guezennec and Nagib, 1986).

This is in good agreement with the results presented in earlier, where positive VITA events were shown to be made up of a Q2 event followed in time by a Q4 event (corresponding to a Q2 event downstream of a Q4 event, as shown in Kim's data). The two cross sections presented in the middle and bottom of Figure 21, illustrate the large scale motions associated with both phases of the VISA (VITA) event. The scale of those structures in the spanwise direction is comparable to the cross-cuts obtained from the present data (see composite Figures 17 and 18). The marking of Q2 and Q4 events on the figure is based on estimates from the present measurements.

This spatial configuration of the VISA (VITA) events is consistent with the findings of the present study. Due to their higher convection velocity (see Guezennec and Nagib, 1986), Q4 events partially overtake Q2 events, creating near the wall the region of sharp acceleration which is so characteristic of positive VITA events. As it has been previously recognized, the positive VITA events may be more important for the production cycle than the negative VITA events. Here, it has been established that the former is the result of Q4-rollers catching up and interacting with Q2-rollers as depicted in Figure 21. The opposite signature of the negative VITA event is consistent with the Q4-rollers running away from the slower Q2-rollers, and hence this interaction is less common.

In spite of the large size of the rollers associated with wall events, most of the production occurs near the wall (Klebanoff, 1954). This can be easily reconciled by recalling that the production is proportional to the shear. Hence, it is clear that the site of maximum production will remain confined to the near-wall region even if the Reynolds stresses associated with the large-scale rollers is constant with height. It is in the near wall layer that most of the turbulent kinetic energy is produced, and where the largest energy transfer between the mean flow and the turbulence occurs. Such mechanisms as vortex tilting and stretching are much more powerful near the wall. This is supported by the results Guezennec and Nagib (1986) who found that most of the high vorticity regions are located on the lower side of the rollers. This is true not only for Q2 events with ejection away from the wall but also for the Q4 rollers that sweep fluid towards the wall.

Based on the present work and the wealth of available literature, a model of the main features of the turbulent boundary layer and their interrelation is given in Figure 22. The least understood part of this model is the evolution of the large-scale coherent rollers from the intermediate scales of hairpin and inverted-hairpin eddies. In particular, no clear mechanism is documented for the growth of their transverse scale as they are tilted and convected. As far as the frequency of their interaction which has been termed the VITA event, one can argue that it must be related to the frequency of their formation. Therefore, it is not inconsistent that it scales with inner variables since the origin of the intermediate hairpin scales lies in the wall layer and its instabilities.

It is quite evident that this proposed model of the turbulence production cycle does not involve the streaky structure as a direct component of the cycle. The streaks are probably related to independent instability mechanisms involving the wall layer only. As pointed out many times previously, the viscous sublayer undergoes a two-dimensional instability which is rendered immediately three-dimensional by the randomizing effect of the turbulence in the buffer layer. The large aspect ratio of the streaks is also governed by the streamwise stretching in that region, and the localization of the three-dimensional disturbances in the sublayer. The important role played by the streaks in the bursting process is to provide concentrations or seeds of spanwise vorticity which, under the excitation provided by the large-scale rollers, can become unstable and break up in a violent way to initiate the bursting motion and the formation of hairpin eddies. This role of the streaks was quite apparent in the most recent work of Moin (1985). In a turbulent channel flow computation, he showed that streaks of low streamwise momentum fluid are ubiquitous and spaced roughly every 100 wall units, but that "hot spots" of normal velocity component are only detected at a few places, resulting in a spacing of the turbulence-producing events of the order of 500 wall units or more. This energy production is much more "spotty" and associated with a much larger spanwise spacing, like that of the rollers.

#### Conclusion

In summary, it has been found that VITA detected events have two distinct contributions to the turbulence production process per event. In fact, they represent pairs of second and fourth quadrant events in rapid succession. This was shown to hold true both for accelerating and decelerating events (positive and negative VITA events).

A new non-intrusive technique based on a V-shaped array of wall-shear sensors was developed to detect strong second and fourth quadrant motions. The events detected by this technique were shown to be highly correlated with events detected by the conventional quadrant technique, provided that only strong events be considered. In addition, this technique allows a better registering of the structures in the spanwise direction over the probe.

Based on these results and those of a related study, a model of the turbulent boundary layer was proposed, whereby the flow is dominated by large-scale counterrotating roller-like structures, and their interaction.

#### Acknowledgment

This investigation was supported by the NASA Langley Research Center and the Air Force Office of Scientific Research under Grant NSG-1591.

#### BIBLIOGRAPHY

- Achia, B. U., and Thompson, D. W. 1976. Structure of the Turbulent Boundary Layer in Drag-Reducing Pipe Flow. *J. Fluid Mech.*, Vol. 81, pp. 439-464.
- Bakewell, H. P. and Lumley, J. L. 1967. Viscous Sublayer and Adjacent Region in Turbulent Pipe Flow. *Phys. Fluids*, Vol. 10, pp. 1880-1889.
- Blackwelder, R. F. 1978. The Bursting Process in Turbulent Boundary Layers. Lehigh Workshop on Coherent Structure in Turbulent Boundary Layers, ed. C. R. Smith and D. E. Abbott, pp. 211-227.
- Blackwelder, R. F. and Kaplan, R. E. 1976. On the Wall Structure of the Turbulent Boundary Layers. *J. Fluid Mech.*, Vol. 76, pp. 89-112.
- Blackwelder, R. F. and Kovaznay, L. S. G. 1972. Time Scales and Correlations in a Turbulent Boundary Layer. *Phys. Fluids*, Vol. 15, pp. 1545-1554.
- Brown, G. L. and Thomas, A. S. W. 1977. Large Structure in Turbulent Boundary Layer. *Phys. Fluids*, Vol. 20, pp. 243-252.
- Chen, C. H. P. and Blackwelder, R. F. 1978. Large Scale Motion in a Turbulent Boundary Layer: A Study Using Temperature Contamination. *J. Fluid Mech.*, Vol. 89, pp. 1-31.
- Corino, E. R. and Brodkey, R. S. 1969. A Visual Investigation of the Wall Region in Turbulent Flows. *J. Fluid Mech.*, Vol. 37, pp. 1-30.
- Corke, T. C., Nagib, H. M. and Guezennec, Y. G. 1982. A New View on Origin, Role and Manipulation of Large Scales in Turbulent Boundary Layers. *NASA CR-165861*.
- Corrsin, S. 1957. Proc. Symp. on Naval Hydrodynamics, Publ. 515, NAS-NRC 373.
- Guezennec, Y. G. and Nagib, H. M. 1985. Documentation of Large Coherent Structures Associated with Wall Events in Turbulent Boundary Layers. Fluid and Heat Transfer Report, Illinois Institute of Technology, Chicago.
- Guezennec, Y. G. and Nagib, H. M. 1986. On the Scaling of VITA Detected Wall Events in Turbulent Boundary Layers. To be submitted to *J. Fluid Mech.*
- Guezennec, Y. G. and Nagib, H. M. 1986. Three-Dimensional Mapping of Wall Events in a Turbulent Boundary Layer. To be submitted to *J. Fluid Mech.*
- Hatzivramidis, D. T. and Hanratty, T. J. 1979. The Representation of the Viscous Wall Region by a Regular Eddy Pattern. *J. Fluid Mech.*, Vol. 95, pp. 655-679.
- Head, M. R. and Bandyopadhyay, P. 1978. Combined Flow Visualization and Hot Wire Measurements in Turbulent Boundary Layers. Lehigh Workshop on Coherent Structure in Turbulent Boundary Layers, ed. C. R. Smith and D. E. Abbott, pp. 98-129.

- Head, M. R. and Bandyopadhyay, P. 1981. New Aspects of Turbulent Boundary Layer Structure. J. Fluid Mech., Vol. 107, pp. 297-337.
- Herzog, S. 1985. Large Scale Structures in the Near Wall Region of Turbulent Pipe Flow. Ph.D. Thesis, Cornell University.
- Hinze, J. O. 1975. Turbulence. 2nd ed., McGraw-Hill, New-York.
- Hogenes, J. H. A. and Hanratty, T. J. 1982. The Use of Multiple Wall Probes to Identify Coherent Flow Patterns in the Viscous Wall Region. J. Fluid Mech., Vol. 124, pp. 363-390.
- Kim, J. 1985. Turbulence Structure Associated with the Bursting Event. Phys. Fluids, Vol. 28, pp. 52-58.
- Kim, J. and Moin, P. 1986. The Structure of the Vorticity Field in Turbulent Channel Flow. Part 2. Study of Ensemble-Averaged Fields. J. Fluid Mech., Vol. 162, pp. 339-363.
- Kim, H. T., Kline, S. J. and Reynolds, W. C. 1971. The Production of Turbulence near a Smooth Wall in a Turbulent Boundary Layer. J. fluid Mech., Vol. 50, pp. 133-160.
- Klebanoff, P. S. 1954. Characteristics of Turbulence in a Boundary Layer with Zero Pressure Gradient. NACA Technical Note No. 3178.
- Kline, S. J., Reynolds, W. C., Schraub, F. A. and Runstadler, P. W. 1967. The Structure of Turbulent Boundary Layers. J. Fluid Mech., Vol. 30, pp. 741-773.
- Moin, P. and Kim, J. 1985. The Structure of the Vorticity Field in Turbulent Channel Flow. Part 1. Analysis of Instantaneous Fields and Statistical Correlations. J. fluid Mech., Vol. 155, pp. 441-464.
- Nakagawa, H. and Nezu, I. 1981. Structure of the Space-Time Correlation of Bursting Phenomenon in an Open Channel Flow. J. fluid Mech., Vol. 104, pp. 1-44.
- Offen, G. R. and Kline, S. J. 1974. Combined Dye-Streak and Hydrogen-Bubble Visual Observations of a Turbulent Boundary Layer. J. Fluid Mech., Vol. 62, pp. 223-239.
- Offen, G. R. and Kline, S. J. 1975. A Proposed Model of the Bursting Process in Turbulent Boundary Layers. J. Fluid Mech., Vol. 70, pp. 209-228.
- Perry, A. E. and Chong, M. S. 1982. On the Mechanisms of Wall Turbulence. J. Fluid Mech., Vol. 119, pp. 173-217.
- Schraub, F. A. and Kline, S. J. 1965. Thermosci. Div., Mech. Eng. Dept. Rep. No. MD-12. Stanford University.
- Smith, C. R. 1978. Visualization of Turbulent Boundary Layer Structure Using a Moving Hydrogen Bubble Wire Probe. Lehigh Workshop on Coherent Structure in Turbulent Boundary Layers, ed. C. R. Smith and D. E. Abbott, pp. 48-97.
- Smith, C. R. and Metzler, S. P. 1983. The Characteristics of Low-Speed Streaks in the Near Wall Region of a Turbulent Boundary Layer. J. Fluid Mech., Vol. 129, pp. 27-46.
- Tiederman, W. G. and Oldaker, D. K. 1977. Phys. Fluid Suppl. II, Vol. 20, S133.
- Williams, D. R. 1985. Vortical Structures in the Breakdown Stage of Transition. Proc. ICASE/NASA Workshop on Stability. August 1985. Springer.
- Willmarth, W. W. and Lu, S. S. 1972. Structure of the Reynolds Stress near the Wall. J. Fluid Mech., Vol. 55, pp. 65-92.

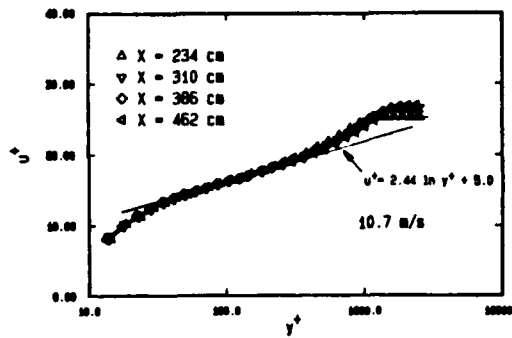


Figure 1. Non-Dimensional Mean Velocity Profiles at Four Downstream Stations.

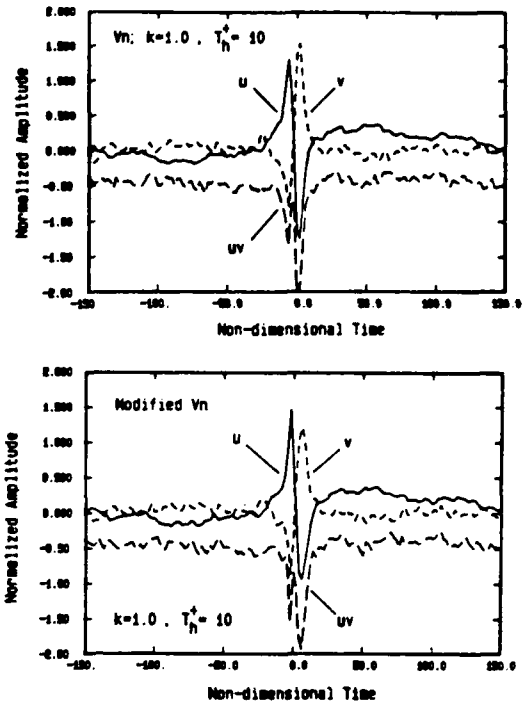


Figure 3. Comparison of Ensemble-Averaged Velocities and Reynolds Stress of Negative VITA Detected Events for Normal and Modified Definition of Point of Detection.

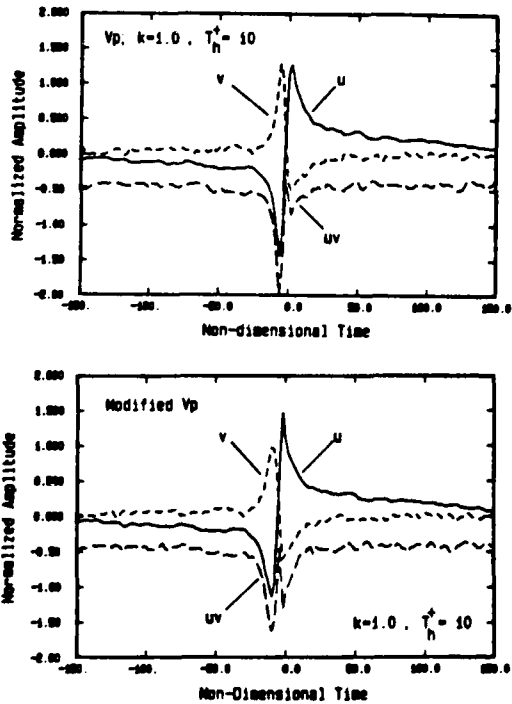


Figure 2. Comparison of Ensemble-Averaged Velocities and Reynolds Stress of Positive VITA Detected Events for Normal and Modified Definition of Point of Detection.

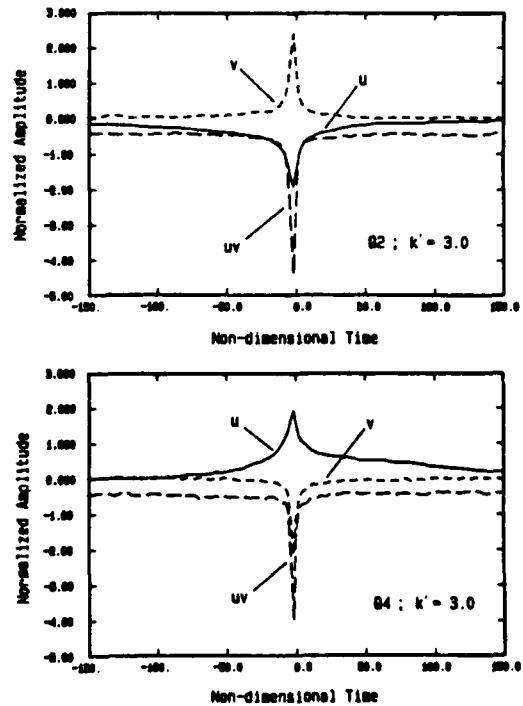


Figure 4. Ensemble-Averaged Velocities and Reynolds Stress of Second Quadrant (Q2) Events (top), and Fourth Quadrant (Q4) Events (bottom).

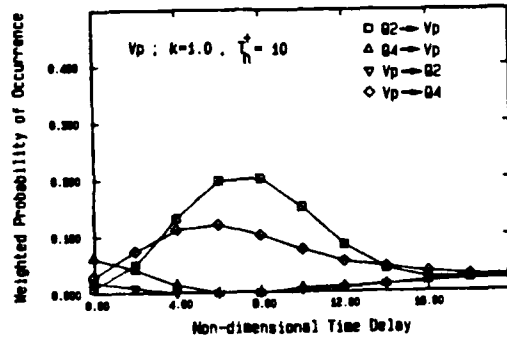
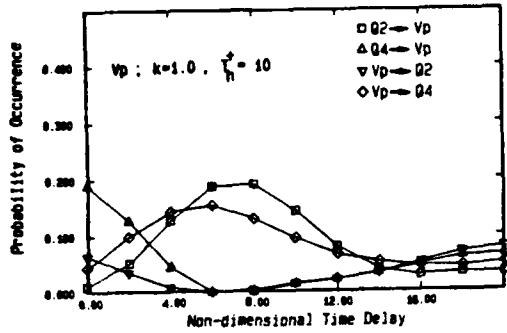


Figure 5. Probability Distributions of Time Delay Between Q2 and Q4 Events and Neighboring Positive VITA Events; Unweighted (top) and Reynolds Stress Weighted (bottom).

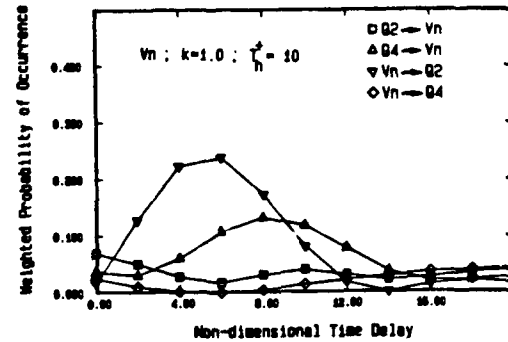
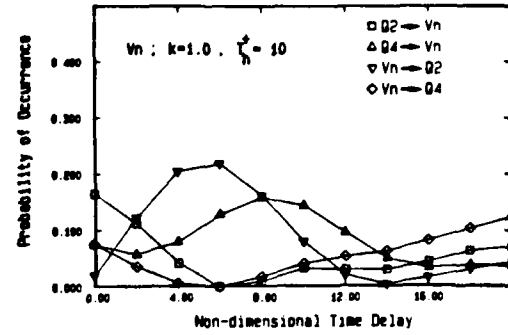


Figure 7. Probability Distributions of Time Delay Between Q2 and Q4 Events and Neighboring Negative VITA Events; Unweighted (top) and Reynolds Stress Weighted (bottom).

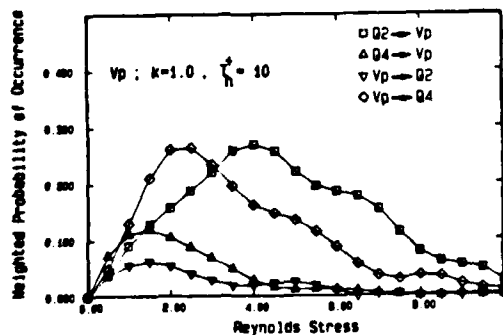
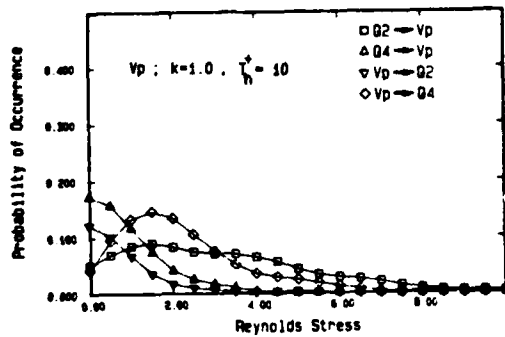


Figure 6. Probability Distributions of Reynolds Stress Intensity of Q2 and Q4 Events Neighboring Positive VITA Events; Unweighted (top) and Reynolds Stress Weighted (bottom).

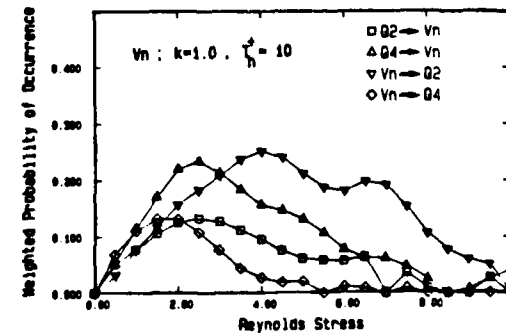
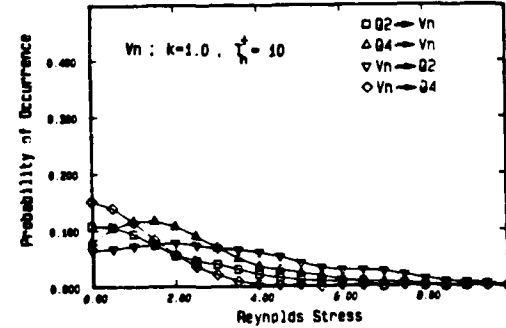


Figure 8. Probability Distributions of Reynolds Stress Intensity of Q2 and Q4 Events Neighboring Negative VITA Events; Unweighted (top) and Reynolds Stress Weighted (bottom).

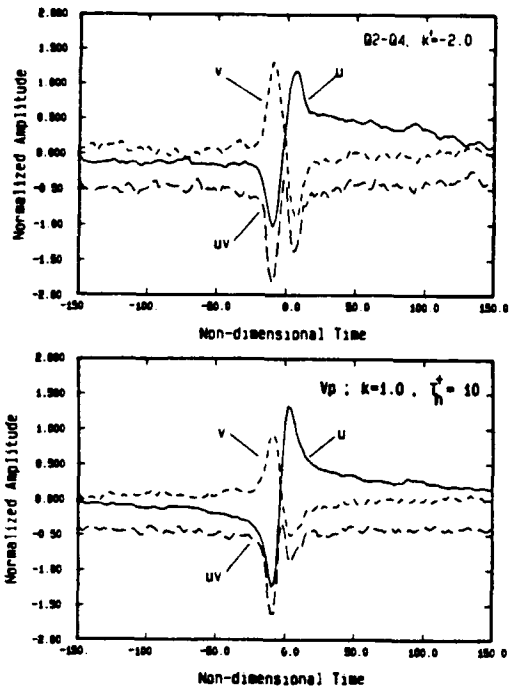


Figure 9. Comparison of Ensemble-Averaged Velocities and Reynolds Stress of Synthetic (Q2/Q4 Pair) and True Positive VITA Events.

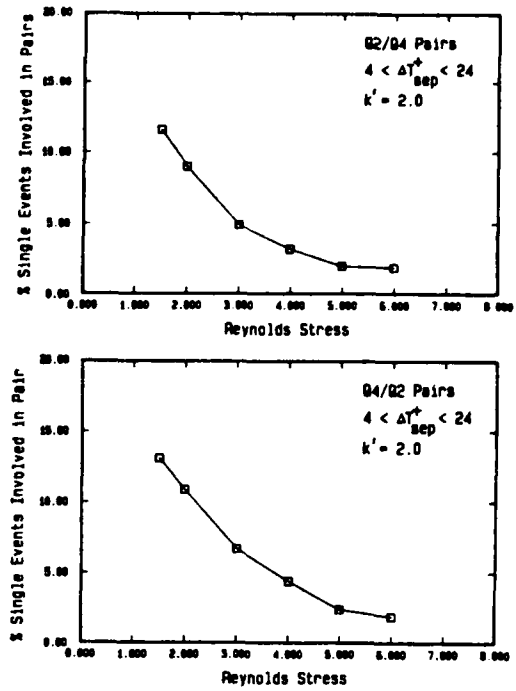


Figure 11. Percentage of Q4 and Q2 Population Representing VITA Events Versus Their Reynolds Stress Intensity; Positive VITA Events (top) and Negative VITA Events (bottom).

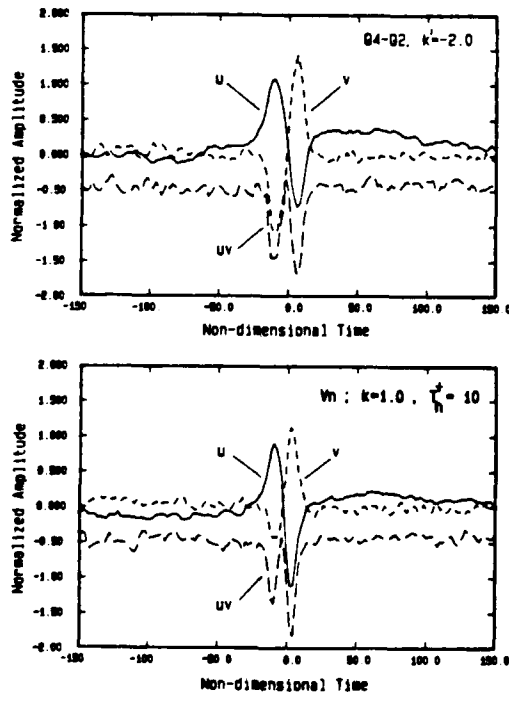


Figure 10. Comparison of Ensemble-Averaged Velocities and Reynolds Stress of Synthetic (Q4/Q2 Pair) and True Negative VITA Events.

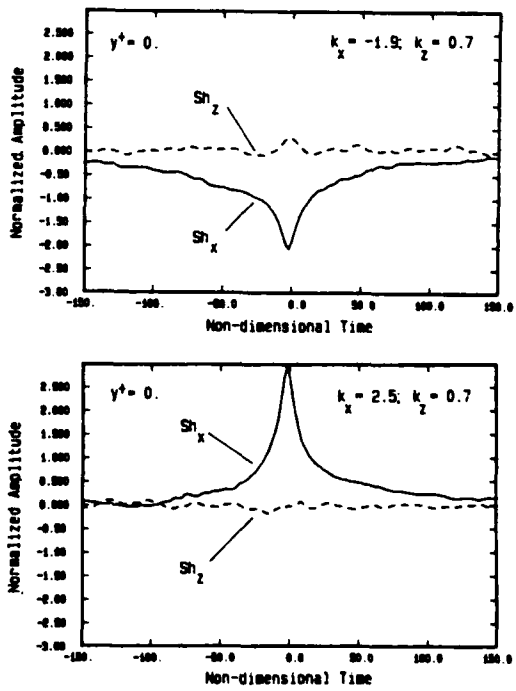


Figure 12. Ensemble-Averaged Streamwise and Transverse Wall-Shear of Second Quadrant (Q2; Events) (top) and Fourth Quadrant (Q4) Events (bottom) Detected at the Wall.

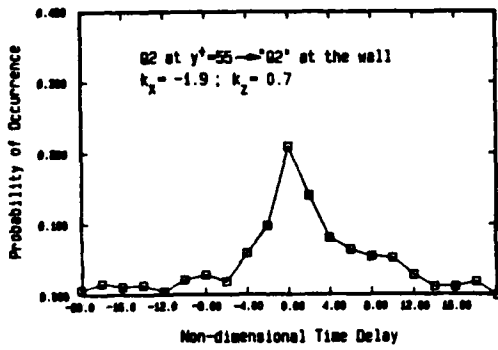


Figure 13. Probability Distribution of Delay Between Q2 Events Detected at the Wall and Q2 Events Detected at  $y^+ = 55$ .

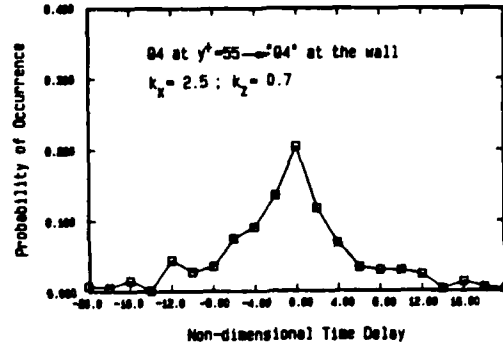


Figure 15. Probability Distribution of Delay Between Q4 Events Detected at the Wall and Q4 Events Detected at  $y^+ = 55$ .

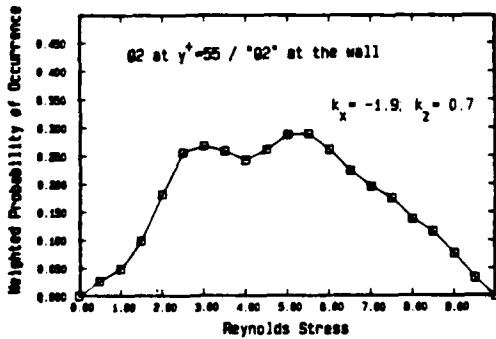
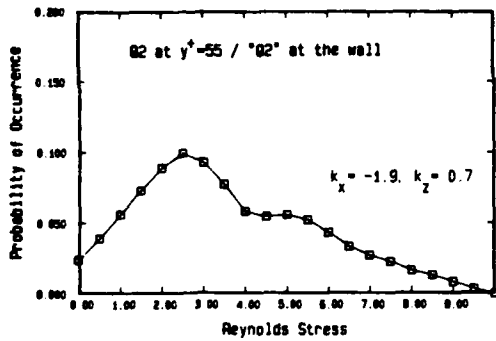


Figure 14. Probability Distribution of Reynolds Stress Strength at  $y^+ = 55$  for Q2 Events Detected at the Wall; Unweighted (top) and Reynolds Stress Weighted (bottom).

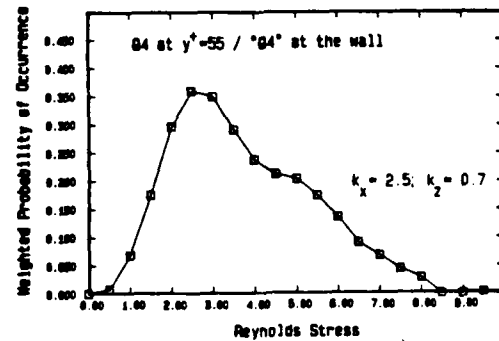
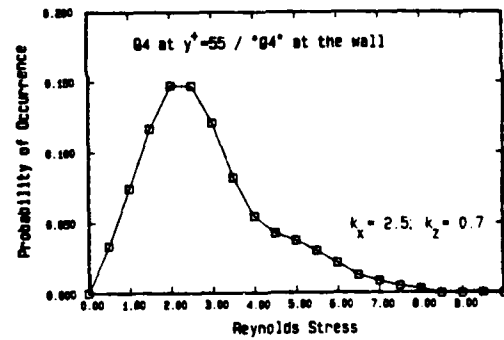


Figure 16. Probability Distribution of Reynolds Stress Strength at  $y^+ = 55$  for Q4 Events Detected at the Wall; Unweighted (top) and Reynolds Stress Weighted (bottom).

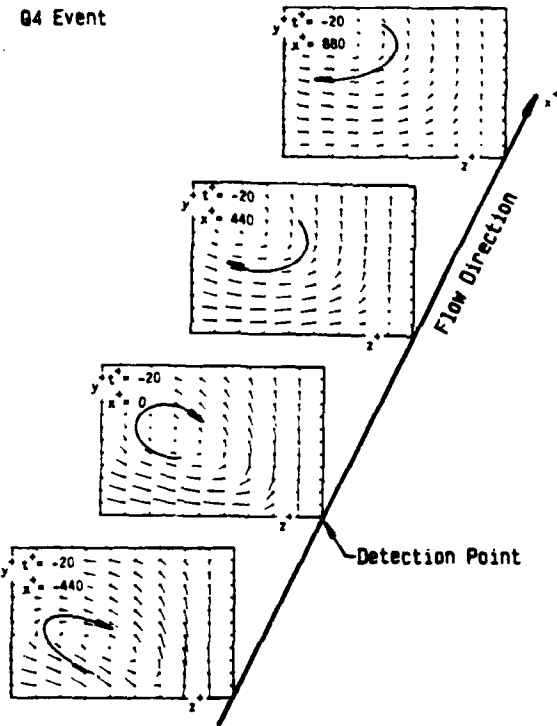


Figure 17. Streamwise Evolution of Vector Maps of Normal and Spanwise Velocity Perturbation Associated with Wall-Detected Q4 Events.

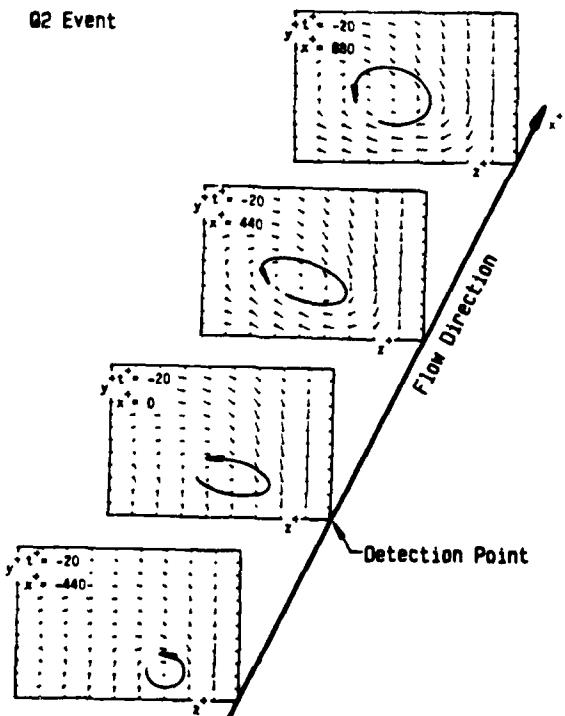


Figure 18. Streamwise Evolution of Vector Maps of Normal and Spanwise Velocity Perturbation Associated with Wall-Detected Q2 Events.

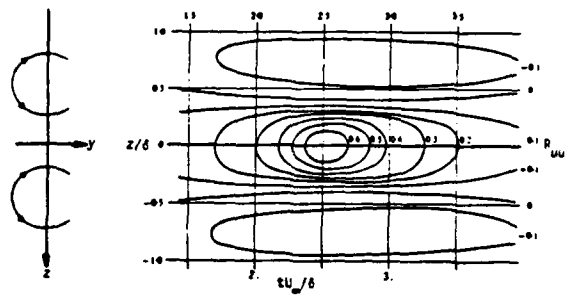
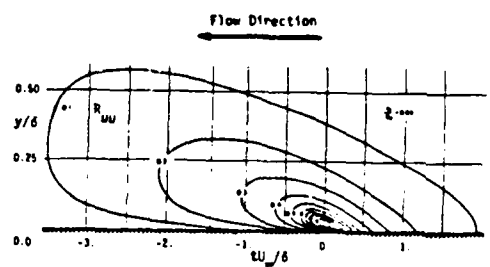


Figure 19. Iso-Correlation Contours of Streamwise Velocity Fluctuations from Blackwelder and Kovaznay (1972), and End View Interpretation Based on Present Results.

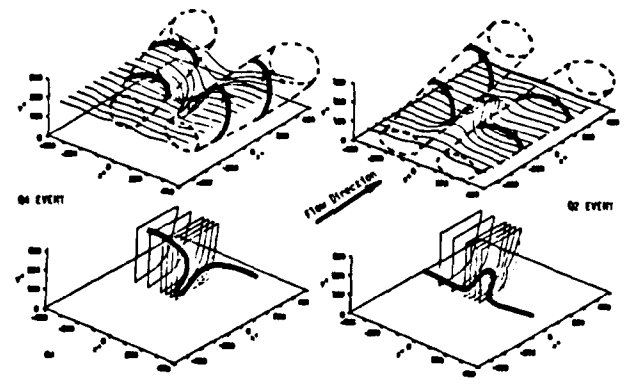


Figure 20. Distortion of Sheet of Vortex Lines for Q4 and Q2 Events from Kim and Moin (1986), Highlighted with Features from Present Study.

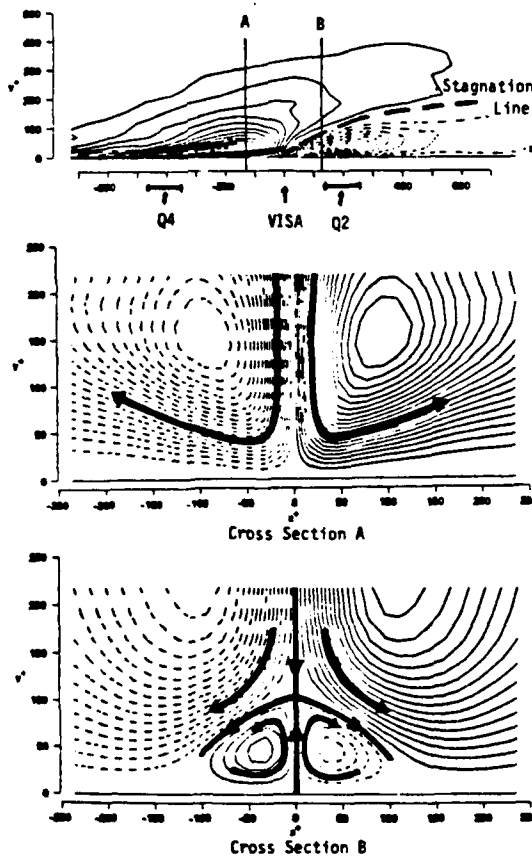


Figure 21. Contours of Fluctuating Streamwise Velocity and Streamlines in Cross-Planes at Two Downstream Positions for VISA Events from Kim (1985), Highlighted with Features from Present Study.

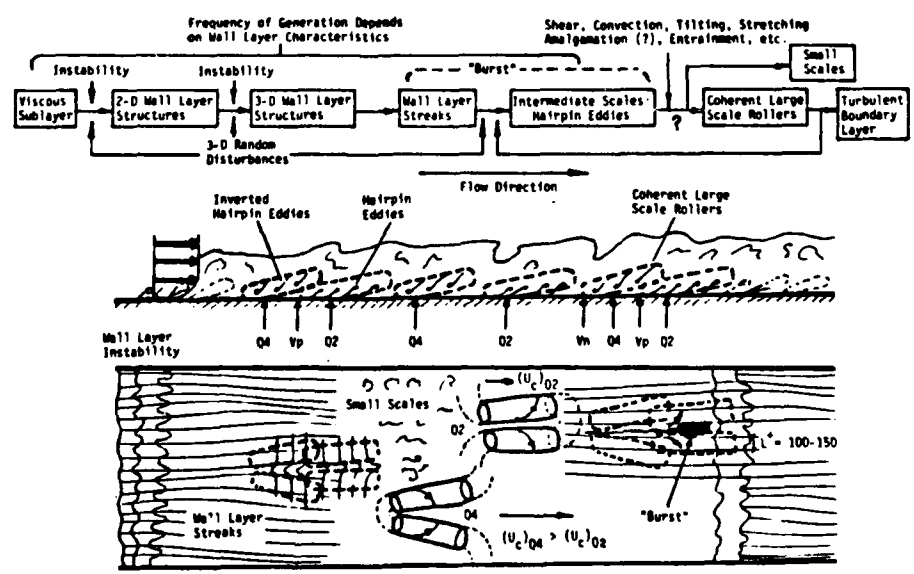


Figure 22. Conjectured View of Turbulent Boundary Layer Features and Their Interrelation.

SPECKLE PHOTOGRAPHIC MEASUREMENT OF  
TURBULENCE IN AN AIR STREAM WITH FLUC-  
TUATING TEMPERATURE

R. Erbeck, W. Merzkirch  
Lehrstuhl für Strömungslehre  
Universität Essen  
D-4300 Essen, F.R.Germany

ABSTRACT

The deflection of laser light passing through the mildly heated, turbulent air stream in a low-speed wind tunnel is measured by means of speckle photography. This optical whole-field method provides a dense distribution of data values of the deflection angle in the field of view. When isotropic turbulence is assumed, it becomes possible to calculate the correlation function of the three-dimensional, turbulent temperature (or density) field from the correlation function of the plane distribution of measured deflection angles. Spectra and characteristic length scales are determined and compared with cold-wire data reported in the literature.

1. INTRODUCTION

Fluctuating values of density and/or temperature in turbulent air flows have been measured by means of the cold-wire technique (see e.g. Petit et al., 1985). Though a number of corrections for the interaction between the mechanical probe and the flow have been proposed, the measured data include a certain, usually unknown error due to this mechanical interaction. If one determines spatial correlation functions of the density or temperature data measured with one probe at a fixed position and as a function of time, it is necessary to make use of Taylor's hypothesis, the application of which requires the existence of a constant mean convective velocity in the flow. This assumption is the less valid the greater the distance over which the spatial correlation is done.

A true spatial correlation is possible if the

data can be derived from a whole-field record (flow visualization). With optical visualization methods, which are sensitive to changes of the fluid density, one integrates the information along the light path through the flow field. It is therefore not possible to determine, by simple means, the instantaneous, three-dimensional density distribution in a turbulent flow. Uberoi and Kovaszny (1955) have proposed a method that allows one for determining the spatial correlation function of the fluid density from the turbulent pattern recorded with a shadowgraph. This method requires the existence of isotropic turbulence in the flow, an assumption that replaces the missing information in the third direction. Uberoi and Kovaszny failed with verifying the proposed procedure because it is not possible to derive quantitative data from a shadowgraph. The same is true for the cases of the schlieren method or interferometry; these classical optical techniques are not appropriate for providing the necessary quantitative data for turbulent flows with fluctuating density.

It had been shown by Wernekinck et al. (1985) that quantitative measurements in turbulent density fields can be performed by means of speckle photography. With this novel technique, originated by Köpf (1972) and by Debrus et al. (1972), one measures the deflection angles of light rays which have passed through a respective flow; i.e. the information is similar to that obtainable with a schlieren system, but the information is quantitative and the technique has a number of advantages over the classical optical methods, as discussed e.g. by Wernekinck and Merzkirch (1986). The method of speckle

photography is applied here for studying the isotropic turbulent flow downstream of a turbulence grid in a low-speed wind tunnel. Weak density fluctuations are generated by means of electrically heated grid wires. The experimental conditions are chosen such that a comparison with cold-wire results from different sources becomes possible. The analytical step, by which the correlation of the measured light deflection is converted into the correlation of the density, is performed in analogy to the proposal by Uberoi and Kovaszny (1955), however with a certain modification because the shadowgraph reacts on density changes in a different way than the speckle technique. The result of the experiments and of the data processing is a true spatial correlation of the turbulent density field, and the flow is not mechanically disturbed since the applied technique is an optical method. A detailed description of these investigations has been given by Erbeck (1986).

## 2. EXPERIMENTAL METHOD AND FLOW CONDITIONS

The experiments have been performed in a small, low-speed wind tunnel with a quadratic test section of  $457 \times 457 \text{ mm}^2$ . Nearly isotropic turbulence is generated by a quadratic grid of mesh size  $M = 41 \text{ mm}$ . One mesh size downstream of the turbulence grid is a system of vertical, electrically heated wires whose spacing is equal to  $M$ . With an applied voltage of 130 V and an electrical current of 18 A, the wire surface temperature is estimated to be  $800^\circ\text{C}$ . This heating of the air flow results in mean values of the temperature fluctuation in the order of  $1^\circ\text{C}$ . The mean flow velocity is kept at 3.5 m/s, and the Reynolds number formed with the mesh size  $M$  is about 10,000. Geometry, heating system, and flow conditions closely match the conditions of a number of reported experiments in which the temperature fluctuations were measured with a cold-wire probe (Mills et al., 1958; van Atta and Yeh, 1972; Sepri, 1976; Warhaft and Lumley, 1978).

The optical set-up is shown in Fig. 1. A horizontal, parallel beam of laser light, 80 mm in diameter, is directed through the test section, normal to the tunnel axis. The vertical mid-plane of the flow is imaged onto a plane ground glass. The pho-

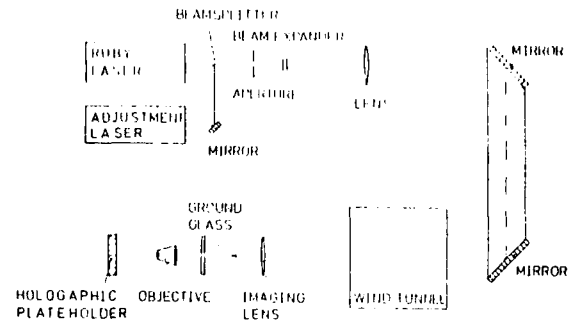


Fig. 1: Optical set-up for taking speckle photographic measurements of the light deflection in a flow with density differences

tographic plane is imaged onto a vertical plane being at a small distance to the left of the ground glass in Fig. 1. This optical arrangement has been described by Wernekinck and Merzkirch (1986). A pulsed ruby laser serves as the light source. Two exposures are taken on the same photographic plate: the first without flow, the second with the flow and the heating system turned on. With the first exposure one generates, on the photographic film, a reference pattern of optical speckles as caused by the granular structure of the ground glass. Due to the light deflection in the density field, the speckle pattern obtained in the second exposure is displaced with respect to the reference pattern, the displacement giving information on the deflection angle  $\epsilon$  in each point  $(x,y)$  of the field of view. This displacement can be measured with the "point-by-point" reconstruction method, a standard method of speckle photography (see e.g. Gärtner et al., 1986). An automated version of this evaluation procedure (Erbeck, 1985) is used here; it provides a large number of data values  $\epsilon(x_i, y_j)$  from each double-exposure. Such a large number of data is necessary for performing a reliable statistical analysis of the measured deflection angles. The data are stored in the memory of a micro-computer that controls the automatic evaluation.

The optical experiments are performed at two axial positions,  $x/M = 18$  and  $x/M = 34$ , downstream of the turbulence grid. It should be noted that the photographic double-exposure ("specklegram") can also be analyzed with a method ("spatial filter-

ing") that provides a visual pattern analogous to a schlieren record (Wernekinck and Merzkirch, 1986).

### 3. DATA ANALYSIS

The distribution of the light deflection angle  $\epsilon(x,y)$  is available in the field of view, a circular area of 80 mm in diameter.  $x,y$  are the coordinates in the recording plane,  $z$  is the direction of the parallel light beam. Instead of  $x,y$  a rectangular coordinate system  $p,q$  is applied which might be rotated with respect to the  $x,y$  system. The speckle photographic measurement delivers the two components,  $\epsilon_p$  and  $\epsilon_q$ , of the deflection angle  $\epsilon$ . The correlation function  $R_{\epsilon_q}$  of the component  $\epsilon_q$  in the points  $(p,q)$  and  $(p+\xi,q+\eta)$  is formed according to

$$R_{\epsilon_q}(\xi,\eta) = \langle \epsilon_q(p,q) \cdot \epsilon_q(p+\xi,q+\eta) \rangle_{AV} \quad (1)$$

where the symbol  $\langle \dots \rangle_{AV}$  designates an integration over the whole field (see e.g. Hinze, 1975). Values of  $\epsilon_q$  exist in a finite number of measured points  $(p_i, q_j)$  with  $0 < p_i < m$ ,  $0 < q_j < n$ . The correlation of  $\epsilon_q$  in  $p$ -direction (symbol  $\perp$ ) is calculated as

$$\begin{aligned} R_{\epsilon_{q\perp}}(\xi=\tau, \eta=0) &= R_{\epsilon_{q\perp}}(\tau) \\ &= \frac{1}{1+m-\tau} \sum_{i=0}^{m-\tau} \epsilon_q(i,q) \cdot \epsilon_q(i+\tau,q) \end{aligned} \quad (2)$$

and the correlation of  $\epsilon_q$  in  $q$ -direction (symbol  $\parallel$ ) is

$$\begin{aligned} R_{\epsilon_{q\parallel}}(\xi=0, \eta=\tau) &= R_{\epsilon_{q\parallel}}(\tau) \\ &= \frac{1}{1+n-\tau} \sum_{j=0}^{n-\tau} \epsilon_q(p,j) \cdot \epsilon_q(p,j+\tau) \end{aligned} \quad (3)$$

Eqs. (2) and (3) are finite approximations of the correlation function (1). The approximation is the better the higher the values of  $m$  and  $n$ .

The two correlation functions of  $\epsilon_q$ , formed in either the  $p$ - or  $q$ -direction, are shown in Fig. 2 for an experiment taken at position  $x/M=18$ .  $R_{\epsilon_{q\parallel}}$  has positive and negative values, while  $R_{\epsilon_{q\perp}}$  is only positive. A change in sign of the correlation function should cause a change from bright to dark or vice versa in the visual pattern obtained by

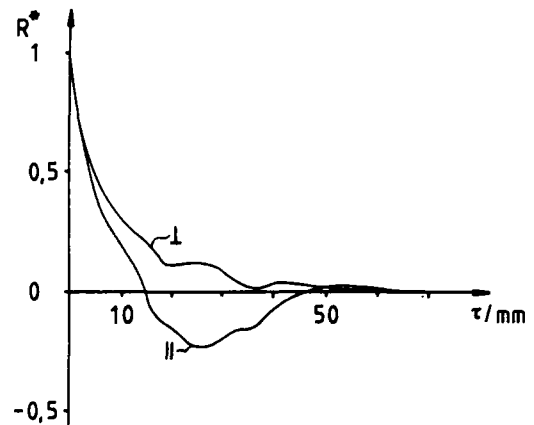


Fig. 2: Normalized correlation function of the deflection angle  $\epsilon_q$  for the correlation taken in  $p$ -direction (symbol  $\perp$ ) and in  $q$ -direction (symbol  $\parallel$ ).

spatial-filtering of the the specklegram (see above). Such a record produced by this reconstruction method (Fig. 3) indeed shows more frequent changes of sign in vertical ( $q$ -) direction than in horizontal ( $p$ -) direction.

The relationship between deflection angle  $\epsilon$  and fluid density  $\rho$

$$\epsilon_q(p,q) = K \int_0^L \frac{\partial \rho(p,q,z)}{\partial q} dz, \quad (4)$$



Fig. 3: Reconstruction and visualization of the turbulent density field by means of spatial filtering.

with  $K$  being the Gladstone-Dale constant and  $L$  the width of the test section in  $z$ -direction, can be introduced in eq. (1). The result is a relationship between  $R_{\varepsilon q}$  and the correlation function of the density,  $R_{\rho}(\xi, \eta, \zeta)$ :

$$R_{\varepsilon q}(\xi, \eta) = -K^2 \int_0^L \int_0^L \frac{\partial^2}{\partial \eta^2} R_{\rho}(\xi, \eta, \zeta) dz' dz'' \quad (5)$$

Correlation is formed between density values at points  $(p, q, z')$  and  $(p+\xi, q+\eta, z'+\zeta)$ , and  $z'' = z' + \zeta$ . Simple integration and setting  $L \rightarrow \infty$  gives

$$R_{\varepsilon q}(\xi, \eta) = -2 K^2 L \int_0^{\infty} \frac{\partial^2}{\partial \eta^2} R_{\rho}(\xi, \eta, \zeta) d\zeta. \quad (6)$$

For isotropic turbulence, the correlation functions do not depend on direction, and they are only functions of the radial distances  $\tau$ , resp.  $r$ :

$$\begin{aligned} \tau &= \sqrt{\xi^2 + \eta^2}, \\ r &= \sqrt{\xi^2 + \eta^2 + \zeta^2} = \sqrt{\tau^2 + \zeta^2}, \\ R_{\varepsilon q}(\tau) &= -2 K^2 L \int_0^{\infty} \frac{\partial^2}{\partial \eta^2} R_{\rho}(\sqrt{\tau^2 + \zeta^2}) d\zeta. \quad (7) \end{aligned}$$

A further simplification is possible for the two cases designated above by the symbols  $\perp$  and  $\parallel$ . The resulting equations can be inverted (for details see Erbeck, 1986), the result of the inversion is

$$R_{\rho}(r) = \frac{1}{\pi L K^2} \int_r^{\infty} \frac{1}{\sqrt{\tau^2 - r^2}} \left\{ \int_0^{\tau} R_{\varepsilon q \parallel}(\tau^*) d\tau^* \right\} d\tau, \quad (8a)$$

$$R_{\rho}(r) = \frac{1}{\pi L K^2} \int_r^{\infty} \frac{\tau}{\sqrt{\tau^2 - r^2}} R_{\varepsilon q \perp}(\tau) d\tau. \quad (8b)$$

With eqs. (8) one has the correlation function of the density expressed explicitly as a function of the correlation function of the measured deflection angles. The integrals in (8a), (8b) can be evaluated by standard methods. With the gas equation and assuming a constant pressure, it is possible to replace the density by the temperature.

#### 4. RESULTS

The normalized correlation function (correlation coefficient) of the temperature,  $R_T^*$ , is shown in Fig. 5 as a function of the non-dimensional ra-

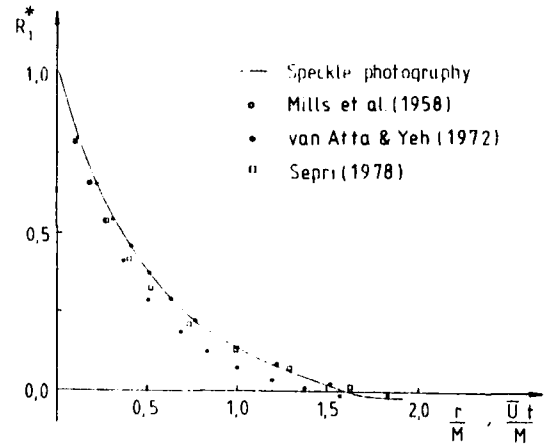


Fig. 4: Normalized correlation function of the temperature,  $R_T^*$ , as function of the non-dimensional radial distance. Speckle measurement taken at the axial position  $x/M=18$ . Referred data were taken for  $x/M$  positions of 17 (Mills et al.), 35 (van Atta and Yeh), 40 (Sepri).

dial distance  $r/M$ . Since measurements have been taken from the specklegram every 0.4 mm, it is not possible to resolve individual measurement points in the speckle results. The maximum distance over which a correlation can be performed is the diameter of the field of view, i.e.  $r=80$  mm or  $r/M=2$ . The speckle photographic result is compared with cold-wire data from different sources. Since these data have been taken as a function of time  $t$  and in a flow with a mean convective velocity  $\bar{U}$ , the spatial correlation of the cold-wire results is referred to a radial distance  $\bar{U} \cdot t$ . It should be noted that there is a difference in the axial position  $x/M$  where the individual experiments have been performed. If one resolves the curve of speckle measurements with a much finer radial scale, it becomes evident that the curve starts at  $r=0$  with nearly horizontal slope.

Fourier analysis of the correlation function allows for determining the one-dimensional energy spectrum  $E_{T1}$ . In Fig. 5, the spectra of the speckle measurements at axial positions  $x/M=18$  and  $x/M=34$  are compared with the result of Sepri (1976). The limiting frequencies or wave numbers  $k_1$  for the speckle results are determined by the diameter of the field of view (80 mm) and the smallest distance between measurement points in evaluating the speck-

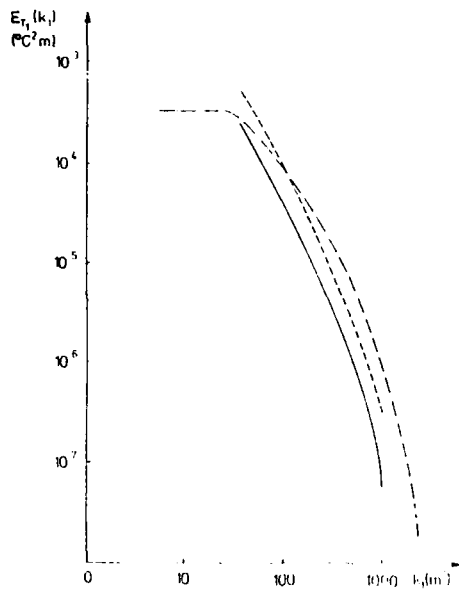


Fig. 5: One-dimensional energy spectrum  $E_{T1}$  as function of wave number  $k_1$ .  
 --- speckle method,  $x/L = 18$   
 — speckle method,  $x/L = 34$   
 -·- Sepri (1976),  $x/L = 39$

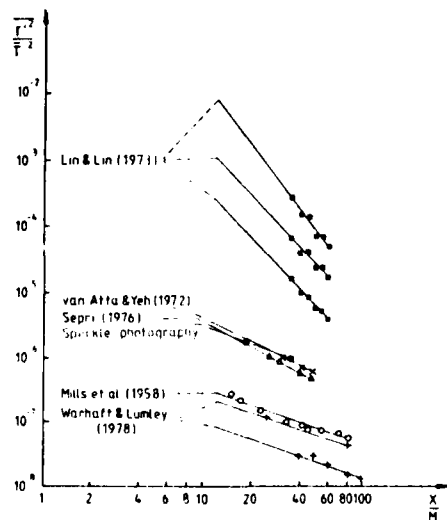


Fig. 6: Decay of the turbulence intensity with increasing axial distance.

igram (0.4 mm). The  $-\frac{5}{3}$  law is not clearly verified.

The mean temperature fluctuation  $T^{T^2}$  is given by the value of the correlation function at  $r = 0$ . These values, plotted as a function of the axial

distance  $x/M$  (Fig. 6), give information on the decay rate of the turbulence. The two data points of the speckle measurements agree well with respective cold-wire data also shown in Fig. 6. From this diagram one can conclude that the heating of the flow and the turbulence intensity in the present experiments were such that a comparison with the referred data is allowed. Only the experiments of Lin and Lin (1973) have been performed with a much higher heat input.

The micro-scale  $\lambda_T$  has been determined both from the curvature of the correlation function for  $r \rightarrow 0$  and from the slope of a straight line through the (two) data points in Fig. 6. The result, given as a function of  $x/M$  (Fig. 7), is in reasonable agreement with the data of Mills et al. (1958) and van Atta and Yeh (1972). A relatively large error is of course attributed to the values that have been derived from the curvature of the correlation function. The turbulent macro-scale  $L_T$  is deter-

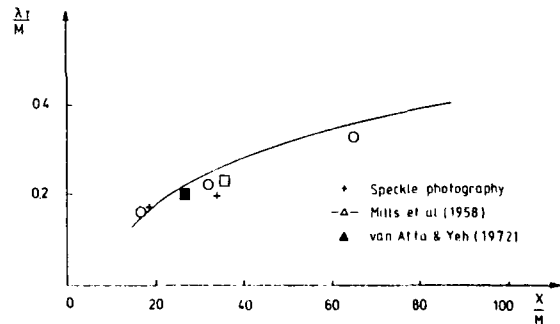


Fig. 7: Turbulent micro-scale  $\lambda_T$ .

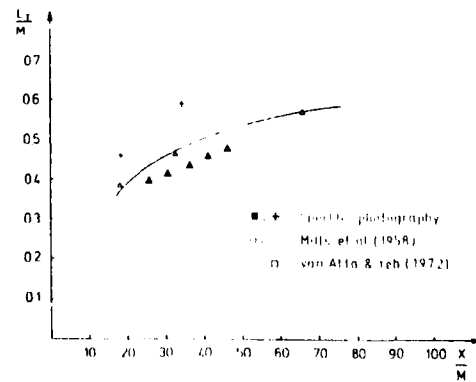


Fig. 8: Turbulent macro-scale  $L_T$ .

mined by an integration of the correlation function, and the values are compared with results from the same sources (Fig. 8).

## 5. DISCUSSION

Correlation measurements in an air flow of isotropic turbulence and with density and temperature fluctuations have been performed with an optical whole-field method based on speckle photography. This experimental method is non-intrusive, and it allows for performing a true spatial correlation of the measured data, without making use of Taylor's hypothesis. First experimental results are in good agreement with respective cold-wire data from different sources. The turbulent macro-scale  $L_T$  determined by an integration of the correlation function exhibits the most pronounced difference between the results from the two experimental methods. With only two experimental points from the new technique available, it is somewhat difficult to come to a definite conclusion explaining this difference. It is believed that the new method is more reliable, when the correlation is performed over large distances. The higher values of  $L_T$  from the speckle measurements are a consequence of the higher values of the correlation function for large  $r$ . Whether the speckle technique delivers the more reliable data for this length scale has to be investigated with additional experiments.

In the present application, the method relies on the existence of isotropic turbulence. If this assumption cannot be made, it becomes necessary either to develop another model that replaces the condition of isotropy, or to directly measure the instantaneous, three-dimensional distribution of the fluid density, e.g. by means of a tomographic processing of the optical data. This will be a subject of future experiments.

## ACKNOWLEDGEMENT

Part of this research has been supported by a grant from Deutsche Forschungsgemeinschaft.

## REFERENCES

Erbeck, R. 1985: Fast image processing with a micro-computer applied to speckle photography. Appl. Opt. 24, 3838-3841.

Erbeck, R. 1986: Die Anwendung der Speckle-Photographie zur statistischen Analyse turbulenter Dichtefelder. Dissertation, Universität Essen (F.R.Germany).

Gärtner, U.; Wernekinck, U.; Merzkirch, W. 1986: Velocity measurements in the field of an internal gravity wave by means of speckle photography. Exp. Fluids 4, 283-287.

Hinze, J.O. 1975: Turbulence. McGraw-Hill, New York.

Lin, Shih-Chun; Lin, Shao-Chi 1973: Study of strong temperature mixing in subsonic grid turbulence. Phys. Fluids 16, 1587-1598.

Mills, R.; Kistler, A.L.; O'Brien, V.; Corrsin, S. 1958: Turbulence and temperature fluctuations behind a heated grid. NACA Technical Note 4288.

Petit, C.; Paranthoen, P.; Lecordier, J.C.; Gajan, P. 1985: Dynamic behaviour of cold wires in heated airflows ( $300 < T < 600$  K). Exp. Fluids 3, 1063-1075.

Sepri, P. 1976: Two-point turbulence measurements downstream of a heated grid. Phys. Fluids 19, 1876-1884.

Uberoi, M.S.; Kovaszny, L.S.G. 1955: Analysis of turbulent density fluctuations by the shadow method. J. Appl. Phys. 26, 19-24.

Van Atta, C.W.; Yeh, T.T. 1972: Spectral transfer of scalar and velocity fields in heated-grid turbulence. J. Fluid Mech. 58, 233-261.

Warhaft, Z.; Lumley, J.L. 1978: An experimental study of the decay of temperature fluctuations in grid-generated turbulence. J. Fluid Mech. 88, 659-684.

Wernekinck, U.; Merzkirch, W.; Fomin, H.A. 1985: Measurement of light deflection in a turbulent density field. Exp. Fluids 3, 206-208.

Wernekinck, U.; Merzkirch, W. 1986: Measurement of natural convection by speckle photography. Proceed. 8th Int. Heat Transfer Conference (San Francisco), Hemisphere, Washington.

A PRELIMINARY INVESTIGATION INTO  
THE REAL-TIME IMAGE ANALYSIS OF A  
VISUALIZED 'TURBULENT' WAKE

N. Toy and C. Wisby,  
Department of Civil Engineering,  
University of Surrey,  
Guildford, Surrey, U.K., GU2 5XH.

ABSTRACT

A novel technique is presented that attempts to utilize modern digital imaging concepts in conjunction with traditional smoke flow visualization to obtain quantitative flow information. Statistical information regarding the turbulent/non-turbulent interface associated with the wake region of a thin, sharp-edged flat-plate model held normal to a uniform flow are presented. Flow information is derived from a real-time video digitization procedure operating with a standard or solid-state video detector device. The information presented includes autocorrelation functions and associated derivative shedding frequencies, probability density distributions, higher-order moments, intermittency functions and mean wake interface locations.

1. INTRODUCTION

It has been appreciated for many years that free turbulent flows such as jets, wakes and boundary layers exhibit a sharp interface between an interior region of turbulent flow and an external region of non-turbulent or irrotational flow. Observations of the signal from a hot-wire probe placed near the outer edge of such a flow were first reported by Corrsin (1943) who identified two distinct signal contributions, indicating slow and smoothly varying velocity fluctuations indispersed with sections of much

more rapid velocity fluctuations. The fraction of the total time that the signal is 'turbulent' is called the intermittency factor  $\Upsilon$ , where the intermittency function  $I(x,t)$  is defined by:

$$I(x,t) = \begin{cases} 1 & \text{: point } (x,t) \text{ in turbulent region} \\ 0 & \text{: point } (x,t) \text{ in non-turbulent region} \end{cases}$$

More extensive studies of intermittency were conducted initially by Townsend (1948) and Corrsin and Kistler (1955).

The mechanism by which a turbulent medium propagates into a non-turbulent medium is a particularly interesting and challenging problem. An easily observable and obvious mechanism for the lateral growth of turbulent shear flows is the large-scale eddies, which have been found to play a central role in the entrainment process (Townsend (1970)). Any complete explanation of entrainment must also include a description of the small-scale activity associated with the turbulent/non-turbulent interface. Theoretical explanations of intermittency and entrainment have been undertaken (Phillips (1972), Corrsin and Kistler, Townsend), but a precise specification of the instantaneous interface position would appear to be a theoretical pre-requisite.

The determination of the intermittency function in experimental Fluid Mechanics generally requires the establishment of an arbitrary

discriminating characteristic in order to define a flow as either turbulent or non-turbulent. Ideally, the condition for a flow to be defined as turbulent or not, involves the determination of the variance of the vorticity fluctuations. In practice, this is not easily obtainable, and a simplified discriminator, such as velocity fluctuations is more often employed. Velocity probes such as the hot-wire and pulsed-wire anemometer are widely used in turbulence measurement, although hot-wire signals used as a turbulent/ non-turbulent discriminator are complicated by potential motions induced in the non-turbulent fluid by pressure fluctuations. Other passive scalars (such as excess temperature) are also used as the discriminating scalar (Fabris (1984)), the turbulence condition being satisfied when the value of the chosen scalar exceeds a given threshold level.

For many years experimenters have introduced tracer elements into flow regimes in order to qualitatively observe instantaneous, large-scale flow patterns. Combined with ciné or time-lapse photography, visualization techniques provide the most direct method of describing detailed complex flow patterns. Flow visualization has also been previously used to provide direct quantitative data, intermittency measurements within a boundary layer being conducted using smoke as a passive contaminant (Fiedler and Head (1966)). In these experiments a photo-electric probe was focussed onto an illuminated boundary layer. When smoke passed through the focal point of the probe lens a signal was generated which was used as the interface detector. A comparison was made between the photo-probe and a hot-wire (situated as close together as possible) and the results reportedly confirmed the identity of smoke with turbulence distributions, although there were some discrepancies. The inconsistencies observed between the photo-probe and hot-wire intermittency functions were thought to be due to the photo-electric probe distinguishing a narrow region of smoke-free fluid in a location where the hot-wire recorded a velocity fluctuation

indistinguishable from turbulence. Fiedler and Head concluded that the photo-electric probe revealed folding in the boundary layer which was later confirmed by results obtained using velocity probe techniques (Imaki (1968)). The use of smoke as a passive contaminant to distinguish turbulent from non-turbulent fluid relies on the smoke being rapidly diffused throughout the entire turbulent fluid. The results obtained appear to indicate that such an assumption would not be unreasonable, although this must remain open to conjecture at present.

More recently, a number of attempts have been made to utilize digital image processing techniques to enhance traditional flow visualization capabilities. Measurements of instantaneous concentration fields have been reported by Schon et al. (1979), this work being developed to study dispersion problems (Balint (1982)) and stack emissions (Schon (1984)). Jimenez (1984) presented an interesting and revealing study of a two-dimensional mixing-layer, the results being presented primarily as pseudo three-dimensional representations, capable of complex viewing orientations. Restrictions were encountered with these and other techniques with respect to obtaining quantitative statistical information, there having been an average of only a few hundred frames considered in each case.

The present study has attempted to incorporate the established technique of flow visualization with a digital image acquisition system in order to obtain quantitative, statistical information regarding the turbulent/ non-turbulent interface. Preliminary studies have been conducted using a thin, sharp-edged flat-plate model held normal to a uniform flow. Real-time video digitization of the visualized wake region combined with a software implemented edge detection algorithm has allowed data analysis concerning the interface motion to be performed. A good statistical population has been ensured by considering samples of no less than 5,000 images, with a possible 100,000 available, if required.

## 2. EXPERIMENTAL DETAILS

A specialised low-speed smoke tunnel facility has been constructed in the Civil Engineering Department of the University of Surrey. The working section of the tunnel is 0.75m x 0.624m and freestream velocities of up to 15 m/s are capable at a turbulence intensity of approximately 0.2%. An efficient smoke filtration system located at the tunnel exit allows the continuous introduction of smoke into the working section whilst maintaining an open-return configuration. Experiments were conducted on the wake of a thin, sharp-edged flat-plate (50.8mm in width) which spanned the side of the tunnel. The wake of the plate was visualized using a passive smoke contaminant and a low-power 5 mW He-Ne laser projected normally through the wake region. When viewed with a video camera of either raster-scan or solid-state technology, the laser beam illuminated a bar of smoke the ends of which coincided with the turbulent/ non-turbulent interface (Figure 1 shows a schematic representation of the experimental arrangement).

## 3. IMAGING EQUIPMENT

A DEC Micro PDP 11/73 has been interfaced with an Imaging Technology IP-512 Imaging System which incorporates a high-speed video digitizer and frame buffer. The IP-512 system allows images to be digitized, stored and displayed to a 512 by 512 pixel resolution at 8-bit accuracy offering 256 grey levels. The frame buffer permits simultaneous host access via an I/O port and paired register configuration. A single 256 Byte input look-up table and three separate output look-up tables (R, G, B signals) are individually programmable allowing variable grey level assignment and pseudo-colour display output. Images are acquired as sequential, non-interlaced fields and have a corresponding resolution of 512 pixels horizontally by 256 pixels vertically. A recent addition to the imaging equipment has been a solid-state 'snap-shot' video camera. This device allows a variable image integration time ranging from 1 to 20 mS whilst maintaining a standard 50 Hz output. The camera is manufactured in the U.K. by E.E.V. Ltd.

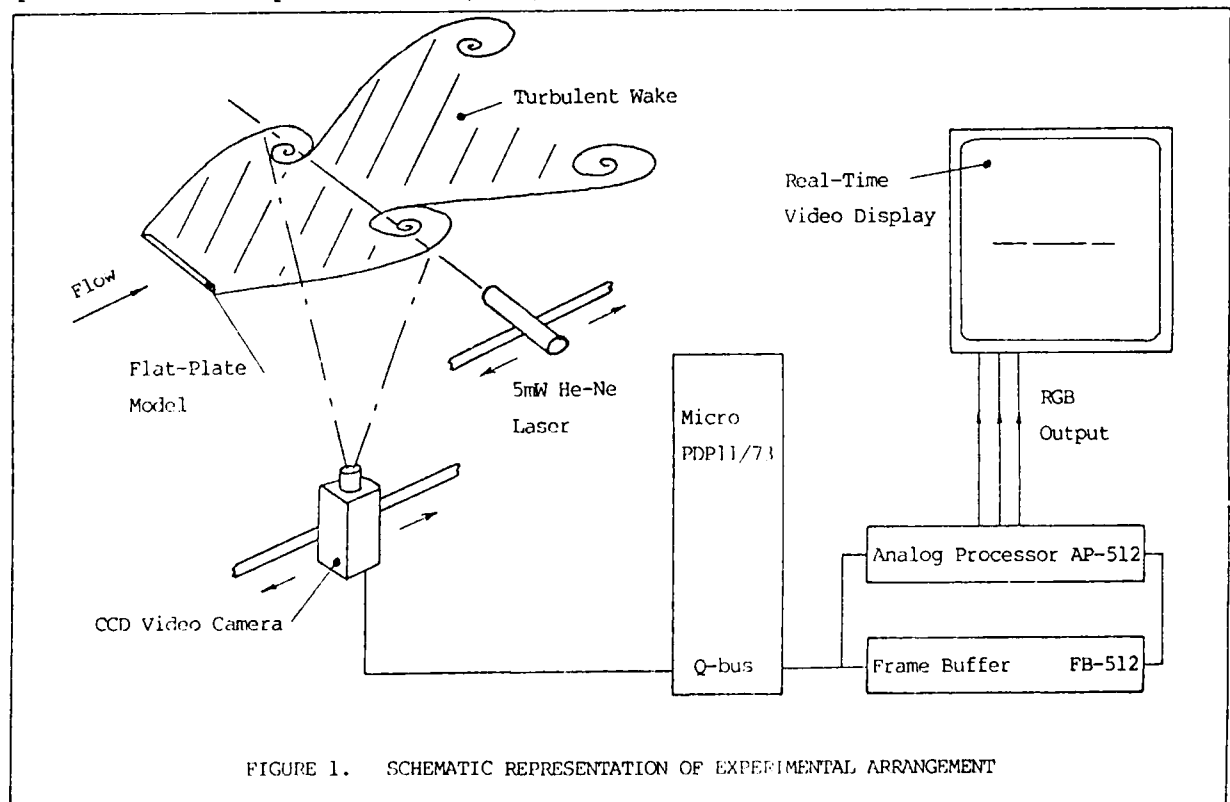


FIGURE 1. SCHEMATIC REPRESENTATION OF EXPERIMENTAL ARRANGEMENT

#### 4. RESULTS

Initial experiments have been undertaken with a thin, sharp-edged flat-plate model held normal to the flow direction. The flat-plate spanned the working section of the tunnel and represented an area blockage of 8.14%, with a length to width aspect ratio of 14.76. The use of end-plates has been restricted in these experiments due to the nature of the video technique. Results have been obtained at downstream locations ranging from 3 plate-widths to 12 plate-widths, and at freestream tunnel velocities of between 1 and 6 m/s representing a Reynold's number ranging from 3,400 to 20,400.

Figure 2 represents a typical 'twin-edge' probability density distribution function obtained using the imaging technique. The functions represent the possibility of encountering the wake interface at any chosen spanwise location at a particular streamwise station, at a given instance in time. Given the symmetrical model and assuming a two-dimensional flow regime, it may be expected that the two probability functions be symmetrical. Associated with the probability density distributions are the higher-order moments such as the skewness (third moment) which in terms of the velocity gradient describes the rate of production of vorticity and kurtosis or 'flatness factor' (fourth moment) which describes the deviation from a normal distribution, as well as the previously described intermittency function which represents the cumulative probability distribution.

Time-dependent interface motion fluctuations were analysed using the autocorrelation function, defined as:

$$R(\tau) = \frac{\lim_{T \rightarrow \infty} \int_{-\tau}^{\tau} f(t) \cdot f(t+\tau) dt}{\lim_{T \rightarrow \infty} \int_{-\tau}^{\tau} f(t) \cdot f(t) dt}$$

A typical autocorrelation function for both wake interfaces is presented in Figure 3. Subsequent spectral analysis of the autocorrelationogram yields any associated dominant frequencies such as the vortex shedding frequency of the turbulent wake.

A series of experiments has been conducted at various downstream locations in the wake of the flat-plate model at the plate mid-span section, at a constant freestream tunnel velocity of 2.0 m/s (Reynold's number of 6,800). Figure 4 represents the calculated mean wake interface locations and variance for various downstream stations. Figure 5 represents the intermittency functions associated with the aforementioned downstream stations, locations X/D = 9.0, X/D = 11.0 and X/D = 12.0 having been omitted in order to avoid confusion caused by the close proximity of the curves.

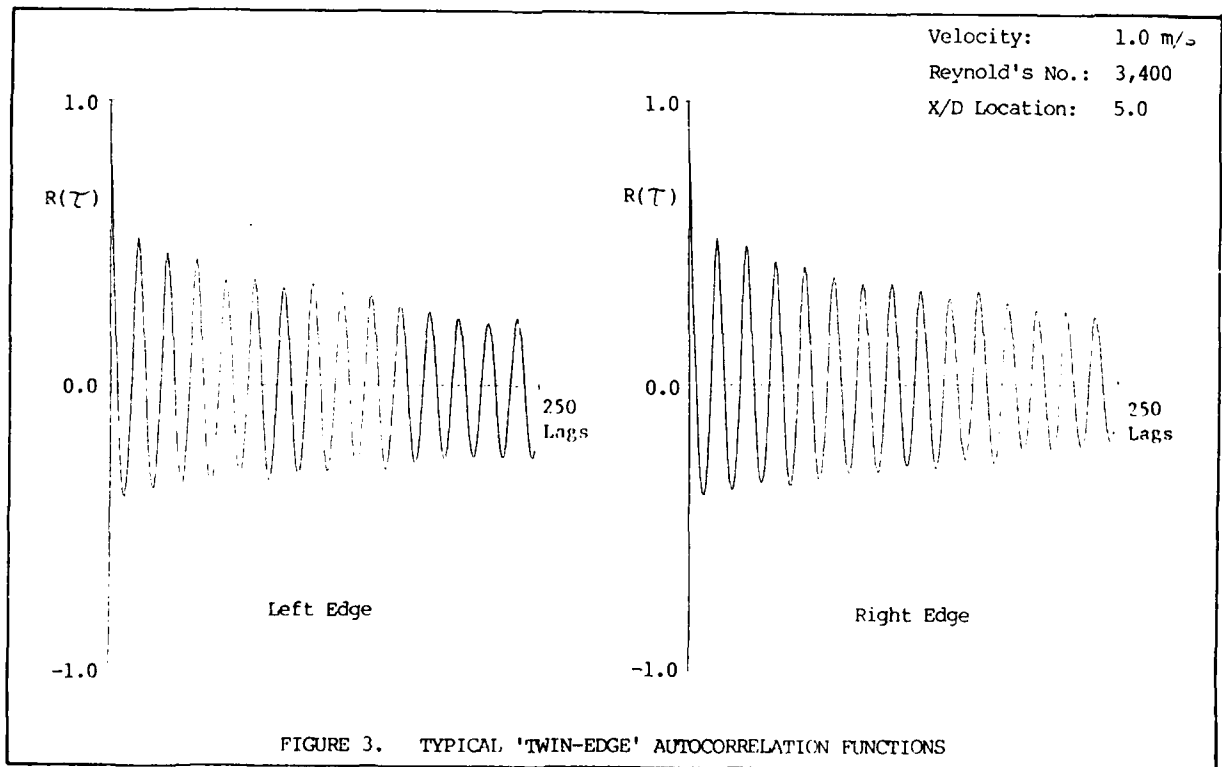
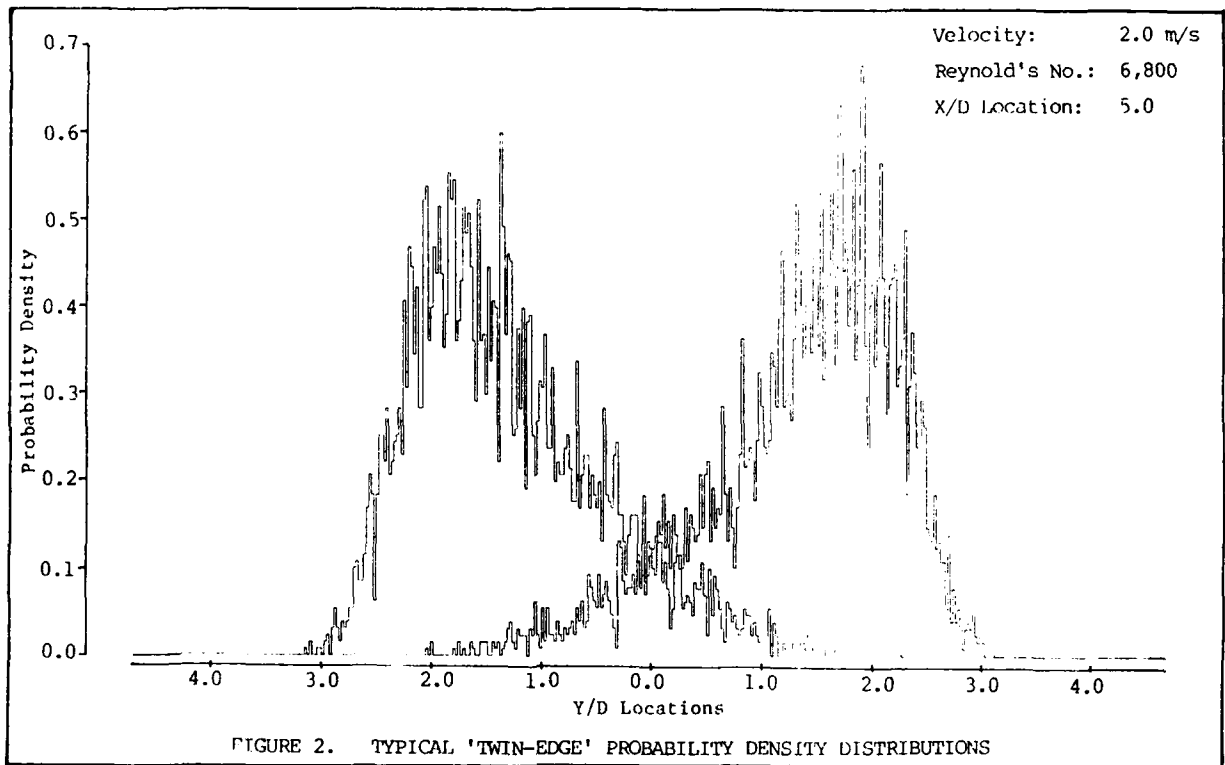
A further series of experiments has been conducted at a single downstream station of X/D = 5.0. The probability moments and vortex shedding frequencies obtained at various freestream velocities are presented in Table 1.

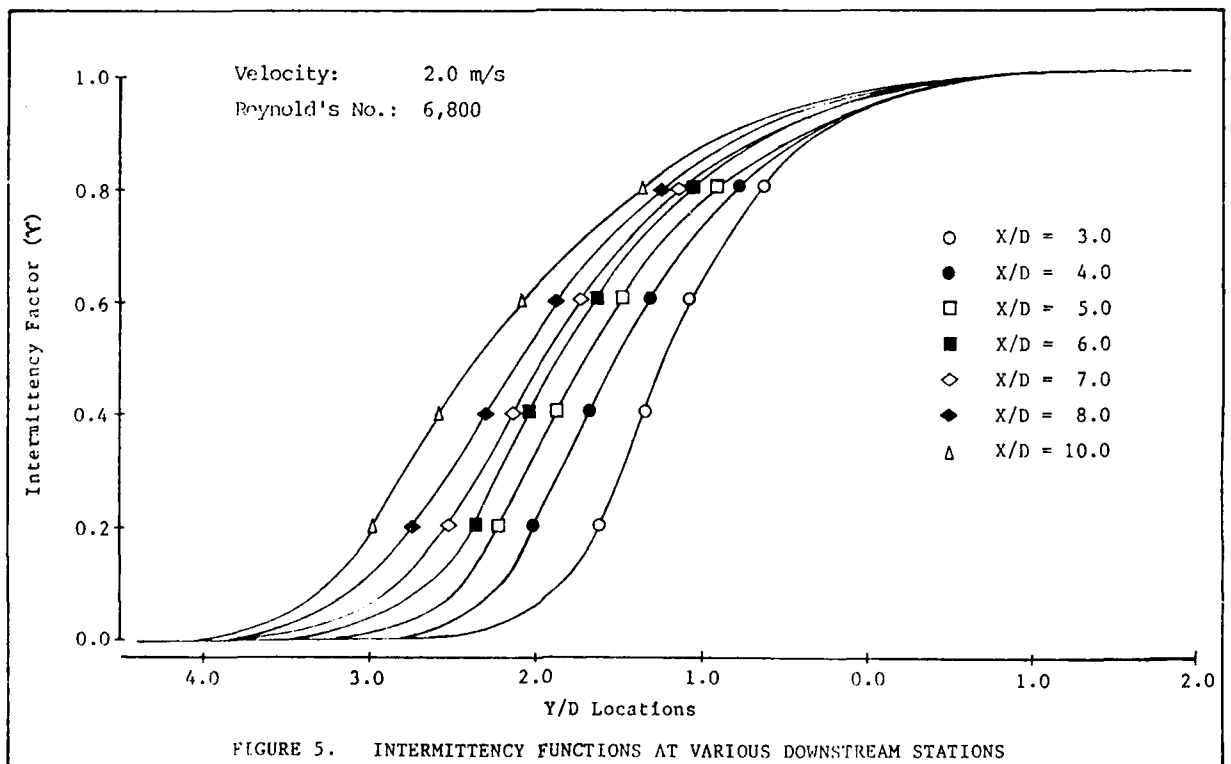
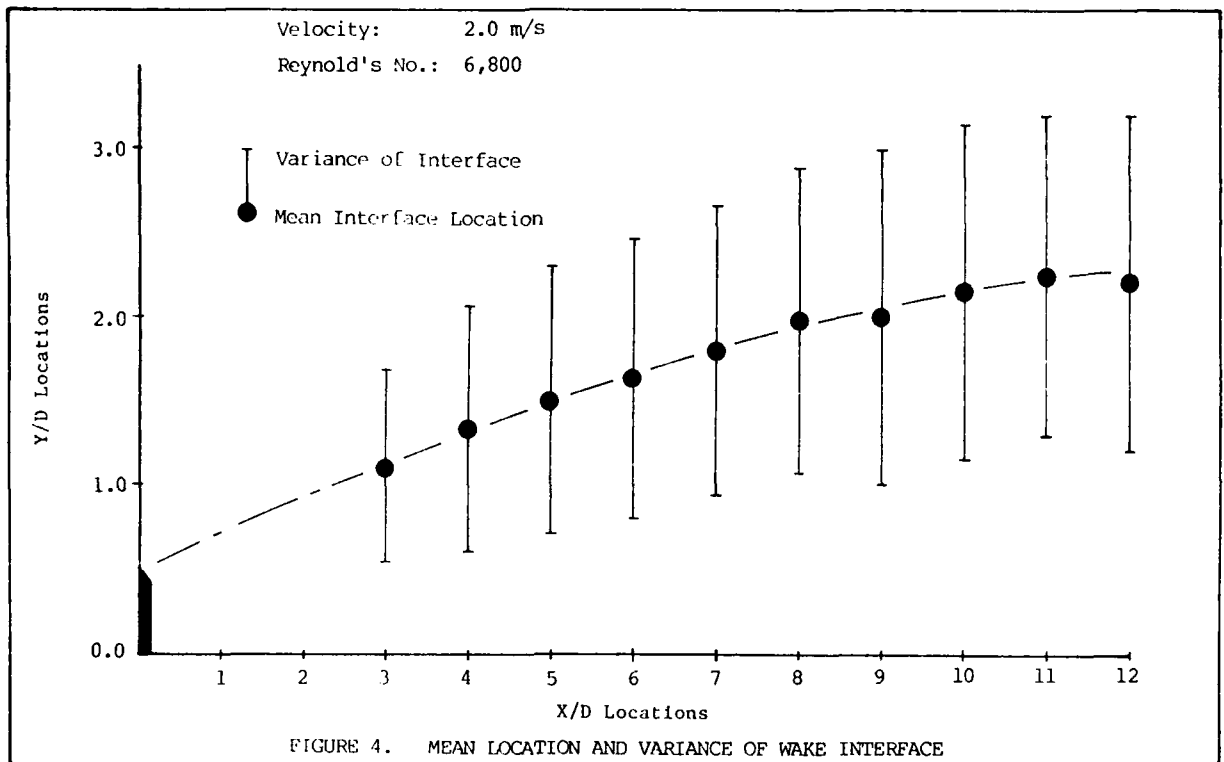
Vel. m/s	Mean X/D	Variance X/D	Skewness	Kurtosis	Freq Hz
1.0	1.485	0.853	0.704	3.190	2.95
2.0	1.419	0.851	0.687	3.130	5.90
3.0	1.371	0.802	0.601	3.002	9.00
4.0	1.283	0.809	0.578	3.441	11.97
5.0	1.265	0.765	0.505	3.564	15.05
6.0	1.240	0.760	0.381	2.953	17.95

Table 1. Moments and Shedding Frequencies

Figure 6 indicates the variation of the non-dimensional Strouhal number (expressed as  $n * D / U$ , where  $n$  is the shedding frequency,  $D$  is the normal dimension of the model and  $U$  is the freestream velocity) with Reynold's number, for the aforementioned downstream location of X/D = 5.0. The Strouhal numbers presented have not been corrected for the blockage effect of the model.

It is not intended to interpret the results obtained at this stage, as this would inevitably require presumptions concerning certain procedural characteristics, some of which are still to be completely evaluated.





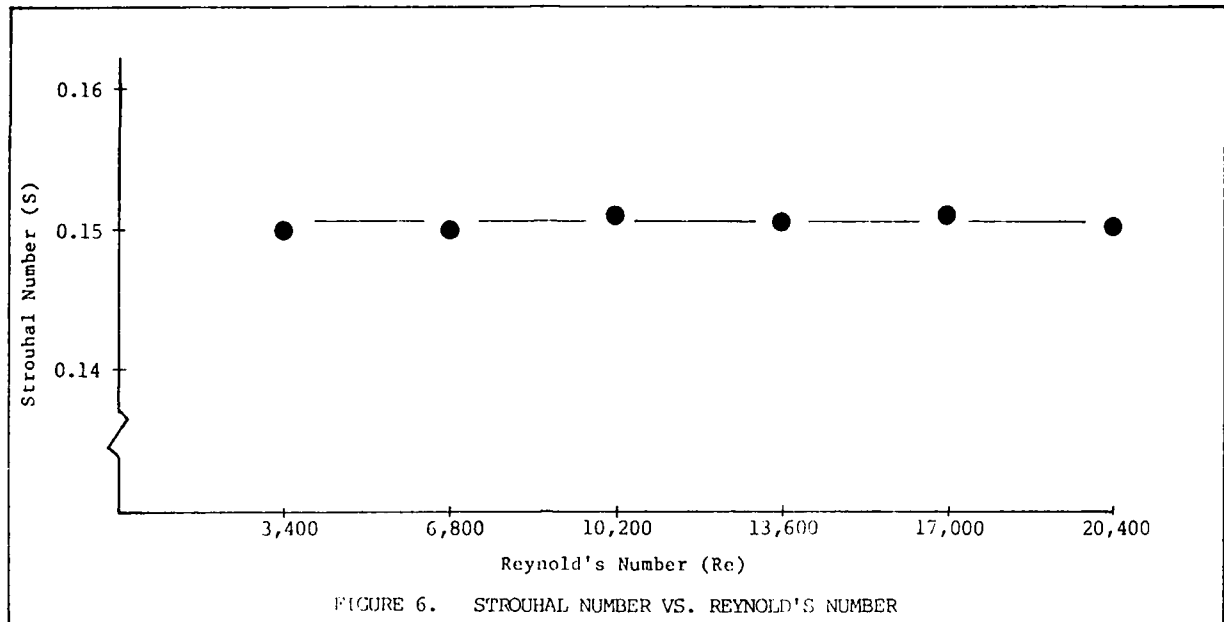


FIGURE 6. STROUHAL NUMBER VS. REYNOLD'S NUMBER

## 5. DISCUSSION

The primary objective of this study has been to examine the possibility of combining the traditional and well-established technique of flow visualization with a modern digital imaging system in order to obtain statistical flow information. The results presented in this paper illustrate that it is possible to obtain statistical information regarding the turbulent/ non-turbulent wake interface. There are, however, inevitable limitations associated with the technique which must be fully appreciated. The restrictions of the present system may be overcome in the future with the implementation of some improved hardware facilities, although it has always been one of the principal objectives of this study to utilize standard, commercially available image analysis and acquisition equipment.

The desire to utilize a real-time video imaging process has some disadvantages compared to the more traditional recording medium of ciné film. The most important considerations when comparing a video system with that of ciné are a loss of sensitivity, a reduction in resolution and a lack of an economic high-speed recording

facility. Video, however, offers real-time, instantaneous image acquisition, recording and playback (if desired). The standard European video rate is 50 Hz which indicates that each image field is normally comprised of a 20 ms integration period (raster timings ignored), thus leading to a degree of image blur for a moving image and providing an upper limitation in frequency analysis of 25 Hz. With regard to the consideration of blur, an attempt has been made to reduce this with the adoption of a variable integration time solid-state camera. This device provides integration periods of between 1 ms and 20 ms whilst maintaining a standard rate video output. Solid-state CCD (Charge-coupled Device) or CID (Charge-injection Device) video cameras also offer a possibility of obtaining higher framing rates in order to increase frequency range capabilities. In comparison to traditional raster-scan type video cameras, a solid-state device offers superior stability in both spatial and temporal characteristics. Individual pixel characteristics often vary within any given CCD array, and it has been established that the statistical analysis of a CCD array line may reveal pixel characteristics with regard to various light intensities.

A further procedure that may also lead to the possibility of a random-sampling technique along similar lines to that described by Gaster and Bradbury (1975) for the pulsed-wire anemometer, may be the adoption of a shuttered light source.

Investigations to-date have been concerned with single location, time-dependent wake interface motions. It is envisaged that the provision of alternative lighting facilities could enable concepts such as spatial and auto-spatial correlations to be investigated. Present investigations are also examining the variation of individual pixel intensities with regard to time across an entire wake line. It is envisaged that further statistical data along such lines will provide a more complete comprehension of the capabilities of this technique and may eventually offer a non-intrusive measurement technique capable of providing a wide range of statistical flow information.

#### 6. CONCLUSIONS

Preliminary statistical information regarding the interface motion of the wake of a thin, flat-plate model has been achieved. The real-time image analysis of a visualized turbulent wake would appear to provide a non-intrusive measurement technique capable of providing statistical information of a relatively unique nature. The results presented in this paper indicate that the technique is capable of yielding both spatial and temporal statistical information. The limitations associated with the European standard video rate of 50 Hz which are comparable with the U.S. video rate have been highlighted. It would seem plausible, however, that future developments in solid-state imagery will provide the possibility of variable framing rates, associated with flexible frame dimensions, allowing greater system flexibility and higher frequency recognition capabilities.

It is envisaged that future investigations concerned with the temporal statistics associated with the light intensity fluctuations of individual pixels from within the wake region will also provide some useful flow information. It is also proposed to study the thin, sharp-edged flat-plate model at varying angles to the freestream flow as well as to consider other two-dimensional model cases.

#### 7. ACKNOWLEDGEMENTS

The author wishes to acknowledge the financial support of the Science and Engineering Research Council.

#### 8. REFERENCES

- Balint, J.L., 1982, "Application d'une methode de visualisation laser et de traitement d'image à l'étude de la dispersion dans les écoulements turbulents", Thèse Lyon.
- Corrsin, S., 1943, N.A.C.A. Wartime Report W-94.
- Corrsin, S., and Kistler, A.L., 1955, "Free-stream Boundaries of Turbulent Shear Flows", N.A.C.A. Report 1244.
- Fabris, G., 1984, "A Conditional Sampling Study of the Interaction of Two Turbulent Wakes", Journal Fluid Mech., Vol. 140, pp 355-372.
- Fiedler, H., and Head, M.R., 1975, "Intermittency Measurements in the Turbulent Boundary Layer", Journal Fluid Mech., Vol. 25, pp 719-735.
- Gaster, M., and Bradbury, L.J.S., 1975, "The Measurement of the Spectra of Highly Turbulent Flows by a Randomly Triggered Pulsed-wire Anemometer", Journal Fluid Mech., Vol. 77, pp 499-509.

Hernan, M.A., and Jimenez, J., 1982, "Computer Analysis of a High Speed Film of the Plane Turbulent Mixing Layer", Journal Fluid Mech., Vol. 119, pp 323-345.

Imaki, K., 1968, "Structure of Superlayer in the Turbulent Boundary Layer", Bull. Inst. Space Aero. Sci., Univ Tokyo 4, pp 323-367.

Jimenez, J., 1984, "Post-processing: Extracting and Displaying Useful Information from Digital Images", von Karman Institute for Fluid Dynamics Lecture Series, Image Processing in Fluid Mechanics.

Phillips, O.M., 1972, "The entrainment interface", Journal Fluid Mech., Vol. 51, pp 97-118.

Schon, J.P., Danel, F., Melinand, J.P., Rey, C. and Charnay, G., 1979, "Measurements of Lagrangian velocities by means of a laser associated to rotating mirrors", Congres LA ROLLA

Schon, J.P., 1984, "Instantaneous Concentration Measurements Through Laser Visualization Associated with a Digital Processing System", von Karman Institute for Fluid Dynamics Lecture Series, Image Processing in Fluid Mechanics.

Townsend, A.A., 1948, Aust. Journal Sci. Res. 1, pp 161-174.

Townsend, A.A., 1970, "Entrainment and the Structure of Turbulent Flow", Journal Fluid Mech., Vol. 25, pp 13-46.

A STUDY OF THE FLOW STRUCTURE  
OF TIP VORTICES ON A HYDROFOIL

T.B.Francis and J.Katz  
Hydraulics Department  
Purdue University  
West Lafayette, Indiana 47907

ABSTRACT

A detailed study of the tip vortices generated on a NACA-66 series hydrofoil was performed in the Purdue University towing tank. The investigation included flow visualization experiments and pressure measurements performed under various test conditions.

Laser induced fluorescence was utilized as the means of flow visualization. An argon ion laser beam was expanded into a thin sheet of light which then sliced a vertical and lateral cross section of the flow field. Rhodamine dye was injected either from the model, or spread in the water upstream of it. This dye then became visible in the laser sheet, unobstructed by the rest of the flow field. The image was then recorded by a TV camera which trailed behind the model.

Pressure measurements were performed with a scanning valve and a specially designed pneumatic control system. An extensive number of ports were located on the model surface from which pressure information was gathered. This information was routed through an A-D conversion and stored in a computer.

Results obtained from the flow visualization experiments showed several clear trends. First, the size of the tip vortex increased as it developed downstream along the hydrofoil chord. Second, the size of the tip vortex increased and its center line became more detached as the angle of attack of the foil was increased. Third, the tip vortex experienced a size reduction and an outward center line shift as the speed (Reynolds Number) was increased. Additionally, secondary vortex structures including shear layer eddies were clearly visible in most flow visualization images.

Results obtained from the pressure measurements provided the information necessary to determine the effect that the tip vortex and secondary vortex structures had on the hydrofoil performance.

INTRODUCTION

Trailing and tip vortices are formed on a lifting surface with a finite span since the pres-

sure difference between the two sides of this surface must disappear at the tip. This fact means that spanwise pressure gradients of opposite signs exist on both sides of an aerofoil. These gradients induce an inward lateral flow on the suction side and an outward flow on the pressure side. When the two flows meet near the tip, a trailing vortex is formed which can cause severe problems in many applications of lifting surfaces. For example, the vortex trailing a helicopter blade will effect the performance of the blade that follows, trailing vortices produced by large planes pose a hazard to small planes passing through them, and the susceptibility of the low pressure region in the vortex core to cavitate can contribute to noise, vibration, and erosion in pump and marine propeller applications. As a result, many studies have been performed to investigate tip vortices, the associated scaling trends, and the various means for alleviating their effects. This subject was reviewed by Platzler and Sounders (1979) who provided a brief summary of about 150 reports. The majority of the literature is associated with the aircraft industry (about 80% according to Platzler and Sounders) and thus concentrates mainly on the wake behind a wing, particularly the far field phenomena. The region of cavitation inception, namely the rollup region near the tip, received much less attention, and very little is known about the flow structure there.

BACKGROUND

Several generations of models that describe the roll-up process of tip vortices have been developed over the years. The original simplified, inviscid, concentrated vortex model was developed by Lamb (1932) and modified by Batchelor (1964) who introduced the axial velocity to the analysis. Moore and Saffman (1973) proceeded further by incorporating the effects of viscosity. Most of the existing predictive schemes that relate the wing load distribution to the vortex structure are based on the work of Betz (1932) which was modified by Donaldson (1975). This theory uses the momentum equation of an inviscid fluid to relate the structure of the vortex sheet behind an isolated wing to the structure of a single fully developed vortex. Donaldson demonstrated that a single rolled-up vortex could not exist in the immediate vicinity of

the lifting surface and developed a criterion for the number of these vortices based on the load distribution. This technique was applied successfully by Yates (1974) to study the wake behind airplanes during take off and landing.

Extensive numerical studies were performed by Bilanin et al (1977) who claimed that Betz's model was satisfactory as long as the trailing vortices did not merge (straining of a vortex on another one). They suggested that substantial reduction of wake hazards could be achieved by proper generation of multiple vortices with wing flaps. This conclusion supported previous experimental observations by Corsiglia et al (1976). Other numerical studies were performed by Shamroth (1979), Chen and Wu (1983), and Mansour (1984). Most of these models, however, cannot describe the fine details of the roll-up process of the tip vortices and, as a result, do not provide a reliable tool for predicting the associated cavitation phenomena.

Some of the main parameters affecting the roll-up process have been identified by experimental studies. McCormick's (1962) cavitation studies, for example, led him to hypothesize that the vortex core radius depended strongly on the boundary layer near the lifting surface tip. This hypothesis was supported by Grow (1969) who measured the tangential velocity near the wing's tip and observed that boundary layer tripping resulted in a substantial increase in the core radius and a decrease in the tangential velocities. Detailed velocity measurements with hot wire anemometers were also carried out by Corsiglia (1973) who identified an inner rotational vortex core, in which the velocity grew with the radius, and an outer irrotational region. This work was followed by Francis' (1976) velocity measurements which demonstrated that the vorticity generated by the boundary layer in the pressure side of the wing migrated around the tip to the suction side. This vorticity and the external flow field induced an outward flow near the tip of the wing's suction side. Platzer and Sounders (1981) confirmed the existence of this outward flow with surface-oil-flow-visualization studies.

Large scale experiments were described by McCormick et al. (1968) who observed that the tangential velocity in the vortex core decreased and the core dimensions increased with increasing distance. The strength of this vortex was found to be much smaller than the predicted theoretical values (about 16 percent). Near-field velocity measurements in the wake of an aircraft were performed by Mertaugh et al (1977) who demonstrated the trend of the vorticity generated at the trailing edge of a wing to roll up into a single vortex core. Detailed surveys of the flow in the wake of rectangular and swept wings were carried out also by El-Ramly and Rainbird (1977). They demonstrated that within the range of experiments (up to 13 times the wing span), the vorticity shed at the wing's trailing edge was never fully rolled up to a single concentrated vortex. Their studies led them to conclude that the strength of the tip vortex depended strongly on the spanwise load distribution, or more accurately on rapid variation of the loading and the nature of boundary layer separation

near the tip. A comparison of their experimental results to the model developed by Betz demonstrated that the theoretical analysis over-estimated both the circulation and velocities in the trailing vortices.

As noted before, the majority of available information about tip vortices is related to the aircraft industry. Experiments with marine propellers, such as the work of Bosswell (1971), Chandrashekhara (1976) and Kuiper (1979) are scarce, most of them are limited to measurements of cavitation inception indices, and some (Kuiper, for example) include surface-oil-flow-visualization studies. Experiments with stationary hydrofoils were carried out by McCormick (1962), the effect of the sweep on hydrofoil cavitation was investigated by Crimi (1970), cavitation on a series of rectangular foils was studied by Billet (1975), and velocity measurements around elliptical wings were performed by Arndt et al. (1985). These studies demonstrated that the conditions for the onset of cavitation (and thus the pressure field) depended strongly on the Reynolds number and the hydrofoil's boundary layer, particularly separation.

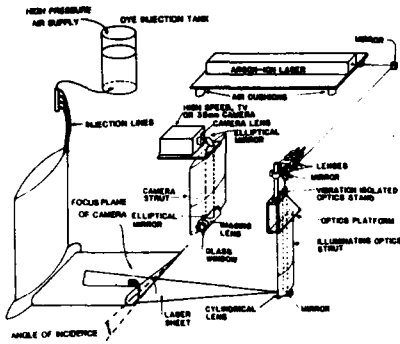
The severe problems associated with the tip vortices motivated the development of various techniques for alleviating their effects. As summarized by Platzer and Sounders (1979), these techniques included the addition of end-plates, splines, bulbs, honeycombs, contravanes, winglets, porous tips, and injection of liquid from various ports located near the tip. Some severe measures, such as the design of wing tip mounted propellers, are discussed by Loth (1984). Since most of these methods result in substantial reduction in performance, only a few can be applied to pumps and marine propellers. Some techniques, namely the roughened or bulbous tip, a porous hydrofoil (passive injection), and several forms of fluid injection were tested in a water tunnel by Sounders and Platzer (1981). They observed that each of these methods resulted in a substantial reduction in the cavitation inception indices and concluded that the roughened tip was the most effective method. This state of knowledge leads to the present project that focuses on detailed observations on the effects of the Reynolds Number, wing geometry, and incidence angle on the flow structure around the tip of a hydrofoil.

#### DESCRIPTION OF THE APPARATUS

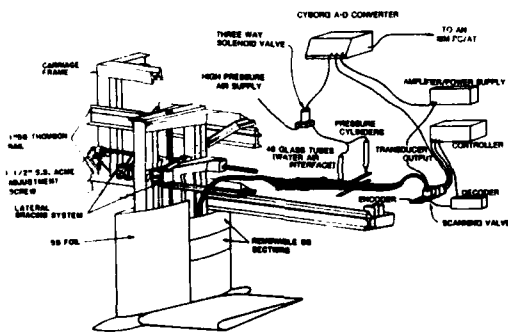
A functional description of the flow visualization system is presented in figure 1a, further details are provided in figures 1b,c and a photograph of the test facility is presented in figure 2. In this setup the 8 watt Argon Ion laser (out of which 3 watts are emitted at 514.5 nanometers) is located on the towing tank carriage, inside a cooled, dust free, vibration isolated container. The output beam is directed by several mirrors into the illuminating foil, expanded to a thin sheet by a cylindrical lens, while its thickness is reduced to about 0.5 mm with a long focal length spherical lens. Rhodamine dye can either be injected from a large number of ports located on the surface of the model, or by seeding the water in the tank shortly

before each run. The image created by the dye in the illuminated sheet is focused by a series of high resolution lenses and recorded either by a TV, 35mm, or a high speed camera. The magnification and resolution of the image is controlled by a proper choice of lenses, and the details in each frame can be varied by changing the concentration of the dye. In the present configuration the mag-

(1a)



(1b)



(1c)

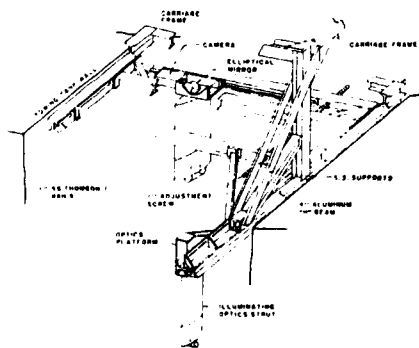


Fig. 1 a: A sketch of the flow visualization system  
 b: A schematic of the main support & pressure system  
 c: A schematic of the illuminating and collecting optics support mechanism

nification can be changed so that the area shown on the entire screen of the TV monitor ranges from 1 x 1 to 20 x 20 inches.

A special transversing system has been designed and constructed for the flow visualization studies to allow for maximum flexibility in testing various types of models. This setup consists of a main strut support that carries the model and two smaller struts, the first one directs the illuminating laser beam, and the second one contains the collecting optics that lead to the camera. All three components are shown schematically in figure 1a, the details of the main strut are displayed in figure 1b, and the smaller struts are presented in figure 1c. The model support can be transversed vertically and laterally, and once the proper location is reached, the entire system can be locked rigidly to a particular position. The entire structure is heavily supported and extremely rugged to minimize the vibrations. The illuminating strut is located six inches from the wall of the towing tank and can be transversed axially (motionwise) so that any desired section on and behind the model can be illuminated. This strut is composed of two overlapping hydrofoils, and its length can be changed by extending the inner foil from the outer shell. The strut containing the periscope that leads to the camera usually trails about 10 feet behind the model. It is also composed of two overlapping parts and mounted on a transversing system that allows motion both in the axial and lateral direction. The axial movement of this periscope can be coupled with the illuminating foil by a lead screw in order to keep the illuminated section focused on the camera when the light sheet is shifted. This feature prevents the need to refocus the camera lens whenever the observed section is changed. If necessary, the location of the two struts can be switched in order to slice the flow field axially and observe the image laterally. The output from the TV camera can be observed on a stationary monitor and recorded on a high resolution video recorder.

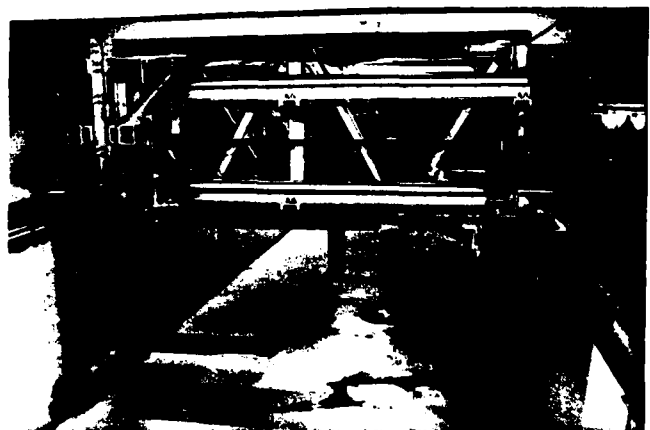


Fig. 2 Towing tank test facility

Figure 1b also contains a description of the pressure measurement system to which the output of the taps on the surface of the model are connected. The plastic tubes leading from the test body are connected to horizontal capillary glass tubes positioned normal to the direction of carriage motion. Each tube contains an air-water interface, so that the lines downstream contain only air. These lines are connected to a scanning valve that contains a pressure transducer. Since the scanning rate of the valve is slow, it cannot cover more than 10 ports during a single run. Therefore, the system requires a mechanism that freezes the pressure in the lines until the valve completes the entire cycle. This system consists of a clamp, two gas cylinders, a solenoid valve that leads to a source of high pressure gas, and a central system. Before the towing tank carriage starts slowing down, an "electronic eye" activates the solenoid valve which directs the high pressure supply to the cylinder. The clamps then squeeze the plastic tubes and freeze the pressure in the lines leading to the scanning valve. After the carriage is brought to rest, the valve is activated, the output of the transducer is digitized and fed into a computer. When the scanning process is completed, the clamp is released and the system is ready for new measurements. This setup has been calibrated carefully, and the maximum error was found to be less than one percent.

## RESULTS

Several samples of the flow structure around the tip of the hydrofoil are presented in figures 3-6. These photographs are organized in three sequences that demonstrate the dependence of the flow geometry on the location along the chord (Fig. 3), the freestream velocity (Fig. 4), and the angle of incidence (Fig. 5). The existence of several secondary flow structures, which will be discussed later, can also be observed in some of the photographs, particularly in figures 3a, 5a, and 6. A large number of such video images have been recorded and analyzed during the course of the present study. The size of the tip vortex is presented in figure 7 and the distance (horizontal and vertical) between its center and the wing tip is summarized in figures 8 and 9. Several clear trends become readily evident from the results. Firstly, the diameter of the vortex, and the location of its center grew with the distance from the leading edge. As a matter of fact, some of the lines in figures 7-9 suggest that the growth rate is almost linear. Secondly, an increase in the freestream velocity resulted in a substantial reduction in the tip vortex size and an outward shift in the location of its center line. This scaling trend is demonstrated both in figure 4 and in the sequence of measured dimensions.

For example, at an incidence angle of  $8^\circ$  and  $x/c = 1$ , the vortex diameter changed from  $D/C = .075$  to  $D/C = .063$  when the free stream velocity was increased from 1 ft/sec to 5 ft/sec. At  $5^\circ$  incidence, and  $x/c = 0.69$  the diameter decreased from  $D/C = .027$  at 1 ft/sec to  $.020$  at 5 ft/sec. This trend has a direct impact on the conditions for the onset of tip vortex cavitation since the

pressure in the core of a Rankine vortex,  $P_c$ , can be expressed as

$$P_c - P_\infty = \frac{\rho \Gamma^2}{2 r^2 r_c^2} \quad (1)$$

where  $r$  is the radius of the core,  $\rho$  is the liquid density,  $\Gamma$  is the circulation and  $P_\infty$  is the pressure at infinity.  $\Gamma$  of a wing can be directly related to the lift coefficient,  $C_L$ , by

$$\Gamma \propto \frac{1}{2} v C C_L \quad (2)$$

The equal sign is replaced by a proportionality relationship since the tip vortex is not fully developed and as a result some of the wing circulation is still outside of the main vortex. Thus:

$$C_{pc} = \frac{P_c - P_\infty}{\frac{1}{2} \rho v^2} \propto - \frac{C^2 C_L^2}{4 r^2 r_c^2} \quad (3)$$

If we assume that the onset of cavitation occurs when  $P_c$  is equal to the vapor pressure,  $P_v$ , then the cavitation inception index,  $\sigma_i$ , defined by

$$\sigma_i = \frac{P_c - P_v}{\frac{1}{2} \rho v^2} \quad (4)$$

is related to the pressure coefficient by

$$\sigma_i + C_{pc} = \frac{P_c - P_v}{\frac{1}{2} \rho v^2} = 0 \quad (5)$$

or

$$\sigma_i \propto \frac{C^2 C_L^2}{r_c^2} \quad (6)$$

Thus, a reduction in the radius of the core results in an increase in the values of  $\sigma_i$ . This scaling trend of the tip vortex radius<sup>1</sup> was already suspected by McCormick (1962, 1968) and an increase in the inception indices with the velocity was observed by Sounders and Platzer (1981) and Arndt et al. (1985).

Thirdly, an increase in the incidence angle resulted in a substantial increase both in vortex size and its distance from the surface. This trend is evident by comparing the photographs in figure 5 and the plotted data in figure 7-9. Since the incidence angle affects the dimensions and extent of the (laminar) separation zone on the foil (particularly at high incidence) the vertical distance between the vortex center and the surface may be related to the extent of separation. This relationship will be investigated in the future, when the chordwise cross section of the flow near the tip will be visualized simultaneously with the transverse sections.

An attempt was made to incorporate the data in figures 7-9 to a single empirical relationship. The resulting expression for the vortex diameter

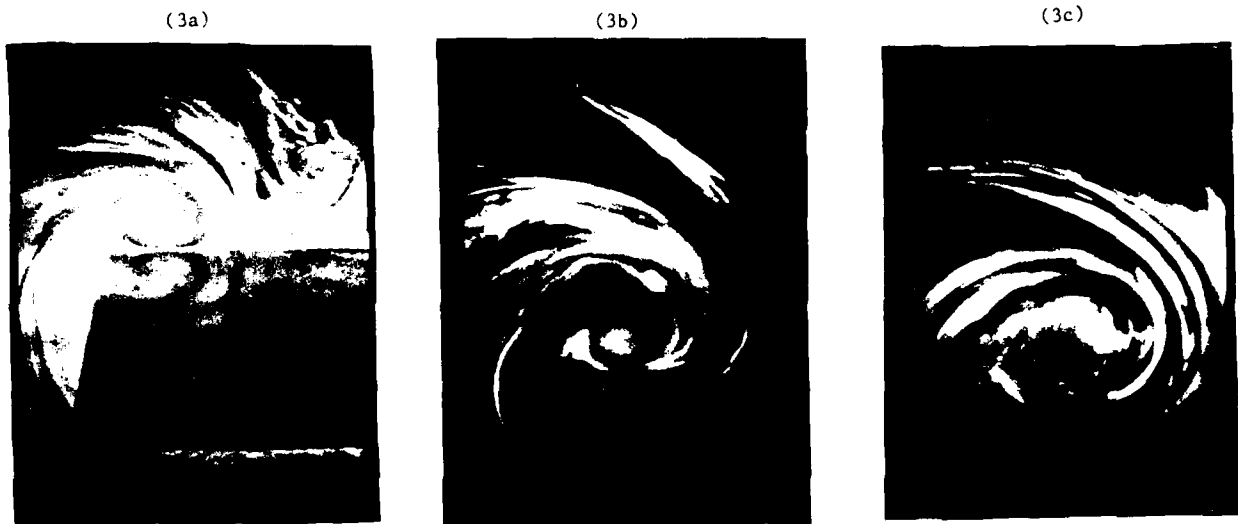


Fig. 3 A sequence of photographs demonstrating the development of a tip vortex at  $5^\circ$  incidence and velocity = 1.5 ft/s  
 (a)  $x/c \approx 0.69$  (b)  $x/c = 0.92$  (c)  $x/c = 1.02$

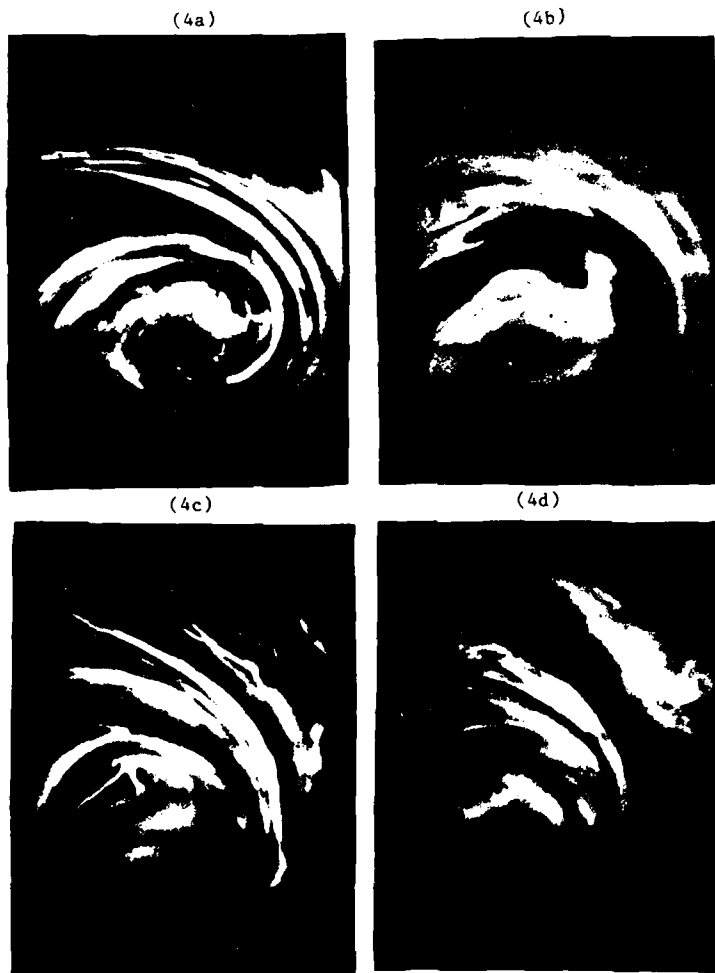


Fig. 4 A sequence of photographs demonstrating the dependence of the vortex size on the free stream velocity just downstream of the trailing edge at  $5^\circ$  incidence. The free stream velocities are:  
 (a) 1.5 ft/s (b) 3.0 ft/s  
 (c) 6.0 ft/s (d) 8.0 ft/s

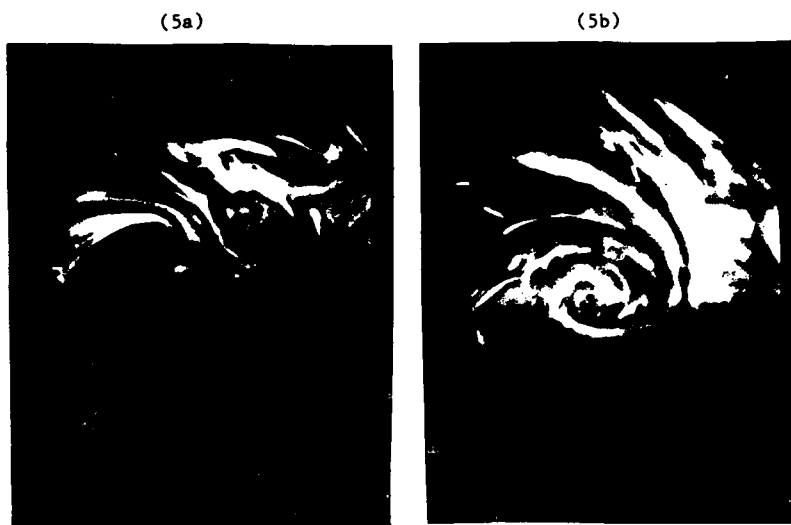


Fig. 5

A sequence of photographs displaying the dependence of a tip vortex on the incidence angle. The velocity is approximately 2.6 ft/sec and the location is  $x/c = 0.82$   
 (a) incidence angle =  $2^\circ$   
 (b) incidence angle =  $5^\circ$

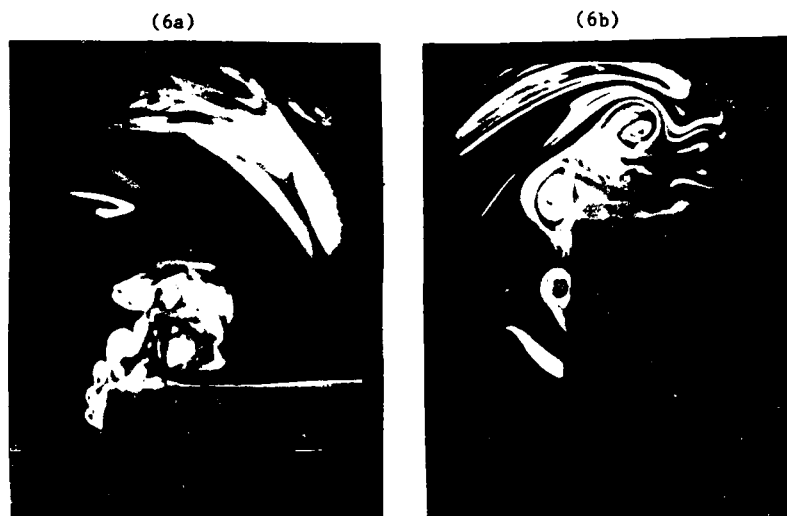


Fig. 6

Primary & secondary flow structures at:

- (6a) cross section ( $x/c$ ) = 0.92  
 angle of incidence =  $5^\circ$   
 speed = 0.4 ft/sec.
- (6b) cross section ( $x/c$ ) = 0.46  
 angle of incidence =  $8^\circ$   
 speed = 0.2 ft/sec

appears to be

$$D/C = F(x/c, \alpha, Re_c) = G(\alpha, x/c)H(Re_c, x/c) \quad (7)$$

where:

$$G(\alpha, x/c) = 0.9(x/c) \{2.1 - 2(\alpha + 1)^{-0.5}(x/c)^{-1}\}$$

$$H(Re_c, x/c) = [0.75 + 1.45 \cdot 10^3(x/c)^{0.6}(Re_c)^{-0.6}]$$

where  $\alpha$  is the incidence angle and  $Re_c$  is the Reynolds  $VC/\nu$ . A comparison between this expression and measured vortex size, is presented in figure 10. Here, the values of  $D/C$  are plotted against a modified horizontal scale defined by the presently obtained empirical relation. The agreement appears to be much better in the lower range of  $F$ , that is higher speeds and lower incidence angles. Finally, as was already noticed before, the region near the tip contains several secondary flow structures. Figures 3a and 5a display counter rotating vortices to the right of the main structure. This secondary vortex appeared first in the upstream regions to

the left of the tip vortex, and then seemed to wrap around the main vortex until it reached the surface. Other secondary structures that appear to be shear layer turbulent eddies are demonstrated in figure 6. These vortices were mostly visible at low speeds and disappeared probably because of the slow recording rate of the video camera at higher velocities. Future studies with high speed photography and shorter exposure times will clarify their role at higher speeds. The effect of these vortices on the size and strength of the main structure will also be verified in the future when the wing geometry at the tip will be modified to a rounded shape.

The spanwise distributions of the surface pressure coefficient for a velocity of 5 ft/sec at various incidence angles and chordwise location ( $X/c$ ) are presented in figure 11. Samples of the chordwise distribution are also presented in figures 12 and 13. A few trends, some of them surprising at first, can be noticed from these results. Firstly, at  $0^\circ$  and  $2^\circ$  incidence there is

a dip in the spanwise distribution around  $Z/S = 0.9$  ( $Z$  being the distance from the root of the foil and  $S$  is the semi span). This dip disappears at higher incidence angles. The explanation to this phenomenon exists in figure 3a and also in 5a that display the secondary structures on the hydrofoil. These counter rotating vortices are much more dominant at lower incidence angles and as a result their effect on the pressure field is noticeable only at  $0^\circ$  and  $2^\circ$ . Unfortunately, the available literature does not provide any measured pressure distributions at low incidence on the NACA-66 hydrofoil close to the tip. As a result the presently observed phenomenon could not be compared to other results. However, discussions with T.J. Mueller revealed that he measured negative lift coefficients on the NACA-66 foil at an incidence angle of  $1^\circ$ . Thus, traces of a counter rotating tip vortex should be expected at these low angles. Secondly, another pressure dip which is probably associated with the main tip vortex exists beyond  $Z/S = 0.95$  on all the distributions of figure 11 irrespective of the incidence angle. This dip is also demonstrated in figure 12 particularly close to the trailing edge, mainly at  $Z/S = 0.96$  but also at  $Z/S = 0.89$  and  $0.94$ . Note that the lowest value of  $C_p$  on the hydrofoil is related to the tip vortex (by comparing the results in figures 12a-12c), and as a result this region which is mostly susceptible to cavitation inception. Thirdly, at incidence angles beyond  $5^\circ$  (Figures 12 and 13) the pressure distribution provides an evidence of boundary layer separation at  $X/C < 0.2$ . The indications of a separation zone still persist close to the hydrofoil's tip (fig. 12c), but the flow becomes three dimensional, and a sharp spanwise pressure gradient in the minimum pressure is clearly evident (see also figure 11). Finally, as shown in figure 13, the root of the hydrofoil affected the pressure distribution, particularly the minimum value of  $C_p$ , mostly up to  $Z/S = 0.2$ . Traces of these root effects are less clear but still evident also in figure 12a.

#### SUMMARY AND CONCLUSIONS

Flow visualization of the rollup process of tip vortices on a rectangular hydrofoil was performed in a towing tank by utilizing laser induced fluorescence. The results demonstrated that the tip vortex size increased with the distance from the leading edge of the foil and with the incidence angle. An increase in the free stream velocity, however, resulted in a reduction in the vortex diameter and in an outward shift in the location of its center. Observations of the fine details of the flow made possible with the experimental setup revealed several secondary structures including a counter rotating vortex on the surface of the foil, and shear layer eddies generated near the wing's tip and entrained by the main vortex. Surface pressure measurements demonstrated the effect of the secondary vortex structures at low incidence. They also revealed that the region with the lowest surface pressure was located near the trailing edge close to the wing tip where the tip vortex was developing.

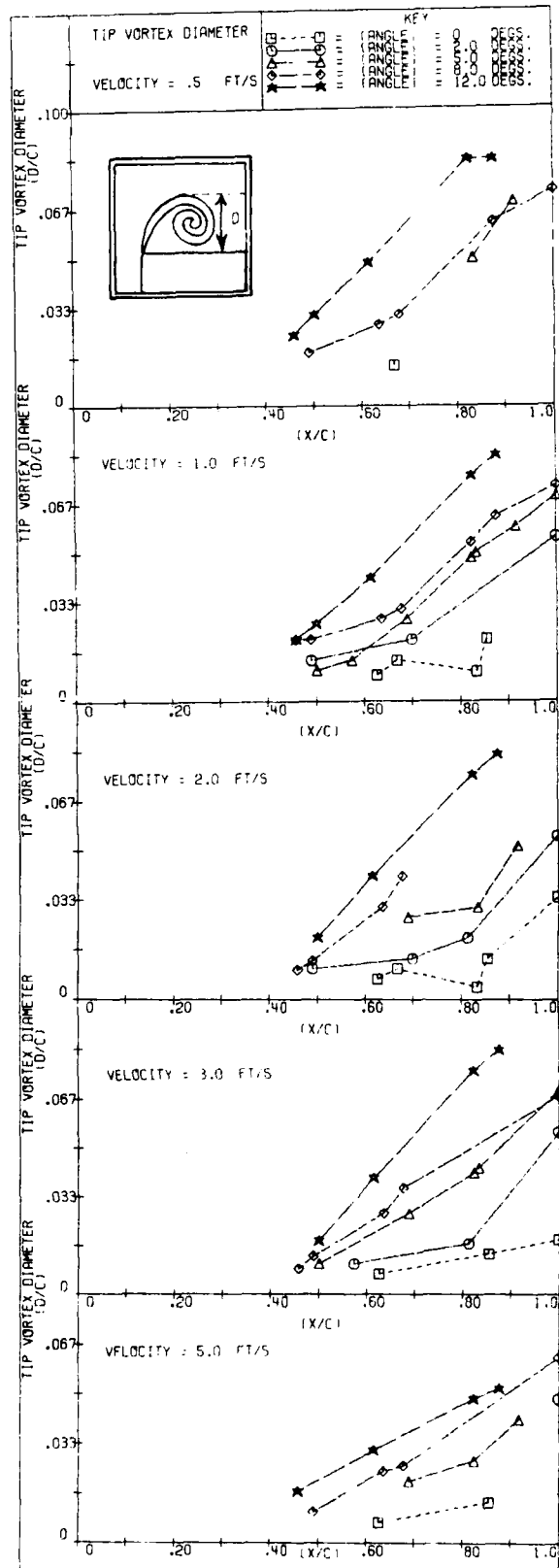


Fig. 7 Measured dimensions of the tip vortex

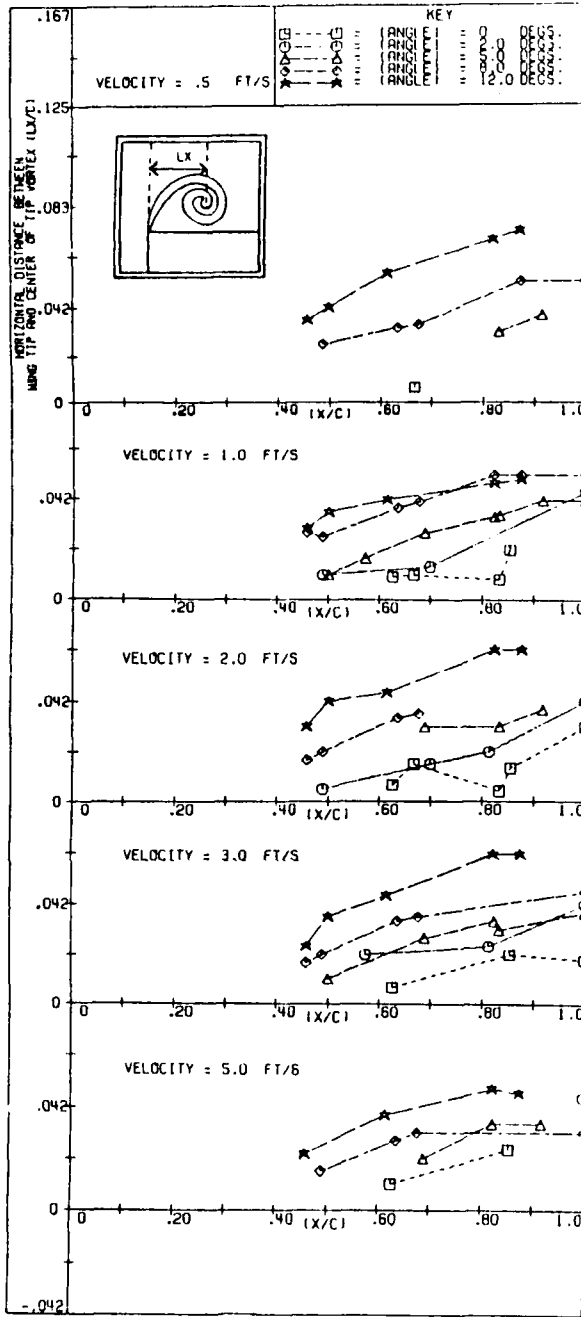


Fig. 8 Horizontal distance between the wing tip and the vortex center

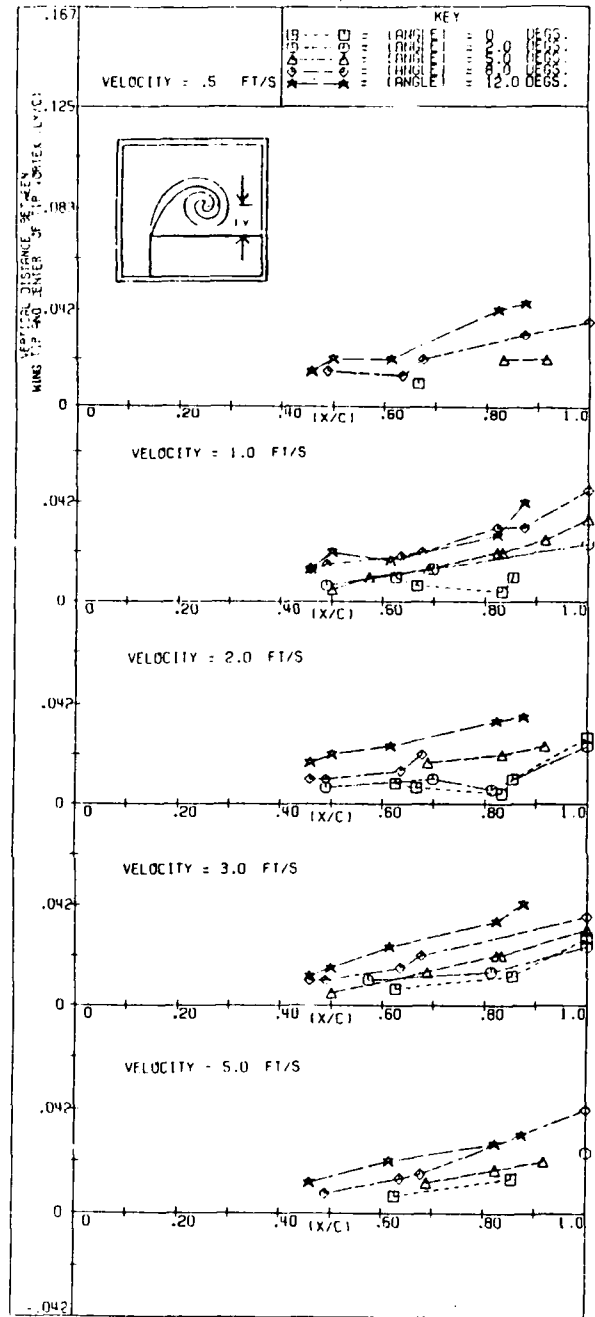


Fig. 9 Vertical distance between the wing tip and the vortex center

**ACKNOWLEDGEMENT**

This work was supported by the Naval Sea Systems Command, General Hydrodynamic Research Program, administered by the David Taylor Naval Ship Research and Development Center under contract number N00014-85-K-0106.

The authors would like to thank Jim Craig for his help in constructing the test body, Tom Cooper and Ken Ward for their help in constructing the test facility.

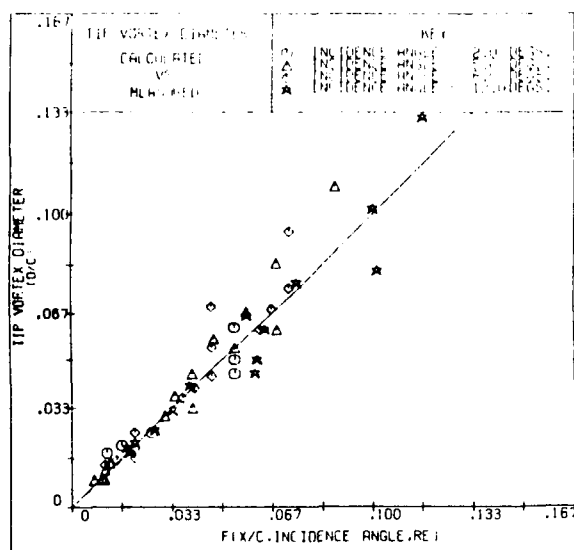


Fig. 10 A comparison between the empirical expression for the tip vortex diameter and measured results.

#### REFERENCES

- Arndt, R.E.A., Higuchi, H., Quadrelli, C.S., (1985), "Tip Vortex Cavitation", ASME Cavitation and Multi-Phase Flow Forum, FED - Vol. 23.
- Batchelor, G.R., (1964), "Axial Flow in Trailing Line Vortices", Journal of Fluid Mechanics, Vol. 20, Part 4, pp. 645-658.
- Betz, A., (1933), "Behavior of Vortex Systems", NACA TM 713, (Translated from ZAMM, Vol. XII, 3, June 1932).
- Bilanin, A.J., Teske, M.E., Williamson G.G., (1977), "Vortex Interactions and Decay of Aircraft Wakes", AIAA Journal, Vol. 15, No. 2, pp. 250-260.
- Billet, M.L., (1975), "Surface and Tip Vortex Cavitation on a Family of Rectangular Foils", Applied Research Laboratory, Pennsylvania State University.
- Bosswell, R.J., (1971), "Design, Cavitation Performance, and Open-Water Performance of a Series of Research Skewed Propellers", NSRDC, Rep. No. 3339.
- Chandrasekhara, N., (1976), "Analysis of Tip Vortex Cavitation Inception of Hydrofoils and Propellers", Hamburgische Schiffbau-Versuchsanstalt GmbH.
- Chen, Z.L., Wu, J.M., (1983), "Jet Wing Vortex Lattice Theory With Nonlinear Wake and Tip Flows", AIAA Paper No. 83-0263.
- Corsiglia, V.R., Schwind, R.K., Chigler, N.A. (1973), "Rapid Scanning Three Dimensional Hot Wire Anemometer Surveys of Wing-Tip Vortices", Journal of Aircraft, Vol. 10, No. 12, pp. 752-757.
- Corsiglia, V.R., Rossow, V.J., Clifone, D.L., (1976), "Experimental Study of the Effect of Span Loading on Aircraft Wakes", Journal of Aircraft, Vol. 13, No. 12, pp. 968-973.
- Crimi, P., (1976), "Experimental Study of the Effects of Span Loading and Cavitation", Journal of Hydrodynamics, Vol. 4, No. 1.
- Donaldson, C. du P., Bilanin, A., (1975), "Vortex Wakes of Conventional Aircraft", AGARDograph 204.
- El-Ramly, Z., Rainbird, W.J., (1977), "Flow Survey of the Vortex Wake Behind Wings", Journal of Aircraft, Vol. 14, No. 11, pp. 1102-1108.
- Francis, M., (1976), "A Wind Tunnel Investigation of the Formation of a Trailing Vortex", University of Colorado, Ph.D. Thesis, Aeronautical Engineering.
- Grow, T.L., (1969), "Effects of a Wing on Its Vortex", Journal of Aircraft, Vol. 6, No. 1.
- Kuiper, G., (1979), "Modeling of Tip Vortex Cavitation on Ship Propellers", 4th Lips Propellers Symposium, Drunen, The Netherlands.
- Lamb, H., (1932), Hydrodynamics, Cambridge, also Dover ed., New York, 1945, pp. 591-592.
- Loth, J.L., Loth, F. (1984), "Induced Drag Reduction with Wing Tep Mounted Propellers", AIAA-84-2149.
- Mansour, N.N. (1984), "Numerical Simulations of the Tip Vortex Off a Low Aspect Ratio Wing at Transonic Speed", AIAA-84-522.
- McCormick, B.W. Jr., (1962), "On Cavitation Produced by a Vortex Trailing from a Lifting Surface", Journal of Basic Engineering, pp. 369-379.
- McCormick, B.W., Tangler, J.L., Sherrieb, H.E., (1968), "Structure of Trailing Vortices", Journal of Aircraft, Vol. 5, No. 3, pp. 260-267.
- Mertaugh, L.J., Damania, R.B., Paillet, F.L., (1977), "An Investigation of the Near-Field Wake Behind a Full Scale Test Aircraft", Journal of Aircraft, Vol. 14, No. 9, pp. 894-902.
- Moore, D.W., Saffman, P.G., (1973), "Axial Flow in Laminar Trailing Vortices", Proc. Royal Soc. London, A. 333, pp. 481-508.
- Mueller, T.J., private communication
- Platzer, G.P., Sounders, W.G., (1979), "Tip Vortex Cavitation Delay With Application to Marine Lifting Surfaces, A Literature Survey", DTNSRDC, Rep. No. 79/051.
- Shamroth, S.J., (1979), "A Viscous Flow Analysis for the Tip Vortex Generation Process", NASA CR 318.

27. Sounders, W.G., Platzer, G.P., (1981), "Tip Vortex Cavitation Characteristics and Delay of Inception on a Three Dimensional Hydrofoil", DTNSRDC, Rep. No. 81/007.
28. Yates, J.E., (1974), "Cavitation of Initial Vortex Roll Up in Aircraft Wakes", Journal of Aircraft, Vol. 11, No. 7, pp. 397-400.

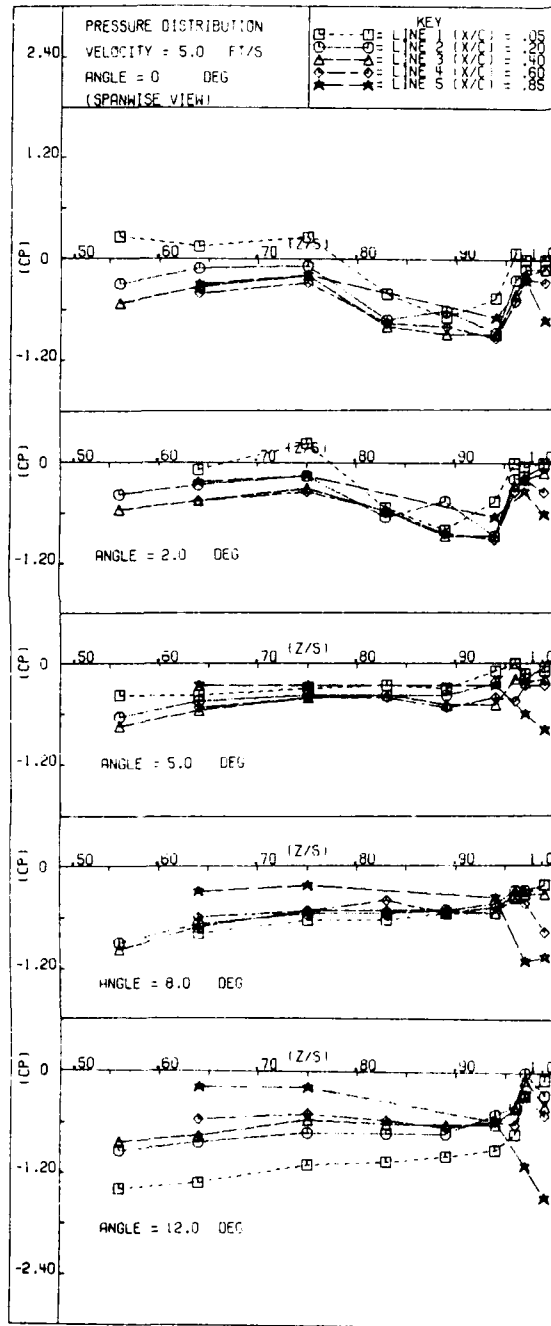


Fig. 11 Spanwise distribution of the pressure coefficient on the hydrofoil

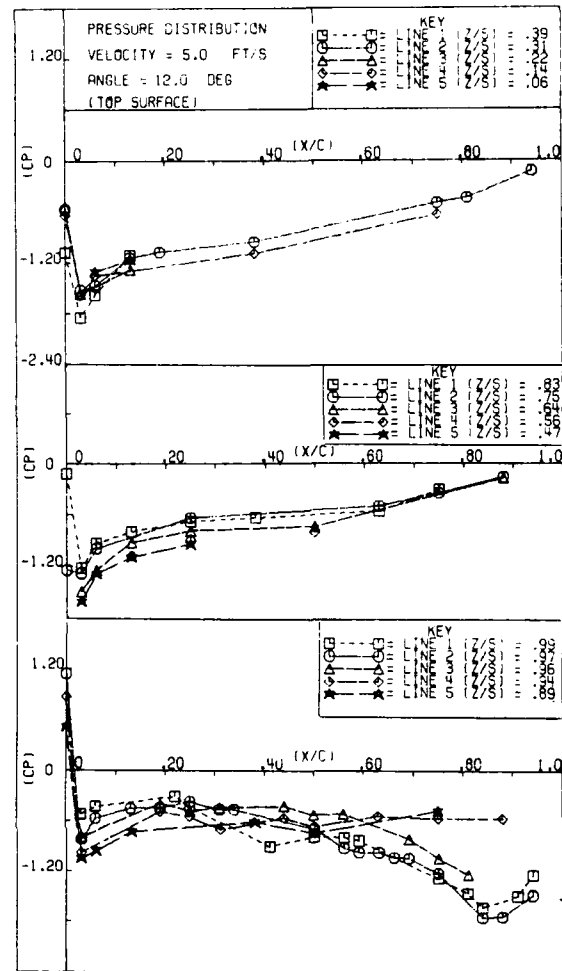


Fig. 12 Chordwise distribution of the pressure coefficient at a 12 degree incidence angle

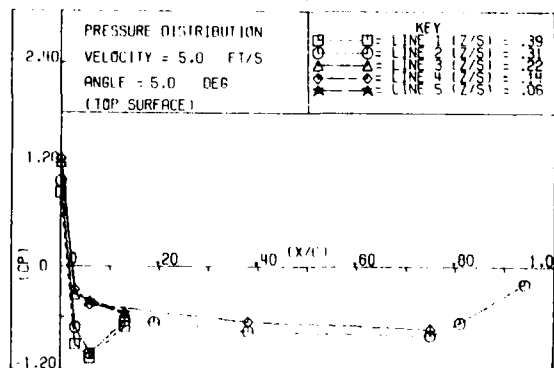


Fig. 13 Chordwise distribution of the pressure coefficient at a 5 degree incidence angle.

VISUALIZED LARGE-SCALE MOTIONS IN THE  
TURBULENT WAKE BEHIND A THIN  
SYMMETRICAL AIRFOIL.

Hiroshi Mackawa, Tsutomu Nozaki,  
Masaki Tao, and Shinichiro Yamasaki  
Faculty of Engineering, Kagoshima  
University, Kagoshima 890, JAPAN

Abstract

The flow structure in the turbulent wake behind a thin symmetrical airfoil was observed by means of a novel smoke wire technique. The smoke emission was conditioned by the detection of low-speed lumps of fluid in the turbulent boundary layer near the trailing edge. The flow visualization pictures reveal that the structure in the near wake flow is affected by the coherent motions in the turbulent boundary layer and that the flow field contains the large-scale motions with roller-like structure at the outer region of the wake and the smaller-scale vortical motion near the wake center. The large-scale motion in the wake is explained by a model of a pair of vortex rings which is similar to that of the coherent motion in the turbulent boundary layer.

1. Introduction

Turbulent wake from the turbulent boundary layers has been investigated hitherto. Turbulence quantities in the near wake of a thin flat plate were measured by Chevray and Kovasznay(1969), Toyota and Hirayama(1979) and calculated by Launder et al.(1974), Pope and Whitelaw(1976), however, few investigations of the organized motion in such a flow has been done. On the other hand, the organized motions in the turbulent boundary layer and in the fully developed turbulent wake have been investigated enormously. But the mechanism of the ordered motions has not been well understood yet. There have been many controversial models for the understanding of the turbulence. The motivation of the present investigation is to research the mechanism which

is common to the organized motion in the boundary layer and that in the wake from a viewpoint of the fundamental mechanism of the turbulence. Therefore, we examined the wake flow from the turbulent boundary layers, which is a non-equilibrium relaxation flow between an upstream equilibrium flow and another downstream self-preserved flow. This paper aims to understand the structural development of the turbulent wake from the turbulent boundary layers : how does the turbulent structure produced in the wall shear flow change along the free shear flow and affect the structure of the wake? The Lagrangian observation is no less important than the Eulerian measurement for understanding the turbulent structure. The evolution of organized structure in the turbulent wake can be observed by means of the flow visualization technique with a conditional sampling.

2. Experiments

2.1 Apparatus

The experiment was carried out in a low-speed wind tunnel with a 50cm x 50cm cross-section. The turbulent intensity in the free stream was 0.4 %. A wood symmetrical airfoil was used, whose dimensions are 180cm chord, 50cm span and 1cm maximum thickness. The leading edge profile is an ellipse whose long axis is 10cm and short axis is 1cm and the trailing edge angle is  $\tan^{-1}(1/80)$ . The airfoil was mounted in the wind tunnel. Tripping wires, 3mm in diameter, were used as turbulence generators installed at 46 cm from the leading edge. The Reynolds number based on the boundary layer momentum thickness  $\theta_0$  at the trailing edge

was  $\theta_0 U_0 / \nu = 735$ . Measurements of the turbulence were taken with a single channel constant temperature hot-wire anemometer. The hot-wires were made of tungsten wire of 0.005mm in diameter and 1.25mm in length (DANTEC miniature probe 55P11). Two dimensional turbulent components were measured by a two-color Laser Doppler Anemometer system (DANTEC: Optical Unit 55X, Counter Processor 55L90a, Frequency Shifter 55N10) and Minicomputer (DATARAM: Minicomputer System DEC: Terminal VT240). The measuring volume is 0.09mm in diameter and 1.1mm in length. A mixture of glycerin and water was used as the seeding liquid and injected from the inlet of the wind tunnel. The free stream velocity was 2.2-2.4m/s. The origin 0 is situated at the midspan of the trailing edge. The x-axis is taken in the streamwise direction, the z-axis is in the spanwise direction and the y-axis is normal to the x-z plane as shown in Figure 1.

## 2.2. Flow visualization system

Flow aspects were visualized by the smoke of paraffin liquid emitted from a heated nickel-chrome wire of 0.2mm in diameter. The smoke wires were suspended in the x-z plane and x-y plane as shown in Figure 2. One or two hot-wire probes were located in the turbulent boundary layer and situated at  $X_{hw}$  upstream of the smoke wire and at  $Y_{hw}$  above the airfoil surface. Those hot-wires can detect the low-speed fluids in the turbulent boundary layer. When the low-speed fluid pass the hot-wire, a trigger signal is generated. The trigger signal is delayed through an electric retardation circuit and turns on a smoke generation switch. The retardation circuit can make various delayed times. Velocity signals of the hot-wire were recorded on a computer memory during the time before and after the trigger signal was produced. The smoke lines were illuminated with a xenon tube which could be triggered several times successively. The pictures of smoke were taken in two directions simultaneously, that is, from side and downstream directions or from above and downstream directions.

## 3. Experimental results

First the two-dimensionality of the flow was checked by measuring the conventional mean velocity

and the turbulence level profiles at different span positions, and the flow was uniform over 75% at the trailing edge and over 70% of the span at the last downstream station,  $x=80\text{cm}$ , where wake measurements were taken. No detectable periodic components or stationary secondary flows were found in the boundary layer near the trailing edge by a wave analyzer measurement.

The characteristics of the turbulent boundary layer near the trailing edge ( $x=-5\text{cm}$ ) were the following: conventional thickness ( $u/U_0=0.99$ )  $\delta=4.5\text{cm}$ , momentum thickness  $\theta=0.41\text{cm}$  and shape parameter  $H=1.4$ . The mean velocity profile and the distribution of intensity of velocity fluctuation at  $x=-5\text{cm}$  are shown in Figure 3. They show the typical turbulent boundary layer. At the trailing edge, the friction velocity is found to be  $u_* / U_0 = 0.043$ . This value is obtained by using Clauser's logarithmic law. The nondimensional thickness of the trailing edge is  $u_* y / \nu = 2$ ; much smaller than the viscous sublayer.

Figure 3 presents the ordinary mean velocity and the velocity fluctuation distributions in the near wake. Symmetry of the distributions is found to be excellent. The flow of the center portion changes rapidly but the outer portion remains the same as the boundary layer at the trailing edge. Figure 4 shows the y components of mean velocity in the near wake measured by LDA. The mean flow toward the wake center can be seen just behind the trailing edge. But the magnitude of y components decreases rapidly at the far downstream station. The velocity profile begins to change to a more "wakelike" appearance beyond  $x=15\text{cm}$ , the wake begins to widen only very gradually. The absence of any significant pressure gradient in the wake is verified by the constancy of the momentum thickness in the downstream direction. Figure 5 shows the distribution of mean velocity defect at the far downstream distances,  $x=60\text{cm}$ ,  $x=70\text{cm}$  and  $x=80\text{cm}$ , where  $b_{1/2}$  represents half the width at half depth of the wake. The self-similar mean velocity profile can be verified. The values of the half-width of the wake are plotted in Figure 6.

Before taking a conditional picture, the frequency of the detection of low-speed fluid in the turbulent boundary layer was examined at

various threshold voltage levels of a hot-wire. We used the frequency of about one time per 30 second.

Figure 7 shows the smoke picture in the x-y plane. The hot-wire probes are located at  $X_{hw}=1\text{cm}$  and  $Y_{hw}=\pm 0.5\text{cm}$ . The smoke is emitted from the last left smoke wire and other wires refer the length scale of  $x=5\text{cm}$  in breadth. A condenser of capacity  $870\mu\text{F}$  was charged up to 180 Volts and many smoke streaks could be emitted. The inhomogeneous large-scale motions, in the scale of order  $\delta$ , can be seen in the outer layer of wake, and which is inclined to the y axis. We can observe the streaks descending and ascending at the forward and backward portions of the large-scale motion, which implies that the large-scale motion has the circulation around itself in the x-y plane. The nonturbulent irrotational flow can be seen between the large-scale motions in the interface layer. Because the low-speed lumps were detected on both upper and lower sides simultaneously, such motions can be seen on both sides in the outer layer of the wake. No holes of vacant smoke can be seen near the wake center. The flow in the inner layer is more homogeneous than the outer layer, but the small-scale vortical motions are observed near the position of maximum turbulent intensity. Figure 8 shows the side and end views of the flow near the trailing edge. The hot-wires are located apart at the distance of  $z_{u*}/v=40$  from the smoke wire. The flow pattern is similar to that of the turbulent boundary layer. The low-speed fluids are lifting up on both sides and the z components of velocity exist.

Figure 9 shows the low-speed streaks in the inner layer of the near wake. The smoke wire is suspended parallel to the trailing edge, where  $X_s=2\text{cm}$  and  $Y_s=0.57\text{cm}$ . Hot-wires are placed at  $Y_{hw}=0.7\text{cm}$ . From the end view the low-speed streak near the hot-wire can be seen lifting up and other streaks are also lifting up. Figure 9 also represents the hot-wire signals before and after the time of trigger signal which is indicated by the arrows in the figure. The sampling interval was 1ms. Figure 10 shows the flow lifting up near the hot-wire, where the smoke wire is located at  $Y_s=1.1\text{cm}$  in the z direction and the hot-wire is

located at  $Y_{hw}=0.7\text{cm}$ .

Figures 11,12,13,14 and 15 are the pictures of one smoke line with multiple exposure. A smoke line is generated by discharging a condenser of capacity  $870\mu\text{F}$  charged up to 300 Volts. A hot-wire is located in the boundary layer of the upper surface, at  $X_{hw}=2.4\text{cm}$  and  $Y_{hw}=8\text{mm}$ . In order to understand the mechanism of the organized motion in the wake, we use a model which was presented in the turbulent boundary layer flow by Kobashi and Ichijo(1984). Figure 16 is a schematic view of the large-scale motion near wake. Figures 11 and 12 are the side view pictures, where a smoke wire is suspended in the y direction through the plate. The photographs of a line smoke were taken by the successive stroboscope light whose flashing interval was 27ms. The last right smoke line arrives at the self-preserved region of the wake. We can observe the large-scale motion in the outer layer which has a transverse vorticity. The smoke streak lifted up in the inner layer of the boundary layer begins to descend in the wake and is merged into the neighborhood of the wake center. On the other hand, the smoke streak in the outer layer is transported with the large-scale organized motion. Some of the pictures show the streak of the opposite side to be transported toward the wake center as shown in Figure 11. Figure 12 shows a rather small coherent motion, but represents the existence of the circulation in the x-y plane. Figures 13 and 14 are the top view pictures, where the interval of a stroboscope light is 55ms. A smoke wire is located at  $Y_s=3.9\text{cm}$  in Figure 13 and at  $Y_s=2.2\text{cm}$  in Figure 14. The low-speed streak behind the hot-wire can be seen and two pairs of high-speed and low-speed streaks exist on both side. The smoke line is contracted in the z direction in Figure 14. We can realize the large-scale motion inducing the z components of velocity from the fact that the streaks are contracted in the spanwise direction. On the other hand, Figure 15 shows the contrary structure, that is, the high-speed streak behind the hot-wire and two low-speed streaks on both sides.

These facts suggest that the large-scale motion in the wake has the structure of a contra-rotating eddies found by Grant(1958) and another

double-roller eddies found by Payne and Lumley(1967). We assume the existence of a pair of vortex rings as illustrated in Figure 16, which have a Grant type and a Payne type structures at the front head and at the tail and the circulation in the x-y plane. The pair vortex rings in the boundary layer lie in the inclined plane at a small angle to the wall and generate a bursting mechanism by stretching in the neighborhood of the wall. They are ejected in the near wake and located in the outer layer of the wake, where their top roof is at the interface layer and the bottom is near the position of maximum turbulent fluctuation in the wake as illustrated in Figure 16. They are inclined at a large angle to the wake center. The structures of the wake are consisted by them.

#### 4. Conclusions

The wake behind a symmetrical thin airfoil was observed by means of a smoke wire technique with a conditional sampling. The counter rotating roller-like vortical motion exists in the wake, which is an inhomogeneous large-scale motion. On the other hand, the smaller-scale motion is homogeneous near the wake center. The organized motion generated in the turbulent boundary layer develops in the wake and has the counter rotating roller-like structure like a Grant type at the front head and a Payne type at the tail. The bottom of large-scale motion is near the position of maximum turbulent fluctuation. These are explained by using a model of the evolution of a pair of vortex rings in the turbulent boundary layer presented by Kobashi and Ichijo.

#### References

1. Chevray, R. and Kovaszny L. S. G. 1969: Turbulent measurements in the wake of a thin flat plate. AIAA J. 7-7, 1641-1643.
2. Grant, H.L. 1958: The large eddies of turbulent motion. J. Fluid Mech., 4, 149-190.
3. Kobashi, Y. and Ichijo, M. 1984: Wall pressure fluctuation and its relation to the structure of turbulence of a boundary layer. Biennial Symp. Turbulence, Missouri-Rolla.
4. Launder, P. E. ; Reece, G. J. and Rodi, W. 1975: Progress in the development of a

Reynolds-stress turbulence closure. J. Fluid Mech. 63-3, 537-566.

5. Toyota, K. and Hirayama, N. 1979: Study on the near wake of a flat plate. Trans. of JSME (in Japanese),40-326, 3021-3028.
6. Payne, F.R. and Lumley, J.L. 1967: Large eddy structure of the turbulent wake behind a circular cylinder. Phys. Fluids, 10, 194-196.
7. Pope, B. and Whitelaw, J. H. 1976: The calculation of near-wake flow. J. Fluid Mech. 73-1 9-32.

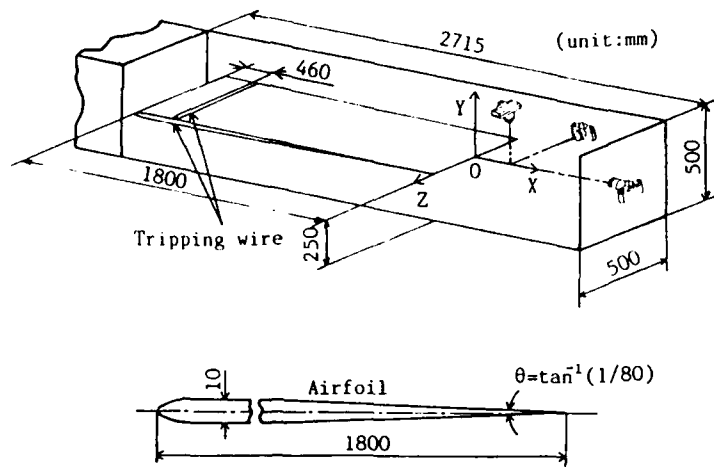


Fig.1 Schematic representation of the apparatus

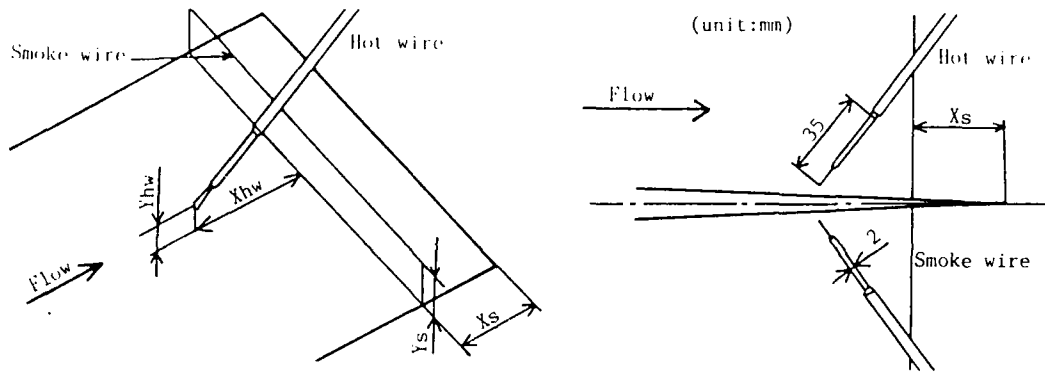


Fig.2 Flow visualization system

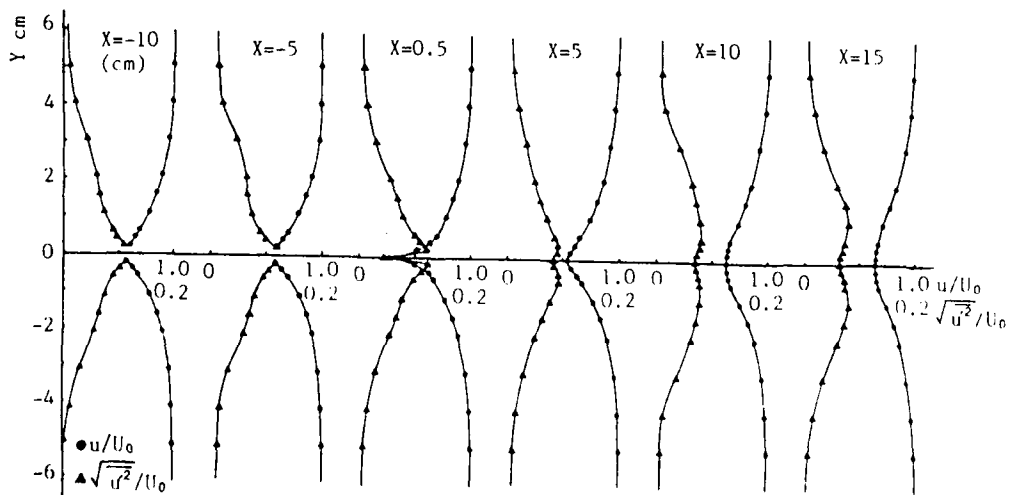


Fig.3 Mean velocity profiles and distributions of intensity of velocity fluctuation

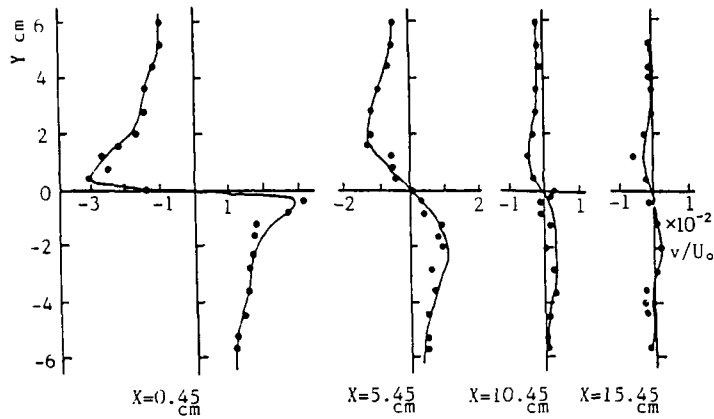


Fig.4 Mean velocity profiles of y components

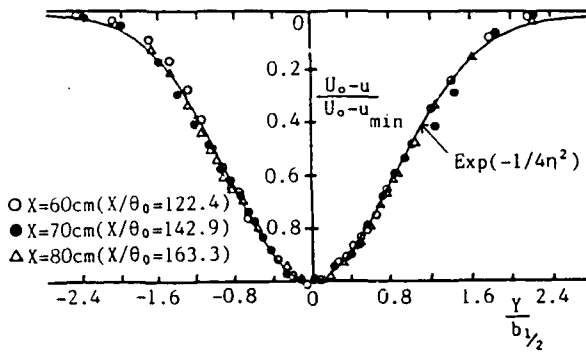


Fig.5 Distribution of mean velocity defect at far downstream distances

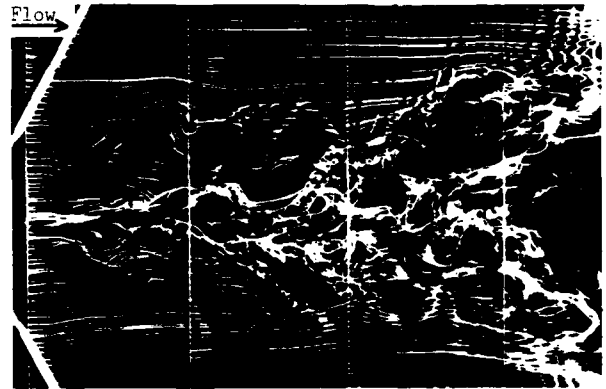


Fig.7 Side view of smoke  
 $X_{hw}=1\text{cm}, Y_{hw}=\pm 0.5\text{cm}, X_s=0\text{cm}$

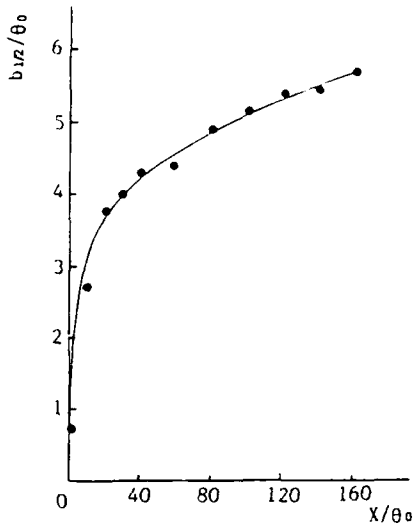


Fig.6 Distribution of half the width at half depth

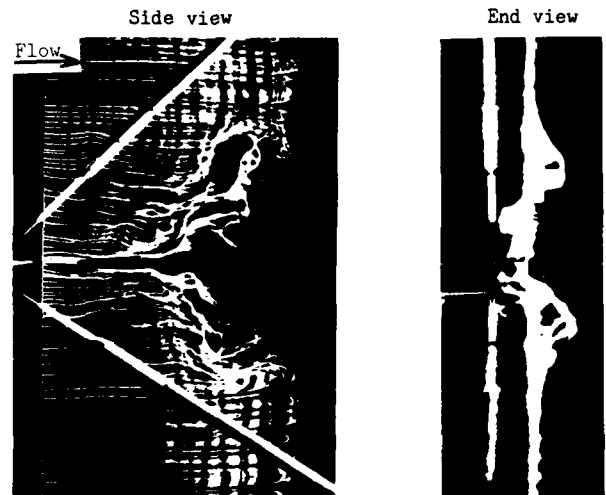


Fig.8 Dual view pictures  
 $X_{hw}=0.5\text{cm}, Y_{hw}=\pm 0.5\text{cm}, X_s=0\text{cm}$

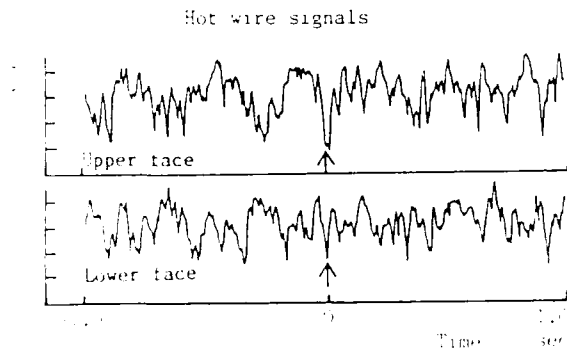
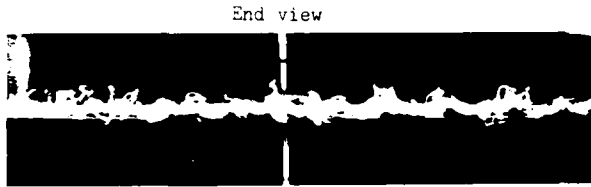


Fig. 9 Dual view pictures  
 $X_{hw}=0.6cm$ ,  $Y_{hw}=0.9cm$ ,  $X_s=2cm$ ,  $Y_s=0.57cm$



Fig. 10 End view of smoke  
 $X_{hw}=2cm$ ,  $Y_{hw}=2cm$ ,  $X_s=2cm$ ,  $Y_s=1.1cm$

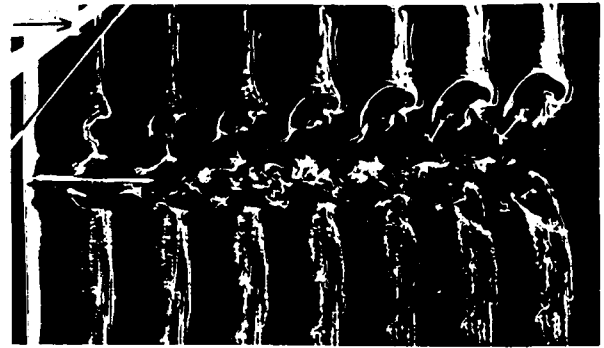


Fig. 11 Side view picture with multiple exposure  
 7 shots time interval 27ms  
 $X_{hw}=2.4cm$ ,  $Y_{hw}=0.8cm$ ,  $X_s=2.5cm$

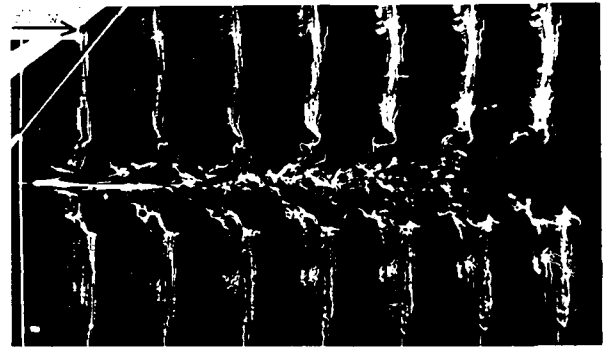


Fig. 12 Side view picture with multiple exposure  
 7 shots time interval 27ms  
 $X_{hw}=2.4cm$ ,  $Y_{hw}=0.8cm$ ,  $X_s=2.5cm$

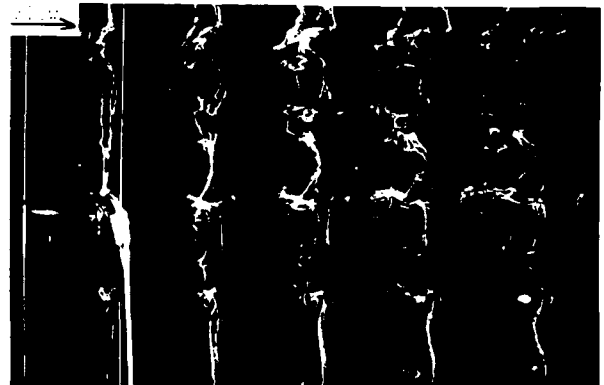


Fig. 13 Top view picture with multiple exposure  
 5 shots time interval 55ms  
 $X_{hw}=2.1cm$ ,  $Y_{hw}=0.8cm$ ,  $X_s=2.4cm$ ,  $Y_s=1.1cm$

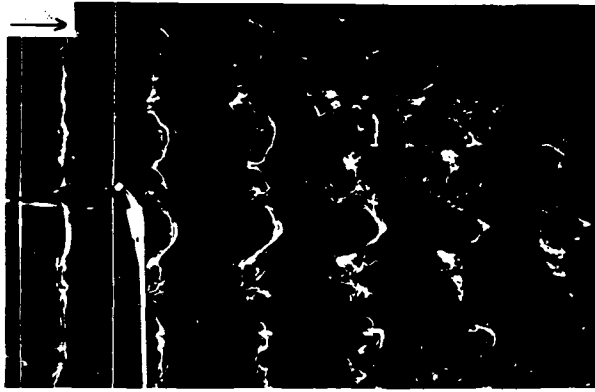


Fig. 14 Top view picture with multiple exposure  
6 shots time interval 5ms  
Xhw=0.2cm, Yhw=0.3cm, Xs=0.5cm, Ys=0.3cm

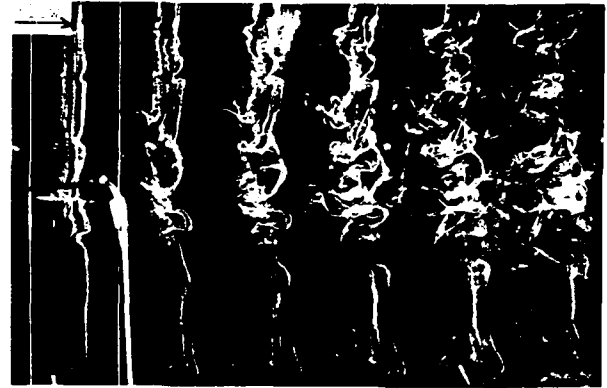


Fig. 15 Top view picture with multiple exposure  
6 shots time interval 5ms  
Xhw=0.4cm, Yhw=0.3cm, Xs=0.5cm, Ys=0.3cm

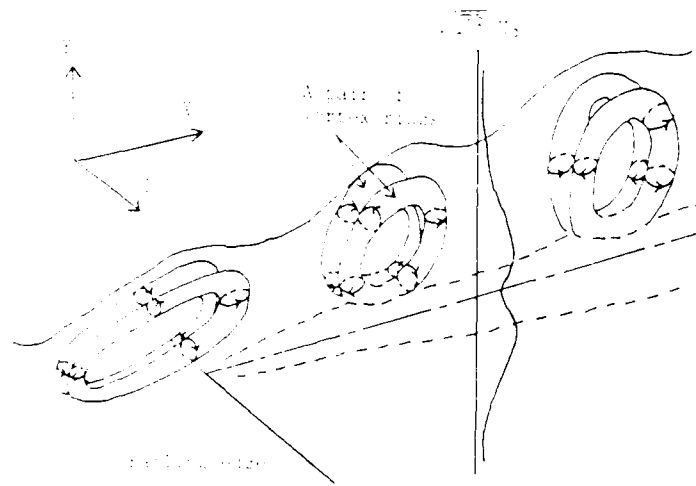


Figure 2 Dynamic model of a pair of vortex rings

A FLOW-VISUALIZATION TECHNIQUE  
FOR EXAMINING COMPLEX THREE-  
DIMENSIONAL FLOW STRUCTURES

J. T. Kegelman

McDonnell Douglas Research  
Laboratories  
St. Louis, Missouri 63166

ABSTRACT

A new flow-visualization technique is presented for examining complex flow structures by use of a scanning laser-light sheet and a high-speed video system together with image-processing techniques. Existing techniques, such as two-dimensional laser-light-sheet techniques, schlieren and shadowgraph methods, are inadequate for characterizing three-dimensional large-scale structures in flows. The new technique allows the three-dimensional images to be reconstructed and transferred to a graphics processor for rotation, translation and close-up examination. The technique is being developed to allow real-time processing of flow images.

1. INTRODUCTION

The flowfield created by a two-dimensional, backward-facing step is being investigated at the McDonnell Douglas Research Laboratories (MDRL) to improve characterization of the dynamics of separating and reattaching shear layers. The large-scale vortical structures that develop in this flowfield are predominantly two-dimensional upstream of reattachment. These structures rapidly become three-dimensional as they interact with the wall

in the reattachment zone. The dominant spanwise and streamwise length scales for the reattached flow are established by the reattachment process. Qualitative information about these processes is best obtained with flow-visualization techniques; however, none of the existing techniques has yielded significant insight into the mechanisms active in large-scale, three-dimensional structures.

The utility of the more common flow-visualization techniques is limited in this flowfield. Flow-seeding techniques, such as smoke and dye injection, allow only visualization of the outermost surface of the large-scale structures. Most schlieren and shadowgraph techniques yield an image that results from diffraction of light due to density changes, integrated along the light path across the flowfield; consequently, spanwise details of the three-dimensional structures are lost. Standard laser-light-sheet, focusing schlieren, and focusing shadowgraph techniques yield only a two-dimensional image of flows which are generally regarded as three-dimensional.

Illumination of the flowfield with a scanning laser-light sheet, the key feature of our technique, leads to a truly three-dimensional image. The quasi-three-dimen-

sional images of Jimenez et al. (1983) were obtained with a fixed light sheet oriented transverse to the flow so that the third dimension of the resulting image was actually simulated by local variation with time.

## 2. OPTICAL SYSTEM

The optical arrangement for the present technique is illustrated in Fig. 1. The beam from a pulsed laser is spread into a sheet by reflection from a cylindrical mirror. The mirror is mounted on the arm of a galvanometer which rotates about an axis perpendicular to the cylinder axis. Because the cylindrical mirror is placed at the focal point of a parabolic mirror, the light sheet is always reflected parallel to the axis of the latter. By applying current to the galvanometer, the light sheet will scan the flowfield. A high-speed video camera is synchronized with both the laser and the motion of the light sheet such that one image is obtained for each position of the light sheet.

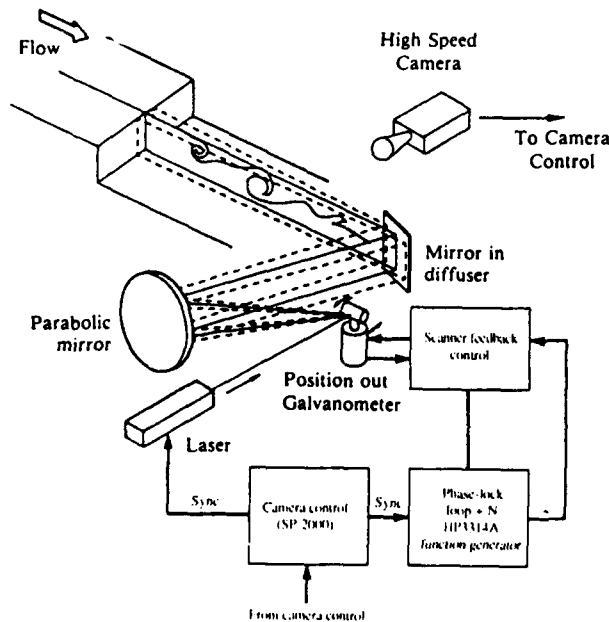


Fig. 1. Scanning-laser-light-sheet arrangement for 3-D image processing.

Three aspects of the optical system require special attention: 1) laser beam divergence, 2) mirror surface quality, and 3) electronic synchronization. The laser used in the present configuration is a 40-W copper vapor laser with a special set of unstable resonator optics which reduce beam divergence to less than 0.7 milliradian. Low beam divergence is essential for producing a thin light at the focal plane of the system. The beam emitted by the laser is 6.0 cm in diameter and can be focused down to a 2.0-mm thick light sheet by the parabolic mirror, as illustrated in Fig. 2. Without the unstable resonator optics in the laser, the light sheet can be made no thinner than 8.0 mm. The parabolic mirror in the current configuration is a 76.2-cm-diameter, 4.572-m focal length, 1/10-wave-length schlieren mirror. The laser produces over 8.5 mJ per pulse at about 6000 pulses per second, and can be externally triggered. The laser can be run at lower repetition rates, down to about 200 pulses per second. However, the energy per pulse does not increase significantly at lower pulse rates, and the duration of the visualization run is then limited as the laser cools, lowering the partial pressure of copper in the laser. Each pulse of the

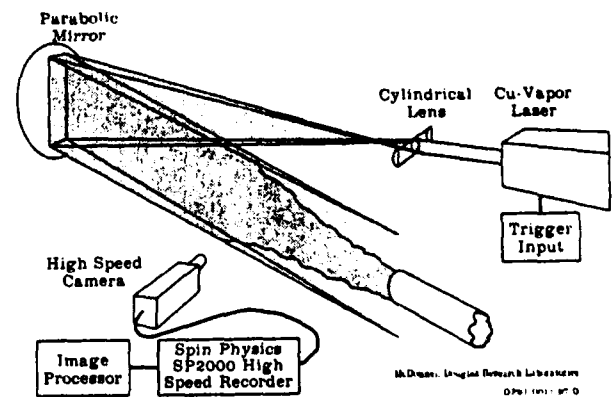


Fig. 2. Optical arrangement for generation of thin light sheet from 6.0 cm. laser beam.

laser has a duration of about 50 ns, sufficient to achieve a low degree of blurring that is caused by motion during each exposure, (the blur distance for a Mach-25 flow is about 0.5 mm).

It is essential that each optical surface in the system be of the highest quality to ensure beam integrity and therefore the thinnest possible light sheet in the field of view. Anti-reflection coatings on each lens, as well as highly reflective coatings on all mirrored surfaces, are desirable for minimizing reflection losses. A clean, uncoated aluminum first-surface mirror scatters about 10% of the light energy during reflection; likewise, an uncoated glass lens loses about 5% per surface, yielding approximately 10% loss to unwanted reflection per lens. Optical coatings can reduce these losses to less than 1% per surface. A typical optical configuration in the MDRL Shear Flow Facility incorporates up to 11 optical components, including the glass walls of the wind tunnel and several mirrors used to steer the beam from the laser, which is mounted in an adjacent room, through the laboratory wall, and to the wind tunnel. Using standard optics with an average 10% reflection loss per element, only  $0.9^{11}$  or 31% of the laser power reaches the flowfield. The use of coated optics, where possible, has reduced losses to about 40%, which include a 25% loss at the large 76.2-cm parabolic mirror and a 10% loss from the glass wind tunnel walls.

There are two key elements in the electronic synchronization system that allow accurate and repeatable positioning of the light sheet during each scan: 1) a phase locked loop "divide by N" circuit to provide one sweep of the flowfield for N pulses of the laser, and 2) a feedback controlled galvanometer amplifier. A Hewlett Packard model HP3314A arbitrary waveform generator has a built-in feature to divide

the incoming trigger pulse train by an integer N and provide a phase-locked output signal with a period N times longer than that of the trigger signal. A General Scanner model CX660HR feedback-controlled scanner amplifier is used to accurately position the light sheet according to the signal from the waveform generator. The scanning system in the current system is limited to about 100 Hz because of the inertia of the scanning mirror; this allows a maximum of 200 flow-volume visualizations per second.

Data are taken with a high-speed video recorder, a Spin Physics SP2000 video system, which provides trigger pulses for both the laser and the "divide by N" circuit. The resolution of the system is limited to 240 by 192 pixels, which can be scanned and recorded 2000 times per second; to increase the frame rate to 6000 pictures per second, partial frames are scanned, further limiting the resolution to 80 by 192. There are six bits, or 64 gray levels available, producing useful images of large structures in the flowfield; however, small-scale features are lost. The effective ASA or equivalent film speed of the video system is about 100, requiring the high levels of illumination afforded by the Copper vapor laser as well as low-f-number lenses to image each visualization pulse. A Fujinon CF50L f/0.7 lens is used with the current system to allow adequate light-gathering capability for the present experiments.

Further improvement in light levels is achieved by using forward scattering; the camera is aligned 30 degrees from the axis of the laser and pointed toward the laser, rather than normal to the plane of the light sheet. The views are obtained by this method are oblique; however, they can be corrected for the off-axis perspective using image processing techniques.

### 3. IMAGE PROCESSING

The data recorded by the visualization technique are processed by the McDonnell Douglas Astronautics Company (MDAC) Image Processing Laboratory. Individual images are digitized and stored on a VAX 780 computer system. Correction for the camera perspective is simplified because the two-dimensional light sheets require only an appropriate stretching, as illustrated in Fig. 3. In this figure, the pressure transducers on the tunnel floor have been used to "calibrate" the stretching function, and the image has been stretched to restore the proper geometric position of the transducers. This view is from the side of the tunnel and the correction applies to horizontal light sheets, in planes parallel to the plane of the tunnel floor.

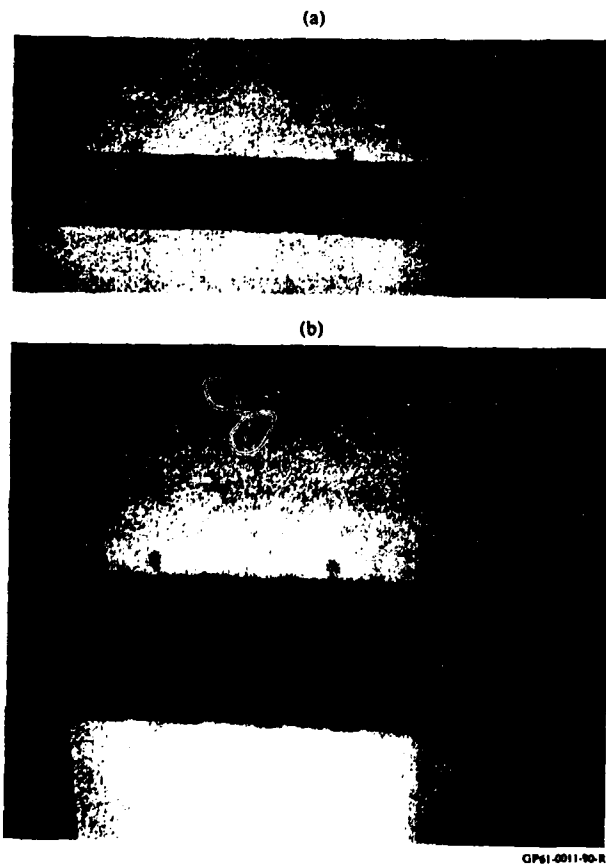


Fig. 3. (a) Raw Video image of test section floor downstream of a backward-facing step and (b) video image after perspective correction.

Figure 4 illustrates the raw video image of a smoke-visualized flow immediately downstream of the backward-facing step. The light sheet in this view is vertical and in the streamwise direction. Raw video images are processed to remove video noise and to correct for nonuniform light intensity as well as perspective distortion. Noise removal is usually accomplished with a neighborhood averaging scheme, whereby the gray-level value of a pixel is modified according to its initial value and an appropriate average of its nearest neighbors.



Fig. 4. Raw video image of reattaching shear layer.



Fig. 5. Image of Fig. (2) after application of binary threshold.



Fig. 6. Result of applying edge-detection scheme to image of Fig. 4.

More sophisticated techniques can be used if the character of the video noise can be identified, as is the case with the Spin Physics video system. In this system, often an entire row or a large portion of a row of pixels will be affected by noise, and the noise removal algorithm will emphasize north and south neighbors by appropriately adjusting coefficients in the weighting scheme.

In Fig. 5, a binary threshold was applied to identify the regions of smoke in the original image. Often a simple binary threshold does not capture the smoke boundaries because of variations in smoke density as it diffuses downstream, and because the scattering angle between the laser beam axis and the camera axis (and therefore the scattered light intensity) varies across the field of view. More sophisticated techniques, such as histogram equalization, or nonuniform binary thresholding, are often required to capture the smoke boundaries. In Fig. 5, a nonuniform binary threshold was applied to the streamwise vertical light sheet shown in Fig. 4. In this view the light intensity varies significantly across the field of view as the smoke density decreases; the threshold was varied across the image to compensate for decreasing light levels. In Fig. 6 a simple edge-detection scheme has been applied to outline the smoke/no-smoke boundary.

The smoke-boundary data from several successive planes can be combined in the computer and displayed so that the three-dimensional character of the flowfield is reconstructed, as illustrated in Fig. 7. These preliminary results were obtained with a standard video scan rate of 30 frames per second, which allowed excessive motion of the flow during a single scan and produced the skewness evident in Fig. 7. As illustrated in Fig. 7, the large-scale structure can be viewed from any angle, and interesting features can be enlarged for

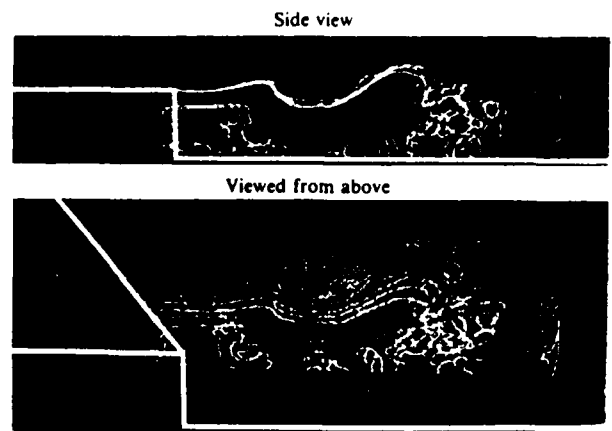


Fig. 7. Computer reconstruction of the 3-D flowfield image.

close-up examination. To further demonstrate the image-reconstruction part of the technique, the procedure of Jiminez et al.

(1983) was used whereby a time sequence of video images from a fixed, transverse light sheet was converted into a quasi-three-dimensional image (Fig. 8) of the large flow-structures defined by the shear-layer smoke/no-smoke boundary. The highly structured image shown in Fig. 8 was produced on a Silicon Graphics IRIS workstation, which allows rotation and enlargement of the image in real time. Although the streamwise dimension in Fig. 8 actually repre-

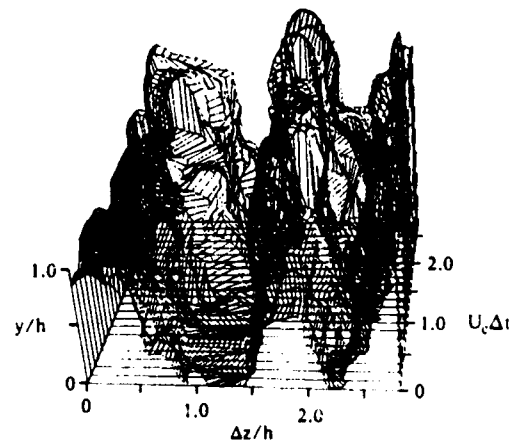


Fig. 8. Quasi-3-D reconstruction of large structures beyond reattachment.

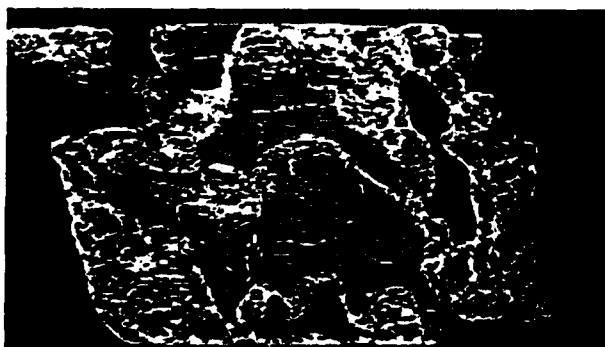
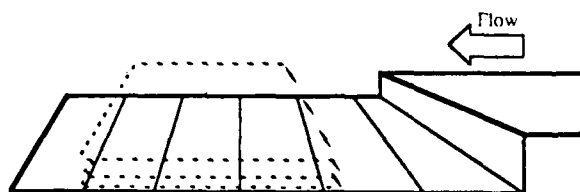
sents time, it is quasi-spatial in that the distance between successive images in the reconstruction is the product of the local mean convection speed  $U_c$ , and  $\Delta t$ , the time elapsed between video images.

True three-dimensional images of these structures have been generated through use of the high-power, high-repetition-rate, pulsed copper-vapor laser synchronized with both the scanning system and a high-speed video system. Fig. 9 shows the results of a three-dimensional reconstruction obtained with a 4000 pulses-per-second scan rate. In this case, a series of horizontal light sheet images was employed to best utilize the resolution of the video system. It is best to choose the scan direction so that the distance between successive planes is approximately equal to the distance between pixels in each plane, thus allowing comparable resolution in all three directions. The three-dimensional features of the flow reconstruction are somewhat difficult to perceive when viewing a stationary photograph as in Figs. 8 and 9. Viewing the reconstruction of these figures on the IRIS

graphics processor, where real time rotation is possible, greatly aids perception of the three-dimensional aspects of the structure.

#### 4. CONCLUSIONS

The technique outlined above has recently been implemented at MDRL and is in the early stages of development. However, useful information regarding the nature of complex three-dimensional flowfields is already being produced. With very high scan rates, as high as 200 flow volumes per second at 6000 frames per second, several complete visualization cycles can be processed into a simulated motion picture of the large-scale-structure development. Alternatively, by synchronizing the visualization cycles with a shear-layer excitation signal, an ensemble-averaged picture of the three-dimensionalization can be constructed from the multiple realizations of that event. Current limitations of the system are the relatively coarse video resolution as well as the time required to process and enhance the video images. A real-time, dedicated image-processing system being developed should substantially reduce the time for processing the video images. Rapid progress in the field of high-speed image acquisition suggests that further improvements in this system will be possible in the near future.



GP81-0011-98-R

Fig. 9. 3-D Reconstruction using horizontal light sheets.

#### REFERENCE

- Jiminez, J., Cogollos, M. and Bernal, L. 1983: A Perspective View of the Plane Mixing Layer, In Proc. Fourth Symp. on Turbulent Shear Flows, Karlsruhe, Germany.

SPANWISE COHERENCE OF VORTICAL  
STRUCTURES IN A REATTACHING  
TURBULENT SHEAR LAYER

Frederick W. Roos and  
Jerome T. Kegelman

McDonnell Douglas Research  
Laboratories  
St. Louis, MO 63166

ABSTRACT

The flow over a backward-facing, two-dimensional step has been investigated in a series of experiments that have emphasized the dynamics of vortical structures in the reattaching shear layer. Low-amplitude oscillation of a flap at the step edge was used to influence the development of the shear-layer vortical structures. In particular, excitation at a variety of frequencies clarified the existence and nature of vortex merging in the fully turbulent reattaching layer. Excitation appreciably reduced shear-layer reattachment length, but only for frequencies consistent with vortex merging. Low-frequency excitation greatly increased the spanwise coherence of the vortical structures, but this effect disappeared for frequencies that allowed vortex merging; if two stages of merging occurred, spanwise coherence became less than in the unexcited case. Low-frequency excitation also increased levels of reattachment-wall pressure fluctuation, but these levels dropped to those of the unexcited case during multiple-vortex merging. Flow visualization showed that three-dimensional vortical-structure fields often showed a high degree of spanwise correlation, demonstrating that strong spanwise correlation is not synonymous with the ex-

istence of highly two-dimensional vortical structures in the reattaching turbulent shear layer.

SYMBOLS

- $C'_p$  Fluctuating pressure coefficient,  
 $C'_p = \frac{p'}{q_0}$
- $f$  Frequency
- $f_x$  Shear-layer excitation frequency
- $h$  Step height
- $p'$  Root-mean-square fluctuating pressure
- $q$  Free-stream dynamic pressure at separation,  $q_0 = \frac{1}{2} \rho U_0^2$
- $R_{pp}$  Zero-time-lag spanwise cross-correlation coefficient for  $p$  (same form as  $R_{uu}$ )
- $R_{pu}$  Temporal correlation coefficient between  $p$  and  $u$ ,  
 $R_{pu} = \lim_{T \rightarrow \infty} \frac{1}{T} \int_0^T \frac{p(t)u(t+\tau)dt}{p'u'}$
- $R_{uu}$  Zero-time-lag spanwise cross-correlation coefficient for  $u$ , Eq. (2)
- $Re_h$  Reynolds number based on step height,  
 $Re_h = \frac{\rho U_0 h}{\mu}$
- $St$  Strouhal number,  $St = \frac{fh}{U_0}$
- $St_x$  Excitation Strouhal number,  $St_x = \frac{f_x h}{U_0}$
- $u$  Fluctuating velocity component in  $x$  direction

$u'$	Root-mean-square value of $u$
$U$	Mean velocity component in $x$ direction
$U_0$	Free-stream value of $U$ at separation
$v$	Fluctuating velocity component in $y$ direction
$x$	Streamwise coordinate, downstream from step face
$x_r$	Reattachment length
$(x_r)_0$	Reattachment length with no excitation
$y$	Cross-stream coordinate, upward from reattachment wall
$y'_{te}$	Root-mean-square displacement of oscillating-flap trailing edge
$z$	Spanwise coordinate
$\delta_0$	Boundary layer thickness at separation
$\mu$	Viscosity
$\phi$	Phase of oscillating-flap displacement
$\rho$	Density
$\tau$	Time lag in temporal correlation

## 1. INTRODUCTION

Despite the simplicity of its boundary geometry, the separating and reattaching flow over a backward-facing step contains several fundamental complexities that present a stimulating and relevant topic for research. Numerous experimental studies of the backstep flow have been conducted. Eaton and Johnston (1981) have provided a review of most of these investigations, while Simpson (1985) has nicely summarized the most recent developments. Much has been learned about the mean flow and turbulence characteristics, and about the effects of initial boundary-layer state and boundary-layer-thickness-to-step-height ratio on such basic variables as the shear-layer reattachment length. However, only recently have studies of the backstep flow begun to concentrate on the dynamics of the coherent vortical structures that evolve in the reattaching turbulent shear layer [e.g., Pronchick and Kline (1983); Troutt

et al. (1984)]. The structure and dynamics of these vortical structures need further definition for at least two reasons. To begin with, satisfactory modeling of reattaching turbulent flows requires that the effects of the vortical structures be taken into account. Secondly these vortical structures provide us with a flow mechanism that can be manipulated for purposes of modifying characteristics of the reattaching flows in which they occur.

An ongoing experimental investigation of large-scale vortical-structure development in the flow over a two-dimensional, backward-facing step is being conducted by the McDonnell Douglas Research Laboratories [Roos and Kegelman (1985, 1986)]. Earlier stages of this effort have concentrated on the two-dimensional aspects of vortical-structure evolution, and have made extensive use of shear-layer excitation to regularize the formation of the vortical structures, allowing ensemble averages of unsteady flowfield variables to be obtained through phase-locked LDV or wall-pressure measurements. The influence of very gentle excitation via a small oscillating flap at the step lip was found to be particularly strong when the separating boundary layer was turbulent, as the flow-visualization photographs in Fig. 1 show. Figure 1(a) shows an unexcited turbulent shear layer,

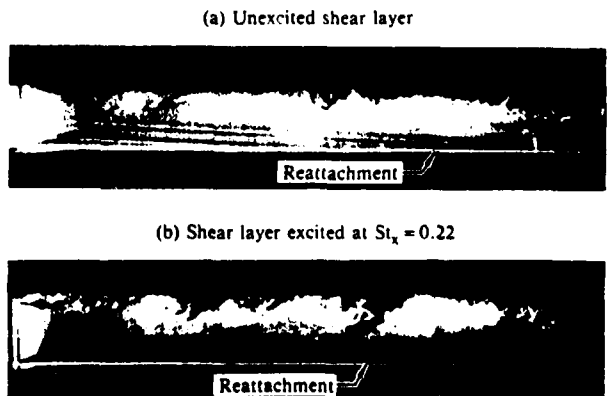


Fig. 1. Influence of excitation on large-scale structures in a reattaching turbulent shear layer ( $Re_h = 39,000$ ).

while Fig. 1(b) shows the same flow excited at  $St_x = 0.22$ . Despite the small excitation amplitude (trailing-edge displacement  $< 1\%$  of boundary-layer thickness), large-scale structures with a wavelength of roughly two step-heights are clearly evident in the excited flow.

One of the most important single characteristics of reattaching shear flows is the reattachment length. Shear-layer excitation has been found to have a considerable influence on reattachment length, and the effect is seen to be very frequency-sensitive, as Fig. 2 shows. This behavior was thought to be a consequence of the vortex-merging process, which became effective only for sufficiently high frequencies ( $St_x > 0.1$ ).

Irregularity in the vortex-merging process interferes with phase-averaged sampling of the velocity field or the fluctuating wall pressures in the reattachment region. In an effort to regularize the merging process, we staggered the streamwise spacing of the excited vortical structures by modulating the period of flap oscillation at the subharmonic frequency. The excitation had the form

$$y_{te}(t) = y_{max} \sin(2\pi f_x t + \alpha \sin \pi f_x t) \quad (1)$$

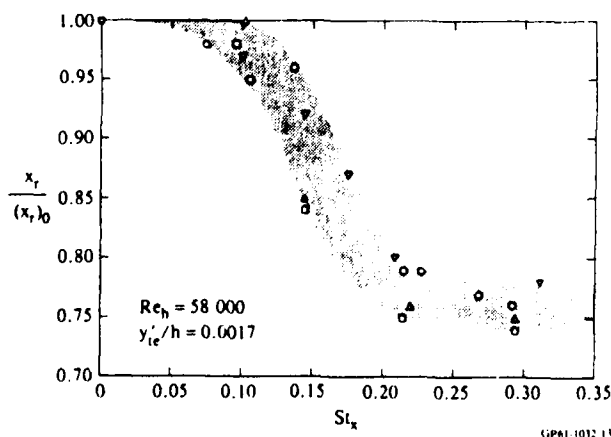


Fig. 2. Influence of frequency on reattachment-length reduction for constant-amplitude shear-layer excitation.

Phase-averaged LDV measurements were made in the turbulent reattachment flow, and the resulting phase-averaged, periodic velocity field was input to a flow-visualization-simulation routine. Figure 3 depicts the results of this procedure. It can clearly be seen that the fully-turbulent shear layer does indeed roll up into coherent vortical structures, initially at the excitation frequency. However, it is apparent that, by about  $x/h = 3$ , every other vortical structure is being merged into the structure following it in response to the subharmonic content of the shear-layer excitation. At the end of the visualized region, only the longer-wavelength (subharmonic) structure is evident, indicating completion of the vortex-merging process.

The vortical structures formed in the turbulent free shear layer rapidly become three-dimensional as they interact with the wall in the reattachment zone. Pronchick and Kline (1983) established that two-dimensionality of the shear-layer vortical structures begins to break down at  $x/h = 2$ , while our own (unpublished) flow-visualiza-

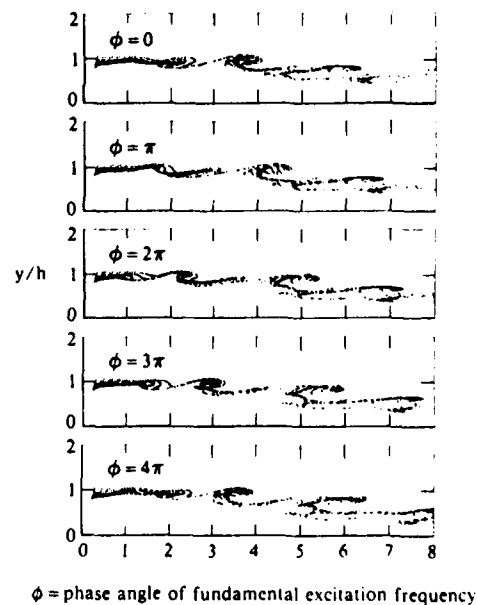


Fig. 3. Turbulent shear-layer streaklines based on phase-averaged LDV measurements with phase-modulated excitation.

tion studies have revealed large, three-dimensional structures erupting in the shear layer in the reattachment region. Such eruptions may arise from distortions in the spanwise vortex, following the description by Müller and Gyr (1982): a downstream kink in the nominally spanwise vortex will be lifted away from the wall via Biot-Savart induction; as this element of the vortex rises and is stretched, it becomes more intense. Pronounced three-dimensionality near and beyond reattachment was also found by Kasagi et al. (1977). The dominant spanwise and streamwise length scales for the reattached flow are established during the reattachment process.

The primary objective of the current study is to extend our earlier results to include the spanwise aspects of vortical-structure development and shear-layer excitation effects.

## 2. EXPERIMENTAL EQUIPMENT AND PROCEDURES

The study of vortical-structure development in reattaching turbulent shear layers is being continued in the McDonnell Douglas Research Laboratories Shear Flow Facility, a low-speed (0-80 m/s), low-turbulence ( $< 0.05\%$ ), closed-circuit wind tunnel developed specifically for investigations of nominally two-dimensional bounded and free shear layers. For the shear-layer reattachment experiments, a backward-facing step (Fig. 4) with aspect ratio 10 has been installed in the test channel. The expansion ratio of the channel at the step is 1.30.

Instrumentation includes centerline rows of static-pressure orifices and an array of fluctuating-pressure transducers embedded in the reattachment wall downstream of the step. A rake of eight hot-wire probes is positioned in the reattaching flow through a remotely driven two-axis traversing unit. The hot wires are operated by standard constant-temperature anemometer units. Hot-wire and pressure-

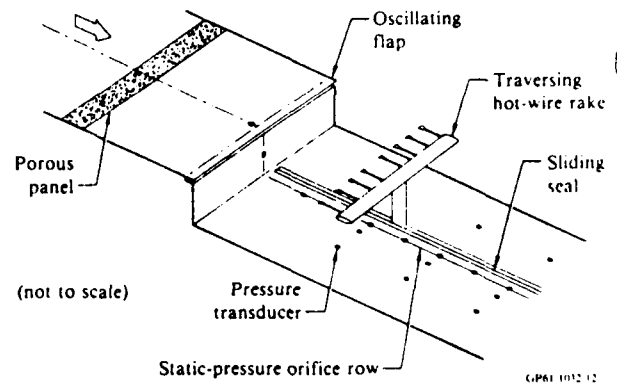


Fig. 4. Backward-facing two-dimensional step geometry and instrumentation.

transducer signals are generally low-pass filtered with a cutoff just above the frequency range associated with the developing shear-layer vortical structures. Acquisition, processing, and plotting of experimental data are handled by digital computer, except that frequency spectra are produced by a spectrum analyzer and plotted on an analog plotter.

Provisions for flow visualization include a porous panel, located upstream of the step, through which smoke (an aerosol of liquid droplets) is introduced into the separating boundary layer. The smoke is illuminated by a light sheet that can be oriented as an x-y, x-z, or y-z plane. A high-pulse-rate, copper-vapor laser generates the light sheet; a high-speed video system can be synchronized with the laser to produce rapidly-sequenced video images of the flow.

Excitation of the separated shear layer is accomplished by a simple, electromagnetically driven trailing-edge flap at the corner of the step. The technique is similar to that originally employed by Wygnanski et al. (1980) to force the development of large-scale vortical structures in turbulent mixing layers. The oscillating flap has a chord of about 15% of the step height, or roughly half the thickness of the separating boundary layer. Flap oscillation amplitude is monitored directly

by tracking the image of a laser spot reflected off the flap surface. In our experiments, the shear-layer excitation provided by the oscillating flap was very gentle. For all experiments reported herein, rms displacement of the flap trailing edge was 0.5% of the step height (equivalent to  $< 2\%$  of  $\delta_0$ .)

To ensure a fully turbulent separating boundary layer, the boundary layer was tripped at the upstream end of the test channel. The trip is three-dimensional, consisting of a spanwise row of small triangular platelets located on the wall and oriented perpendicular to the flow. Height of the trip was always less than the local laminar boundary-layer thickness.

### 3. RESULTS AND DISCUSSION

#### 3.1. Vortex Merging and Excitation Effects

Further evidence and definition of the vortical-structure merging process is provided by the hot-wire rake data. To maximize the hot-wire response to streamwise velocity fluctuations associated with the vortical structures, the hot-wire rake was always positioned at the outer edge of the turbulent shear layer. In this location, the hot wires were no longer seeing bursts of turbulence within the layer but were still responding strongly to the outer-flow fluctuations related to the convective passage of the large-scale vortices. The upper portion of Fig. 5, for example, compares amplitude spectra at three streamwise stations in the unexcited reattaching flow. There is a clear reduction in the center frequency of the spectral peak with increasing distance downstream of separation, strongly suggesting that the passage frequency of large structures is being reduced through the vortex-merging process as the flow proceeds from separation to reattachment; these results are comparable to those discussed by Bhattacharjee et al. (1986) and Roos and Kegelmann (1985). The broad, low character of the spectral peaks and the

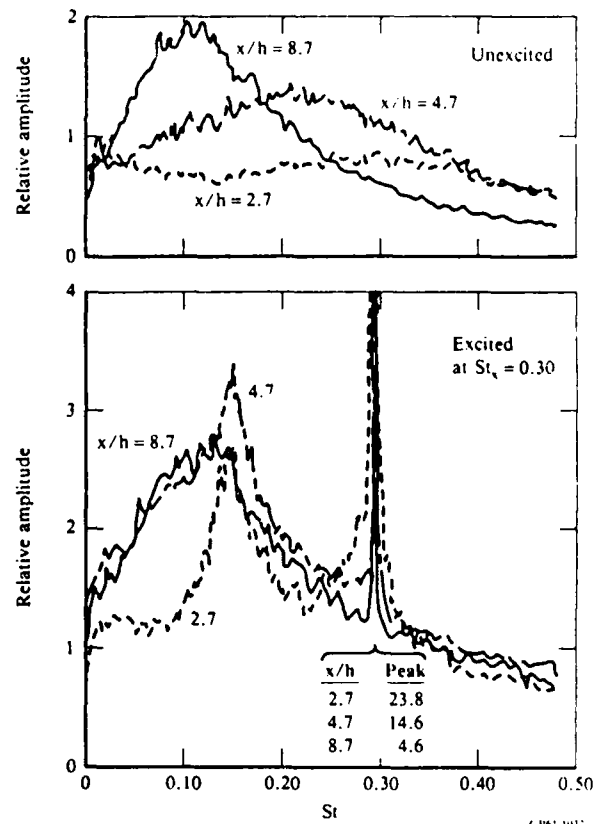


Fig. 5. Streamwise development of hot-wire spectra for unexcited and excited turbulent shear layers.

gradual shift to lower frequencies result from the spatial and temporal randomizing influence that the initial boundary-layer turbulence has on the vortical-structure formation and merging processes. For reference, it might be noted that the most-unstable frequency at the upstream end of the free shear layer corresponds roughly to  $St = 0.4$ .

Excitation of the free shear layer at a frequency corresponding to the broad peak in the upstream shear-layer spectrum produces the spectra shown in the lower part of Fig. 5. The strong, highly organized response of the layer to the excitation is obvious, and the transfer of fluctuation energy to the subharmonic of the excitation is a clear indication of vortex merging. As the flow passes downstream from  $x/h = 2.7$  to 4.7, the amplitude of the excitation peak diminishes while the subharmonic

peak grows. But there also is considerable increase in spectral level around the second subharmonic; this level is maintained as the flow proceeds through the reattachment zone, even though the peaks at the fundamental and first subharmonic decline. It is evident, then, that two stages of vortex merging are occurring before the shear layer reattaches.

Another comparison is shown in Fig. 6, which presents spectra at  $x/h = 8.7$  for two distinctly different excitation frequencies as well as for the unexcited case. Although both the low- and high-frequency cases were excited at the same amplitude, the excitation peak in the  $St_x = 0.30$  case has almost disappeared (due to two stages of vortex merging) while the  $St_x = 0.11$  peak is very strong, showing essentially no indication of energy transfer to subharmonic via vortex merging.

In an effort to define where and for which frequencies the merging process is active, we have plotted the amplitude of the excitation-frequency spectral peak for a range of excitation frequencies at each of the three streamwise measuring stations (Fig. 7). For the lowest excitation frequencies, the peak amplitude grows with distance downstream, the rate of growth

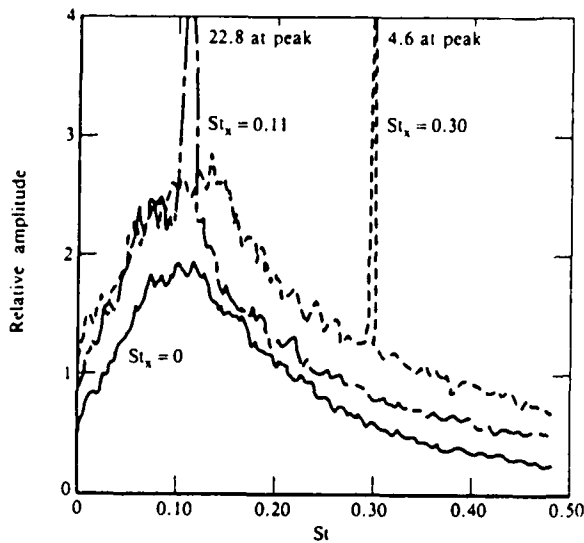


Fig. 6. Hot-wire spectra at  $x/h = 8.7$ .

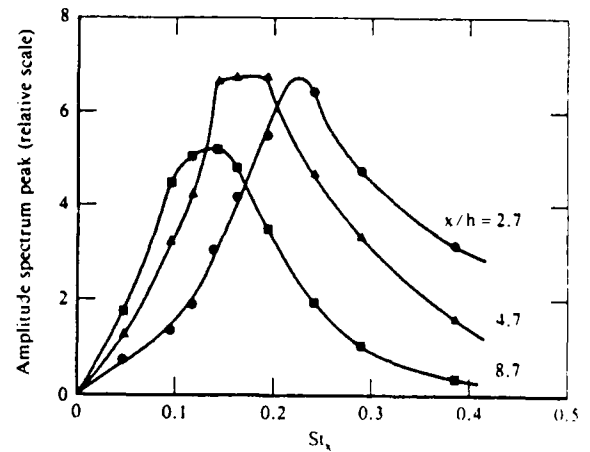


Fig. 7. Influence of excitation frequency on response peak in hot-wire spectra.

increasing with frequency. Around  $St_x = 0.11$ , however, the excitation stops growing by  $x/h = 8.7$ . For excitation frequencies higher than this, growth will cease upstream of  $x/h = 8.7$ , and energy will begin to appear in the subharmonic, i.e., vortex merging will begin. For excitation frequencies above  $St_x = 0.15$ , the excited mode stops growing before  $x/h = 4.7$ , i.e., merging will be evident at  $x/h = 4.7$  for all  $St_x > 0.15$ . Continuing, for all  $St_x > 0.22$ , subharmonic energy (i.e., evidence of merging) will appear even at the most upstream measuring station,  $x/h = 2.7$ . For example, recall that the  $x/h = 2.7$  spectrum in the lower part of Fig. 4, for a case with  $St_x = 0.30$ , showed substantial energy at the subharmonic frequency ( $St = 0.15$ ).

Measurements of wall-pressure fluctuation have been made in the reattachment region. To confirm that the flow structures being sensed and measured by the hot wires were in fact the same ones being monitored by the pressure transducers, pressure fluctuations at the wall and streamwise velocity fluctuations at the shear-layer outer edge were cross-correlated at the same streamwise station ( $x/h = 4.7$ ). The results are shown in Fig. 8 for both an excited and an unexcited case.

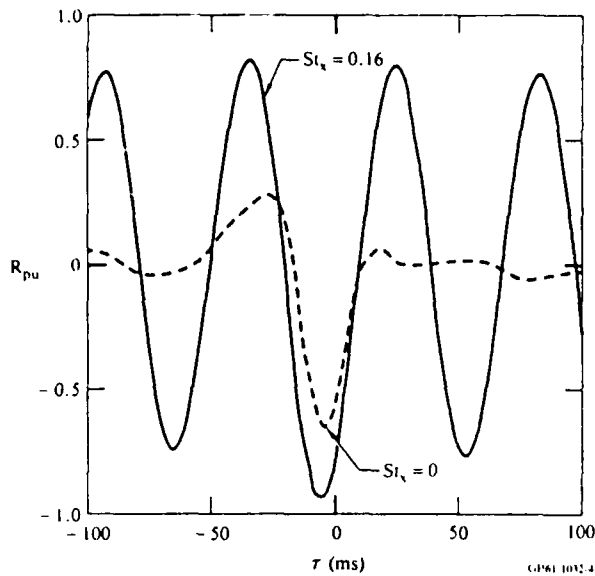


Fig. 8. Pressure-velocity correlation at  $x/h = 4.7$  for unexcited and excited reattaching turbulent shear layers ( $Re_h = 58,000$ ).

The pronounced negative correlation peak, especially for the case of the unexcited shear layer, makes it clear that the same structure is indeed being monitored by both instruments. Furthermore, the sense of the correlation is consistent with the passage of a vortical structure (i.e., simultaneous velocity increase at the hot-wire location and pressure decrease at the wall beneath the vortex). The offset of the correlation peaks from  $\tau = 0$  results from a combination of imprecise positioning of the hot wire and differences in filtering of the two circuits.

The intensity of wall-pressure fluctuations in the reattachment zone reflects the influence of excitation frequency. Figure 9 shows  $C'_p$  data for several excitation frequencies. Although reattachment lengths were not measured in this series of experiments, Roos and Kegelmann (1986) demonstrated that the peak intensity of wall-pressure fluctuation approximately coincides with the mean reattachment point. The data in Fig. 9 show that the only effect of excitation at frequencies for which merging does not occur is to increase the

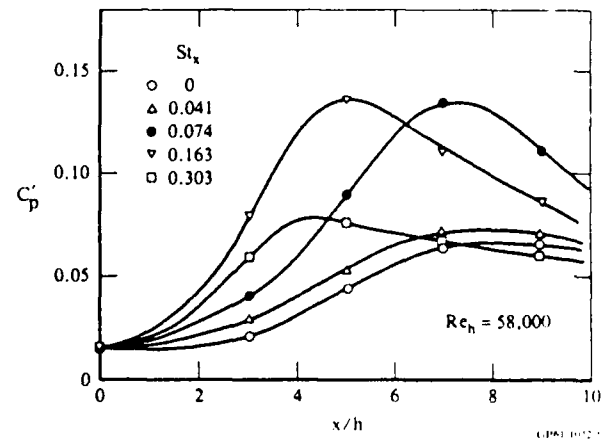


Fig. 9. Influence of excitation frequency on reattachment-wall pressure fluctuation intensity distribution.

intensity of wall-pressure fluctuations; the reattachment point is not affected. Once vortex merging becomes established (i.e., for  $St_x > 0.10$ ), the reattachment length is substantially reduced. Notice that a further increase in excitation frequency continues to reduce the reattachment length but no longer produces such intense pressure fluctuations. Because these higher excitation frequencies lead to two stages of vortex merging, it is suggested that the increasing structural disorganization that accompanies the merging process is responsible for the reduced intensity of vortex/wall interaction.

### 3.2. Spanwise Structure

The influence of excitation frequency on the spanwise structure of the reattaching shear layer was studied primarily through cross-correlation of the velocity fluctuations sensed by the probes in the hot-wire rake. These correlations were cast in the form of the spanwise cross-correlation coefficient  $R_{uu}$ , defined by

$$R_{uu}(\Delta z) = \lim_{T \rightarrow \infty} \frac{1}{T} \int_0^T \frac{u(z, t)u(z + \Delta z, t) dt}{(u')^2} \quad (2)$$

Examples of these cross-correlations are

given in Fig. 10. The upper plots, which represent the unexcited shear layer, show the spanwise correlation dropping off completely over a spanwise range of about three step-heights at  $x/h = 4.7$ ; the correlation improves with distance downstream, evidently from increasing growth and organization of the vortical structures. These results are similar to those presented by Troutt et al. (1984).

As Bhattacharjee et al. (1986) have also shown, the spanwise correlation is much greater when the shear layer is excited (middle plots in Fig. 10). Since the excitation is at a frequency too low for merging to occur, there is continuing growth and hence increasing spanwise correlation of the vortical structures with increasing streamwise distance. However, when the frequency of the excitation is sufficiently high to cause merging before reattachment, as in the lower plots of Fig.

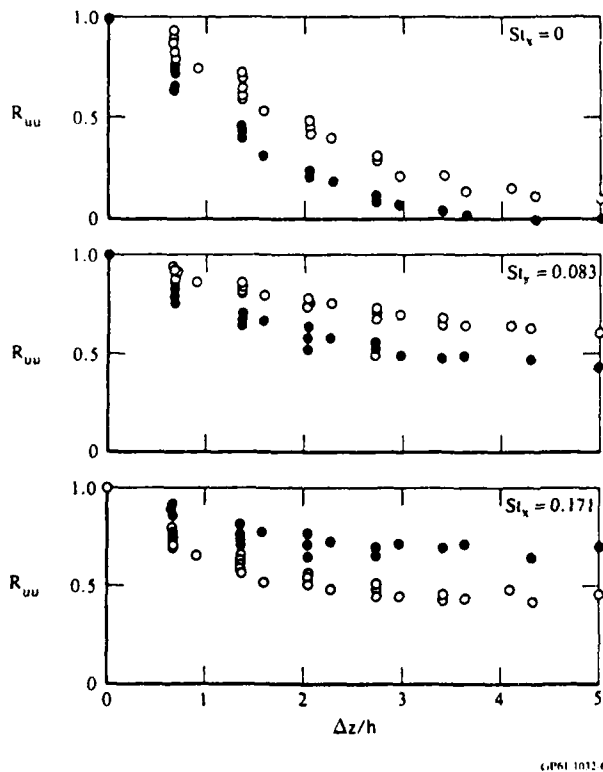


Fig. 10. Spanwise hot-wire cross-correlations for reattaching turbulent shear layers at (●)  $x/h = 4.7$  and (○) 8.7 ( $Re_h = 58,000$ ).

10, the situation reverses and we see the spanwise correlation decrease with distance downstream; this situation reflects the disorganizing and three-dimensionalizing effects of vortex merging in the reattaching shear layer.

For the downstream measuring station, Fig. 11 shows a set of spanwise cross-correlation curves (with data points omitted for clarity) covering the range from no excitation to excitation that leads to two-stage vortex merging. The spanwise correlation increases with excitation frequency until merging becomes significant, and decreases thereafter. Again, the three-dimensionalizing effects of vortex merging, especially of multiple-stage merging, are substantial: the spanwise correlation for  $St_x = 0.394$  is less than that of the unexcited flow.

As might be expected, the spanwise cross-correlations computed from pressure-fluctuation measurements agree well with the hot-wire correlations. Two spanwise pressure correlations are compared with the corresponding hot-wire results in Fig. 12.

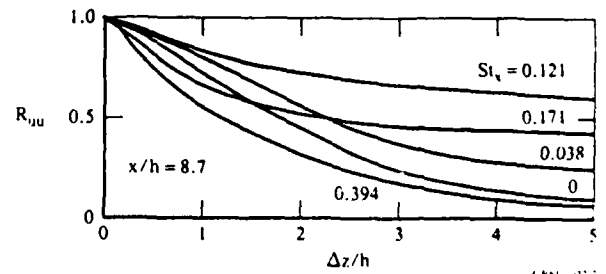


Fig. 11. Influence of excitation frequency on spanwise hot-wire cross-correlation ( $Re_h = 58,000$ ).

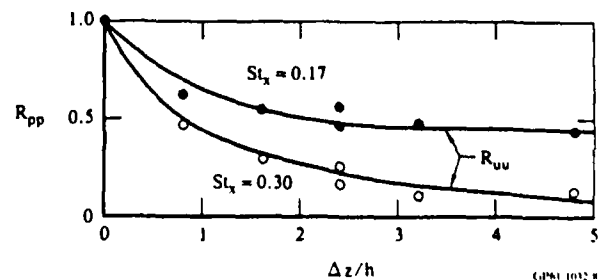


Fig. 12. Comparison of spanwise wall-pressure and hot-wire cross-correlations at  $x/h = 8.7$ .

Unfortunately, there is more to the character of spanwise structure in the reattaching shear layer than is indicated by the zero-time-lag cross-correlations. In fact, the cross-correlations can give misleading impressions. Since initial development of the vortical structures is quite two-dimensional, especially if shear-layer excitation is involved, the spanwise invariance of the mean flow tends to keep the different spanwise elements of a vortical structure convecting downstream at the same rate, even if the spanwise organization of that structure is in the process of breaking down. The result can be a spanwise array of distinct vortical lumps, all of which are convected past a streamwise measuring station at the same time; hence fluctuations that are synchronized across the span are produced, despite the three-dimensionality of the vortical structures. The spanwise cross-correlation indicates a high degree of spanwise coherence, much as if the structure were indeed two-dimensional.

The phenomenon just described can be seen in the results of flow-visualization studies of the reattaching shear layer. Figure 13 presents two images of a transverse ( $y-z$ ) plane at  $x/h = 8.7$  for a case of shear-layer excitation at  $St_x = 0.111$ . These images are frames from a high-speed video sequence (framing rate = 2000/s), computer-corrected for view angle and intensity variation. The interval between the images shown is approximately one-half the period of the fundamental excitation, i.e., the images are about one-half cycle apart. The two most important features of this sequence are (1) the very pronounced spanwise structure in the reattached shear layer, and (2) the very evident, spanwise-organized thinning of the layer from the first image to the second. Referring back to Figs. 10 and 11, we recall that a high degree of spanwise temporal correlation exists for this case, despite the pro-

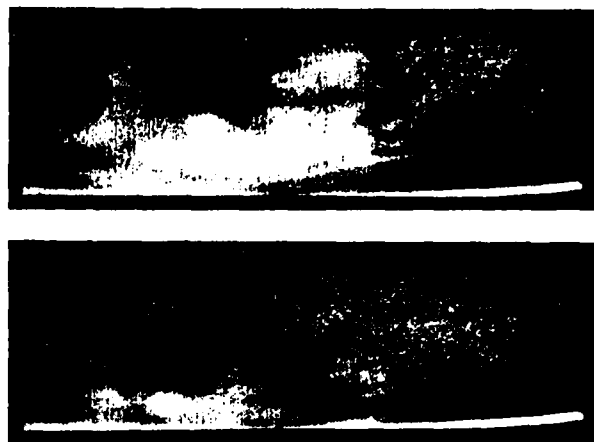


Fig. 13. Transverse-plane images at half-cycle intervals of reattached turbulent shear layer at  $x/h = 8.7$  ( $St_x = 0.111$ ).

nounced three-dimensionality of the vortical structures passing through the light sheet.

Two more transverse-plane images, shown in Fig. 14, were selected at random from a high-speed video sequence taken with no shear-layer excitation. Figure 14(a) shows that the reattached shear layer occasionally presents a rather uniform, well-ordered cross-section: there appear to be four structures of similar size across the span. In addition to showing considerably greater irregularity, the image in Fig. 14(b) shows a significant feature that appears quite frequently: the sweeping of

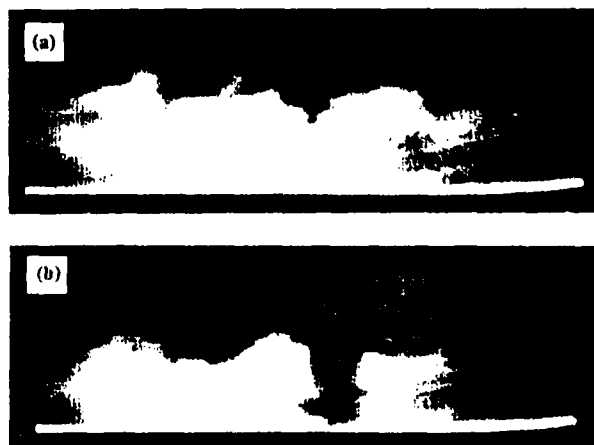


Fig. 14. Transverse-plane images of reattached turbulent shear layer at  $x/h = 8.7$  ( $St_x = 0$ ).

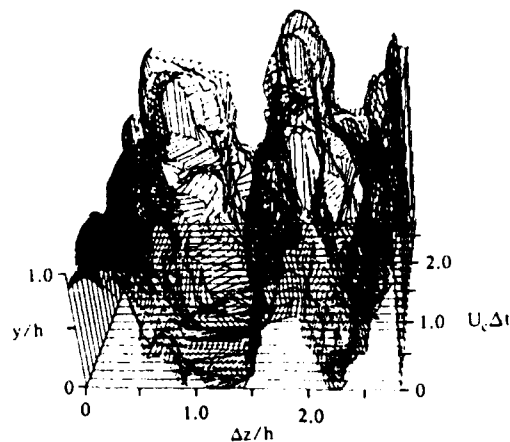


Fig. 15. Quasi-3-D reconstruction of large-scale structures downstream of reattachment (laminar separation).

smoke-free outer flow all the way down to the reattachment wall, as evidenced by the dark gap in the shear-layer image. Efforts are presently under way to apply digital image-analysis techniques to these shear-layer images to extract information concerning characteristic spatial features of the three-dimensional vortical structures. A preliminary example of a form of analysis of transverse-plane flow-visualization information is shown in Fig. 15, a quasi-three-dimensional reconstruction of the evolving spanwise structure in a low-speed (laminar separation) shear layer. The techniques involved in producing this reconstruction are discussed in the companion paper by Kegelman (1986).

#### 4. CONCLUSIONS

The development and evolution of vortical structures in a reattaching turbulent shear layer have been studied in a series of experiments on the flow over a backward-facing, two-dimensional step. Excitation of the shear layer by low amplitude oscillation of a flap at the point of flow separation has proved to be very effective in enhancing and controlling the development of vortical structures in the reattaching flow.

Excitation at a variety of frequencies clarified the existence and nature of vortex merging in the fully turbulent reattaching layer.

Reattachment length was reduced substantially with excitation, but only for frequencies that permitted vortex merging to occur prior to reattachment.

Spanwise coherence of shear-layer vortical structures increased greatly with excitation at low frequencies, but diminished with increasing excitation frequency once vortex merging developed. For frequencies that permitted two stages of vortex merging before reattachment, spanwise coherence decreased in comparison to the unexcited case.

Similarly, reattachment-wall pressure fluctuations increased in intensity with low-frequency shear-layer excitation, but reduced to unexcited-case levels when multiple merging occurred.

Flow-visualization results showed that a high degree of spanwise correlation is not synonymous with the existence of highly two-dimensional vortical structures. In fact, strongly three-dimensional vortical-structure fields often show strong spanwise correlation as they are convected through and beyond reattachment.

#### REFERENCES

- Bhattacharjee, S.; Scheelke, B.; Trout, T. R. 1986: Modification of vortex interactions in a reattaching separated flow. *AIAA J.* 24, 623-629.
- Eaton, J. K.; Johnston, J. P. 1981: A review of research on subsonic turbulent flow reattachment. *AIAA J.* 19, 1093-1100.
- Kasagi, N.; Hirata, M.; Yokobori, S. 1977: Visual studies of large eddy structures in turbulent shear flows by means of smoke-wire method. In: *Flow visualization* (ed. Asanuma, T.). pp. 245-250, Washington-New York-London: Hemisphere.

- Kegelman, J. T. 1986: A flow-visualization technique for examining complex three-dimensional flow structures. Tenth symposium on turbulence, University of Missouri-Rolla, Rolla, Missouri.
- Müller, A.; Gyr, A. 1981: Visualization of the mixing layer behind dunes. In Euro-mech 156, The mechanics of Sediment-transport, Istanbul.
- Pronchick, S. W.; Kline, S. J. 1983: An experimental investigation of the structure of a turbulent reattaching flow behind a backward-facing step. Report MD-42. Thermosciences Division, Dept. of Mechanical Engineering, Stanford University.
- Roos, F. W.; Kegelman, J. T. 1985: Control of coherent structures in reattaching laminar and turbulent shear layers. AIAA Paper No. 85-0554.
- Roos, F. W.; Kegelman, J. T. 1986: Influence of excitation on coherent structures in reattaching turbulent shear layers. AIAA Paper No. 86-0112.
- Simpson, R. L. 1985: Two-dimensional turbulent separated flow. AGARDograph No. 287, Vol. 1. Advisory Group for Aerospace Research and Development, North Atlantic Treaty Organization.
- Troutt, T. R.; Scheelke, B.; Norman, T. R. 1984: Organized structures in a reattaching separated flow field. J. Fluid Mech. 143, 413-427.
- Wynanski, I.; Oster, D.; Fiedler, H. 1980: A forced, plane, turbulent mixing layer: A challenge for the predictor. In: turbulent shear flow 2. pp. 314-326, Berlin-Heidelberg-New York: Springer-Verlag.

A VORTEX RING/VISCOUS WALL LAYER  
INTERACTION MODEL OF THE  
TURBULENCE PRODUCTION PROCESS  
NEAR WALLS

C. C. Chu and R. E. Falco  
Turbulence Structure Laboratory  
Department of Mechanical  
Engineering  
Michigan State University  
East Lansing, MI 48824

ABSTRACT

Vortex ring-like microscale eddies which were found to exist across the turbulent boundary layer (Falco 1977, 1983) initiate the turbulence production process near walls through interaction with the wall region. An experimental simulation involving an artificially generated vortex ring interacting with a Stokes layer enables investigation of the interaction with reproducible initial conditions and in the absence of background turbulence. All of the observed features in the turbulent boundary layer production process such as the streaky structure, the pockets and the lift-up, and the hairpin vortices, have been observed to form. Interestingly, the model includes interactions that occur with low probability in the turbulent boundary layer, but which contribute significantly to transport, and may be the events most readily controllable.

LIST OF SYMBOLS

D	the diameter of a vortex ring
$U_c$	convection velocity of a Typical eddy
$U_r$	velocity of a vortex ring
$U_{inf}$	freestream velocity
$U_w$	velocity of the moving belt
$\delta$	the Stokes layer thickness
$\nu$	kinematic viscosity
$( )^+$	non-dimensionalized by $\nu/u_0$
y	coordinate normal to the surface
x	coordinate in the main flow direction
$\theta$	momentum thickness of the shear layer
R	Reynolds number
$\omega$	vorticity
$u_f$	friction velocity
$\lambda$	streamwise wavelength

1. Introduction

We present a moderately extensive review of the important structural features associated with the wall region events, and then discuss new boundary layer observations that further complete our understanding. Then we present the vortex ring/moving wall simulation

experiments, and show where they give us insights and extend our understanding of boundary layer processes. We conclude by briefly discussing the use of the simulation to a) help us further understand the turbulent boundary layer production process, and b) to help establish a rational basis for boundary layer control studies.

1.1 Long streaks found in the wall region

Early investigations of Runstadler, Kline and Reynolds (1963) in the near wall region of turbulent boundary layers discussed the existence of regions of both low speed fluid and of high speed fluid. In general both regions were extended in the streamwise direction. Estimates of the length of the low speed regions, which were marked by a build up of dye they seeped into the sublayer, indicated streaks of  $1000 x^+$  or more existed. Estimates of the high speed streak length were not obtainable, because they were not marked by dye. High speed streaks were found using Hydrogen bubbles emanating from a wire laid parallel to the wall and perpendicular to the flow. The persistence time at the wire was considerable, but estimates were not made. The width of low speed streaks was also estimated to be about 20 wall layer units. They found that the high speed streaks were usually wider, and that they extended across the region between a pair of low speed streaks.

1.1.1 Low speed streaks come in pairs

A number of investigators have studied the formation of low speed streaks. Oldaker and Tiederman (1977) observed that a pair of low speed streaks formed as a result of the response to what appeared to be a sequence of local high speed outer region eddies interacting with the wall and aligned along a streamwise direction. The path left by the outer region disturbances clearly formed a high speed streak. Falco (1980a) observed the formation of low speed streaks in pairs by a similar mechanism. Although low speed streaks are often observed to exist singly, care must be taken when interpreting low speed streak formation, because once formed the low speed streaks can persist for very long times (see Smith and Metzler 1983).

1.1.2 High speed streaks come singly

The formation of pairs of high speed streaks has not been reported, although high speed streaks have been observed to alternated with low speed streaks for short distances near Hydrogen bubble wires.

1.1.3 Spacing of the low speed streaks

Schraub and Kline (1965) have determined that the low speed streaks are spaced  $102 \pm 10$  wall layer units. Smith and Metzler (1983) extended the counting to higher Reynolds numbers ( $Re = 5800$ ), and concluded that the spacing was Reynolds number independent.

#### 1.1.4 Stability of the low speed streaks

The low speed streaks break up. This has been observed by all investigators, starting with Runstadler, Kline, and Reynolds (1963). The stability of the high speed streaks has not been similarly investigated.

Low speed streaks have been observed to break down by first lifting up, then showing a growing waviness, which is followed by rapid breakdown. More recently, Acarlar and Smith (1984) have observed that low speed streaks can breakdown by the formation of hairpin vortices growing out of them. Falco (unpublished) has also observed this form of breakdown of the long streaks, but it is much rarer than the wavy breakdown. Falco (1978) observed another mechanism of long streak breakup that appeared to be most common. Streaks were observed to break up because of the movement towards the wall of coherent outer region eddies, which simply pushed the marker that gathered into the streak away from their path. Schraub and Kline (1965) also appeared to have observed this form of streak breakup. Looking upstream they observed "the ejection of sublayer fluid appears to be usually initiated by the sudden spreading or widening of a relatively high u-velocity region. This faster fluid then "interacts" with the slower fluid on both sides as it spreads." They noted that a pair of counter rotating patterns emerged when high speed fluid came down to the wall, pushing low speed fluid, marked by the presence of Hydrogen bubbles, sideways.

#### 1.1.5 Reynolds stress

There is very little Reynolds stress associated with streaks that are stably present on the wall. When streaks lift-up, we can get significant Reynolds stress. However, we have observed that the streak lift-up is associated with the presence of a specific outer region coherent motion called a Typical eddy (Falco 1977).

#### 1.1.6 Streak formation

Since the mid fifties, it has been suggested that long counter rotating streamwise vortices exist in the wall region and that pairs of these vortices produce a gathering of wall layer dye between them that we see as the low speed

streaks. A high speed streak would be the result of high speed fluid being induced towards the wall between a pair of these streamwise vortices rotating the other way. A number of authors have suggested causes for these streamwise vortices. The currently most popular suggestion is that they are the 'legs' of hairpin vortices that are also observed in the wall region. However, as Acarlar and Smith (1984) have pointed out, it is very hard to understand how the hairpin legs could extend upstream as far as would be necessary to produce streaks of length  $1000 x^+$ . Thus, there is still no experiment evidence supporting the various rational physical hypothesis describing the formation of streaks.

### 1.2 Pockets

Another feature of the wall region structure that is clearly present close to the dye slit, is the frequent rearrangement of marker that moves it away from a local region, leaving a scoured pocket of low marker concentration.

#### 1.2.1 What they look like

Figure 1 shows two pockets as seen in a layer of smoke marked sublayer fluid. Falco (1980a) described the evolution of pockets and conditionally sampled their Reynolds stress and other quantities. The lateral boundaries of each pocket are a pair of streaks. These are low speed streaks, but are much shorter than the low speed streaks (also see Fig. 1) discussed above. The existence of both these short streak pairs and of the long streaks led Falco (1980b) to suggest that a double structure existed in the wall region.

#### 1.2.2 Pocket scales

The lateral scale and longitudinal scale of the pockets has been measured. Falco (1983) showed that the lateral scale of pockets increases when non-dimensionalized by wall layer variables. At low Reynolds numbers pockets are smaller in scale than the low speed streak spacing, but at about  $Re = 5000$ , they are about the same, and would be considerably larger at technologically important Reynolds numbers.

#### 1.2.3 Pocket frequency

The frequency of occurrence of pockets has been measured by Falco (1983). Pockets scale on wall layer variables, and are spaced on average approximately 27 wall time scales. This is approximately four times as frequent as the time between bursts detected by VITA, the currently most popular 'turbulence detector' (see Blackwelder and Kaplan 1976).

#### 1.2.4 The evolution of pockets

Pockets are footprints of outer

region motions that interact with the wall. Falco (1980a) showed that they start out as a movement of wall layer fluid away from a point as a high speed outer region eddy (a Typical eddy, discussed below), nears the wall. The interaction results in the footprint opening up into a developed pocket shape, which has a pair of short streaks at its lateral boundaries. Next, fluid is seen to lift-up from the downstream end of the pocket. This lifted fluid takes on the characteristics of a hairpin vortex (Falco 1982).

#### 1.2.5 Reynolds stress associated with pockets

Significant Reynolds stress is associated with all of the stages of pocket formation. Falco (1980a) discussed the distributions in detail. He found that during the early part of the interaction ensemble averaged Reynolds stress signatures of the order of 10 times the long time average existed, which were the result of the sweep. Later, Reynolds stress signatures of equal magnitude were found that were the result of the lift-up and ejection of fluid from the downstream end of the pocket.

### 1.3 Hairpins

Vortex lines are constantly being bent in a turbulent boundary layer. Although flow visualization of a passive contaminant can not be used to observe vorticity directly, smoke marked features in the wall region that appear to be hairpin vortices have been observed by Falco (1982). The concentration of distorted vortex lines into hairpin vortices has been observed to result from two mechanisms.

#### 1.3.1 Formation and stability of hairpins emerging from the lift-up of fluid out of pockets

As mentioned above, in the later stages of pocket evolution, wall layer fluid is lifted and at times ejected out of the pocket. This fluid takes the form of a hairpin vortex (see Falco 1982). Depending upon the type of interaction that occurs, the hairpin may a) remain in the sublayer, b) lift above the sublayer and then return to the wall, c) lift above the sublayer and undergo an evolution that leads to necking down and pinch-off into a vortex ring, and d) lift-up and get ingested into the Typical eddy that induced it up. In general, the hairpins do not remain stable for very long. In particular, we have never observed a hairpin to remain 'in tact' long enough to move across the boundary layer as suggested by Head and Bandyopadhyay (1981).

#### 1.3.1.1 Strength of hairpins emerging from pockets

An estimate of the strength of the hairpins that emerge out of the pockets can be made from the data of Falco (1980a) who ensemble averaged the vorticity (as represented by  $du/dy$  only) at the downstream end of the pockets at  $y^+ = 16$ . Although this is not a direct measure because the probe is not within the hairpin at its strongest time, and furthermore, the hairpin in some cases has been ingested, it is a conservative estimate. We see that  $\omega_x$  is 4 times the mean shear.

#### 1.3.2 Hairpins forming over streaks

We have observed hairpins forming out of a single streak. The streak is seen to become lumpy, and one of the lumps grows and a hairpin emerges from it. Acarlar and Smith (1984) have also observed hairpins growing over simulated streaks, and it appears, in a turbulent boundary layer.

#### 1.3.2.1 Strength and stability of hairpins

As far as we are aware, no measurements of the strength of these hairpins has been made. We have made very few observations of them. Because of the fact that their formation is due to an instability of the streak, which may be similar to the lumping instability mode found by Swearington (private communication) to occur in some cases of streak breakdown in Taylor Gortler experiments, and not to the presence of some coherent motion in the region above them, once they form they may not be subjected to strong ambient perturbations that destroy them for some time, and may move a little further out into the layer. However, as mentioned above, we have never observed a hairpin to remain stable and move across an appreciable fraction of a fully turbulent boundary layer.

#### 1.3.3 Hairpin formation at other times

We have also observed hairpins to form between two streaks under conditions in which no pocket was present. As with the findings in the previous section, this was a rare observation. Our observations discussed below shed light on these occurrences.

### 1.4 Typical eddies

The microscale coherent motions which are similar to laminar vortex rings are called Typical eddies. They have been studied by Falco (1974, 1977, 1983) who showed that they contribute significantly to the Reynolds stress in the outer part

of the boundary layer, and that they are the excitation eddies that create the pockets.

#### 1.4.1 Typical eddies are vortex rings

All available evidence suggests that the Typical eddies are laminar vortex rings. Experiments using two mutually orthogonal sheets of laser light enabled us to determine, as far as the smoked marking allows, that the coherent feature was a ring. Falco (1980b) presented evidence of this type. More recently, Falco (1982, 1983) presented additional evidence showing the existence and importance of Typical eddies in the inner region.

#### 1.4.2 Typical eddies create pockets

Typical eddies found near the wall are directly responsible for the formation of pockets and play a large part in their evolution. Falco (1982, 1983, 1984) and Lovett (1982) have described these interactions, the specific outcomes of which are too detailed to present here.

#### 1.4.3 Direction of Typical eddy motion

Typical eddies have been observed to move both towards and away from the wall. In general, we have found Typical eddies orientated so that they induce themselves away from the wall. However, if they are in a large scale wallward flow, then the net velocity may be wallward. Eddies moving towards the wall have been observed positioned in the valleys between the large scale bulges. Eddies in this position have also been observed to move away from the wall, but most often Typical eddies moving away from the wall are found under the large scale bulges, which have a net outward flow (Falco 1977). Most of the observed angles--whether towards or away from the wall--have been shallow, often no more than a few degrees.

#### 1.4.4 Convection velocities

The average convection velocity of Typical eddies has been measured in the outer region by Falco (unpublished). It was found that the eddies move with approximately the local mean velocity of their center of mass.

#### 1.4.5 Formation in the outer region

Typical eddies have been observed to form in the outer region of turbulent boundary layers, on the upstream side of the large scale motions (Falco 1977). Recently, Moin, Leonard, and Kim (1986) have performed numerical studies using the full Navier Stokes equations, and demonstrated that the straining field of a large scale loop of vorticity can induce

ambient vorticity to reorganize into a vortex ring. The reorganization takes place on the upstream side of the large scale coherent vortex motion, essentially confirming the observations made in the boundary layer.

#### 1.4.6 Formation from lifted hairpins

Both types of hairpin creation mechanisms described above can produce hairpins that can pinch-off and form new vortex rings. Falco (1983) showed visual evidence of a hairpin lifting from the downstream end of a pocket, contorting and pinching off to form a new vortex ring-like Typical eddy. This pinch-off mechanism has also been clearly shown to occur in the calculations of Moin, Leonard and Kim (1986).

### 1.5 Streamwise vorticity

Many investigators have noted the presence of streamwise vortices in the wall region. Almost without exception, the vortices have been of short extent ( see Praturi and Brodkey (1978), Falco (1980b) Smith (1982)). A number of investigators have suggested that streamwise vortices of much greater extent exist in the wall region, essentially laying just above the wall in pairs, which are responsible for the creation of both low and high speed streaks, however, no one has ever observed them, and recent calculations of turbulent channel flow using the full Navier Stokes equations (see Kim 1986), have shown that the eddies which have streamwise vorticity are not elongated in the stream direction.

## 2. Experimental techniques

### 2.1 Boundary layer observations

The boundary layer motions were made visible by seeding the flow with .5 - 5 micron oil droplets, and illuminating the oil fog with laser light spread into sheets that could be placed parallel to the wall in the wall region, or perpendicular to the wall and parallel to the flow, or both. The technique has been described by Falco (1980c), so we will not repeat the details here. A new twist, used in these new experiments, which was of particular value in finding the long streaks and their correspondence with the coherent motions above the wall, was the capability to observe the washout of smoke in a laser sheet parallel to the wall while we could simultaneously observe the motion above the wall in a laser sheet perpendicular to the wall and parallel to the flow.

### 2.2 Vortex ring/moving wall simulations

We can simulate the interaction of a

Typical eddy with the viscous wall region of a turbulent boundary layer by creating a vortex ring and having it convect towards or away from a moving wall. For convenience, we have used an impulsively started wall. It has the advantages of being an exact solution of the Navier-Stokes equations (Stokes first problem), and therefore is well defined. Furthermore, it is approximately linear in the wall region which is similar to the viscous sublayer of a turbulent boundary layer.

#### 2.2.1 Experimental apparatus

Experimental simulations were performed in a water tank which is 16" deep by 12 3/4" wide by 96" long. Figure 2 shows the side view and end view of the experimental apparatus which includes a vortex ring generating device, a moving belt and driving arrangement, a synchronizing timer, and visualization recording devices.

#### 2.2.2 Vortex ring generating device

The vortex ring generating device includes a constant head reservoir from which fluid, which could be dyed, passes through a solenoid valve whose opening time could be varied, and an orifice of prescribed size (see Figure 2 items 1,2,3). The constant head reservoir (1) is filled with a mixture of 10 ppm Fluorescent Sodium Salt Sigma No. F-6377, green dye and water solution. As the solenoid valve (2) opens, a slug of dyed fluid is released from the orifice (3) by the pressure head, and rolls up into a vortex ring. Three different inner diameters of the orifice have been used; 1", 1/2", and 3/8". The size and speed of the vortex ring generated depends upon both the height of the dye reservoir and the opening duration time of the solenoid valve for a fixed orifice. The details were discussed in Liang (1984).

#### 2.2.3 Moving belt and driving device

The wall upon which the vortex ring interacted is actually a moving belt (4) made of transparent plastic which has a smooth surface. Two ends of the belt are joined together to form a loop, which circulates around two rollers (5) as shown in Figure 2. The width of the belt is 7 inches; and the distance between the two rollers is 60 inches. The test section is at 30 inches downstream from one of the rollers, giving us a Stokes layer for this distance (if the belt is run longer Blasius effects begin to enter into the problem). This width/length ratio is sufficient to prevent the disturbances generated in the corners from reaching the center of the belt at the test section. Therefore, the wall layer flow on the

moving belt could be considered two-dimensional. One of the rollers is driven by a 1/4 HP DC motor (6). The speed of the belt is adjustable within the range from 1 in/sec. to 9 in/sec. The belt reaches a constant speed very soon (within a second) after power is on. This hard-start character allows us to consider the belt to be impulsively started. As the belt moves, a Stokes layer builds up on the belt. A mixture of red food coloring and water is used to mark the wall layer for visualization. The belt is covered with dye before each run in a 'dye run' using a dye injector near the leading roller of the belt, shown in Figure 2 (7).

#### 2.2.4 Timing

The opening duration time of the solenoid valve, and the time delay between the onset of the belt movement and release of the vortex ring are controlled by a 115 VAC/60 HZ timer designed in the laboratory. Since the thickness of the Stokes layer,  $\delta$ , is a function of the square root of the belt run time, by carefully adjusting the time delay, we can adjust  $\delta/D$  as desired.

#### 2.2.5 Visualization and recording

The primary visual data consisted of simultaneous plan and side view time resolved images which were collected using a standard VCR, a video camera, and a monitor, shown in the end view of Figure 2. The side view was often illuminated by a laser sheet emitted from an 8 W Coherent CR-8 Supergraphite Argon Ion Laser. The visual data were analyzed on a high resolution monitor with a superimposed calibrated scale, using the slow motion capabilities of the recorder.

### 3. New boundary layer observations

#### 3.1 Typical eddy wall interactions create both streaks and pockets

The major discovery is that as a Typical eddy convects over the wall, it causes a far field interaction that results in the formation of a pair of long streaks. If the Typical eddy is convecting towards the wall, when it gets close enough, it will create a pocket, and have one of four types of interactions defined below. The far field effect of the Typical eddies has been surprising. Eddies as far as 3.5 wall region thicknesses (greater than 100 wall units) which are convecting at shallow angles either towards or away from the wall have been observed to create streaks. Thus, only one mechanism is necessary to create all of the structure found in the wall region.

This long range effect has made the

observations connecting the formation of a streak pair with the passage of a Typical eddy very difficult. For a long time the connection was dismissed, because it was thought that other motions (for example, the large eddies) or other mechanisms within the boundary layer must have had the governing influence, and here we include any of the classical hypothesis. However, using the vortex ring/moving wall model we describe below, we found that the interaction of the coherent vortex rings definitely does occur over these distances. With the model, which doesn't have any additional influences present, we could be certain that the interaction was the effect of the passage of the eddy. This evidence does not remove the possibility that other coherent motions in the boundary layer can create a pair of streaks, however, Falco (1977) has pointed out that their are only two important coherent motions, the Typical eddies and the large scale motions. This, combined with the fact that if all other scales of motion in the boundary layer contributed to the creation of streaks, we would not have a preferred streak spacing of approximately 100 wall units (Schraub and Kline 1965), lends support to the argument that Typical eddies are primarily responsible. The possibility of interaction of the large scale motions can not be ruled out, but at high Reynolds numbers the large scale motions may have scales many thousands of wall layer units, and thus could not be the primary streak producing mechanism.

3.2 All occurrences of hairpin vortices connected with Typical Eddy/wall interaction.

Observations mentioned above have indicated that hairpin vortices can form as a result of pocket evolution and as a result of lumping instability of existing low speed streaks. We also indicated that there were occurrences where neither of these mechanisms appeared to be the cause. We have now identified another mechanism that can result in the formation of hairpin vortices. When a Typical eddy is moving away from the wall at a shallow angle and when it is moving relatively slowly, say  $U_c/U_{inf} < .4$ , it will create a pair of long very stable streaks that trail behind a hairpin vortex that lifts-up slowly. The fraction of the remaining hairpins that this accounts for is not known, but it may well be an important percentage. These hairpins are in general more stable and last longer than those created by the other two mechanisms.

3.3 Pinch-off of lifted hairpins

Falco (1983) has previously observed

the pinch-off of a lifted hairpin vortex. The circumstance of the characteristics of the excitation eddy could not be ascertained because it was not in the laser sheet illuminating the flow above the wall at the time the pocket was formed.

3.4 Most often observed Typical eddy/wall region interactions

In laser sheet side view studies, we have most often observed a well defined lift-up of sublayer fluid, sometimes a couple of lift-ups, which take(s) on a hairpin configuration. This fluid does not get ingested into the Typical eddy, which moves away from the wall perturbed, but still a stable Typical eddy. The hairpin(s) have most often been observed to twist and lose their coherence, or just move back down towards the wall and dissipate. We call this a Type II interaction. The other commonly observed interaction, called Type III, results in a lifted hairpin of sublayer fluid which almost upon forming, gets ingested into the Typical eddy, resulting in a chaotic breakdown of both the lifted hairpin and the eddy, as the eddy is moving away from the wall.

In plan view studies the above mentioned interactions are accompanied by the formation and evolution of a pocket.

4. Vortex ring/moving wall interactions

4.1 Vortex ring interacting with a moving belt

We can simulate the interaction of a Typical eddy with the wall region of a turbulent boundary layer by creating a vortex ring and having it convect towards a moving wall. Figure 3 shows the basic idea behind the simulation. The vortex ring can be aimed at or away from the wall at shallow angles. Both the wall and the ring move in the same direction. The Reynolds numbers based upon the initial ring velocity and diameter of the dyed ring bubble,  $D$ , ranges between 900 and 2000. When created away from walls, these rings remain stable to azimuthal instabilities over durations longer than those used in the interaction experiments. By performing a Galilean transformation on the simulation, we recover the essential aspects of the turbulent boundary layer flow.

4.2 Evolutions of the model

We will describe the model in terms of the velocity ratios and spatial relationships of the simulation. Later in the discussion, we will invoke the Galilean transformation to relate the findings to the turbulent boundary layer

case.

#### 4.2.1 Fast rings ( $U_r/U_w > .45$ ) moving towards the wall

Interactions which result from these rings have been described by Liang, Falco and Bartholomew (1983). They result in the formation of a pocket, and varying degrees of lift-up of wall layer fluid. The interactions have been divided into four types. Figure 4 shows sketches of the four types of interaction. Type I results in a minor rearrangement of the wall layer fluid; followed by the ring moving away from the wall essentially undisturbed. Type II (same as described for boundary layer interactions) results in a well defined lift-up of wall layer fluid, which takes on a hairpin configuration. This fluid does not get ingested into the ring, and the ring moves away from the wall perturbed, but still a stable ring. The hairpin has been observed to pinch-off, or just move back down towards the wall and dissipate. Type III (also described in section 3.4) results in a lifted hairpin of wall layer fluid which gets ingested into the ring, resulting in a chaotic breakdown of both the lifted hairpin and the vortex ring, as the vortex ring is moving away from the wall. Type IV also initiates a hairpin vortex, but in this case the hairpin vortex is ingested into the ring on a much shorter timescale, and the ring and lifted wall layer fluid both breakdown while the ring is very close to the wall.

Liang et al. used vortex rings with  $D^+ > 250$  and  $\delta^+$  between 20 and 50, and they observed only the above four types of interactions. Our experiments indicate that if  $D^+ < 150$  and  $\delta^+$  is between 20 and 50, we can also obtain the four types of interactions noted above, but in addition, we found that long streaks also formed. In these cases, a hairpin grew out of the open end of the pocket, its legs stretched and a pair of streamwise streaks formed along side the hairpin legs. The streaks grew to several hundred wall units. This observation is in contrast to the suggestions of a number of investigators that a lifted hairpin vortex would induce a single streak to form between its legs.

#### 4.2.2 Slow rings ( $U_r/U_w < .35$ ) moving towards the wall at a shallow angle

These initial conditions result in a pair of long low speed streaks, a pocket and a hairpin lift-up. Figure 5 shows six photos of this happening prior to the onset of a Type III interaction. We can see the formation of the pair of low speed streaks, followed by the formation of the pocket, and the associated hairpin lift-up, then partial ingestion. The ring later breaks up. The streaks that form under

these conditions become wavy and slowly breakdown resulting in additional lift-up and transport. The initial conditions are two-dimensional. The moving belt is started from rest, so that the layer approximates a Stokes layer. These streaks have obviously not formed as the result of the existence of streamwise vortices, but it is clear from the Navier Stokes equations that streamwise vorticity has been generated at the wall.

#### 4.2.3 Fast rings ( $U_r/U_w > .45$ ) moving away from the wall at a shallow angle (less than 3 degrees)

These initial conditions result in a hairpin vortex which is linked to the distributed streamwise vorticity that has formed a pair of long, very stable, low speed streaks. A pocket is not observed. The evolution of the hairpin in this case can lead to the pinch-off of this hairpin, forming a vortex ring, and another hairpin. Figure 6 shows four photos of the evolution leading to the creation of a new vortex ring. The long stable streaks which form, come closer and closer together, indicating that the streamwise vorticity which caused them, and which is of opposite sign, is being stretched and brought very close together. Diffusion is accelerated, and the vorticity is redistributed into a vortex ring and a hairpin loop. Figure 7 shows long very stable streaks and a long stretched hairpin which does not pinch-off over the distance available due to size limitations of the experimental facility--more than 2500 wall layer units. There are two initial conditions that may cause this kind of long stretched streamwise vorticity to evolve into a hairpin: 1)  $\delta/D$  is very small; 2) the ring is far away from the wall. Further study concerning the effects of ring to wall distance is needed.

#### 4.2.4 Slow rings ( $U_r/U_w < .45$ ) moving away from the wall at a shallow angle

These initial conditions result in a hairpin from which a pair of long stable low speed streaks emerge. A pocket is also not observed. The phenomena of hairpin pinch-off, for this case, appears to depend upon  $\delta/D$ . If  $\delta/D < .15$  we get pinch-off, but only a part of the fluid involved in the hairpin is observed to pinch-off and form the ring. If  $\delta/D$  is greater, and the ring moves away from the wall without ingesting any wall layer fluid (Type I or II), the lifted hairpin appears to do very little. Figure 8 shows four photos of the evolution for  $\delta/D > .15$ . In this case a pocket does not form, and it appears that the hairpin has been generated by the initial vortex ring/wall interaction, and that a pair of streamwise vortices--which could be called its legs--trail behind, creating the steak pair.

Pinch-off does not occur. Figure 9 shows four photos of the interaction for  $\delta/D < .15$ . In this case pinch-off of a portion of the lifted hairpin does occur creating a new small vortex ring.

#### 4.2.5 Summary of interactions

A summary of the vortex ring/wall interactions which result in streak formation and evolution is shown as a function of the parameters  $U_r/U_w$ ,  $\delta/D$  and ring angle in Fig. 10 and 11. Figure 10 shows the dependence of the formations and evolutions of streaks on  $\delta/D$  and  $U_r/U_w$  for  $D^+ > 250$  and a 3 degree incidence angle. The indicated boundaries are between different evolutions are approximate; additional data is necessary to precisely locate their positions. The information available suggests that the streak development is essentially independent of  $\delta/D$ . Furthermore, streaks are only observed to form for speed ratios less than approximately .45. Figure 11 shows the dependence of  $\delta/D$  on  $U_r/U_w$  for rings moving away from the wall at 2.5 degrees.  $\delta/D$  now plays a much more important role, and long streaks are generated over the entire speed ratio range studied.

#### 4.3 Scaling associated with the vortex ring/moving wall interactions

From our perspective of a turbulence production model, the streak spacing, streak length and wavelength of the streak instability are quantities of interest.

##### 4.3.1 Streak spacing

Figure 12 shows the dependence of the streak spacing in wall units on the size of the vortex ring in wall units, for an incidence angle of 3 degrees and  $U_r/U_w = .31$ . The thickness of the wall layer (in wall units) is shown next to each data point. The streak spacing,  $Z^+$ , is within 10% of the ring diameter for wall layer thicknesses between 20 and 50 wall units. Results show that decreasing  $U_r/U_w$  will decrease the average streak spacing relative to the ring size for fixed incidence angles. Furthermore, increasing the incidence angle of the vortex ring will increase the average streak spacing for a given ring size and speed ratio. Figure 13 shows the dependence of the streak spacing on the speed ratio and angle.

##### 4.3.2 Streak length

Measurements show that streak lengths greater than  $x^+ = 500$  were obtained for many of the interactions in ranges where the streaks are stable (for rings with  $D^+ = 100$ , streaks as long as  $x^+ = 1000$  were found).

##### 4.3.3 Wavelength associated with wavy streak instability

Figure 14 shows the non-dimensionalized streamwise wavelength that sets in as a function of  $\delta^+$  for different  $U_r/U_w$ . The wavelength is the same order as the ring diameter. It decreases as the ring/wall speed ratio.

#### 4.4 Stability considerations

##### 4.4.1 Vortex ring stability

Some additional data has been obtained, which confirms and extends the results of Liang (1984), showing the boundary between stable ring wall interactions (Types I and II), and unstable interactions (Types III and IV) depends upon  $\delta/D$ . Figure 15 shows a stability map of the interactions for 3 degree rings. We can see that for low ring/wall speed ratios, the ring stability depends primarily upon the relative thickness of the wall layer and the size of the ring; for thicker wall layers, or smaller rings the interactions are more stable. Furthermore, the shallower the incidence angle the more stable the interaction.

##### 4.4.2 Stability of the streaks

We spent considerable time deciding upon a measure of the time to instability of the streaks which exhibited wavy instability. Figure 16 shows the dependence of the time to instability of the streaks on the wall layer thickness (both quantities non-dimensionalized by wall layer variables) for 3 degree incidence rings. We can see that for each convection velocity ratio, there is a value of  $\delta^+$  above which the time to instability becomes much longer. As the ring/wall speed ratio increases, the critical thickness of the wall layer needed to increase the time to instability decreases.

##### 4.4.3 Comparison between ring and streak stability

Both the rings and the streaks are more stable when the wall layer is thicker. Figure 15 shows a comparison of the stability boundaries of a three degree ring moving towards the wall, and of the boundaries of stable streak formation those rings can create. It turns out that the ring stability curves for different size rings collapse when plotted this way, but the streak formation boundaries remain a function of the size of the ring. As the ring size increases, the unstable region, where streaks breakup as they are forming, increases.

The streak formation boundaries in

this figure represent the boundaries between conditions that will enable a pair of long streaks to form. For  $\delta/D$  below the boundaries, we have a very unstable situation in which the fluid in the region around the eddy seems to rearrange itself into the beginnings of a streak, but the streak pair is not stable, and immediately breaks up. For  $\delta/D$  values above the boundaries, a pair of long streamwise streaks form. However,, once formed the streaks are susceptible to breakdown by the wavy or lumpy instabilities noted above, where the time to instability is a function of angle, convection velocity, and the instantaneous wall layer thickness ( for example, see figure 16 ).

## 5. Implications for turbulent boundary layers

### 5.1 Connection between vortex ring/wall layer description and the Typical Eddy wall layer interaction

To interpret the results of the vortex ring/moving wall interactions in terms of turbulent boundary layer interactions, we must perform a Galilean transformation on the velocity field. Our interpretation of the simulation has been to identify the Stokes layer with the viscous wall region which extends to  $y^+$  approximately 30-50. The mean velocity at this height is approximately 70 -80% of  $U_{inf}$ . Thus,

$$U_c / U_{inf} = a(1 - U_r/U_w)$$

where 'a' represents the outer region velocity defect which we can not simulate (20 -30%). Thus, in thinking about the implications for the turbulent boundary layer, basically high speed ratios in the simulations correspond to low convection velocities of the Typical eddies in the boundary layer. As a result, we expect the Typical eddies that emerge from wall layer fluid (through a pinch-off of lifted hairpin vortices, for example) to have a low convection velocity. Since these are moving away from the wall, they will correspond to fast rings moving away from the wall. These exhibit long streak formation which is stable, and pinch-off, depending upon the thickness of the wall layer. We do see long stable low speed streaks in the boundary layer, and we have limited evidence of hairpin pinch-off. On the other hand, Typical eddies that are convecting towards the wall will be of relatively high speed, and thus simulated by low speed vortex rings moving towards the wall. These will produce long streaks which go unstable (undergoing either wavy or lumpy instabilities), short streaks which go unstable, and pockets in all cases. Again we see all these events in the turbulent boundary layer.

The wide range of interactions that can be simulated using the vortex ring/moving wall experiments are not all admitted by the turbulent boundary layer with equal frequency. Some are not admitted at all. The range of the parameters (angle, wall layer thickness, convection velocity) found in the boundary layer are limited, and in all cases they have skewed probability distributions (towards higher values) that are approximately lognormal. When these distributions are used to determine the events that are most probable, we begin to see what to expect.

Figure 17 shows the distribution of  $D^+$  obtained from the diameter of the Typical eddies of a turbulent boundary layer at  $R_\theta = 1176$ , superimposed upon the streak spacing obtained for various size rings. When the simulation outcomes are conditioned by the probabilities of scales found in the boundary layer, we see that the simulation gives a most likely streak spacing of approximately 100 wall units. This is an important quantitative test of the quality of the simulation.

We have very limited information about distributions of this type for the angles of incidence and/or movement away from the wall, for the convection velocity, and for the instantaneous wall layer thickness, but the evidence indicates that the frequency of occurrence of many of the interactions which we can simulate is quite low in the turbulent boundary layer. Often these interactions are very intense. The conditions in the boundary layer that exist which keep their probability low are essential to the measured values of the drag. We need to explore ways to further limit the occurrence of the violent breakups if we are to pursue a rational program of drag reduction ( and noise reduction ) in the boundary layer. The model allows us to isolate a specific high drag producing event, and carefully study the parameters that it depends upon. We are currently building the sample sizes necessary to more accurately obtain the distributions mentioned above.

### 5.2 Implications for drag modifications

As we have seen, small changes in the parameters of Typical eddy size, incidence angle, convection velocity, and wall layer thickness can alter the evolutions that result when a Typical eddy interacts with the wall. Changes in any of these variables which cause a cross over in the boundaries (such as those shown in Fig. 10 and 11), will result in a change in the drag at the wall.

Consider, for example the angle of

incidence. If we can change the strength of the large scale motions, say, by outer layer manipulators, we can easily change the angle of a Typical eddy that is moving towards the wall, and may even be able to change the direction if it is at a shallow angle, so as to make it move away from the wall. This will effect the stability of both the local eddy wall interaction (interactions of Type I-IV), and the stability of the streaky structure which is created, as well as the formation of new Typical eddies via the pinch-off process. Thus, we can affect not only the local drag, but alter the drag downstream by directly interfering with the cyclic production process.

Modifications to the wall that result in small changes in the effective wall region thickness, for example NASA riblets, will also have an effect on the drag. If increases in wall region thickness above the critical thicknesses can be made (see for example, Fig. 11 and 15), streaks are more likely to remain stable. Furthermore, the local interactions (Types I-IV) will also tend to be of Type I and II. Thus, the drag can also be reduced.

## 6. Conclusions

New findings in the turbulent boundary layer have suggested that long low speed streaks are formed in pairs as the result of the interactions of microscale very coherent vortex ring-like eddies (Typical eddies) propagating over the wall. Depending upon the distance from the wall, the angle of incidence of the eddy with the wall (both magnitude and sign), the convection velocity of the eddy, and the local thickness of the viscous wall region, different structural features can evolve out of the evolution. The distance over which a Typical eddy could interact with the wall and wall layer flow was a surprise, but means that many coherent microscale eddies that are in the outer region take part in the production process.

The vortex ring/moving wall simulation incorporates all of the evolutions and structural features. It dramatically demonstrates that streamwise vortices are not required to produce streamwise streaks. When the streak spacings obtained in the simulation are conditioned by the probability of occurrence of Typical eddy scales found in the boundary layer, we see that the simulation provides the correct streak spacing (approximately 100 wall units). Other possible outcomes of the simulation need to be weighed by the measured probabilities of occurrence of the angles, convection velocities, and length scales of the Typical eddies in the turbulent

boundary layer to enable us to obtain a picture of the most probable interactions, and to gain insight into the causes of the interactions which occur with lower probability, that may contribute significantly to the transport. It appears that turbulent boundary layer control leading to drag reduction can be realized by fostering the conditions suggested by the simulations which will increase the probability of having stable interactions.

## Acknowledgements

This research was sponsored by the Air Force Office of Scientific Research under Contract No. F49620-85-C-0002. We would like to thank Dr. Jim Michaels for his encouragement and advise as contract monitor.

## References

- Acarlar, M.S. and Smith, C.R. 1984: An experimental study of hairpin-type vortices as a potential flow structure of turbulent boundary layers. Rept. FM-5, Dept. of M.E./Mech., Lehigh Univ.
- Blackwelder, R.F. and Kaplan, R.E. 1976: Burst detection in turbulent boundary layers. J. Fluid Mech. 76, pp. 89-101.
- Falco, R.E. 1974: Some comments on turbulent boundary layer structure inferred from the movements of a passive contaminant. AIAA Paper 74-99.
- Falco, R.E. 1977: Coherent motions in the outer region of turbulent boundary layers. Phys. Fluids Suppl. II 20, S124-S132.
- Falco, R.E. 1978: The role of outer flow coherent motions in the production of turbulence near a wall. in Coherent Structure of Turbulent Boundary Layers ed. C.R. Smith and D.E. Abbott pp. 448-461.
- Falco, R.E. 1980a: The production of turbulence near a wall. AIAA Paper No. 80-1356.
- Falco, R.E. 1980b: Structural aspects of turbulence in boundary layer flows. in "Turbulence in Liquids" ed. Patterson and Zakin, pp. 1-15.
- Falco, R.E. 1980c: Combined simultaneous flow visualization/hot-wire anemometry for the study of turbulent flows. J. of Fluids Engr. 102, pp. 174-183.
- Falco, R.E. 1982: A synthesis an model of wall region turbulence structure. In "The Structure of Turbulence, Heat an Mass Transfer" ed. by Z. Zoric', pp. 124-135, Hemisphere Press.

Falco, R.E. 1983: New results, a review and synthesis of the mechanism of turbulence production in boundary layers and its modification. AIAA Paper No. 83-0377.

Head, M.R. and Bandyopadhyay, P. 1981: New aspects of turbulent boundary layer structure. J. Fluid Mech. 107, pp. 297-337.

Kim, J. 1986: Investigation of turbulent shear flows by numerical simulation. Tenth Congress of Applied Mechanics, Austin TX June 16-20.

Liang, S. 1984: Experimental investigation of vortex ring/moving wall interactions. MS Thesis, Dept. Mech. Engr. Michigan State Univ.

Liang, S., Falco, R.E. and Bartholomew, R.W. 1983: Vortex ring/moving wall interactions: experiments and numerical modeling. Bull. Am. Phy. Soc., Series II, 28, p. 1397.

Lovett, J. 1982: The flow fields responsible for the generation of turbulence near the wall in turbulent shear flows. MS. Thesis, Dept. Mech. Engr. Michigan State Univ.

Moin, P., Leonard, A. and Kim, J. 1986: Evolution of a curved vortex filament into a vortex ring. Phy. Fluids 29, pp.955-963.

Oldaker, D.K. and Tiederman, W.G. 1977: Spatial structure of the viscous sublayer in drag reducing channel flow. Phy. Fluids 20 (10), pp. 133-44.

Praturi, A.K. and Brodkey, R.S. 1978: A stereoscopic visual study of coherent structures in turbulent shear flow. J. Fluid Mech. 89, pp. 251-272.

Runstadler, P.W., Kline, S.J. and Reynolds, W.C. 1963: An experimental investigation of the flow structure of the turbulent boundary layer. Dept. of Mech. Engr. Rep. MD-8, Stanford Univ.

Schraub, F.A. and Kline, S.J. 1965: Study of the structure of the turbulent boundary layer with and without longitudinal pressure gradients. Dept. of Mech. Engr. Rep. MD-12, Stanford Univ.

Smith, C.R. 1982: Application of high speed videography for study of complex, three-dimensional water flows. SPIE 348, "High Speed Photography (San Diego), pp. 345-352.

Smith, C.R. and Metzler, S.P. 1983: The characteristics of low-speed streaks in the near-wall region of a turbulent boundary layer. J. Fluid Mech. 129, p. 27.

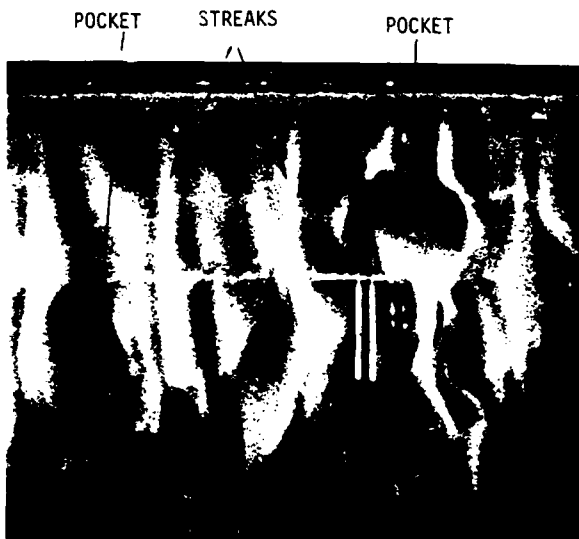


Fig. 1. Two pockets and a pair of streaks as seen in wall slit visualization of the sublayer of a turbulent boundary layer using smoke as the contaminant in air. The slit is at the top of the photo, and the flow is from top to bottom.

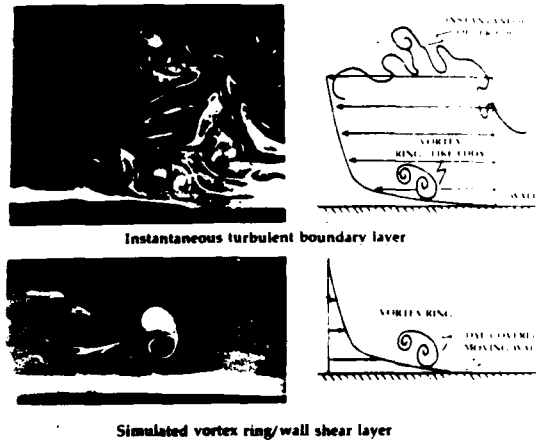


Fig. 3. The basic idea behind the simulation. Performing a Galilean transformation on the vortex ring/moving wall interaction makes it a model of the turbulent boundary layer production process.

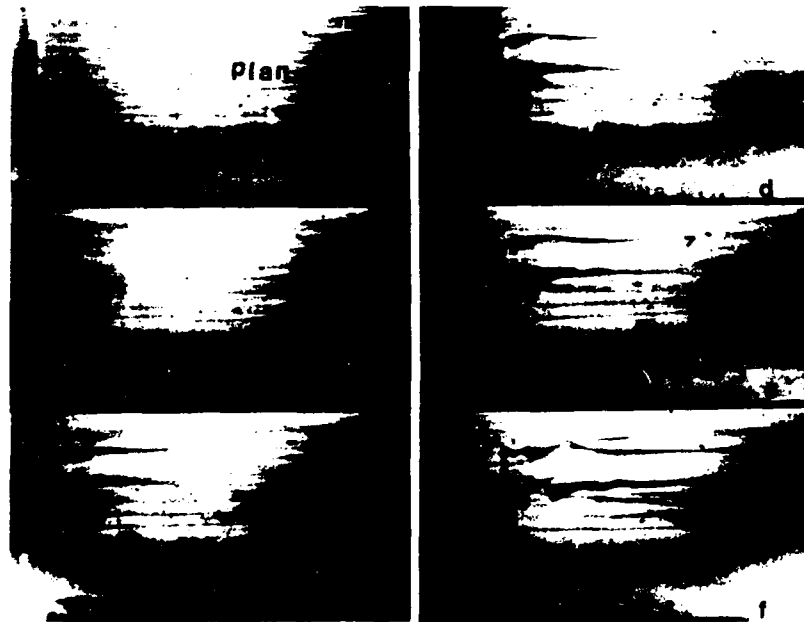


Fig. 5. Six photos of a vortex ring/moving wall interaction for  $U_r/U_w < .35$  when the ring moves toward the wall at a 3 degree angle. Both plan and side views are shown; the ring and the wall are moving to the right; only the wallward side of the ring has dye in it. The interaction results in a pair of long streaks prior to the onset of a pocket and its associated hairpin lift-up, which then gets partially ingested into the ring.

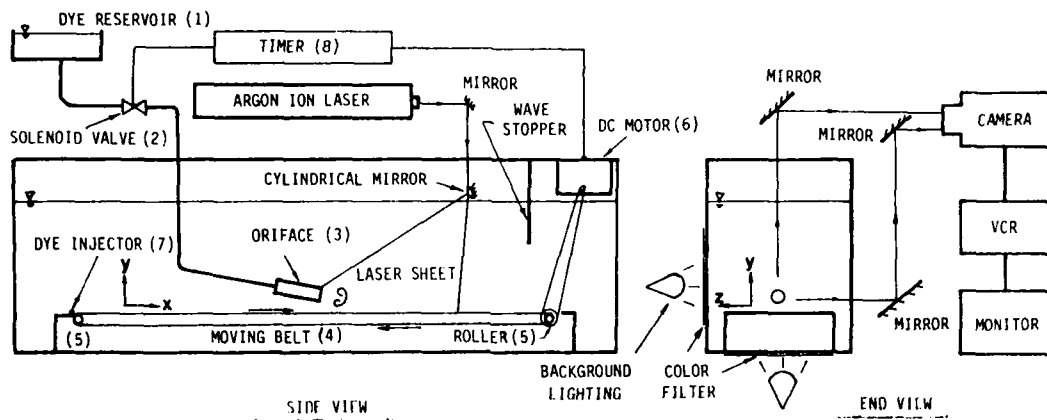


Fig. 2. Side and end views of a schematic of the experimental apparatus used in the vortex ring/moving wall simulations.

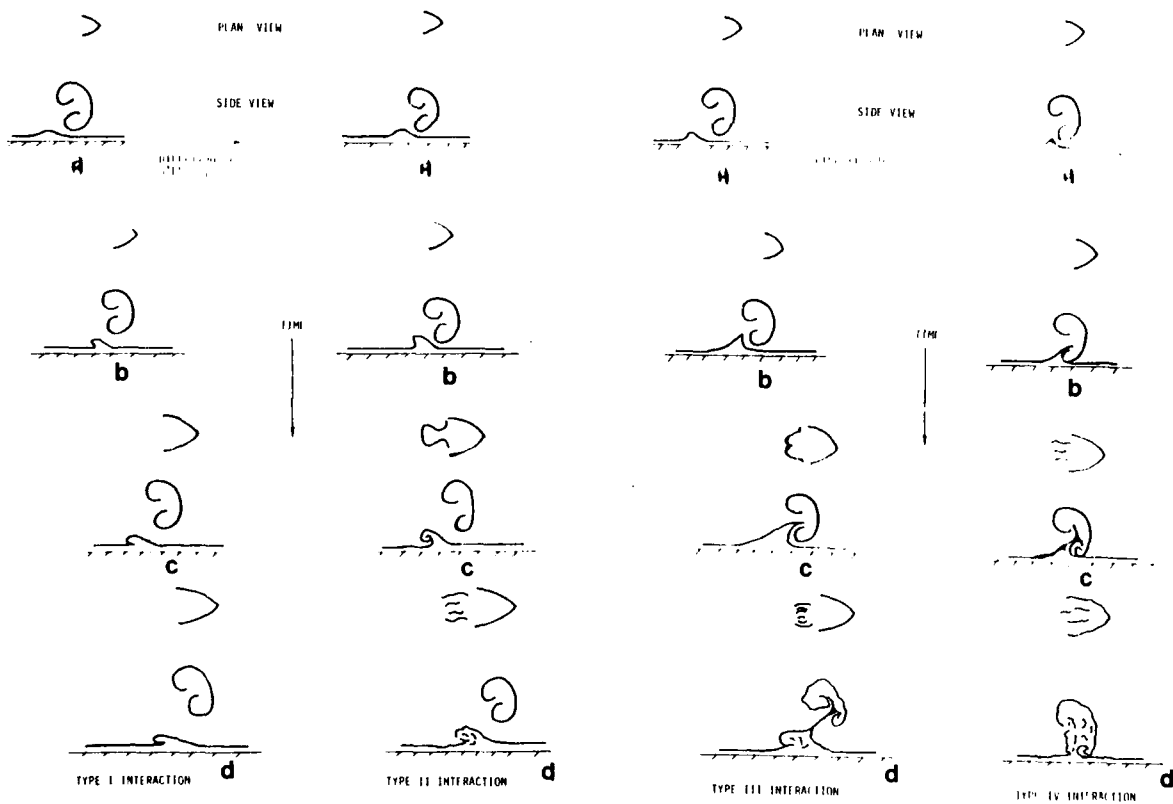


Fig. 4. Sketches of the four types of local vortex ring/moving wall interactions (see text for explanation).

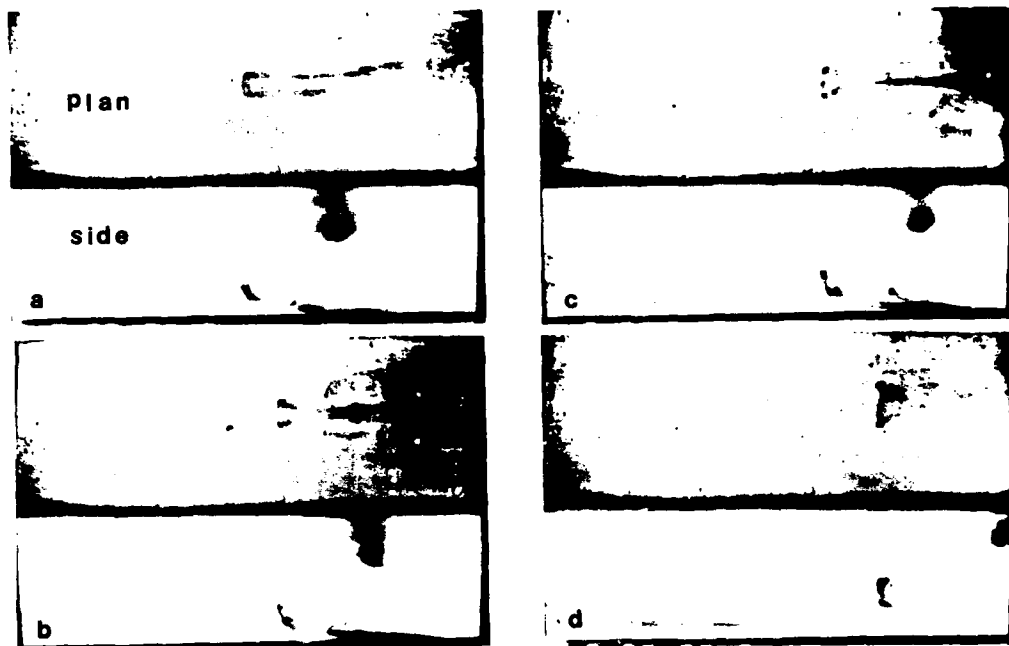


Fig. 6. Four photos of a vortex/ring moving wall interaction for  $U_r/U_w > .45$  when the ring is moving away from the wall at a 2.5 degree angle. Both plan and side views are shown; the ring is at the upper right of the side view; ring and wall are moving to the right. A hairpin forms when the interaction starts. The long stable streamwise streaks which also form, come closer and closer together, indicating that the streamwise vorticity which caused them, and which is of opposite sign, is being stretched and coming closer together. This evolution leads to 'pinch-off' and the creation of a new vortex ring.

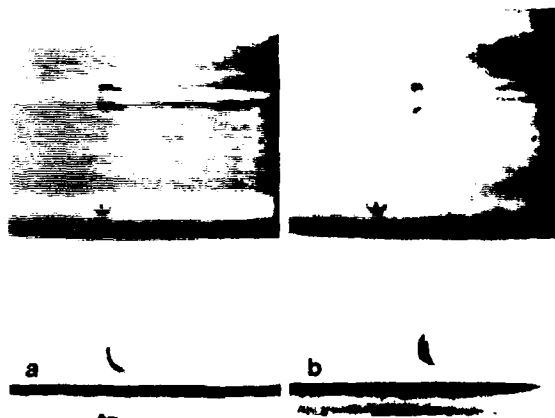


Fig. 7. Same conditions as Fig. 6, except that the wall layer is very thin, so  $b/D$  is small. We obtain long very stable streaks and a long stretched hairpin which does not pinch-off over the 2500 wall layer distance of the facility. The time between each photo is approximately 50 wall units.

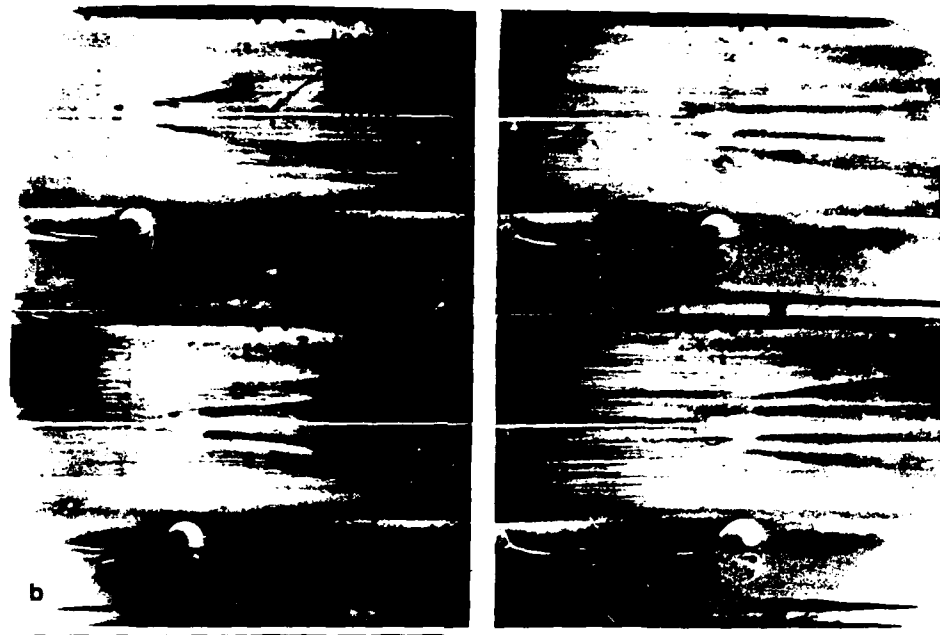


Fig. 8. Four photos of a vortex/ring moving wall interaction for  $U_r/U_w < .45$  when the ring is moving away from the wall at a 2.5 degree angle and  $\delta/D > .15$ . Both plan and side views are shown; the ring has most of its dye in the upper part; ring and wall are moving to the right. Again a pair of long stable streaks is created, a pocket does not form, and a weak hairpin which forms does not pinch-off. There is evidence of a second pair of streaks forming.



Fig. 9. Same conditions as Fig. 8, except that  $\delta/D < .15$ . In this case we again obtain a pair of long stable streaks and a hairpin. Pinch-off of a portion of the lifted hairpin does occur creating a new small vortex ring. We don't have the secondary streak pair forming.

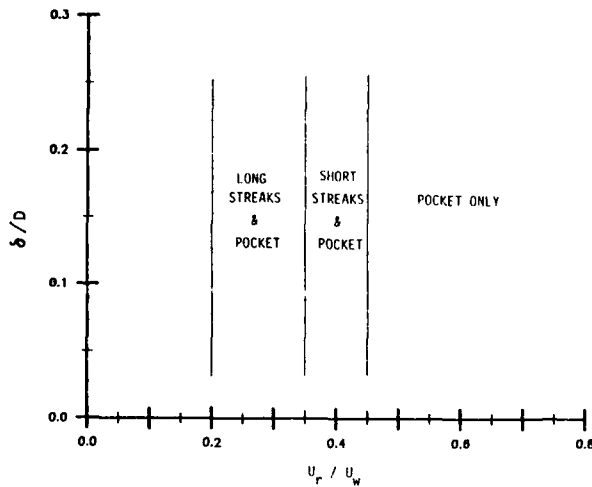


Fig. 10. The dependence of the formation and evolution of streaks on  $\delta/D$  and  $U_r/U_w$  for  $D^+ > 250$  and a 3 degree incidence angle. The indicated boundaries between different evolutions are approximate. Streaks are only observed to form for  $U_r/U_w < .45$ .

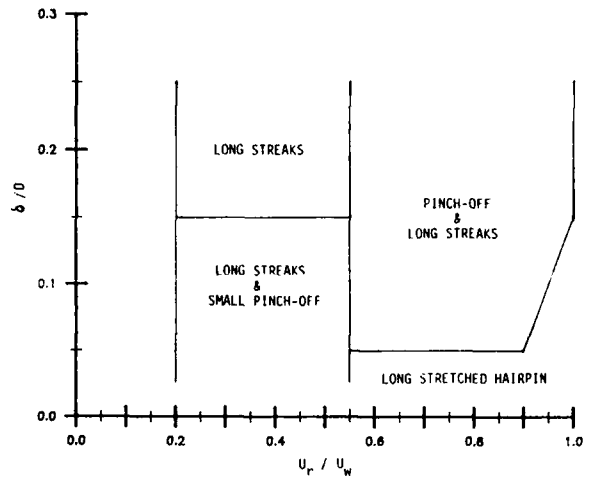


Fig. 11. The dependence of the formation and evolution of streaks on  $\delta/D$  and  $U_r/U_w$  for rings moving away from the wall at 2.5 degrees.  $\delta/D$  now plays a much more important role, and long streaks are generated over the entire speed ratio range studied.

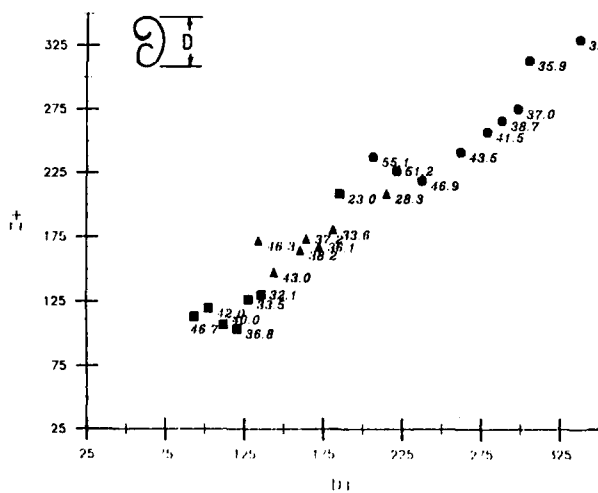


Fig. 12. The dependence of the long streak spacing in wall units on the size of the vortex ring in wall units, for an incidence angle of 3 degrees and  $U_r/U_w = .31$ . The thickness of the wall layer (in wall units) is shown next to each data point.

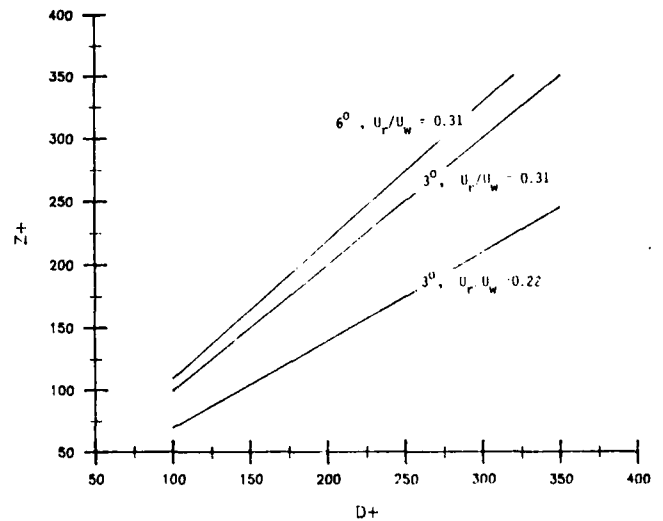


Fig. 13. The dependence of the streak spacing on the speed ratio and ring interaction angle.

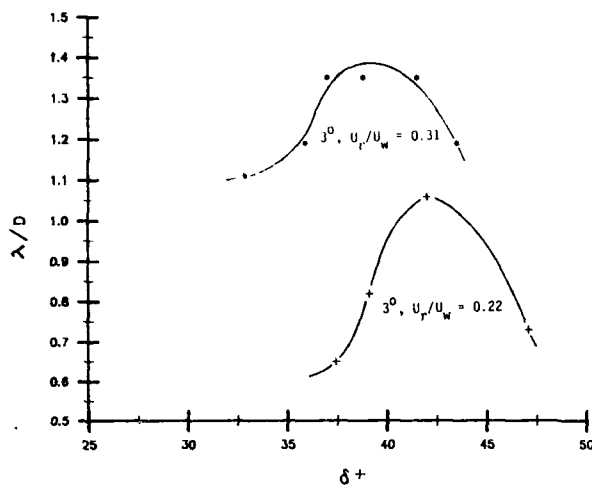


Fig. 14. The non-dimensionalized streamwise wavelength of streaks subjected to wavy instabilities.

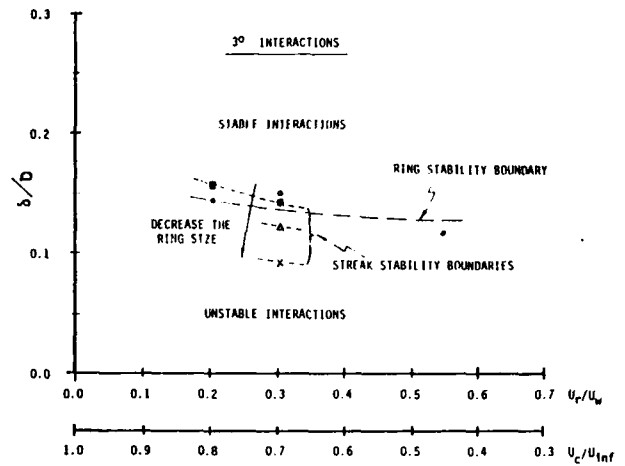


Fig. 15. Comparison of the 'stability boundaries' of a three degree ring moving towards the wall, and of the boundaries of stable streak formation those rings can create. The ring stability curves for different size rings collapse when plotted this way, but the streak stability boundaries remain a function of the size of the ring.

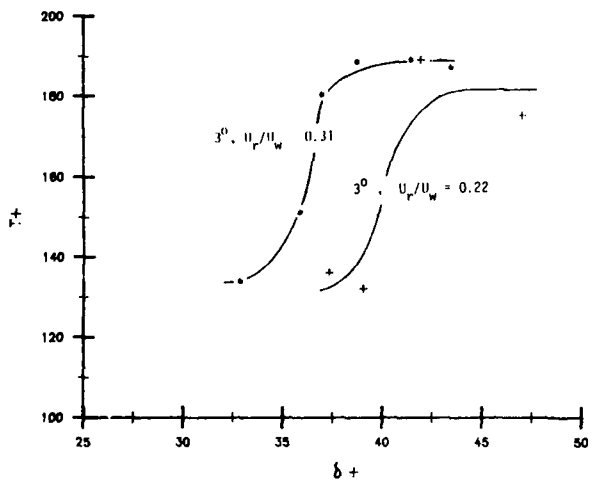


Fig. 16. The dependence of the time to instability of the streaks on the wall layer thickness (both quantities non-dimensionalized by wall layer variables) for 3 degree incidence rings.

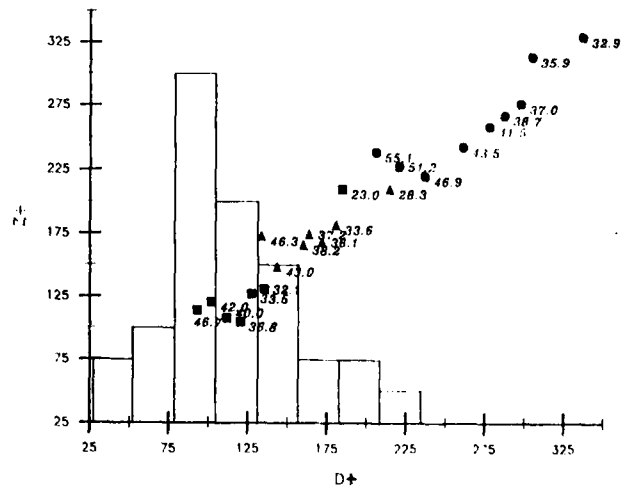


Fig. 17. The distribution of  $D^+$  obtained from the diameter of the Typical eddies of a turbulent boundary layer at  $Re_{\theta} = 1176$ , superimposed upon the streak spacing obtained for various size rings.

## New developments in 3-component LDA techniques

by

Preben Buchhave

DANTEC Electronics, Allendale, N. J.

### Abstract:

To gain the full potential advantage of the laser Doppler measuring technique, the instrumentation must be flexible enough to be configured in a way, which is optimal for a given flow problem. At DANTEC we are continually working on a dual improvement programme: On the one hand, we learn from the use of LDA equipment in many different situations and are able to determine the requirements to an optimum configuration, and on the other hand, we use our experience to continually improve the specifications and performance of the equipment. We are grateful to be given this opportunity to summarize our latest advances, and to explain the underlying ideas. In this talk, we shall present results in the areas of optical configurations for 3-component measurements in turbulent flow, improvements in interface and software, and the use of fiber optic technology.

Two opposing requirements often clash in the application of LDA to 3-component measurements in turbulent flows: good resolution of all three velocity components and optical accessibility. With a fringe-mode LDA it is necessary to access the measuring volume with laser beams from significantly different directions. It is also desirable to maintain control of the fringe distance in the MV. The only way to achieve this is by establishing three independent fringe systems in the measuring volume by transmitting three independent pairs of laser beams, which are coded either by laser wavelength (color), carrier frequency (frequency shift) and/or polarization of the laser light. A combination of fringe-mode and reference-mode LDA techniques requires such different operating conditions that it does not seem to work under normal circumstances. To reduce the number of optical components a commonly used technique is to combine a two-component system, which measures two orthogonal components normal to one axis, with a single component system. The primary measured components, as shown in Fig. 1, consist of two generally non-orthogonal components,  $u_1$  and  $u_2$ , and a third component,  $u_3$ , normal to the plane of the first two. The transformation from these primary measured components to a desired orthogonal system is given in many references, see e. g. Ref. 1. The problem with this arrangement occurs because the two non-orthogonal primary components are often separated by a small angle due to necessary constraints in the optical accessibility of the measuring volume. This reduces the resolution (smallest measurable velocity component) of the so-called axial component (the z-component in Fig. 1)

when it is computed from the primary components. With the orthogonal system shown in Fig. 1, the transformation formulas for the x- and z-components reduce to the sum and differences of the  $u_1$ - and  $u_2$ -components. The problem can be visualized by considering a set of virtual fringes normal to the x- and z-axes. These virtual fringes define the number of zero crossings of a hypothetical signal formed by the sum and difference of the primary Doppler signals from the  $u_1$  and  $u_2$  systems. The resolution of a resulting component depends on the transit time and the number of virtual fringes (shift subtracted) in such a way that the resolution becomes very poor for the z-component in the commonly used configuration of Fig. 2. The best result (most similar resolution of all three fluctuating velocity components) is obtained when the longest direction of the MV is aligned with the mean flow direction as shown in fig. 3.

The need to control independently the fringe spacing through the beam angle and the resolution through the component separation angle motivates the optical arrangement of the DANTEC 3-component LDA as shown in Fig. 4. In this system it is possible to control the angles as well as the focal distance independently, and thus adapt the system to a wide range of applications.

Having the opto/mechanical configuration of Fig. 4. we often go a step further and recommend an off-axis backscatter configuration. This can be achieved simply by exchanging the photodetector optics from one side of the optics to the other. The measuring volume is then defined by the intersection of the focussed laser beams from one optics with the projection of the pinhole from the other optics, which significantly reduces the length of the MV. The effect is not only to improve the spatial resolution of the instrument, but also to significantly improve the signal-to-noise ratio of the detected signal due to the reduction of scatter from small particles surrounding the MV.

The ultimate step in obtaining an equal resolution on all three components in an orthogonal system and the smallest possible measuring volume is a configuration as shown in Fig. 5. Obviously such a system requires a careful mechanical design, but it is our experience that the demands to mechanical rigidity can be met.

A special problem in LDA measurements occur when an attempt is made to measure through a window into a waterfilled tank. The LDA optics is carefully designed for minimum optical aberrations in air, and by applying the same optics through an air-water interface severe aberrations are introduced. These aberrations are least visible in a direct backscatter optics, because some signals will still be detected, but the definition of the measuring volume becomes very poor, and the signal-to-noise ratio is severely degraded. DANTEC recommends that, whenever possible, the front optics be placed inside the liquid and that the front lenses be designed for operation in the liquid. If this is not possible, we recommend that the tank be surrounded by an additional tank, which houses the front optics and allows the front optics to be designed for operation in the same index of refraction as in the tank. This is of course an added expense and inconvenience, but considering the investment in time and money normally associated with 3-component measurements it is a relatively small effort, but one that may make a big difference.

The second problem complex we shall address here is that of the computer data processing. The same type of general considerations we used when considering the optics are applicable here. The problem is the huge range of possible velocities and spacial and temporal scales. To achieve optimum operation the data processing parameters such as sample size, sample rate and number of batches and also such signal processor characteristics as velocity offset and range (frequency shift and filter settings) must be fine tuned. These requirements translate into necessary specifications for the interface and software.

At DANTEC we have long used a buffered computer interface with the capability of measuring both velocity, transit time and time between samples on three channels simultaneously (with programmable coincidence time). The random data rate combined with the required number of data words from each 3-component measurement dictate a transfer speed of up around 1 M words per sec. Data must often be timed relative to an external trigger, e. g. from an encoder on a piece of rotating machinery. Our new IBM compatible interface board has an on-board buffer capacity of 32 k measurement points, a transfer speed of 1 M samples per sec, ability to write either directly to a hard disc or directly to memory, programmable coincidence filter and on-board timing circuits for timing of external trigger pulses. It will also allow the signal processors to be operated in the so called controlled processor mode.

The most important part of the equipment with respect to user friendliness, however, is the software. In a previous publication (Ref. 2 and 3) we have considered the requirements to the sampling process, and shown the enormous range of sampling parameters required for optimal operation. As a specific example we considered the velocity field around a ship model in a towing tank. If the goal is measurement of mean and moments of the three-dimensional velocity field around the stern and propellor at a number of points in a grid, it was shown that a required 5 pct. accuracy of the measured mean values translated into a requirement for sample frequency and sample size of 5 Hz and 36 samples per grid point, respectively. If the goal, however, was measurement of spectral characteristics in the boundara layer along the side of the model, the requirements changed to something like a 30 kHz sample rate and a sample size of 230 k samples per measuring point. Obviously, it is preferable to have an idea about the required sample size before starting a measurement. In the references it was discussed how one can make some preliminary estimates from the known or estimated scales of the experiment. However we have also tried to accomodate this estimation proces by providing two different modes of operation of the software: the estimate mode and the measure mode. In the estimate mode it is possible to wiew on-line two important characteristics of the flow: the velocity pdf or histogram and the velocity autocorrelation function. The on-line histogram allows the user to check if the processor shift and bandwidth are correctly adjusted by allowing him to see the velocity distribution within the limits set by the processor. It is then clearly seen if the processor is limiting the measured velocity range or if there is a possibility of filter bias. The on-line correlation function allows the user in a similar fashion to check the temporal characteristics of the flow, in particular the

integral time constant, which plays a crucial role determining the optimum sample rate. As is well known, multiple samples within the integral time scale are redundant from the point of view of averaging the statistical fluctuations of the velocity. On the other hand, if batch sampling is being employed, it is necessary to extend each batch over at least two integral time scales to get an unbiased spectral estimate. The on-line correlogram allows the user to estimate the integral time scale and the form of the correlation function before starting a time consuming measurement. The measure mode on the other hand allows a completely computer controlled, automatic measurement program including three-dimensional traversing of the measuring point. Data is collected on storage media, and will be available for subsequent analysis at any time.

The last item we wish to address is the use of fiber optic technology in LDA measurements. In our view the advantage of the fiber optic probes is primarily a practical one, in that the fiber technology allows LDA optics to be employed at positions, where the standard optical systems have no access. Also positioning and moving the optical system becomes easier, when the laser can be connected through a fiber optic link. However, as all good things, the fiber optics has a price, and this is primarily a loss of light in the transmission fiber and an increased number of adjustments, in particular for coupling the light into the fiber. This problem occurs because of the properties of the gas laser such as mode instability and beam shifting, which makes it hard to design a coupling, which does not have to be adjusted once in a while. The greatest problem in the use of fiber optic LDAs seems to be the incorporation of frequency shift in such a way that the system operation is not degraded. To avoid interference effect in two separate fibers, DANTEC has employed a technique in which the shifted and unshifted beams are combined and transmitted through a polarization preserving fiber as two independent, orthogonally polarized beams (Fig. 6). This method may produce unacceptable cross coupling in longer fibers, and therefore a slightly larger probe has been designed for such cases. This two-color Ar-laser probe contains both dispersive prism color separation and two-channel Bragg cell frequency shift internally, and thus avoids the problems of interference effects and cross coupling entirely (Fig. 7).

#### References:

1. Buchhave, P (1984) "Three-component LDA measurements" DISA Information 29, pp 3 - 9.
2. Larsen, P. S. and Buchhave, P. (1986) Flow measurements: Why, What and How?" Pt. 2, DANTEC Information 2, pp 2 - 6.

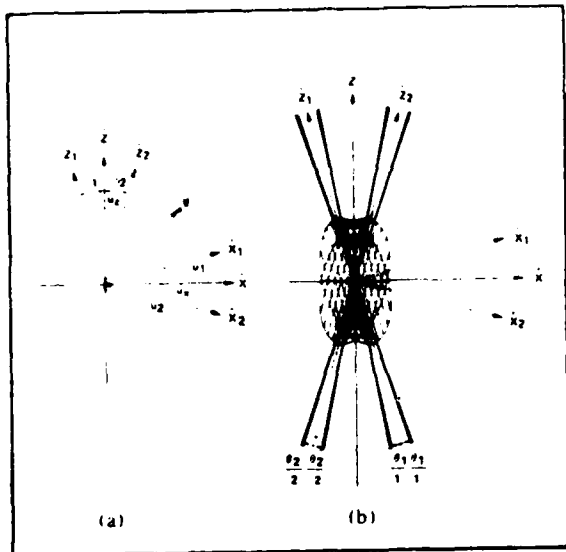


Fig. 1. Primary measured velocity components.

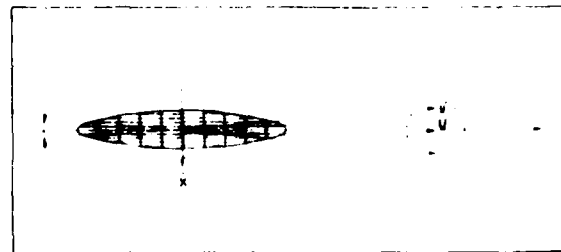


Fig. 3. Best orientation of measuring volume

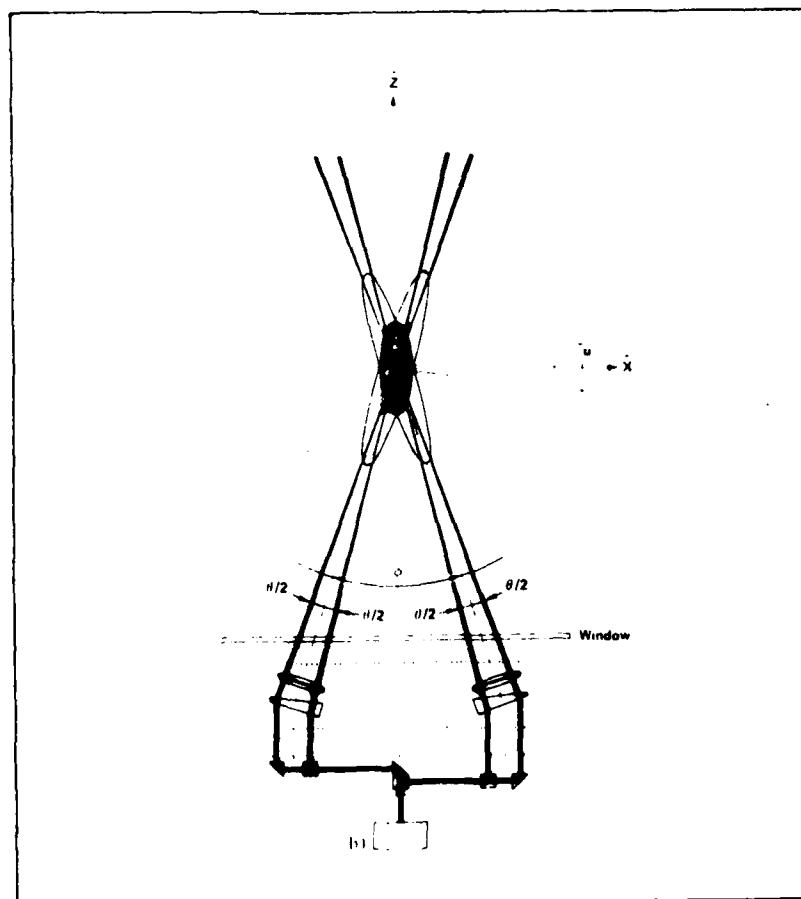


Fig. 2. Commonly used 3-component LDA configuration.

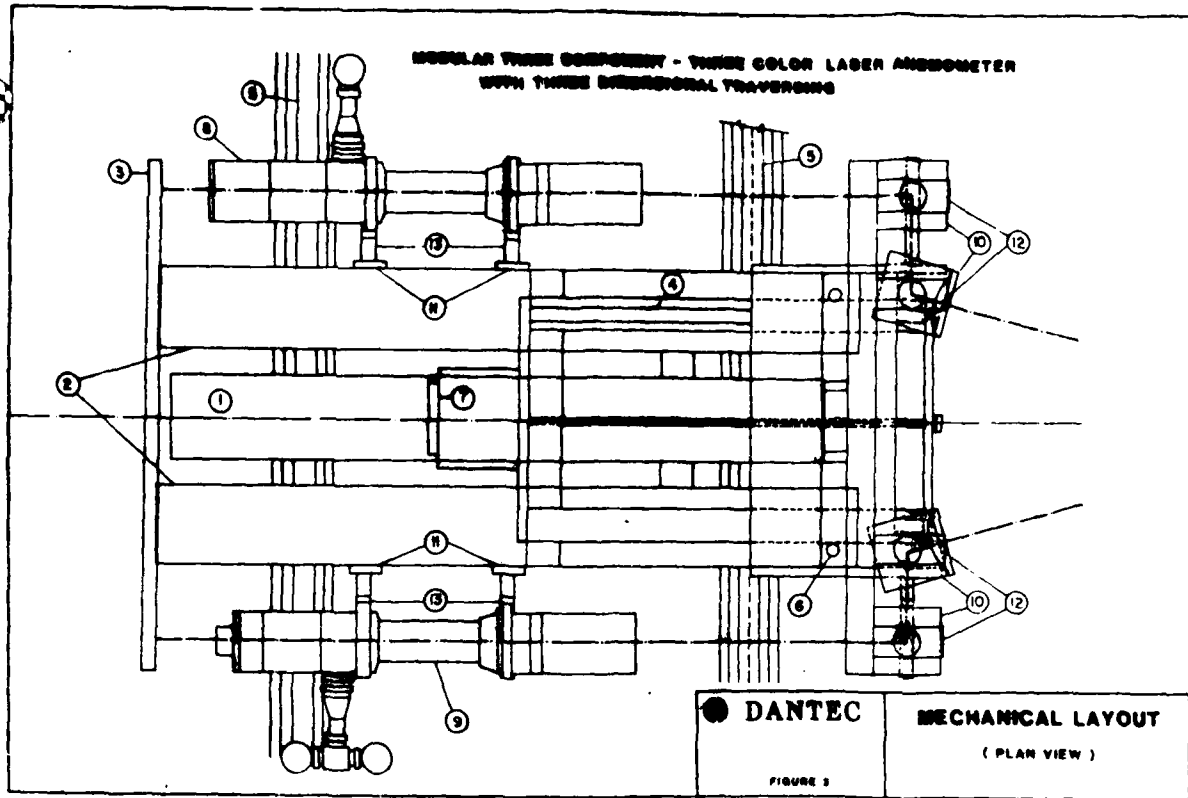


Fig. 4. 3-component LDA opto/mechanical arrangement.

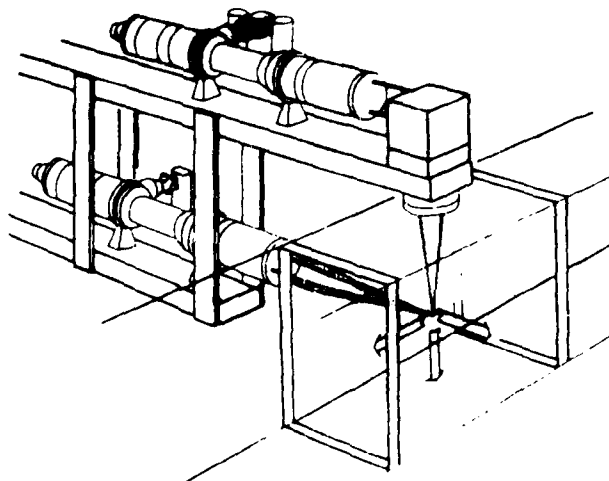
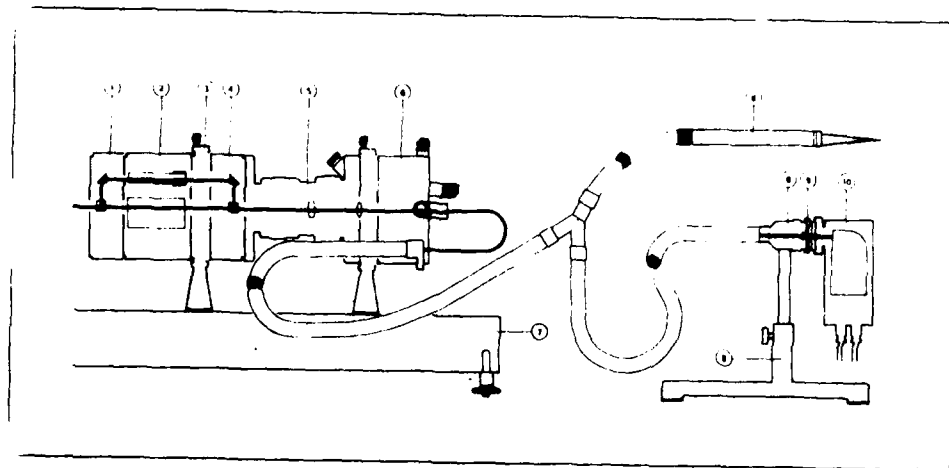


Fig. 5. Orthonormal 3-component LDA.



Code No.	Description	Qty.	Pos. No.
55X08	PM Section	1	10
55X23	Support	2	3
55X29	Bragg Cell Section	1	2
55X38	Interference Filter 632.8 nm	1	9
55X41	Mounting Bench	1	7
55X60	Beam Compressor	1	5
55X61	Fiber Manipulator	1	6
55X62	Optical Probe Head	1	8
55X63	Side-looking Probe Section	1	-
55X64	Beam Splitter pol.	1	1
55X65	Beam Splitter pol. turned	1	4

Fig. 6. FOLDA optics using two coaxial optical beams in one fiber.

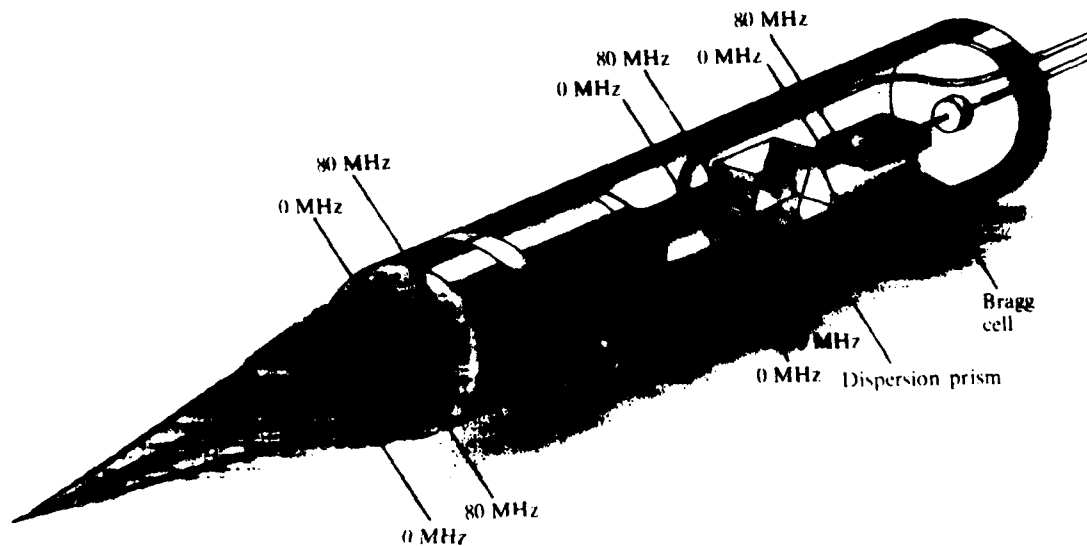
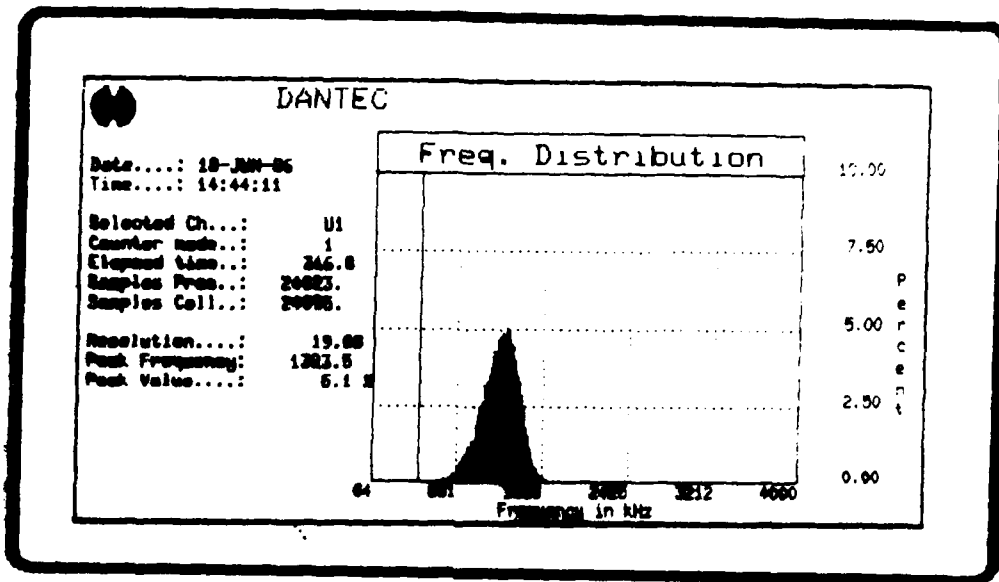
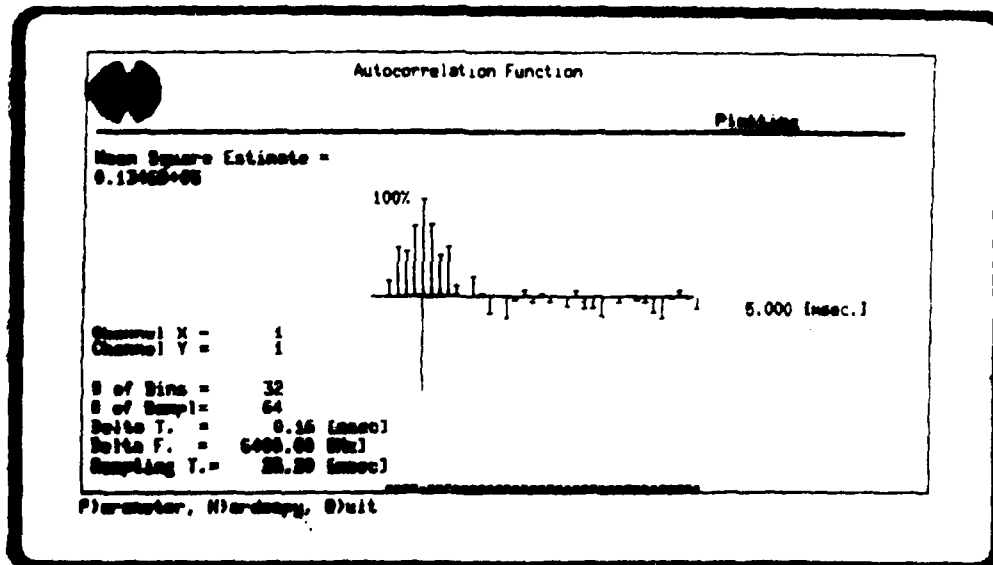


Fig. 7. Complete backscatter fiber optic LDA including internal dispersing prism color separator and Bragg cell.



**PANEL 2: On-Line Histogram**  
**TEST PROGRAM**

A single channel is opened and the signal frequency content is displayed as a histogram.



**PANEL 3: On-Line Auto-Correlation**  
**TEST PROGRAM**

Allows evaluation of data-arrival rate.

ON THE DECOMPOSITION OF TURBULENT  
FLOW FIELDS FOR THE ANALYSIS OF  
COHERENT STRUCTURES

Charles G. Speziale

The George W. Woodruff School of  
Mechanical Engineering  
Georgia Institute of Technology  
Atlanta, GA 30332

ABSTRACT

The decomposition of the turbulent velocity, pressure, and vorticity fields for the analysis of coherent structures is examined from a fundamental theoretical standpoint. It is shown that the commonly used double and triple decompositions yield coherent and incoherent parts of the turbulence that are not Galilean invariant and, consequently, severe doubts are raised concerning their general usefulness for the eduction of coherent structures. Alternative triple decompositions are proposed which are invariant under an arbitrary change of observer. Applications of this triple decomposition to the construction of helicity fluctuations which are more suitable for the study of coherent structures are also discussed.

1. INTRODUCTION

During the past decade, a significant research effort has been directed toward the study of coherent structures in turbulence (c.f., Roshko (1976) and Cantwell (1981)). Although large-scale organized motions had been observed in turbulent flows many years before (c.f., Townsend (1956)), it is only through this more recent work that the widespread occurrence and important role of coherent structures in turbulence have come to be recognized. Most of this recent research on coherent structures, however, has been limited to flow visualization which can, at times, be misleading. The need for more quantitative experimental and theoretical analyses of coherent

structures has recently been emphasized by Lumley (1981) and Hussain (1983, 1986). Great difficulties arise in accomplishing this task for more general turbulent flows which are not being strongly excited at some unique characteristic frequency. For such turbulent flows, the eduction of coherent structures is a painstaking experimental effort in which great caution must be taken to insure that freak modes are not captured.

Two different decompositions of the turbulent flow fields have primarily been utilized in the analysis of coherent structures: triple decompositions consisting of time-averaged, coherent, and incoherent parts (see Reynolds and Hussain (1970)) and double decompositions consisting of just coherent and incoherent parts (see Hussain (1983)). The purpose of this paper is to analyze in more detail these various methods of decomposing turbulent flows for the analysis of coherent structures. It will be shown that the commonly used double and triple decompositions are not Galilean invariant. In particular, it will be demonstrated that the temporal phase averages used to represent the coherent part of the turbulence are not unique for all inertial frames of reference. Consequently, serious doubts are cast on the general applicability of these double and triple decompositions for the eduction of coherent structures since they are overly biased by the observer. Alternative triple decompositions will be proposed which are invariant under an arbitrary change of frame and, thus, appear to be more suitable for the general eduction of coherent structures. These triple decompositions will be

utilized to construct helicity fluctuations that are properly invariant for the description of coherent structures unlike previously used measures which were not Galilean invariant (see Speziale (1985)). Potential applications of these results to the analysis of turbulent shear flows will be discussed briefly along with other possible avenues of future research.

## 2. THE STANDARD DOUBLE AND TRIPLE DECOMPOSITIONS

The turbulent flow of an incompressible viscous fluid will be considered for which the velocity  $\underline{v}$  and pressure  $P$  are solutions of the Navier-Stokes and continuity equations given by

$$\frac{\partial \underline{v}}{\partial t} + \underline{v} \cdot \nabla \underline{v} = -\nabla P + \nu \nabla^2 \underline{v} \quad (1)$$

$$\nabla \cdot \underline{v} = 0 \quad (2)$$

where  $\nu$  is the kinematic viscosity of the fluid. Additionally, the vorticity vector  $\underline{\omega} = \nabla \times \underline{v}$  is a solution of the transport equation

$$\frac{\partial \underline{\omega}}{\partial t} + \underline{v} \cdot \nabla \underline{\omega} = \underline{\omega} \cdot \nabla \underline{v} + \nu \nabla^2 \underline{\omega} \quad (3)$$

which is obtained by taking the curl of equation (1). In the earliest analysis of coherent structures, the triple decomposition was introduced where the turbulent fields  $\phi = (\underline{v}, \underline{\omega})$  were decomposed as follows (see Reynolds and Hussain (1970) and Hussain (1983)):

$$\phi = \bar{\phi} + \phi_c + \phi_r \quad (4)$$

In (4),  $\bar{\phi}$  is the time-mean,  $\phi_c$  is the coherent part, and  $\phi_r$  is the incoherent (or random) part which, respectively, are given by

$$\bar{\phi} = \lim_{T \rightarrow \infty} \frac{1}{2T} \int_{-T}^T \phi(\underline{x}, t + \tau) d\tau \quad (5)$$

$$\phi_c = \langle \phi' \rangle = \lim_{N \rightarrow \infty} \frac{1}{N} \sum_{i=1}^N \phi'(\underline{x}, t + \tau_i) \quad (6)$$

$$\phi_r = \phi' - \langle \phi' \rangle \quad (7)$$

where  $\phi'$  is the usual turbulent fluctuating part such that

$$\phi = \bar{\phi} + \phi' \quad (8)$$

From (6), it is clear that the coherent part of the turbulence in this formalism is based on an ensemble average of turbulent flow structures at the same phase of their evolution which occurs at the time intervals  $\tau_i$  (consequently,  $\langle \cdot \rangle$  is called the phase average).

The alternative approach that has been used consists of viewing the turbulence as a superposition of coherent and incoherent parts as follows (see Hussain (1983))

$$\phi = \langle \phi \rangle + \phi_r \quad (9)$$

which constitutes the double decomposition. Since,

$$\begin{aligned} \langle \phi \rangle &= \bar{\phi} + \langle \phi' \rangle \\ &= \bar{\phi} + \phi_c \end{aligned} \quad (10)$$

it is clear that the double and triple decompositions are only equivalent in their coherent parts when

$$\bar{\phi} \ll \langle \phi \rangle,$$

i.e., when the coherent structures are dominant relative to the time-mean fields. Since the triple decompositions can describe the growth of coherent structures by the extraction of energy from the time-mean flow (a process which the double decompositions are fundamentally unable to describe), they have been the preferred approach for the analysis of coherent structures that are small perturbations of the mean flow. Double decompositions have been useful in the analysis of coherent structures that are dominant relative to the time-mean flow (c.f., Hussain (1983)).

It will now be shown that the coherent part of the turbulence defined by both the double and

triple decompositions discussed above are not Galilean invariant and, hence, are not suitable for the analysis of general turbulent flows. A Galilean transformation is defined by

$$\underline{x}^* = \underline{x} - \underline{V}_0 t, \quad t^* = t \quad (11)$$

where  $\underline{V}_0$  is any constant vector. If  $\underline{x}$  is an inertial frame of reference, then  $\underline{x}^*$  will constitute the class of inertial frames. Under a Galilean transformation it is a simple matter to show that

$$P^* = P, \quad \underline{v}^* = \underline{v} - \underline{V}_0, \quad \underline{\omega}^* = \underline{\omega} \quad (12)$$

where the notation

$$f^*(\underline{x}^*, t^*) \equiv f(\underline{x} - \underline{V}_0 t, t) \quad (13)$$

is utilized. While  $P$  and  $\underline{\omega}$  are Galilean invariant, their time means are not since, e.g.,

$$\begin{aligned} \overline{P^*} &= \lim_{T \rightarrow \infty} \frac{1}{2T} \int_{-T}^T P^*(\underline{x}^*, t^* + \tau) d\tau \\ &= \lim_{T \rightarrow \infty} \frac{1}{2T} \int_{-T}^T P(\underline{x} - \underline{V}_0 t, t + \tau) d\tau \\ &\neq \overline{P}. \end{aligned} \quad (14)$$

This is not at all surprising since the existence of a time mean requires that the turbulence be statistically steady. It is well-known that the Galilean transformation of a steady flow is not necessarily steady (c.f., Milne-Thomson (1968)). This problem is easily overcome by the substitution of ensemble averages defined by

$$\overline{\phi}_E(\underline{x}, t) = \lim_{N \rightarrow \infty} \frac{1}{N} \sum_{i=1}^N \phi^{(i)}(\underline{x}, t) \quad (15)$$

where an average is taken over  $N$  repeated experiments (for a statistically steady turbulence, the ergodic hypothesis of  $\overline{\phi} = \overline{\phi}_E$  can be invoked). The fluctuating fields  $\phi''$  based on an ensemble mean, defined by

$$\phi = \overline{\phi}_E + \phi'', \quad (16)$$

are invariant under an arbitrary change of frame (see Speziale (1979)).

There is, however, an additional problem with the coherent part of the turbulence defined by the phase average (6). Such a phase average is not Galilean invariant. More specifically, given that

$$f^* = f, \quad (17)$$

then, in general,

$$\langle f^* \rangle \neq \langle f \rangle. \quad (18)$$

The detailed proof of this is as follows:

$$\begin{aligned} \langle f^* \rangle &= \lim_{N \rightarrow \infty} \frac{1}{N} \sum_{i=1}^N f^*(\underline{x}^*, t^* + t_1) \\ &= \lim_{N \rightarrow \infty} \frac{1}{N} \sum_{i=1}^N f(\underline{x} - \underline{V}_0 t, t + t_1) \\ &\neq \langle f \rangle \end{aligned} \quad (19)$$

and, hence, the phase average is not a Galilean invariant. This result is not all that surprising if one considers the fact for

$$t_1 = 1/F \quad (20)$$

the phase average is nothing more than an ensemble average with respect to some characteristic frequency  $F$ . It is well-known that the measured temporal frequency of a disturbance depends on the motion of the observer.

In the next section, a triple decomposition which is independent of the observer will be introduced.

### 3. TRIPLE DECOMPOSITIONS THAT ARE INDEPENDENT OF THE OBSERVER

As discussed in the last section, in order to be able to analyze coherent structures in turbulent flows which are not necessarily statistically steady, ensemble averages defined by (15) should be used. The fluctuating fields will

be split into coherent and incoherent parts as follows

$$\phi'' = \phi_C + \phi_R. \quad (21)$$

In lieu of the frame-dependent phase averages (given by (6)) that have been traditionally used, phase averages based on either Eulerian space or Lagrangian time ensembles are proposed. To be specific,  $\phi_C$  will be taken to be of the form

$$\phi_C = \langle \phi'' \rangle_e \equiv \lim_{N \rightarrow \infty} \frac{1}{N} \sum_{i=1}^N \phi''(\underline{x} + \underline{x}_i, t) \quad (22)$$

or

$$\phi_C = \langle \phi'' \rangle_L \equiv \lim_{N \rightarrow \infty} \frac{1}{N} \sum_{i=1}^N \phi''(\underline{x}, t + t_i). \quad (23)$$

In (22) - (23),  $\underline{x}_i$  are position vectors placed from  $\underline{x}$  at spatial intervals where the reference phase occurs,  $\phi''(\underline{x}, t)$  is the Lagrangian representation defined by

$$\phi''(\underline{x}, t) \equiv \phi''(\underline{x}(\underline{x}, t), t) \quad (24)$$

where  $\underline{x}(\underline{x}, t)$  is the time-dependent topological mapping that describes the fluid motion (e.g.,  $\underline{x}(\underline{x}, t) \equiv \underline{x}(X(\underline{x}, t), t)$ ), and  $t_i$  are the time intervals at which the reference phase occurs for a given fluid particle  $\underline{x}$ .

If we take

$$\phi = \bar{\phi}_E + \phi_C + \phi_R \quad (25)$$

(where  $\phi_C$  is taken to be either  $\langle \phi'' \rangle_e$  or  $\langle \phi'' \rangle_L$ ) the coherent and incoherent parts of the turbulence will be independent of the observer. More precisely,

$$\phi_C^* = \phi_C, \quad \phi_R^* = \phi_R \quad (26)$$

under arbitrary time-dependent rotations and translations of the spatial frame of reference

$$\underline{x}^* = Q(t)\underline{x} + \underline{h}(t). \quad (27)$$

In (27),  $\underline{h}(t)$  is any time-dependent vector and  $Q(t)$  is any time-dependent proper orthogonal tensor such that

$$Q Q^T = Q^T Q = \underline{I}, \quad \det Q = 1 \quad (28)$$

where  $\det(\cdot)$  represents the determinant and the superscript T denotes the transpose. Equation (26) results from the fact that the fluctuating velocity, pressure, and vorticity fields based on an ensemble mean are frame-independent (see Speziale (1979)), i.e.,

$$\phi^{**} = \phi'' \quad (29)$$

and that any properly posed Eulerian space or Lagrangian time average are observer independent (see Truesdell and Noll (1965)). Of course, as demonstrated in the last section, Eulerian time averages depend strongly on the motion of the observer. Hence, beyond satisfying the obvious physical constraint of Galilean invariance, this new triple decomposition defined by (22), (23), and (25), gives rise to coherent parts that are completely independent of the observer. This is as it should be since turbulence consists of a superposition of organized and random time-dependent deformations whose fundamental properties should not be affected by a rigid body motion of the observer. It should be kept in mind that the traditional turbulence correlations (i.e., the Reynolds stresses, dissipation rate, etc.) which have shed considerable light on the structure of random turbulence are invariant under a change of observer.

One important application of these results could lie in the analysis of the helical nature of turbulence. Recently, computations of the helicity density

$$h = \underline{v} \cdot \underline{\omega} \quad (30)$$

have been conducted with the hope that some important new insights could be gained on the nature of coherent structures (c.f., Levich and Tsinober (1983) and Pelz, et al., (1985)). However, it was shown by Speziale (1985) that

fluctuations in the helicity density  $h$  transform as

$$h^{**} = h'' - \underline{v}_0 \cdot \underline{\omega}'' \quad (31)$$

under a Galilean transformation and are, thus, not invariant. While the alternative helicity

$$h_1 = \underline{v}'' \cdot \underline{\omega}'' \quad (32)$$

is invariant under a change of observer, it is overly biased by the incoherent turbulence and, thus, could not be directly correlated with such turbulence activity as coherent structures (see Pelz, et al., (1985)). Consequently, no measure of local helicity that was defined in this previous body of research on helical structures is appropriate for the general analysis of coherent structures as pointed out by Speziale (1985). It appears, perhaps, that these difficulties could be overcome by the use of the coherent helicity density

$$h_c = \underline{v}_c \cdot \underline{\omega}_c \quad (33)$$

which is invariant under a change of observer and provides a measure of the alignment of the velocity and vorticity vectors of the organized structures which may be related to turbulence activity. It would be of considerable value if (33) could be measured or computed for some turbulent shear flow in the future.

#### 4. CONCLUSIONS

It has been demonstrated that the commonly used double and triple decompositions are not Galilean invariant and are, thus, not suitable for the general eduction of coherent structures. They can only be used for such analyses if a reference frame exists relative to which the turbulence is approximately statistically steady and all organized structures possess (or are created by excitations at) a dominant temporal frequency. For such a case, the triple decompositions (4) would constitute an appropriate representation with the double decompositions serving as a convenient alternative when the coherent structures dominate the flow. An alternative triple

decomposition was proposed which was based on an ensemble mean and Eulerian space or Lagrangian time phase averages of the turbulent flow fields. It was proven that this decomposition gives rise to coherent and incoherent parts of the turbulence that are completely independent of the observer—a property which should be satisfied if one is to develop a framework suitable for the general eduction of coherent structures. It was argued that an alternative measure of local helicity based on the coherent velocity and vorticity obtained from this decomposition is preferable to the non-Galilean invariant helicity density which has formed the basis for some recent computations.

Further experimental and computational research is needed to test the efficacy of this new triple decomposition in the eduction of coherent structures. In addition, it would be of interest to apply these ideas to the analysis of helical structures in turbulence. It appears that coherent structures will be an active and fertile area of research for many years to come. However, the ultimate value of any scientific theory lies in its predictive value. It is only through the development of a sound theoretical framework that this will become possible.

#### ACKNOWLEDGMENT

This research was supported by the Office of Naval Research under Contract No. N00014-85-K-0238 for which Dr. Chung Lee served as the Project Monitor.

#### REFERENCES

- Cantwell, B. 1981 Organized Motion in Turbulent Flow, Ann. Rev. Fluid Mech. 64, 457.
- Hussain, A.K.M.F. 1983 Coherent Structures: Reality and Myth, Phys. Fluids 26, 2816.
- Hussain, A.K.M.F. 1986 Coherent Structures and Turbulence, G. I. Taylor Symposium on Fluid Mechanics, Cambridge University.
- Levich, E. and Tsinober, A. 1983 On the Role of Helical Structures in Three-Dimensional Turbulent Flow, Phys. Letters 93A, 293.

- Lumley, J. L. 1981 Coherent Structures in Turbulence, Transition and Turbulence, R. E. Meyer, ed., Academic Press, 215.
- Milne-Thomson, L. M. 1968 Theoretical Hydrodynamics, MacMillan.
- Felz, R. B., Yakhot, V., Orszag, S. A., Shtilman, L. and Levich, E. 1985 Velocity-Vorticity Patterns in Turbulent Flow, Phys. Review Letters 54, 2505.
- Reynolds, W. C. and Hussain, A.K.M.F. 1970 The Mechanics of an Organized Wave in Turbulent Shear Flow, J. Fluid Mech. 41, 241.
- Roshko, A. 1976 Structure of Turbulent Shear Flows: A New Look, AIAA J. 14, 1349.
- Speziale, C. G. 1979 Invariance of Turbulent Closure Models, Phys. Fluids 22, 1033.
- Speziale, C. G. 1985 On Helicity Fluctuations in Turbulence, Quart. Appl. Math. (in press).
- Townsend, A. A. 1956 The Structure of Turbulent Shear Flow, Cambridge University Press.
- Truesdell, C. and Noll, W. 1965 The Non-linear Field Theories of Mechanics, Handbuch der Physik, Vol. III/3, Springer-Verlag.

FORMATION OF A CONCENTRATED VORTEX STRUCTURE INDUCED BY INTERACTION OF A SINGLE VORTEX WITH UNSTEADY VORTEX LAYER SHEDDING FROM AN AIRFOIL

Jerzy Świrzydźczuk  
Institute of Fluid Flow Machinery  
Polish Academy of Sciences  
Gdańsk, Poland

ABSTRACT

The paper contains the results of theoretical and experimental investigations of deformation of unsteady vortex layer formed behind an airfoil in a plane parallel flow. The variable intensity of the layer is caused by the concentrated vortex structure flowing in the vicinity of the airfoil. The theoretical calculations were performed for a symmetric Joukovsky airfoil, using conformal mapping and point vortices methods. The experimental investigations were conducted in a wind tunnel at velocity  $U = 2.16$  m/s and  $Re = 4 \times 10^3$ . A "smoke wire" visualization technique was used supplemented by standard hot-wire anemometer measurements. Both experiment and theory indicate that the generated layer quickly deforms forming in many cases a new concentrated structure of comparable intensity but of rotation opposite to the primary vortex. Results of intensity measurements of both vortices are presented.

1. INTRODUCTION

The investigations of airfoil behaviour in unsteady flow conditions, when the character of changes of flow is known, are a significant part of the whole airfoil studies. They tend to evaluate the changes f.e. of aerodynamic lift, pressure or vorticity distribution on the airfoil contour due to short-lived or local changes of velocity field. The significance of above investigations results from the fact, that these changes can involve effects, which cannot be predicted basing on the theory of stationary flow about an airfoil, but which can make the airfoil operating conditions worse to a considerable degree, f.e. by vibrations or strong instantaneous overload. Therefore ma-

ny efforts were - and still are - made to construct a model allowing to predict and analyse the unsteady flow about an airfoil as completely as possible in a theoretical way.

The changes of flow conditions describing cases often occurring in aeronautical engineering i.e. changes of velocity or of an inclination angle, sharp-edged gusts or airfoil vibrations, were examined in details basing on both analytical and numerical models (f.e. Basu and Hancock (1978), Giesing (1968)). It is possible to point at a case that has been less thoroughly examined. It is the case closely connected with operation of rotor elements of fluid-flow machinery, namely presence of concentrated vortex structures in flow oncoming towards an airfoil. This case of flow disturbance is sometimes analysed as a solution of given, definite configuration of profile palisades in a definite machinery design, but there are only a few publications treating the problem generally - as an elementary case of vortex-airfoil interaction. Saffman and Sheffield (1977) analysed theoretically potential flow over a flat plate with a single attached vortex. They found the possible positions of the vortex zero-velocity equilibrium and demonstrated that the lift was significantly increased in that way. A similar analysis, but related to Joukovski airfoil, was done by Huang and Chow (1982). Timm (1985) investigated experimentally so-

und effects of the vortex-airfoil interaction in a subsonic flow. He demonstrated many examples of flows, where new vortex structures were generated as a result of the primary vortex interaction with the airfoil boundary layer. Poling and Telionis (1986) studied flow about a fixed airfoil immersed in the vortex wake generated by a pitching airfoil. Basing on the precise measurements they concluded that the unsteady Kutta condition did not correctly describe the flow in the immediate vicinity of the airfoil trailing edge.

This paper describes theoretical and experimental investigations of development of the unsteady vortex layer, generated behind an airfoil by a single concentrated free vortex, treated in the paper as a primary, elementary flow disturbance. A course of changes of the vortex layer intensity as well as the particular stages of its deformation and interaction with the primary vortex are examined. Intensities of the investigated structures are estimated. The results should be useful in theoretical analysis of many more complicated cases of flow about bodies and simultaneously they should yield new information about regularities of vortex interaction in real flows.

## 2. THEORY

The existence of vorticity in the flow, both concentrated and having continuous distribution, is often described by placing the groups of point or discrete vortices in the potential flow model (see Saffman(1979)). The results presented here were obtained using the model of flow of ideal fluid about a symmetric Joukovsky airfoil, which shape resulted from:

$$z = \zeta - A + \frac{(a - A)^2}{\zeta - A} \quad (1)$$

where:  $z = x + iy$ ,  $\zeta = \xi + i\eta$

It is assumed that a group of point vortices is present in the flow near the airfoil. One of these vortices, which was coming

with the stream from infinity, causes generation of new vortices close behind the trailing edge of the airfoil - as a result of fulfilling the Kutta condition. These path vortices create in the flow a single row, growing with time and deforming simultaneously. The point of gene-



Fig. 1. The model of vortex flow near the airfoil

ration of the new path vortex in the considered time step is taken basing on the equality of the distance between this point and the trailing edge and product of local  $x$  - component of the velocity vector calculated at this point and half a time step. This requirement is a close adaptation of the requirement used by Basu and Hancock.

The instantaneous velocities of the vortices were calculated using the Kirchhoff-Routh function, which for a considered step  $s$  can be stated as:

$$W_s = \sum_{j=0}^s K_j \left[ \frac{1}{2} K_0 \ln \frac{\xi_j^2 + \eta_j^2}{a^2} - U y_j \left( 1 - \frac{a^2}{\xi_j^2 + \eta_j^2} \right) \right] + \frac{1}{4} \sum_{\substack{j,k=0 \\ j \neq k}}^s K_j K_k \ln \frac{a^2 [(\xi_k - \xi_j)^2 + (\eta_k - \eta_j)^2]}{(\xi_j \xi_k + \eta_j \eta_k - a^2)^2 + (\xi_j \eta_k - \eta_j \xi_k)^2} + \frac{1}{2} \sum_{j=0}^s K_j^2 \ln \frac{\xi_j^2 + \eta_j^2 - a^2}{a} + \frac{1}{2} \sum_{j=0}^s K_j^2 \ln \frac{(\xi_j - A)^2 + \eta_j^2}{\sqrt{[(\xi_j - a)^2 + \eta_j^2][(\xi_j + a - 2A)^2 + \eta_j^2]}} \quad (2)$$

The velocity components are given by:

$$v_{xj} = \frac{v_{\xi j}^A - v_{\eta j}^B}{A^2 + B^2}, \quad v_{yj} = \frac{v_{\eta j}^A + v_{\xi j}^B}{A^2 + B^2} \quad (3)$$

where:

$$v_{\xi_j} = -\frac{1}{K_j} \frac{\partial W_s}{\partial \eta_j} \quad v_{\eta_j} = \frac{1}{K_j} \frac{\partial W_s}{\partial \xi_j} \quad (4)$$

$$A = \operatorname{Re} \left( \frac{dz}{d\xi} \right) \quad B = \operatorname{Im} \left( \frac{dz}{d\xi} \right) \quad (5)$$

In each time step the calculations are divided into three stages:

- calculations of the location and intensity of the new path vortex,
- calculations of the instantaneous velocities and displacement of vortices to their new positions,
- estimation of the error resulting from the assumed value of the time step.

The displacement of the vortices is realized using two-step method called the "predictor-corrector" method. The estimation of the displacement error is executed basing on the Kirchhoff-Routh function as an invariant of vortex motion. When the value of the error  $\delta W$  exceeds the assumed value, the calculations in considered step are repeated with realization of vortex displacement in some intermediate steps, in which the Kutta condition is not satisfied.

The passage of the single concentrated vortex structure in vicinity of the airfoil causes generation of an unsteady vortex layer. The examples of the vortex layer distribution are shown in Fig. 2. It is impos-

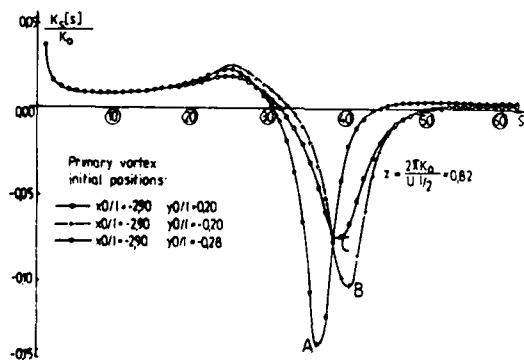


Fig. 2. Intensities of vortices constituting the vortex layer generated by the moving primary vortex.

sible to find two symmetric cases of vortex-airfoil interaction in regions above and below the airfoil because the vortex is accelerated in the first region and decelerated in the second region by the potential of the airfoil. Therefore in Fig. 2 three curves are demonstrated, among them curves A and B are characterized by the symmetry of the initial positions of the primary vortex while curves A and C - by the same value of the smallest distance between vortex trajectories and the airfoil contour. It can be added that in all cases the strongest part of the layer is generated at the moment, when the primary vortex passes the trailing edge/steps no 35 + 40/.

Basing on the executed calculations it can be proved that mutual interaction of the particular elements of the layer, intensified by the influence of the primary vortex leads to formation of a new concentrated vortex structure heving comparable intensity but rotation opposite to the primary vortex. The deformation of the layer begins in its part placed nearest the primary vortex (it is also the most intensive part of the layer) and ends by formation of the interactional vortex before or behind the primary vortex - depending on the direction of the interaction between the primary vortex and the vortex layer. These two cases of the vortex layer deformation are shown in Fig. 3.

Formation of the new vortex in the flow causes certain changes in density and velocity distribution in vicinity of the vortex. As an example of these changes the trajectories of the primary and interactional vortices are shown in Fig. 4. It is clearly noticeable that the vortices do not move, in general in direction marked by the main, parallel flow.

The results presented in this chapter are only a part of the possible analysis of the considered flow. The selection of results to be presented was guided by the possibility of comparison with experimental

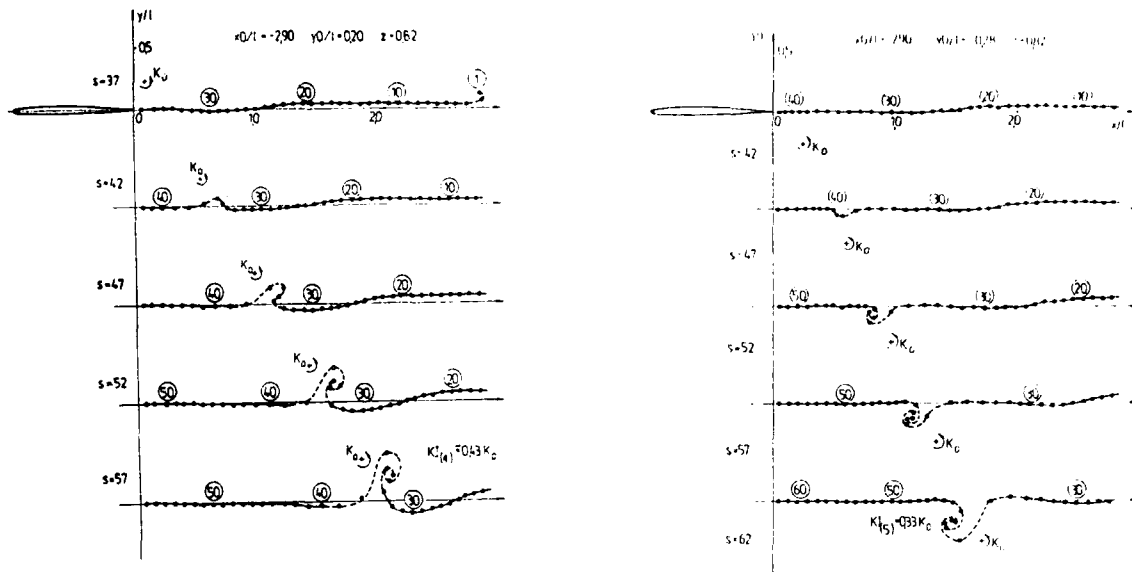


Fig. 3. Formation of the interactional vortex induced by the primary vortex passing above (left) and below (right) the airfoil

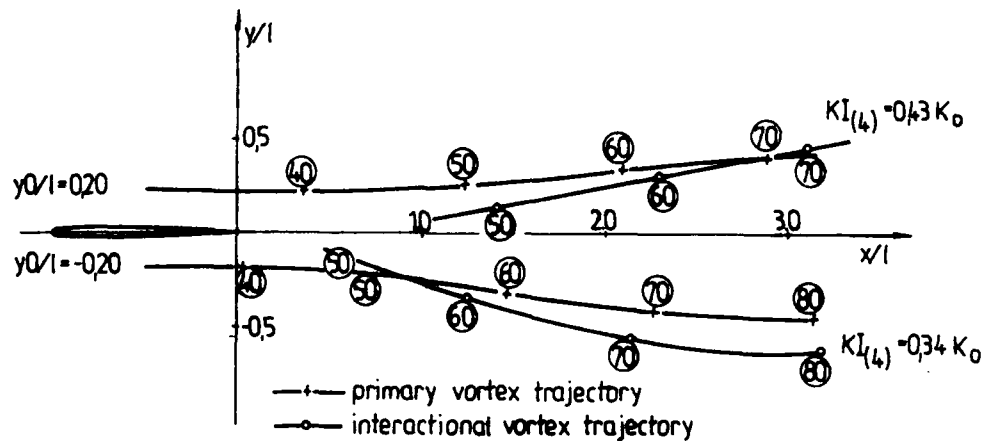


Fig. 4. Trajectories of the primary and interactional vortices.

results described in the next Chapters.

### 3. EXPERIMENTAL CONDITIONS

The results presented in the foregoing Chapter may be easily accepted within the limits of the considered model, however it is more difficult to answer the question how far these results are representative for description of the course of the continuous vortex layer deformation occurring in real

flow. The experimental investigations of the interaction between a single vortex and an unsteady vortex layer were performed in an open circuit low turbulence wind tunnel. The aim of the experiment was to find certain regularities of the vortex layer development and to compare - only in a qualitative aspect - with the theoretical results.

A symmetrical airfoil of 7 per cent thickness and  $l = 25$  mm chord length was

placed in a 120x120x750 mm test section in the stream of velocity  $U = 2,16$  m/s. Such a low flow velocity resulted from the desire of obtaining the most readable course of the phenomenon. Corresponding Reynolds number based on the airfoil chord length was  $4 \times 10^3$ . The single primary vortex was generated by an additional airfoil placed in some distance before the tested airfoil. The impulse change in the angle of inclination of this airfoil by the amount of  $\Delta\alpha \approx 3.3^\circ$  allowed to generate a vortex structure, intensity of which was estimated using two-exposure method as equal  $K = \Gamma/2\pi = 28.1 \text{ cm}^2/\text{s}$  (Swirydczuk (1985)). The airfoil rotation was realized using a specially designed generator with a core moved by the electromagnetic field of an electromagnet coil supplied with a current pulse. The design of the generator allowed to obtain, at a required rotation angle, a course of the core velocity nearly diminishing to zero at the latter part of rotation, that was the basic requirement warranting generation of a single concentrated vortex, as it had been proved in many trials with different kinds of generator construction. A short discussion of features of the vortex structure generated in above manner is presented by Swirydczuk (1985).

The investigations of particular stages of the primary vortex development allowed to choose the distance between the airfoils warranting relative constancy of vortex features during its interaction with the airfoil and the vortex layer.

The phenomenon was visualized using the smoke-wire technique. The possible positions of the heating wire during experiment are shown in Fig. 5. The experiment was recorded using a photographic camera and a system of flash-guns, securing proper illumination of smoke streaklines flowing from the heating wire. The control apparatus designed in IF-FM, Pol.Ac.Sci. controlled automatically the course of particular stages of the experiment, that is wire sm-

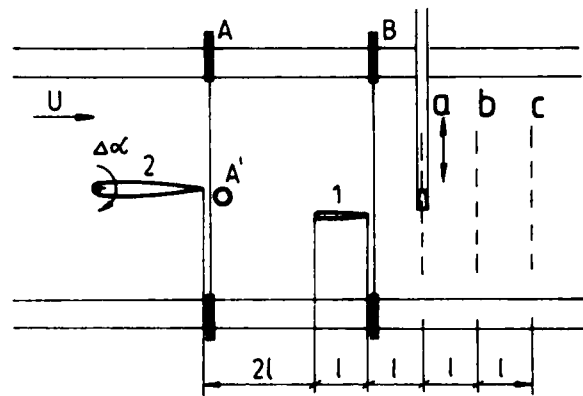


Fig. 5. Variants of visualizing wire positions: A, A', B and of anemometer probe: a, b, c in the tunnel, 1-tested airfoil, 2-generator airfoil.

king, airfoil rotation and lighting of the flash-guns. In each cycle consisting of the above stages a single photograph was obtained, described by a dimensionless time delay  $T = \Delta t \cdot U/l$  measured from the beginning of airfoil rotation till flash-guns flash. High repeatability of the phenomenon allowed to consider the photographs made in different cycles as a film sequence describing a single, general case of the vortex layer deformation.

Discussion of the visualization results is presented in Chapter 4. In supplement to these investigations a series of velocity modulus measurements were done, using a CT hot wire anemometer. The results of these measurements are described in Chapter 5.

#### 4. VISUALIZATION RESULTS

A series of recordings of the unsteady vortex layer behaviour was done using the above described instrumentation. The dimensionless minimum value  $y/l$  of the distance between the primary vortex trajectory and the airfoil surface was assumed as a specific parameter of each series. Basing on the changes of this parameter one can divide collected results into three groups, namely:

- passage of the vortex above the airfoil in a large distance from its surface ( $0,21 < y/l < 0,58$ );

- passage of the vortex close by the airfoil surface ( $0 < y/l < 0.17$ );
- passage of the vortex below the airfoil ( $y/l < 0$ ).

4.1 The primary vortex passing far from the airfoil surface.

"A large distance" is interpreted as a distance warranting passage of the whole vortex region treated as a vortex core on

one side of the airfoil. A typical course of the vortex layer deformation in this case is shown in Fig. 6 ( $y/l = 0.41$ ). It must be noticed, that time  $T$  is measured starting from the additional airfoil rotation, so the moment, in which the primary vortex passes the trailing edge of the tested airfoil, is approximately equal to time  $T = 3.0$ . The photograph a/ presents the flow directly befo-



a/  $T = 3.47$



d/  $T = 6.06$



b/  $T = 4.32$



e/  $T = 6.92$



c/  $T = 5.19$



f/  $T = 7.79$

0 5 cm

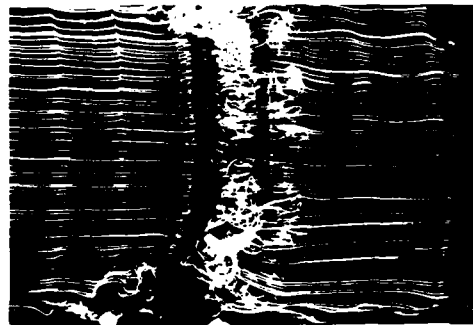
Fig. 6 Deformation of the unsteady vortex layer behind the airfoil:  $y/l = 0.41$ , wire in position B.

re appearance of the primary vortex. One can recognize only two parts of von Karman's vortex streets forming behind the tested airfoil below and the generator airfoil above. The primary vortex appears in the photograph b/. Strong bending of the smoke streaklines in such a short time evidences the relatively large intensity of the vortex. In photograph c/ the first effect of the interaction between the primary vortex and the unsteady vortex layer is shown. A new vortex structure, qualitatively similar to the interactional vortex predicted theoretically, is forming just below the primary vortex. The following particular stages of formation of the new vortex are presented in photographs d/ + e/. The growing destabilization of the primary vortex is also observable.

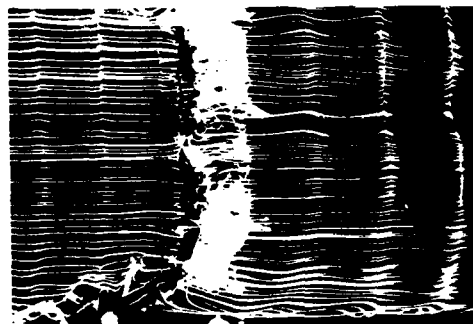
It was stated, that investigated phenomenon, two-dimensional in its early stages, strongly tends to become three-dimensional, both in respect to the inner structure of the vortices and to their external shape. Basing on the recorded material it was assumed that the moment  $T = 7.0$  is the time limit of two-dimensionality of the phenomenon, in respect to longitudinal deformation of the shape of vortices. Fig. 7 shows the visualization results of the flow in the plane parallel to the airfoil trailing edge (wire in position A'). The photograph a/ presents the primary and the interactional vortices moving together while in the photograph b/ only the single primary vortex is shown in comparable stage of development. A distinct separation line between both vortices can be indicated in photograph a/ while it is absent in photograph b/.

Basing on the recorded photographs the diagram of trajectories of the studied vortices was prepared. The results are shown in Fig. 8.

The above described course of vortex layer deformation is typical for the considered case. Effects of the interactional vor-



a/  $T = 6.91$



b/  $T = 6.79$

Fig. 7. Planform view on the moving vortices: a/ primary and interactional vortices, b/ primary vortex moving alone.

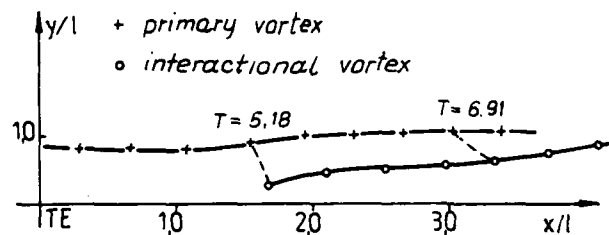


Fig. 8. Experimental trajectories of primary and interactional vortices:  $y/l = 0.41$ . Vortex formation from the continuous unsteady vortex layer were observed in all recorded series, for  $y/l = 0.21 + 0.58$ , with higher values of  $y/l$  corresponding to the slower course of vortex formation. In the case of the maximum value  $y/l = 0.58$  the rudimentary effects of the vortex presence were observed in the distance of  $5l$  behind the airfoil trailing edge, in other words at the moment of possible nearly full natural dis-

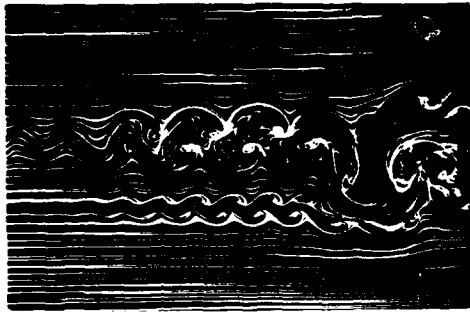


Fig. 9. Formation of a weak interactional vortex:  $y/l = 0.58$ ,  $T = 9.51$

It was found that in the case of faster formation of the interactional vortex the destabilization of the primary vortex is also more intensive.

#### 4.2 The primary vortex passing close by the airfoil surface

The properties of the primary vortex generated in manner described in Chapt. 3 differ, in their nature from properties of the potential, point vortex. The vorticity distribution of fluid treated as a vortex core is one of these differences. When the vortex passes sufficiently close to the airfoil surface, there is a possibility, that one part of vorticity may pass on one side while the second - on the other side of the airfoil. If one of these parts is of considerably larger intensity than the other, it behaves like a single isolated vortex. Course of its interaction with the airfoil and the vortex layer is similar to that discussed in Chapt. 4.1, only the rate of the primary vortex transformation into the interactional vortex is considerably larger. Simultaneously vorticity collected in the second part of core causes, in interaction with vortex layer, formation of the new vortices of intensity much smaller than vortex generated by the first part. The regularities of formation of these weak vortices were not found. A supposition is posed, that both the properties of the vortices and the range of values  $y/l$  corresponding to their formation depend to a con-



a/  $T = 4.76$



b/  $T = 5.18$

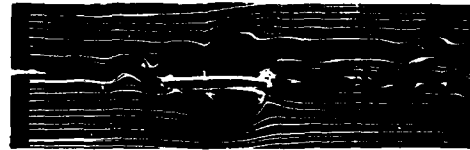


c/  $T = 6.15$

Fig.10. Interactional vortex formation as a result of primary vortex passage close by the airfoil surface:  $y/l = 0.17$

siderable degree on the properties of the primary vortex, which are strongly connected with the manner of vortex generation. Therefore it is impossible to find any common regularities of their behaviour, except the fact of their formation.

The head-on vortex collision with the airfoil is the external case of considered type of interaction. The only one interesting result recorded in this case is unequal velocity of motion of both vortex parts Fig. 11. These parts dissipate their rotation so



$T = 2.16$

Fig.11. Head-on vortex-airfoil collision (wire in pos. A).

strongly on their way along the airfoil surface that they provoke any visible changes in the vortex path region.

#### 4.3 The Primary vortex passing below the airfoil

The attempts of the research into the interactional vortex formation have ended in this case with a negative result.

It is possible to point two possible reasons for this result:

- Diagram in Fig. 2 shows, that in the case of vortex moving below the airfoil the extremum local intensity of the generated vortex is considerably smaller than in the case of vortex moving above the airfoil. Therefore the vortex layer deformation also should take place slower in the considered case.

- Contrary to the case described in Chapt. 4.1 requirement of obtaining certain  $y/l$  value was connected with necessity of the airfoil location in the region of von Karman's vortex street forming behind the generator airfoil. As a result the research of effects of the interactional vortex formation was performed in a region of strong influence of two stationary vortex paths.

## 5. MEASUREMENTS

The standard measurements of velocity vector moduli were performed with aim to verify obtained visualization results and to estimate intensities of the primary and interactional vortices. A constant temperature hot wire anemometer was used. The velocity signal recorded in certain number of points lying on three lines: a, b and c, (shown in Fig. 5) was examined. The measurements were realized for two cases of flow conditions:

- a case of the free primary vortex moving in the tunnel;
- a selected case of the interactional vortex formation ( $y/l = 0.41$ ).

The measurements allowed preparing of the diagram of instantaneous changes of velocity modulus  $\Delta V/V_m$  recorded in different points at the moment, when the tested vortex was passing by the measurement point. The distribution of  $\Delta V/V_m$  along  $y$ -axis for the case of free primary vortex motion is presented in Fig. 12 (probe in the position a). Basing on obtained results one can estimate the primary vortex intensity. Assuming that the diameter  $dr$  of the vortex core is mar-

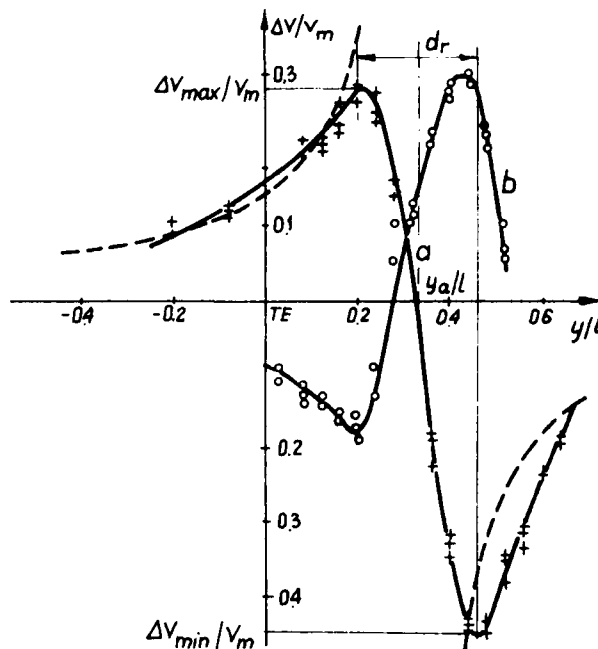


Fig. 12. The changes of the velocity increment recorded at the moment of the passage of the primary vortex (curve a) and the interactional vortex (curve b).

ked by the extremum values  $\Delta V_{\max}/V_m$  and  $\Delta V_{\min}/V_m$  of the velocity increments it is possible to calculate the modulus of the vortex intensity as:

$$K_0 = 0.25 dr (\Delta V_{\max}/V_m - \Delta V_{\min}/V_m) \quad (6)$$

As a result of calculations following values of  $K_0$  were obtained:

23.16  $\text{cm}^2/\text{s}$ , 30.33  $\text{cm}^2/\text{s}$  and 30.80  $\text{cm}^2/\text{s}$  i.e. values similar to that presented in Chapt. 3. These values should be interpreted as an intensity of the point potential vortex inducing at the distance  $dr/2$  from its centre the velocity difference equal to that generated by the real primary vortex. It must be stated, that the error of estimation of  $K_0$  values, resulting from differences between properties of the theoretical and real vortices, cannot be exactly determined. A velocity increment distribution generated by the free potential vortex of intensity  $K_0$ , is presented in Fig. 12 as a dashed curve.

The selected result of analogical measurements made in the case of the interactional vortex formation is also shown in Fig. 12 (probe in the position c).

The measurements were performed only in

the cases b/ and c/ from the possible probe positions, because in case a/ it was impossible to separate the part generated by the interactional vortex from the total signal. Basing on the formula (6) the following values of the vortex intensity were calculated: 16.19 cm<sup>2</sup>/s, 13.95 cm<sup>2</sup>/s

Estimation of the ratio of the interactional and primary vortex intensities based on their values presented earlier leads to result in limits: 0.45 + 0.70 i.e. value of the same order as calculated numerically see Fig. 3+5.

## 6. CONCLUSIONS

The results are presented of the investigations of an interaction of a single vortex flowing in vicinity of a symmetric airfoil with an unsteady, continuous vortex layer shedding from its training edge. A good qualitative agreement was obtained between the theoretical and experimental results in the region placed above the airfoil i.e. in the region, where the airfoil influence accelerates the moving vortex. It was proved, that the vortex layer deformation leads to formation of a new, concentrated vortex having a comparable intensity but rotation opposite to the primary vortex. The beginning of the new vortex formation takes place in the part of vortex layer situated below the primary vortex, but the subsequent development moves the forming vortex into position before the primary vortex. A similarity was observed between the theoretical and experimental trajectories of the investigated vortices, especially visible in the initial period of their common motion, before destabilization of the primary vortex.

It must be emphasized, that the theoretical results were obtained basing on a simple model of an ideal fluid with the standard Kutta condition used for evaluation of the rate of the shedding vorticity. Good agreement with the experimental data in such a complicated case of vortex interaction suggests that reliable results can be obtained, basing on this model, in many similar cases

of flow about airfoils occurring i.e. in the fluid-flow machinery. Particularly, the Kutta condition, although not taking into consideration the complicated course of local changes of the velocity in the neighbourhood of the trailing edge, in general, seems to describe rightly the unsteady conditions of flow about an airfoil in the considered case.

The experimental investigations demonstrated, that the phenomenon of creation of the opposite vorticity, as a result of the vortex passage in vicinity of the airfoil, is stable and its intensity, at the whole tested region, monotonically depends on the distance  $y/l$ , in which the vortex passes by the airfoil. In this connection one may point the reason of this vorticity formation not only in the direct interaction between the primary vortex and the airfoil boundary layer, as it was proved by Timm, but also in the way that can be defined as the potential vortex-airfoil interaction.

## REFERENCES

1. Basu, B.C.; Hancock, G.J. 1981: The unsteady motion of a two dimensional aerofoil in incompressible inviscid flow. *J. Fluid Mech.* 87, 159-178.
2. Giesing, J.P. 1968: Nonlinear two-dimensional unsteady potential flow with lift. *J. Aircraft.* 5, 135-143.
3. Huang, M.K.; Chow, C.Y. 1982: Trapping of a free vortex by Joukowski airfoils. *AIAA J.* 20, 292-298.
4. Poling, D.R.; Telions, D.P. 1986: The response of airfoils to periodic disturbances - the unsteady Kutta condition. *AIAA J.* 24, 193-199.
5. Saffman, P.G.; Sheffield, J.A. 1977: Flow over a wing with an attached free vortex. *Stud. App. Math.* 57, 107-117.
6. Saffman, P.G.; Baker, G.R. 1979: Vortex interaction. *Ann. Rev. Fluid Mech.* 11, 95-122.
7. Świryczuk, J. 1985: Behaviour of the vortex layer generated in the flow by an impulse change of circulation around a profile. In: *Optical Methods in Dynamics of Fluid and Solids /proc. IUTAM Symp. Liblice, Czechoslovakia, 1984 -ed. Pichal, M./*, pp. 241-247, Berlin, Heidelberg, Springer-Verlag.
8. Timm, R. 1985: Schallentstechung bei der Wechselwirkung von Wirbeln mit einer Tragflügelumströmung, Mitt. no. 80, Göttingen: Max-Planck Inst. Strömungsforsch.

## SOME NUMERICAL RESULTS BEARING ON STABLY STRATIFIED TURBULENCE

Jackson R. Herring and Olivier Metais

### ABSTRACT

We examine stably stratified, randomly forced turbulence numerically, with forcing and damping selected to give insight into the question of whether cascade of energy to large scales is possible for strongly stratified three-dimensional turbulence, in a manner similar to two-dimensional turbulence. We consider narrow-wave number band forcing, whose angular distribution is strictly two-dimensional. For sufficiently small Froude number, the statistically steady state is characterised by a weakly inverse-cascading horizontally velocity variance field. The vertical variability is pronounced, and for large Brunt-Väisälä frequencies  $N$  seemingly independent of  $N$ . If, on the other hand, the Froude number exceeds a critical value, the vertical variability is weak, and the statics of the scales larger than the forcing scale is near that predicted by inviscid equipartitioning. For all forcing functions considered, the vertical motion and temperature field ( $w, T$ )—centered at smaller scales—are more three-dimensionally isotropic, with no large scale organisation. At large  $N$  (small Froude number) the  $w-T$  fields scales as  $1/N$ , with the horizontal motion field independent of  $N$ . Furthermore, at large  $N$  and for horizontal forcing, the horizontal motion field is consistent with the condition that a substantial fraction of the total dissipation is attributable to it. In simple terms, this implies a drag acting on all horizontal scales of motion, which in turn flattens the slope of the energy spectrum in the putative inverse-cascade range, and increases it in the enstrophy-cascade range. We further estimate, via this mechanism and the numerical results, that increasing resolution decreases the effects of the drag on the spectral shape.

### 1. INTRODUCTION

Mesoscale variability in the range (10-1000 km) shows a horizontal scale distribution ( $k^{-5/3}$ ) whose physics seems to be a combination of strongly stable turbulence and wave motion. Gage (1979, 1986) proposed that the observed horizontal variability may be explained as an inverse cascading two-dimensional turbulence, whose physics is similar to that deduced by Kraichnan (1967) for strictly two-dimensional turbulence. In later papers (see e.g., Gage, (1986) for review) he generalized the discussion to include quasi-geostrophic turbulence a la Charney (1971). Lilly (1983) subsequently argued that strong stratification alone implies a dominantly two-dimensional motion. The argument relied on earlier scaling analysis (Riley, Metcalfe, and Weissman, 1981). The energy source is at small scales—in the range of large-scale thunderstorm activity. An inverse-cascade then operates to distribute the energy to progressive larger scales. We should stress that the motion here envisioned is not two-dimensional; its horizontal components ( $u, v$ ) have vertical variability which is dynamically determined through dissipative mechanisms,

which may involve breaking waves in patches of sufficiently low Richardson's number. In addition, an effective radiation damping of the wave component should also be introduced in order to properly represent the effects of exiting of waves from the region of study. At the large scale end of this region (1000 km) the effects of rotation must undoubtedly play a significant role, and stratified turbulence merges with a Charney (1971) -type quasi-geostrophic turbulence.

Fig. 1 shows some data reported by Nastrom (*et. al.*, 1984), which may support these ideas. It shows the zonal (east-west) and meridional (north-south) winds in the high regions of the troposphere. We note that a relatively shallow  $k^{-5/3}$  spectrum blends in with the steeper  $k^{-3}$  planetary-scale at about 1000 km. The energy source for this motion is hypothesized by Gage and Lilly to be at about 1 km.

That forced two-dimensional flow cascade energy to large scales was first suggested by Kraichnan (1967), and confirmed by several numerical experiments. For the larger-scales of the atmosphere, two-dimensionality can be largely understood by the rapid rotation of the atmosphere, combined with its (on average) stable stratification. The basic theory for such a regime is known as quasi-geostrophic flow, and Charney (1972) proposed simplified equations to understand turbulence in the homogeneous context. His equations are simply conservation of potential vorticity (for our purposes, vertical vorticity) as convected along the horizontal motion field. Such equations are shown to have energy and enstrophy (squared vorticity) as inviscid constants of motion, the same conditions that lead to inverse cascade of flows. The conditions of validity for the quasi-geostrophic regime are that the Rossby number ( $u/L\Omega$ ) be much less than one. Here, ( $u, L$ ) are typical velocity and length scales of the motion, and  $\Omega$  is the earth's rotation rate. An examination of the data in Fig. 1 suggests that these conditions are met at the large scale end of the  $k^{-5/3}$  range, but within roughly a factor of 10-20 into this spectral range  $R_0$  becomes of order unity.

There then remains the question of whether strong stable stratification alone is sufficient to keep the flow essentially two-dimensional. The thought here is that a certain type of quasi-two-dimensional motion may be the low Mach number analogue of ordinary turbulence, and the internal gravity waves the analogue of acoustic motion. In the present case, we may attempt to expand the complete motion field about a component that survives at "zero Mach-type number" (here for Froude number  $= u/LN$ , where  $N$  is the gravity wave [Brunt-Väisälä] frequency) and a wave component, which may have vanishingly small amplitude as  $N \rightarrow \infty$ . The appropriate scaling has been discussed by Riley *et al.*, (1983). It turns out that the turbulence analogue here is two-dimensional flow but with a vertical variability that depends on the wave component. If this two-dimensional component is to survive the effects on non-linear mixing, some enhanced wave dissipation seems necessary. This may be furnished by some form of wave breaking, followed by viscous dissipation.

We need not stress that our arguments above supporting the layered two-dimensional flow (stratified turbulence) are speculative. In order to understand their relevance and validity, we examine here stratified flows for a variety of stratifications (values of  $N^2 = g(-dT/dz)/\alpha$ . Here,  $g$  is the acceleration of gravity,  $\alpha$  the expansivity of air, and  $T$  the temperature.) To pursue the atmospheric analogy, we shall be particularly interested in the statistics of such flows if forced (in our analogy, randomly forced!) at small scales.

Our equations for this investigation are Boussinesq Navier-Stokes, with a "hyper-viscosity and conductivity" to attenuate the smallest scales. These are solved, pseudo-spectrally in the homogeneous context, starting from random initial conditions. Before examining forced flows, we examine the basic qualitative physics of such flows, under the influence of viscous decay. We do this by discussing some initial value problems, similar to those of Reilly *et al.*, but at higher resolution ( $64 \times 64 \times 64$  instead of  $32 \times 32 \times 32$ ), and stronger stratification.

We consider first the behavior of the flow at moderate Brunt-Väisälä frequency. Put non-dimensionally,  $Fr = (\text{the Froude number}) = uL/N \approx 0.2$ . Figure 2 shows the energetics of viscous decay for three initial value problems; (1) in which the flow starts as randomly distributed horizontal motion field (all vertical vorticity), (2) a random flow consisting of pure waves (all horizontal vorticity), and (3) a random flow in which waves and turbulence are near equipartition. We note that the vertical-vorticity initial value problem remains strongly two-dimensional, and in fact, towards the end of the run becomes more so. This tends to support the above conjecture that stratified flows evolve to a dominantly two-dimensional state. Moreover, other numerical calculations at stronger stratification and the same initial  $(u, T)$ -fields have even more dominant horizontal fields. However, if such a two-dimensional dominance is universal, we should also be able to demonstrate the converse—that pure (random) wave initial conditions evolve into dominantly vertical-vorticity modes.

Figure 2b shows, for a pure wave initial value problem, the equivalent information as in Fig. 2a. Interestingly, the wave component remains dominant throughout the course of the run. This is a puzzling aspect of all our stratified runs; the flow prefers either: (1) two-dimensional turbulence in layers; or (2) wave-dominated flow; or (3) an equipartitioned state, in which  $(u, v, w, T)$  have the same variance, as in Fig. 2c. The latter does not correspond to the equipartitioning of strict thermal equilibrium, but a quasi-equilibrium in which the degrees of freedom  $(w, T)$  are frozen together.

In Fig. 3a and 3b we show iso-surfaces of the total temperature field,  $T(\underline{x}, t)$ , for two stratifications  $Fr = 1$ , and  $Fr = .2$ . Here the time beyond the initial random state is about one large-scale eddy circulation time. The initial conditions here are purely random (vertical) vorticity. We note that at  $Fr = 1$ , a considerable amount of vertical moving, entrainment, and engulfment. On the other hand, at

stronger stratification,  $T(\underline{x}, 1.0)$ , is much more uniform, but has occasional cusp-like features, which lead to a dissipation.

We now turn to the forced flows. The forcing here is two-dimensional, so that without any three-dimensional perturbation, the flow—in response to the random forcing—is two-dimensional, inverse-cascading turbulence. The spectrum of kinetic energy is shown in Fig. 4. A Markov forcing is applied only at wave-numbers ( $10 < k < 12$ ). We note the typical inverse cascade range for  $k < 10$ , and the "enstrophy cascade range"  $k > 10$ , followed by a dissipation range,  $k > 20$ .

We next examine the behavior of this flow if, at  $t = 0$ , a small temperature perturbation is introduced. We do this for a range of Brunt-Väisälä frequencies (and hence Froude numbers). We may expect, for a given forcing, that as  $N$  increases, a given horizontal flow is able to tolerate progressively more vertical shear before "turning over" in the vertical: the equipartitioning or "isotropizing" tendency which would equilibrate all components of shear is opposed by the stable stratification. This surmise is based on the classical stability analysis of a (constant) shear flow: the shear is stable to small perturbation if  $(N/(\partial u/\partial z)^2)^{1/2} > (1/4) =$  the Richardson number,  $R_i$ .

Fig. 5 shows the course of the energetics of a forced flow, identical to that described in Fig. 4 except that a small perturbation is introduced in the temperature field at  $t = 0$ . The flow is strongly stratified, having an equilibrium  $R_i = N/(\partial u/\partial z)^2 > 1/2 = 10$ , and  $Fr = .11$ . We note the initial exponential increase of the perturbation in vertical velocity and temperature: this linear growth phase is in accordance with our ideas about the tendency towards isotropy. This and studies at other  $N$ , however, seem to suggest—surprisingly—that the growth rates are insensitive to  $N$ . The equilibrium level of the wave component ( $= [w, T]$ , where  $w$  is the vertical velocity field) is considerably reduced from the  $N = 0$  value. A series of runs with various  $N$ 's indicate that the wave component attenuates as  $1/N$ , in accordance with a perturbation analysis of the present system. This is true provided  $N$  is above a critical value set by the condition that the rms  $R_i \gtrsim 1$ . Below this critical  $N$  the (single-time) statistics of the flow are rather indifferent to  $N$ , and the flow (exterior to the forcing wave-number band) rapidly becomes isotropic. Figure 6 compares (isotropically accumulated) spectra for horizontal energy (a) and wave energy (b) for two values of  $N = (20, 80)\pi$ ; these frequencies correspond to  $Fr = (1, .2)$ . The two values of  $N$  lie respectively below and above the critical value of  $N$ . The spectral bulge for  $N = 80\pi$ , on closer examination, is seen to represent a strongly two-dimensionally layered random flow, whose three-dimensional features may be noted in Fig. 7, which shows the iso-surfaces of  $u(x, y, z, t)$ . The strongly layered aspect of the flow is clearly discernible. But note the billowing nature of the  $u = 0$  interface. A vertical sounding of

$(u, v, w)$  is shown in Fig. 8. Note the irregular fluctuations of the horizontal motion, and the fact that  $w(x)$  is more rapidly changing, centered at higher wave number.

The question whether this forced motion represents, in any sense, two-dimensional, inverse-cascading flow is addressed in Fig. 9. Here we show spectra, equivalent to those in Fig. 5, except that energies are accumulated in wave-number bins labeled by increments of  $K_{\perp} = (K_x^2 + K_y^2)^{1/2}$ , where the  $K$ s represent Cartesian components of the wave number vector  $k$ . The spectrum  $\phi_1(K_{\perp})$  represents a two-dimensional energy—based on the vertical vorticity, the prescription for which is given in the figure caption. Similarly,  $\phi_2(K_{\perp})$  is the velocity-component of the wave energy, and  $P(K_{\perp})$ , the potential energy. Two observations may be made about these figures: (1) the horizontal energy spectrum,  $\phi_1(K_{\perp})$ , has an appreciable energy transferred to large scales; (2) the wave energy is centered at much smaller scales; it is, in fact, very flat and attenuated only by dissipation. We notice also that, for  $\phi_1(K_{\perp})$ —an appreciable amount of energy accumulates near the forcing wave number. Figure 9 may be compared directly to Fig. 4, for two-dimensional flow. Thus, inverse cascade occurs, but is much attenuated by the three dimensionality of the flow.

It is also interesting to examine the influence of stable stratification on the (differential) distribution of shear,  $\partial u/\partial x$ , since it is this quantity that determines the stability of the flow against vertical overturning. This is presented in Fig. 10 for  $N = (0.1, 20, 80)\pi$ . For near isotropy,  $P(x = \partial u/\partial x)$  has a significant  $\exp(-c|x|)$  region. At strong stratification, it is more nearly Gaussian. We note that  $|\partial u/\partial x| > N$  ceases to exist above  $N = 20\pi$ .

Another interesting quantity is the helicity,  $H = \underline{u} \cdot (\nabla \times \underline{u})$ , whose distribution is shown in Fig. 11 for the same range of  $N$  as for Fig. 10. This distribution has been calculated in the context of homogeneous isotropic flow, and for shear flows (Shtilman, *et al.*, 1986; Kerr *et al.*, 1986). Some of these authors note that the more relevant quantity to examine is the conditional distribution. The conditional factor is that some putative stability indicator—for example, regions of low strain or dissipation. In all cases, however, it seems plausible that a distribution peaked near  $(x = \pm 1)$  indicates that regions of  $\underline{u} \cdot (\nabla \times \underline{u})$  are significantly stable. The stratified studies reported here suggest the contrary.

## 2. CONCLUSIONS AND INTERPRETATION OF RESULTS

We have briefly examined here a sequence of randomly forced, homogeneous flows, of progressively increasing (stable) stratification, specified here by the stability parameter  $N^2 \equiv \alpha g \beta$ . If the  $N$  is large enough to stabilize the flow, a further increase produces flows that become progressively more two-dimensional, but in horizontal layers, whose thickness is set by the condition that the dissipation of kinetic energy input to the flow be attributable to the vertical variability of the horizontal flow. The onset

of the stable layered-flow regime seems to be set by the condition that the local Richardson number—based on the r.m.s.  $\partial u/\partial x$ —be larger than unity. This stabilizes the flow against both shear and buoyant overturning. The wave component of the flow becomes progressively attenuated, with amplitude  $\sim N^{-1}$ . The wave-spectrum, on the other hand, is quite flat, and tails off only because of dissipative effects, suggesting the possibility of sharp wave fronts. Our results on this point are similar to the findings of Farge and Sadourny (1986) for two-dimensional shallow water waves. The amplitude of the wave component is in accordance with a wave perturbation analysis.

The particular numerical experiments stressed here consist of a two-dimensionally forced, inverse cascading flow, upon which a small, random temperature perturbation is introduced. The perturbations so introduced grew exponentially, and in accordance with the ( $N = 0$ ) two-point closure analysis, but with growth rates independent of  $N$ . It may be that the linear phase of this problem can be understood as an instability of near static, two-dimensional set of vortices.

Our results indicate a degree of inverse cascade to large scales, but not yet a  $k^{-6/3}$  range (the numerical results are more like  $k^{-1/2}$ ). We also note an appreciable accumulation of energy near the forcing wave number, and an associated wave-vortex interaction transferring (two-dimensional) energy into waves. Nonetheless, it may be that higher resolution will allow a potential  $k^{-6/3}$  range to emerge. Note in this connection that the dissipation is distributed over the full range of  $K_{\perp}$ , not just large  $K_{\perp}$ . This is because it is primarily attributable to the vertical variability of  $(u, v)$ . Thus, the dynamics of the large-scale range is not purely inertial, but contains an appreciable frictional component.

We may form a rough estimate of the friction effects (taken here, for simplicity, as  $-\mu \underline{u}$ ) on the spectrum  $\Phi_1(K_{\perp})$  by writing an effective two-dimensional equation for  $\underline{u}$

$$\partial \underline{u} / \partial t = \mu \underline{u} - \nabla p + \underline{E} + \dots \quad (1)$$

and requiring that at the r.m.s. statistically steady level

$$\mu \langle u^2 \rangle = \langle F^2 \rangle \tau, \quad (2)$$

where  $\tau$  is the correlation time of  $F$ . The magnitude of the right hand side of (2) may be fixed by the requirement that  $\langle F^2 \rangle \tau K_f^2$  be the dissipation of enstrophy. If the flow then has a smallest wave number,  $K_L$ , and—as found here—a degree of inverse cascade, we may expect, from (29), that  $\langle u^2 \rangle$  increases as  $K_L$  decreases. (For notational simplicity, we drop the “ $\perp$ ” subscript on  $K$  from here on.) Hence the effect of  $\mu$  decreases with decreasing  $K_L$ . Assuming an inverse cascade  $K^{-6/3}$ ,  $K < K_f$  and  $K^{-3} K > K_f$  spectrum would lead to:

$$\mu = (\langle F^2 \rangle \tau) K_L^{2/3} \quad (3)$$

To assess the quantitative effect of  $\mu$  on the spectrum, we must have a detailed model of the inverse cascade process. A simple way of doing this is to utilize a diffusion approximation for the transfer process (Lesieur and Herring, 1985). The results of such a model predict that the friction  $\mu$  will lessen the inverse cascade spectral slope and increase the enstrophy cascade slope. The effectiveness of  $\mu$  is determined by the ratio of  $\mu$  to the total enstrophy. For the  $-5/3$  cascade this is:

$$\Gamma = [K_L(K_f \ln K_r / K_f)]^{2/3} \quad (4)$$

where  $K_r$  is the beginning of the enstrophy dissipation range. Thus the assumption of a  $-5/3$  range is consistent with the idea that the effect of  $\mu$  decreases with the low wave number cut-off, a necessary requirement for the existence of  $K^{-5/3}$  inverse cascade.

For inverse cascade to occur, there remains the additional requirement that the inviscid form of the flow studied conserve both energy and enstrophy. Here the small scales are a potential problem, because the equipartitioning by the nonlinear terms may lead to  $\Phi_1 = \Phi_2$  as  $K \rightarrow \infty$ . There is also the fact that the vertical variability of  $(u, v)$  causes enstrophy to be non-conserved even if  $(w, T)$  are strictly zero. With regard to the first issue, we may note that as  $N \rightarrow \infty$ , the flow remains strongly anisotropic throughout the dissipation range. The second problem is more difficult. It appears that vertical variability of  $(u, v)$  induces  $(w, T)$  (as in the Taylor-Green problem), but the waves are strongly dissipated—perhaps because they tend to shock—and hence have no chance to equilibrate with the horizontal component. From the perspective of a layer of two-dimensional turbulence, this would appear to be tantamount to a rather strong leakage of energy. The result may again be a friction on the two-dimensional component similar to that just discussed. The establishment of a near enstrophy conservation property suitable to induce an inverse cascade may then depend sensitively on the shape of the vertical variability.

We also examined, briefly, the certain distribution functions for the flow, in particular that for vertical shear, and the helicity density. The distribution of shear for those calculations having significant inverse cascade were surprisingly stable. This parallels the fact, discussed above, that dissipation is attributable to vertical shear, almost exclusively. It should be noted that the dissipation range found here for large  $N$  is strongly anisotropic. The helicity distribution suggested that for stratified turbulence, regions of high relative helicity were not as favored as for other homogeneous flows previously investigated.

## FIGURE CAPTIONS

- Fig. 1 Kinetic energy spectrum near the tropopause from the GASP aircraft data. After Nastrom *et al.*, (1984).
- Fig. 2 Energetics of the decay of stratified turbulence. The energy is decomposed by writing  $u(k) = \hat{e}_1(k)\phi_1(k) + \hat{e}_2(k)\phi_2(k)$ ,  $\hat{e}_1(k) = k \times \hat{n}/(|k| \times \hat{n})$ ,  $\hat{e}_2(k) = k \times \hat{e}_1(k)/|k \times \hat{e}_1(k)|$ , where  $u(k)$  is the Fourier decomposition of  $u(x)$ , the velocity field, and  $\phi_1(k)$ , and  $\phi_2(k)$  are called the vortical and wave components of  $u(k)$ , and  $\hat{n}$  in the unit vertical vector. Solid line is potential energy  $P(t)$ ; long dashed, variances of  $\phi_1$ ; and short dashed, variance of  $\phi_2$ . Curve (a) is for random initial data  $\phi_1(0) \neq 0$ ,  $\phi_2 = 0$ ; (b)  $\phi_1(0) = 0$ ,  $\phi_2(0) \neq 0$ ; (c)  $\phi_1(0) = \phi_2(0) \neq 0$ ,  $P(0) = 0$ .
- Fig. 3 (a); Iso-surfaces of temperature for "strongly" stratified flow ( $Fr = .2$ ); (b); for weakly ( $Fr = 1$ ) stratified flow. Initial conditions correspond to conditions in Fig. 2(a).
- Fig. 4 Kinetic energy spectrum for randomly forced ( $F \neq 0$ ) for  $10 \leq k \leq 12$  two-dimensional flow. Forcing region is indicated by  $(k)$ . The arrow marked by "vis" indicates the region of strong dissipation.
- Fig. 5 Energetics of randomly forced flow (same forcing as for Fig. 4) but with small initial temperature perturbation. Curves are:  $\langle u^2 \rangle$ ,  $\langle v^2 \rangle$ ; the horizontal variance;  $\langle w^2 \rangle$ ; the vertical variance of the motion field; and  $P$  the potential energy. Conditions are strongly stratified:  $Fr = .1$ .
- Fig. 6 Spectra  $\phi_1(k)$ ,  $\phi_2(k)$ ,  $\phi_1(k) + \phi_2(k)$ , and  $P(k)$  for: (a) weakly stratified flow ( $Fr = 1$ ); (b) strongly stratified flow ( $Fr = .1$ ). Forcing is strictly two-dimensional, and the same as in Fig. 4. Spectra are shown for a time during the stationary portion of the flow.
- Fig. 7 Iso-surfaces of  $u(x, y, z, t)$  for strongly stratified case of Fig's. 5 and 6. Note two-dimensional layering of the flow.
- Fig. 8 Vertical soundings of the flow shown in Fig. 7.
- Fig. 9 Spectra of  $\phi_1(K_\perp)$ ,  $\phi_2(K_\perp)$ ,  $\phi_1(K_\perp) + \phi_2(K_\perp)$ , and  $P(K_\perp)$ , for the same flow of Fig's. 6, 7, 8. Here  $K_\perp = \sqrt{k_x^2 + k_y^2}$ .
- Fig. 10 Differential distribution function of  $\partial u / \partial z$  for three stratifications: (a)  $N = .01$ , (b)  $N = 20\pi$ , and (c)  $N = 80\pi$ . Flow is stationary.
- Fig. 11 Distribution of relative helicity ( $\alpha = u \cdot (\nabla \times u)$ ), for the three flows described in Fig. 10 during stationary phase of flow.

## REFERENCES

- Charney, J. G., 1971: Geostrophic turbulence. *J. Atmos. Sci.*, **28**, 1087-1095.
- Farge, M., and R. Sadourny, 1986: Inertial-gravity wave effects on a decaying two-dimensional turbulence in rotation. Preprint, to be submitted to *J. Fluid Mech.*
- Gage, K. S., 1979: Evidence for a  $k^{-5/3}$  law inertial range in mesoscale two-dimensional turbulence. *J. Atmos. Sci.*, **36**, 1950-1954.
- Gage, K. S., and G. D. Nastrom, 1986: Theoretical interpretation of atmospheric spectra of wind and temperature observed by commercial aircraft during GASP. Preprint.
- Kerr, R. M., W. Ashurst, A. Borja, A. Kerstein, and C. Gibson, 1986: Velocity and scalar histograms of helicity and skewness in numerical turbulence. Preprint.
- Kraichnan, R. H., 1967: Inertial range in two-dimensional turbulence. *Phys. Fluids.*, **10**, 1417-1423.
- Lesieur, M., and J. R. Herring, 1985: Diffusion of a passive scalar in two-dimensional turbulence. *J. Fluid Mech.*, **161**, 77-95.
- Levich, E., 1985: Certain problems in the theory of developed hydrodynamical turbulence (preprint).
- Lilly, D. K., 1983: Stratified turbulence and the mesoscale variability of the atmosphere. *J. Atmos. Sci.*, **40**, 749-761.
- Nastrom, G. D., K. S. Gage, and W. H. Jasperson, 1984: *Nature*, **310**, 36.
- Orsag, S. A., and G. S. Patterson, 1972: Numerical simulation of turbulence. In *Statistical Models and Turbulence*. M. Rosenblatt and C. VanAtta, Eds. *Lecture Notes in Physics*, Vol. 12, pp. 127-147.
- Riley, J. J., A review of turbulence in stably-stratified fluids. Nov. 1985, preprint.
- Riley, J. J., R. W. Metcalfe, and M. A. Weissman, 1981: Direct numerical simulations of homogeneous turbulence in density stratified fluids. *Proc. AIP Conf. Nonlinear properties of internal waves*. Bruce J. West, Ed., 79-112.
- Shtilman, L., R. Pels, E. Levich, and A. Tsnober, 1985: On the role of helicity in turbulent flows. *Euromech*, **195**. Munich, 1985. Also Preprint; to appear in *Phys. Fluids*.
- Van Zandt, T. E., 1982: A universal spectrum of buoyancy waves in the (1982) atmosphere, *Geophys. Res. Lett.*, **9**, 575-578.
- Yakhot, V., and R. Pels, 1986: Large-scale structure generation by anisotropic small-scale flows. Preprint, to appear in *Phys. Fluids*.

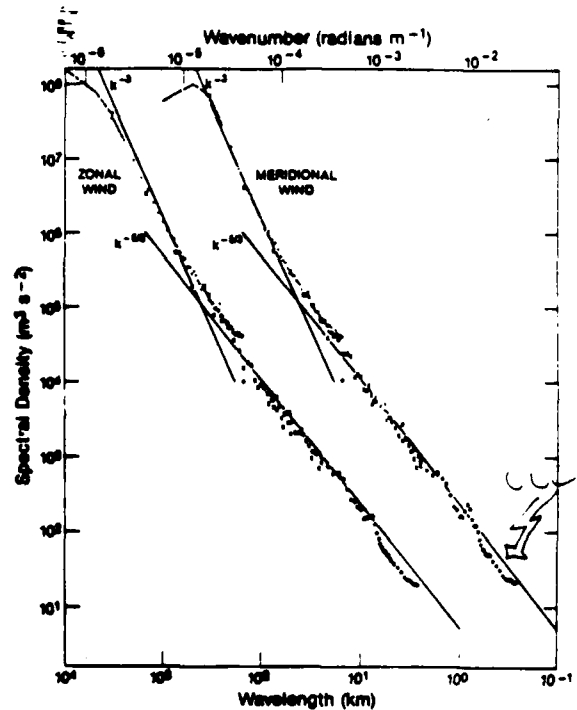


Figure 1

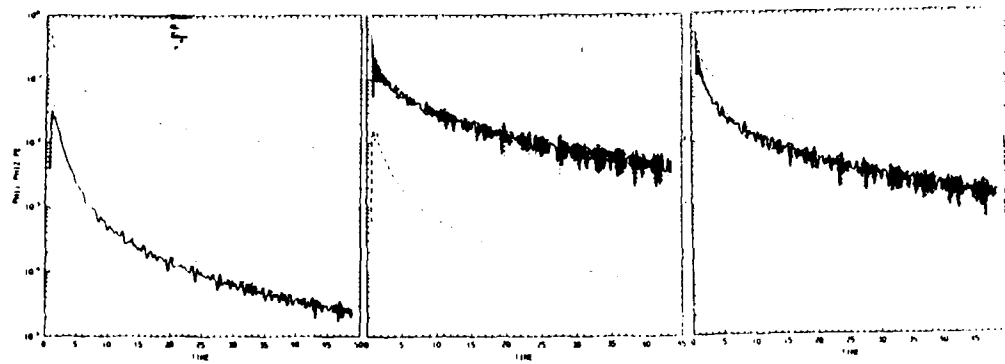


Figure 2

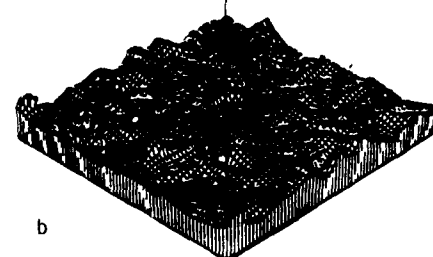
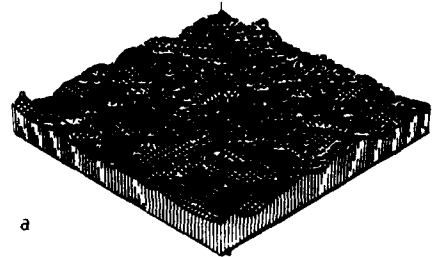


Figure 3

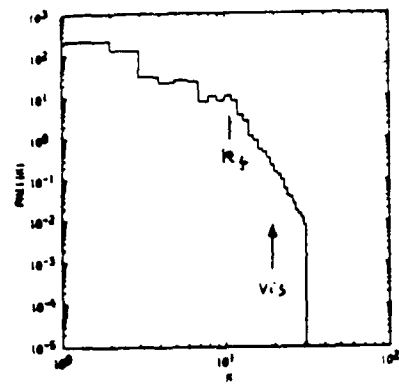


Figure 4

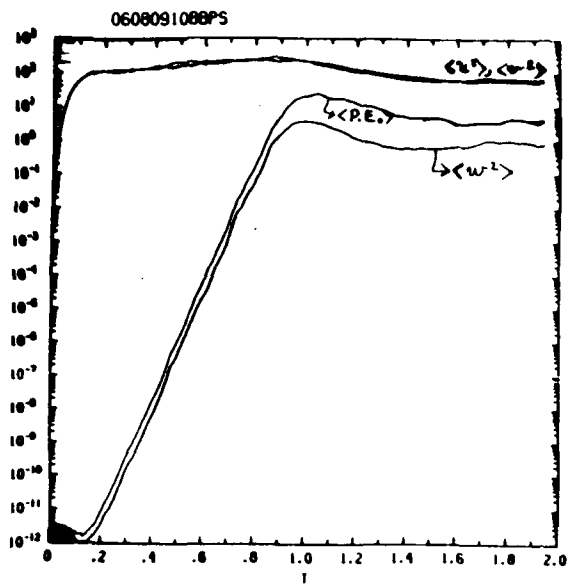


Figure 5

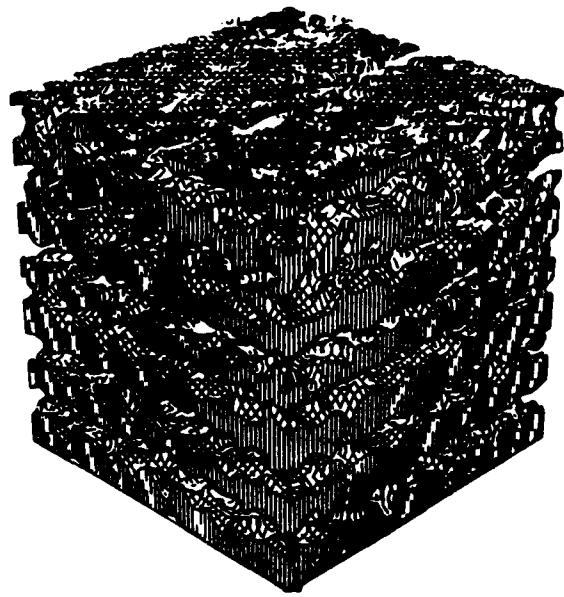


Figure 7

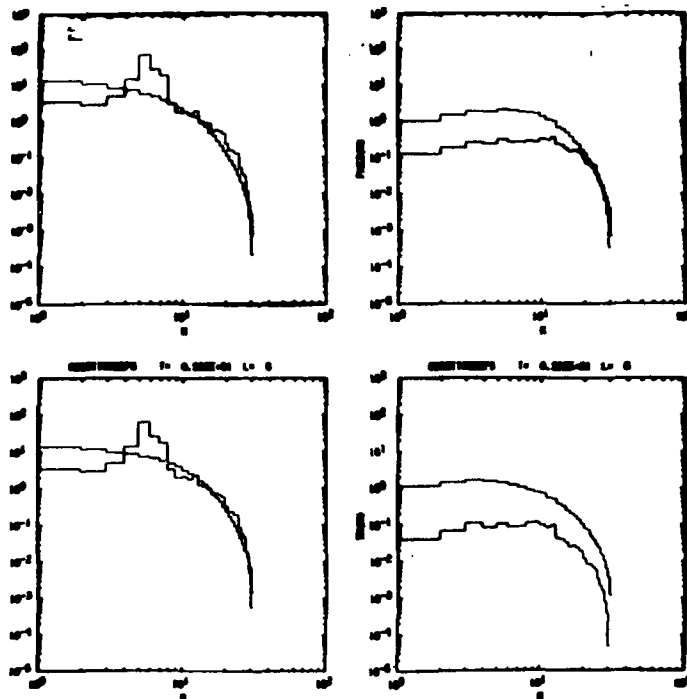


Figure 6

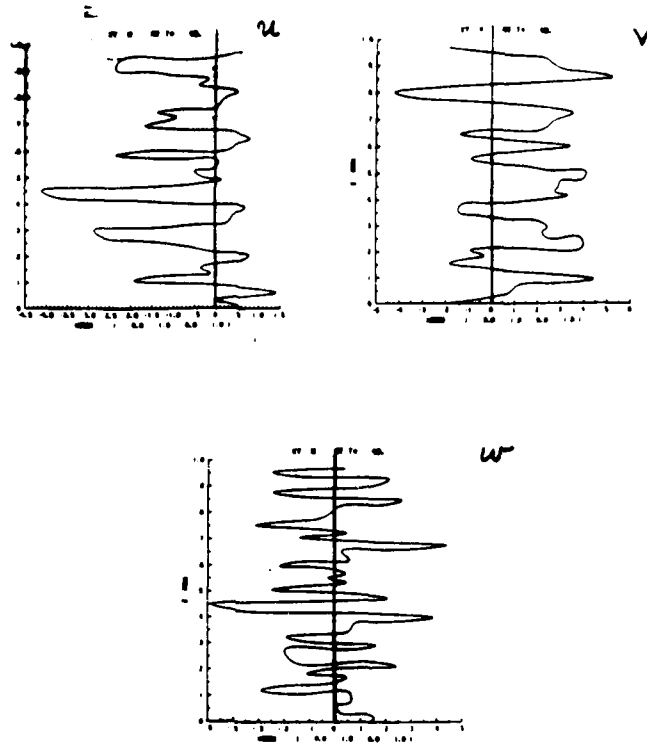


Figure 8

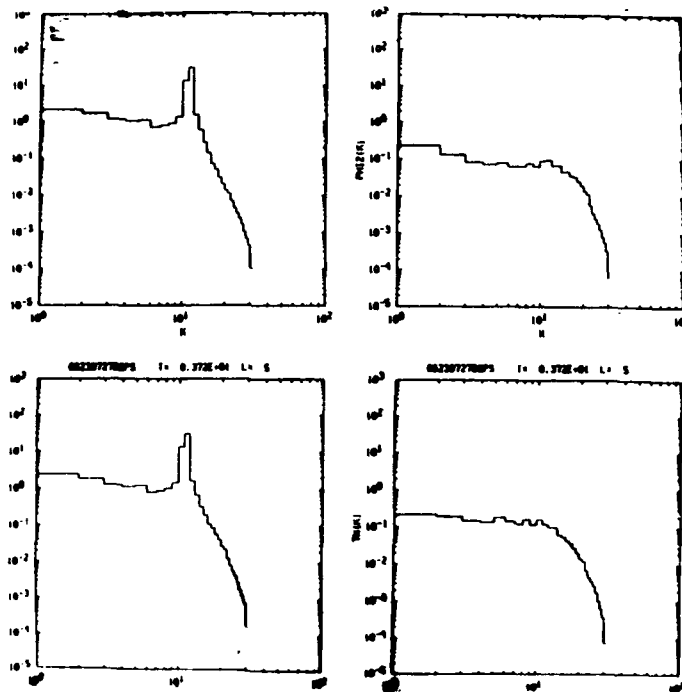


Figure 9

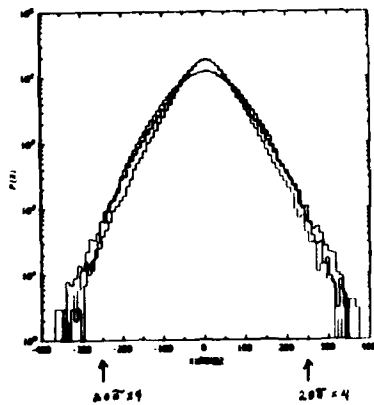


Figure 10

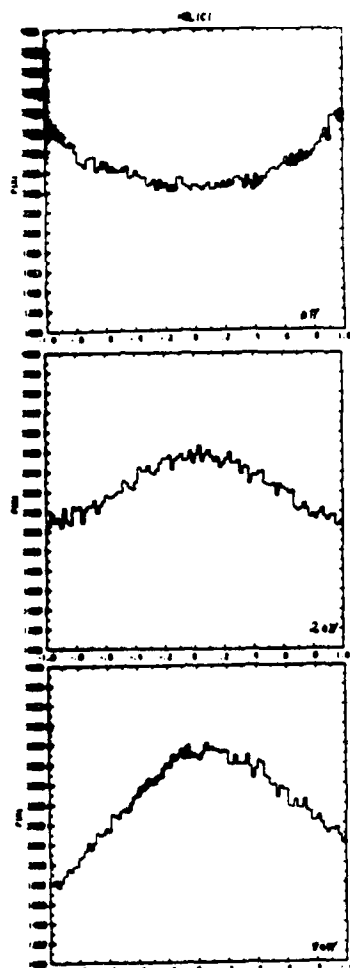


Figure 11

**A NUMERICAL INVESTIGATION OF THE  
TURBULENT PULSATING FLOW IN A PIPE**

P. ANDRE, R. CREFF, J. BATINA  
J.E. CNRS 034 936  
Laboratoire de Mécanique et Energé-  
tique - Université d'Orléans  
B.P. 6749 - 45067 ORLEANS Cedex 2 -  
FRANCE

**ABSTRACT**

A numerical model for turbulent pulsating flows in a pipe has been worked out and some of the most significant results are shown. One of the aims of that paper is to discuss the different hypothesis which are used in the model by comparison to other theoretical investigations and some experimental data. Conditions of the quasi-steady behaviour of the flow are studied.

**1. INTRODUCTION**

Two of the most interesting questions arising from studies upon turbulent pulsating flow are :  
i) the interaction between turbulence and the forced pulsation applied to the flow ; ii) would this pulsation be responsible for drastic changes in transport properties and, as an example, on convective heat transfer ?

Most of the informations brought up on those two points come mainly from experiments. On the other hand, a theoretical treatment of turbulent pulsating flows needs some assumptions and particularly an as appropriate as possible choice for a turbulence model. As an approach and looking for some criteria on the above questions the following hypothesis have been used in the proposed model :

A fully developed turbulent air flow is established in a tube. The axial pressure gradient is supposed to change sinusoidally with time around a steady value and consequently the velocity in the same manner. To check the ability of such a flow to modify convective heat transfer, the tube wall is maintained at a constant and uniform temperature and then a developing thermal fluid field is observed from the entry of the heated tube section. A modified mixing length model adapted to heat transfer in tubes is used.

The different equations, continuity, momentum and energy, are solved by means of a finite difference scheme using asymptotic developments for the pressure the velocity and the fluid temperature. Then, the equations are separated according the

different orders of the asymptotic developments : steady and unsteady. Radial distributions for amplitudes and phases of the velocity and the temperature are shown for various conditions of mean Reynolds number and frequency. A discussion on the quasi-steady behaviour of the flow resulting from the present model is proposed by comparison to some experimental criteria.

**2. PHYSICAL MODEL**

A fully developed turbulent flow of air is considered in a pipe of radius R with the assumptions of constant physical properties. Beyond a certain cross-section, taken here as the origin of the axial coordinate x, the tube wall is heated at a constant and uniform temperature over the ambient fluid temperature. With these hypothesis the development of the steady and unsteady thermal fluid flow will be shown by the model. The region of a fully developed turbulent flow, both dynamically and thermally, will be also depicted.

As a first approximation and because no closure law is available between the random turbulent agitation and the periodic modulation applied to the pressure gradient, it is assumed that the superimposed unsteady perturbation does not affect the overall turbulent behaviour averaged over time. Then, the eddy properties are supposed to remain constant along a pulsation period. However, it is expected that the model will give informations on the unsteady quantities such as amplitude and phase-lag for the velocity and the fluid temperature, the thermal gradient at the wall.

To depict the mean turbulent flow behaviour, the CEBECI's mixing length model (1973) modified by HABIB and NA (1974) for specific applications in pipe flows is retained here. In this model, the turbulent kinematic viscosity is given by :

$$v_t^+ = \frac{v_t}{v_m} = R^{+2} \left[ 0,4 \frac{y^+}{R^+} - 0,44 \left( \frac{y^+}{R^+} \right)^2 + 0,24 \left( \frac{y^+}{R^+} \right)^3 - 0,06 \left( \frac{y^+}{R^+} \right)^4 \right] \left[ 1 - \exp(-y^+/A^+) \right]^2 \cdot \frac{\partial u^+}{\partial y^+} \quad (1)$$

where A is a damping factor, R the tube radius, y the transverse coordinate, u the velocity and :

$$y^+ = yu^*/\nu \quad ; \quad A^+ = Au^*/\nu \quad ; \quad u^+ = u/u^*$$

with  $u^* = \sqrt{\tau_w/\rho}$  the usual friction velocity

$\tau_w$  the wall shear stress  
 $\nu_m$  the molecular kinetic viscosity

The thermal turbulent dimensionless diffusivity is written as :

$$a_t^+ = \frac{a_t}{m} = (R^+)^2 \left[ 0,4 \frac{y^+}{R^+} - 0,44 \left( \frac{y^+}{R^+} \right)^2 + 0,24 \left( \frac{y^+}{R^+} \right)^3 - 0,06 \left( \frac{y^+}{R^+} \right)^4 \right]^2 [1 - \exp(-y^+/A^+)] \quad (2)$$

$$\left[ 1 - \exp(-y^+ \sqrt{Pr/B^+}) \right] \cdot \frac{\partial u^+}{\partial y^+}$$

where the thermal damping parameter  $B^+$  is expressed as a function of the Prandtl number  $Pr$ , by means of some experimental data :

$$B^+ = \sum_{i=1}^5 C_i (\log Pr)^{i-1} \quad (3)$$

with  $C_i$  : five numerical coefficients.

The turbulent Prandtl number may be written as :

$$Pr_t = \nu_t / a_t = \left[ 1 - \exp(-y^+/A^+) \right] / \left[ 1 - \exp(-y^+ Pr/B^+) \right]$$

which, at the wall, gives :

$$Pr_t = B^+ / A^+ \sqrt{Pr} \quad (5)$$

with those definitions, good correlations have been obtained with experiments for a large range of Prandtl numbers : 0.02 to 15 and Reynolds numbers exceeding  $10^4$ . The two different conditions of constant heat flux at the wall or uniform wall temperature have been successfully used in those correlations. However, they were achieved for fully developed steady, dynamically and thermally flows. In our conditions, where a thermally developing flow has to be investigated, the reliability of the proposed model can be discussed. In the growth of the thermal boundary layer, one may expect some relation between the mixing length and the longitudinal coordinate  $x$ . However, and according to the study of CHEN and CHIOU (1981) for moderate molecular Prandtl numbers as for an air flow, no modification of the damping parameter  $B^+$  is requested in the thermal entrance region.

Other semi-empirical models such those given by DEISSLER (1955) and REICHARDT (1951) could be experimented in the application to unsteady flows but numerical computations of the velocity and temperature profiles from the friction law and the thermal gradient at the wall appear to be more complicated and more time consuming. On the other hand, the  $k - \epsilon$  turbulence model was used by COUSTEIX et al (1977) in the computation of unsteady boundary layers and compared to the mixing-length model : however, in the  $k - \epsilon$  model, some

corrections are needed for high Reynolds numbers and in the vicinity of the wall, to fit results brought up by the mixing-length model.

The physical and boundary conditions are finally summarized in Fig. 1

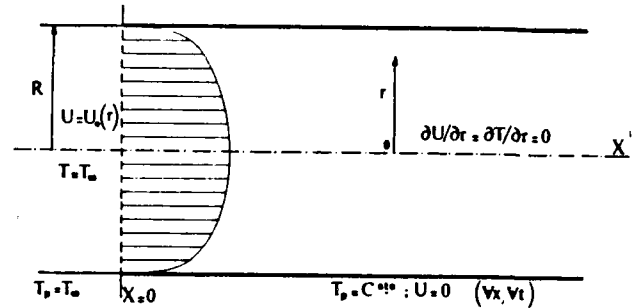


Fig.1 - Boundary conditions of the physical problem

### 3. ANALYSIS

The different quantities are made dimensionless in a classical manner by using the friction velocity  $u^*$  for the velocities and cylindrical coordinates :

$$u^+ = u/u^*$$

$$r^+ = r \frac{\sqrt{\tau_p/\rho}}{v_m} ; R^+ = R \frac{\sqrt{\tau_p/\rho}}{v_m} ; x^+ = x \frac{\sqrt{\tau_p/\rho}}{v_m}$$

The axial pressure gradient existing in the fully developed steady flow is used as a reference value for the pressure gradients with :

$$-\frac{1}{\rho} \frac{\partial p}{\partial x} = \frac{2\tau_p}{\rho R} \quad (6)$$

With  $R^2/v_m$  a time scale, we obtain a reduced time  $t^+$  and a reduced frequency such as :

$$t^+ = t/(R^2/v_m) \quad \Omega = \omega R^2/v_m \quad (7)$$

The dimensionless temperature is given as :

$$\theta = (T_p - T)/(T_p - T_\infty) \quad (8)$$

where  $T_p$  and  $T_\infty$  are the wall and ambient fluid temperatures respectively. The reduced equations are then

$$[AX] \quad \frac{r^+}{R^{+2}} \cdot \frac{\partial u^+}{\partial t^+} - 2 \frac{r^+}{R^+} = \frac{\partial}{\partial r^+} \left[ r^+ \left( 1 + \frac{v_t}{v_m} \right) \frac{\partial u^+}{\partial r^+} \right] \quad (9)$$

$$[III] : \quad (10)$$

$$\frac{1}{R^{+2}} \cdot \frac{\partial \theta}{\partial t^+} + u^+ \frac{\partial \theta}{\partial x^+} = \frac{1}{r^+} \frac{\partial}{\partial r^+} \left[ r^+ \left( \frac{1}{Pr} + \frac{a_t}{v_m} \right) \frac{\partial \theta}{\partial r^+} \right]$$

using the boundary layer approximation and neglecting the heat conduction along the x coordinate. Then, the boundary conditions are expressed as :

$$(11)$$

$$x^+ = 0 : \theta = 1 \quad \forall r^+, v_t^+$$

$$r^+ = 0 : \frac{\partial u^+}{\partial r^+} = \frac{\partial \theta}{\partial r^+} = 0 \quad \forall x^+, v_t^+$$

$$r^+ = R^+ : u^+ = 0, \theta = 0 \quad \forall x^+, v_t^+$$

The forcing unsteady pressure gradient is written as an asymptotic development in the following form :

$$\frac{\partial p}{\partial x} = \left( \frac{\partial p}{\partial x} \right)_0 \left[ 1 + \epsilon \tau e^{j\Omega t^+} + \epsilon^2 \tau^2 e^{2j\Omega t^+} + \dots \right]$$

with  $\epsilon$  a perturbation parameter,  $\tau$  an amplitude coefficient. Then, the velocity is supposed to be :

$$(13)$$

$$u^+ = u_0^+ + \epsilon u_1^+ e^{j\Omega t^+} + \epsilon^2 u_2^+ e^{2j\Omega t^+} + \dots$$

while for the fluid temperature we have :

$$\frac{T_p - T}{T_p - T_\infty} = \frac{T_p - T_0}{T_p - T_\infty} - \frac{T_1}{T_p - T_\infty} e^{j\Omega t^+} - \epsilon^2 \frac{T_2}{T_p - T_\infty} e^{2j\Omega t^+}$$

$$\text{or: } \theta = \theta_0 - \epsilon \theta_1 e^{j\Omega t^+} - \epsilon^2 \theta_2 e^{2j\Omega t^+}$$

$$(14)$$

After having introduced those developments in Equations (9) and (10) the different order equations are separated with respect to  $\epsilon^0, \epsilon^1, \epsilon^2, \dots$ . Then, a generalized form for the n-order x-momentum equation can be expressed as :

$$[AX]_n : \quad (15)$$

$$nj\Omega \frac{r^+}{R^{+2}} \frac{u_n^+}{r^+} - 2 \frac{r^+}{R^+} = \frac{\partial}{\partial r^+} \left[ r^+ \left( 1 + \frac{v_t}{v_m} \right) \frac{\partial (u_n^+/r^+)}{\partial r^+} \right]$$

For  $n = 0$ , the steady form is obtained. To illustrate the thermal problem, the first-order energy equation is given :

$$[III]_1 : \quad (16)$$

$$-j \frac{\Omega}{R^{+2}} \cdot \theta_1 - u_0^+ \frac{\partial \theta_1}{\partial x^+} + u_1^+ \frac{\partial \theta_0}{\partial x^+} = - \frac{1}{r^+} \frac{\partial}{\partial r^+} \left[ r^+ \left( \frac{1}{Pr} + \frac{a_t}{v_m} \right) \frac{\partial \theta_1}{\partial r^+} \right]$$

$$\text{with } \theta_1 = \theta_1 / \tau ; u^+ = u_1^+ / \tau$$

The resolution of momentum and energy equations is made using a finite difference scheme in which the dynamic field is first computed and after the developing thermal fluid field starting from the entry section is then calculated. More details are given in ANDRE et al (1986). Mean Reynolds numbers are ranging from  $10^4$  to  $10^5$  according to hypothesis and reduced frequencies used in the computation were equal to  $10\Omega$ ,  $50\Omega$ ,  $100\Omega$  and  $250\Omega$ . To illustrate this, a reduced frequency of  $10\Omega$  corresponds to a true frequency equal to 0.75 Hz for an air flow in a 1 cm tube radius while  $250\Omega$  corresponds to 18.75 Hz in the same conditions.

#### 4. DYNAMIC AND THERMAL FLUID FIELDS - STEADY FLOW

To check the accuracy of the Cebeci-s model for the eddy viscosity, the axial velocity profile computed from the zero-order momentum equation is compared to some experimental data obtained by NIKURADSE (1932) in Fig. 2

The classical logarithmic law :

$$\frac{u}{u_0} = 5,75 \log y^+ + 5,5 \quad (17)$$

is also represented.

To describe the steady development, the temperature is expressed by  $\theta_c/\theta_{0c}$  versus  $r/R$  where  $C$  refers to the center axis. Temperature profiles obtained for a mean Reynolds number of  $10^5$  are given in Fig. 3 for different cross-sections denoted by  $x^+$ . In the fully thermally developed flow, the reduced temperature is expressed for different mean Reynolds numbers and compared to the classical law  $(1 - r^*)^{1/N}$  with  $N = 1 + 0,75 (Pr/3 - 1)$  (Fig. 4). The weak influence of the Reynolds number on the profiles is clearly shown out excepted for  $10^4$  which is the lowest limit of applicability of the model. This is confirmed by the longitudinal

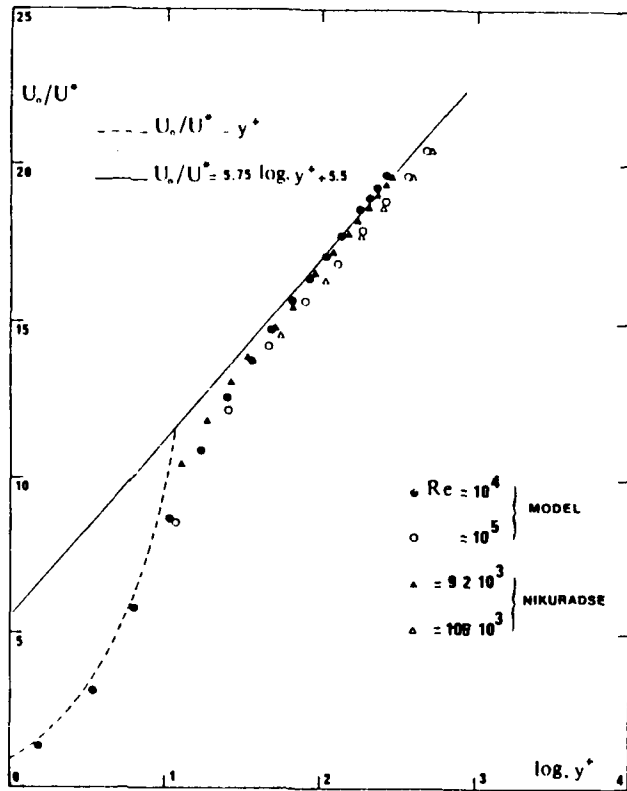


Fig. 2 - Axial steady velocity profiles

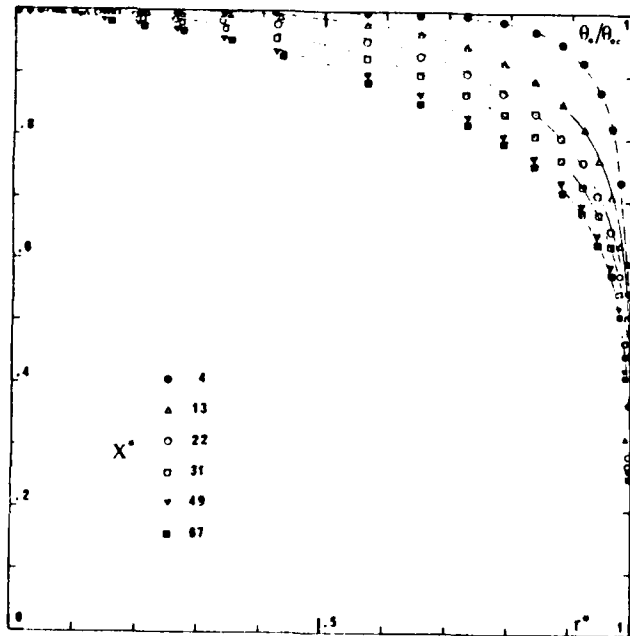


Fig. 3 - Steady temperature profiles for the developing thermal fluid field,  $Re = 10^5$

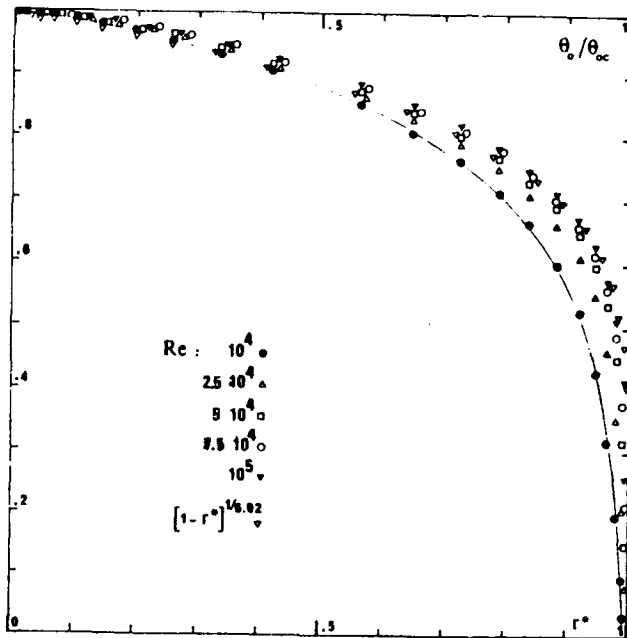


Fig. 4 - Steady temperature profiles for the fully developed thermal fluid field

evolution of the steady Nusselt number  $Nu_0$ , expressed as :

$$Nu_0 = \frac{2(\partial\theta_0/\partial r^*)_p}{\theta_p - \bar{\theta}_0} p \quad (18)$$

where  $r^* = r/R$ ,  $p$  refers to the wall and coefficient 2 defines a Nusselt number on the tube diameter. Results are compared in Fig. 5 to those given by SLEICHER and TRIBUS (1957) and SIEGEL and SPARROW (1960) where, in both cases, the fluid flow was assumed with equal dynamic and thermal eddy diffusivities ( $Pr_t = 1$ ). A turbulent Prandtl number equal to unity does not induce strong differences in the thermal development as far as the molecular Prandtl number is itself not far from unity. This is confirmed by CHEN and CHIOU.

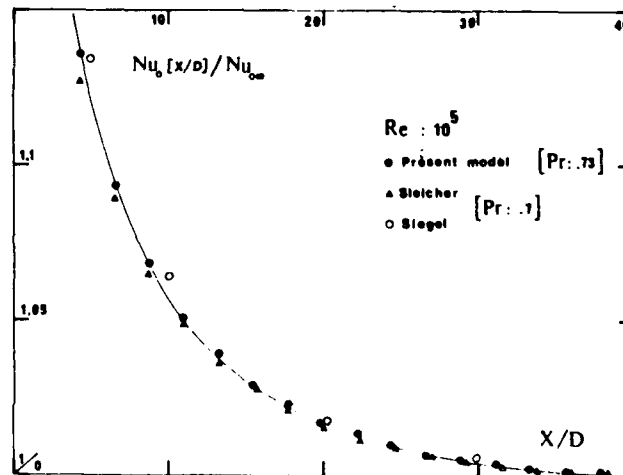


Fig. 5 - Longitudinal evolution for the steady heat transfer

### 5. DYNAMIC FLUID FIELD - UNSTEADY FLOW

As for the dynamic steady-flow, the unsteady regime is assumed to be fully established leading to repetitive unsteady velocity profiles along the tube axis. The velocity  $U_1$  expressed as :

$$u_1(r, \Omega, t) = |u_1(r, \Omega)| \cdot \cos[\omega t + \phi(r, \Omega)] \quad (19)$$

is shown at different angles for two frequencies,  $10\Omega$  and  $250\Omega$ , on Fig.6 and 7 respectively and for a same Reynolds number :  $10^4$ . As the frequency increases, the velocity amplitude decreases whereas a maximum is reached near the wall instead of the center axis as it occurs for the lowest frequency. This leads to an annular effect.

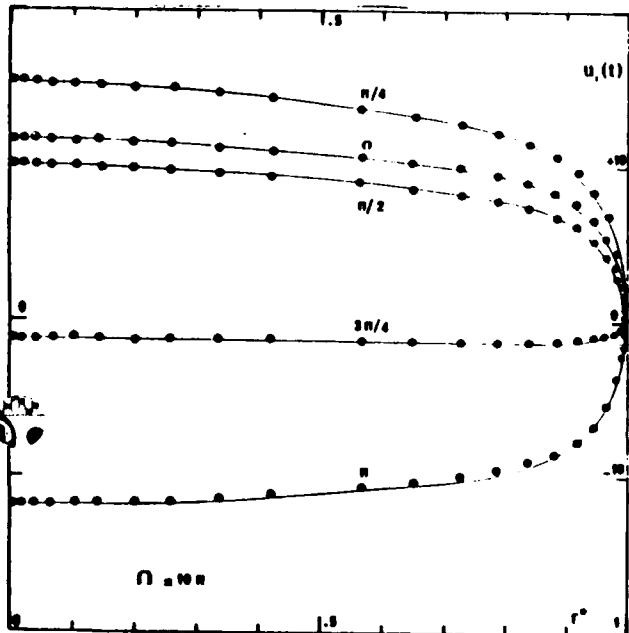


Fig.6 - Unsteady velocity distributions for  $Re = 10^4$  and a low frequency

To complete this, it can be seen from fig.8 that the radial variation of the phase angle is nearly negligible for the lowest frequency : the fluid oscillates "as a whole" all along the tube radius for this condition.

The velocity amplitudes for the first and second orders (fundamental and first harmonics) are compared to the steady velocity amplitude in Fig. 9. Whereas the three profiles remain the same for a low frequency, a strong annular effect appears for the high frequency of  $250\Omega$  ; this effect is even more pronounced for the second order velocity than for the first order and confirms the trend for increasing frequencies. On the other hand, for a mean Reynolds number equal to  $10^5$ , no annular effect is shown even for the highest studied frequency.

If now, we consider a constant frequency but variable mean Reynolds number, increasing velocity amplitudes are obtained for increasing

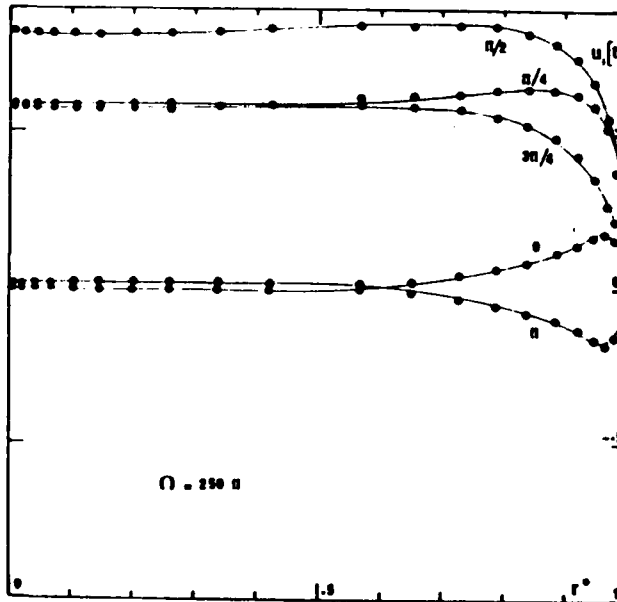


Fig.7 - Unsteady velocity distributions for  $Re=10^4$  and a high frequency

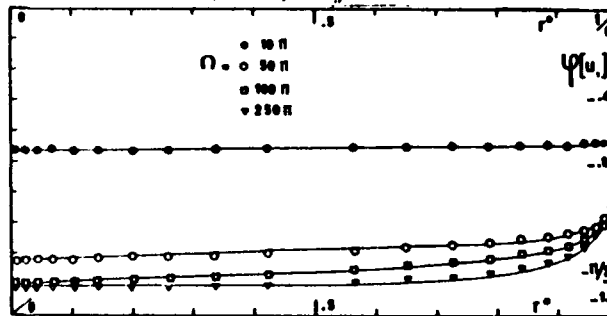


Fig.8 - Radial profiles for the velocity phase,  $Re = 10^4$ , and different frequencies

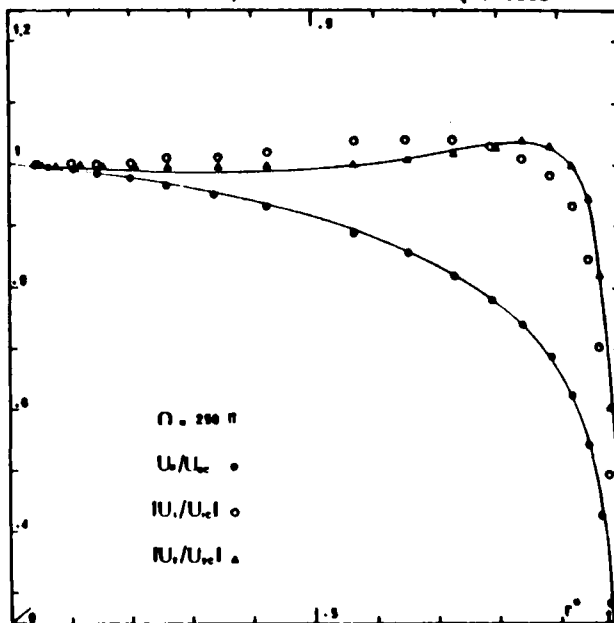


Fig.9 - Amplitude profiles for the steady, first order and second order velocities;  $Re=10^4$

Reynolds numbers but the dimensionless velocity profiles tend gradually towards an homothetic shape to that of the steady velocity. This will be discussed in section 7.

### 6. THERMAL FLUID FIELD - UNSTEADY FLOW

Both amplitude and phase angle for the unsteady temperature are function of the two space coordinates, the frequency and this is formulated as follows :

$$\theta_1(x^*, r^*, \Omega, t) = \tau \cdot \theta_1(x^*, r^*, \Omega) \quad (20)$$

$$\cos[\omega t + \psi(x^*, r^*, \Omega)]$$

where  $x^* = x/R$ . Unsteady temperature profiles may be expressed at different angles and such profiles are shown in Fig.10 for a tube section not very far from the heated length entry ( $x^* = 13$ ). From computations, it may be observed that the phase angle does not change along the radius for low frequencies whereas for highest frequencies a phase-lag exists between the wall and the center axis which increases as the thermal field is developing.

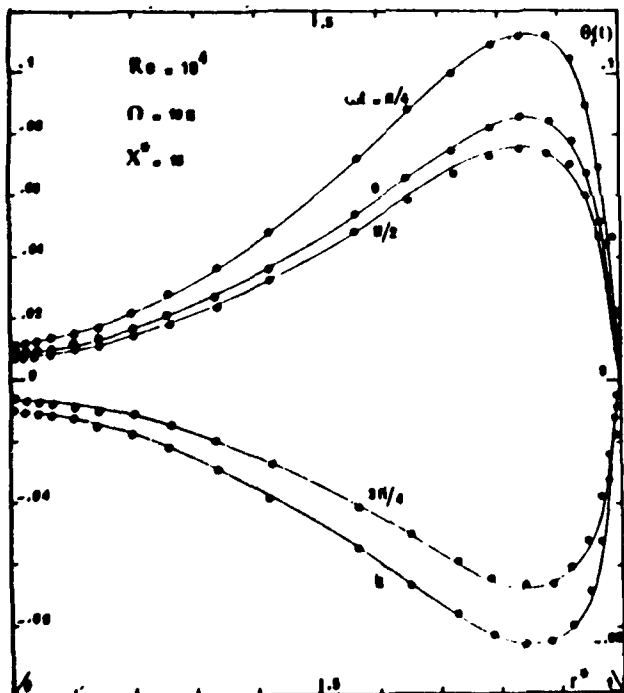


Fig.10 - Unsteady temperature profiles in the developing thermal fluid field

For the amplitudes, an annular effect appears in the first sections and is developing with the flow such as its maximum tends from the wall towards the axis and amplitudes increase. On Fig. 11 and 12 amplitude profiles are given for the same frequency but two different Reynolds numbers ( $10^4$  and  $10^5$  respectively).

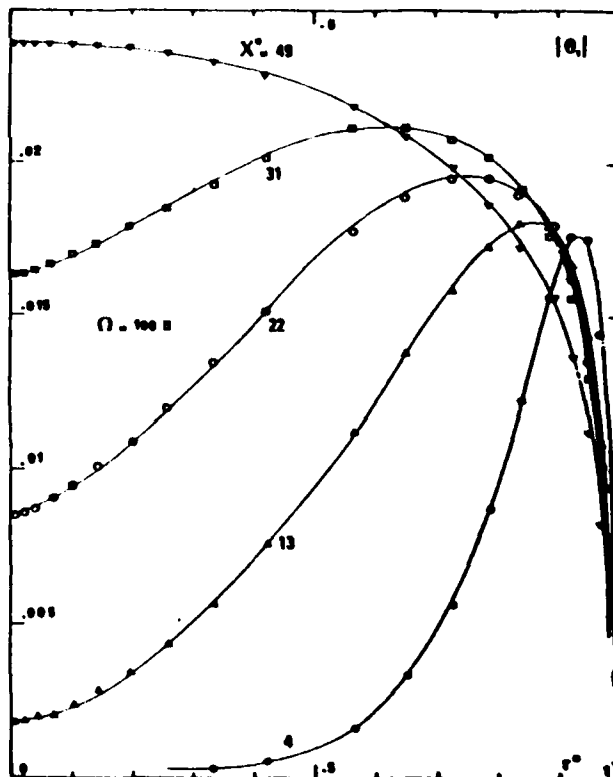


Fig.11 - Amplitude profiles for the unsteady temperature,  $Re = 10^4$

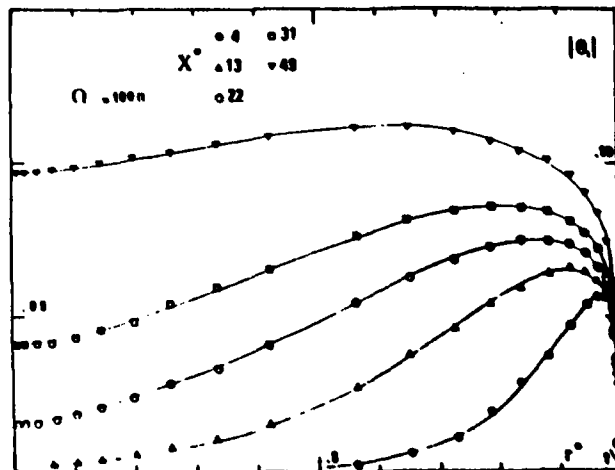


Fig.12 - Amplitude profiles for the unsteady temperature,  $Re = 10^5$

From the different results brought up by the model two different characteristics may be summarized as follows :

i) for a given Reynolds number, unsteady temperature amplitudes decrease when the frequency increases ;

ii) for a given frequency, amplitudes increase with the Reynolds number.

These trends are similar to those shown for the unsteady velocity.

If now, we consider the temperature gradient at the wall, it can be shown, Fig. 13, that its amplitude vanishes shortly after the heated section entry for the highest frequency, whereas it remains significant on a long axial distance and even grows for the lowest frequency. In the same way, the phase angle, expressed as the phase difference with the forcing unsteady pressure, shows a very slow variation along the wall for a low frequency, whereas it changes strongly in the high frequency case (Fig. 14). The instantaneous transport of heat from the wall to the fluid and then the unsteady thermal fluid field are vanishing and disappearing on a short axial distance from the entry and for increasing frequencies.

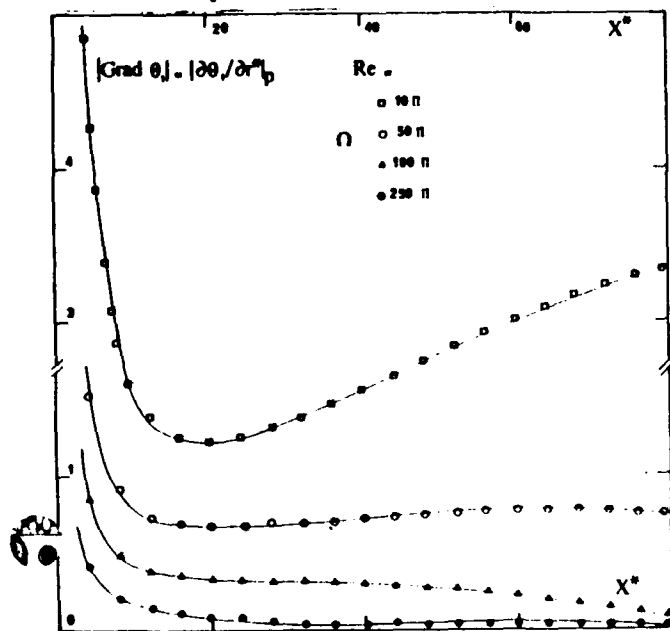


Fig. 13 - Longitudinal variation for the temperature gradient at the wall (amplitudes)

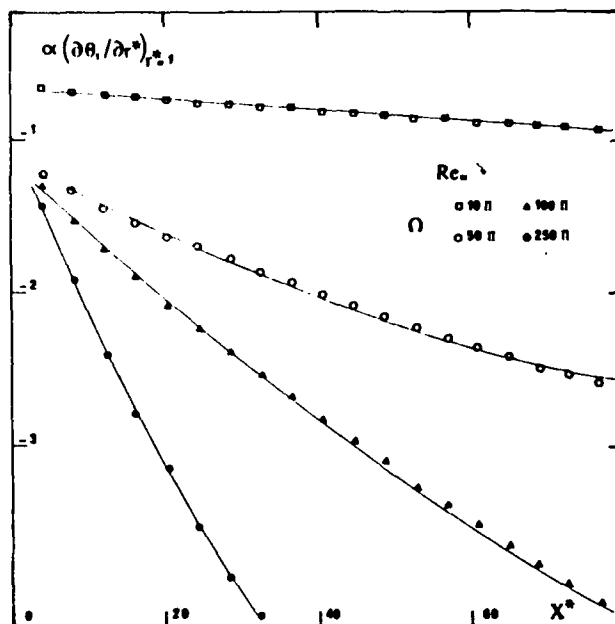


Fig. 14 - Longitudinal variation for the temperature gradient at the wall (phases)

#### 7. DISCUSSION AND CONCLUDING REMARKS

Unsteady effects may be discussed from the x-momentum equation. From the generalized form, Eq. (15), it can be seen that if the first term on the left hand side vanishes, then, any unsteady dynamic effect will disappear. This is normally obtained for frequency decreasing towards zero. In that limit case,  $[AX]_n$  becomes similar to  $[AX]_0$ . By reminding that  $u_n$  is equal to  $u/u^*$ , the modulus of the first term in Eq. 15 is written as :

$$C_n = \frac{n\Omega r^+}{R^{+2}} \cdot \frac{|u_n^+|}{\tau^n} = \frac{n\Omega r^+}{R^{+2}} \cdot \frac{|u_n^+|}{u^*} \cdot \frac{1}{\tau^n} \quad (21)$$

Considering  $\frac{r^+}{R^{+2}} \sim \frac{1}{R^+}$  and the usual definition for the friction velocity in the studied range of mean Reynolds numbers, the coefficient of the unsteady velocity amplitude may be formulated such as :

$$K_n = \frac{160n}{\tau^n} \cdot \frac{D}{v_m} \cdot \frac{\Omega}{Re^{1,75}} \quad (22)$$

Then for a fluid of a given kinematic viscosity flowing in a tube of diameter D, the influence of the unsteady term is traduced by the factor  $\Omega/Re^{1,75}$ . It comes clear that for a given constant frequency the increase in Reynolds number leads to vanishing unsteady dynamic effects. A same trend may be also shown for the thermal fluid field from the unsteady term in the energy equation, Eq. (16). On the other hand, for a given mean Reynolds number, the increase in frequency induces typical unsteady effects such as the annular effect but, at the same time, decreasing unsteady velocity or temperature amplitudes. This corresponds, in a sense, to vanishing

unsteady effects. Therefore, it can be assumed that two opposite limits may be achieved for a fixed  $Re$ : low modulation frequency where the flow may be described as steady or quasi steady and high frequencies where unsteady effects exist but with very small amplitudes if they are not negligible when compared to steady values. Between those two limits, the analysis shows that it could exist a range of critical values for  $\Omega/Re^{1.75}$  for which unsteady dynamic and thermal effects would be significant.

In their analytical studies, OHMI and USUI (1976) have shown the existence of the same two opposite limits confirmed by experiments (1976). However, this was depicted with no analytical criterion. In another work, OHMI et al (1978) have made an analytical approach for the quasi-steady approximation using a time variable friction velocity. For low frequencies, the eddy viscosity is then considered as the sum of a steady component and an unsteady viscosity. This last term is not still existing as the frequency increases due to inertia effects of the turbulent flow. To define a limit for the frequency domain where the quasi-steady approximation applies a criterion is given by OHMI et al such as: no more than 1% in the relative variation between steady velocities calculated for each instantaneous value of the forcing pressure gradient and unsteady velocities calculated with the hypothesis of an oscillating friction velocity. From this, a curve was obtained showing the frequency as a monotonic growing function of the Reynolds number: below that curve a quasi steady behaviour may be considered whereas above it the flow is in a purely unsteady regime. From the present analysis and the major role held by the factor  $\Omega/Re^{1.75}$  a slightly different criterion may be proposed and based upon the numerical values for  $U_0$  and  $U_1$ : for a frequency equal to  $100\Omega$  and a mean Reynolds number equal to  $10^5$ , the model shows a relative difference not greater than 1% all along the radial profiles. In that situation and according to OHMI, the corresponding flow regime should be considered as quasi-steady which gives:

$$\Omega/Re^{1.75} < 5.6 \cdot 10^{-7}$$

Such a criterion has to be considered as a rather crude one for it is only based upon velocity profiles. At least, it may be used as an extreme limit for quasi-steadiness. However the present analysis induces the existence of a frequency range for which unsteady effects could be not negligible when compared to analog steady effects. In their experimental work, BINDEL et al (1985) have studied the wall region of a turbulent channel flow submitted to large amplitude periodic oscillations. Using the Stokes layer thickness,  $L_s$ , as a typical parameter to depict the possible interaction between oscillations and the wall region flow it has been shown that for:

$$L^+ = \frac{L_s}{L_v} = \frac{\sqrt{2\nu/\omega}}{\nu/u_*} < 10$$

where  $L_v$  is the viscous length scale, viscous diffusion alone governs the removal of unsteady

vorticity from the wall and, then, turbulence is not active in the diffusion (Stokes flow situation) For values of  $L^+$  contained between 10 and 20, which means for lower frequencies, a departure from the Stokes flow is observed. For  $L^+$  larger than 20 a general trend towards quasi-steady flow occurs. A different expression for the dimensionless criterion,  $L^+$ , may be obtained, with the friction velocity defined according to the classical Blasius formulae it may be shown that:

$$\Omega/Re^{1.75} = 0.048/L^{+2}$$

Then the trend to quasi-steady flow would occur for values of  $\Omega/Re^{1.75}$  smaller than  $1.2 \cdot 10^{-4}$  which is less restrictive than proposed by the present analysis.

In an other experimental study, on turbulent pulsating pipe flows, SHEMER and KIT (1984) have made out a slight different criterion, namely, quasi-steady flow behaviour occurs for  $St/Re$  smaller than  $3.24 \cdot 10^{-4}$  where  $St$  is the Strouhal number. This ratio may be redefined such as:

$$\Omega/Re^{1.75} < 0.81 \cdot 10^{-4} Re^{-1/4}$$

which for the average Reynolds number ( $Re=5500$ ) used in those experiments would give:

$$\Omega/Re^{1.75} < 6.97 \cdot 10^{-4}$$

which is again less restrictive than above. Therefore, experimental data show that quasi steady flows may be still obtained for larger frequencies than those predicted by the present analysis with a given  $Re$ .

From these different results, it appears that a specific combination of the frequency and the mean Reynolds number is closely related to the ratio of the oscillating Stokes layer thickness to the viscous layer thickness. Any efficient interaction between oscillations and turbulence may be then expressed in terms of that ratio or in terms of  $\Omega/Re^{1.75}$ . As a typical example, GALITSEISKII et al (1976), studying convective heat transfer in a pulsating turbulent pipe flow, have shown that the maximum enhancement for heat transfer was correlated to a ratio  $L/5 L_v$ , equal to 30 which may be expressed also as  $\Omega/Re^{1.75} \approx 10^{-6}$ . However, further experimental studies are needed to correlate the dynamic interactions between oscillations and turbulence to observed changes in transport or diffusion throughout the flowfield. In other words, such changes as those on convective heat transfer may result from other dynamic effects such as: large amplitudes, periodic reverse flows, second-order terms in developing flow field, etc ...

#### REFERENCES

- BINDER G., TARDU S., BLACKWELDER R.F., KUENY J.L., 1985, Large amplitude periodic oscillations in the wall region of a turbulent channel flow. Symposium on Shear Flows, Cornell University, (N-7), 16-1, 16-6

CEBECI T., 1973, A model for eddy conductivity and turbulent Prandtl number, J. of heat transfer, vol. 95, 227-234

CHEN C.J., SHING CHIOU J., 1981, Laminar and turbulent heat transfer in the pipe entrance for liquid metals, Int.J.of Heat, Mass transfer, vol.24, n°7, 1179-1190

COUSTEIX J., HOUEVILLE R., DESOPPER A., 1977, Résultats expérimentaux et méthodes de calcul relatifs aux couches limites turbulentes en écoulement instationnaire, Unsteady aerodynamics, AGARD CONF. PROC. n° 227, Ottawa, 26-28 Sept.

DEISSLER R.G., 1955, Turbulent heat transfer and friction in the entrance regions of smooth passages, Trans. ASME vol. 88, 1221-1233

GALITSEISKII B.M., NOZDRIN A.A., RYZHOV Y.A., YAKUSH E.V., 1976, Investigation of local heat transfer coefficients under conditions of the resonance oscillations of a gas in channels. Inzhenerno-Fizicheskii Zhurnal, vol.31, n°2, 197-201

HABIB I.S., NA T.Y., 1974, Prediction of heat transfer in turbulent pipe flow with constant wall temperature, J. of Heat Transfer, vol.96, 253-254, May

NIKURADSE J., 1932, Gesetzmässigkeiten der Turbulenten Strömung in glatten Rohren, Forschung auf dem Gebiete des Ingenieurwesens, Ausgabe B., Band 3, 1-35

OHMI M., USUI T., 1976, Pressure and velocity distributions in pulsating turbulent pipe flow, Part 1 : theoretical treatments, Bull.J.S.M.E., Vol. 19, n° 129, 307-313

OHMI M., USUI T., TANAKA O., TOYAMA M., 1976, Pressure and velocity distributions in pulsating turbulent pipe flow, Part.2 : experimental investigations, Bull. J.S.M.E., vol.19, n° 134, 951-957

OHMI M., KYOMEN S., USI T., 1978, Analysis of velocity distribution in pulsating turbulent pipe flow with time-dependent friction velocity, Bull. J.S.M.E., vol.21, n° 157, 1137-1143

REICHARDT H., 1951, Vollständige Darstellung der turbulenten Geschwindigkeitsverteilung in glatten Leitungen, Z. für ang. Mathematik und Mechanik, vol.31, 208-219

SHEMER L., KIT E., 1984, An experimental investigation of the quasisteady turbulent pulsating flow in a pipe, Phys.Fluids 27, (1), 72-76

SIEGEL R., SPARROW E.M., 1960, Comparison of turbulent heat transfer results for uniform wall heat flux and uniform wall temperature, J. of heat transfer, vol.82, 152-153

SLEICHER C.A., TRIBUS M., 1957, Heat transfer in a pipe with turbulent flow and arbitrary wall-temperature distribution, Trans. ASME, vol.79, 789-797

NUMERICAL SIMULATION OF THE  
VISCIOUS WALL REGION

Karam Azab and John B. McLaughlin  
Clarkson University  
Potsdam, New York 13676

ABSTRACT

It is shown that the viscous wall region can be simulated by solving the Navier-Stokes equation subject to an extra constraint at large distances from the wall. Periodic boundary conditions are applied in the streamwise and spanwise directions with periodicity lengths that are several times larger than the experimental mean streak spacing, and no subgrid scale modelling is used. The model yields results which are in reasonably good agreement with results obtained from direct simulation of turbulent boundary layers and fully developed turbulent channel flow in spite of the fact that the calculations are two orders of magnitude smaller.

LATIN SYMBOLS

$i$	$\sqrt{-1}$
$j$	integer
$k_x, k_z$	wavenumbers in x and z directions
$l, L, m, M$	integers
$N$	time step index
$p$	integer or fluctuating part of pressure
$P$	integer
$dP_{ext}/dx$	external pressure gradient
$Re$	Reynolds number
$t$	time
$u$	x-component of velocity
$u_\infty$	x-component of velocity at infinity
$u^*$	friction velocity
$v$	y-component of velocity
$\vec{v}$	velocity vector
$v_0$	reference speed
$w$	z-component of velocity
$x$	streamwise coordinate
$X$	periodicity length in the x direction

$\hat{x}$	unit vector in the x direction
$y$	normal coordinate
$y_1, y_2$	log profile imposed for $y_1 < y < y_2$
$y_m$	map parameter
$\hat{y}$	unit vector in the y direction
$z$	spanwise coordinate
$\hat{z}$	unit vector in the z direction

GREEK SYMBOLS

$\nu$	kinematic viscosity
$\vec{\omega}$	vorticity vector
$\pi$	pressure head
$\rho$	mass density
$\zeta$	argument of Chebyshev polynomials

1. INTRODUCTION

Deardorff (1970) carried out a numerical study of high Reynolds number turbulent channel flow using only 6720 grid volumes and was able to obtain fair to good agreement with Laufer's (1950) experimental statistics in the core of the channel. As a consequence of the low spatial resolution, Deardorff's simulation did not treat the viscous wall regions explicitly. Instead, he developed a set of artificial boundary conditions which forced the horizontal average of the streamwise component to agree with the law of the wall at the grid point closest to the wall. Subgrid scale modelling was used in order to account for neglected small scales.

In the years since Deardorff's contribution, numerical simulation of turbulent flows has emerged as a useful supplement to laboratory experiments. Recently, Kim et al. (1986) have performed direct numerical simulations of turbulent channel flow using pseudospectral methods in which the nonlinear terms of the Navier-Stokes equation were evaluated

on a grid containing  $4.10^6$  grid points. The Reynolds number of the flow was 3300, based on the mean centerline velocity and channel half-width. No subgrid scale modelling was used since the grid spacings were small enough to account for all essential scales of motion.

Unfortunately, direct simulation of turbulent flow is limited to small Reynolds number because the computational work is proportional to  $Re^3$ , and Orszag and Yakhat (1986) have argued that such calculations will be even more expensive with cellular-automaton methods. Thus, turbulence modelling will be needed in numerical simulation of high Reynolds number flows for the foreseeable future. In this paper, a model will be described which is, in a sense, complementary to Deardorff's approach. Deardorff's simulation does not explicitly deal with the viscous wall region, but the viscous wall region is of some interest since laboratory experiments by Laufer (1954) and Kim et al. (1971) indicate that most turbulence production takes place in that region. In our approach, all details of the outer part of the flow are eliminated by setting the horizontal average of the streamwise component of velocity equal to a constant at points outside the viscous wall region. Rigid boundary conditions are imposed at the wall and velocity fluctuations are required to vanish at infinite distance from the wall. Periodic boundary conditions are imposed in both horizontal directions and pseudospectral methods are used to solve the governing equations.

Ideally, one would use periodicity lengths which are much larger than any of the natural length scales of the flows of interest, but this would make the size of the computation prohibitive. Instead, the periodicity lengths are chosen to be several times larger than the mean spanwise spacing between low speed streaks which Kline et al. (1967) determined to be 100 wall units (in wall units, the units of length and time are  $\nu/u_*$  and  $\nu/u_*^2$ .) Corino and Brodkey's (1969) experiments indicated that the low speed streaks played an important role in turbulence production and that the spanwise and streamwise lengths of turbulent bursts were somewhat smaller than the mean streak spacing. Our choice of periodicity lengths is motivated by

the notion that the most important length scales in the viscous wall region are on the order of the mean streak spacing or smaller and that larger length scales can be treated crudely.

No subgrid scale modelling is used in the calculations to be reported. As a consequence, it was necessary to use small grid intervals, but, since the periodicity lengths were small compared to the largest length scales present in turbulent shear flows, only 34000 grid points were needed in order to achieve grid spacings comparable to those used by Kim et al. (1986).

In spite of the fact that the calculations to be reported were two orders of magnitude smaller than direct simulations of channel flow and boundary layers, it will be shown that the computed intensities are in good agreement with those obtained by direct simulation. In addition, the energy balance is satisfied within the viscous wall region and the mean streak spacing is correctly predicted.

## 2. GOVERNING EQUATIONS

The system to be discussed is an incompressible flow over an infinite, flat, impermeable, and rigid wall. The origin of the coordinate is located on the wall and the  $x$ ,  $y$ , and  $z$  axes point in the streamwise, normal, and spanwise directions, respectively. All physical quantities will be made dimensionless in terms of a reference speed,  $v_0$ , the kinematic viscosity,  $\nu$ , and the mass density,  $\rho$ .

The primary goal is to formulate a model of the viscous wall region of turbulent shear flows such as fully developed turbulent channel flow or pipe flow. When expressed in wall units (i.e.,  $v_0 = u_*$ ), the external pressure gradient for such flows vanishes in the limit of large Reynolds numbers. Thus, one needs a means of supplying energy to the viscous wall region in order to sustain the turbulence in that region. In an actual channel or pipe flow, the external pressure gradient supplies the energy that drives the flow. In the model, the flow is maintained by setting the horizontal ( $x$  and  $z$ ) average of the  $x$ -component of velocity equal to a fixed profile for  $y > y_1$ . In its simplest formulation, a constant profile would

be used, but this would eliminate all turbulence production for  $y > y_1$  and, since values for  $y_1$  on the order of 30 to 40 wall units yield intensity profiles that agree best with experiment in the region  $y < 30$  wall units, this would eliminate a significant amount of turbulence production. For this reason, a logarithmic profile is imposed for  $y_1 < y < y_2$ . For  $y > y_2$ , a constant profile is imposed. In the calculations to be reported,  $y_1$  and  $y_2$  were approximately 33 and 55 wall units, respectively.

Since the horizontal average of the x-component of velocity is fixed for  $y > y_1$ , the imposed velocity at  $y = y_1$  acts as a source of energy for the viscous wall region in a manner similar to the moving wall in a plane Couette flow. However, unlike plane Couette flow, fluctuations in all three components of velocity exist for  $y > y_1$ .

The governing equations of the model are:

$$\frac{\partial \bar{v}}{\partial t} + \bar{v} \cdot \nabla \bar{v} = -\bar{\nabla} p - (d_{p_{ext}}/dx)\hat{x} + \bar{v}^2 \bar{v} \quad (1)$$

$$\bar{\nabla} \cdot \bar{v} = 0 \quad (2)$$

$$\langle u \rangle = 2.4 \ln(y) + 5.34, \quad y_1 < y < y_2 \quad (3)$$

$$\langle u \rangle = 2.4 \ln(y_2) + 5.34 \equiv u_\infty, \quad y_2 < y \quad (4)$$

$$\bar{v} = 0, \quad y = 0 \quad (5)$$

$$v = w = 0, \quad y = \infty \quad (6)$$

$$u = u_\infty, \quad y = \infty \quad (7)$$

$$\bar{v}(x+mX, y, z+nZ, t) = \bar{v}(x, y, z, t). \quad (8)$$

In Eqs. (3) and (4), the brackets denote an average over  $x$  and  $z$ . In writing Eqs. (3) and (4), it is assumed that  $v_0$  is the friction velocity based on the initial value of the horizontally averaged velocity. If  $v_0$  were the steady-state friction velocity, the right hand side of Eq. (3) would be a good approximation to Laufer's (1954) experimental data. However, for the parameter choices used in the calculations to be reported, the horizontally averaged wall shear stress drops by about 15% during the initial transient period and all variables must be rescaled in order to obtain their values in wall units based on the steady-state friction velocity. As a consequence, the profile in Eq. (3) is about

8% larger than Laufer's experimental profile.

### 3. PARAMETER CHOICES

There are four adjustable parameters in the model which was formulated in the previous section:  $y_1$ ,  $y_2$ ,  $X$ , and  $Z$ . Experimental results are used in choosing all four parameters. Laufer's (1954) energy balance suggests that the region  $y^+ < 30$  is a net source of turbulence kinetic energy and this finding is consistent with the channel flow simulation results reported by Moser and Moin (1984). Corino and Brodkey (1969) stress the importance of the region  $y < 30$  wall units in the "ejection" processes which are important in the production of turbulence. These results suggest that  $y_1$  should be roughly 30 wall units. Experimentation with various values of  $y_1$  reveals that large values of  $y_1$  lead to small wall shear stresses (and, hence, large deviations from Laufer's profile for  $y > y_1$ ) and fluctuation intensities which are too small near the wall. Values of  $y_1$  which are much smaller than 30 wall units yield fluctuation intensities which are considerably smaller than the experimental values for  $y > y_1$ .

Since a significant amount of turbulence production occurs for  $y > 30$  wall units, it is desirable to choose  $y_2$  to be considerably larger than  $y_1$ . In the calculations to be reported,  $y_2$  was approximately 55 wall units, based on the steady-state friction velocity.

In the calculations to be reported,  $X$  and  $Z$  were approximately 581 and 249 wall units, respectively, based on the steady-state friction velocity. The choice of  $X$  was suggested by the experiments of Morrison et al. (1971) who found that, in the viscous wall region, the frequency-wavenumber spectrum showed a maximum at a wavelength equal to 630 wall units. Based on the initial value of the friction velocity, the value of  $X$  was 630 wall units in the calculations to be reported.

The value of  $Z$  was sufficiently large that one should typically find two low speed streaks in the computational region. Larger values of  $Z$  would have increased the size of the computation considerably since the number of grid points in the spanwise direction would have had to be

increased and the number of grid points is required to be an integer power of two by the fast Fourier transform routines used in our calculations.

#### 4. NUMERICAL METHODS

The Marcus (1984) technique was used to solve the governing equations. In this approach, three fractional steps are used to advance the velocity from time step  $N$  to time step  $N+1$ . In the first fractional step, the nonlinear terms are computed. The method used to obtain the results to be reported differs from the one described by Marcus in that an Adams-Bashforth-Crank-Nicholson (ABCN) scheme (see Orszag and Kells (1980)) instead of an Adams-Bashforth scheme is used to compute the nonlinear terms. The two methods differ in that, in the ABCN method, the convective term is divided into two parts and the larger part is treated implicitly:

$$\frac{\vec{v}^{N+1}}{\Delta t} = \frac{\vec{v}^N}{\Delta t} - \frac{U}{2} \left( \frac{\partial \vec{v}}{\partial x} \right)^{N+\frac{1}{3}} + \frac{\partial v}{\partial x} \left( \frac{N-\frac{2}{3}}{2} \right) \Delta t + \frac{3}{2} \vec{f}^N - \frac{2}{3} \frac{1-N}{2} \vec{f}^N - \frac{5}{3} \vec{f}^N \quad (9)$$

$$\vec{f} = (\vec{v} \times \vec{\omega}) + U \frac{\partial \vec{v}}{\partial x} - (d_{pext}/dx) \hat{x} \Delta t \quad (10)$$

In Eqs. (9) and (10),  $U$  is a fit to Laufer's experimental profile for  $y < y_2$  and a constant for  $y > y_2$  and  $\vec{\omega}$  is the vorticity.

The second fractional step incorporates the pressure head,  $\pi$ :

$$\frac{\vec{v}^{N+1}}{\Delta t} = \frac{\vec{v}^N}{\Delta t} + \frac{1}{3} \Delta T \vec{\nabla} \pi^{N+1} \quad (11)$$

The pressure head is divided into inviscid and viscous parts:

$$\pi^{N+1} = \pi_i^{N+1} + \pi_v^{N+1} \quad (12)$$

The inviscid and viscous parts of the pressure head satisfy the following equations:

$$\Delta t \vec{\nabla}^2 \pi_i^{N+1} = \vec{\nabla} \cdot \frac{\vec{v}^N}{\Delta t} \quad (13)$$

$$\frac{\partial \pi_i}{\partial y} = 0, \quad y = 0 \text{ and } y = \infty \quad (14)$$

$$\vec{\nabla}^2 \pi_v^{N+1} = 0 \quad (15)$$

$$\frac{\partial \pi_v^{N+1}}{\partial y} = \frac{\partial^2 v^{N+1}}{\partial y^2}, \quad y = 0 \quad (16)$$

$$\frac{\partial \pi_v^{N+1}}{\partial y} = 0, \quad y = \infty \quad (17)$$

Finally, the third fractional step accounts for the viscous term:

$$\frac{\vec{v}^{N+1}}{\Delta t} = \frac{\vec{v}^N}{\Delta t} + \frac{2}{3} \Delta t \vec{\nabla}^2 \frac{\vec{v}^N}{\Delta t} \quad (18)$$

The velocity field at time step  $N+1$  appears on the right hand side of Eq. (16). Thus, Eqs. (15-18) must be simultaneously solved, and, for that purpose,  $\pi_v$  is expanded in a set of Green's functions in a manner similar to that described by Marcus (1984).

Pseudospectral methods are used to solve Eqs. (9-18) and each variable  $Q(x,y,z,t)$  is expanded as a spectral sum:

$$Q(x,y,z,t) = \sum_{k_x} \sum_{k_z} \sum_{p=0}^P Q(k_x, k_z, p, t) e^{i(k_x x + k_z z)} T_p(\zeta) \quad (19)$$

where

$$k_x = \frac{\partial \pi}{\partial x} \ell, \quad -L \leq \ell \leq L-1 \quad (20)$$

$$k_z = \frac{\partial \pi}{\partial z} m, \quad -M \leq m \leq M-1 \quad (21)$$

The quantities  $k_x$  and  $k_z$  in Eqs. (19-21) are the wavenumbers in the  $x$  and  $z$  directions, respectively. The quantity  $\zeta$  in Eq. (19) is defined as follows:

$$\zeta = \frac{y-y_m}{y+y_m} \quad (22)$$

The parameter  $y_m$  in Eq. (22) determines the distribution of the collocation points in the  $y$  direction which is given by

$$y_j = y_m \left( \frac{1+\zeta_j}{1-\zeta_j} \right) \quad (23)$$

$$\zeta_j = \cos\left(\frac{\pi j}{P}\right), \quad 0 \leq j \leq P \quad (24)$$

It is also helpful to introduce a mixed representation which is defined as follows:

$$Q(x,y,z,T) = \sum_{k_x} \sum_{k_z} \hat{Q}(k_x, k_z, y, T) e^{i(k_x x + k_z z)}, \quad (25)$$

where  $k_x$  and  $k_z$  are given in Eqs. (20) and (21).

For all the Fourier components of the velocity field except  $\ell=m=0$ , the tau method (see Gottlieb and Orszag (1977)) and the Haidvogel-Zang (1979) factorization are used to solve Eq. (18). However, the constraint on the  $x$ -component of velocity given by Eq. (3) introduces a discontinuity into the derivative of  $\hat{u}(0,0,y,T)$

at  $y = y_1$ , and this would result in poor convergence if spectral methods were used to compute this Fourier component of the velocity field. As a consequence, central difference methods are used to compute the viscous term for the  $l = m = 0$  Fourier component of the velocity field.

In order to compute the nonlinear terms in Eq. (9), the velocity and vorticity fields are evaluated on a grid of points and the cross product,  $\vec{v} \times \vec{\omega}$ , is computed. The grid points are equally spaced in the  $x$  and  $z$  directions and the distribution of grid points in the  $y$  direction is given by Eqs. (23) and (24). The numbers of grid points in the  $x$  and  $z$  periodicity lengths are  $2M$  and  $2N$ , respectively, and the number of grid points in  $y$  is  $2P+1$ . The results to be presented were obtained with 32 grid points in the  $x$  and  $z$  directions and 33 grid points in the  $y$  direction. Based on the steady-state friction velocity, the grid spacings in the  $x$  and  $z$  directions were 18.2 and 7.8 wall units, respectively. The grid spacings in the  $y$  direction varied from 0.067 to 4.9 wall units, respectively.

The results to be presented were obtained with a time step equal to 0.21 wall units. It was found that when the time step was reduced to one half that value, there was virtually no difference in statistical quantities.

Moser, Moin, and Leonard (1983) have shown that aliasing errors in the calculation of the nonlinear terms can lead to qualitatively incorrect behavior in time-dependent problems with marginal resolution, and, for that reason, the two-thirds rule was used to reduce the aliasing errors in the results to be reported.

A variety of different initial conditions was explored and it was found that the statistical results predicted by the model were insensitive to the choice of initial conditions. In the initial condition for the results to be presented, the horizontal average of the  $x$ -component of velocity was set equal to Laufer's experimental profile for  $y < y_2$  and a constant for  $y > y_2$ . The vertical component of velocity and the fluctuating part of the  $x$ -component of velocity were set equal to random numbers multiplied by smooth functions that

guaranteed the correct behavior at the wall. The initial spanwise component of velocity was computed from the incompressibility condition.

The computer program which was used to solve the governing equations was tested by computing the decay rate of Orr-Sommerfeld eigenmodes of a base profile which was equal to Laufer's profile for  $y < 60$  wall units and a constant for  $y > 60$  wall units. When considered as a function of the real part of the wave speed, the magnitude of the imaginary part exhibits a local minimum, and Bark (1975) has shown that the magnitudes of the  $x$ ,  $y$ , and  $z$  components of velocity for these least damped eigenmodes exhibit a  $y$ -dependence which is qualitatively similar to the  $y$ -dependence of the turbulent intensities provided that the wavelengths in the  $x$  and  $z$  directions are comparable to the preferred wavelengths measured by Morrison et al. (1971). Three-dimensional eigenmodes for a wide variety of values of  $k_x$  and  $k_z$  were used to test the program and it was found that, provided  $y_m$  was in the range  $15 \leq y_m \leq 60$  wall units, the program correctly predicted the decay rates to within less than 1%. The results to be reported were obtained with  $y_m$  equal to 30 wall units, based on the initial friction velocity.

## 5. RESULTS

In Figure 1, the horizontally and time averaged  $x$ -component of velocity is compared with Laufer's (1954) experimental profile. The difference between the two profiles in the region  $33.7 < y < 55.3$  wall units is due to the fact that the steady-state wall shear stress is 15% smaller than the initial wall shear stress as explained in chapter 2.

In Figures 2 and 3, the computed intensities of the  $x$ ,  $y$ , and  $z$  components of velocity are compared with Kim et al.'s (1986) direct simulation channel flow results and Laufer's (1954) experimental data. Perry et al. (1985) have argued that hot wire  $x$  probes may yield spuriously low values for the  $y$ -component of velocity in the viscous wall region and this may account for part of the discrepancy between the computed and measured intensities. Perry et al. (1986) have also suggested that the statistics of the viscous

wall may exhibit a mild Reynolds number dependence, and, in that case, the present formulation of the model would appear to be more suitable for low Reynolds numbers since the Reynolds numbers for Kim et al.'s simulations was 3300 while the Reynolds number for Laufer's data was 50000.

In Figure 4, the terms of energy balance are plotted versus distance from the wall. Although there is a significant error in the balance at the edge of viscous wall where the constraint is imposed on the x-component of velocity, the balance is satisfied well through the rest of the viscous wall region.

One of the main motivations for the present study was to develop a model which can correctly yield information about turbulence structure in the viscous wall region. Figure 5 is a plot of the contours of the x-component of velocity for which the x-component of velocity is smaller than the horizontal average of the x-component of velocity. The highly elongated nature of the low speed regions is apparent.

Finally, in Figures 6 and 7 the streamwise and spanwise autocorrelations of the three components of velocity are shown at approximately 5 wall units from the wall. The rapid decay of the v and w autocorrelations as a function of streamwise separation is also seen in the direct simulation results of Kim et al. (1986). The u autocorrelation exhibits a minimum as a function of spanwise separation at approximately 45 wall units, which corresponds to a mean streak spacing equal to 90 wall units. The v autocorrelation exhibits a minimum at approximately 23 wall units. The latter value is very close to the value obtained by Kim et al. who have suggested that it may be interpreted as the diameter of isolated streamwise vortices which are responsible for the streaks.

## 6. CONCLUSION

The model which has been described yields predictions which are in accord with results obtained by direct simulations requiring two orders of magnitude more spatial resolution. The model can be thought of as complementing Deardorff's simulation of the core of a high Reynolds number

channel flow, and it appears possible that one may be able to match the two simulation techniques in a simulation of a high Reynolds number channel flow. We hope to report the results of such an approach in the future.

## REFERENCES

- Bark, F.H. 1975: On the wave structure of the wall region of a turbulent boundary layer. *J. Fluid Mech.* 70, 229-250
- Corino, E.R.; Brodkey, R.S. 1969: A visual investigation of the wall region in turbulent flow. *J. Fluid Mech.* 37, 1-30.
- Deardorff, J.W. 1970: A numerical study of three-dimensional turbulent channel flow at large Reynolds numbers. *J. Fluid Mech.* 41, 453-480.
- Gottlieb, D.; Orszag, S.A. 1977: *Numerical Analysis of Spectral Methods*. Philadelphia: Society for Industrial and Applied Mathematics.
- Haidvogel, D.B.; Zang, T.: The accurate solution of Poisson's Equation by Expansion in Chebyshev Polynomials. *J. Comp. Phys.* 30, 167-180.
- Kim, J.; Moin, P.; Moser, R.D. 1986: Turbulence statistics in fully developed channel flow at low Reynolds number. unpublished paper, NASA Ames Research Center.
- Kline, S.J.; Reynolds, W.C.; Schraub, F.A.; Runstadler, P.W. 1967: The structure of turbulent boundary layers. *J. Fluid Mech.* 30, 741-773.
- Laufer, J. 1950: Investigation of turbulent flow in a two-dimensional channel. *NACA T.N.* 2123, 1-67.
- Laufer, J. 1954: The structure of turbulence in fully developed pipe flow. *NACA Report* 1174, 417-434.
- Marcus, P.S. 1984: Simulation of Taylor-Couette flow. Part 1. Numerical methods and comparison with experiment. *J. Fluid Mech.* 146, 45-64.
- Morrison, W.R.B.; Bullock, K.J.; Kronauer, R.E. 1971: Experimental evidence of waves in the sublayer. *J. Fluid Mech.* 47, 639-656.
- Moser, R.D.; Moin, P. 1984: Direct numerical simulation of curved turbulent channel flow. *NASA T.M.* 85974.
- Moser, R.D.; Moin, P.; Leonard, A. 1983: A spectral numerical method for the Navier-Stokes equations with applications to Taylor-Couette flow. *J. Comp. Phys.* 52, 524-544.
- Orszag, S.A.; Kells, L.C. 1980: Transition to turbulence in plane Poiseuille and plane Couette flow. *J. Fluid Mech.* 96, 159-205.
- Orszag, S.A.; Yakhat, V. 1986: Reynolds number scaling of cellular-automaton hydrodynamics. *Phys. Rev. Lett.* 56, 1691-1693.
- Perry, A.E.; Henbest, S.; Chong, M.S. 1986: A theoretical and experimental study of wall turbulence. *J. Fluid Mech.* 165, 163-199.

Perry, A.E.; Lim, K.L.; Henbest, S.M. 1985: A spectral analysis of smooth flat-plate boundary layers. Fifth Symposium on Turbulent Shear Flows, Cornell University, 9.29-9.34.

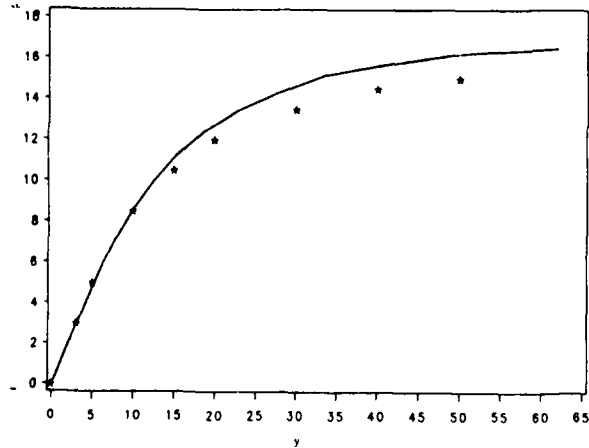


Figure 1. Horizontal and time average of computed  $u$  (—) compared to Laufer's (1954) experimental results ( $\star$ ).

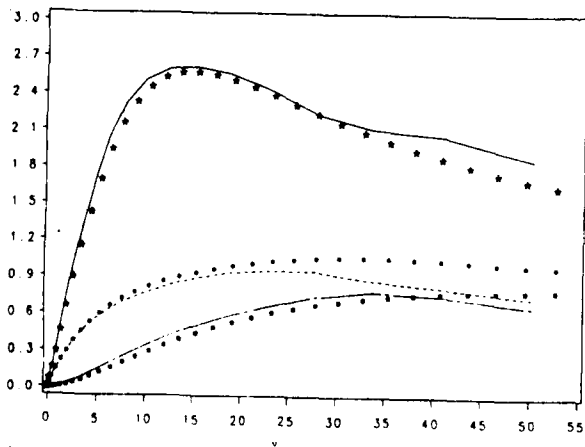


Figure 2. Computed intensities of  $u$  (—),  $v$  (---), and  $w$  (···) compared to Kim et al.'s (1986) experimental results for  $u$  ( $\star$ ),  $v$  ( $\blacksquare$ ), and  $w$  ( $\bullet$ ).

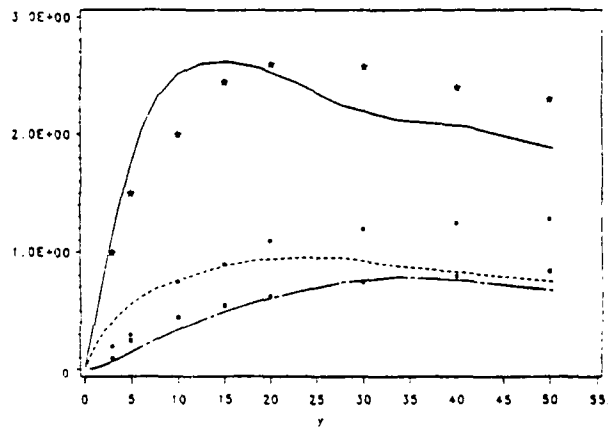


Figure 3. Computed intensities of  $u$  (—),  $v$  (---), and  $w$  (···) compared to Laufer's (1954) experimental results for  $u$  ( $\star$ ),  $v$  ( $\blacksquare$ ), and  $w$  ( $\bullet$ ).

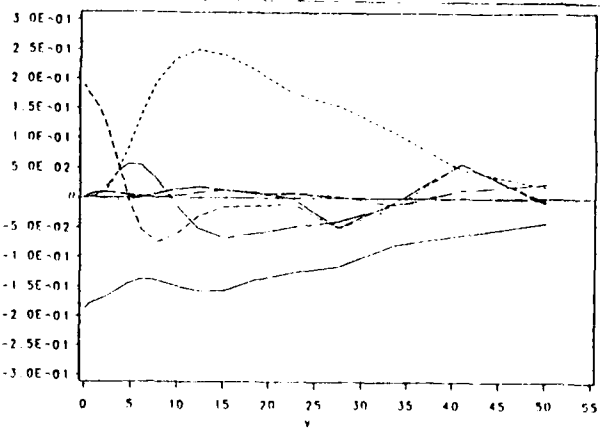


Figure 4. Energy balance: production (···), dissipation (—), kinetic energy diffusion (---), pressure diffusion (— · —), viscous diffusion (— — —), net (— · — · —).

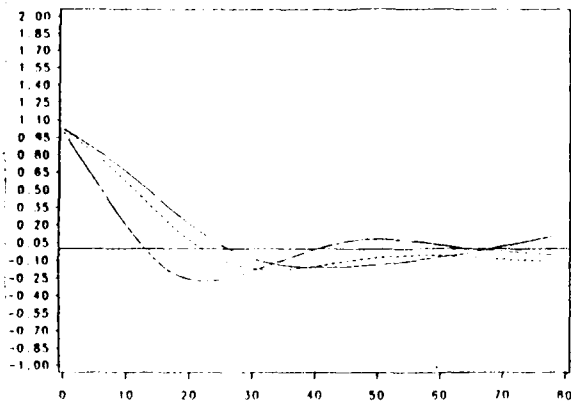
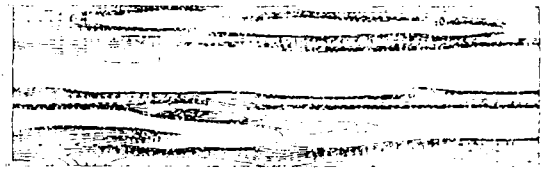


Figure 5. Spanwise correlation functions of u (—), v (---), and w(---).



2.00 1.75 1.50 1.25 1.00  
0.75 0.50 0.25 0.00

Figure 7. Negative contours of the fluctuating part of the x-component of velocity for  $y=5.9$  wall units.

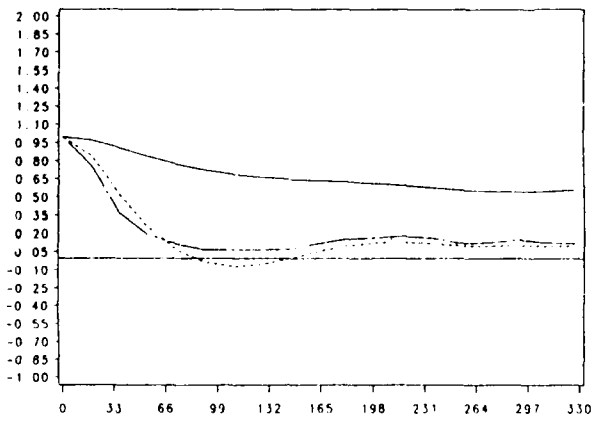


Figure 6. Streamwise correlation functions of u (—), v (---), and w (---).

# NUMERICAL STUDY OF THE MEAN STATIC PRESSURE FIELD OF AN AXISYMMETRIC FREE JET\*

F.F. Grinstein†, E.S. Oran, J.P. Boris, and A.K.M.F. Hussain‡  
Laboratory for Computational Physics  
U.S. Naval Research Laboratory  
Washington, D.C. 20375

## ABSTRACT

We present numerical simulations of the evolution of the Kelvin-Helmholtz instability in a spatially evolving two-dimensional shear layer. The results of these simulations are used to study the transitional region of a subsonic, compressible, axisymmetric free jet, at very high Reynolds number, and to calculate pressures and momentum fluxes based on the primitive flow variables. The results indicate that the mean static pressure drops significantly within the jet accounting for growth in the streamwise momentum flux. This supports the experimental results of Hussain and Clark (1976). The sensitivity of the results to unsteady initial conditions is investigated.

## 1. INTRODUCTION

Traditionally, it is assumed that the mean static pressure gradients in a free jet are everywhere negligibly small compared to other mean forces on the fluid. Thus, the pressure in a jet is considered to be virtually constant and equal to the ambient pressure (Abramovich, 1963). As a consequence, the mean longitudinal momentum flux is a constant at each axial location moving streamwise from the nozzle. Hussain and Clark (1976) measured the momentum flux in a planar jet with hot wires and found that it increases in the streamwise direction, and that the extent of the increase depends on the initial conditions. They also noted that the pressure can drop considerably within the turbulent regions of a free jet. Although Hussain and Clark also measured decreases in the static pressure that were consistent with the observed increases in the momentum flux, a total quantitative balance between the pressure and momentum changes could not be obtained. They noted that that they did not expect perfect balance because of the large uncertainties in both velocity and pressure measurements at the high turbulence levels. The extent of the momentum flux increase and its dependence on the initial conditions remain unresolved; this is because the

---

\* Presented at the Tenth Symposium on Turbulence, University of Missouri-Rolla, September 22-24, 1986

† Berkeley Research Associates, Springfield, VA

‡ Department of Mechanical Engineering, University of Houston

measurement uncertainties cannot be evaluated experimentally, but can perhaps be determined accurately via numerical simulation. In this paper we analyze numerical simulations of jet flows to help clarify these apparent inconsistencies.

Numerical investigations of shear flows have used spectral (Metcalfe et al., 1986), vortex dynamics (Ghoniem, 1986), and finite-difference (Corcos and Sherman, 1984; Davis and Moore, 1985; Grinstein et al., 1985, 1986ab; Kailasanath et al., 1986) techniques. Numerical studies of the evolution of flows similar to those seen in the laboratory experiments have been considered for both two-dimensional planar and axisymmetric shear layers. Previous finite-difference calculations have modeled either temporally-developing mixing layers (Corcos and Sherman, 1984), where it is assumed that the vortex dynamics takes place in a relatively compact region of space, or spatially developing layers (Davis and Moore, 1985; Grinstein et al., 1985, 1986ab, Kailasanath et al., 1986), which correspond more closely to the laboratory experiments.

Recent numerical simulations of unforced, subsonic, compressible, spatially-evolving two-dimensional shear layers have produced new information about mixing in shear layers and the development of this two-dimensional unstable flow (Grinstein et al., 1985, 1986ab). A number of important features of the flow field in the transitional region were noted in these calculations. The mixing layer composition was observed to be asymmetric, containing more of the faster fluid (Grinstein et al., 1986a), in qualitative agreement with experimental results (Koochesfahani et al., 1985). The calculated distribution of merging locations was in good agreement with the distributions obtained with weakly excited planar (Ho and Huang, 1982) and axisymmetric (Kibens, 1980) shear layers. In addition, evidence of spatial and temporal coherence observed between the first few roll-ups (Grinstein et al., 1986b), suggested the presence of an underlying degree of organization in the unforced two-dimensional shear layers due to downstream feedback on the inflowing fluid.

In this paper we present numerical simulations of the evolution of the Kelvin-Helmholtz instability in a spatially-evolving two dimensional shear layer. The results of these simulations are used to study the transitional region of a subsonic, compressible, axisymmetric free jet and to calculate pressures and momentum fluxes based on the primitive flow variables. The results indicate that the mean static pressure drops significantly within the jet which accounts for the growth in the streamwise momentum flux. This supports the experimental results of Hussain and Clark (1976). The sensitivity of the results to unsteady initial conditions is also investigated.

## 2. THE AXISYMMETRIC JET

The system studied is an air high-speed free jet emerging into a quiescent air background. A schematic diagram of the flow configuration is given in Fig. 1. The jet is initialized with a top-hat axial velocity profile and uniform standard temperature and pressure everywhere. The jet is subsonic, with Mach number  $M=0.57$ , and corresponding free stream velocity  $U_o = 2.0 \times 10^4$  cm/s. The calculation is fully compressible, sound waves are resolved and acoustic delay times for pressure waves are properly included. Excitation has been extensively used in the investigation of the basic mechanisms of shear flows (Crow and Champagne, 1971; Ho and Huang, 1982; Hussain et al., 1986). Excitation of the jet at the inflow is provided here by imposing a sinusoidal perturbation of fixed frequency  $f_1$  and relative amplitude  $a_1$  on the free stream inflow velocity  $U_o$ , i.e.,

$$U_o \rightarrow U_o \times [1 + a_1 \sin(2\pi f_1 t)]. \quad (1)$$

In this way we simulate a controllable planar excitation of the jet stream at the nozzle exit. In the laboratory experiments this forcing is usually introduced acoustically by means of speakers in settling chambers upstream of the nozzle exit (e.g., Zaman and Hussain, 1980). In addition, we can simulate the effects of fluctuations in the experimental flows due to turbulence and boundary layers in the nozzle by superposing random inflow perturbations of the axial velocity (Grinstein et al., 1986b).

## 3. THE NUMERICAL MODEL

The numerical model used to perform the simulations solves the two-dimensional time-dependent conservation equations for mass, momentum and energy for an ideal gas

$$\frac{\partial \rho}{\partial t} = -\nabla \cdot \rho \mathbf{V}, \quad (2)$$

$$\frac{\partial(\rho \mathbf{V})}{\partial t} = -\nabla \cdot \rho \mathbf{V} \mathbf{V} - \nabla P, \quad (3)$$

$$\frac{\partial \epsilon}{\partial t} = -\nabla \cdot \epsilon \mathbf{V} - \nabla \cdot P \mathbf{V}, \quad (4)$$

where  $\epsilon = P/(\gamma - 1) + (1/2)\rho V^2$ , is the internal energy, and  $\mathbf{V}$ ,  $P$ ,  $\rho$ , and  $\gamma$ , are the velocity, pressure, mass density, and the ratio of specific heats. The equations are solved using the Flux-Corrected Transport (FCT) algorithm (Boris and Book, 1976) and timestep-splitting techniques. FCT is a nonlinear, explicit, fourth-order, compressible finite-difference algorithm which ensures

that all conserved quantities remain monotonic and positive. It accomplishes this through a two-step process. First it modifies the linear properties of a high-order algorithm by adding diffusion during convective transport to prevent dispersive ripples from arising. The added diffusion is then subtracted out in an anti-diffusion phase of the integration cycle. These processes maintain high-order accuracy without artificial viscosity to stabilize the algorithm. No subgrid turbulence has been included at this stage beyond the natural FCT filtering. The nonlinear properties of the FCT algorithm ensure that energy in wavelengths smaller than a few computational cells is dissipated. In this way, the algorithm mimics the behavior of physical viscosity at high Reynolds numbers.

In the case of initially laminar flows with very large Reynolds numbers, the shear stresses and dissipation terms are significant only in very thin layers of the flow on the surface of the nozzle and across the shear layers that separate the jet stream from the surroundings. For this type of flow, the vorticity contribution from the boundary layers is much smaller than that due to the shear layers, and a purely inviscid description of the large scale features of the gas phase flow such as provided by the present model can be expected to be adequate.

Inflow and outflow boundary conditions are needed to ensure the proper behavior of the fluids near the boundaries and throughout computational domain. However, accurate transparent boundary conditions that provide adequate information about the region outside of the computational domain are very difficult to define for the numerical simulation of compressible subsonic flows. Most of the simulations performed until fairly recently involved temporally developing shear layers. Such simulations replace inflow and outflow conditions with periodic boundary conditions, and concentrate on the vorticity dynamics in compact regions. A detailed simulation that investigates spatially developing flows requires a model for inflow and outflow boundary conditions.

The calculations presented below use inflow and outflow boundary conditions which have been developed and tested for multidimensional FCT calculations (Boris et al., 1985, Grinstein et al., 1986a) The density and inflow velocity of the jet are specified and the energy at the inflow guard cells is determined from a zero-slope condition on the pressure:

$$\rho_g = \rho_{\text{inflow}}, \quad (5a)$$

$$v_g = v_{\text{inflow}}, \quad (5b)$$

$$P_g = P_1, \quad (5c)$$

where  $P_1$  is the pressure at the first inflow cell. This allows the pressure at the inflow to vary in response to disturbances originated by the fluid accelerations downstream. Equation (5c) requires the acoustic waves to reflect at the inflow, which is physically reasonable because the density and velocity at the inflow are fixed. To make a smoother and more realistic transition to the region of interest behind the lip of the nozzle, we have included a portion of the nozzle inside the computational domain. The conditions allow feedback to occur between the fluid accelerations downstream and the inflowing material, thus allowing the instability to evolve naturally in the calculation.

The conditions at the outflow guard cells define the density and velocity through zeroth- and first-order extrapolations, respectively, from the last two cells:

$$\rho_g = \rho_n, \quad (6a)$$

$$v_g = 2v_n - v_{n-1}. \quad (6b)$$

These are standard conditions consistent with fixing the inflow velocity of the jet. The energy at the guard cells is defined in terms of the density and velocity given by (6a-b) and the pressure defined by

$$P_g = P_n + \frac{(Y_g - Y_n)}{(Y_g - Y_j)}(P_{amb} - P_n), \quad (6c)$$

where  $Y$  is either the radial or axial coordinate, and the subscript  $j$  refers to the trailing edge of the nozzle. Equation 6c is the result of interpolating between the pressure values at the boundary,  $P_n$ , and at infinity,  $P_{amb}$ . It enforces a trend in which the pressure gradient vanishes and the pressure equals  $P_{amb}$  at infinite distances from the nozzle. The slow relaxation of the pressure towards the known ambient value is necessary because the pressure at the inflow is not specified, but calculated from other variables. By giving a reference pressure value we avoid secular errors in the calculations.

The computational grid is set up initially and held fixed in time. The timesteps are chosen by requiring the Courant number to be about 0.4. The finite-difference grids have 100-126 cells in the cross-stream (radial) direction and 220-382 in the streamwise (axial) direction. The mesh spacings vary in the ranges  $0.05 \leq \Delta Z \leq 0.52$  cm and  $0.02 \leq \Delta R \leq 0.67$  cm for the coarser grids, and in the ranges  $0.03 \leq \Delta Z \leq 0.29$  cm and  $0.01 \leq \Delta R \leq 0.67$  cm for the finer grids. Using the finer grids is expensive, so they are used only sparingly to check the stability of the results of the numerical calculations.

The effects due to boundary layers in the nozzle have not been included in our calculations. Thus the initial thickness of the shear layer  $\theta_o$  is effectively equal to the thickness of the rim of the nozzle in the simulations, i.e., one cell across the shear layer. We define the Strouhal number,  $St_{\theta_o} = f\theta_o/U_o$ , associated with the natural instability frequency of the shear layer. Then using a typical longitudinal phase velocity  $u_p = f\lambda \approx 0.6U_o$ , we can estimate  $\theta_o/\lambda \approx St/0.6$ . For  $St$  in the range 0.0125 - 0.0155 (Husain and Hussain, 1983) one wavelength ( $\lambda$ ) of the natural oscillation of the shear layer ahead of the nozzle exit is resolved with 39 - 48 cells in the cross-stream direction and 16 - 19 in the streamwise direction. Thus the spatial-evolution of the large scale features of the shear layer can be adequately resolved by the gridding in the numerical model.

Figure 2 shows a schematic diagram of a typical grid used in the calculations. The cells are closely spaced in the radial ( $R$ ) direction across the shear layer, where the large structures form, and they become farther apart as the distance from the shear layer increases for  $R > R_o$ . The cell separations in the streamwise direction ( $Z$ ) also increase in size as we move away from the trailing edge of the nozzle, located at  $R_o = 0.7$  cm and  $Z = Z_o \approx 1.67$  cm. The cell spacing chosen takes advantage of the fact that the structures merge and grow downstream, so that fewer cells are necessary to keep the resolution effectively the same as that near the nozzle.

## 4. RESULTS AND DISCUSSION

### 4.1 The Unexcited Jet

The instabilities were triggered at the beginning of the calculation by a small (order 0.1%) transient pressure pulse at the shear layer, just ahead of the nozzle edge (Grinstein et al., 1985, 1986ab). This is closely analogous to exciting the jet with a weak, spark-produced N-wave perturbation as in the experimental studies by Heavens (1980).

Figure 3 shows typical instantaneous contours of static pressure and vorticity, which are calculated using the information given by the primitive flow variables. Local minima of the static pressure occur where the vorticity rolls up. At those locations, the pressure drops up to 22% below ambient, in contrast with pressure increases of up to 8% that occur between the roll-ups and within the potential core of the jet. Vortex rings first develop at an essentially fixed distance  $Z \approx 0.4D$ , where  $D$  is the diameter of the jet. The newly formed structures move along the interface, interact with each other and thereby spread the vorticity until the central, potential core region disappears, at approximately  $Z = 5D$ .

Figure 4a shows contours of the time-averaged axial velocity  $U/U_o$ . The radial variation of the longitudinal turbulence intensity,  $\langle u^2 \rangle^{1/2}/U_o$ , is shown in Figure 4b as a function of  $(R - R_o)/\theta$ . Here,  $\theta = (R_{0.1} - R_{0.9})$  is the local width of the shear layer, with  $R_x$  defined for a given  $Z$  as the radial location at which  $U = xU_o$ . Figures 4a and 4b show the approximately linear growth of the mixing layers in the axial direction. Figure 4c shows the spectra of the axial velocity fluctuations at  $R/D = 0.5$ , centerline of the shear layer, and at  $Z = 0.4D$ , the streamwise location where the first roll-up takes place, as a function of the Strouhal number  $St_\theta$ . The spectra in Fig. 4c shows a main peak at  $St_\theta = 0.015$ . This corresponds to the natural instability frequency of the shear layer.

Figure 5 shows the result of time-averaging the static pressure and the vorticity. The mean static pressure is generally below ambient in the mixing layers and above ambient in the potential core of the jet. The mean static pressure varies within 2% of ambient pressure. Local minima of the static pressure are found at  $z = 1.7 D$ , in the neighborhood of the first merging location, and at  $z = 3.7 D$ , in the region where the second merging takes place near the end of the potential core (see Fig. 3). The mean vorticity is concentrated in the region of vortex shedding from where it spreads following the approximate linear growth of the shear layer.

#### 4.2 The Excited Jet

Excitation is imposed by means of a controlled perturbation introduced at the inflow according to Eq. 1. Figures 6-8 show the effect of such perturbations on the jet flow. Although the excitation level in the calculations,  $a_1$ , was varied in the range 0.01 - 0.1, only the results of low level (1%) excitation are reported below. Figure 6 shows the longitudinal turbulence intensity at the centerline of the jet as a function of streamwise distance  $z/D$ , for excitation frequencies  $f_1$  defined by  $St_D = f_1 D/U_o = 0.35, 0.85$ , and by  $St_\theta$  (corresponding to  $St_D = 1.05$ ). These frequencies are associated with characteristic excitation modes of the axisymmetric jet, namely to the jet preferred mode, the stable jet column pairing mode, and the shear layer instability mode (Zaman and Hussain, 1980, 1981ab). Figures 7 and 8 show the effect of changing the excitation frequency on the mean static pressure and streamwise velocity profiles.

Controlled excitation of the jet affects the scale of the structures that roll up in the near field of the jet. As a consequence, excitation modifies the turbulence intensity level at the shear layers. For the purpose of our discussion, excitation at  $St_D = 0.35$  and at  $St_\theta$  represent two extremes. For excitation at  $St_D=0.35$ , roll-up at the preferred jet mode frequency is favored. This is indicated by

the hump of the longitudinal turbulence intensity between  $1-2D$  in Fig. 6, by the local minimum in the contours of mean static pressure in Fig. 7b, and by the widening of the mean velocity profiles in Fig. 8b, at those same streamwise locations. This is the natural mode of the jet, associated with the largest characteristic scale present in the flow. As can be seen by comparison of Figs. 8b and 8a, excitation of these large scales causes the shear layers to grow faster so that the potential core length becomes shorter. The largest decrease in the mean static pressure at the shear layer is 3.3%, compared to an increase of about 2.4% in the centerline of the jet. This shows the largest growth among all of the excited cases considered.

Excitation at  $St_{\theta_0}$  eliminates the formation of energetic large scale structures downstream. These structures tend to form further downstream where the flow becomes independent of the initial conditions. As a consequence the streamwise extent of the potential core becomes larger, as can be seen by comparing Figs. 8c and 8a. The resulting turbulence suppression can also be observed in the longitudinal turbulence intensity curve in Fig. 6. Excitation at  $St_D = 0.85$  enhances the turbulence production almost everywhere, as indicated in Fig. 6, and the length of the potential core is somewhat shortened. The streamwise stretching of the minimum of the mean static pressure between  $2.5$  and  $5D$  in Fig. 8d suggests the streamwise interval of stable vortex pairing observed with this type of excitation in the experiments by Zaman and Hussain (1980). As in the unexcited case, the mean static pressure varies within 2% of ambient pressure for the latter two cases.

#### 4.3 The Streamwise Momentum Flux

We need an expression for the mean streamwise momentum flux as a function of streamwise direction that we can obtain from the primitive variables we calculate. We can obtain this by: 1) integrating Eq. 3 in the  $R$ -direction (with the boundary condition  $\mathbf{V} = 0$  for  $R \rightarrow \infty$ ), and 2) time averaging the resulting expression. The result of this process is

$$\int_0^{\infty} \rho [U^2 + \langle u^2 \rangle + \langle P \rangle] R dR = constant. \quad (7)$$

From Eq. 7 it follows that the isobaric jet flow hypothesis implies that the streamwise momentum flux is constant. However, Eq. 7 states that it is consistent with conservation of momentum to have an increase in the average momentum flux as long as it is balanced by appropriate decreases in the mean static pressure. Measurements of such pressure decreases, have been reported in the literature by Miller and Comings (1957), Bradbury (1965), Sami et al (1967), Sunyach and

Mathiew (1969), Maestrello and McDaid (1971) and by Hussain and Clark (1976). Variation of the streamwise momentum in the case of planar jets was first reported by Hussain and Clark (1976). The authors found that the extent of increase in momentum flux depended on the initial conditions and they were able to measure consistent decreases in the static pressure. However, due to the high turbulence levels, they could not determine a total quantitative balance between the changes because of the large uncertainties in both velocity and pressure measurements.

We define the streamwise components of the total average momentum flux  $\mathcal{M}_T(Z)$ , mean momentum flux  $\mathcal{M}(Z)$ , and the pressure integral  $\mathcal{P}(Z)$ , as follows

$$\mathcal{M}_T(Z) = \int_0^\infty \rho(R, Z) \left( U(R, Z)^2 + \langle u(R, Z)^2 \rangle \right) R dR, \quad (8)$$

$$\mathcal{M}(Z) = \int_0^\infty \rho(R, Z) U^2(R, Z) R dr, \quad (9)$$

$$\mathcal{P}(Z) = \int_0^\infty \langle P(R, Z) \rangle R dR. \quad (10)$$

Equation 7 can be rewritten in terms of these quantities, using the values at the nozzle exit as reference,

$$\frac{\mathcal{M}_T(Z) - \mathcal{M}_T(Z_0)}{\mathcal{M}_T(Z_0)} + \frac{\mathcal{P}(Z) - \mathcal{P}(Z_0)}{\mathcal{M}_T(Z_0)} = 0. \quad (11)$$

Figure 9a compares the two terms of Eq. 11 along the first five diameters downstream from the nozzle in the case of the unexcited jet. The momentum flux increases up to 9% relative to its value at the nozzle exit and exactly balances the decrease in the pressure integral. Thus the low pressure regions in the shear layer are directly associated with the increase in momentum flux. Comparing Figs. 9a and 3, we see that vortex rings roll up at the locations  $z_1, z_2$ , and  $z_3$ , and at these locations the static pressure has local minima. The location  $z_4$  corresponds to the approximate location of the end of the potential core. Three-dimensional effects not considered in the simulations are important beyond  $z_4$ , so that any discussions of structures beyond this point are questionable physically.

A comparison of the streamwise growth of the total momentum flux and the mean momentum flux is presented in Fig. 9b. Since the mean momentum flux decreases relative to its value at the

nozzle exit, the increase in the total momentum flux is here largely due to the longitudinal turbulent contribution  $\mathcal{M}_T(Z) - \mathcal{M}(Z)$ .

Figure 10 compares the streamwise momentum flux variation along the first five diameters with typical data reported by Hussain and Clark (1976) for the first five nozzle widths of a planar jet, and with results calculated by these authors using the data of Crow and Champagne (1971) for a circular jet. The figure shows a reasonable agreement between the results corresponding to the higher jet velocities, in spite of the broad differences between the jets involved.

The effect of unsteady initial conditions on the variation of the streamwise momentum flux is shown in Figure 11. The variations of the streamwise momentum flux are closely related to those of the mean static pressure and the longitudinal turbulence intensity, and thus they are strongly dependent on the nature of the excitation. In particular, there is a clear correspondence between the maxima in streamwise momentum flux and the minima in the profiles of mean static pressure in Fig. 7. Thus the discussion of Fig. 7 in Sec. 4.2 is also relevant here.

In all of the excited cases there is an increase of  $\mathcal{M}_T(Z)$  for  $Z$  between 1 and  $2D$  associated with the increased turbulence production near the nozzle. The greatest growth corresponds to excitation at the frequency of the preferred jet mode  $St_D=0.35$ , as shown in Fig. 11b. As the excitation frequency is increased to  $St_D=0.85$  (Fig. 11d), the total momentum flux increase becomes less pronounced between 1 and  $2D$  and enhanced further on downstream, especially in the region of the local minima in mean static pressure.

As mentioned earlier, an effect of excitation at  $St_{\theta_0}$  is to inhibit the formation of the larger scales in the near field of the jet. This mainly involves the suppression of the structures that roll up with the second subharmonic of  $St_{\theta_0}$  near the end of the potential core. This suppression is clearly noted in Fig. 11c for  $Z$  between 2 and  $4D$ , and tends to fade as we move further downstream, where the influence of the excitation is progressively reduced. The lengthening of the potential core is apparent in this case by noting the slower decrease in the mean momentum flux  $\mathcal{M}(Z)$ .

## 5. CONCLUSIONS

We have presented results from finite difference numerical simulations of the transitional region of a subsonic, compressible axisymmetric jet at very high Reynolds number. The following conclusions may be drawn from the results of this work.

- 1) The static pressure may vary significantly within a compressible jet relative to that of the surroundings. It decreases at the shear layers and increases in the potential core. Instantaneous

pressure drops of the order of 20% were observed at the locations where the vortex rings roll up, in contrast with pressure increases of order 8% elsewhere in the jet. The mean static pressure variations ranged between 2% for the unexcited jet to up to 3.3% for the jet excited at the jet preferred mode frequency  $St_D=0.35$ .

2) The total momentum flux increases in the transitional region of the jet up to a maximum value in the range 9 - 11 %, depending on the initial conditions. Following momentum conservation, the increases are exactly balanced by decreases in mean static pressure and agree very reasonably with experimental results. The increases in total momentum flux are mainly due to the longitudinal turbulence intensity.

#### ACKNOWLEDGEMENTS

This work was performed under Office of Naval Research project #RR024-03-01 and Naval Research Laboratory project #RR011-09-43.

#### REFERENCES

- Abramovich, G.N., *The Theory of Turbulent Jets*, MIT press (1963)
- Bradbury, L.J.S., *The Structure of a Self-Preserving Turbulent Plane Jet*, *J. Fluid Mech.* **23**, 31 (1965).
- Boris, J.P. & Book, D.L., in *Methods in Computational Physics*, Vol. 16, pp. 85-129, Academic Press, New York (1976).
- Boris, J.P., Oran, E.S., Gardner, J.H., Grinstein, F.F. & Oswald, C.E., in *Ninth International Conference on Numerical Methods in Fluid Dynamics*, ed. by Soubbaramayer and J.P. Boujot, pp. 98-102, Springer Verlag, New York (1985).
- Corcus, G. M. and Sherman, F. S., *J. Fluid Mech.* **139**, 29 (1984).
- Crow, S.C. and Champagne, F.H., *Orderly Structure in Jet Turbulence*, *J. Fluid Mech.* **48**, 547 (1971).
- Davis, R. W. and Moore, E. F., *A Numerical Study of Vortex Merging in Mixing Layers*, *Phys. Fluids* **28**, 1626 (1985).
- Ghoniem, A.F. and Ng, K.K., *Effect of Harmonic Modulation on Rates of Entrainment in a Confined Shear Layer*, *AIAA paper 86-0056* (1986), Reno.
- Grinstein, F.F., Oran, E.S. & Boris, J.P., *Numerical Simulation of Asymmetric Mixing in Planar Shear Flows*, *J. Fluid Mech.* **165**, 201 (1986a).
- Grinstein, F.F., Oran, E.S. & Boris, J.P., *Numerical Simulations of Unforced Spatially-Developing Mixing Layers*, submitted to *J. Fluid Mech.* (1985).
- Grinstein, F.F., Oran, E.S. & Boris, J.P., *Direct Numerical Simulations of Axisymmetric Jets*, *AIAA paper 86-0039*, Reno, to appear in *AIAA J.* (1986b).
- Heavens, S.N., *Visualization of the Acoustic Excitation of a Subsonic Jet*, *J. Fluid Mech.* **100**, 185 (1980).
- Ho C.M. and Huang L.S., *Subharmonics and Vortex Merging in Mixing Layers*, *J. Fluid Mech.* **119**, 443 (1982).

- Hussain A.K.M.F. and Clark A.R., Upstream Influence on the Near Field of a Plane Turbulent Jet, *Phys. Fluids* **20**, 1416 (1976).
- Hussain, A.K.M.F., Husain, H.S., Zaman, K.B.M.Q., Tso, J., Hayakawa, M., Takaki, R., and Hasan, M.A.Z., Free Shear Flows: Organized Structures and Effects of Excitation, *AIAA* paper 86-0235, Reno (1986).
- Kailasanath, K., Gardner, J., Boris, J., and Oran, E., Interactions Between Acoustics and Vortex Structures in a Central Dump Combustor, *AIAA* paper 86-1609, Huntsville, to appear in *AIAA J. Prop. Power* (1986).
- Kibens, V., Discrete Noise Spectrum Generated by an Acoustically Excited Jet, *AIAA J.* **18**, 434 (1979).
- Maestrello, L. and McDaid, E., *AIAA J.* **9**, 1058 (1971).
- Miller, D.R. and Comings, E.W., Static Pressure Distribution in the Free Turbulent Jet, *J. Fluid Mech.* **3**, 1 (1957).
- Metcalf, R. W., Orszag, S.A., Brachet, M.E., Menon, S., and Riley, J.J, Secondary Instability of a Temporally Growing Mixing Layer, to appear in *J. Fluid Mech.* (1986).
- Sami, S., Carmody, T., and Rouse, H., *J. Fluid Mech.* **27**, 231 (1967).
- Sunyach, M. and Mathiew, J., *J. Heat Mass Transfer* **12**, 1679 (1969).
- Zaman, K.B.M.Q., and Hussain, A.K.M.F., Vortex Pairing in a Circular Jet Under Controlled Excitation. Part 1. General Jet Response, *J. Fluid Mech.* **101**, 449 (1980).
- Zaman, K.B.M.Q., and Hussain, A.K.M.F., Turbulence Suppression in Free Shear Flows by Controlled Excitation, *J. Fluid Mech.* **103**, 133 (1981a).
- Zaman, K.B.M.Q., and Hussain, A.K.M.F., The 'Preferred Mode' of the Axisymmetric Jet *J. Fluid Mech.* **110**, 39 (1981b).

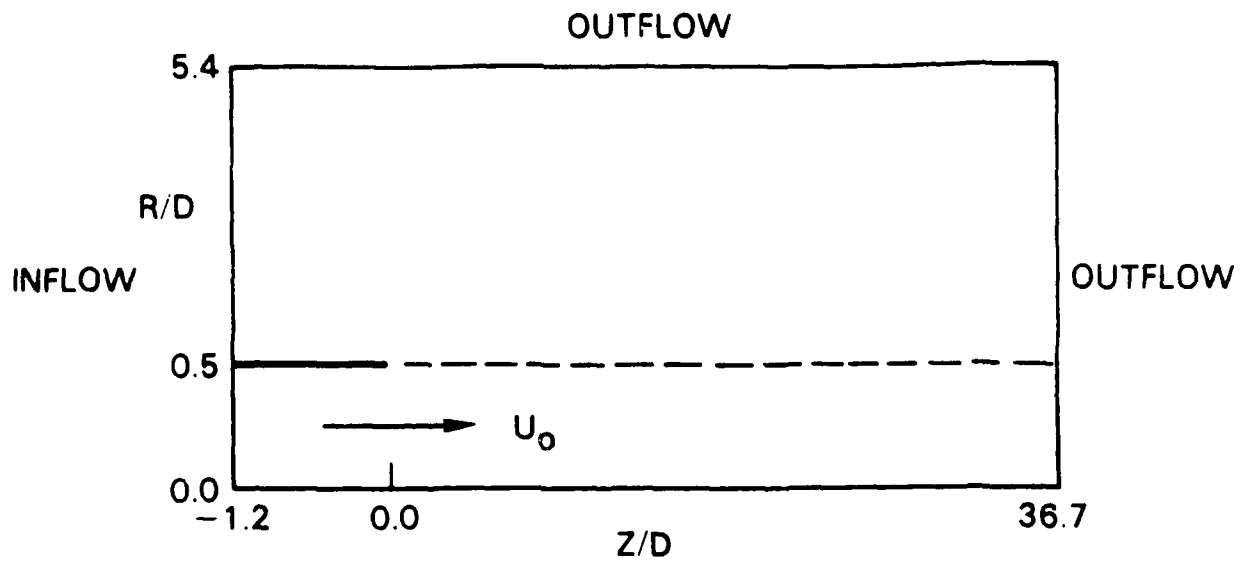


Figure 1 - Flow configuration

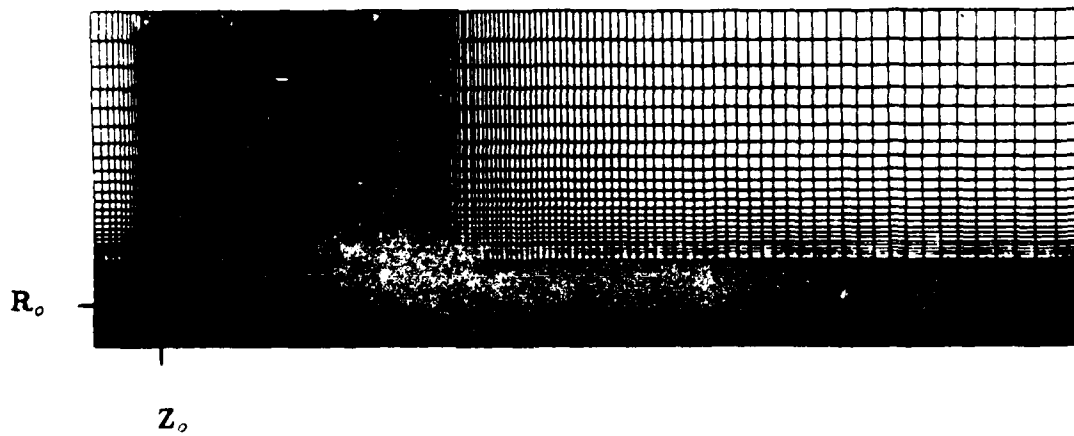


Figure 2- Typical grid used in the calculations

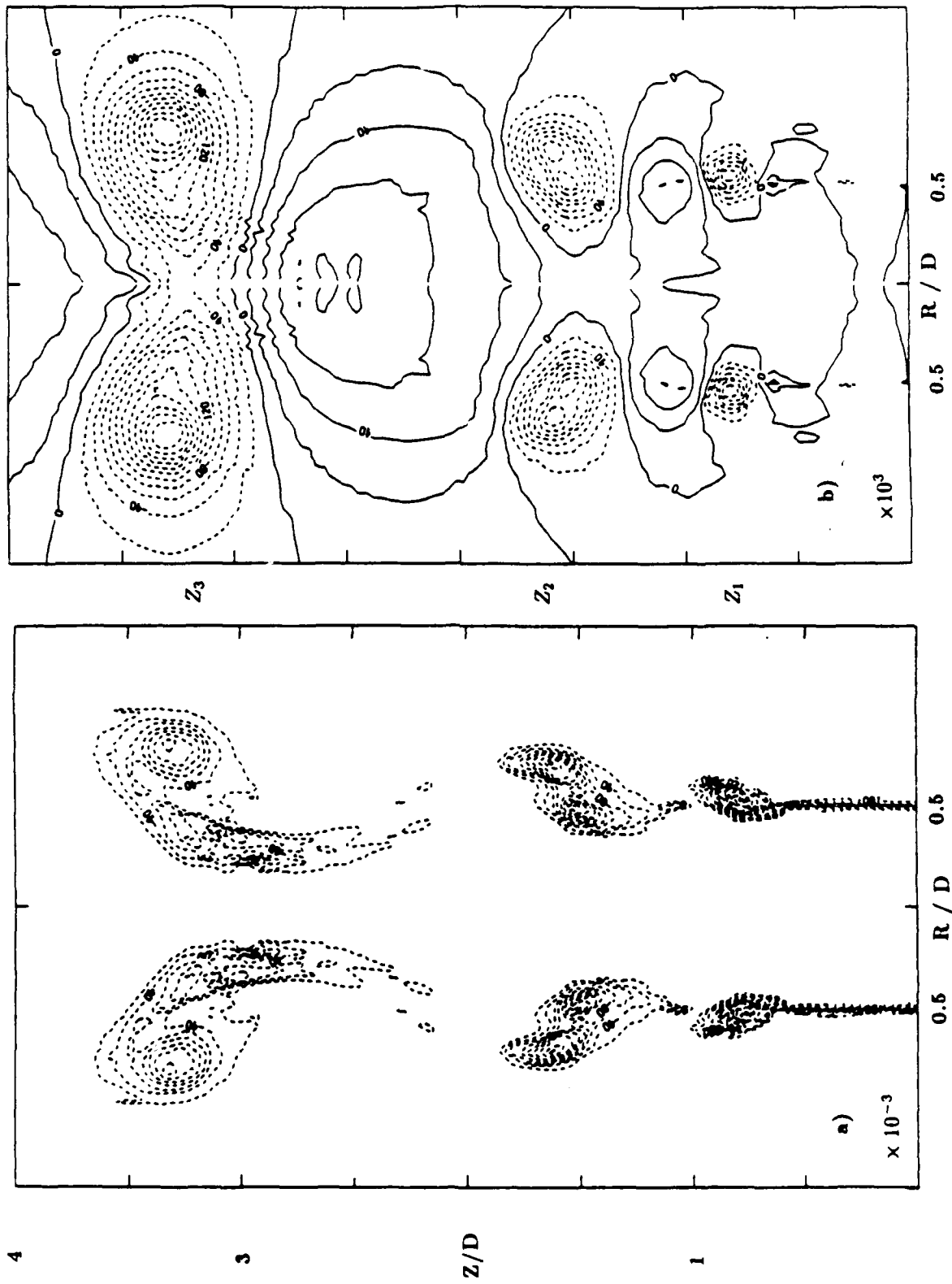


Figure 3 - Instantaneous flow visualization. a) Eddy vorticity contours. The minimum value is  $-4.8 \times 10^5 \text{ s}^{-1}$  increasing to  $-2 \times 10^4 \text{ s}^{-1}$  with an interval of  $2 \times 10^4 \text{ s}^{-1}$ ; b) relative static pressure difference,  $(P - P_{inlet})/P_{inlet} \times 10^3$ , ---  $(P - P_{inlet}) > 0$ , - - -  $(P - P_{inlet}) < 0$ .

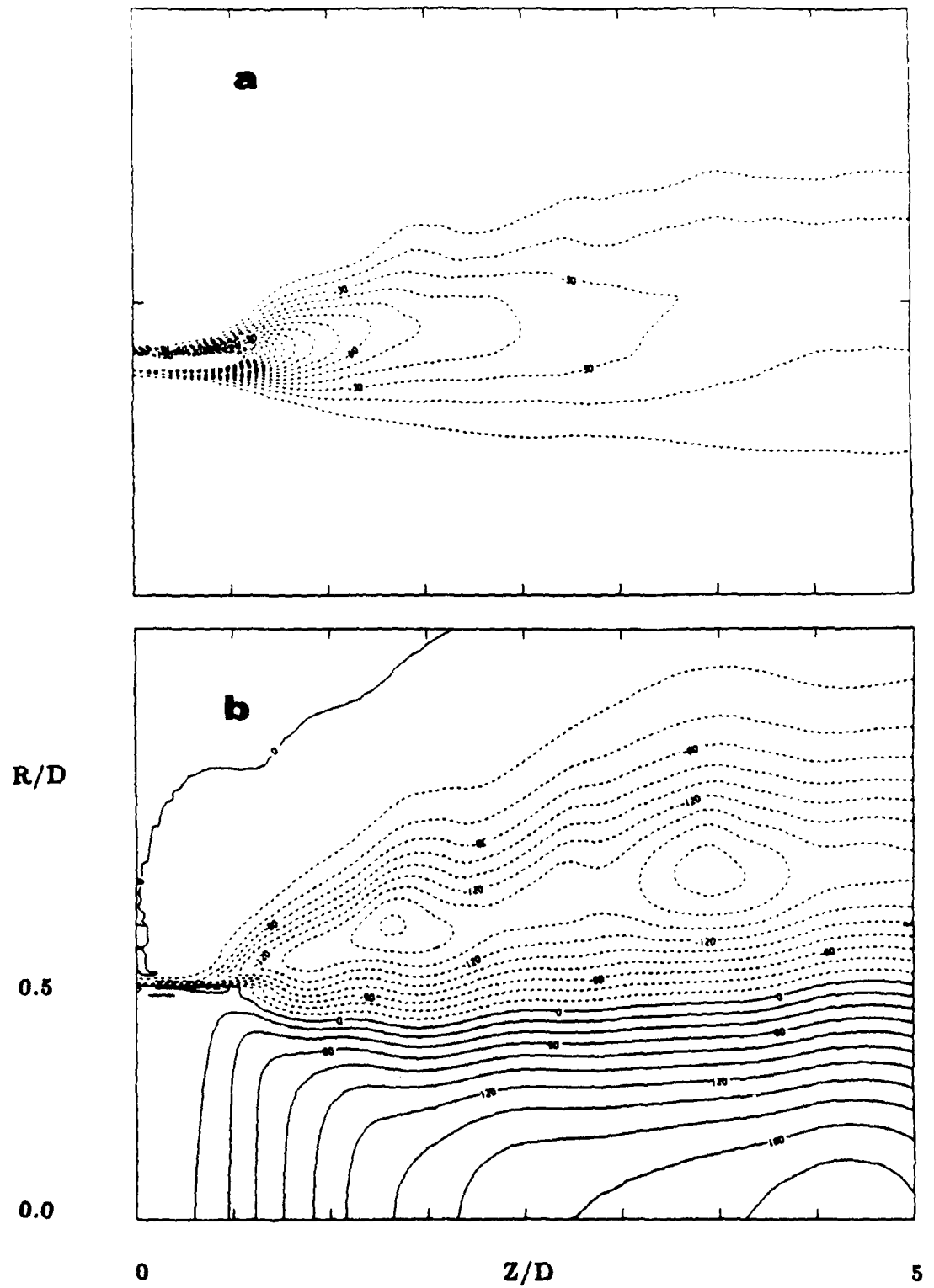
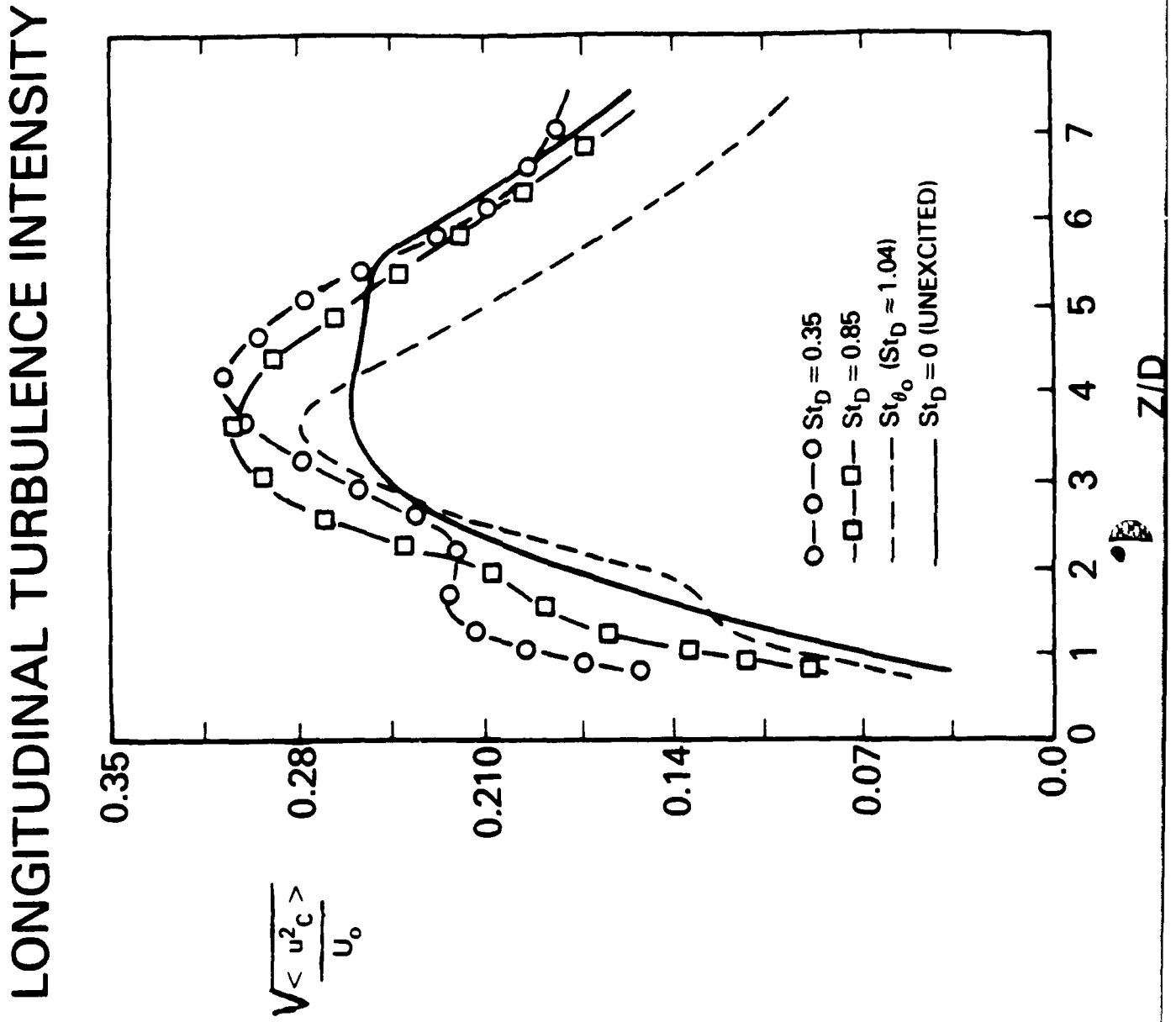


Figure 5 - a) Mean Vorticity. Equally spaced contours, interval:  $2 \times 10^5 \text{ s}^{-1}$ , scale by  $10^{-3}$ ; b) Mean relative pressure difference, equally spaced contours, scaled by  $10^4$

Figure 6



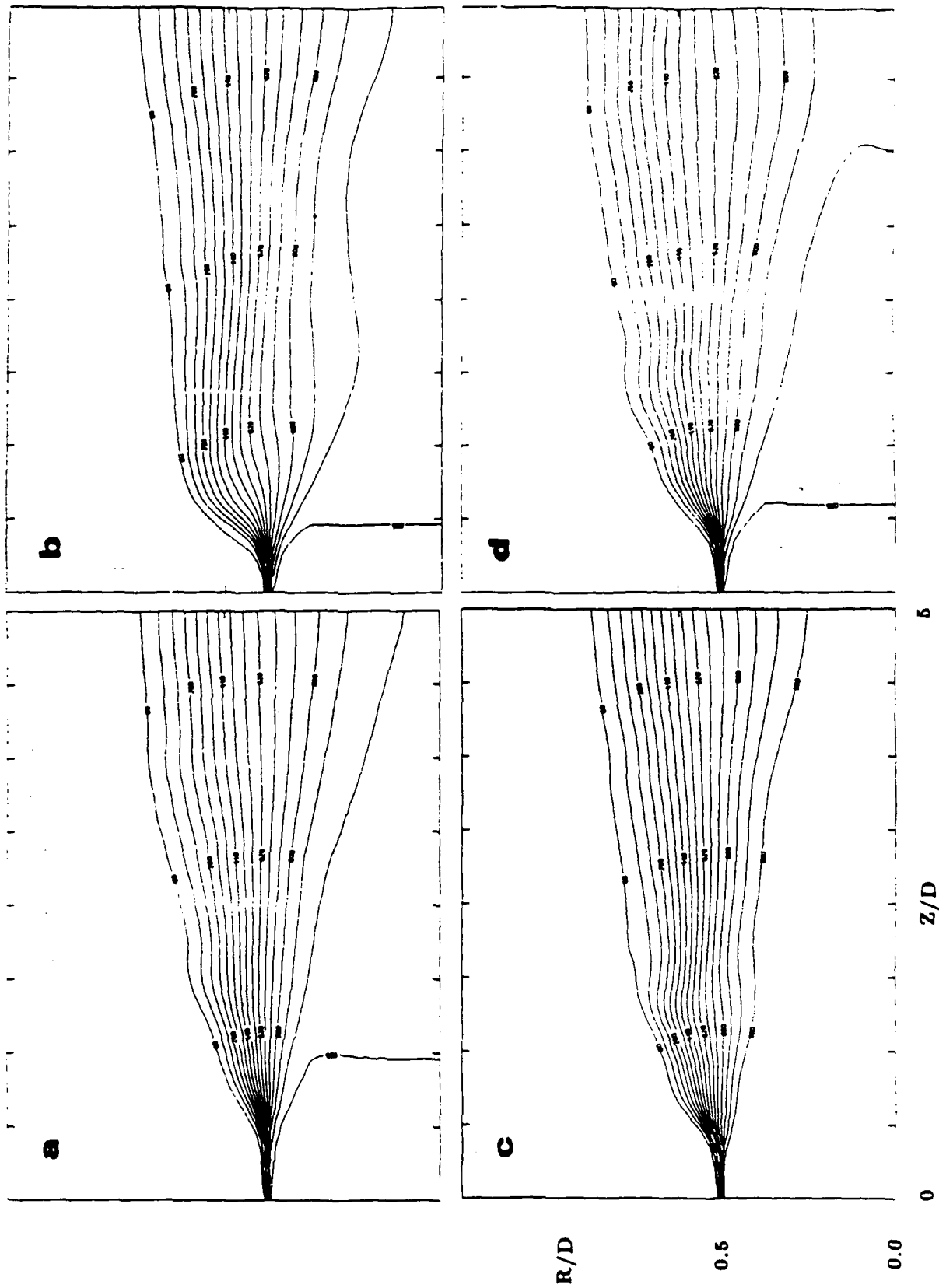


Figure 7 - Profiles of mean longitudinal velocity ( $U/U_0$ ), scaled by  $10^3$ . a) Unex-

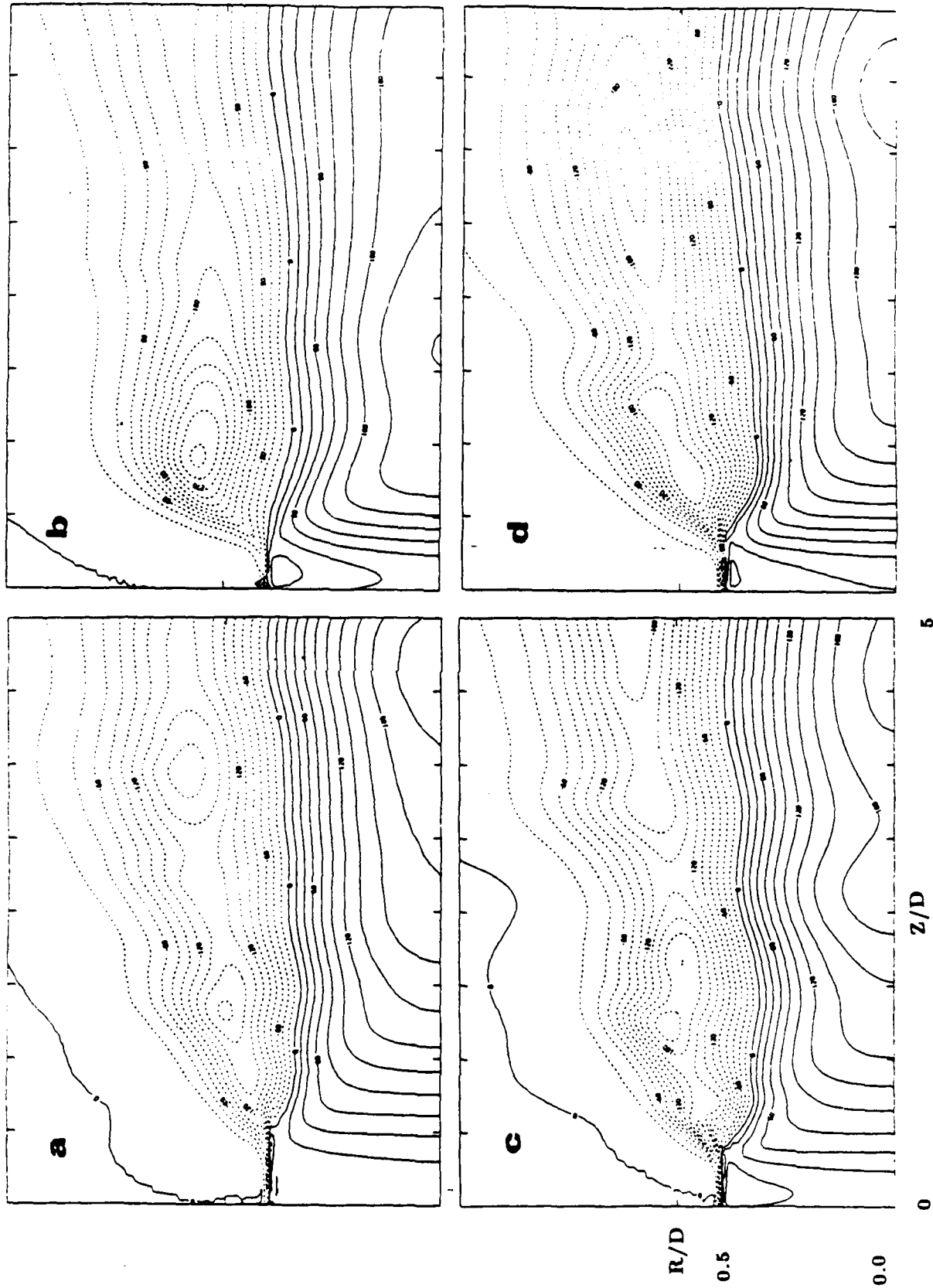


Figure 8 - Mean Relative Pressure Difference, scaled by  $10^4$ . a) Unex-  
 cited, b)  $St_D = 0.35$ , c)  $St_D = 0.85$ , d)  $St_D = 0.85$ .

Figure 9a - Total longitudinal momentum flux increase vs. static pressure decrease.

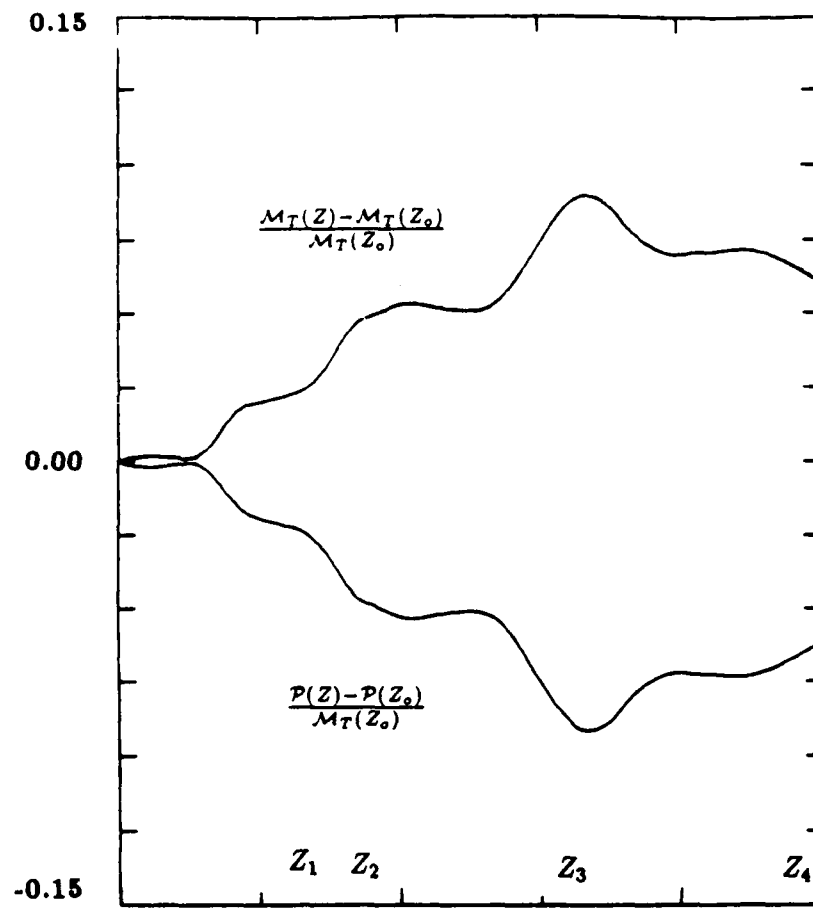


Figure 9b - Variation of the total and mean longitudinal momentum fluxes.

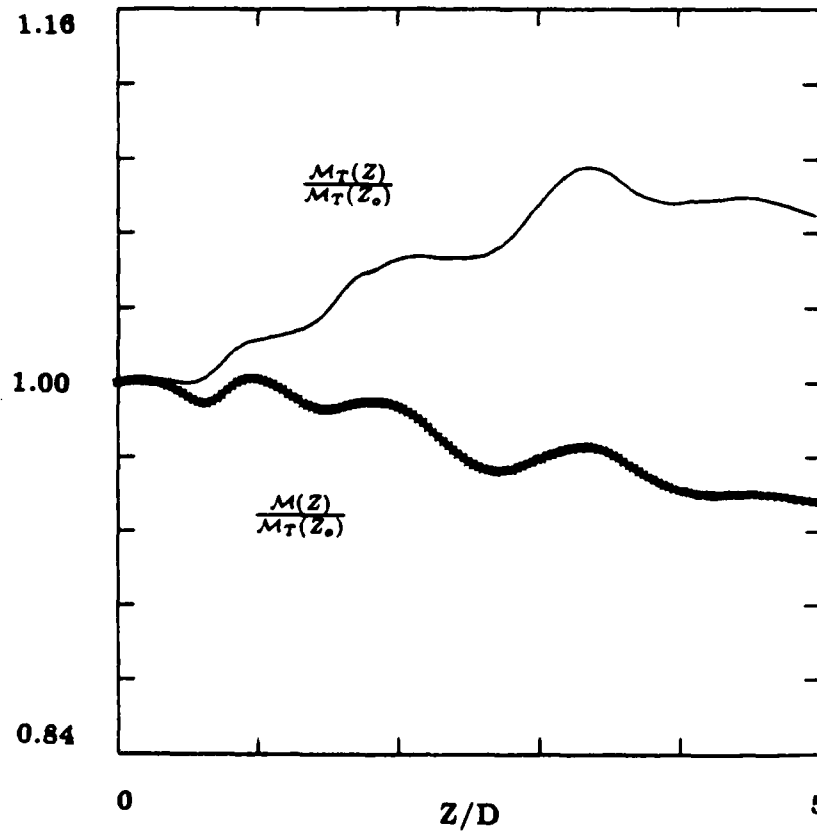
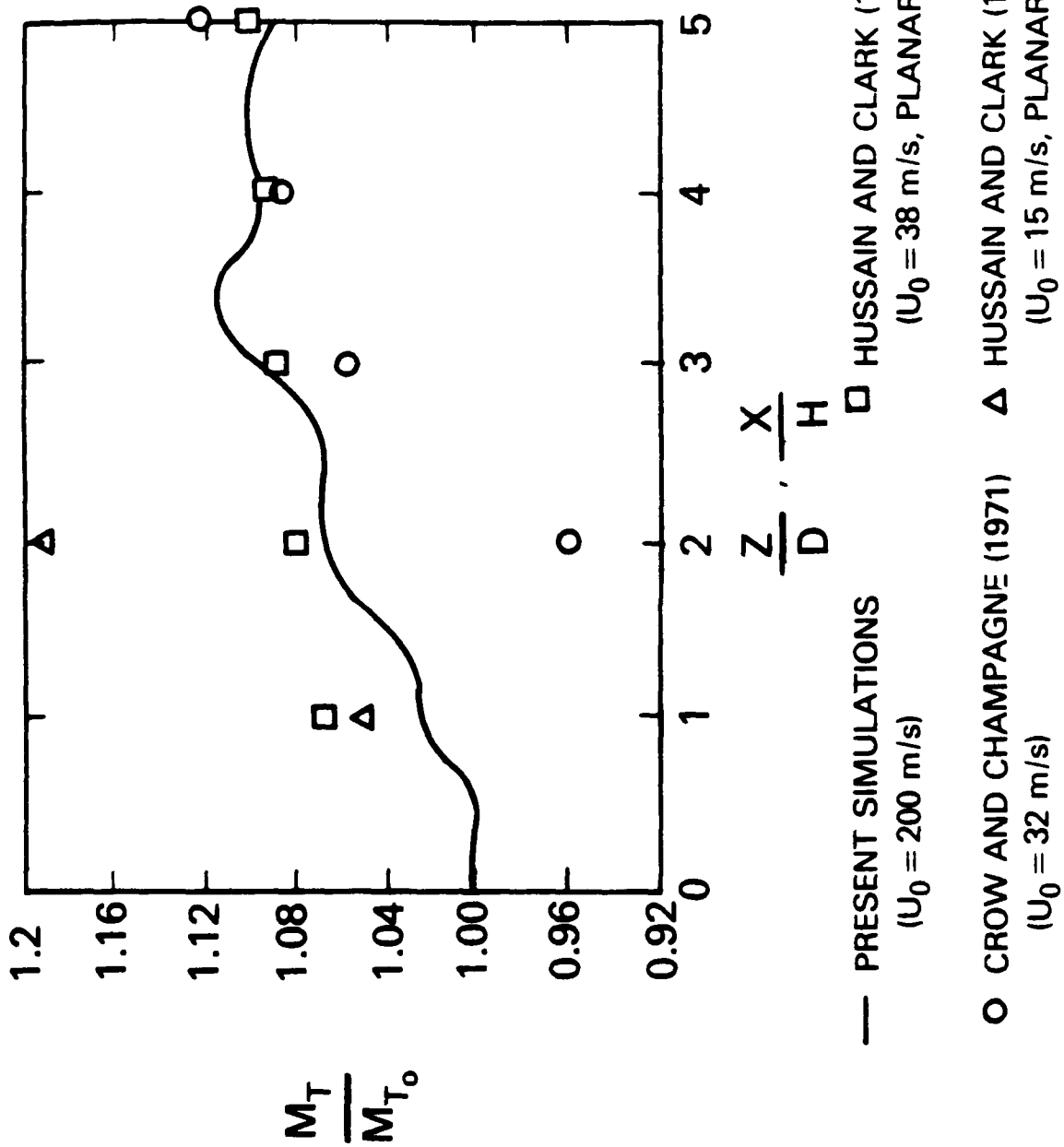


Figure 10

# STREAMWISE MOMENTUM FLUX VARIATION



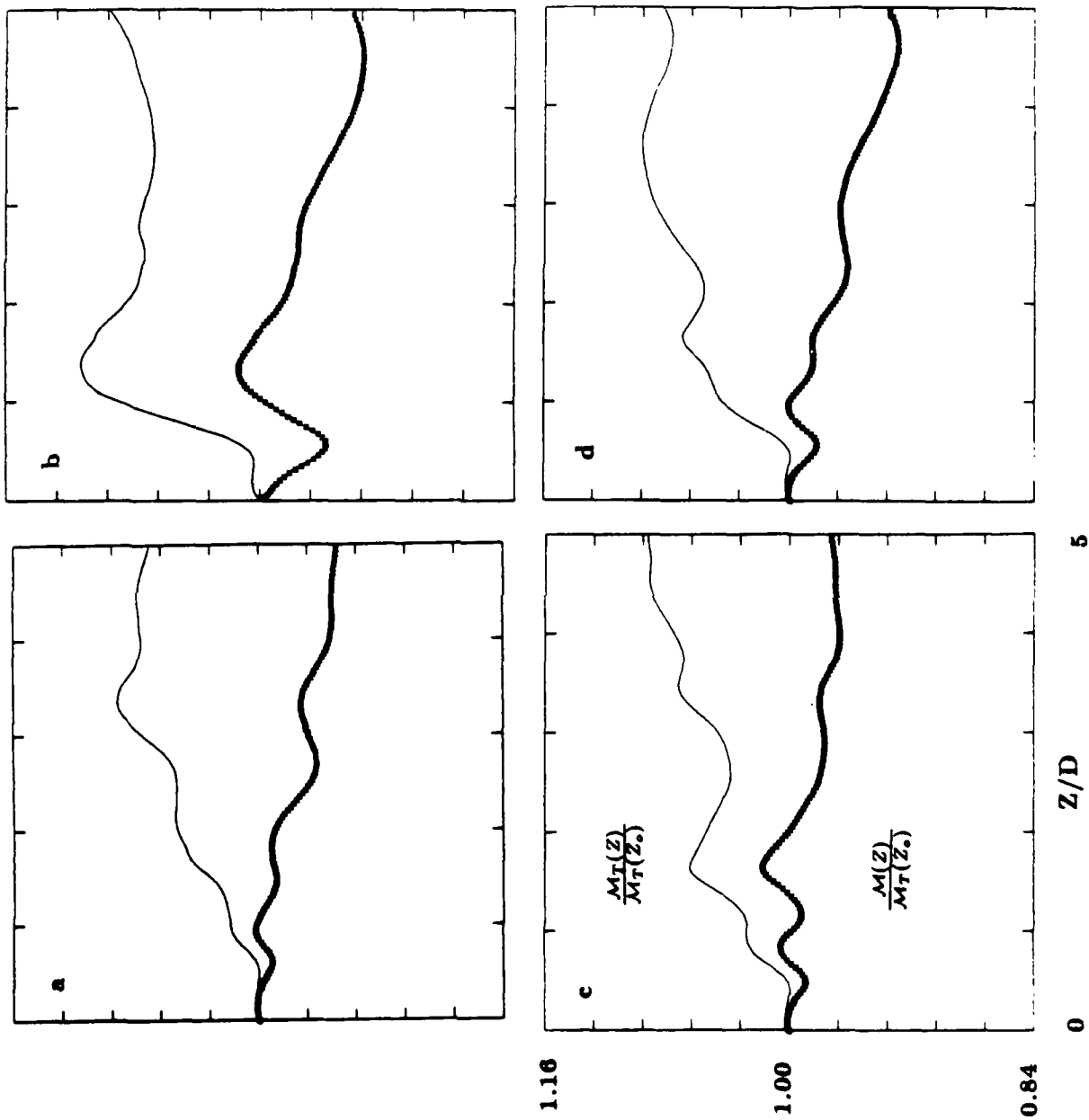


Figure 11 - Total and mean longitudinal momentum fluxes. a) Unexcited, b)  $St_0 =$

NUMERICAL INVESTIGATION OF  
HELICITY IN TURBULENT FLOW

Leonid Shtilman\*, Richard B. Pelz\*\*  
and Arkady Tsinober\*\*\*

\*Inst. Appl. Chem. Phys., CUNY,  
New York, NY 10031

\*\*Dept. Mech. & Aero. Engr., Rutgers  
Univ., Piscataway, NJ 08854

\*\*\*Dept. of Fluid Mech. & Heat Transfer  
Tel-Aviv University, Tel-Aviv 69978

Results of direct numerical simulation of decaying, nearly isotropic turbulence are presented. The angular orientation between vorticity and velocity evolves from a state that is initially random to one in which there is a high probability of vector alignment. Helicity evolves in a qualitatively different manner than the energy or enstrophy, reflecting changes of flow topology. From a random, zero-helicity field it is seen that viscosity can be a source of helicity generation. Probability distributions of the gradient quantities  $|\nabla(P+u^2/2)|$ ,  $|\mathbf{v}\cdot\boldsymbol{\omega}|$  and  $|\mathbf{v}\times\boldsymbol{\omega}|$  show their most probable states are much lower than their average.

One of the most exciting topics of current research in fluid mechanics is that of coherent structures in turbulent flows<sup>1</sup>. They are a spatio-temporal self-organization, an order or structure that contradicts the long-held belief of the quasi-randomness of turbulence.

A coherent structure can be observed and tracked in experiment; thus, it exists for a relatively long time (greater than, say, a turnover time). For a structure to remain intact, it must be largely impervious to the nonlinear transfer or cascade of energy. If the interaction term,  $\mathbf{v}\times\boldsymbol{\omega}$ , is small in a region, then the energy transfer there is small. For nonzero velocity and vorticity, minimization of this term at a point is accomplished by the alignment of the vectors. Helicity density,  $h$ , defined as  $h = \mathbf{v}\cdot\boldsymbol{\omega}$ , is a measure of this alignment. This quantity, along with the total helicity, defined as

$$H = \int_V \mathbf{v}\cdot\boldsymbol{\omega} dV, \quad (1)$$

are important quantities in the physics of coherent structures.

In this work we present results of direct numerical simulations of decaying turbulence for a variety of nearly isotropic, initial conditions. The goal of our simulations was to find some qualitative aspects of helicity in a decaying isotropic flow.

Aside from its importance for coherent structures, helicity is a quantity with some interesting properties. Firstly, like energy, it is an invariant of the Euler equations. Helicity is also a measure of how the vortex lines in a flow are knotted given some unit vorticity. Indeed, Moffatt<sup>2</sup> found that the inviscid solution of  $n$  interlinked vortex rings has helicity equal to  $n$ . This result was generalized by Arnold<sup>3</sup>. Lastly, helicity, like energy, is not Galilean invariant, and care should be taken in choosing the reference frame<sup>4</sup>.

Helicity has been investigated by theoreticians<sup>5</sup> and numericists<sup>6-9</sup>. The numerical results are as follows. Pelz *et al*<sup>6</sup> detected high pointwise alignment of velocity and vorticity vectors in turbulent channel flow. Shtilman *et al*<sup>7</sup> found the same phenomenon in the turbulent flow that evolved from the Taylor-Green vortex. In both cases, it was equally probable to find vectors pointing in the opposite direction (anti-parallel) as in the same direction (parallel). In the numerical experiments of Kerr and Gibson<sup>8</sup> a randomly stirred fluid was

found to have a high probability of parallel alignment. It is believed that the external forcing caused this asymmetry. To increase the generality of the previous work<sup>6,7</sup> we present here the results of direct numerical simulations of the complex flows in which there are no mean flow, forcing or special, deterministic initial conditions that could favor the natural (or favor the artificial) organizational tendencies of turbulence.

Calculations were performed in a domain periodic in all three directions. For an accurate spatial representation and natural adherence to the boundary conditions, the dependent variables were expanded in a trigonometric series and a pseudo-spectral method was employed. A semi-implicit, time-stepping scheme was used, whereby the nonlinear and linear terms were handled explicitly and implicitly, respectively<sup>10</sup>.

Table I contains the information concerning the three cases presented here. Incompressible, initial fields were constructed by, firstly, computing fields having Gaussian probability in wave-number and then by multiplying these fields by a function of wave-number as to give the power spectrum the functional form  $f(k)$  (see Table I). The column labelled  $Re_\tau$  contains the initial Reynolds number based on Taylor microscale, characteristic velocity and viscosity.

With an incompressible velocity field as the initial condition, the Navier-Stokes equations are integrated in time. The calculation is stopped periodically, and the flow field is saved. This is opposite to the collection method in experiments where data is saved at a few points in space but throughout the time of the experiment. Some standard analysis techniques of experimen-

tal data, power spectra and probabilities, are used. One sample time was chosen for presentation in this report. Table II contains quantities that were calculated at this time.

Run	time	$k_{peak}$	$k_d$	Hel	S	$Re_\tau$
L	0.693	4.	19.2	0.072	0.529	11.6
F	0.760	2.	27.8	-0.116	0.531	72.2
C	0.495	5.	33.4	-0.020	0.337	18.0

Table II. Quantities calculated at sampling times including the wavenumber of the maximum energy  $k_{peak}$ , the Kolmogorov wavenumber  $k_d$ , the total helicity Hel, the skewness S, and the Reynolds number based on Taylor microscale  $Re_\tau$ .

With an instantaneous, spectral representation of the complete flow field, one can calculate quantities containing highly accurate spatial derivatives. One such quantity, the relative helicity,  $\vec{v} \cdot \vec{\omega} / |\vec{v}| |\vec{\omega}|$ , gives the cosine of the angle between velocity and vorticity (the angle is denoted  $\theta$ ).

In Figures 1 and 2 we present the power spectra of energy and enstrophy at the initial and sampled time for Run L and Run F respectively. Both runs have initial power spectra similar to those obtained in experiments and to the standard spectra for nearly all simulations to date. Because the computational domain is finite, one cannot produce a field that is truly homogeneous and isotropic for all modes. Nevertheless, the power spectra for u, v and w shown in Figures 1 and 2 show the fields are nearly isotropic, deviations occur-

Run	$f(k)$	$c_1, c_2$	$k_{peak}$	$\nu$	$k_d$	Hel	$Re_\tau$
L	$c_1 k^4 \exp(-c_2 k^2)$	0.012, 0.08	5.0	0.017	23.0	0.478	20.7
F	$c_1 k^6 \exp(-c_2 k^2)$	0.314, 0.75	2.0	0.010	22.1	-0.075	114.4
C	$c_1 k^4 \exp(-c_2 k^2)$	0.020, 0.125	5.0	0.010	35.9	0.0	33.9

Table I. Parameters and calculated quantities for  $t=0$  including the shape function for the power spectra  $f(k)$ , the wavenumber of the maximum energy  $k_{peak}$ , the viscosity  $\nu$ , the Kolmogorov wavenumber  $k_d$ , the total helicity Hel, and the Reynolds number based on Taylor microscale  $Re_\tau$ .

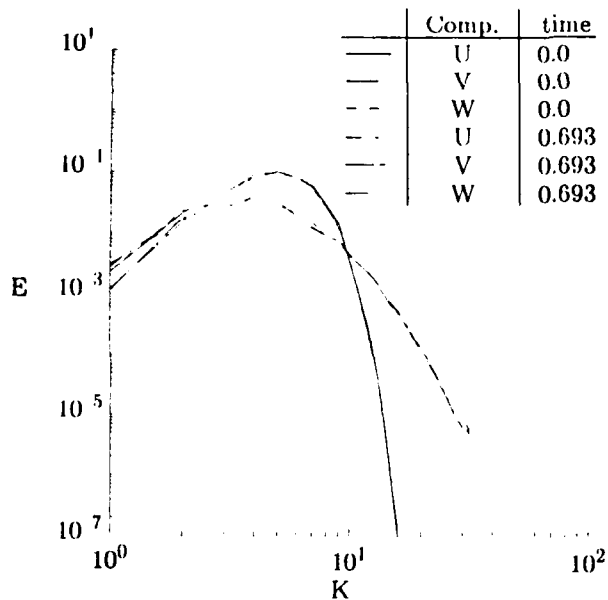


Figure 1. Run L: Six power spectra, the components  $u(k)^2$ ,  $v(k)^2$  and  $w(k)^2$  at  $t=0.0$  and  $t=0.693$ , are presented. The three spectra for each time nearly coincide.

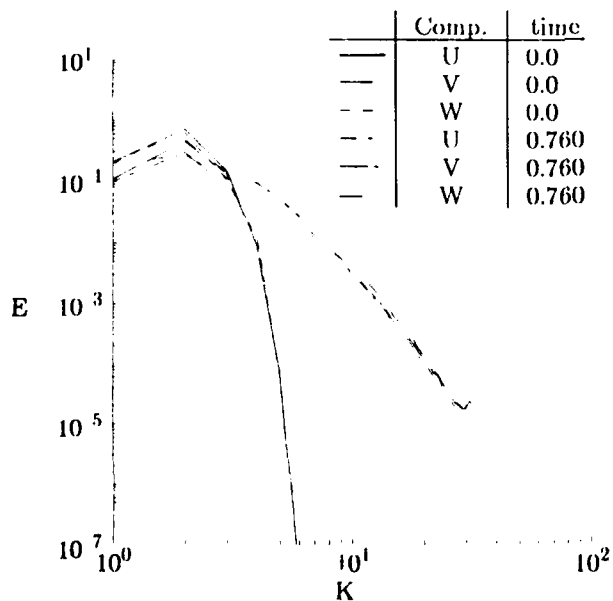


Figure 2. Run F: Six power spectra, the components  $u(k)^2$ ,  $v(k)^2$  and  $w(k)^2$  at  $t=0.0$  and  $t=0.760$ , are presented. The three spectra for each time nearly coincide.

ring in the low wave-number range. The skewness, a measure of energy transfer, compares well with experiments of isotropic turbulence (see Table II). In Figures 3 and 4 the non-normalized, probability distribution functions (PDD) of relative helicity for initial and sample times are shown. The relative helicity is shown as  $\cos\theta$  on the axis labels. Initially, the histograms are not symmetric with respect to a vertical line at  $\cos\theta=0$  (the histogram of the Taylor-Green vortex has this symmetry<sup>7</sup>). As the flow evolves, peaks or "horns" at  $\cos\theta = \pm 1$  develop. At the sample time the histograms shown in figures 3 and 4 are statistically steady. Thus, the velocity and vorticity fields which were randomly oriented initially evolve to a state in which there is a higher probability for the vectors to be aligned at each point. Their orientation with respect to a coordinate axis is still random, however.

The evolution of peaks in turbulent flows seems to be independent of geometry and initial conditions, since this same phenomenon was found in the channel and the Taylor-Green vortex problem.

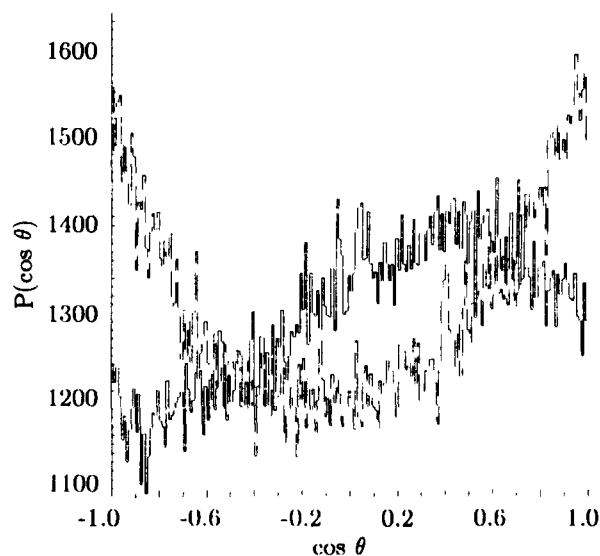


Figure 3. Run L: The probability density  $P(\cos\theta)$  for the distribution of the angle  $\theta$  between velocity and vorticity (relative helicity) for  $t=0.0$  (solid line) and for  $t=0.693$  (dashed line).

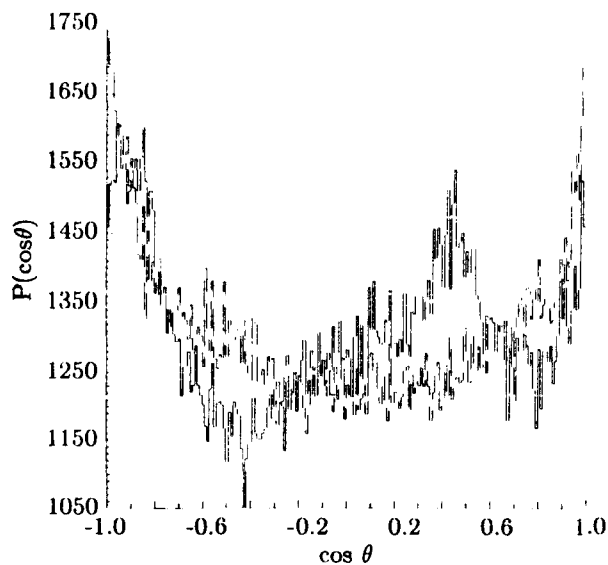


Figure 4. Run F: The probability density  $P(\cos\theta)$  for the distribution of the angle  $\theta$  between velocity and vorticity (relative helicity) for  $t=0.0$  (solid line) and for  $t=0.760$  (dashed line).

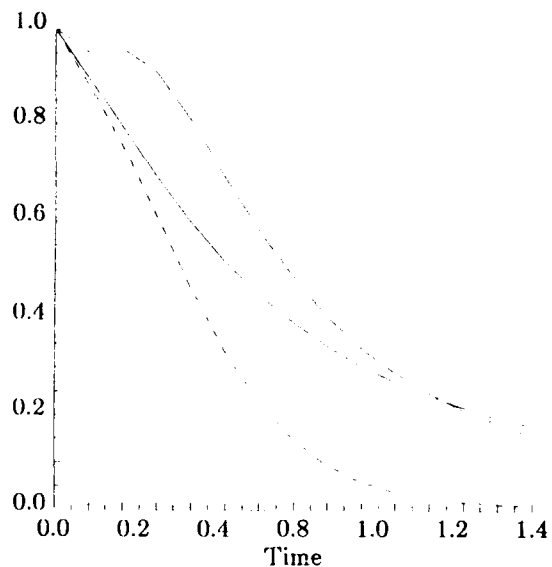


Figure 5. Run L: The time history of energy (solid), enstrophy (long dash) and helicity (short dash) normalized by their initial values.

Figure 5 presents the time history of the energy, enstrophy and helicity normalized by their initial values. The decreasing value of the helicity with time is linked not only to the decrease of energy and enstrophy, but to a process of symmetrization of the helicity. Indeed, the plot shows that the helicity decreases faster than either of the other quantities, which indicates that there is a balancing of positive and negative values of helicity within the domain. When the histograms in Figures 3 and 4 are compared with those of the Taylor-Green vortex (see ref. 7), the peak-to-valley ratio is considerably higher in the latter case. The severity of the ratio is believed to be a function of Reynolds number, which is considerably higher in the Taylor-Green case.

An example of the effect of Reynolds number on the relative helicity, we present a result from a Taylor-Green simulation. In Figure 6 the PDD for  $R = 100$  and  $t = 9.6$  is shown. The peaks at  $\pm 1$  are developed but thin, and memory of the initial conditions (zero relative helicity) still remains. The peak at zero does not disappear for this Reynolds number: however, for a simulation where  $R = 1500$ , the peak at  $\cos\theta = 0$  is gone after  $t = 1$  (see Shtilman *et al*<sup>7</sup>).

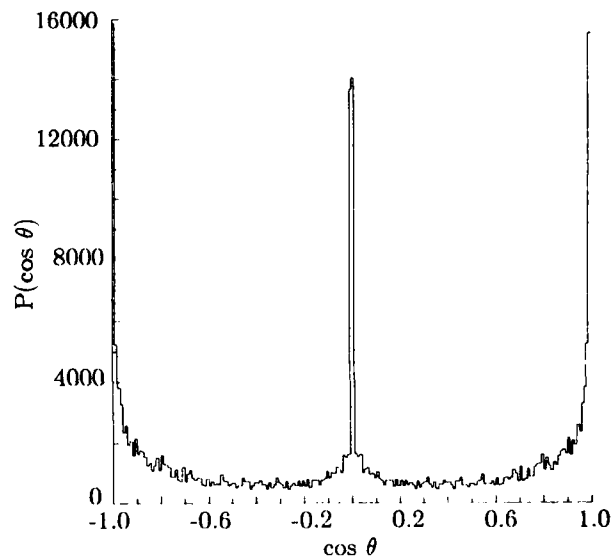


Figure 6. Taylor-Green vortex problem: The probability density  $P(\cos\theta)$  for the distribution of the angle  $\theta$  between velocity and vorticity (relative helicity) for  $t=9.6$  and  $R=100$ .

Run F has an initial condition that is far away from the similarity solution of decaying turbulence. Because the low wavenumbers contain a large amount of energy initially, a long transient period occurs in which energy is transferred towards the higher wavenumbers. Figure 7 shows the time history of the energy, enstrophy and helicity normalized as in Figure 5. The rise in enstrophy is an indication of the saturation of the high wavenumbers modes. The energy is a monotonically decreasing function reflecting the loss of energy in the large scales. The helicity follows neither of these curves closely. After an initial period of little change, the helicity increases. It turns sharply downwards, possible due to the symmetrization of local values of helicity. At  $t=1.7$  the helicity again starts to increase. This is quite surprising since both energy and enstrophy are decreasing by that time.

To determine whether the initial helicity distributions play a role in the evolution of the helicity, an initial condition was generated with the constraint that the helicity is zero. The subsequent evolution of this field was called Run C. The initial condition was gen-

erated through the use of a Clebsch representation of the velocity<sup>11</sup>. One can choose an initial flow field in the form

$$\vec{v} = \lambda \vec{\nabla} \mu - \vec{\nabla} \psi, \quad \Delta \psi = \vec{\nabla} \cdot \lambda \vec{\nabla} \mu \quad (2)$$

where  $\lambda$  and  $\mu$  are random functions and  $\psi$  enforces incompressibility. Zero helicity, a necessary but not a sufficient condition of the Clebsch variable representation of the velocity field (Frenkel, Cassidy<sup>12</sup>), can be demonstrated by substituting expression (2) into equation (1). The spectra of  $\lambda$ ,  $\mu$  and initial energy are presented in Figure 8.

One can derive the equations of motion for the variables  $\lambda$  and  $\mu$  from the Navier-Stokes equations (see Grossmann<sup>13</sup>). It should be mentioned that not all flow fields with zero helicity can be represented in the Clebsch form (e.g., the Taylor-Green vortex). Solutions of the inviscid equations will be solutions of the Euler equations since the helicity is a constant of motion for Euler solutions. Even if an initial field does have a Clebsch representation, its time evolution (using the

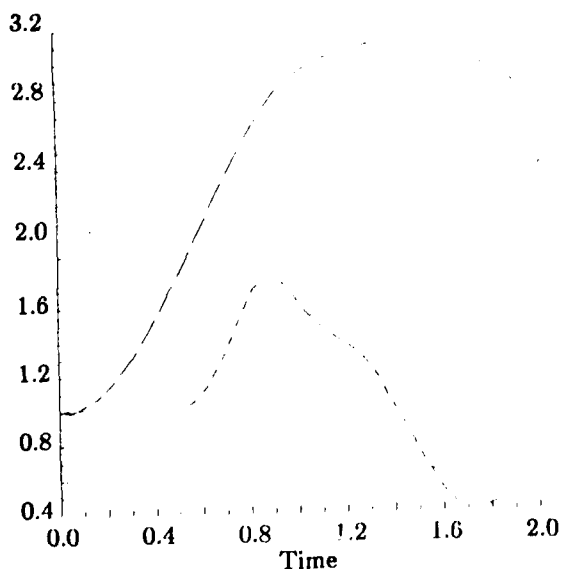


Figure 7. Run F: The time history of energy (solid), enstrophy (long dash) and helicity (short dash) normalized by their initial values.

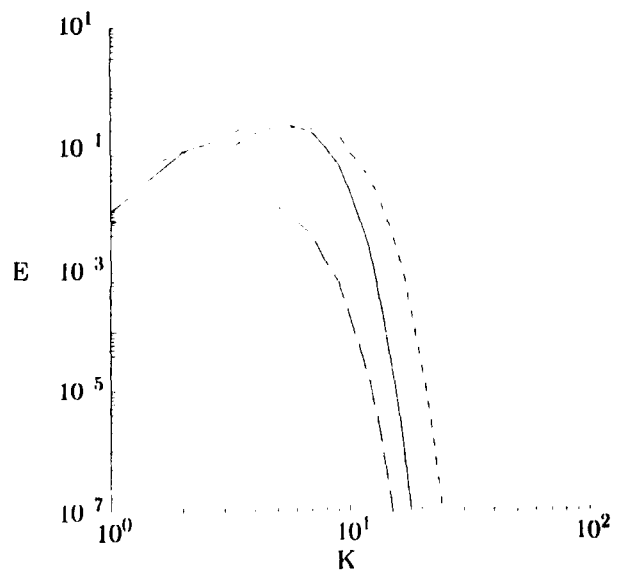


Figure 8. Run C: Spectra of  $\lambda$  (solid),  $\mu$  (long dash) and energy at  $t=0$  (short dash).

viscous equations) will not, in general, be equivalent to the evolution based on the Navier-Stokes equations<sup>12</sup>. Indeed, Figure 9 shows the time history of the normalized energy and enstrophy (a) and helicity (b) for Run C. While the curves of energy and enstrophy follow an expected course, the helicity fluctuations oscillate through zero. Thus, there is spontaneous generation and fluctuation of helicity in unforced turbulent flows. The Clebsch equations are unable to predict this.

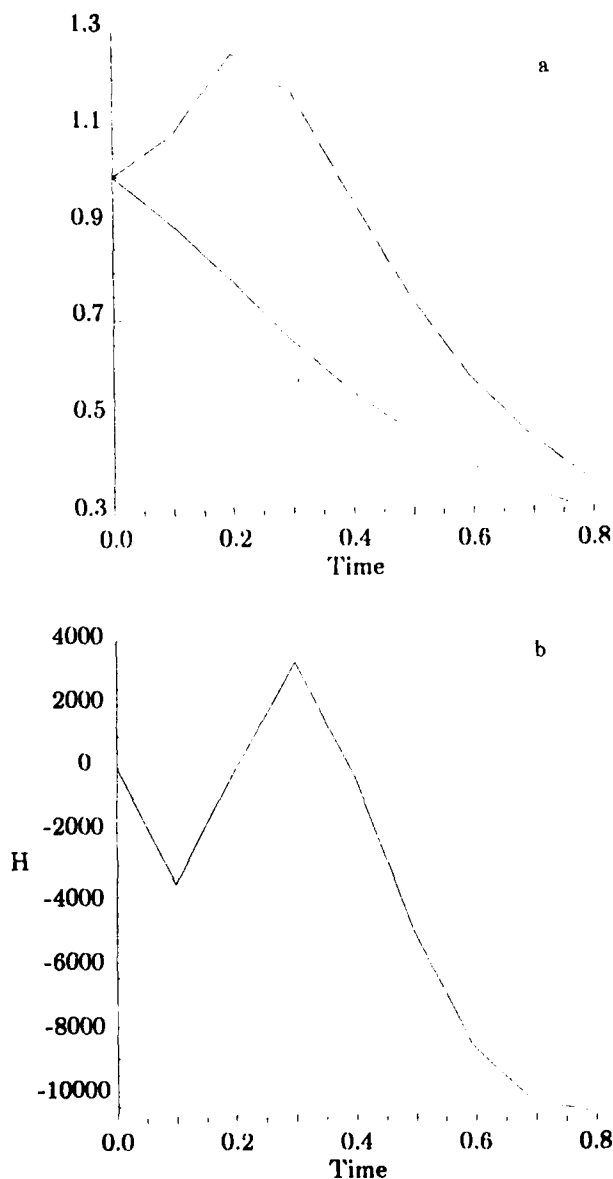


Figure 9. Run C: (a) The time history of energy (solid) and enstrophy (dash) normalized by their initial values. (b) The time history of helicity.

The phenomenon of generation and fluctuation of helicity can be explained by examining the equation of motion for helicity.

$$\frac{d}{dt} \int_V \vec{v} \cdot \vec{\omega} dV = \int [\vec{\omega} \cdot (-P + u^2/2) + \nu(\vec{v} \times \nabla \times \vec{\omega})] \cdot d\vec{s} + 2\nu \int_V \vec{\omega} \cdot \nabla \times \vec{\omega} dV \quad (3)$$

The last term is viscosity dependent but not positive definite. *Viscosity can act as a source as well as a sink of helicity.* Recall, viscosity only acts as a sink for energy. Initially the PDD of relative helicity for Run C showed that the velocity and vorticity vectors are orthogonal was highly probable. The final PDD, however, has a shape much like the final PDDs of Run L and F.

In references<sup>6,7</sup> it is reported that conditional sampling of the PDD of helicity showed that the alignment of the velocity and vorticity is much more profound in the regions of small dissipation. However, the analysis of the conditional sampling in the regions of large dissipation is difficult. In ref.<sup>8</sup> the shape of the PDD of helicity density was found to be the same in the whole volume and in the volume with large dissipation. One of the reasons for this might be the fact that in turbulent field only small fraction of volume has large dissipation. It is important to investigate this question in more detail.

Figure 10 shows a plot of the PDD of the non-linear potential term  $|\vec{\nabla} \cdot (-P + u^2/2)|$ , the helicity density  $|\vec{v} \cdot \vec{\omega}|$  and interaction term  $|\vec{v} \times \vec{\omega}|$  for Run L. It is clear that the most probable value of all quantities is very small when compared to their maximum and average values. Similar results have been found in laboratory experiments<sup>14</sup>. Figure 10 shows that the most probable value of  $|\vec{v} \cdot \vec{\omega}|$  is much less than the value of  $|\vec{v} \times \vec{\omega}|$ . This means that for small values of  $|\vec{v}| |\vec{\omega}|$ , vorticity and velocity have a tendency to align, while for larger values, they have more of a tendency to be perpendicular. It also can be seen in Figure 10 that the peak of the PDD for  $|\vec{\nabla} \cdot (-P + u^2/2)|$  is located between the peaks of  $|\vec{v} \cdot \vec{\omega}|$  and  $|\vec{v} \times \vec{\omega}|$ . E. Levich has given an explanation of this result from an

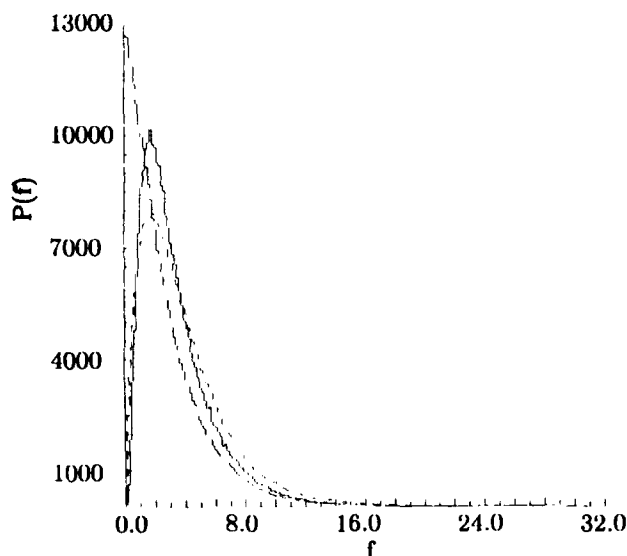


Figure 10. Run L: The probability density distributions of nonlinear potential term  $|\vec{\nabla}(P+u^2/2)|$  (solid), the helicity density  $|\vec{v}\cdot\vec{\omega}|$  (long dash) and interaction term  $|\vec{v}\times\vec{\omega}|$  (short dash) at time  $t=0.693$ .

analysis with path integrals (see Ref. 5).

The results of the runs presented above are typical of all runs with various initial conditions, which we performed. In all these runs the formation of the maxima at  $\pm 1$  in the PDDs are pronounced. However, the shape of the curve and severity of the peaks are a function of Reynolds number and initial conditions.

between the peaks of  $|\vec{v}\cdot\vec{\omega}|$  and  $|\vec{v}\times\vec{\omega}|$ . E. Levich has given an explanation of this result from an analysis with path integrals (see Ref. 5).

The results of the runs presented above are typical of all runs with various initial conditions, which we performed. In all these runs the formation of the maxima at  $\pm 1$  in the PDDs are pronounced. However, the shape of the curve and severity of the peaks are a function of Reynolds number and initial conditions.

#### ACKNOWLEDGEMENTS

We would like to thank Professors E. Levich, B. Levich, A. Frenkel, S.A. Orszag, and V. Yakhot for

helpful discussions. Professor Orszag was also of great assistance in providing the original computer code and computing facilities. This work was supported in part by Air Force Office of Scientific Research under contract F49620-85-C-0026, the Office of Naval Research under Contract N00014-82-C-0451 and by the US Department of Energy grant under Contract NDE-AC02-80ER 10559. Computing was done at the National Center for Atmospheric Sciences and Lawrence Livermore Laboratory.

#### REFERENCES

- <sup>1</sup>see the review by Hussein, A.K.M.F., Coherent structures in turbulence. presented at G.I. Taylor Symposium, March 1986, to be published in *J. Fluid Mech.*
- <sup>2</sup>Moffatt, H.K. 1969 The degree of knottedness of tangled vortex lines. *J. Fluid Mech.* **35**, 117-129.
- <sup>3</sup>Arnol'd, V. 1974 The asymptotic Hopf invariant and its applications. *Proc. Summer School in Differential Equations*, Erevan, Armenian S.S.R. Acad. Sci., 229-256.
- <sup>4</sup>Speziale, C. private communication.
- <sup>5</sup>Levich, E. 1986 Some recent developments in turbulence theory. to be published in *Phys. Rep.*
- <sup>6</sup>Pelz, R.B., Yakhot, V., Orszag, S.A., Shtilman, L., Levich, E. 1985 Velocity-vorticity patterns in turbulent flow. *Phys. Rev. Lett.* **54**.
- <sup>7</sup>Shtilman, L., Levich, E., Orszag, S.A., Pelz, R.B., Tsinober, A. 1985 On the role of helicity in complex fluid flows. *Phys. Lett.* **113A**.
- <sup>8</sup>Kerr, R.M., Gibson, C.H. 1985 *Bull. Am. Phys. Soc.* **30**.
- <sup>9</sup>Pelz, R.B., Shtilman, L., Tsinober, A. 1986 On the helical nature of unforced, turbulent flows. accepted to *Phys. Fluids*.
- <sup>10</sup>Patterson, G.S., Orszag, S.A. 1972 *Phys. Fluids* **14**, 2538.
- <sup>11</sup>Lamb, H. 1932 *Hydrodynamics* (Cambridge University Press) 6th ed.
- <sup>12</sup>Frenkel, A., Cassidy, W. to be published.
- <sup>13</sup>Grossman, S.S. 1975 An order parameter field theory for turbulent fluctuation. *Phys. Rev.* **A11**, 2165.
- <sup>14</sup>Balint, J.-L. 1986 These de Docteur d'Etat es Sciences, University of Lyon.

SPECTRAL PROPERTIES OF EXACT RANDOM SOLUTIONS TO  
BURGERS' EQUATION FOR MODIFIED THOMAS INITIAL CONDITIONS

Steven Keleti and X B Reed, Jr.  
Chemical Engineering Department,  
University of Missouri-Rolla, Rolla, MO 65401 USA

Abstract

Random sawtooth Thomas initial conditions can be specified on a fixed spatial mesh [50, 44] or on a random one, termed modified Thomas initial conditions. Beyond the white-noise band common to both at small  $k$ , modified Thomas has  $E(k,0) \sim k^{-3}$ , whereas Thomas has pronounced ringing. For modified Thomas, there is (i) a narrow band (small  $k$ ) white-noise spectrum  $E(k,t) = E_0$  like that for Thomas [18, 20], (ii) a  $k^{-2}$  subrange of increasing bandwidth with increasing  $Re_0$ , and (iii) an exponential viscous cutoff at high wave numbers which decays more rapidly with decreasing  $Re_0$ . The small time spectral transfer,  $T(k,t)$ , for modified Thomas does not have a spike at  $k = 2\pi/d_n$ , whereas it does for Thomas at  $k = 2\pi/d$  [18]. The evolution of  $E(k,t)$ ,  $D(k,t)$ , and  $T(k,t)$  for modified Thomas are otherwise similar in form to that for Thomas for [20]  $t > 1$ .

1. Introduction

Theoretical turbulence may be described as standing in need of the next generation of supercomputers or as suffering from the lack of random solutions to the Navier-Stokes equations. Burgers' equation, a one-dimensional analog which is often used to test numerical methods and theoretical closures, can be solved exactly in terms of standard functions of mathematical physics by means of the Cole-Hopf [9, 15] transformation, provided:

- (i) The initial conditions for Burgers' equation map under the inverse Cole-Hopf transformation into mathematically tractable initial conditions for the heat conduction equation (i.e., so that more than a purely formal solution is obtained).
- (ii) The boundary conditions for Burgers' equation are either to be imposed as, say, asymptotically vanishing or constant on infinite domains [3] or have counterparts which make for tractable boundary value problems for the heat conduction equation (e.g., [40, 38]).

Burgers devoted most of his life to the analysis of the equation,  $\partial u / \partial t + u \partial u / \partial x = \nu \partial^2 u / \partial x^2$ , which bears his name (see especially [5-8]), including its statistical properties. Many closures have been tried on Burgers' equation prior to the use of their three-dimensional generalizations ([25, 39, 58], to name but a few). In his continuing development

of the Wiener-Hermite expansion, Meecham, with a number of collaborators, has obtained significant results on Burgers' equation *per se* (e.g., [29, 30]). In particular, he and several co-workers [16, 17] were the first to obtain an exact, (almost) statistically homogeneous, solution to Burgers' equation on an infinite domain for nonzero random piecewise constant initial conditions on a large but finite domain (evaluated at  $Re_0 = 200$ ). Shih and Reed [44] observed that the Laplace solution to the heat conduction equation could also be used -- certainly with more calculational difficulty -- to obtain a solution to Burgers' equation (also evaluated at  $Re_0 = 200$ ) on an infinite domain for nonzero random piecewise linear continuous initial conditions. These physically more realistic initial conditions were also used in the study of exact solutions to Burgers' equation on a finite domain with vanishing [43] and with spatially periodic [45] boundary conditions at  $Re_0 = 200$ .

The above investigations provided detailed behavior of all but the fine scale structure for  $\langle u(x,t)u(x+r,t) \rangle$  and its Fourier transform  $E(k,t)$ , with  $\langle \rangle$  denoting ensemble averaging. In [44, 45, 43], histograms and the first nine (single-point) moments were obtained, with  $\langle u^2(x,t)u(x+r,t) \rangle$  also being computed in [45]. The ensembles in [44, 45, 43] were large by the standards of Jeng, *et al.* [17], consisting of 12 realizations on the IBM equipment, but being small by the standards necessary to accurately compute estimators of two-point statistical properties. Moreover, the spatial mesh on which the exact solutions were numerically evaluated [44, 45, 43] were inadequate to obtain spatial correlations for extremely small separations and equivalently high wave-number spectral results.

For large ensembles (50, occasionally even 100 members), Keleti and Reed [18] obtained preliminary energy, dissipation, and transfer spectra at  $Re_0 = 400$  and 1000 on an FPS-164. These and subsequent results also extended well into the high wave-number range through the use of a rapid, accurate algorithm for the evaluation of exact solutions to Burgers' equation on a very fine spatial mesh [18, 20, 19]. The initial conditions were those first employed by Thomas [50] and subsequently used by Shih and Reed [44, 45, 43]: values of velocity  $\{u_n\}$  selected at random from a uniform  $(-1,1)$  distribution on a fixed spatial mesh  $\{x_n - x_{n-1}\} = d$  ( $d = 1$ ) were connected linearly. The random piecewise linear continuous initial conditions generated in this way are called *Thomas initial conditions*.

Piecewise linear continuous random initial conditions for Burgers' equation have several advantages, among which are features analogous to velocity records for homogeneous turbulent velocity fluctuations [44]. Thomas [50] initial conditions have a *distribution of velocity scales but only a single length scale*. This manifests itself in several ways, for instance in a spectral peak at  $k = 2\pi$  for small times [20]. The question that therefore arises is whether or not the statistical properties of velocity fields evolving from Thomas initial conditions are representative of a larger class of exact random solutions to Burgers' equation, this being a basic tenet of homogeneous turbulence (e.g., [1]) and more generally of statistical mechanics [52]. (For a brief discussion and a demonstration of a stronger result for a specific pair of classes of initial conditions, see [37]). An obvious way to test the hypothesis is to consider initial conditions with a *distribution of length scales, as well as a distribution of velocity scales*. The simplest version of these initial conditions, which we have termed *modified Thomas initial conditions*, may be generated by selecting the  $\{d_n\} = \{x_n - x_{n-1}\}$  from a uniform (0,2) distribution, as well as selecting the  $\{u_n\}$  from a uniform (-1,1) distribution, with the two random variates being statistically independent and therefore uncorrelated.

## 2. Initial Conditions, Velocity Fields, and Some Single-point Statistical Properties

The initial conditions are specified by the random location of  $\{x_n\}$  at which the random velocity  $\{u_n\}$  is specified. The  $\{u_n\}$  are selected from a uniform distribution on (-1,1). The  $\{x_n\}$  are selected from a uniform distribution on (0,2). In both cases, basically, the IMSL (pseudo)random number generator algorithm was used [23, 27], except that intermediate (pseudo)random numbers  $\xi_k'$  were used as seeds to generate the actual random numbers  $\xi_k$  instead of the recommended seeds,  $\xi_{k-1}$ :

$$\xi_k' = \text{MOD}(16807.0\xi_{k-1}, 2^{32}-1),$$

$$\xi_k = \text{MOD}(16807.0\xi_k', 2^{32}-1).$$

Normalization to (0,1) was by division by  $2^{32}$  and the first seed was  $\xi_0 = 123457$ . The  $u_n$  on (-1,1) were then obtained as  $u_n = (2\xi_n/2^{32}-1)$ . Similarly,  $d_n = x_n - x_{n-1}$  on (0,2) was obtained as  $d_n = 2\xi_n/2^{32}$ . There are pitfalls in the generation of (pseudo)random numbers [23], but the above use of a random seed has been investigated by, for instance, MacElroy and Suh [27] and shown to avoid most difficulties. The number of (pseudo)random numbers  $\{d_n\}$  and  $\{u_n\}$  was significantly less than the cycling that can arise, assuring negligible correlation between the (pseudo)random numbers [23, 27].

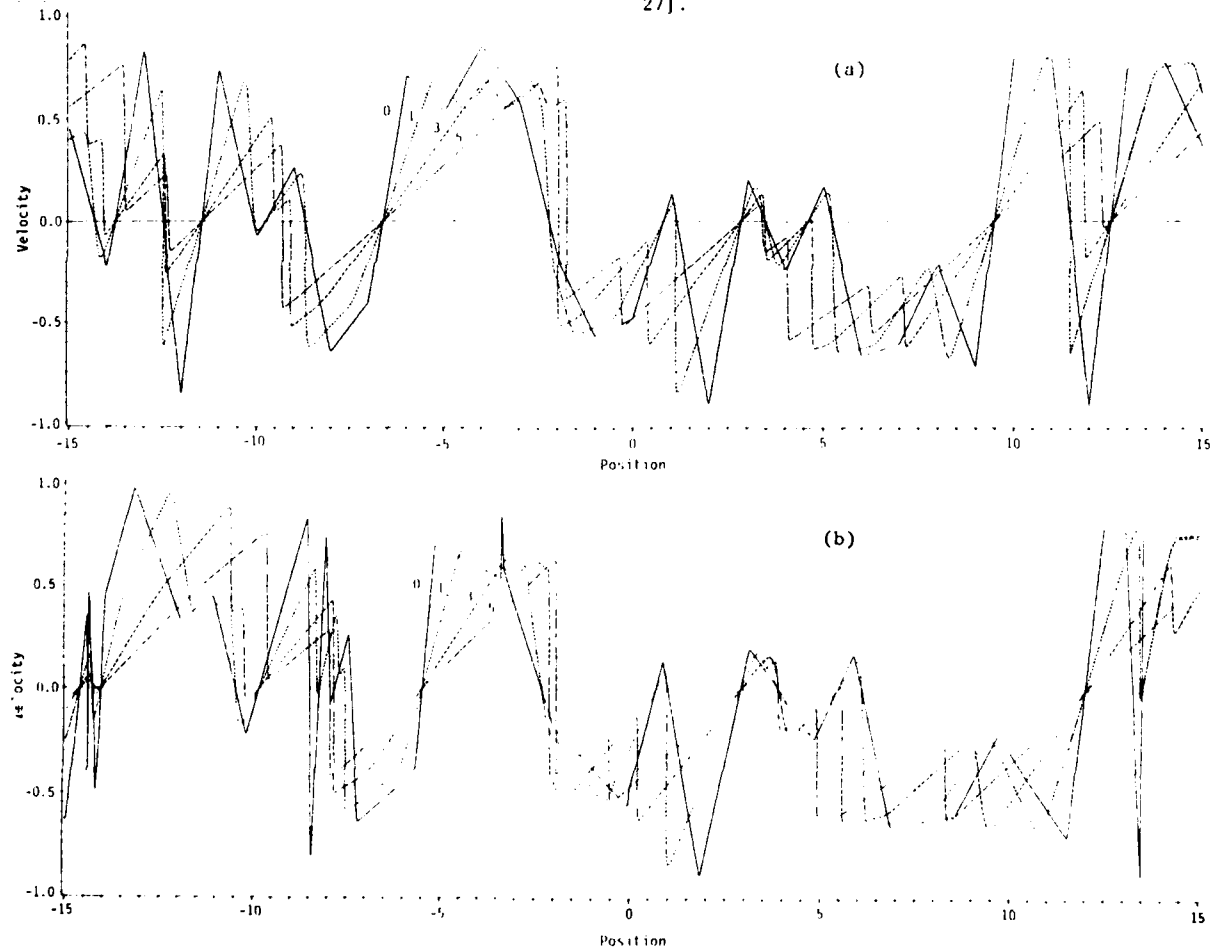


Figure 1. Comparison of velocity profiles for short time:  $t = 0, 1, 3, 5$ .

(a) For Thomas initial conditions  
(b) For modified Thomas initial conditions

The modified Thomas initial conditions are selected with the uniformly (0,2) distributed  $\{d_n\}$  being renormalized such that over each ensemble member  $\langle d_n \rangle = d = 1$ . Each member is selected on a periodic domain of length  $2L = 200d$ , the domain size selected for the Thomas initial conditions [44, 45, 18, 20]. Using a solution over a periodic domain allows an investigation of the spectral properties of Burgers' equation without addressing issues concerning the use of the Fourier transform over a finite domain.

The differences between the velocity profiles for Thomas and modified Thomas initial conditions are shown in Figure 1 for short times. The values of the  $\{u_n\}$  are identical in Figures 1(a) and 1(b), being selected at random from a uniform (-1,1) distribution, as explained above. The fixed spatial mesh  $\{x_n - x_{n-1}\} = d = 1$  for  $t = 0$  is apparent in Figure 1(a), as is the random spatial mesh  $\{x_n - x_{n-1}\} = \{d_n\}$ ,  $\langle d_n \rangle = 1$  in Figure 1(b) with  $\{x_n - x_{n-1}\}$  selected as explained above. Both Figures 1(a) and 1(b) show the temporal evolution of velocity profiles at  $Re_0 = \langle d_n \rangle u_0 / \nu = 400$  with  $u_0 = \sup |u_n| = 1$ . The effect of the distribution of spatial scales on the velocity field and thence on the spectral properties for modified Thomas initial conditions were the object of the present study.

The modified Thomas initial conditions have the same initial turbulence energy as do the Thomas ones, a consequence of the  $\{u_n\}$  being selected from the same distribution and independently of the  $\{d_n\}$  (see Appendix A). The distribution of that energy is quite different, however, and one would therefore expect an effect of the initial conditions on the turbulence energy decay. Such is the case.

Three inviscid ingredients provide a basis for the explanation (see, e.g., [53]):  
 (i) corners  $u_n$  move at a constant speed until they form or are swept up by a shock,  
 (ii) segments with negative slopes form shocks, and  
 (iii)  $|u_n(t)|$  decays for shocks.

The distribution of initial length scales of modified Thomas conditions insures that more shocks will form much sooner than for Thomas initial conditions. Once a shock is formed, its energy decays, and thus the energy of modified Thomas initial conditions initially decays faster than that of Thomas initial conditions. By  $t \sim 1$ , in contrast, most negative slopes for Thomas initial conditions have become shocks and an accelerated energy decay is observed, relative to modified Thomas initial conditions. The last shock can form much later for modified Thomas initial conditions, thus delaying the approach of modified Thomas initial conditions to the asymptotic decay rate which it has in common with Thomas initial conditions.

Table 1: Modified Thomas Statistics

t	$u' = \langle u^2 \rangle^{1/2}$		$\langle u_x^2 \rangle$		$\lambda = (\langle u^2 \rangle / \langle u_x^2 \rangle)^{1/2}$		$Re_\lambda = u' \lambda / \nu$	
	$Re_0=400$	$Re_0=1000$	$Re_0=400$	$Re_0=1000$	$Re_0=400$	$Re_0=1000$	$Re_0=400$	$Re_0=1000$
0	0.46904	0.46904	2.36421	2.36421	0.30505	0.30505	57.23219	143.08047
1	0.45020	0.45180	5.69081	14.14681	0.18872	0.12012	33.98509	54.27158
3	0.38009	0.38129	4.46540	11.25774	0.17987	0.11364	27.34645	43.32853
5	0.33293	0.33382	2.52408	6.37163	0.20956	0.13225	27.90740	44.14654
10	0.27110	0.27166	0.92464	2.32827	0.28193	0.17804	30.57163	48.36505
15	0.23861	0.23903	0.47594	1.19714	0.34586	0.21846	33.00973	52.21941
20	0.21774	0.21810	0.30608	0.76941	0.39357	0.24864	34.27918	54.22796
25	0.20244	0.20274	0.21366	0.53736	0.43796	0.27658	35.46457	56.07402

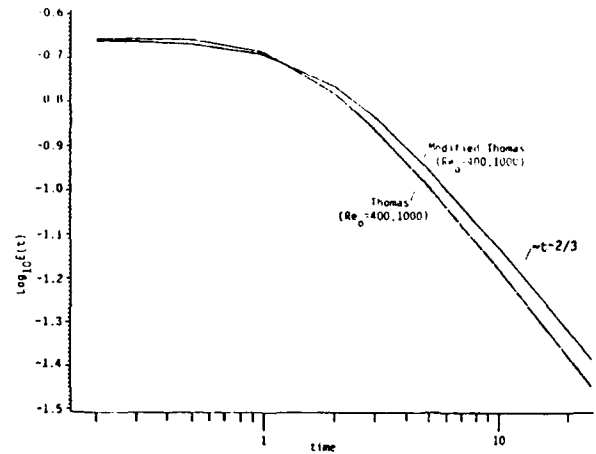


Figure 2. Comparison of energy decay curves:  
 (a) For Thomas initial conditions  
 (b) For modified Thomas initial conditions

There is no appreciable effect of Reynolds' number on the energy decay rate because  $Re_0$  is sufficiently high [1]. Both initial conditions have an energy decay rate which asymptotically approaches  $t^{-2/3}$ , consistent with the original theory of Burgers [7] and with other later research (e.g., [31, 47, 21]).

Other basic single-point statistical properties are tabulated in Table 1 for comparison with those for Thomas initial conditions [20]. The rms velocity  $u'(t)$  decays monotonically, and the effect of  $Re_0$  is in the third or fourth decimal place. The variance of  $u_x$ , in contrast, depends markedly on  $Re_0$ , increasing initially and then decreasing, with  $\langle u_x^2 \rangle_{max}$  being much higher for  $Re_0 = 1000$  than for 400. The Taylor microscale  $\lambda(t)$  may be determined from energy decay rates. The values in Table 1 were obtained from

$$\lambda^2(t) = \frac{\langle u^2 \rangle}{\langle u_x^2 \rangle} = \frac{\int_0^\infty E(k,t) dk}{\int_0^\infty k^2 E(k,t) dk}$$

estimated by

$$\sum_{f=0}^{N-1} E(k=2\pi f / \Delta x, t) / \sum_{f=0}^{N-1} k^2 E(k=2\pi f / \Delta x, t).$$

With  $\lambda$  initially decreasing and then increasing, consonant with the behavior of  $\langle u_x^2 \rangle$ ,  $Re_\lambda$  decreases sharply at first -- the decrease being the more precipitous, the higher the  $Re_0$  -- and then gradually increases. An increase in  $Re_0$  by a factor of 2.5 produces an asymptotic increase in  $Re_\lambda$  by a factor of 1.6. Burgers (eq. (94) of [7]) derived

$$\lambda^2 = 3\nu t,$$

which together with the  $\langle u^2 \rangle$  asymptote of  $t^{-2/3}$  gives

$$Re_\lambda = \langle u^2 \rangle^{1/2} \lambda / \nu \sim 3^{1/2} t^{1/6} / \nu^{1/2},$$

from which follows

$$\frac{Re_\lambda(Re_0=1000)}{Re_\lambda(Re_0=400)} = \left( \frac{1000}{400} \right) = 1.6.$$

Although the evolution of  $Re_\lambda$  is available in the literature, for instance, from modified 0-4th cumulant expansions [33] ( $t^{0.08} - 0.13$ ) and from the finite difference computations of Mizushima and Saito [32] ( $t^{0.106}$ ), the results presented here ( $t^{0.169}$ ) are the first computations accurate enough to confirm the  $Re_\lambda \sim t^{1/6} / \nu^{1/2}$  asymptote for Burgers' equation. Burgers (eq. (92b) of [7]) also found  $\langle u_x^2 \rangle \sim t^{-1/3}$ . These asymptotes may be compared with those calculated from the last four points and presented in Table 2. Typical values of  $Re_\lambda$  for wind tunnel and locally isotropic turbulence for comparison with values in Table 1 are 50 by Van Atta and Chen [56], 70 by Uberoi [54], and 500 by Kistler and Vrebalovich [22], compared to about 2000 by Grant, Stewart, and Moilliet [11].

The above statistical measures may be compared with those for Thomas initial conditions [20] as follows (see also Figure 2). The variance  $\langle u_x^2 \rangle$  for Thomas initial conditions [20] is initially much smaller but grows to a much higher maximum and then decays to lower values than do those for the modified Thomas. The initial decay of  $\lambda(t)$  to a minimum is more rapid for the Thomas, but then its gradual growth recovers to that for the modified Thomas. Consequently,  $Re_\lambda$  for Thomas initial conditions begins roughly a factor of 2 higher but ends (at  $t = 25$ ) slightly lower than  $Re_\lambda$  for modified Thomas.

Table 2: Asymptotic statistics

	$Re_0=400$	$Re_0=1000$
$\langle u^2 \rangle$	0.3187 $t^{-0.6367}$	0.3211 $t^{-0.6388}$
$\langle u_x^2 \rangle$	36.1446 $t^{-1.5945}$	91.3089 $t^{-1.5968}$
$\lambda$	0.09391 $t^{0.4789}$	0.05929 $t^{0.4798}$
$Re_\lambda$	21.2070 $t^{0.1606}$	33.5920 $t^{0.1601}$

### 3. Computational Methods

Here and in [20]  $u(x,t)$  has been computed with high accuracy (greater than 10 decimal places) on a fine spatial mesh ( $200/2^{16}$ ) for a quite large ensemble (50 members, which gave results that were imperceptibly distinct from preliminary studies with 100 members), allowing spectral resolution far into the viscous cutoff.

The consistent discrete Fourier transform pair which was used in the present computations was

$$\hat{u}(k=2\pi f/N\Delta x, t) = \Delta x \sum_{n=0}^{N-1} u(x=n\Delta x, t) \exp[-i2\pi fn/N]$$

$$f = \{0, 1, \dots, N-1\}$$

$$u(x=n\Delta x, t) = \frac{1}{N\Delta x} \sum_{f=0}^{N-1} \hat{u}(k=2\pi f/N\Delta x, t) \exp[i2\pi fn/N]$$

$$n = \{0, 1, \dots, N-1\}.$$

Computations were implemented on the FPS-164 using FFT techniques [28] such as have been used in turbulence by Van Atta and Chen [55]. Energy spectra were computed from

$$E(k=2\pi f/N\Delta x, t) = \hat{u}^*(k, t) \hat{u}(k, t) / N\Delta x,$$

which is the Fourier transform of the autocorrelation function

$$Q(r=n\Delta x, t) = \frac{1}{N\Delta x} \sum_{f=0}^{N-1} E(k=2\pi f/N\Delta x, t) \exp[i2\pi fn/N]$$

$$n = \{0, 1, \dots, N-1\}$$

$$= \langle u(x, t) u(x+r, t) \rangle.$$

The dissipation spectrum  $D(k, t)$  can be computed by first computing  $u_x(x, t)$  and then employing the Fourier transform (in this case, FFT) or by recognizing that  $D(k, t) = k^2 E(k, t)$ . The latter is obviously simpler and computationally less intensive. That it is also more accurate at a given spatial mesh may be seen by recognizing that a spatial mesh just fine enough to replicate the steep velocity profile through a shock is insufficiently fine to provide a good representation of the velocity gradient itself. A demonstration of this may be seen in Keleti and Reed [19].

The spectral transfer

$$T(k, t) = -\frac{1}{2} ik [\hat{u}(k, t) \hat{u}^*(k, t) - \hat{u}^{2*}(k, t) \hat{u}(k, t)] / N\Delta x$$

is the Fourier transform of

$$-\frac{1}{2} \partial \langle u(x, t) u^2(x+r, t) \rangle - \langle u^2(x, t) u(x+r, t) \rangle / \partial r.$$

The cumulative transfer spectra

$$S(k=2\pi f_0/N\Delta x, t) = -\int_0^k T(k', t) dk'$$

$$= \sum_{f=0}^{f_0} T(k=2\pi f/N\Delta x, t)$$

$$f_0 < \frac{1}{2} N \quad (k < \pi/\Delta x)$$

These terms appear in the spectral form of the von Kármán-Howarth equation for Burgers' equation,

$$dE(k, t)/dt = T(k, t) - 2\nu k^2 E(k, t).$$

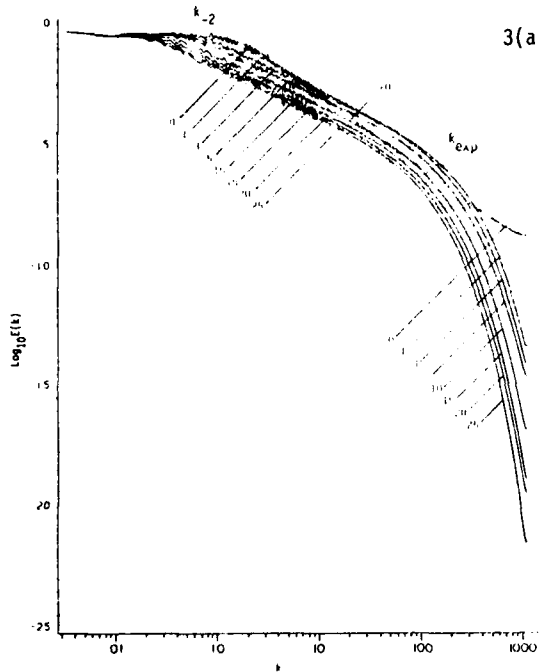
### 4. Energy Spectra

The energy spectrum of Burgers' equation for modified Thomas initial conditions is characterized by:

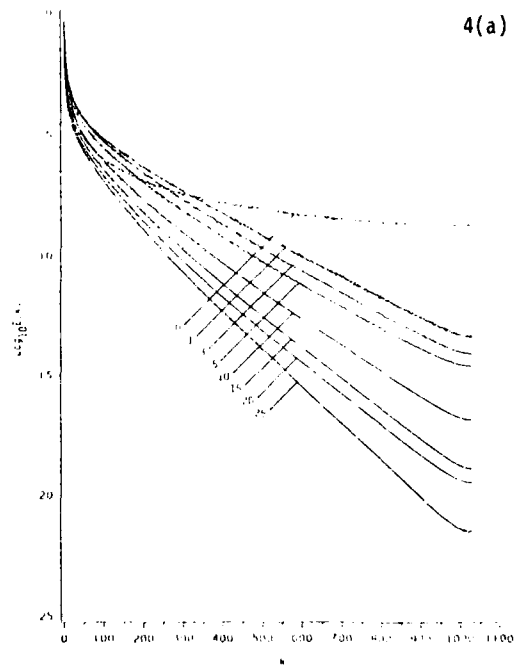
- (i) a low wave-number white-noise energy-containing subrange,  $0 < k < k_{-2}$  (Figure 3),
- (ii) a  $k^{-2}$  subrange,  $k_{-2} < k < k_{exp}$  (Figure 3), and
- (iii) an exponential viscous cutoff,  $k_{exp} < k$  (Figure 4).

The small white-noise domain is characteristic of energy spectra evolving from both Thomas [18, 20] and modified Thomas initial conditions; although the modified Thomas has more total energy, the spectra here and in Keleti and Reed [20] have the same low wave-number level. The location of the transition wave number  $k_{-2}$  at which the white noise gives way to the  $k^{-2}$  subrange decreases with increasing time at a given  $Re_0 = 400, 1000$ , a qualitative observation which is quantified in Figures 3(a) and 3(b).

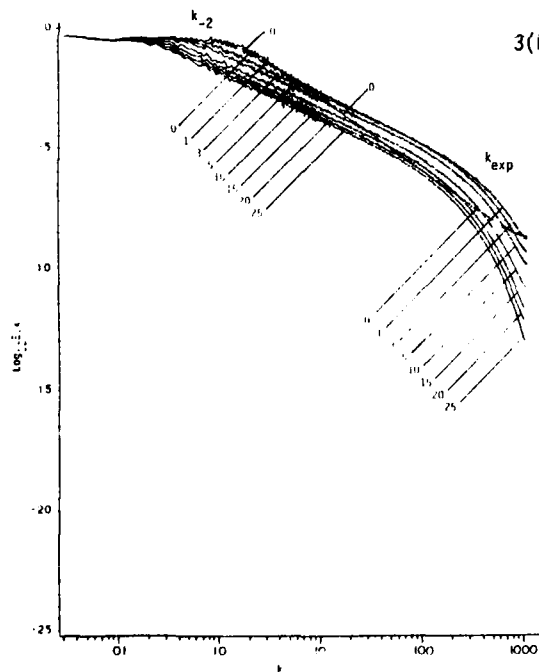
Evolution of Energy Spectra:  
 $E(k, t)$  for  $t=0, 1, 3, 5, 10, 15, 20, 25$



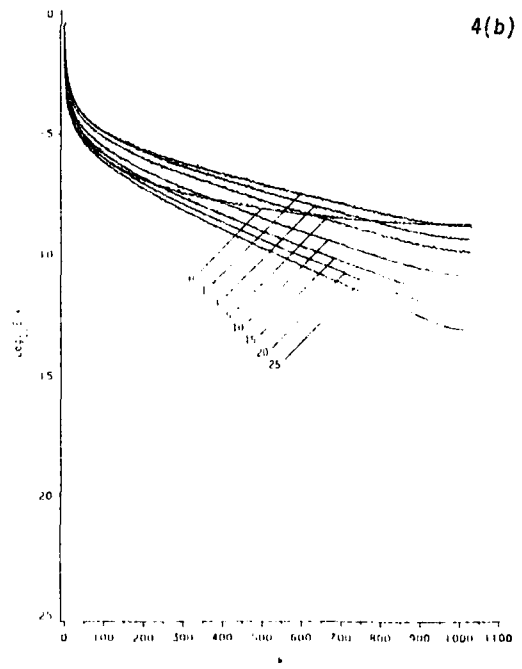
3(a)



4(a)



3(b)



4(b)

Figure 3. Log-Log plot emphasizing white noise and  $k^{-2}$  subranges:  
 (a) at  $Re_0=400$   
 (b) at  $Re_0=1000$

Figure 4. Semi-Log plot emphasizing exponential viscous cutoff:  
 (a) at  $Re_0=400$   
 (b) at  $Re_0=1000$

Burgers was the first to obtain the  $k^{-2}$  spectrum (eq. (85b), [7]). The  $k^{-2}$  subrange is usually discussed by comparing and contrasting it with the  $k^{-5/3}$  subrange for three-dimensional isotropic turbulence [24, 1, 14, 34, 49]. We elect instead to discuss it in straightforward terms of properties of Fourier transforms.

The Fourier transform of Burgers' equation is

$$d\hat{u}(k,t)/dt + ik \int_{-\infty}^{\infty} \hat{u}(m,t) \hat{u}(k-m,t) dm / 4\pi = -\nu k^2 \hat{u}(k,t)$$

with  $\hat{u}(k,t)$  the Fourier transform of  $u(x,t)$ . The asymptotic behavior of  $\hat{u}(k,t)$  may be seen by considering the limits  $k \rightarrow 0$  and  $k \rightarrow \infty$  in this equation.

The former yields

$$\lim_{k \rightarrow 0} d\hat{u}(k,t)/dt = 0$$

under the mild restriction that the energy density of the field be bounded, i.e.,

$$\lim_{L \rightarrow \infty} (1/2L) \int_{-L}^L u^2(x,t) dx < C.$$

Although this implies nothing about the wave-number dependence of  $E(k,t) = \hat{u}^*(k,t) \hat{u}(k,t)$  for small  $k$ , it does indicate that the large scale structures are slowly varying and that the mean velocity is time invariant, i.e.,  $\hat{u}(0,t) = \langle u \rangle$ .

The latter yields a one-dimensional version of the weak turbulence limit,

$$\lim_{k \rightarrow \infty} \hat{u}(k,t) = \hat{u}(k,0) \exp(-\nu k^2 t),$$

provided the inertial term (the convolution term with prefactor  $k$ ) grows less rapidly than the dissipation term (the energy term with prefactor  $k^2$ ). This is a variant of plausible arguments sometimes invoked for spectral behavior at high wave numbers [1, 34, 49]. Unfortunately for such arguments, there is the further implication that

$$\lim_{k \rightarrow \infty} E(k,t) = E(k,0) \exp(-2\nu k^2 t),$$

in clear disagreement with the results in Figure 4. The exponential viscous cutoff makes clear that convolution terms cannot be ignored in the high wave-number limit and must be handled with care in the theoretical estimation of spectral behavior. Consequently, equations which have solutions which behave like solutions to Burgers' equation -- equations which are unforced or are weakly forced on scales larger than typical intershock distances (macroscales) -- lead to fallacious high wave-number spectra if the convolution term is neglected on the basis of physical arguments, dimensional analysis, and ordering arguments predicated only upon local scales.

Finally, the mathematical form of the high wave-number energy spectra evolving from Thomas [18, 20] and from modified Thomas (see especially Figure 4) statistical initial conditions agrees with that for a single Burgers' "eddy" [2, 42]; Mizushima [31] also obtained an exponential viscous cutoff as a consequence of similarity and invariance of the large scale motions.

Convolution produces broadening and smoothing effects (pp 143-149 of [4]). The energy spectrum of a function with jumps has an asymptote of  $k^{-4}$  (as does the Thomas initial condition  $E(k,0)$ ), whereas one with corners has an asymptote of  $k^{-2}$  (which is the asymptote to which the energy spectra  $E(k,t)$  quickly evolve in the absence of viscosity). Functions with discontinuities intermediate in severity between jumps and corners may have intermediate asymptotes. Modified Thomas initial conditions have corners, but with  $\{d_n\}$  selected on  $(0,2)$ , jumps are not excluded (as they are for Thomas initial conditions), and there is a  $k^{-3}$  asymptote.

Moreover, if the  $m$ th derivative of a function becomes impulsive, then for large  $k$  its transform behaves as  $|k|^{-m}$  and its energy spectrum as  $|k|^{-2m}$ . As solutions to Burgers' equation for  $\nu > 0$ ,  $t > 0$  are everywhere smooth (all derivatives exist), their energy spectra must fall off faster than any polynomial at large  $k$ . This the above exponential viscous cutoff does.

The  $k^{-2}$  subrange passes smoothly into the exponential viscous cutoff at a transition wave number  $k_{exp}$ , which decreases with time. The bandwidth of the  $k^{-2}$  subrange remains virtually constant (Figure 3), with the migration of the center frequency to the lower wave numbers thus accounting for the energy decay.

An exponential viscous cutoff for three-dimensional isotropic turbulence has been proposed by Dugstead (p. 239 of [14] and derived by Tatsumi and Kida [47] for the modified 0-4th cumulant expansion. Both Corrsin [10] and Pao [35] have obtained exponential functions for high wave numbers with, however, powers of  $k$  in the exponential; Tatsumi, Kida, and Mizushima [48] obtained  $\exp(-\beta k^{1.5})$  by multiple-scale cumulant expansion. The so-called Gaussian falloff has also been derived by Saffman [42], and is widely used in studies of Burgers' equation (e.g., [30, 33, 59]).

The exponential viscous cutoff for Burgers' equation dates from one of his early analyses (eq. (85a) [7]) in the form  $A/\sinh^2 \beta k$ ; Benton [2], Saffman [41], and Mizushima [31] subsequently obtained the same form. Tokunaga's [51] two-equation one-dimensional compressible turbulence investigation led to an exponential viscous cutoff, as have several closure hypotheses (e.g., [33]). Love [26], in the context of subgrid-scale modelling of Burgers' equation, shows without comment a log-semi plot with a high wave-number band which is nearly linear. Other than Love, there have been no computations into the high wave-number domain until Keleti and Reed's [18, 20] studies of the Thomas initial condition, although a belief in the exponential cutoff was widespread. The situation may be likened to that for the Navier-Stokes equations, except that the requisite delicate measurement with sufficiently high spatial and temporal resolution of fluctuating velocity fields at sufficiently high  $Re_\lambda$  had been lacking. Indeed, until 1962, the  $k^{-5/3}$  spectrum had not been comfortably confirmed [11]. The difficulty cannot be overcome through direct numerical simulation of the Navier-Stokes equations because of the hardware requirements of high  $Re_\lambda$  computations.

## 5. Dissipation Spectra

With  $D(k,t)$  given by  $k^2 E(k,t)$  and with  $E(k,t)$  already described, little needs to be said about the dissipation spectrum. It is characterized by

- (i) a quadratic low wave-number domain (Figure 5),
- (ii) a white-noise subrange (Figure 5), and
- (iii) a viscous cutoff of  $k^2 \exp(-\alpha k)$  (Figure 6).

Dissipation spectra for Burgers' equation have customarily been discussed in terms of a uniform distribution of dissipation described in (ii). Equipartition of dissipation obviously requires two caveats, *viz.*, (i) and (iii), with (i) conceivably restricted to Thomas and modified Thomas initial conditions.

The dissipation spectrum  $D(k,t)$  is of special interest in the high wave-number range, for which computations for small ensembles and relatively coarse meshes [16, 17, 44, 45, 43] were admittedly lacking until recently [18, 20].

## 6. Spectral Transfer and Cumulative Spectral Transfer

Spectral transfer along the energy spectrum is at the heart of an understanding of the mechanics of homogeneous turbulence [12, 1, 14, 34]. Two-point closures which focus on the structure of homogeneous turbulence require not only empirical results for the energy spectrum, they require them also for the transfer spectrum. The temporal evolution of the two-point spatial correlation of third order,  $\langle u^2(x,t)u(x+r,t) \rangle$  has been computed using the Lagrangian history direct interaction approximation of Kraichnan [25] by Walton [57] and has been computed from exact solutions [45] on what, by comparison to the present spatial mesh, may be described as coarse; and as there was an ensemble of only 12 realizations, no attempt was then made to compute transfer spectra. Subsequently,  $T(k,t)$  were computed for single-point Gaussian initial conditions [46], but those results were not adequate for the present purposes because they were also for a small ensemble (12 realizations), as well as being limited in  $k$ -space and in accuracy.

The spectral transfer function  $T(k,t)$  is shown in Figures 7 and 8. The former emphasizes how  $T(k,t)$  evolves in the  $k^{-2}$  energy subrange, whereas the latter emphasizes spectral transfer in the viscous cutoff range. The effect of  $Re_0$  is to extend the far wave-number range into which energy is transferred from the low wave modes. The higher the value of  $Re_0$ , the less  $T(k,t)$  extends into the viscous cutoff range and the more  $T(k,t)$  is dominated by inviscid mechanics typified by  $E(k) \sim k^{-2}$  (cf. Figures 7(b) and 7(a)). The more rapid falloff of  $T(k,t)$  with increasing viscosity in the viscous cutoff range is clear by comparing Figures 8(a) and 8(b). Initial spectral transfer functions  $T(k,0)$  are quite noisy, but their general location (Figures 7, 8) provides a ready reference for comparing  $T(k)$  at different  $Re_0$ , as well as different  $t$ , much as  $E(k,0)$  does for  $E(k,t;Re_0)$ . Because  $T(k,t)$  and  $S(k,t)$  take on negative values, log-log and log-semi coordinates can be used only if the absolute values are plotted or if the negative values are omitted. The latter option was chosen here. The log-log and log-semi plots (Figure 7)

of  $T(k,t)$  do not show any power law subranges but do reflect the more extensive viscous cutoff at  $Re_0 = 400$  and the more extensive inviscid subrange at  $Re_0 = 1000$ . The log-semi plots (Figure 8), in contrast, suggest exponential cutoffs for  $T(k,t)$ , just as  $E(k,t)$  has an exponential viscous cutoff. However, the log-semi plots of dissipation spectra (Figure 6) also give the appearance of being exponential but are known to be of the form  $k^2 E(k) \sim k^2 \exp(-\beta k)$ . Upon closer scrutiny, several of the  $T(k,t)$  lines (Figure 8) may be seen to have a slight curvature, comparable to that of the  $D(k,t)$  plots (Figure 6). Consequently, one infers that  $T(k,t) \sim P_m(k) \exp(-\beta k)$  for high wave numbers, with  $P_m(k)$  a polynomial in  $k$ . For a single "eddy", the asymptotic curve according to Benton [2] would have the form  $(k^2 - k) \exp(-\beta k)$ .

The cumulative spectra are shown in Figures 9 and 10, with similar comments holding.

Log-semi plots of both  $T(k,t)$  and  $S(k,t)$  are displayed in Figures 11 ( $Re_0 = 400$ ) and 12 ( $Re_0 = 1000$ ), for short times in 11a and 12a and longer times in 11b and 12b. The forms, except for the "noisy" nature of  $T(k,t)$ , are quite like those for three-dimensional transfer spectra [36, 54, 56, 13, 48]. The most spectacular observation has little physics but reflects the well known smoothing role played by integration. More stringent windowing -- or french curve smoothing -- would yield  $T(k,t)$  vs.  $k$  resembling even more the published less noisy three-dimensional results. The only window we have used for  $T(k,t)$  is that used throughout, as in [20], which does not affect the visual character of the curves.

For the modified Thomas initial conditions, the spectrum of initial eddy sizes assures that for small  $k$ , its spectral transfer is greater than that for Thomas initial conditions (due to the greater energy distributed in the larger "eddies"). This "signature" of the modified Thomas initial conditions persists through all of the times for which the spectra were evaluated. The other feature distinguishing  $T(k,t)$  for modified Thomas from Thomas initial conditions is the lack of spikes for small times.

## 7. Discussion

The modified Thomas initial conditions introduced here provide for a distribution of initial spatial scales, whereas a period of evolution is necessary for Thomas initial conditions to evolve into a state having a distribution of spatial scales. This has consequences for the energy decay rate (Figure 2), for the evolution of the Taylor microscale  $\lambda(t)$  (Table 1), and for the corresponding turbulence Reynolds' number  $Re_\lambda(t) = u'\lambda/\nu$  (Table 1).

The implications of the distribution of initial spatial scales -- which may be likened to initial eddy sizes -- on the initial turbulence energy spectrum are profound. For all but short times, nevertheless, the energy spectra for the two classes of initial conditions are qualitatively quite similar. This suggests that they are two-point statistical properties which, when appropriately normalized, are characteristic of random solutions to Burgers' equation ("turbulence") and not characteristic of initial conditions ("specific grid geometry") [1].

Evolution of Dissipation Spectra:  
 $D(k,t)=k^2 E(k,t)$  for  $t=0,1,3,5,10,15,20,25$

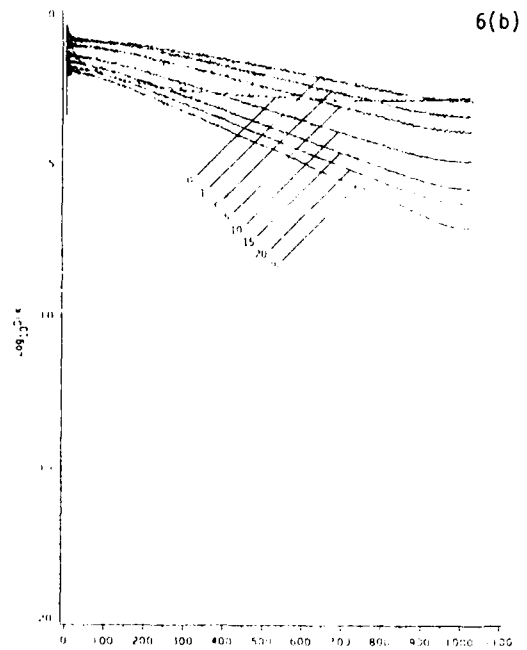
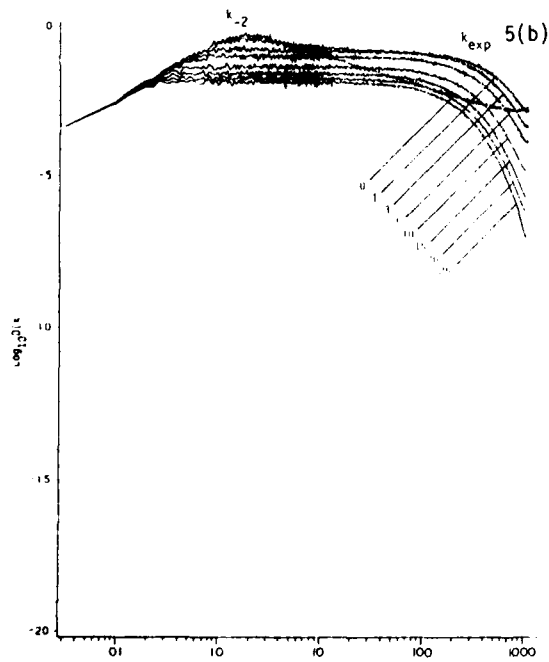
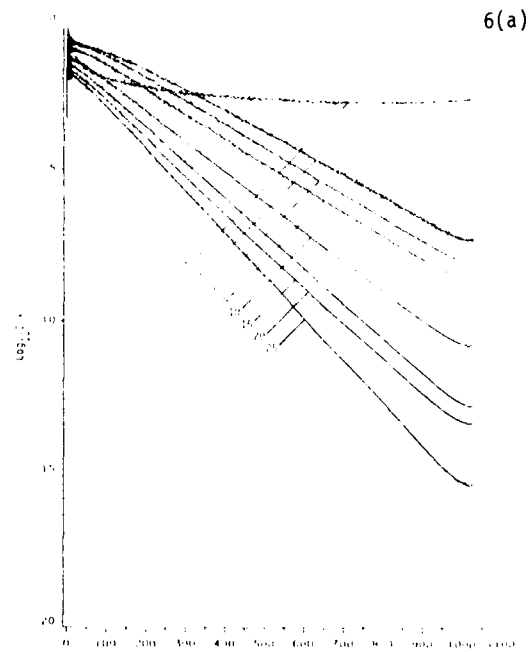
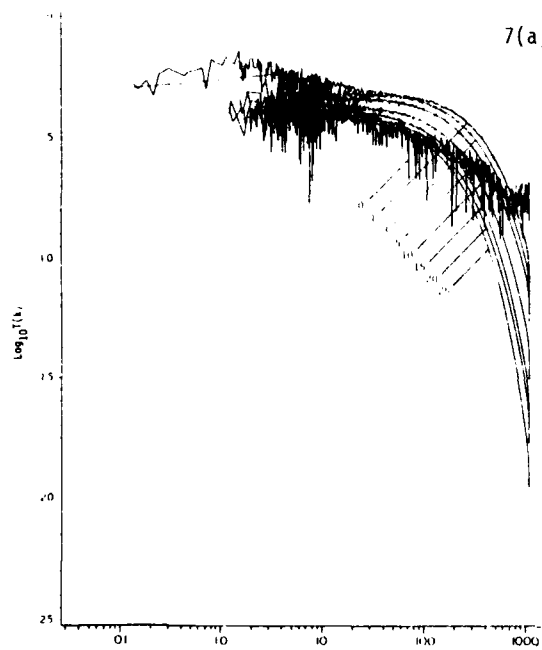


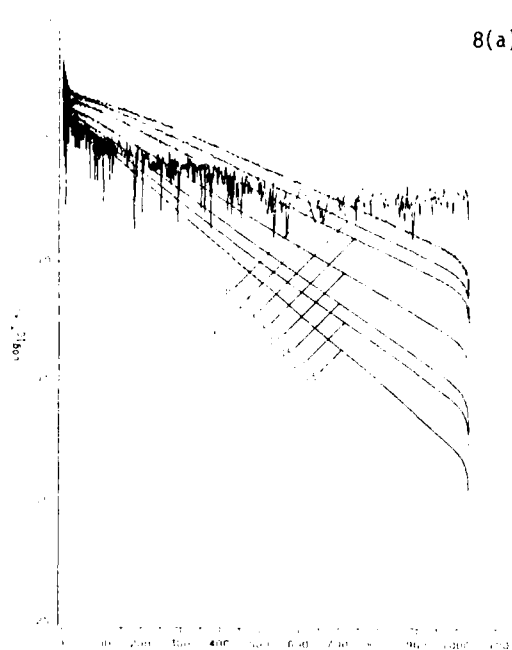
Figure 5. Log-Log plot emphasizing equipartition subrange for dissipation:  
 (a) at  $Re_0=400$   
 (b) at  $Re_0=1000$

Figure 6. Semi-log plot emphasizing effect of viscosity on dissipation at high wave numbers:  
 (a) at  $Re_0=400$   
 (b) at  $Re_0=1000$

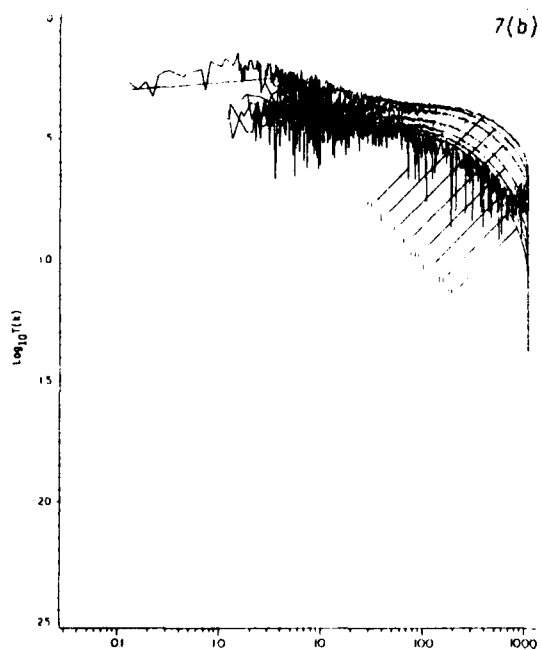
Evolution of Spectral Transfer:  
 $T(k, t)$  for  $t=0, 1, 3, 5, 10, 15, 20, 25$



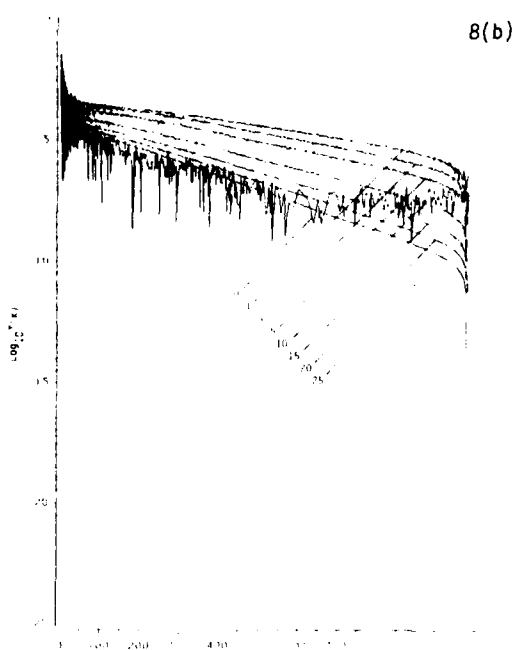
7(a)



8(a)



7(b)

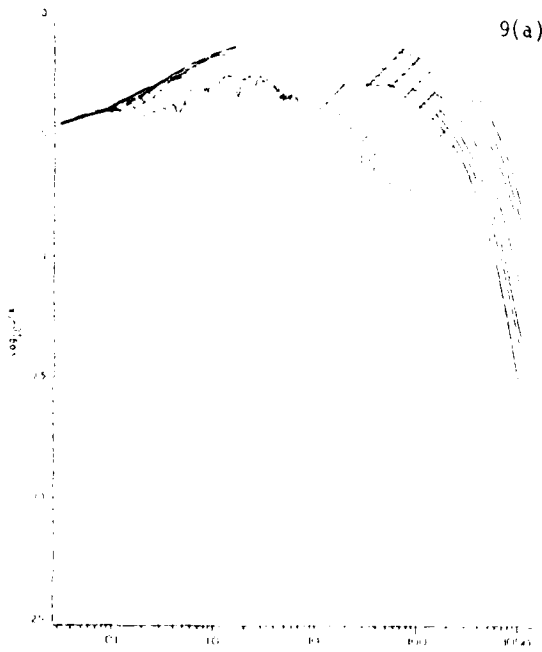


8(b)

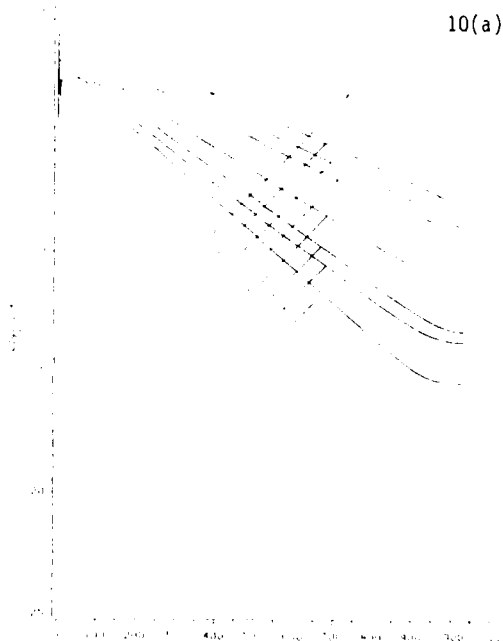
Figure 7. Log-log plot:  
 (a) at  $Re_0=400$   
 (b) at  $Re_0=1000$

Figure 8. Semi-log plot:  
 (a) at  $Re_0=400$   
 (b) at  $Re_0=1000$

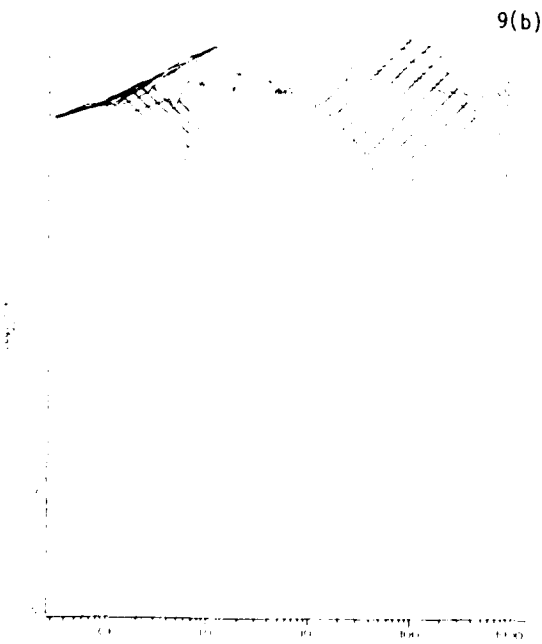
Evolution of Cumulative Transfer Spectra:  
 $S(k,t) = -\int_0^k T(k',t) dk'$  for  $t=0,1,3,5,10,15,20,25$



9(a)



10(a)



9(b)



10(b)

Figure 9. Log-Log plot:  
 (a) at  $Re_0=400$   
 (b) at  $Re_0=1000$

Figure 10. Semi-Log plot:  
 (a) at  $Re_0=400$   
 (b) at  $Re_0=1000$

Evolution of Transfer and Cumulative Transfer Spectra:  
 $T(k,t)$ ,  $S(k,t)$  for  $t=0,1,3,5,10,15,20,25$

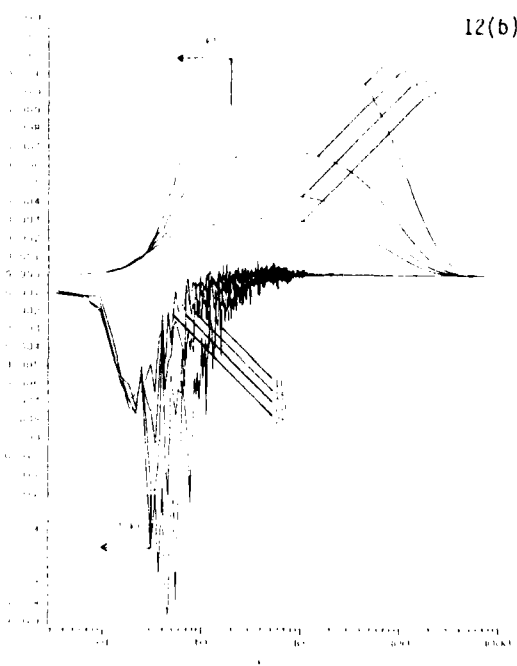
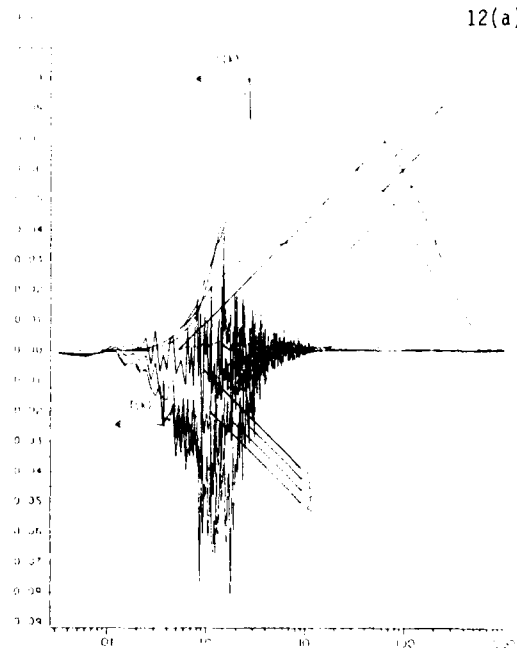
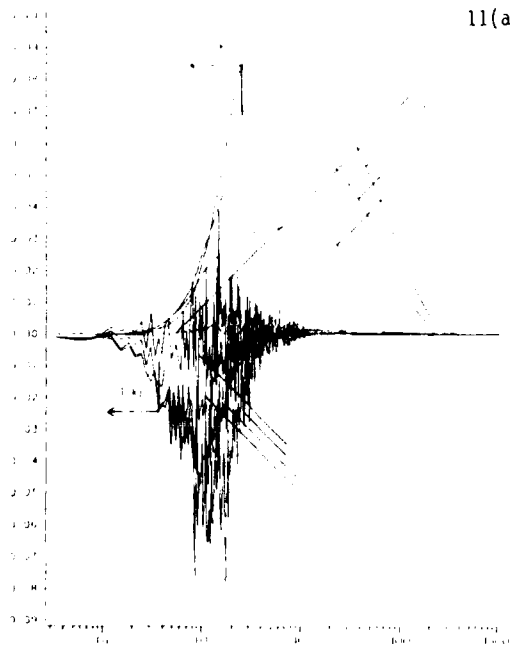


Figure 11. Log-Semi plot at  $Re_0=400$ :  
 (a)  $t=0,1,3,5$   
 (b)  $t=10,15,20,25$

Figure 12. Log-Semi plot at  $Re_0=1000$ :  
 (a)  $t=0,1,3,5$   
 (b)  $t=10,15,20,25$

These spectra' results (Figures 3, 4), together with those for Thomas initial conditions [20], thus invite formulation of a conceptual framework which would provide a unifying mathematical description of the results for Burgers' equation which would be (virtually) independent of initial conditions.

The dissipation spectra for the two classes of initial conditions, being simply and directly related to the energy spectra, have corresponding similarities and dissimilarities. The most noteworthy feature of  $D(k,t)$  for modified Thomas initial conditions is the dissipative equipartition on  $k_{-2} < k < k_{exp}$ , which it has in common with that for Thomas initial conditions [20]. These observations themselves are hardly new. What is novel is the discovered limit  $k_{exp}(t, Re_0)$  and the quantitative demonstration of the asymptote  $k^2 \exp(-\alpha(t)k)$  as a function of  $Re_\lambda$ .

Spectral transfer results for Burgers' equation have seldom been presented (but see, e.g., [39]), other than very limited ones [46], before our study of Thomas initial conditions [18, 20]. Except for short times, spectral transfer for Thomas [20] and for modified Thomas is hardly dissimilar. Initial transients, as expected, are strongly dependent on initial conditions.

In conclusion, through the use of numerical procedures to compute the exact solution to Burgers' equation with random initial conditions, spectral solutions over a range of 20 decades -- up to 16 decades in the viscous cutoff at  $Re_0 = 400$  -- have been computed for the modified Thomas initial conditions. These results reveal unequivocally an exponential viscous cutoff for Burgers' equation.

#### Acknowledgements:

The first author was supported during the course of this research by a Shell Fellowship, for which we are both indebted. It is also a pleasure for us to acknowledge the encouragement of J. W. Johnson and the cooperation of D. W. Bearth, both of whom helped in different ways to hasten completion of the research. Finally, we are indebted to H. Haddad who carried out extensive computations on earlier versions of the velocity and spectral codes [18].

#### Appendix A:

The expectation for the initial turbulence energy for the Thomas and modified Thomas initial conditions can be determined from the expectation of the energy for an individual interval, as the velocity endpoints are statistically independent. Taking the linear velocity defined between the endpoints  $u_{n-1}$  and  $u_n$  over the segment  $d_n$ , one has at  $t=0$  an energy of

$$E_n = \left\{ \int_0^{d_n} [(u_n - u_{n-1})x/d_n + u_{n-1}]^2 dx \right\} / d_n \\ = [u_n^2 + u_n u_{n-1} + u_{n-1}^2] / 3.$$

From statistical independence and the assumption that the endpoints are selected with zero mean, one obtains

$$E(t=0) = \langle E_n \rangle = (2/3) \cdot u_n^2 = 2/9$$

because  $\langle u_n^2 \rangle = 1/3$  for the uniform distribution of the Thomas and modified Thomas initial conditions.

#### References:

1. G.K. Batchelor, The Theory of Homogeneous Turbulence, Cambridge Univ. Press, Cambridge (1953).
2. E.R. Benton, "Solutions illustrating the decay of dissipation layers in Burgers' nonlinear diffusion equation", Phys. Fluids 10, 2113-2119 (1967).
3. E.R. Benton and G.W. Platzman, "A table of solutions of the one-dimensional Burgers equation", Quart. Appl. Math. 30, 195-212 (1972).
4. R. Bracewell, The Fourier Transform and Its Applications, McGraw-Hill, New York (1965).
5. J.M. Burgers, "Mathematical examples illustrating relations occurring in the theory of turbulent motion", Verh. Kon. Nederl. Akad. v. Wetenschappen, Amsterdam, Afd. Natuurk. (1st Sect.) 17, No.2, 1-53 (1939).
6. J.M. Burgers, "A mathematical model illustrating the theory of turbulence", Advances in Applied Mechanics, vol. 1, R. von Mises and T. von Karman (eds.) Academic, New York, 171-199 (1948).
7. J.M. Burgers, "Correlation problems in a one-dimensional model of turbulence I-IV", Proc. Acad. Sci. Amsterdam, 53, 247-260, 393-406, 718-742 (1950).
8. J.M. Burgers, The Nonlinear Diffusion Equation, Reidel, Dordrecht (1974).
9. J.D. Cole, "On a quasi-linear parabolic equation occurring in aerodynamics", Quart. Appl. Math. 9, 225-236 (1951) (see also P.A. Lagerstrom, J.D. Cole, and L. Trilling, Problems in the theory of viscous compressible fluids, Cal. Inst. Tech., Pasadena, CA, (1949)).
10. S. Corrsin, "Further generalization of Onsager's cascade model for turbulent spectra", Phys. Fluids 7, 1156-1159 (1964).
11. H.L. Grant, R.W. Stewart, and A. Moilliet, "Turbulence spectra from a tidal channel", J. Fluid Mech. 12, 241-263 (1962).
12. W. Heisenberg, "Zur statistischen Theorie der Turbulenz", Z. Physik 124, 628-657 (1948).
13. K.N. Helland, C.W. Van Atta and G.R. Stegen, "Spectral energy transfer in high Reynolds number turbulence", J. Fluid Mech. 79, 337-359 (1977).
14. J.O. Hinze, Turbulence, 2nd ed., McGraw-Hill, New York (1975).
15. E. Hopf, "The partial differential equation  $u_t + uu_x = \nu u_{xx}$ ", Commun. Pure Appl. Math. 3, 201-230 (1950).

16. D.T. Jeng, A Study of Burgers' Model Equation of Turbulence, Magistral thesis, U. Minn. (1965).
17. D.T. Jeng, R. Foerster, S. Haaland, and W.C. Meecham, "Statistical initial-value problem for Burgers' model equation of turbulence", *Phys. Fluids* 9, 2114-2120 (1966).
18. S. Keleti and X B Reed, Jr., "Spectral considerations for exact random solutions of Burgers' equation at  $Re_0=400$ , including high wave numbers", 5th Symposium on Turbulent Shear Flows, Cornell Univ. (1985).
19. S. Keleti and X B Reed, Jr., "Exact solutions to Burgers' equation at high Reynolds' numbers: II. Efficient accurate numerical evaluation", to be submitted (1986).
20. S. Keleti and X B Reed, Jr., "Evaluation of spectra for large ensembles of exact solutions to Burgers' equation for Thomas initial conditions", to be submitted (1986).
21. S. Kida, "Asymptotic properties of Burgers turbulence", *J. Fluid Mech.* 93, 337-377 (1979).
22. A.L. Kistler and T. Vrebalovich, "Grid turbulence at large Reynolds numbers", *J. Fluid Mech.* 26, 37-47 (1966).
23. D.E. Knuth, The Art of Computer Programming, vol. 2 Seminumerical Algorithms, Addison-Wesley, Reading, Mass., pp 9-37 (1981).
24. A.N. Kolmogorov, "The local structure of turbulence in incompressible viscous fluid for very large Reynolds' numbers", *C. R. (Doklady) de l'Acad. des Sci. de l'URSS* 30, 301-305 (1941). (see pp 151-161 of Turbulence: Classic Papers on Statistical Theory, S. K. Friedlander and L. Topper (eds.), Interscience, New York, (1961).
25. R.H. Kraichnan, "Lagrangian-history statistical theory for Burgers' equation", *Phys. Fluids* 11, 265-277 (1968).
26. M.D. Love, "Subgrid modelling studies with Burgers' equation", *J. Fluid Mech.* 100, 87-110 (1980).
27. J.M.D. MacElroy and S. H. Suh, "Concentration and noncontinuum effects in size-exclusion partitioning", *AIChE Symp. Ser.*, No. 248, 82, 133-148 (1986).
28. M. Martell, "Computing very large FFTs efficiently on the FPS-164", *Checkpoint* 2, 5-18 (Oct. 1970, Floating Point Systems, Inc.).
29. W.C. Meecham, P. Iyer, and W.C. Clever, "Burgers' model with a renormalized Wiener-Hermite representation", *Phys. Fluids* 18, 1610-1616 (1975).
30. W.C. Meecham and A. Siegel, "Wiener-Hermite expansion in model turbulence at large Reynolds numbers", *Phys. Fluids* 7, 1178-1180 (1964).
31. J. Mizushima, "Similarity law and renormalization for Burgers' turbulence", *Phys. Fluids* 21, 512-514 (1978).
32. J. Mizushima and Y. Saito, "Numerical study of the initial condition dependence of Burgers' turbulence", *Phys. Fluids* 28, 1294-1298 (1985).
33. J. Mizushima and T. Tatsumi, "The modified zero-forth cumulant approximation for turbulence", *J. Phys. Soc. Jpn.* 50, 1765-1773 (1981).
34. A.S. Monin and A.M. Yaglom, Statistical Fluid Mechanics, vol. 2, (J.L. Lumley, ed.) MIT Press, Cambridge, MA (1975).
35. Y.H. Pao, "Structure of turbulent velocity and scalar fields at large wavenumbers", *Phys. Fluids* 8, 1063-1075 (1965).
36. I. Proudman and W.H. Reid, "On the decay of a normally distributed and homogeneous turbulent velocity field", *Philos. Trans. R. Soc.* A247, 163-189 (1954).
37. X B Reed, Jr. and Y.-C. Shih, "A serendipitous discovery", to be submitted (1986).
38. X B Reed, Jr. and Y.-C. Shih, "Application of the Cole-Hopf transformation to boundary value problems for Burgers' equation", to be submitted (1986).
39. W.H. Reid, "On the transfer of energy in Burgers' model of turbulence", *Appl. Sci. Res.* A6, 85-91 (1957).
40. E.Y. Rodin, "On some approximate and exact solutions of boundary value problems for Burgers' equation", *J. Math. Anal. and Appl.* 30, 401-414 (1970).
41. P.G. Saffman, "Lectures on Homogeneous Turbulence", pp 485-614 in Topics in Nonlinear Physics, N.J. Zabusky (ed.) Springer, New York (1968).
42. P.G. Saffman, "On the fine-scale structure of vector fields convected by a turbulent fluid", *J. Fluid Mech.* 16, 545-572 (1963).
43. Y.-C. Shih and X B Reed, Jr., "Solution to Burgers' equation on a finite domain with random initial and zero boundary conditions", pp 301-338, Symp. of Fluid Dynamics, A.L. Addy, et al. (eds.), Dept. Mech. and Ind. Engg, U. Ill. 301-338 (1984).
44. Y.-C. Shih and X B Reed, Jr., "Solution to the piecewise linear continuous random initial value problem for Burgers' equation", *Phys. Fluids* 28, 2088-2099 (1985).

45. Y.-C. Shih and X B Reed, Jr., "Exact solution to Burgers' equation for spatially periodic boundary conditions", *PhysicoChemical Hydrodynamics* 6, 853-861 (1985).
46. Y.-C. Shih and X B Reed, Jr., "Can exact random solutions to Burgers' equation be normally distributed?", submitted to *PhysicoChemical Hydrodynamics*
47. T. Tatsumi and S. Kida, "The modified cumulant expansion for isotropic turbulence at large Reynolds numbers", *J. Phys. Soc. Jpn.* 49, 2014-2025 (1980).
48. T. Tatsumi, S. Kida and J. Mizushima, "The multiple-scale cumulant expansion for isotropic turbulence", *J. Fluid Mech.* 85, 97-142 (1978).
49. H. Tennekes and J.L. Lumley, A First Course in Turbulence, MIT Press, Cambridge, Mass. (1972).
50. J.H. Thomas, "Numerical experiments on a model system for magnetohydrodynamic turbulence", *Phys. Fluids* 11, 1245-1250 (1968).
51. H. Tokunaga, "The statistical theory of one-dimensional turbulence in a compressible fluid", *J. Phys. Soc. Jpn.* 41, 328-337 (1976).
52. R.C. Tolman, The Principles of Statistical Mechanics, 1st ed., Oxford University Press, London (1959; orig., 1938).
53. P.-L. Tseng and X B Reed, Jr., "Exact solutions to Burgers' equation at high Reynolds' numbers: 1. Inviscid solutions", to be submitted (1986).
54. M.S. Uberoi, "Energy transfer in isotropic turbulence", *Phys. Fluids* 6, 1048-1056 (1963).
55. C.W. Van Atta and W.Y. Chen, "Correlation measurements in grid turbulence using digital harmonic analysis", *J. Fluid Mech.* 34, 497-515 (1968).
56. C.W. Van Atta and W.Y. Chen, "Measurements of spectral energy transfer in grid turbulence", *J. Fluid Mech.* 38, 743-763 (1969).
57. J.J. Walton, "Integration of the Lagrangian-history approximation to Burgers' equation", *Phys. Fluids* 13, 1934-1435 (1970).
58. H.W. Wyld, Jr., "Formulation of the theory of turbulence in an incompressible fluid", *Annals of Physics* 14, 143-165 (1961).
59. K. Yamamoto and I. Hosokawa, "Energy decay of Burgers' model of turbulence", *Phys. Fluids* 19, 1423-1424 (1976).

BOUNDARY-LAYER TRANSITION TO  
TURBULENCE: THE LAST FIVE YEARS

William S. Saric  
Mechanical and Aerospace Eng.  
Arizona State University  
Tempe, AZ 85287

ABSTRACT

Within the last five years, increased emphasis on secondary instability analysis along with the experimental observations of subharmonic instabilities have changed the picture of the transition process for boundary layers in low-disturbance environments. Additional efforts with Navier-Stokes computations have formed an impressive triad of tools that are beginning to unravel the details of the early stages of transition. This paper reviews these recent efforts.

SYMBOLS

a chordwise complex wavenumber normalized by  $L$   
A disturbance amplitude  
 $A_0$  amplitude at  $R=R_0$ , usually Branch I  
 $C_p$  pressure coefficient  
F  $w/R = 6.28fv/U_0^2$  : dimensionless frequency  
f dimensional frequency [hz]  
L  $\sqrt{vx^*/U_0}$  : boundary-layer reference length.  
N  $\ln(A/A_0)$  : amplification factor  
R  $\sqrt{R_x} = U_0 L/v$  : boundary-layer Reynolds number  
 $R_0$  initial boundary-layer Reynolds number, usually Branch I  
 $R_x$   $U_0 x^*/v$  : x-Reynolds number or chord Reynolds number  
U basic-state chordwise velocity normalized by  $U_0$

$U_0$  freestream velocity, [m/s]  
 $\nu$  kinematic viscosity [ $m^2/s$ ]  
w  $6.28fL/U_0$ : dimensionless circular frequency  
W basic-state spanwise velocity normalized by  $U_0$   
 $x^*$  dimensional chordwise coordinate [m]  
x chordwise coordinate normalized with L  
y normal-to-the-wall coordinate  
z spanwise coordinate

1. INTRODUCTION

The problems of understanding the origins of turbulent flow and transition to turbulent flow are the most important unsolved problems of fluid mechanics and aerodynamics. There is no dearth of applications for information regarding transition location and the details of the subsequent turbulent flow. A few examples can be given here. (1) Nose cone and heat shield requirements on reentry vehicles and the "aerospace airplane" are critical functions of transition altitude. (2) Vehicle dynamics and "observables" are modulated by the occurrence of laminar-turbulent transition. (3) Should transition be delayed with Laminar Flow Control on the wings of large transport aircraft, a 25% savings in fuel will result. (4) Lack of a reliable transition prediction scheme hampers efforts to accurately predict airfoil surface heat transfer and to cool the blades and vanes in gas turbine

engines. (5) The performance and detection of submarines and torpedoes are significantly influenced by turbulent boundary-layer flows and efforts directed toward drag reduction require the details of the turbulent processes. (6) Separation and stall on low-Reynolds-number airfoils and turbine blades strongly depends on whether the boundary layer is laminar, transitional, or turbulent.

The common thread connecting each of these applications is the fact that they all deal with bounded shear flows (boundary layers) in open systems (with different upstream or initial amplitude conditions). It is well known that the stability, transition, and turbulent characteristics of bounded shear layers are fundamentally different from those of free shear layers (Morkovin, 1969; Tani, 1969; Reshotko, 1976). Likewise, the stability, transition, and turbulent characteristics of open systems are fundamentally different from those of closed systems (Tatsumi, 1984). The distinctions are vital. Because of the influence of indigenous disturbances, surface geometry and roughness, sound, heat transfer, and ablation, it is not possible to develop general prediction schemes for transition location and the nature of turbulent structures in boundary-layer flows.

There have been a number of recent advances in the mathematical theory of chaos that have been applied to closed systems. Sreenivasan and Strykowski (1984), among others, discuss the extension of these ideas to open systems and conclude that the relationship is still uncertain. It appears from a recent workshop and panel discussion (Liepmann et al. 1986) that the direct application of chaos theory to open systems is still some distance away. However, the prospect of incorporating some of the mathematical ideas of chaos into open system problems and of encouraging the

transfer of data to the mathematicians is good. Since there is still some uncertainty in the direct application of chaos theory to transition no further mention of this will be given here.

The purpose of this report is to bring into perspective certain advances to our understanding of laminar-turbulent transition that have occurred within the last five years. In particular, these advances have been made by simultaneous experimental, theoretical, and computational efforts.

### 1.1 Basic Ideas of Transition

With the increased interest in turbulent drag reduction and in large scale structures within the turbulent boundary layer, researchers in turbulence have been required to pay more attention to nature of laminar-turbulent transition processes. It is generally accepted that the transition from laminar to turbulent flow occurs because of an incipient instability of the basic flow field. This instability intimately depends on subtle, and sometimes obscure, details of the flow. The process of transition for boundary layers in external flows can be qualitatively described using the following (albeit, oversimplified) scenario.

Disturbances in the freestream, such as sound or vorticity, enter the boundary layer as steady and/or unsteady fluctuations of the basic state. This part of the process is called receptivity (Morkovin, 1969) and although it is still not well understood, it provides the vital initial conditions of amplitude, frequency, and phase for the breakdown of laminar flow. Initially these disturbances may be too small to measure and they are observed only after the onset of an instability. The type of instability that occurs depends on Reynolds number, wall curvature, sweep, roughness, and initial conditions. The

initial growth of these disturbances is described by linear stability theory. This growth is weak, occurs over a viscous length scale, and can be modulated by pressure gradients, mass flow, temperature gradients, etc. As the amplitude grows, three-dimensional and nonlinear interactions occur in the form of secondary instabilities. Disturbance growth is very rapid in this case (now over a convective length scale) and breakdown to turbulence occurs.

For many years, linear stability theory, with the Orr-Sommerfeld equation as its keystone, served as the basic tool for predictors and designers. Since the initial growth is linear and its behavior can be easily calculated, transition prediction schemes are usually based on linear theory. However, since the initial conditions (receptivity) are not generally known, only correlations are possible and, most importantly, these correlations must be between two systems with similar environmental conditions. The impossibility of matching or fully understanding these environmental conditions has led to the failure of any absolute transition prediction scheme for even the simple Blasius flat-plate boundary layer.

The preceding is not always follow the observed behavior. At times, the initial instability can be so strong that the growth of linear disturbances is by-passed (Morkovin, 1969) in such a way that turbulent spots appear or secondary instabilities occur and the flow quickly becomes turbulent. This phenomenon is not well understood but has been documented in cases of roughness and high freestream turbulence (Reshotko, 1986). In this case, transition prediction schemes based on linear theory fail completely.

## 1.2 Review of the Literature

The literature review follows the outline of the process described above and

begins with Reshotko (1984a, 1986) on receptivity (i.e. the means by which freestream disturbances enter the boundary layer). In these papers, Reshotko summarizes the recent work in this area and points out the difficulties in understanding the problem. Indeed, the receptivity question and the knowledge of the initial conditions are the key issues regarding a transition prediction scheme. Of particular concern to the transition problem are the quantitative details of the roles of freestream sound and turbulence. Aside from some general correlations, this is still an opaque area. However, in section 3.2 below, a demonstration of the role of initial conditions on the observed transition phenomenon is discussed.

The details of linear stability theory are given in Mack (1984b). This is actually a monograph on boundary-layer stability theory and should be considered required reading for those interested in all aspects of the subject. It covers 58 pages of text with 170 references. In particular, his report updates the three-dimensional (3-D) material in Mack (1969), covering in large part Mack's own contributions to the area.

The foundation paper with regard to nonlinear instabilities is Klebanoff et al. (1962). This seminal work spawned numerous experimental and theoretical works (not all successful) for the period of 20 years after its publication. It was not until the experimental observations of subharmonic instabilities by Kachanov et al. (1977), Kachanov and Levchenko (1984), and Saric and Thomas (1984), along with the work on secondary instabilities, that additional progress was made in this area. Recent papers of Herbert (1984a,b,c; 1985; 1986a,b) cover the problems of secondary instabilities and nonlinearities i.e. those aspects of the breakdown process that succeed the growth of linear disturbances. It should be emphasized that two-

dimensional waves do not completely represent the breakdown process since the transition process is always three-dimensional in bounded shear flows. Herbert describes the recent efforts in extending the stability analysis into regions of wave interactions that produce higher harmonics, three-dimensionality, subharmonics, and large growth rates--all harbingers of transition to turbulence. Recent 3-D Navier-Stokes computations by Fasel (1980,1986), Spalart (1984), Spalart and Yang (1986), Kleiser and Laurien (1985, 1986) Reed and co-workers (Singer et al. 1986, 1987; Yang et al. 1987) have added additional understanding to the phenomena. More is said about this in section 3.2.

The paper by Arnal (1984) is an extensive description and review of transition prediction and correlation schemes for two-dimensional flows that covers 34 pages of text and over 100 citations. An analysis of the different mechanisms that cause transition such as Tollmien-Schlichting (T-S) waves, Görtler vortices, and turbulent spots is given. The effects that modulate the transition behavior are presented. These include the influence of freestream turbulence, sound, roughness, pressure gradient, suction, and unsteadiness. A good deal of the data comes from the work of the group at ONERA/CERT part of which has only been available in report form. The different transition criteria that have been developed over the years are also described which gives an overall historical perspective of transition prediction methods.

In a companion paper, Poll (1984b) extends the description of transition to 3-D flows. When the basic state is three-dimensional, not only are 3-D disturbances important, but completely different types of instabilities can occur. Poll concentrates on the problems of leading-edge contamination and crossflow vortices, both

of which are characteristic of swept-wing flows. The history of these problems as well as the recent work on transition prediction and control schemes are discussed. We return to a discussion of 3-D flows in section 4.

Reshotko (1984b, 1985, 1986) and Saric (1985b) review the application of stability and transition information to problems of drag reduction and in particular, laminar flow control. They discuss a variety of the laminar flow control and transition control issues which will not be covered here.

## 2. REVIEW OF T-S WAVES

The disturbance state is restricted to two dimensions with a one-dimensional basic state. The 2-D instability to be considered is a viscous instability in that the boundary-layer velocity profile is stable in the inviscid limit and thus, an increase in viscosity (a decrease in Reynolds number) causes the instability to occur in the form of 2-D traveling waves called T-S waves. All of this is contained within the framework of the Orr-Sommerfeld equation, OSE. The historical development of this work is given in Mack (1984b) and a tutorial is given by Saric (1985a).

The OSE is linear and homogeneous and forms an eigenvalue problem which consists of determining the wavenumber,  $a$ , as a function of frequency,  $w$ , Reynolds number,  $R$ , and the basic state,  $U(y)$ . The Reynolds number is usually defined as  $R = U_0 L / \nu = \sqrt{R_x}$  and is used to represent distance along the surface. In general,  $L = \sqrt{v x^* / U_0}$  is the most straightforward reference length to use because of the simple form of  $R$  and because the Blasius variable is the same as  $y$  in the OSE. When comparing the solutions of the OSE with experiments, the dimensionless frequency,  $F$ , is introduced as  $F = w/R = 6.28fv/U_0^2$  where  $f$  is the frequency in Hertz.

Usually, an experiment designed to observe T-S waves and to verify the 2-D theory is conducted in a low-turbulence wind tunnel ( $u'/U_0$  from 0.02% to 0.06%) on a flat plate with zero pressure gradient (determined from the shape factor = 2.59 and not from pressure measurements!) where the virtual-leading-edge effect is taken into account by carefully controlled boundary-layer measurements. Disturbances are introduced by means of a 2-D vibrating ribbon using single-frequency, multiple-frequency, step-function, or random inputs (Costis and Saric, 1982) taking into account finite-span effects (Mack, 1984a). Hot wires measure the  $U + u'$  component of velocity in the boundary layer and d-c coupling separates the mean from the fluctuating part. The frequency,  $F$ , for single-frequency waves remains a constant.

When the measurements of are repeated along a series of chordwise stations, the maximum amplitude of the waves varies. At constant frequency, the disturbance amplitude initially decays until the Reynolds number at which the flow first becomes unstable is reached. This point is called the Branch I neutral stability point and is given by  $R_1$ . The amplitude grows exponentially until the Branch II neutral stability point is reached which is given by  $R_{11}$ . The locus of  $R_1$  and  $R_{11}$  points as a function of frequency gives the neutral stability curve shown in Fig. 1. If the growth rate of the disturbances is defined as  $s=s(R,F)$ , Fig. 1 is the locus of  $s(R,F)=0$ . For  $R > 600$  the theory and experiment agree very well for Blasius flow. For  $R < 600$  the agreement is not as good because the theory is influenced by nonparallel effects and the experiment is influenced by low growth rates and nearness to the disturbance source. Virtually all problems of practical interest have  $R > 1000$  in which case the parallel theory seems quite adequate (Gaster, 1974; Saric and Nayfeh, 1977).

By assuming that the growth rate,  $s = s(R,F)$ , to hold locally (within the quasi-parallel flow approximation), the disturbance equations are integrated along the surface with  $R = R(x)$  to give:

$$A/A_0 = \exp(N)$$

where  $dN/dR = s$ ,  $A$  and  $A_0$  are the disturbance amplitudes at  $R$  and  $R_0$ , respectively, and  $R_0$  is the Reynolds number at which the constant-frequency disturbance first becomes unstable (Branch I of the neutral stability curve).

The basic design tool is the correlation of  $N$  with transition Reynolds number,  $R_0$ , for a variety of observations. The correlation will produce a number for  $N$  (say 9) which is now used to predict  $R_0$  for cases in which experimental data are not available. This is the celebrated  $e^N$  method of Smith and von Ingen (e.g. Arnal, 1984; Mack, 1984b). The basic LFC technique changes the physical parameters and keeps  $N$  within reasonable limits in order to prevent transition. As long as laminar flow is maintained and the disturbances remain linear, this method contains all of the necessary physics to accurately predict disturbance behavior. As a transition prediction device, the  $e^N$  method is certainly the most popular technique used today. It works within some error limits only if comparisons are made with experiments with identical disturbance environments. Since no account can be made of the initial disturbance amplitude this method will always be suspect to large errors and should be used with extreme care. When bypasses occur, this method does not work at all. Mack (1984b) and Arnal(1984) give examples of growth-rate and  $e^N$  calculations showing the effects of pressure gradients, Mach number, wall temperature, and three dimensionality for a wide variety of flows. These reports contain the most up-to-date stability information.

### 3. SECONDARY INSTABILITIES AND TRANSITION

There are different possible scenarios for the transition process, but it is generally accepted that transition is the result of the uncontrolled growth of unstable three-dimensional waves. Secondary instabilities with T-S waves are reviewed in some detail by Herbert (1984b, 1985, 1986), Saric and Thomas (1984) and Saric et al. (1984). Therefore, only a brief outline is given in section 3.1 in order to give the reader some perspective of the different types of breakdown. Section 3.2 discusses the very recent results.

#### 3.1 Secondary Instabilities

The occurrence of three-dimensional phenomena in an otherwise two-dimensional flow is a necessary prerequisite for transition (Tani, 1981). Such phenomena were observed in detail by Klebanoff et al. (1962) and were attributed to a spanwise differential amplification of T-S waves through corrugations of the boundary layer. The process leads rapidly to spanwise alternating "peaks" and "valleys", i.e., regions of enhanced and reduced wave amplitude, and an associated system of streamwise vortices. The peak-valley structure evolves at a rate much faster than the (viscous) amplification rates of T-S waves. The schematic of a smoke-streakline photograph (Saric et al. 1981) in Fig. 2 shows the sequence of events after the onset of "peak-valley splitting". This represents the path to transition under conditions similar to Klebanoff et al. (1962) and is called a K-type breakdown. The lambda-shaped (Hama and Nutant, 1963) spanwise corrugations of streaklines, which correspond to the peak-valley structure of amplitude variation, are a result of weak 3-D displacements of fluid particles across the critical layer and precede the appearance of Klebanoff's "hair-pin" vortices. This has been

supported by hot-wire measurements and Lagrangian-type streakline prediction codes (Saric et al., 1981; Herbert and Bertolotti, 1985). Note that the lambda vortices are ordered in that peaks follow peaks and valleys follow valleys.

Since the pioneering work of Nishioka et al. (1975, 1980), it is accepted that the basic transition phenomena observed in plane channel flow are the same as those observed in boundary layers. Therefore, little distinction will be given here as to whether work was done in a channel or a boundary layer. From the theoretical and computational viewpoint, the plane channel is particularly convenient since the Reynolds number is constant, the mean flow is strictly parallel, certain symmetry conditions apply, and one is able to do temporal theory. Thus progress has been first made with the channel flow problem.

Different types of three-dimensional transition phenomena recently observed (e.g. Kachanov et al. 1977; Kachanov and Levchenko, 1984; Saric and Thomas, 1984; Saric et al. 1984, Kozlov and Ramanosov, 1984) are characterized by staggered patterns of peaks and valleys (see Fig. 3) and by their occurrence at very low amplitudes of the fundamental T-S wave. This pattern also evolves rapidly into transition. These experiments showed that the subharmonic of the fundamental wave (a necessary feature of the staggered pattern) was excited in the boundary layer and produced either the resonant wave interaction predicted by Craik (1971) (called the C-type) or the secondary instability of Herbert (1983) (called the H-type). Spectral broadening to turbulence with self-excited subharmonics has been observed in acoustics, convection, and free shear layers and was not identified in boundary layers until the results of Kachanov et al. (1977). This paper re-initiated the interest in subharmonics and prompted the simultaneous verification of

C-type resonance (Thomas and Saric, 1981; Kachanov and Levchenko, 1984). Subharmonics have also been confirmed for channel flows (Kozlov and Ramazanov, 1984) and by direct integration of the Navier-Stokes equations (Spalart, 1984). There is visual evidence of subharmonic breakdown before Kachanov et al. (1977) in the work of Hama (1959) and Knapp and Roache (1968) which was not recognized as such at the time of their publication. The recent work on subharmonics is found in Herbert (1985, 1986a,b), Saric, Kozlov and Levchenko (1984), and Thomas (1986).

The important issues that have come out of the subharmonic research is that the secondary instability depends not only on disturbance amplitude, but on phase and fetch as well. Fetch means here the distance over which the T-S wave grows in the presence of the 3-D background disturbances. If T-S waves are permitted to grow for long distances at low amplitudes, subharmonic secondary instabilities are initiated at disturbance amplitudes of less than  $0.3U_0$ . Whereas, if larger amplitudes are introduced, the breakdown occurs as K-type at amplitudes of  $1U_0$ . Thus, there no longer exists a "magic" amplitude criterion for breakdown.

A consequence of this requirement of a long enough fetch for the subharmonic to be entrained from the background disturbances is that the subharmonic interaction will occur at or to the right of the Branch II neutral stability point (see Fig. 1). Since this is in the stable region of the fundamental wave, it was not likely to be observed because the experimenters quite naturally concentrated their attention of measurements between Branch I and Branch II.

### 3.2 Recent Results

The surprise that results from the analytical model of Herbert (1986a,b) and

the Navier-Stokes computations of Singer, Reed, and Ferziger (1986), is that under conditions of the experimentally observed K-Type breakdown, the subharmonic H-Type is still the dominant breakdown mechanism instead of the fundamental mode. This is in contrast to Klebanoff's experiment, confirmed by Nishioka et al. (1975, 1980), Kachanov et al. (1977), Saric and Thomas (1984), Saric et al. (1984), and Kozlov and Ramazanov (1984) where only the breakdown of the fundamental into higher harmonics was observed. Only Kozlov and Ramazanov (1984) observed the H-type in their channel experiments and only when they artificially introduced the subharmonic.

This apparent contradiction was resolved by Singer, Reed, and Ferziger (1987). Here the full three-dimensional, time-dependent incompressible Navier-Stokes equations are solved with no-slip and impermeability conditions at the walls. Periodicity was assumed in both the streamwise and spanwise directions. The implementation of the method and its validation are described by Singer, Reed and Ferziger (1986). Initial conditions include a two-dimensional T-S wave, random noise, and streamwise vortices. No shape assumptions are necessary, the spectrum is larger, and random disturbances whether freestream or already in the boundary layer can be introduced and monitored for growth and interactions (Singer, Reed, and Ferziger, 1986). Other advantages realized by computations are 1) the inclusion of boundary-layer growth, neglected in linear theory but important to the growth of secondary instabilities, 2) the generation of ensemble averages, 3) the visualization of flow phenomena for comparison with experiments (advanced graphics capability), and 4) the calculation of vorticity and energy spectra, often unavailable from experiments.

The streamwise vortices can alter the relative importance of the subharmonic and fundamental modes. Streamwise vortices of approximately the strength of those that might be found in transition experiments can explain the difficulty in experimentally identifying the subharmonic route to turbulence (Herbert 1983).

The corresponding computational visualizations of Singer et al. (1987) are shown in Figs. 4 and 5; flow is from lower right to upper left. Figure 4 shows the vortex structures, commonly seen in the transition process, under the conditions of a forced 2-D T-S wave and random noise as initial conditions. The subharmonic mode is present as predicted by theory but not seen experimentally. Other views of the vortical structure are given by Herbert (1986a). However, when streamwise vorticity (as is present in the flow from the turbulence screens upstream of the nozzle) is also included, the subharmonic mode is overshadowed by the fundamental mode (as in the experiments!). The resulting pattern, ordered peak-valley structure, is seen in Fig. 5. Here is a case in which the computations have explained discrepancies between theory and experiments.

In the presence of streamwise vorticity, the fundamental mode is preferred over the subharmonic; this agrees with experimental observations, but not with theory (which does not account for this presence). Without streamwise vorticity, the subharmonic modes dominate as predicted by theory and confirmed by computational simulations. In the presence of streamwise vorticity characteristic of wind-tunnel experiments, the K-type instability dominates and the numerical simulations predict the experimental results.

Direct numerical simulations are playing an increasingly important role in the investigation of transition; the

literature is growing, especially recently. This trend is likely to continue as considerable progress is expected towards the development of new, extremely powerful supercomputers. In such simulations, the full Navier-Stokes equations are solved directly by employing numerical methods, such as finite-difference or spectral methods. The direct simulation approach is widely applicable since it avoids many of the restrictions that usually have to be imposed in theoretical models.

The Navier-Stokes solutions are taken hand-in-hand with the wind tunnel experiments in a complementary manner. The example of Singer, Reed, and Ferziger (1987) illustrate that these two techniques cannot be separated. The next step in the simulations will be to predict the growing body of detailed data being developed by Nishioka et al. (1980, 1981, 1984, 1985) on the latter stages of the breakdown process.

#### 4. THREE-DIMENSIONAL BOUNDARY LAYERS

Three-dimensional flows offer a rich variety of instability mechanisms and the 3-D boundary-layer flow over the swept-wing is no exception. This type of flow is susceptible to four types of instabilities that lead to transition. They are leading-edge contamination, streamwise instability, centrifugal instability, and the topic of this section, crossflow instability. Leading-edge contamination occurs along the attachment line and is caused by disturbances that propagate along the wing edge (Poll 1979, 1984a,b). Streamwise instability is associated with the chordwise component of flow and is quite similar to processes in two-dimensional flows, where T-S waves generally develop. This usually occurs in zero or positive pressure-gradient regions on a wing. The general theory is given by Nayfeh (1980). Centrifugal instabilities occur in the shear flow over a concave surface and appear in the form of Görtler vortices

(Floryan and Saric, 1979; Hall, 1983). Attachment-line contamination problems are important for transition control but not discussed here because of the existing reviews cited above. At the same time, a review of Görtler vortices is beyond the goal of this report.

A wide body of literature exists on stability and transition problems of rotating disks, cones, and spheres. These are classic problems of three-dimensional boundary layers that exhibit the same generic stability characteristics. The protagonists are Malik et al. (1981), Kobayashi and Kohama (1984), and Kohama and Kobayashi (1983). These, along with others, are reviewed by Reed and Saric (1986) and will not be discussed here.

The focus of this section is on the crossflow instability which occurs in strong negative pressure gradient regions on swept wings. In the leading-edge region both the surface and flow streamlines are highly curved. The combination of pressure gradient and wing sweep deflects the inviscid-flow streamlines inboard as shown in the schematic of Fig. 6. This mechanism re-occurs in the positive pressure gradient region near the trailing edge. Because of viscous effects, this deflection is made larger in the boundary layer, and causes crossflow, i.e. the development of a velocity component inside the boundary layer that is perpendicular to the inviscid-flow velocity vector. This is illustrated in the schematic of Fig. 7. This profile is characteristic of many different three-dimensional boundary-layer flows. The crossflow profile has a maximum velocity somewhere in the middle of the boundary layer, going to zero on the plate surface and at the boundary-layer edge. This profile exhibits an inflection point (a condition which is known to be dynamically unstable) causing so-called crossflow vortex structures to form with their axes in the streamwise direction.

These crossflow vortices all rotate in the same direction. Descriptions of this instability are given in the classic paper by Gregory, Stuart and Walker (1955) and in the reports by Mack (1984b) and Poll (1984b).

In the past ten years considerable progress has been achieved in calculating the stability characteristics of three-dimensional flows. The state-of-the-art transition prediction method still involves linear stability theory coupled with an  $e^N$  transition prediction scheme (Mack, 1984b; Poll, 1984b). Malik and Poll (1984) extend the stability analysis of three-dimensional flows, analyzing the flow over a yawed cylinder, to include curvature of the surface and streamlines. They show that curvature has a very stabilizing effect on the disturbances in the flow. This is compared with the experimental results of Poll (1984a) which show good agreement with the transition prediction scheme. They also find that the most highly amplified disturbances are traveling waves and not stationary waves. Here again Malik and Poll (1984) obtain good agreement with Poll's (1984a) recent experimental work where Poll identifies a highly amplified traveling wave around one kHz near transition. Malik and Poll obtain  $N$  factors for the fixed-frequency disturbances between 11 and 12 which agreed with the work of Malik, Wilkinson and Orszag (1981) on the rotating disk. In both cases (the disk and cylinder), when the extra terms involving curvature and Coriolis effects are omitted in the stability analysis, the  $N$  factors are much larger which illustrates the need to do the realistic stability calculations.

Michel, Arnal and Coustols (1984) develop transition criteria for incompressible two- and three-dimensional flows and in particular for the case of a swept wing with infinite span. They correlate transition onset on the swept

wing using three parameters: a Reynolds number based on the displacement thickness in the most unstable direction of flow, the streamwise shape parameter, and the external turbulence level. They simplify the problem by not including curvature effects and assuming locally parallel flow and even with these simplifications, the comparison with experiment shows good agreement.

The current experimental work of Poll (1984a) focuses on the crossflow instability where he shows that increasing yaw has a very destabilizing effect on the flow over a swept cylinder. He characterizes the instability in two ways. The first is by fixed disturbances visualized by either surface evaporation or oil-flow techniques. These disturbances are characterized by regularly spaced streaks aligned approximately in the inviscid-flow direction, leading to a "saw-tooth" pattern at the transition location. The second way is with unsteady disturbances in the form of a large-amplitude high-frequency harmonic wave at frequencies near one kHz. At transition near the wall surface, he obtains disturbance amplitudes greater than 20% of the local mean velocity. Initially he tries to use two parameters to predict transition. They are the crossflow Reynolds number and a shape factor based on the streamwise profile. However, based on the results of his research, he found that two parameters alone are not enough to predict transition, and that one needs at least three parameters to accurately describe the crossflow instability.

Michel, Arnal, Coustol, and Juillen (1984) present some very good experimental results on the crossflow instability, conducted on a swept airfoil model. By surface visualization techniques they show regularly spaced streaks that are aligned practically in the inviscid-flow direction,

with a "saw-tooth" pattern near the transition area. They perform hot-wire measurements on the stationary waves. Their results show a spanwise variation of the boundary layer before transition that becomes chaotic in the transition region. The variations are damped in the turbulent region. They also find a small peak in the spectra around one kHz (like Poll, 1984a), which is due to a streamwise instability. In addition to this they provide some theoretical work on the secondary velocities, and show counter rotating vortices in the streamwise direction. However, when these components are added to the mean velocities the vortices are no longer clearly visible. Even with all this progress there are very little experimental data with which to compare the theoretical models.

A major unanswered question concerning swept-wing flows is the interaction of crossflow vortices with T-S waves. If the vortex structure continues aft into the mid-chord region where T-S waves are amplified, some type of interaction could cause premature transition. In fact, the unsteadiness at transition observed by Poll and Michel et al. could be due to this phenomenon. Indeed early LFC work of Bacon et al. (1962) show a somewhat anomalous behavior of transition when sound is introduced in the presence of crossflow vortices. It is well known that streamwise vortices in a boundary layer strongly influence the behavior of other disturbances. Nayfeh (1981) shows that Görtler vortices produce a double-exponential growth of T-S waves. Malik (1986) in a computational simulation of the full Navier-Stokes equations is unable to find this interaction however, indicating a need for more work in this area. Herbert and Morkovin (1980) show that the presence of T-S waves produces a double-exponential growth of Görtler vortices, while Floryan

and Saric (1980) show a similar behavior for streamwise vortices interacting with Görtler vortices. Reed (1984) analyzes the crossflow/T-S interaction in the leading-edge region by using a parametric-resonance model. Reed shows that the interaction of the crossflow vortices with T-S waves produces a double exponential growth of the T-S waves. The results of Bacon, Pfenninger and Moore (1962) and Reed (1984) clearly show the need to experimentally study problems of this kind.

Saric and Yeates (1985) established a three-dimensional boundary layer on a flat plate that is typical of infinite swept-wing flows. This is done by having a swept leading edge and contoured walls to produce the pressure gradients. The experimentally measured  $C_p$  distribution is used along with the 3-D boundary-layer code of Kaups and Cebeci (1977) to establish the crossflow experiment and to compare with the theory. Some of the results of Saric and Yeates (1985) are discussed below because they illustrate that not everything is as it should be in three-dimensional boundary layers.

Boundary-layer profiles are taken at different locations along the plate with both the slant-wire and straight-wire probes. Reduction of both the straight-wire and slant-wire data at one location produces a crossflow profile which provides comparison with the theory. The velocity component perpendicular to the inviscid-flow velocity vector is called the crossflow velocity. By definition, since the crossflow profile is perpendicular to the edge velocity, the crossflow velocity is zero in the inviscid flow.

Disturbance measurements of the mean flow are conducted (Saric and Yeates, 1985) within the boundary layer by making a spanwise traverse (parallel to the leading edge) of the hot wire at a constant  $y$  location with respect to the plate. These

measurements are carried out at many different  $x$  and  $y$  locations using two different mean velocities. The results show a steady vortex structure with a dominant spanwise wavelength of approximately 0.5 cm. The corresponding spectrum for this disturbance measurement shows a sharp peak at a wavelength of about 0.5 cm, but it also shows a broad peak at a larger wavelength of 1.0 cm, generally at a lower amplitude. The cause of this broad peak at the larger wavelength is explained by the linear-theory predictions (Dagenhart, 1981) for crossflow vortices. This 0.5 cm wavelength does not agree with the flow-visualization results nor with the theoretical calculations of the MARIA code (Dagenhart, 1981).

The naphthalene flow-visualization technique shows that there exists a steady crossflow vortex structure on the swept flat plate. The pattern of disturbance vortices is nearly equally spaced and aligned approximately in the inviscid-flow direction. The wavelength of the vortices is on the scale of 1 cm and this spacing agrees quite well with the calculated wavelength from the MARIA code.

While the flow visualization clearly indicates a spanwise wavelength of 1 cm on the surface, the spectra of the hot-wire measurements show a dominant sharp peak at 0.5 cm and a smaller broad-band peak at 1 cm. This apparent incongruity can be explained with the wave interaction theory of Reed (1985), who uses the actual test conditions of this experiment. Reed shows that it is possible for a parametric resonance to occur between a previously amplified 0.5 cm vortex and a presently amplified 1 cm vortex and that measurements taken near the maximum of the crossflow velocity would show a strong periodicity of 0.5 cm. Moreover, Reed's wall-shear calculations and streamline calculations show the 0.5 cm periodicity dying out near the wall and the 1 cm periodicity dominating.

These phenomena are not observed by Michel et al. (1984) who measure phenomena not measured by Poll nor Saric and Yeates.

Two important points need to be emphasized. First, one must, whenever possible, use multiple independent measurements. This was the only way the 0.5 cm and the 1.0 cm vortex structure could be reconciled. Second, the steadiness of the vortex structure in the wind tunnel experiments in contrast to the unsteady predictions of the theory, indicates that some characteristic of the wind tunnel is fixing the vortex structure. This is directly analogous to the biasing of the K-type secondary instability in the flat plate flow. Perhaps some very weak freestream vorticity is providing the fix for the crossflow vortex structure. All of this serves notice that stability and transition phenomena are extremely dependent on initial conditions.

#### 5. TRANSITION PREDICTION AND CONTROL

When the recent work on subharmonics is added to the discussion at the end of section 3 on the limitations of the  $e^N$  method, one indeed has an uncertainty principle for transition (Morkovin, 1978). Transition prediction methods will remain conditional until the receptivity problem is adequately solved and the bypass mechanisms are well understood. In the mean time, extreme care must be exercised when using correlation methods to predict transition. Additional problems of transition prediction and laminar flow control are discussed by Reshotko (1985, 1986). The main principle of laminar flow control is to keep the disturbance levels low enough so that secondary instabilities and transition do not occur. Under these conditions, linear theory is quite adequate and  $e^N$  methods can be used to calculate the effectiveness of a particular LFC device.

The idea of transition control through active feedback systems is an area that has

received considerable recent attention (Liepmann and Nosenchuck, 1982; Thomas, 1983; Kleiser and Laurien, 1984, 1985; Metcalfe et al., 1985). The technique consists of first sensing the amplitude and phase of an unstable disturbance and then introducing an appropriate out-of-phase disturbance that cancels the original disturbance. In spite of some early success, this method is no panacea for the transition problem. Besides the technical problems of the implementation of such a system on an aircraft, the issue of three-dimensional wave cancellation must be addressed. As Thomas (1983) showed, when the 2-D wave is canceled, all of the features of the 3-D disturbances remain to cause transition at yet another location. Some clear advantage over passive systems have yet to be demonstrated for this technique.

#### ACKNOWLEDGEMENTS

The author would like to thank Dr. H. Reed for her helpful comments and for sharing her recent work. The author is also grateful to Dr. T. Herbert for his comments and ideas during our collaboration. This work is supported by the Air Force Office of Scientific Research Contract AFOSR-85-NA-077.

#### REFERENCES

- Arnal D. 1984. Description and prediction of transition in two-dimensional incompressible flow. AGARD Report No. 709 (Special course on stability and transition of laminar flows) VKI, Brussels.
- Bacon, J.W. Jr., Pfenninger, W. and Moore, C.R. 1962. Influence of acoustical disturbances on the behavior of a swept laminar suction wing. Northrup Report NOR-62-124.

- Costis, C.E. and Saric, W.S. 1982. Excitation of wave packets and random disturbances in a boundary layer. V.P.I. & S.U. Report No. VPI-E-82.26.
- Craik, A.D.D. 1971. Nonlinear resonant instability in boundary layers. *J. Fluid Mech.*, vol. 50, 393.
- Dagenhart, J.R. 1981. Amplified crossflow disturbances in the laminar boundary layer on swept wings with suction. NASA TP-1902.
- Fasel, H. 1980. Recent developments in the numerical solution of the Navier-Stokes equations and hydrodynamic stability problems. *Comp. Fluid Dyn.*, (Kollman, Wolfgang, ed.), Hemisphere.
- Fasel, H. 1986. Numerical simulation of laminar-turbulent transition. Invited Paper, U.S. National Congress of Applied Mechanics, ASME, June 1986.
- Floryan, J.M. and Saric, W.S. 1979. Stability of Görtler vortices in boundary layers. AIAA Paper No. 79-1497 and AIAA J., vol. 20, 316.
- Floryan, J.M. and Saric, W.S. 1980. Wavelength selection and growth of Görtler vortices. AIAA paper no. 80-1376 and AIAA J., vol. 22, 1529.
- Gaster, M. 1974. On the effects of boundary-layer growth on flow stability. *J. Fluid Mech.*, vol. 66, 465.
- Gregory, N., Stuart, J.T. and Walker, W.S. 1955. On the stability of three-dimensional boundary layers with applications to the flow due to a rotating disk. *Phil. Trans. Roy. Soc. Lon.*, vol. A248, 155.
- Hall, P. 1983. The linear development of Gortler vortices in growing boundary layers. *J. Fluid Mech.*, vol. 130, 41.
- Hama, F.R. 1959. Some transition patterns in axisymmetric boundary layers. *Phys. Fluids*, vol. 2, 664.
- Hama, F.R. and Nutant, J. 1963. Detailed flow-field observations in the transition process in a thick boundary layer. *Proc. 1963 Heat Trans. Fluid Mech. Inst.*, 77.
- Herbert, T. 1983. Subharmonic three-dimensional disturbances in unstable plane shear flows. AIAA Paper No. 83-0009.
- Herbert, T. 1984a. Analysis of the Subharmonic Route to Transition in Boundary Layers. AIAA Paper No. 84-0009.
- Herbert, T. 1984b. Secondary instability of shear flows. AGARD Report No. 709 (Special course on stability and transition of laminar flows) VKI, Brussels.
- Herbert, T. 1984c. Nonlinear effects in boundary-layer stability. AGARD Report No. 709 (Special course on stability and transition of laminar flows) VKI, Brussels.
- Herbert, T. 1985. Three-dimensional phenomena in the transitional flat-plate boundary layer. AIAA Paper No. 85-0489.
- Herbert, T. 1986a. Vortical Mechanisms in Shear Flow Transition. *Euromech 199 Colloquium, Direct and Large Eddy Simulation*, Vieweg Verlag.
- Herbert, T. 1986b. Analysis of secondary instabilities in boundary layers. Invited Paper, U.S. National Congress of Applied Mechanics, ASME, June 1986.
- Herbert, T. and Bertolotti, F.P. 1985. Effect of pressure gradients on the growth of subharmonic disturbances in boundary layers, in *Proc. Conf. on Low Reynolds Number Airfoil Aerodynamics*, ed. T.J. Mueller, Univ. of Notre Dame.
- Herbert, T., Bertolotti, F.P. and Santos, G.R. 1985. Floquet analysis of secondary instability in shear flows. ICASE/NASA Workshop on Stability of Time-Dependent and Spatially Varying Flows, August 19-20, Hampton, VA.
- Herbert, T. and Morkovin, M. V. 1980. Dialogue on bridging some gaps in

- stability and transition research. Laminar-Turbulent Transition, ed: R. Eppler and H. Fasel, Springer.
- Kobayashi, R. and Kohama, Y. 1985. Spiral vortices in boundary layer transition on a rotating cone. Proc. 2nd IUTAM Symp. on Laminar-Turbulent Transition, Novosibirsk.
- Kachanov, Yu.S., Kozlov, V.V. and Levchenko, V.Ya. 1977. Nonlinear development of a wave in a boundary layer (in Russian). Mekhanika Zhidkosti i Gaza, no. 3, 49.
- Kachanov, Yu.S. and Levchenko, V.Ya. 1984. Resonant interactions of disturbances in transition to turbulence in a boundary layer. J. Fluid Mech., vol. 138, 209. (in Russian in 1982).
- Kaups, K. and Cebeci, T. 1977. Compressible laminar boundary layers with suction on swept and tapered wings. J. Aircraft, vol. 14, 661.
- Klebanoff, P.S., Tidstrom, K.D. and Sargent, L.M. 1962. The three-dimensional nature of boundary-layer instability. J. Fluid Mech., vol. 12, 1.
- Kleiser, L. and Laurien, E. 1984. Three-dimensional numerical simulation of laminar-turbulent transition and its control by periodic disturbances. Proc. 2nd IUTAM Symp. Laminar-Turbulent Transition, Novosibirsk, USSR.
- Kleiser, L. and Laurien, E. 1985. Numerical investigation of interactive transition control. AIAA Paper No. 85-0566.
- Knapp, C.F. and Roache, P.J. 1968. A combined visual and hot-wire anemometer investigation of boundary-layer transition. AIAA J., vol. 6, 29.
- Kohama, Y. and Kobayashi, R. 1983. Boundary layer transition and the behavior of spiral vortices on rotating spheres. J. Fluid Mech. 137, pp 153-164.
- Kozlov, V.V. and Ramazanov, M.P. 1984. Development of finite amplitude disturbances in a Poiseuille flow. J. Fluid Mech., vol. 147, 149.
- Liepmann, H.W. and Nosenchuck, D.M. 1982. Active control of laminar-turbulent transition. J. Fluid Mech., vol. 118, 201.
- Liepmann, H., Ghil, M., Newell, A., Roshko, A., and Saric, W. 1986. "Is chaos relevant to shear flows?" Chaotic Motion in Open Flows, UC Institute for Nonlinear Studies Workshop, Lake Arrowhead, California, Feb. 7-9, 1986.
- Mack, L.M. 1969. Boundary-layer stability theory. Jet Propulsion Lab. Rpt. 900-277, Rev. A.
- Mack, L.M. 1984a. Line sources of instability waves in a Blasius boundary layer. AIAA Paper 84-0168.
- Mack, L.M. 1984b. Boundary-layer linear stability theory. AGARD Report No. 709 (Special course on stability and transition of laminar flows) VKI, Brussels.
- Malik, M.R. 1986. Wave interactions in three-dimensional boundary layers. AIAA Paper No. 86-1129.
- Malik, M.R. and Poll, D.I.A. 1984. Effect of curvature on three-dimensional boundary layer stability. AIAA Paper No. 84-1672.
- Malik, M.R., Wilkinson, S.P. and Orszag, S.A. 1981. Instability and transition in rotating disk flow. AIAA J., vol. 19, 1131.
- Metcalfe, R.W., Rutland, C., Duncan, J.H. and Riley, J.J. 1985. Numerical simulations of active stabilization of laminar boundary layers. AIAA Paper No. 85-0567.
- Michel, R., Arnal, D. and Coustols, E. 1984. Stability calculations and transition criteria in two- or three-dimensional flows. Proc. 2nd IUTAM Symp. on Laminar-Turbulent Transition, Novosibirsk.
- Michel, R., Arnal, D., Coustols, E. and Juillen, J.C. 1984. Experimental and

- theoretical studies of boundary layer transition on a swept infinite wing. Proc. 2nd IUTAM Symp. on Laminar-Turbulent Transition, Novosibirsk.
- Morkovin, M.V. 1969. On the many faces of transition. Viscous Drag Reduction ed: C.S. Wells. Plenum.
- Morkovin, M.V. 1978. Instability, transition to turbulence and predictability. AGARDograph No. 236.
- Morkovin, M.V. 1983. Understanding transition to turbulence in shear layers - 1983. AFOSR Final Report, Contract F49620-77-C-0013.
- Nayfeh, A.H. 1980. Three-dimensional stability of growing boundary layers. Laminar-Turbulent Transition, ed: R. Eppler and H. Fasel, Springer.
- Nayfeh, A.H. 1981. Effect of streamwise vortices on Tollmien-Schlichting waves. J. Fluid Mech., vol. 107, 441.
- Nishioka, M., Iida, S., and Ichikawa, Y. 1975. An experimental investigation of the stability of plane Poiseuille flow, J. Fluid Mech., 72, pp. 731-751.
- Nishioka, M., Asai, M. and Iida, S. 1980. An experimental investigation of secondary instability. Laminar-Turbulent Transition, ed: R. Eppler and H. Fasel, Springer.
- Nishioka, M., Asai, M. and Iida, S. 1981. Wall phenomena in the final stages of transition to turbulence. Transition and Turbulence, ed. R.E. Meyer, Academic Press.
- Nishioka, M. and Asai, M. 1984. Evolution of Tollmien-Schlichting waves into wall turbulence. Turbulence and Chaotic Phenomena in Fluids, ed: T. Tatsumi, North-Holland.
- Nishioka, M. and Asai, M. 1985. 3-D wave disturbances in plane Poiseuille flow. Laminar-Turbulent Transition, Vol 2. ed. V. Kozlov, Springer.
- Poll, D.I.A. 1979. Transition in the infinite swept attachment line boundary layer. Aeronautical Quart., vol. XXX, 607.
- Poll, D.I.A. 1984a. Some observations of the transition process on the windward face of a yawed cylinder. Cranfield College of Aeronautics Report 8407.
- Poll, D.I.A. 1984b. Transition description and prediction in three-dimensional flows. AGARD Report No. 709 (Special course on stability and transition of laminar flows) VKI, Brussels.
- Reed, H.L. 1984. Wave interactions in swept-wing flows. AIAA paper no. 84-1678.
- Reed, H.L. 1985. Disturbance-wave interactions in flows with crossflow. AIAA Paper No. 85-0494.
- Reed, H.L. and Saric, W.S. 1986. Stability and transition of three-dimensional flows. Invited Paper, U.S. National Congress of Applied Mechanics, ASME, June 1986.
- Reshotko, E. 1976. Boundary-layer stability and transition. Ann. Rev. Fluid Mech. 8, 311.
- Reshotko, E. 1984a. Environment and receptivity. AGARD Report No. 709 (Special course on stability and transition of laminar flows) VKI, Brussels.
- Reshotko, E. 1984b. Laminar flow control - Viscous simulation. AGARD Report No. 709 (Special course on stability and transition of laminar flows) VKI, Brussels.
- Reshotko, E. 1985. Control of boundary-layer transition. AIAA Paper No. 85-0562.
- Reshotko, E. 1986. Stability and Transition, how much do we know? Invited Paper, U.S. National Congress of Applied Mechanics, ASME, June 1986.
- Saric, W.S. 1985a. Boundary-layer transition: T-S waves and crossflow mechanisms. Proc. AGARD Special Course on Aircraft Drag Prediction and Reduction. VKI, Belgium. May 1985.

- Saric, W.S. 1985b. Laminar flow control with suction: theory and experiment. Proc. AGARD Special Course on Aircraft Drag Prediction and Reduction, VKI, Belgium, May 1985.
- Saric, W.S., Carter, J.D. and Reynolds, G.A. 1981. Computation and visualization of unstable-wave streaklines in a boundary layer. Bull. Amer. Phys. Soc., vol.26, 1252.
- Saric, W.S., Kozlov, V.V. and Levchenko, V.YA. 1984. Forced and unforced subharmonic resonance in boundary-layer transition. AIAA Paper No. 84-0007.
- Saric, W.S. and Nayfeh, A.H. 1977. Nonparallel stability of boundary layers with pressure gradients and suction. AGARD C-P No. 224, 6.
- Saric, W.S. and Thomas, A.S.W. 1984. Experiments on the subharmonic route to transition. Turbulence and Chaotic Phenomena in Fluids, ed: T. Tatsumi, North-Holland.
- Saric, W.S. and Yeates, L.G. 1985. Experiments on the stability of crossflow vortices in swept-wing flows. AIAA Paper No. 85-0493.
- Singer, B.A., Reed, H.L. and Ferziger, J.H. 1986. Investigation of the effects of initial disturbances on plane channel transition. AIAA Paper No. 86-0433.
- Singer, B.A., Reed, H.L., and Ferziger, J.H. 1987. Effect of streamwise vortices on transition in plane channel flow, accepted, 1987 AIAA Aerospace Sciences Meeting, Reno.
- Spalart, P. and Yang, K.S. 1986. Numerical simulation of boundary layers. Part 2. Ribbon-induced transition in Blasius flow, accepted Journal of Fluid Mechanics.
- Spalart, P.R. 1984. Numerical simulation of boundary-layer transition. NASA TM-85984.
- Sreenivasan, K.R. and Strykowski, P.J. 1984. On analogies between turbulence in open flows and chaotic dynamical systems, Turbulence and Chaotic Phenomena in Fluids (Tatsumi, T., ed.), IUTAM Proc., Kyoto, Japan, Sept. 5-10, 1983.
- Tani, I. 1969. Boundary layer transition. Ann. Rev. Fluid Mech. 1, 169-196.
- Tani, I. 1981. Three-dimensional aspects of boundary-layer transition. Proc. Indian Acad. Sci., vol. 4, 219.
- Tatsumi, T. (ed.) 1984. Turbulence and Chaotic Phenomena in Fluids. Proc. IUTAM Symp., Kyoto, Japan, Sept. 5-10, 1983.
- Thomas, A.S.W. 1983. The control of boundary-layer transition using a wave superposition principle. J. Fluid Mech., vol. 137, 233.
- Thomas, A.S.W. 1986. Experiments on secondary instabilities in boundary layers. Invited Paper, U.S. National Congress of Applied Mechanics, ASME, June 1986.
- Thomas, A.S.W. and Saric, W.S. 1981. Harmonic and subharmonic waves during boundary-layer transition. Bull. Amer. Phys. Soc., vol. 26, 1252.
- Yang, K.S., Spalart, P.S., Reed, H.L., and Ferziger, J.H. 1987. Navier-Stokes computations of pressure-gradient effects on transition in a boundary layer, accepted: IUTAM Symposium on Turbulence Management and Relaminarization, Bangalore, India, 19-23 January.

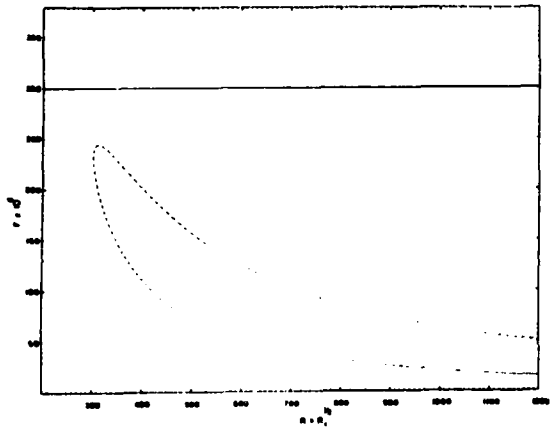


Figure 1. Neutral stability curve for Blasius boundary layer from parallel stability theory

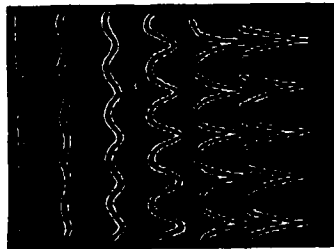


Figure 2 Streaklines in the boundary layer from flow visualization reproduced by Herbert et al. 1985. Ordered peak-valley structure of lambda vortices. K-Type

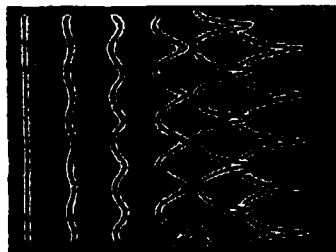


Figure 3. Streaklines in the boundary layer from flow visualization reproduced by Herbert et al. 1985. Staggered peak-valley structure of lambda vortices. H-Type.



Figure 4. Computer visualization of vortex lines by Singer et al. 1987. No imposed streamwise vortices H-Type

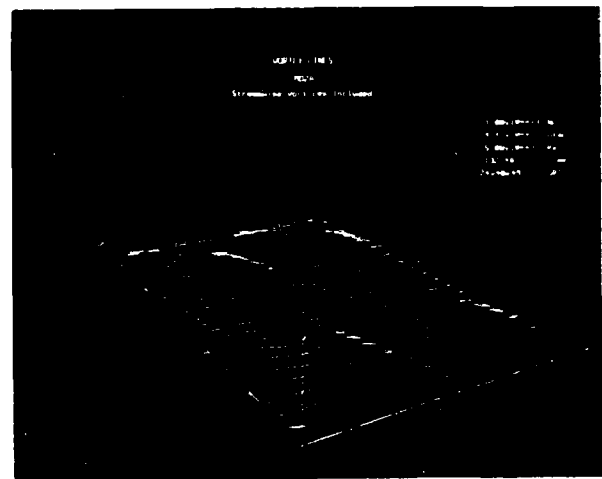


Figure 5. Computer visualization of vortex lines by Singer et al. 1987. Imposed streamwise vortices K Type

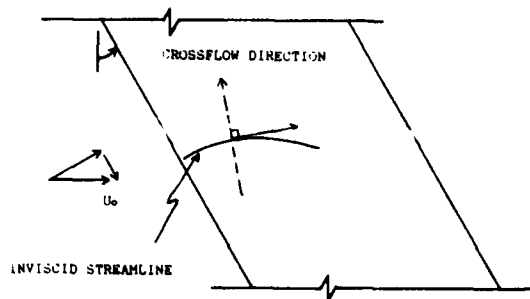


Figure 6. Schematic of flow over a swept wing

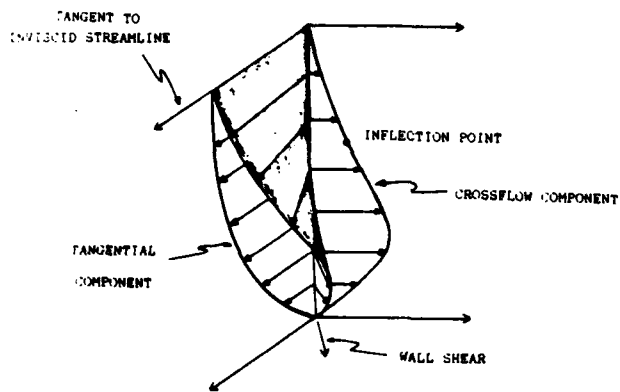


Figure 7 Schematic of velocity components on a swept wing illustrating the definition of crossflow velocity.

**AN EXPERIMENTAL INVESTIGATION OF A  
GLOBAL RESONANCE MECHANISM IN THE  
TWO-DIMENSIONAL TURBULENT JET**

Flint O. Thomas and K. M. K. Prakash  
School of Mechanical and Aerospace  
Engineering  
Oklahoma State University  
Stillwater, Oklahoma 74078

**ABSTRACT**

An experimental investigation of the transition and related structural development of a two-dimensional turbulent jet is presented. The data obtained suggest the presence of a global resonance mechanism which operates in the jet and strongly influences its large-scale development. This resonance appears to take the form of near exit perturbations which are each related to particular vortex pairing/destruction events occurring downstream, both in the developing jet shear layers and in the interaction region of the flow. These perturbations excite the nascent jet shear layers and affect the subsequent structural evolution of the flow. Thus the transition of the jet is noted to be governed both by the initial thin shear layer instability and the requirements for global resonance.

**1. INTRODUCTION**

The existence of a resonance mechanism in impinging jets was clearly demonstrated by Ho and Nossler (1981). As a natural extension of this work Laufer (1981) questioned whether a similar resonance mechanism may occur in free jets as well. Indeed preliminary measurements by Laufer and Monkewitz (1980) in an axisymmetric jet indicated that hot-wire signals obtained in the initial shear layer exhibit modulation at a frequency corresponding to the "jet column mode or downstream vortex passage frequency near the end of the potential core. More detailed study of this phenomenon by Monkewitz (1983) revealed that the signal modulation is due to a modulation of the receptivity of the shear layer. Related work by Dimotakis and Brown (1976) in mixing layers led to the conclusion that the flow dynamics at any

point is coupled to the flow structures occurring farther downstream. Ho and Huang (1982) indicate that both the local instability process and global resonance requirements play crucial roles in determining the dynamic behavior of the mixing layer. In fact, the global resonance mechanism appears responsible for determining the location of vortex pairing events which are directly responsible for mixing layer growth. Evidence was found by Thomas and Goldschmidt (1986) which suggests that a global resonance mechanism also plays an important role in the evolution of planar jets. Preliminary data suggesting such a feedback phenomenon are presented and discussed in Thomas and Goldschmidt(1985).

The primary objective of the work to be reported was to experimentally investigate the nature of the global resonance mechanism as it occurs in the planar turbulent jet and its implications for jet development.

**2. MEASUREMENT APPARATUS AND FLOW FIELD**

The experimental facility is the same as that described in Thomas and Brehob (1986). It is powered by a three-stage centrifugal blower which supplies air to a large cubic plenum chamber. The blower and plenum are coupled by means of a flexible rubber duct for vibration isolation. A large slab of fiberglass insulation material is contained within the plenum in order to filter the air and to decouple the flow field from any blower pulsation. A rectangular duct containing flow straighteners and turbulence reducing screens connects the plenum to the nozzle assembly. The two-dimensional nozzle has a contraction ratio of 16 to 1 and ends in a slot that is 1.27 cm wide and 45.7 cm in height. The nozzle contour was

based on a design by Jordinson (1961). Twin faceplates mounted flush with the nozzle exit extend laterally to the edge of the flow field. The flow field is formed by two large horizontal plates 2.13 m in length and 1.52 m wide which keep the basic flow two-dimensional. All other sides of the flow field remain open.

All measurements to be reported were made with commercial anemometers operated in the constant temperature mode. For measurement of the instantaneous longitudinal fluctuating component standard straight wire probes were used. The analog signals from the anemometers were passed through anti-alias filters and then digitized with an HP-98640A A/D board. The resulting signals were then processed on line with an HP-9920S microcomputer which performed all data reduction. Further details concerning the experimental facilities may be found in Prakash (1986).

In the work to be reported, all measurements were made at an exit Reynolds number of 7700 (based on nozzle exit slot width and mean exit velocity). This corresponds to a mean exit velocity of  $U_0 = 8.84$  m/s. The exit mean velocity profile was flat except for two very thin shear layers which bounded the potential core. The mean velocity variation in the shear layers was very closely approximated by a hyperbolic tangent type profile. The exit centerline fluctuation intensity was quite low; less than 0.30 percent. The nozzle exit boundary layers were found to be laminar and had a momentum thickness of  $\theta = 0.0085$  cm. The corresponding displacement thickness was  $\delta^* = 0.0232$  cm. The initial mean velocity development is characterized by the widening of the shear layers resulting in a "shearing down" of the initially flat profile and the jet potential core is completely engulfed by  $x/D = 4.5$  ( $x =$  the longitudinal spatial coordinate,  $D =$  the nozzle slot width). The downstream variation of jet shear layer momentum thickness  $\theta$  is documented in Figure 1. Initial development is characterized by localized increases in  $\theta$  which will be shown to correspond to large-scale vortex formation and interaction events.

In order to validate the flow field an extensive set of mean flow and turbulence data was obtained. These data were compared with other published values in order to insure no unusual behavior that might jeopardize the generality of

the conclusions to be made from this work. Though space limitations prevent presentation of these data it may be said that the jet exhibited no unusual characteristics with regard to both mean flow and turbulence quantities. Approximate mean velocity similarity was noted for  $x/D > 11$ .

### 3. MEASUREMENTS CHARACTERIZING JET DEVELOPMENT

This section describes the results of measurements that detail the development of structural patterns in the two-dimensional turbulent jet. These data will subsequently be examined in light of the requirements for global resonance in section 4.

#### 3.1 Spectral Measurements

Spectral measurements of the longitudinal velocity fluctuations were made both on the centerline of the jet and in the jet shear layer ( $y/b = 1.0$ , where  $y$  is the lateral spatial coordinate and  $b$  is the mean velocity half-width) at several selected streamwise locations ( $0.25 < x/D < 20$ ). FFT techniques were used to compute the spectra and in order to obtain smooth repeatable values the measurements were typically averaged over 200 ensembles. The frequency resolution of the spectra is approximately 9 Hz.

##### 3.1.1 Linear Amplification Region

Shear layer spectra obtained in the region  $0.25 < x/D < 1.0$  indicate frequency dependent amplification of instabilities which is in good agreement with linear stability theory for spatially amplified disturbances. Figure 2 presents experimentally measured spatial amplification rates obtained in the nascent jet shear layer compared with predicted values from Michalke's (1965) linear stability theory for the hyperbolic tangent profile. The good agreement verifies the exponential amplification of small disturbances for  $x/D < 1.0$ . Phase velocities (not shown here) also exhibit good agreement with linearized small disturbance theory. The dimensionless frequency for maximum amplification is  $\beta = 2\pi f\delta/U = 0.21$  ( $f =$  frequency in Hz,  $\delta =$  maximum slope shear layer thickness and  $U$  is the mean speed of the high and low speed sides of the shear layer, in this case  $0.5U_0$ ) or  $f\theta/U = 0.0320$  which corresponds to a frequency of approximately 750 Hz.

One unexpected result of energy spectra obtained in the linear region of the jet is the existence of a dominant, albeit low level,

spectral peak at approximately 20 Hz as is seen in Figure 3. Such a low frequency mode is very uncharacteristic of thin shear layer instability frequencies as it is at least an order of magnitude less than the expected values. This mode behaves as a neutral mode in the linear region. Plausible sources for the production of this unexpected near exit low frequency wave were investigated. Pulsing of the exit flow was considered as a possible source. However, it was found that lateral profiles of the low frequency mode indicate it to be highly localized in the jet shear layers. It was also thought that this wave could originate due to a boundary layer instability from inside the nozzle. However the measured  $Re_x$  is far below the critical value as computed from the instability characteristics of the Blasius boundary layer profile which makes this an unlikely source as well. A kinematic effect arising because of a lateral flapping of the shear layer past the stationary probe was also ruled out as a possible origin. Hence it was concluded that the low frequency mode is highly localized in the shear layer adjoining the potential core and is not linked to any source external to the flow field. Since the frequency corresponds to downstream vortex passage rather than typical shear layer instabilities it served as early evidence of a possible coupling with the downstream flow. Similar low frequency near exit oscillations were reported in other planar jet test rigs by Sato (1960) and Thomas and Goldschmidt (1986).

### 3.1.2 Nonlinear Spectral Development

The exponential growth of the most amplified instability wave saturates by  $x/D = 1.25$  (approximately 2.6 initial instability wavelengths), marking the end of linear growth and the onset of nonlinear interaction between fluctuations. Previous research in free shear layers has indicated that the onset of nonlinear effects is marked by the rolling up of the most amplified instability into a periodic array of compact spanwise vortices (see Ho and Huang (1982), Ho and Huerre (1984)). Since the initial region of the planar jet, basically consists of two nominally self preserving shear layers it seems natural to expect similar behavior. However the results of the spectral measurements indicate that the vortex roll up frequency does not correspond to the initially most amplified frequency.

Figure 4 presents the shear layer power spectrum obtained at  $x/D = 2.25$  which shows the formation of a dominant mode at approximately 250 Hz corresponding to the local vortex passage frequency. This figure also illustrates another characteristic of spectra obtained in this region which is the development of "sidebands" on the primary modes. The frequency spacing between the sidebands corresponds to the low frequency mode noted previously in the linear amplification region. The presence of these bands here suggests modulation of the primary mode by the low frequency wave. These sidebands are asymmetric about the primary mode they modulate, favoring the low frequency side.

Figure 5 shows the streamwise growth and decay of the 250 Hz mode along with its subharmonic at 125 Hz (the bandwidth for this figure is 10 Hz). Ho and Huerre (1984) related the completion of the roll up process to the downstream location where the fundamental reaches maximum amplitude which from Figure 5 suggests that in this case  $x/D = 2.25$  may be considered as an average location for structural formation. It has also been demonstrated that the location of subharmonic saturation corresponds to the streamwise location where vortex pairing is accomplished in free shear layers, though it is difficult to pinpoint an exact location since it requires some streamwise distance to occur. From Figure 5 the subharmonic is seen to saturate at  $x/D = 4.5$  indicating a vortex pairing event occurs on average at that approximate location. This location also marks the end of the potential core and Figure 1 suggests that the increased shear layer widening associated with this pairing event is responsible for its termination. Figure 6 clearly shows this sequence of halving of modal frequency which suggests the pairing of vortical structures at the approximate location described above. With increasing downstream distance there is a gradual shift in the energy of fluctuations to lower frequencies. Modulation effects play an important role in this process due to the formation of multiple sidebands on the primary modes. These interact among themselves to enrich the broadband energy content of the spectra. Miksad (1972) noted that the nonlinear interaction between modes at two different frequencies in a free shear layer resulted in the formation of sum and difference modes as well as the harmonics and

subharmonics of the interacting waves. Such nonlinear interactions appear to be a primary source for the energy transfer to lower frequencies noted in the jet shear layer spectra as each of the fine scale spectral peaks could be traced to sum and difference interactions between other components. The shear layer spectra beyond  $x/D = 8$  are basically broadband in nature making it extremely difficult to discern any further aspects regarding structural development.

It is expected that certain velocity fluctuations on the jet centerline are induced by large-scale structural events occurring in the shear layers. Hence centerline power spectra show more distinct peaks as compared to those obtained in the shear layer where the levels of fine-grained turbulence are higher. Evidence of the interaction between structures beyond the potential core is noted in the centerline spectral sequence of Figure 7. It may be observed that the dominant spectral frequency near 125 Hz is halved over the range  $7 < x/D < 9$ . A more gradual approximate halving of the resulting mode near 60 Hz is accomplished by  $x/D = 17$  (not shown here) suggesting an additional merging/destruction event is involved. It will be shown in the following sections that this event is associated with the loss of flow symmetry.

### 3.2 Space-time Correlation Measurements

Normalized space-time correlation functions of longitudinal fluctuations were obtained with probes positioned on opposite sides of the jet centerline at  $y/b = \pm 1.0$  for selected streamwise locations throughout the developing jet. Figure 8 shows selected representative space-time correlation coefficient functions. The positive zero time-delay value for the coefficient function at  $x/D = 4$  suggests that the jet shear layer structures are arranged symmetrically with respect to the centerline (this has also been confirmed in separate flow visualization studies in our laboratory). There is a decrease in the level of zero time-delay positive correlation with downstream distance due to the increasing randomization of the waveforms as the flow progresses downstream (which was also noted in a spectral sense as a broadening of peaks). The average local frequencies of oscillation of the coefficient functions were found to be in good agreement with the passage frequencies inferred from the dominant modes of the power spectra. The

structural symmetry is gradually lost beyond the end of the potential core as the shear layers interact to form the self-preserving anti-symmetric structural array that has been shown to characterize the similarity region of planar jets (see Thomas and Brehob (1986)). Figure 8 shows the corresponding change in the form of the correlation function as the shear layers interact. The formation of a negative lobe at zero time-delay (as noted in the correlations obtained at  $x/D = 16$  and  $17$ ) indicates the onset of anti-symmetric longitudinal velocity fluctuations which characterize the similarity region of the jet. This transformation appears complete near  $x/D = 16-17$  as is evidenced by Figure 9 which shows the variation of zero time-delay correlation coefficient with downstream distance. It may be noted that the negative correlation persists well into the similarity region. Of interest in Figure 8 is the similarity between the correlation function in the near exit region (shown for example is  $x/D = 0.75$ ) with those obtained in the early self-preserving region. This further suggests that the low frequency near exit mode may be related to downstream structures and that unlike the primary shear layer modes these near exit fluctuations are anti-symmetric.

### 3.3 Spectral Coherence and Phase Spectrum Measurements

In the first coherence measurements to be reported the probe positioning was identical to that for the correlation measurements reported above. The purpose of these measurements was to obtain information regarding the relation between corresponding spectral modes occurring on opposite sides of the jet in the developing and interacting shear layers. The space-time correlation measurements presented in the previous section were performed in the time domain and result from superposition of the multiple spectral modes present. Hence, this measurement is not complete in detailing the relationship between corresponding spectral modes in the developing jet shear layers.

Of particular interest are the near exit coherence measurements which show peaks at the dominant frequencies noted from the previously presented spectral analysis. For example, Figure 10 presents the coherence spectrum obtained at  $x/D = 0.50$ . Elevated coherence is noted near

20 Hz, 60 Hz and 250 Hz as well as for a range of higher frequencies associated with instability waves in the linear region. The 20 Hz mode was noted previously in the near exit spectral measurements as well as in spectra obtained near  $x/D = 16$  (near the formation of flow asymmetry). The corresponding near exit phase spectrum (not shown here) indicates this mode to be anti-symmetric. Significant is the occurrence of strong coherence across the near exit region for the 60 Hz mode which was noted from spectra to correspond to the passage frequency resulting from vortex merging just beyond the end of the potential core. This suggests the possibility of a particularly strong influence from this downstream event. The 60 Hz mode may also be noted from the previously presented near exit correlation function by defining the frequency as a reciprocal of the time delay between consecutive maxima. The phase spectrum obtained at  $x/D = 0.50$  indicates that this mode is symmetric. The fact that the correlation function shows negative correlation at zero time-delay does not indicate asymmetry of the 60 Hz component but instead reflects the influence of the 20 Hz mode. The 250 Hz and 125 Hz modes are noted to be symmetric and correspond to the downstream vortex roll up frequency and subharmonic formation, respectively. A complete study of the downstream evolution of the coherence and phase spectra was performed. These data confirm that the jet shear layer structures form and evolve symmetrically and that while pairing near  $x/D = 4.5$  causes small phase excursions the symmetric pattern is rapidly recovered. These measurements were of limited value beyond  $x/D = 8$  due to the low levels of coherence associated with the chaotic nature of the flow in the interaction region.

In the second set of measurements to be reported two straight wire probes were placed on opposite sides of the jet centerline with one probe fixed in the nascent jet shear layer at  $x/D = 0.25$ . The other probe was movable and was placed in the opposite jet shear layer at  $y/b = 1.0$  over streamwise locations between  $0.25 < x/D < 20$ . The spectral coherence and phase spectra were computed via FFT techniques for selected streamwise positions of the movable probe. Figure 11 presents the measured frequencies corresponding to local maximum spectral coherence for various positions of the

movable probe. A discontinuous distribution involving four nearly constant frequency regimes is noted from this figure. The figure suggests a downstream coupling with the near exit flow at certain preferred discrete frequencies. These frequencies were each noted from previous measurements to be associated with structural interaction events. The region  $0.25 < x/D < 2.0$  indicates that the spectral mode near 250 Hz (which corresponds to the vortex roll up frequency) is most coherent with the nascent shear layer flow. A sudden drop to 125 Hz is noted to occur soon after roll-up ( $x/D = 2.0$ ). This subharmonic frequency is seen to exhibit peak coherence up to  $x/D = 5.0$ . It may be recalled that spectral measurements indicate a pairing event occurs over this region which suggests that this event is coupled with the near exit flow field. From the previously presented centerline spectral measurements,  $x/D = 7$  was noted as the location initiating a halving of the characteristic structural passage frequency. This is consistent with Figure 11 which shows that the frequency for maximum coherence drops to approximately 60 Hz over the range  $5 < x/D < 8$ . This initiates a second interaction event which results in maximum coherence near 20 Hz for  $x/D > 16.0$ . It may also be noted from Figure 11 that each of the the events which lead to a discontinuous shift in frequency for maximum coherence are associated with an approximate doubling in downstream distance between the occurrence of the events. A similar phenomenon was noted by Ho and Huang (1982) in mixing layers.

It is interesting to compare the above measurement with coherence measurements made at corresponding streamwise locations but with the probes side by side at  $y/b = \pm 1.0$ . Figure 12 makes such a comparison between the two measurements for  $x/D = 8.0$ . Of significance is the observation that the coherence levels are much greater when the probes possess large streamwise separation. The comparatively high levels of coherence exhibited for the cases involving streamwise probe separation even in this chaotic region is further evidence of the presence of a coupling between the near exit flow and downstream locations.

#### 4. GLOBAL RESONANCE MECHANISM

The experimental results presented in the

previous section document the occurrence of localized large-scale structure interaction events in the developing two-dimensional turbulent jet. The experiments also suggest that these events are strongly coupled with the near exit shear layers. In this section a simple model for global resonance is examined in light of the experimental results presented. The model is based upon a feedback model proposed by Ho and Nossier (1981) for impinging jet flows and extended by Ho and Huang (1982) to mixing layers.

A requirement for resonance to occur between two streamwise locations in a flow separated by a distance  $\Delta x$  is that the time for convection of vortical structures downstream plus the time for acoustic disturbances to propagate upstream must equal an integral multiple of the resonance period. This assumes that the feedback loop consists of downstream propagating coherent vortical structures whose subsequent interactions produce upstream propagating acoustic waves. These are believed to excite the nascent jet shear layers to complete the feedback loop. Mathematically the above relation is then

$$\int_{x_0}^{x_0 + \Delta x} \frac{dx}{KU_m(x)} + \frac{\Delta x}{a} = \frac{N}{f_{res}} \quad (1)$$

where  $N = \text{integer}$ ,  $K = \text{constant} = U_c(x)/U_m(x)$ ,  $U_c(x)$  is a structural convective velocity,  $U_m(x)$  is the local mean centerline velocity,  $a = \text{acoustic speed}$ ,  $x_0 = \text{the streamwise near exit location for the feedback node}$ ,  $f_{res} = \text{the resonant frequency associated with the structural interaction event}$  and  $x_0 + \Delta x = \text{the downstream location associated with the vortex interaction event}$ . Measurements suggest that  $K = 0.6$  which is in general agreement with the results of Goldschmidt et al (1972). The value for  $N$  was taken to be 1. It may be noted that Laufer and Monkewitz (1980) have suggested that  $N = 2$  is appropriate for axisymmetric jets. Since in the case considered here  $x_0$  is approximately at the nozzle lip and the flow is a low speed subsonic flow equation (1) reduces to

$$\int_0^{x_1} \frac{dx}{KU_m(x)} = \frac{N}{f_{res_i}} \quad (2)$$

where  $x_1$  is the location of the  $i$ th downstream large-scale structural interaction event and  $f_{res_i}$  is the corresponding frequency. If global

resonance is to exist in the jet then the above relation must be satisfied throughout the flow field; in both the developing shear layers and in the interaction region and early similarity regions beyond the jet potential core. It is apparent that the merging of the shear layers near the end of the potential core results in vortex pairing/destruction events as the symmetrically arranged shear layer structures are forced to interact. It is necessary that the characteristic resonant frequency  $f_{pc}$  associated with the first structural interaction beyond the end of the potential core at  $x_{pc}$  (which will equal twice the length of the potential core) should satisfy the requirements of global resonance. Thus it follows that

$$f_{pc} = \frac{N}{\int_0^{x_{pc}} \frac{dx}{KU_m(x)}} \quad (3)$$

The measurements presented also indicate that significant changes in passage frequency with downstream distance occur primarily from vortex pairing events. Since a passage frequency halving occurs at pairing locations it is possible to predict the occurrence of all vortex pairing events from the requirements of global resonance when one pairing event location along with the corresponding structural frequency is known. With this in mind it could be said that

$$f_i = 2^i f_{pc} \quad (4)$$

where  $i$  corresponds to the " $i$ th" event prior to the interaction event at  $x_{pc}$  and  $f_i$  is the structural passage frequency associated with the completion of the  $i$ th pairing event. In this manner negative  $i$  values correspond to events downstream of  $x_{pc}$ . Substituting (4) in equation (3) we obtain an implicit relation for event locations  $x_i$

$$2^i f_{pc} = \frac{N}{\int_0^{x_i} \frac{dx}{KU_m(x)}} \quad (5)$$

Figure 11 compares the resonant frequencies and streamwise locations predicted by the requirements for global resonance (given that the potential core nominally ends at  $x/D = 4.5$  due to the pairing event that occurs there) with modal frequencies based upon measurement of spectral coherence. The agreement is seen to be

favorable.

## 5. CONCLUSION

The measurements of jet development that have been presented are in support of the existence of a global resonance mechanism operating in the planar turbulent jet. Measurements have documented the following key events which are important in the development of the flow: The roll-up of shear layer instability waves into a symmetric array of vortices near  $x/D = 2.25$ , symmetric structural merging events near  $x/D = 4.5$  and  $x/D = 9.0$  and a merging /destruction event associated with the loss of flow symmetry which occurs near  $x/D = 17$ . Each of these events are thought to be coupled to the nozzle exit flow by a feedback loop. Phase spectra show that the near exit perturbations induced by these events are symmetric with the exception of the mode near 20 Hz which appears to be associated with the formation of the self-preserving anti-symmetric array that characterizes the similarity region of planar jets. Several studies have shown this array to exhibit a local passage frequency given by  $fb/U_m = 0.11$  (see Thomas and Brehob (1986)). Values near the location of formation at  $x/D = 17$  are in agreement yielding  $(fb/U_m)_{x/D=17} = 0.1$ . While the near exit mode near 20 Hz exhibits the greatest amplitude, the mode near 60 Hz appears substantially more coherent across the jet exit and both experiment and resonance model suggest that it has a more pronounced effect on jet development. In particular, merging of structures beyond the potential core is seen to be a most important event as it largely determines the global flow dynamics through the selection of  $x_{pc}$  and  $f_{pc}$  in accordance with the requirements for global resonance. Both model and experiment indicate that the structural roll-up ( and consequently the subsequent flow evolution) is significantly altered over that which has been documented in single mixing layers and that the shear layer interaction beyond the potential core is primarily responsible for the modification. The roll-up at a frequency of approximately 250 Hz instead of the initially most amplified frequency of 750 Hz is required to satisfy the resonant condition at the end of the potential core imposed by the length scale  $D$ . Such a scale is absent in the mixing layer where the instability characteristics scale with the initial shear layer

thickness. The dynamic mechanism by which the roll up is altered is not presently completely understood. However, detailed spectral measurements reported in Prakash (1986) suggest an interaction between the subharmonic of the most amplified shear layer instability and the mode  $f_{pc}$  is responsible. Additional work involving application of higher order spectra (i.e. the bicoherence spectra) are required to quantify this interaction.

## ACKNOWLEDGMENTS

This work was completed in part under NSF Grant No. MEA-8403893. Additional support was provided by Dow Chemical Corporation. This support is gratefully acknowledged.

## REFERENCES

1. Dimotakis, P. E.; Brown, G. L. 1976: The Mixing Layer at High Reynolds Number : Large Structure Dynamics and Entrainment. *J. Fluid Mech.* 78, 535-345.
2. Goldschmidt, V. W.; Young, M. F. ; Ott, E. S. 1981: Turbulent Convective Velocities (Broadband and Wavenumber Dependent) in a Plane Jet. *J. Fluid Mech.* 108, 327-345.
3. Gutmark, E.; Wygnanski, I. 1976: The Planar Turbulent Jet. *J. Fluid Mech.* 73, 465-495.
4. Ho, C. M.; Huang, L. S. 1982: Subharmonics and Vortex Merging in Mixing Layers. *J. Fluid Mech.* 119, 443-473.
5. Ho, C. M.; Huerre, P. 1984: Perturbed Free Shear Layers. In : *Ann. Rev. Fluid Mech.* Vol 16, pp. 365-424, Annual Reviews Inc.
6. Ho, C. M.; Nossier, N. S. 1981: Dynamics of an Impinging Jet. Part 1. The Feedback Phenomenon. *J. Fluid Mech.* 105, 119-142.
7. Jordinson, R. 1961: Design of Wind Tunnel Contractions. *Aircraft Eng.* 33, 294-297.
8. Laufer, J. 1981: Transition and Turbulence. pp. 63-76, New York: Academic Press.
9. Laufer, J.; Monkewitz, P. 1980: AIAA paper No. 80-0962.
10. Michalke, A. 1965: On Spatially Growing Disturbances in an Inviscid Shear Layer. *J. Fluid Mech.* 23, 521-544.
11. Miksad, R. W. 1972: Experiments on the Nonlinear Stages of Free Shear Layer Transition. *J. Fluid Mech.* 56, 695-719.
12. Monkewitz, P. 1983: On the Nature of the Amplitude Modulation of Jet Shear Layer Instability Waves. *Phys. of Fluids.* 26, 3180-3184.
13. Prakash, K. M. K. 1986: An Experimental Investigation of a Resonance Mechanism in a Two-Dimensional Turbulent Jet. M.S. Thesis, School of Mechanical and Aerospace Engineering, Oklahoma State University.
14. Sato, H. J. 1960: The Stability and Transition of a Two-Dimensional Jet. *J. Fluid Mech.* 1, 53-80.

15. Thomas, F. O.; Brehob, E. G. 1986: An Investigation of Large-Scale Structure in the Similarity Region of a Two-Dimensional Turbulent Jet. *Phys. of Fluids*, 29, 1788-1795.
16. Thomas, F. O.; Goldschmidt, V. W. 1985: The Possibility of a Resonance Mechanism in the Developing Two-Dimensional Jet. *Phys. of Fluids*, 28, 3510-3514.
17. Thomas, F. O.; Goldschmidt, V. W. 1986: Structural Characteristics of a Developing Turbulent Planar Jet. *J. Fluid Mech.* 163, 227-256.

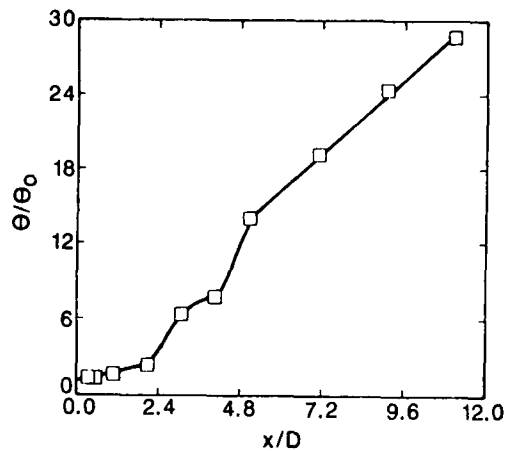


Figure 1. Downstream variation of shear layer  $\theta$

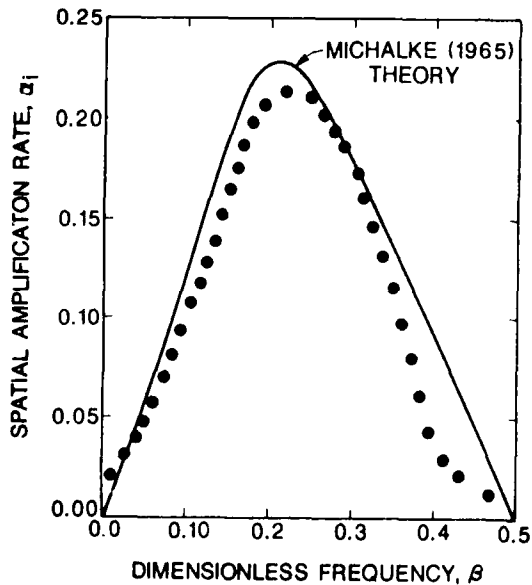


Figure 2. Spatial amplification rates

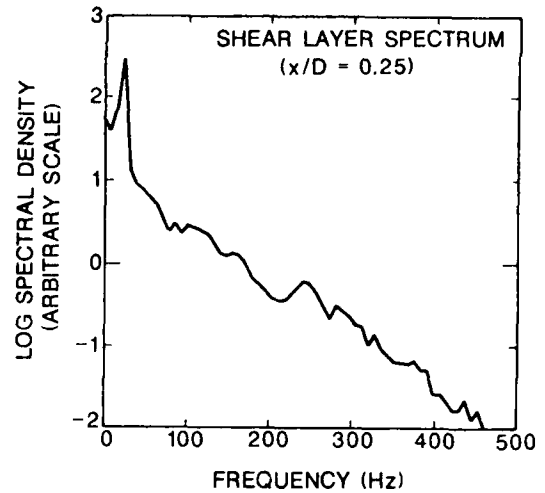


Figure 3. Shear layer spectrum at  $x/D = 0.25$

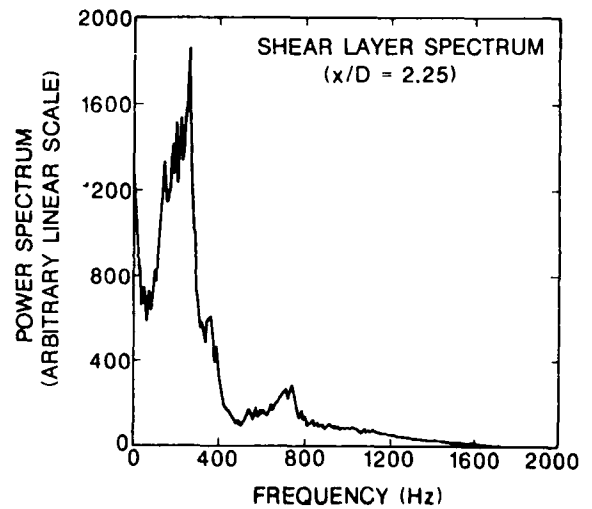


Figure 4. Shear layer spectrum at  $x/D = 2.25$

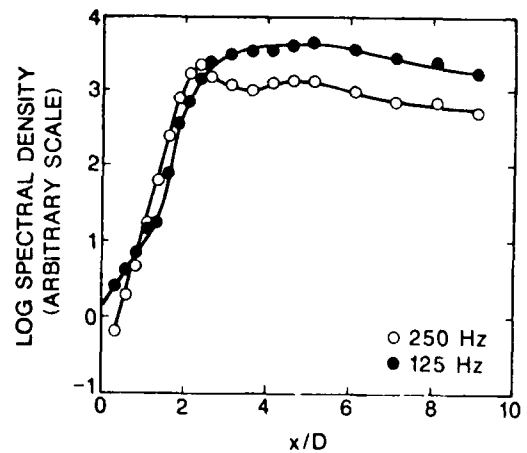


Figure 5. Downstream spectral evolution

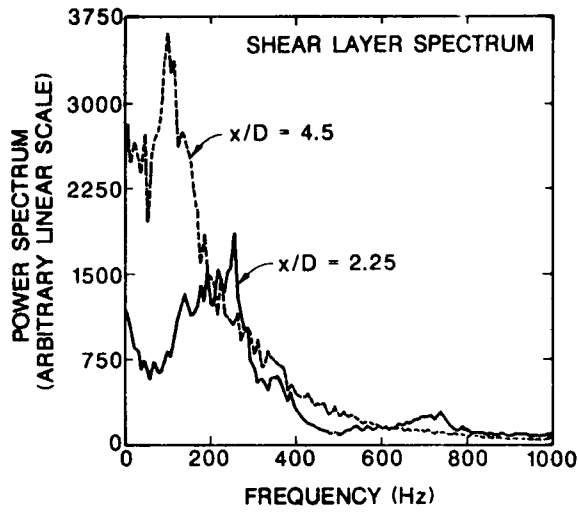


Figure 6. Comparison of shear layer spectra at  $x/D = 2.25$  and  $4.5$

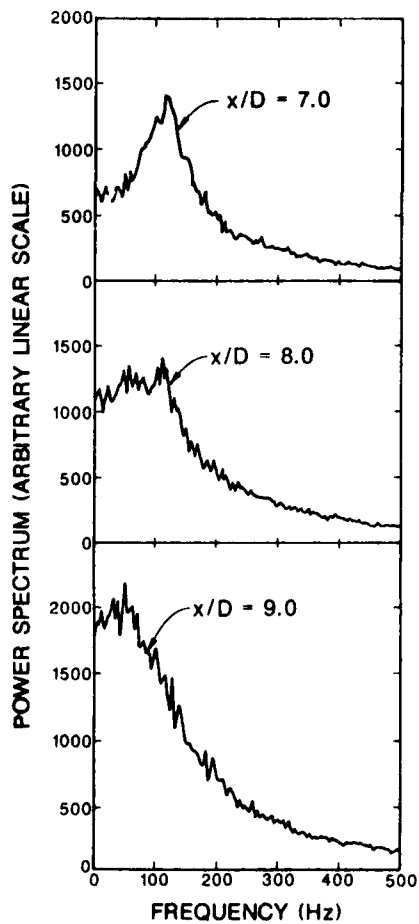


Figure 7. Centerline spectral sequence

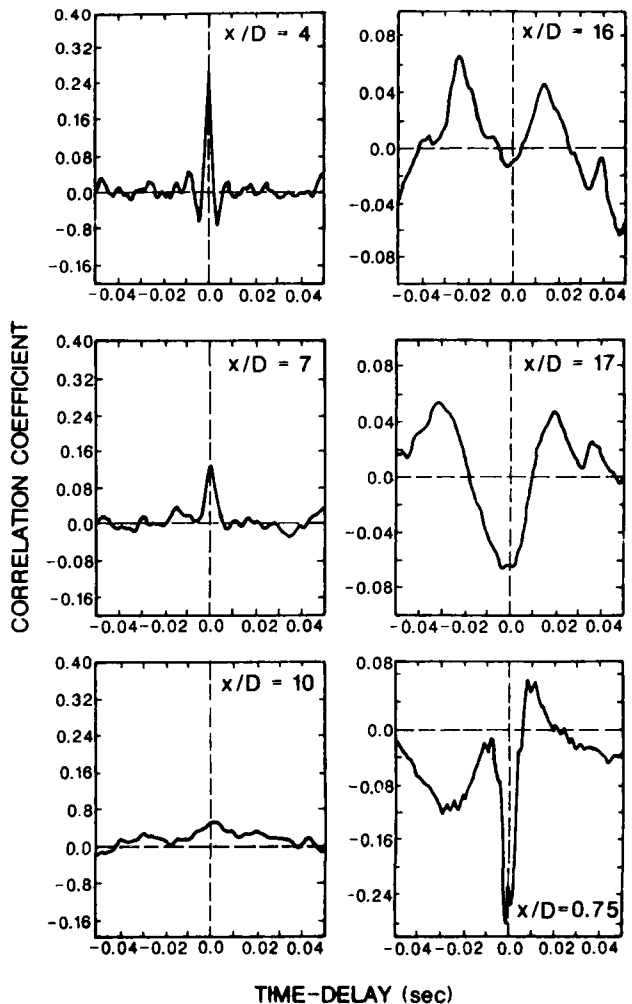


Figure 8. Measured correlation coefficient functions (probes at  $y/b = +1.0$ )

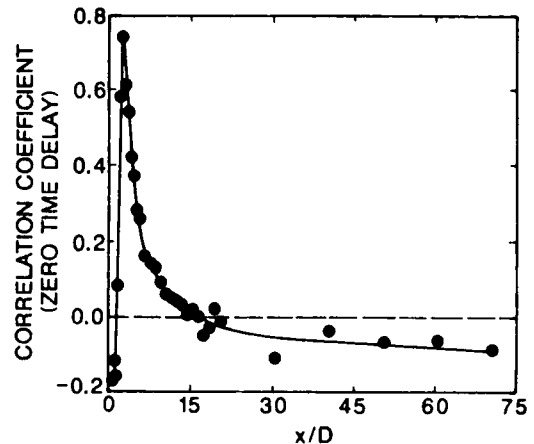


Figure 9. Downstream variation of zero time delay correlation coefficient (probes at  $y/b = \pm 1.0$ )

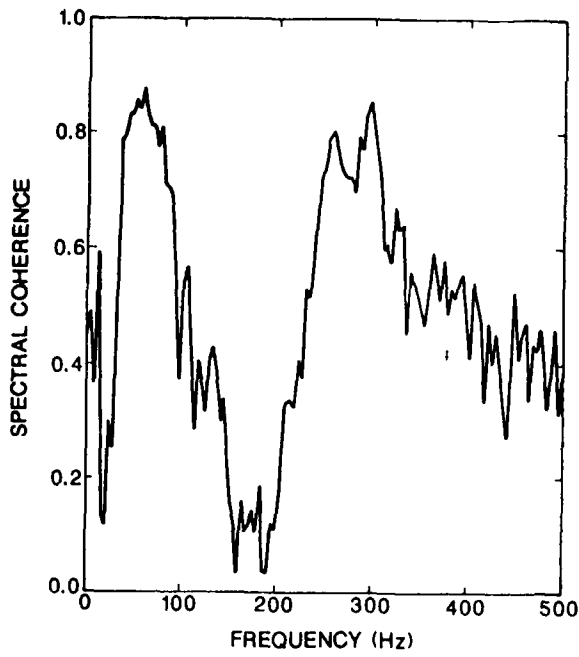


Figure 10. Spectral coherence at  $x/D = 0.5$  (probes at  $y/b = \pm 1.0$ )

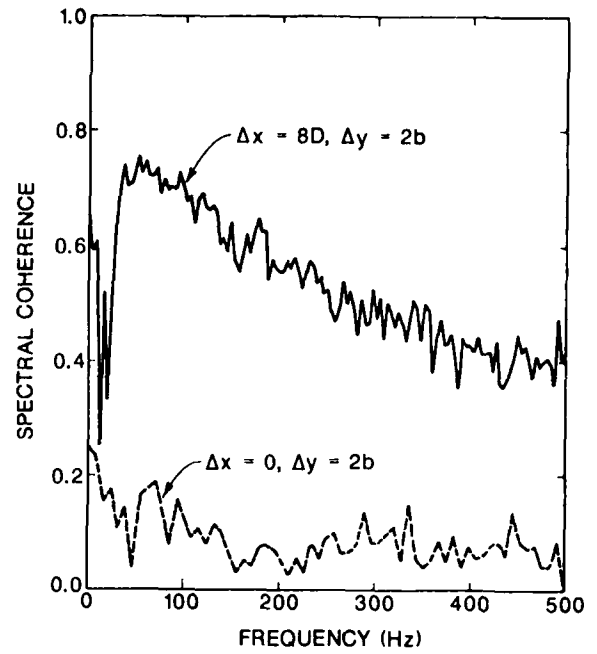


Figure 12. Comparison of spectral coherence with and without streamwise probe separation

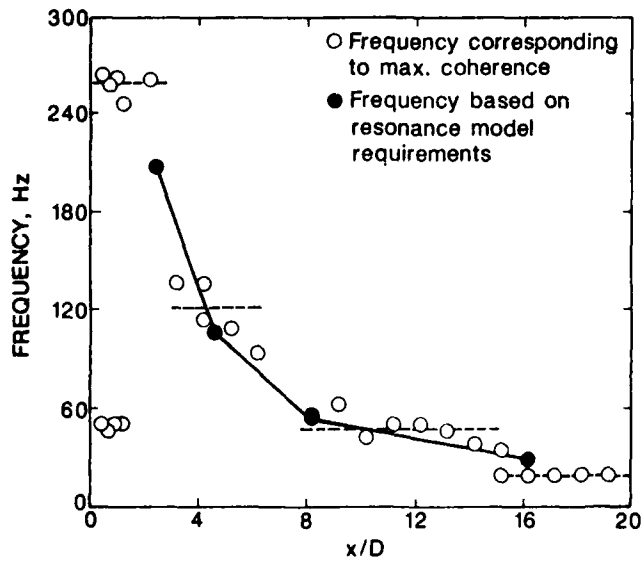


Figure 11. Downstream variation of modal frequency

**RAYLEIGH-BENARD CONVECTION:  
EXPERIMENTAL STUDY OF  
TIME-DEPENDENT INSTABILITIES**

Beatrice Martinet and Ronald J. Adrian  
Department of Theoretical and  
Applied Mechanics  
University of Illinois  
Urbana, IL 61801, USA

**ABSTRACT**

The transition from steady thermal convection to turbulent thermal convection in a horizontal layer of water (Prandtl number = 5.8) contained by a square cavity of large aspect ratio (48.5) has been studied using laser Doppler velocimetry. Power spectra of the horizontal velocity fluctuations were measured in the Rayleigh number range from 30,000 and 99,000, wherein periodic, quasi-periodic, and broad-band time-dependent instabilities coexist. At Rayleigh numbers greater than 32,000 a narrow band spectrum emerges that is probably associated with the oscillatory instability of Busse (1972). The frequency of this motion scales with  $\kappa^2/d$  modified by a Prandtl number factor.

Between  $10Ra_c$  and  $30Ra_c$  the frequency undergoes three abrupt jumps while increasing along an  $Ra^{2/3}$  power law.

**LIST OF SYMBOLS**

c	heat capacity
d	depth of fluid layer
f	frequency
g	gravitational acceleration
H	heat flux
k	thermal conductivity
Nu	Nusselt number = $Hd/k\Delta T$
Pr	Prandtl number = $\nu/\kappa$
Ra	Rayleigh number
$Ra_c$	critical Rayleigh number = 1708
$\Delta T$	temperature difference across the fluid layer
$\beta$	thermal coefficient of expansion

$\Gamma_y$	aspect ratio = width/depth
$\kappa$	thermometric conductivity = $K/\rho c$
$\nu$	kinematic viscosity
$\rho$	density

**1. INTRODUCTION**

Horizontal fluid layers heated from below become unstable to infinitesimal perturbations at a critical Rayleigh number  $Ra_c = 1708$ . They subsequently undergo a sequence of instabilities as the Rayleigh number is increased, and at Rayleigh number around  $10^5$  they become generally chaotic, with smooth, broad-band spectra having no discernable peaks. At sufficiently large Rayleigh numbers, perhaps as large as  $10^7$  or  $10^8$ , the buoyancy-driven motions become fully turbulent.

The succession of instabilities has been investigated extensively using linear and non-linear stability analysis and flow visualization. Steady instabilities that have been identified include the basic infinitesimal amplitude roll cells, (c.f. Chandrasekhar 1961, Busse 1978), finite amplitude roll cells, and hexagonal Benard cells (Busse 1967), the zig-zag instability of roll cells (Busse and Whitehead 1971), the cross-roll instability (Busse 1971), and the skewed varicose and knot instabilities (Busse and Clever 1979). Time-dependent instabilities include the fundamental three-dimensional oscillatory motion of roll cells (Willis and Deardorff 1970, Busse 1972), time-dependent bimodal convection (Busse and Whitehead 1974), the time-dependent knot or collective instability (Busse and Whitehead 1974, Clever and

Busse 1979), and the transient skewed varicose instability (Clever and Busse 1979). At high Rayleigh numbers a "spoke" convection pattern has also been identified (Clever and Busse 1979). Most of these mechanisms are reviewed by Busse (1978).

The existence of one or more of these instabilities in a given convection system depends in a complicated, and sometimes sensitive, manner on the Rayleigh number, the Prandtl number, the initial conditions of the experiment (including hysteresis effects), and the boundary conditions including geometry of the necessary finite convection cavity, and the thermal properties of the cavity walls (Riahi 1984, Busse and Riahi 1980). The parametric map of all these effects is far from being fully developed.

Time-dependent instabilities have been studied experimentally for various Prandtl numbers and aspect ratios by Chen and Whitehead (1968), Willis and Deardorff (1970), Krishnamurti (1970, 1973), Busse and Whitehead (1974), Gollub, Hulbert, Dolny and Swinney (1977), Ahlers and Behringer (1979), Gollub and Benson (1980), Gollub, McCarriar, and Steinman (1982), and Gollub and McCarriar (1982). The studies by Gollub and co-workers involved LDV measurements of velocity power spectra to study the transition to chaos and evaluate the applicability of modern chaos theories such as Ruelle and Takens' (1971) conjecture on the production of chaos from the interaction of multiple independent but weakly nonlinearly coupled instability modes. McLaughlin and Orszag (1982) addressed similar questions by means of numerical simulations.

The purpose of this paper is to report a study of the frequency spectra of convection at moderate Prandtl number (5.8) in a very wide layer with highly conducting boundaries. The spectra are measured using an LDV to sense the horizontal velocity at a single point near the center of the convection chamber, and the Rayleigh number is varied from a value below the onset of oscillatory instability, 30,000, to a value where the spectrum indicates fully chaotic motion, 99,000. Frequency

peaks are identified with various instabilities, and the frequency of the oscillatory instability is studied as a function Rayleigh number.

Our reasons for undertaking this study are to determine the transitional behavior for a previously unexamined set of parameters, and to correlate these results with existing data in an effort to construct a unified description of the frequencies of the instabilities.

## 2. EXPERIMENTAL APPARATUS

### 2.1 Convection chamber

The test section consisted of a rectangular cavity 485 mm x 485 mm in horizontal dimension, by 10 mm height. The upper and lower boundaries were aluminum plates, and the sidewalls were plexiglass. Figure 1 shows a vertical cross-section of the apparatus. The lower plate (b) rested in close thermal contact on a second plate (a) of 38 mm thickness. The heat through the lower plate was supplied by a resistance wire heating mat bonded to the bottom of Plate (a), and the thickness of Plate (a) was used to diffuse the heat uniformly, providing homogenous conditions of the surface of Plate (b). The upper plate (c) consisted of a 27 mm thick aluminum plate with two counterflow cooling channels machined into it. Cooling water was supplied from a temperature bath maintained constant with a temperature stability of  $\pm 0.01^\circ \text{C}$ .

Temperature uniformity of the upper thermal boundary was studied by placing 14 thermocouples in the upper surface. The temperature of the lower surface was monitored using a single thermocouple inserted through a horizontal hole to the middle of the test section. It was found that in the central 60% of the upper plate the temperature was constant with an accuracy of  $\pm .01^\circ \text{C}$ . Over the entire plate the temperature varied by no more than  $.07^\circ \text{C}$ . from minimum to maximum. The largest changes occurred under operating conditions near the edges of the plate due to sidewall heat loss.

The thickness of the water layer was 10.0 mm, and its mean temperature range was  $26.4^\circ\text{--}29.0^\circ \text{C}$ .

corresponding to a Prandtl number variation from 6 to 5.6. The temperature drop across the fluid layer varied from 1.41C up to 4C at the maximum Rayleigh numbers studied in this experiment.

## 2.2 Laser Doppler velocimeter

A single-channel, frequency-shifted laser Doppler velocimeter was used to measure horizontal velocity fluctuations at the midpoint of the convection layer, i.e. at the geometric center of rectangular plan form and halfway between the upper and lower plates.

The optical arrangement of the laser velocimeter is shown in Figure 2. The focal length of lens L1 was 380 mm, producing a measurement volume 3.4 mm long and 0.22 mm in diameter defined at the  $e^{-2}$  points. Light was collected through a lens L2 which viewed the measurement volume at an angle of 30° to the optic axis. Using a 0.2 mm pin hole in front of the photomultiplier tube, the off-axis light collection reduced the length of the measurement volume to approximately 0.3 mm.

The signal from the PM tube was demodulated using a TSI model 1090 frequency tracker, modified by the addition of a 0-50 KHz low frequency range. After low pass filtering, the tracker's output signal was digitized at a rate of 20 Hz and recorded for a period of 820 seconds. The 16 Kword data record was analyzed by fast Fourier transform to obtain power spectra, and 5 to 12 records were obtained for each Rayleigh number and averaged to produce the power spectra used in the data analysis.

## 2.3 Experimental Procedure

Changes in the Rayleigh number were produced by incremental changes of the heat flux in the lower plate. Following each change, the convection underwent transient adjustment to the new heat flux. The transient was judged to be over when the temperature fluctuations in the temperature difference between the two plates caused Rayleigh number fluctuations less than  $\pm 0.8\%$ . Typically, the stabilization time was 12 hours, but in some instances the period was as short as 5 hours, and in other

instances it was as long as 48 hours. These times were shorter than the times reported by Gollub, et al. (1982) to achieve full pattern adjustment, but long enough to give stable frequency spectra.

## 3. EXPERIMENTAL RESULTS

### 3.1 Spectra

Measurements of velocity versus time and associated power spectra are presented in Figure 3. The Rayleigh number is defined as

$$Ra = \frac{\beta g \Delta T d^3}{\nu \kappa}, \quad (1)$$

where  $\beta$  is the thermal coefficient of expansion,  $g$  is gravity,  $\Delta T$  is the mean temperature drop across the fluid layer,  $d$  is the depth of fluid layer and  $\nu$  and  $\kappa$  are the kinematic viscosity and kinematic conductivity, respectively.

At  $Ra = 30,000$ , spectral energy is concentrated in a peak at very low frequency, dropping down to a uniform level of nearly white instrumental noise. At  $Ra = 32,000$ , a second spectral peak approximately 10 times larger than the instrumental noise level appears at a frequency of approximately 20 mHz. Increasing  $Ra$  to 38,500 produces a third spectral peak, increases the broad band noise, and increases the amplitude of the first spectral peak. Thereafter, increasing the Rayleigh number also increases the high frequency spectral energy density of the first peak and broadens each peak, making the third peak less recognizable. At  $Ra = 64,500$  the third peak can no longer be recognized, and the spectrum exhibits the broadband frequency behavior characteristic of chaotic motion. Between  $Ra = 50,000$  and 64,000, the level of the broad band spectrum increases substantially in the low frequency range up to 50 mHz, and between  $Ra = 64,500$  and 99,000 the energy level of the broad band component increases by a factor of ten over the entire frequency band.

The behavior of the present spectral data is entirely consistent with that of Gollub, et.al. (1982) who also measured spatial patterns in horizontal planes using a scanning LDV. They

identified the large spectral peak centered at zero frequency with the time-dependent form of the skewed varicose instability. Its time scale, of order 400 seconds, is much shorter than the time scale for evolution of the horizontal plan form of the convection pattern. The time scale of the latter is of order 100 hours, much longer even than the time for horizontal diffusion of heat across the width of the convection cell. Gollub, et.al. (1982) associate the second spectral peak with Busse's oscillatory instability, on the basis of the undulating roll-like patterns they observed. This identification is not entirely consistent with stability theory, since Busse and Clever (1979) argue that the dominant mechanisms at Prandtl numbers of order unity are the skewed varicose instability and the knot instability, the oscillatory mechanism normally being restricted to small Prandtl numbers. However, several facts support the idea that the oscillatory instability is present in our experiments. First, it is generally agreed that the time scale of the oscillatory instability corresponds to the time for a fluid element to circulate around a roll cell, (Krishnamurti 1970, Busse and Whitehead, 1974). In our experiments the velocities are of order 0.02 cm/s and the depth is 1 cm, yielding a 50 second time scale, in close agreement with the frequency of the second peak. Second, the value of  $Ra = 32,000$  at which the second peak first occurs is close to the stability boundary for the transition from steady 2-D roll cells to time dependent flow presented by Krishnamurti (1973) at  $Pr = 5$ .

The frequency of the third spectral peak that arises at  $Ra = 38,500$  is nearly double that of the second peak, indicating that it is a harmonic of the oscillatory instability arising, presumably, from non-linear interactions. It is certainly plausible that oscillatory instability waves propagating along the axes of adjacent or neighboring roll cells would produce harmonics. Lateral displacement of each roll with respect to the other would be proportional to the sum of the instability waves, and the non-linear relationship

between velocity and displacement would produce a harmonic by two-wave mixing.

The spectral peaks of the oscillations in the present experiment have much broader line-width than those observed in a small aspect ratio chamber by Gollub and Benson (1980), indicating that the frequency is much more deeply modulated. This increased modulation probably is the result of less restrictive side-wall conditions which permit many different patterns of convection to form. In the limit of  $\Gamma_v \rightarrow \infty$ , it is well known (Busse 1978) that the orientation of roll cell patterns suffers pattern degeneracy, while in finite cavities the rolls tend to orient themselves so as to terminate perpendicular to the lateral boundaries.

In further contrast to Gollub and Benson's small  $\Gamma_v$  spectra, our spectra exhibit no evident sub-harmonic instabilities nor do they exhibit significant energy in spectral peaks located at frequencies incommensurable with the fundamental frequency of the oscillatory instability.

### 3.2 Frequency of Oscillation

The mean frequency of the second peak increases with increasing Rayleigh number, Fig. 5. Comparison with results of other investigations at approximately similar Prandtl numbers indicates a strong effect. When scaled with the thermal diffusion time scale  $d^2/\kappa$  the frequencies measured in these experiments correlate better, Fig. 6. In Fig. 6 the cross-hatched region indicates the range of frequencies found by Krishnamurti (1970) for Prandtl numbers between 0.71 and 8500. Krishnamurti's (1970) water data at  $Pr = 6.8$  agrees well with our results at  $Pr = 5.8$ , but our results continue to differ significantly from the water data of Gollub et. al. (1982) at  $Pr = 2.5$ . Each of the foregoing experiments were performed in cavities of reasonably large aspect ratio, so the discrepancy between the present data and those of Gollub, et. al. (1982) is probably a Prandtl number effect.

In Fig. 7 the Prandtl number dependence has been reduced by re-scaling that dimensionless frequency with a factor  $Pr^{-0.3}$ . The correlation

proposed by Willis and Deardorff on the basis of limited data used a  $Pr^{-0.6}$  power that does not collapse the present data as well. The re-scaled data correlate along a single curve corresponding to the frequency of the oscillatory instability peak. The data labeled  $f_2$  were found from the second fundamental frequency identified in the Gollub and Benson (1980) experiment. They are clearly isolated from the main body of data, and the conclusion must be that they are associated with an instability mechanism distinct from the oscillatory instability. The mechanism of the higher frequency instability may be the knot instability that Busse and Clever (1979) expected in this range of Rayleigh numbers and Prandtl numbers, in which case the data show the co-existence of three modes of instability: skewed varicose, oscillatory and knot. The co-existence may not be simultaneous. Velocity traces indicate intermittent hopping between modes. Scatter of the data in the range  $Ra > 37 Ra_c$  where  $f_2$  exists may be the result of intermediate frequencies produced by non-linear mixing of  $f_1$  and  $f_2$ .

Below  $37 Ra_c$  the dimensionless frequency repeatedly remains constant over significant ranges of Rayleigh number, then jumps abruptly to a higher value. Three frequency jumps are evident at Rayleigh numbers 15, 23 and 39 times critical. The jump at 23 times critical is close to the value for transition to time-dependent flow found by Krishnamurti (1970). At each jump the frequency increases by a factor of approximately 1.25. Data along this portion of the curve all correspond to aspect ratio greater than 10, and they consist mainly of results for moderate Prandtl numbers, with the exception of one point for air. Thus, each of these experiments is expected to have essentially similar combinations of instabilities, and it is reasonable to find correlation of the frequency jumps in the various experiments once the Prandtl number dependence is removed.

The frequency jumps suggest a resonance phenomenon in which the average wave-length of the instability remains constant over a range of

increasing Rayleigh numbers, and then changes abruptly. The occurrence of such phenomenon at large aspect ratios argues against the wave length being determined by a condition imposed by the side walls on the number of roll cells, especially since the fractional magnitudes of the frequency jumps are large compared to the change that might be expected if the number of roll cells across the width of the cavity were to change by one. However, it is difficult to avoid concluding that the jumps are the consequence of some form of resonance condition.

Various studies of the frequency of oscillations in convection have indicated the prevalence of an  $Ra^{2/3}$  power law relationship. As noted by Busse and Whitehead (1979) their data and the data of Rossby (1966) and Krishnamurti (1970) could be represented by  $fd^2\kappa = Ra^{2/3}$ , albeit with considerable spread. Howard's (1966) high Rayleigh number thermal boundary layer theory predicts an  $Ra^{2/3}$  law, as does Foster and Waller's (1985) more recent work, in the case where the Nusselt number is proportional to  $Ra^{1/3}$  so that the heat transfer ratio is independent of the layer depth.

An examination of Fig. 7 shows that the mean shape of the staircase curve formed by the succession of frequency jumps also follows an  $Ra^{2/3}$  power law relatively well. This appears in fact, to be the explanation for the success of fitting an  $Ra^{2/3}$  curve to earlier data. The fact that the frequency jumps occur along an average  $Ra^{2/3}$  curve suggests that they are manifestations of transitions made by the flow structure to minimize the influence of the layer depth parameter. These adjustments may in fact be transitions from one mode of flow instability to another. For example, the jump at  $23Ra_c$  is close to the location of the transition to time-dependent flow found by Krishnamurti (1970). However, transitions at  $15Ra_c$  and  $29Ra_c$  are not predicted by existing theories for moderate Prandtl numbers, and it should be born in mind that the frequency data do not correspond to a jump from one spectral peak to another.

It is obvious that the frequency is independent of depth when the dimensionless frequency obeys a two-thirds law. More detailed dimensional arguments show further that the two-thirds law also corresponds to an  $Ra^{1/3}$  law for the Nusselt number, implying that the heat transfer state is also independent of the layer depth. Hence, the transitions occur in such a way as to render to heat flux and the frequency dependent only upon the diffusive processes at the wall.

As noted earlier, the period of the oscillatory instability is determined by the time for a fluid particle to orbit around a roll cell from the bottom to the top of the layer and back again. For this period to be independent of layer depth, the fluid velocity must be exactly right so as to match the time period of the diffusive processes at the wall. For a given type of spatial structure, this relation can only be maintained over a limited range of Rayleigh numbers. Beyond that range, it may be necessary for a new structure to emerge which will again sustain the proper relationship between velocity in the core of the convection layer and thermal diffusion in the conduction layer.

Foster and Waller (1985) have recently reported data for the period of intermittent convection motions at high Rayleigh number. When recast into a form containing the Rayleigh number, and using the  $Nu = 0.19 Ra^{0.283}$ , their equation predicts the curve shown by the dotted line in Fig. 7. The close correspondence with the frequency of the second mode observed by Gollub, et al. (1980) in a small aspect ratio container suggests a close relationship between this instability and the motions in highly turbulent convection. Both experiments were performed in low aspect ratio cavities.

#### SUMMARY AND CONCLUSIONS

Power spectra of horizontal velocity have been measured in a horizontal water layer of aspect ratio 48.5. At moderate Prandtl number (5.8) three instabilities are found. The spectra indicate a skewed varicose instability with very

low frequency (1 mHz) associated with slow lateral motion of the roll cells. The skewed varicose instability accounts for a large fraction of the spectral energy, its amplitude being comparable to or larger than the amplitude of a faster ( $\approx 20$  mHz) oscillatory instability. With increasing Rayleigh number the oscillatory instability produces a second harmonic, and a broad-band spectrum grows until the spectral peaks are no longer evident at  $Ra = 99,000$ .

Frequencies of the oscillatory spectral peak have been correlated for a range of Prandtl numbers centered around  $Pr = 5$ . Between  $10 Ra_c$  and  $30 Ra_c$  the frequency makes three abrupt transitions, only one which, at  $23 Ra_c$ , may be associated with a known transition from steady to time-dependent instability. The frequency jumps generally occur around a curve that follows on  $Ra^{2/3}$  power law.

#### ACKNOWLEDGEMENT

The research reported here was supported by NSF grant ATM-82-03521.

#### REFERENCES

- Ahlers, G.; Behringer, R. P. 1979: The Rayleigh-Benard instability and the evolution of turbulence. *Prog. Theor. Phys. Suppl.* 64, 186-201.
- Busse, F. H. 1967: On the stability of two-dimensional convection in a layer heated from below. *J. Math. & Phys.* 46, 140-150.
- Busse, F. H. 1972: The oscillatory instability of convection rolls in a low Prandtl number fluid. *J. Fluid Mech.* 52, 97-112.
- Busse, F. H. 1978: Non-linear properties of thermal convection. *Rep. Prog. Phys.* 41, 1931-1967.
- Busse, F. H.; Clever, R. M. 1979: Instabilities of convection rolls in a fluid of moderate Prandtl number. *J. Fluid Mech.* 91, 319-335.
- Busse, F. H.; Riahi, N. 1980: Non-linear convection in a layer with nearly insulating boundaries. *J. Fluid Mech.* 96, 243-256.
- Busse, F. H.; Whitehead, J. A. 1971: Instabilities of convection rolls in a high Prandtl number fluid. *J. Fluid Mech.* 47, 305-320.
- Busse, F. H.; Whitehead, J. A. 1974: Oscillatory and collective instabilities in large Prandtl number convection. *J. Fluid Mech.* 66, 67-79.

Chandrasekhar, S. 1961: Hydrodynamic and Hydromagnetic Stability. Oxford: Clarendon Press.

Chen, M. M.; Whitehead, J. A. 1968: Evolution of two-dimensional periodic Rayleigh convection cells of arbitrary wave numbers. *J. Fluid Mech.* 31, 1-15.

Clever, R. M.; Busse, F. H. 1974: Transition to time dependent convection. *J. Fluid Mech.* 65, 625-645.

Cross, M. C. 1982: Ingredients of a theory of convective textures close to onset. *Phys. Rev. A.* 25, 1065-1076.

Foster, T. D. 1971: Intermittent convection. *Geophys. Fluid Dyn.* 2, 201-217.

Foster, T. D.; Waller, S. 1985: Experiments on convection at very high Rayleigh numbers. *Phys. Fluids.* 28, 455-461.

Gollub, J. P.; Benson, S. V., 1980: Many routes to turbulent convection. *J. Fluid Mech.* 100, 449-470.

Gollub, J. P.; Hulbert, S. L.; Dolny, G. M.; Swinney, H. L. 1977: Laser Doppler study of the onset of turbulent convection at low Prandtl number. In: *Photon Correlation Spectroscopy and Velocimetry.* (ed. Cummins, H. F.; Pike, E. R.). New York: Plenum.

Gollub, J. P.; McCarriar, A. R. 1982: Convective patterns in Fourier space. *Phys. Rev. A.* 26, 3470-3476.

Gollub, J. P.; McCarriar, A. R.; Steinman, J. G. 1982: Convective pattern evolution and secondary instabilities. *J. Fluid Mech.* 125, 259-281.

Howard, L. N. 1966: Convection at high Rayleigh number. *Proc. 11th Intl. Cong. of Appl. Mech., Munich, 1964,* ed. H. Gortler, Berlin: Springer-Verlag.

Krishnamurti, R. 1970: On the transition to turbulent convection. Part 2. The transition to time dependent flow. *J. Fluid Mech.* 42, 309-320.

Krishnamurti, R. 1973: Some further studies on the transition of thermal convection. *J. Fluid Mech.* 60, 285-303.

Malkus, W. V. R. 1954: The heat transport and spectrum of thermal turbulence. *Proc. Roy. Soc., A225* 196-212.

McLaughlin, J. B.; Orszag, S. A. 1982: Transition from periodic to chaotic thermal convection. *J. Fluid Mech.* 122, 123-142.

Riahi, N. 1984: Non-linear thermal convection with finite conducting boundaries. *J. Fluid Mech.* 152, 113-123.

Rossby, T. 1966: Dept. of Geology and Geophysics, M.I.T. Sci. Rep. HRF/SR27.

Ruelle, D.; Takens, F. 1971: On the nature of turbulence. *Comm. Math. Phys.* 20, 167-192.

Willis, G. E.; Deardorff, J. W. 1970: The oscillatory motions of Rayleigh convection. *J. Fluid Mech.* 44, 661-672.

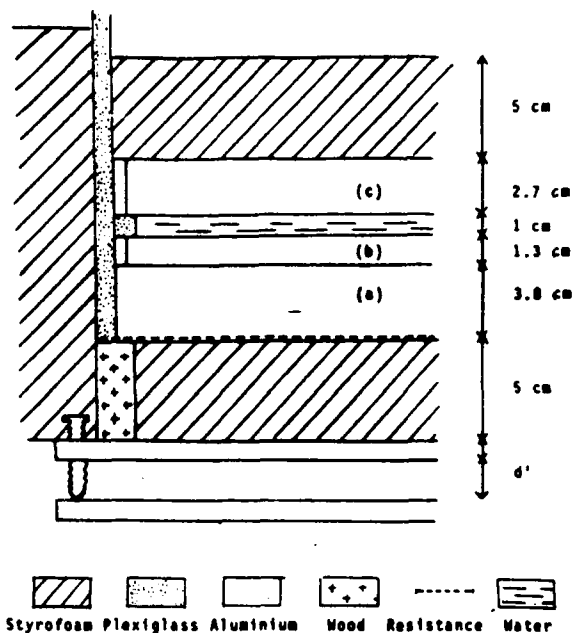


Fig. 1. Convection test section. (a) Heated plate; (b) lower plate of the convection cavity; (c) upper plate of the cavity and cooling water channels.

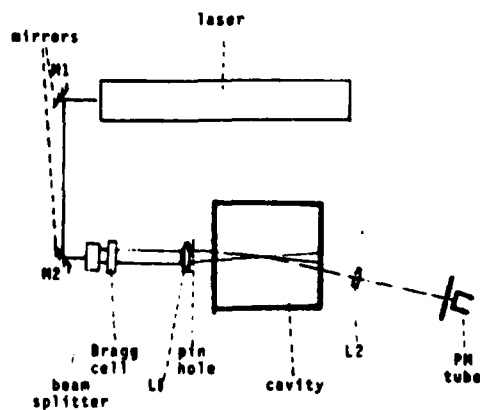


Fig. 2. Laser Doppler velocimeter geometry for measurement of horizontal velocity.

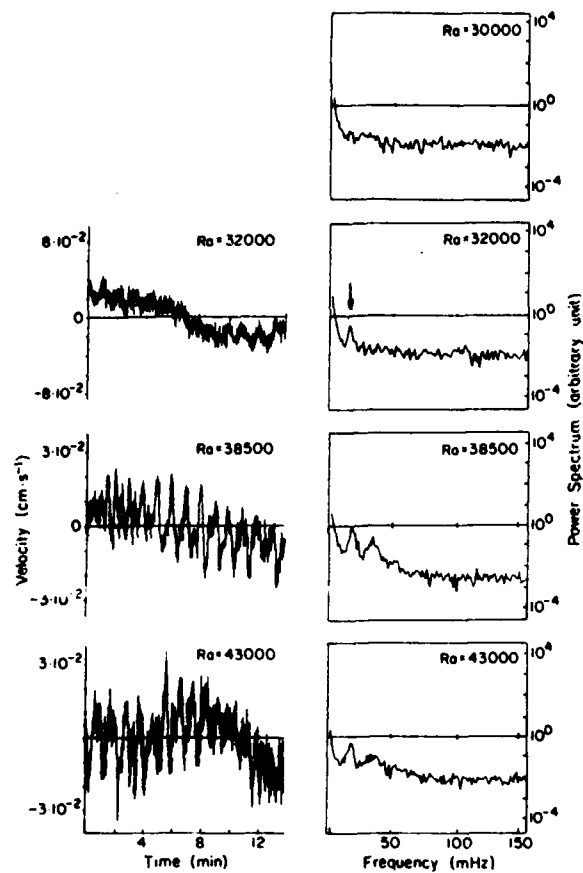


Fig. 3. Temporal evolution and power spectral density of the horizontal velocity for  $30,000 < Ra < 43,000$ .

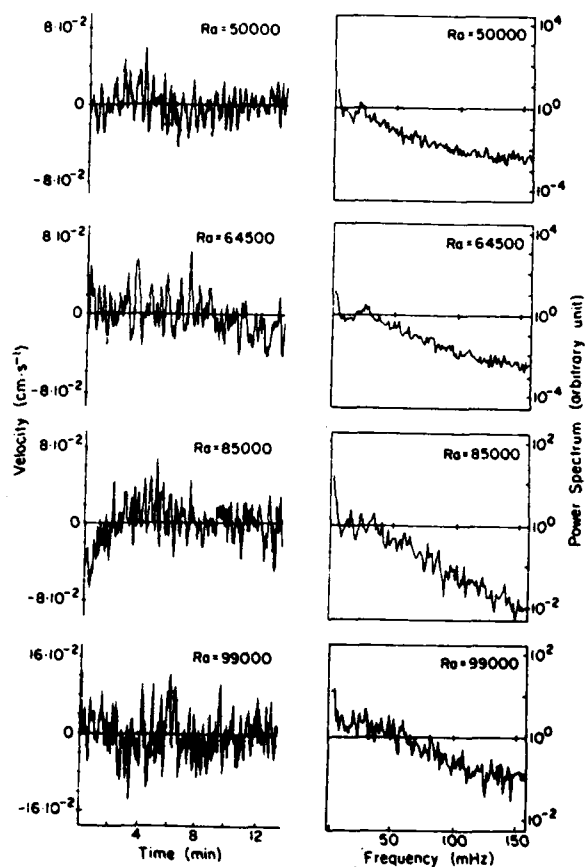
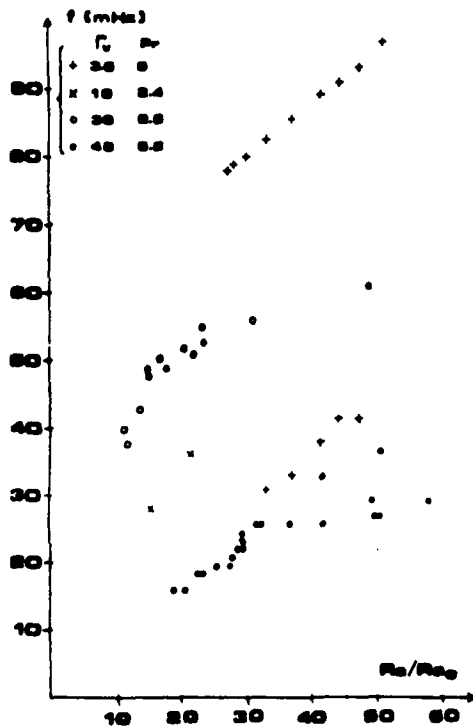
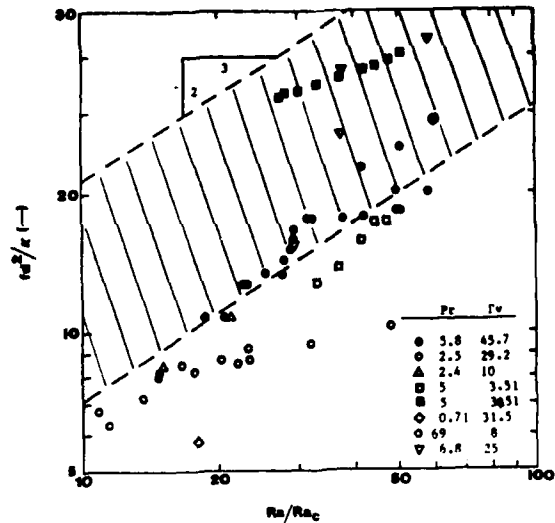


Fig. 4. Temporal evolution and power spectral density of the horizontal velocity for  $50,000 < Ra < 99,000$ . Note the change of scale on the power spectra for  $Ra = 85,000$  and  $99,000$ .



**Fig. 5.** Frequency of the second spectral peak associated with oscillatory motion.  
 + Gollub and Benson, 1980 (first and second peaks);  
 X Gollub, et al. 1977;  
 ● Gollub, et al. 1982;  
 ● present measurement.



**Fig. 6.** Dimensionless frequency of the instabilities.  
 ○ Gollub, et al. 1982;  
 △ Gollub et al. 1977;  
 □ Gollub and Benson 1980 ( $f_1$ );  
 ■ Gollub and Benson 1980 ( $f_2$ );  
 ◇ Willis and Deardorff 1970;  
 ⊕ Busse and Whitehead 1974;  
 ▽ Krishnamurti 1970 (water);  
 /// Krishnamurti 1970 (range of data for  $0.71 < Pr < 8500$ );  
 ● present data.

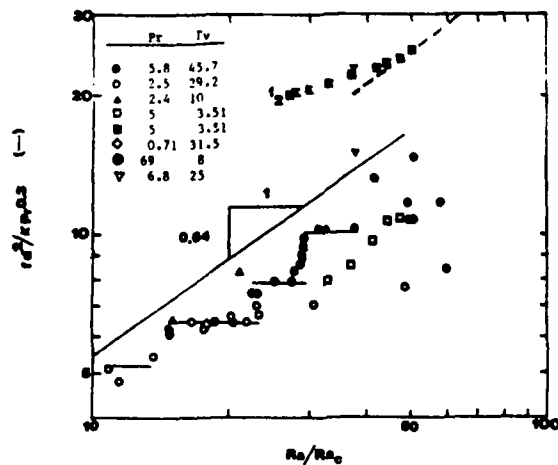


**Fig. 7.** Dimensionless frequency correlation with Prandtl number. Symbols are the same as in Fig. 6.  
 ---- Foster and Waller 1985,  $Pr = 5$ ,  $fd^2/k = 0.0031 Ra^{0.64}$ .

EXPERIMENTS ON THE INFLUENCE OF MEAN FLOW  
UNSTEADINESS ON THE LAMINAR-TURBULENT  
TRANSITION OF A WAKE

R.S. Solis, R.W. Miksad, and E.J. Powers  
College of Engineering  
The University of Texas at Austin  
Austin, Texas 78712

ABSTRACT

The role of low frequency mean flow unsteadiness on the transition to turbulence of a laminar wake was investigated. Low frequency unsteadiness was generated in a low turbulence wind tunnel test section by periodically varying the cross-sectional area of a sonic throat located downstream of the test section. In the linear stage of fluctuation growth in the wake, mean flow unsteadiness acts to modulate the amplitude and phase of the growing instabilities and leads to the generation of sidebands in the velocity power spectrum. Low frequency modulations, whether induced by mean flow unsteadiness, or by nonlinear interactions of growing instability modes, act to accelerate the redistribution of spectral energy as the flow evolves to turbulence.

1. INTRODUCTION

The importance of low frequency modulations on the transition of a laminar wake to turbulence has been studied by Miksad, et al. (1982, 1983) and Jones (1982). In steady mean flow experiments cited above, low frequency modulations at frequencies  $f_{n1}$ , generated via *nonlinear interactions* between unstable modes, were found to produce amplitude and phase modulations of growing instability fluctuations in the wake. One effect of amplitude and phase modulations, at frequency  $f_{n1}$  for example, is to "broaden" the sideband structure which surrounds the fundamental instability frequency,  $f_0$ , by adding additional frequency components with energy at frequencies  $f_0 \pm n f_{n1}$ . In addition to spectrum sideband broadening, low frequency modulation appears to be linked to the sudden interruptions in the instantaneous velocity trace which seem to presage the final randomization stage in the transition to turbulence

(Miksad, et al., 1985). The frequency of occurrence of these events was found to correspond to the modulation frequency,  $f_{n1}$ .

The present set of experiments was conducted in order to study the effects of low frequency modulations, at frequencies  $f_m$ , generated by *mean flow unsteadiness* on the transition. Experiments were conducted for six sets of flow conditions. These include steady and unsteady mean flow experiments under "natural" and "controlled" conditions. A description of the unsteady mean flow is given in Section 2. In "controlled" transition, low level sound is used to excite instability modes of the wake at frequencies which fall within the band of the naturally most unstable frequencies in the wake. Two types of controlled transition experiments were conducted. In the first type, called "single instability excited" transition, the most unstable mode of the wake, at frequency  $f_0=587$  Hz, was acoustically excited. In the second type, called "double instability excited" transition, both the most unstable mode at  $f_0$  and a second instability mode at frequency  $f_1=567$  Hz were acoustically excited. This gave a difference frequency mode due to nonlinear interactions between  $f_0$  and  $f_1$  of  $f_{n1}=20$  Hz. Results are presented here for three conditions: I) steady mean flow, one instability mode excited, II) unsteady mean flow, one instability mode excited, and III) unsteady mean flow, two instability modes excited.

All experiments were conducted in a low turbulence wind tunnel. Fluctuation measurements were taken in the wake of a thin airfoil of maximum thickness

.31 cm and chord length 20 cm. The wind tunnel test section is 20 cm x 20 cm by 80 cm in length. The mean flow velocity,  $U_0$ , was 8.3 m/s. The Reynolds number based on the mean flow velocity and the initial half width of the wake,  $b_0$ , was 640. The wake flow generated was initially laminar, but unstable. The basic flow geometry is shown in Figure 1.

## 2. GENERATION OF UNSTEADY MEAN FLOW

Periodic, small amplitude mean flow unsteadiness of the form  $U(y,t) = [1 + \epsilon \sin(2\pi f_m t + \phi)] \cdot U_0(y)$  was introduced in the wind tunnel test section by varying the cross sectional flow area of a sonic throat located downstream of the test section. In the free stream, the ratio of the mean flow variation amplitude,  $\epsilon U_0$ , to the mean flow amplitude,  $U_0$ , was  $\epsilon = .03$ . The phase,  $\phi$ , of the mean flow variation was essentially constant throughout the freestream, but was found to vary across the wake. The ratio of the unsteady mean flow frequency,  $f_m = 33$  Hz, to the natural instability frequency of the wake,  $f_0$ , was  $(f_m/f_0) = .057$ . Spectra of the mean flow variations in the free stream showed no harmonic distortion in the sinusoidal mean flow waveform.

## 3. EXPERIMENTAL RESULTS

The initial most evident effect of mean flow unsteadiness on instabilities growing in the early region of the transition is the production of amplitude and phase modulations. Shown in Figure 2 are measurements for single acoustic control experiments, both steady mean flow (top set of figures) and unsteady mean flow (bottom set of figures). Shown for each set are, from top to bottom: a) normalized free stream velocity,  $U_{fs}(t)/U_0$ , b) normalized streamwise velocity component of the wake fluctuation,  $u(t)/U_0$ , c) computed amplitude demodulates of the wake fluctuations,  $AM(t)$ , and d) computed phase demodulates of the wake fluctuations,  $PM(t)$ . The amplitude and phase demodulates are defined:

$$u = C \cdot (1 + AM(t)) \cdot \cos(2\pi f_0 t + PM(t)).$$

Digital complex demodulation at frequency  $f_0$  yields  $AM(t)$  and  $PM(t)$  (Khadra, et al., 1981). Wake velocity fluctuation measurements shown in Figure 2(b) were taken at downstream location  $x/b_0 = 9.1$  and lie within the

linear growth region of the growing instabilities. The cross stream location of the wake fluctuation measurements coincides with the location of the maximum rms fluctuation amplitude. Amplitude and phase modulations of the velocity fluctuations are clearly evident in the set of experiments in which mean flow unsteadiness has been imposed (bottom figures), whereas modulations are absent the top set of figures representing steady mean flow conditions.

Modulation of the velocity fluctuations in the linear region was studied by Shen (1961), who considered the effect of mean flow unsteadiness on the growth and decay of instabilities for a general class of shear flows of the form:

$$U(y,t) = T(t) \cdot U(y) \quad (1).$$

In such flows, instability fluctuations will exhibit amplitude and phase modulations. The stream function solution for the instability fluctuations can be expressed:

$$\Psi = f(y) \cdot \exp(\alpha x + C_1 \epsilon \sin 2\pi f_m t) \cdot \exp[i(kx - 2\pi f_0 t + C_2 \epsilon \sin 2\pi f_m t)]$$

$$= g(x,y) \cdot (1 + \epsilon \sin 2\pi f_m t) \cdot \exp[i(kx - 2\pi f_0 t + C_2 \epsilon \sin 2\pi f_m t)]$$

The resulting velocity fluctuations can thus be viewed as consisting of a carrier wave,  $\exp[i(kx - 2\pi f_0 t)]$ , modulated in amplitude and phase at the unsteadiness frequency,  $f_m$ . The frequency of the carrier wave,  $f_0$ , corresponds to the frequency of the most unstable mode in the wake. To a first order approximation, the mean flow velocity variations in the present experiments can be expressed in the form given in equation (1), and the generation of modulations at  $f_m$  is expected.

The effect of modulations at frequency  $f_m$  on the velocity power spectrum is to introduce sidebands about the carrier frequency,  $f_0$ , at frequency components  $f_0 \pm n f_m$ , where  $n$  is integer. A similar sideband structure also appears about the harmonics of the fundamental,  $n f_0$ , as nonlinear effects induce growth of the harmonics. The type of sideband structure described is evident in Figure 3, which shows the velocity spectrum of the unsteady mean flow time trace shown in Figure 3. In Figure 3, it is seen that the carrier frequency,  $f_0 = 587$  Hz, is flanked above and below by waves at frequencies  $f_{\text{sideband}} = f_0 \pm n f_m$ , where  $f_m = 33$  Hz.

When two instability modes are excited, as in the experiments conducted by Miksad, et al. (1982,1983), a second independent source (the first being mean flow unsteadiness) of amplitude and phase modulations is introduced. When both mean flow unsteadiness and multiple instabilities are introduced into the flow, each acting as an independent source of modulations on the velocity fluctuations, one is naturally led to search for multiple tone modulation effects. In multiple tone modulation, modulations produced by independent mechanisms at frequencies  $f_i$  and  $f_j$  generate sidebands, at frequencies  $f_0 \pm nf_i$  and  $f_0 \pm nf_j$  about the fundamental, as in single tone modulation. However, sidebands also appear at new frequencies  $f_0 \pm nf_i \pm mf_j$ . Multiple sidebands of this type can be seen in Figure 4, which shows the velocity spectrum for unsteady flow, double instability excited experiments. Measurements in Figure 4 were taken at the same streamwise location as for the spectrum shown in Figure 3. In Figure 4, the carrier frequency is at  $f_0 = 587$  Hz. Modulations occur at frequencies  $f_m = 33$  Hz due to mean flow unsteadiness, and  $f_{n1} = 20$  Hz due to nonlinear interactions between modes  $f_0 = 587$  Hz and  $f_1 = 567$  Hz. For example, the spectrum in Figure 3 shows the carrier mode,  $f_0$ , sideband components  $f_0 \pm nf_{n1}$  and  $f_0 \pm nf_m$ , and cross modulation sidebands at frequencies  $f_0 + 2f_m - f_{n1}$  (633 Hz),  $f_0 - 2f_m + f_{n1}$  (541 Hz), etc. Simultaneous modulations of the velocity fluctuations by both mean flow unsteadiness,  $f_m$ , and the low frequency mode,  $f_{n1}$ , generated by nonlinear interactions, clearly act to broaden the spectrum surrounding the fundamental instability more completely than if either modulation mechanism were operating alone.

The final stages of the transition to turbulence of the laminar wake are characterized by a spectral broadening about the fundamental and harmonics; a redistribution of fluctuation energy from regions high in energy to those low in energy (i.e., a filling in of spectral valleys); and by a decay of the coherent energy at the fundamental and harmonics. One mechanism by which energy can be redistributed from regions of high energy, spectral peaks, to those of low energy, spectral valleys, is that of cross-sideband nonlinear interactions. That is, new fluctuations produced by nonlinear interactions between sidebands of the fundamental,  $f_0 \pm nf_i$ , and

sidebands of the harmonics,  $mf_0 \pm nf_j$ , will act to fill the spectral valleys. (See Figure 4.) More sidebands appear in the fluctuation spectra of unsteady flow, double instability excited experiments than in spectra of either of the other two cases. Because of this, one might expect a higher degree of nonlinear activity in unsteady, double frequency excited experiments, than for either of the other two sets of experimental conditions. Squared bicoherence spectrum measurements, presented in Figure 6, indicate that this is the case.

The squared bicoherence spectrum is defined (Kim, et al., 1978, 1979):

$$b^2(f_i, f_j) = \frac{|B(f_i, f_j)|^2}{E[|X(f_i)X(f_j)|^2]E[|X(f_i+f_j)|^2]}$$

where  $B(f_i, f_j) = E[X(f_i)X(f_j)X^*(f_i+f_j)]$ ,  $E[ ]$  is the expected value operator, the superscript \* denotes the complex conjugate, and  $X(f_i)$  is the Fourier amplitude of the time series  $x(t)$ , in this case of the velocity fluctuation in the wake. The bicoherence,  $b^2$ , is bounded by  $0 < b^2 < 1$ , where values near 1 indicate strong nonlinear coupling between waves at frequencies  $f_i$ ,  $f_j$ , and  $f_i+f_j$ . Values of  $b^2$  near zero indicate the lack of nonlinear wave coupling.

Presented in Figure 6 are bicoherence measurements for all three experimental conditions. Contour levels in Figure 6 are for  $b^2 = .3, .6, \text{ and } .9$ . Regions for which  $b^2 > .9$  are shaded black. Those for which  $.6 < b^2 < .9$  are stippled. Each measurement was taken at downstream location  $x/b_0 = 91$ . (This streamwise location is between the linear growth region and the fully turbulent region of the wake.) Note first that for steady flow, single instability excitation, nonlinear wave coupling, as indicated by high levels of  $b^2$ , is restricted to the fundamental and to its harmonics. That is, the fundamental,  $f_0$ , is nonlinearly coupled to the first and second harmonics,  $2f_0$  and  $3f_0$  respectively, and the first harmonic is nonlinearly coupled to the second and third harmonics. Wave coupling combinations which might broaden the spectrum by generating frequency components other than those at  $nf_0$  are simply not evident.

With mean flow unsteadiness imposed, bicoherence contours at  $(f_m, nf_0 \pm mf_m)$  in Figure 6

indicate that low frequency modes are coupled with the fundamental and harmonics to generate a sideband structure about the fundamental and the harmonics. Thus, some spectral broadening, in the form of sidebands, is indicated.

When both mean flow unsteadiness and multiple instabilities are present, the bicoherence contours take on shapes different than those in the first two cases. In this case, high levels of bicoherence lie along diagonal bands of  $f_i + f_j = \text{constant}$ , where the constant corresponds to frequencies lying in spectrum valleys between the fundamental and harmonics. This type of band structure, similar to that documented by Jones(1982), is indicative of nonlinear coupling conducive to spectral valley filling.

Shown in Figure 7 are spectra for all three experimental conditions at downstream location  $x/b_0=364$ , in the final stage of the wake flow before full turbulence is attained. Clearly, in the two experiments in which mean flow unsteadiness was imposed, a more complete distribution of fluctuation energy to spectrum valleys exists by this streamwise location. In both unsteady flow experiments, not only are the spectral valleys more completely filled, but the amplitude of the coherent modes, at frequencies  $nf_0$ , are diminished in comparison to the steady flow spectrum.

A final measure of the accelerating effect of mean flow unsteadiness on the transition to turbulence is presented in Figure 8. Shown in Figure 8 is the streamwise evolution of the ratio of energy in the "random" components of the spectrum (i.e., those modes not at frequencies  $nf_0$ ) to the total fluctuation energy. This quantity, called the "randomness factor", approaches 1 as the flow becomes turbulent (Sato and Saito, 1975). Basically, the randomness factor gives an indication of the completeness of spectrum valley filling and of the decay of coherent modes,  $nf_0$ .

As shown in Figure 8, the randomness factor remains small in the transition region  $x/b_0 < 300$  for steady mean flow, single instability excitation experiments. In this region, most of the fluctuation energy is contained in the coherent modes. The final stages of flow transition to turbulence occur, for this case, between  $300 < x/b_0 < 550$ . At  $x=550$ , the randomness factor approaches 1, indicating that energy

has become evenly spread throughout the spectrum by this point.

Under both unsteady mean flow conditions, the randomness factor, Figure 8, is relatively large even in the early stages of the transition. This is due, in part, to the energy contained in the sidebands,  $nf_0 \pm mf_m$ . The randomness factor is larger for double instability experiments than for single instability excited experiments under unsteady mean flow conditions. This reflects the enhanced sideband structure (Figure 4) and nonlinear activity (Figure 6) seen in unsteady mean flow, double instability excited experiments. Finally, the randomness factor approaches 1 more rapidly (at  $x/b_0=400$ ) under both unsteady mean flow conditions than in steady flow, showing that mean flow unsteadiness has the effect of accelerating the overall transition.

#### 4. CONCLUSIONS

Experiments were conducted in order to study the effects of mean flow unsteadiness on the transition of a laminar wake to turbulence. Results presented for three sets of experiments under controlled conditions show that mean flow unsteadiness induces amplitude and phase modulations in the linear region of the transition. Mean flow unsteadiness and multiple instability modes can each generate modulations independently. These modulation mechanisms, when combined, produce multiple tone modulations in the linear region which broaden the velocity spectrum. Further downstream, mean flow unsteadiness aids in the overall redistribution, or randomization, of energy in the velocity spectrum, leading to an overall acceleration in the transition to turbulence. Results of experiments conducted under "natural" conditions (i.e., in the absence of acoustic excitation), not presented here, indicate that mean flow unsteadiness also accelerates the overall transition under those conditions.

#### 5. ACKNOWLEDGEMENTS

This work was supported by the National Science Foundation under Grant MSM-8211205 and the Department of Defense Joint Services Electronics Program through the Air Force Office of Scientific Research under Contract F 49620-86-C-0045.

## REFERENCES

- Jones, F.L., 1982, An Experimental Study of Nonlinear Wave Interactions and Modulations During Transition of a Symmetric Wake, Ph. D. Dissertation, UT Report No. LTT-83-02.
- Khadra, L., Kim, Y.C., Powers, E.J., Jones, F.L., and Miksad, R.W., 1981, "Digital complex demodulation of unsteady fluid flow measurements", Computers in Flow Predictions and Fluid Dynamic Experiments, ASME.
- Kim, Y.C., and Powers, E.J., 1978, "Digital bispectral analysis of self-excited fluctuation spectra", Phys. Fluids, 21, 8, 1452.
- Kim, Y.C., and Powers, E.J., 1979, "Digital bispectral analysis and its applications to nonlinear wave interactions", IEEE Trans. on Plasma Science, PS-7, No. 2, 120.
- Miksad, R.W., Jones, F.L., Powers, E.J., Kim Y.C., and Khadra, L., 1982, "Experiments on the role of amplitude and phase modulations during transition to turbulence", J. Fluid Mech., 44, 3, 741-765.
- Miksad, R.W., Jones, F.L., and Powers, E.J., 1983, "Measurements of nonlinear interactions during natural transition of a symmetric wake", Phys. Fluids, 26, 1402-1409.
- Miksad, R.W., Jones, F.L., and Powers, E.J., 1985, "Experiments on nonlinear interactions in wake transition", Laminar-Turbulent Transition, IUTAM Symposium Novosibirsk 1984, ed. V.V., Kozlov, Springer-Verlag, Berlin, Heidelberg.
- Panter, P.F., 1965, Modulation, Noise, and Spectral Analysis, Applied to Information Transmission, New York, McGraw-Hill.
- Sato, H., and Saito, H., 1975, "Fine-structure of energy spectra of velocity fluctuations in the transition region of a two-dimensional wake", J. Fluid Mech., 67, 3, 539-559.
- Shen, S.F., 1961, "Some considerations on the laminar stability of time-dependent basic flows", J. Aerospace Sci., 28, pp. 297-404,417.

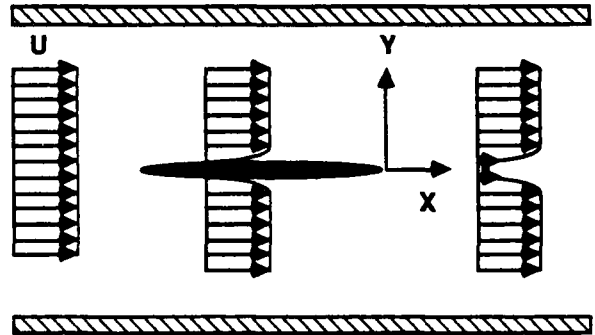


FIGURE 1. WAKE FLOW GEOMETRY.

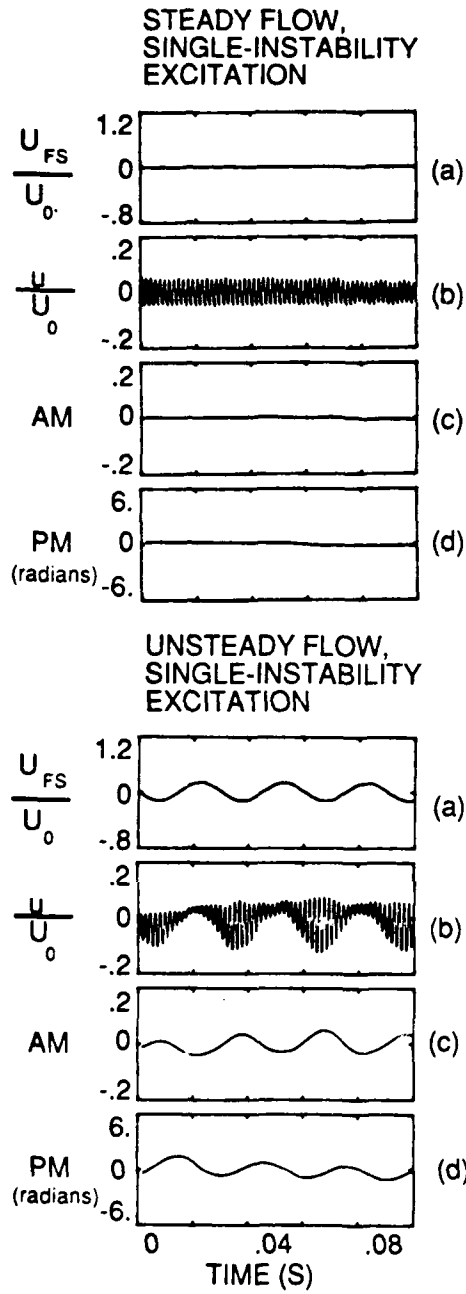


FIGURE 2. FREE-STREAM, WAKE, AND DEMODULATES, STEADY AND UNSTEADY FLOW.

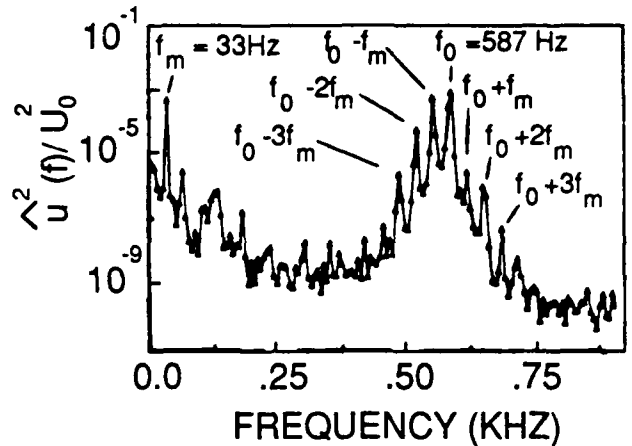


FIGURE 3. VELOCITY SPECTRUM, UNSTEADY FLOW, SINGLE INSTABILITY EXCITATION.

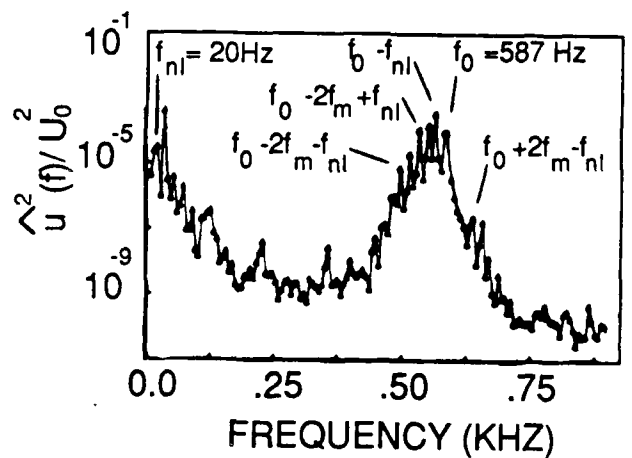


FIGURE 4. VELOCITY SPECTRUM, UNSTEADY FLOW, DOUBLE INSTABILITY EXCITATION

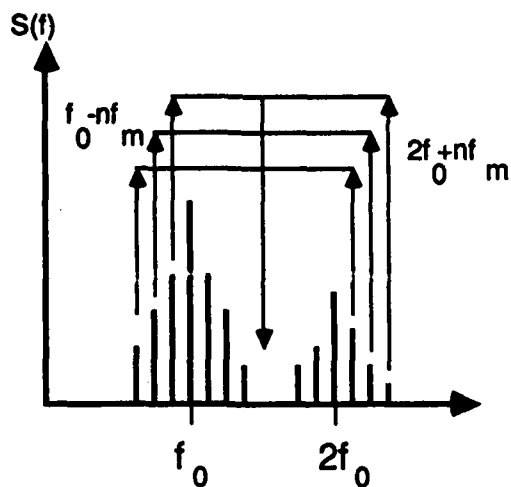


FIGURE 5. SCHEMATIC OF CROSS-SIDEBAND INTERACTIONS LEADING TO SPECTRAL VALLEY FILLING.

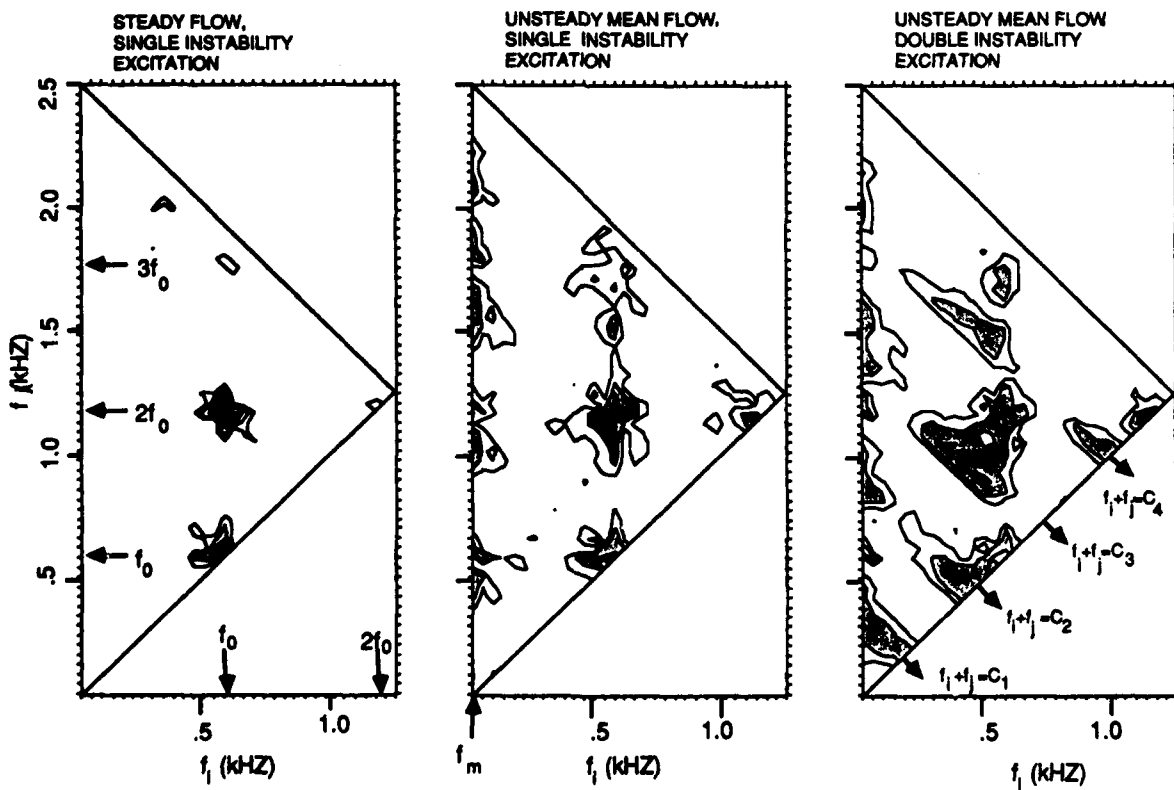


FIGURE 6. BICOHERENCE SPECTRUM,  $b^2(i,j)$ ,  $x/b_0=91$ .

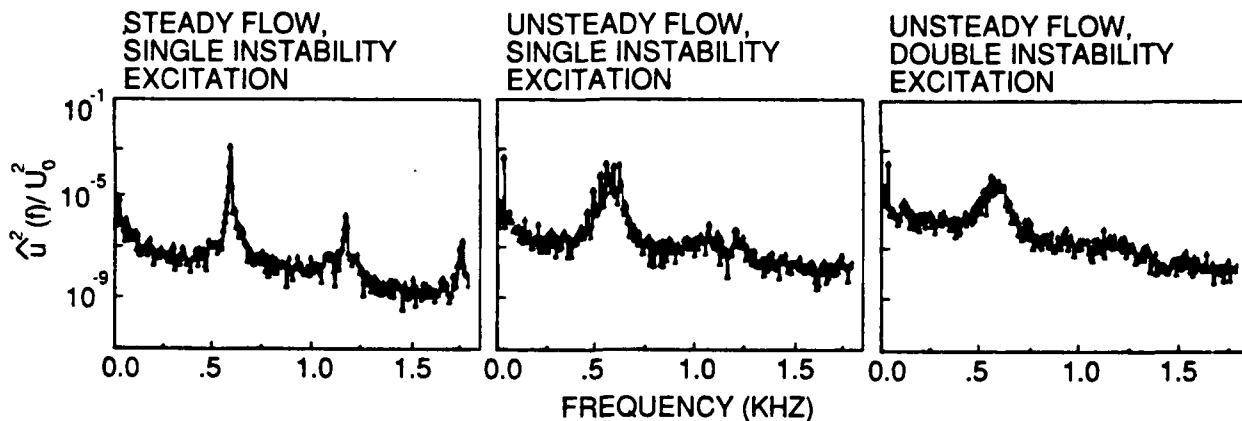


FIGURE 7. VELOCITY SPECTRA.  
 $X/b = 364.$   
 $0$

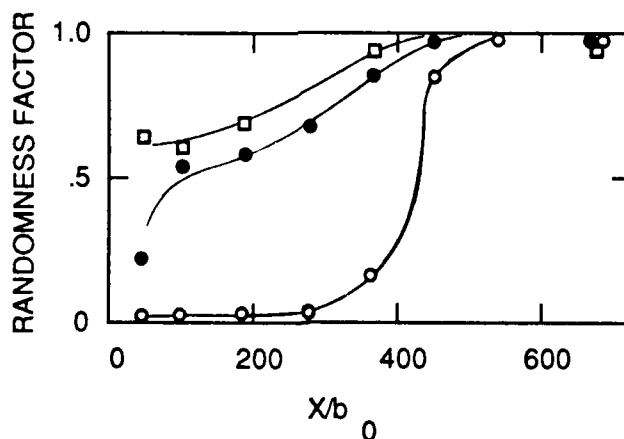


FIGURE 8. RANDOMNESS FACTOR.  
 STEADY FLOW, SINGLE  
 FREQUENCY EXCITATION -  $\circ$  ,  
 UNSTEADY FLOW, SINGLE  
 FREQUENCY EXCITATION -  $\bullet$  ,  
 UNSTEADY FLOW, DOUBLE  
 FREQUENCY EXCITATION -  $\square$  .

A NEW METHOD FOR MEASURING IN  
STREAM SMALL SCALE STATIC PRESSURE  
FLUCTUATIONS WITH APPLICATION TO  
WIND-WAVE INTERACTIONS

Jean-Paul GIOVANANGELI  
Institut de Mécanique Statistique  
de la Turbulence, Marseille, France

ABSTRACT

A new method for measuring in stream small-scale pressure fluctuations is presented. The higher capability of the method with regard to the classical one, particularly over laboratory wind waves, is proved. First observations of the air pressure fluctuations have been done over the air water interface during laboratory experiments on wave generation. The results show that, for pure laboratory wind waves at short fetches, a strong coupling exists between air and water motions and that the energy transfer from wind to the waves seems due mainly to the work done by the wave induced pressure fluctuations.

LIST OF SYMBOLS

$C$  : wave phase celerity  
 $C_g$  : wave group celerity  
 $Coh$  : coherency  
 $C_{ps}$  : pressure coefficient for a static pressure sensing head  
 $C_{pt}$  : pressure coefficient for a total pressure sensing head  
 $g$  : gravitational acceleration  
 $n$  : frequency  
 $p$  : instantaneous static pressure  
 $p_m$  : measured instantaneous static pressure  
 $p_t$  : instantaneous total pressure  
 $p_{tm}$  : measured instantaneous total pressure  
 $p'(t)$  : static pressure fluctuation  
 $Q_{pn}$  : quadrspectrum between static pressure fluctuations and water level deflections  
 $S_p$  : static pressure fluctuations spectrum  
 $S_{pt}$  : total pressure fluctuations spectrum

$S_\eta$  : wave spectrum  
 $\vec{u}$  : instantaneous air velocity vector  
 $U$  : air velocity outside the boundary layer  
 $X$  : fetch  
 $\alpha$  : instantaneous incidence angle of the air velocity  
 $\eta$  : instantaneous water level  
 $\phi$  : phase shift  
 $\xi$  : wave energy amplification ratio  
 $\xi^P$  : non dimensional energy transfer ratio by pressure work  
 $\xi^M$  : non dimensional energy transfer ratio predicted by Miles theory  
 $\rho_a$  : air density  
 $\rho_w$  : water density

1. INTRODUCTION

The determination of the static pressure fluctuations is known to be of crucial importance in many fluid flow studies. Of particular interest here is the fluctuating pressure in air right above the air-water interface during the stages of wave generation (Phillips, 1957 ; Miles, 1957). Some experimental works were done in the past in this respect. They are limited and have been confined to measurements either above ocean gravity waves (Longuet-Higgins et al., 1963 ; Dobson, 1971 ; Elliott, 1972 ; Snyder et al., 1981) or over two dimensional laboratory mechanically generated waves (Shemdin and Hsu, 1967 ; Latif, 1974 ; Papadimitrakis et al., 1984 ; Young and Sobey, 1985).

The air pressure fluctuations were measured

using static pressure sensing heads. The results concerning open field observations show a large scatter and are in poor agreement with theory. Laboratory experiments are difficult to make and to analyze because mainly the small amplitude of pressure fluctuations, the dynamic pressure noise and the acoustic effects due to the wave maker and the fan. Further specific observations are thus needed and particularly over waves generated by the wind in wind wave facilities.

This article reports on a series of experiments conducted in laboratory in order to measure small scale static pressure fluctuations in a turbulent boundary layer above a wind wave field. A critical analysis combined with the results of experiments intended to better precise the response of a static pressure tube for the flow configuration lead us to raise basic questions about the accuracy of the classical method. A new technique is consequently proposed.

Comparisons of the performances of the new method and the classical ones were conducted during a series of tests and experiments. Finally the newly designed device was used to determine the wind pressure field in the close vicinity of the air-water interface during experiments on wave generation by the wind in a laboratory air-water facility. First measurements of the work done by the pressure forces are given and compared to the wave amplification ratio.

## 2. THE FLOW CONFIGURATION AND THE EXPERIMENTAL SET UP

The experiments were carried out in the 1/5 scale model of the large I.M.S.T. wind-wave facility described in detail by Coantic and Favre (1974). It is an air-water facility with a water tank of 8.6m long, 0.60m large and 0.26m deep. The air tunnel is 0.28m high and the flow speed can be varied from 0.5 to 15 m/s.

The water surface deflection was measured using two capacitance wave gauges of 0.3mm outer diameter with DISA model 55E capacitance measuring units. The typical sensitivity of the probes was of 0.6 V/cm.

The three instantaneous air velocity

components were measured using simultaneously two X wires DISA model P61 with four constant temperature anemometers DISA model 55M01. The order of magnitude of velocity fluctuations lead us to use digital techniques and a non-linear cooling law for the wires (Giovanangeli, 1980).

The pressure sensor T.S.I. model 1412J which has been used is a bleed type pressure transducer described in detail by Jones (1981). The main characteristics (sensivities and frequency response) of the probe have been studied by Giovanangeli (1986). The pressure sensitivity of the sensor is equal to 10 mV/mm H<sub>2</sub>O and is constant up to 1 KHz. Furthermore, the phase shift between mechanically generated pressure fluctuations and probe voltage fluctuations is equal to zero.

The static pressure sensing head which has been used is described on the Figure 1. It consists in a classical static pressure tube of 2mm outer diameter with four pressure holes. The distance between the hemispherical tip and the holes is equal to 13mm. The sensor was located inside the tip.

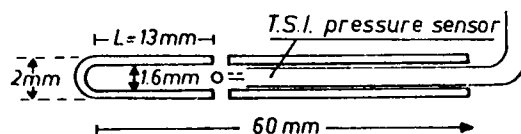


Fig. 1 - THE STATIC PRESSURE PROBE

A total pressure sensing head has been used likewise. It is a 2mm outer diameter tube, 1.6mm inner diameter, 50mm long (see figure 2).

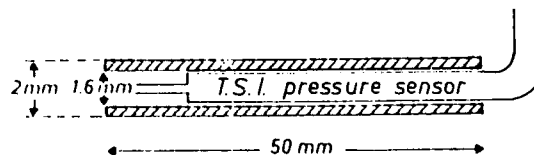


Fig. 2 - THE TOTAL PRESSURE PROBE

For data processing, the output voltage of each sensor were stored numerically on a Hewlett-Packard model 2100 A computer after digitization at 312.5 Hz. Low-pass analog linear filters were used to prevent aliasing. Fast Fourier Transform techniques were used to estimate statistical

properties (auto and cross-spectra).

For the greater part of the experiments, the probes were operated at a fetch  $X$  equal to 3.5m. The mean value  $U$  of the air velocity outside the boundary layer was equal to 6 m/s or 7.5 m/s

### 3. THE NEW METHOD

#### 3.1 Response of a static pressure tube in a turbulent flow

The use of steady-flow techniques for static pressure fluctuations measurements lead to raise four basic questions are : the magnitude of the turbulent scales which can be observed taking into account the measuring volume of the probe (Bradshaw, 1971 ; Hinze, 1975) the dynamic pressure effect when the flow velocity direction is misaligned with the probe axis (Dobson, 1974), the development of a wake on the probe (Fohr, 1979) and the acoustic noise effect.

Each particular point cited above was considered in a series of tests and experiments which consisted to study the response of the static pressure tube described in figure 1 and operated in a turbulent boundary layer over a laboratory wind-wave field.

Considering the values of the scales of the generated waves and of the turbulence, it appeared at first that the size of the classical static pressure probes used by others is not suitable for wind tunnel observations. The probe described in figure 1 doesn't allow to observe scales smaller than 13 mm.

As far as the second point is concerned, it is well known that when the angle  $\alpha$  between the axis probe and the air velocity  $\vec{u}$  is different from zero, the measured pressure  $p_m$  is equal to :

$$p_m = p + \frac{1}{2} \rho_a \cdot C_{p_s}(\alpha) \cdot |\vec{u}|^2 \quad (1)$$

where  $\rho_a$  is the air density,  $C_{p_s}$  is a negative value "pressure coefficient" depending upon  $\alpha$ . Various investigators considered from statistical considerations (Jones et al., 1979 ; George et al., 1984 ; Elliott, 1972 ; Snyder et al., 1974 ; Miksaad, 1976) that pressure coefficient  $C_{p_s}$  could be considered as constant and approximately equal to zero. The figure 3 shows the evolution of  $C_{p_s}$

defined by the formula (1) for  $U = 7.5$  m/s and for different values of  $\alpha$ . Each point of the curve has been obtained using a pressure sensor Baratron Model MK2 because the velocity sensitivity of the sensor at low wind speeds (Giovanangeli, 1986).

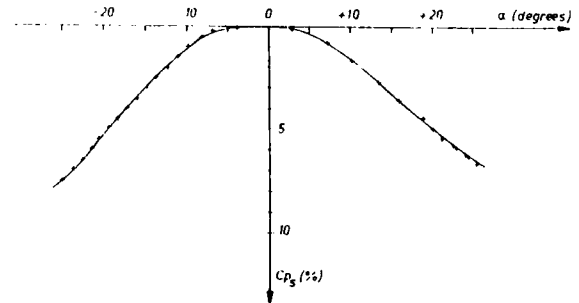


Fig. 3 - PRESSURE COEFFICIENT OF THE STATIC PROBE VERSUS WIND DIRECTION

$C_{p_s}$  is different from zero if  $\alpha$  is different from zero. The relationship  $C_{p_s} = C_{p_s}(\alpha)$  has been fitted by a fifth degree polynomial curve. Preliminary experiments using the two X wires in the close vicinity of the waves showed that the instantaneous angle  $\alpha(t)$  can be largely greater than ten degrees and then  $C_{p_s}$  cannot be considered as zero.

The other important point is concerned with the development of a turbulent wake on the probe when  $\alpha$  is not equal to zero as shown by Fohr (1979) using visualization techniques. It can be shown here that this effect can largely modify the measured pressure spectrum. For this purpose, the probe was operated in the turbulent boundary layer for different values of the mean angle  $\bar{\alpha}$ . For each experiment the air velocity was equal to 7.5 m/s and the distance of the probe above the mean level of the interface was constant.

The figure 4 presents the evolution of the pressure spectra determined for  $\bar{\alpha} = 0^\circ, 5^\circ, 10^\circ,$  and  $15^\circ$ . For the frequencies lower than 60 Hz, the spectra are clearly different. For example at 5 Hz the pressure spectrum determined for  $\bar{\alpha} = 15^\circ$  is equal to seven times the spectrum determined for  $\alpha = 0^\circ$ .

Finally, the acoustic effects have been determined roughly by operating successively the

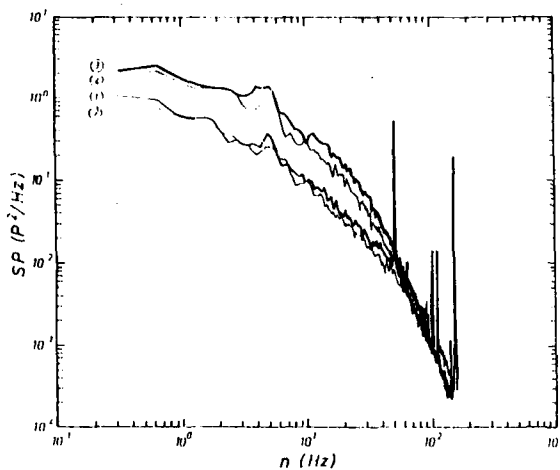


Fig. 4 - STATIC PRESSURE SPECTRA MEASURED USING THE STATIC PROBE FOR DIFFERENT VALUES OF THE MEAN WIND DIRECTION

1 :  $\bar{\alpha} = 0^\circ$ , 2 :  $\bar{\alpha} = 5^\circ$ , 3 :  $\bar{\alpha} = 10^\circ$ , 4 :  $\bar{\alpha} = 15^\circ$

probe, with  $U = 6$  m/s and  $\alpha = 0^\circ$ , inside and outside the turbulent boundary layer. The figure 5 shows the measured pressure spectra for the two cases. The signal to noise ratio depends on the frequency and is equal to 10 db at 1 Hz and to 0 db at 100 Hz.

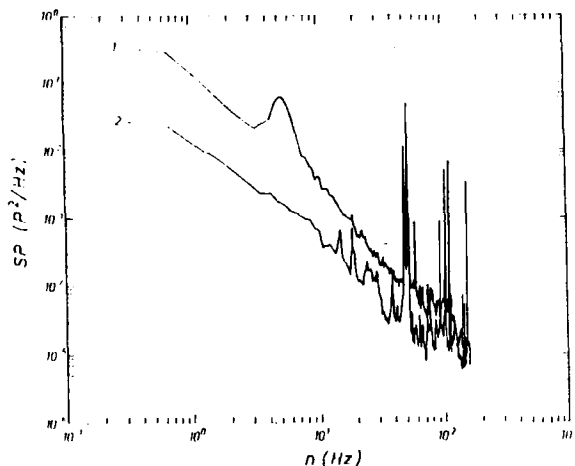


Fig. 5 - PRESSURE SPECTRA MEASURED USING THE STATIC PROBE INSIDE (1) AND OUTSIDE (2) THE BOUNDARY LAYER

Considering the above results and taking into account the order of magnitude of the instantaneous angle  $\alpha$  close to the waves, it appears clearly that for the flow configuration of interest here the small scale pressure fluctuations

cannot be measured with an acceptable accuracy by using a classical pitot static tube.

### 3.2 Response of a total pressure tube in a turbulent flow

As for the static pressure tube, the response of the total pressure tube, shown in figure 2, was studied for the same flow conditions. One can considered at first sight that the total pressure fluctuation can be measured for turbulence scales which are an order of magnitude less than for static pressure fluctuation by using static pitot tube.

As far as the velocity incidence effects are concerned, the Figure 6 presents the evolution of the "total pressure coefficient"  $C_{pt}$  defined by :

$$p_{tm} = p_t + \frac{1}{2} \rho_a \cdot C_{pt}(\alpha) \cdot |\vec{u}|^2 \quad (2)$$

where  $p_{tm}$  is the measured total pressure,  $p_t$  the true total pressure and  $\alpha$  the incidence angle of the air velocity. As found by others investigators, the value of  $C_{pt}$  can be considered equal to zero for  $\alpha$  laying between  $\pm 12^\circ$ . It reaches 0.01 for  $\alpha = \pm 15^\circ$ . The curve  $C_{pt} = C_{pt}(\alpha)$  has been fitted too by a fifth polynomial curve in  $\alpha$  for  $\alpha > 12^\circ$ .

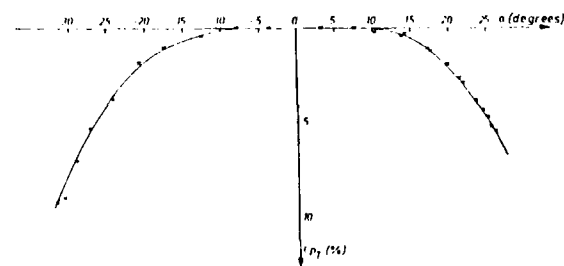


Fig. 6 - PRESSURE COEFFICIENT OF THE TOTAL PRESSURE PROBE VERSUS WIND DIRECTION

The wake effects have been investigated by measuring the total pressure fluctuations spectra for two values of the mean incidence angle keeping constant  $U = 7.5$  m/s and the distance of the probe above the mean water surface level. Figure 7 shows the evolution of the measured total pressure spectra for  $\bar{\alpha} = 0^\circ$  and  $\bar{\alpha} = 15^\circ$ .

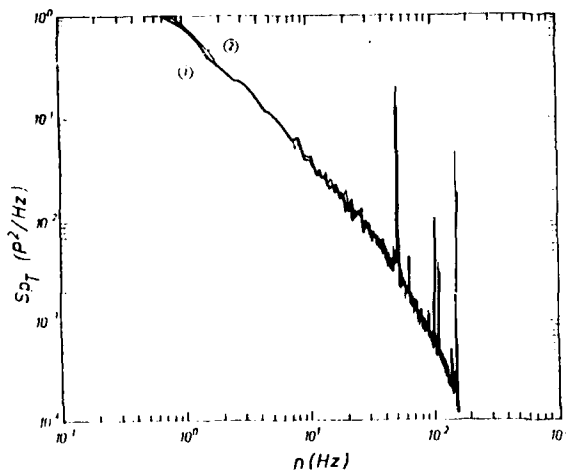


Fig. 7 - TOTAL PRESSURE SPECTRA MEASURED WITH THE TOTAL PRESSURE PROBE FOR  $\bar{\alpha} = 0^\circ$  (1) and  $\bar{\alpha} = 15^\circ$

This picture shows that, contrarily to the measurements of static pressure using a static pressure tube, the velocity incidence has no effect on the measurement of total pressure fluctuations. This could be explained considering that the wake develops downstream the total pressure hole.

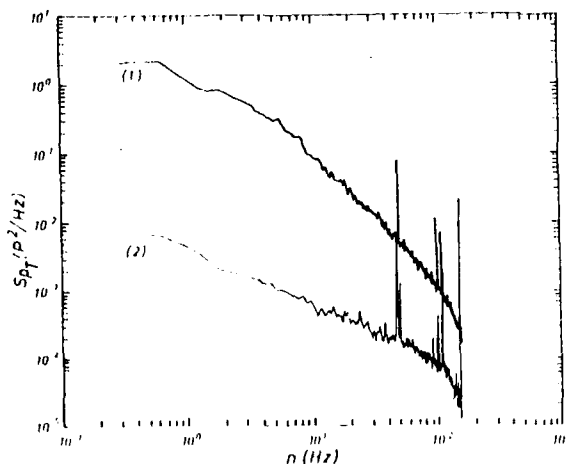


Fig. 8 - TOTAL PRESSURE SPECTRA INSIDE (1) AND OUTSIDE (2) THE BOUNDARY LAYER

The signal to acoustic noise ratio has been measured in the same way that for the static pressure tube. Figure 8 presents the total pres-

sure fluctuations spectra measured inside and outside the turbulent boundary layer. The signal to noise ratio is much greater than for static pressure measurements. It depends too upon the frequency and reaches the values of 24 db for 1 Hz and 10 db for 100 Hz.

### 3.3 The method

The results presented above show that, as suggested by Bradshaw (1971), the in stream small scale fluctuating static pressure cannot be measured in wind facilities using the classical method and particularly in the vicinity of wind waves. On the other hand, the fluctuating total pressure measurements can probably be done with an acceptable accuracy because the small measurement volume of the total pressure sensing head, the insignificant effects of the incidence of the air velocity and of the turbulent wake and the higher value of the signal to noise ratio. This lead us to propose a new method with consists to measure simultaneously the instantaneous total pressure and the dynamical pressure by means of an arrangement of hot wires. The instantaneous static pressure  $p(t)$  is then determined using the following equation :

$$p(t) = p_{tm}(t) - \frac{1}{2} \cdot \rho_a \cdot C_{pt}(\alpha(t)) \cdot |\vec{u}(t)|^2 - \frac{1}{2} \rho_a |\vec{u}(t)|^2 \quad (3)$$

where the first term  $p_{tm}(t)$  is the measured total pressure, the second one the incidence effect correction and the third term is the instantaneous dynamical pressure.

In the classical way, the incidence effects have been considered too as following :

$$p(t) = p_m(t) - \frac{1}{2} \rho_a C_{ps}(\alpha(t)) \cdot |\vec{u}(t)|^2 \quad (4)$$

where the first term  $p_m(t)$  is the measured static pressure and the second one the correction term for the static pressure tube.

The classical and the new method were operated for the same experimental flow configuration in order to compare their relative capabilities to measure small scale in stream pressure fluctuations over wind waves. The results are discussed on the basis of theoretical models of wind wave generation and results of open field measurements made by others.

The experimental configuration of the probes corresponding to the classical method is shown on Figure 9.

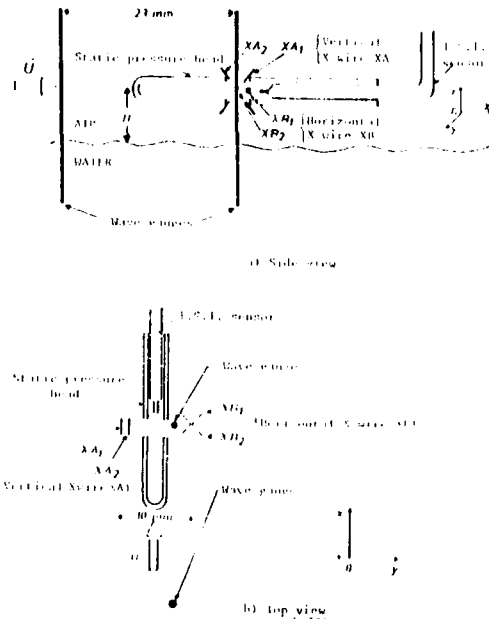


Fig. 9 - EXPERIMENTAL SET UP USED FOR STATIC PRESSURE MEASUREMENTS USING THE CLASSICAL METHOD

The vertical X wire XA and the horizontal X wire XB have been located on both sides of the pressure holes at the same height  $H = 12$  mm as the probe above the mean water level. The two wave gauges were separated from 23 mm in the wind direction. The downstream wave probe was located between the static holes and the horizontal X wire XA.

The experimental configuration of the probes is similar (Figure 10a). Picture 10b displays a view of the total pressure probe and the X wires.

#### 4. EXPERIMENTAL RESULTS

The results are concerned mainly with experiments carried out for  $U = 7.5$  m/s. Figure 11 shows the wave spectra  $S_n(n)$ . It presents a well peaked maximum energy at 4 Hz and two peaks at 8 Hz and 12 Hz. The wave energy considered at 4, 8 and 12 Hz decreases as  $n^{-5}$ , as predicted by Phillips (1958). Between 4 Hz and 8 Hz and between 8 Hz and 12 Hz, the wave spectra evolves as  $n^{-8.5}$ .

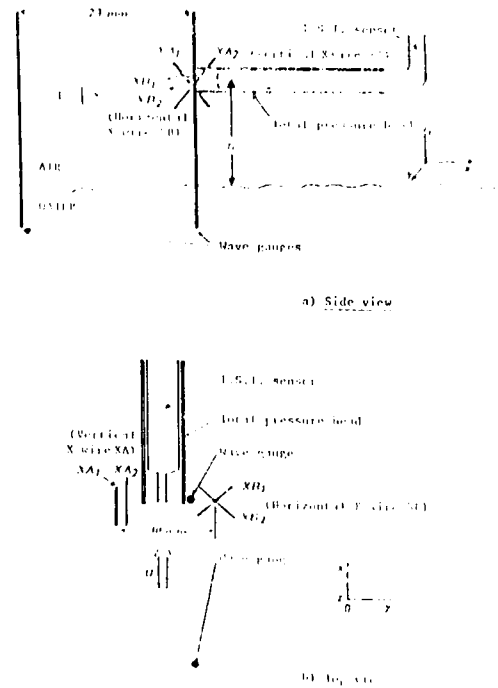


Fig. 10a - EXPERIMENTAL SET UP USED IN THE NEW METHOD

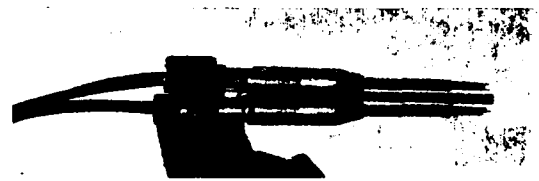


Fig. 10b - TOTAL PRESSURE PROBE AND THE X WIRE

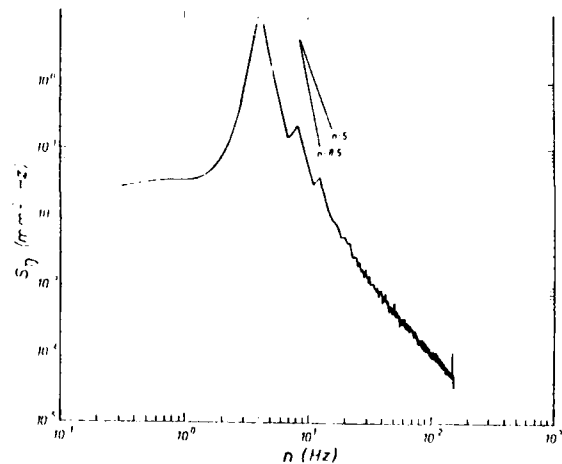


Fig. 11 - WAVE SPECTRUM ( $U = 7.5$  m/s)

Figure 12 shows the wave celerity  $C(n)$  in the range 4 Hz-10 Hz.  $C(n)$  is approximately constant as observed by others (Ramamonjariisoa, 1974).

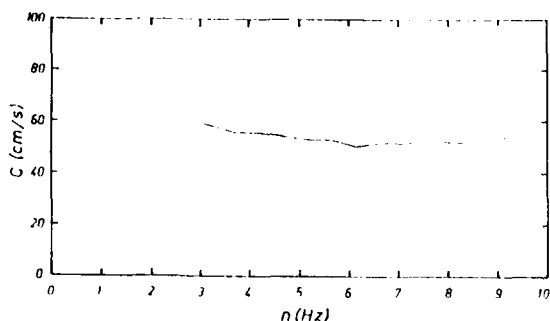


Fig. 12 - WAVE PHASE CELERITY ( $U = 7.5$  m/s)

The Figure 13 presents the evolution in time of the interface  $\eta(t)$  measured at the downstream wave gauge and of the static pressure fluctuation  $p'(t)$  determined by the classical method and by the new method proposed here. It seems at first sight that  $p'(t)$  measured by the new method is significantly coupled with the interface motions as expected by theoretical considerations (Lamb, 1939 ; Miles, 1957) or open field measurements. On the other hand, this doesn't appear if  $p'(t)$  is determined by the classical method.

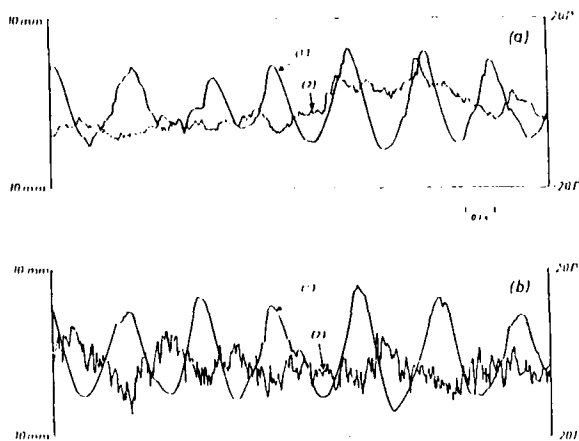


Fig. 13 - SAMPLE OF TIME VARIATIONS OF : (1) WATER SURFACE LEVEL  $\eta(t)$  AND (2) STATIC PRESSURE FLUCTUATION  $p'(t)$  DETERMINED BY THE CLASSICAL METHOD (UPPER) AND BY THE NEW METHOD (LOWER)

The Figure 14 gives the pressure spectra measured using the classical (curve 1) and the new

(curve 2) methods. The general shape of the two spectra is similar to those measured by other over ocean waves (Elliott, 1972 ; Dobson, 1972 ; Snyder et al., 1981) i.e. a turbulent pressure spectra which decreases when the frequency increases and on which appears two "humps" corresponding to the first or second harmonic of the wave field components. However, the peak considered at 4 Hz is well defined on the curve 2 contrarily to the curve 1. The two spectra differ largely when the frequencies increase. For the frequencies lower than 3 Hz the two methods give similar spectra. This is not surprising since for large scales the two methods must be equivalent.

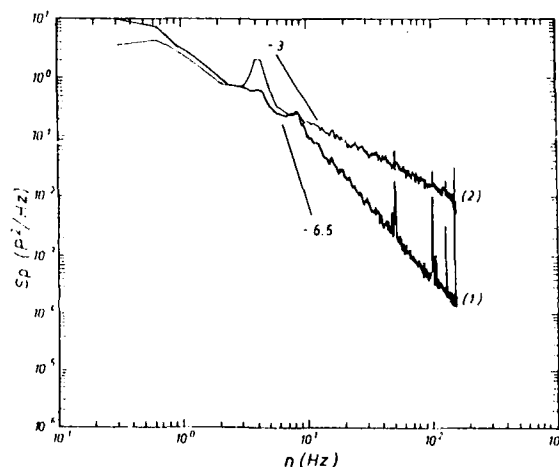


Fig. 14 - STATIC PRESSURE SPECTRA USING THE CLASSICAL METHOD (1) AND THE NEW METHOD (2)

The higher capability of the new method can be proved at first considering the pressure spectra slopes in the frequency range corresponding to the wave induced fluctuations. As a matter of fact it can be shown that since the phase celerity of waves is constant, as observed here, the linear theory, which can be considered here, allow to predict the following relation :

$$S_p(n) = A \cdot n^2 \cdot S_\eta(n) \quad (5)$$

where A is a constant. Taking into account the evolution of  $S_\eta(n)$  with frequency n, as shown above, the pressure spectra should evolve as  $n^{-5}$  for  $n = 4$  Hz, 8 Hz and 12 Hz and as  $n^{-6.5}$  in the range laying from 4 Hz to 8 Hz.

It appears on Figure 14 that the pressure spectrum determined using the new method has

evolutions with frequency which agree with the predicted ones. This doesn't appear if the pressure is measured by the classical method.

The Figure 15 displays the coherency function  $Coh(n)$  between  $p'(t)$  and  $\eta(t)$  determined by the two methods. If  $p'(t)$  is measured by the new method,  $Coh(n)$  reaches at  $n = 4$  Hz a higher value than for the classical method. Furthermore with the classical method,  $Coh(n)$  is greater for  $n = 8$  Hz than for  $n = 4$  Hz. This shows that the correction term of equation (2) is not well measured or, as proposed by others (Barat, 1965), that  $C_{ps}$  depends upon the observed scales.

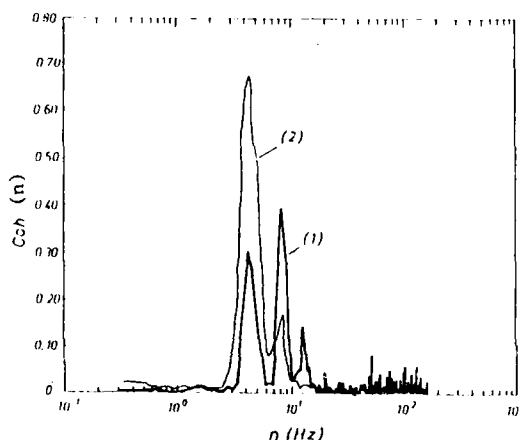


Fig. 15 - COHERENCY FUNCTION BETWEEN  $\eta(t)$  AND  $p'(t)$  DETERMINED USING THE CLASSICAL METHOD (1) AND THE NEW METHOD (2)

On the other hand, for the pure turbulent pressure components others investigators (Elliott, 1972 ; Jones et al., 1979 ; George et al., 1984) showed that the wave number pressure spectra can be grouped using the parameter  $\rho_a U^2$ . The Figure 16 and 17 present respectively the normalized wave number pressure spectra, measured for  $U = 6$  m/s and  $U = 7.5$  m/s, for  $p'(t)$  determined by the classical and the new method.

The spectra can be grouped if  $p(t)$  is measured by the new method. They can't with the classical one. In the range of frequencies corresponding to the wave induced pressure components, the normalized spectra are not grouped since for the wave components the  $\rho_a U^2$  parameter is not a normalization parameter

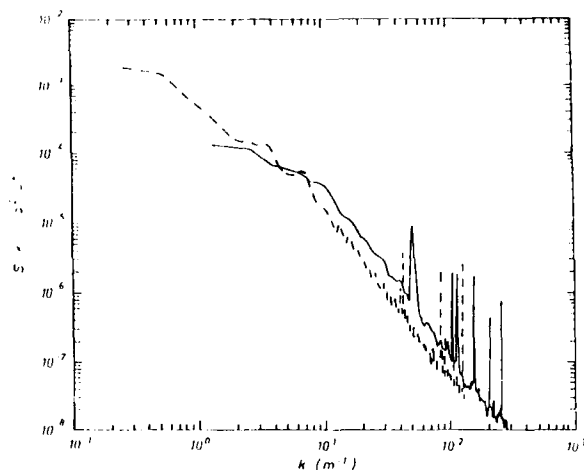


Fig. 16 - NON DIMENSIONAL WAVE NUMBER PRESSURE SPECTRA USING THE CLASSICAL METHOD FOR  $U = 6$  m/s (---) AND  $U = 7.5$  m/s (—)

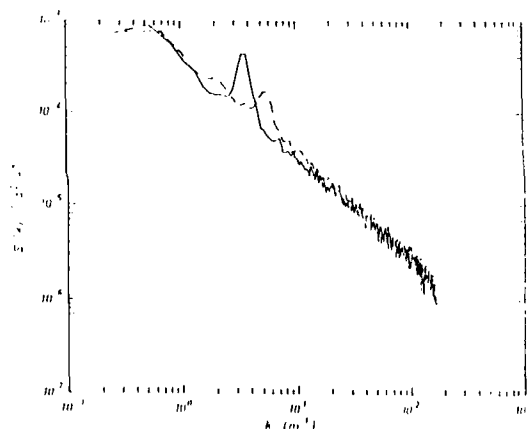


Fig. 17 - NON DIMENSIONAL WAVE NUMBER PRESSURE SPECTRA USING THE NEW METHOD FOR  $U = 6$  m/s (---) AND  $U = 7.5$  m/s (—)

The results presented above show that for the particular experimental flow configuration the new method seems to be clearly powerful to measure in stream small scale pressure fluctuations contrarily to the classical one. However the experimental procedure is rather complex since it is necessary to operate simultaneously a total pressure probe and two X wires. A simplified method and a prototype probe has been successfully developed (Giovanangeli, 1986). It consist mainly in a total pressure probe coupled to a single hot wire of a particular shape. This last sensor allows

to measure directly the instantaneous velocity modulus.

Finally first estimates of the energy transfer from wind to waves by pressure fluctuations measured by the new method have been done. The results have been compared to the wave amplification ratio measured for the dominant wave component between  $X = 3.5$  m and 4 m for  $U = 6$  m/s. It has been observed that over this distance the frequency  $n_0$  of the dominant wave was constant. The Figure 18 shows the quadspectrum  $Q_{p\eta}$  between  $p'(t)$  and  $\eta(t)$  at  $X = 3.5$  m. The curve is sharply peaked at  $n_0 = 5$  Hz.

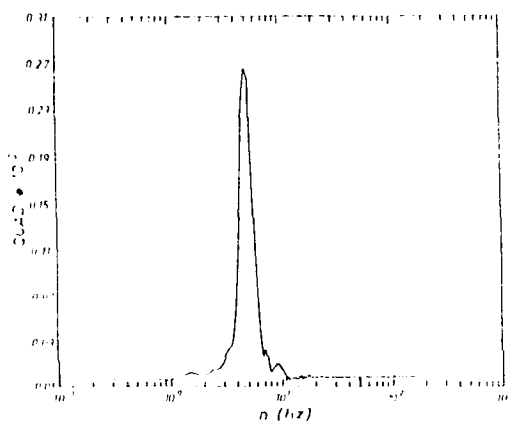


Fig. 18 - QUADSPECTRUM BETWEEN AIR PRESSURE FLUCTUATIONS AND WATER SURFACE DEFLECTIONS ( $U = 6$  m/s)

The non dimensional ratio of work done by the pressure fluctuations is equal to :

$$P(n) = \frac{Q_{p\eta}(n)}{\rho_w g S_n(n)} \quad (6)$$

where  $\rho_w$  is the water density.

The wave amplification ratio is defined as :

$$E(n) = \frac{Cg \cdot P(n)}{2\pi n \cdot X} \quad (7)$$

where  $Cg$  is the wave group velocity.

The following table gives the respective values of the above parameters measured for  $U = 6$  m/s and  $n_0 = 5$  Hz.

$P$	$E$	$E_{sc}$	$E_M$
$14.6 \cdot 10^{-3}$	$15.3 \cdot 10^{-3}$	$15.7 \cdot 10^{-3}$	$3.5 \cdot 10^{-3}$

where  $E_{sc} = \frac{E_a}{\rho_w} (1 - \frac{U}{c})$  is the empirical formula given by Snyder and Cox (1961) and  $E_M$  the value given by Miles theory. As observed by other investigators in open field experiments, it is shown that even for pure laboratory wind wave the coupling between the wave and air motion is strong. Furthermore, the energy transfer from wind to wave seems mainly due to wave induced pressure components and largely greater than the Miles predicted value.

## 5. CONCLUSION

The response of a classical static pressure tube and of a total pressure tube in a turbulent boundary layer over laboratory water waves has been studied by means of a series of tests and experiments. The results show that for the flow configuration considered here the classical method doesn't allow to measure in stream small scale static pressure fluctuations with an acceptable accuracy. A new method combining a total pressure sensing head and hot wires anemometers is presented. The performances of the two methods have been compared. The higher capability of the new method to determine small scale static pressure fluctuations is clearly proved. First observations of wind pressure field in the close vicinity of the air water interface show that, as observed by others in open sea or over mechanically generated waves, a strong coupling exists between air and water motions and that the energy transfer from air to waves is mainly due to the wave induced pressure fluctuations and largely higher than the value predicted by the linear stability theory. These results are the first obtained for pure laboratory wind waves at very short fetches.

## Acknowledgements

This work has been sponsored by the Etablissement d'Etudes et de Recherches Météorologiques and the Centre National de la Recherche Scientifique (France). We would like to thank all the technical staff of I.M.S.T. Laboratory of Luminy, especially P. Chambaud for his assistance and A.M. Rugliéro for drawings and for typing the manuscript. We thank also Drs. A. Ramamonjirisoa,

R. Dumas, M. Coantic and E. Mollo-Christensen for their useful remarks.

#### References

- Barat, M. 1965 : Contribution à la mesure des pressions dans les écoulements turbulents. Thèse de Docteur ès Sciences, Paris.
- Bradshaw, P. 1971 : An introduction to turbulence and its measurements. Pergamon Press.
- Coantic, M; Favre A. 1974 : Activities in, and preliminary results of, air-sea interactions research at I.M.S.T., Adv. Geophys., 18A, 391-405.
- Dobson, F.W. 1971 : Measurements of atmospheric pressure on wind-generated sea waves. J.F.M., vol. 48, 91-127.
- Dobson, F.W. 1974 : Air pressure measurement techniques. Air-Sea Interaction, Instruments and Method, Plenum Press, New York and London.
- Elliott, J.A. 1972 : Microscale pressure fluctuations near waves being generated by the wind. J.F.M., 54, 427-448.
- Fohr, J.P. 1979 : Contribution à l'étude du comportement des antennes de pression statique dans divers écoulements. Thèse de Doctorat ès Sciences, Université de Poitiers.
- George, W.K.; Beuther, P; Arndt, R. 1984 : Pressure spectra in turbulent free shear flows, J.F.M., vol. 48, 155-191.
- Giovanangeli, J.P. 1980 : A non dimensional heat-transfer law for a slanted hot-film in water flow. DISA Info. n° 25.
- Giovanangeli, J.P. 1986 : Mécanismes physiques d'évolution des vagues de vent : observations et analyses. Thèse de Doctorat d'Etat, Université d'Aix-Marseille II.
- Giovanangeli, J.P. 1986 : Velocity and temperature sensitivities of a bleed type pressure sensor. To be published.
- Hinze, J.O. 1975 : Turbulence (2nd Edit.), Mac Graw Hill.
- Jones, B.G. 1981 : A bleed-type pressure transducer for in stream fluctuating static pressure sensing. T.S.I. Quarterly.
- Jones, B.G; Adrian, R.J; Nithianandan, C.K. 1979 : Spectra of turbulent static pressure fluctuations in jet mixing layers. A.I.A.A. Journal, vol. 17, 449-457.
- Lamb, H. 1932 : Hydrodynamics. Cambridge University Press.
- Latif, M.A. 1974 : Acoustic effects on pressure measurements over water waves in the laboratory. Coastal and Oceanographic Engineering Laboratory, Technical Report n° 25.
- Longuet-Higgins, M.S; Cartwright, D.; Smith, N.D. 1963 : Observations of the directional spectrum of sea waves using the motions of a floating buoy. Ocean Wave Spectra, 111-136, Englewood Cliffs, Prentice-Hall Inc.
- Miksad R.W. (1976) - An omnidirectional static pressure probe. Journal of Applied Meteorology, 15, pp.1215-1225.
- Miles, J.W. 1957 : On the generation of surface waves by shear flows. J.F.M., vol. 3, 185-204.
- Papadimitrakis, Y; Hsu, E; Street, R. 1984 : Measurements of the fluctuating pressure in the turbulent boundary layer over progressive mechanically generated water waves. Gas Transfer at Water Surface, 201-209, W. Brutsaert and G.H. Jirka (eds.), D. Reidel Publ. Company.
- Phillips, O.M. 1957 : On the generation of waves by turbulent wind. J.F.M., vol. 2, 417-445.
- Phillips, O.M. 1958 : The equilibrium range in the spectrum of wind generated waves. J.F.M., vol. 4, 426-434.
- Ramamonjariisoa, A. 1974 : Contribution à l'étude de la structure statistique et des mécanismes de génération des vagues de vent. Thèse de Doctorat ès Sciences, Université de Provence.
- Shemdin, O.H; Hsu, E.Y. 1967 : The dynamics of wind in the vicinity of progressive water waves. Depart. of Civ. Eng. Stanford University, Tech. Rep. n° 66.
- Snyder, R.L; COX C.S. 1961 : A field study of the wind generated ocean waves. J. of Marine Res., vol. 24, n° 2.
- Snyder, R.L; Dobson, F.N; Elliott, J.A; Long R.B. 1981 : Array measurements of atmospheric pressure fluctuations above surface gravity waves. J.F.M., vol. 12, 1-59.
- Young, I; Sobey, R. 1985 : Measurements of the wind-wave energy flux in an opposing wind. J.F.M., vol. 51, 427-442

EXPERIMENTAL STUDY OF MUTUAL  
INTERFERENCE BETWEEN TWO SPHERES  
PLACED ON PLANE BOUNDARY

Shiki Okamoto  
Department of Mechanical Engineering  
Shibaura Institute of Technology  
Tokyo, Japan

ABSTRACT

This paper describes an experimental study of the mutual interference between two spheres placed on a plane boundary. The experiment was carried out in an N. P. L. type wind-tunnel having a working section of 500mm x 500mm x 2000mm in size at a Reynolds number of  $4.74 \times 10^4$ .

The surface-pressure distributions of two spheres were measured for the various relative positions of two spheres and the drag, side-force, and lift coefficients were determined from surface-pressure distributions. The separation of the flow and the formation of vortices were observed by the method of visualization. The distributions of velocities, and turbulent intensities of the flow past two spheres were measured. The experimental results for two spheres were compared with those of a single sphere.

Nomenclature

$C_D$	: drag coefficient
$C_L$	: lift coefficient
$C_p$	: surface-pressure coefficient of sphere = $(P - P_\infty) / (\rho U_\infty^2 / 2)$
$C_S$	: coefficient of side force
$D$	: diameter of sphere [mm]
$P$	: static pressure [Pa]
$P_\infty$	: static pressure in free stream [Pa]
$Re$	: Reynolds number = $DU_\infty / \nu$
$S$	: spacing between the centers of two adjoining spheres in plane view [mm]
$U$	: time-mean velocity in X-direction [m/s]
$U_\infty$	: free stream velocity [m/s]
$u', v', w'$	: X, Y and Z-components of velocity fluctuation [m/s]
$X, Y, Z$	: coordinate axes with origin at the bottom center of test sphere, X, Y, Z axis being taken in the streamwise, lateral and vertical directions respectively. [mm] (see Fig. 1)
$\alpha$	: latitude angle [deg.]
$\theta$	: longitude angle [deg.]
$\phi$	: angle between the line connected with the centers of two spheres and wind direction [deg.] (see Fig. 2)
$\nu$	: kinematic viscosity of air [ $m^2/s$ ]
$\rho$	: density of air [ $N/m^3$ ]

1. INTRODUCTION

In designing structures and improving the atmospheric environment, it is necessary to obtain experimental data concerning flow-fields and the aerodynamic forces of a structure such as high buildings, smokestacks and gas tanks.

The flow past a three-dimensional blunt obstacle placed on a plane boundary was first studied by Schlichting (1936) in connection with the effect of surface roughness. Since then, numerous studies have been performed in connection with the air flow past buildings, cooling towers, smokestacks, spherical gas tanks and other structures. Klemm et al. (1939) studied the drag of a sphere placed on a ground plate, and Hunt (1971) investigated the flow past a building in a uniform stream. Peterka & Cermak (1977) studied the wake behind a rectangular cylinder, and Sakamoto et al. (1980) studied the flow past a flat plate of finite length and a rectangular cylinder. Furthermore, Okamoto & Yagita (1973, 1977) studied the flow past a circular cylinder and a cone, and Okamoto (1980, 1982) investigated the flow past a sphere and a hemisphere cylinder.

The above-mentioned investigations were limited to cases of a single blunt obstacle placed on a plane boundary. However, since, in practice, two or more obstacles have often been located in rows as seen in concentrations of high buildings in city centers and gas tanks in storage and plant areas, it is necessary to investigate the flowfield past a number of obstacles placed on a ground plane. Concerning the interference between two blunt obstacles, a number of experimental investigations by Biermann (1933), Hori (1959), Bearman (1973), Price (1976) and Barnes et al. (1986) have hitherto been performed on the flow past two-dimensional blunt cylinders in a uniform stream, but only a few studies of the flow past blunt obstacles placed on a ground plane have been performed. Taniguchi et al. (1982) have investigated the interference between two circular cylinders of finite length vertically immersed in a turbulent boundary layer, and Takano et al. (1981) have studied the flow past two and three rectangular cylinders embedded in a turbulent boundary layer.

This paper describes an experimental study of the interference between two spheres on a ground plane with varied relative positions. The surface-pressure distributions on two spheres were measured

and the drag, lift and side force coefficients were determined from the surface-pressure distributions. The surface-pressure distributions on the ground plane were also measured and the flow patterns past two spheres were visualized. The velocity distributions and turbulent intensities in the far wake behind two spheres were measured. The flows caused by the interference between two spheres were compared with the flow past a single sphere.

## 2. EXPERIMENTAL APPARATUS AND MEASUREMENT PROCEDURES

The experiment was carried out in an N. P. L. type wind-tunnel having a 500mm x 500mm working section of 2000mm length. The ground plate, an aluminium plate of 4mm thickness, was set with a spacing of 25mm from the lower wall of the tunnel exit in order to avoid the boundary layer developed on the tunnel wall, as shown in Fig. 1. The test sphere was placed at a downstream distance of 500mm from the leading edge of the ground plate. The boundary layer at the position of the test sphere was transitional and its thickness was about 6 mm.

Two kinds of two spheres, of 70mm diameter and 40mm diameter were provided, the former being used for measurements of the surface pressure and the latter for measurements of velocity, and turbulence intensities of the flow. The point on the surface of the sphere was represented by latitude angle ( $\alpha$ ) and longitude angle ( $\theta$ ), ( $\alpha=0^\circ$  and  $\theta=0^\circ$ ) taken at the center of the frontal face of test sphere (see Fig. 1). Pressure holes of 0.5mm diameter were bored with an angular spacing of  $\alpha=10$  degrees on the surface of the sphere in the vertical plane ( $\theta=0^\circ$ ). Measurements of the surface pressure for any value of  $\theta$  were made by rotating the test sphere about the vertical Z-axis. The surface pressure was transmitted to a manometer passing through the base of the test sphere. Many pressure holes of 0.5mm diameter were bored to measure the pressure on the surface of the ground plate. The separation of the flow on the ground plate was observed by smearing a solution of tooth powder on the ground plate. The

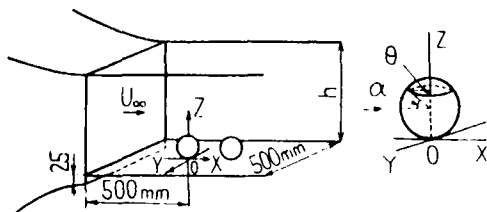


Fig. 1. Schema of apparatus and nomenclature

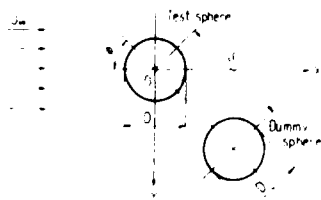


Fig. 2. Relative position of two spheres

generation of vortices behind the spheres were visualized by ink shedding in a water channel. The time-mean velocity and turbulence were measured by the Pitot and static-pressure tubes, and a constant-temperature hot-wire anemometer.

The angle between the line connected to the centers of the two spheres and the wind direction, or the incidence angle, was varied at  $\phi=0^\circ$  (tandem) and  $90^\circ$  (side-by-side) arrangements. The spacing between the centers of the two spheres was varied at  $S/D=1.3, 1.5, 1.7$  and  $2.5$  for each set of values of  $\alpha$  and  $\theta$ , and  $S/D=3.5$  was added in the case of the tandem arrangement ( $\phi=0^\circ$ ).

Measurements were done at a wind velocity of  $U_\infty=10.2\text{m/s}$  and  $U_\infty=17.9\text{m/s}$  for the spheres of  $D=70\text{mm}$  and  $D=40\text{mm}$  respectively, that is at a Reynolds number of  $Re=4.74 \times 10^4$ . This Reynolds number was situated in the subcritical region where the drag of the sphere is independent of the Reynolds number.

## 3. EXPERIMENTAL RESULTS AND DISCUSSIONS

### 3.1. Case of Tandem Arrangement ( $\phi=0^\circ$ )

#### (1) Surface-pressure distribution

Figure 3 shows the variation of surface-pressure distributions on the upstream and downstream spheres in the horizontal center section ( $\alpha=0^\circ$ ) with  $S/D$ , where the dotted and broken lines denote the measured result (Okamoto 1980) and a theoretical value based on the potential-flow theory of a single sphere respectively.

The pressure distribution on the upstream sphere is varied slightly with  $S/D$  and has, as a whole, a pressure distribution which is similar to that of a single sphere, except near the rear portion influenced the downstream sphere. The pressure on the surface of the two spheres in the range of  $0 \leq \theta < 90^\circ$  is slightly larger than that of a single sphere owing to the effect of the downstream sphere.

The pressure distribution on the downstream sphere is different from that of the upstream sphere because the downstream sphere is located in the wake of the upstream sphere. The pressure on the frontal surface of the downstream sphere is negative when  $S/D < 2.5$  and becomes positive when  $S/D \geq 2.5$  and approaches the value of a single sphere as the spacing between both spheres further increases. Since the length of the recirculation region behind a single sphere is  $2.5D$ , the downstream sphere is supposed to leave the recirculation region behind the upstream



(a) upstream sphere (b) downstream sphere

Fig. 3. Surface pressure distributions in horizontal center section ( $\alpha=0^\circ$ ) of two spheres in tandem arrangement ( $\phi=0^\circ$ )

sphere when  $S/D=3.0$ . The negative pressure at  $\theta=180^\circ$  of the upstream sphere is nearly equal to that at  $\theta=0^\circ$  of the downstream sphere in the case of  $S/D \leq 1.5$ , this region between both spheres is considered to be stagnant.

Figures 4 and 5 show the surface-pressure distributions on the upstream and downstream spheres in the vertical center section ( $\theta=0^\circ$ ). The pressure distribution on the upstream sphere agrees with that of a single sphere independently of  $S/D$  when  $\alpha \leq 60^\circ$ . The stagnation point on the frontal face is located at  $\alpha=5^\circ$ . The pressure distribution on the downstream sphere is varied with  $S/D$  and approaches that of a single sphere with the increase in  $S/D$ . The critical value of  $S/D$  at which the interference between two spheres practically vanishes is estimated to be  $S/D=10$  according to Fig. 6 which shows the variations of  $C_p$  at  $\theta=0$  and  $\alpha=0$  of the downstream sphere with  $D/S$ .

Figures 7 and 8 show the isopressure lines on the frontal and rear faces of an upstream sphere in the cases of  $S/D=1.3$  and 2.5. The isopressure lines for both cases of  $S/D$  are nearly the same on the frontal face, but are different on the rear face.

Figures 9 and 10 show the isopressure lines on the frontal and rear faces of the downstream sphere in the cases of  $S/D=1.3$  and 2.5. The pressure is negative on the greater part of the frontal face when  $S/D=1.3$ , but becomes positive on the upper half part when  $S/D=2.5$ .

## (2) Lift and drag

The coefficients of aerodynamic forces are defined by aerodynamic forces divided by the product of dynamic pressure of a free stream times the frontal projected area of a sphere. The drag, side force, and lift are the forces in the X-, Y- and Z-directions respectively, and their coefficients are determined by the measured surface-pressure using the following equations :

$$C_D = \frac{2}{\pi} \int_{-\pi/2}^{\pi/2} \int_0^\pi C_p \cos^2 \alpha \cos \theta d\alpha d\theta$$

$$C_S = \frac{2}{\pi} \int_{-\pi/2}^{\pi/2} \int_0^\pi C_p \cos^2 \alpha \sin \theta d\alpha d\theta$$

$$C_L = -\frac{1}{\pi} \int_{-\pi/2}^{\pi/2} \int_0^\pi C_p \sin 2\alpha d\alpha d\theta$$

There is no side force in the case of a tandem arrangement ( $\phi=0^\circ$ ). The above-mentioned drag is, strictly speaking, the pressure drag, but it may be seen to be the total drag, because the frictional drag of a sphere is negligible as compared with the pressure drag. Denoting the drag and lift coefficients of a single sphere by  $C_{D0}$  and  $C_{L0}$  respective-



Fig. 4. Surface pressure distribution on upstream sphere in vertical center section ( $\theta=0^\circ$ )

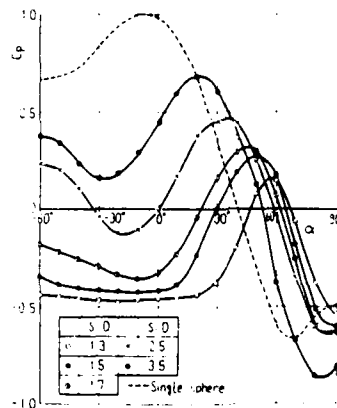


Fig. 5. Surface pressure distribution on downstream sphere in vertical center section ( $\theta=0^\circ$ )

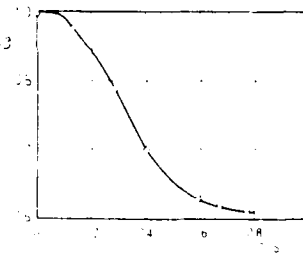


Fig. 6. Variation of  $C_p$  at  $\theta=0^\circ$  and  $\alpha=0^\circ$  of downstream sphere with  $D/S$

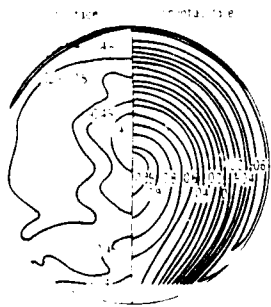


Fig. 7. Isopressure lines on upstream sphere ( $S/D=1.3$ )

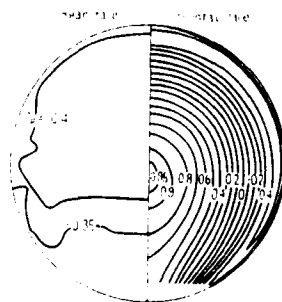


Fig. 8. Isopressure lines on upstream sphere ( $S/D=2.5$ )



Fig. 9. Isopressure lines on downstream sphere ( $S/D=1.3$ )

ly, the results of the experiment (Okamoto 1980) were  $C_{D0} = 0.627$  and  $C_{L0} = 0.242$ .

Figures 11 and 12 show the variation of  $C_D/C_{D0}$  of the upstream and downstream spheres with  $S/D$ . The drag coefficient of the upstream sphere decreases when  $S/D \leq 3$  and then increases gradually towards the value of single sphere as  $S/D$  increases. The drag coefficient of the downstream sphere is negative when  $S/D \leq 1.3$ , but becomes positive and increases towards the value of single sphere as  $S/D$  increases. The value of  $S/D$  corresponding to  $C_D/C_{D0} = 1$  seems to be  $S/D = 10$ , as mentioned previously. Figures 11 and 12 show Taniguchi's (1982) experimental results using a circular cylinder (height/diameter=3) and Takano's (1981) results using a rectangular cylinder (height/width=1) for the sake of comparison. Both results show similar tendencies to those of spheres. Figure 13 shows the lift coefficients of two spheres. The lift coefficients of the upstream sphere increases when  $S/D \leq 1.5$  and then decreases towards the value of a single sphere as  $S/D$  increases, while that of the downstream sphere increases with increasing  $S/D$ .

### (3) Flow patterns

Figure 14 shows the flow past two spheres visualized by the ink shedding method in a water channel under a Reynolds number of  $Re = 1.06 \times 10^3$ . Although the Reynolds number in the water channel experiment is different from that in the wind tunnel, the behavior of the vortex formation in the wind tunnel is considered to be practically the same as that in the water channel. Figure 14(a) where  $S/D = 1.3$ , shows that the flow in the intermediate region

between two spheres is stagnant like a dead water region and the arch vortices are generated behind the downstream sphere. Figure 14 (b) where  $S/D = 2.5$ , shows that the arch vortices are generated behind the upstream sphere as well as behind the downstream sphere.

Furthermore the flow patterns on the ground plane caused by two spheres were visualized by smearing a solution of tooth powder on the ground plate. Figure 15 shows that a separation line shaped like a horse-shoe appears around the spheres, suggesting the existence of a horse-shoe vortex inside the separation line.

The flow past the spheres can also be read from the surface pressure distribution on the ground plane shown in Fig. 16. The broken lines in this figure represent the separation lines. The pressure in front of the downstream sphere is negative when  $S/D \leq 1.7$ , but it becomes positive when  $S/D = 2.5$ . This happens because the downwash from the upstream sphere impinges on the frontal face of the downstream sphere

### (4) Velocity profile and turbulence intensity in far wake

The recirculation region generated in the near wake behind two spheres, ends at  $X/D \approx 4$  even for  $S/D = 2.5$ , as surmised from the pressure distribution on the ground plane, and a turbulent shear layer is formed along the ground at  $X/D \approx 4$ . The profiles of mean velocity and turbulence intensity in the turbulent shear layer were measured for the cases of  $S/D = 1.3$  and 2.5. It has been found from previous

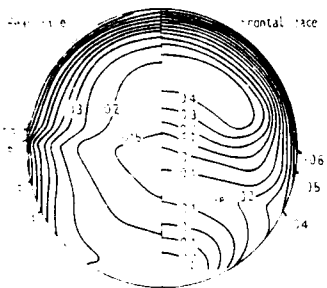


Fig. 10. Isopressure lines on downstream sphere ( $S/D = 2.5$ )

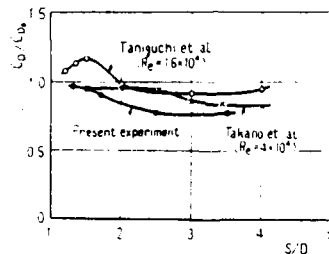


Fig. 11. Drag coefficient of upstream sphere in tandem arrangement ( $\phi = 0^\circ$ ). (● sphere, ○ circular cylinder, x rectangular cylinder)

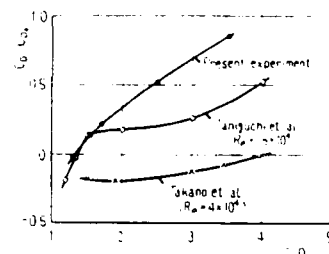


Fig. 12. Drag coefficient of downstream sphere in tandem arrangement ( $\phi = 0^\circ$ ). (● sphere, ○ circular cylinder, x rectangular cylinder)

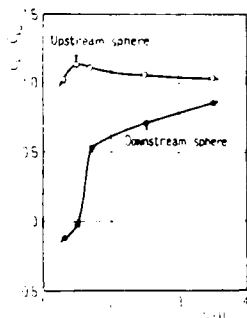


Fig. 13. Lift coefficients of spheres in tandem arrangement ( $\phi = 0^\circ$ )



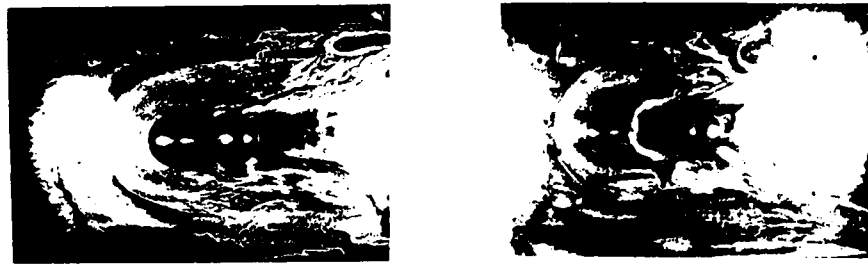
(a)  $S/D = 1.3$  (b)  $S/D = 2.5$   
Fig. 14. Flow past two spheres in tandem arrangement ( $\phi = 0^\circ$ )

paper that the wall wake behind a single sphere becomes thin and spreads transversely with an increase in the downstream distance. Such feature of flow pattern is caused by strong downwash due to the existence of horse-shoe vortices generated near the root of a sphere.

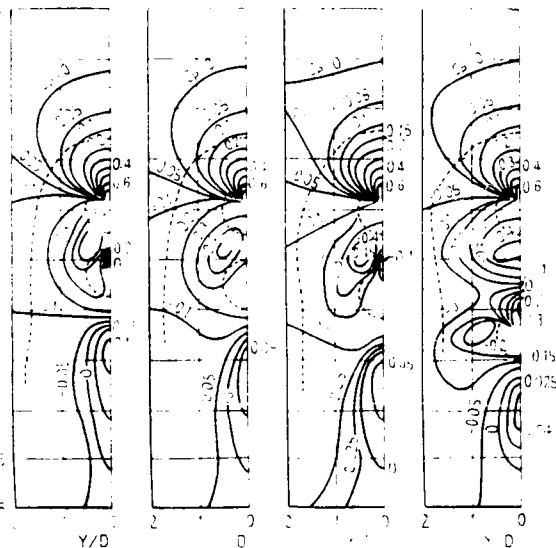
The downstream change of the profiles of mean velocity defect and the decay of turbulence in the far wall-wake in the horizontal center section ( $Z/D=0.5$ ) are shown in Figs. 17~20. The profile of velocity defect for  $S/D=1.3$  has two peaks in the like manner as that of a single sphere. On the other hand, for the case of  $S/D=2.5$  the profile of velocity defect has one peak at the center ( $Y=0$ ) at  $X/D=5$  immediately behind the downstream sphere, and it comes to have two peaks as the downstream distance increases. The velocity defect decreases and the width of wall wake increases with increasing downstream distance. The profile of velocity defect even for  $S/D=2.5$  approaches to those of  $S/D=1.3$  and a single sphere at  $X/D=14$ , though it differs considerably from them at  $X/D=5$ .

The three-components of turbulence intensity take similar form as the velocity defect. The profiles of turbulence intensities for  $S/D=1.3$  agree almost with that of a single sphere. The profiles of turbulence intensities for  $S/D=2.5$  have one peak at the center at  $X/D=5$ , but they come to have two peaks as the downstream distance increases and approach to the result of a single sphere at  $X/D=14$ . The X-component of turbulence intensity is larger than the Y- and Z-components, while the Y-component equals almost to the Z-component at the downstream distance  $X/D=25$ , as shown in Figs. 18~20.

Figures 21 and 22 shows the profiles of the velocity defect and the X-component of turbulence intensity in the wake at  $X/D=10$ . At  $Z/D=0.2$  the velocity defect becomes large and two peaks appear in the profiles. The velocity defect decreases with increasing vertical distance from the ground plane, but two peaks still remain at  $Z/D=1.0$ . The transverse spread of the velocity defect profile is large at lower value of  $Z/D$ , and it decreases with increasing upward distance from the ground plate.



(a)  $S/D=1.3$  (b)  $S/D=2.5$   
Fig. 15. Separation line on ground plane due to two spheres in tandem arrangement ( $\phi=0^\circ$ )



(a)  $S/D=1.3$  (b)  $S/D=1.5$  (c)  $S/D=1.7$  (d)  $S/D=2.5$   
Fig. 16. Surface pressure distribution on ground plane in tandem arrangement ( $\phi=0^\circ$ )

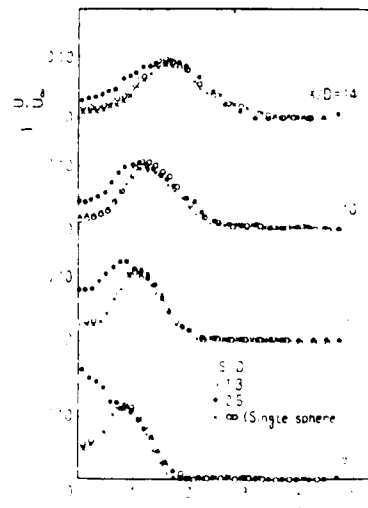


Fig. 17 Profiles of velocity defect at  $Z/D=0.5$

Two peaks almost disappear at  $Z/D=1.2$  and the velocity defect approaches to zero. It is found from this figure that the profiles of velocity defect for  $S/D=1.3$  agree well with that of a single sphere. On the other hand the profiles of velocity defect for  $S/D=2.5$  have larger value at  $Z/D=0.6$  as compared with those of  $S/D=1.3$  and a single sphere, but they approach to those for  $S/D=1.3$  and a single sphere at  $Z/D=1.2$ .

The profile of X-component of turbulence intensity has almost similar form as the velocity defect, while it has still two peaks at  $Z/D=1.2$  as shown in Fig. 22. The profiles for  $S/D=1.3$  are close to those of a single sphere. The turbulence intensity for  $S/D=2.5$  becomes slightly larger than that for  $S/D=1.3$  and a single sphere at  $Z/D=0.8$  and approaches to them at  $Z/D=1.0$ .

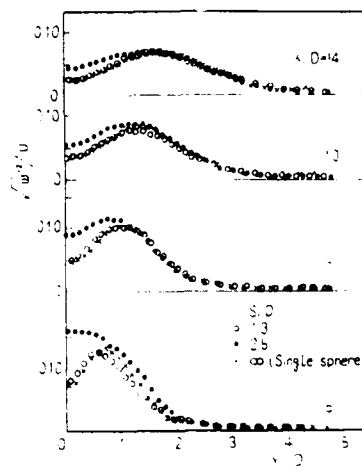
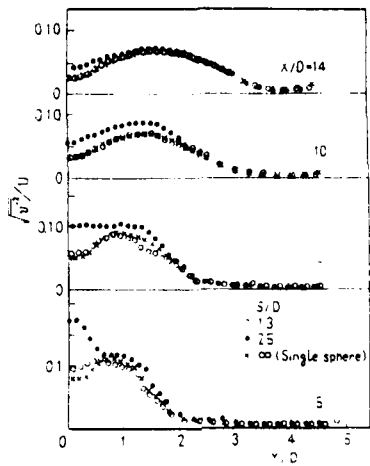
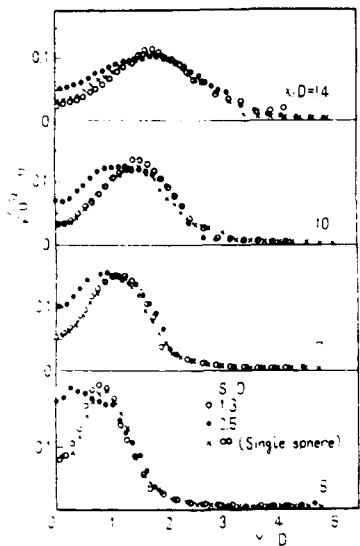


Fig. 18 X-component of turbulence intensity at  $Z/D=0.5$

Fig. 19 Y-component of turbulence intensity at  $Z/D=0.5$

Fig. 20 Z-component of turbulence intensity at  $Z/D=0.5$

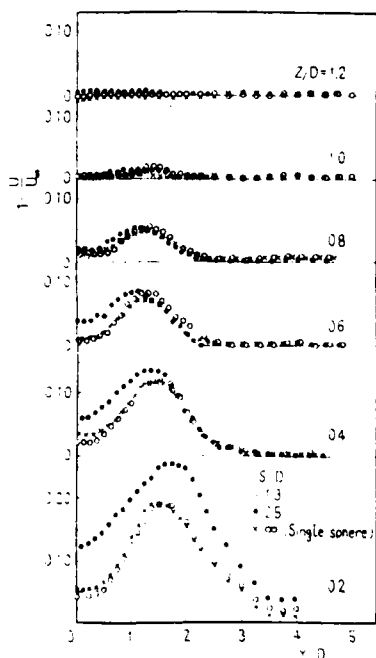


Fig. 21 Profiles of velocity defect at  $X/D=10$

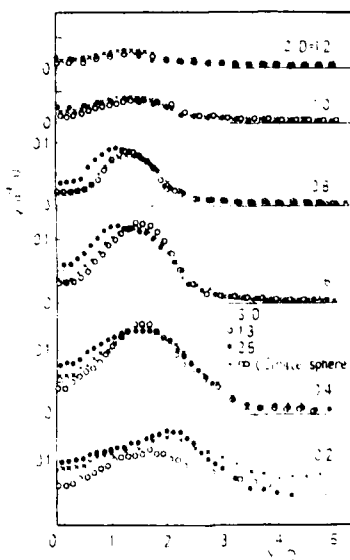


Fig. 22 X-component of turbulence intensity at  $X/D=10$

### 3.2. Case of Side-by-side Arrangement ( $\phi=90^\circ$ )

#### (1) Surface-pressure distribution

Figure 23 shows the surface-pressure distributions on a sphere in the horizontal center section ( $\alpha=0^\circ$ ) for various values of S/D. The inner and outer sides of a sphere are represented by  $\theta=0^\circ\sim 180^\circ$  and  $\theta=0^\circ\sim -180^\circ$  respectively. Since the inner side is under the influence of the opposite sphere, the pressure distribution is asymmetrical about the center plane ( $\theta=0$ ), inducing a side force on the sphere. The degree of asymmetry increases with the decrease in the value of S/D. The angle of maximum pressure, which enables us to estimate the asymmetry of pressure distributions, shifts to the inner side of the sphere with a decrease in the value of S/D.

The pressure distribution on the outer side is practically unaltered in the many cases of S/D when  $S/D \geq 1.5$ , while the pressure distribution on the inner side is varied remarkably with S/D. The minimum pressure on the inner side becomes lower and the point of minimum pressure is shifted downstream as S/D decreases.

#### (2) Lift, drag and side force

Figures 24~26 show that the lift, drag and side force coefficients of one sphere in a side-by-side arrangement decreases gradually as S/D increases. These figures show that the mutual interference between two spheres in a side-by-side arrangement may be ignored when  $S/D \geq 3$ .

Figures 25 and 26 show Taniguchi's (1982) and Takano's (1981) results for the sake of comparison. The critical value of S/D at which the mutual interference may be ignored is greater for circular and

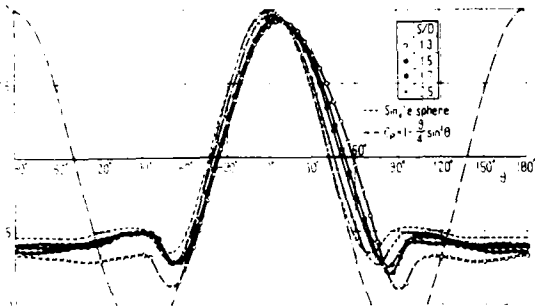


Fig. 23. Surface pressure distribution in horizontal center section ( $\alpha=0^\circ$ ) of sphere in side-by-side arrangement ( $\phi=90^\circ$ )

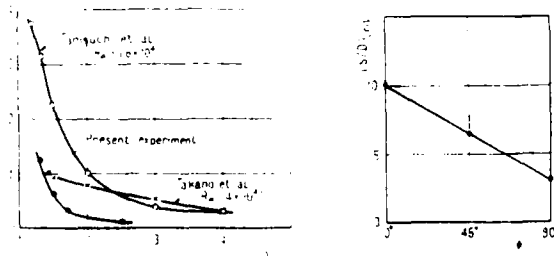


Fig. 26. Side-force coefficient of one sphere in side-by-side arrangement ( $\phi=90^\circ$ ).  
(● sphere, ○ circular cylinder, x rectangular cylinder)

rectangular cylinders than for spheres. Then the measurement of lift, drag and side-force coefficients was added in the case of the oblique arrangement for  $\phi=45^\circ$ . This critical value of S/D is shown in Fig. 27 in terms of incidence angle  $\phi$  and expressed as :

$$(S/D)_{crit} = 10 - 7\left(\frac{\phi}{90^\circ}\right), \quad (\phi: \text{degree})$$

#### (3) Flow patterns

Figure 28 shows the flow past two spheres visualized by the ink-shedding method in a water channel under a Reynolds number of  $Re=1.06 \times 10^3$ . This figure shows that the arch vortices are generated from the spheres as if they were one body when  $S/D=1.3$ , but they shed separately when  $S/D=2.5$ .

Figure 29 shows the pressure distributions on the ground plane in a side-by-side arrangement ( $\phi=90^\circ$ ). A separation line is formed around the spheres as if they were one body when  $S/D \leq 1.7$ , because the flow in the intermediate region between two spheres is stagnant, but the separation lines are formed around individual spheres when  $S/D=2.5$ .

#### (4) Velocity profile and turbulence intensity in far wake

The recirculation region generated in the near wake behind two spheres ends at  $X/D \approx 3$  even for  $S/D=1.3$  like tandem arrangement, as seen from the pressure distribution on the ground plane, and a turbulent shear layer is formed along the ground at  $X/D \approx 3$ . The profiles of velocity and turbulence intensity were measured for  $S/D=1.3$  and 2.5. The profiles of mean velocity defect and three components of turbulence intensity in the wake in the horizontal

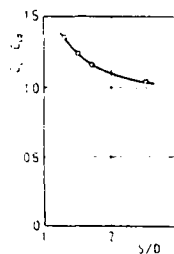


Fig. 24. Lift coefficient of one sphere in side-by-side arrangement ( $\phi=90^\circ$ )

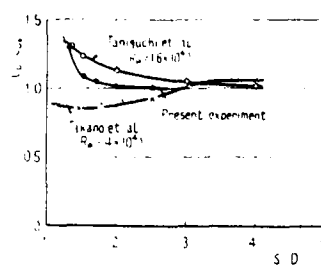
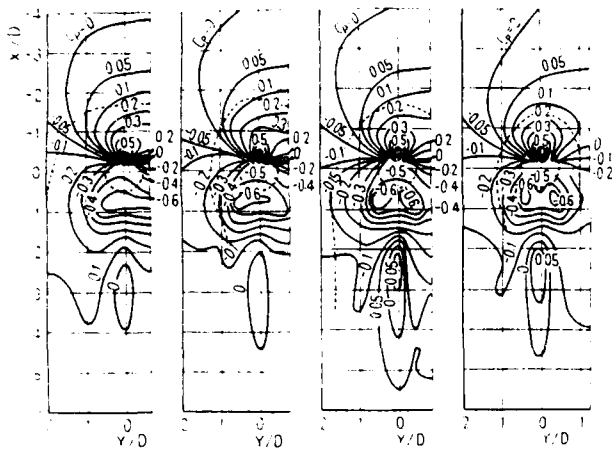


Fig. 25. Drag coefficient of one sphere in side-by-side arrangement ( $\phi=90^\circ$ ).  
(● sphere, ○ circular cylinder, x rectangular cylinder)



(a)  $S/D=1.3$  (b)  $S/D=2.5$   
Fig. 28. Flow past two spheres in side-by-side arrangement ( $\phi=90^\circ$ )

Fig. 27. Critical value of S/D



(a)  $S/D=1.3$  (b)  $S/D=1.5$  (c)  $S/D=1.7$  (d)  $S/D=2.5$   
 Fig. 29. Surface pressure distribution on ground plane in side-by-side arrangement ( $\phi=90^\circ$ )

center section ( $Z/D=0.5$ ) are shown in Figs. 30~33 respectively. The profiles being plotted in the half right side from the center of spacing between two spheres. The velocity defect profile has a large peak at  $X/D=5-10$  for  $S/D=1.3$  as if two spheres were one body, because two spheres are located closely. Though the velocity defect has the smallest value at  $Y=0$  for a single sphere, the velocity defect for  $S/D=1.3$  is not smallest at  $Y=0$ .

On the other hand, the profile of velocity defect has three peaks for the case of  $S/D=2.5$ , which differs from the profiles for  $S/D=1.3$ . The peak appeared at the center of spacing between two spheres is largest, and the other peak at  $Y/D>0$  is close to that of a single sphere. The velocity defect at  $Y=0$  for  $S/D=1.3$  is larger than that for  $S/D=2.5$  at  $X/D=5$ , but it becomes smaller than that for  $S/D=2.5$  at  $X/D \geq 7$ .

The profiles of turbulence intensity have three peaks for  $S/D=1.3$ , which differs from the profiles of velocity defect, and the other peak at  $Y/D>0$  approaches to that for  $S/D=2.5$  and a single sphere with an increase of  $X/D$ . The profile for  $S/D=2.5$  at  $Y/D>0$  agrees well with that of a single sphere at  $X/D \geq 10$ . The X-component of turbulence intensity is larger than the Y- and Z-components, while the Y-component equals almost to the Z-component except near the peak at  $Y/D>0$  at the downstream distance  $X/D \geq 5$ , as shown in Figs. 31~33. But the value of other peak of Y-component at  $Y/D>0$  is slightly smaller than that of Z-component.

Figures 34 and 35 show the profiles of the velocity defect and the X-component of turbulence intensity in the wall wake at  $X/D=10$ . The large velocity defect appears at the center of spacing between two spheres for both cases of  $S/D=1.3$  and 2.5. It remains still at  $Z/D=1.0$  and 1.2 differently from the result of a single sphere. On the other hand, the peak velocity defect near  $Y/D=1.5$  decreases gradually as the upward distance increases. Three peaks appear in the profile for  $S/D=1.3$  and 2.5 at  $Z/D \leq 0.4$  but they change to one peak at the center of spacing between two spheres at  $Z/D \geq 1.0$ . It is found from this figure that the

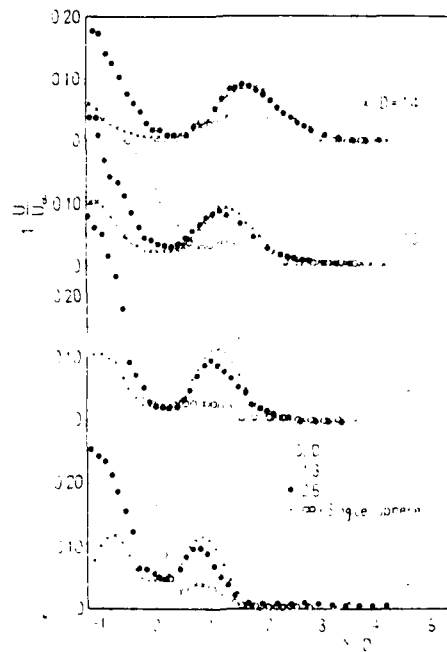


Fig. 30 Profiles of velocity defect at  $Z/D=0.5$

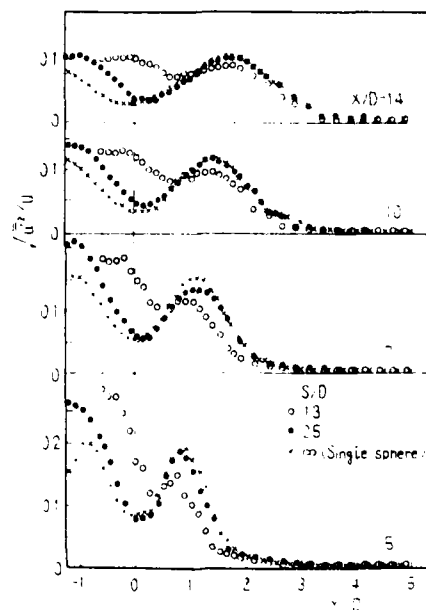


Fig. 31 X-component of turbulence intensity at  $Z/D=0.5$

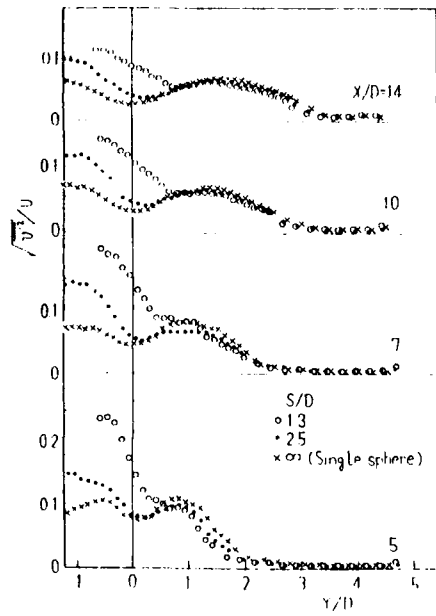


Fig. 32. Y-component of turbulence intensity at  $Z/D=0.5$

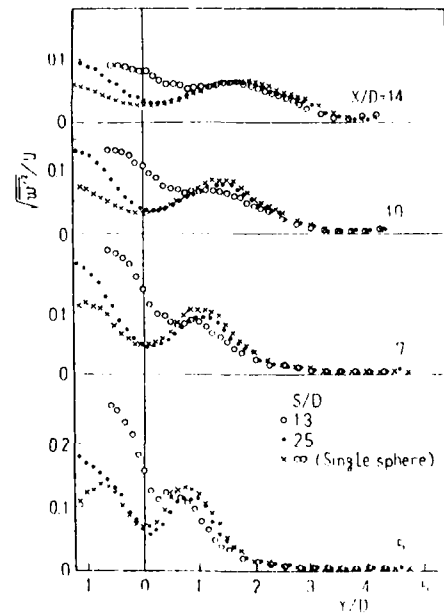


Fig. 33. Z-component of turbulence intensity at  $Z/D=0.5$

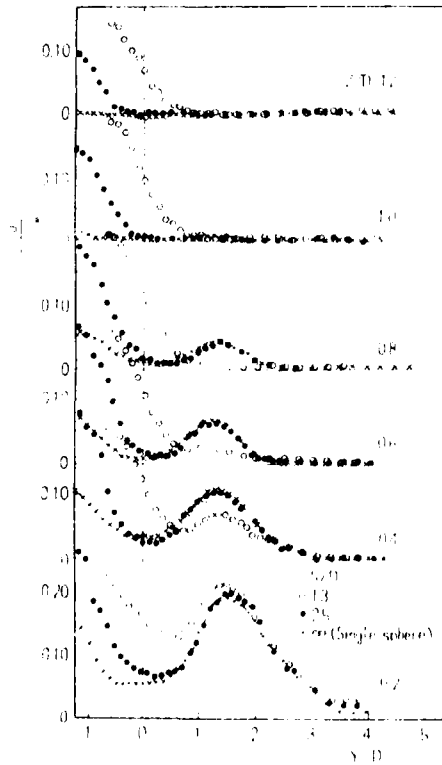


Fig. 34. Profiles of velocity defect at  $X/D=10$

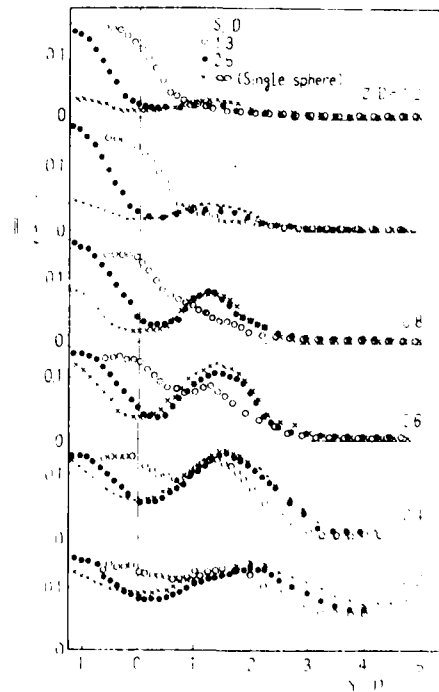


Fig. 35. X-component of turbulence intensity at  $X/D=10$

profile for  $S/D=2.5$  at  $Y>0$  agrees with that of a single sphere.

The profiles of the X-component of turbulence intensity shows same tendency as those of velocity defect. The turbulence intensity at the center of spacing between two spheres equals to the peak intensity at  $Y \approx 0$  at  $Z/D=0.2$  and  $0.4$ . Three peaks appear in the profiles for  $S/D=2.5$  at  $Z/D \leq 1.0$  and a peak appears for  $S/D=1.3$  near the center between two spheres at  $Z/D \approx 0.8$ . The profile of turbulence intensity for  $S/D=2.5$  at  $Y>0$  is close to that of a single sphere.

#### 4. CONCLUSIONS

This paper presents an experimental study of the mutual interference between flows past two spheres placed on a ground plane. The results of the study are summarized as follows :

(1) In the case of a tandem arrangement ( $\phi=0^\circ$ ), the surface pressure distribution on the upstream sphere is almost exactly the same as that on a single sphere, except on the rear face. The downstream sphere is strongly affected by the upstream sphere for  $S/D \geq 1.7$ , so that the pressure is negative on the frontal face of a downstream sphere. The pressure on both spheres tends to approach the value of a single sphere when  $S/D \geq 2.5$ .

(2) In the side-by-side arrangement ( $\phi=90^\circ$ ), the asymmetry of pressure distribution is augmented with a decrease in  $S/D$ . The location of the maximum pressure and the minimum pressure on the inner side of a sphere shifts to the downstream direction as  $S/D$  decreases. The pressure distribution on the outer side is similar to that of a single sphere.

(3) In the case of a tandem arrangement ( $\phi=0^\circ$ ), the lift coefficient of the upstream sphere is larger than that of the downstream sphere. The drag coefficient of the upstream sphere is slightly smaller than that of a single sphere, and the drag coefficient of the downstream sphere has a negative value when  $S/D=1.3$  and then increases with an increase in  $S/D$ . The lift and drag coefficients of both spheres approach the values of a single sphere as  $S/D$  increases.

In the case of a side-by-side arrangement ( $\phi=90^\circ$ ), the lift, drag and side force coefficients of a sphere decrease with an increase in  $S/D$ , approaching the values of a single sphere.

(4) The critical value of  $S/D$ , for which the mutual interference between two spheres may be ignored, is expressed as :

$$(S/D)_{\text{crit}} = 10 - 7 \left( \frac{\phi}{90^\circ} \right),$$

where  $\phi$  is incidence angle in degree.

(5) In the case of tandem arrangement, the profiles of mean velocity defect and the turbulence intensities for  $S/D=1.3$  agree with those for a single sphere.

On the other hand, in the side-by-side arrangement the profiles of mean velocity defect and the turbulence intensity for  $S/D=2.5$  at  $Y>0$  agree with that for a single sphere.

#### REFERENCES

- Barnes, F. H. ; Baxendale, A. J., Grant, I., 1986: A lock-in effect in the flow over two cylinders. *Aero. Jour.* 90, 128-138
- Bearman, P. W., Wadcock, A.J., 1973: The interaction between a pair of circular cylinders normal to a stream. *J. Fluid. Mech.* 61, 499-512
- Biermann, D.; Herrstein, W. H., 1933: The interference between struts in various combinations. *NACA TR 468*, 515-524
- Hori, E., 1959: Experiments on flow around a pair of parallel circular cylinders. *Proc. 9th Japan Nat. Congr. Appl. Mech.*, 231-234
- Hunt, J. C. R., 1971: The effects of single buildings and structures. *Phil. Trans. Roy. Soc., Lond. A.* 269, 457-467
- Klemin, A.; Schaefer, E. B.; Beerer, J. G., 1939: Aerodynamics of the perisphere and trylon at world's fair. *Trans. Am. Soc. Civ. Engr.* 2042, 1449-1472
- Okamoto, S. 1980: Turbulent shear flow behind a sphere placed on a plane boundary. In: *Turbulent Shear Flows 2.* (ed. Bradbury, L.J.S., Durst, F., Launder, B. E., Schmidt, F. W., Whitelaw, J. H.), pp. 246-256, Berlin Heidelberg : Springer
- Okamoto, S. 1982: Turbulent shear flow behind hemisphere-cylinder placed on ground plane. In: *Turbulent Shear Flows* (ed. Bradbury, L. J. S., Durst, F., Launder, B. E., Schmidt, F. W., Whitelaw, J. H.), pp. 171-185, Berlin Heidelberg : Springer
- Okamoto, T.; Yaqita, M., 1973: The experimental investigation on the flow past a circular cylinder of finite length. *Bull. Jpn. Soc. Mech. Eng.* 16, 805-814
- Okamoto, T. et al., 1977: Flow past cone placed on flat plate. *Bull. Jpn. Soc. Mech. Eng.* 20, 329-336
- Peterka, J. A.; Cermak, J. E., 1977: Turbulence in building wakes. *Proc. 4th Int. Conf. on Wind Effects on Building and Structures*, 447-463
- Price, S. J., 1976: The origin and nature of the lift force on the leeward of two bluff bodies. *Aeronaut. Q.* 26, 154-168
- Sakamoto, H. et al., 1980: A study on the flow around cubes immersed in turbulent boundary layer. *Trans. Jpn. Soc. Mech. Eng.* 46, 1437-1446 (in Japanese)
- Schlichting, H., 1936: Experimentelle Untersuchungen zum Rauigkeitsproblem. *Ing. Arch.* 7, 1-34
- Takano, A. et al., 1981: Experimental studies on the flow around rectangular cylinders. *Trans. Jpn. Soc. Mech. Eng.* 47, 982-991 (in Japanese)
- Taniguchi, S. et al., 1982: Interference between two circular cylinders of finite height vertically immersed in a turbulent boundary layer. *Trans. ASME, Ser. I*, 104, 529-536

DOUBLE PULSED LASER VELOCIMETER  
WITH DIRECTIONAL RESOLUTION FOR  
COMPLEX FLOWS

Christopher C. Landreth, Ronald J.  
Adrian and Chung-Sheng Yao  
Department of Theoretical and  
Applied Mechanics  
University of Illinois at  
Urbana-Champaign  
Urbana, IL 61801

ABSTRACT

An automated pulsed laser velocimeter has been constructed which determines fluid velocity fields by directly measuring particle image separations. A new image shifting technique eliminates directional ambiguity from velocity measurements. Theoretical and practical considerations in implementing the PLV system are presented. Using a simple, known flow field to investigate system performance, RMS errors of less than 0.7% of full scale are achieved, and at low seeding density fewer than 10% of velocity measurements produce bad data. Applications of system measurements to the instantaneous velocity field of an axisymmetric jet are presented.

1. INTRODUCTION

Pulsed laser velocimetry (PLV) is a technique to measure simultaneous and quantitative velocity data for fluid flows. The state of the art in PLV is summarized in a number of recent papers by Lourenco and Krothapalli (1986), Short and Whiffen (1986), Arnold, et al. (1986), Adrian (1986), and others. In the double-pulsed, 2-D version of this technique using the particle image velocimetry (PIV) mode of operation (Adrian and Yao, 1983), fluid is seeded with small particles, typically of order  $10\mu\text{m}$  in size. The fluid is illuminated by a thin sheet of double-pulsed laser light having a pulse interval  $\Delta t$  (Fig. 1), and images of particles moving within the light sheet are recorded in pairs on photographic film, at some image magnification  $M$ . The photograph is then interrogated at a location  $\mathbf{x}$  by illuminating a

small 'interrogation region' within a thin light beam and analyzing the displacement  $\Delta \mathbf{x}$  of particle image pairs within that region (Fig. 2). By successively interrogating the photograph at many adjacent interrogation regions, particle velocity  $\mathbf{u}$  in the plane of the light sheet may be inferred at many points in the flow field:

$$\Delta \mathbf{x}(\mathbf{x}) = \mathbf{u}(\mathbf{x}) \Delta t M, \quad (1)$$

where  $\mathbf{x}$  refers to particle position in the flow plane. Provided the particle image density is sufficiently high and the interrogation regions on the photograph sufficiently small, the measured velocity vector field may be considered nearly continuous over the 2-D flow field.

A fundamental problem with the basic PLV method is directional ambiguity. Although the magnitude of the image pair separation may be

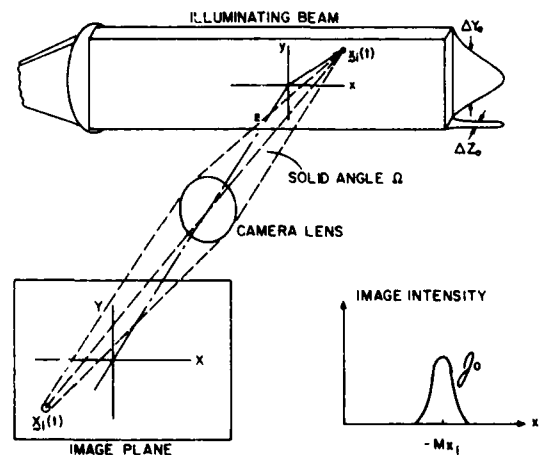


Fig. 1: Image recording system of a pulsed laser velocimeter

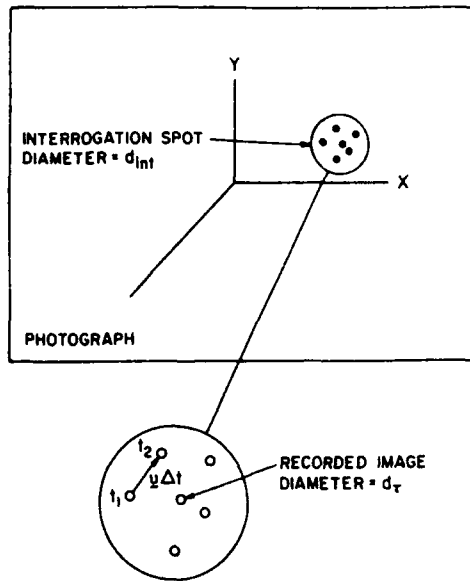


Fig. 2: Interrogation of the recorded image

determined, the polarity of the measured velocity vector is not known. However, directional ambiguity may be eliminated if the image field is shifted between the two illumination pulses, such that the second image of every particle image pair is positively displaced from the first image.

The optimal method of interrogating PLV photographs largely depends on the image density  $N_I$  (Adrian and Yao, 1983), defined as the mean number of particle image pairs per interrogation region. If we assume a light sheet thickness  $\Delta z_0$  and a particle seeding concentration  $C$ , then for a square region of size  $d_{int}^2$

$$N_I = C\Delta z_0 d_{int}^2 / M. \quad (2)$$

If  $N_I < 1$ , particle images are observed as sparse, infrequently overlapping pairs, and only a small fraction of interrogation regions may yield velocity data. One may thus directly measure the separation  $\Delta X$  of each pair to determine the velocity vector. If  $N_I$  is large, each interrogation region generally contains many particle image pairs, and every region is capable of yielding velocity information. For large values of image density, statistical methods such as Young's fringe analysis (Burch and Tokarski, 1968; Hinsch, Schipper and Mach, 1984; et al.) or

spatial correlation (Adrian and Yao, 1983) are required to extract the correct pairings of particle images.

The computational time required to evaluate a 2-D interrogation region may be reduced substantially if the 2-D information is appropriately integrated into 1-D format before computation. For example, 1-D integration of Young's fringes has been demonstrated by Maddux, et al. (1980) using a cylindrical compression lens and linear detector array, and by Ineichen, et al. (1980) using a video raster line. A method called 'orthogonal image compression' (Fig. 3) has been developed, in which the 2-D image of an interrogation region is split, and optically compressed onto two orthogonally-aligned linear detector arrays (Yao and Adrian, 1984). Particle images in the 2-D region appear as peaks in the 1-D distributions of each of the two array signals. The separations of the peaks may be directly measured in each orthogonal direction if  $N_I < 1$ , or evaluated using 1-D spatial correlation if  $N_I > 1$ .

The purpose of this paper is to describe a complete double-pulsed PLV system for measurement of complex flows with small scales of motion and flow reversals. As discussed by Landreth (1986), the system uses the orthogonal image compression method in an automated interrogation device, in which a PDP 11/23 minicomputer regulates the interrogation procedure. The system also employs

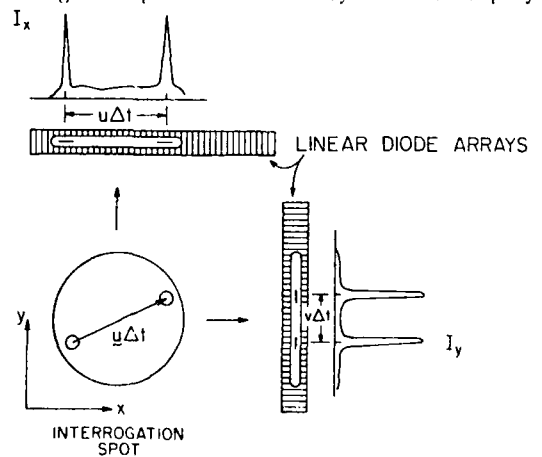


Fig. 3: Interrogation by 1-D orthogonal image compression

a new method for determining the direction of displacement from double-pulsed images. The performance of the system is evaluated for the case of low image density. PLV-generated vectors of solid-body rotation flow are compared to corresponding known values to determine the quality of the PLV measurements. Then, the PLV system is used to produce a vector map of axisymmetric jet flow to reveal with detail its instantaneous flow structure.

## 2. DIRECTIONAL RESOLUTION IN PLV

Given identical conditions in recording each of the two exposures on a PLV photograph, there exist no characteristics identifying the order of particle image exposure. As a result, measuring the separation of the image pairs on the photograph is insufficient to determine the polarity of the velocity vector field. For a given displacement measurement in two dimensions, the velocity vector is ambiguous in sign:  $\pm u$ . For a given measurement using 1-D orthogonal image compression, each component of the velocity vector is ambiguous in sign, resulting in four possible velocity measurements:  $(u,v)$ ,  $(-u,v)$ ,  $(u,-v)$  and  $(-u,-v)$ .

An effective and versatile technique proposed by Adrian (1986) and referred to as spatial 'image shifting' has been developed for resolving directional ambiguity in PLV. The method involves rectilinearly shifting the photographic field of view by an appropriate, known distance between the first and second illumination pulses. As a result, the second image of each particle image pair is shifted by a fixed, known displacement such that the most negative fluid velocity still produces a positive displacement of the second particle image with respect to the first.

Figure 4 illustrates the use of image shifting in PLV. Figure 4a shows a 2-D turbulent flow having a region of flow reversal. Corresponding to this flow field is a domain, in the  $\Delta X$ - $\Delta Y$  plane, of the probable displacement of the fluid during the pulse interval  $\Delta t$ , at all points within the flow field (Fig. 4b). The domain is enclosed within an iso-probability contour  $C_d$ . For a PLV

photograph of the flow,  $C_d$  encloses the domain of every probable location of a second particle image with respect to its corresponding first image. With 1-D orthogonal compression, this domain is enclosed within rectangle  $R_d$ , defined by the upper and lower bounds of  $C_d$ :  $\Delta X_L$ ,  $\Delta X_U$ ,  $\Delta Y_L$  and  $\Delta Y_U$ .

If, for the same flow field, an appropriate uniform image shift  $X_s$  is provided between illumination pulses, the resulting image displacement domains  $C_d'$  and  $R_d'$  appear as in Fig. 4c. The shift  $X_s$  is chosen such that

$$X_s > -\Delta X_L \quad (3a)$$

$$Y_s > -\Delta Y_L \quad (3b)$$

An image pair having a displacement  $\Delta X$  in the unshifted field (Fig. 4b) now has a displacement  $\Delta X_\tau$  in the shifted field (Fig. 4c), given as

$$\Delta X_\tau = \Delta X + X_s \quad (4)$$

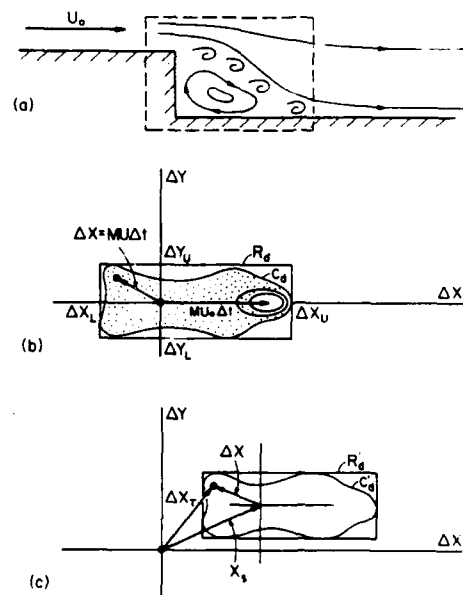


Fig. 4: Use of image shifting in PLV. (a) Flow field having recirculation (b) Displacement domain of recirculating flow (c) Displacement domain after shifting all second images by  $X_s$

At every point on the PLV photograph, the measured displacement  $\Delta X_t$  has components which are positive, and is thus free of directional ambiguity. The fluid velocity  $u$  may then be solved using equations (4) and (1).

For the PLV system described in this paper, image shifting is performed using a rotating mirror placed in front of the photographing lens (Fig. 5). The flow field is photographed while the mirror rotates at a constant angular velocity  $\omega_m$ , and the resulting image shift  $X_s$  is given as

$$|X_s| = 2M\Delta t(s_o - s_m)\omega_m \quad (5)$$

where  $s_o$  is the object distance from the camera lens to the flow plane, and  $s_m$  is the distance from the lens to the mirror.

In effect, image shifting in PLV is analogous to frequency shifting in laser Doppler velocimetry. As with frequency shifting, the method requires some prior knowledge of the velocity domain of the flow field, in particular, the upper and lower bounds of each velocity component.

### 3. INTERROGATION METHODS

#### 3.1 Interrogation by 1-D Spatial Correlation

Originally, the interrogation system developed by Yao and Adrian (1984) employed an algorithm of 1-D spatial correlation, with orthogonal image compression, to extract velocity data from PLV photographs of flow fields having  $N_T > 1$ . The algorithm employed a constant interrogation region size  $d_{int} = 1$  mm. The correlation distributions yielded by the algorithm were found to include random peaks of appreciable magnitude in addition to peaks produced by particle image pairs, often resulting in incorrect measurements. A numerical simulation of the 1-D correlation analysis (Adrian, 1985) similarly produced correlation distributions with random peaks which often exceeded the true correlation peaks. The investigation indicated that for a given interrogation, small noise peaks which occur in the 2-D correlation plane due to random image pairings are effectively integrated by 1-D compression, and are superposed to form large random composite peaks.

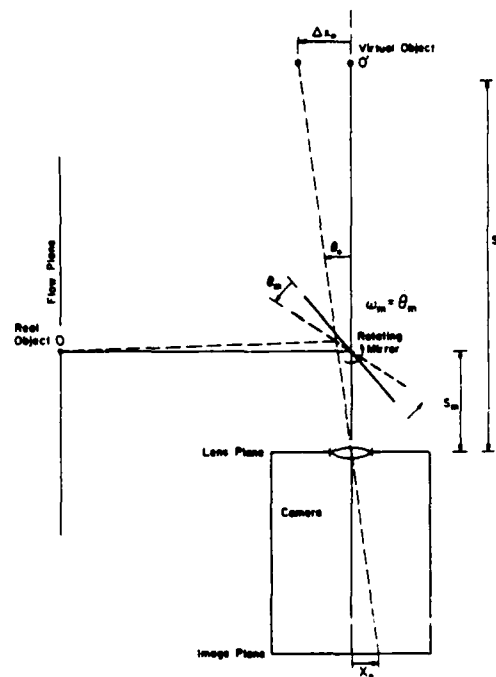


Fig. 5: Rotating mirror apparatus to implement image shifting

The 1-D correlation method is thus expected to produce a significant number of erroneous measurements. Several modifications to this method are anticipated to increase significantly its reliability, and are currently being investigated. However, present development of the interrogation system has instead focused on techniques intended for PLV photographs of low image density, in which particle image pair separations are measured directly.

#### 3.2 Direct-Measurement Interrogations

A computer-based algorithm has been developed to measure image pair displacements by successively interrogating square interrogation regions of size  $d_{int} = 1$  mm. For a given particle image pair, the algorithm measures the separation of the two images by isolating two 'windows' within the interrogation region, and locating a single image within each window. It is intended for PLV photographs having image-shifted fields, in which the second particle image of every image pair is displaced positively (that is, 'above' and 'to the right') with respect to the first image.

Figure 6 illustrates a typical interrogation using the 'two-window' algorithm. The computer begins the interrogation by positioning a 1 mm x 1 mm region on the PLV photograph within the interrogation laser beam (Fig. 6a). The image from the illuminated region is orthogonally compressed onto the two linear detector arrays. The array scans are digitized and stored into the computer memory as two 1024-element vector arrays. From the two vector arrays the computer isolates a small, fixed rectangular window  $W_I$  in the lower left corner of the interrogation region (Fig. 6b).

If the photographic field has been image-shifted with  $X_s$  having positive X and Y components, and if the window  $W_I$  encloses a first image of a particle image pair, then the second image of the pair should be contained within the interrogation region, above and to the right of  $W_I$ , within the image-shifted displacement domain  $R_d'$ . The domain  $R_d'$  thus defines a second computational window  $W_{II}$  enclosing the second image for a given first image within  $W_I$ .

The computer searches the 'first image window'  $W_I$  for a single particle image. If the number of images located in the search is unequal to one, the computer aborts the interrogation. If a single image is located, the computer isolates a 'second image window'  $W_{II}$  within the interrogation region (Fig. 6c), based on the presumed position and geometry of  $R_d'$  with respect to the first image in  $W_I$ . The computer then searches  $W_{II}$  for a second isolated particle image.

If the particle image in  $W_I$  is not a first image of a pair but is instead a second or an unpaired image, and if  $N_I$  is sufficiently low, then  $W_{II}$  is generally empty of any particle images, and as a result the interrogation is aborted without a measurement. If the image within  $W_I$  is a first image, as in Fig. 6, the second image generally appears isolated within  $W_{II}$ . As a result, the computer recognizes the two peaks in each array as components in a single image pair, and measures the separation  $\Delta X_r$  between the two images (Fig. 6d). From  $\Delta X_r$  the computer calculates the velocity vector as by

equations (4) and (1). Finally, the computer records the velocity measurement, and records the location in the flow field of the velocity vector.

Following the interrogation, the computer shifts the photograph, as in Fig. 6a, by a distance equal to the size of  $W_I$ . Between interrogations, the photograph is shifted such that  $W_I$  successively encloses adjacent, non-overlapping regions which incrementally cover the entire photograph. As a result, the first image of every particle image pair on the photograph is at one time contained within  $W_I$  during a single interrogation. Therefore, a large fraction of all image pairs should produce successful measurements.

At low values of image density  $N_I$ , particle image pairs are generally separated by large regions of void, and thus a two-window interrogation procedure generally encounters image pairs one at a time. However, because the distribution of the image pairs is random, more than one image pair may appear within a given interrogation

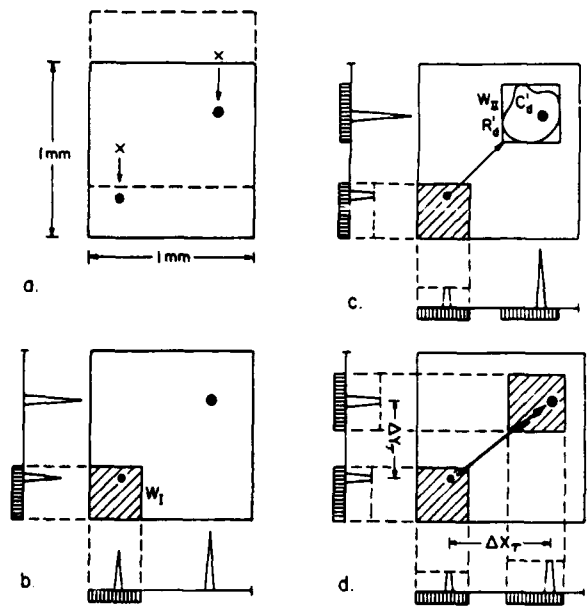


Fig. 6: Typical 2-window interrogation. (a) Position new interrogation region (b) Locate 1<sup>st</sup> image within  $W_I$  (c) Define  $W_{II}$ , locate 2<sup>nd</sup> image within  $W_{II}$  (d) Measure displacement  $\Delta X_r$

region. As a result, confusion may occasionally arise in determining particle image displacement. In particular, if an image pair enclosed within  $W_I$  and  $W_{II}$  is accompanied by additional spurious images in either window, measurement failure occurs since the correct pairing of images cannot be determined. Further, if an unpaired image in  $W_I$  is accompanied by an image from a differing image pair in  $W_{II}$ , the interrogation produces an erroneous measurement. Evaluation of a PLV photograph is thus expected to produce a certain fraction of incorrect velocity measurements.

Choosing the size of the first image window involves addressing constraints governing the interrogation procedure. Increasing the size of  $W_I$  decreases the number of interrogations required to cover a photograph and leads to a faster interrogation speed; however, it also increases the likelihood of failed measurements due to spurious particle images occurring within  $W_I$ .

Failed or erroneous measurements may frequently occur due to 1-D compression of the 2-D interrogation region. In Fig. 7a, for example, the image pair  $\tau_1 - \tau_2$  fails to produce a measurement, since the spurious image  $\tau_a$  is horizontally compressed onto  $W_I$  and vertically compressed onto  $W_{II}$ . Spurious image compression may be minimized by the use of masking, in which a physical mask is placed in front of the image of the interrogation region, before the image is compressed. Masking the interrogation region of Fig. 7a, for example, eliminates the compression of  $\tau_a$  in both directions (Fig. 7b), resulting in a successful measurement of  $\tau_1 - \tau_2$ .

#### 4. EXPERIMENTAL APPARATUS AND PROCEDURE

##### 4.1 Recording System

The illumination source used for all experiments was a double-pulsed ruby laser from Apollo Lasers, Inc. The laser employs an 8" x 0.625" ruby rod and Pockels cell Q-switching, capable of delivering extremely short pulses of 25 ns duration. The pulse separations are time-adjustable over seven orders of magnitude between  $\Delta t \sim 1 \mu s$  and  $\Delta t \sim 10 s$ , suitable for illuminating

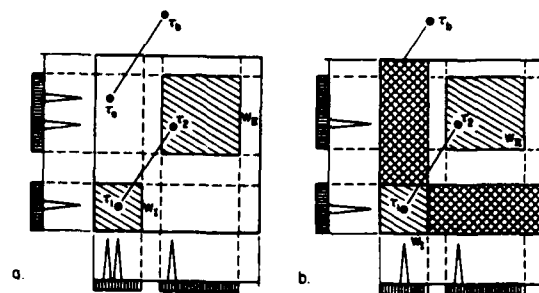


Fig. 7: Use of masking with 2-window interrogations.  
 (a) Without mask: failed measurement  
 (b) With mask: successful measurement

flows having maximum velocities ranging from 0.05 mm/s up to 500 m/s. The maximum energy output of the laser is 2.5 J per pulse, or 5.0 J total.

The illuminated flow fields were recorded using a 4" x 5" view camera fitted with a Nikkor 120 mm f5.6 process lens, and all photographs were recorded on 4" x 5" sheets of Kodak Technical Pan 2415 film. The Nikkor lens uses a symmetrical design for reproducing flat fields, at a magnification of order one, with extremely low optical distortion, typically 0.1% or less. Technical Pan film was chosen because of its high contrast and resolution (320 lines/mm), and comparatively high speed, which exceeds that of most holographic films by two orders of magnitude or more.

To provide image shifting during the recording procedure, a rotating mirror assembly was mounted on the camera directly in front of the photographing lens. The assembly consists of a 60 mm x 40 mm flat rectangular mirror mounted on the rotor of a galvanometer scanner made by General Scanning, Inc. The mirror oscillates at an angular velocity adjustable between 0 and 25 rad/sec, suitable for image-shifting fields with reversed velocities of up to 10 m/sec.

For evaluating system performance, PLV measurements were made of fluid in solid-body rotation. In these experiments, water was placed in a cylindrical dish of 190 mm diameter and 100 mm height, and was particle-seeded with 15.7  $\mu m$  polystyrene spheres manufactured by Dow, Inc. The dish and water were rotated on a phonographic turntable at a constant angular velocity  $\omega = 3.491$  rad/sec (33 1/3 RPM). The pulsed beam, having an

energy output of 2.2 J per pulse and a separation  $\Delta t = 3.500$  ms, was optically shaped into a sheet of width  $\Delta y_0 \sim 100$  mm and thickness  $\Delta z_0 \sim 1$  mm, and transmitted horizontally through the dish. The illuminated flow field was photographed from above using a magnification of 0.94 and a lens setting of f8.

All negatives were processed with Kodak D-19 developer, using a developing time of 12 minutes. A two-step processing method discussed by Pickering and Halliwell (1985) was employed for minimizing film noise, in which a contact-print positive was reproduced from every negative, again using Kodak 2415 film and D-19 developer. All interrogations were performed using the contact print photographs.

#### 4.2 Interrogation System

The interrogation stage of the PLV system is an automated computer-controlled instrument, consisting of two hardware packages working in tandem during the interrogation process. An interrogation table illuminates and images PLV photograph information, and a computer processes the information to compute velocity, and positions the PLV photograph.

A diagram of the interrogation table (Fig. 8) details the arrangement of its components. The PLV photograph is held within an X-Y translation stage manufactured by Daedal, Inc., which is positioned by two stepper motors, one for each direction of translation. The photograph is illuminated by a spatially-filtered, parallel 8 mW He-Ne laser beam having a diameter of 2mm. Light scattered off the interrogation region is transmitted through a high-pass spatial filter, which is arranged to eliminate the background 'pedestal' from the region. The projected image beam is magnified, and divided into two identical beams using a pellicle beamsplitter.

The two image beams are orthogonally compressed into 1-D images using two mutually perpendicular cylindrical lenses. For masking the 2-D image before compression, a paper mask is placed in front of each of the two lenses. The

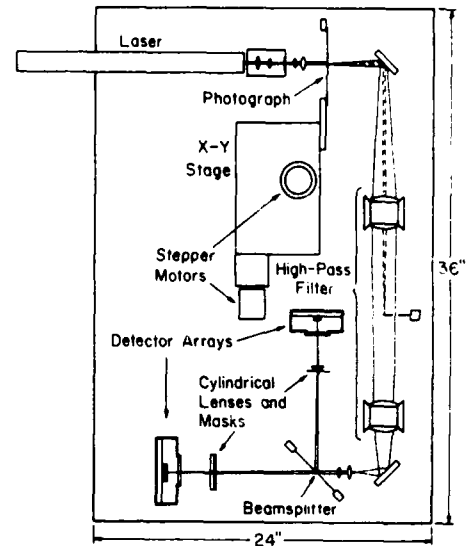


Fig. 8: Top view of the interrogation table

1-D images are projected onto two 1024-element linear detector arrays from EG&G Reticon, Inc., which convert the light intensity of the image into a time-varying analog signal.

All processing and control of the interrogation procedure is performed by a PDP 11/23 minicomputer having an attached SKYMNK array processor. For vector operations used during interrogation, the SKYMNK increases the speed of the PDP computer by more than two orders of magnitude. The detector array signals are digitized with a DT 2782 A/D converter from Data Translation, Inc., and control is provided to the X-Y stage via a dedicated stepper-motor driver board in concert with the parallel output of the PDP console.

The two-window interrogation algorithm is carried out using a single FORTRAN program. Under this program, the computer opens and names a file to store all measurement data, and performs successive two-window interrogations using the SKYMNK to analyze the vector arrays for each interrogation. In operation, the computer performs a single interrogation in 0.125 seconds, and is capable of interrogating an entire 100 mm x 120 mm PLV photograph in less than 3 1/2 hours.

## 5. SYSTEM PERFORMANCE

The quality of PLV measurements was evaluated using solid-body rotation flow, whose velocity  $u_0$  is a known function of the fluid location in 2-D space. If the angular velocity  $\omega$  is assumed positive clockwise, then

$$u_0(x,y) = \omega y \quad (6a)$$

$$v_0(x,y) = -\omega x. \quad (6b)$$

### 5.1 Data Yield and Reliability

Using PLV measurements of turntable flow, an investigation was conducted to determine the system's data yield and reliability as functions of image density and interrogation window geometry. An ensemble of fourteen photographs was recorded in which the particle concentration was varied between photographs to produce image densities ranging between 0.2 and 1.5. Image shifting was not used in this ensemble. Each photograph was interrogated four times, each time using a different interrogation window geometry. The four geometries were:  $W_I$  of dimensions  $1/4 \text{ mm} \times 1/4 \text{ mm}$ , with and without masking, and  $W_I$  of dimensions  $1/3 \text{ mm} \times 1/3 \text{ mm}$ , with and without masking. On every photograph, a single square region of dimensions  $27 \text{ mm} \times 27 \text{ mm}$ , located above and to the left of the apparent center of rotation, was isolated on the photograph. The bounded region was chosen to provide a known displacement domain  $C_d$ , located above and to the right of the origin in the  $\Delta X$ - $\Delta Y$  plane, which could be analyzed by all four interrogation geometries, without image shifting.

Before the interrogation analysis, the number of particle image pairs on each photograph was counted, both manually and computationally, to determine the image pair density  $N_I$  for that photograph. During the interrogation procedure for each photograph, each measured velocity vector  $u$  was compared with the vector  $u_0$  predicted from equation 6. A given measurement was recorded by the computer as 'erroneous' if  $u$  and  $u_0$  differed significantly and 'successful' if they did not. For each photograph, the data yield was calculated as

$$\text{data yield} = \frac{\text{number of successful measurements}}{\text{area of photograph}} \quad (7)$$

Figure 9 shows vector maps generated from a single PLV photograph, using each of the four interrogation window geometries. In Figures 9a and 9c, where masking was employed during interrogation, the yield of data is clearly higher than that of Figures 9b and 9d, where masking was not used. The yield is also higher using the smaller of the two first image windows,  $W_I = (1/4 \text{ mm})^2$  (Figures 9a and 9b). Furthermore, the measurements produced by the masked interrogations are seen to contain a lower percentage of spurious data than those produced without masking, and thus the reliability of the masked measurements in Fig. 9 appears higher.

Measurements of data yield and reliability are graphed in Figures 10a and 10b. In Figure 10a, the masked interrogations are seen to produce data yields which increase with  $N_I$ , while unmasked interrogations produce yields which level off and decrease with increasing  $N_I$ . Masking is thus

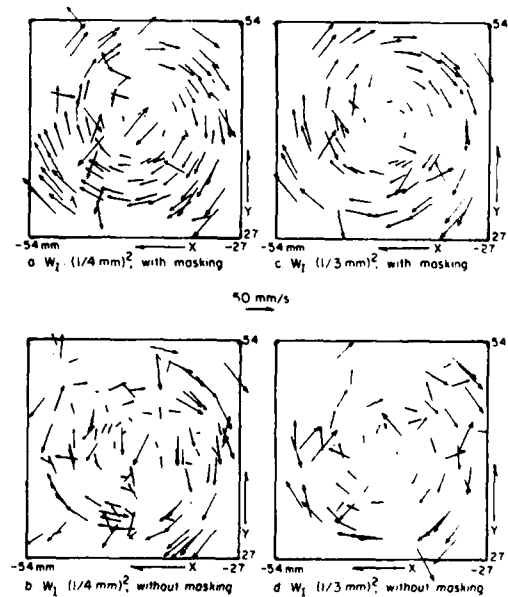


Fig. 9: Four vector maps produced from a single photograph of solid-body rotation, shown after subtracting the mean velocity at the center of each map from all vectors. X and Y are measured from the apparent center of rotation on the PLV photograph.

shown to increase data yield substantially. The reliability of the PLV measurements may be determined from the fraction of all measurements which are erroneous (Fig. 10b). The masked configurations produces a consistently lower fraction of bad data than their unmasked counterparts for all sampled values of image density, and thus are concluded to provide measurements of higher reliability.

Figures 10a and 10b indicate two trends in the data yield and reliability, for masked interrogations, as a function of  $N_I$ . First, at very low image densities ( $N_I < 0.3$ ), the reliability is excellent, with fewer than 10% of all measurements producing bad data. However, the data yield is correspondingly low. Second, at high image densities ( $N_I > 1.5$ ), data yield is relatively high, but measurements are significantly unreliable. However, if the data yield is high

enough to reveal flow structure with detail, then PLV maps in the high-yield regime may be filtered to remove many of the bad measurements.

## 5.2 Accuracy

For the investigation of system accuracy, an error value was determined for each successful measurement as a percentage of the maximum (full-scale) velocity recorded on the photograph. A distribution of accumulated error values was then compiled to determine the overall accuracy of PLV measurements. For this investigation, five photographs were recorded without image shifting and were interrogated in a region above and to the left of the apparent center of fluid rotation; and five photographs were recorded with substantial image shifting and were interrogated in a region enclosing the apparent center of rotation. The full-scale velocity of the interrogated shifted region was 1/4 that of the shifted region. All photographs were interrogated using a  $(1/3 \text{ mm})^2$  first-image window, with masking.

For each group of measurements from a PLV photograph, error values were found to be distributed around a non-zero mean error value. This 'sample mean error' is presumed due to the uncertainty in precisely locating measurements with respect to the photograph's apparent center of rotation. When the sample mean error was subtracted from the error distribution for each photograph, and the errors for all photographs compiled into a histogram (Fig. 11), the statistical accuracy for the PLV system could be determined. Figures 11a and 11b show the distribution for all unshifted measurements, and all full-scale image-shifted measurements, respectively.

From the error values of unshifted measurements, the RMS full-scale error is calculated to be 0.7% and 0.4% for the two orthogonal directions of interrogation. From the error values of full-scale shifted measurements, the RMS error is calculated as 2.4% and 2.2% in the two directions. The errors of the shifted measurements are approximately four times larger than the corresponding unshifted values, corresponding to

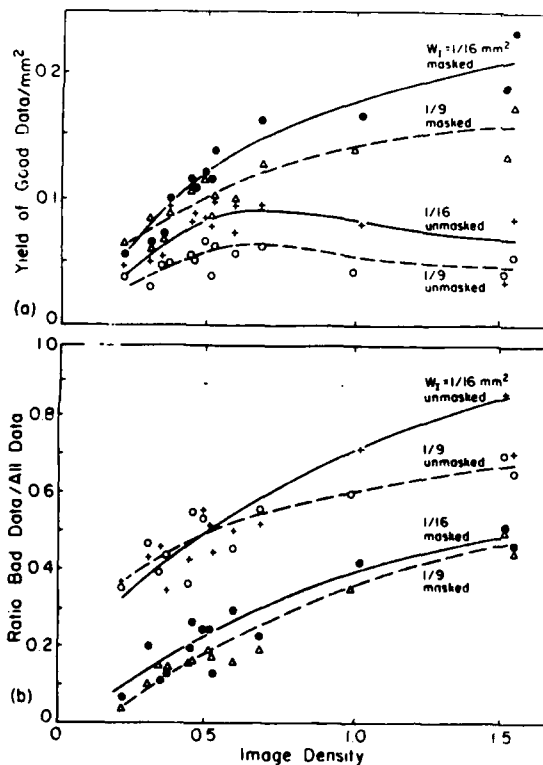


Fig. 10: Data yield and reliability as functions of image density and interrogation window geometry. (a) yield of good data vs.  $N_I$  (b) ratio of bad data to all data vs.  $N_I$

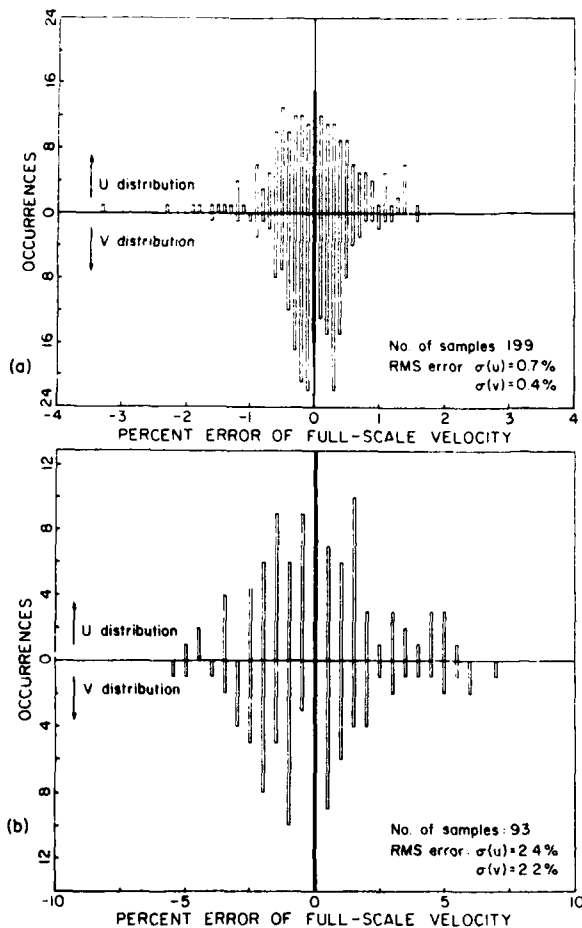


Fig. 11: Histogram of statistical error distribution.  
 (a) All unshifted fields  
 (b) All shifted fields

the fourfold decrease in the full-scale velocity in the shifted region. Thus, the absolute RMS error is apparently unaffected by image shifting.

#### 6. JET FLOW VECTOR MAPS

The PLV system was demonstrated in the investigation of a turbulent, axisymmetric water jet. Photographs were recorded of the flow within a 10-gallon glass tank, in which water was circulated through a vertical tube mounted above the tank. The water exited downward through a 36 mm diameter nozzle into the fluid in the tank, as a round jet having a potential velocity  $U_j = 89$  mm/sec, and a Reynolds number of 3500.

A large region of a jet flow PLV photograph was analyzed and the measured vectors were plotted

in 2-D maps. A map of the jet flow from a stationary frame of reference is shown in Figure 12a, after a visual filtering operation was used to locate and remove erroneous vectors. The filtered field, consisting of 911 vectors, clearly shows the core region of the jet, surrounded by smaller-scale undulations within a diverging shear layer. The internal structure of the jet is revealed in Fig. 12b, a map of the same photograph in which a streamwise component equal to  $0.92 U_j$  has been subtracted from every vector. Four distinct regions of vorticity are visible in the mixing layer, two on each side of the core, and the potential core is clearly seen to decay downstream of the exit. Scales of motion as small as a few millimeters are readily visible in Fig. 12c, an enlargement of one of the vortices within the mixing layer.

#### 7. CONCLUSIONS

A pulsed laser velocimetry system has been constructed for evaluating fluid flow properties of experimental interest. By using the spatial image shifting technique, which offsets all negative displacements of particle image pairs on a PLV photograph, the system can resolve directional ambiguity in reversing flow fields. The use of the 'two-window' interrogation method, in which image pairs are directly measured from photographs having low image density, capitalizes on the offset displacements produced by image shifting. By masking the interrogation windows, the data yield and reliability of interrogations are improved substantially.

In performance, the full-scale accuracy of system measurements are as low as a fraction of a percent, comparable to those of state-of-the-art single point measurement systems. In measuring extended regions of complex flows, the system generates vector maps of high data yield which reveal instantaneous flow structure, with considerable detail, down to a length scale of a few millimeters. These measurements are quantitative, unlike the qualitative measurements of conventional flow visualization methods, and

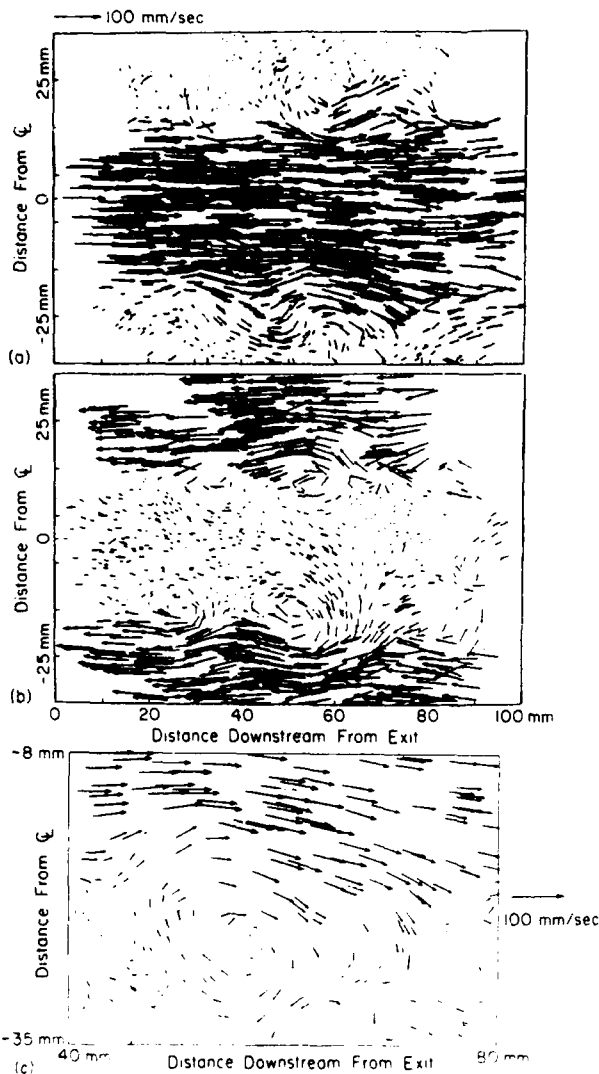


Fig. 12: PLV vector maps of axisymmetric jet flow.  
 (a) Stationary reference frame  
 (b) Reference frame moving at  $0.92 U_j$   
 (c) Enlargement of single vortex in the flow, reference frame moving at  $0.20 U_j$

can thus be used to determine spatially-varying statistical and derivative flow properties.

#### ACKNOWLEDGEMENT

This material is based on work supported by the National Science Foundation under Grant No. ATM 86-00509.

#### REFERENCES

- Adrian, R. J., 1985: Multi-Point Vector Measurement by Pulsed Laser Velocimetry with Image Compression. Proc. Int'l. Sym. on Fluid Control and Measurement, Tokyo, 1985. Pergamon Press, 1087-1093.
- Adrian, R. J., 1986: Statistical Properties of Particle Image Velocimetry Measurements in Turbulent Flow. Proc. Third Int'l. Sym. Applications of Laser Anemometry to Fluid Mechanics, Lisbon, Port. 1986.
- Adrian, R. J., 1986: An Image Shifting Technique to Resolve Directional Ambiguity in Double-Pulsed Laser Velocimetry. Manuscript awaiting publication.
- Adrian, R. J., and Yao, C. S., 1983: Development of Pulsed Laser Velocimetry for Measurement of Fluid Flow. Proc. Eighth Sym. on Turbulence, University of Missouri, Rolla, 170-186.
- Arnold, W., Hinsch, K., and Platen, W., 1986: Analysis of Non-stationary Flows by Evaluating the Fringe Visibility in Speckle Velocimetry. Proc. Third Int'l. Sym. Applications of Laser Anemometry to Fluid Mechanics, Lisbon, Port. 1986.
- Burch, J. M., and Tokarski, J.M.J., 1968: Production of Multiple Beam Fringes from Photographic Scatterers. Optica Acta, 15, 101-111.
- Hinsch, K., Schipper, W., and Mach, D., 1984: Fringe Visibility in Speckle Velocimetry and the Analysis of Random Flow Components. Appl. Optics, 23, 4460-4461.
- Ineichen, B., Eglin, P., and Dandliker, R., 1980: Hybrid Optical and Electronic Image Processing for Strain Measurements by Speckle Photography. Appl. Optics, 19, 2192-2195.
- Landreth, C., 1986: Two-Dimensional Measurements of Complex Flows Using Pulsed Laser Velocimetry with Directional Resolution. M. S. Thesis, University of Illinois, Urbana-Champaign
- Lourenco, L. M., and Krothapalli, A., 1986: Application of PIDV to the Study of the Temporal Evolution of the Flow Past a Circular Cylinder. Proc. Third Int'l. Sym. Applications of Laser Anemometry to Fluid Mechanics, Lisbon, Port. 1986.
- Maddux, G. E., Corwin, R. R., and Moorman, S. L., 1981: Proc. Spring Meeting of Soc. for Exp. Stress Analysis, 1981.
- Pickering, C.J.D., and Halliwell, N. A., 1985: Particle Image Velocimetry: Improving Fringe Signal-to-noise Ratio with a Two-step Photographic Process. J. Opt. Soc. Amer. A, 2, 610-615.
- Short, M., and Whiffen, M. C., 1986: The Relationship Between Seeding Density and Analysis Methodology in Particle Imaging Velocimetry. Proc. Third Int'l. Sym. Applications of Laser Anemometry to Fluid Mechanics, Lisbon, Port. 1986.
- Yao, C. S., and Adrian, R. J., 1984: Orthogonal Compression and 1-D Analysis Technique for Measurement of Particle Displacements in Pulsed Laser Velocimetry. Appl. Optics, 24, 44-52.

THE GENERATION OF TURBULENCE FROM  
DISPLACED CROSS-MEMBERS IN UNIFORM  
FLOW

N. Toy and T.A. Fox,  
Department of Civil Engineering,  
University of Surrey,  
Guildford, Surrey, U.K., GU2 5XH.

ABSTRACT

This paper presents details of an experimental investigation into the nature of turbulence generated in the wake of a single grid node. The latter has been considered as two members placed perpendicular to each other in the geometry of a cross, with square and circular sections representing bars and rods respectively. The effect of member spacing has been examined in an attempt to identify the complex flow phenomena associated with such a configuration, and in this respect a critical gap width has been found.

1. INTRODUCTION

The turbulence characteristics of a flow can be altered significantly by forcing the fluid to pass through a series of elements arranged in a grid configuration, Van der Hiege Zijnen (1957) and Rose (1970). In the wake of such an obstruction, a highly complex three-dimensional flow field is created which has practical importance in many engineering problems, for example:-

- (i) the generation of specific turbulence levels for use in wind tunnel studies;
- (ii) the efficiency of thermal cooling in a heat exchanger composed of heated tubes arranged as a series of grids;

- (iii) the loading of individual members in a lattice structure subjected to a wind environment.

Many of the principal investigations into the flow regimes associated with grid configurations have been reviewed by Laws and Livesey (1978). These concentrate on the effect of mesh geometry, size and solidity in the production of turbulence, with the mechanism of generation being generally represented as the coalescence of a number of jets emerging from each orifice in the grid, Baines and Peterson (1951). However, little information has been published with regard to the effect upon the turbulence field of the individual nodal points which make-up the whole grid.

The geometry of a grid node may be considered in its simplest form as two members perpendicular to each other in the shape of a cross. A number of investigations have been recently undertaken to examine the flow phenomena produced by this configuration when the members intersect in a single plane. Osaka et al (1983 a, b) and Zdravkovich (1985), have studied circular cylinders arranged in such a geometry, and Donoso et al (1983) examined the case of sharp-edged flat plates normal to the freestream. These authors found evidence of strong secondary flows in the wake which produce trailing vortices with centres located near the node. At spanwise positions beyond this disturbance quasi two-dimensional conditions were recorded.

Zdravkovich (1983) has also determined limited details of the interference to flow caused by two circular cylinders placed one behind the other to form a cross with members in contact at the centre. In this case, a similar regime was found with the addition of a pair of horseshoe vortices generated symmetrically about the point of contact. These remain attached over the surface of the downstream cylinder and converge in the wake.

Consideration has not, however, been given to the effect upon these flow regimes of the introduction of a gap at the node of the geometry. The experiments reported in this paper were therefore devised to investigate the flow around a cross composed of non-connecting members perpendicular to each other. The initial study being confined to the node of configurations composed of circular cylinders and square bars.

## 2. EXPERIMENTAL DETAILS

The tests were performed in a uniform airflow with a freestream turbulence intensity of 0.17%, at a Reynolds number based on model diameter of  $2 \times 10^4$ . The wind tunnel facility was of the low-speed, blow down open circuit type with working section dimensions of 1.067m x 1.372m x 9.0m, and has been described in Savory and Toy (1984).

Two 30mm square sectional aluminium bars formed one cross, with a pair of 30mm diameter circular cylinders forming the other. Both elements completely spanned the working section and could be displaced to produce a gap at the node. The co-ordinate system based on this geometry is illustrated in Figure 1, which also defines the separation distance, L. The blockage percentage associated with each member was calculated in accordance with E.S.D.U. 80024 (1980), and was found to be 2.2% and 1.8% for the horizontal and vertical elements respectively. It was therefore considered unnecessary to apply a

correction factor to the experimental data. End plates were not fitted to either member as they produce interference effects that would complicate the analysis of the flow conditions in the wake of the perpendicular geometry, Toy and Fox (1986).

Mean pressures on the surface of each model were measured from 0.5mm tapings connected to a Furness low pressure transducer via a Scanivalve switch mechanism. The latter was controlled by a microcomputer, which also performed data acquisition via a 10-bit A-D converter, and on-line analysis, Savory and Toy (1984). The freestream reference pressures were obtained from a pitot tube positioned in the uniform flow. The total head was connected to the Scanivalve, and the static to the transducer. This system produced values of  $C_p$  with a repeatable accuracy of 1.5%.

Velocity and turbulence intensity data was obtained with a pulsed-wire anemometer of the type described by Bradbury and Castro (1971), this being an appropriate instrument for use in highly turbulent flows. On-line data acquisition and analysis was again performed by the microcomputer. Values of the velocity components and turbulence intensities were calculated from the mean of 10,000 samples taken at each measurement position. Data collection over the near wake of the models was achieved by mounting the probe on a three-dimensional traversing system, which has a positional accuracy of  $\pm 0.02$ mm.

In order to calculate the distribution of x-direction vorticity,  $\omega_x$ , over related planes in the wake, it was necessary to obtain normalised mean velocity components;  $\bar{v}/U_0$ ,  $\bar{w}/U_0$  and  $\bar{u}/U_0$ . To achieve this, each two-dimensional traverse over the measurements plane was repeated five times with the probe at yaw angles of  $0^\circ$  and  $\pm 45^\circ$ , and the data was reduced by the method of Cheun (1981). From these results an approximate differentiation of the mean velocity profiles was

undertaken to give the x-direction vorticity;

$$\omega_x = \frac{\partial w}{\partial y} - \frac{\partial v}{\partial z}$$

Autocorrelation measurements were made on-line by the microcomputer with the pulsed-wire anemometer. The software calculated correlation coefficients for a specified range of lags. By extrapolation of the recorded data, using the method of Stone (1978), autocorrelations were obtained to a minimum coefficient of  $\pm 0.01$ . A cosine-law power spectral analysis was performed on this data to determine the energy distribution with regard to periodic frequency.

### 3. DISCUSSION

Measurements of the mean pressure distribution on the surface of each model were made for a range of member spacings varying from elements in contact ( $L=1D$ ), to a separation of ten diameters ( $L=10D$ ). Figure 2 shows the coefficient of stagnation pressure,  $C_{ps}$  and coefficient of base pressure,  $C_{pb}$  recorded at the centre of each span, together with the corresponding single element values. In the case of the upstream members, the stagnation pressure,  $C_{ps1}$  remained approximately constant over the range of spacings examined and implies a negligible interference to the flow conditions upstream of the model. However, the stagnation pressures recorded on the downstream element,  $C_{ps2}$ , exhibit a significant variation with member spacing. At separation distances in excess of five diameters,  $L>5D$ , the value of  $C_{ps2}$  is almost constant at  $C_{ps2}=0.5$ , indicating that the flow conditions in the gap are stable for larger spacings. Whereas at low gap widths, when  $L<5D$ , the stagnation pressure shows a considerable dependence upon member spacing, and this is associated with a change in the nature of the flow conditions within the gap. The "local" minimum value of  $C_{ps2}$  recorded at a spacing of three diameters,  $L=3D$ , marking the division between two different flow regimes.

The nature of these two flow regimes can be assessed by examination of the power spectra determined from the autocorrelation measurements made within the gap. Figure 3 shows the results obtained with the square bars. At a member spacing of ten diameters,  $L=10D$ , the peak energy measured at the dominant frequency is 25% greater than that found in the wake of a single bar, also shown, and the corresponding Strouhal Number is slightly reduced. This suggests that at large spacings the central portion of the upstream member sheds vortices in a periodic manner similar to that associated with a single bar at the same Reynolds Number. Further evidence for this may be deduced from the base pressure,  $C_{pb1}$  recorded at  $L=10D$ , Figure 2, which is equivalent to the single bar value. As the bars are brought closer together, the dominant frequency associated with vortex shedding steadily decreases, as shown by the reduction in Strouhal Number, and the peak energy levels rise to a maximum at five diameters before decreasing rapidly. At the critical spacing of three diameters,  $L=3D$ , the peak energy level is reduced to a minimum of 11% of the single bar value and this marks a distinct division in the characteristics of the energy distributions. For spacing less than three diameters,  $L<3D$ , the Strouhal Number in the gap continues to decrease and the energy levels recover slightly, but the distributions show a greater spread of energy over a larger range of frequencies than those found for  $L>3D$ . These are indicative of a disturbance to the periodic vortex shedding from the central region of the upstream bar. This is also indicated by the values of  $C_{pb1}$  in this range, Figure 2, which rise rapidly with decreasing gap width and become positive at  $L=1.5D$ .

A similar result was found in the wake of the upstream circular cylinder, Figure 4. In this case, the peak energy levels recorded at the predominant frequencies were below the single cylinder values at all member spacings. For example, at ten diameters,  $L=10D$ , the energy was reduced by 50%, and the corresponding Strouhal

Number was slightly less than that found in the wake of the single cylinder. However, despite this reduction, the base pressure measured on the upstream cylinder when  $L=10D$ , Figure 2, is equivalent to that found on the single cylinder shedding quasi two-dimensional vortices. This regime continues to be present in the gap as the spacing is decreased, with the Strouhal Number and the peak energy also decreasing. At a spacing of  $L=2.75D$ , the critical gap width is reached and the regime changes to one characterised by a greater distribution of energy over a larger range of frequencies. This indicates a similar disturbance to vortex shedding from the central portion of the upstream cylinder as was found with the square bars, and this is further confirmed by the rise of  $C_{pb_1}$  at  $L<3D$ , Figure 2.

These distinct changes to the flow regime in the gap affect the flow conditions around the downstream member, and consequently those in the wake of the perpendicular geometry. For spacings larger than the critical,  $L>3D$ , when vortices are shed periodically from the centre of the upstream member, the nature of the disturbance appears to be independent of gap width over the range examined. This is evident in the base pressures recorded at the centre of the downstream span,  $C_{pb_2}$  in Figure 2, which remain approximately constant over the larger spacings at a value considerably higher than that of a single element. This reduction in suction may be the result of turbulence produced by the vortices from the upstream member. The presence of turbulence in an approach flow having been found to cause a downstream movement of the vortex formation region in the wake of single elements, with a consequent rise in base pressure, Surry (1972) and Lee (1975).

When the flow regime within the gap changes, at member spacings below three diameters,  $L<3D$ , the conditions in the wake of the node become significantly more disturbed. In this respect, the values of  $C_{pb_2}$  exhibit a considerable variation with gap width, and both section types

display a maximum in suction in the region  $L=2D$ . To examine in detail the effects of this disturbance on the near wake of the geometry, vorticity and turbulence intensity distributions have been recorded immediately downstream of the node. Measurements of these quantities were made over the  $y-z$  plane shown in Figure 1 with the members in contact,  $L=1D$ , and at subsequent spacings of  $L=2D$  and  $L=3D$ .

The vorticity distributions recorded at one diameter downstream,  $x/D=1.0$ , with the members in contact ( $L=1D$ ) are shown in Figures 5(a) and (b) for the square and circular sections respectively. The general flow pattern is composed of a dominant area of negative-wise vorticity, and a smaller region of positive-wise vorticity. In the case of the circular cylinders, these features appear to corroborate the existence of the surface flow regimes proposed by Zdravkovich (1983) for a similar model. The negative circulations at the centre of the wake corresponding to the location of a horseshoe vortex generated on the downstream cylinder adjacent to the point of contact, whilst the positive circulation is produced by secondary flow along the rear of the upstream member. The distribution in the wake of the square bars is slightly different with the negative-wise vortex exhibiting greater vorticity and considerably more consolidation. There appears to be no spanwise secondary flow along the rear of the downstream square bar, although the positive-wise trailing vortex does suggest that such a flow is present in the wake of the upstream member.

To determine the effects of these secondary circulations upon the turbulence levels in the near wake,  $u$ -component intensities have been collected over the same  $y-z$  planes as the vorticity. The recorded distributions are shown as Figures 6(a) and (b) for the square and circular sections respectively. The general contour pattern is influenced to a large degree by the geometry of the cross, particularly in the case of the circular cylinders, where the main contours are parallel to each element except in

the centre of the wake. In this respect, the distribution is similar to that found in the far wake of intersecting cylinders investigated by Osaka et al (1983b). The lateral position of the peak intensity is clearly seen in both Figure 6(a) and 6(b), and each of these values has been recorded in Table 1. From this it can be deduced that the maximum turbulence intensity in the wake of each node is below that associated with corresponding downstream locations in the wakes of the single two-dimensional models.

The vorticity distribution diagrams for the same y-z plane at x/D=1.0 when a gap of one diameter is introduced, L=2D, are shown for both model geometries as Figures 5(c) and 5(d). Both distributions show that although the influence on the flow pattern of the positive-wise trailing vortex is reduced, the regime is again dominated by the presence of an area of negative-wise vorticity. However, the precise effect of the introduction of a gap between the members upon the structure of this secondary flow appears to be dependent upon section geometry. For the square model, Figure 5(c), the value of the maximum vorticity at the vortex centre seems to have decreased, and moved laterally away from the node in the z-direction, relative to that recorded when the bars are in contact. The vortex has also spread more fully in the immediate wake, converging on the z-axis within the plane to produce a spanwise secondary flow along the rear of the downstream bar. In the wake of the circular geometry, Figure 5(d), the opposite is evident in that the maximum intensity of the vortex has increased, and its centre has moved towards the node. In addition, the vortex seems to have consolidated, the several centres evident in Figure 5(b) having been replaced by a single centre of much greater intensity.

These changes in the fluid motion are reflected in the turbulence levels recorded in the y-z planes shown in Figures 6(c) and (d). As with the members in contact case, the distribution is influenced by the cross geometry and the contours

are generally parallel to the cylinder axis except in the centre of the wake. For both section types the maximum intensity is located laterally away from the node and the corresponding values are recorded in Table 1. Reference to the latter reveals that the turbulence level in the plane has increased immediately behind the cross relative to the L=1D case, although the values are still below those found in the wakes of the single models.

Table 1 Maximum Turbulence Intensity Recorded at x/D=1 in the Near Wake

GAP WIDTH	SQUARE	CIRCULAR
L/D	$\frac{\sqrt{u'^2}}{U_0}$	$\frac{\sqrt{u'^2}}{U_0}$
1	0.15	0.12
2	0.20	0.16
3	0.21	0.24
Single	0.30	0.29

Increasing the gap width to two diameters, L=3D, leads to a further reduction in the vorticity found in the wake of both models. The distribution for the square section is shown in Figure 5(e), and reveals a re-alignment of the negative-wise vortex relative to the node. The value of the maximum contour is reduced in comparison with Figure 5(c), and the vortex is less intense. In addition, the positive-wise vortex generated by the upstream member is no longer evident. In the wake of the circular cylinders, Figure 5(f), the effects are similar, a significant decrease in negative-wise vorticity being found in comparison with Figure 5(d). Both distributions therefore indicate a decrease in the interference effects of the node with increasing gap width.

This decrease in the influence of the node on the fluid motion in the wake of the cross has a subsequent effect upon the distribution of the turbulence intensities. These are shown in Figures 6(e) and 6(f), and both reveal a wide

spread of turbulence with a reduction in the influence of the cross geometry. Instead, it is the downstream member that dominates the distribution, even at the centre of the wake, and the contour pattern in this region is becoming quasi two-dimensional. This is reflected in the maximum values recorded in Table 1, which are tending, with increasing gap width, towards those measured at the same locations in the wakes of the single two-dimensional models.

#### 4. CONCLUDING REMARKS

This paper has attempted to outline the effect of member spacing upon the flow regime and turbulence levels associated with a single grid node. It has shown that the distance between the members has a significant effect upon the flow conditions in the gap at the centre of the geometry, together with the vorticity in the wake of the configuration, and therefore the degree of turbulence generated by the node.

Two distinct flow patterns were found at the node and these were separated by a critical gap width. In the range of member spacings greater than three diameters,  $L > 3D$ , periodic vortex shedding occurs in the wake of the central portion of the upstream member. For spacings less than three diameters,  $L < 3D$ , the vortex shedding in the gap is disturbed and secondary circulations are established in the wake of the configuration. These produce a turbulence field with a distribution that is influenced by the cross geometry, and with maximum intensities below those associated with the wake of a single two-dimensional member.

#### ACKNOWLEDGEMENTS

This research has been supported by a Science and Engineering Research Council Studentship awarded to T. A. Fox.

#### NOTATION

$C_p$	pressure coefficient, $(p-p_0)/\frac{1}{2}\rho U_0^2$
$D$	diameter of model
$L$	distance between model centres
$n$	vortex shedding frequency
$p$	pressure on models surface
$P_0$	static pressure
$Re$	Reynolds number, $DU_0/\nu$
$St$	Strouhal number, $nD/U_0$
$U_0$	freestream reference velocity
$\bar{u}, \bar{v}, \bar{w}$	local mean velocity components in x, y, and z directions
$u'$	u-component velocity fluctuation
x, y, z	co-ordinate system of geometry
$\phi$	power spectra energy
$\nu$	kinematic viscosity of fluid
$\rho$	density of fluid
$\omega_x$	x-direction vorticity, $\frac{\partial w}{\partial y} - \frac{\partial v}{\partial z}$

#### REFERENCES

- Baines, W.D.; Peterson, E.G. 1951: An investigation of the flow through screens. *J. Fluid Eng., Trans. ASME* 73, 467-480.
- Bradbury, L.J.S.; Castro, I.P. 1971: A pulsed wire technique for velocity measurements in highly turbulent flows. *J. Fluid Mech.* 49, 657-691.
- Cheun, B.S. 1981: Separated shear layers behind two-dimensional square-edged bodies. Ph.D. Thesis, University of Surrey.
- Donoso, J.A.; Hillier, R.; Yeung, C.K. 1983: The effect of strong three-dimensional disturbance on vortex shedding. *J. Wind Eng. and Ind. Aero.* 11, 381-392.
- E.S.D.U. 1980: Blockage corrections for bluff bodies in confined flows. No. 80024, Engineering Sciences Data Unit.

Laws, E.M.; Livesey, J.L. 1978: Flow through screens. *Ann. Rev. Fluid Mech.* 10, 247-266.

Lee, B.E. 1975: The effect of turbulence on the surface pressure field of a square prism. *J. Fluid Mech.* 69, 263-282.

Osaka, H.; Nakamura, I.; Yamada, H.; Kuwata, Y.; Kageyama, Y. 1983a: The structure of a turbulent wake behind a cruciform circular cylinder 1st Report: the mean velocity field. *Bull. Japan Soc. Mech. Engrs.* 26, 356-363.

Osaka, H.; Yamada, H.; Nakamura, I.; Kuwata, Y.; Kageyama, Y. 1983b: The structure of a turbulent wake behind a cruciform circular cylinder 2nd Report: the streamwise development of turbulent flow fields. *Bull. Japan Soc. Mech. Engrs.* 26, 521-528.

Rose, W.G.. 1970: Interaction of grid turbulence with a uniform shear. *J. Fluid Mech.* 44, 767-779.

Savory, E.; Toy, N. 1984: Microcomputer control of wind tunnel instrumentation with on-line data acquisition and analysis. *Software and Microsystems.* 3, 93-97.

Stone, P. 1978: Use of the autocorrelation matrix in spectral analysis. Ph.D. Thesis, University of Surrey.

Surry, D. 1972: Some effects of intense turbulence on the aerodynamics of a circular cylinder at subcritical Reynolds number. *J. Fluid Mech.* 52, 543-563.

Toy, N.; Fox, T.A. 1986: The effect of aspect ratio of end plate separation upon base pressures recorded on a square bar. *Experiments in Fluids.* 4, 266-268.

Van der Hiege Zignen, B.G. 1957: Measurement of the intensity, integral scale and microscale of turbulence downstream of three grids in a stream of air. *Appl. Sci. Res.* 7A, 149-174.

Zdravkovich, M.M. 1983: Interference between two circular cylinders forming a cross. *J. Fluid Mech.* 128, 231-246.

Zdravkovich, M.M. 1985: Flow around two intersecting circular cylinders. *J. Fluid Eng., Trans. ASME.* 107, 507-511.

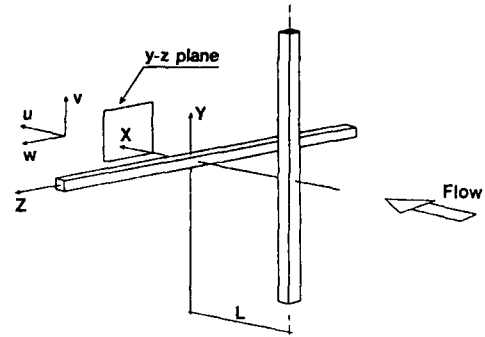


Figure 1: Cross geometry and co-ordinate system.

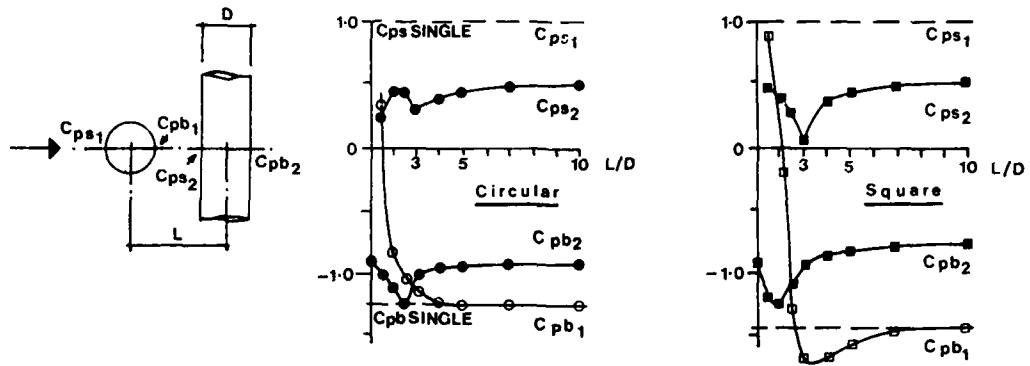


Figure 2: Relationship between the principal pressure coefficients at the centre of each span and member spacings in the range:  $1 \leq L/D \leq 10$ .

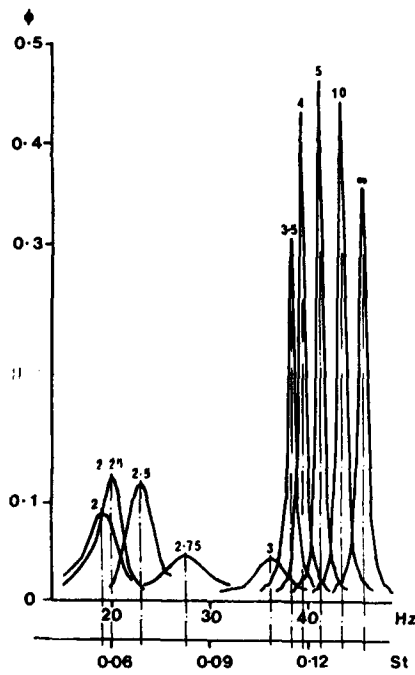


Figure 3: Power Spectra recorded in the gap between the square bars for member spacings in the range:  $2 \leq L/D \leq 10$ .

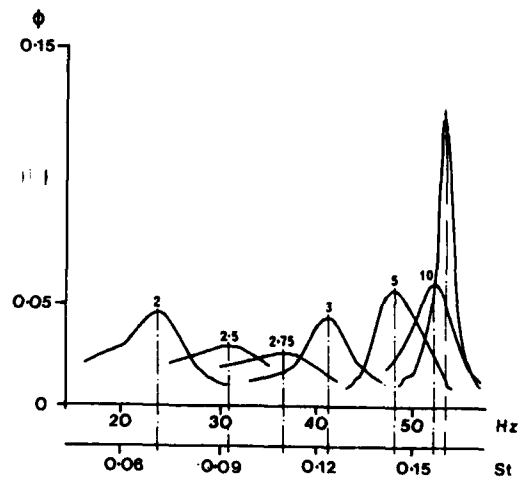
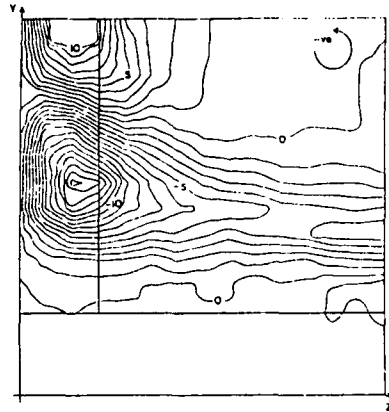
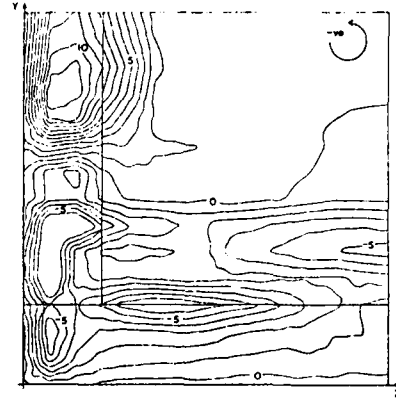


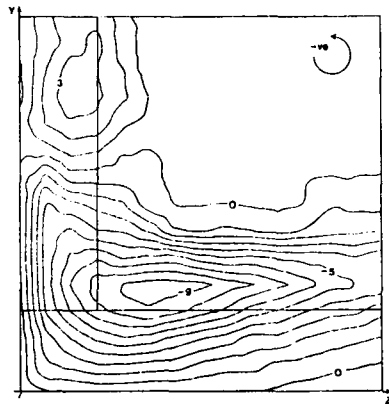
Figure 4: Power Spectra recorded in the gap between the circular cylinders for member spacings in the range:  $2 \leq L/D \leq 10$ .



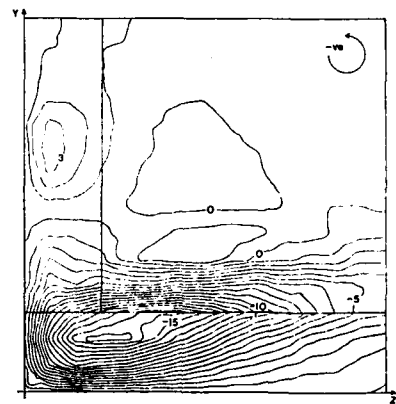
(a) Square bars,  $L = 10$



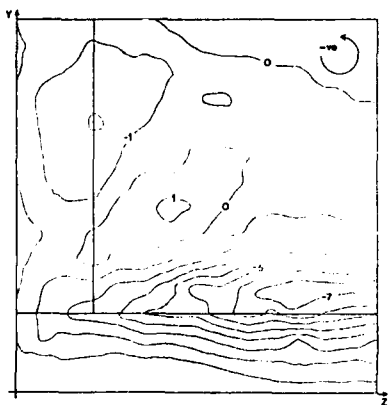
(b) Circular cylinders,  $L = 10$



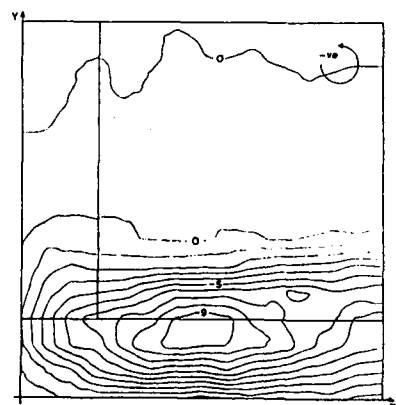
(c) Square bars,  $L = 20$



(d) Circular cylinders,  $L = 20$

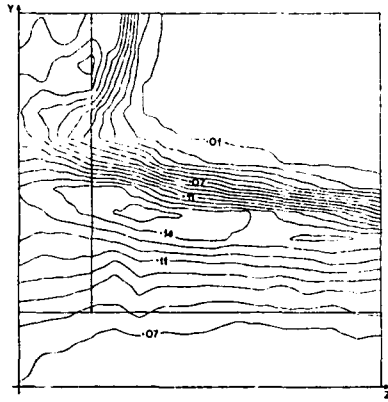


(e) Square bars,  $L = 30$

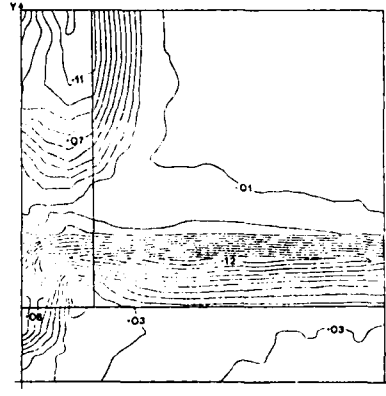


(f) Circular cylinders,  $L = 30$

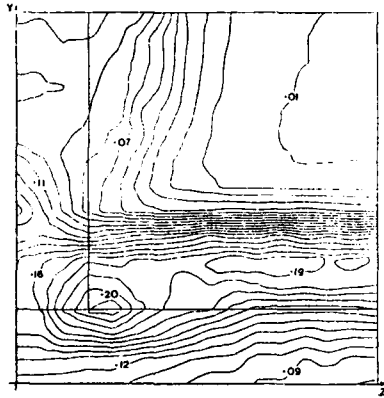
Figure 5: Vorticity distribution at  $X = 10$  in the near wake of the node of both crosses.  
Contours =  $10 D_{wx}/U_0$ .



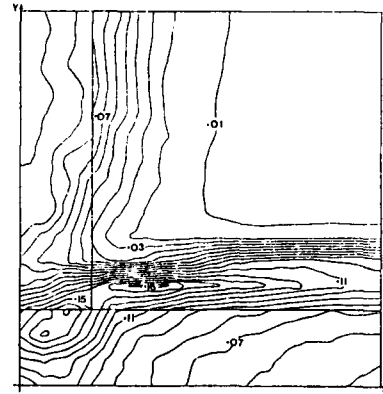
(a) Square bars,  $L = 1D$



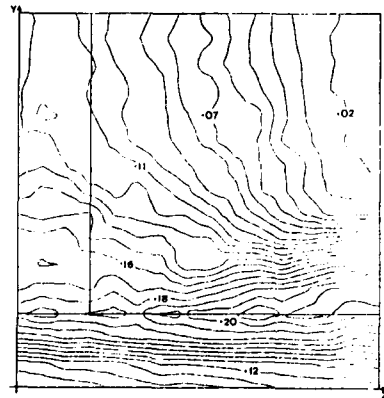
(b) Circular cylinders,  $L = 1D$



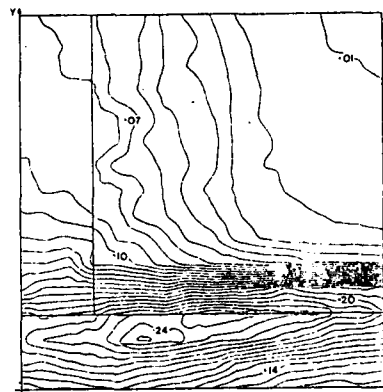
(c) Square bars,  $L = 2D$



(d) Circular cylinders,  $L = 2D$



(e) Square bars,  $L = 3D$



(f) Circular cylinders,  $L = 3D$

Figure 6: Turbulence intensities at  $X = 1D$  in the near wake of the node of both crosses.  
Contours =  $\sqrt{u'^2}/U_0$ .

A COMPARISON OF ANALOG AND DIGITAL  
SYSTEMS OF MEASUREMENTS OF  
TURBULENCE PARAMETERS

By R. S. AZAD\* and L. G. OZIMEK  
Department of Mechanical Engineering  
The University of Manitoba  
Winnipeg, Manitoba, Canada R3T 2N2

\* Professor of Fluid Dynamics

ABSTRACT

An experimental investigation of analog and digital data for measurement of various flow parameters has been undertaken with view to find whether the digital method is superior to the analog one. Towards this end, comparative measurements of skewness, flatness, and velocity spectra taken by different experimenters were examined for a turbulent boundary layer flow at a free stream velocity of 8 m/sec. In addition, comparative measurement of skewness, flatness, mixed moments and spectra were examined for flow in an 8° conical diffuser with fully developed pipe flow at the entry. The Reynolds number based on the pipe diameter and pipe bulk velocity to the inlet of the diffuser was 130,000. All measurements were made on a line normal to the surface.

Single wire measurements taken in the boundary layer flow show no significant difference between analog and digital measurements. Single wire and X-wire measurements taken in the diffuser flow show the digital results cross the zero value ahead of corresponding analog results in such measurements as skewness and certain fourth order mixed moments.

It can be concluded from this research that there is no difference between analog and digital values obtained for any physical quantity in turbulent flow provided adequate analog and digital systems are properly used.

NOMENCLATURE

$f_K = U/2\pi\eta$	Kolmogorov frequency
$K ( )$	flatness factor or Kurtosis
rms	root mean square
$S ( )$	skewness factor
$U$	mean axial velocity component
$u$	fluctuating axial velocity component
$u^1 = (\overline{u^2})^{1/2}$	rms of fluctuating axial velocity component
$u^*$	friction velocity
$v$	fluctuating transverse or radial velocity component
$v^1 = (\overline{v^2})^{1/2}$	rms of fluctuating transverse velocity component
$\overline{uv}$	Reynolds shear stress per unit mass
$y$	normal distance from a surface
$Y^+ = yu^*/\nu$	nondimensional distance from a surface
$\delta$	boundary layer thickness
$\epsilon$	mean turbulent energy dissipation rate
$\eta = (\nu^3/\epsilon)^{1/4}$	Kolmogorov length scale
$\mu$	dynamic viscosity of a fluid
$\nu = \mu/\rho$	kinematic viscosity of a fluid
$\rho$	fluid density

1. INTRODUCTION

Originally, most statistical measurements in turbulent flows were obtained with analog devices. Special circuits were constructed to add, subtract, multiply, integrate, differentiate, time delay and filter the fluctuating electrical signals. The development of analog-to-digital

converters over the past twenty years has made digital computing of turbulent signals practical. Bearman (1968) outlined digital methods and equipment to compute mean square values, autocorrelation and cross correlation functions, power and cross spectral density functions. Errors due to aliasing and quantizing were also discussed. Introduction of the fast Fourier transform technique by Cooley and Tukey (1965) has greatly reduced the computer time required to calculate various statistics from that of the discrete Fourier transform. Other aspects of digital processing and analysis have been discussed by Bendat and Piersol (1966), Oppenheim and Schaffer (1975), Chen (1979), Beauchamp and Yuen (1979), and many others.

In turbulence research, Frenkiel and Klebanoff (1967 a,b) were among the first to report results obtained from digital techniques and they were followed by Van Atta and Chen (1968) who obtained different values for odd moments. This discrepancy was due to using two different operations of anemometer, i.e., constant current and constant temperature. Otherwise their results agreed with each other. Tennekes and Wyngaard (1972) found that accurate measurement of the fourth moment of the velocity derivative at a turbulent Reynolds number in the order of 5000 required a dynamic range of forty standard deviations. They concluded that measurement of moments beyond the fourth for velocity derivatives in geophysical turbulence were practically impossible with the current instrumentation, design and execution of the experiments. However, Pierce (1972) found that only twelve standard deviations of the signal for measurement of the streamwise velocity derivatives were required to determine Kurtosis at the centerline of a free jet with a turbulent Reynold number of 640.

No thorough comparison of analog and digital results are available in literature apart from some passing remarks by Gibson, Stegen and McConnell (1970) and Sastry (1984). Hence a direct comparison of some experimental parameters obtained through analog and digital techniques was undertaken in this study. Measurements were made in a simple boundary layer flow and in a more

complex flow, like that of a conical diffuser, in order to determine possible differences in the parameters obtained by these two methods. The present digital results of skewness and flatness factors of the streamwise velocity component from single normal hot-wire were compared with analog measurements of Derksen (1981) and Kasab (1986) throughout the same boundary layer flow. The analog and digital measurements of the flow in conical diffuser were taken simultaneously. Single hot-wire measurements of third and fourth order moments of the velocity were taken and compared. In addition five spectra were measured at five different locations on a line normal to the diffuser wall. Measurements from X-wire consisted of mixed moments up to the fourth order and five spectra each of the longitudinal velocity and the transverse velocity fluctuations.

## 2. APPARATUS AND METHODS

### 2.1 Wind tunnels details

Two low speed, open return wind tunnels were used in the experiments: a boundary layer tunnel and a fully developed pipe flow tunnel with an 8° conical diffuser at its outlet. The boundary layer tunnel consists of wooden inlet duct, a radial vane damper, four stage axial fans driven by two-speed four-pole ball bearing motors, a silencer, two 8° total angle rectangular diffusers with two turning sections, a settling duct with screens, a circular contraction cone of an area ratio of 16 : 1, a number 16 sandpaper flow trip, and finally a 2.67 m length of pipe of inside diameter of 27.0 cm. The boundary layer growth is obtained on the inside wall of the pipe. Detailed description and the operation of the boundary layer tunnel are described in Serag (1978) and Burhanuddin (1980). Measurements across the turbulent boundary layer were taken perpendicular to the pipe wall, 15 cm from the pipe exit for a free stream velocity of 8 m/sec.

The second wind tunnel was a straight open return type. It consisted of a centrifugal fan driven by a 2½ HP DC motor, a rectangular diffuser, three sets of screens, a settling chamber, a contraction cone of an area ratio of 89 : 1, a

combined vibration isolator and a number 16 sandpaper for flow trip, two straight sections of 10.16 cm ID steel pipe of total length of 7.95 m and 8° conical diffuser of area ratio of 4 : 1. The flow from the diffuser was discharging in the open space of the laboratory. The overall length of the diffuser was 72 cm. The single and cross wire measurements were taken normal to the wall, 9 cm from the diffuser exit. All tests were conducted with fully developed pipe flow at the diffuser entry at the Reynolds number of 130,000 based on the entry pipe diameter of 10.16 cm and pipe bulk velocity.

## 2.2 Turbulence measurements

The anemometers used in the series of comparative tests were the DISA55M system together with two types of linearizers, DISA55D10 and DISA55M25. A DISA55D35 rms voltmeter was used to measure the local turbulence components of the flow. Two turbulence processors were available to obtain analogly manipulated parameters. They were DISA52B25 turbulence processor and Tri-Met Instruments model type 377 multifunction turbulence processor. The latter instrument was developed specifically for use in the Turbulence Laboratory at the University of Manitoba. The circuit details are given in Hummel (1978). All outputs, the  $u$ -component, the  $v$ -component, and their products were instantaneous values and as such were averaged with an external integrator before a numerical value could be read from the external DC voltmeter in the analog series of measurements. Other auxiliary instruments used in this investigation were DISA55D26 signal conditioner, Krohn-Hite 3550 filters, and three oscilloscopes - Tektronic 466 storage scope, Tektronic 2213A and Tequipment D1011.

The hot-wire probes used in the experiments were DISA55P05 gold plated, single wire, boundary layer types and DISA55P51 gold plated X-array types. Hot-wires were platinum plated tungsten of 5  $\mu$ m in diameter with an overall length of 3 mm and a sensitive length of 1.25 mm. The hot-wires were operated at an overheat ratio of 0.8 in the constant temperature mode.

## 2.3 Computer Facilities

The Computer facilities developed in the Turbulence Laboratory at the University of Manitoba consisted of a PDP-11/34A central processing unit, an FP11-A floating point processor, two RL01 random access disc drives for secondary storage, and a VT-100 video display terminal. The computer was equipped with an LPA-11K laboratory peripheral accelerator with a KW-11K dual programmable clock and an AD-11K 12 bit A/D converter for data acquisition. An RSX-11M operating system was used with a DEC FORTRAN compiler to run the computer. The software packages for data acquisition and analysis of the turbulent signal were developed in the laboratory. Hard copy output was obtained through an LA-180, 180 character per second line printer and an HP747a, six pen plotter.

Further details of the apparatus and techniques are given in Ozimek (1986).

## 3. RESULTS AND DISCUSSION

The turbulence parameters from the hot-wire measurements were obtained by both analog and digital means and subsequently the results from these two methods were compared. Here the measurements in the boundary layer flow are first described and then the report on diffuser flow follows.

### 3.1 Boundary layer flow

Analog and digital results obtained from measurements by boundary layer hot-wire probes are compared. In digital measurements, 200 data buffers were filled at a rate of  $3 \times 10^3$  samples/sec. Values of third and fourth order moments obtained by analog and digital means are shown in Figures 1 and 2. Analog values were obtained from Derksen (1981) and Kassab (1986). Digital values were given by the PDP 11/34A computer after processing the linearized signal from the hot-wire. Figure 1 shows the skewness distribution in the boundary layer for a free stream velocity of 8 m/sec in the logarithmic and wake regions of the flow to be predominantly negatively skewed. Basically, the probability distribution of the mean velocity,  $U$ , for values of  $Y^+ < 15$  is positively skewed,  $Y^+ > 15$  is symmetric about the

mean velocity, and  $Y^+ > 15$  is negatively skewed. The minimum value of skewness occurs at approximately 45 mm, the outer edge of the boundary layer. Flatness factor or Kurtosis for the same free stream velocity is illustrated in Figure 2. This has a nearly constant value of 2.8 below the Gaussian value of 3 for the first 20 mm from the wall or  $y/\delta < 0.4$  where  $\delta$  is the boundary layer thickness.

A comparison of the plotted analog and digital results shows good agreement between both methods of data analysis. Discrepancies in results near the wall may be due to spatial resolution of the hot-wire, inaccurate distance measurements and variation in turbulent flows from day to day. Variability in the results further from the wall may be attributed to the intermittent nature of the flow. Both under amplification and over amplification of the turbulent signal result in inaccurate values of the processed signal.

### 3.2 Diffuser flow

Analog and digital measurements in the adverse pressure gradient flow were simultaneously made with single wire and X-wire probes. Linearization of the hot-wire anemometer was performed in situ. The digital data were collected into 2000 buffers at a rate of  $2 \times 10^6$  samples/sec for a total of 2053120 data points at each probe position.

The trend of the Reynolds shear stress  $\overline{uv}$  shown in Figure 3 exhibits a linear region in the first 20 mm from the wall before increasing in slope and reaching a maximum value which is called critical point (CP). Two distinct linear regions are observed from CP to the diffuser axis. The first extends for approximately the following 20 mm and has a slightly negative slope. The second has a large negative slope and extends beyond the diffuser axis. The Reynolds shear stress,  $\overline{uv}$ , in the pipe is linear between the wall and axis in contrast to the diffuser result. Figure 3 shows clearly no significant difference between analog and digital results.

The skewnesses obtained by both analog and digital means via boundary layer and cross wire

probes are shown in Figure 4. The skewness of the axial velocity component is highly positive and hence asymmetric in the first few millimeters from the wall and gradually approaches zero (indicating symmetrical probability density distribution about the mean velocity) at a position in line with the pipe wall at the diffuser entry. The skewness values continue to increase in the negative direction until a minimum is reached at the diffuser axis, then due to symmetry about the axis, the skewness values begin to increase. The skewness of the radial velocity component ( $v$ ) is negative in the first two thirds of the flow and reaches a positive peak just before the centerline before dropping to zero at the diffuser axis. The digitally obtained skewness results,  $S(u)$  and  $S(v)$ , cross the zero value ahead of the corresponding analog results, otherwise there is no difference between analog and digital results. Normalized third order moments of  $\overline{uv^2}$  and  $\overline{u^2v}$  are shown in Figures 5 and 6 respectively and show similar trend to the skewness distributions of  $u$  and  $v$ . The central moment of the  $\overline{uv^2}$  correlation, although smaller in magnitude, is of the same sign as  $S(u)$ , i.e., positive in the wall region, negative in the core region of the flow with zero at CP and relative minimum, due to symmetry occurring at the diffuser axis. The central moment of the  $\overline{u^2v}$  correlation is smaller in magnitude but of the same trend as  $S(v)$  (see Figure 6). Like the  $S(v)$  distribution, the distribution of  $\overline{u^2v}/u'^2v'$  changes sign twice: first just after CP and second at the axis of the diffuser. No discernable difference can be observed between the analog and digital measurements of these two moments shown in Figures 5 and 6. The triple velocity correlations in the diffuser-flow are distributed differently from those in fully developed pipe flow or boundary layer flow. Turbulence seems to have a completely different physical mechanism in the former flow than the latter ones.

The flatness factors by both analog and digital means through boundary layer and X-wire probes are shown in Figure 7. The fourth order moments,  $K(u)$ , decrease in value from the wall to a minimum

value of 2.5 below that of the Gaussian value of 3 at a distance of approximately 5 cm from the axis of the diffuser; this distance is in line with the wall of the pipe at the inlet of the diffuser. The increasing values of the flatness factors reach a relative maximum at the diffuser axis. The flatness factors of the radial velocity component,  $K(v)$ , are larger in value than corresponding axial values between the wall and CP. The flatness values decrease in magnitude, approaching the Gaussian value of 3 in the region of about 5 cm from the axis of the diffuser before increasing in value and peaking at diffuser axis. The flatness values of the radial component in the core region of the diffuser flow are lower in magnitude than corresponding flatness values of axial component. Analog and digital results in Figure 7 show no appreciable difference after taking experimental errors into account. Other fourth order moments measured are  $\overline{u^2v^2}/\overline{u^2v}^2$ ,  $\overline{uv^3}/\overline{u^3v}$  and  $\overline{u^3v^3}/\overline{u^3v}^3$  and they are shown in Figures 8, 9 and 10, respectively. The magnitudes of these central moments are lower than flatness factors of either u or v velocity components everywhere in the field. The  $\overline{u^2v^2}/\overline{u^2v}^2$  wave-like distribution (see Figure 8) fluctuates between values of 1 at CP and 3 in proximity of the wall. Since both components are even powered, central moment is positive and has a definite value at the axis. Except in close proximity to the wall, little scatter is observed between the analog and digital points. The fourth order moments with odd powered components have the same sign as the Reynolds shear stress  $\overline{uv}$ , and as such they are passing through zero at the diffuser axis. Both central moments collapse onto the same curve in the core region of the flow, but near the wall, the value of  $\overline{uv^3}/\overline{u^3v}$  is higher than value of  $\overline{u^3v^3}/\overline{u^3v}^3$ . At CP their values have a magnitude of about 1. Again, no significant difference between the analog and digital data exists.

The analog and digital data for the comparison of the velocity spectra in diffuser-flow were collected and processed at different times. The hot-wire signal for the digital results was

filtered at the Kolmogorov frequency  $f_k = U/2\pi\eta$  by means of the signal conditioner. The DC component of the signal was subtracted, leaving the fluctuating component to be amplified to within the 0.5 volts limits accepted by the A/D converter. The digital spectral results were calculated using the fast Fourier transform and spectra subroutines supplied by DEC. The spectra were calculated by two passes of the data: a 'high frequency' spectrum calculated from the data as it is and a low frequency spectrum calculated from the data stream filtered using a second order Butterworth infinite-impulse-response (IIR) filter. The 'low frequency' data were then sampled at 1/64 of the sampling rate, spectrum calculated, and multiplied by a factor of 64 to account for the shift in bandwidth. The spectra were finally plotted by HP plotter.

The analog spectral results were collected by low pass filtering the signal at  $f_k$  and then band pass filtering the signal for frequencies between 2 Hz and 35 KHz. Eight measurements of spectral density per decade were made. Spectral results of u and v velocity components obtained by a single and cross wire probes and processed with analog and digital means are shown in Figure 11. This figure shows that the velocity spectra display the same trends: some scatter in low frequency range, digital noise occurring at lower frequencies than analog noise. No significant difference is seen between the plotted analog and digital spectral results.

#### 4. CONCLUDING REMARKS

In both flows, boundary layer and diffuser, the analog and digital data compared well in most parameters measured. Differences in them may be due to the effects of imperfect amplification, imperfect matching of the frequency and sensitivity of the input signals of x-wires and non-repeatable turbulent flow.

Analog and digital techniques may be considered from other points of view, such as, time, versatility, convenience and future prospects. The analog technique generally takes more time to accomplish a task than the digital one. Any

specific task of measurement is better executed by analog technique, since it is designed for that purpose. On the other hand the digital techniques have the advantage that once the data have been collected and stored on tape, it can be re-analyzed at a later date to investigate additional parameters or other physical hypothesis. Future developments in measurements belong to digital techniques in one form or other.

#### 5. ACKNOWLEDGMENTS

The authors greatly appreciate the financial assistance given by NSERC Canada for the research.

#### 6. REFERENCES

- Bearman, P.W. 1968 Digital analysis of hot-wire data. NPL Rep. No. 1273.
- Beauchamp, K.G. & Yuen, C.K. 1979 Digital methods for signal analysis. George Allen and Unwin, London.
- Bendat, J.S. & Piersol, A.G. 1966 Measurement and analysis of random data. John Wiley and Sons, New York.
- Burhanuddin, S. 1980 Measurement of wall shear stress with hot-wire anemometer. M.Sc. Thesis, The University of Manitoba.
- Chen, C-T. 1979 One-dimensional digital signal processing. Marcel Dekker, New York.
- Cooley, J.W. & Tukey, J.W. 1965 An algorithm for machine calculation of complex Fourier Series. Math Comp. 19, 297-301.
- Derksen, R.W. 1981 The response of a hot-wire of finite length to fine-scale structure in a turbulent flow. M.Sc. Thesis, The University of Manitoba.
- Frenkiel, F.N. & Klebanoff, P.S. 1967a High-order Correlations in a turbulent field. Phys. Fluids 10, 507-520.
- Frenkiel, F.N. & Klebanoff, P.S. 1967b Correlation measurement in a turbulent flow using high-speed computing methods. Phys. Fluids 10, 1737-1747.
- Gibson, C.H., Stegen, G.R. & McConnel, S. 1970 Measurements of the universal constant in Kolmogoroff's third hypothesis for high Reynolds number. Phys. Fluids 13, 2448-2451.
- Hummel, R.H. 1978 Turbulence structure in a conical diffuser. Ph.D. Thesis, The University of Manitoba.
- Kazub, S.Z. 1986 Turbulence structure in axisymmetric-wall bounded shear flows. Ph.D. Thesis, The University of Manitoba.
- Oppenheim, A.V. & Schaffer, R.W. 1975 Digital signal processing. Prentice-Hall, New Jersey.
- Ozimek, L.G. 1986 A comparison of analog and digital data for measurements of turbulence parameters. M.Sc. Thesis, The University of Manitoba.
- Pierce, R.E. 1972 Statistical analysis of turbulence using a large scale digital computing system. Ph.D. Thesis, The Pennsylvania State University.
- Sastry, M.S. 1984 Comparison of turbulence data obtained from hot-wire signals by different methods. Proceedings of the Western Michigan Conference on Mechanical Engineering, Kalamazoo, Michigan, 284-289.
- Serag, M.A.-A. E.-S. 1978 The influence of the length and the diameter on the response characteristics of a hot-wire probe to the fine scale structure of turbulence. M.Sc. Thesis, The University of Manitoba.
- Tennekes, H. & Wyngaard, J.C. 1972 The intermittent small-scale structure of turbulence: data processing hazards. J. Fluid Mech. 55, 93-103.
- Van Atta, C.W. & Chen, W.Y. 1968 Correlation measurements in grid turbulence. J. Fluid Mech. 34, 497-515.

FIGURES

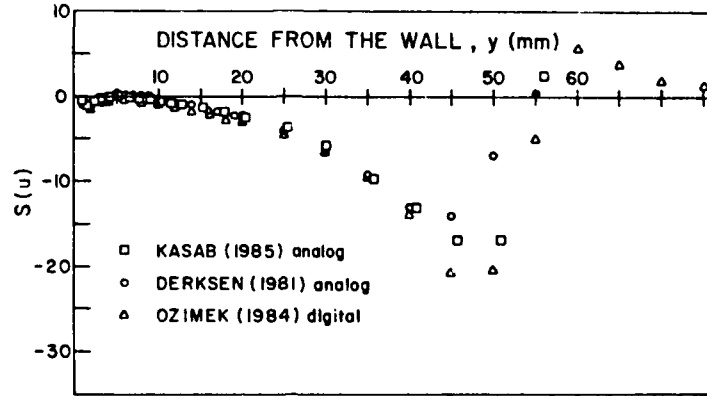


Figure 1. Skewness of  $u$  in the boundary layer flow.

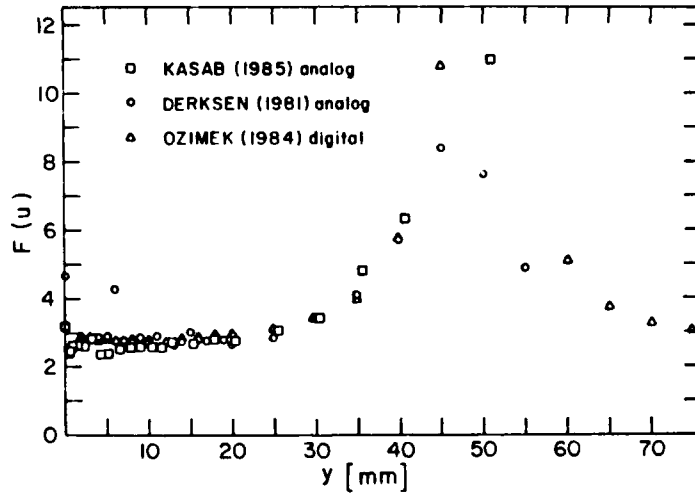


Figure 2. Flatness factor of  $u$  in the boundary layer flow.

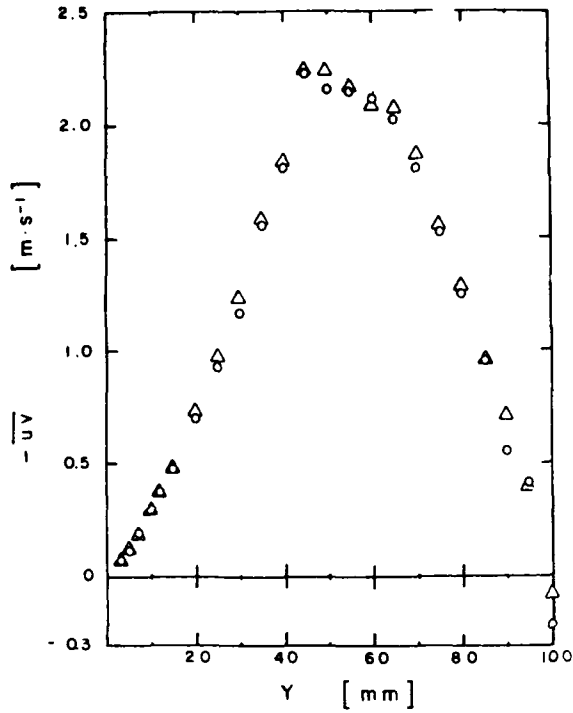


Figure 3. Reynolds shear stress,  $\overline{uv}$ , in the diffuser-flow.

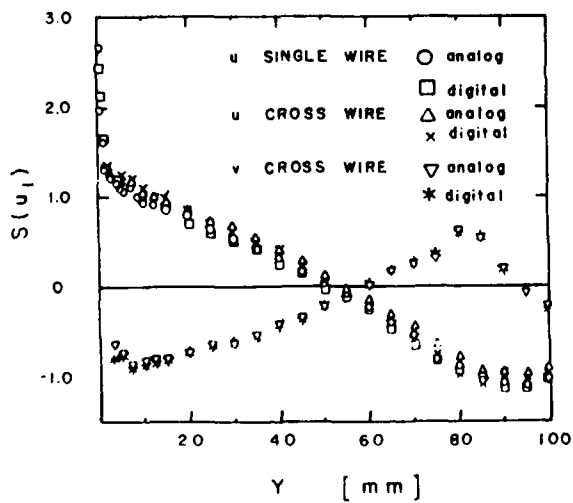


Figure 4. Skewness of  $u$  and  $v$  in the diffuser flow.

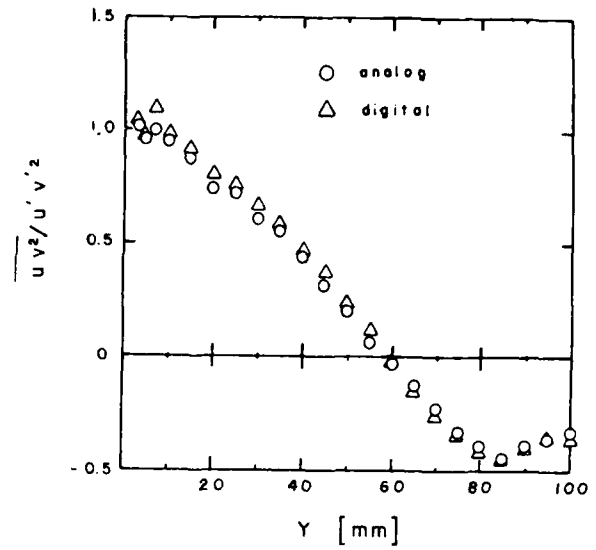


Figure 5. Central moment,  $\overline{uv^2}$ , in the diffuser-flow.

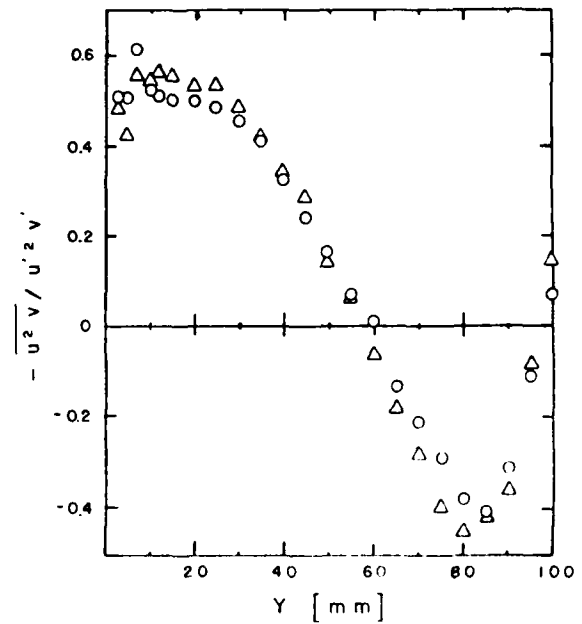


Figure 6. Central moment,  $\overline{u^2v}$ , in the diffuser flow.

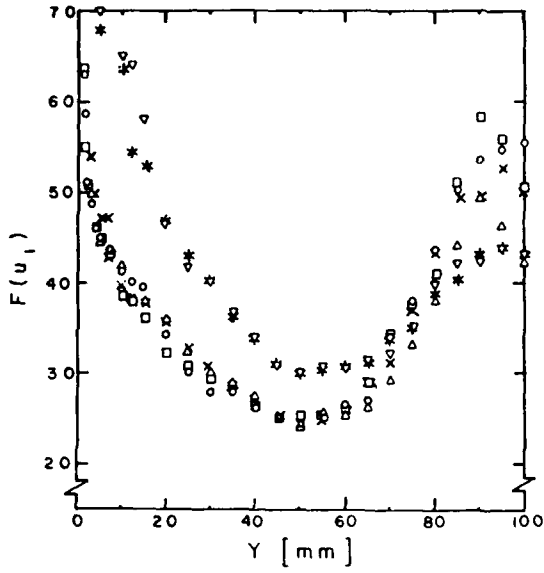


Figure 7. Flatness factor of  $u$  and  $v$  in the diffuser-flow.

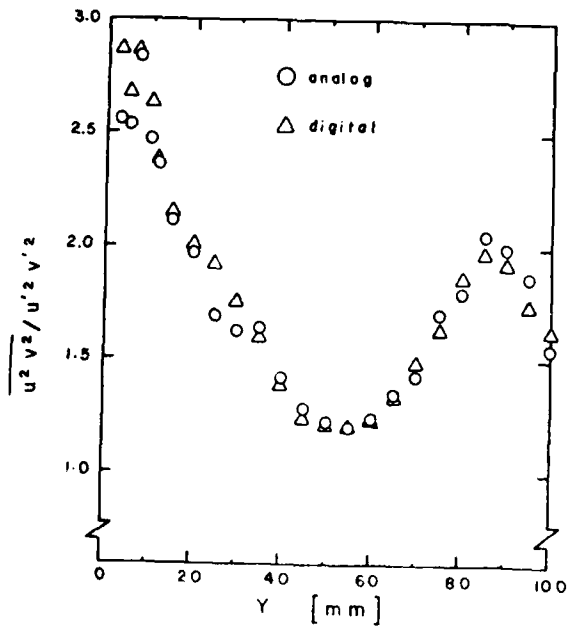


Figure 8. Central moment,  $\overline{u^2 v^2}$ , in the diffuser-flow.

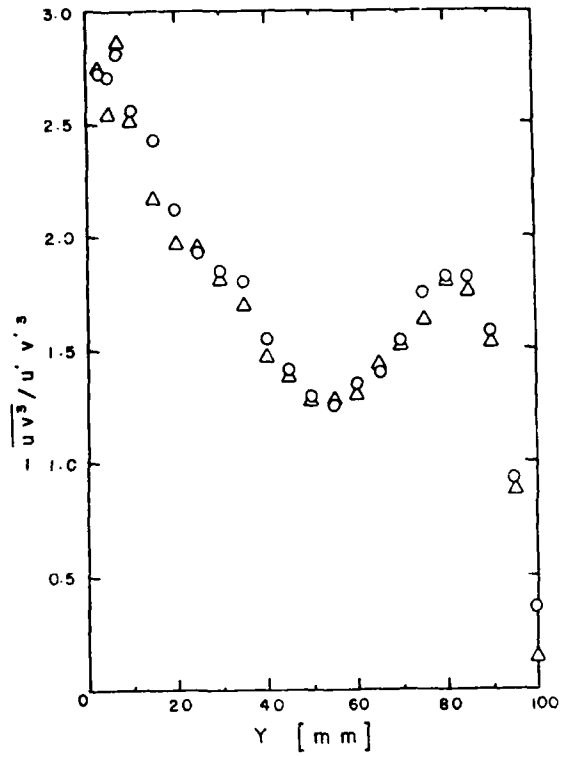


Figure 9. Central moment,  $\overline{u v^3}$ , in the diffuser-flow.

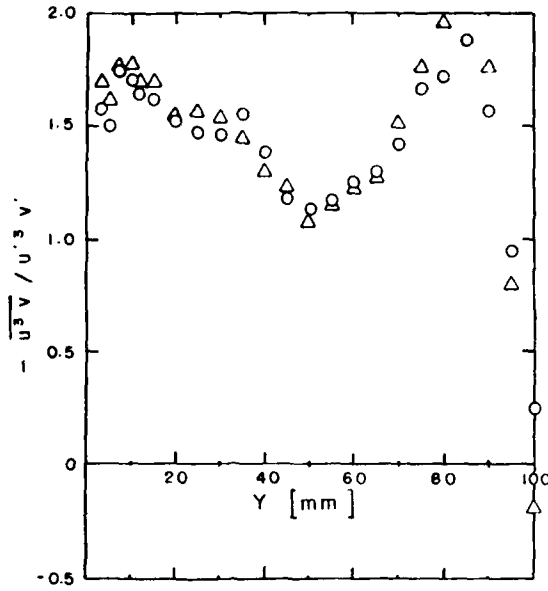


Figure 10. Central moment,  $\overline{u^3v}$ , in the diffuser-flow.

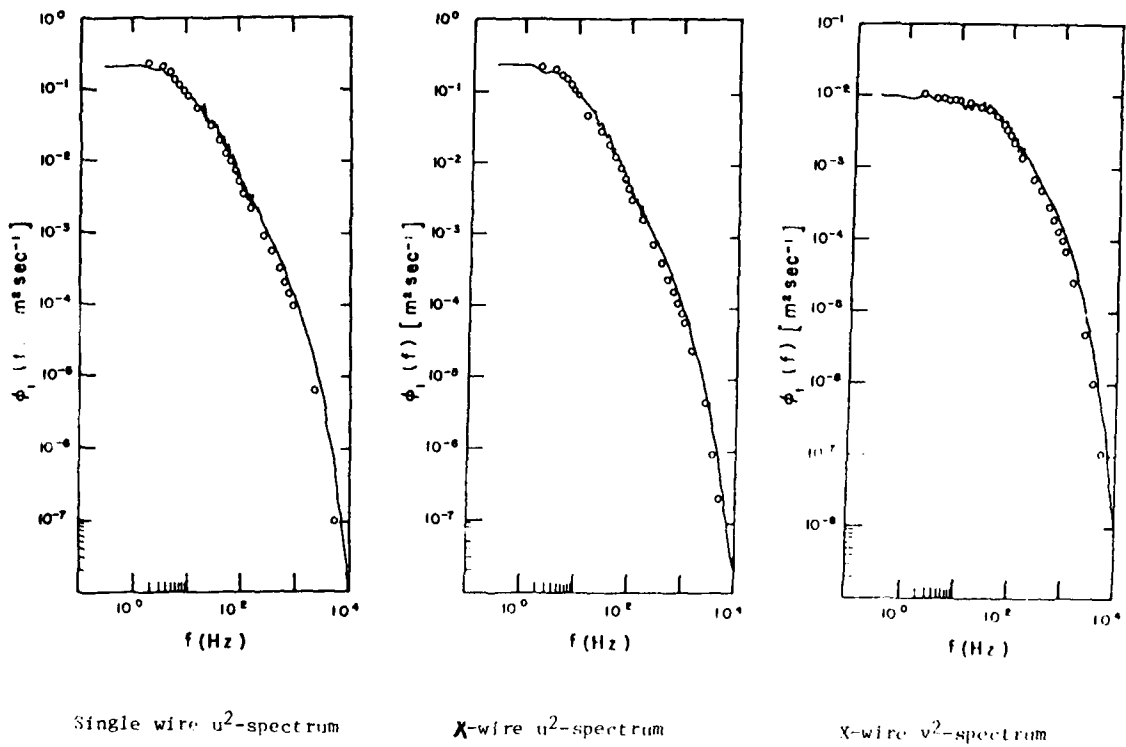


Figure 11. Spectra in the diffuser-flow at  $y = 25$  mm.

MODELING OF EXHAUST FUME  
CONCENTRATIONS NEAR BUILDINGS

Paul Dawson\*, Brian Lamb\*\*, Daniel  
Martin\*, and David Stock\*  
College of Engineering and  
Architecture  
Washington State University  
Pullman, WA 99164-2920

ABSTRACT

The flow field and concentration field were computed for a cubic building in a neutral atmospheric boundary layer. The numerical results were then compared with a wind tunnel simulation of the same flow. The results agreed closely except at ground level.

1. INTRODUCTION

Physical modeling of the flow and dispersion of pollutants about three-dimensional objects has been a well developed science since the early 1970's, but only recently have numerical techniques been used to compute this type of flow. Wind tunnel models are useful for evaluating a particular configuration but they are expensive and the testing time-consuming. Physical models are also limited in that the data they provide can only in a few special cases be generalized. With the availability of large, high speed computers, it is now possible to compute three-dimensional flows with recirculation, the type of flow found around buildings and other complex topographical features. Although such computations are also expensive and time consuming, we will gain experience that can be used to develop more efficient schemes which, with the advent of still larger computers, will become practical tools in the near future. This paper compares

the results of a numerical calculation of the flow and exhaust-gas dispersion about a cubic body in the atmospheric boundary layer with the results of an atmospheric wind tunnel simulation of the same flow. Although we would prefer to compare the calculation against full-scale field data, field data generally does not contain enough information for a complete comparison and it often includes changes in the direction and magnitude of the wind during data acquisition (Ryan et al. 1980).

Two- and three-dimensional numerical schemes have been used to compute the fluid flow and heat transfer in small-scale systems of interest to engineers. Using these schemes, it has been possible to compute flows that contain recirculation zones using appropriate numerical models. Through experience, the models have been tuned to give acceptable results for small-scale flows. Computations of atmospheric flows, on the other hand, have mostly focused on large-scale phenomena in which recirculation zones were either not present or much smaller than the computational grid scale used in the calculation. Between these two scales lies the area of flow about buildings and smaller landforms. We have attempted to combine these two scales by modifying the turbulence schemes used by engineers so that they apply to the atmospheric boundary layer.

\* Department of Mechanical Engineering

\*\*Laboratory for Atmospheric Research

## 2. COMPUTATIONAL TECHNIQUES - FLOW FIELD

We used the TEMPEST code (Trent et al. 1983) to compute the fluid flow, then used the PEST code to compute diffusion of the tracer gas. TEMPEST is a three-dimensional, finite difference program that solves the time-dependent equations of motion, continuity, and energy for incompressible turbulent flows, but includes the ability to account for small density variations through the Boussinesq approximation. It uses a Cartesian coordinate system and a solution technique similar to the Los Alamos Marker-and-Cell technique (Amsden and Harlow 1970) by solving the momentum and energy equations explicitly, and the continuity/pressure equations implicitly. A second-order accurate predictor-corrector advection scheme has been incorporated into the momentum equations of TEMPEST. The turbulent equations were closed using the  $k$ - $\epsilon$  first-order scheme. The Reynolds stresses were modeled as

$$\rho \overline{U_i U_j} = \frac{2}{3} \rho k \delta_{ij} - \mu_t \left( \frac{\partial U_i}{\partial x_j} + \frac{\partial U_j}{\partial x_i} \right) \quad (1)$$

where  $k$  is the turbulent kinetic energy and  $\mu_t$  is the turbulent viscosity. The turbulent viscosity was then modeled as

$$\mu_t = C_\mu \frac{\rho k^2}{\epsilon} \quad (2)$$

where  $C_\mu$  is a constant and  $\epsilon$  is the turbulent kinetic energy dissipation. In the first-order closure scheme, the turbulent viscosity is related to a turbulent velocity scale and to a length scale. In the two-equation form of the first-order closure, the turbulent velocity scale is equated to the square root of turbulent kinetic energy.  $k$  is found by solving the modeled turbulent kinetic energy equation

$$\rho \left( \frac{\partial k}{\partial t} + U_i \frac{\partial k}{\partial x_i} \right) = \frac{\partial}{\partial x_j} \left( \frac{\mu_t}{\sigma_k} \frac{\partial k}{\partial x_j} \right) + \mu_t \left( \frac{\partial U_i}{\partial x_j} + \frac{\partial U_j}{\partial x_i} \right) \frac{\partial U_i}{\partial x_j} - \rho \epsilon - \frac{\mu_t}{\rho \omega_T} k \frac{\partial \rho}{\partial z} \quad (3)$$

where  $\sigma_k$  and  $\omega_T$  are constants and  $g$  is the acceleration of gravity acting in the  $-z$  direction. The last term on the righthand side accounts for production of turbulent kinetic energy due to buoyancy. This same form of the turbulent kinetic energy equation is used in both engineering and atmospheric calculations.

The turbulent energy dissipation  $\epsilon$  is used to represent the length scale in the two-equation model. The link between the energy dissipation and length scale is the least understood part of the two-equation turbulence model and the proper form of the modeled  $\epsilon$  equation is still questionable. By comparing their one-dimensional calculations to the Leipzig wind profile (Leltau 1962), Detering and Ertling (1985) showed that the standard engineering form the  $k$ - $\epsilon$  model overpredicts the turbulent viscosity. They trace the difference to the surface layer value for  $k$  and to the length scale calculated by the standard form of the  $\epsilon$  equation. The constant  $C_\mu$  is usually evaluated in the constant flux layer near a wall, which gives

$$k = \frac{u_*^3}{\sqrt{C_\mu}} \quad (4)$$

where  $u_*$  is the friction velocity. Within the constant flux layer of the atmospheric boundary layer measurements indicate  $C_\mu = 0.076$  (Panofsky et al. 1977). This value was taken for  $C_\mu$  instead of the standard engineering value of 0.09.

The standard engineering form of the  $\epsilon$  equation is

$$\rho \left( \frac{\partial \epsilon}{\partial t} + U_i \frac{\partial \epsilon}{\partial x_j} \right) = \frac{\partial}{\partial x_j} \left( \frac{\mu_t}{\sigma_\epsilon} \frac{\partial \epsilon}{\partial x_j} \right) +$$

$$C_1 \frac{\epsilon}{k} \mu_t \left( \frac{\partial U_i}{\partial x_j} + \frac{\partial U_j}{\partial x_i} \right) \frac{\partial U_i}{\partial x_j} -$$

$$C_2 \rho \frac{\epsilon}{k} - \frac{C_3 \mu_t}{\rho \sigma_T} \frac{1}{k} g \frac{\partial \rho}{\partial z} \quad (5)$$

where the last term on the righthand side represents buoyancy effects. The two-equation model assumes the length scale is given by

$$l = \frac{C_\mu^{3/4} k^{3/2}}{\epsilon} \quad (6)$$

Detering and Etling (1985) used this relation to compare the length scale given by the two-equation model to the atmospheric form given by Blackadar (1962). They found that the mixing length predicted by Blackadar's equation increased linearly with height near the surface and then become constant near  $l = 0.03 \delta$  where  $\delta$  is the boundary layer height evaluated from mean wind profiles. The mixing length predicted by the standard two-equation model grows linearly and reaches a maximum of  $l = 0.16 \delta$ . To correct for this difference, Detering and Etling (1985) suggested modifying the dissipation equation to account for the decreased shear found in the middle and upper part of the atmospheric boundary layer. They proposed reducing dissipation relative to production with height or, for complex flows, making  $C_1$  in equation (5) depend on the characteristic length scales of the turbulence using

$$C'_1 = \frac{C_1 l}{h} \quad (7)$$

where  $l$  is a turbulent length scale and  $h$  is a characteristic scale for the atmospheric boundary layer. They used equation (6) for the length scale  $l$  and

$$h = \frac{C_h U_*}{f} \quad (8)$$

for  $h$ , where  $f$  is the Coriolis parameter and  $C_h$  is a constant. Combining this gives

$$C'_1 = \frac{C_1 f C_\mu^{3/4} k^{3/2}}{C_h U_* \epsilon} \quad (9)$$

They suggest setting  $C_h = 0.0015$ .

We used this modified form of the turbulent dissipation equation in the calculations along with the following constants:

$$C_\mu = .026, C_1 = 1.13, C_2 = 1.92, C_3 = 1.13$$

$$\sigma_k = 0.7, \sigma_\epsilon = 1.3, \sigma_T = 0.7, C_h = 0.0015$$

$$U_* = 0.65 \text{ ms}^{-1}, \quad f = 1 \times 10^{-4} \text{ s}^{-1}$$

Using a grid spacing of 21 long by 22 wide by 12 high with no obstructions, the Leipzig data were used to compare the modified turbulence closure scheme with the standard engineering closure. As found by Detering and Etling (1985), the modified closure was superior to the other closure schemes. The computed results matched the Leipzig data except in the lower part of the surface layer.

3. COMPUTATIONAL TECHNIQUES—CONCENTRATION FIELD  
PEST (Pollution Equation Solver in Three Dimensions) solves the three-dimensional steady state scalar convection and turbulent diffusion equation

$$U_j \frac{\partial C}{\partial x_j} + \frac{\partial}{\partial x_j} (\overline{U'_j C'}) = S \quad (10)$$

where  $S$  is a source or sink term. Equation (10) is solved using the velocity field calculated by TEMPFST. For this neutrally stable flow, the first-order turbulence closure was used in the following form

$$\overline{U'_j C'} = -D_{ij} \frac{\partial C}{\partial x_j} \quad (11)$$

where  $D_{ij}$  is the turbulent diffusivity tensor. Assuming a turbulent Schmidt number of one and an isotropic diffusivity,  $D_{ij}$  is then equal to the turbulent viscosity which is determined as part of the fluid flow calculation. The modeled diffusion equation was solved using an implicit ADI finite difference scheme (Douglas 1962) which incorporated an upwind differencing scheme.

#### 4. SIMULATION

Thompson and Lombardi (1977) measured the concentration field resulting from a roof-top emission from an isolated cubic building in the EPA meteorological wind tunnel. They also measured the velocity and turbulence intensity in the longitudinal direction. We modeled this same flow and emission using TEMPEST and PFST. The wind tunnel model was a 0.18 m cube placed in a 1.8 m deep simulated neutral atmospheric boundary layer with a wind speed of 1.46 m/s at the building height. The velocity profile without the building followed the 1/7 power law with elevation,  $z$ , measured from a plane 0.025 m above the floor of the tunnel and 0.025 m below the top of the roughness elements. The effluent was emitted through a central port in the roof with negligible momentum and negligible buoyancy.

The numerical simulation used a variable space grid of 40 long by 32 wide by 32 high. Figure 1 shows a top view of the grid and building. The building occupied six nodes in the vertical direction and was offset slightly to one side due to the odd number of nodes used for the building width. The roof top point emission was simulated by setting the concentration of the computational cell centered above the roof top to match the emission rate and the net flow through that computational node.

#### 5. RESULTS

TEMPEST was run until the computed velocity did not change with time and the velocity field, turbulent kinetic energy, and turbulent kinetic energy dissipation were stored and later used in PEST. Figure 2 shows the downwind velocity profiles at three locations and compares the

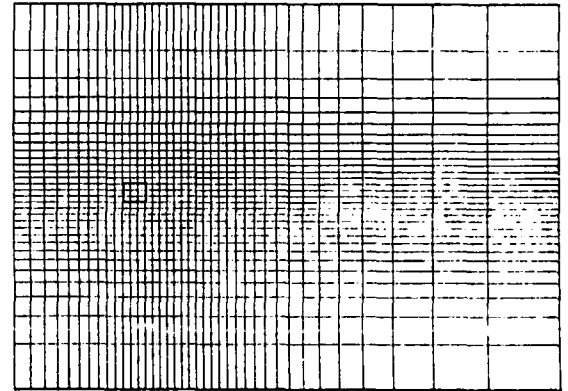


Figure 1. PLAN VIEW OF THE NONUNIFORM GRID USED IN 'TEMPEST' AND 'PEST'. THE POSITION OF THE BUILDING IS INDICATED BY BOLDER LINES. THE LIMITS OF THE HORIZONTAL AXIS ARE  $x/H = -5.05$  AND  $17.89$ , WHERE  $x$  IS MEASURED FROM THE CENTER OF THE BUILDING. THE LIMITS OF THE LATERAL AXIS ARE  $y/H = -10.06$  AND  $9.75$  WHERE  $y$  IS MEASURED FROM THE CENTER OF THE BUILDING ( $H = .1868$  m). THE CELLS SHOWN ARE 2 THROUGH 39 IN THE  $x$  DIRECTION, AND 2 THROUGH 31 IN THE  $y$  DIRECTION.

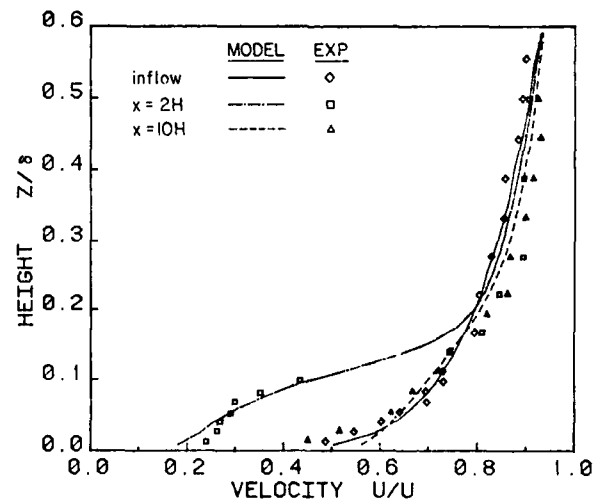


Figure 2. MEAN VELOCITY PROFILES FOR EXPERIMENTAL AND SIMULATED RESULTS. ( $x = 0$ ).  $U_\infty = 2.0$  m/s

computed results with the wind tunnel simulation. Close agreement was found in the mean velocity field. Figures 3 and 4 show the computed turbulent kinetic energy and turbulent kinetic energy dissipation. Unfortunately, these quantities were not measured in the model study. The velocity field in a vertical plane through the center of the building is shown in Figure 5. Figures 6 and 7 show the velocity vectors in two different horizontal planes. The recirculation zone in front and behind the building can be seen in these figures, but the grid was too coarse to show the recirculation zone on the top of the building.

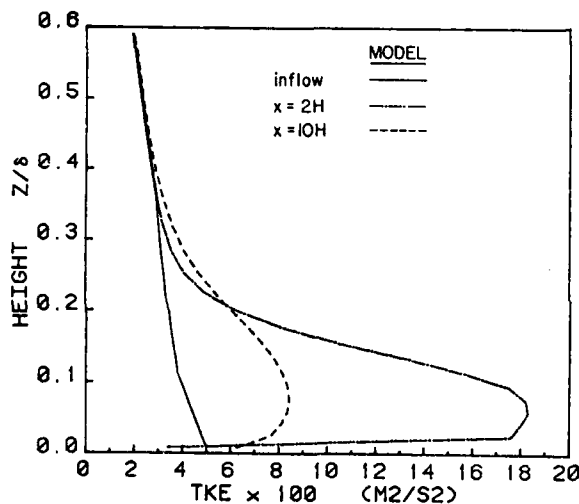


Figure 3. VERTICAL PROFILES OF THE INFLOW AND COMPUTED TURBULENT KINETIC ENERGY (k). INFLOW CONDITIONS FOR k WERE TAKEN FROM PROFILES GIVEN BY ROBINS (1978) FOR RURAL CONDITIONS.

Concentration isopleths computed by PEST are shown in Figures 8, 9, and 10. In these plots, the vertical and lateral scales have been enlarged. The asymmetry in the lateral isopleths is caused by very small differences in the transverse velocities caused by the building being slightly offcenter relative to the grid. The computed concentration profiles are compared with measurements made in the wind tunnel simulation

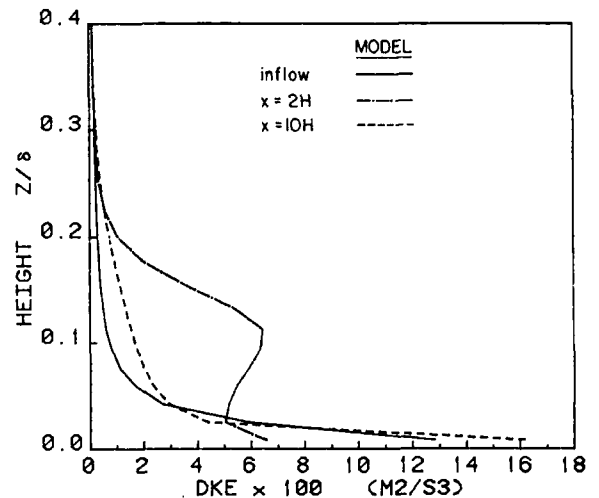


Figure 4. VERTICAL PROFILES OF THE INFLOW AND COMPUTED DISSIPATION OF TURBULENT KINETIC ENERGY. INFLOW CONDITIONS WERE COMPUTED FROM k AND EDDY VISCOSITY PROFILES GIVEN BY ROBINS (1987) FOR RURAL CONDITIONS.

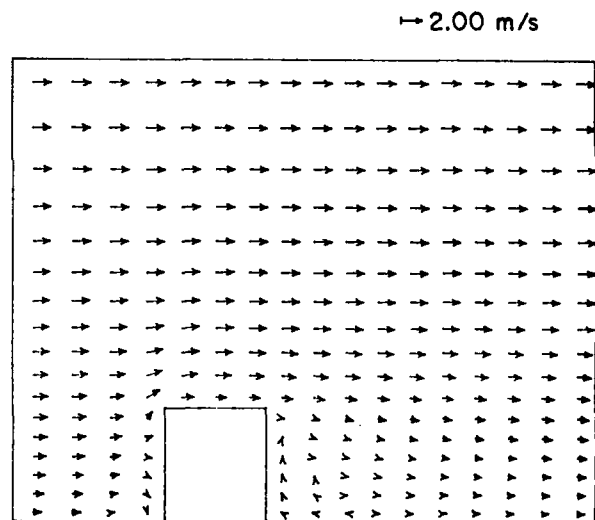


Figure 5. VELOCITY VECTOR FIELD IN THE VERTICAL PLANE AT THE CENTER OF THE BUILDING.

in Figures 11, 12, and 13. In these figures the nondimensional concentration  $\chi$  is given by  $C_H U_H^2 / Q$ , where  $U_H$  is the wind speed at the building height and  $Q$  is the emission rate. These figures show reasonable agreement except near the ground.

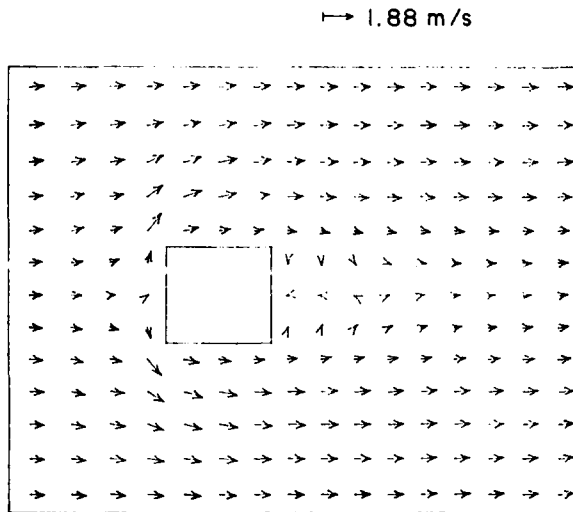


Figure 6. VELOCITY VECTOR FIELD IN THE HORIZONTAL PLANE ADJACENT TO THE GROUND SURFACE ( $z/H = 0.080$ ).

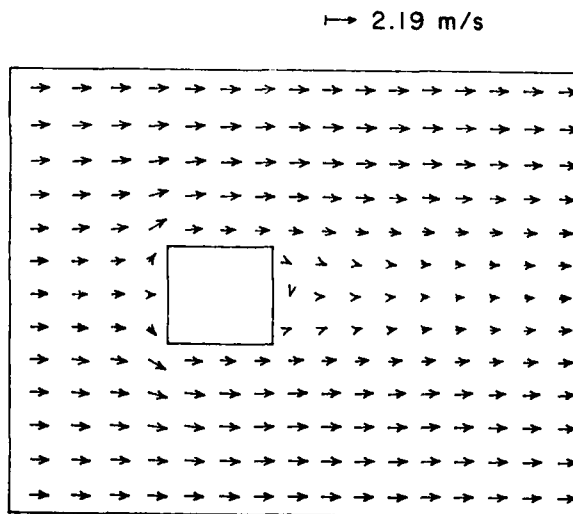


Figure 7. VELOCITY VECTOR FIELD IN THE HORIZONTAL PLANE ABOVE THE MIDPOINT OF THE BUILDING ( $z/H = 0.567$ ).

## 6. DISCUSSION

The TEMPEST and PFST Programs were able to reproduce the flow field and concentrations field around an isolated cubic building. Since our results were compared with a wind tunnel simulation of the actual atmospheric flow, there still remains the question of how well the wind tunnel

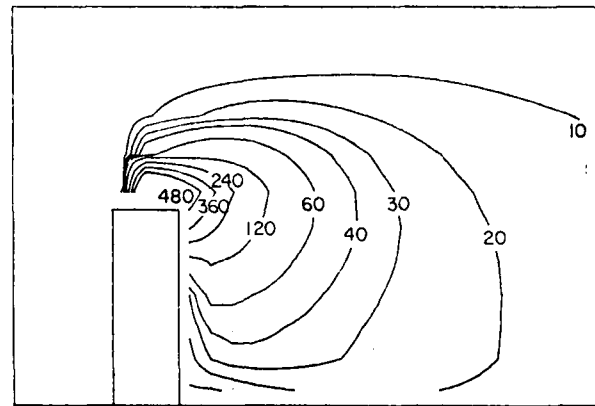


Figure 8. CONCENTRATION ISOPLETHS (IN MILLIGRAMS/ $m^3$ ) IN THE VERTICAL PLANE AT THE CENTER OF THE BUILDING. THE VERTICAL DIRECTION HAS BEEN EXAGGERATED. THE LIMITS OF THE VERTICAL AXIS ARE  $z/H = 0$  AND 2.05, AND THE LIMITS OF THE HORIZONTAL AXIS ARE  $z/H = -1.90$  AND 6.52.

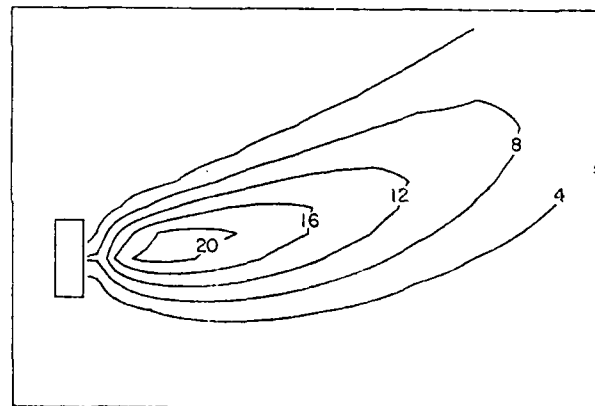


Figure 9. GROUND LEVEL CONCENTRATION ISOPLETHS (IN MILLIGRAMS/ $m^3$ ). THE LATERAL DIRECTION OF THE FIGURE HAS BEEN EXAGGERATED. THE LIMITS OF THE LATERAL AXIS ARE  $y/H = -1.77$  AND 3.07, AND THE LIMITS OF THE WINDWARD DIRECTION ARE  $x/H = -1.90$  AND 6.52.

simulation models the real flow. The computed concentrations showed the poorest agreement with the model study at ground level. This result is not surprising since this is the area that is hardest to simulate both in the tunnel study and in the numerical program. Most natural atmospheric boundary layers are full rough and characterized by a  $z_0$  and a zero plane displacement. In both the model study and the numerical simu-

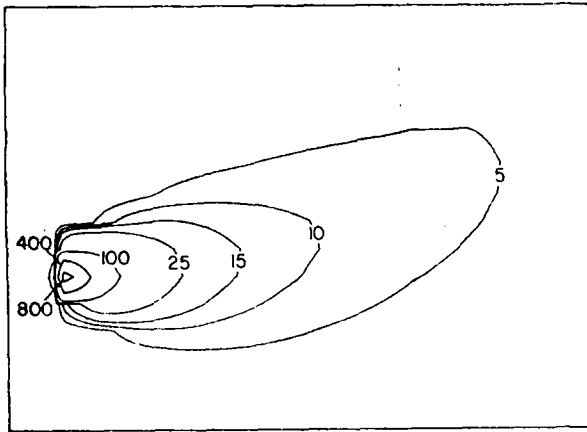


Figure 10. CONCENTRATION ISOPLATHS (IN MILLI-GRAMS/m<sup>3</sup>) IN THE HORIZONTAL PLANE OF THE ELEVATED POINT SOURCE ( $z/H = 1.093$ ). THE LIMITS OF THE AXES IN THE FIGURE ARE THE SAME AS THOSE IN FIG. 9.

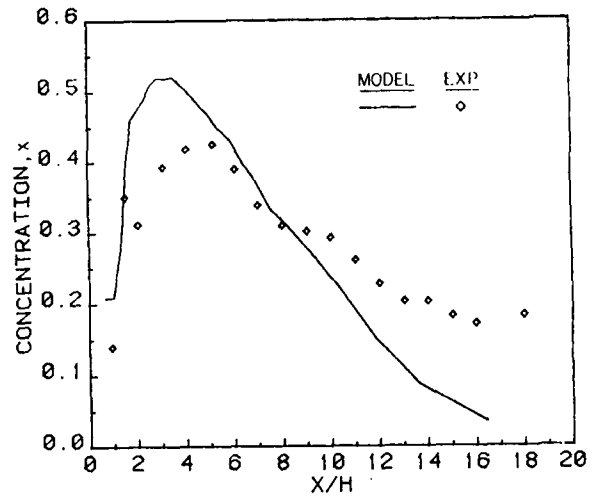


Figure 12. NONDIMENSIONAL GROUND LEVEL CONCENTRATIONS FOR EXPERIMENTAL AND SIMULATED RESULTS.  $y = 0$ ,  $z = 0.025$  m FOR THE EXPERIMENTAL RESULTS AND  $z = 0.015$  m FOR THE NUMERICAL RESULTS.

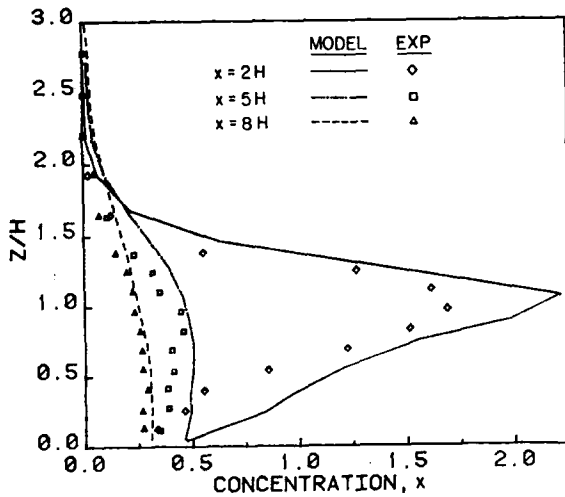


Figure 11. NONDIMENSIONAL VERTICAL CONCENTRATION PROFILES.  $y = 0$

lation, this ground level velocity profile had to be approximated.

#### 7. ACKNOWLEDGEMENTS

We thank Don Trent and Loren Fyler for their help with TFMEST, and Bob Lentz and Mike Shook for their help with the computing systems used for the computations and plotting. This work was supported by EPA Grant R-811877-01 and the com-

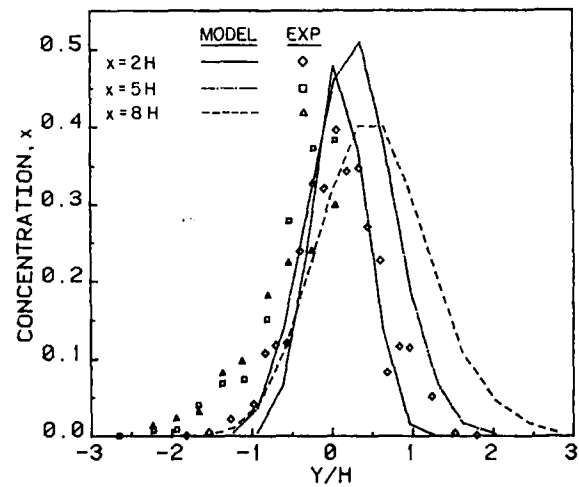


Figure 13. NONDIMENSIONAL LATERAL GROUND LEVEL CONCENTRATIONS PROFILES.

puting was done at the Washington State University Computing Center on an IBM 3090.

#### 8. REFERENCES

Amsden, A.A. and Harlow, F.H. 1970. The SMAC method: a numerical technique for calculating incompressible flows. Los Alamos Scientific Laboratory Report LA-4370.

- Blackadar, A.K. 1962. The vertical distribution of wind and turbulence exchange in a neutral atmosphere. *J. Geophys. Res.* 67: 3094-3102.
- Detering, H.W. and Etling, D. 1985. Application of the F- $\epsilon$  turbulence model to the atmospheric boundary layer. *Boundary Layer Meteor.* 33: 113-133.
- Douglas, J. 1962. Alternating direction methods for three space variables. *Numerische Mathematik.* 4: 41-63.
- Lettau, H.H. 1962. Theoretical wind spirals in the boundary layer of a barotropic atmosphere. *Beitr. Phys. Arm.* 35: 195-212.
- Panofsky, H.A., Tennekes, H., Lenschow, D.H., and Wyngaard, J.C. The characteristics of turbulent velocity components in the surface layer under convective conditions. *Boundary Layer Meteorol.* 11: 355-361.
- Robins, A.G. 1987. Plume dispersion from ground level sources in simulated atmospheric boundary layers. *Atm. Env.* 12: 1033-1044.
- Ryan, W., Lamb, B., and Robinson, E. 1984. An atmospheric tracer investigation of transport and dispersion around a large isolated hill-part I-daytime and day-night transitions periods. *Atm. Env.* 18:10 2003-2021.
- Thompson, R.S. and Lombardi, D.J. 1977. Dispersion of roof-top emission from isolated buildings: a wind tunnel study. EPA-600/4-77-006.
- Trent, D.S., Eyler, L.L., and Budden, M.J. 1983. TEMPEST a three-dimensional time-dependent computer program for hydrothermal analysis. Pacific Northwest Laboratory, PNL-4348 Vol. 1.

FLOWS WITH STRONGLY ANISOTROPIC TURBULENCE - DYNAMIC AND HEAT  
TRANSFER ASPECTS

H. Branover and S. Sukoriansky

Center for MHD Studies

Ben Gurion University of the Negev

P.O.B. 653, Beer Sheva 84105, Israel

**ABSTRACT**

Turbulent flows with clearly expressed inverse energy cascades have been arranged and studied. The experiments have been performed with mercury flows submitted to the influence of external magnetic fields. Turbulence intensity data, and even more energy spectra, indicated the existence of an inverse energy cascade. Such small scale flows can possibly be used for simulation of some phenomena in atmospheric turbulence.

The present work was undertaken with the goal of providing additional evidence for verification of hypotheses on turbulence structure and transfer mechanism changes developed in previous studies. For this purpose, provisions have been made which allowed intensity and spectrum measurements at different distances from flow entrance into the magnetic field so that time dependent expansion of magnetic field influence on different parts of spectra could be detected. Furthermore, different turbulizing grids have been introduced which permitted making comparisons between small and large scale forced turbulence with different directions of turbulizing elements in respect to the magnetic field (rods with axes perpendicular or parallel to magnetic field direction).

Heat transfer processes in such flows have been assessed and strong enhancement of heat transfer have been predicted. This prediction has been confirmed also experimentally. These results are important for a number of technological applications, specifically for the design of nuclear fusion reactors.

## NOMENCLATURE

B	=	magnetic field induction
D	=	hydraulic diameter of the channel's cross-section
Ha	=	$BD (\sigma/\rho\nu)^{1/2}$ = Hartmann number
f	=	pulsation frequency
k	=	wave number
N	=	$\sigma B^2 D/\rho U$ = Stuart number (interaction parameter)
Re	=	$UD/\nu$ = Reynolds number
U	=	mean velocity
u'	=	velocity fluctuation
$\epsilon$	=	energy transfer rate
$\nu$	=	kinematic viscosity
$\rho$	=	density
$\sigma$	=	electrical conductivity
$\chi$	=	thermal diffusivity
$c_p$	=	specific heat capacity

## INTRODUCTION

Over the last two decades there has been a permanently growing interest in unusual structures in general and in two-dimensional turbulence in particular and in modification of turbulent transfer properties. Typical examples of two-dimensional turbulence can be observed in atmospheric motions influenced by Coriolis forces. However, it is quite difficult to arrange an experiment reproducing this type of turbulence and in any case it is achievable only in very big experimental facilities. An interesting alternative way to study two-dimensional turbulence with strongly modified transfer properties (inverse energy cascades, strong anisotropy of transfer properties, etc) is presented by flows of electro-conductive fluids in the presence of external magnetic field producing an additional, easily controlled, body force.

A number of experimental studies of this kind have been performed by using mercury flows in the presence of transverse magnetic field.<sup>1-14</sup> A review of most of these experimental studies can be found in Ref.15. The earliest studies already discovered striking phenomena that, while judging upon experimental data of pressure drop, an initially turbulent flow could be laminarized by means of applying a strong enough magnetic field; however, local velocity measurements indicated persistence or even growth of disturbances. Taking into account the fact that a magnetic field does not influence the structure of a flow, which is two-dimensional in the plane transverse to the field,<sup>15</sup> and considering also theoretical results<sup>16</sup> predicting anisotropy of turbulence in magnetic fields, it was concluded that while the magnetic field suppresses the normal mechanism of generation of shear turbulence, residual two-dimensional turbulence can have a very high intensity and a very low decay rate. Later, unconventional -3 slopes in experimental spectra were detected

and in some, although few, cases existence of a -3 slope in the high wave number region along with a -5/3 slope in the lower wave number region was found. All that has been interpreted as manifestation of an inverse energy cascade (where -5/3 slope existed) and enstrophy cascade (where -3 slope existed) - both predicted by two-dimensional turbulence theory.<sup>17-19</sup>

Despite the fact that a relatively great effort was done to investigate the peculiarities of turbulence in electroconductive flows affected by magnetic fields, and that the number of above referred-to publications which appeared over the last two decades is quite impressive, little evidence was obtained regarding the mechanism in which a two-dimensional turbulence with amplified low frequency fluctuations was established. In other words, little light was shed on the question how does a "normal" three-dimensional turbulence with a conventional energy cascade and energy dissipation process develop - after a magnetic field is applied - into a two-dimensional amplified low frequency turbulence with a supposedly inverse energy cascade and low rate of energy dissipation, and what are the transient states. Moreover, in all experimental studies the obstacle placed into the flow for generation of forced turbulence had a relatively very large scale and therefore it was difficult to make the distinction between two possibilities:

- (a) that the amplification of low wave number disturbances in flows with strong magnetic fields is due to the establishment of an inverse energy cascade, transferring turbulent energy from the high wave number region down the spectrum, or
- (b) that the magnetic field directly influences the forced turbulence generation process, and the higher the magnetic fields the lower wave number high-energy disturbances are generated.

Those are just a few examples which illustrate some (out of many more) uncertainties which remained. As a matter of fact, the only relatively well established fact was that in magnetic fields turbulence disturbances have a tendency toward two-dimensionality. Whether they actually become ultimately two-dimensional depends, as shown by Sommeria and Moreau<sup>11</sup> on the geometry of the boundaries. As regards the existence of inverse energy cascades, the only supporting evidence has been the observation of a -5/3 slope and increase of energy of low frequency disturbances in very few of the measured spectra.

In view of all the above the present study has been undertaken with the following main goals:

- 1) To clarify with possible trustworthiness the existence of an inverse energy cascade;
- 2) To ascertain details (qualitative and, if possible, also quantitative) of mechanisms and transient states in the process of rearrangement of turbulence structure;
- 3) To assess the possible technological implications of observed phenomena.

Elaboration of this program is going on already for a number of years and is still quite far from completion. Preliminary results have been published in.<sup>20,21</sup> Since then, a substantial amount of new experimental data has been obtained, and its analysis now permits to present a satisfactory, although not yet comprehensive, description and explanation of the phenomena considered.

## Some General Definitions and Descriptions of Experimental Facility and Instrumentation

While considering turbulent phenomena in a flow of the above described type, it is desirable to introduce the following characteristic time scale for an eddy of size  $l$  ( $\sim 2\pi/k$ )

$$t_{tu} = l/u_1 - \text{eddy turnover time}$$

$$t_j = \rho / \sigma B^2 - \text{Joule time}$$

where  $u_1$  is velocity of the  $l$ -scale fluctuation.

The interaction parameter  $N_k = t_{tu}/t_j$  expresses the ratio of intensities of the Joule dissipation and eddy distortion processes.

It should be emphasized that the Joule time scale is independent of the fluctuation scale and can easily be controlled by changing the magnetic field flux density  $B$ . In this way, the magnetic field influence can be "tuned" to different scales of turbulence influencing substantially only fluctuations with lowest wave number at weak field and progressively expanding this influence towards ever larger wave number when the field increases. Indeed,  $t_{tu}$  represents the characteristic time required for the eddy to be distorted, and as a result, small scale eddies to be generated (direct energy cascade).  $t_j$  represents the characteristic time in which a fluctuation is substantially changing its structure due to Joule mechanism of energy dissipation. Therefore, if  $t_{tu} < t_j$  the fluctuation breaks up before it experiences the influence of the magnetic field. If the scale for which  $t_{tu} = t_j$  is designated by  $l_{em}$  then for the region where  $l < l_{em}$  conventional turbulence persists, however, with reduced energy transfer rate  $\epsilon$ . Obviously,  $k = 2\pi/l$  value corresponds to  $N_k = 1$ . In this way, it is possible to divide the whole turbulent scales region into two different parts by setting a definite value of magnetic field  $B$ . In one of these parts turbulence does not undergo principal qualitative changes, as shown above, while in the other part of the region it changes very dramatically in a way which will be described below.

For accomplishing the goals of the present work provisions were made which allowed intensity and spectrum measurements at different distances from flow entrance into the magnetic field, so that time-dependent expansion of magnetic field influence on different parts of spectra could be detected. Furthermore, different turbulizing grids have been introduced which permitted making the comparisons between small and large scale forced turbulence with different directions of turbulizing elements in respect to the magnetic field (rods with axes perpendicular or parallel to magnetic field direction and combination of both).

The schematic diagram of the experimental facility is presented in Fig. 1. The facility has a pump, an overflow constant level tank with a number of dense meshes for quietening the entering flow disturbances and a constant level sump tank. The tanks are provided with water cooling which keeps the mercury temperature constant within an  $0.5^\circ\text{C}$  accuracy.

The experimental channel, made from perspex, has a rectangular  $2 \times 4.8 \text{ cm}^2$  cross-section. Magnetic field is directed transverse to the longer side of the channel cross-section. In one part of the experiments different honeycombs, made of an assembly of electrically insulated tubes, were used. The external diameter of the pipes of the first honeycomb is 2.4 mm, the second 3.5 mm,

and the third 5.4 mm. The corresponding wall thicknesses of the honeycomb tubes are 0.3, 0.1 and 0.18 mm. The solidity of the honeycombs is  $\sim 0.25$  for the first honeycomb, 0.1 for the second, and 0.06 for the third. The length of the honeycomb in the flow direction is 25 cm. A variety of grids was used for creating different kinds of flow disturbances. Three grids were made from plastic rods approximately 5 mm in diameter, which were placed at intervals equal to their diameter. The rods of the first grid are oriented perpendicular to the magnetic field, of the second parallel to the field, and in the third grid the rods are placed crosswise. The solidity of this last grid is  $\sim 0.66$ . The fourth grid was made from very thin strings, 0.2 mm in diameter, placed crosswise with a distance between the strings of 4 mm. The solidity of this grid is  $\sim 0.2$ .

The electromagnet pole length is 90 cm and magnetic field can vary from 0 to 1.1 T. The magnet can easily be moved along the channel. In this way a different situation can be created, as follows. The source of forced turbulence can be placed either in the magnetic field or at different distances upstream of the magnet. In the last case, providing that the distance from the turbulent source to the poles of the magnet were greater than the pole height it was possible to neglect magnetic field influence on turbulence generation. The only magnetic interaction is with the turbulence existing at the entrance to the magnetic gap.

The mercury flow rate is measured by a venturi flow meter with liquid manometers. Experiments have been performed at mean velocity value  $U = 0.3$  m/sec corresponding to  $Re = 73.3 \times 10^3$ . In several experiments  $Re$  was  $78.5 \times 10^3$ .

Local velocity measurements have been performed by means of TSI quartz-coated hot film probes (1212-20 HG model with 0.05 mm sensor diameter and 1 mm sensor length). The signal was processed through a Disa 55M system with a 55M10 constant temperature standard anemometric bridge. The usual probe overheating ratio was 5%. Spectral functions were obtained by means of FFT Spectrum Analyzer (Spectral Dynamics Model SD 340). The spectrum analyzer performed the calculations for frequencies up to 500 Hz with 1.25 Hz resolution (time window 0.8 sec), using 64 ensembles for averaging. Using the Taylor hypothesis, corresponding wave numbers  $k = 2\pi f/U$  have been established.

#### **Attempts to Use a Honeycomb for Elimination of Background Turbulence and Mean Flow Profile Disturbances in a Flow Entering a Magnetic Field, and Actual Results**

For accomplishing the goals of this study it was assumed that one of the necessary preconditions is the elimination of penetration of any turbulence from upstream into the test section with magnetic field. To achieve that placing of fine honeycombs into the flow upstream of the test section was suggested. It seemed obvious that to be efficient the honeycomb has to be extended into the section with magnetic field since the entrance of a flow in a magnetic field is accompanied by a substantial rearrangement of velocity profiles which can yield new turbulence disturbances also in a case when all fluctuations carried from upstream have been suppressed.

It was expected that with the honeycomb placed in the way described above, the flow in the

test section with magnetic field will have an extremely low background turbulence level which would permit performance of experiments at "clean" and well-controlled conditions. It was also believed that very small scale and arbitrary oriented disturbances generated by the tail section of the honeycomb will not have any substantial impact on the flow. However, already the first measurements of turbulence intensity and later of spectra lead to unexpected and quite dramatic results.

Fig. 2 shows turbulence intensity as a function of the magnetic field strength (which is represented by the ratio of  $Ha/Re$ ) for different flow situations: (I) honeycomb is covered by the magnetic field, (II) the magnetic field begins at a distance of  $5.5 D$  downstream from the honeycomb ( $D$  is the hydraulic diameter of the channel's cross-section), and (III) there is no honeycomb in the channel. Comparing Fig. 2.II and 2.III one can observe that turbulent intensity is slightly smaller in case of a honeycomb placed upstream of the magnet, than without a honeycomb. Changes of turbulence intensity when  $Ha/Re$  is increasing are identical in cases II and III. Namely,  $u'/U$  reaches approximately 30-40% of the initial level without magnetic field at  $Ha/Re \sim (2:3) \times 10^{-3}$  and then remains practically constant up to the highest experimental value of  $Ha/Re$ . However, when the magnetic field is applied over the honeycomb section, the influence of the field on intensity of turbulence is significantly different (Fig. 2.I): intensity reaches a minimal value, exactly as in the cases above, but after that intensity increases strongly with further increase of the  $Ha/Re$  value, reaching a level two or more times higher than the initial level without magnetic field.

Experimental spectra are presented in Figs. 3,4. When the honeycomb is not covered by the magnetic field (Fig. 4), energy density in the low wave number region gradually decreases with the increase in the value of  $Ha/Re$ . There is a slight tendency in the low wave number region towards steeper slope and simultaneously the energy density at higher wave numbers decreases while the  $-5/3$  slope is preserved in the inertial range (conventional energy cascade with lower  $\epsilon$ ). At  $Ha/Re \sim 5 \cdot 10^{-3}$  and higher low wave number energy density remains almost constant, but at  $k > 5 \cdot 10^2$  (former inertial range) the slope becomes clearly  $-3$ .

When the field covers the honeycomb (Fig. 3), energy density at low  $k$  initially goes down when  $Ha/Re$  increases as in the previous case. However, at higher  $Ha/Re$  values energy density *increases* in the low  $k$  region. This coincides with intensity measurements for the same case presented above.

The striking results described above permit to formulate the following working hypothesis.

In a gradually increasing magnetic field three-dimensional components of flow disturbances are increasingly suppressed (starting from the largest scales) so that for a given wave number  $k_i$  there is a value of magnetic field  $B_{ki}$  at which  $N_{ki} \sim 1$  and for  $B > B_{ki}$  only close to two dimensional components of disturbances with wave numbers  $k \leq k_i$  remain. Providing that at  $k_i$  there is turbulent energy injection the turbulent energy in the  $k \leq k_i$  is transferred to the lower wave number end of the spectrum (inverse cascade) and this results in amplification of energy density in

the low  $k$  region. At  $k < k_i$  the slope of spectra should be  $-5/3$ . The development of the inverse cascade demands time and therefore the  $-5/3$  slope zone should gradually expand from  $k \approx k_i$  towards the lowest  $k$  region.

Regarding the experiment with a honeycomb described above, the working hypothesis permits the following explanation of the results obtained. The turbulence observed in the channel without a magnetic field is the developing wall shear turbulence. The tail part of the honeycomb generates turbulence at high frequencies (from characteristic wave number  $k_i$  and up) and without a magnetic field disturbances of such frequencies disappear fast because of viscose dissipation and in practice do not influence the residual turbulence. Since generation of wall shear turbulence occurs in the low frequency part of the spectrum, the increase of magnetic field results in decrease of the energy flux towards high frequencies. When the field becomes strong enough ( $N_{ki} \sim 1$ ) the influence of the field reaches the disturbances generated by the honeycomb's tail, and from that moment and further the energy of those disturbances is no more dissipated but rather transferred towards lower frequencies. This results in the increase of energy of low  $k$  disturbances and in an increase of turbulence intensity.

#### Scrutiny of the Working Hypothesis

First of all let us investigate whether the reason of all the observed phenomena is not the change of disturbance generation conditions. A comparison of turbulence intensities in the case when the honeycomb tail is not covered by the magnetic field with the case without a honeycomb shows that turbulent intensity is almost equal at all magnetic field values (Figs. 2.II and 2.III). Comparison of turbulence spectra for flows with different honeycombs (solidity 0.25 and 0.1) placed upstream of the entrance to magnetic field shows almost completely identical results for all the measured  $k$  ranges for different magnetic field values (Fig. 4). Hence, the influence of pulsations generated by the honeycomb outside the field on turbulence development is negligible.

For the further analysis it is desirable to assess the characteristic value of  $k_i$  for pulsations appearing as a result of mixing adjacent jets exiting the honeycomb. Since the pipe diameter for the first honeycomb is 2.4 mm and pipe wall thickness 0.3 mm, one can assume that the characteristic scale of pulsation is  $\sim 1$  mm which corresponds to  $k_i \sim 6,000 \text{ m}^{-1}$ .

As it was described above, in the case when the honeycomb is in the magnetic field, energy of the low frequency part of the spectrum is growing fast, starting from a definite magnetic field value (Fig. 3). The energy at  $k < 3 \cdot 10^2$  grows approximately ten times. Those wave numbers are more than by an order of magnitude different from  $k_i$  and therefore it is impossible to assume generation of disturbances with such wave numbers directly at the exit from the honeycomb pipes. This confirms again the hypothesis about the existence of an inverse energy cascade.

Let us now assess the value of the magnetic interaction parameter  $N_{ki}$  at which phenomena characteristic for the inverse energy cascade appear. One can make an estimation for  $N_{ki}$  from the following expression:

$$N_{ki} \sim \sigma B^2 / \rho k_i u_{ki} \quad (1)$$

where  $u_{ki}$  is the characteristic velocity of the pulsation with wave number  $k_i$ . This velocity can be evaluated from  $u_k \sim (kE(k))^{0.5}$ . Taking  $k_i \sim 6,000 \text{ m}^{-1}$  one can find that  $E(k_i) \sim 10^{-9} \text{ m}^3 \text{ s}^{-2}$  (see Fig. 3). This implies a value  $u_{ki} \sim 2.4 \cdot 10^{-3} \text{ m/s}$ . Results presented in Fig. 3 show that the inversion of energy cascade occurs at  $3.5 < Ha/Re \cdot 10^3 < 5.5$  which corresponds to magnetic flux density values  $0.35 \text{ T} < B < 0.55 \text{ T}$ . Taking for the critical value of magnetic field flux density the middle of this interval, we obtain  $B = 0.45 \text{ T}$  and  $N_{ki} \sim 1.1$ .

For further verification of the working hypothesis experiments with honeycombs having different solidity were performed. Energy spectra were measured at different distances (10.5, 23 and 43 cm) from the honeycomb (Figs. 5 - 7). Different solidity resulted in a different level of energy transfer rate  $\epsilon$  in the inverse cascade and, consequently, in slightly different levels of energy at low frequencies in strong magnetic fields. Thus, the energy was higher the greater the solidity. In other respects the spectra were completely analogous in cases with different honeycombs. The evaluation of  $N_{ki}$  resulted in values  $\sim 1$  in all cases.

Very similar results were obtained also in the measurements of turbulence behind the grid made from cross-wise strings (solidity 0.2, string diameter  $\sim 0.2 \text{ mm}$ ) (Fig. 8).

For the low  $k$  region ( $10^2 < k < 10^3$  at all probe locations application of medium magnetic field causes a decrease of energy density, while at stronger magnetic field energy density increases beyond the values without magnetic field. This is a general qualitative tendency.

Quantitatively, there are differences in magnetic field influence for different probe locations. It should also be mentioned that energy density without magnetic field slowly increases with the increase of distance. For higher  $k$  values without magnetic field there is no clearly expressed inertial range with  $-5/3$  slope (except for the largest distance from honeycomb where there is a rather short  $k$  range with slope close to  $-5/3$ ). However, for the higher value of  $Ha/Re$  the shape of the spectra curves undergoes the two following major changes:

- a) a range with slopes close to  $-5/3$  appears becoming clearer expressed with the increase of distance;
- b) while in the curve obtained with the probe closest to honeycomb there is a strongly-manifested plateau with  $E(k) \sim \text{const.}$ , stretching up to  $k \approx 10^3$  values, with increase of distance this plateau is reduced (remaining only in lower  $k$  range) and disappears almost completely at the largest distance; simultaneously, the  $-5/3$  slope region expands towards lower  $k$  values and ultimately becomes dominating for almost the entire experimental  $k$  range (see for illustration Fig. 5.d).

It is reasonable to assume, that the establishment of the  $-5/3$  slope of the spectra at higher magnetic field values, with simultaneous increase of energy density at low  $k$  values, reflects the existence of an inverse energy cascade. In this respect, it is interesting to check how the expansion of the  $-5/3$  range with increase of distance from the forced turbulence source (tails of honeycomb

tubes) coincides with assessment based on energy conservation considerations.<sup>22</sup>

$$k_{\min}(t) \sim \epsilon^{-1/3} t^{-3/2} \quad (2)$$

where  $k_{\min}$  is the smallest wave number reached by the inverse energy cascade in time  $t$ . (In spite of the fact that in our case there is no continuous forcing of turbulence, as in Ref. 22, one can suppose that kinematic of turbulent movement is similar.)

In our case time  $t$  is connected with the distance  $x$  between the forced turbulence source and the probe ( $x \sim t$ ). Since for a flow with an inverse energy cascade  $\epsilon$  is independent of distance (time) at a given magnetic field,

$$\frac{k_{\min}(x_1)}{k_{\min}(x)} \sim \left( \frac{x_1}{x} \right)^{-3/2} \quad (3)$$

where  $x$  and  $x_1$  are 2 different distances from the forced turbulence source to the probe.  $x_1$  designates the maximal distance. The values of  $x$  were 43.5, 23 and 10.5 in experiments with honeycombs and 40, 20 and 7.8 in experiments with a string-made grid. Corresponding values of  $k_{\min}(x)$  were taken from the spectra curves. Results are given in Fig. 9. The deviation of experimental values from the expression 3 is greater for weaker turbulizers. It permits to assume that the reason of such deviation is the dissipation of turbulence energy.

The next series of experiments were made with dense grids of different configurations. Typical for those grids is generation of strong turbulence in the wide frequency interval, including low frequencies. The level of grid generated turbulence is so high that it is possible to neglect the influence of the honeycomb. Use of grids with different configurations permit generation of turbulent disturbances differently oriented in respect of the magnetic field. It is reasonable to assume that in the case when grid elements are perpendicular to the magnetic field, inverse energy cascade does not appear, since in such cascade only two-dimensional pulsations which are not suppressed by the magnetic field can participate. In the case considered here, however, the generated disturbances are strongly suppressed through Joule dissipation. On the other hand, in the case of a grid with elements parallel to the field one can expect that the inverse energy cascade will be manifested very strongly.

Intensity measurements given in Figs. 10-11 and spectra in Figs. 12-13 completely confirm these considerations. Decrease of turbulence intensity in Fig. 11 in strong fields is very dramatic and the residual level is only slightly higher than the level in experiments without any grids or honeycombs (Fig. 2.III). At the same time for cases with rods parallel to the field a very strong intensity increase was observed and the intensity in strong fields were by an order of magnitude higher than in a free channel.

Analysis of experimental spectra leads to the following conclusions. For grid elements perpendicular to magnetic field,  $E(k)$  decreases strongly at all  $k$  when the  $k > 10^3$ , while  $k \sim 10^3$  corresponds to the size of forced eddies, generated by the grid. At this stage, it is not enough evidence to conclude whether the  $-3$  slope indicates an enstrophy cascade or it has to be attributed to the angular energy transfer in magnetic fields, as discussed in Ref.10.

In the case when grid elements are parallel to the magnetic field, an extremely "clean"  $-5/3$  slope persisting in the entire experimental range  $10^2 < k < 10^4$  is manifested in strong magnetic field. This is best seen in the case when the measurements were done closest to the grid (Fig. 13a). Energy density increases with increase of field first at low  $k$  values, but later this phenomenon expands at the entire  $k$  range. With distance from grid increasing substantial dissipation is observed, the level of  $E(k)$  is going down but at higher field values the  $-5/3$  slope still persists.

Results of experiments with dense crosswise grid are given in Fig. 14. Since this grid can be regarded as a superposition of both cases discussed above, one can expect results having features common with each of those cases. In particular the influence of a magnetic field should be manifested in suppression of pulsations perpendicular to the field (leading to initial decrease of turbulence intensity) and for stronger fields in the establishment of an inverse cascade in which the two-dimensional pulsations take part. Thus, in this case one can also expect the appearance of  $-5/3$  slopes in the spectra and in the gross of the total turbulence intensity. Indeed, these features can be easily observed in Fig. 14. In weak magnetic fields the energy of all wave numbers comes down, however, when the field increases (beginning from  $B \approx 0.25$  T), the energy of low wave numbers begins to increase. The above value of  $B$  is considerably lower than in the honeycomb experiments. This is consistent with the fact that the minimal frequency generated by the grid is substantially lower than that of honeycomb generated pulsations.

As mentioned above, dense grids generate turbulence in a wide interval of frequencies. This gives an additional opportunity to verify our working hypothesis, namely to check that  $N_{k_i} \approx 1$ . Indeed, for frequencies generated by the grid, the spectrum curve is flat with a slight slope. In the region of two-dimensional pulsations the slope has to be characteristic for an inverse cascade, namely  $-5/3$ . This enables the location of the point where the change of slope occurs on the spectral curves for different fields. The wave number at this point corresponds to the maximum extent of the magnetic field where its effect is significant in making the disturbances two-dimensional. Among all the figures presented in the paper two such points are clearly indicated: wave number  $k \sim 400 \text{ m}^{-1}$  at  $B = 0.3 \text{ T}$  (Fig. 13b) and  $k \sim 450 \text{ m}^{-1}$  at  $B = 0.4 \text{ T}$  (Figs. 14b and 14d). Corresponding values of energy density equal to  $2.2 \cdot 10^{-7} \text{ m}^3/\text{s}^2$  and  $1.3 \cdot 10^{-6} \text{ m}^3/\text{s}^2$  respectively. Using formula (1),  $N_k$  is evaluated  $\sim 1.9$  in the first case and  $\sim 1.1$  in the second.

The change of slope on the spectrum moves towards greater  $k$  values when the magnetic field increases. Unfortunately it is not easy to detect the exact position of this point in strong fields since for high  $k$  the spectrum has a sharp slope even without the magnetic field.

One more proof of the working hypothesis can be found using Fig. 15, where spectra for different magnetic fields are presented in the case when a grid with elements parallel to the field was placed at a distance of 18 cm upstream from the beginning of the magnetic field region. At such distances, as mentioned above, the influence of the magnetic field on turbulent generation is negligible. Therefore the peculiarities of the spectrum in Fig. 15 in strong magnetic fields ( $E(k) \sim k^{-5/3}$  and the amplification of energy on low frequencies) can be explained only as the influence of the magnetic field on turbulence generated by the grid and brought by the flow into the magnetic field region.

### Assessment of Heat Transfer Enhancement

The strongly anisotropic turbulent flow, described above, is characterized by an almost two-dimensional turbulent velocity field in the plane perpendicular to the magnetic field. This two-dimensional turbulence does not cause substantial momentum transfer. Nevertheless, it can have a very strong effect on the transfer of passive scalar quantities, such as heat and mass.

Obviously, practical utilization of the turbulent enhancement effect of magnetic fields is much dependent on the rate of decay of such anisotropic turbulence. As follows from Ref. 11, turbulence disturbances in strong fields in channels with insulated walls can be described as a multitude of vortices with axis parallel to the field and perpendicular to channel walls. The two-dimensionality of the flow is disturbed only in the very narrow Hartmann layer near the walls. As is well known, two-dimensional vortices parallel to the field are not affected by the magnetic field. Therefore, the only mechanism, through which energy of those vortices can be dissipated, is the Hartmann friction in the very narrow wall layer. This leads to braking of those vortices. In Ref. 11 evaluation of characteristic time  $t_H$  of such braking is given:

$$t_H = D/B (\rho/\sigma\nu)^{1/2} = D \cdot Re/UHa,$$

which is independent of the vortex size, if the Ha parameter for such vortex is large.

In most practical cases  $Re/Ha \gg 1$ , hence quasi-two-dimensional vortices will persist over a long period of time.

To illustrate the effect of turbulence enhancement in magnetic fields on heat transfer rate, we treated numerically the problem of a liquid metal flow between two parallel plates (with distance  $L$  between them), one of which is subject to a constant heat flux

$$\chi \rho c_p \frac{\partial T}{\partial y} \Big|_{y=0} = q'' \quad (4)$$

and the other is thermally insulated

$$\frac{\partial T}{\partial y} \Big|_{y=L} = 0 \quad (5)$$

The corresponding stationary heat transfer equation is

$$U(y) \frac{\partial T}{\partial x} = \frac{\partial}{\partial y} \left( \chi(y) \frac{\partial T}{\partial y} \right) + \frac{Q(y)}{\rho c_p} \quad (6)$$

The total thermal diffusivity,  $\chi(y)$ , required in this equation, was deduced from the theoretical model for locally isotropic turbulent flows, developed in Ref. 23. This model, which proved to be accurate for heat transfer calculations of fully developed turbulent liquid metal flows in ducts, cannot be applied directly to strongly non-isotropic turbulent flows. Therefore, additional semiempirical considerations were used. From semiempirical theories it is known that turbulent heat diffusivity is proportional to the product of the integral scale of turbulence and the turbulence intensity. The experimental results of the present work can be used to estimate the effect of a magnetic field on these factors.

Thus, the procedure adopted for the calculation of the flow temperature distribution in the presence of a strong transverse magnetic field was as follows. The first step was to calculate the heat diffusivity in locally isotropic turbulence. This parameter was then scaled by an amplification factor, based on our experimental results (of 20 in the results presented below) to account for the effect of the inverse energy cascade. Equation (6) was solved using this heat diffusivity and an MHD flow velocity profile.

The heat generation term has the form

$$Q = Q_0 e^{-cy}.$$

Furthermore, the flow is assumed to be thermally fully developed, (i.e.  $T(x,y)$  is the superposition of a linear function of  $x$  and an unknown function of  $y$ ).

The illustration was carried out for channel conditions typical for poloidal-flow blankets of fusion reactors: the channel depth was 0.4 m, the first wall was subjected to a heat flux  $q'' = 0.5 \text{ MW/m}^2$ , a total power of 5.9 MW was deposited in the blanket per square meter of the first wall area, and the factor  $c$  in the heat generation term was set to 3.5. The laminar Prandtl number for lithium was taken to be 0.0362.

Fig. 16 compares the Nusselt number, calculated for the nonisotropic turbulent flow in a strong traverse magnetic field, with the corresponding Nusselt number, calculated for a magnetic field free isotropic turbulent flow and for a laminar flow. The latter corresponds to the flow regime assumed, up until now, to prevail in a fusion reactor blanket environment.

The Nusselt number is defined to be

$$Nu = \frac{2q''L}{c_p \rho \chi_0 (T_w - \bar{T})} \quad (8)$$

where  $\bar{T}$  is the average liquid metal bulk temperature,  $T_w$  is the interface temperature between the

first wall and the liquid metal, and  $\chi_0$  is laminar thermal diffusivity. In the laminar case the large difference between  $T_w$  and  $\bar{T}$  occurs because the flow is assumed to be thermally fully-developed. For the poloidal-flow blanket geometry this assumption is not valid. Nevertheless, for enhanced turbulence heat transfer the flow can be treated with reasonable accuracy as thermally fully-developed, since the estimated Fourier number (i.e., the ratio of the fluid residence time to the cross-channel conduction time) was greater than one.

The above calculations predict the enhancement of heat transfer an order of magnitude compared with locally isotropic turbulence in the channel free from any obstacles, and two orders of magnitude compared with heat transfer in laminar flow. Of course, the calculation is based on a very approximate model and should be treated as a preliminary indication of expected phenomena. Further experiments must be carried out in order to verify the existence of the effect of heat transfer enhancement in magnetic fields in channels with turbulence inducing means. These experiments are at present in preparation at BGU, and the first one of its kind has recently been made in the experimental facility described above.

A flat heating element, 1 m long and its width equal to the channel width, was placed on the bottom of the channel. This element was covered by copper plate 5 mm thick. For generation of eddies with the axis parallel to the magnetic field, the grid with rods parallel to the field was placed in the entrance section of the channel. Thermocouples were used for temperature measurements in the middle of the channel and on the surface of the heated plate. The measured difference between the temperature of the wall and the average bulk temperature is presented in Fig. 17.

At this preliminary stage only few °C overheat of the copper plate was attainable and it was impossible to exclude influence of some turbulence inducing factors, generating strong disturbances with orientation transverse to the magnetic field. However, even under such unfavorable conditions the effect of heat transfer enhancement due to rearrangement of turbulence was clearly manifested.

#### ACKNOWLEDGMENTS

This work was supported by SOLMECS (ISRAEL) LTD. We are also grateful to Ilya Zilberman, Aharon Ratner, Dov Kleiman and Moshe Poizner for their help in the preparation and performance of experiments; to Prof. Ehud Greenspan, who made us aware of the importance of the phenomena researched in this paper towards the development of fusion reactors, and for his great help in preparing the section dealing with this aspect.

## REFERENCES

1. Branover, H.H., Slyusarev, N.M., and Scherbinin, E.V., 1965, "Some Results of Measuring Turbulent Pulsation of Velocity in a Mercury Flow in the Presence of a Transverse Magnetic Field," *Magnitnaya Gidrodinamika*, Vol. 1, p. 33.
2. Branover, H.H., Gelfgat, Yu.M., Kit, L.G. and Platnick, E.A., 1974, "Effect of a Transverse Magnetic Field on the Intensity Profiles of Turbulent Velocity Fluctuations in a Channel of Rectangular Cross Section," *Magnitnaya Gidrodinamika*, Vol. 3, p. 41.
3. Gardner, R.A. and Lykoudis, P.S., 1971, "Magneto-Fluid-Mechanic Pipe Flow in a Transverse Magnetic Field. Part I, Isothermal Flow," *Journal of Fluid Mechanics*, Vol. 47, p. 737.
4. Kolesnikov, Yu.B. and Tsinober, A.B., 1972, "Two-Dimensional Turbulent Flow behind a Circular Cylinder," *Magnitnaya Gidrodinamika*, Vol. 3, p. 23.
5. Kolesnikov, Yu.B. and Tsinober, A.B., 1974, "An Experimental Study of Two-Dimensional Turbulence behind an Array," *Mekhanika Zhidkosti i Gasa*, N.4, pp. 146-151.
6. Hua, H.M. and Lykoudis, P.S., 1974, "Turbulence Measurements in a Magneto-Fluid-Mechanic Channel," *Nuclear Science and Engineering*, Vol. 54, p. 445.
7. Votsish, A.D. and Kolesnikov, Yu.B., 1976, "Transition from Three-Dimensional to Two-Dimensional Turbulence in a Magnetic Field," *Magnitnaya Gidrodinamika*, Vol. 3, pp. 141-142.
8. Votsish, A.D. and Kolesnikov, Yu.B., 1976, "Spatial Correlation and Vorticity in Two-Dimensional Turbulence," *Magnitnaya Gidrodinamika*, N.3, pp. 25-28.
9. Branover, H.H. and Gershon, P., 1979, "Experimental Investigation of the Origin of Residual Disturbances in Turbulent MHD Flows after Laminarization," *Journal of Fluid Mechanics*, Vol. 94, p. 629.
10. Alemany, A., Moreau, R., Sulem, P.L., & Frish, V., 1979, "Influence of an External Magnetic Field on Homogenous MHD Turbulence," *Journal de Mecanique*, Vol. 18, No. 2, pp. 277-313..
11. Sommeria, J. & Moreau, R., 1982, "Why, How, and When, MHD Turbulence becomes Two-Dimensional," *Journal of Fluid Mechanics*, Vol. 118, pp. 507-518.
12. Sommeria, J., 1983, "Two-Dimensional Behaviour of MHD Fully-Developed Turbulence," *Journal de Mecanique Theorique et Appliquee*, Numero Special, p. 169.
13. Seluto, S.F., 1984, "Influence of Magnetic Field on Formation of Turbulent Structure Behind the Grids with Different Configurations," *Magnitnaya Gidrodinamica*, N.3, pp. 55-60.

14. Sommeria, J., 1985, "Two-Dimensional Behavior of Electrically Driven Flows at High Hartmann Numbers," Single- and Multi-Phase Flows in an Electromagnetic Field. Progress in Astronautics and Aeronautics, H. Branover, P.L. Lykoudis and M. Mond, Eds., AIAA, N.Y., V. 100, p. 77-78.
15. Branover, H.H., 1978, Magnetohydrodynamic Flow in Ducts, Halsted Press.
16. Moffatt, H.K., 1967, "On the Suppression of Turbulence by a Uniform Magnetic Field," Journal of Fluid Mechanics, Vol. 28, p. 571.
17. Kraichnan, R.H., 1967, "Inertial Ranges in Two-Dimensional Turbulence," Physics of Fluids, Vol. 10, p. 1417.
18. Leith, C.E., 1967, "Diffusion Approximation for Two-Dimensional Turbulence," Physics of Fluids, Vol. 11, p. 671.
19. Batchelor, G.K., 1969, "Computation of the Energy Spectrum in Homogeneous Two-Dimensional Turbulence," Physics of Fluids, (Suppl. 2), Vol. 12, p. 233.
20. Sukoriansky, S., Zilberman, I., and Branover, H., 1985, "Experiments in Duct Flows with Reversed Turbulent Energy Cascades," Single- and Multi-Phase Flows in an Electromagnetic Field. Progress in Astronautics and Aeronautics, H. Branover, P.L. Lykoudis and M. Mond, Eds., AIAA, N.Y., Vol. 100, p. 111-124.
21. Sukoriansky, S., Zilberman, I., & Branover, H., 1986, "Experimental Studies of Turbulence in Mercury Flows with Transverse Magnetic Fields," Experiments in Fluids, Vol. 4, pp. 11-16.
22. Rose, H.A. and Sulem, P.L., 1978, "Fully Developed Turbulence and Statistical Mechanics," Le Journal de Physique, Vol. 39, No. 5, pp. 441-484.
23. Yachot, V. and Orszag, S., 1986, "Renormalization Group Analysis of Turbulence. I. Basic Theory," J. Scientific Computations, Vol. 1, p. 1.

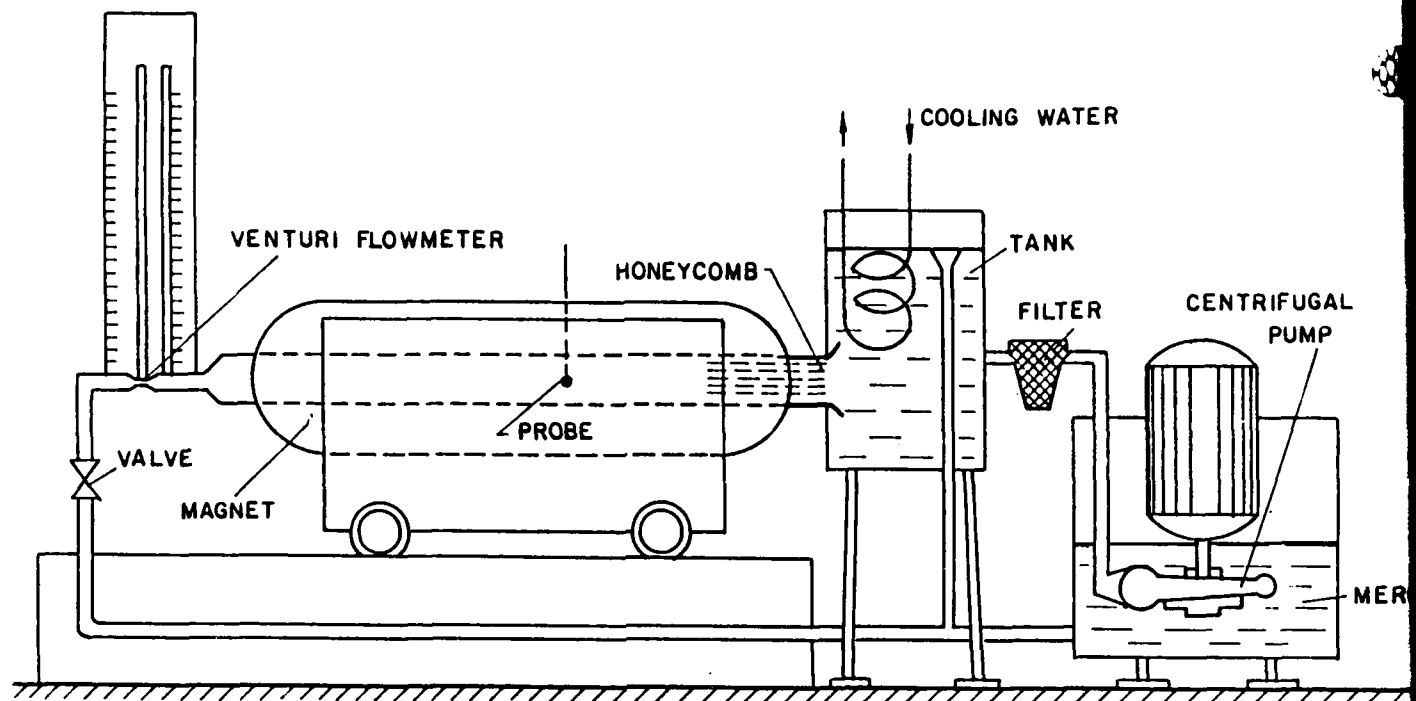


Fig. 1. Schematic diagram of experimental facility

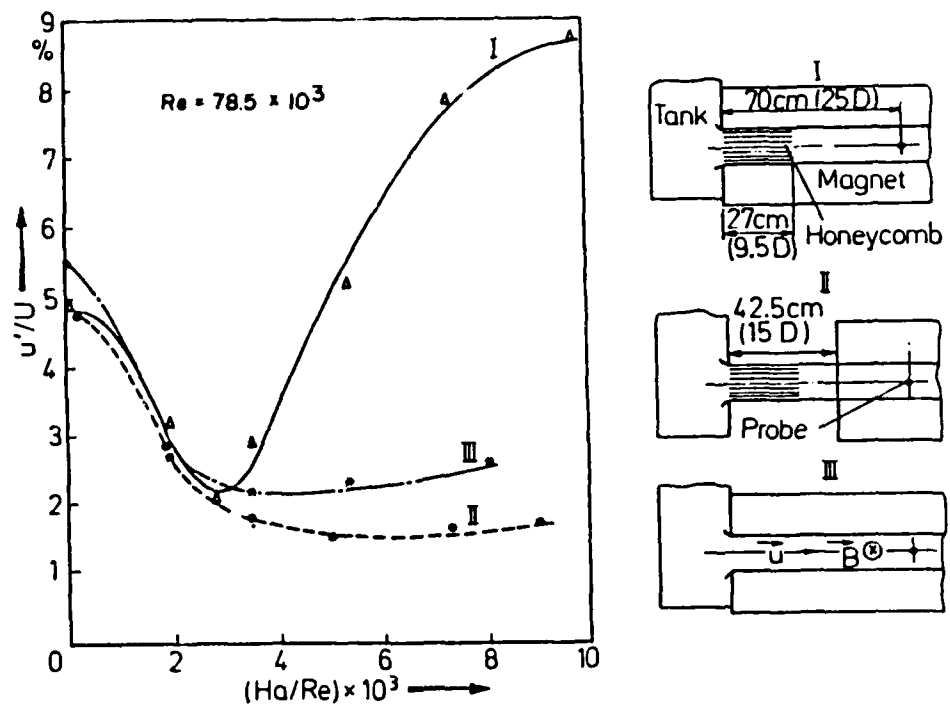


Fig. 2. Turbulence intensities as a function of  $Ha/Re$  at different positions of the magnet with and without honeycomb (solidity of the honeycomb is 0.25)

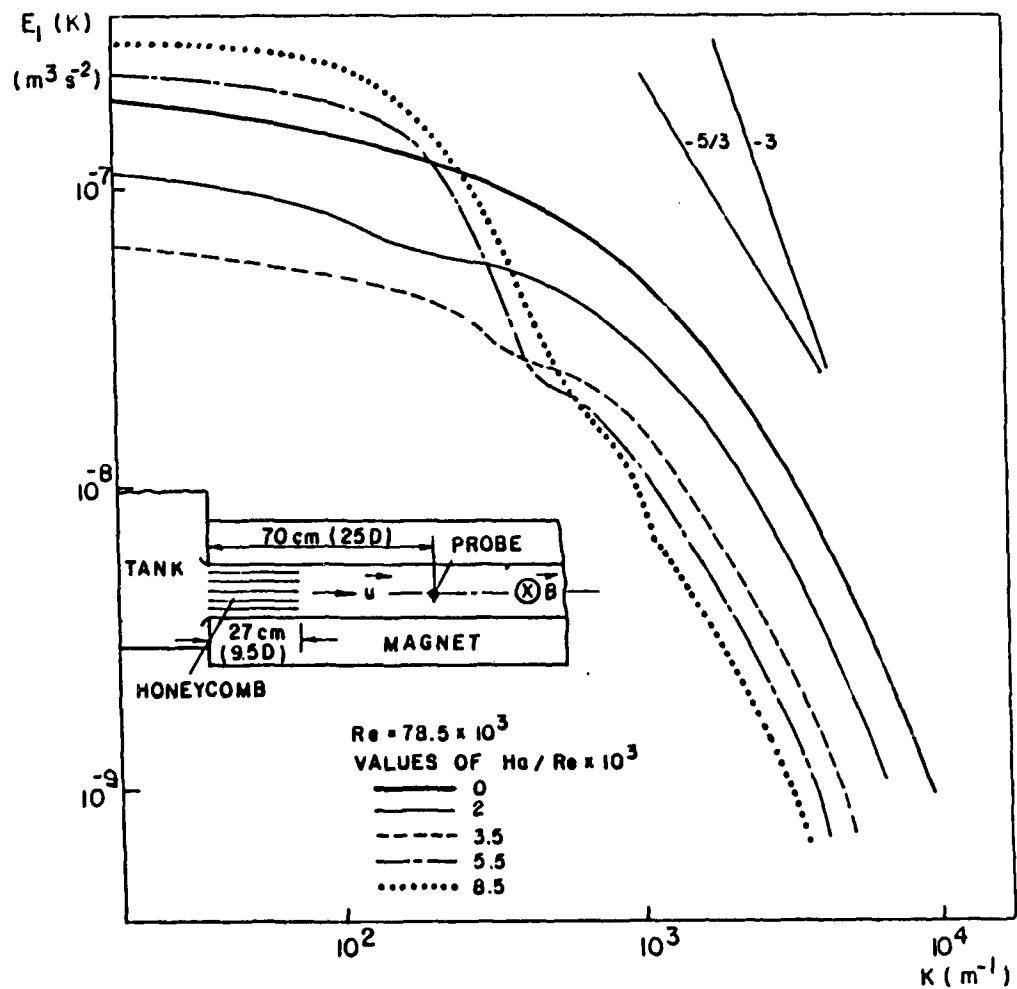


Fig. 3. Turbulence spectra at different  $Ha/Re$  values with the magnet covering the honeycomb

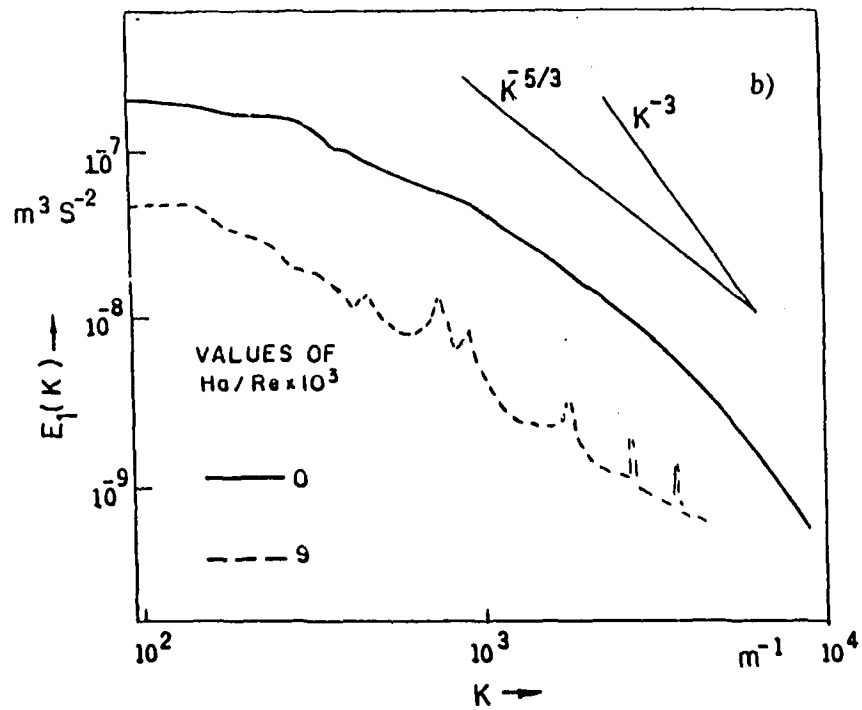
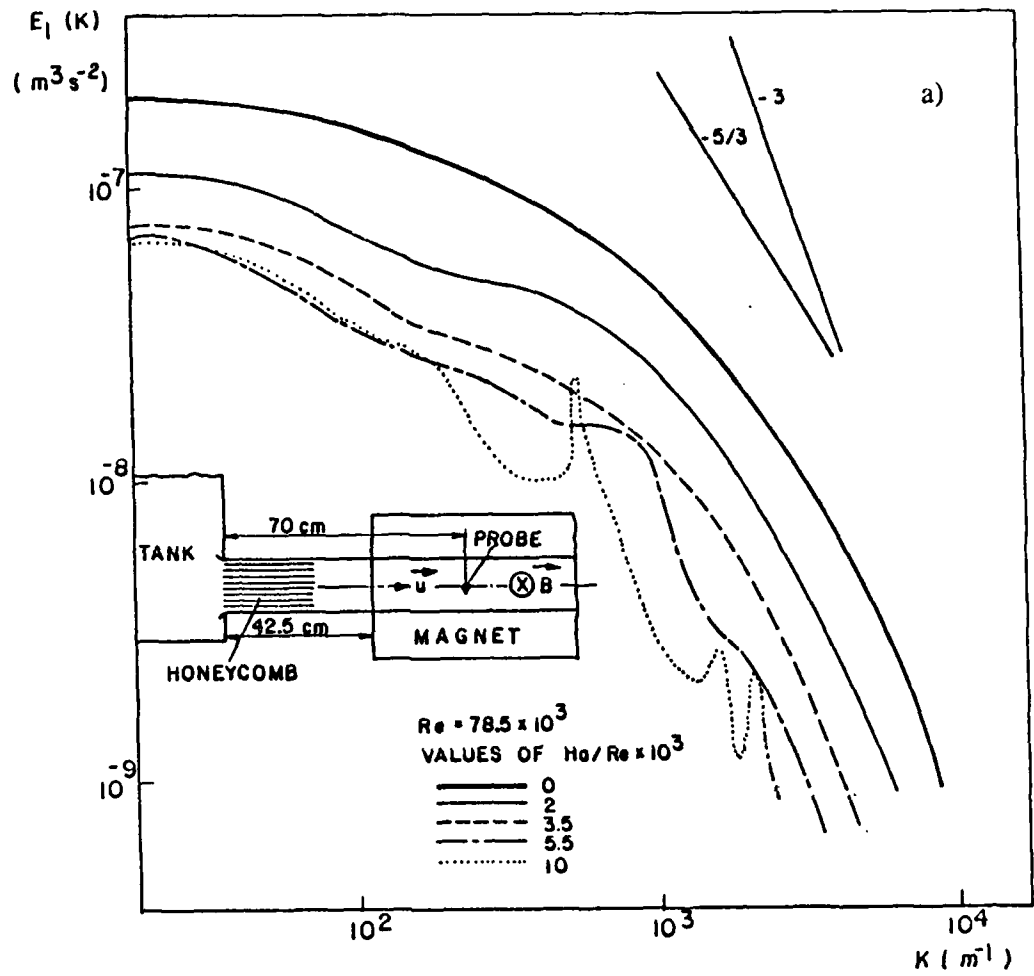
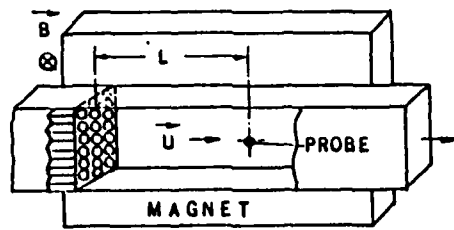


Fig. 4. Turbulence spectra at different  $Ha/Re$  values with the magnet positioned downflow of the honeycombs: a) solidity = 0.25; b) solidity = 0.1



VALUES OF  $Ha/Re \times 10^3$

— 0  
 - - - 3  
 - - - 10

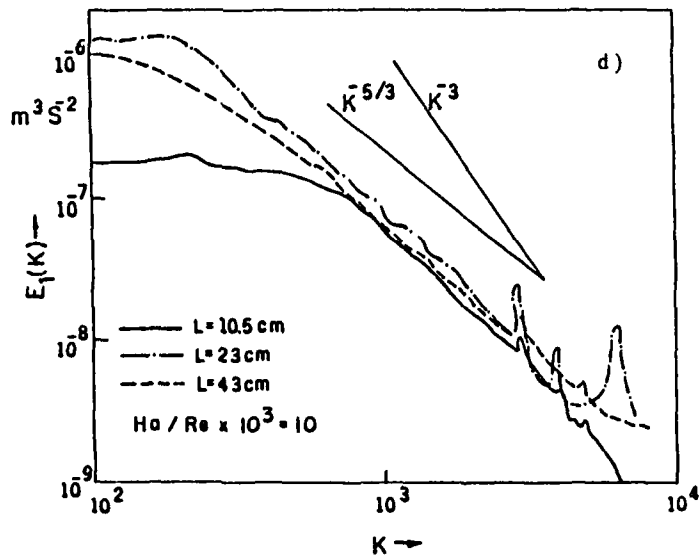
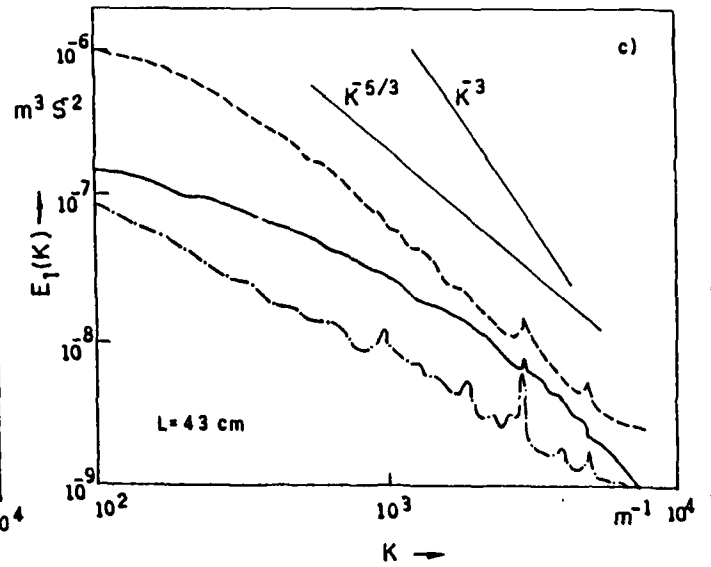
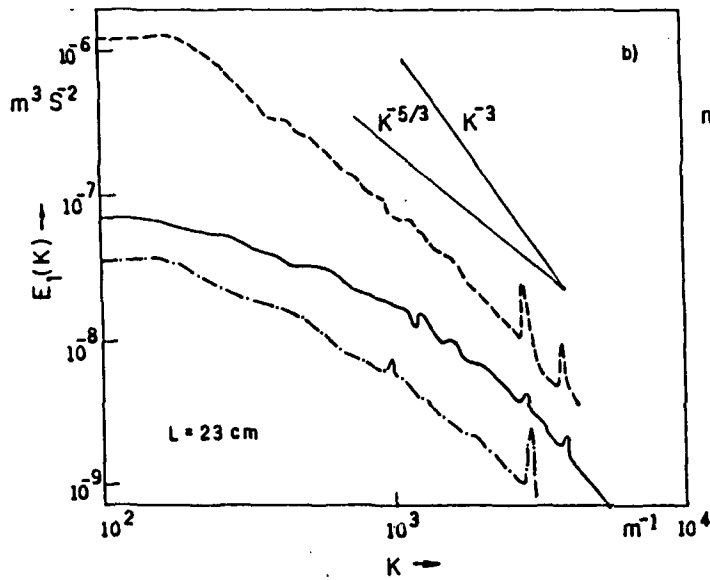
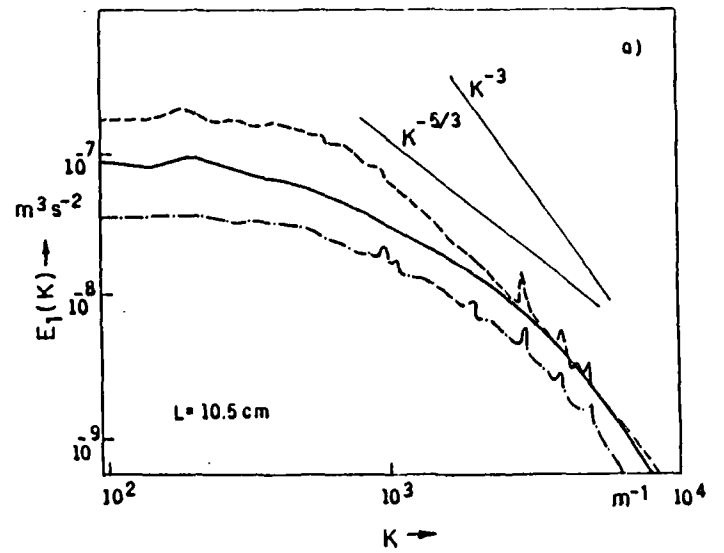
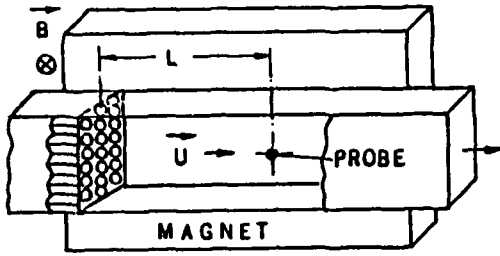


Fig. 5. Turbulence spectra measured at different distances from the honeycomb and for different values of  $Ha/Re$  (solidity of the honeycomb is 0.25)



VALUES OF  $Ha/Re \times 10^3$

- 0
- · - 3
- - - 10

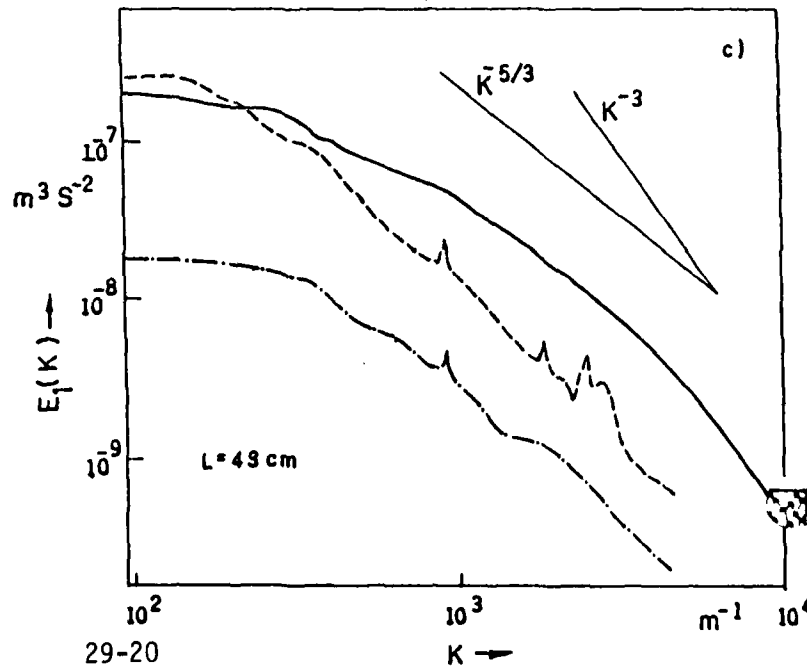
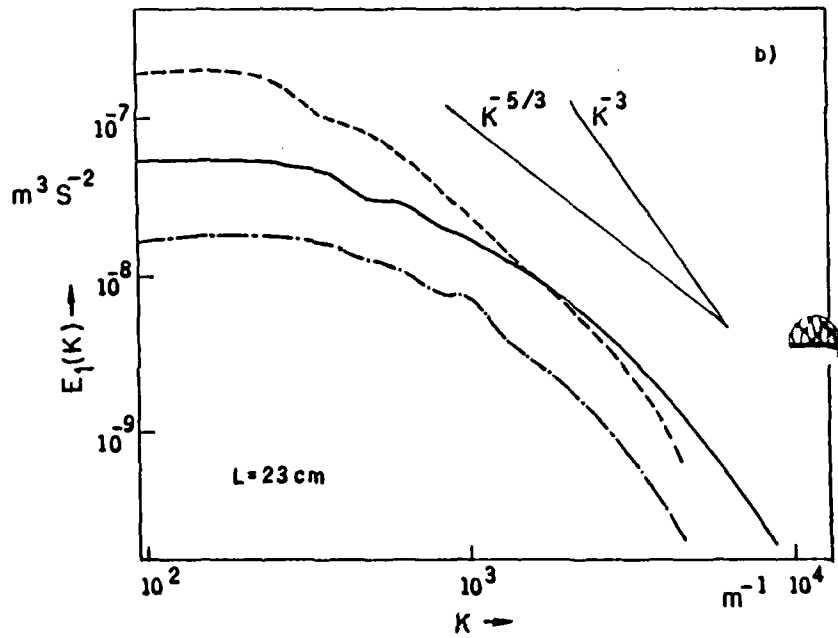
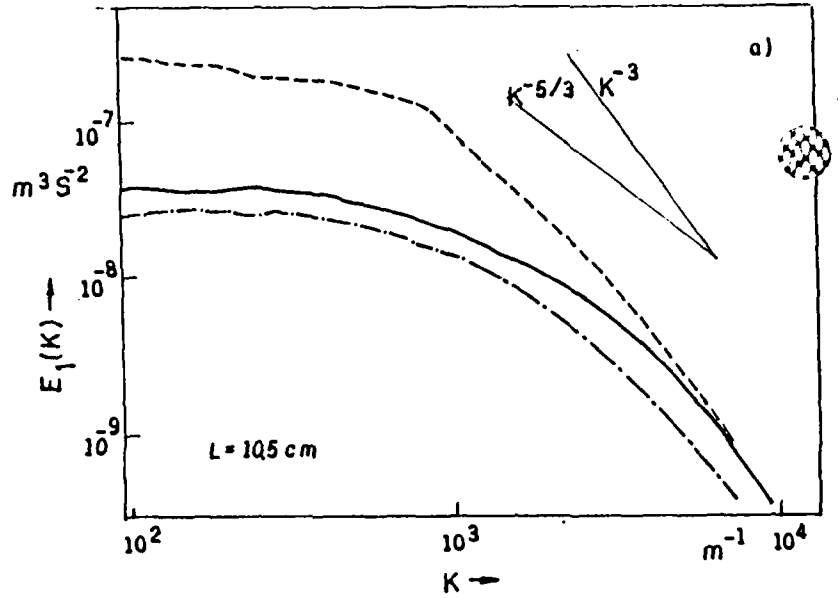
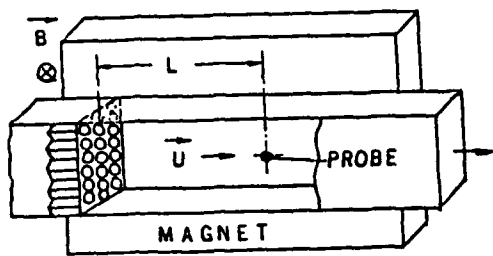


Fig. 6. Turbulence spectra measured at different distances from the honeycomb and for different values of  $Ha/Re$  (solidity of the honeycomb is 0.1)



VALUES OF  $Ha/Re \times 10^3$

- 0
- - - 3
- - - 10

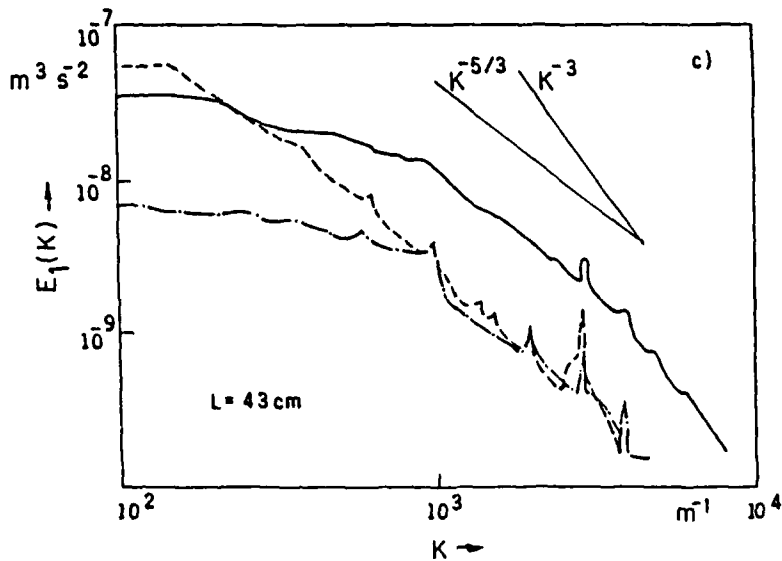
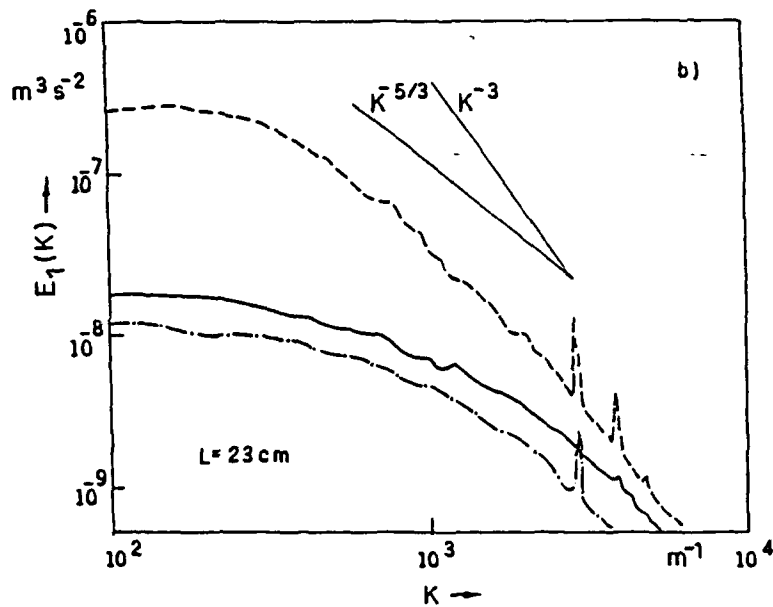
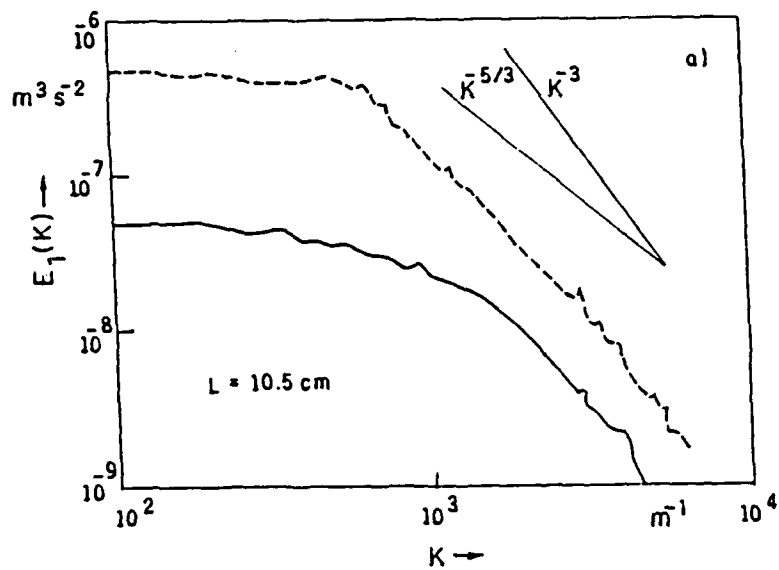
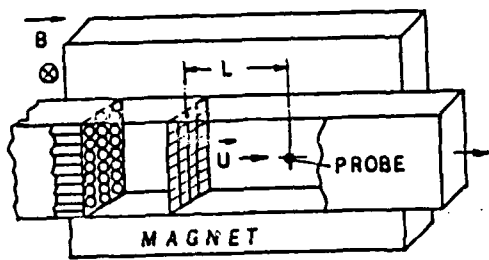


Fig. 7. Turbulence spectra measured at different distances from the honeycomb and for different values of  $Ha/Re$  (solidity of the honeycomb is 0.06)



VALUES OF  $Ha/Re \times 10^3$

- 0
- - - 3
- ⋯ 5
- - - 10

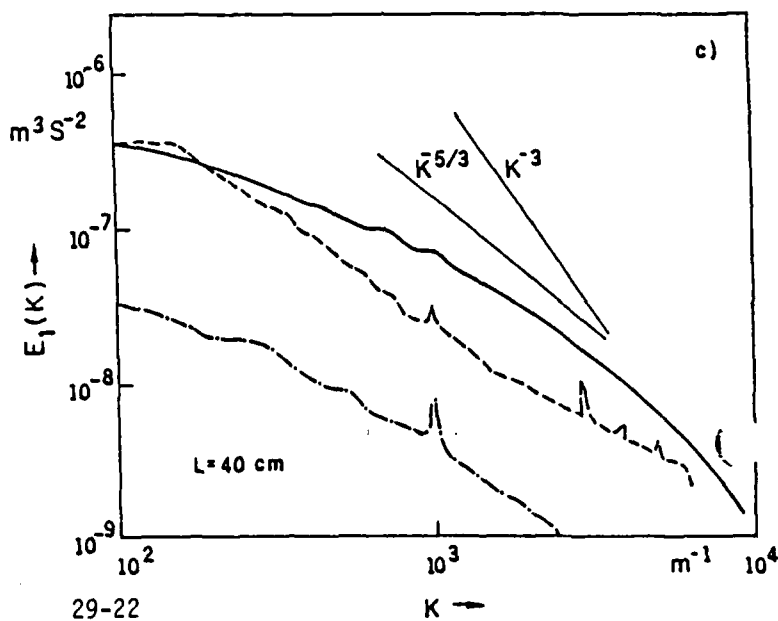
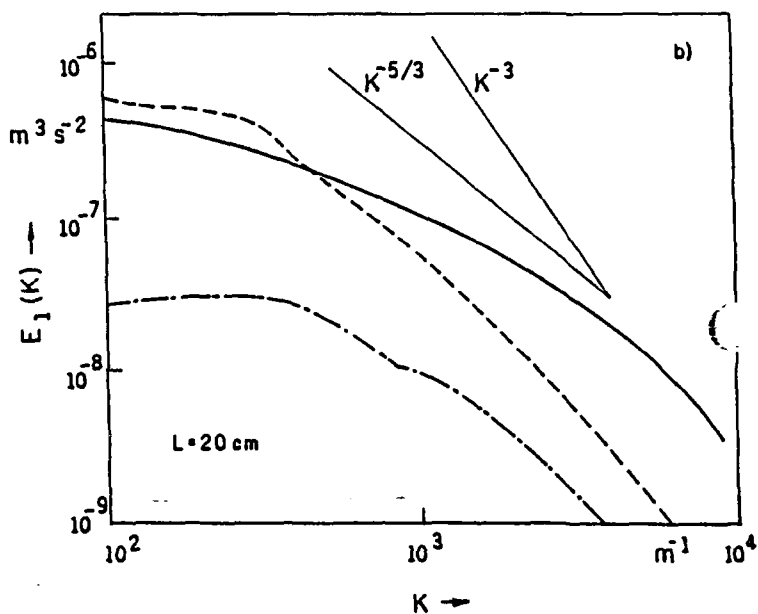
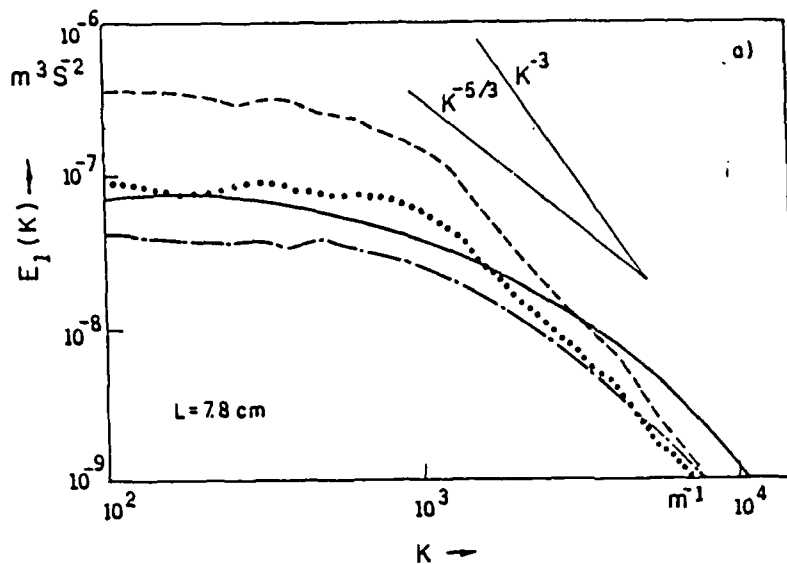


Fig. 8. Turbulence spectra measured at different distances from the crosswise-strings grid and for different values of  $Ha/Re$

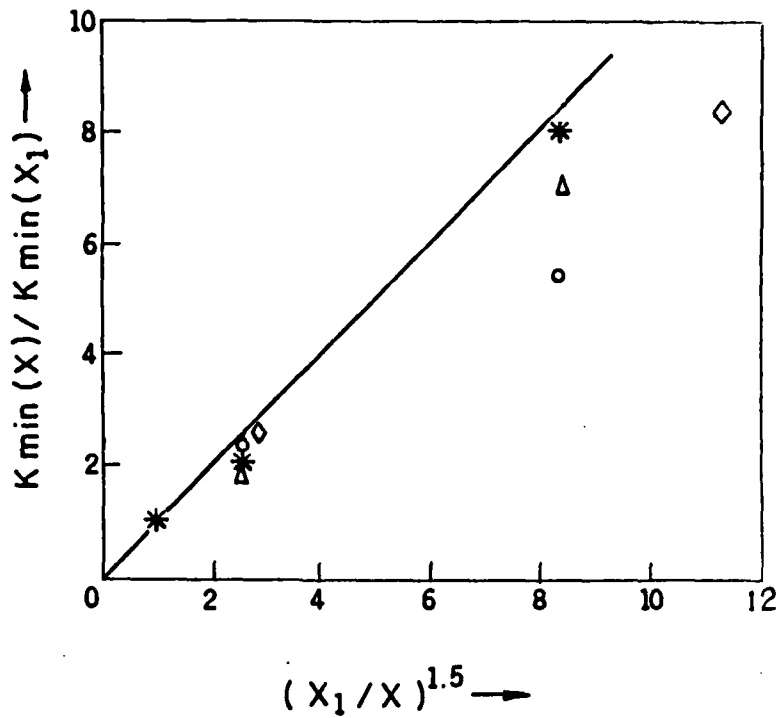


Fig. 9. The expansion of the inertial range with increase of distance from the source of forced turbulence:

- \* honeycomb with solidity 0.25
- Δ honeycomb with solidity 0.1
- o honeycomb with solidity 0.06
- ◇ grid of crosswise strings

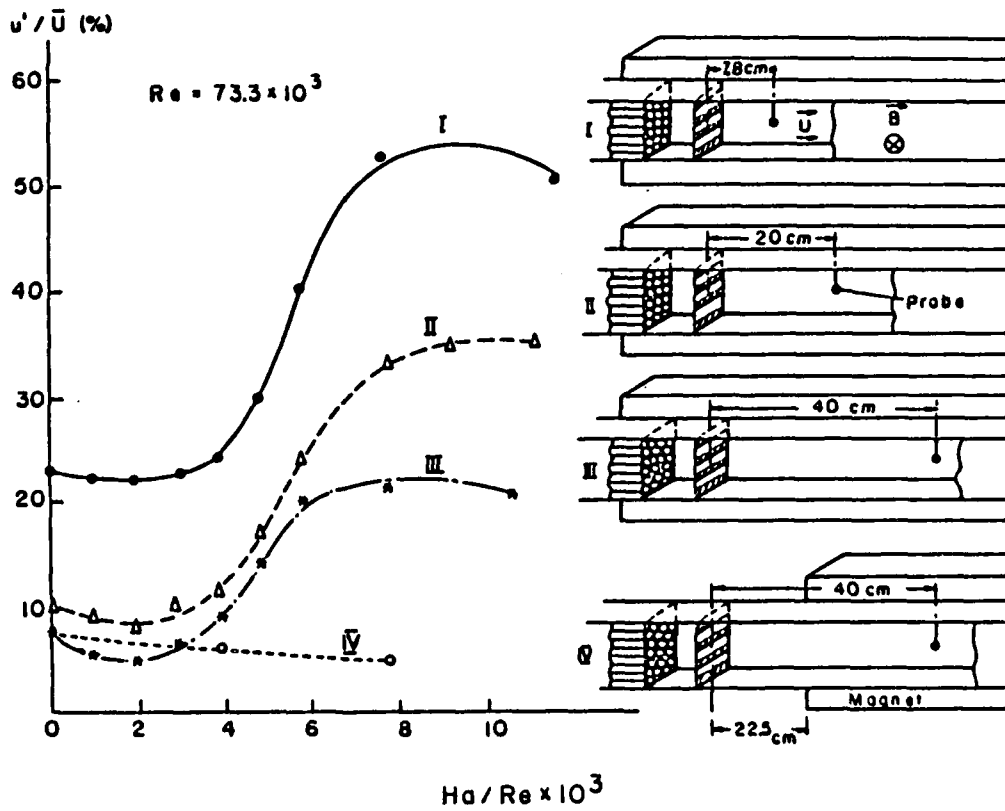


Fig. 10. Turbulence intensities measured at different distances from the grid with bars parallel to the field, and for different values of  $Ha/Re$

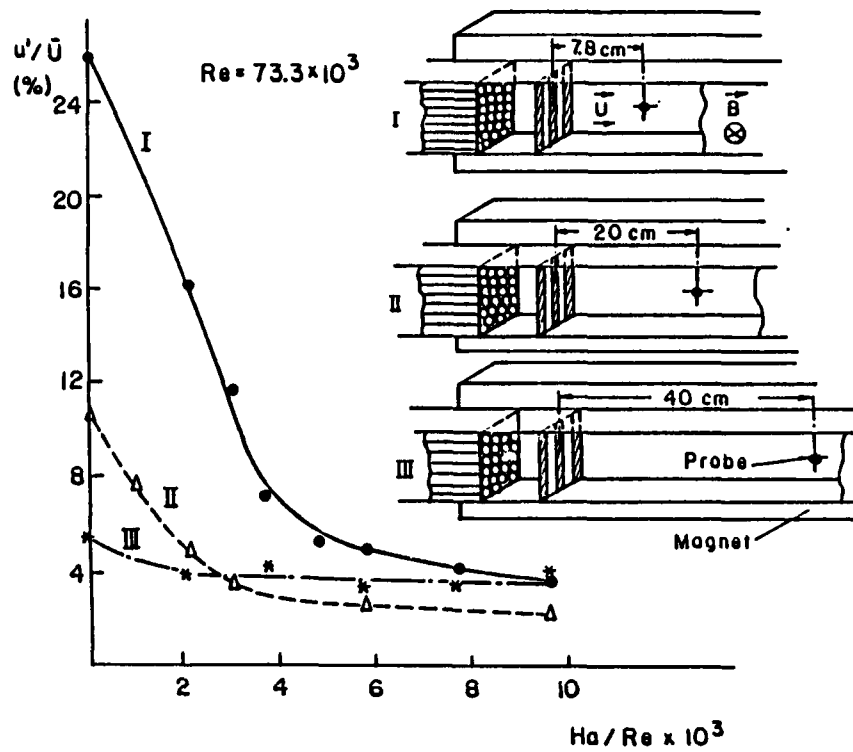


Fig. 11. Turbulence intensities measured at different distances from the grid with bars perpendicular to the field, and for different values of  $Ha/Re$

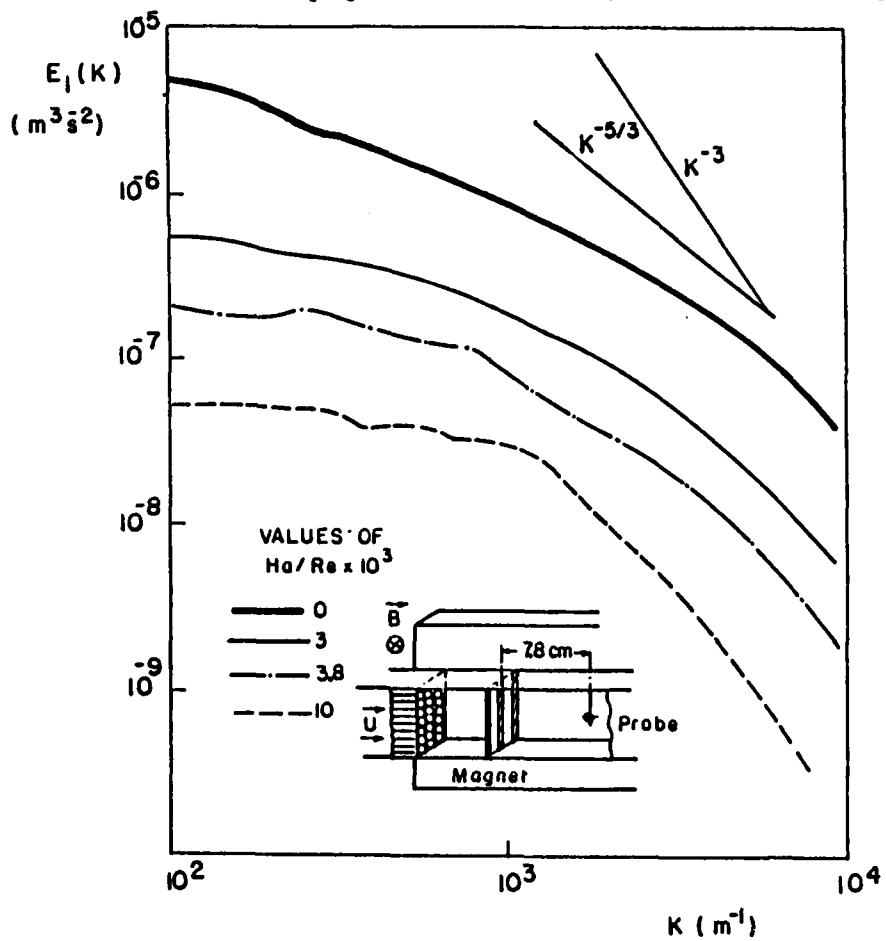


Fig. 12. Turbulence spectra measured at different values of  $Ha/Re$  (grid with bars perpendicular to the field)

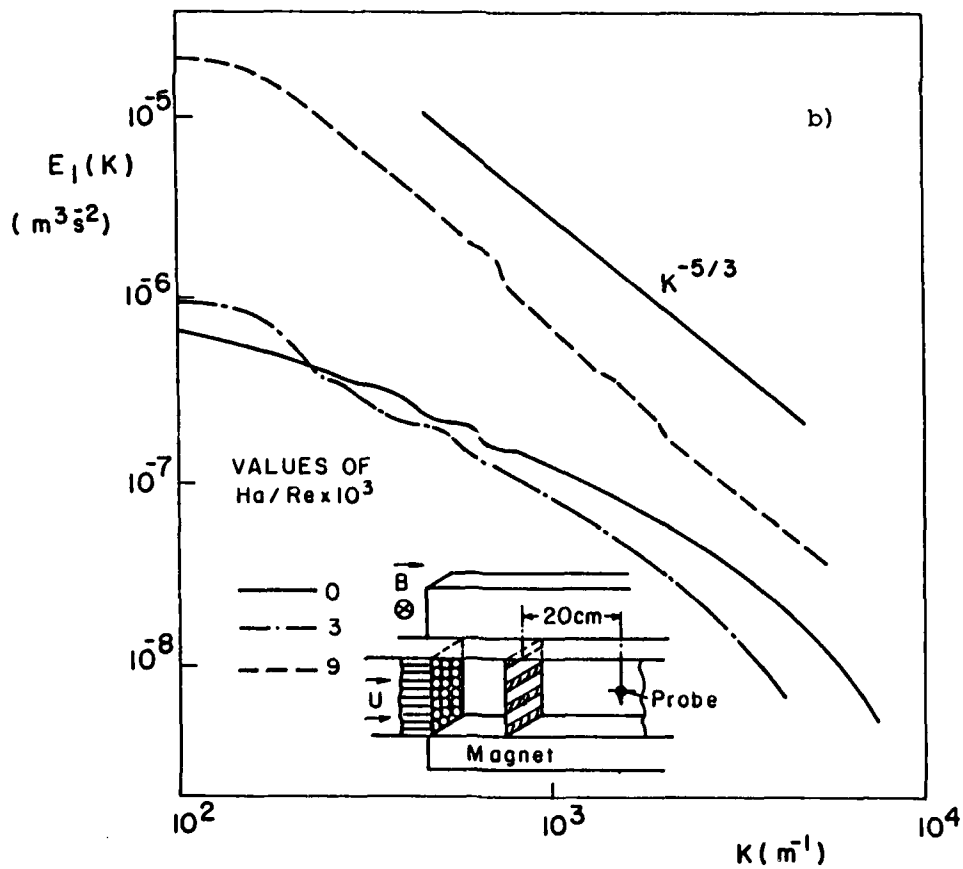
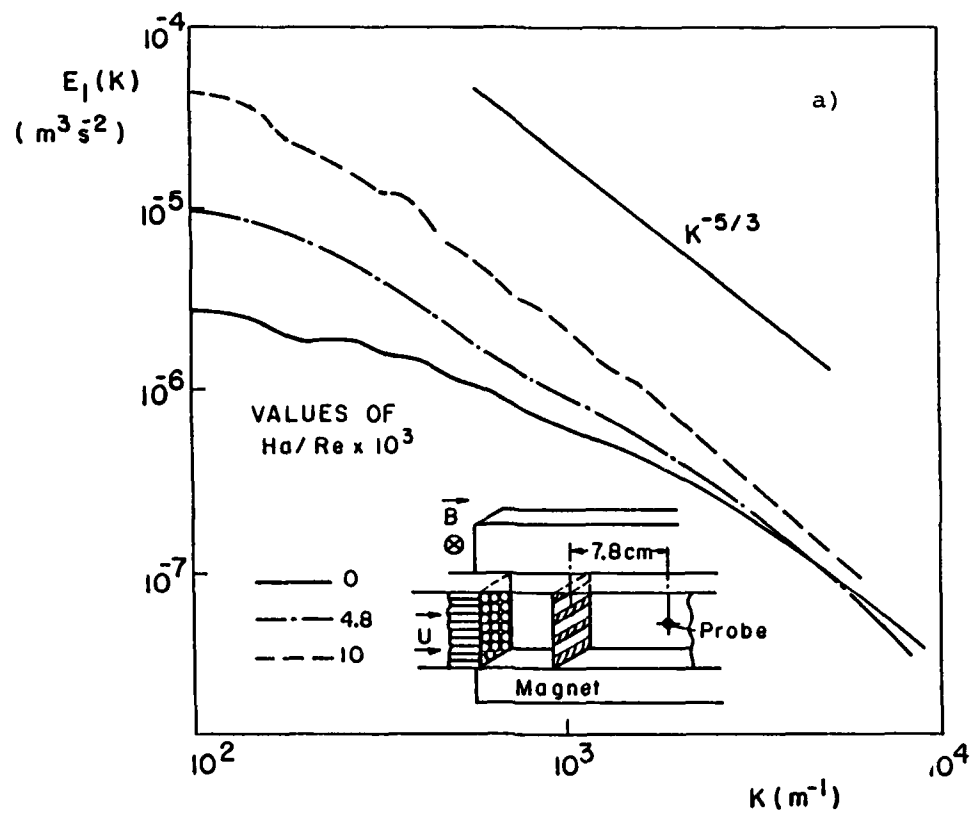


Fig. 13. Turbulence spectra measured at different distances from the grid with bars parallel to the field, and for different values of  $Ha/Re$

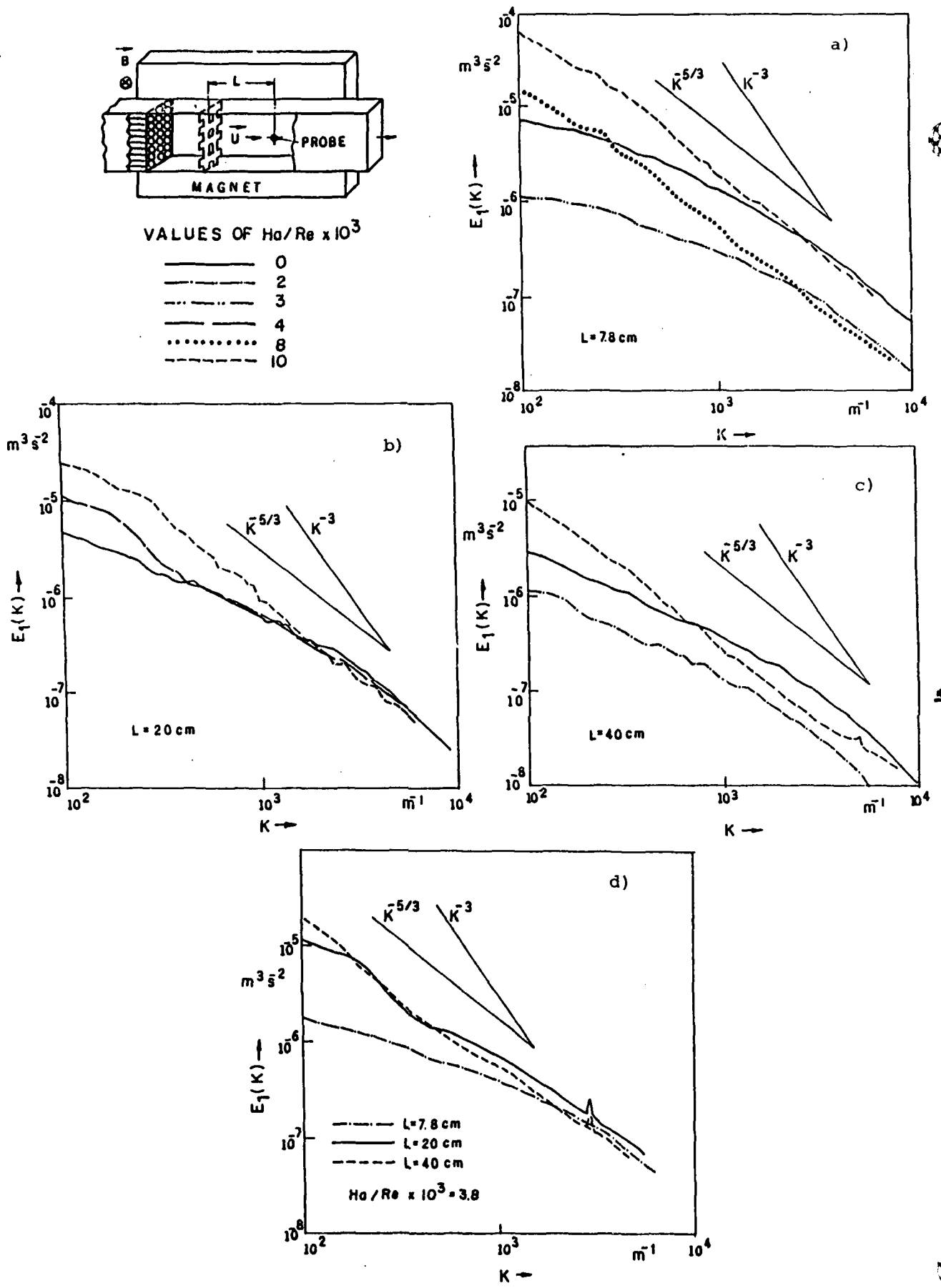


Fig. 14. Turbulence spectra measured at different distances from the grid with crosswise bars, and for different values of  $Ha/Re$

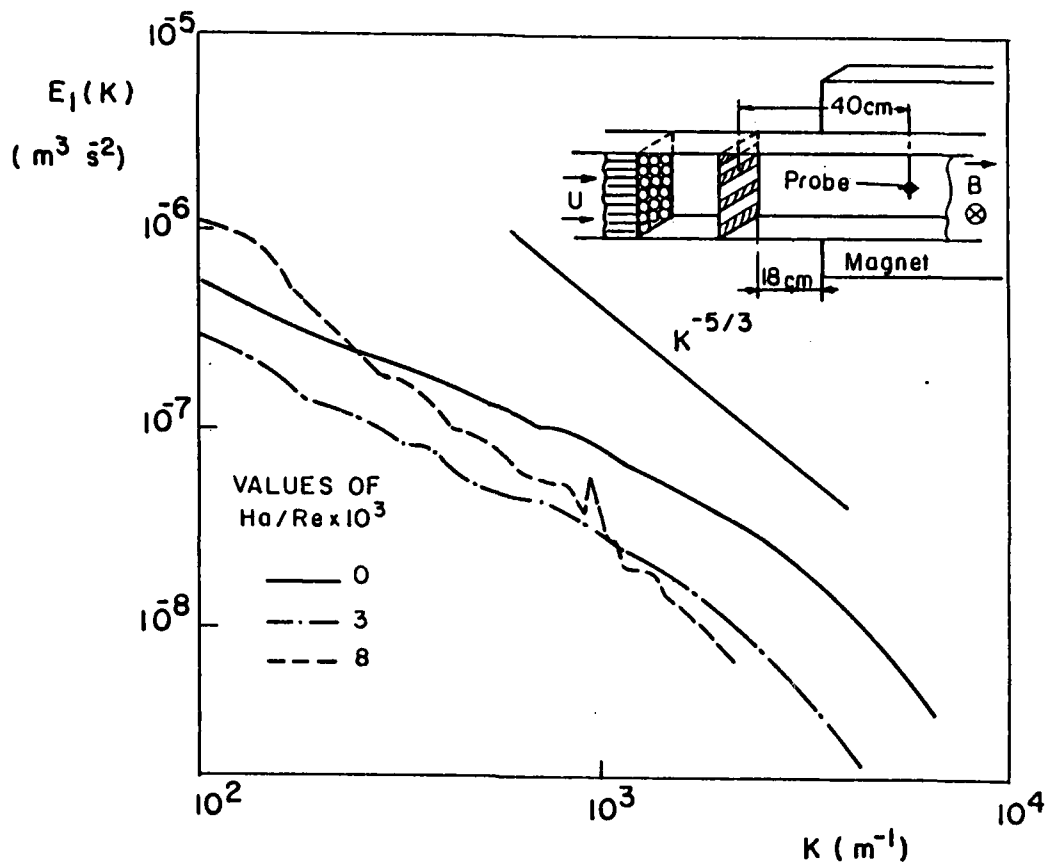


Fig. 15. Turbulence spectra at different  $Ha/Re$  values with the magnet positioned downflow of the grid with bars parallel to the field

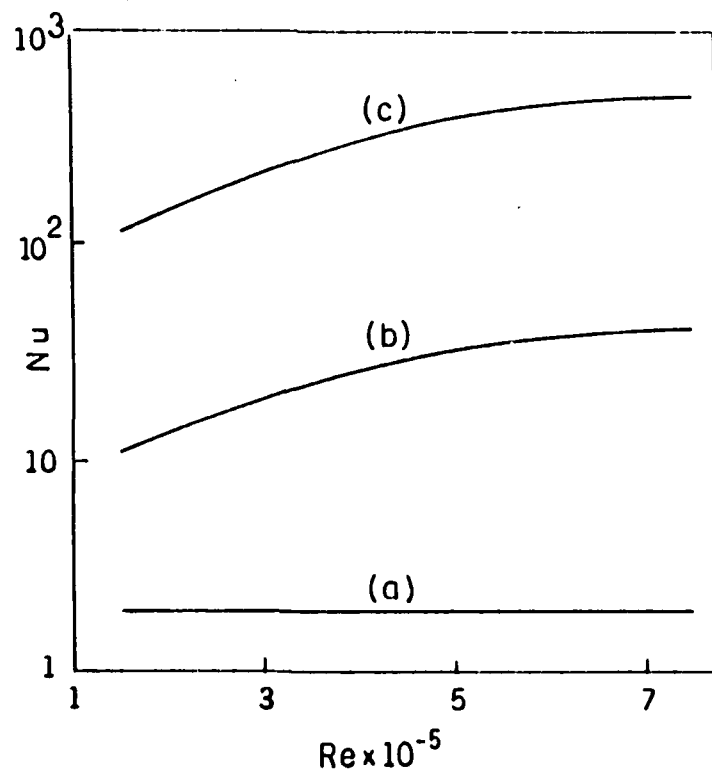


Fig. 16. Nusselt number as a function of  $Re$ . The calculations are based on:  
 (a) Laminar thermal diffusivity  
 (b) Thermal diffusivity of locally isotropic turbulence (no magnetic field).  
 (c) Thermal diffusivity of turbulence enhanced by a magnetic field.

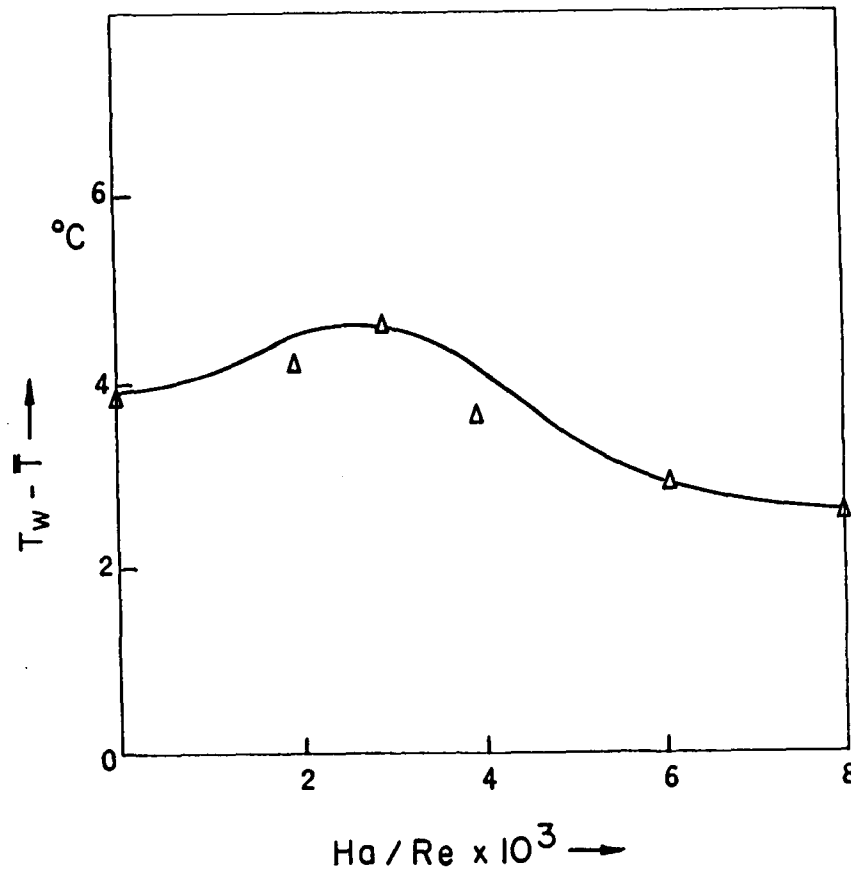


Fig. 17. The difference between the wall and bulk temperatures measured at different values of  $Ha/Re$

NUMERICAL COMPUTATIONS OF FLOW PATTERN  
IN ALUMINIUM REDUCTION CELLS

Essam Eldin Khalil, Ph.D, DIC, M. ASME, AIAA  
Faculty of Engineering,  
Cairo University,  
Cairo,  
EGYPT.

ABSTRACT

Numerical prediction methods, based on the solution of the conservation equations governing the mass, three momentum and energy, had been widely developed, modified and tested. These methods became powerful design tools as they put readily meaningful predictions of trends and performance figures under various parametric operation conditions.

The present work describes a computer program that solves the governing equations in the finite difference form and is applied to an Aluminium Reduction cell. The cell considered here is that of Egyptalum at Nage Hammady, Egypt with cell current of 150 kA, and producing one ton per day. The present predictions clearly demonstrate the capability to adequately predict local flow pattern and turbulence characteristics, in Aluminium cells.

1) Introduction

Recently, extended efforts were devoted to the analysis and modelling of Hall-Heroult Aluminium Reduction cells, Ziegler et al (1985), Arita et al (1981), Lee et al (1985). These mathematical prediction procedure concentrated on the numerical calculations of current densities, magnetic fields, metal and bath velocities and the wave interface surface pattern between the metal and bath. These mathematical models ranged from simple laminar flows to fully turbulent recirculating ones. The model assumptions were naturally assessed prior to their application into cell modelling. To assess the aerodynamic model assumption, comparisons with measured velocities and turbulence characteristics are essential. Measurements of current efficiency and metal topography are straightforward, but those of mean and fluctuating velocity components are not routine and can hardly be obtained in a real full scale cell. Lee et al (1985)

designed and built an experimental cell using wood's metal and measured velocities at various points in the cell. Arita et al (1981) used a flow prediction procedure to obtain the bath and metal velocity patterns as well as their intersecting surface.

However, the present work made use of the TEACH-T computer code of Gosman et al (1974), modified here to present an aluminium reduction cell, to predict local flow pattern. The present procedure solves the governing equation together with the appropriate boundary conditions to yield velocity vectors and flow pattern under various operational conditions.

The following section describes the numerical procedure and modelling assumptions while section three describes the numerical computations. The paper ends with a brief concluding section.

2) Numerical Procedure :  
2.1. Problem Identification:

Flow pattern in Aluminium Reduction cells is naturally complicated with multiphase and magnetic field effects. The problem is better visualized by considering the strong secondary flows and flow reversal yielding the elliptic nature of the governing conservation equations. It is clear by now that analytical solution of the governing equations of mass, momentum and energy is indeed very difficult. The present work used a numerical procedure that solves the governing differential equations in the finite difference mode using an iterative procedure with "SIMPLE" Algorithm of Spalding et al (1972). The full Navier-Stokes equation are to be solved at discrete nodes in the numerical grid superimposed on the cell horizontal plane. The mathematical formulation of the problem is considered in terms of geometrical configuration and governing equations and boundary conditions.

### 2.1.1. Geometrical Configuration

The geometrical configuration under investigation is shown in figure 1. It consists of a three dimensional chamber with a rectangular horizontal cross section. The top is occupied by the anode and the bottom is the cathode with molten Alumina and electrolyte filling the space. Magnetic field is in effect between the two terminal surfaces and results in the motion of the molten fluid and consequent agglomeration of the cell constituents.

### 2.1.2. Governing Equations:

The governing equations described in the open literature are put here in the general form as follows :

$$\frac{\partial}{\partial x_j} \bar{\rho} \bar{U}_j \bar{\phi} + \frac{\partial}{\partial x_j} \bar{\rho} \bar{U}_j \bar{\phi} = \frac{\partial}{\partial x_j} \gamma_\phi \frac{\partial \bar{\phi}}{\partial x_j} + \bar{S}_\phi \quad (1)$$

where

$\bar{\rho}$  is the time averaged local density,  
 $\gamma_\phi$  is the local laminar exchange coefficient.  
 $\bar{\phi}$  is the time averaged general dependent variable.  
 $\bar{U}_j$  is the time averaged velocity component in the  $x_j$  coordinate direction.  
 $\bar{S}_\phi$  is the average value of the source/sink term of the entity  $\bar{\phi}$ . The variable  $\bar{\phi}$  can take the form of any of the three velocity components  $U_j$ , i.e.  $\bar{\phi} = U$  or  $V$  or  $W$  thus yielding the three momentum equations in the  $x, y$  and  $z$  coordinates directions. The term  $\bar{S}_\phi$  is the momentum source/sink term in the  $U, V$ , and  $W$  conservation equations. Each of these terms combine the shear and Reynolds stresses effects, pressure gradients and the body force. For example in the  $U$  momentum equation,  $\bar{\phi} = U$ ,  $\gamma_\phi = \mu$  and  $\bar{S}_u = \bar{F}_x - \frac{\partial \bar{P}}{\partial x}$  where  $\bar{F}_x$  is the body force due to the magnetic field effect in the  $x$  direction.

To yield the above equations solvable, closure of the momentum equations is necessary; this is achieved through the application of turbulence modelling assumptions to calculate the terms  $\bar{u}_i \bar{u}_j$  as explained later. The continuity equation can be readily obtained from the general equation (1) by introducing  $\bar{\rho} = 1$  and putting  $\bar{S}_\rho = \text{Zero}$ .

### 2.2. Turbulence Modelling:

The turbulent characteristics of the flow in the cell are obtained with the aid of a two equation ( $k-\epsilon$ ) turbulence model of Launder et al (1974). The model estimates the local shear and Reynolds stresses  $\bar{u}_i \bar{u}_j$  in the momentum equations as:

$$-\overline{u_i u_j} = -\mu_t \left[ \frac{\partial \bar{U}_i}{\partial x_j} + \frac{\partial \bar{U}_j}{\partial x_i} \right] + \frac{2}{3} \bar{k} \delta_{ij} \quad (2)$$

where the values of  $\mu_t$  the turbulent viscosity are obtained as:

$$\mu_t = 0.09 \rho k^2 / \epsilon \quad (3)$$

The values of  $k$  the kinetic energy of turbulence and  $\epsilon$  its dissipation rate are obtained from their respective transport equations, expressed in the form (1), with  $\bar{\phi} = k$  and  $\epsilon$  respectively. The constants of the model were those of Launder et al and were kept unchanged. The validity of this model assumptions was extensively assessed by way of comparisons with available experiments in a wide range of flow configurations, Ziegler et al (1985), El-Maghraby et al (1985), Gosman et al (1974) and Khalil (1983).

### 2.3. Boundary Conditions:

In this paper, four boundaries are to be specified; the longside wall, the two shortside walls and the symmetry line. At all walls, velocities are prescribed as zero with the application of a wall function to relate the near wall nodes to wall values and to obtain the resultant shear stresses. The values of  $k$  and  $\epsilon$  at the rear wall region are also obtained from the wall function expressions. At centreline, zero velocity gradient is assumed.

The present work considered a symmetrical half section of the cell; figure 2 shows the various boundaries of the computational scheme.

The magnetic field effects were represented in the momentum equation by the term  $F_x$  and  $F_y$  denoting the magnetic forces. These were obtained from a separate computer program of El-Maghraby et al (1985) that calculates the electromagnetic fields at all grid nodes in the computational cell.

Further details of the nature of the equations and their derivations can be found in previous reports.

### 2.4. Finite difference grid:

The grid utilized in the present work is of the orthogonal type and is to be superimposed on the horizontal plane across the cell. The grid is constructed of orthogonal grid lines with grid nodes at their intersection points. The governing equations are discretized at these locations. The grid arrangement for the  $U$  and  $V$  is different from those for  $\bar{\phi}$ . This is to allow for the easy storing of the boundary values of  $U$  and  $V$  at the control volume edges to ease continuity equation verification. The grid in this form allows

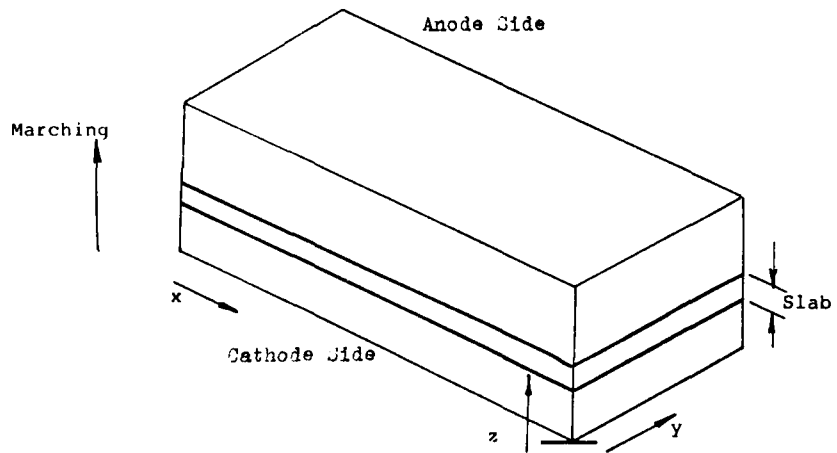


Fig.1 : Aluminium Reduction Cell Configuration

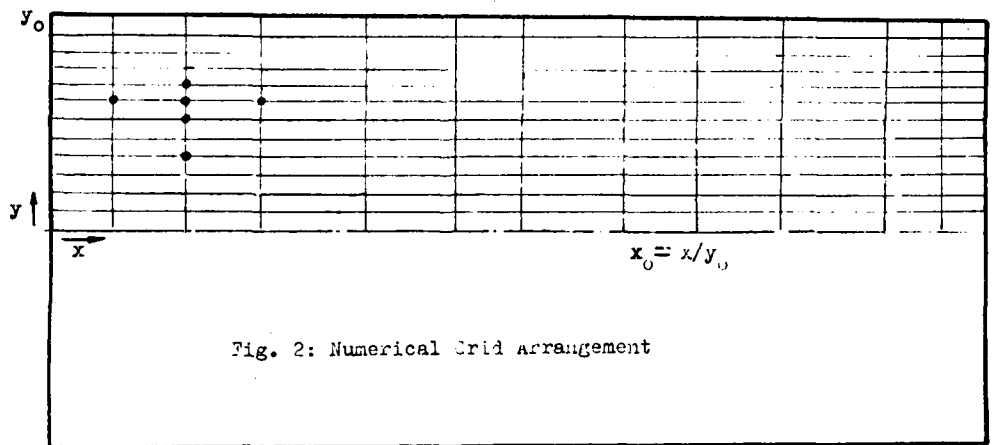


Fig. 2: Numerical Grid Arrangement

also for the input body forces to be located at the same locations as the velocities  $U$  and  $V$ . The grid was of the non-uniform type with grid lines condensed near steep gradient zones.

The finite difference discretization of the governing equation would yield the following equation;

$$A_n \phi_n + A_s \phi_s + A_e \phi_e + A_w \phi_w + S_\phi = A_p \phi_p \quad (4)$$

where the terms  $n, s, e, w$  denote the north, east and west neighbouring nodes and  $p$  denotes the polar node. The term  $S_\phi$  is to be represented in the linearized form as;

$$S_\phi = S_u + S_p \phi_p \quad (5)$$

The term  $A_p$  combines the coefficients  $A_n, A_s, A_e,$  and  $A_w,$  and  $A_n$  is the convection and diffusion coefficient of the term  $\phi$ . The calculated coefficients are incorporated in the momentum equations which are then solved iteratively to satisfy the convergence criteria. Two loops of iterations are generally performed; an inner loop and an outer one. Final convergence is obtained when all governing equations satisfy the convergence criteria.

### 3. Numerical computations:

The present program was set to predict the electrolyte and the molten metal flow patterns at two different locations under the anode surface. The first case pertains to  $Z=0.004$  m which is just under the anode. The predicted mean axial velocity distribution is shown in figure 3. The maximum velocity was less than 0.2 m/s. The velocity profiles at various stations along the cell long side axis indicated forward and backward flow zones. In the left hand side of the cell, velocity profiles in the long wall region behaved in a wall jet manner with the velocity peak in this region moving towards the centre away from the wall. The velocity decays due to the adverse pressure effect and a flow reversal occurs as indicated at  $x/1.25$  and  $y/y_0$  of 0.55. The strength of the flow motion decreases as  $x$  increases which is due to the smaller effect of magnetic fields at the central core of the cell. In the middle of the cell the flow became nearly stagnant. It is worth noting that the summation of the velocity yields zero due to the fact that no mass is externally added, i.e.

$$\int_0^{y_0} u \, dy = 0$$

This is also true in the  $x$  direction as;

$$\int_0^x u \, dx = 0$$

Figure 4 illustrates the axial velocity variation along the  $x$  direction at various values of  $y$ . At  $x_0$  greater than 4.6 and at  $y/y_0$  less than about 0.5, the flow is positive in the forward direction with peak positive velocities occurring at the centreline. The velocity decays towards the long wall and diminishes to zero with a consequent recirculation zone in the wall region. The flow field can be visualized by the eddies counter rotating in such a manner that the fluid is brought from the two sides towards the central zone near the long wall and is being forced out towards the side walls in the central plane. The velocity vector contours are shown in figure 5 for this particular case.

Figure 5 demonstrates the complexity of the fluid motion under magnetic force and clearly identifies two anti-rotating vortex zones. The vectors shown are drawn to scale and were calculated from the predicted values of the axial and radial velocity components profiles as;

$$U_R = \sqrt{u^2 + v^2}$$

at an angle defined as;

$$\tan \theta = \frac{v}{u}$$

The magnitudes of the resultant velocities were less than 0.2 m/s with zones of zero velocities well identified. Figure 5 is being constructed of two mirror images of the half-sectioned velocity vectors to present a more appreciable view of the flow pattern.

The significance of the present technique can be well realized by the parametric investigations; this is effected by changing some of the major factors and parameters influencing the cell performance. Figure 6 shows the radial profiles of mean axial velocity distribution in the situation where the magnetic forces are 10% of those of the actual cell. That is to say, what would happen if the magnetic forces and field were reduced. Apparently, the velocity pattern would remain unchanged in a broad sense but would be reduced in value. The maximum velocity is less than 0.04 m/s as compared to 0.2 m/s for the actual case. The size of the forward and backward zone is insignificantly changed as compared to fig. 3. The technological cell practice recommended the minimum flow motion in the cell and hence, smaller magnetic forces are required. The question is how small, what distribution of forces and consequently the burbars.

Another exercise was to calculate the flow field under the original actual cell conditions but with a magnetic field that yields same  $F_y$  but with new  $F_{x1} = -F_x$ . The

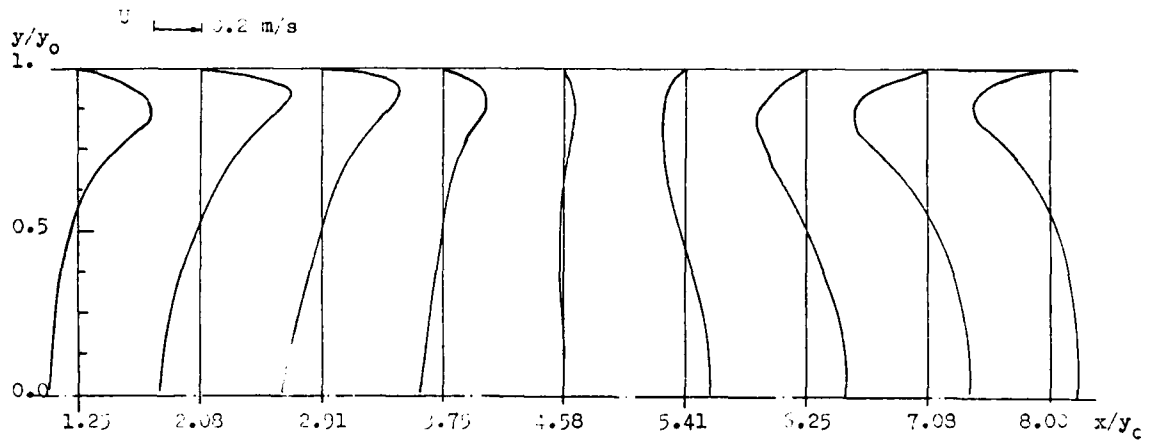


Fig.3 : Calculated Mean Axial Velocity Profiles.

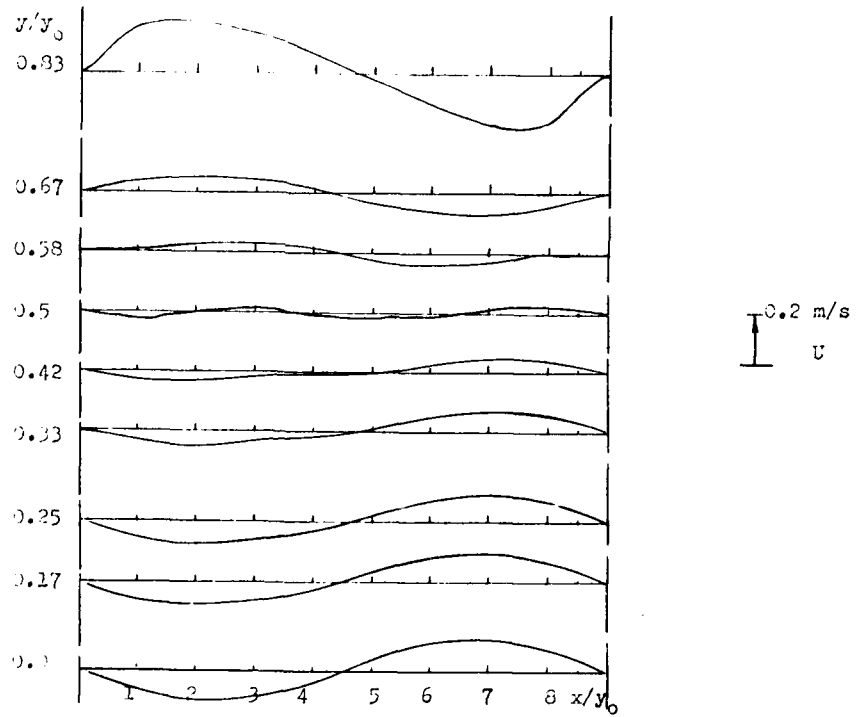


Fig.4 : Predicted Axial Velocity Profiles

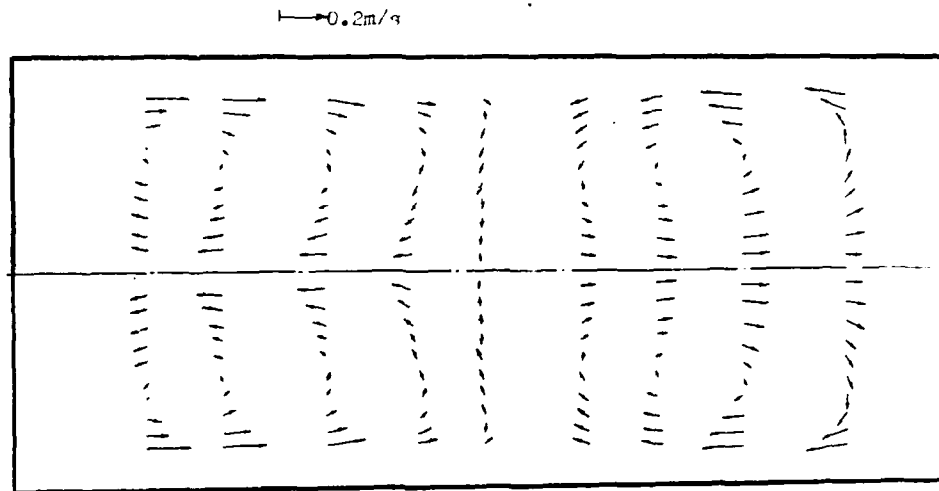


Fig.5 : Predicted Flow Pattern in the Aluminium Reduction Cells of Wage-Hannady, Egypt.

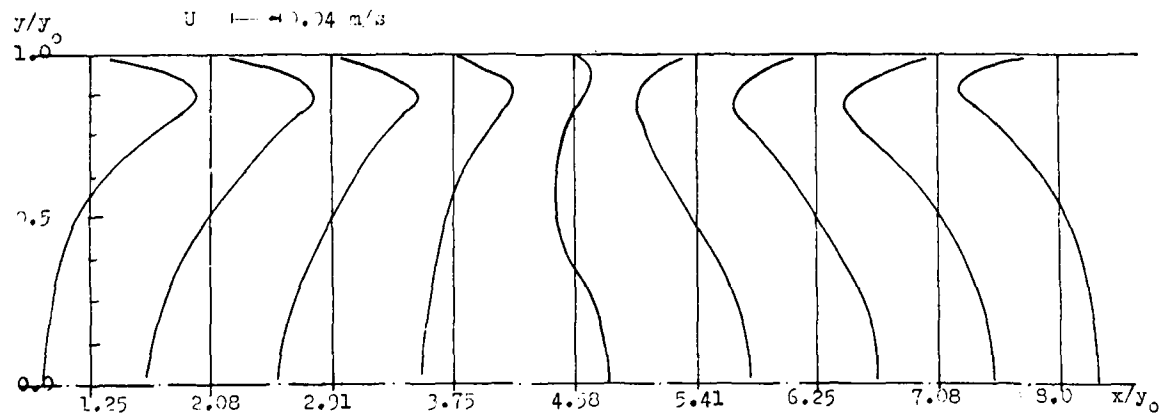


Fig.6 : Calculated Mean Axial Velocity Profiles for Reduced Magnetic Forces(10% of Base Case.)

resultant velocity vector is shown in figure 7. The flow field is totally changed with one big eddy rotating the whole fluid bulk.

The second test case is that for a horizontal plane at 0.4m under the anode in the molten metal bath; the magnetic forces were obtained from the solution of the electromagnetic field. The predicted molten metal flow pattern for this case is shown in figure 8. The obtained distribution is similar in nature to that of figure 6. The vector in figure 5 indicated stronger inward flow in the centre of the cell while those in figure 8 showed less diffusion force in the middle of the cell. The size of the eddies was nearly the same.

#### 4. Closure :

The present section demonstrated the capability of the computer program MAC to predict the local flow pattern in Aluminium cell under various operating conditions. The obtained predictions indicated calculated peak velocities of the order of 0.15 m/s which is consistent with previous work of Arita et al (1981) for a similar cell with prebaked anode. The calculated flow pattern demonstrated the existence of zones of steep velocity gradients and recirculation. It is anticipated to perform some more calculation tests to be compared with available experiments in the next report.

#### Acknowledgement :

The author wishes to acknowledge the help and cooperation of the staff of the Aluminium Company of Egypt. Thanks are due to Profs. M.G. El Maghraby and S.M. El Raghy for their encouragement and interest. Part of this work was carried out with the financial support of the FRCU-AID Grant, Project FRCU 842014 which is greatly acknowledged.

#### References :

- Arita, T. and Ikeuchi, H., 1981 "Light Metals, 1981", G.M. Bell (Ed.), AIME, 357.
- El Maghraby, M.G. et al 1985 " Analysis and Modelling of Aluminium Reduction cells at Nage-Hammady, FRCU 842014, Egypt.
- Gosman, A.D., Pun, W.M., 1974, Calculation of Turbulent Recirculating flows, Imperial college HTS/74/2.
- Khalil, E.E., 1982, Modelling of Furnaces and combustors, Abacus Press.
- Launder, B.E., Spalding, D.B., 1974, Numerical Computations of Turbulent Flows, Comp. Methods in Applied Mechanics and Engineering, vol. 3, 269.

Lee, H.C. and Evans, J.W., 1985, Light Metals 1985", H.O. Bohner (Ed.), AIME, 569.

Spalding D.B and Patankar S.V. 1972, A calculation Procedure for Heat and mass Transfer in 3D flows, Int. J. Heat and Mass Transfer, vol. 15, 1787.

Ziegler, D. and Evans, J.W., 1985, Mathematical Modelling of Electrolyte circulation in cells with Planar vertical Electrodes, J. Electrochemical society.

0.2 m/s

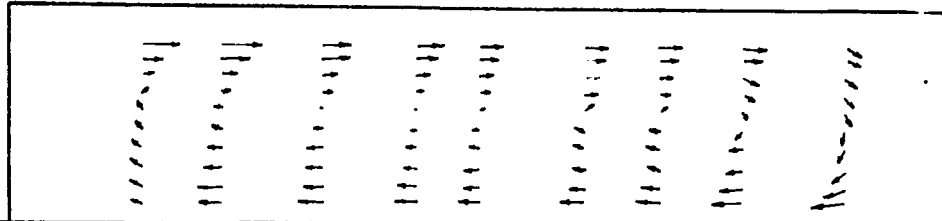


Fig.7 : Predicted Flow Pattern in the Cell for a Reversed Axial Magnetic Force Component

0 0.2 m/s

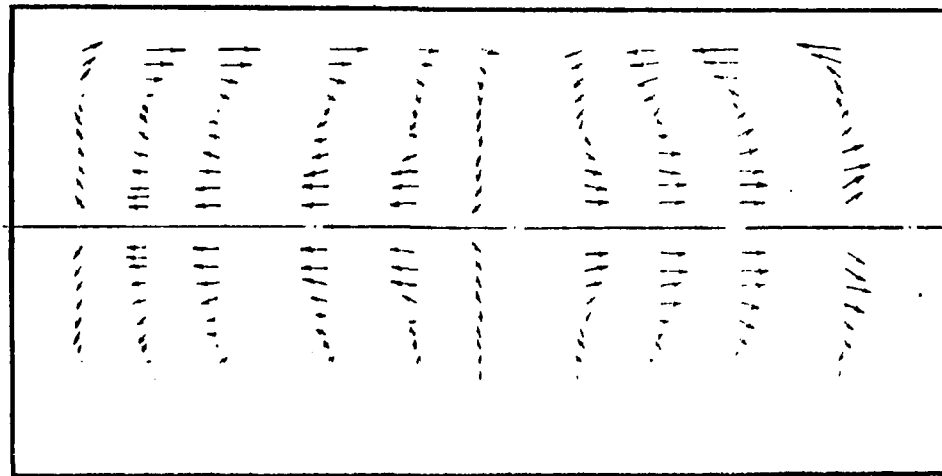


Fig.8 : Molten Metal flow Pattern in the aluminium Reduction Cells of Nage Hammady

TURBULENCE MEASUREMENTS IN A FLOW  
GENERATED BY THE COLLISION OF RADIALLY  
FLOWING WALL JETS\*

Barry Gilbert  
Grumman Corporate Research Center  
Bethpage, New York 11714-3580

ABSTRACT

Early results of an experimental investigation of the abnormally high turbulence level and mixing layer growth rate characteristics found in the upwash regions of aircraft with vertical short takeoff and landing (V/STOL) flows in ground effect are presented. The upwash flow is formed from the collision of two opposing radially flowing wall jets. The wall jets are created in a unique way that allows the upwash to form without any interference due to the source jets. The objective of this work is to systematically characterize the development and structure of the flow. The upwash flow exhibits very large mixing rates compared to turbulent free or wall jet flows. A unique set of two component velocity profiles was taken in the upwash flow field. These measurements include several higher moment terms that appear in the turbulent kinetic energy equations, as well as length scales and intermittency determinations. Measurements were taken along the axis connecting the two source jets as well as off this axis at six measurement stations above ground. The results provide detailed data on an important class of flows where none existed, and they are expected to significantly improve the computational empirical tools available for predicting V/STOL behavior near the ground.

\* This work was funded by the Air Force Office of Scientific Research under contract No. F49620-85-C-0111 by Dr. James Wilson.

1. INTRODUCTION

A unique turbulent mixing phenomenon results from the collision of opposing wall jets. The mean velocity profile of the generated flow appears to be similar to those found in free and wall jet turbulent flows. However, the macroscopic properties of mixing layer growth rate and the corresponding mean velocity decay rate are significantly different. This combined effect means that there is a different distribution of average momentum in the flow. It is important to properly understand the mixing process and the dynamics of the resulting flow in order to take full advantage of this effect in some applications.

One such flow has recently been identified due to the development of aircraft with V/STOL capability. When a V/STOL aircraft is in ground effect, the exhaust from the aircraft lift jets interacts with the ground, producing an upwash flow directed toward the underside of the aircraft. This upwash flow (including fountains, in the case of more than two jets) has profound aerodynamic implications on the aircraft design by virtue of the additional lift force it imparts to the aircraft at its most critical point of operation, in hover. The induced aerodynamic effects due to upwash augmentation of lift forces and suckdown entrainment over the lower surfaces of only 5% of engine thrust may translate into as much as a 40% difference in mission payload or endurance as described by and Kalemari and York

(1979). An understanding of the basic physical mechanisms acting in the flow field between the aircraft and the ground is vital to the successful development of a practical V/STOL aircraft.

The upwash flow is very difficult to analyze because of the much greater mixing layer growth rate compared to other types of turbulent flows as described by Rajaratnam (1976). The problem is made computationally difficult by the intrinsic three-dimensionality of the upwash and because the turbulence in this type of flow is not understood. Numerical codes require better definition of the turbulent structure in order to make reliable predictions of the fountain flow and, later, the fountain/aircraft interaction.

Although the upwash flow field is very complex, the analysis that is most often used is based on a very simple model. The mean velocity profile along a line connecting the source wall jets looks like the profile found in a free radial wall jet. A simple momentum balance along the collision line requires that a fan forms long the symmetry plane between the two jets (see Fig. 1). Extrapolating these velocity vectors back to their virtual origin is equivalent to folding the ground plane down. The flow is then analyzed simply as a radial free jet with its origin located at the impingement point of the source jets. The most obvious problem with this type of analysis is the much faster growth rate found in the upwash compared to a free jet. This has profound influence on both the distribution of momentum in the upwash and the magnitude of the entrainment field contributing to the suckdown on the aircraft. As diagrammed in the Fig. 1, the real upwash fan extends over a much broader region than the free radial upwash model would predict.

This program is designed to investigate the mechanisms that control turbulence levels, mixing layer spread rate, and mean velocity decay rate in the upwash fan, thereby determining the pertinent scaling parameters of the flow. The goal is to provide a reliable data base for use in predictive computational models and to provide the foundation necessary to properly model the basic V/STOL turbulence equations.

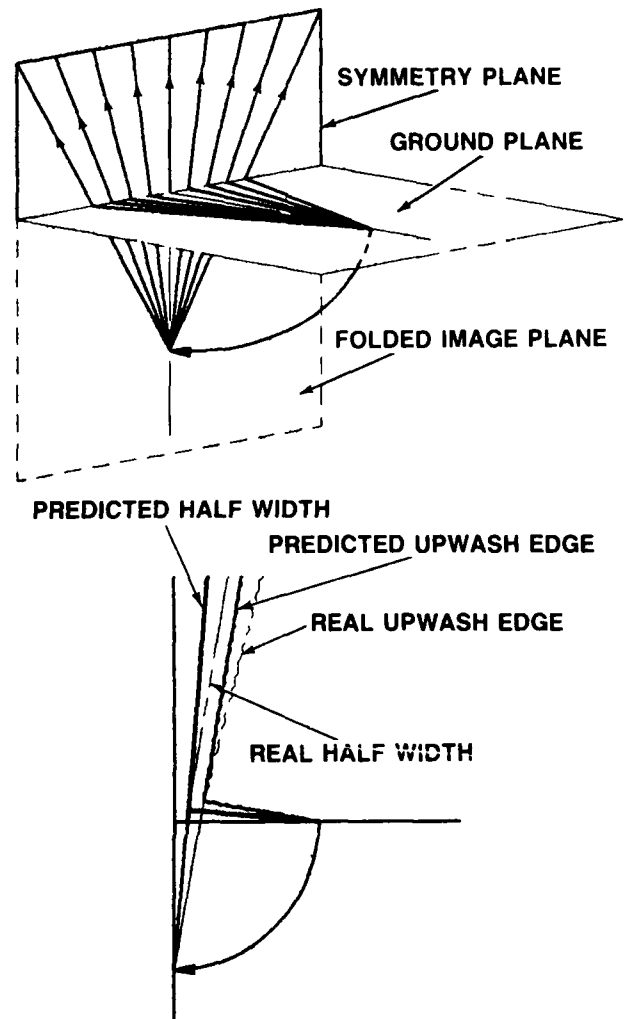


FIG. 1. DIAGRAM SHOWING CURRENT ANALYSIS USING A FOLDED IMAGE PLANE

The approach adopted was to initially examine the turbulence found in a very simple two-dimensional flow configuration. The lifting jet impingement region with the ground was eliminated. The radially spreading wall jets were replaced by simple two-dimensional wall jets. Specific characteristics contributing to the high turbulence level and to the increased mixing rate were isolated and identified. In addition the upwash turbulence structure was examined in fine detail, providing a detailed data base for the first time. These results were reported previously by Gilbert (1983, 1984, 1985).

The results presented in this paper represent some of the measurements taken in the flow created by the collision of radially flowing wall jets. This configuration more closely approximates the actual V/STOL flow behavior. We have made detailed surveys of the three velocity components and several of their statistical moments. Profiles have been made through the flow domain of the upwash for equal strength wall jets. This is the first time that these data have been measured.

In the sections that follow, we will describe the new flow facility designed to study radial wall jets. The wall jet characteristic will be given. It is important that these characteristics are well-documented and well-behaved because they form the starting conditions for the upwash. The basic upwash mean and turbulent properties will be given. These are compared to free jet and two-dimensional upwash results obtained in an earlier investigation. Finally, a discussion of the results and implications to modeling of these types of flow is given.

## 2. RESULTS

### 2.1 Apparatus and Instrumentation

A new wind tunnel facility was designed and

constructed for the study of the upwash created from the collision of radially flowing wall jets. The usual method employed for the generation of this sort of wall jet is the impingement of a circular free jet into a ground plane. While this method undoubtedly creates a radial wall jet in the case of an upwash, it also introduces an additional complication. It is impossible to isolate the effects of the presence of circular free jets on the development of the upwash physically located between them. The downward-flowing free jets set up a strongly coupled secondary rotating flow with the upward-flowing upwash.

We wanted to generate a highly controllable upwash flow whose characteristics would not be affected by the presence of a large secondary flow. The geometry chosen was one that employed a circular source jet flowing through the ground plane from below. The circular jet is diverted into the radial direction along the ground by impinging it on a circular deflector plate.

The new flow facility is shown in Fig. 2. Various different permutations of gap height and deflector plate diameter were tried. The

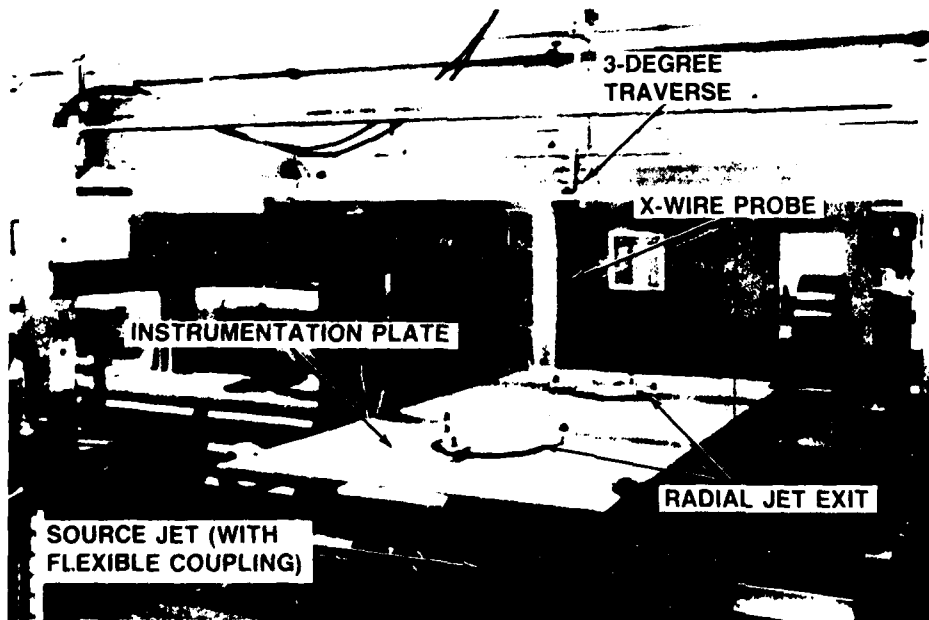


FIG. 2. PHOTOGRAPH OF RADIAL WALL JET UPWASH FACILITY

resulting mean velocity profiles were compared to those obtained from a conventional free jet impingement radial wall jet flow. The final geometric combination chosen was the one that had the same mean velocity decay profile and radial wall jet half velocity height growth rate as the impinging free jet.

The photograph shows the two source jets exhausting from the two independent plenum chambers below the instrumentation plate. The source nozzles are coupled to the instrumentation plate via a flexible collar to provide vibration isolation. The plate is supported by the plenum chambers in such a way as to isolate the flow from any fan vibration that may be transmitted through the chambers. The deflection plates are mounted by three support cantilevers with the gap set by machined spacers. The circular disk in the center contains a series of eight static pressure taps. By rotating this disk, the entire static pressure field between the two source jets may be mapped. The gap height is 5 mm, and the deflection plate has a 15.25 cm diameter. The source nozzle has a 50 cm diameter. The plate is 100 cm x 50 cm, with a jet center distance of 50 cm or 100 gap heights. The radial jet exit velocity is typically 95.5 mps.

The data reported in this report were taken with a commercial X-probe hot film anemometer calibrated in our facility. The experiment and data acquisition are controlled by our real-time mini-computer system. Two time series from the anemometers and various other flow conditions are taken at each point. The time series are pre-processed in real-time and stored before the program increments the probe position. At each point, 32768 data pairs are taken at 2500 pairs/sec for about 13 sec.

The coordinate system that was chosen for these experiments makes it easy to compare wall jet data with traditional wall jet data, and upwash data with free jet data. A system was chosen that allows the X direction to be in the direction of the largest velocity component; that is, X is toward the symmetry plane in the wall

jets and along the symmetry plane in the upwash. For clarity, wall jet parameters are indicated with a 'w' subscript.

## 2.2 Wall Jets

Figure 3 shows typical velocity profiles taken at the exit and slightly downstream of the radial jet, and includes the entrained flow over the top of the deflector plate. Profiles taken at three radial positions around the exit for both jets show very similar profiles. Notice that the flow seems to stick to the deflector plate at the exit but begins to form a normal wall jet profile at only 5 gap heights downstream.

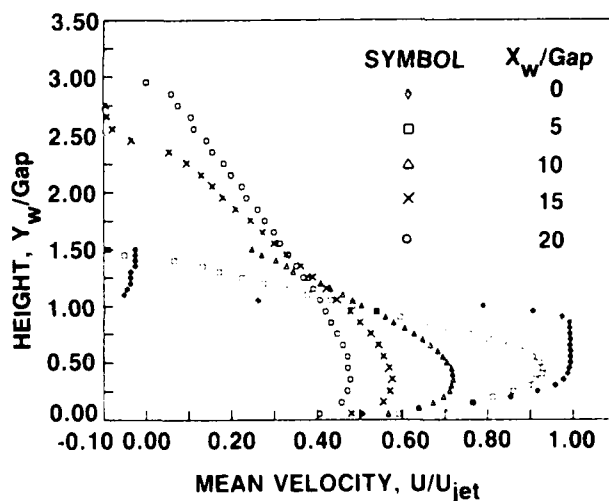


FIG. 3. TYPICAL EXIT JET PROFILES

Wall jet mean and turbulence profiles were taken at 16 locations from the jet exit nozzle to a position beyond the instrumentation center-line. The position of these profiles is noted by the numbers along the instrumentation plate shown in Fig. 4. These measurements were made at equal distances along the plate in increments of approximately 4 gap heights. Each profile contains 26 points spanning 12 gap heights. The height is shown by the brackets at stations 15 and 16 in the figure. The data acquisition and movement of the single-element hot film probe were controlled by the automatic digital data system.

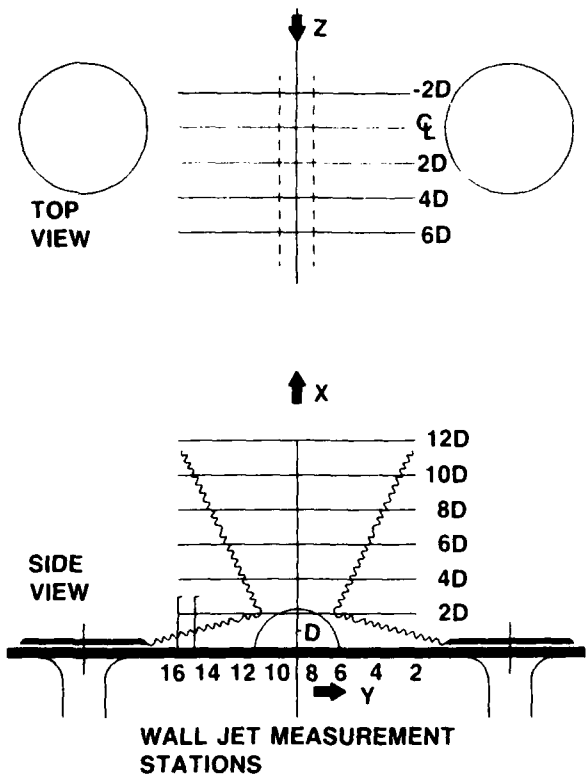


FIG. 4. DIAGRAM SHOWING MEASUREMENT STATIONS AND COORDINATE SYSTEM USED

A plot of the wall jet growth rate as characterized by the half velocity height versus the distance downstream is given in Fig. 5A for each wall jet. A linear least squares curve fit of the data from stations 4 through 16 ( $X_w/\text{Gap} > 14$ ) gives a growth rate of 0.097. The first stations were not used in the curve fit because they are in the developing region. Figure 5B shows the linear decay of the maximum velocity versus distance. This relationship is required by conservation of momentum considerations. The data were normalized by the characteristic half height dimension and alternate profiles were plotted. Figure 6 shows that the mean velocity similarity exists as early as  $X_w/\text{Gap} = 13$ , much sooner than usual. The turbulence energy profiles show similarity at about  $X_w/\text{Gap} = 20$ .

The generally accepted growth rate value for an axisymmetric wall jet is 0.078. However, wall

jets produced by impinging circular jets on a plate give a value of 0.087, and that value seems to be independent of the height of the impinging jet from the plate. The virtual origins, defined by the half velocity growth curve, are -7.14 and -7.20 gap heights which are about half-way between the geometric centerline and the exit.

Matching the maximum velocity values at the physical centerline alone was not enough to ensure that the upwash fan would form vertically. In early tests, the maximum velocity criterion produced an upwash fan that formed at the physical centerline but that was not vertical. Careful

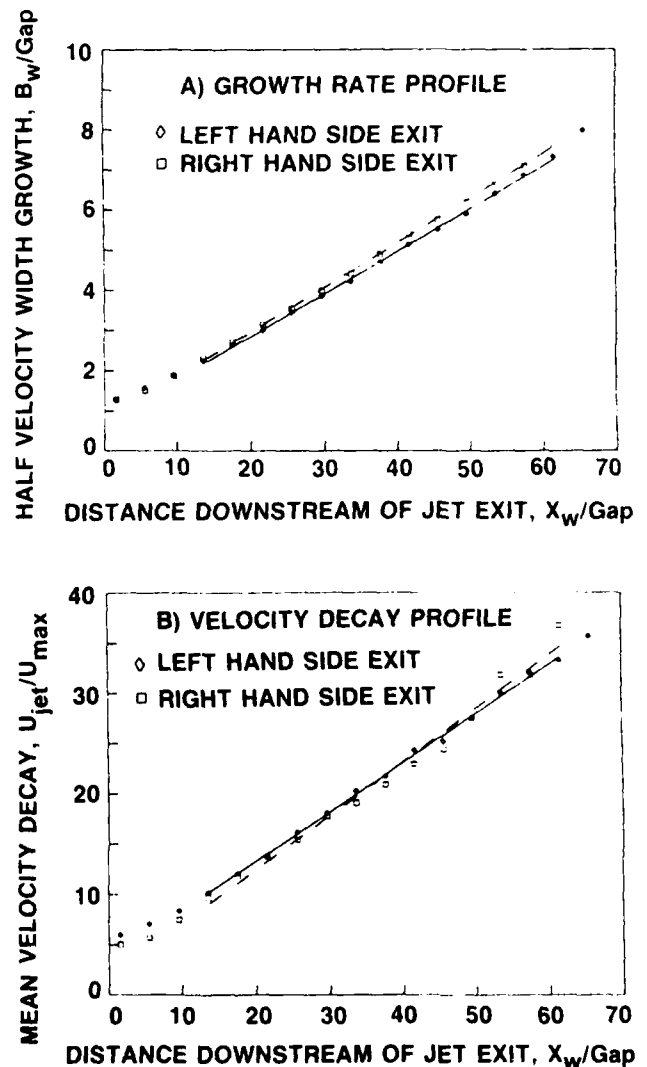


FIG. 5. RADIAL WALL JET CHARACTERISTICS

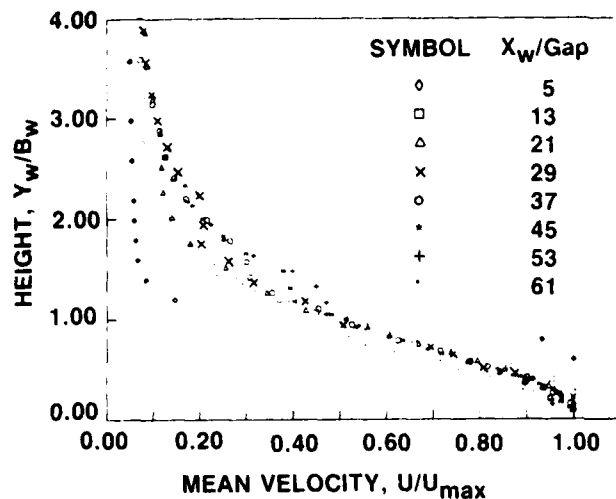


FIG. 6. NORMALIZED RADIAL WALL JET MEAN VELOCITY PROFILES

measurement of each velocity profile at the centerline showed that one flow had an excess of momentum above the maximum velocity point. This caused the flow to slant away from that side showing the strong sensitivity of the flow to very small differences in the velocity profile. The source wall jets were manipulated to give nearly identical profiles; therefore, momentum distributions at the collision point also were nearly identical.

The wall jet characteristics at the centerline may be determined at  $X_w/\text{Gap} = 50$ . The wall jet parameters when no collision occurs should be used to normalize upwash data in a manner similar to using the wall jet nozzle height and source jet velocity as characteristic parameters in a wall jet flow. At the centerline, the wall jet half velocity height is  $B_w/\text{Gap} = 4.0 = D = 20.50$  mm, and the characteristic velocity is  $U_{c2}/U_{\text{jet}} = 0.218 = U = 20.8$  mps. The value  $D$  now becomes the characteristic height for the upwash and is used to determine all the measurement stations in the upwash. The region of influence of the collision extends to about  $2D$ . This is shown as a semi-circle in Fig. 4.

### 2.3 Upwash Measurements

Figure 4 shows the location of the measurement stations in the upwash. The value  $D$ , the

half velocity height at the collision point of an individual radial wall jet, is the characteristic dimension of the upwash. Measurements were made along the centerline connecting the two jets at 6 heights from  $2D$  to  $12D$ . Measurements at  $12D$  may have been affected by the presences of the probe transverse mechanism and support structure. Profiles also were taken at four cross-stream locations in the  $Z$ -direction. These profiles at  $2D$  increments were  $6D$  to  $-2D$  and at the same four lower heights as the centerline. Additional profiles were taken along the  $Z$ -plane in the symmetry plane and at one-half width to either side of the symmetry plane at heights of  $4D$  and  $6D$ . Each profile contained 60 points positioned approximately  $0.23D$  ( $4.8$  mm) apart, except at the lowest station where they were at half that value. Each profile was repeated with the  $X$ -probe rotated  $90$  degrees so that all three velocity components at each point were measured. Since this procedure repeats the measurement, it is a good check on the reproducibility of the data.

There are two forms of data acquisition programs. These programs are responsible for taking the real-time data, performing some pre-processing, storing the processed data, and controlling the probe movement and timing. The longer form of the program does a complete turbulence analysis; the other computes only means, turbulence energy, and one component Reynolds stress. The long form computes, in addition, third and fourth moments, auto-correlations and cross-correlations, Taylor microscales, and integral scales. These allow calculation of various terms in the turbulent kinetic energy equation, and intermittency. The length scales are calculated by computing the turbulence energy spectra from the time series by using fast Fourier transforms and then computing the correlation using the inverse transform. The Taylor scales also were computed from the derivative of the time series for comparison. Taking time derivatives inherently adds noise so that these values are not as reliable as those obtained from the correlation method. The values agreed well at the symmetry plane where the intermittency

is one. Along the centerline, a complete data analysis was done. Only the first and second moments will be shown here. At all other points, a shorter analysis was performed that gives only the first and second moments (means, turbulence energy, and Reynolds stress).

The mean velocity profiles in the upwash direction were curve fit with a least squares curve of the form  $U = A+C \exp [-(Y-Y_0)^2/2S^2]$ , where  $Y_0$  is the symmetry coordinate,  $A+C$  is the maximum velocity, and  $S$  may be used to define the half velocity width as  $B(U=U_{max}/2) = 1.177 S$ . This curve fit procedure is superior to the usual determination of half width that relies on interpolating between data points to find  $U_{max}/2$ . That method suffers severely from data scatter in both the determination of  $U_{max}$  and the interpolation at  $U_{max}/2$ , and rarely gives symmetric half velocity positions.

The half velocity growth rate curve defined by the curve fit technique is shown in Fig. 7A. The growth rate shown is about 0.25. This value is essentially the same one found in the previous two-dimensional upwash and is more than twice the free jet value. The mean velocity decay curve is shown in Fig. 7B. The data are plotted in a form to give the linear relationship required by conservation of momentum considerations.

The normalized mean velocity profiles at six heights are shown in Fig. 8. The profiles have been shifted to their symmetry point and normalized by the local half velocity width and local maximum mean velocity as determined by the curve fit. It was found in the two-dimensional wall jet studies that the zone of influence of the collision is on the order of two characteristic length scales  $D$ . Therefore, there is still some evidence of the turning of the flow at  $X/D = 2$ . The residual velocities shown in the tails of the velocity distribution are similar to those found previously. This entrainment flow is also very evident in the smoke flow visualization studies. The mean velocity profiles are symmetric. These similarity profiles may be expressed as  $U/U_{max} = \exp \{-0.693 \eta^2\}$  where  $\eta = Y/B$ . The constants in

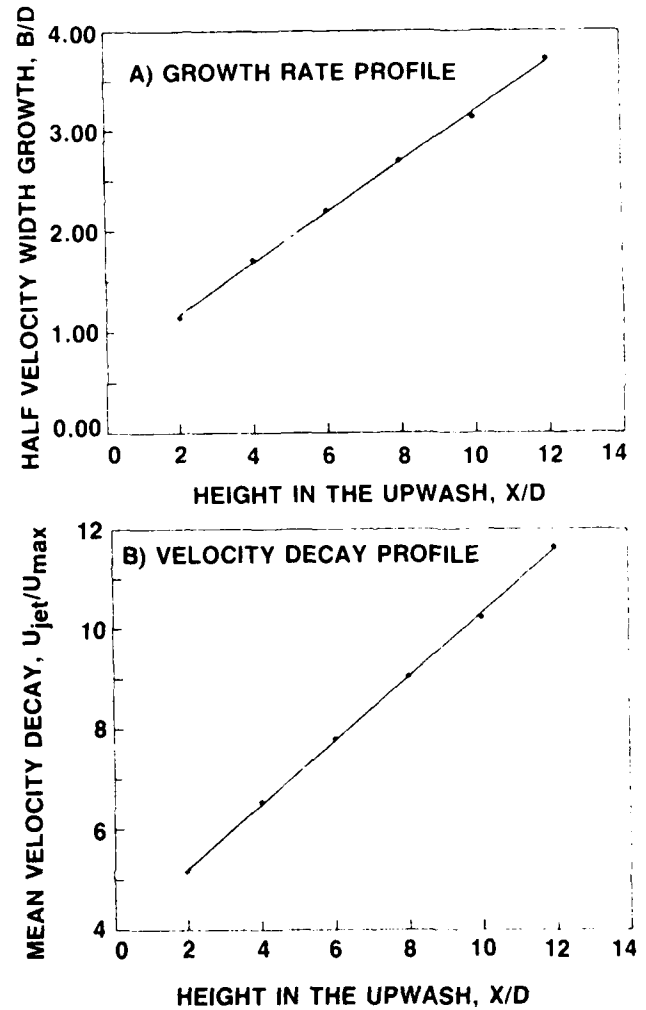


FIG. 7. RADIAL UPWASH CHARACTERISTICS ALONG THE CENTERLINE

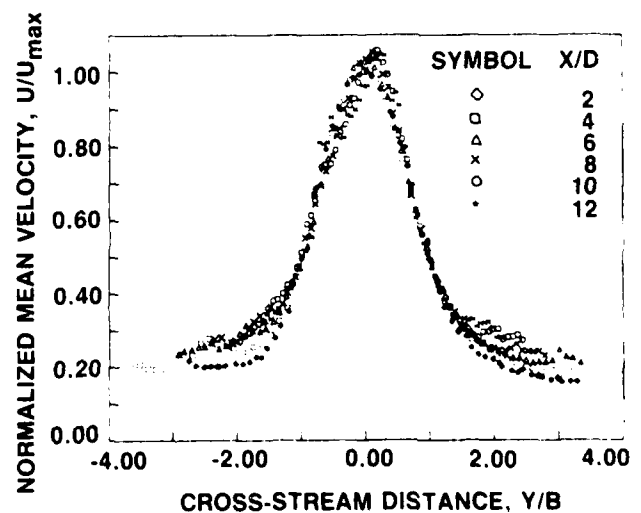


FIG. 8. NORMALIZED MEAN VELOCITY PROFILES

the curve fits have been absorbed into the virtual origin shift. However, the mixing layer growth rate is about twice the free jet value. The similarity profile for this flow can be written as  $U/U_{max} = \exp(-12.0 (Y/X)^2)$  where the free jet coefficient is between 70.7 and 75.0. Since the mixing layer growth rate is higher, the mean velocity decay must be correspondingly lower. Our decay curve is  $U_{max}/U_0 = 1.5/(X/D)$  compared to a coefficient of about 3.5 in the free jet case.

The entrainment coefficient can now be estimated from the mean velocity decay and growth rate relations used in the conservation equations. By assuming the entrainment velocity as a constant fraction of the local maximum velocity, the fraction is given as 0.53 times the growth rate. In a free radial jet, the growth rate is 0.1, which gives an entrainment velocity of 0.053. For the radial upwash, the entrainment velocity is significantly higher at 0.125 of the local maximum. This can readily be seen in smoke flow visualization studies. The entrainment velocity represents only the magnitude of the velocity carrying mass into the upwash and is not expected to appear strictly as a transverse velocity component.

The component turbulence energy in the mean flow direction is shown in Fig. 9A. Similarity is reached at about  $X/D = 4$ , which is much faster than usually found in radial free jets and is about the same found for the two-dimensional upwash. This may be due to the fact that there is no core region that needs to decay before the similarity jet can form. These profiles are normalized in a manner similar to the mean profiles. The magnitude and form of these profiles are exactly those expected to be found in a two-dimensional plane jet. These turbulent velocity profiles are symmetric and have symmetric peaks. The components in the two cross-stream directions, obtained by rotating the probe, are shown in Fig. 9B and 9C. These two figures show the expected form and values. Figure 10 shows the total turbulent kinetic energy profile at six measurement stations normalized as before. The total energy  $q^2$  reaches similarity quite rapidly,

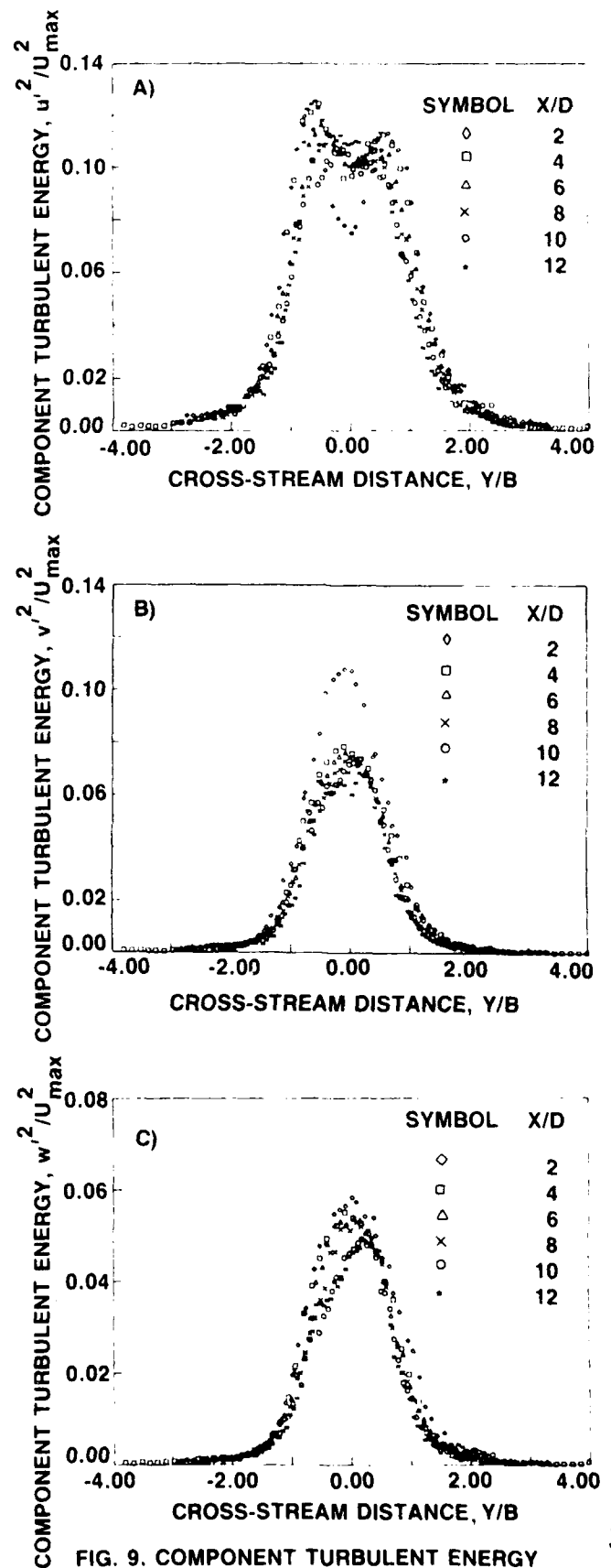


FIG. 9. COMPONENT TURBULENT ENERGY

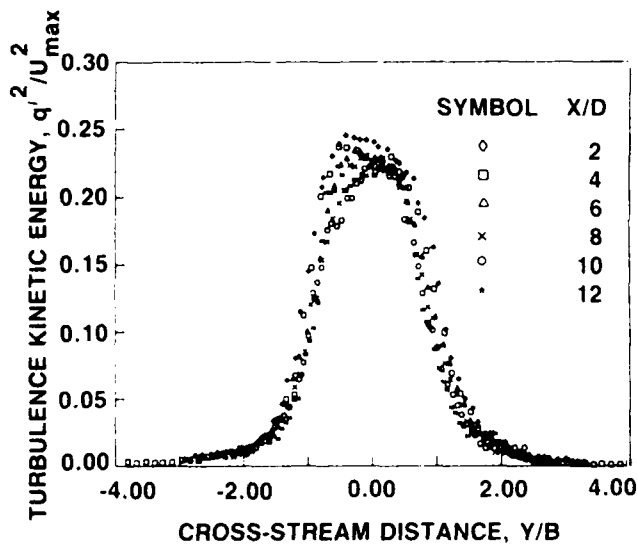


FIG. 10. TOTAL TURBULENCE KINETIC ENERGY

showing that the slower development of the individual components is really due to a redistribution of turbulence among the various components as they approach local isotropy. Examination of the component turbulence energy and total kinetic energy levels found in the upwash shows these values to be exactly the same as those found in ordinary radial and two-dimensional free jet flows.

Figure 11 shows one component of the Reynolds stress,  $\overline{uv}$ . Across the center region, the Reynolds stress profiles are anti-symmetric about the centerline passing through zero and have the same magnitude on either side. Since Reynolds stress measurements are particularly sensitive to measurement techniques, these plots are a good indication of the precision of the entire experiment. The form and magnitude are again exactly those expected for radial and two-dimensional jets.

In addition to growth rate, another departure from free jet characteristics is found in the intermittency. Figure 12 shows the normalized intermittency. The intermittency is determined by the flatness factor normalized by the centerline value. An intermittency factor of one indicates fully turbulent flow. The form of these curves is

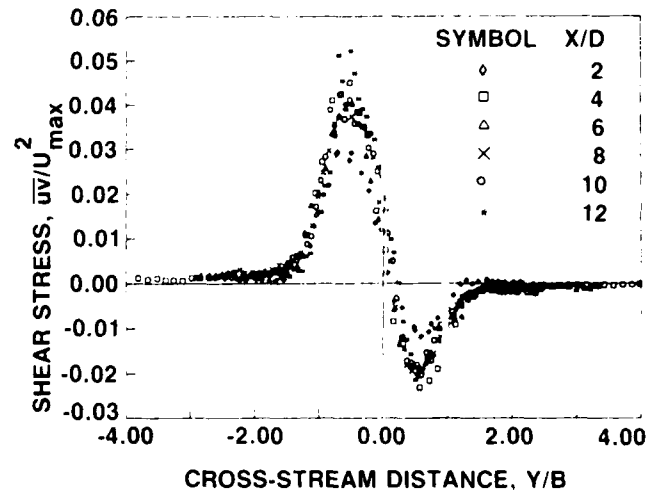


FIG. 11. SHEAR STRESS COMPONENT

the expected normal distribution. However, in all free shear flows, the ratio of the intermittency half width to mean velocity half width is two as shown by Townsend (1980). Our measurements in the upwash give this ratio as one. As indicated, all of the profiles shown have been normalized by local mean velocity half widths. So, while the form looks absolutely correct, the widths of the profiles are about twice the free jet widths. Because of the method of normalization, this means that the intermittency profile is really very similar to the free jet profile. Because the upwash intermittency profile does not have a flat region at the centerline, the non-turbulent flow

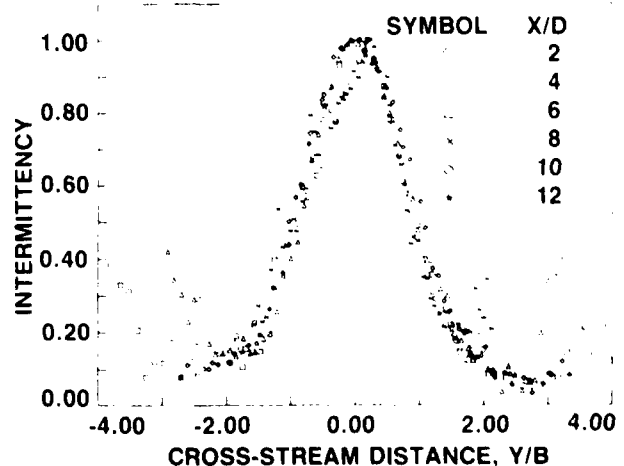


FIG. 12. INTERMITTENCY PROFILES

outside the upwash is penetrating nearly to the centerline; that is, the mixing layer must have a penetration length scale nearly equal to the half velocity width.

The results of the profiles taken off the centerline were very similar. The processing of these data was performed just like the centerline data. The growth and decay characteristics are shown in Fig. 13. The mean velocity vector used in the calculations was the true vector computed from the three mean velocity components. These show that the centerline values of growth and decay also appear off axis.

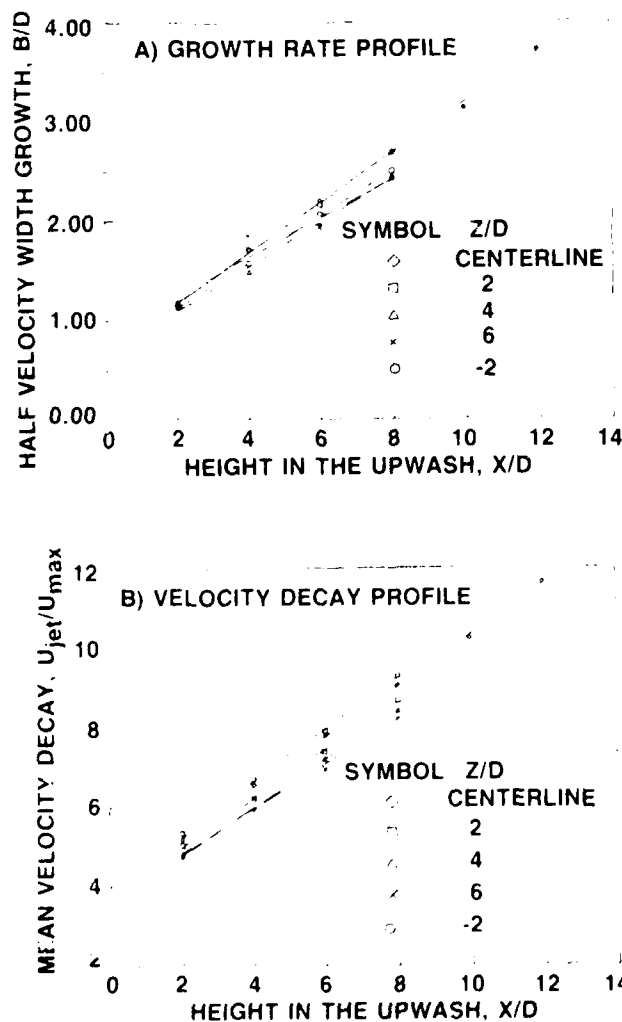


FIG. 13. RADIAL UPWASH CHARACTERISTICS OFF THE CENTERLINE

From these data, it is possible to compute the velocity vector in the plane perpendicular to the line connecting the source jets. The plane that lies halfway between the two source jets is a symmetry plane. The theory derived from a simple conservation criterion requires that these vectors all are straight and emanate from the same virtual origin. The measured values with the theoretical prediction are shown in Fig. 14. To the positive Z-side, the agreement is very good. On the negative side, the vectors seem to point more closely to the vertical. Planes parallel to the symmetry plane show that the vectors turn more toward the vertical as you go away from the symmetry plane. This is reasonable since this flow is more influenced by entrainment and less by the direct collision with the opposing wall jet. The reason the negative side vectors are different from the positive is a small wrinkle in the upwash fan. Throughout the initial stages of setting up this experiment, it was continuously re-emphasized that even a small variation in the wall jet profiles along the collision line would result in a slanting or wrinkling of the upwash fan.

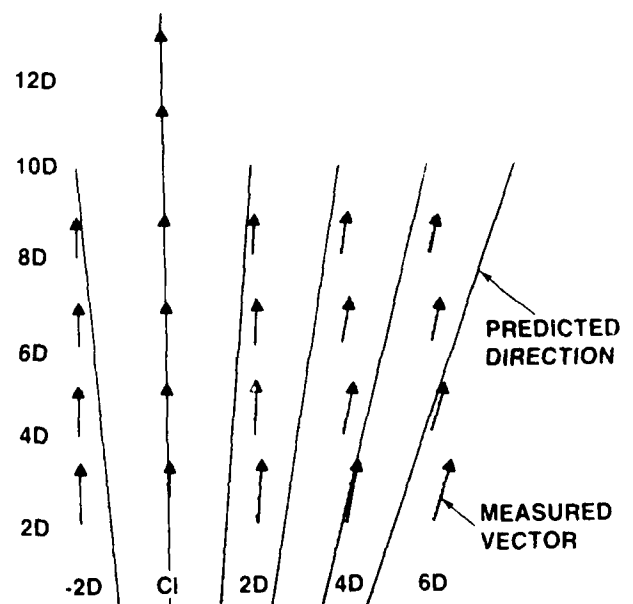


FIG. 14. MEASURED AND PREDICTED VELOCITY VECTORS IN THE SYMMETRY PLANE

### 3. SUMMARY

The data reported in this paper represent initial results of a fundamental investigation of the turbulence structure found in the flow created by the collision of radially flowing wall jets. This type of flow is found in the upwash region of V/STOL aircraft. The experiment is a continuation of a study that started with a simplified two-dimensional wall jet geometry that has been generalized here to radial jets. A new method of producing a radial wall jet was developed that avoids the complications introduced by the presence of impinging jets. Radial wall jet profiles were taken to assure that the wall jet characteristics of an impinging jet were faithfully reproduced. These surveys showed the rapid development and turbulence similarity profiles. They exhibited the well-established mixing layer growth rate and mean velocity decay rate that characterize radial wall jets. Measurements were made in the upwash region which resulted from the collision of radial wall jets. These are the most complete turbulence measurements in this type of flow. Profiles were taken at six measurement stations along the line connecting the source jets, and four measurement stations along planes parallel to the centerline plane and along the symmetry plane using X-probe hot film anemometry. All three velocity components were measured. The results corresponded very well to those obtained in the two-dimensional experiment. The collision region of influence is about two characteristic heights. The characteristic height is the half velocity height of the wall jet that would exist at the collision point for a single jet. The upwash forms at the point where the maximum mean

velocity from each jet is equal. However, the characteristics of the upwash also are very sensitive to the profile or distribution of momentum in the wall jet. A small variation in the wall jet profile will cause the upwash to slant significantly. The expected, abnormally high mixing layer growth rate was found in the radial upwash. The result predicted by other investigators of abnormally high turbulence energy was not found in either set of experiments. The linear trends for upwash growth rate and local maximum velocity decay rate were found. The upwash flow reaches similarity very quickly due to the very high mixing rate and the lack of a core region that has to be consumed. The very sharp intermittency profile of the upwash also differs from the one found in a free jet. This indicates that the non-turbulent flow outside the upwash is penetrating nearly to the centerline of the upwash; that is, the mixing layer has a penetration length scale nearly equal to the half velocity width of the upwash fan.

### REFERENCES

- Gilbert, B.L. July 12-14, 1983: Detailed turbulent measurements in a two-dimensional upwash. AIAA No. 83-1678, AIAA 16th Fluid & Plasma Dynamics Conf., Danvers, MA.
- Gilbert, B.L. Aug. 1984: An investigation of turbulence mechanisms in V/STOL upwash flow fields. Grumman R&D Center Report RE-688.
- Gilbert, B.L. Sept. 1985: An investigation of turbulence mechanisms in V/STOL upwash flow fields. Grumman R&D Center Report RE-707.
- Kalemaris, S.G.; York, P. May 1979: Weight impact on VTOL, SAWE Paper No. 1326, 38th Annual Conf. of SAWE, New York, NY.
- Rajaratnam, N. 1976: Turbulent jets. In: Developments in water science. Vol. 5., Amsterdam: Elsevier Scientific Publishing Co.
- Townsend, A.A. 1980: The structure of turbulent shear flow, 2 ed. Great Britain: Cambridge University Press.

ELECTROMAGNETIC METHODS OF TURBULENCE  
MEASUREMENTS, SHORTCOMINGS AND ADVANTAGES

A. Tsinober<sup>1</sup>, E. Kit<sup>1</sup>, M. Teitel

Department of Fluid Mechanics and Heat  
Transfer, Faculty of Engineering  
Tel-Aviv University, Ramat Aviv  
Tel-Aviv 69978, Israel

Current Address:

<sup>1</sup>Department of Mechanical Engineering  
University of Maryland  
College Park, MD 20742 USA

ABSTRACT

Two major electromagnetic methods of turbulence measurements are discussed. Both methods are based on the measurement of the electrical field induced by the fluid motion in the presence of a magnetic field. In the first method a multielectrode potential difference probe (PDP) is used in the presence of an external magnetic field, while in the second one the source of the magnetic field is incorporated in the probe itself and the magnetic field is strongly localized around the probe. Shortcomings and advantages of both methods are discussed along with recent developments.

1. INTRODUCTION AND BASIC RELATIONS

The idea of electromagnetic methods is to deduce velocity  $u = [u_i](i=1,2,3)$  and other flow characteristics from the measurements of electrical field  $e = [e_i] = [\partial\phi/\partial x_i]$  (magnetic field), induced by the motion of an (electrically conducting) fluid in the presence of magnetic field.

These methods are realized in two different ways. In the first the measurements of the induced electrical field are made by a probe consisting of two or more electrodes while the magnetic field (mostly homogeneous) is created by an external (to the probe) source. The main feature of the second way is that the source of the magnetic field is an integral part of the probe itself and thus is strongly localized in the vicinity of the probe. Each method has its own advantages and shortcomings

with respect to each other and to nonelectromagnetic methods which will be discussed in sequel.

In the following it is assumed that the conductivity of the fluid is constant and large, the frequencies in the flow are not very large and the magnetic Reynolds number is small, i.e., that  $\epsilon(\sigma T)^{-1} \ll 1$ ,  $\sigma\mu_0 L^2 T^{-1} \ll 1$  and  $\mu_0\sigma V L \ll 1$ , where  $V$ ,  $L$ ,  $T$  are the characteristic scales of velocity, length and time respectively,  $\sigma$  and  $\epsilon$  are the electrical conductivity and permittivity of the fluid respectively and  $\mu_0$  the permeability of free space. These conditions are mostly well fulfilled for electrolytes and liquid metals up to frequencies at least as large as  $10^5 \text{ sec}^{-1}$ . Under these conditions the Ohm's law in the form

$$j = \sigma(e + u \times B) \quad (1)$$

is valid, the electrical field is a potential one  $e = -\text{grad}\phi$  and the induced magnetic field is negligible, i.e.,  $\text{rot}B = 0$ .

As it was pointed out by many authors that the main difficulty of the induction velometry method is the problem of Ohm's losses (Grossman, et al. (1957), Shercliff (1962), Kit (1970) and others). It follows from the Ohm's law that the quantity  $u \times B$  cannot be measured precisely unless the current  $j = 0$  or is small in comparison with either  $\sigma u \times B$  or  $-\sigma \text{grad}\phi$ . This occurs in some special cases as for example in two-dimensional flow with the magnetic field perpendicular to the plane of the flow in which the potential  $\phi$  of the electrical field is equal to the stream function  $\psi$

(the same is true for an analogous axisymmetric flow. On the other hand, for the two-dimensional flow with the magnetic field parallel to the plane of the flow the electrical field is constant and is defined by the flow rate (or the velocity at infinity) and the characteristics of the external electrical circuit leaving no hope to measure any local characteristics at all.

Thus in general the measured electric field  $-\nabla\phi$  cannot be considered as  $\mathbf{u} \times \mathbf{B}$ . As was pointed out by Professor J.A. Shercliff. "This is particularly important when measurements of turbulent velocities are being attempted by induction velocimetry ... the question as to how measurements of fluctuating electric fields and their correlations in turbulent shear flow or even in homogeneous turbulence under a uniform imposed magnetic field can be related to the statistical kinematic properties of the turbulence has not yet been answered, but certainly deserves investigation".

In fact there is little hope to obtain this relation in the general case of three-dimensional non-homogeneous non-isotropic turbulent flow since the electrical field is uniquely defined by only one component of vorticity (the one which is parallel to the magnetic field) and boundary conditions. This follows from the equation  $\text{div} \mathbf{j} = \mathbf{u} \cdot \nabla \times \mathbf{B}$  and Ohm's law (1) from which follows the Poisson equation for the electrical field potential.

$$\nabla^2 \phi = \text{div}(\mathbf{u} \times \mathbf{B}) = \mathbf{B} \cdot \boldsymbol{\omega}, \text{ where } \boldsymbol{\omega} = \text{rot} \mathbf{u}, \quad (2)$$

which together with appropriate boundary conditions defines uniquely the electrical field. Thus the electric field does not "feel" the two other vorticity components of the flow field, which are perpendicular to the magnetic field. Therefore, the only information about the flow field which could be obtained from the electrical field measurements, is that which follows from the knowledge of  $\boldsymbol{\omega}_B$ .

In spite of this limitation the electromagnetic methods of turbulence measurements appear to be useful in many respects. Their shortcomings and advantages as well as recent developments are discussed in the following.

## 11. POTENTIAL DIFFERENCE PROBE (PDP) METHOD WITH AN EXTERNAL MAGNETIC FIELD

Grossman, et al. (1957) were the first to introduce a three electrode probe (schematically shown in figure 1) with the third electrode on the OY axis parallel to the external magnetic field. This allowed to measure  $-\partial\phi/\partial y = e_y = j_y/\sigma$  and in this way to obtain an estimate of the induced electrical current  $j$ . Their measurements were performed in a pipe flow of slightly salted water in a transverse magnetic field. The main result of Grossman, et al (1957) was that the rms value of  $e_y = j_y/\sigma$  appeared to be of the same order as the rms value of  $e_z$ . Therefore they concluded that measurements of  $e_z$  do not provide the correct value of the longitudinal component of velocity fluctuations  $u_x$  as was hoped before. Kit (1970) extended the work of Grossman, et al. (1957) in the MHU channel flow of mercury and obtained similar results for weak magnetic field (small interaction parameter). He showed that in a strong enough magnetic field when the flow becomes almost two-dimensional in the plane perpendicular to the magnetic field the rms value of  $e_y$  was two orders of magnitude smaller than that of  $e_z$ . It was shown in this way that the PDP method is applicable for velocity measurements in two-dimensional flows.

Kolesnikov and Tsinober (1972) showed that in homogeneous and isotropic turbulent flow the ratio  $\kappa = 2\overline{e_y^2}/\overline{e_z^2} = 1$ . On the other hand in two-dimensional flow  $\kappa = 0$ . Therefore measurements of  $\kappa$  in turbulent flow provides a measure of its deviation from isotropy.

As it was mentioned in the introduction it is impossible in principle to obtain precise relations between the velocity and the induced electrical field fluctuations in the general case of three-dimensional turbulent flow. There exists a case, however, for which it is possible to obtain relations of this kind between statistical characteristics of velocity and electrical fields. This is the case of homogeneous and isotropic turbulent flow in which the components of velocity, vorticity, etc. are statistically the "same" and this makes it possible to obtain these relations. This was done theoretically and checked experimentally

by Tsinober, et al. (1986) and is briefly reviewed here. As a consequence of isotropy they obtained a number of relations i) between the intensity of turbulence  $u^2$  and the first derivatives potential of the electrical field  $\phi$ , ii) between the different first derivatives of  $\phi$ , iii) correlation coefficients between the velocity fluctuation  $u_x$  and  $u_z$  and  $\partial\phi/\partial z$  and  $\partial\phi/\partial x$  respectively, iv) between second derivatives of  $\phi$  and v) a relation between the longitudinal velocity correlation function  $f(r)$  and correlation functions of the three derivatives

$$\frac{\partial\phi(x)}{\partial x} \frac{\partial\phi(x+r)}{\partial x}, \frac{\partial\phi(x)}{\partial y} \frac{\partial\phi(x+r)}{\partial y}, \frac{\partial\phi(x)}{\partial z} \frac{\partial\phi(x+r)}{\partial z}$$

Some of these relations are shown below (the magnetic field is oriented as in fig. 1). For the full set of relations and details see Tsinober, et al. (1986).

$$i) \quad \overline{u^2} = 2,5(\overline{\partial\phi/\partial z^2}) \quad (3)$$

$$ii) \quad \overline{(\partial\phi/\partial x)^2} = 2(\overline{\partial\phi/\partial y})^2 = \overline{(\partial\phi/\partial z)^2} \quad (4)$$

$$iii) \quad \overline{u_x(\partial\phi/\partial z)/(u_x^2)^{1/2}} \{(\overline{\partial\phi/\partial z})^2\}^{1/2} \\ = (5/11)^{1/2} = 0,79 \quad (5)$$

These and other mentioned relations were checked in a flow of salted water past a grid on a small scale facility.

In order to produce a reasonably measurable signal it was necessary: i) to have rather strong external magnetic field in the region the probe was placed (the smaller the probe the stronger magnetic field is necessary); ii) to specially process the electrodes to reduce the electrochemical noise. A probe of an overall scale of about 1 mm (with electrodes = 0.1 mm) was used to measure flow characteristics past a grid in a test section of 5 x 5 cm<sup>2</sup> in cross section. The use of salted water (low electrical conductivity) ensured that the dynamic interaction of the flow and the magnetic field is entirely negligible (which is not the case with mercury), since for salted water flow even in very strong magnetic fields the electromagnetic force is several orders of magnitude smaller than the viscous and inertia forces. Measurements of first and second derivatives of  $\phi$  as well as  $\nabla^2\phi = \omega_B$  were performed at three positions past the

grid. In some cases hot-film and laser-doppler measurements were performed along with PDP (potential difference probe) measurements. In most of the cases the correlation relations for the first and second derivatives of  $\phi$  were in good agreement with the theoretical values for isotropic flow. Some of the experimental results are shown in figure 2. It is remarkable that the value of the correlation coefficient in (5) obtained from experiments was  $0,74 \pm 0,01$  (see fig. 3).

Another extremely important application of the potential difference method was suggested by Grossman, et al. (1957). It follows from eq. (2), which enables one to measure the component of the vorticity parallel to the magnetic field, by measuring the  $\nabla^2\phi$  which in turn could be measured using a 7-electrodes probe realizing a central difference approximation of the Laplacian. The first qualitative attempt to implement this method was made by Baker (1971) using a five-electrode probe in a laminar flow. Tsinober, et al. (1986) made an attempt to check the performance of this method in the above mentioned experiments by measuring  $\nabla^2\phi = \omega_B$  by a seven electrode probe schematically shown in figure 4. As a test of the vorticity probe performance the isotropy relations for the second derivatives of  $\phi$  were checked from measurements in the frame of 1.2.3. Some results related to vorticity measurements are shown in figures 5 and 6.

### III. THE CASE OF LOCALIZED MAGNETIC FIELD

Along with oceanographic applications there were made recently attempts to build a probe for velocity measurements (in laboratory conditions) using a miniature permanent magnet as a source of magnetic field localized in the vicinity of the point of measurement. This was made possible due to the advances in the technology of strong permanent magnets (Müller and Ihun (1977), Ricou and Vives (1982), Weisenfluh (1985)). Though these developments were made for liquid metal flows (MHU) the method used can be successively applied in ordinary fluid flows like slightly salted water flows, etc.

As in most methods of local measurements using a probe introduced into the flow this method is based on the assumption that the flow in the vic-

nity of the probe is uniform but may be time dependent. The method could be illustrated as follows: Suppose a cylindrical permanent magnet is placed in a uniform flow perpendicular to the axis of the cylinder as shown in figure 7. Two antipode electrodes A and C are placed on the surface of the cylinder measuring the potential difference of the electrical field reduced by the flow past the cylinder. For the illustration purposes we suppose that the flow is two-dimensional and potential, the magnetic field is directed along the OZ axis and the cylinder is electrically insulated from the fluid. In the frame of these assumptions the induced electrical potential is two-dimensional and is to be found from the following boundary-value problem

$$\frac{\partial^2 \phi}{\partial r^2} + \frac{1}{r} \frac{\partial \phi}{\partial r} + \frac{1}{r^2} \frac{\partial^2 \phi}{\partial \theta^2} = 0$$

$$\left. \frac{\partial \phi}{\partial r} \right|_{r=a} = 2UB_{r=a} \sin \theta \quad (6)$$

The solution is elementary and  $\phi = 2UB a^2/r \sin \theta$ . In particular the potential difference between the electrodes A and C  $\Delta \phi_{AC} = 4BaU \sin \theta$ , i.e., proportional to the velocity component perpendicular to AC. Obviously a pair of antipode electrodes located at the ends of the diameter perpendicular to AC will produce a potential difference proportional to the velocity component parallel to AC. Evidently in this configuration there is no possibility to obtain any information about the third velocity component without changing the orientation of the probe. Analogous relations for a potential flow past a spherical permanent magnet (magnet dipole) were obtained by Weissenfluh (1985).

The relevance of the above illustrations for the real fluid flows is a consequence of two main reasons: i) the vorticity induced by probe presence is mostly concentrated in the boundary layer, ii) strong localization of the magnetic field near the probe. As we have seen above the potential of the induced electrical field is defined by the boundary value problem

$$\nabla^2 \phi = \text{div}(u \times B) = B \cdot \text{rot} u$$

$$\left. \frac{\partial \phi}{\partial n} \right|_s = 0 \quad (7)$$

while when the flow is assumed potential the corresponding boundary value problem is

$$\nabla^2 \phi = 0$$

$$\left. \frac{\partial \phi}{\partial n} \right|_s = (u \times B)_n \quad (8)$$

The solutions of (7) and (8) correspondingly

$$\phi(r) = \int_{V'} G(r-r') \text{div}(u \times B) dV' \quad (9)$$

$$\phi(r) = \int_S G(r-r') (u \times B) \cdot n ds' \quad (10)$$

where G is the Green function of the problem, V' is the volume of the flow region and s' is the surface of the body (probe).

If the boundary layer is thin and the normal vorticity component could be neglected comparing to the tangential ones in the boundary layer then the volume integral in (9)

$$\int G \text{div}(u \times B) dV' \sim \int G \frac{\partial}{\partial r'_n} (u \times B)_n dr'_n ds' \sim$$

$$\sim \int G (u \times B) \cdot n ds'$$

which is precisely (10).

The above result is altered by the presence of vorticity in the separation region and the wake past the probe. This alteration, however, is significantly reduced due to strong decrease of the intensity of magnetic field in these regions.

The above arguments indicate that the response of a probe schematically shown in figure 7 as a function of velocity could be expected to be linear. Indeed the experiments by Ricou and Vives (1982) and Weissenfluh (1985) demonstrated that the calibration coefficients of the type  $K = \Delta \phi_{AC} / BUa$  are practically velocity independent for the probe Reynolds number in the range  $200 < Re < 15000$ .

#### IV. DISCUSSION AND CONCLUSIVE REMARKS

The main shortcoming of the potential difference probe method is that generally it does not

make it possible to get quantitative information about the velocity field from the measurements of the three components of the induced electrical field. The main reasons for this are i) that the potential of the electrical field at any point depends on the flow in the whole volume and ii) that it depends on one component of the vorticity  $\omega_z$  only. Therefore, in general, calibration of a potential difference probe consisting, for example, of two electrodes in some flow is meaningless.

Nevertheless the PDP method is very useful for a number of applications. The first example is homogeneous and isotropic flow and the possibility to assess the deviation of turbulence from isotropy. It is noteworthy also that it could be used in nonisotropic turbulence for determining the spectral interval where the turbulence becomes locally isotropic by using high pass filters and checking if the isotropy relations are valid. One of the most important applications of this method is the possibility to measure one component of vorticity (parallel to the imposed magnetic field) directly; i.e., the method does not require calibration. Since the relation (2) is local this method of vorticity measurements is applicable to any flow (not only homogeneous and isotropic). The PDP method has some other advantages as compared to other methods for turbulence measurements. Some of them are as follows: i) possibility to distinguish between velocity components due to the vector nature of the basic relation and sensitivity to the direction of the flow; ii) it is linear and does not require any calibration procedure (in fact no calibration procedure can be applied to this method); iii) it is insensitive to the physical properties of the fluid medium; iv) it yields an instantaneous measure of quantities fluctuating in time; i.e., its response time is extremely small; v) it operates in flows of complex nature (recirculating flows, flows without mean velocity, flows with varying temperature), and it enables to determine the separation and reattachment points and the moment and position of the turbulence onset of relaminarization.

The method utilizing the localized magnetic field has the advantage that it could be used to

obtain quantitative information about the velocity field (two of its components at a time). This becomes possible due to two of its main features. The probe "feels" mostly the vorticity induced by its presence in the flow. This vorticity is linearly related to the velocity in the vicinity of the probe and is almost parallel to the magnetic field in the flow region adjacent to the probe. The probe does not feel the vorticity out of this region due to the strong localization of the magnetic field around the probe.

This method does not allow to measure vorticity without using more than one probe.

It has a number of advantages, the main of which is that it is equally applicable in flows of complex nature like flows without mean velocity, complicated three-dimensional flows, separated flows, etc.

#### REFERENCES

- Baker, R.C., 1971, On the electromagnetic vortex probe, *J. Phys.* E4, 99-101.
- Grossman, L.M., Li, H. and Einstein, H., 1957, Turbulence in civil engineering. Investigation of Liquid Shear Flow by Electromagnetic Induction. *Proc. Amer. Soc. Civ. Engrs, J. Hydr. Div.* 83, No. 1394, 1-5.
- Kit, L.G., 1970, Turbulent velocity fluctuation measurements using a conduction anemometer with three-electrode Probe, *MagnetoHydrodynamics*, 6, No. 4, 480-487.
- Kolesnikov, Yu. B. and Tsinober, A.B., 1972, Two dimensional turbulent flow behind a circular cylinder. *MagnetoHydrodynamics*, 8, No. 3, 300-307.
- Müller, S.F. and Thun, G., 1977, Permanentmagnetische Durchflugsnehmer-Sonde für flüssige Metalle, Institut für Reaktorbauelemente KFK 2479, Karlsruhe.
- Ricou, R. and Vives, C., 1982, Local velocity and mass transfer measurement in molten metals using an incorporated magnet probe. *Int. J. Heat Mass Transfer*, 25, No. 10, 1579-1588.

Shercliff, J.A., 1962, The theory of Electromagnetic Flow Measurement, Cambridge, Cambridge University Press.

Tsinober, A., Kit, E. and Teitel, M., 1986, On the relevance of the potential difference method for turbulence measurements, J. Fluid Mechanics (accepted for publication).

von Weissenfluh, T., 1985, Probes for local velocity and temperature measurements in liquid metal flow. Int. J. Heat Mass Transfer 28, No. 8, 1563-1574.

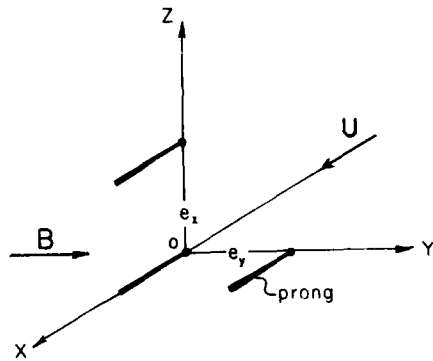


Figure 1 A scheme of a three-electrode potential difference probe.

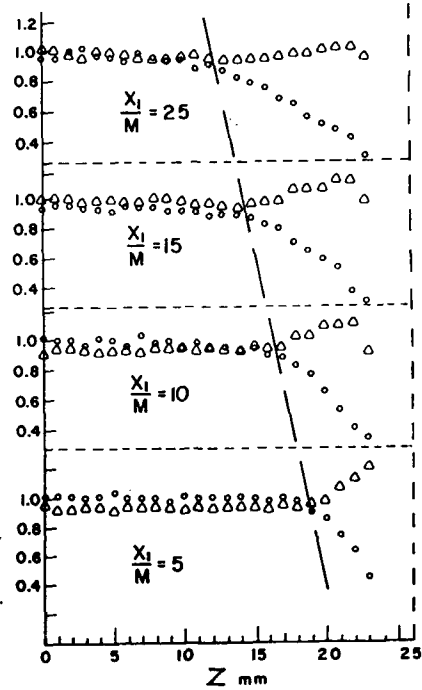


Figure 2 Checking the isotropy relations along the flow cross section at different distances from the grid, M = mesh of the grid.

$$\Delta - \frac{\{(\partial\phi/\partial z)^2\}^{1/2} / 2^{1/2} \{(\partial\phi/\partial y)^2\}^{1/2}}{\{(\partial\phi/\partial x)^2\}^{1/2} / \{(\partial\phi/\partial z)^2\}^{1/2}}$$

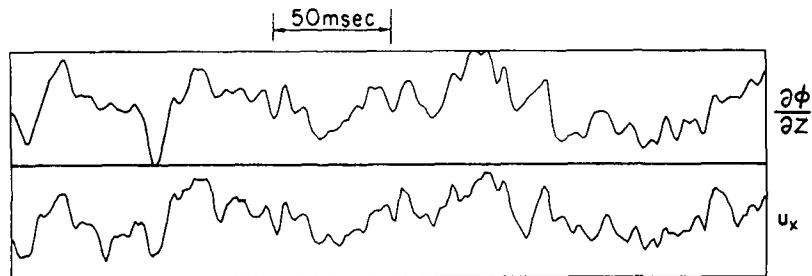


Figure 3 An example of oscillograms of  $u_x$  signal measured by a wire hot-film probe and of  $\partial\phi/\partial z$  signal measured by potential difference probe.

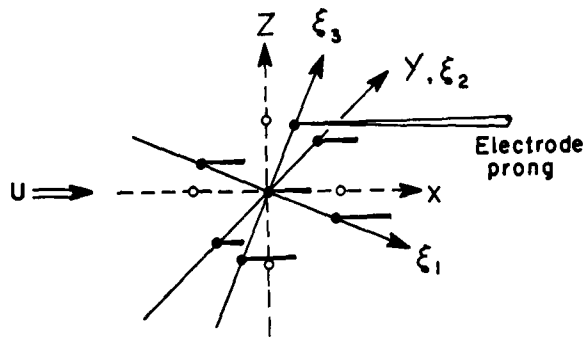


Figure 4 A scheme of the tip of a seven-electrode vorticity probe. The seven tips of the electrodes in the plane xOZ are turned  $22.5^\circ$  relative to the OY axis in order to minimize the disturbances between them.

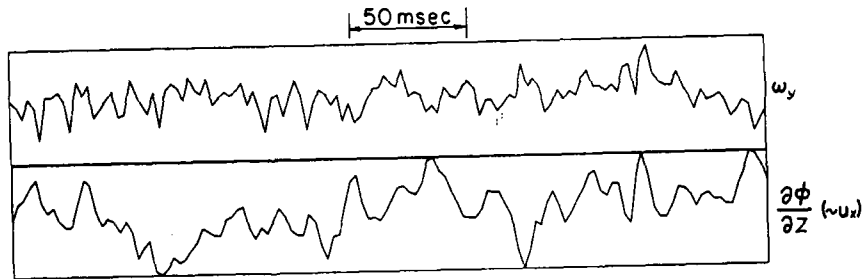


Figure 5 Comparing of oscillograms of simultaneous signals  $\omega_y$  and  $\frac{\partial \phi}{\partial z}$  ( $\sim u_x$ ) illustrating larger content of high frequencies in the  $\omega_y$  signal.

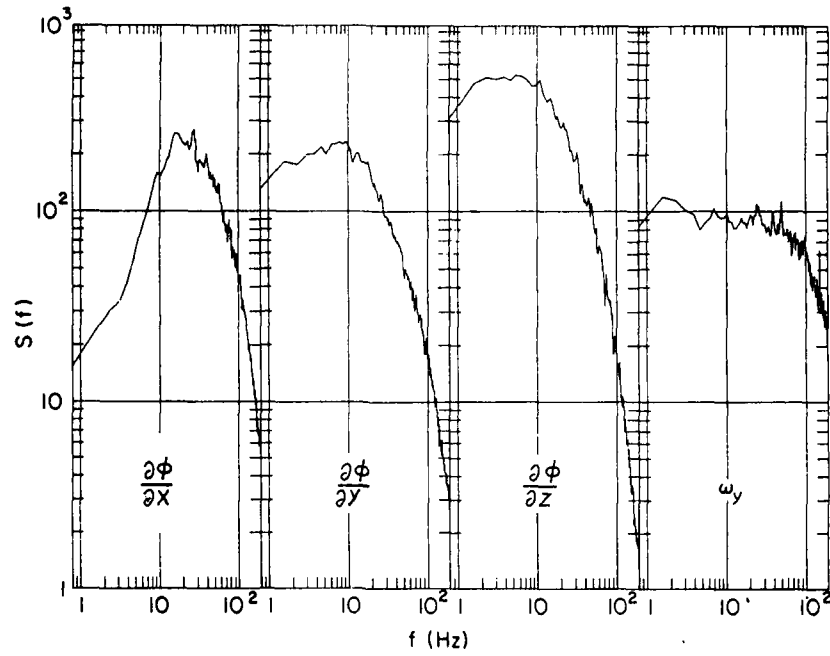


Figure 6 One dimensional spectra of  $\omega_y$  and electrical field components,  $\partial\phi/\partial x$ ,  $\partial\phi/\partial y$ ,  $\partial\phi/\partial z$ .

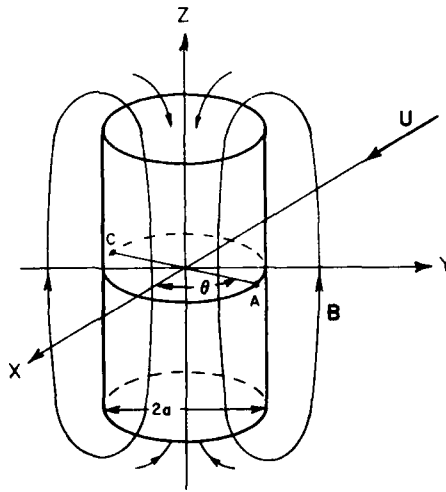


Figure 7 A scheme of a cylindrical probe with a local magnetic field.

EXPERIMENTAL AND NUMERICAL STUDY  
ON THE  
AERODYNAMICS OF JETS IN GROUND EFFECT

by

J.M.M. Barata, D.F.G. Durão and M.V. Heitor

Mechanical Engineering Department  
Instituto Superior Técnico  
Av. Rovisco Pais  
1096 Lisboa Codex  
Portugal

ABSTRACT

The flow field resulting from the impingement of an axisymmetric jet against a wall through a cross flow is analysed by visualization techniques and quantified by laser anemometry and numerical calculations. The experimental study has been carried out for a Reynolds number based on the jet-exit of 60000, for a velocity ratio between the jet and the cross flow of 25 and for the jet exit 5 jet-diameters above the ground plate. This paper describes the experimental method, identifies the main sources of imprecisions, evaluates the estimate of the related errors and compares sample results obtained with laser anemometry in the central plane with numerical predictions using the "k- $\epsilon$ " turbulence model. The experimental results were used to identify the zones of the flow where grid refinement was required to minimise numerical errors.

The study was extended by numerical predictions to investigate the effect on the flow field of the velocity ratio between the jet and the cross-flow and of the height of the jet exit above the ground plate.

NOMENCLATURE

$C_1, C_2, C_{\mu}$	- constants in turbulence model
$D$	- diameter of jet
$H$	- height of crossflow tunnel
$K$	- turbulent kinetic energy
$R_e$	- Reynolds number
$R_{uv}$	- shear stress correlation coefficient
$P$	- static pressure
$U$	- horizontal velocity, $U = \bar{u} + u'$
$V$	- vertical velocity, $V = \bar{v} + v'$
$x$	- horizontal coordinate
$y$	- vertical coordinate
$\delta_{ij}$	- Kronecker delta
$\epsilon$	- dissipation rate of $K$
$C_{\epsilon}, C_{\mu}$	- turbulent Prandtl numbers for $K$ and $\epsilon$
$\mu$	- molecular dynamic viscosity
$\mu_T$	- turbulent viscosity
$\rho$	- density

SUBSCRIPTS

$J$	- jet-exit value
$O$	- crossflow value

1. INTRODUCTION

Flow fields containing impinging jets against a wall through a low-velocity crossflow occur frequently in industrial environments, namely where the jets compete with any cross-wind present. If the crossflow is confined a further complexity is introduced and an example of a practical application is the flow field created underneath a vertical take-off aircraft which is lifting off with zero or small forward momentum. Ground effect phenomena may occur and change the lift forces on the aircraft, cause re-ingestion of exhaust gases into the engine intake and raise fuselage skin temperatures.

The study of a single jet impingement in ground effect through a crossflow provides a basis to understanding the more complex practical flow fields and to evaluate the numerical solutions of the equations of motion which use turbulence models in order to predict these flows. This paper presents laser-Doppler measurements of the mean and fluctuating velocity characteristics for an axisymmetric jet in ground effect through a confined crossflow, and compares sample results with numerical predictions using the "k- $\epsilon$ " turbulence model. The numerical results are based on the solution of the finite difference form of the fully tridimensional Navier-Stokes equations, incorporating the turbulence viscosity concept.

Measurements of the velocity characteristics of normal impinging free jets on a flat surface have been reported for relatively large ratios between the height of the jet exit above the ground plate and the jet diameter (at least  $H/D > 10$ ), using either probe and optical techniques, as reviewed for example by Araújo et al (1982). Qualitative information on the effect of that ratio (up to  $H/D=0.4$ ) in a confined flow field has only been given by the visualization studies of Seripalli (1983). Experiments on the aerodynamics of jets through a confined crossflow are much scarcer, and have been reported not only for large values of the height of the jet exit above the ground plate, but also for low velocity ratios between the jet and the crossflow  $V_j/U_0$ . Sugiyama and Usami (1979), Andreopoulos and Rodi (1984) and Shayesteh et al (1985) report hot-wire measurements for ratios  $H/D$  higher than 24 and for values of  $V_j/U_0$  respectively up to 1.96, 2 and 16. Kamotani and Greber (1984) present results for  $H/D=12$  and Stoy and Ben-Hain (1973)

give pitot-tube measurements for values of  $H/D$  of 3.05 and for jet to cross-stream velocity ratios up to 6.8. Only Crabb, Durso and Whitelaw (1981) report LDV measurements, including those of the shear stress, but for values of  $H/D=12$  and for velocity ratios up to 2.3.

This paper reports LDV measurements for a jet Reynolds number of  $Re = 60000$ , a velocity ratio between the jet and the crossflow of 25 and for the jet exit 5 jet-diameters above the ground plate. The measurements are extended by numerical predictions of the flow for velocity ratios between the jet and the crossflow between 5 and 25, and for the jet exit between 3 and 5 jet diameters above the ground plate.

Much of the published computational work on jets in crossflow has centered on integral methods based on simplifying assumptions, which are only capable of predicting global effects, such as jet trajectories and jet cross-section shapes, as shown for example by Stoy and Ben-Haim (1973) and Adler and Baron (1979). Patankar et al (1979) employed a finite-difference numerical procedure together with a two-equation turbulence model to predict a single jet in an unconfined crossflow, and obtained good agreement with the experiments of Keffer and Baines (1963) and Ramsey and Goldstein (1972) for velocity ratios from 2 to 10. A similar approach was used by Jones and McGuirk (1980) to calculate the confined flow measured by kamotani and Greber (1974). The gross features of the flow are well predicted but the calculations appear to exhibit diffusion rates larger than those consistent with measured profiles, which can be attributed either to numerical or "turbulence model" errors. Grids up to  $20 \times 15 \times 15$  nodes were used, but further grid refinement would be desirable to identify the precise source of disagreement between measurements and predictions. Demuren (1983) presented predictions of the flow measured by Sugiyama and Usami (1979) using a three-dimensional finite-difference scheme together with the "K- $\epsilon$ " turbulence model and has shown, for example, the importance in prescribing the correct boundary conditions at the jet discharge, although for velocity ratios of 1.96 and values of  $H/D=25$ .

This paper presents an application of a finite-difference scheme similar to that used by Jones and McGuirk (1980). Here it is used a comparatively fine grid to predict the flow field for low values of the ratio between the height of the jet-exit above the ground plate and the jet diameter.

Next section describes the experimental method, gives details of the flow configuration, of the laser-Doppler velocimeter and of the errors incurred in the measurements. Section 3 describes the calculation method. Section 4 presents the experimental results and compares them with numerical calculations, which are extended to a large set of flow conditions in section 5. Section 6 summarises the main findings and conclusions of this work.

## 2. EXPERIMENTAL METHOD

### 2.1 Flow Configuration

The experiments were performed on a horizontal water tunnel, 1.50 m long and 0.5m wide, made of perspex, in which the crossflow was driven by the pressure difference between a constant head and a discharge tank and was passed through straighteners and screens upstream of the tunnel inlet, as schematically shown in figure 1.

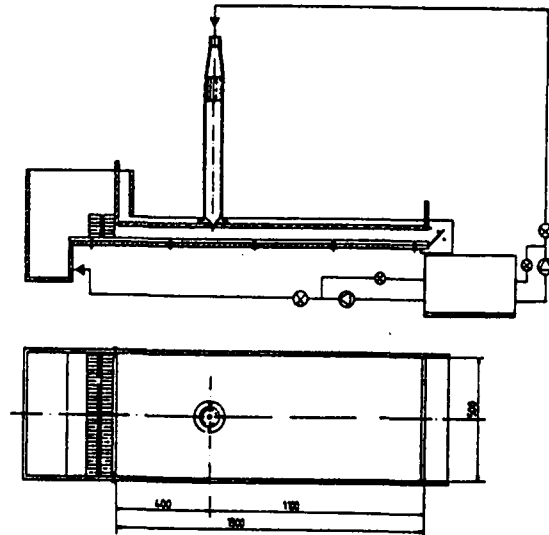


Figure 1 - Diagram of the flow configuration

The apparatus was built to allow multi-jet impingement experiments with variable height of the jet-exit above the ground plate, but in the present study a single jet of 20mm exit diameter,  $D$ , has been used, 5 jet-diameters above the ground plate (i.e.  $H/D=5$ ). The tunnel extends for 20  $D$  upstream and for 55  $D$  downstream of the jet and for 12.5  $D$  from the jet to the side walls. The jet unit comprises a nozzle with a contraction ratio of 16 and a settling chamber 0.56 m long, which encloses a flow distributor at  $7^\circ$  and flow straighteners. The system is recirculatory, with the water drawn from the discharge tank pumped into the constant-head tank and supplying the jet through control valves.

The present results were obtained for a jet Reynolds number of  $Re_j=60000$ , a jet exit mean velocity of  $V_j=3$  m/s and a local turbulence intensity of 2%, and for a velocity ratio between the jet and the cross flow of  $V_j/U_\infty=25$ . Measurements obtained in the tunnel without the jet assembly have shown that the local turbulence intensity of the crossflow was 18% and that the wall boundary layer around the jet impingement region was 10 mm thick.

The origin of the horizontal,  $X$ , and vertical,  $Y$ , coordinates in the tunnel is taken at the centre of the jet exit.

## 2.2 Experimental Technique

Flow visualization has been conducted by introducing a fluorescent dye into the jet flow and illuminating the central plane of the tunnel with a sheet of light obtained by spreading a laser beam. A solution of fluorescein-sodium has been used and, in agreement with Saripalli (1983), found to be an ideal tracer fluid for the present application. The light source was a 1W argon-ion laser in the 488 nm line, under which the fluorescein-sodium fluoresces a bright yellowish-green. Visualisation using air bubbles as tracer has also been performed using a similar illumination system.

Velocity was measured by a laser-Doppler velocimeter operated in the dual-beam, forward-scatter mode with sensitivity to the flow direction provided by light-frequency shifting from acousto-optic modulation (bragg cells). The resulting frequency shift was normally set between 1 and 2MHz. The principal characteristics of the laser-Doppler velocimeter, in particular those of the transmitting optics, are summarised in Table 1.

TABLE 1

Principal Characteristics of the Laser-Doppler Velocimeter

- 1 W (nominal) Argon-Ion laser; wavelength:	514 nm
- focal length of focussing lens:	310 mm
- beam diameter, at $e^{-2}$ intensity, of laser:	1.5 mm
- measured half-angle of beam intersection (in air):	4.64°
- calculated half-angle of beam intersection (in water):	3.48°
- fringe separation (line pair spacing):	3.18 $\mu$ m
- calculated dimensions of measuring volume, at a intensity, (major and minor axis of ellipsoid in water):	2.25; 0.135 mm
- velocimeter transfer constant:	0.3145 MHz/ms <sup>-1</sup>

The light scattered by naturally-occurring centres in the water was collected by a lens (focal length of 150 mm) and focussed onto the pinhole aperture (0.3 mm) of a photomultiplier (OEI, type LD-0-810) with a magnification of 0.76. The output of the photomultiplier was band-pass filtered and the resulting signal processed by a laboratory-built frequency counter. Each measurement is subject to preset validations in the amplitude and time domains and, if valid, is digitised as a floating point number and transferred to a 8-bit microcomputer, as described by Heitor et al (1984).

Figure 2 shows a schematic diagram of the data acquisition and processing system.

The complete LDV system is mounted on a three dimensional manual traversing unit, allowing the positioning of the laser-velocimeter control volume within  $\pm 0.5$  mm. The horizontal, U, and vertical, V, mean velocity components and corresponding normal and shear Reynolds stresses were determined from measurements with the laser beams in the horizontal and vertical planes and at 45°. In order to measure the vertical component in near wall regions, the transmitting optics were inclined by half-angle of beam intersection, and the scattered light was collected off-axis. Measurements could then be obtained up to 2mm from the ground plate without

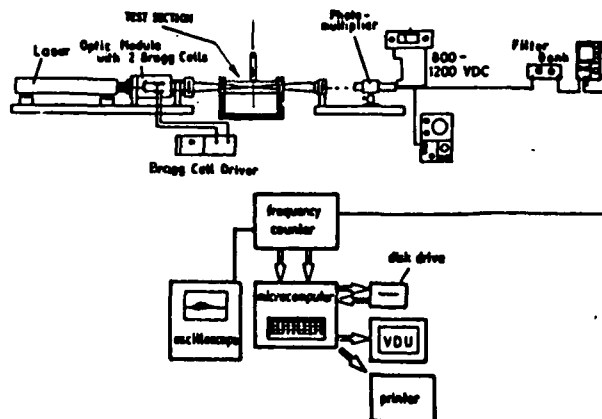


Figure 2 - Diagram of LDV system

a significant deterioration of the Doppler signal. Results obtained 20 mm above the ground plate with both the on-axis and the off-axis arrangements have shown a close agreement, within the precision of the equipment.

## 2.3 Experimental Accuracy

Errors incurred in the measurement of velocity by displacement and distortion of the measuring volume due to refraction on the duct walls and the change in refractive index were found to be negligibly small and within the accuracy of the measuring equipment. The tolerance on the output of the counter derives from the error in the clock count and from the resolution of the floating point format of the data: the maximum error is always less than 1%. Non-turbulent Doppler broadening errors due to gradients of mean velocity across the measuring volume (e.g., Durst et al, 1981) may affect essentially the variance of the velocity fluctuations, but for the present experimental conditions are of the order of  $10^{-4} V_r^2$  and, therefore, sufficiently small for their effect to be neglected. The largest statistical (random) errors derived from populations of, at least, 10000 velocity values were of 1.5 and 3%, respectively for the mean and variance values, according to the analysis referred by Yanta and Smith (1978) for a 95% confidence interval. No corrections were made for sampling bias, but even in the zones of the flow characterized by low particle arrival rates (about 80 particles per second) no correlations were found between Doppler frequencies and time interval between consecutive bursts, suggesting that such bias effects are unimportant for the present flow conditions (e.g., Durao, Laker and Velho, 1985).

## 3. CALCULATION METHOD

### 3.1 Governing Equations

The numerical results presented are based on the solution of the full three-dimensional form of the differential conservation equations for momentum and mass. The time-averaged form of

these equations may be written in cartesian tensor notation as follows:

$$\rho \bar{U}_j \frac{\partial \bar{U}_i}{\partial x_j} = - \frac{\partial \bar{P}}{\partial x_i} + \frac{\partial}{\partial x_j} (\nu \frac{\partial \bar{U}_i}{\partial x_j} - \rho \overline{u'_i u'_j})$$

$$\frac{\partial \bar{U}_i}{\partial x_i} = 0$$

where the over bars represent averaged quantities. The turbulent diffusion fluxes are approximated with the high Reynolds number version of the two-equation "k-ε" model, described in detail by Launder and Spalding (1974). The Reynolds shear stress is linearly related to the mean rate of strain via a scalar turbulent viscosity:

$$\rho \overline{u'_i u'_j} = \frac{2}{3} \delta_{ij} K - \mu_T \left( \frac{\partial \bar{U}_i}{\partial x_j} + \frac{\partial \bar{U}_j}{\partial x_i} \right)$$

The turbulent viscosity, which is derived from the turbulence model is expressed as:

$$\mu_T = C_\mu \rho K^2 / \epsilon$$

The values for the turbulent kinetic energy, K, and the dissipation rate of turbulent energy, ε, are obtained by solving the following transport equations:

$$\rho \bar{U}_j \frac{\partial K}{\partial x_j} = \frac{\partial}{\partial x_j} \left( \frac{\mu_T}{\sigma_k} \frac{\partial K}{\partial x_j} \right) - \rho \overline{u'_i u'_j} \frac{\partial \bar{U}_i}{\partial x_j} - \rho \epsilon$$

$$\rho \bar{U}_j \frac{\partial \epsilon}{\partial x_j} = \frac{\partial}{\partial x_j} \left( \frac{\mu_T}{c} \frac{\partial \epsilon}{\partial x_j} \right) - C_1 \frac{\epsilon}{K} \rho \overline{u'_i u'_j} \frac{\partial \bar{U}_i}{\partial x_j} - C_2 \rho \frac{\epsilon^2}{K}$$

The turbulence model constants which were used are those found to give good agreement in a wide range of 2D shear flows (see, e.g., Launder and Spalding, 1974):

$$C_\mu = 0.09 \quad ; \quad C_1 = 1.44 \quad ; \quad C_2 = 1.92 \quad ; \quad \sigma_k = 1.0 \quad \text{and} \quad c = 1.3$$

### 3.2 Computational Procedure and Boundary Conditions

The solutions of the equations were obtained using a finite-difference formulation comprising a linearised, implicit, conservative scheme using centred differencing except where mean flow convective fluxes dominate diffusive processes. In that case donor cell differencing is used. The

solution procedure is based on the SIMPLE algorithm widely used and reported in the literature (see Barata, 1985 for details).

The computational domain has six boundaries where dependent variables values were specified: an inlet and outlet plane, a symmetry plane and three solid walls at the top, bottom and side of the channel. The sensitivity of the solutions to the location of the inlet and outlet boundaries was investigated. Their final position is sufficiently far away from the jet so that the boundary conditions have negligible influence on the computed flow in the vicinity of the jet. The inflow boundary is located 7.5 diameters upstream the jet-exit and the outflow is located 12.5 diameters downstream. At the inlet boundary uniform profiles of all the dependent variables were specified according to the experimental values. At the outflow boundary the zero normal gradient condition is prescribed for all the dependent variables. On the symmetry plane passing through the impinging jet the normal velocity vanishes, and the derivatives of the other velocity components with respect to the normal coordinate are zero. The normal gradients of the turbulence quantities, K and ε, also vanish on the symmetry plane. On the solid surfaces the velocity, the turbulent kinetic energy and the dissipation of turbulent energy follow the impermeable-wall condition. At the grid points nearest the wall the mean velocities and turbulence quantities are prescribed using turbulent local equilibrium wall law profiles (see Launder and Spalding, 1974). At the upper surface the exact shape of the jet exit, from which the jet is issued, is defined. This was obtained by modifying the cell surface areas where the hole boundary bisected the surface area of the adjacent finite-difference control volume, so that the specified jet velocity produce the correct fluxes. The jet exit boundary conditions are prescribed from experimental measurements.

The numerical results presented in the next sections were obtained using a grid consisting of 30x17x17 nodes (in the x,y,z directions respectively), as schematically shown in figure 3. Non-uniform spacing was used in order to get

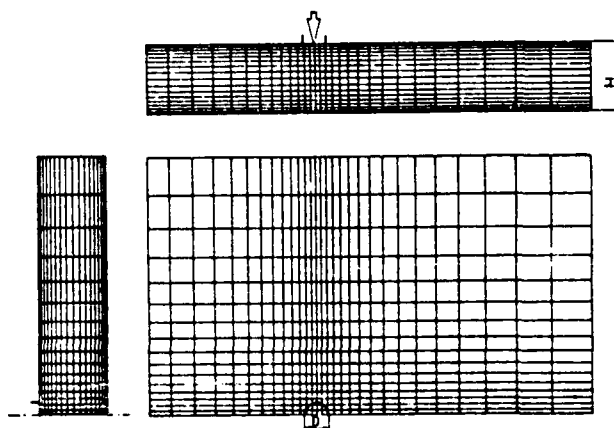


Figure 3 - Finite Difference grid (30x17x17 nodes)

fine grid spacing near the jet, where rapid variations were expected. Grid expansion factors up to 1.2 have been used. These calculations required approximately 800 K 32-bits-words of memory, which represents the maximum accessible storage on the Instituto Superior Tecnico VAX 11/750. A typical converged solution involved approximately 500 iterations, and required about 11 hours of execution time. Preliminary tests performed on the Imperial College VAX 8600 required about 2 hours of execution time.

#### 4. THE FLOW FIELD FOR $H/D=5$ AND $V_j/U_0=25$ .

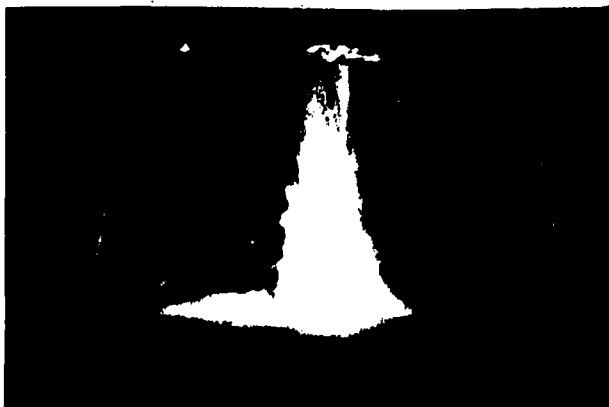
##### 4.1 Experimental Results and Discussion

Figures 4 to 8 provide a detailed set of results to characterize the flow-field created by a single jet impinging on a ground plane through a cross flow, for  $Re=60000$ ,  $H/D=5$  and  $V_j/U_0=25$ . The measurements include mean and variance values of horizontal,  $U$ , and vertical,  $V$ , components of velocity and corresponding Reynolds shear stress.

Prior to the detailed measurements, visualization of the flow was performed to guide the choice of measurement locations and to provide a qualitative picture of the flow.



(b) Flow visualization using air bubbles as tracer particles.



(a) Flow visualization by introducing a fluorescent dye into the jet flow.

Figure 4 - Visualization of the flow for

$$Re_j=60000, H/D=5; V_j/U_0=25$$

Figure 4 identifies the initial potential-core jet region, where the flow characteristics are identical to those of a free jet, and the impingement region, characterised by considerable deflection of the jet after to be slightly bent by the pressure difference between the upstream and downstream sides of the jet. The deflected jet becomes almost parallel to the ground plane and exhibit a behaviour similar to that of a radial wall jet where the upstream effects of interaction due to impingement are no longer important. It appears that the flow in the vicinity of the jet is largely controlled by complex inviscid dynamics, so that the influence of turbulence on the flow development may be weak and limited to the far flow-field, as discussed by Andreopoulos (1985). The figure suggests that the crossflow is deflected sideways by the penetration of the jet and may cause a recirculation region just downstream of the discharge, away of the ground plane. In the ground-plane region the approaching crossflow is decelerated and a further recirculating flow region occurs far upstream of the jet.

Figure 5 and 6 show horizontal and vertical profiles of  $U$  and  $V$ , which confirm the above description and quantify the mean flow characteristics of the impinging jet and of the radial wall-jet. Based on the horizontal profile of  $U$  at  $Y/D=4.7$ , figura 5(a), it is expected that the impingement point on the ground plane occurs about  $0.2D$  downstream of the axis of the jet-exit. The inclination of the impinging jet is associated with the peaks in the horizontal profiles of  $U$  at  $Y/D=0.75$  and  $4.0$ , figure 5(a), in the downstream edge of the jet, and is confirmed by the flow asymmetry shown by the vertical profiles of  $V$  at  $X/D=\pm 0.75$ , figure 6(b). The peaks in the horizontal profiles of  $U$  are followed by near zero and negative horizontal velocities. The latter are clearly observed in the vertical profile of  $U$  at  $X/D=+0.75$ , figure 6(a), between  $Y/D=2$  and  $4$ , and correspond to the recirculation zone formed just downstream of the impinging jet by the deflection of the crossflow around the jet. Examination of the vertical profiles of  $U$ , figure 6(a), shows the deceleration of the part of the wall-jet upstream of the jet-exit relative to the downstream part. The former is associated with near-zero and positive (downward) vertical mean velocities, figure 6(b), and follows the ground plane, while the later is associated with negative (upward) vertical mean velocities and, therefore, is slightly directed away from the ground with a maximum inclination of  $3.8^\circ$  at  $X/D=2.5$ . This behaviour explains the horizontal profile of  $U$  at  $Y/D=4.7$ , figure 5(a), in that  $U$  increases in absolute value upstream of the jet exit, at least up to  $X/R=-8$ , while it decreases downstream of the jet exit for  $X/R>+9$ . Far upstream, for  $X/R<-8$ , it is expected the horizontal mean flow changes its direction, giving rise to the recirculation zone observed by the visualization studies.

Figures 7 and 8 show horizontal and vertical profiles of  $\overline{u'^2}$ ,  $\overline{v'^2}$  and  $\overline{u'v'}$  and quantify the turbulence characteristics of the impinging and wall jets. The shear layer surrounding the jets is a region of intense velocity fluctuations. The

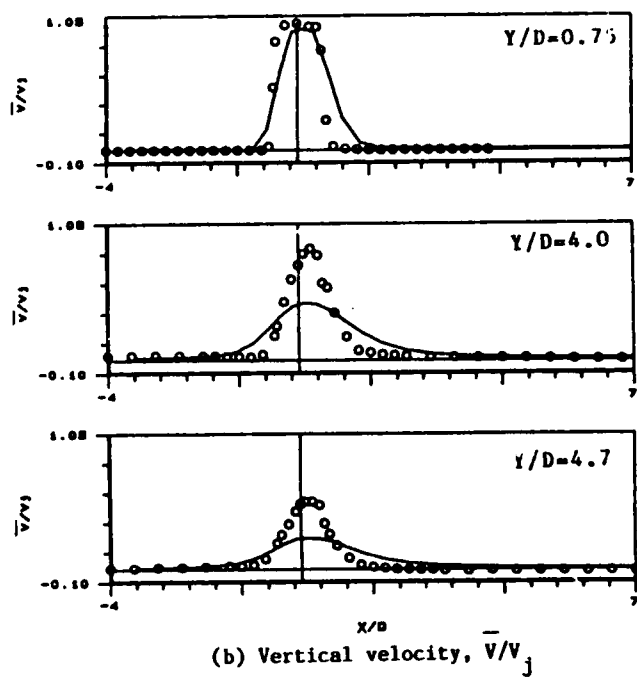
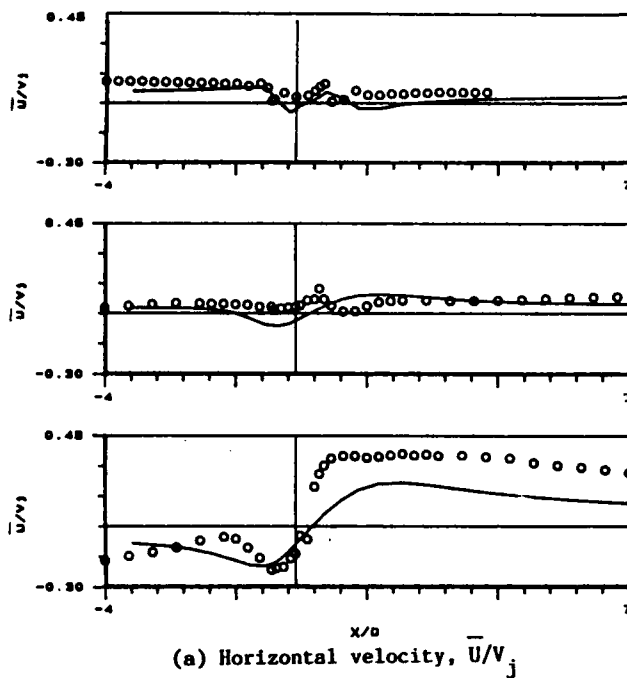


Figure 5 - Horizontal profiles of mean velocity characteristics for  $Re_j=60000$ ,  $H/D=5$  and  $V_j/U_o=25$ .

KEY: o MEASUREMENTS; — CALCULATIONS

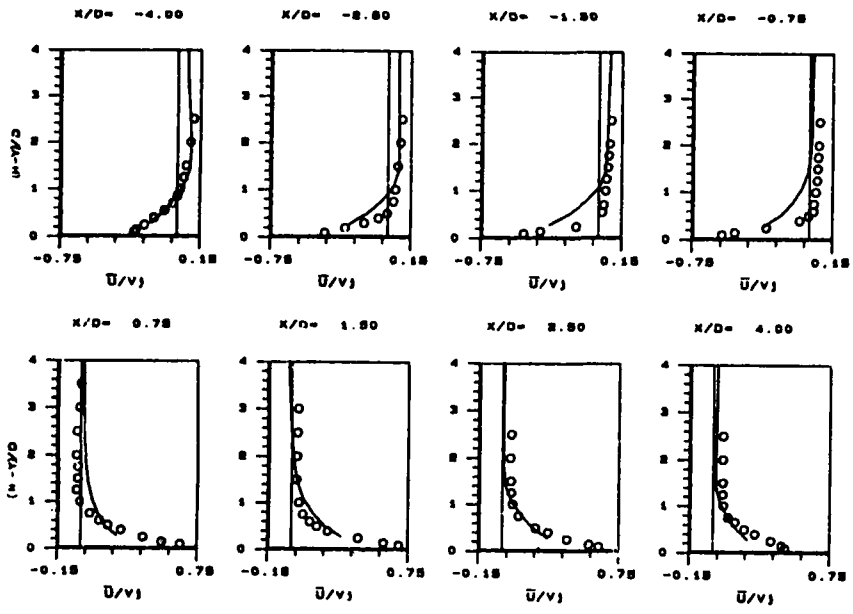
profiles exhibit maximum values consistently located in the region of the highest mean velocity gradients around the edge of the jets. The velocity probability distributions indicate a near-Gaussian behaviour and suggest the absence of discrete-frequency oscillations associated with these peaks. The development of the horizontal profiles shown in figure 7, quantify the turbulent diffusion process along the impinging jet. The peaks spread along the jet and the minima at the centre of the jet increase its magnitude. The upstream peak of  $\overline{v'^2}$  is consistently larger than the downstream and both are larger than the corresponding peaks of  $\overline{u'^2}$ . The flow is anisotropic in that, with exception of the initial potential core,  $\overline{v'^2}$  is largest around the jet, with  $\sqrt{\overline{u'^2}}/\sqrt{\overline{v'^2}} \geq 0.7$ , while  $\overline{u'^2}$  is largest away from the vicinity of the jet, with  $\sqrt{\overline{u'^2}}/\sqrt{\overline{v'^2}} < 1.4$ , as shown in figure 7 (c).

The profiles of shear stress, figure 7 (d), are consistent with the direction of the mean flow, with near-zero values at the centre of the jet. The shear stress is positive along the downstream edge of the jet suggesting that faster moving elements of jet-fluid ( $v' > 0$ ) tend to move outward into the wake of the jet ( $u' > 0$ ). Similarly, the shear stress along the upstream edge is negative because the outward movement of fluid particles corresponds to negative horizontal velocity fluctuations ( $u' < 0$ ). Also, the sign of shear stress is in agreement with the sign of the shear strain  $\partial \overline{V}/\partial x$  in the sense that  $\overline{u'v'} = -\nu_t \partial \overline{V}/\partial x$  (with  $\partial \overline{U}/\partial y \neq 0$ ), where  $\nu_t$  is the turbulence viscosity. With the approach of the ground plane the shear strain  $\partial \overline{U}/\partial y$  increases, and the magnitude of the peaks of shear stress decreases. This is because the flow

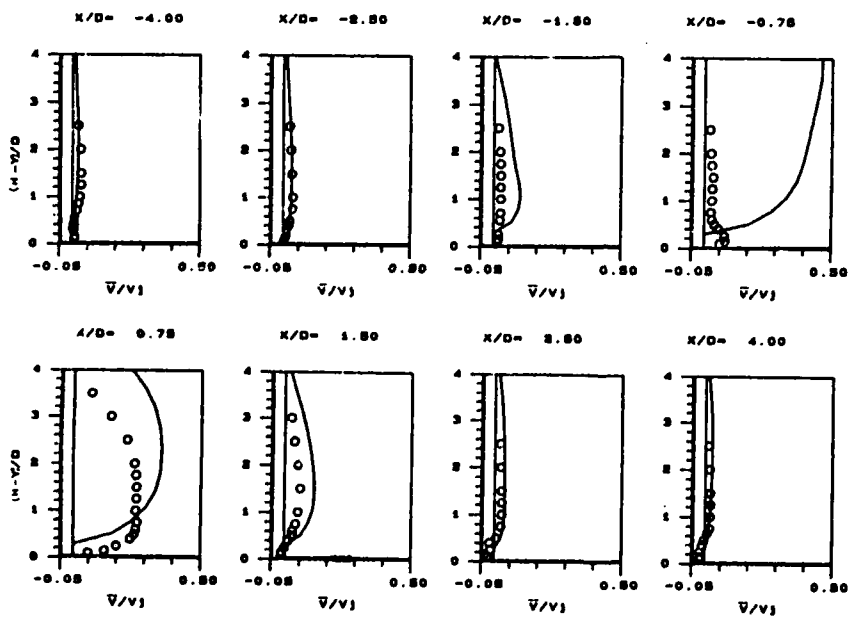
in this region is subjected to strongly stabilizing curvature and it is well known (see, e.g., Andreopoulos and Rodi, 1984) that the curvature reduces the shear stress more than the turbulent kinetic energy. Far away from the vicinity of the impinging jet,  $|\partial \overline{U}/\partial y| > |\partial \overline{V}/\partial x|$  and the shear stress changes its sign, as shown in figure 7 (d) for  $Y/D=4.7$ .

The results suggest that the generation of turbulence up to around  $Y/D=4$  is dominated by shear stress production, while the turbulent structure of the impingement region is influenced by extra rates of strain, such as those resulting from streamwise curvature and lateral divergence (see, for example, Bradshaw, 1973). The effective-viscosity hypotheses may, therefore, be of the limited use in the impingement zone. In fact, the similarity between  $\partial \overline{V}/\partial x$  and  $\partial \overline{U}/\partial y$  in this zone suggests that the "thin shear layer" approximation, as discussed by Cebeci and Bradshaw (1977), is inapplicable.

Figure 8 quantifies the turbulence characteristics of the wall-jet. The peak values of  $\overline{u'^2}$  are the largest with the level of turbulence anisotropy,  $\sqrt{\overline{u'^2}}/\sqrt{\overline{v'^2}}$ , reaching 2.3 at  $X/D=1.5$ . The shear stress, figure 8 (c), is negative downstream of the jet exit and positive otherwise, confirming the above analysis. The figure shows, for example, that in the downstream wall-jet, the faster elements of fluid ( $u' > 0$ ) tend to move away from the wall ( $v' < 0$ ). Out of the impingement region the sign of the shear stress is consistent with that of  $\partial \overline{U}/\partial y$  on the basis of mean gradient transport modelling (i.e.,  $\overline{u'v'} = -\nu_t \partial \overline{U}/\partial y$ , with  $\partial \overline{V}/\partial x \approx 0$ ). Eddy-viscosity models should then be capable of simulating the shear-stress distribution. However, the complexity in the variation of the



(a) Horizontal velocity,  
 $\bar{U}/v_j$



(b) Vertical velocity  
 $\bar{V}/v_j$

Figure 6 - Vertical profiles of mean velocity characteristics for  $Re_j=60000$ ,  $H/D=5$  and  $v_j/U_o=25$

KEY: o MEASUREMENTS  
— CALCULATIONS

eddy-viscosity itself, as shown by Andreopoulos and Rodi (1984) for low jet to crossflow velocity ratios and high values of  $H/D$ , limits the applicability of such models.

Horizontal and vertical profiles of the shear stress correlation coefficient,  $R_{uv}$ , have been calculated from the results and show maximum peak values about 0.55, that is the value found usually in well-behaved shear flows. Also, the profiles of the structure parameter given by the ratio of  $\overline{u'v'}$  upon  $K$  (which is taken as  $3/4 (\overline{u'^2} + \overline{v'^2})$ ) show peak values between 0.3 and 0.4 along the edges of the impinging jet, which are close to the values found in undisturbed shear layers. The structure parameter decreases in the impingement region, as a result of the decrease in the shear stress analysed before.

#### 4.2 The Prediction of the flow field

Figures 5 to 8 present numerical results of the mean and turbulent velocity fields together with the measurements discussed above, and have been used to assess the validity of the turbulence model and numerical scheme described in section 3. Figures 5 and 6 show that the gross features of the mean flow field are well predicted, although important local differences occur between measurements and calculations, particularly in the near field of the jet and with the approach of the ground plane. The calculated rate of decay of the impinging jet is higher than actually occurred in the experiments, its deflection is attenuated suggesting diffusion rates higher than those consistent with the measured profiles and the near-wall velocities

are under predicted. Also, the recirculation zone measured in the wake of the jet is not calculated.

The precise reason of these discrepancies is difficult to identify, since they are attributed to numerical and "turbulence model" errors. The three-dimensional nature of the present flow, together with the computer storage available precludes the use of more refined grids and the

achievement of grid independence. Numerical diffusion (see, e.g., McGuirk et al, 1985) is therefore, expected to occur. These limitations together with the prescription of the wall boundary conditions are an important source of disagreement between measurements and predictions. The other potential source of error is the "k-ε" turbulence model, as readily observed by the comparison of the turbulent

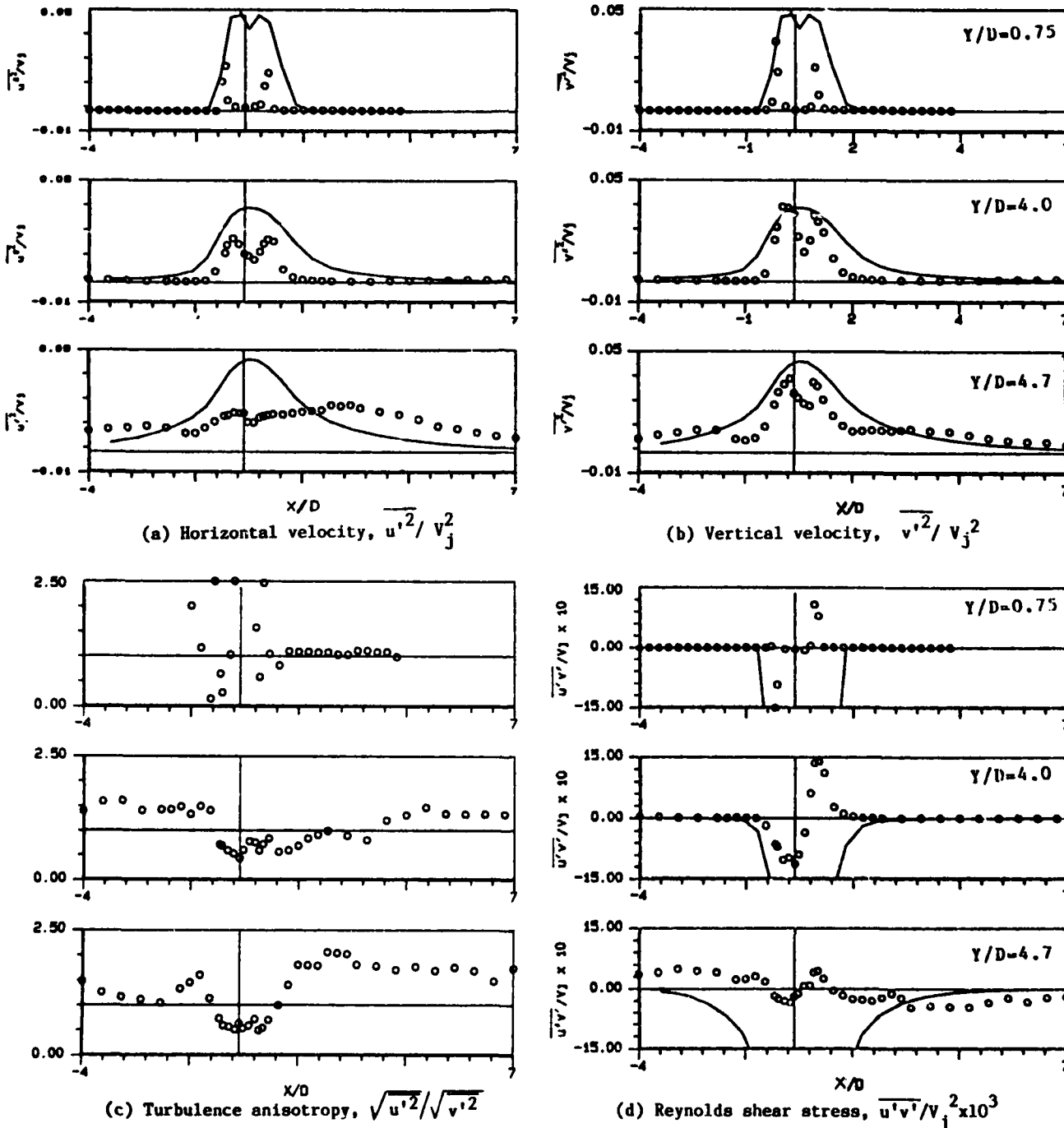


Figure 7 - Horizontal profiles of fluctuating velocity characteristics for Re=60000, H/D=5 and  $V_j/U_o=25$

KEY: ○ MEASUREMENTS; — CALCULATIONS ( $\overline{u'^2}$  and  $\overline{v'^2}$  as 2/3 K)

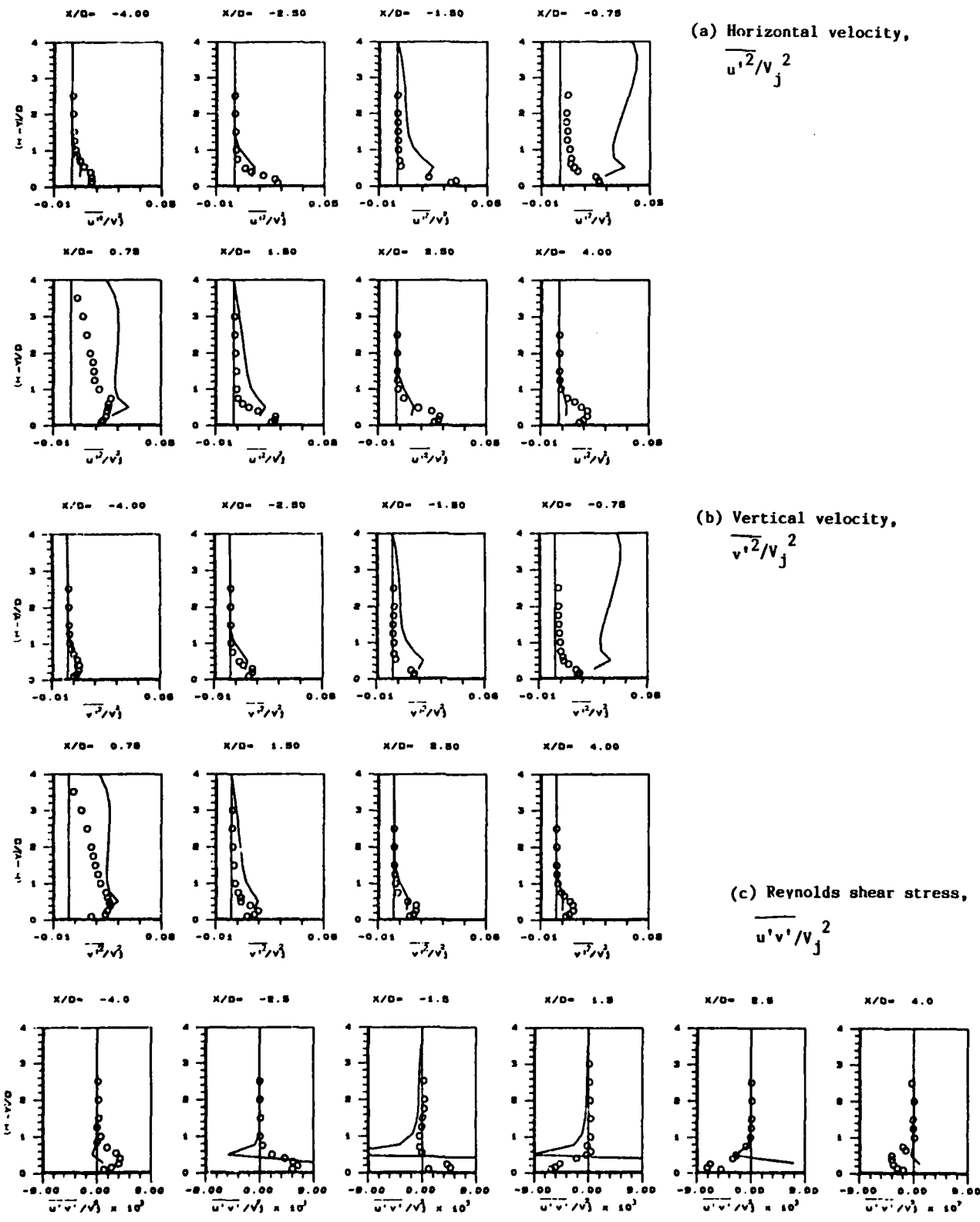


Figure 8 - Vertical profiles of fluctuating velocity characteristics for  $Re=60000$ ,  $V_j/U_o=25$ ,  $H/D=5$   
 KEY: o MEASUREMENTS ; — CALCULATIONS ( $\overline{u'^2}$  and  $\overline{v'^2}$  as  $2/3 K$ )

velocity values.

Figure 7 and 8 show that the Reynolds, normal and shear, stresses associated with the edges of the impinging jet are overpredicted, as well as the total turbulent field in the vicinity of the jet. Modelling errors are large in these zone, as discussed in section 4.1 and confirmed by the change in sign of the predicted shear stress values in the impinging zone. On the contrary, the far field is under predicted due mainly to the insufficiently fine grid used.

Based on the above comments it can be concluded that, in spite of the local differences mentioned before, the numerical results provide a fair qualitative picture of the flow, particularly of the mean velocity field. This can be further analysed from the calculated distribution of mean velocity vectors plotted in figure 9. The formation of the recirculation zone due to deceleration of the upstream wall-jet occurs for  $X/D < -4$  and agrees with the visualization experiments. Also, the jet trajectory is well predicted, with the impingement point at  $X/D=+0.11$ .

#### 5. PARAMETRIC STUDY ON THE EFFECT OF $V_j/U_0$ AND $H/D$ ON THE MEAN FLOW FIELD.

The previous section compared measurements with numerical predictions of the flow for the experimental conditions, assessed the accuracy of the calculation method and identified the main sources of imprecisions. Here an attempt is made to simulate numerically the effect of the jet to crossflow velocity ratio,  $V_j/U_0$ , and of the height of the jet-exit above the ground plane,  $H/D$ , on the mean flow field.

Figure 10 shows streaklines calculated at the symmetry plane for velocity ratios,  $V_j/U_0$ , between 4 and 20, for  $H/D=3$ . The decrease in the ratio  $V_j/U_0$  moves the upstream recirculation zone close to the jet and the impingement point away of the axis of the jet-exit, increasing the inclination of the jet trajectory. Also, the recirculation zone measured in the wake of the jet for the experimental conditions is now observed for  $V_j/U_0 < 10$  by the negative horizontal velocities associated with the streaklines just downstream of the discharge. The errors incurred in these calculations are expected to decrease for low jet to crossflow velocity ratios but, even in figure 10 (d) for  $V_j/U_0=5$ , the diffusion rates appear to be larger than those expected

from the measurements analysed before, due to both numerical and "turbulence model" errors.

Figure 11 shows the effect of decreasing the height of the jet-exit above the ground plane together with the increase of the crossflow velocity, keeping constant the velocity ratio  $V_j/U_0$ . The trajectory of the jet is unaltered but the formation of the upstream vortex occurs far downstream, close to the jet, due to the decrease in the crossflow velocity. Again, numerical and modelling errors influence the distributions plotted, particularly for the lowest value of the ratio  $H/D$ , but the general features of the flow are expected to be correct. The results suggest that the flow is largely controlled by the pressure distributions associated with the impinging and wall jets. The impinging-jet trajectory is particularly influenced by the ratio  $V_j/U_0$ , while the location of the upstream vortex results from a balance between the pressure fields associated with the wall-jet and the upstream crossflow and, therefore, is influenced more by  $U_0$  than  $V_j/U_0$ .

#### CONCLUSIONS

Flow visualization studies and LDV measurements have provided information of the flow field created by a single jet impinging on a ground plane through a crossflow, for  $Re=60000$ ,  $H/D=5$  and  $V_j/U_0=25$ . The measurements are compared with numerical results based on the solution of the finite difference form of the fully tridimensional Navier-Stokes equations, incorporating the turbulence viscosity concept. The following is a summary of the more important findings and conclusions of this work.

- The experiments have shown a large penetration of the impinging jet through the crossflow. The jet is slightly bent and gives rise to a recirculation zone on its wake by deflection of the crossflow. The deflected jet becomes almost parallel to the ground plane and originates a further recirculating flow region far upstream of the impinging jet.

- The shear layer surrounding the jets is a region of intense velocity fluctuations with maximum values located in the region of highest mean velocity gradients. The sign of the shear stress is consistent with the direction of the mean flow and with the sign of the shear strain with the exception of the impingement zone, where

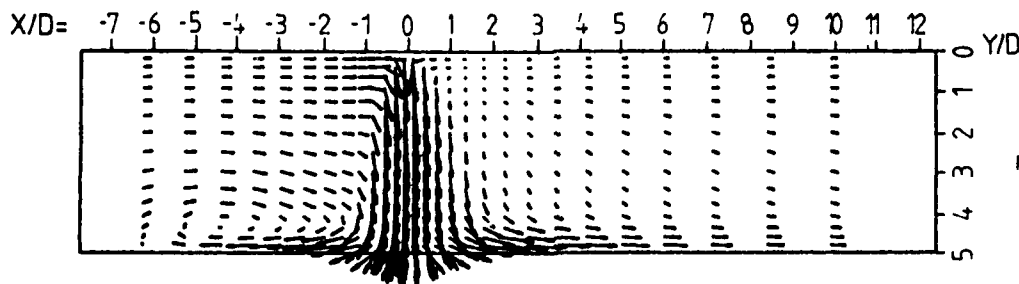


Figure 9 - Calculated mean velocity vectors at the symmetry plane for  $Re_j=60000$ ,  $H/D=5$  and  $V_j/U_0=25$

the flow is dominated by strong curvature effects.

• The gross features of the mean flow field are well predicted, but important local differences occur between measurements and calculations of the mean and turbulent fields, due to numerical and "turbulence model" errors.

• The numerical predictions are extended to cover a large set of flow conditions and allow to analyse the effect of the ratios  $V_j/U_0$  and  $H/D$  on the jet trajectory and on the location of the recirculating flow region upstream of the impinging jet.

#### ACKNOWLEDGEMENTS

We are pleased to be able to acknowledge many useful discussions with Dr. J.J. McGuirk. The preliminary tests of the calculation method were performed using the computational facilities of the Fluids Section of the Imperial College, University of London. The assistance of Mr. Rui Chaves in plotting the results is gratefully acknowledged. Thanks are also due to Mrs. Rosário Lucas and Mrs. Isabel Nunes for their speedy typing of this report.

This work was partially supported by the Procurement Executive of the Ministry of Defence of U.K. and made at the Centro de Termodinâmica Aplicada e Mecânica dos Fluidos da Universidade Técnica de Lisboa.

#### REFERENCES

- Adler, D. and Baron, A. (1979). Prediction of a three-dimensional circular turbulent jet in crossflow. *AIAA J.*, 17.
- Andreopoulos, J. (1985). On the structure of jets in a crossflow. *J. Fluid Mech.*, 157, pp. 163-197.
- Andreopoulos, J. and Rodi, W. (1984). Experimental investigation of jets in a crossflow. *J. Fluid Mech.*, 138, pp. 93-127.
- Araújo, S.R.B., Durão, D.F.G. and Firmino, F.J.C. (1982). Jets impinging normally and obliquely to a wall. AGARD CPP308, paper 5.
- Barata, J.M.M. (1985). Estudo Numérico de jactos incidentes sobre superfícies planas. M. Sc. Thesis, Instituto Superior Técnico, Technical University of Lisbon.
- Bradshaw, P. (1973). Effects of streamline curvature on turbulent flow. *Agardograph* 169.
- Cebeci, T. and Bradshaw, P. (1977). Momentum transfer in boundary layers. Hemisphere Publishing Corp. Washington.
- Crabb, D., Durão, D.F.G. and Whitelaw, J.H. (1981). A round jet normal to a crossflow. *J. Fluids Engng.*, 103, pp. 142-153.
- Demuren, A.O. (1983). Numerical calculations of steady three-dimensional turbulent jets in crossflow. *Comp. Meth. in Appl. Mech. and Engng.*, 37, pp. 309-328.
- Durão, D.F.G., Laker, J.R. and Velho, A. (1985). Velocity and amplitude bias and the development of laser anemometry counters. ASME Winter Annual Meeting, Miami Beach, Florida, November 17-22.
- Durst, F., Melling, A. and Whitelaw, J.H. (1981). Principles and Practice of Laser-Doppler Anemometry, 2nd ed., Academic Press, New York.
- Heitor, M.V., Laker, J.R., Taylor, A.M.K.P. and Vafidis, G. (1984). Instruction Manual for the FS "model 2" Doppler-Frequency Counter. Imperial College, Mech. Eng. Dept., Report FS/84/10.
- Jones, W.P. and McGuirk, J.J. (1980). Computation of a round turbulent jet discharging into a confined crossflow. Turb. Shear Flows 2, pp. 223-245 (ed by et al). Springer Verlag.
- Kamotani, Y. Bradebury and Greber, I. (1974). Experiments on confined turbulent jets in a cross-flow. NASA CR-2392.
- Keffer, J.F. and Baines, W.D. (1963). The round turbulent jet in a cross-wind. *J. Fluid Mech.*, 15, pp. 481-496.
- McGuirk, J.J., Taylor, A.M.K.P. and Whitelaw, J.H. (1985). The assessment of numerical diffusion in upwind difference calculations of turbulent recirculating flows. In "Turbulent Shear Flows-3", pp. 206-224 (ed. by Bradebury et al). Springer Verlag.
- Lauder, B.E. and Spalding, D.B. (1974). The numerical computation of turbulent flows, *Comput. Meths. Appl. Mech. Engng.*, 3, pp. 269-289.
- Patankar, S.V., Basu, D.K. and Alpay, S.A. (1977). Prediction of the three-dimensional velocity field of a deflected jet. *J. Fluids Engng.*, 99, pp. 758-762.
- Ramsey, J.W. and Goldstein, R.J. (1972). Interaction of a heated jet with a deflecting stream. NASA CR 72613.
- Saripalli, K.R. (1983). Visualization studies of jet impingement flows at McDonnell Douglas Research Laboratories. In "Flow Visualization III", Proc. 3rd Int. Symp. on Flow Visualization (ed. W.J. Young), Univ. Michigan, Sept. 6-9.
- Shayesteh, M.V., Shabaka, I.M.N.A. and Bradshaw, P. (1985). Turbulent structure of a three dimensional impinging jet in a cross flow. Paper AIAA-85-0044, AIAA 23rd Aerospace Sciences Meeting, Reno, January, 14-17.
- Stoy, R.C. and Ben-Haim, Y. (1973). Turbulent jets in a confined crossflow. *J. Fluids Engng.*, 95, pp. 551-556.
- Sugiyama, Y. and Usami, Y. (1979). Experiments on the flow in and around jets directed normal to a cross flow. *Bulletin JSME*, 22, pp. 1736-1745.
- Yanta, W.J. and Smith, R.A. (1978). Measurements of turbulent-transport properties with a laser Doppler velocimeter. AIAA paper 73-169, 11th Aerospace Science Meeting, Washington.

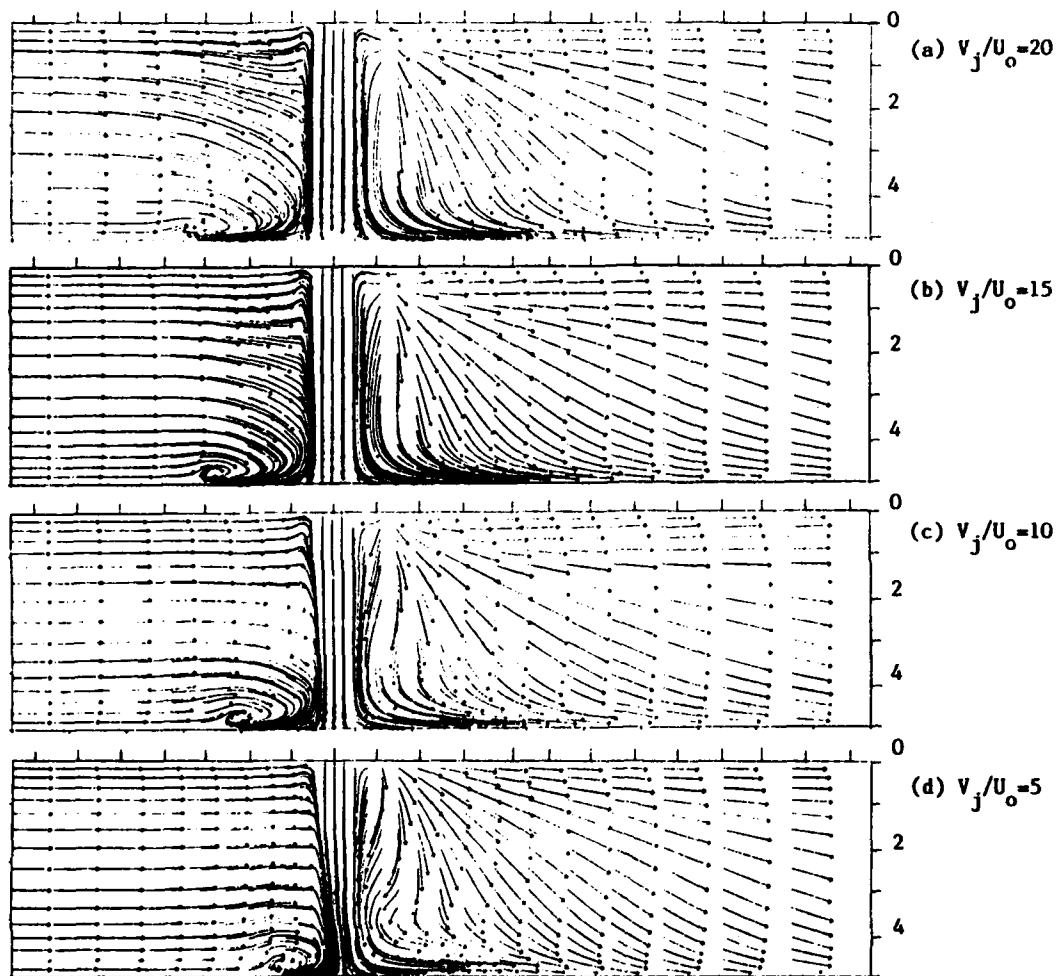


Figure 10 - Numerical study of the effect of the jet to crossflow velocity ratio on the mean flow field, for  $H/D=3$ . (Streaklines over 0.2 s).

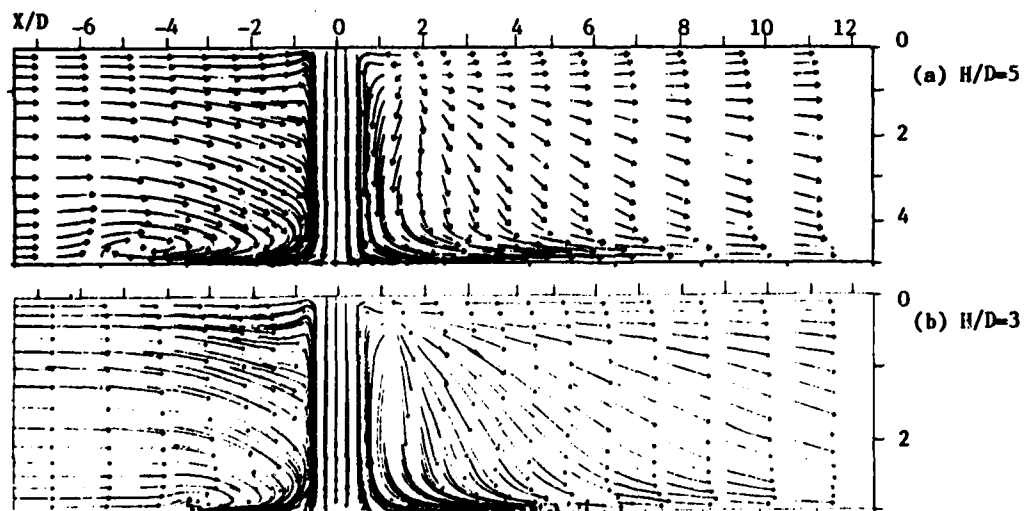


Figure 11 - Numerical study of the effect of the height of the jet-exit above the ground plane on the mean flow field, for  $V_j/U_0=20$  (Streaklines over 0.2 s).

TECHNIQUES FOR MEASUREMENT OF VELOCITY  
IN LIQUID-METAL MHD FLOWS\*

C. B. Reed, B. F. Picologlou,  
P. V. Dauzvardis, and J. L. Bailey  
Argonne National Laboratory  
Argonne, IL 60439

ABSTRACT

Three instruments for measuring local velocities in liquid-metal MHD experiments for fusion blanket applications are being evaluated. The devices are used in room-temperature NaK experiments to measure three-dimensional flow field patterns anticipated in complex blanket geometries. Hot film anemometry, a standard technique in ordinary fluids, is being used, as well as two developmental devices. One is called the Liquid Metal Electromagnetic Velocity Instrument (LEVI), and performs essentially as a local DC electromagnetic flow meter. The third device, a Thermal Transient Anemometer (TTA) is a rugged, yet relatively simple device, which measures local velocity through the mechanism of convective heat transfer, in some ways similar to hot-film anemometry. Results are presented showing the kinds of data collected thus far with each instrument. Measurements include both local velocity measurements and some preliminary frequency analyses of the fluctuating signals from both a hot-film sensor and the LEVI device.

INTRODUCTION

Recent blanket studies have demonstrated that MHD presents a critical feasibility issue for liquid-metal self-cooled Tokamak blankets, Abdou et al. (1983). Although successful designs have been developed using available theory and data on liquid metal MHD, a number of uncertainties related to MHD effects remain unresolved

Abdou et al. (1983) and Picologlou et al. (1984). To improve the level of understanding of the details of MHD flows as they apply to magnetically confined fusion blankets, an experimental program is being carried out in a facility at Argonne National Laboratory (ANL). The experimental facility (Argonne's Liquid-Metal Engineering Experiment (ALEX) described in detail elsewhere, Reed et al. (1985) is capable of attaining maximum Hartmann numbers (M) and interaction parameters (N) in the range of  $10^3$ - $10^4$ , which is close to the range of  $10^4$ - $10^5$  that these parameters attain in the reactor blanket.

The experimental program is aimed towards measurement of detailed flow structure characteristics. This is of fundamental importance because existing theories predict, in the cases where 3-D effects become dominant, unconventional velocity profiles with high velocity wall jets and low velocity core regions. Since 3-D effects are virtually unavoidable in the blanket, and because the flow profiles have a strong influence on heat transfer and corrosion rates, data validating existing theories are indispensable to design efforts seeking to either minimize or take advantage of such effects.

Local velocity measurements have been made previously in a number of room temperature liquid-metal MHD experiments. In these experiments mercury has been the working fluid of choice, although one paper, Fabris et al. (1978) gives very qualitative results in room temperature NaK. Although hot-film anemometry has been used to collect most relevant local velocity

\*Work supported by the Office of Fusion Energy/  
U. S. Department of Energy.

data, difficulties associated with operating this instrument in mercury, R. A. Gardner (1971) suggest that additional means should be developed for acquiring the necessary local velocity data.

To this end, an instrumentation development program is being carried out at ALEX, in parallel with the baseline experimental program on MHD effects. Three distinct instruments are being used or developed at this time, i.e., the hot-film anemometer (HFA), the liquid-metal electromagnetic velocity instrument (LEVI), and the thermal transient anemometer (TTA). Only HFA has been widely used previously; the other two devices are undergoing significant development work for the first time.

#### Hot Film Anemometry

Hot film anemometry has been used in similar liquid-metal applications previously, but sensor fouling and calibration stability problems make its use very tedious and time consuming. Nevertheless, previous successes with HFA in room temperature liquid-metal MHD experiments, Reed and Lykoudis (1978) dictated that its development be pursued in this application. Ordinary, commercially available, hot-film electronic equipment and quartz coated hot-film sensors were used in the present investigation. Figure 1 shows a typical cylindrical HFA sensor and probe. A further description of HFA can be found in numerous texts and publications.

#### Liquid Metal Electromagnetic Velocity Instrument

The LEVI is essentially a miniature local electromagnetic flowmeter; a device that can measure the local component of the velocity,  $u$ , normal to an applied magnetic field, by measuring the magnitude of the local voltage gradient. The LEVI used here requires an applied magnetic field and that the local current density,  $j$ , be much smaller than  $\sigma u B$ . Here  $\sigma$  is the fluid's conductivity and  $B$  the magnetic flux density of the externally applied field. Fortunately, the latter condition on the magnitude of  $j$  is satisfied in virtually all cases of MHD flows in thin-walled and insulating wall ducts. The measured velocity component is related to other measured quantities as follows:

$$u = \frac{\Delta\phi}{d \cdot B}$$

where  $\Delta\phi$  is the local voltage difference, and  $d$  is the LEVI electrode separation. A sketch of the LEVI geometry used here is shown in Fig. 2. These instruments were fabricated from HFA probes, similar to the one shown in Fig. 1, from which the cylindrical hot film sensor had been removed. The two probe tips were each hand-worked to produce a bare metal tip which comprised the two instrument electrodes. Typical electrode separations were  $\sim 1.5$  mm. Voltages produced by the LEVI were measured with a 12-bit A/D converter system having 2.44  $\mu V$  resolution.

#### Thermal Transient Anemometer

The thermal transient anemometer (TTA) is a velocity measurement device that is based on established thermal anemometry principles. However, by applying a pulsed heat input to the sensor, several significant advantages result when compared to conventional steady state thermal anemometers, perhaps the most important of which is a far simpler and more durable sensor.

The device consists of a sensor located in the flow path of the fluid and externally located support electronics. The sensor is essentially a sheathed thermocouple that is alternately heated and cooled; heated by pulsing an electric current through its hot junction and then convectively cooled by the moving fluid. The cooling rate is measured and then, using a microprocessor algorithm, is correlated to the local flow velocity. A schematic of the TTA system is shown in Fig. 3.

Motivation for development of the TTA in liquid metal flows is primarily based on two functional considerations. First, the TTA probe is easily configured to measure local velocity in a very small flow cross section. This high resolution is advantageous to flow measurements in the ALEX tests where large velocity gradients are encountered. Secondly, the TTA probe has good corrosion resistance in the NaK fluid environment both at ambient temperature as well as at the elevated temperature conditions anticipated for future tests.

#### INSTRUMENT DESCRIPTIONS AND RESULTS

##### HFA

Because of its previous widespread use in a number of R&D applications, a detailed description of the theory and operation of HFA will not

be given here. The primary questions that arise when considering HFA for liquid-metal MHD (LMMHD) application in NaK are: chemical compatibility, surface effects, and heat transfer effects related to the fluid properties of the liquid metal. Chemical compatibility questions were favorably resolved by testing commercially available hot-film sensors in a quiescent pool of NaK inside a glove box. No evidence of degradation of either the quartz coating or of the organic electrical insulating material on the sensor support fingers was observed following as many as 67 days of powered operation at overheat ratios (OHR)<sup>\*</sup> of up to 1.4. Cylindrical sensors, similar to that shown in Fig. 1, operated up to 31 days at power with OHR up to 1.2. Hence, it was established that no fundamental chemical incompatibility exists between ordinary commercially available hot-film sensors and room temperature NaK under operating conditions of interest for fusion applications.

Surface effects are responsible for the commonly encountered, Gardner (1971) erratic behavior of HFA in liquid metals. These surface effects have been reported almost exclusively in the working fluid mercury and include poor wetting of the sensor heat transfer surfaces and buildup of impurities on these surfaces. The impurity issue is handled in the present experiments by routinely filtering the NaK in both the large ALEX loop and in the instrumentation development loop. In the large loop, both 100  $\mu$  and 40  $\mu$  elements are used; in the small loop, 40 $\mu$ . Additionally, the strong reactivity of NaK dictates that a very clean system be maintained. Here, an argon covergas having less than 1 ppm of O<sub>2</sub> and water vapor is used. This feature minimizes the formation of oxides and other impurities which exacerbate the surface effects problem.

Heat transfer considerations associated with hot-film sensors in liquid metals are related to the low Prandtl number (Pr) of NaK (~0.04) and its high boiling point. The low Pr translates to a reduced sensitivity to convective cooling of the sensor, compared to conductive cooling. The

<sup>\*</sup>The sensor OHR is defined as  $OHR = R_{hot}/R_{cold}$ , where  $R_{hot}$  and  $R_{cold}$  are the operating and ambient resistances, respectively, of the sensor.

high boiling point makes possible higher sensor operating temperatures, thus improving measurement sensitivity and reducing the influence of environmental temperature changes. This gain in performance, however, comes at the expense of sensor longevity. Data presented here were collected at an OHR of 1.05, a modest value intended to avoid sensor failure in these initial investigations. Future work will be carried out at higher OHR.

Local velocity measurements comprise most of the HFA results presented here, but some turbulence measurements collected with HFA are presented later. Figure 4 shows HFA bridge voltage variations along the length of the ALEX thin-walled, round test section; further details of the test section and experimental arrangement are given in Reed et al. (1985) and Picologlou et al. (1986). The figure is centered on the corner of the magnet pole face, showing variations up- and downstream from the pole face corner ( $X = 0.0$ ). Upstream is negative and downstream is positive in X. The hot-film sensor is positioned at the pipe centerline and M and N are as shown on the figure. Since the anemometer bridge voltage,  $E_b$ , is related to the local velocity in the following way:

$$E_b^2 = A + B\sqrt{u},$$

the bridge voltage follows the velocity. One can see that the HFA reveals trends in the local flow velocity in the vicinity of the inlet (or outlet, shown here) of the magnetic field at M and N values of interest in fusion reactor blanket design. For example, Fig. 4 shows the voltage (velocity) at the centerline decreasing as the outlet of the magnet is approached, reaching a minimum before fully exiting the field, and finally increasing toward the centerline flow velocity. Figure 5 shows similar behavior at the test section centerline for  $M = 3,500$  and  $N = 3,050$ , with one notable exception, i.e., the hot-film data suggest that the distance downstream from the edge of the pole face, over which the centerline velocity is influenced by the magnetic field is less for the lower values of M and N than for the high.

An additional example of the kinds of results the HFA can produce is shown in Fig. 6. Here the probe is placed at 90% of the distance

from the pipe centerline to the wall,  $r/a = 0.9$  (the centerline being  $r/a = 0.0$ , the wall being  $r/a = 1.0$ ). The probe is in the horizontal plane of symmetry for the pipe. It can be seen that the HFA indicates first a rise and then a fall in velocity as the wall jets are first formed and then die out on exiting the magnet. Further details on the method of data acquisition and interpretation of the results can be found in Picologlou et al (1986).

#### LEVI

Ohm's law for a moving conductor is

$$\vec{j} = \sigma(\vec{E} + \vec{u} \times \vec{B})$$

neglecting the Hall effect. In all cases of interest for liquid-metal cooled fusion blankets, the MHD flows will be confined to thin-walled or insulated ducts where

$$c \ll 1.$$

In these cases, it can be shown that

$$\vec{j} \ll \sigma \vec{u} \times \vec{B}.$$

Hence, Ohm's law reduces to

$$\vec{E} = -\vec{u} \times \vec{B}.$$

Dropping the vector notation, expressing the electric field  $E$  as  $\Delta\phi/d$ , and solving for  $u$ , we have

$$u = \frac{\Delta\phi}{d \cdot B}.$$

This argument forms the theoretical basis for use of the LEVI probe, but experimental verification of its performance is required. Figure 7 shows a velocity profile across the horizontal midplane of the ALEX test section inside the magnetic field obtained with a LEVI. (The asymmetries of the profile are associated with some early difficulties in completely and uniformly removing the  $Cr_2O_3$  layer from the inside surface of the stainless steel test section.) Nevertheless, the average velocity was known from loop flow meters and should agree with the value obtained by integrating the velocity profile across the pipe. Care was taken to observe the fact that the flow is uniform along magnetic field

lines in the presence of a transverse magnetic field as shown in Fig. 7. Comparison of the average velocity obtained by graphical integration of Fig. 7 to that given by the loop flow meter yielded 0.72 m/s and 0.70 m/s, respectively; a roughly 3% difference.

Since resolving the  $Cr_2O_3$  surface layer problem, a number of additional velocity profiles have been collected in the round test section using the LEVI. All LEVI velocity profiles obtained have been graphically integrated and compared with the known average velocity reading. Table 1 summarizes the results of this comparison. It can be seen that with the exception of the two profiles taken in the far fringes of the B-field (E and H), all comparisons are within very respectable limits. An example profile (F) is shown in Fig. 8.

Table 1. LEVI Velocity Profile Integral Summary

ID	Location <sup>a</sup>	B <sub>o</sub> (T)	B/B <sub>o</sub>	N <sub>o</sub>	M <sub>o</sub>	$\frac{\bar{u}_{LEVI}}{\bar{u}_{flowmeter}}$
A	mid-plane	2	1	10 <sup>4</sup>	6500	1.03
B	mid-plane	2	1	10 <sup>4</sup>	6500	0.92
C	mid-plane	1	1	3x10 <sup>3</sup>	3250	0.88
D	inlet	2	0.5	10 <sup>4</sup>	6500	0.96
E	inlet	2	0.1	10 <sup>4</sup>	6500	1.17
F	inlet	1	0.5	3x10 <sup>3</sup>	3250	0.88
G	outlet	2	0.5	10 <sup>4</sup>	6500	0.95
H	outlet	2	0.1	10 <sup>4</sup>	6500	1.35
I	outlet	1	0.5	3x10 <sup>3</sup>	3250	0.95

<sup>a</sup>Profile Location W.R.T. Magnet.

In Fig. 9 velocity variations in the axial direction, as measured by the LEVI, are shown. This figure is to be compared with Fig. 4, taken with the HFA at the same conditions. It can be seen that the LEVI gives good quantitative information until it gets outside the B-field where the LEVI measurement goes to unrealistically high values. There are a number of possible explanations for this behavior, among them the decrease in both the applied field and in the induced voltage to levels which may be below reliable limits of the instrumentation. Another possible cause of this behavior could be the presence of

B-field gradients across the width of the pipe, which undoubtedly increase in the fringing areas.

Further examples of LEVI velocity distributions in the axial direction are shown in Figs. 10 and 11. These two figures complement Figs. 5 and 6, respectively. At this point, the LEVI has given very good quantitative velocity data inside the field and partially into the fringing region. The HFA currently gives qualitative velocity information in the entire inlet/outlet region of the magnet, showing the extent of the three-dimensional region both inside and outside the field. The HFA also shows regions of rising or falling velocity inside and outside the field.

#### TTA

A schematic of the TTA system is shown in Fig. 3. The system consists of a sensor located in the flow path of the fluid and externally located support electronics. The sensor is essentially a sheathed thermocouple that is alternately heated and cooled; heated by pulsing an electric current through its hot junction and then convectively cooled by the moving fluid. The cooling rate is measured and then, using a microprocessor algorithm, is correlated to the local flow velocity over the probe.

Referring to Fig. 12, the operation of the probe can be described as follows:

- At time  $t_{-1}$ , a constant, relatively high, voltage (10-30 V) is applied directly across the calibration wires for a time ( $t_0 - t_{-1}$ ). Hence, by resistance heating, the temperature of thermocouple junction is raised above the bulk fluid temperature. This power pulse (voltage) does not have to be accurately controlled or measured.
- At time  $t_0$ , the power pulse is switched off and the temperature distribution in the thermocouple begins to relax.
- At time  $t_1$ , an instantaneous junction temperature is recorded,  $T_1$ .
- At time  $t_2$ , a second instantaneous junction temperature is recorded,  $T_2$ .
- Then, using readings  $T_1$  and  $T_2$ , the preprogrammed microprocessor calculates the corresponding flow velocity.
- At time  $t_3$ , the power pulse is reapplied and the cycle is repeated.

After the initial cooldown time,  $t_0 - t_{-1}$ , the temperature decay of the thermocouple junction

is characterized by:

$$T = A_1 e^{-k\alpha_1^2 t} \quad (1)$$

where

- T = temperature at a given time,
- t = time,
- H = convective coefficient at a cylinder surface,
- K = thermal conductivity within the cylinder,
- k = K/ρc, ρ = density, c = heat capacity of the cylinder,

and  $\alpha_1$  is a function of H only for a given probe.  $A_1$  is a constant for fixed initial conditions and probe thermal properties.

A semilog plot of Eq. (1) starting at time,  $t_1$ , and normalized to temperature,  $T_1$ , is shown in Fig. 13. The slope of this curve is constant and approximated by:

$$\frac{\ln T_2/T_1}{t_2 - t_1} = -k\alpha_1^2 \quad (2)$$

Thus with measured temperature values,  $T_1$  and  $T_2$ , at a given time interval,  $t_2 - t_1$ , the slope is calculated using Eq. (2) and, from the calculated H, the local fluid velocity is determined.

Testing to date in air and water have established feasibility of the TTA device. Typical results are shown in Fig. 14 for two sizes of thermocouple sensor. The anticipated operating region for NaK is also identified. Presently, flow tests are being performed at ALEX using a test arrangement and test procedures similar to those for the air and water tests. Results to date in NaK have been reasonably successful. However, the very high thermal convection encountered in NaK flow requires higher magnitude power pulses and faster response thermocouples to achieve good data resolution. A normalized log plot of the NaK flow test results is shown in Fig. 15. Note the fast temperature decay and the scattering of the data.

#### Turbulence Measurements

Power spectral density measurements and RMS measurements were collected from both the HFA and the LEVI. A variable gain, differential amplifier was used to isolate the LEVI from an RMS meter and/or a digital fast Fourier transform

spectrum analyzer. Turbulence and energy spectrum studies are not a primary focus of the present work because, based on past LMMHD work in this area at much lower M and N [see Miyazaki et al. (1983) for example], turbulence is expected to play a negligible role in fusion blanket related issues, if it is present at all. Indeed, the preliminary data gathered thus far from both the HFA and the LEVI indicate that ordinary turbulence is damped by more than two orders of magnitude, to near the noise level of the system. For example, Fig. 16 shows two energy spectra obtained from the HFA at  $r/a = 0.9$ , the region very near the wall where turbulence production is the strongest. The upper curve represents the amplitude vs frequency of turbulent fluctuations (in arbitrary units) rather far downstream from the exit of the magnet ( $X = 0.9$  m) where the flow has nearly returned to ordinary turbulent pipe flow. The lower curve represents the turbulent energy spectrum at roughly  $X = 0$ . ( $B/B_0 = 0.5$ ), i.e., near the edge of the B-field. Yet the turbulent spectra is down more than two orders of magnitude, only slightly above the system noise level. The lower curve in Fig. 16 is fully representative of all hot-film spectra obtained once inside the fringing area of the B-field, at all values of  $r/a$ . Hence, our conclusion is that turbulence, in the cases of interest for liquid-metal cooled fusion blankets, is of academic interest at most.

It was shown earlier that the LEVI gives meaningful local velocity results away from the edges of the fringing field only. This same result is true of its ability to generate meaningful velocity fluctuation signals as well. A significant number of power spectral density (PSD) measurements were collected from the LEVI probe. LEVI spectra were collected while the mean velocity profiles listed in Table 1 were being taken and while the data in Figs. 9, 10, and 11 were being taken. All these PSD results from the LEVI probe can be represented by the two curves in Fig. 17. The upper curve represents spectra collected from all regions of the pipe within the magnetic field except the two essentially stagnant regions, one at each end of the magnet. In these two central regions of nearly stagnant fluid, not only is the mean velocity very low, but the LEVI fluctuations are also

lower (lower curve in Fig. 17), by roughly an order of magnitude than those in the other regions of the pipe.

It is important to put these PSD measurements in perspective. Within the magnetic field, the HFA and the LEVI PSD measurements are essentially consistent. In this preliminary work, the HFA has not been able to resolve the same detail as the LEVI PSD distributions shown by Fig. 17, perhaps because of the influence of the magnetic field on the HFA heat transfer. However, the important picture to keep in mind is that presented in Fig. 16, where it is seen that all the possible fine points in the PSD distributions exhibited by the LEVI data of Fig. 17 are at least two orders of magnitude below the freestream turbulence levels. Hence, our preliminary conclusion is that turbulence is not a major technical issue here.

#### SUMMARY AND CONCLUSIONS

Three instruments for measuring local velocity in LMMHD experiments are being tested and developed. The HFA has proven to be chemically compatible with NaK and thus far a powerful though qualitative tool for the task at hand. It is also useful in overviewing the importance of turbulence. Future HFA work will focus on increasing the instrument sensitivity by using higher OHR and developing calibration procedures to yield quantitative results as well.

The LEVI has turned out to be a rugged, accurate, reliable, easy to use, and inexpensive instrument. It has become the workhorse of the velocity measuring effort at ALEX and is expected to remain so. Future enhancements will focus on such details as electrode geometry improvements and increasing the adherence of the organic coating.

A methodology for determining performance of a given thermocouple in TTA-NaK applications has been developed using air and water flow measurements to characterize the probe. From these results, baseline decay curves have been calculated which represent the limiting case of the fastest decay for a given probe, i.e., infinite surface conductance. Baselines for 1.66 mm and 0.33 mm diameter probes were presented. At present, 0.25 mm diameter sheathed, ungrounded, BN insulated thermocouples are being baselined. These probes

show promise in the TTA velocity measurement system under NaK flow conditions.

REFERENCES

Abdou, M. A., et al. 1983: Blanket comparison and selection study. ANL/FPP-83-1, Argonne National Laboratory

Fabris, G. et al. 1978: Local measurements in two-phase liquid-metal MHD. In Proceedings of the Second Beersheva Int'l Seminar, Beersheva. pp. 157-171

Gardner, R. A. 1971: Hot film anemometry in a liquid mercury magneto-fluid mechanic pipe flow. Presented at Symposium on Flow Its Measurement and Control in Science and Industry, Pittsburgh, Pennsylvania. Paper No. 2-2-55

Miyazaki, K. et al. 1983: Flow and heat transfer characteristics in lithium loops under transverse magnetic field. Nucl. Tech. Fusion 4, 773-778

Picologlou, B. F.; Reed, C. B.; Dauzvardis, P. V.; Walker, J. S. 1986: Analytical and experimental investigations of magnetohydrodynamic flows near the entrance to a strong magnetic field. Presented at 7th Topical Meeting on the Technology of Fusion Energy, Reno, Nevada

Picologlou, B. F.; Reed, C. B.; Nygren, R.; Roberts, J. 1984: Magneto-fluid-dynamic issues for fusion first wall and blanket systems. Presented at the Fourth Beersheva Int'l Seminar on Magnetohydrodynamic Flows and Turbulence, Ben Gurion University of the Negev, Beersheva, Israel

Reed, C. B.; Lykoudis, P. S. 1978: The effect of a transverse magnetic field on shear turbulence. J. Fluid Mech. 89, 147-171

Reed, C. B.; Picologlou, B. F.; Dauzvardis, P. V. 1985. Experimental facility for studying MHD effects in liquid metal cooled blankets. Fusion Technology 8, 257-268

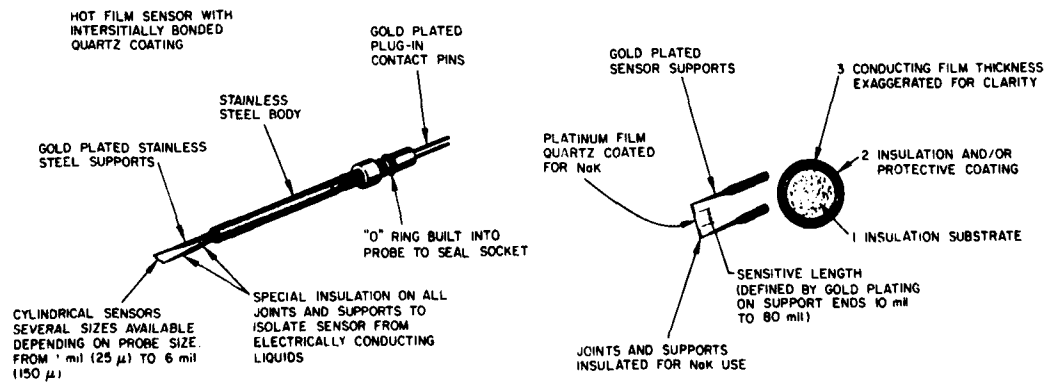


Fig. 1. Hot-film probe and cross section of hot-film sensor

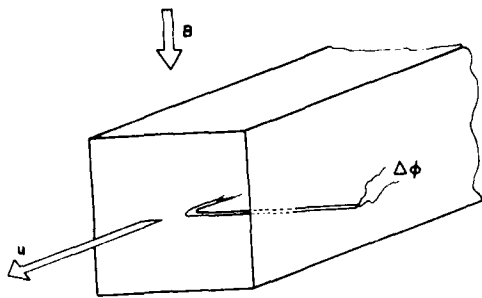


Fig. 2. LEVI geometry

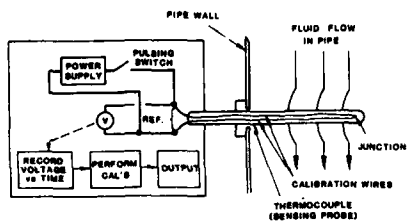


Fig. 3. Schematic of the TTA system

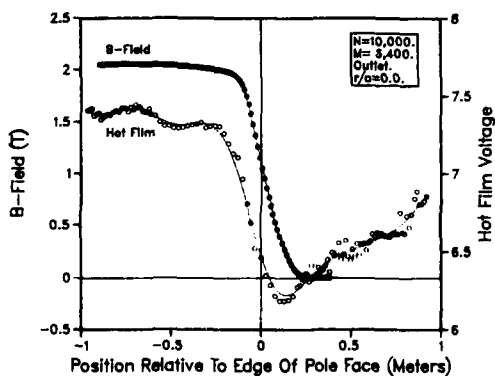


Fig. 4. Hot-film voltage axial variation,  $N = 10,000$ ;  $r/a = 0.0$

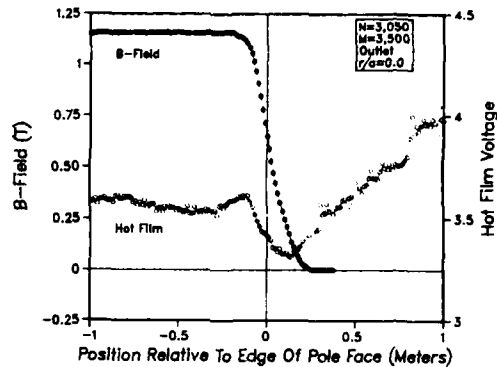


Fig. 5. Hot-film voltage axial variation,  $N = 3,050$ ;  $r/a = 0.0$

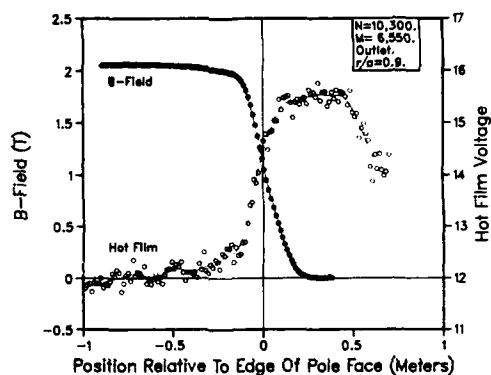


Fig. 6. Hot-film voltage axial variation,  $N = 10,300$ ;  $r/a = 0.0$

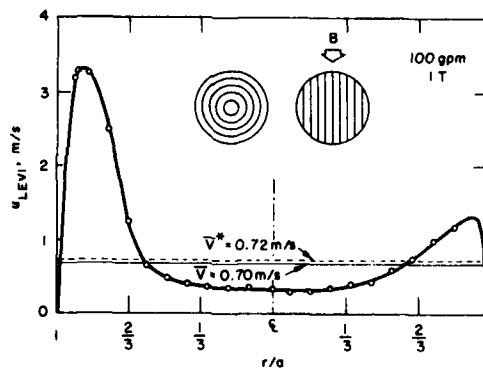


Fig. 7. LEVI velocity profile integration

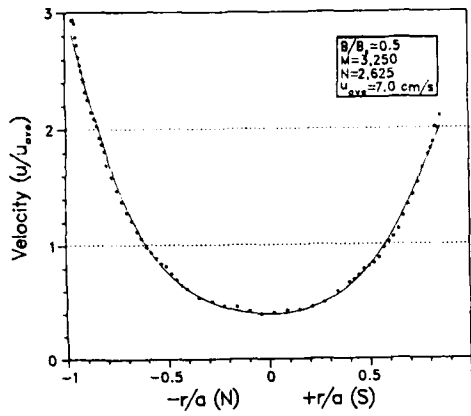


Fig. 8. LEVI velocity profile in fringing magnetic field

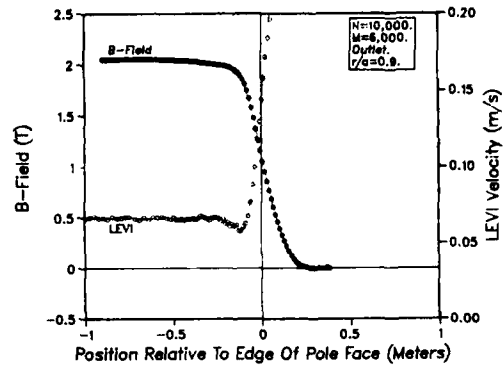


Fig. 11. LEVI velocity axial variation,  $N = 10,000$ ;  $r/a = 0.9$

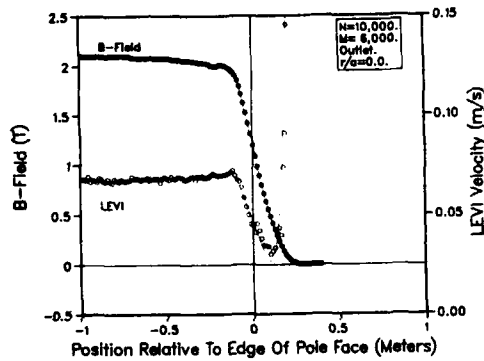


Fig. 9. LEVI velocity axial variation,  $N = 10,000$ ;  $r/a = 0.0$

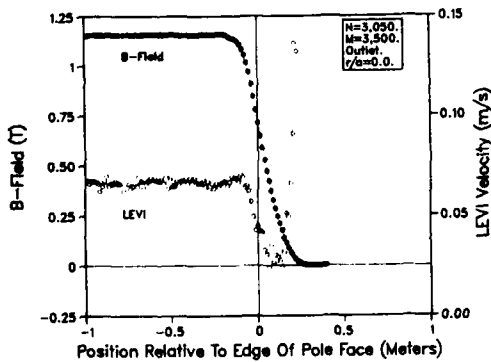


Fig. 10. LEVI velocity axial variation,  $N = 3,050$ ;  $r/a = 0.0$

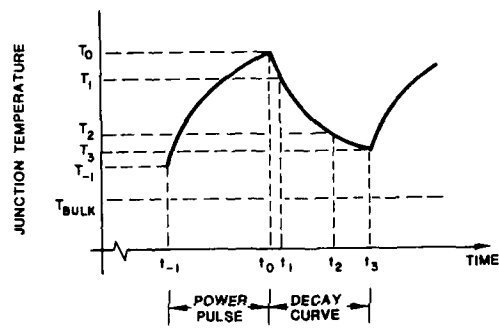


Fig. 12. Cyclic operation of the TTA probe

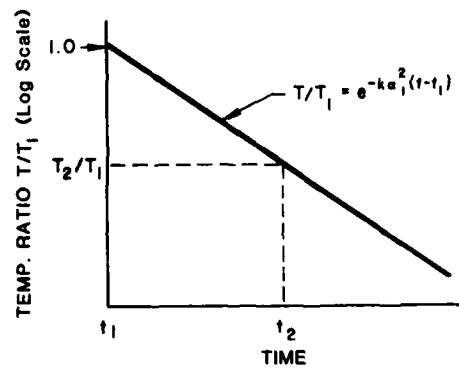


Fig. 13. Normalized TTA temperature decay starting from time  $T_1$

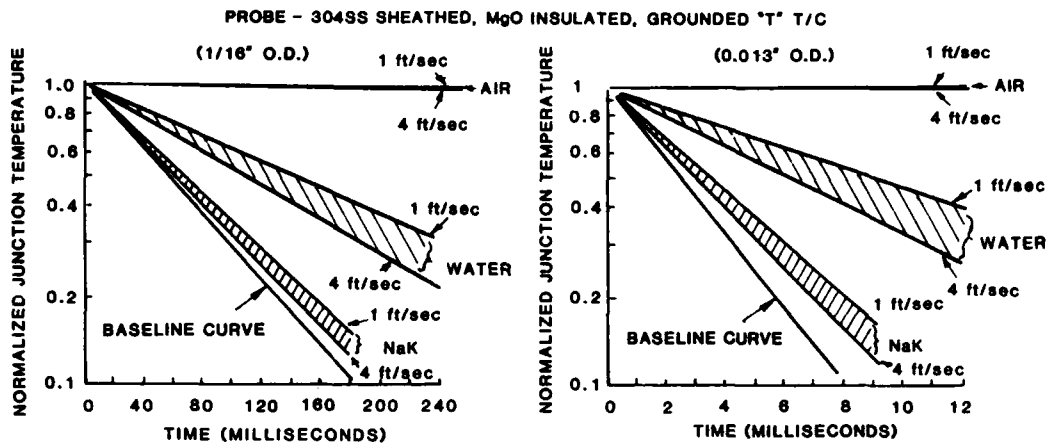


Fig. 14. Normalized TTA temperature vs time-theoretical slope comparisons

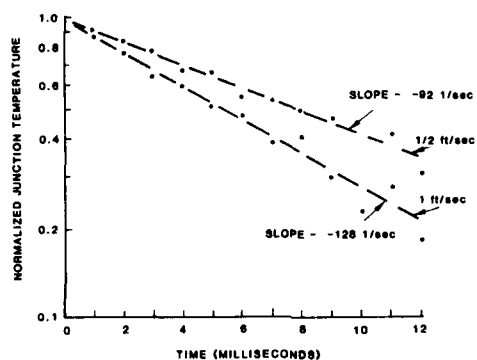


Fig. 15. Normalized TTA temperature plot for NaK flow

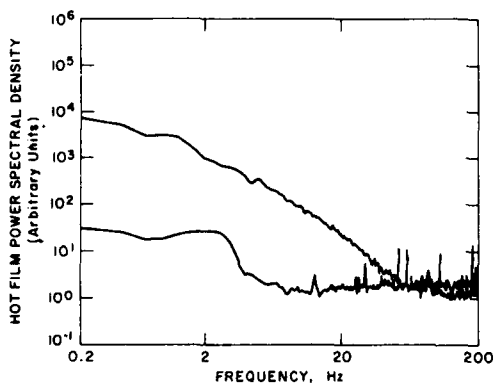


Fig. 16. Hot-film power spectra

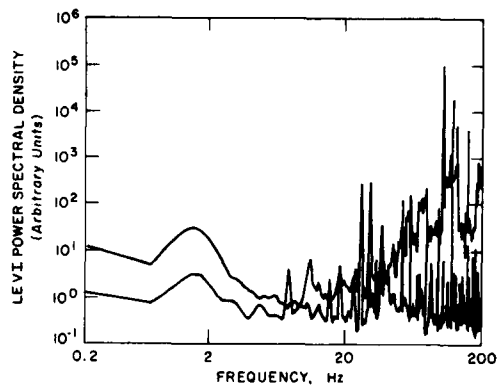


Fig. 17. LEVI power spectra

Experimental and Computational Investigation  
of Turbulent Transport in an Axisymmetric  
Sudden Expansion

Richard D. Gould, Warren H. Stevenson  
and H. Doyle Thompson

Purdue University  
School of Mechanical Engineering  
West Lafayette, IN 47907

ABSTRACT

Simultaneous two-component laser velocimeter measurements were made in the incompressible turbulent flow field following an axisymmetric sudden expansion. Mean velocities, Reynolds stresses and triple-products were measured and are presented at axial positions ranging from  $X/H = 0.2$  to 14. A balance of the turbulent kinetic energy in the flow was also performed. The production, convection and diffusion of turbulent kinetic energy were computed directly from the experimental data using central differencing. A specially designed correction lens was employed to correct for optical aberrations introduced by the circular tube. This lens system allowed the accurate simultaneous measurement of axial and radial velocities in the test section. The experimental measurements were compared to predictions generated by a code which employed the  $k-\epsilon$  turbulence model. Possible sources of differences observed between model predictions and the measurements are discussed.

INTRODUCTION

The flow downstream of a sudden pipe expansion is of both theoretical and practical importance, since it involves a number of fundamental flow phenomena and is found in a wide variety of important applications. Due to the axial symmetry of the flow, experimental measurements can be compared directly with numerical models without the difficulties which arise in 2-D rectangular cross-sections as a result of sidewall boundary layer effects. Therefore a complete and accurate experimental mapping of the flowfield would provide a significant data base for testing of various models. The present study was initiated with this in mind.

Flowfield properties of interest include axial and radial mean velocities and turbulent normal stresses as well as Reynolds stresses. Triple products are also measured. A two-color two component laser velocimeter was used to make these measurements. Aberrations introduced by the circular tube were compensated for by a specially designed

correction lens system developed by Durrett et al. (1985b). Special attention was given to the velocity bias issue, since bias error can be significant in regions of high turbulence which are of most interest.

BACKGROUND

The separated flow following a sudden expansion is complex, consisting of a potential core, a curved free shear layer with high turbulence levels, a primary recirculation zone and a secondary recirculation zone or corner eddy very close to the step. Following reattachment of the shear layer at the wall, the flow proceeds to develop and in the case of an axisymmetric sudden expansion a fully developed turbulent pipe flow is achieved.

Numerous studies of 2-D and axisymmetric sudden expansions have been conducted. Comprehensive reviews of 2-D step flow studies have been presented by Eaton and Johnston (1980) and Bremner et al. (1980). Driver and Seegmiller (1982) present a rather complete data set of two component LDV measurements in a 2-D step flow and compare them with state of the art turbulence modelling predictions. Pitz and Daily (1983) investigated the reacting flowfield following a 2-D step. Stevenson, Thompson and Luchik (1982) reviewed a number of axisymmetric sudden expansion flow investigations including those of Freeman (1975) and Moon and Rudinger (1977) which were the first in which LDV measurements were reported. Freeman's work was conducted with water while Moon and Rudinger used air as the working medium. Gould, et al. (1983) investigated both air flow and flow with combustion in a sudden expansion. In all of the above axisymmetric sudden expansion studies single component LDV systems were used and measurements were confined to the tube diameter coinciding with the optical axis of the LDV system. Radial velocity measurements in an axisymmetric geometry were first performed by Durrett, et al. (1985a) by using a specially designed correction lens system to compensate for the aberrations introduced by the circular tube wall. Velocity measurements in the secondary recirculation zone were also made in the latter study.

## EXPERIMENTAL APPARATUS

### LDV System

A two-color, two component LDV system operating in forward scatter was developed to make simultaneous measurements of axial,  $u$ , and radial,  $v$ , velocity components in the axisymmetric sudden expansion flow. The LDV system includes Bragg cell modulators in the four beam paths to allow a net frequency shift of 5MHz in both the green and blue beams. This permits an unambiguous measurement of negative velocities and also eliminates incomplete signal bias. Probe volume diameters of the green and blue beams are 0.250 mm and 0.150 mm, respectively. The probe volume lengths are approximately 2 mm and the fringe spacings are 5.33  $\mu$ m for the green probe volume and 5.11  $\mu$ m for the blue probe volume. Scattered light from the probe volume is separated with a dichroic filter so that approximately 80% of each color passes to its respective photomultiplier tube. Narrow bandpass filters are used to further reduce signal cross talk.

The data collection and processing system consists of two TSI Model 1990 counter-type processors (one for each channel), a TSI Model 1998 interface with coincidence timing electronics and a PDP 11/40 mini-computer with DMA capability. With this system it is theoretically possible to acquire velocity data from individual Doppler burst signals at rates up to 100,000 samples per second. (In practice the rates are less due to seed density limits.) The mini-computer and counter processors are also interfaced so that sampling can be controlled. This is accomplished with a hardware clock controlling the data ready-inhibit handshaking signals.

### FLOW SYSTEM

The flow system used for this experiment is illustrated in Figure 1. It consists of a converging inlet nozzle with an exit diameter of 76.2 mm followed by a 152.4 mm diameter downstream section. This inlet was chosen to give a uniform inlet velocity profile. The test section was extruded from optical quality fused quartz and allows measurements throughout the flowfield for  $x/H$  values ranging from 0.2 to 14. The test section design is shown in Figure 2.

Air flow was provided by a radial fan blower followed by a flow conditioning section consisting of honeycomb flow straighteners. The static pressure drop across the nozzle was used to monitor inlet flow conditions and was maintained constant to within  $\pm 0.25$  inches of water throughout the experiment.

Seeding was supplied by two TSI model 3076 liquid atomizers each followed by a TSI model 3072 evaporation-condensation monodisperse aerosol generator. This produced seeding particles one micron or less in diameter using a 100% solution of dioctyl phthalate (DOP). The seeders were capable of providing seed densities sufficient to give data validation rates in excess of 30,000 per second for each channel (green and blue beams) over most of the flowfield. The two-channel "coincident" data validation rate which is controlled by the coin-

idence timing logic circuit in the TSI 1998 master interface was somewhat less than the asynchronous data validation rates that the individual counter processors detect. With the coincidence window set to 10  $\mu$ s, as it was for this experiment, the maximum "coincident" data validation rate was approximately one-half the value of the data rate reading on the counter processor with the lower of the two data rates. For this experiment, two-channel "coincident" data validation rates ranged between 10,000 and 15,000 per second over most of the flowfield. This "coincident" data validation rate was high enough to use the experimental technique for eliminating velocity bias by inhibiting the counter processors for a fixed time interval between samples, approximating equal time sampling. This method has previously been described by Stevenson, Thompson and Roesler (1982) and its effectiveness confirmed in subsequent studies, including the work by Gould, et al. (1983); Durrett, et al. (1985a) and Johnson, et al. (1982).

### CORRECTION LENS

A correction lens to allow simultaneous axial and radial velocity measurements in a cylindrical tube has been designed using the procedure described by Durrett, et al. (1985b). The planar-concave cylindrical lens that corrects for the aberration induced by the quartz test section has a radius of curvature of 3.3528 m, a thickness at its center of 17.93 mm and a refractive index of 1.52. The correction lens insures that the orthogonal probe volumes (green and blue) intersect to within 100  $\mu$ m along the length and to within 25  $\mu$ m along the diameter. The correction lens system is comprised of two lenses, one on the transmitting side and one on the receiving side of the test section. This is due to the symmetry of the system. The lenses have to be moved away from the test section as the measurement point moves further off axis. A ray tracing program is used to determine the placement of the lenses and also gives the real probe volume intersection relative to the beam intersection if no test section or lens was present. Simultaneous axial-radial velocity measurements can be made out to a non-dimensional radius of approximately 83% with this system.

### EXPERIMENTAL TECHNIQUE

The simultaneous axial and radial velocities were sampled at 100 Hz using the interval sampling technique for velocity bias elimination discussed earlier. In all cases 6400 individual realizations were accumulated for each velocity component at each measurement point to form velocity histograms. The relatively long sampling time (64 seconds) ensures that all low frequency phenomena are included in the sample. Using statistical analysis and assuming Gaussian distributions and local turbulence intensity levels of 70%, the expected sampling error for the 6400 sample size was found to be less than 1% for mean velocities and less than 2% for turbulence intensities for a 95% confidence level. All data points lying outside  $\pm 3 \sigma$  were discarded and revised statistics were calculated. Typically, less than 100 data points out of the 6400 were discarded.

## COMPUTATIONAL FLOW PREDICTIONS

An existing TEACH computer program originally developed by Pun and Spalding (1976) and subsequently modified by Chiappetta (1983), for predicting the turbulent swirling and reacting flow in an axisymmetric bluff body combustor was further modified to predict the flowfield in an axisymmetric sudden expansion for this study. The code employs the two equation k- $\epsilon$  turbulence model and the combustion model of Magnussen and Hjertaher (1978). Conservation equations for swirl and chemical reaction were not solved for this study. The standard turbulence constants given by Pun and Spalding were used.

Basically, the boundary conditions for all the dependent variables were changed to those for an axisymmetric sudden expansion. The inlet boundary condition was set to a uniform axial velocity of 22 m/s. Inlet radial velocity was set to zero while the inlet turbulent kinetic energy was set to 1% of the mean kinetic energy. The outlet boundary condition requires that the axial gradient of the dependent variables vanish at the exit plane. A skewed upwind numerical differencing scheme, added by Chiappetta (1983), was used to finite difference the conservation equations. This numerical differencing method uses a nine point stencil and thereby accounts for the flow angle of the fluid into the control cells.

The predictions were made using a 22 x 87 grid in the radial and axial direction, respectively. Location of the exit boundary, where the gradient boundary condition is applied, was varied from a non-dimensional axial distance of 20 step heights to 40 step heights. This test was performed to see if the outlet boundary condition was influencing the upstream flowfield. The predictions showed no noticeable change in the flowfield when the location of the exit plane was changed.

An additional study was performed to demonstrate how well the eddy viscosity model embodied in the k- $\epsilon$  turbulence model predicts the Reynolds stresses. The turbulent viscosity,  $\mu_t$ , in the k- $\epsilon$  model is given by

$$\mu_t = \frac{C_D \rho k^2}{\epsilon} \quad (1)$$

where  $C_D$  is an empirical coefficient,  $\rho$  is the density,  $k$  is the turbulent kinetic energy and  $\epsilon$  is the rate of turbulence dissipation. The unknown Reynolds stresses are then found using  $\mu_t$  and the mean velocity gradients through the modified Boussinesq approximation

$$-\rho u_i u_j = \mu_t \left[ \frac{\partial u_i}{\partial x_j} + \frac{\partial u_j}{\partial x_i} \right] - \frac{2}{3} \delta_{ij} \left[ \mu_t \frac{\partial u_k}{\partial x_k} + \frac{1}{2} \rho \bar{u}^2 \right] \quad (2)$$

The last term insures that the two sides of the equation balance when  $i$  and  $j$  are set equal and summed. The TEACH code was allowed to converge upon a solution giving the final mean values of all the dependent variables ( $U$ ,  $V$ ,  $p$ ,  $k$ ,  $\epsilon$ ) throughout the flowfield. Knowing the mean velocity distributions allows one to numerically differentiate and find the mean velocity gradient at each point in the flow. Knowing the mean gradients and the turbulent viscosity given by (1), (which is known because we have  $k$  and  $\epsilon$  throughout the flowfield) we can calculate the modelled turbulent stresses that the code substitutes in the momentum equations at each location to close the problem. It should be noted that care must be taken when numerically differentiating the dependent variables due to the staggered grid used in TEACH codes.

## EXPERIMENTAL RESULTS AND DISCUSSION

### MEAN VELOCITY DATA

Measurements of the axial and radial mean velocity and turbulent normal stress as well as Reynolds stress and turbulent kinetic energy were previously made in an axisymmetric sudden expansion flow, Gould et al. (1986), and are included here for completeness. Turbulent triple products were measured as part of the present study. The measurements were all direct and were made at 21 radial locations across the test section and at 12 axial planes located at non-dimensional axial distances based on step height of  $X/H = 0.2$  to 14. Figures 3 through 12 are profile plots of the normalized measurements and the k- $\epsilon$  model predicted values. Triple products are not used in the k- $\epsilon$  model, so no predicted values are shown. The mean inlet centerline velocity of 22 m/sec was used to normalize all measurements for this experiment.

Figure 3 shows the measured mean axial velocity profiles (solid lines) throughout the sudden expansion flowfield. The inlet velocity profile was measured experimentally at  $x/H = 0.2$  and was found to be very flat across the entire diameter of the inlet. Velocity measurements from both sides of the centerline are plotted at this axial location. The dashed lines represent the predicted axial mean velocity profiles. Fairly good agreement exists between the measurements and the prediction, although the centerline velocity is first underpredicted and then overpredicted. This was also found in previous studies by Stevenson, et al. (1982) and Durrett, et al. (1985a). The model also predicts higher negative axial velocities in the recirculation zone than the experimental measurements indicate. Reattachment occurs at approximately 8 step heights downstream of the inlet plane and also agrees with published results.

The mean radial velocity measurements show more data scatter than the axial velocity component as can be seen in Figure 4. This would be expected, since the mean radial velocity is more than an order of magnitude less than the mean axial velocity over much of the flow. The error bar shown on this plot takes into account the beam steering errors due to slight surface ripples on the extruded quartz tube wall and the uncertainty in the orientation of the blue fringes with respect

to the flow. The blue fringe orientation is estimated to be perpendicular to the flow to within  $\pm 0.25$  degrees. This corresponds to an uncertainty in radial velocity of  $\pm 0.1$  m/s in the core region of the flow due to the axial velocity component. The measured mean radial velocity is zero to within the uncertainty estimate across the diameter of the inlet. The measured mean radial velocity profiles presented here agree qualitatively with those measured by Durrett, et al. (1985a), but velocity magnitudes here were approximately half the values reported in that study. The source of this discrepancy is not obvious, but the present results are internally consistent and exhibit no anomalies. The predicted mean radial velocity agrees qualitatively with the measured values and is within the uncertainty estimate over most of the flow. The main differences between the predicted and measured mean radial velocities occur in the recirculation zone.

#### TURBULENT REYNOLDS STRESSES

Figures 5 and 6 show profiles of the measured and predicted axial and radial turbulent normal stresses, respectively. Peak values of axial normalized turbulent intensity (i.e., the square root of what is presented) occur in the shear layer and reach values of 25%. This is in good agreement with earlier studies performed by Gould et al. (1983) and Stevenson, Thompson and Luchik (1982). The peak value of radial normalized turbulence intensity was found to be approximately 15%. This agrees closely with the findings of Durrett et al. (1985a) who found peak radial normalized intensities of 17%. *It is interesting to note that the peak radial normalized turbulence intensity is approximately two-thirds the value of the peak axial normalized turbulence intensity.* This behavior is also found in free jet flows as shown by Wygnanski and Piedler (1969). The values of normal stresses used by the k- $\epsilon$  model to close the computation are calculated from equation (2) as discussed earlier and are shown by the dashed lines. For incompressible flow, the normal stresses are composed of two terms: the term due to mean velocity gradients, which accounts for approximately 30% of the total normal stress and can be positive or negative depending on the local mean velocity gradient, and the term due to the turbulent kinetic energy. This second term can be thought of as a pseudo-pressure due to turbulent normal stresses. Hence, when using the eddy viscosity constitutive relationship of equation (2), near isotropic normal stresses result due to the overwhelming contribution to the normal stress from this second term. This constraint will lead to poorly predicted mean velocities in highly anisotropic flow fields.

The values of Reynolds stress used by the k- $\epsilon$  model are shown along with measured values in Figure 7. Peak values of normalized Reynolds stress occur in the shear layer as expected and reach values of 0.015. This result agrees well with the results obtained by Durrett, et al. (1985a), which used a rotatable one-component LDV system along with Logan's method (1972) to calculate Reynolds stresses from two independent measurements oriented at  $\pm 45^\circ$  to the flow direction. Reynolds stress

values used by the code are high compared to measured values in the shear layer and the recirculation zone. This may be due to the fact that predicted turbulent kinetic energy is higher than the measured value in the recirculation zone as shown in Figure 8. This would tend to give a higher value of turbulent viscosity for a given dissipation (see Equation 1). It should be noted that Figure 8 shows profiles of measured turbulent kinetic energy calculated by assuming that the unknown tangential turbulence intensity equalled the measured radial turbulence intensity. Free jet experiments show this behavior, and it appears to be a reasonable assumption for the bounded axisymmetric sudden expansion flow studied here.

The k- $\epsilon$  model also fails to predict the correct turbulence level in the central region downstream of  $x/h = 6$ . Predicted values of turbulent kinetic energy are very low in this part of the flow. This result explains why the values of modelled normal stress that the code uses are low.

Care must be taken with the kind of analysis presented here. One must remember that the k- $\epsilon$  model does not predict Reynolds stresses; it attempts to solve two additional conservation equations, one for turbulent kinetic energy and one for turbulent dissipation rate, in order to define an eddy viscosity. Knowing the eddy viscosity allows one to estimate or model the unknown Reynolds stresses in each of the conservation of momentum equations and therefore close the problem. The purpose of this analysis was to compare the estimated Reynolds stresses used by the k- $\epsilon$  model with experimentally measured values. The insight gained by doing this may give rise to new turbulence models or to improvements of existing models.

#### TURBULENT-TRIPLE PRODUCTS

The turbulent triple products that were measured in this study are  $uuu$ ,  $uuv$ ,  $uvv$  and  $vvv$ . The normalized values are shown in Figures 9 through 12. The triple products are antisymmetric about the centerline of the shear layer, peaking to either side of the centerline of the shear layer and approaching zero at the edges of the shear layer. This behavior is characteristic of free shear layers in early stages of separation. Very little data exists to compare the present data with at this time. Driver and Seegmiller present limited triple product data (i.e. the sum of  $uuv$  and  $vvv$ ) in the flow field downstream of a 2-D backward facing step. The triple product data from the present study and Driver and Seegmiller's study exhibit similar shape but differ in peak magnitudes. The peak normalized values of ( $uuv + vvv$ ) were found to be approximately 5 times greater in this study than those reported by Driver and Seegmiller. It should also be noted that normalized peak values of Reynolds stress in this study were found to be 1.5 times greater than those reported for the 2-D backward facing step flow.

The reason for this difference in peak values is unknown. One possible reason may be the large disparity in expansion ratio used in the two stu-

dies. Driver and Seegmiller used an expansion ratio of 1.125:1 while an expansion ratio of 4:1 was used for the present study. Driver and Seegmiller also reported that  $(uuu + uvv)$ , which was not shown, exhibited similar behavior to  $(uuv + vvv)$  but was opposite in sign. All the triple product data measured in this study had the same sign. Again, the reason for this difference is not obvious, but the present results are internally consistent. It is interesting to note the rather high value of  $uuu$  on the centerline of the sudden expansion at  $X/H = 10$  (Figure 9). The high value found at this location may indicate the passage of large eddy structures. The value of  $uu$  at this location is reasonable which strongly suggests that  $uuu$  is also reasonable.

#### TURBULENT KINETIC ENERGY BALANCE

The  $k-\epsilon$  turbulence model uses the turbulent kinetic energy,  $k$ , and the rate of turbulent dissipation,  $\epsilon$ , to calculate a value for the eddy viscosity as given by Equation (1). This eddy viscosity is then used, along with mean velocity gradients, in the eddy viscosity turbulence model (given by Equation (2)), to give the "modelled" turbulent stresses needed to solve the time averaged momentum equations for  $U$ ,  $V$  and  $P$ . In an effort to validate the transport equation for turbulent kinetic energy, an energy balance was performed as part of this study.

For steady incompressible, axisymmetric flow the conservation equation for turbulent kinetic energy is as follows:

$$\begin{aligned} \left[ v \frac{\partial k}{\partial r} + u \frac{\partial k}{\partial x} \right] = \frac{1}{\rho} \frac{\partial}{\partial x} \left[ \mu \frac{\partial k}{\partial x} - \rho \frac{uvv}{2} - \rho \frac{vww}{2} - \rho \frac{uuu}{2} - \overline{uvp} \right] \\ + \frac{1}{\rho r} \frac{\partial}{\partial r} \left[ \mu r \frac{\partial k}{\partial r} - \rho r \frac{vrv}{2} - \rho r \frac{vwr}{2} - \rho r \frac{uuv}{2} - r \overline{vfp} \right] \\ - \left[ \frac{2}{\rho} \frac{v^2}{r^2} + \frac{\mu}{\rho} \frac{v^2}{r^2} \right] - \left[ \overline{vrv} \frac{\partial v}{\partial r} + \overline{uvu} \frac{\partial u}{\partial r} + \overline{vuv} \frac{\partial v}{\partial x} + \overline{uuu} \frac{\partial u}{\partial x} + \overline{vrv} \frac{v}{r} \right] \\ - \frac{\mu}{\rho} \left[ \left| \frac{\partial v}{\partial r} \right|^2 + \left| \frac{\partial w}{\partial r} \right|^2 + \left| \frac{\partial u}{\partial r} \right|^2 + \left| \frac{\partial v}{\partial x} \right|^2 + \left| \frac{\partial w}{\partial x} \right|^2 + \left| \frac{\partial u}{\partial x} \right|^2 \right] \quad (3) \end{aligned}$$

where the fluctuating axial, radial and tangential velocities are denoted by  $u$ ,  $v$  and  $w$ , respectively. The equation is composed of the following terms from left to right: 1) radial and axial convection, 2) axial diffusion, 3) radial diffusion, 4) additional diffusion due to cylindrical coordinates, 5) production and 6) viscous dissipation. As can be seen from Equation (3), the exact turbulent kinetic energy equation has many additional unknowns including triple products, pressure diffusion terms and viscous dissipation terms. In order to simplify the turbulent kinetic energy equation so that it can be employed in the  $k-\epsilon$  model, the unknown terms are either modelled as a function of some

known quantity or are completely ignored. The modelled turbulent kinetic energy equation for steady, incompressible, axisymmetric flow is given by:

$$\begin{aligned} v \frac{\partial k}{\partial r} + u \frac{\partial k}{\partial x} = \frac{1}{\rho} \frac{\partial}{\partial x} \left[ \mu_{\text{eff}} \frac{\partial k}{\partial x} \right] + \frac{1}{\rho r} \frac{\partial}{\partial r} \left[ \mu_{\text{eff}} r \frac{\partial k}{\partial r} \right] \\ + \frac{\mu_t}{\rho} \left[ 2 \left| \frac{\partial u}{\partial x} \right|^2 + 2 \left| \frac{\partial v}{\partial r} \right|^2 + 2 \left| \frac{v}{r} \right|^2 + \frac{\partial v}{\partial x} + \frac{\partial u}{\partial r} \right] - \epsilon \quad (4) \end{aligned}$$

where

$$\mu_{\text{eff}} = \mu_t + \mu_{\text{lam}} \quad (5)$$

Comparing Equations (3) and (4), one can readily conclude that many simplifications have been made so that the modelled equation is in terms of five dependent variables, which then leads to a closed form solution.

In order to validate the modelled equation, each group of terms (i.e., convection, diffusion, production and dissipation) in Equations (3) and (4) was compared. The turbulent kinetic energy was defined as  $k = uu + 2vv$ , as mentioned earlier. This assumption enables us to determine the convection terms from the experimental data. Central differencing was used to numerically differentiate the data. It should be noted that all experimental data was smoothed first, using a least squares cubic spline smoothing package, before it was differentiated. The modelled convection terms were found in a similar fashion using the converged solution as "predicted" data. The "exact" diffusion terms contain parameters that were not measured in this study. In order to calculate the total diffusion,  $vww$  was assumed to equal  $vuv$  and  $uvw$  was assumed to equal  $uvv$ . The pressure-diffusion terms were assumed negligible in this analysis. This assumption is reasonable at locations away from the wall. Again, the modelled total diffusion (i.e. axial and radial) was also calculated. The production terms were computed directly from the experimental data by assuming  $w = vv$ . The "modelled" production terms were calculated according to equation (4). The "measured" dissipation was inferred by balancing the turbulent kinetic energy equation while the modelled dissipation is a direct output of the TEACH code. Figure 13 shows radial profiles of the loss and gain of turbulent kinetic energy due to convection, production, diffusion and dissipation at axial locations ranging from  $x/H = 2$  to 12. A number of conclusions can be drawn from these results. First, the predicted production was found to be higher than the measured production throughout most of the shear layer. This is because the predicted value of  $uv$  was higher than the measured value as mentioned earlier. The total production of turbulent kinetic energy is dominated by  $uv \partial u / \partial r$  in this flow field. The measured convection of turbulent kinetic energy was found to be higher than the predicted convection in the central region of the flow downstream of  $x/H = 6$ . This is probably due primarily to the diffusion term. The radial gra-

dients of  $u_{uv}$  and  $v_{vv}$  give rise to high values of measured turbulent diffusion in this region. Apparently, the transport coefficient,  $\mu_t$ , used in the modelled diffusion terms does a poor job of modelling the real diffusion in this region of the flow.

#### CONCLUSIONS

Overall, it can be concluded that the  $k-\epsilon$  turbulence model does a good job in predicting the mean flow parameters of an axisymmetric sudden expansion flow. This has been confirmed in several studies. However, there are areas in the flowfield where the prediction fails to match the experimental results. These include the recirculation zone and the central core region downstream of  $x/h = 6$ . The  $k-\epsilon$  turbulence model uses values of Reynolds and normal stresses that qualitatively agree with the measured values, but differ in magnitude. The isotropic normal stress assumption used in the model contributes to errors in the predicted flowfield, as shown in the present study. A modification to the eddy viscosity model aimed at correcting this may be a fruitful area of study. Turbulent triple products were measured and found to contribute significantly to the transport of turbulent kinetic energy. Lastly, a turbulent kinetic energy balance identified the various areas of the flow where different turbulent transport mechanisms dominate.

#### ACKNOWLEDGMENTS

This investigation was supported by NASA Lewis Research Center under grant NAG3-502.

#### BIBLIOGRAPHY

- Bremmer, R., Thompson, H.D. and Stevenson, W.H. (1980) "An Experimental and Numerical Comparison of Turbulent Flow Over a Step," AFWAL-TR-80-22105, Air Force Wright Aeronautical Laboratories.
- Chiappetta, L.M. (1983) "User's Manual for a TEACH Computer Program for the Analysis of Turbulent, Swirling Reacting Flow in a Research Combustor." NASA Report #R83-915540-27.
- Driver, D.M. and Seegmiller, H.L. (1982) "Features of a Reattaching Turbulent Shear Layer Subject to an Adverse Pressure Gradient," AIAA-82-1029.
- Durrett, R.P., Stevenson, W.H. and Thompson, H.D. (1985a) "Radial and Axial Turbulent Flow Measurements with an LDV in an Axisymmetric Sudden Expansion Air Flow," International Symposium on Laser Anemometry, ASME Winter Annual Meeting, Nov. 17-22, Miami Beach, Florida, pp. 127-133.
- Durrett, R.P., Gould, R.D., Stevenson, W.H. and Thompson, H.D. (1985b) "A Correction Lens for Laser Doppler Velocimeter Measurements in a Cylindrical Tube," AIAA Journal, 23, 1387-1391.
- Eaton, J.K. and Johnston, J.P. (1980) "An Evaluation of Data for Backward Facing Step Flow," 1980/81 Conferences on Complex Turbulent Flows, Stanford University, Department of Mechanical Engineering.
- Freeman, A.R. (1975) "Laser Anemometer Measurements in the Recirculating Region Downstream of a Sudden Pipe Expansion" Proceedings of the LDA-Symposium, Copenhagen.
- Gould, R.D., Stevenson, W.H. and Thompson, H.D. (1986) "Two Component Laser Velocimeter Measurements of Turbulence Parameters Downstream of an Axisymmetric Sudden Expansion," Third International Symposium on Applications of Laser Anemometry to Fluid Mechanics, Lisbon.
- Gould, R.D., Stevenson, W.H. and Thompson, H.D. (1983) "Laser Velocimeter Measurements in a Dump Combustor" ASME Paper 83-HT-47.
- Logan, S.E. (1972) "A Laser Velocimeter for Reynolds Stresses and Other Turbulence Parameters," AIAA Journal, 19, 933-935.
- Moon, L.F. and Rudinger, G. (1977) "Velocity Distribution in an Abruptly Expanding Circular Duct," ASME Journal of Fluids Engineering, 99, 226-230.
- Pitz, R.W. and Dailey, J.W. (1983), "Combustion in a Turbulent Mixing Layer Formed at a Rearward-Facing Step," AIAA Journal, 11, 1565-1570.
- Pun, W.M. and Spalding, D.B. (1976) "A General Computer Program for Two-Dimensional Elliptic Flows," HTS/76/2, Imperial College, Mechanical Engineering Department.
- Stevenson, W.H., Thompson, H.D. and Craig, R.R. (1982) "Laser Velocimeter Measurements in Highly Turbulent Recirculating Flows," Proceedings of the Symposium on Engineering Applications of Laser Velocimetry, ASME Winter Annual Meeting, Phoenix, Arizona.
- Stevenson, W.H., Thompson, H.D. and Luchik, T.S. (1982) "Laser Velocimeter Measurements and Analysis in Turbulent Flows with Combustion," AFWAL-TR-82-2076, Part I, Air Force Wright Aeronautical Laboratories.
- Stevenson, W.H., Thompson, H.D. and Roesler, T.C. (1982) "Direct Measurement of Laser Velocimeter Bias Errors in a Turbulent Flow," AIAA Journal, 20, 1720-1723.
- Wynanski, I. and Fiedler (1969) "Some Measurements in the Self-Preserving Jet," J. of Fluid Mechanics, 38, p. 577.

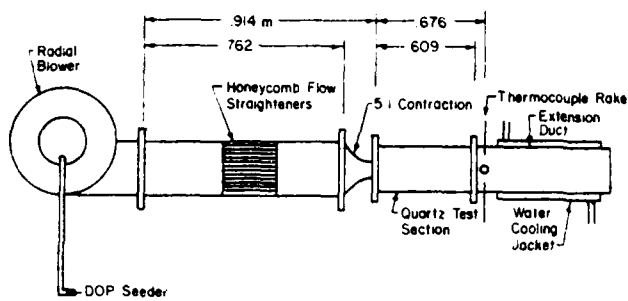


Figure 1. The flow system

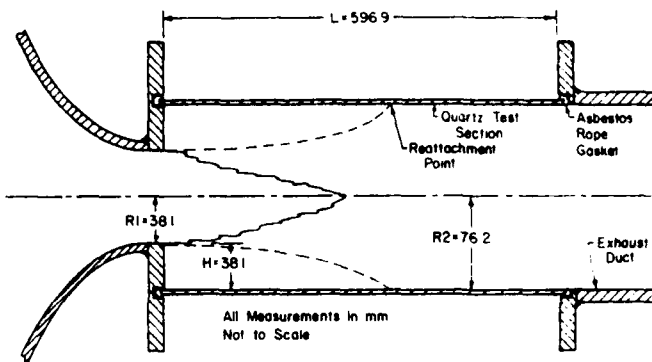


Figure 2. The test section

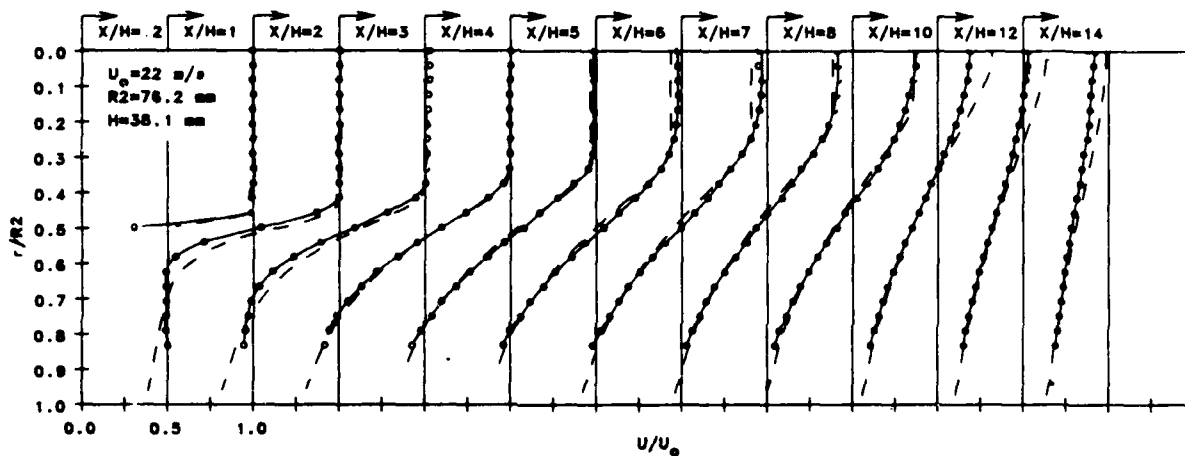


Figure 3. Mean axial velocity profiles (o - measurements, --- prediction)

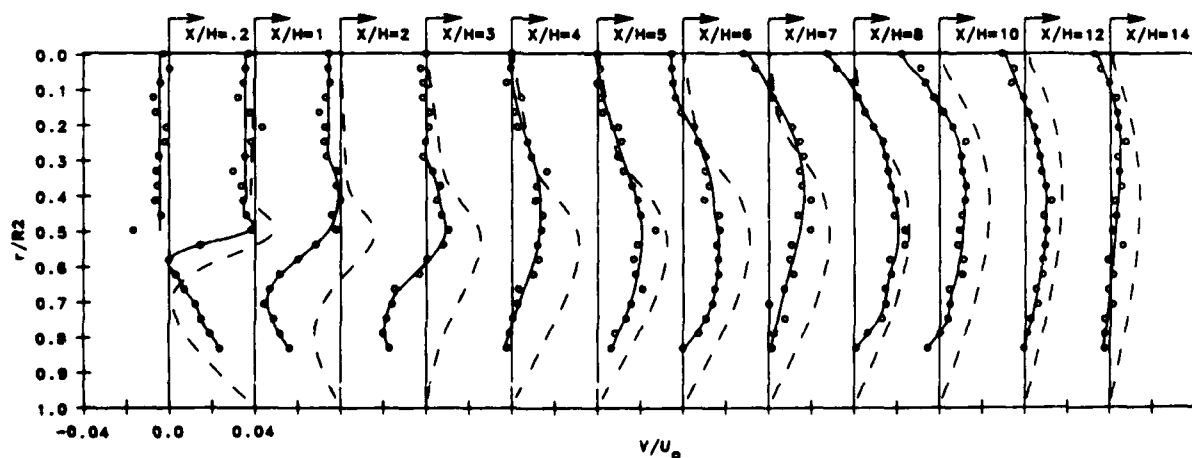


Figure 4. Mean radial velocity profiles (o - measurements, --- prediction)

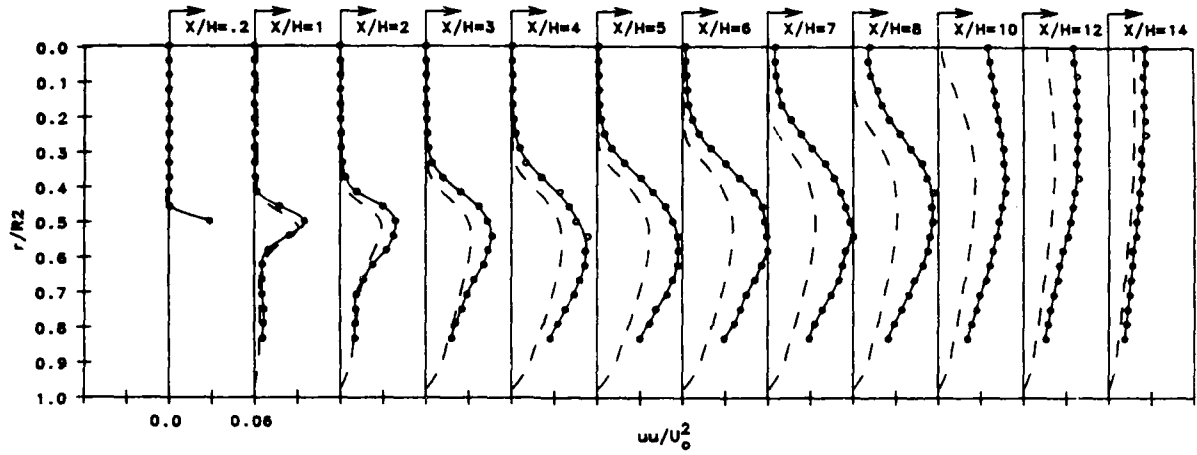


Figure 5. Normalized axial turbulent normal stress profiles (o - measurements, --- prediction)

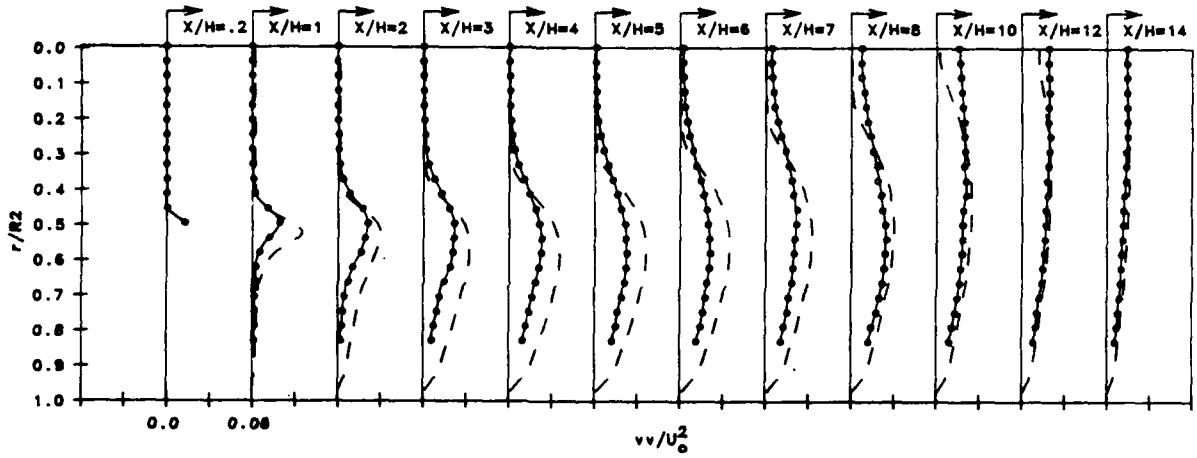


Figure 6. Normalized radial turbulent normal stress profiles (o - measurements, --- prediction)

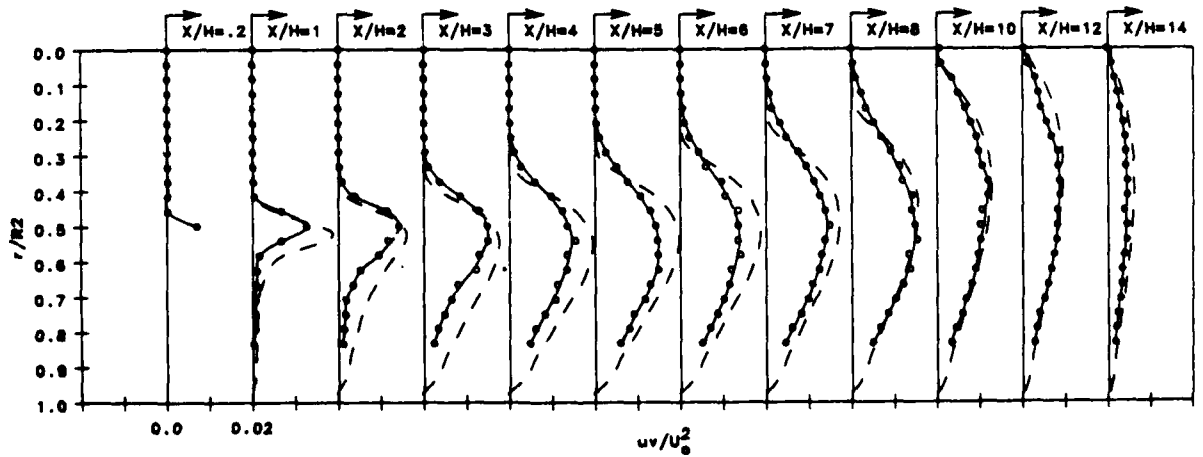


Figure 7. Normalized shear stress profiles (o - measurements, --- prediction)

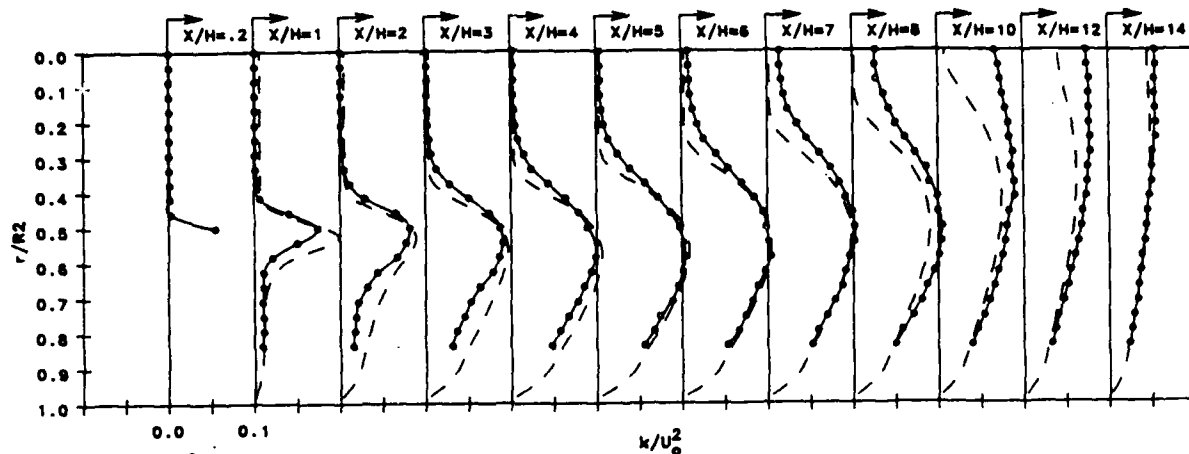


Figure 8. Normalized turbulent kinetic energy profiles (o - measurements, --- prediction)

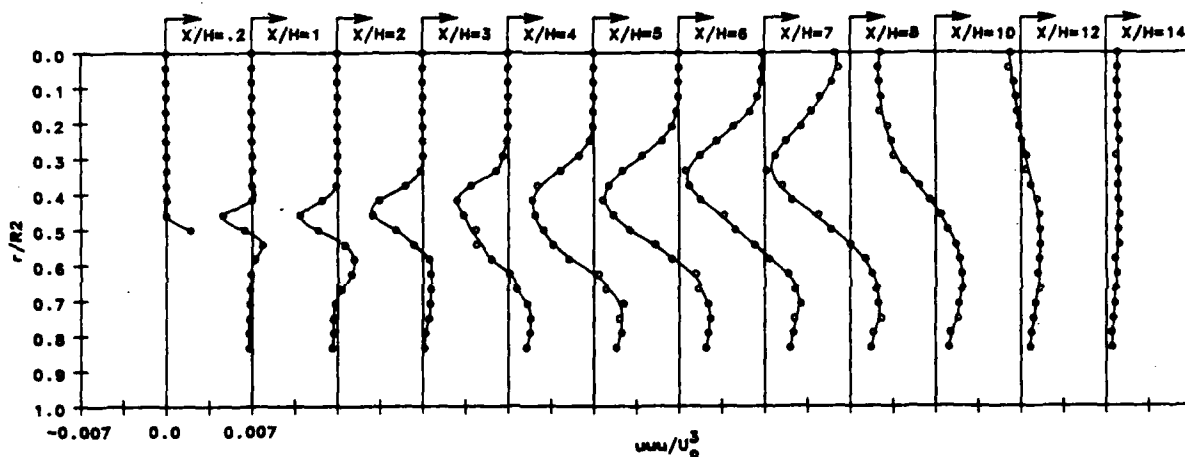


Figure 9. Normalized  $uuu$  turbulent triple-product profiles (o - measurements)

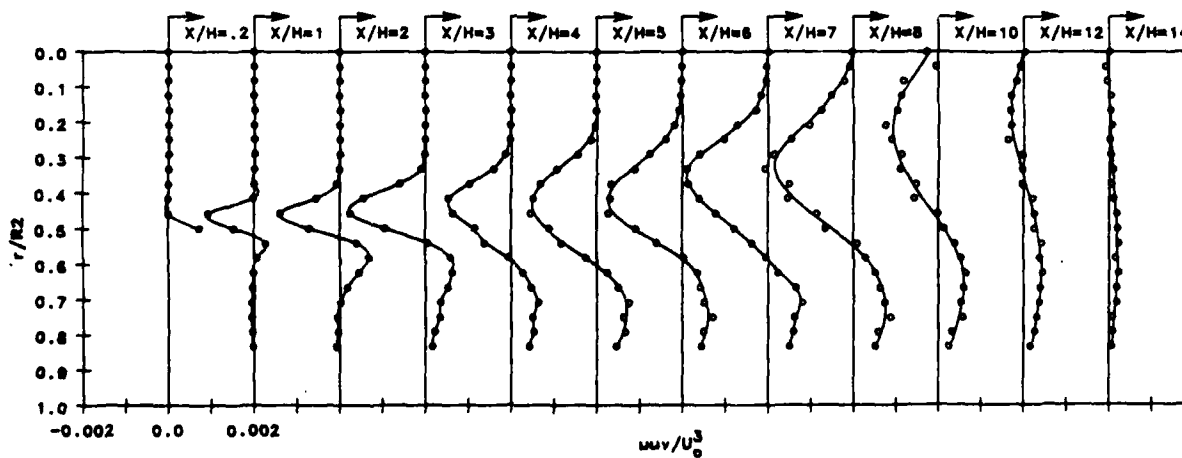


Figure 10. Normalized  $uvv$  turbulent triple-product profiles (o - measurements)

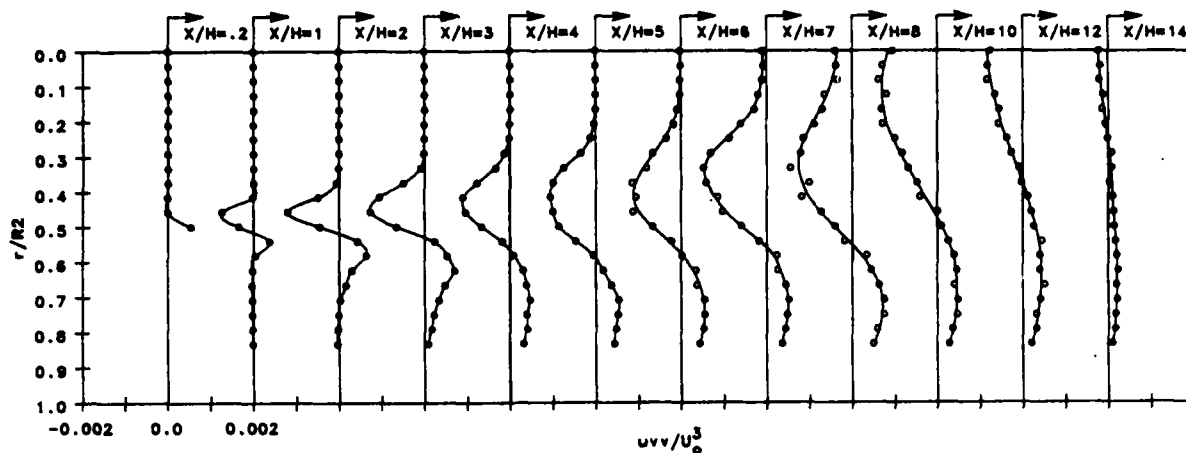


Figure 12. Normalized vvv turbulent triple-product profiles (o - measurements)

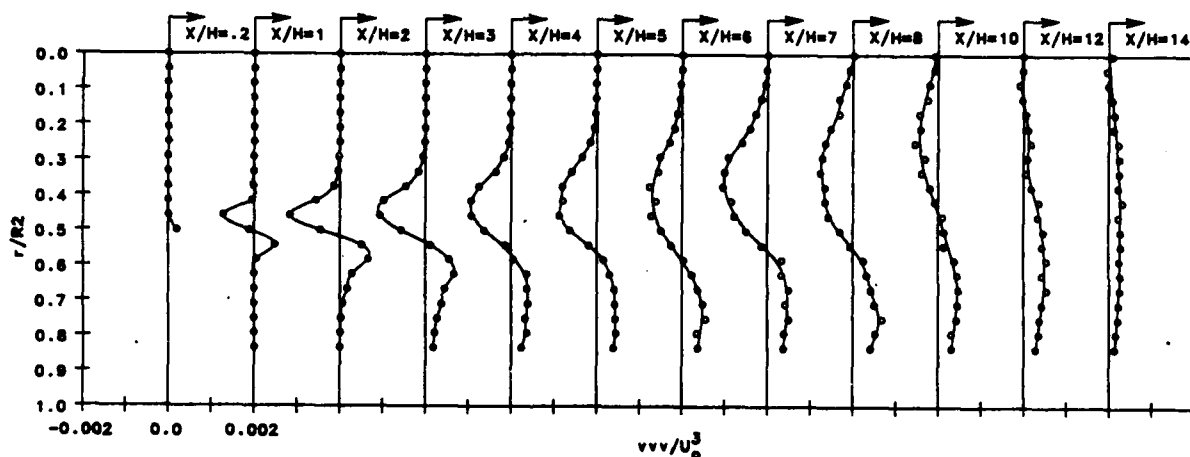


Figure 11. Normalized uvv turbulent triple-product profiles (o - measurements)

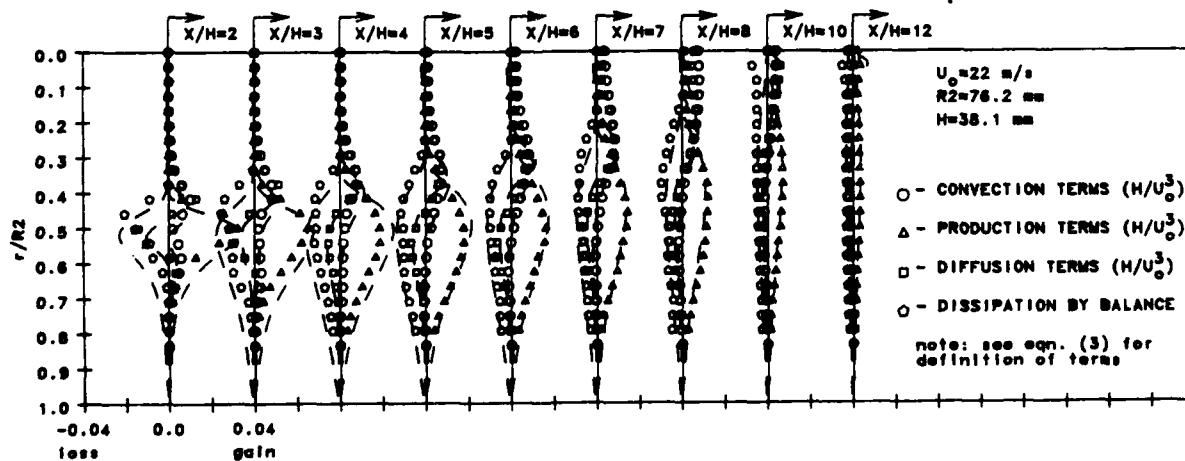


Figure 13. Normalized turbulent kinetic energy balance (symbols - measurements, --- prediction)

MEASUREMENTS OF FULLY DEVELOPED  
TURBULENT FLOW IN A TRAPEZOIDAL  
DUCT

M.M.A. Khalifa and A.C. Trupp  
Department of Mechanical Engineering  
University of Manitoba  
Winnipeg, Manitoba, Canada R3T 2N2

ABSTRACT

The turbulence characteristics of fully developed isothermal air flows through a symmetric trapezoidal duct were examined experimentally using Pitot tube and hot-wire anemometry over a Reynolds number range of  $3.7-11.6 \times 10^4$ . The measurements included local wall shear stress and the cross-sectional distributions of mean axial velocity, secondary velocities and Reynolds stresses. Four secondary flow cells were detected in a symmetric half of the duct. Although secondary velocity components were typically less than about 1% of the bulk axial velocity, their effect was especially pronounced on the distributions of turbulent kinetic energy and local wall shear stress.

SYMBOLS

a, b, c, d trapezoidal duct dimensions; see Fig. 1.  
A, B coefficients in log law (see Table 1)  
 $D_h$  equivalent hydraulic diameter  
f Darcy friction factor,  $(2D_h/\rho U_b^2)(dP/dx)$   
k turbulent kinetic energy per unit mass,  $1/2 (\bar{u}^2 + \bar{v}^2 + \bar{w}^2)$   
 $k^+$  dimensionless turbulent kinetic energy,  $k/(\bar{u}^*)^2$ .  
P static pressure  
Re Reynolds number,  $\rho U_b D_h/\mu$   
s distance along inclined wall, measured from top corner, see Fig. 1  
u, v, w fluctuating components of the velocities in the x, y, z directions

$u^+, v^+, w^+$  dimensionless turbulence intensities;  
 $\sqrt{\bar{u}^2/\bar{u}^*}, \sqrt{\bar{v}^2/\bar{u}^*}, \sqrt{\bar{w}^2/\bar{u}^*}$   
 $u^*$  local friction velocity,  $(\tau_w/\rho)^{1/2}$   
 $\bar{u}^*$  average friction velocity,  $(\bar{\tau}/\rho)^{1/2}$   
 $\bar{U}$  axial mean velocity (time-average)  
 $U_b$  average mean axial velocity  
 $U_{sec}$  resultant of  $\bar{V}$  and  $\bar{W}$ ,  $(\bar{V}^2 + \bar{W}^2)^{1/2}$   
 $U^+$  dimensionless velocity,  $\bar{U}/u^*$   
 $\bar{V}, \bar{W}$  mean velocities in the y, z directions (secondary velocities)  
x axial direction  
y, z horizontal and vertical directions, see Fig. 1  
 $z^+$  dimensionless distance from (and normal to) a wall,  $z u^*/\nu$   
z distance from wall (at  $y = 0$ ) to location of maximum axial velocity  
 $\mu$  laminar dynamic viscosity  
 $\nu$  kinematic viscosity  
 $\rho$  air density  
 $\tau_w$  local wall shear stress  
 $\bar{\tau}_w$  average of local wall shear stresses over all walls  
 $\bar{\tau}$  average wall shear stress,  $(dP/dx)(D_h/4)$   
 $\phi$  corner angle of trapezoidal duct, see Fig. 1

1. INTRODUCTION

The flow distribution, pressure drop and heat transfer characteristics of fluid flow through a straight duct of uniform cross-section depend on a number of factors especially cross-sectional shape. There are an infinite number of possible

cross-section geometries. Of these, one possibility is the circular tube which is unique in that the flow is axi-symmetric. Circular pipes have, of course, been very widely used and extensively studied over many years. For non-circular ducts, substantial thermal-hydraulic data are now available for laminar flow and heat transfer for a wide assortment of shapes, however new geometries (related to specific applications) continue to emerge for analysis. On the other hand, there is still relatively little information available for many non-circular ducts under turbulent flow conditions. Perhaps the main exception to this is for rod bundles which have continued to receive special attention because of the nuclear power industry.

Fully developed, single phase, turbulent flows through straight non-circular ducts are much more complicated than laminar flows. Apart from anisotropic turbulent diffusion, geometric asymmetries give rise to secondary flows (shallow helical streamlines) which are driven by Reynolds stress gradients. Experimental studies have been conducted on turbulent flow structure for fully developed flows through several straight non-circular ducts. These include rectangular ducts, triangular ducts, parallel-flow rod bundles, internally finned tubes, eccentric annuli, etc. The flow cross-section for each of these ducts is usually symmetric in two or more parts; each symmetric part being called a primary flow cell. Due to symmetry, there can be no net transfer of momentum or energy across the boundaries of a primary flow cell. For the same reason, secondary flows cannot cross a primary flow cell boundary.

In terms of secondary flow, non-circular ducts may be placed into three classes according to the number of secondary flow cells in each primary flow cell. These classes are:

- Class 1: 1 cell; e.g. square duct, equilateral triangular duct, eccentric annuli, infinite square rod bundle arrays, etc.
- Class 2: 2 cells; e.g. rectangular (non-square) ducts, internally finned tubes, etc.
- Class 3: 3 or more cells (multi-cells).

For Class 3 ducts, there are only two known cases where multi-cells have been confirmed experimentally.

These are the two square interconnected sub-channels by Lyall (1971) and the simulated rod bundle by Seale (1982). Other cases have been predicted numerically; e.g. an isosceles triangular duct by Rapley and Gosman (1984) and a trapezoidal duct by Nakayama et al. (1983).

Concerning trapezoidal ducts, there are an infinite number of possible cross-sections. However, for trapezoidal ducts of the symmetric type shown in Fig. 1, the shape of any family member can be specified by  $\phi$  and the ratio  $2 a/b$ . For  $\phi = 60^\circ$ , for example, the limiting cases are the equilateral triangular duct ( $a = 0$ ) and infinite parallel plates ( $b \rightarrow 0$ ). For fully developed laminar flow, theoretical results for  $fRe$  and average Nusselt number have been documented by Shah and London (1978) for  $30^\circ \leq \phi \leq 90^\circ$  and  $0 \leq 2 a/b \leq \infty$ . For fully developed turbulent flows, the only experimental data known to the authors are those due to Nikuradse (1930), Rodet (1960) and Chiranjivi and Sankara Rao (1971). In his pioneering work, Nikuradse (1930) measured pressure drop and mean velocity distribution for a trapezoidal duct characterized by  $\phi = 61^\circ$  and  $2 a/b = 1.02$ . From his velocity data, he also calculated the distribution along the duct perimeter of a parameter proportional to local wall shear stress. Thirty years later, Rodet (1960) obtained the first turbulence data for a trapezoidal duct defined by  $\phi = 75^\circ$  and  $2 a/b = 0.536$ . He measured the local wall shear stresses and the cross-sectional distributions of mean axial velocity and Reynolds stresses, however he did not attempt to measure the secondary velocities. Chiranjivi and Sankara Rao (1971) did experiments with a trapezoidal duct with  $\phi = 70^\circ$  and  $2 a/b = 0.280$ , but the measurements were confined to bulk heat transfer only.

As indicated above, little turbulence data exist for trapezoidal channels. Since a symmetric trapezoidal duct is a Class 3 geometry, accurate experimental data (including secondary flow measurements) should be extremely useful as a test case regarding development of numerical prediction schemes. This was the main motivating factor leading to the selection of the present trapezoidal duct for experimental exploration. In

addition, there is a growing interest in developing multi-passage tubes for compact heat exchangers. The symmetric trapezoidal duct is akin to the annular sector duct which is a common element in multi-passage tubes.

The actual dimensions of the cross-section of the present trapezoidal duct were (see Fig. 1)  $a = 25.4$  mm,  $b = 66.0$  mm,  $c = 63.5$  mm and  $\phi = 60^\circ$ . The equivalent hydraulic diameter of the cross-section was 71.1 mm. The geometry of the present duct ( $\phi = 60^\circ$ ,  $2 a/b = 0.770$ ) relative to those used previously is such that the ratio  $2 a/b$  for the four ducts form (roughly) the progression  $1/4$ ,  $1/2$ ,  $3/4$  and 1. In terms of actual shape, the present duct is quite different from those used by Rodet (1960) and Chiranjivi and Sankara Rao (1971), but it is fairly similar to the duct employed by Nikuradse (1930).

As indicated in Fig. 1, symmetry permits the flow cross-section to be divided along the z-axis into two parts, i.e. two primary flow cells. Accordingly, following checks to confirm flow symmetry, the measurements were confined to the right half. The measurements included axial pressure drop, the cross-sectional distributions of mean axial velocity, secondary velocities and five of the six Reynolds stresses (not  $\rho \overline{vw}$ ), and the distributions of local wall shear stress on the three walls. The main measurements were conducted at Reynolds numbers of 79,000 and 99,000 and involved both Pitot tubes and hot-wire anemometry. The purpose of this paper is simply to communicate our experimental results for fully developed turbulent isothermal air flows.

## 2. EXPERIMENTAL FACILITY AND EQUIPMENT

A complete description of the test rig, test section, traversing mechanism and instrumentation have been documented by the present authors (1985), however space allows only a few details to be given here.

The present trapezoidal duct was obtained by modifying the equilateral triangular duct used by Gerrard (1976) and by Aly et al. (1978). This triangular duct was changed to a trapezoidal cross-section by installing an isocetes fillet at

the upper vertex of the triangle. The complete test section, which consisted of a wooden entrance length (4.88 m) and a final precision acrylic section (2.44 m), was installed in a simple wind tunnel operating in the open circuit mode. Room temperature air was blown through the trapezoidal duct, and measurements were made from the discharge end of the acrylic test section. Since the measuring station (30 mm from end) was located 102 equivalent hydraulic diameters from the inlet, the flow was assumed to be fully developed.

Measurements were made on the basis of a cartesian coordinate system (see Fig. 1). Accurate relative positioning of either a Pitot tube or a hot-wire probe was achieved using a traversing mechanism having resolutions of 0.01 mm in the z-direction and 0.02 mm in the y-direction. The turbulence measurements were made using constant temperature linearized hot-wire anemometry manufactured by DISA. The miniature probes included a 55P11 single wire, a 55P61 X-probe and a 55P12 45° slanting probe. All hot-wire probes were calibrated insitu against the Pitot tube, with the probe located along the z-axis in the region of maximum axial velocity. The secondary velocity components were measured using both the X-probe and the 45° slanting probe: the latter using the rotation technique. In addition,  $\bar{V}$  was determined by the symmetry technique used by Gerrard (1976). The hot-wire data presented here have been corrected (as applicable) for tangential cooling effects as suggested by Lawn (1969). The yaw sensitivity factor was taken as 0.23 for DISA probes.

## 3. RESULTS AND DISCUSSION

### 3.1. General

As mentioned above, the measuring station was located 102 equivalent hydraulic diameters from the test section inlet, and about 30 mm from the discharge end of the trapezoidal duct. Prior to undertaking detailed measurements, the apparatus was investigated for end/blockage effects and for flow symmetry between the two halves. The latter was tested at both the mean velocity and turbulence levels and by checking the local wall shear stresses over the entire duct perimeter. The

results were satisfactory and have been documented in our internal report (1985). Detailed measurements were subsequently taken in the right half of the trapezoidal duct at several Reynolds numbers but mainly at Reynolds numbers of 79,000 and 99,000. Both Pitot tube and hot-wire measurements were made at typically about 100 locations constituting the nodes of Cartesian measurement grids. Bulk velocities for the primary flow cell were obtained by numerical integration of the mean axial velocity fields with appropriate log law shaping near the solid boundaries. Most of the experimental data presented here have been normalized by either  $U_b$  (via Pitot tube) or  $\bar{u}^*$  (via  $\partial P/\partial x$ ).

### 3.2. Friction Factors

With the wind tunnel stabilized at a fixed setting, the axial pressure distribution was determined from pressure measurements at 20 static pressure taps/piezometer rings spanning the length of the last half of the test section. For all Reynolds numbers, pressure decreased linearly with axial distance. The fully developed axial pressure gradient for each Reynolds number was determined from a straight line least-squares-fit to the data. Friction factors were then computed (using  $U_b$  via Pitot tube) to an accuracy estimated to be within 4%.

The present results are shown in Fig. 2 which also includes the experimental data of Rodet (1960) and the Nikuradse (1930) data line. The present results for isothermal friction factor were correlated by:  $f = 0.1976 (Re)^{-0.21}$ . Relative to pipe flow, the present data lie typically about 8% below the standard correlation shown in Fig. 2 for circular pipe. This deviation, as is the case for many other non-circular ducts, reflects a long-recognized deficiency in the equivalent hydraulic diameter approach.

Fig. 2 also shows the prediction of Malak et al. (1975) for the present duct and Rodet's duct. The present results generally fall slightly below the line of Malak et al. by an average of about 2 1/2% which is within the experimental accuracy.

\* This outcome stems from the fact that the  $fRe$  products for the three ducts are almost equal under fully developed laminar flow conditions.

According to Malak et al., friction factors for the present duct and for Rodet's duct fall within 2% of each other, whereas Nikuradse's duct lies between the two\*. As shown in Fig. 2, Rodet's data are in good agreement with the prediction of Malak et al. This, in turn, explains the good consistency between the present data and that of Rodet, despite substantial differences in duct cross-sectional shape. On the other hand, the data of Nikuradse (1930) is noticeably above the prediction of Malak et al., but only at the lower Reynolds numbers. Overall, the present results appear to be consistent with expectations and with the limited experimental data for other trapezoidal ducts.

### 3.3. Secondary Flow

The secondary flow results are presented next so that interpretation of the remaining results may benefit from a secondary flow perspective. Some of the data are shown in Figs. 3-5 inclusive. The data have been normalized by the average mean axial velocity,  $U_b$ . Like other secondary flow geometries, the present data seem to scale reasonably on either  $U_b$  or  $\bar{u}^*$ . As shown in our internal report (1985), the distributions of  $\bar{V}/U_b$  and  $\bar{W}/U_b$  via X-probe showed good consistency at the two main Reynolds numbers of 79,000 and 99,000.

Fig. 3 shows the z-direction component ( $\bar{W}$ ) of the secondary flow for three horizontal traverses. For the traverse at  $z/b = 0.182$ , for example, the data shows an upflow near the duct symmetry line, a downflow in the mid-span region and a second upflow near the inclined wall. As drawn, the line faired through the data does not strictly satisfy conservation of mass. To comply with continuity, the zero position would have to be lowered to about -0.2%, or (alternatively)  $\bar{W}/U_b$  must reach about 3% adjacent to the inclined wall. Otherwise, considering the small quantities being measured, the agreement between the 45° slanting probe and the X-probe is quite reasonable except near the inclined wall where the X-probe consistently gave lower values. This is likely due to error induced on the separated wires by the steep axial velocity gradients near the wall.

Axial velocity gradient errors associated

with the X-probe can also be seen in Fig. 4 which shows the  $\bar{V}/U_b$  distributions for three vertical traverses each with three sets of measurements. The X-probe generally registered too high near the top wall and too low near the bottom wall. Again, the faired lines do not completely satisfy continuity as drawn, however near-wall secondary flows may be under-estimated. Overall, the three data sets show considerable scatter, but there is general agreement in trend.

Fig. 5 shows the resultant secondary flow ( $U_{sec}$ ) in the primary flow cell cross-section at  $Re = 99,000$ . The construction is based on  $\bar{V}$  and  $\bar{W}$  via the  $45^\circ$  slanting probe using the rotation technique for each component. Each arrow indicates the magnitude (see scale) and direction; location corresponds to the center of the arrow. Four counter-rotating cells of secondary flow can be seen with the pattern shown in the inset to Fig. 5. This pattern is precisely that inferred by Nikuradse (1930) based on the distortions seen in his measured axial velocity distribution. Flow from the highest axial momentum region (maximum  $\bar{U}$ ; located at  $y = 0, z/b = 0.48$ ) is convected into each corner where it splits for the return flow. For the flow into the  $60^\circ$  corner, the largest observed secondary velocity was about 1.6% of  $U_b$ . The global maximum was indicated to be just under 2.2% of  $U_b$  and this was located adjacent to the inclined wall. Compared to other Class 3 geometries, this maximum value is a little larger than that found by Seale (1982) for a simulated rod bundle (about 1 1/2% of  $U_b$ ), but smaller than that determined by Lyall (1971) for two square interconnected sub-channels (about 3 1/2% of the local axial velocity).

### 3.4. Mean Axial Velocity

Mean axial velocities ( $\bar{U}$ ) were measured using both Pitot tube and hot-wire anemometry to within estimated accuracies of about 1% and 2% respectively. No corrections were made for velocity gradient or turbulence effects, however the wall proximity correction suggested by Ower and Pankhurst (1966) was applied for the Pitot tube. For the same nominal mass flow rate through the duct, the bulk velocity ( $U_b$ ) for the Pitot tube

transverse was found to be generally about 2% higher than the  $U_b$  value for the single hot-wire probe traverse. But as shown in Fig. 6, when each is normalized by its own  $U_b$ , the distributions of  $\bar{U}/U_b$  were very similar. Also whereas Fig. 6 is for  $Re = 99,000$ , isovel plots of  $\bar{U}/U_b$  for other mass flow rates were found to be essentially independent of Reynolds number. There was, however, a slight tendency for the profiles to become flatter with increasing Reynolds number. For example, for  $Re=79,000$  the maximum  $\bar{U}/U_b$  value was about 1.22 and this value decreased slightly to about 1.21 for  $Re = 99,000$ .

A close examination of Fig. 6 shows some bulging of the contours towards the corners and away from the horizontal walls in the mid-wall regions. The latter is particularly noticeable for the top wall. These distortions are caused by secondary flows in the pattern shown in Fig. 5. Similar distortions were present for the trapezoidal ducts of Nikuradse (1930) and Rodet (1960). In fact, the isovels for Rodet's duct also show bulging to reflect the return flow off the inclined wall. Evidence of this for the present duct is shown later in the distributions of wall shear stress and turbulent kinetic energy.

In addition to velocity measurements at various grid points throughout the domain, special Pitot tube traverse were made normal to each wall in the near-wall regions for the purpose of obtaining data to compare to the universal log law distribution. These results are summarized in Table 1 and illustrated in Fig. 7. As can be seen, logarithmic velocity distributions do indeed exist and the least-squares-fit coefficients do not differ much from the conventional values. Hence if one excludes the immediate corner regions (where the flow is influenced by the presence of both walls) and providing scaling is done with the local friction velocity, then it appears that the universal law of the wall holds reasonable for the near-wall regions for the present Class 3 geometry.

### 3.5. Local Wall Shear Stress

Local wall shear stresses ( $\tau_w$ ) were measured along all three walls by the Preston technique

using the appropriate relation of Patel (1965). For each Reynolds number, the overall average wall shear stress ( $\bar{\tau}_w$ ) was determined by numerical integration (over all walls) of the measured values of the axial component of local wall shear stress. The  $\bar{\tau}_w$  values derived in this manner via Preston tube were found to be within 3% of the duct average values ( $\bar{\tau}$ ) corresponding to the measured axial pressure gradients.

The distributions of local wall shear stress (normalized by  $\bar{\tau}_w$ ) are shown in Fig. 8 for two Reynolds numbers. The data for both Reynolds numbers form essentially a single distribution. From the data for each Reynolds number, separate averages were calculated for each wall. The average wall shear stress for the top wall was about 12% higher than the overall average, whereas the bottom wall and the inclined wall were about 1 1/2% and 3% lower than  $\bar{\tau}_w$  respectively. A similar deviation for the top wall was present in the results of Nikuradse (1930) whose duct, as noted earlier, was quite similar to the present trapezoidal duct. The average wall shear stress for his top wall was about 10% above the overall average while his bottom wall and inclined wall were about 2% and 4% lower than the overall average respectively. On the other hand, the average for each of the three walls of the duct of Rodet (1960) was approximately equal to the overall average. This outcome is in keeping with one of the roles of secondary flow, namely, to tend to equalize the wall shear stress around the entire duct perimeter. It is not known why this was not achieved for the present duct (and also for Nikuradse's duct), but it may be related to aspect ratio. In any event, Fig. 8 does contain evidence of secondary flow effect. In particular, attention is drawn to the small dip in the distribution of  $\tau/\bar{\tau}_w$  for the inclined wall at  $s/d = 0.4$  which is about where the returning secondary flow leaves this wall.

### 3.6. Reynolds Stresses

Space permits only a few samples to be given from a rather large set of experimental data. The data presented here are for  $Re = 99,000$ . As shown in our internal report (1985), scaling by  $\bar{u}^*$

renders the data fairly independent of Reynolds number.

In Fig. 9, the data for the Reynolds normal stresses which were obtained from traverses along the duct symmetry line, are presented and compared to the results of corresponding traverses for circular pipe [Laufer (1954)], square duct [Brundrett and Baines (1964)] and equilateral triangular duct [Aly (1977)]. The distributions for the present data lie between the square duct and pipe flow and (not surprisingly) are very similar to the results for the equilateral triangular duct. In general, the present turbulence intensities exceed their counterparts for pipe flow by roughly about 15%. Part of this may be attributable to the fact that the local friction velocities for each end of the symmetry line are 4 to 5% higher than the duct average friction velocity (see Fig. 8). The remainder may partly be due to the secondary flow which moves fluid from each wall towards the central region. highly turbulent fluid which has been generated near the wall, is convected towards the central region thus causing turbulence intensities at a given location to be higher than would otherwise be.

Fig. 10 shows the distributions of turbulence intensities along three selected horizontal traverses. For a given location, as would be expected,  $\sqrt{\bar{u}^2/\bar{u}^*}$  (axial) is generally larger than  $\sqrt{\bar{v}^2/\bar{u}^*}$  (parallel to top and bottom walls) and  $\sqrt{\bar{w}^2/\bar{u}^*}$  (normal to top and bottom walls). In the region of maximum axial velocity, the turbulence intensities reach their lowest level and are almost equal. For  $z/b = 0.5$ , as the traverse moves from the core region, the turbulence levels increase monotonically to attain high values adjacent to the inclined wall. This pattern is fairly standard. The patterns for both  $z/b = 0.124$  and  $0.875$ , however, are more complicated and have been influenced by secondary flow. Although each traverse is exactly parallel to a horizontal wall, at  $y/c = 0$  turbulence levels are relatively high because of the secondary flow from the wall to the core region. As  $y/c$  increases, the turbulence intensities decrease (rather than

hold constant) and then bottom-out corresponding to where the secondary flow moves into the corner, having brought low turbulent fluid from the core region. As these traverses finally approach the inclined wall, the normal stress distributions consistently register an increasing trend entering the high turbulence production zone near the inclined wall.

The contour plots for the Reynolds normal stresses were qualitatively similar to that for the turbulent kinetic energy ( $k$ ) which is shown in Fig. 11 for two Reynolds numbers. Clear indications of the secondary flow pattern can be seen from the strong distortions of the contours towards the corners of the trapezoidal duct. The results shown in Fig. 11 are qualitatively similar to those obtained by Rodet (1960) for his duct.

Relationships between the turbulence intensities of the type described by Alshamani (1978, 1979) were also explored. The results, based on both local and average friction velocities, will be described in detail by Khalifa (1986). For now, Fig. 12 gives a sample result. Each least-squares-fit equation shown in this figure is capable of describing the data with a standard deviation of about 4% (or less) of the range average. The coefficients for each linear equation are fairly similar to the corresponding results found by Seale (1982) for a simulated rod bundle. This similarity for two Class 3 geometries implies that the vorticity source model of Seale (1982) may be capable of handling other Class 3 geometries.

Turning next to the Reynolds shear stresses, Fig. 13 shows the contours of  $\overline{uv}$  and  $\overline{uw}$  in the primary flow cell. No data were gathered for  $\overline{pvw}$ , however this shear stress is known from theory to be zero along the symmetry line ( $y/c = 0$ ) and is expected elsewhere to be small. The shear stress  $\overline{puv}$  was also found to be essentially zero along the symmetry line. This agrees with the theoretical conclusion that  $\overline{puv}$  acting on the  $xz$  plane at  $y/c = 0$ , must be zero since  $\overline{uv}/(\overline{u^*})^2$  (like  $\overline{V}$ ) has an antisymmetric distribution on each side of the symmetry plane. The contour map for each shear stress contains both positive and negative

regions. For  $\overline{uw}$ , the split is roughly top-bottom whereas for  $\overline{uv}$ , it is left-right. Attention is also drawn to evidence of secondary flow. In particular, for  $\overline{uw}$  there are bulges towards the top corner, while for  $\overline{uv}$  there are bulges adjacent to the inclined wall in the return flow region.

For fluid in the central region or adjacent to the top or bottom wall,  $\overline{puw}$  is the primary shear stress. As expected, along the duct symmetry line ( $y/c = 0$ ), this normalized shear stress varies (see Fig. 13) monotonically from roughly -1 to +1. For fluid adjacent to the inclined wall, the primary shear stress on a surface parallel to this wall would be a mixture of  $\overline{puv}$  and  $\overline{puw}$ . Contour values shown in Fig. 13 of  $\overline{uv}/(\overline{u^*})^2$  of about 0.7 and  $\overline{uw}/(\overline{u^*})^2$  of about 0.3, are consistent with this expectation.

Further information on  $\overline{uw}$  is given by Fig. 14 which shows the distribution of  $\overline{uw}/(\overline{u^*})^2$  along three vertical traverses. One of these is the duct symmetry line ( $y/c = 0$ ) over which the variation is slightly non-linear and ranges from about -1.1 to 0.8. A linear variation from -1 to +1 is, of course, characteristic along a diameter of fully developed pipe flow. For non-circular ducts, departures from linearity along a symmetry line are not uncommon and dimensionless magnitudes may readily exceed unity (e.g. square duct). Departures here from unity and from linearity are due to both secondary flow and to the  $\overline{uv}$  distribution (Fig. 13). Along the duct symmetry line, the axial momentum equation become (neglecting the viscous term):

$$\overline{w} \frac{\partial \overline{U}}{\partial z} = -\frac{1}{\rho} \frac{\partial p}{\partial x} + \frac{\partial \overline{uv}}{\partial y} + \frac{\partial \overline{uw}}{\partial z}$$

where the pressure gradient term is a constant for fully developed flow. Hence the gradient of  $\overline{uw}$  along the symmetry line, depends on the modifications to this pressure gradient constant by the local values of  $\overline{w} \partial \overline{U} / \partial z$  and  $\partial \overline{uv} / \partial y$ . Concerning the latter, although  $\overline{uv}$  is zero along the symmetry line,  $\partial \overline{uv} / \partial y$  is non-zero since  $\overline{uv}$  has an antisymm-

metric distribution about the symmetry line. Based on Fig. 13, peak values for  $uv/(\bar{u}^*)^2$  are about -0.5 near the top wall but only about -0.14 near the bottom wall. Hence along  $y/c = 0$ ,  $\partial uv/\partial y$  values are likely to be quite different for these two regions. On the other hand, based on the known secondary flow pattern, the term  $\bar{w} \partial \bar{u}/\partial z$  has a single polarity and should be of about the same magnitude for points equidistant from each wall. Hence it appears that the  $uv$  distribution exerts the asymmetric effect on  $uw$  along the  $z$ -direction.

#### 4. CONCLUDING REMARKS

An experimental investigation was made of the flow structure of fully developed isothermal air flow through a  $60^\circ$  acute angle symmetric trapezoidal duct with aspect ratio  $2 a/b = 0.770$ . This research revealed the following key features:

- a) Within each symmetric half of the duct, there exists four counter-rotating cells of secondary flow with secondary velocity components typically less than about 1% of the bulk axial velocity. This secondary flow pattern exerts a very significant influence on the distributions of turbulent kinetic energy and local wall shear stress and is expected to influence heat transfer.
- b) Near-wall axial velocity distributions are logarithmic with conventional coefficients when scaling is done with local friction velocity. Turbulence intensities are interrelated linearly with coefficients similar to those found by Seale (1982) for another Class 3 geometry. Both of these facts are relevant to turbulence modelling for non-circular ducts.

#### ACKNOWLEDGEMENT

The authors gratefully acknowledge the support provided for this research by the Natural Sciences and Engineering Research Council Canada.

#### REFERENCES

- Alshamani, K.M.M. 1978: Correlations Among Turbulent Shear Stress, Turbulent Kinetic Energy and Axial Turbulent Intensity, AIAA J. 16, No. 8, pp. 859-861.
- Alshamani, K.M.M. 1979: Relationships Between Turbulent Intensities in Turbulent Pipe and Channel Flow, Aero. J. 83, pp. 159-161.

- Aly, A.M.M. 1977: Turbulent Flows in Equilateral Triangular Ducts and Rod Bundle Sub-Channels, Ph.D. Thesis, University of Manitoba.
- Aly, A.M.M.; Trupp, A.C.; Gerrard, A.D. 1978: Measurements and Predictions of Fully Developed Turbulent Flow in an Equilateral Triangular Duct, J. Fluid Mech. 85, pp. 57-83.
- Brundrett, E.; Baines, W.D. 1964: The Production and Diffusion of Vorticity in duct Flow, J. Fluid Mech. 19, pp. 375-394.
- Chiranjivi, C.; Sankara Rao, P.S. 1971: Laminar and Turbulent Forced Convection Heat Transfer in a Symmetric Trapezoidal Channel, Ind. J. Technology 9, pp. 416-420.
- Gerrard, A.D. 1976: Turbulent Flow in an Equilateral Triangular Duct, M.Sc. Thesis, University of Manitoba.
- Khalifa, M.M.A.; Trupp, A.C. 1985: Turbulent Flow Characteristics in a Trapezoidal Duct-Experimental Results, Dept. of Mech. Eng., University of Manitoba Report No. ER 25-39.
- Khalifa, M.M.A. 1986: Measurements and Predictions of Turbulent Flow and Heat Transfer in Trapezoidal Ducts, Ph.D. Thesis (In Preparation), University of Manitoba.
- Laufer, J. 1954: The Structure of Turbulence in Fully Developed Pipe Flows, NACA Report TN 1174.
- Lawn, C.J. 1969: Turbulent Measurements with Hot Wires at B.N.L., Central Elec. Gen. Board, Berkeley Nuclear Labs. Rep. RD/B/M 1277.
- Lyall, H.G. 1971: Measurements of Flow Distribution and Secondary Flow in Ducts Composed of Two Square Interconnected Sub-Channels, Symposium on Internal Flows, University of Salford, Apr. 20-22, 1971, pp. E16-E23.
- Malak, J.; Hejna, J.; Schmid, J. 1975: Pressure Losses and Heat Transfer in Non-Circular Channels with Hydraulically Smooth Walls, Int. J. Heat Mass Transfer, 18, pp. 139-149.
- Nakayama, A.; Chow, W.L.; Sharma, D. 1983: Calculation of Fully Developed Turbulent Flows in Ducts of Arbitrary Cross-section, J. Fluid Mech. 128, pp. 199-217.
- Nikuradse, J. 1930: Turbulent Stromung in nicht kreisförmigen Röhren, Ing.-Arch-1, pp. 306-332.
- Ower, E.; Pankhurst, R.C. 1966: The Measurement of Air Flow, 4th Ed. Pergamon, Oxford.
- Patel, V.C. 1965: Calibration of the Preston Tube and Limitations on Its use in Pressure Gradients, J. Fluid Mech., 25, pp. 185-208.
- Rapley, C.W.; Gosman, A.D. 1984: The Prediction of Turbulent Flow and Heat Transfer in a Narrow Isosceles Triangular Duct, Int. J. Heat Mass Transfer, 27, pp. 253-262.
- Rodet, E. 1960: Etude De L'écoulement D'un Fluide Dans Un Tunnel Prismatique De Section Trapezoidale, Publ. Sci et Tech. du Min. de l'Air, No. 369.
- Seale, W.J. 1982: Measurements and Predictions of Fully Developed Turbulent Flow in a Simulated Rod Bundle, J. Fluid Mech. 123, pp. 399-423.
- Shah, R.K.; London, A.L. 1978: Laminar Flow Forced Convection in Ducts, Advances in Heat Transfer, Supplement 1, Academic Press.

Table 1

Near-wall Velocity Distributions (Re=99,000)

Form:  $U^+ = A \ln z^+ + B$

Wall:	Top	Inclined	Bottom
A	2.25	2.36	2.26
B	6.32	6.34	6.48
Max. $z^+$ in range	700	700	400
No. of data points	66	37	60
No. of Traverses	3	3	4
Std. Dev. (%): (Measured vs LSF $U^+$ ; expressed as a percentage of the average $U^+$ in the range)	2.08	2.56	0.88

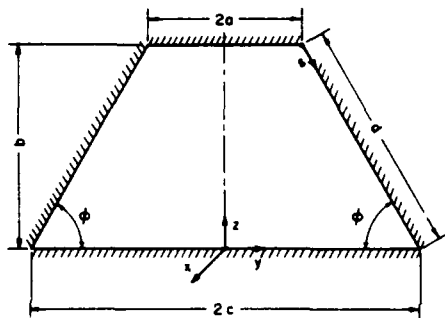


Fig. 1: Trapezoidal Duct and Coordinate System

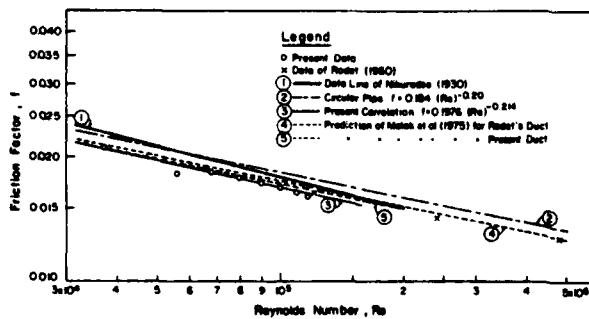


Fig. 2: Friction Factor versus Reynolds Number

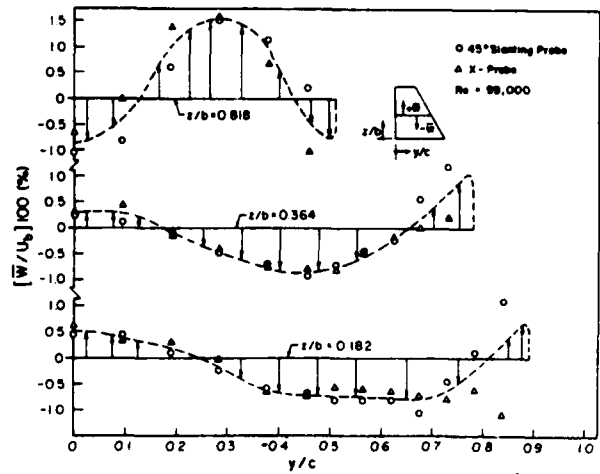


Fig. 3: Distribution of  $\bar{W}$  for Three Horizontal Traverses;  $Re = 99,000$ .

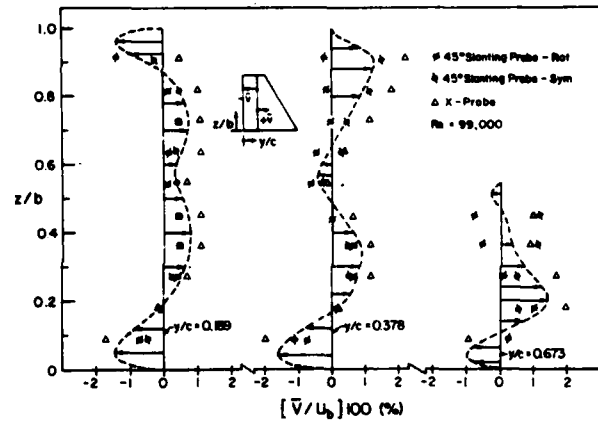


Fig. 4: Distributions of  $\bar{V}$  for Three Vertical Traverses;  $Re = 99,000$

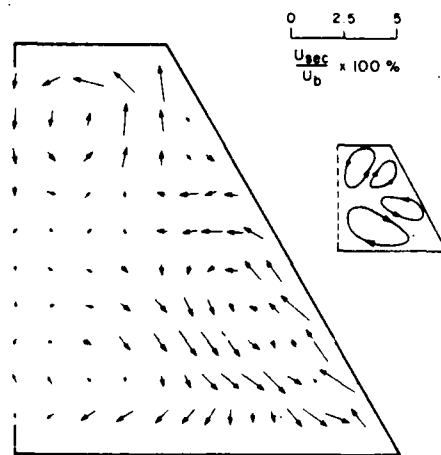


Fig. 5: Secondary Flow in a Trapezoidal Duct;  $Re = 99,000$ .

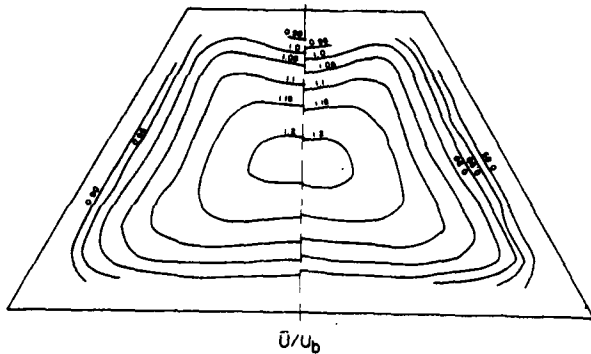


Fig. 6: Contours of Axial Velocity;  
 $R_e = 99,000$ . Right: Data via Hot-wire  
 Left: Data via Pitot-tube

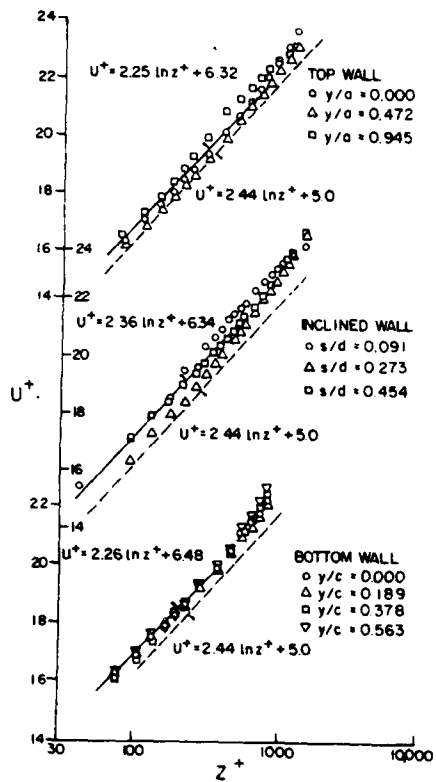


Fig. 7: Near-Wall Velocity Distributions;  
 $R_e = 99,000$ .

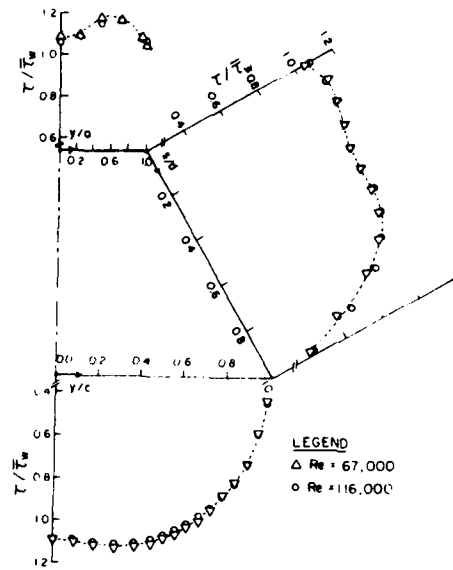


Fig. 8: Local Wall Shear Stress Distributions

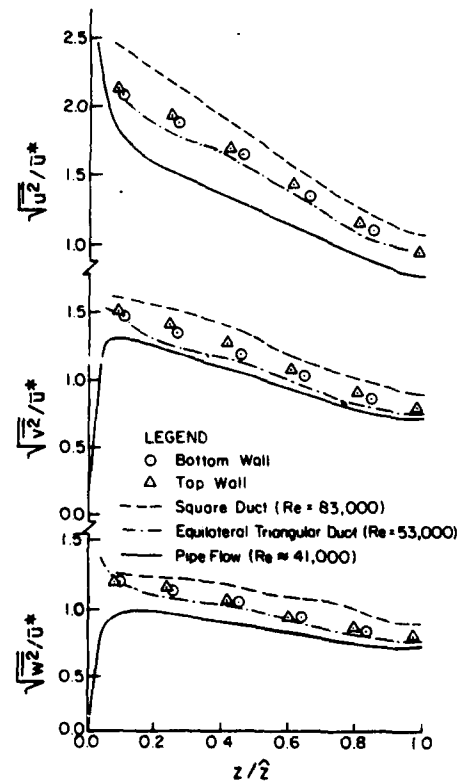


Fig. 9: Distribution of Reynolds Normal Stresses Along Duct Symmetry Line ( $y = 0$ );  $R_e = 99,000$ .

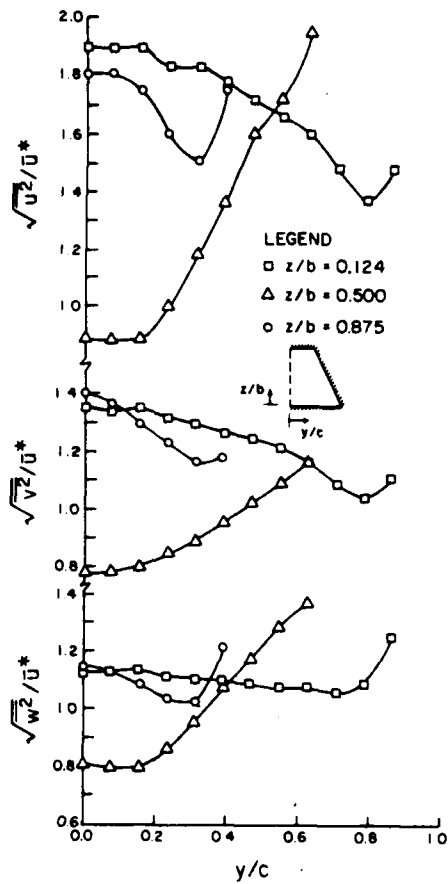


Fig. 10: Distribution of Reynolds Normal Stresses Along Horizontal Traverses;  $R_e = 99,000$ .

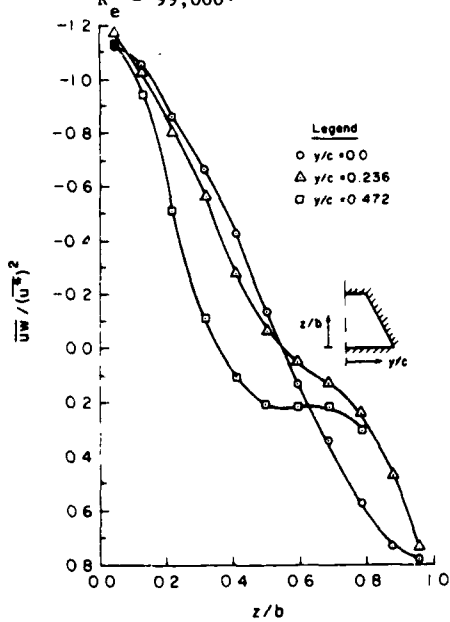


Fig. 14: Distribution of Shear Stress  $\overline{\rho u w}$ ;  $R_e = 99,000$ .

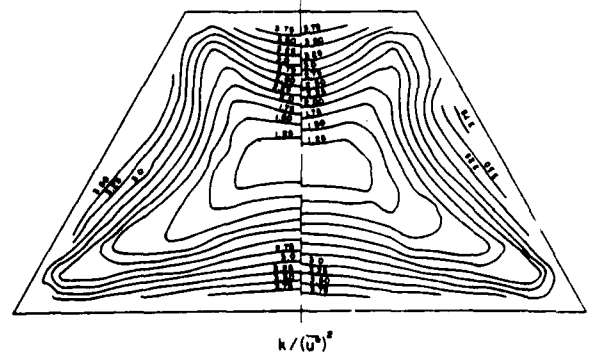


Fig. 11: Contours of Turbulent Kinetic Energy  
Right:  $R_e = 99,000$ .  
Left:  $R_e = 79,000$ .

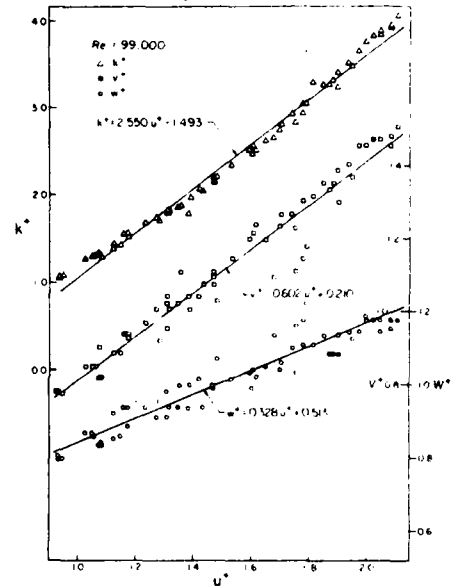


Fig. 12: Relationships Between  $u^+$  and  $k^+, v^+$  and  $w^+$  for the Rectangular Domain:  $0 \leq y/a \leq 1, 0 \leq z/b \leq 1; R_e = 99,000$ .

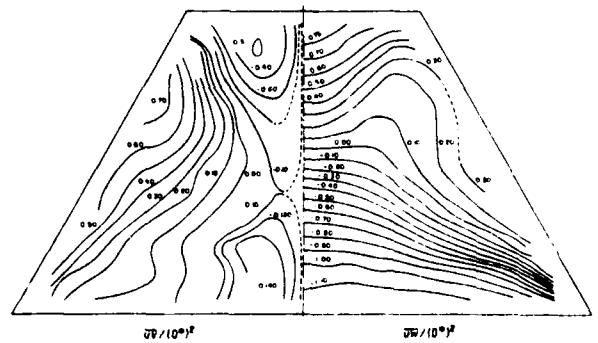


Fig. 13: Reynolds Shear Stress Contours;  $R_e = 99,000$ .

## EXPERIMENTAL AND COMPUTATIONAL STUDIES OF PLANE MIXING LAYERS

R. D. Mehta\*, O. Inoue†,  
L.S. King† and J.H. Bell\*

\* Stanford University, Ca

† NASA Ames Research Center, Ca

**Abstract.** Some experimental and computational studies of forced and unforced plane turbulent mixing layers have been completed. The experimental results include flow-visualization data using the smoke-laser technique and mean flow and turbulence measurements using X-wires and a two-component Laser-Doppler Velocimeter (LDV). Two computational studies of the measured mixing layers have been conducted in a coordinated effort: one using the discrete vortex method and the other based on Reynolds averaged Navier-Stokes equations. The present paper contains an overall comparison and discussion of the measured and computed results.

### 1. INTRODUCTION

Turbulent mixing layers are often found to dominate the flow field in engineering applications. Apart from governing the rate of mixing in combustion chambers and flow reactors, mixing layers are also responsible for most of the broad-band noise generated in propulsion systems. Furthermore, mixing layers exhibit certain universal flow features that have made them very attractive for experimental and computational studies.

Experimental investigations of mixing layers were revived when Brown and Roshko (1974) performed flow visualization studies of a plane mixing layer and reported the presence of large, quasi-two-dimensional vortical structures. Most of the subsequent studies concentrated on the search and identification of these large scale structures (see Ho and Huerre, 1984 for a review). Apart from spectacular flow visualizations, mixing layers are also well suited for probe-type measurements since spatial problems are reduced due to the absence of bounding walls and the fast growth rate of the layer compared to other shear flows (Mehta and Westphal, 1986). For computational studies, mesh specification is simpler in general, again due to the absence of bounding walls. In addition, mixing layers are thought to be more sensitive to the modeling of turbulence than boundary layers (Rodi, 1975), thus making them more suitable for the development and testing of new turbulence models. The plane mixing layer is also popular because the asymptotic behavior of this flow is thought to be quite simple in the-

ory. Townsend (1976) shows that the governing equations and boundary conditions for the plane turbulent mixing layer can yield "self-preserving" solutions for sufficiently high Reynolds number and downstream distance. The necessary conditions for self-preservation are that the mixing layer grows linearly and that the shapes of the mean velocity and turbulence profiles are independent of downstream distance when scaled by local mixing layer thickness. In particular, peak values of the turbulence stresses should be independent of streamwise position.

The formation of the two-dimensional vortex structure is primarily due to the inviscid Kelvin-Helmholtz instability operating on the vorticity distribution across the mixing layer. The layer grows through pairing of adjacent spanwise vortices. The pairing process is random in space and time and this results in a linear, continuous growth of the mixing layer. However, the onset of the initial instability, the position of the merging processes, and the number of vortices involved in the merging are extremely sensitive to small perturbations anywhere in the flow field (Ho and Huang, 1982). In particular, small oscillations in a direction normal to the free stream and at frequencies even an order of magnitude lower than the initial instability frequency are found to affect the growth rate and turbulence structure of the mixing layer significantly (Oster and Wignanski, 1982).

The main objective of the present research was to study plane turbulent mixing layers with and without forcing at the mixing layer origin using two experimental techniques and two computational approaches. In particular, the aim was to assess the performance of these techniques in this type of shear flow by comparing the results and identifying possible problems in the individual approaches.

### 2. EXPERIMENTAL AND COMPUTATIONAL TECHNIQUES

#### 2.1 Experimental Techniques

A 38 X 15 cm open-circuit blower wind tunnel (Fig. 1) located in the Fluid Mechanics Laboratory at Ames Research Center was used for the experiments. The two-stream mixing layer was generated by installing a sheet of dense foam over the upper half of the last screen and dividing the flow in the contraction with a 1.5 mm thick splitter plate. This arrangement produced two streams with a velocity ratio of about 0.5. Both ends of the splitter plate were tapered to zero thickness, the upstream end to minimize disturbance and the downstream end to minimize wake effects in the two-stream layer. For the tripped cases, round wire trips (1.0 and 1.5 mm diameter) were attached at the entry to the constant-area exit duct. This provided a region for boundary layer development at nearly zero pressure gradient prior to the formation of the mixing layers. For the forced mixing layer experiments, a hinged flap (1 cm long) was attached to the downstream end of the splitter plate and driven from one end using a linear oscillator. Excitation frequencies of up to 100 Hz and amplitudes of up to 2 mm could be achieved with this mechanism.

The mixing layer exhausted into the still laboratory air where the measurements were made. The absence of a test section around the mixing layer was previously shown to have negligible effect in the measurement region,  $0 < x < 30$  cm (Mehta and Westphal, 1986). The free-stream velocity on the high speed side was about 21 m/s with a turbulence level of 0.2% at the duct exit. The forced mixing layer measurements were made at lower speeds; high speed side velocity was set at 10 m/s.

The smoke flow visualization study was conducted by injecting heated mineral oil smoke on the splitter plate just downstream of the last screen. Cuts in the  $x$ - $y$  plane through the seeded mixing layer were illuminated by projecting a thin ( $\sim 2$  mm) laser sheet through a cylindrical lens.

Hot-wire measurements were made using X-wire probes with  $5 \mu\text{m}$  Tungsten sensing elements about 1 mm long welded to the supports; the spacing between the wires was also about 1 mm. The probes were calibrated statically in the potential core of the high-speed duct exit flow assuming a 'cosine-law' response to yaw, with the effective angle determined by calibration. The analog signals were filtered (low pass at 25 KHz), DC offset, and amplified ( $\times 10$ ) before being fed into a NASA-built computer interface. The interface contained a fast sample-and-hold A/D converter with 12 bit resolution and a multiplexer for connection with another interface to an HP 9845 computer (Westphal and Mehta, 1983). The software included a correction for ambient temperature drift.

Mean velocity and turbulence measurements were also made with a three-component laser velocimeter system (Rodman et al., 1985), used in the two-component mode for the present studies. The system utilized two wavelengths (0.488 and 0.5145  $\mu\text{m}$ ) from an argon-ion laser. Bragg cell frequency shifting (40 MHz) was introduced in both lines to enable directional discrimination and to reduce fringe bias. The orthogonal four-beam matrix with a beam separation of 1.3 cm was focused into the flow field through a 38 cm focal length lens. Scattered light was collected in the off-axis forward scatter mode. An effective sensing volume was formed by the focused laser beams and the off-axis collection optics that was approximately 200  $\mu\text{m}$  in diameter and 1.5 mm long. The signals from the photomultiplier tubes were mixed electronically with sine waves of known frequency, fed into single particle burst counters for processing and then multiplexed to the HP 9845 computer via a NASA-built LDV interface. The flow was seeded by injecting 1  $\mu\text{m}$  diameter (measured) mineral oil smoke particles at the blower inlet.

## 2.2 Computational Techniques

For the two-dimensional discrete vortex method, let us consider an unbounded flow produced by an infinite row of discrete vortices with the same sign and the same strength which are moving along the  $x$ -axis with a constant velocity. Let the circulation of each vortex be denoted by  $\Gamma$ , the fixed distance between the two neighboring vortices by  $l$ ,

the constant velocity of the vortices by  $U_c$ , and the higher- and lower-speed velocities of the flow far from the  $x$ -axis by  $U_1$  and  $U_2$ , respectively. Then the following relations are satisfied:

$$\Gamma = \Delta U l, \quad \Delta U = U_1 - U_2, \quad U_c = (U_1 + U_2)/2 \quad (1)$$

Next, let us suppose that at an initial time,  $t = 0$ , vortices in the "test section" ( $x > 0$ ) are suddenly removed. At all subsequent times the vortices upstream of the test section ( $x < 0$ ) are constrained to move along the  $x$ -axis with the convection velocity  $U_c$ . Once it enters the test section, each vortex is free to move under the influence of the potential field induced by individual vortices including the upstream ( $x < 0$ ) vortices, in addition to the contribution of the convection velocity. Our main interest lies in the motion of the discrete vortices in the test section. In order to prevent excessive bending of the mixing layer towards the low-speed side, upper and lower walls were simulated by two rows of vortices. These vortices have circulation  $\Gamma/2$  and are located at the image positions with respect to the upper and the lower walls. Note that the strength of these vortices is prescribed such that total circulation of the flow field is zero. The complex velocity potential,  $f$ , which governs the flow development for  $N$  vortices, is given by:

$$f = U_c z - i \sum_{n=1}^N \frac{\Gamma}{2\pi} \log(z - z_n) - i \sum_{n=1}^N \frac{\Gamma}{4\pi} \log(z - z_{u,n}) - i \sum_{n=1}^N \frac{\Gamma}{4\pi} \log(z - z_{l,n}) \quad (2)$$

where  $z = x + iy$ , and the subscripts  $u$  and  $l$  denote the upper- and lower-image vortices, respectively. The velocity components  $u$  in the  $x$ -direction and  $v$  in the  $y$ -direction are given by:

$$u - iv = \frac{\partial f}{\partial z} \quad (3)$$

The time development of an individual vortex is determined from the relation:

$$\frac{dx_n}{dt} = u_n, \quad \frac{dy_n}{dt} = v_n \quad (4)$$

In cases where forcing is applied, each new discrete vortex that arrives at the origin (entry to the test section) is assigned the velocity,  $u = U_c$ ,  $v = v_f(t)$ , in addition to the velocity induced by individual discrete vortices. Periodic disturbances of the form,  $v_f(t) = A \sin(2\pi ft)$ , are assumed. In this simulation a first-order Euler scheme is employed for time integration. A detailed account of the method is given in Inoue and Leonard (1986). While this inviscid vortex method is suitable for studying the far-field behavior (in the self-similar region) of both forced and unforced mixing layers, in its present form, where only one sign of vorticity is shed, it cannot be used to simulate the near-field development which includes the viscous wake from the splitter plate.

In order to compute the near-field development of the mixing layer, starting with the boundary layers on the splitter plate, a second two-dimensional computational approach was developed which involved solving the Reynolds averaged Navier-Stokes equations for an incompressible, constant-density fluid. Since the experimental results used in the present comparisons were obtained for mixing layers in which the static pressure was essentially constant, the pressure-gradient terms in the Navier-Stokes equations was neglected. Also, viscous stress terms are assumed small, except for the transverse shear  $\nu \partial u / \partial y$ . The steady two-dimensional, incompressible, constant-density Navier-Stokes equations may thus be simplified to a system parabolic in the streamwise direction,  $x$ .

$$\frac{\partial u}{\partial x} - \frac{\partial v}{\partial y} = 0 \quad (5)$$

$$u \frac{\partial u}{\partial x} + v \frac{\partial u}{\partial y} = \frac{\partial}{\partial y} \left( \nu \frac{\partial u}{\partial y} \right) \quad (6)$$

These equations are solved both on the splitter plate and in the mixing region downstream of the plate. The velocity defect arising from the confluent boundary layers is convected into the mixing-layer region. In contrast, most mixing-layer analyses have been derived based on the assumption of self-similarity, for which no account may be taken of the viscous layers on the plate.

Finite-difference forms of eqns. 5 and 6 are solved on a rectangular mesh with variable spacing in both directions, in order to concentrate mesh points near the splitter plate trailing edge and in the mixing layer itself. The solution is advanced in the streamwise direction using a Crank-Nicholson scheme centered at half-integer points for the momentum equation. The continuity equation is then enforced at integer points. For  $\nu = \text{const}$ , the difference form of the nondimensional momentum equation is

$$\bar{u}_{i,j} \frac{u_{i,j}^n - u_{i-1,j}}{x_i - x_{i-1}} - \frac{1}{2} \bar{v}_{i,j} \left[ \left( \frac{\partial u}{\partial y} \right)_{i,j}^n + \left( \frac{\partial u}{\partial y} \right)_{i-1,j} \right] = \frac{1}{2Re} \left[ \left( \frac{\partial^2 u}{\partial y^2} \right)_{i,j}^n - \left( \frac{\partial^2 u}{\partial y^2} \right)_{i-1,j} \right] \quad (7)$$

where the superscript  $n$  signifies the  $n$ -th iteration at station  $x_i$ , and

$$\bar{u}_{i,j} = \frac{1}{2} (u_{i-1,j} + u_{i,j}^{n-1}) \quad (8)$$

$$\bar{v}_{i,j} = \frac{1}{2} (v_{i-1,j} + v_{i,j}^{n-1}) \quad (9)$$

Iteration at each  $x$ -station is required since the convection terms are nonlinear. With the definitions

$$\Delta y_f = y_{j-1} - y_j \quad (10)$$

$$\Delta y_m = y_j - y_{j-1} \quad (11)$$

derivatives in the  $y$ -direction are approximated as

$$\left( \frac{\partial u}{\partial y} \right)_{i,j} =$$

$$\frac{\Delta y_m^2 u_{i,j+1} - (\Delta y_f^2 + \Delta y_m^2) u_{i,j} + \Delta y_f^2 u_{i,j-1}}{\Delta y_m \Delta y_f (\Delta y_m + \Delta y_f)} \quad (12)$$

and

$$\left( \frac{\partial^2 u}{\partial y^2} \right)_{i,j} =$$

$$2 \frac{\Delta y_m u_{i,j+1} - (\Delta y_f + \Delta y_m) u_{i,j} + \Delta y_f u_{i,j-1}}{\Delta y_m \Delta y_f (\Delta y_m + \Delta y_f)} \quad (13)$$

For turbulent flows,  $\nu$  is replaced by  $\nu + \nu_t$ , where

$$\nu_t = \nu_u + (\nu_t - \nu_u) e^{-1.2(x_i - x_{i-1})} \quad (14)$$

$$\nu_u = 0.0115 Re_s \quad (15)$$

where  $\nu_t$  is the eddy viscosity at the trailing edge of the splitter plate (obtained using the Cebeci-Smith turbulence model),  $\nu_u$  is the eddy viscosity of a self-similar mixing layer,  $\delta_{t,e}$  is the sum of the boundary layer thicknesses at the trailing edge and  $Re_s$  is the Reynolds number based on mixing layer thickness. This formulation allows a smooth transition from merging boundary layers in the near region to asymptotically approach the self-similar mixing layer in the far region. Exponential blending of eddy viscosities in this manner is in the spirit of the method proposed for airfoil wakes by Chang et al. (1984).

### 3. RESULTS AND DISCUSSION

Following Townsend (1976), the normalizing velocity scale is chosen as the velocity difference across the layer, and the shear layer thickness (given by a least-squares fit of the mean data to the error function profile shape) is used to normalize the  $y$ -coordinate. The mean profiles were found to fit the error function (plotted on all the mean velocity plots) extremely well in the range  $0.1 < U < 0.9$ , thus justifying the use of this procedure for providing an accurate and objective method for defining shear layer thickness.

#### 3.1 Unforced Mixing Layer

The plane unforced two-stream mixing layer with a velocity ratio of about 0.5 was investigated using each of the four techniques (experimental and computational) described above in Section 2.

Fig. 2 shows a comparison between X-wire and LDV measurements of mean flow and turbulence quantities in the self-preserving region of the two-stream mixing layer. Also included in the figure are mean flow and turbulence statistics given by time averaging instantaneous velocities evaluated in the vortex simulation. Previous detailed measurements in the near-field of the two-stream mixing layer had shown that the layer reached self-similarity for  $x > 12$  cm, for both tripped and untripped initial conditions (Mehta and Westphal, 1986). In the vortex simulations, once

the mixing layer achieved a quasi-steady state ( $t > 200$ ), the mean flow and turbulence statistics indicated a self-preserved condition for  $x > 60$  (the length scale is arbitrary in the simulations). The measurements shown in Fig. 2 are for untripped initial boundary layers and at  $x = 23$  cm and the vortex simulation results are for  $x = 100$ , both in the self-similar region.

The validity and consistency of cross-wire measurements was previously confirmed for this shear flow through comparison with existing data and application of the two-dimensional conservation laws (Mehta and Westphal, 1986). The cross-wire data are therefore used here as base cases for comparisons. The agreement between the two experimental techniques of the mean flow behavior and distribution and peak levels of the Reynolds normal stresses ( $\overline{u'^2}$  and  $\overline{v'^2}$ ), is extremely good, to well within 10% (Figs. 2a and b). The peak level of the shear stress ( $\overline{u'v'}$ ) and its distribution on the higher-speed side of the mixing layer also agree well (Fig. 2c). However, the LDV measurements on the low-speed side of the layer are somewhat below the other data. As a more severe test of the comparison, the triple product ( $\overline{u'v'^2}$ ), representing normal transport of the shear stress, and the shear correlation coefficient ( $R_{uv} = \overline{u'v'} / \sqrt{\overline{u'^2} \overline{v'^2}}$ ), which is useful in identifying turbulence structure are also plotted (Figs. 2e and f). Since  $R_{uv}$  is the ratio of the shear stress to the intensities, it will tend to magnify discrepancies in the measured stresses. The slightly higher normal stresses and lower shear stress, measured by the LDV, especially on the low-speed side of the mixing layer are clearly reflected in this plot. The triple products compare reasonably well, except again for the low-speed side.

Not surprisingly, the normal stress values obtained with the LDV are slightly higher than the X-wire measurements due to the inferior signal-to-noise ratio. LDV measurements can also suffer from biasing due to strong seed concentration gradients and sampling bias towards higher velocities. Since a relatively dense foam was used to produce the low speed side of the mixing layer, there was concern that seed particles may be blocked by the foam, thus resulting in a concentration gradient. However, on monitoring the data rate across the mixing layer, it was found to be proportional to the mean velocity, thus indicating an absence of a significant seed concentration gradient. As for sampling bias, a correction was applied such that each sample was weighted inversely to the magnitude of the instantaneous velocity, in the way used by Johnson et al. (1984). The effects of this correction on the mean streamwise velocity and the primary shear stress are shown in Figs. 3a and b. Clearly, for the turbulence intensities encountered in the present mixing layer (less than 20%), the LDV measurements do not seem to be markedly affected by sampling bias. So, on the whole, for measurements in mixing layers of mean velocities and turbulence Reynolds stresses, the two techniques seem to agree reasonably well; to an extent where either technique may be used in assessing the computational results.

The mean flow results computed using the vortex method in the self preserving region are in good agreement with the measurements. The peak level of the streamwise fluctuation  $\overline{u'^2}$  also compares well, although the computed levels fall-off more slowly towards the mixing layer outer edges. However, the computed values of the normal fluctuation,  $\overline{v'^2}$ , are clearly higher, by a factor of about four. Somewhat surprisingly, in spite of this large disagreement in  $\overline{v'^2}$ , the primary shear stress  $\overline{u'v'}$  results compare extremely well with the measurements. Once again, the differences in the computed values of the stresses are reflected clearly in the distribution of the higher order terms (Figs. 2e and f). The high computed values of the normal fluctuation are attributed to the observed presence in experiments of three-dimensionality in the form of longitudinal (streamwise) vortices which ride within the spanwise vortices (Jimenez et al., 1985). The longitudinal vortices tend to relax  $\overline{v'^2}$  in practical mixing layers. This conclusion is further supported by the results for the forced case presented and discussed below in Section 3.2. This relaxation can obviously not be modeled in the 2-D computation, although work is in progress on developing a 3-D code where this hypothesis will be tested more directly.

The results from the Reynolds averaged Navier-Stokes equations are compared to the cross-wire data in Figs. 4a-d. For these results, the sum of the initial boundary layer thicknesses is used to normalize the y coordinate. The computation was started from the splitter plate edge using the measured (tripped) boundary layer profiles as input (Fig. 4a). The computed mean velocity profile just downstream of the splitter plate reproduces the plate wake extremely well (Fig. 4b). Although the wake defect is still in evidence, it is clear that the velocity profile is rapidly evolving toward self-similarity. For that reason, the value of the constant C in eqn. 14 was chosen as 2.5. This is in contrast to the value of 20 used by Chang et al. (1984) for airfoil wakes. Further downstream, in the self similar region, the computed results for both the mean velocity and shear stress compare well with the measurements (Figs. 4c and d). The present computational scheme was thus able to capture the near-field behavior, which includes the plate wake, and then relaxes to a self-similar solution in the far-field, in agreement with the experimentally observed trends.

### 3.2 Forced Mixing Layer

Experimental data for the forced mixing layer were obtained for a velocity ratio of 0.5 whereas the vortex simulations were run for a velocity ratio of 0.6. However, as shown in Oster and Wygnanski's (1982) measurements, the effect of velocity ratio on the Reynolds stress distribution is minimal, especially in a given streamwise development region. We therefore feel that the present comparisons, even on a quantitative level, are justified.

Oster and Wygnanski (1982) identified three distinct regions in the streamwise development (or rate of growth) of forced mixing layers. The onset of each region is determined by the forcing frequency, the average velocity of the

two streams and the sum of the initial boundary layer momentum thicknesses. This classification is well illustrated in the comparisons between some flow visualization results and the distribution of discrete vortices as given by the vortex simulations (Figs. 5a and b). In Fig. 5a, where the forcing is at half the "natural" frequency, the position for the onset of instability and the rapid vortex pairing and hence a high growth rate (compared to the unforced layer) are well reproduced by the computations; this represents region I. Further downstream (not shown in the present results), the mixing layer growth would be expected to reduce to zero (region II) before regaining the initial high growth rate (region III). However, when the mixing layer is forced at twice the natural frequency, region II is entered straightaway and vortex pairing and hence growth are inhibited right from the start, as shown in Fig. 5b. So qualitatively, the vortex simulations are able to reproduce the trends observed in the flow visualizations extremely well.

The quantitative data from the vortex method are compared to LDV measurements for the case when the mixing layer is forced at half the natural frequency in Figs. 6a-h. (The forcing amplitude in the experiments was 1 mm and  $A = 0.5l$  in the vortex simulation.) The first streamwise station shown in Fig. 6 is at the end of region I with the subsequent stations being in region II. As found by Oster and Wygnanski (1982), for the value of forcing frequency and amplitude considered in the present study, the mean velocities (Figs. 6a and b) are not affected: the velocity distribution is still well represented by an error function. However, the effect of forcing on the Reynolds stresses is significant. The peculiar double-peaked distribution of  $\overline{u'^2}$  is seen in both results (Figs. 6c and d) and this is attributed to the passage (through the measurement plane) of well aligned vortices which have relatively quiescent cores and increased  $u$ -activity at the periphery (Oster and Wygnanski, 1982). The computed maximum levels of  $\overline{u'^2}$  also compare very well with the measured values. The effect of forcing on  $\overline{v'^2}$  is to increase it by a factor of almost five over the unforced values. This is in response to increased two-dimensionality in the mixing layer, a notion which is further supported by the observance (Oster and Wygnanski, 1982) that  $\overline{u'^2}$  is reduced by the forcing. The increased levels in  $\overline{v'^2}$  compare well between the two techniques (Figs. 6e and f) and this again confirms the feeling that, in practice, the unforced mixing layer contains significant three-dimensionality which tends to relax  $\overline{v'^2}$ . The maximum effect of forcing occurs on the primary shear stress,  $\overline{u'v'}$  (Figs. 6g and h). At the first streamwise station shown, the shear stress has a familiar shape although the peak levels are somewhat higher than the unforced case; this is consistent with the accelerated growth encountered in region I. However, with increasing streamwise distance, the shear stress begins to drop and eventually changes sign so that there is a negative correlation between the shear stress and the mean velocity profile. This change in sign is more easily understood by considering the mean-momentum equation and remembering that  $\partial U / \partial x$  is zero in region II (Oster

and Wygnanski, 1982). The overall trend is very well reproduced in the computations. In the experiments, data could only be obtained up to a streamwise position where the primary shear stress dropped to near-zero values. So for forced mixing layers, the 2-D vortex simulations give results which seem to agree extremely well with experimentally observed trends.

#### 4. CONCLUDING REMARKS

Results from experimental and computational investigations of plane turbulent mixing layers (with and without forcing) have been compared and discussed. Reasonably good agreement was found between the two measurement techniques, at least for turbulence quantities up to second order. The implication of the good agreement, that sample bias corrections to the LDV data were minimal for this type of shear flow, was further confirmed by evaluating the corrections. The Reynolds averaged computations were successful at capturing the complete evolution of the mixing layer, including wake effects in the near-field and approach to self-preservation in the far-field. For the far-field behavior, the vortex method showed excellent qualitative and quantitative agreement with measured data for the forced mixing layer. However, for the unforced layer, the results seemed to indicate that a 3-D computation, which includes the modeling of the longitudinal vortices, may be necessary. Further coordinated computational/experimental studies are being conducted in continuing search for a better physical understanding of the underlying mixing layer structure and behavior. Particular attention is being paid to the three-dimensional interaction between streamwise and spanwise vortices in a turbulent mixing layer.

#### ACKNOWLEDGEMENTS

Two of the authors (R.D.M. and J.H.B.) were supported by the Fluid Dynamics Research Branch, NASA Ames Research Center under Grant NCC-2-294. O.I. was supported by a National Research Council Fellowship.

#### REFERENCES

- Brown, G.L.; Roshko A. 1974: On density effects and large structure in turbulent mixing layers. *J. Fluid Mech.* 64, 775-816
- Chang, K.C.; Bui, M.N.; Cebeci, T.; Whitelaw, J.H. 1984: The Calculation of turbulent wakes. Dept. of Mech. Eng., Calif. State Univ., Long Beach, Report ME-84-3
- Ho, C.-M.; Huang L.-S. 1982: Subharmonics and vortex merging in mixing layers. *J. Fluid Mech.* 119, 443-473
- Ho, C.-M.; Huerre P. 1984: Perturbed free shear layers. *Ann. Rev. Fluid Mech.* 16, 365-424
- Inoue, O.; Leonard, A. 1986: Vortex simulation of forced mixing layers. NASA-TM 88235

Jimenez, J.; Cogollos, M.; Bernal, L.P. 1985: A perspective view of the plane mixing layer. *J. Fluid Mech.* 152, 125-143

Johnson, D.A.; Modarress, D.; Owen, F.K.: 1984: An experimental verification of Laser-Velocimeter sampling bias and its correction. *ASME J. Fluids Eng.* 106, 5-10

Mehta R.D.; Westphal, R.V. 1984: Near-field turbulence properties of single- and two-stream plane mixing layers. *AIAA Paper 84-0538*. To appear in *Experiments in Fluids*. 1986

Oster, D.; Wagnanski I.J. 1982: The forced mixing layer between two parallel streams. *J. Fluid Mech.* 123, 91-130

Rodi, W. 1975: A review of experimental data of uniform density free turbulent boundary layers. In: *studies in convection* (ed. Launder, B.E.). Vol. 1. pp 79-166. London: Academic Press

Rodman, L.C.; Bell J.H.; Mehta, R.D. 1986: A three-component Laser-Doppler Velocimeter data acquisition and reduction system." Dept. of Aero. and Astro., Stanford University, JIAA Report TR-63. Also NASA-CR 177390. January 1986

Townsend, A.A. 1976: *Structure of turbulent shear flow*. Second edition. Cambridge Univ. Press esp. pp. 227-230

Westphal, R.V.; Mehta R.D. 1983: Cross hot-wire data acquisition and reduction system. NASA-TM 85871

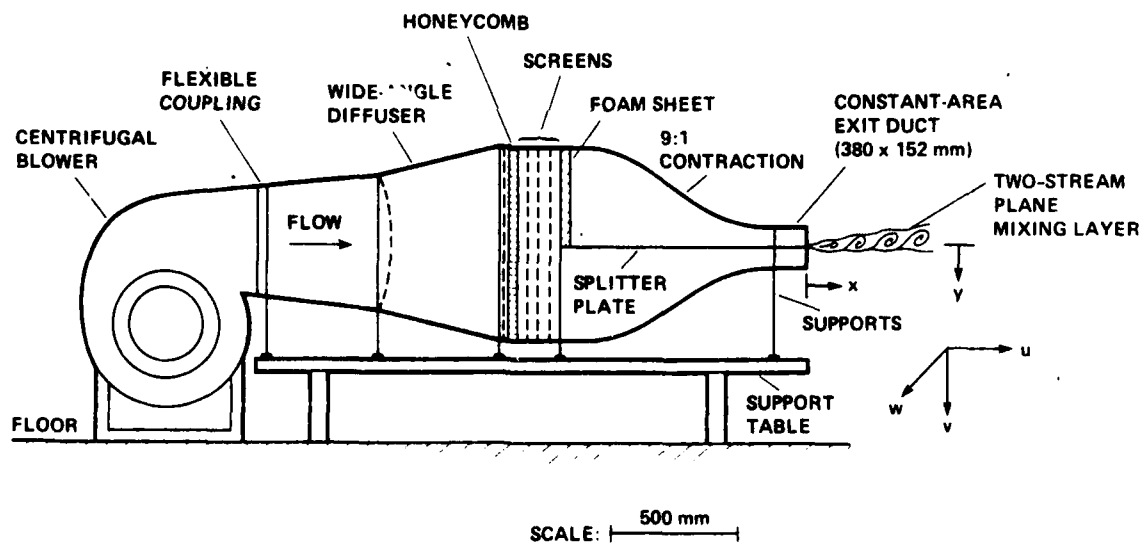


Fig. 1. Schematic of 38 X 15 cm Shear Layer Wind Tunnel.

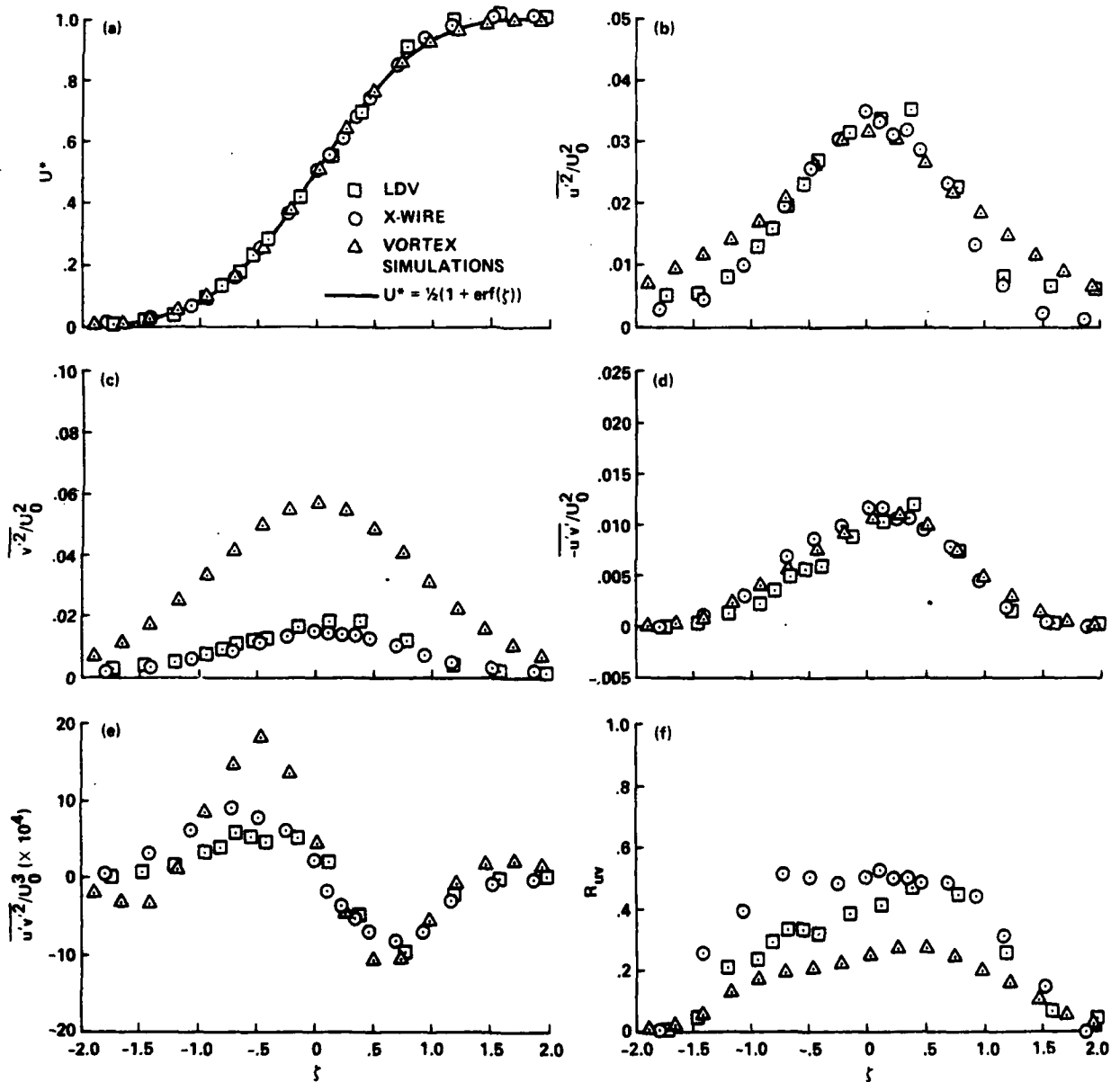


Fig. 2. Comparison of X-wire and LDV Measurements and Vortex Method Computations for the Unforced Mixing Layer in the Self-Similar Region. Velocity Ratio = 0.5.

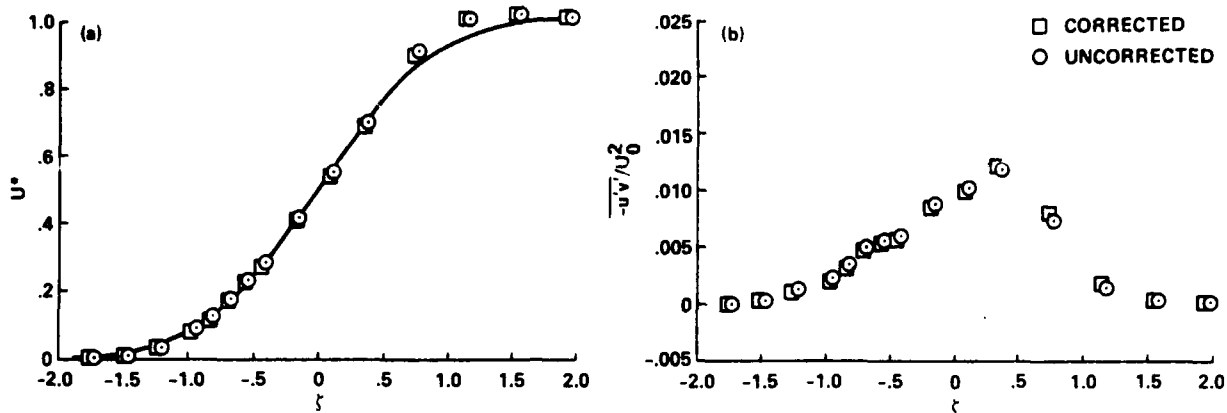


Fig. 3. Effects of Sampling Bias Corrections on LDV data: (a) Mean Velocity Data; (b) Turbulence Shear Stress Data.

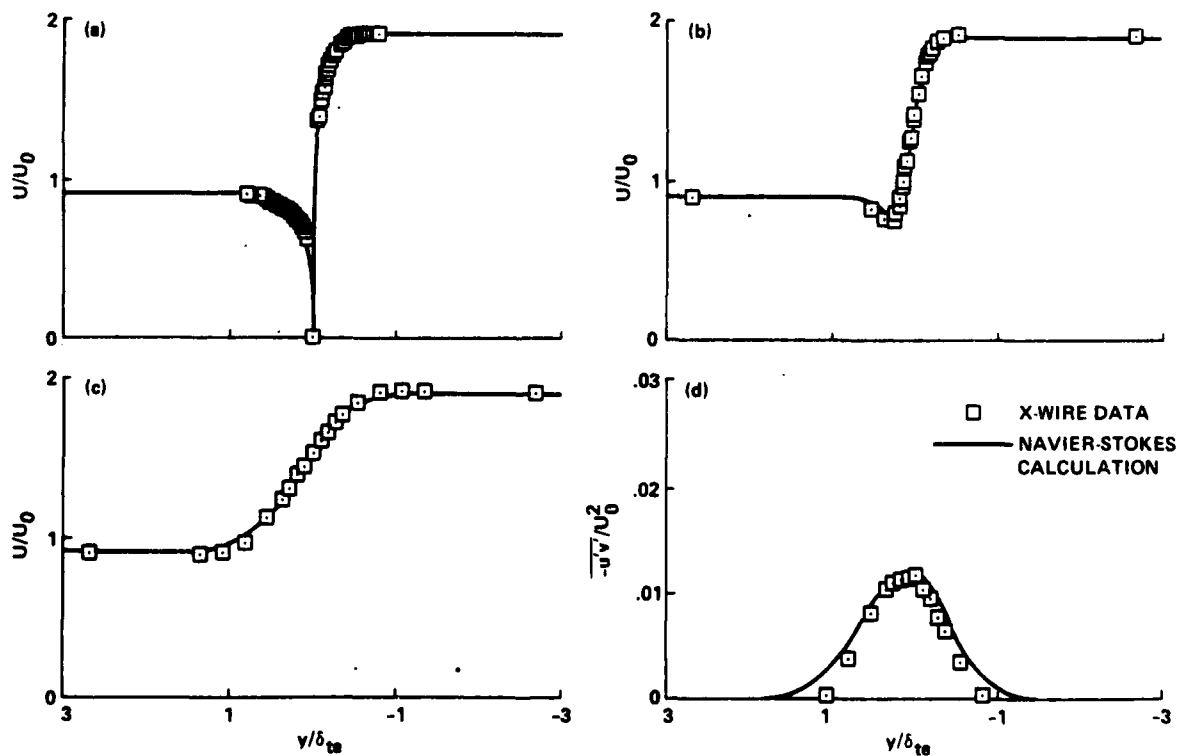
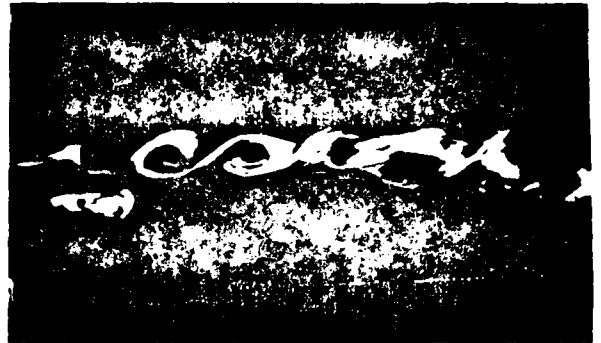


Fig. 4. Computation using Reynolds Averaged N-S Equations compared with X-Wire Measurements: (a) Input Boundary Layer Profiles at Splitter Plate Edge; (b) Mean Velocity Computation in the Near-Field Region; (c) Mean Velocity Computation in the Self-Similar Region; (d) Shear stress Computation in the Self-Similar Region.

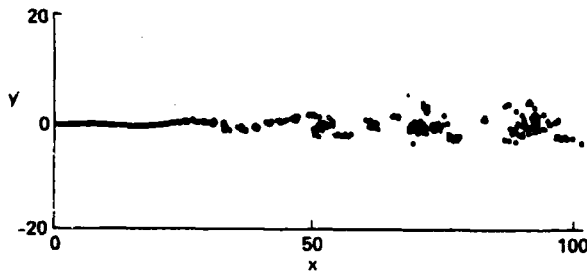
Smoke Flow Visualization



Smoke Flow Visualization



Vortex Method Simulation



Vortex Method Simulation

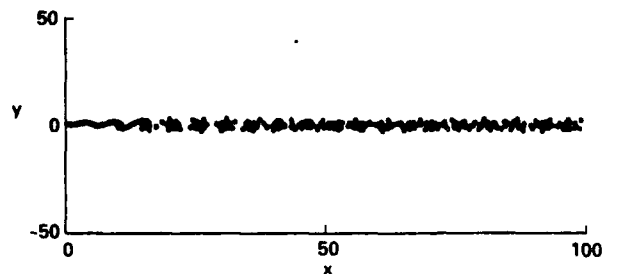


Fig. 5a. Qualitative Comparison for Forced Mixing Layer. Forcing at Forcing at Half the Natural Frequency, velocity ratio = 0.5.

Fig. 5b. Qualitative Comparison for Forced Mixing Layer. Forcing at Forcing at Twice the Natural Frequency, velocity ratio = 0.5.

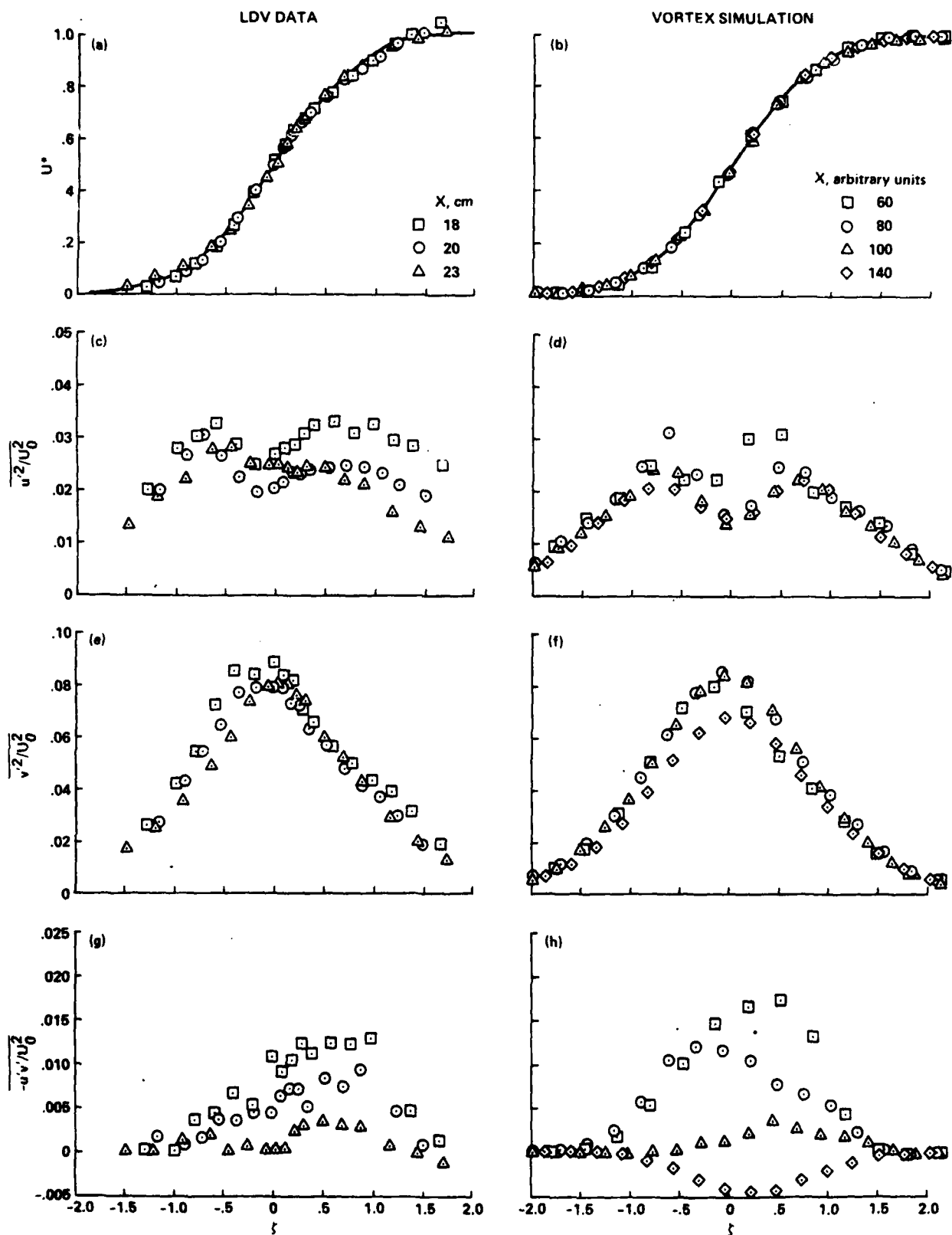


Fig. 6. Comparison of LDV data and Vortex Method Computation for Forced Mixing Layers. Forcing at Twice the Natural Frequency.

# THE TURBULENT AND PERIODIC FLOWS BEHIND A SQUARED OBSTACLE

by

D.F.G. Durao, M.V. Heitor and J.C.F. Pereira

Instituto Superior Tecnico

Mechanical Engineering, Department

1096 Lisbon Codex

Portugal

## ABSTRACT

Laser-Doppler measurements of the velocity characteristics are presented for the turbulent flow around a squared obstacle mounted in a water channel for  $Re=14000$ . The study involved spectral analysis and digital filtering of the LDV data obtained behind the obstacle.

The purpose of the measurements is to separate and quantify the turbulent and the periodic, non-turbulent, motions of the wake flow, in order to improve knowledge of the nature of the fluctuations in the near-wake region of two-dimensional bodies.

The results show, for example, that in the zone of highest velocity oscillations the energy associated with the turbulent fluctuations is about 40% of the total energy.

## 1. INTRODUCTION

The quasi-periodic nature of the flow around two-dimensional bluff-bodies is relevant for many design purposes, but very little information is available on the details of the aerodynamics of near wake flows.

The present study follows those of Durao et al (1986-a and -b), which provide a basis to understanding the nature of the fluctuations in the wake region of two-dimensional bodies and to assess the accuracy of calculation procedures in recirculating flows. In those previous works detailed laser-Doppler measurements were presented for the turbulent flow around a squared obstacle mounted in a water channel for  $Re=14000$ . Also, analogue spectral analysis was conducted by sampling and holding the velocity at each new Doppler burst until another valid signal arrives. The results have shown a single spectral peak at the predominant frequency of 4.7 Hz for  $Re=14000$ , for the normal velocity fluctuations in the centreline of the obstacle. In agreement with the results of Okajima (1982), the Strouhal number is approximately constant and equal to 0.133 for obstacle heights, between 8 and 20 mm in the range  $10^3 < Re < 2 \times 10^4$ . The results have suggested that the fluctuating velocity distributions measured by

the laser-Doppler velocimeter are a result of the time averaging measuring process in which the turbulent and the periodic, non turbulent, contributions to the total, normal and shear, stresses are not decomposed. Similarly, Yeh et al (1982) have shown that in the near wake around a strut mounted in a circular pipe, the shape of the radial profiles of the normal stresses is qualitatively similar to that of the turbulent variances, although the magnitude of the peaks of the turbulent variances is about half of the time-averaged measured values. These results suggest that a steady-state numerical calculation of the aerodynamic field requires the modeling of the relative motion of the turbulent and non-turbulent zones, for example, as proposed by Celenligil and Mellor (1985). Also, the calculations of Majundar and Rodi (1985) have shown that the separated turbulent flow past circular cylinders cannot be predicted realistically with a standard steady-flow model ignoring the periodic vortex-shedding motion.

The purpose of the present paper is to separate and quantify the energy associated with the turbulent and the periodic, non-turbulent, motions of the flow previously investigated for  $Re=14000$ , in order to bring new physical understanding of the nature of the fluctuations in the near wake region of two-dimensional bodies. Fast Fourier transforms and digital filtering techniques are applied to the output of the laser velocimeter, which was digitised and sampled at a constant frequency.

Section 2 summarizes the flow configuration and the experimental method and gives details of the data processing procedures. Section 3 presents and discusses the new results in the context of the previous works. The last section summarizes the main findings and conclusions.

## 2. EXPERIMENTAL METHOD AND ACCURACY

The experiments were performed on an horizontal, 120 x 156 mm, water tunnel made of perspex with a 20 x 20 mm obstacle, W, set across the narrow dimension, W, and completely spanning the duct as schematically shown by Durao et al (1986-a, b).

The results were obtained with the obstacle centered between the top and the bottom of the duct, for a reference velocity of  $U_0=0.68$  m/s and a freestream turbulence intensity of 6%. The effects of the proximity of the wall, of the size of the obstacle and of the Reynolds number on the wake-flow have been discussed by Durao et al (1986-a). Measurements obtained in the tunnel without the obstacle have shown that the flow was symmetric and that the wall boundary layer around the region where the obstacle was located, was 15 mm thick.

The origin of the axial, X, and vertical, Y, coordinates in the duct is taken at the centre of the upstream face of the obstacle.

Flow visualization has been conducted by injecting at the upstream face of the obstacle (at  $X=0, Y=0$ ) fluorescein-sodium, a fluorescent dye found to be an ideal tracer fluid for the present application. Fluorescein-sodium is soluble in water, is used in small concentrations such that density differences are negligible and the contamination of the water with the colour of the fluorescein-sodium dye is slow, so that a good contrast could be maintained without frequent replacement of the water in the system. The flow was illuminated by a sheet of laser light obtained by using a cylindrical lens to spread the laser beam. The light source was a 1W argon-ion laser in the 488 nm line, under which the fluorescein-sodium fluoresces a bright yellowish-green. Visualisation using air bubbles as tracer particles has also been performed using a similar illumination system.

Velocity was measured by a laser-Doppler velocimeter operated in the dual-beam, forward-scatter mode with sensitivity to the flow direction provided by light-frequency shifting from acousto-optic modulation (Bragg cells). The resulting frequency shift was normally set at 700 KHz. The principal characteristics of the laser-Doppler velocimeter, in particular those of the transmitting optics, are summarized in Table 1.

TABLE 1  
PRINCIPAL CHARACTERISTICS OF THE LASER-DOPPLER VELOCIMETER

- 15 mW (nominal) He - Ne Laser; wavelength:	632.8 nm
- focal length of focussing lens	300 mm
- beam diameter, at $e^{-2}$ intensity, of laser	1.1 mm
- measured half-angle of beam intersection (in air)	$4.81^\circ$
- calculated half-angle of beam intersection (in water)	$3.61^\circ$
- fringe separation (line pair spacing)	3.77 $\mu$ m
- calculated dimensions of measuring volume, at $e^{-2}$ intensity, (major and minor axis of ellipsoid in water)	3.489; 0.220 mm
- velocimeter transfer constant	0.2650 MHz/(ms <sup>-1</sup> )

The light scattered by naturally-occurring centres in the water was collected by a lens (focal length of 200 mm) and focused onto the pinhole aperture (0.3 mm) of a photomultiplier (OEI, type LD-0-810) with a magnification of 1.55. The output of the photomultiplier was band-pass filtered and the resulting signal processed by a laboratory-built frequency counter, as described

by Heitor et al (1984).

Estimates of the maximum inaccuracy and precision associated with each measurement have been presented by Durao et al (1986-b). Systematic errors due to non-turbulent Doppler ambiguity and velocity bias effects are small and the largest statistical (random) errors were of 0.5 and 3%, respectively for the mean and variance values, according to the analysis referred by Yanta and Smith (1978) for a 95% confidence interval.

The concentration of the naturally-occurring scattering centers in water, which give rise to Doppler signals, is such that the probability of finding more than one particle in the measuring volume of the anemometer is negligibly small: hence the occurrence of Doppler signals is a discrete, rather than a continuous process. This fact eliminates power spectrum aliasing but limits the spectral analysis of the velocity characteristics, once fast Fourier transform methods cannot be directly used. Several methods have been proposed for spectral estimation of LDV information (see, for example, Srikantiah and Coleman, 1985; Lading, 1985; Saxena, 1985) and the procedure adopted here has consisted in frequency analysing the output of the counter after to be digitized, transferred to the memory of a MicroVAX II computer, and sampled at a constant frequency of 2KHz, using linear interpolation between the measurements. This procedure requires a mean sampling rate at least three times the Nyquist rate and, as also discussed by Saxena (1985), limits the frequency range for spectral analysis but is considerable better than the sample-and-hold technique. Adrian and Yao (1985) have shown that holding results in missing high frequency information, with a low pass filter frequency equal to the mean data rate / 2 and that the attenuation is about 10% at a frequency equal to one-twentieth of the data rate. In the present study the data rate varied between 200 and 2000 Hz and, therefore, is high enough to avoid biasing errors and render the analysis valid at the low frequency range of interest here (i.e. about 5Hz).

Two procedures have been used to quantify the relative contributions of the turbulent and the periodic, non-turbulent, motions to the total flow field. First, the velocity fields were decomposed into a sum of mean, periodic, and random velocity components, as described by Yeh et al (1982). For a component  $u_i(t)$ :

$$U_i(t) = \bar{U}_i + \sqrt{2} u_{pi} \sin(2\pi ft + \phi) + u_i'(t) \quad (1)$$

where  $\bar{U}_i$  is the mean velocity,  $u_{pi}$  the rms amplitude of the velocity component occurring at the first harmonic,  $f$ , of the vortex shedding, with a corresponding phase of  $\phi$ , and  $u_i'(t)$  is the remaining turbulence velocity. Higher harmonics of the periodic flow have not been detected. Second, digital band-reject filters were used. Chebyshev filters of 7th order (e.g. Bendat and Piersol, 1971) were chosen with an attenuation of 100dB at the predominant frequency,  $f$ , and of 3dB at  $\pm 1$ Hz.

The accuracy of the variance of the filtered signals is limited mainly by the mean data rate and the finite sample size and is estimated to be within 9% of the maximum values measured.

### 3. EXPERIMENTAL RESULTS AND DISCUSSION

Part of this study was devoted to observing the periodic flow structure behind the squared obstacle which might, at least qualitatively, explain the vortex shedding mechanism.

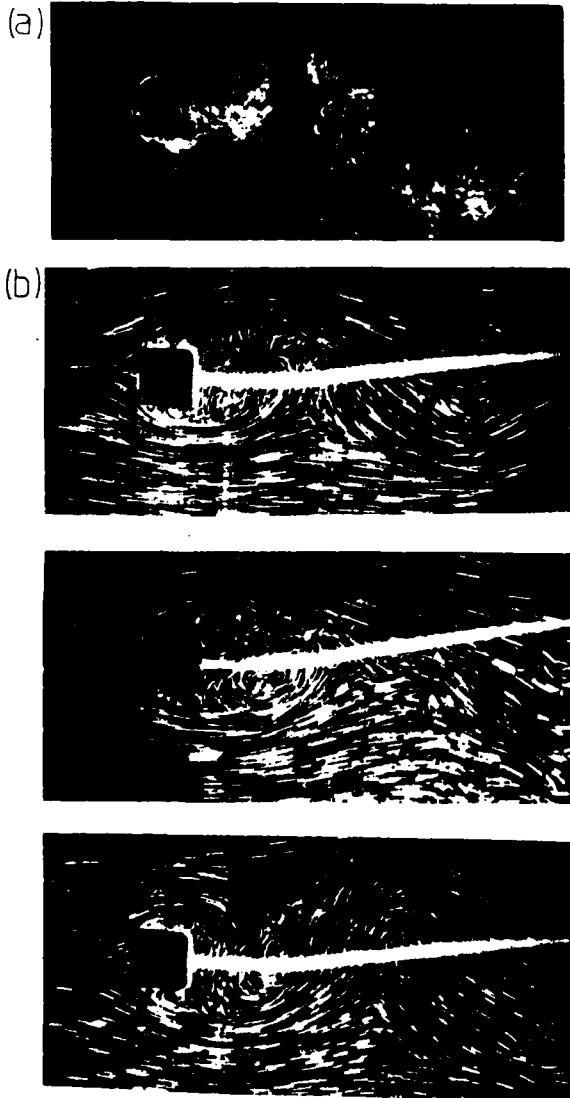


Figure 1 - Visualization of the flow around the obstacle for  $Re=14000$ .

- (a) Flow visualization by injecting a solution of Fluorescein-sodium at the upstream face of the obstacle (at  $X=0, Y=0$ )
- (b) Flow visualization using air bubbles as tracer particles.

The visualization experiments of figure 1(a) show a large amplitude vortex-street wake as a result of the mutual interaction between the top and bottom separating shear layers. It is postulated by Gerrard (1966) and discussed by Bearman (1984) that the vortex continues to grow, fed by circulation from its connected shear layer, until it is strong enough to draw the opposing shear layer across the near wake. In figure 1 the interaction between one shear layer and the vortex forming on the opposite side of the wake is clearly seen. The streaklines of figure 1(b) identify the accelerating flow upstream of, and around, the obstacle, the recirculating flow behind the obstacle and the development of the wake flow far downstream.

The important features of the time-averaged flow are summarised by the distribution of mean flow streamlines and the turbulent kinetic energy, discussed in detail by Durao et al (1986-b) and shown in figure 2(a) and (b).

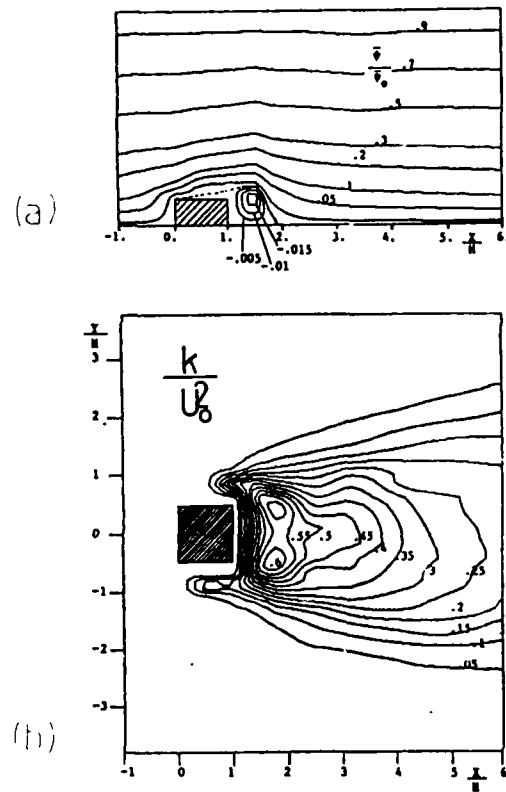


Figure 2 - The time-averaged mean and turbulent flow field for  $Re=14000$ .

- (a) Mean flow streamlines.  $\Psi_0 = \int_0^L \bar{u}(y) dy$ ;  
 $L$  - half length of the channel, 78mm.  
 (see Durao et al, 1986-b)

- (b) Distribution of turbulent kinetic energy,  $k/u_0^2$ . (see Durao et al, 1986-b)

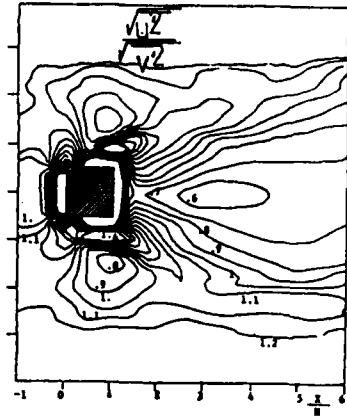


Figure 2-(c) Distribution of turbulence anisotropy,  $\sqrt{u'^2} / \sqrt{v'^2}$

The stream function was defined considering the flow two-dimensional, which is a particularly good approximation at the central plane of the channel, where the measurements were made. In general, the flow accord with previous separated flows with a free stagnation point.

The distribution of the turbulent kinetic energy,  $k$ , was calculated on the basis of local isotropy, i.e.  $k = 3/4(u'^2 + v'^2)$ . The contours reveal distributions which are qualitatively similar to those in the confined arrangements of Fujii et al (1978), McKillop and Durst (1986), Taylor and Whitelaw (1984) and Yeh et al (1982) and in the unconfined flows of Durao and Whitelaw (1978) and Durao et al (1984). The shear layer surrounding the recirculation bubble is a region of intense velocity fluctuations: the level of turbulent kinetic energy rises as the downstream distance increase, with maximum values around the reverse flow boundary at the stagnation zone; the individual stresses are anisotropic in that  $v'^2$  is largest close to the rear stagnation point, while the highest values of  $u'^2$  lie along the curved shear layer.

Comparison with the flows listed above indicates that the magnitude of the peaks are significantly higher than those reported in non-periodic turbulent wakes; on the contrary, the values are similar to those reported by Yeh et al (1982) and, for example, Bradbury (1976), and explained as the result of vortex shedding. Also, the structure parameters calculated by Durao et al (1986-b), such as  $u'v'/U_{max}$ ,  $R_{uv}$  and  $u'v'/k$ , show that the shear stress in the present near-wake flow is higher than that in non-periodic turbulent shear layers and suggest the existence of local periodic oscillations.

The distribution of the levels of measured anisotropy is shown in figure 2(c). The anisotropy of the Reynolds stresses is particularly high along the separating shear layer, with maxima at the plane of the downstream face of the obstacle, where  $\sqrt{u'^2} / \sqrt{v'^2} = 2.2$  at  $Y/H = (0.875 \pm 0.025)$ . The measured turbulent anisotropy on the centreline is also high, reaching a value of  $\sqrt{u'^2} / \sqrt{v'^2} = 0.45$  at

$X/H=3.25$  ( $\sqrt{u'^2} / \sqrt{v'^2} = 0.65$  at stagnation).

Figure 3 shows a characteristic digital spectral analysis of LDV data (at  $X/H=5, Y/H=0$ ) and confirms the oscillating nature of the present flow with a predominant frequency of 4.7 Hz for  $Re=14000$ .

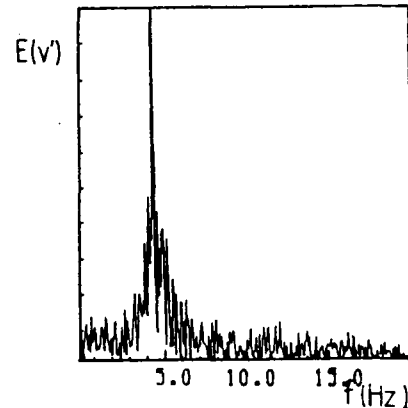


Figure 3 - Digital power spectra of normal velocity fluctuations in the centreline of the wake flow for  $Re=14000$ .  $X/H=5$ ;  $Y/H=0$ ;  $\bar{V}/U_0=0$ ;  $f=4.7$  Hz

The corresponding time-resolved output of the counter over 4 seconds is shown in figure 4(a) after to be linearly interpolated and sampled with a frequency of 2KHz. The signal follows a "noisy" sinusoidal wave with a corresponding bimodal probability density function, shown in figure 5(a).

Band-reject filtering of the measured signal centered at the predominant frequency, have allowed to decompose the turbulent fluctuations from the periodic oscillations. The former are shown in figure 4(b) and are characterized by a near-Gaussian probability density function, figure 5(b), with the mean value of the total flow but with a variance 37% of that of the measured signal.

This analysis has been extended to the whole flow field and figures 6(a) and (b) show the centreline development of  $u'^2$  and  $v'^2$ , both measured and filtered using the two procedures defined previously, together with the distribution of the mean axial velocity. The variance of the band reject filtered signal of the normal velocity fluctuations,  $v'^2$ , is consistently lower than that of the turbulent fluctuations decomposed from a sine wave because of the large attenuation of the former in the band filter. Nevertheless, the agreement between the two filtered curves reveals the well defined sinusoidal signals measured for the normal velocity.

The time-resolved axial velocity fluctuations,  $U(t)$ , exhibit comparatively low intensity peaks in the power spectrum and badly

defined sinusoidal signals, such that only the band reject filter could be used to decompose the turbulent and the periodic axial flows.

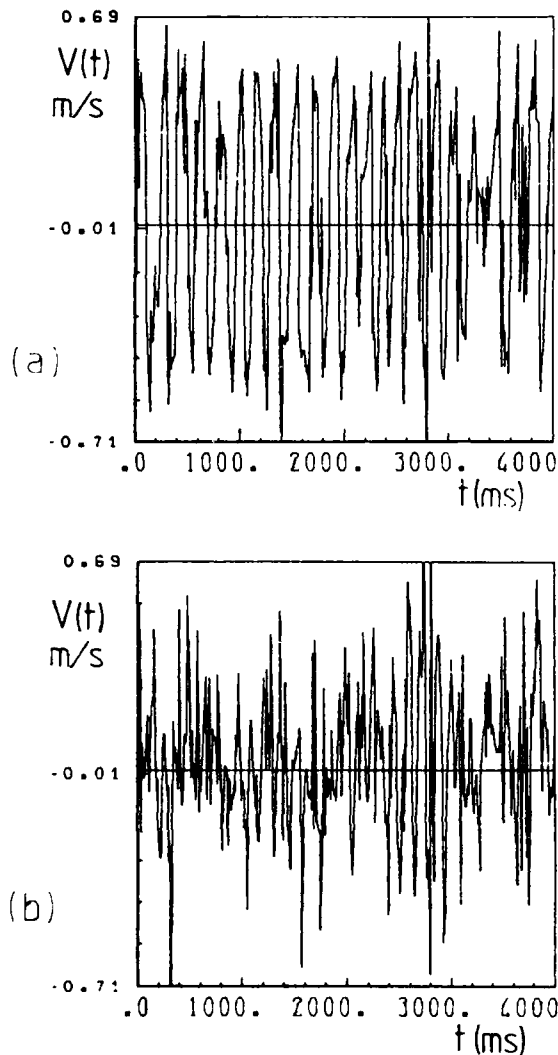


Figure 4 - Time-resolved normal velocity fluctuations at  $X/H=5$ ,  $Y/H=0$ . (Flow conditions of Figure 3).  
 (a) Measured signal  
 (b) Filtered signal (using a band-reject filter centered at the predominant frequency).

In general, the results show that the filtered distributions of  $u'^2$  and  $v'^2$  reveal the same trends of the measured signal with the maximum values located in the same points, but with lower values, respectively about 30% and 65% for the normal and axial velocity fluctuations. As a consequence, the anisotropy of the filtered Reynolds stresses has decreased substantially, as shown in figure 6(c): turbulence anisotropy (i.e.

$\sqrt{u'^2}/\sqrt{v'^2}$ ) on the centerline has a maximum value of 0.7 in comparison with 0.45 of the measured signal.

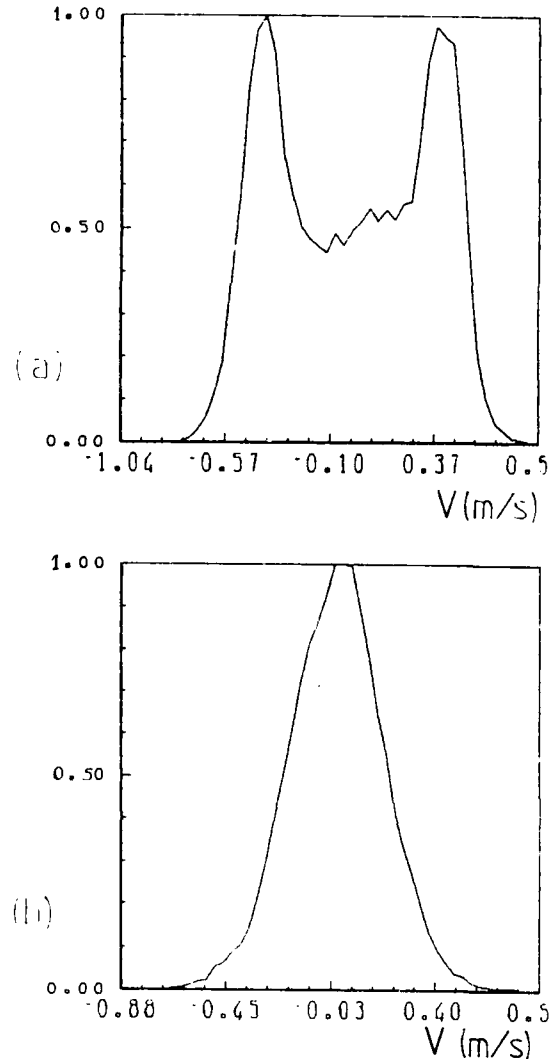


Figure 5 - Histogram of normal velocity fluctuations at  $X/H=5$ ,  $Y/H=0$ . (Flow conditions of Figure 3).  
 (a) Measured signal  
 (b) Filtered signal (using a band-reject filter centered at the predominant frequency).

Figure 7 shows vertical profiles of filtered and measured normal and shear stresses downstream of the stagnation point, at  $X/H=2.5$ , and agrees with the above analysis: the qualitative trends are maintained but the filtered variances are lower. In particular, the peaks in the filtered profiles of  $u'^2$  are still located around the separation streamline and are associated with the maximum transversal gradients of  $u$  but are about 53% of the measured values. It is interesting to note that in the context of the

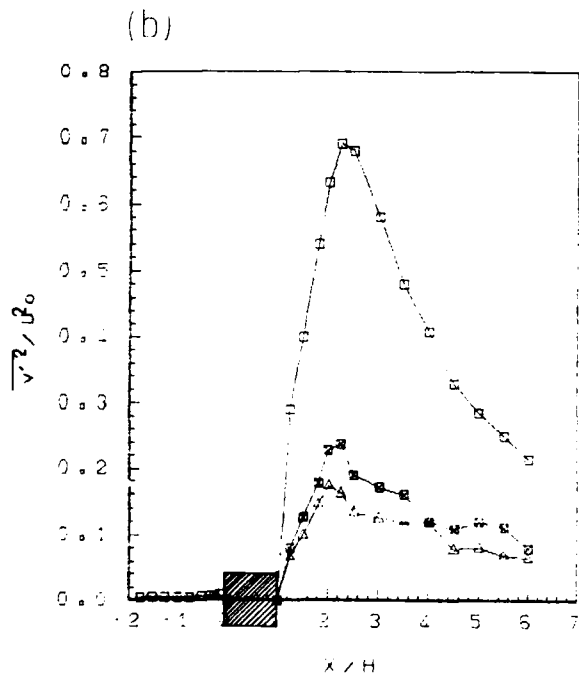
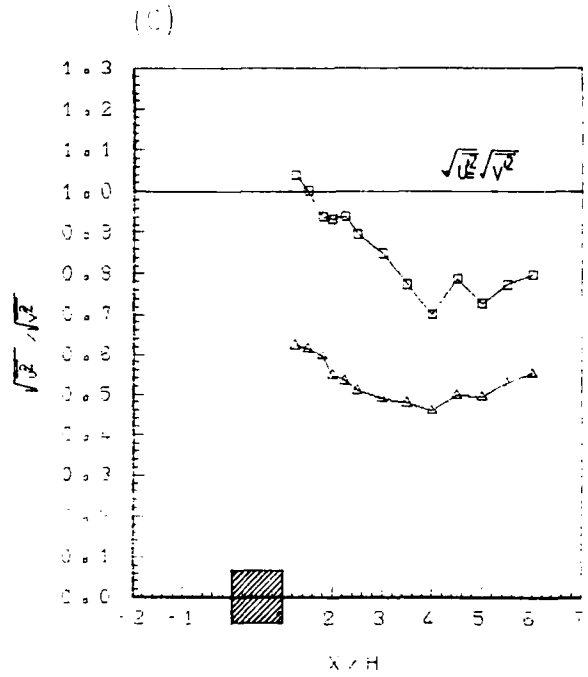
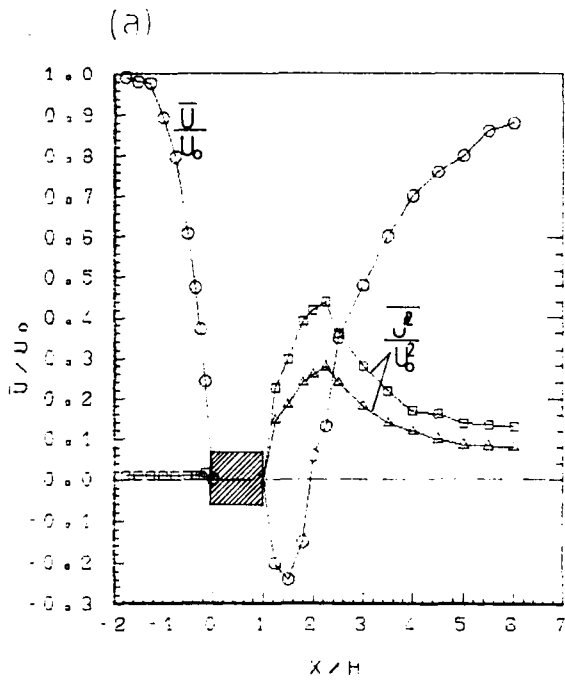


Figure 6 - Centreline distribution of velocity characteristics.  $Re=14000$

- (a) Axial velocity:  $\circ \bar{U}/U_0$   
 $\square U'^2/U_0^2$  measured  
 $\triangle U'^2/U_0^2$  filtered (band-reject)
- (b) Normal velocity:  $\square \bar{v}^2/v_0^2$  measured  
 $\triangle v'^2/v_0^2$  filtered (band-reject)  
 $\circ v'^2/v_0^2$  decomposed from sine wave, as in equation 1
- (c) Turbulence anisotropy:  
 $\square \sqrt{u'^2}/\sqrt{v'^2}$  measured  
 $\triangle \sqrt{u'^2}/\sqrt{v'^2}$  filtered (band-reject)

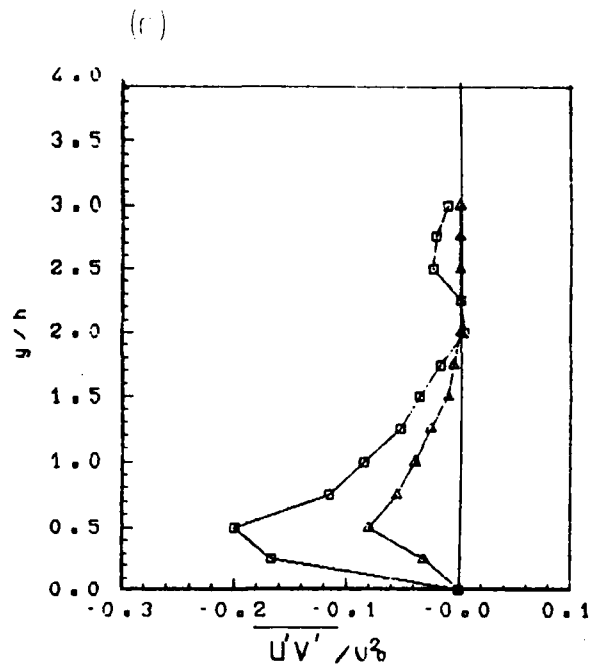
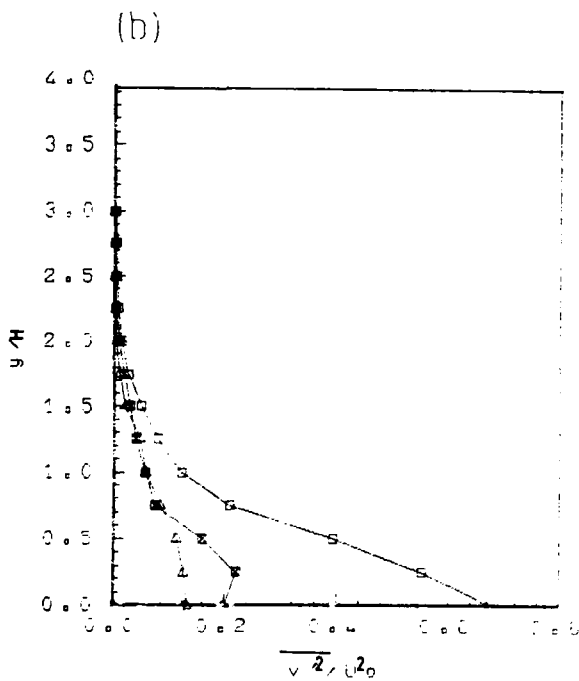
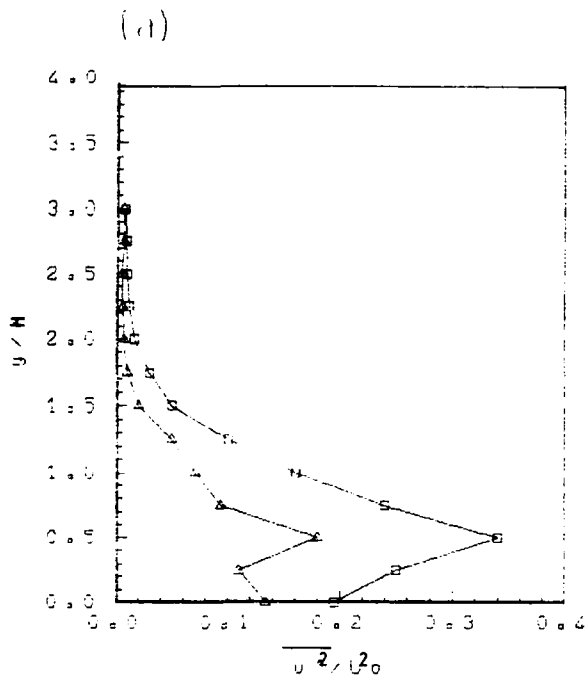


Figure 7 - Vertical profiles of normal and shear Reynolds stresses at  $X/H=2.5$  (upper half profiles).  $Re=14000$

- (a) Axial velocity:  $\square$   $\overline{u'^2}/U_0^2$  measured  
 $\triangle$   $\overline{u'^2}/U_0^2$  filtered (band-reject)  
 $\times$   $\overline{u'^2}/U_0^2$  decomposed from sine wave, as in equation 1
- (b) Normal velocity:  $\square$   $\overline{v'^2}/U_0^2$  measured  
 $\triangle$   $\overline{v'^2}/U_0^2$  filtered (band-reject)  
 $\times$   $\overline{v'^2}/U_0^2$  decomposed from sine wave, as in equation 1
- (c) Shear stress:  $\square$   $\overline{u'v'}/U_0^2$  measured  
 $\triangle$   $\overline{u'v'}/U_0^2$  filtered (band-reject)

analysis reported by Durao et al (1986-b), the maximum filtered values of  $\overline{u'^2}$  and  $\overline{v'^2}$  are similar to those reported in non-periodic turbulent wakes, for example by Fujii et al (1978), Mckillop and Durst (1986) and Taylor and Whitelaw (1984).

The decrease in the values of the filtered turbulent energy relative to those measured is associated to a comparatively large variation between the measured and filtered shear stress. The peaks in the filtered profiles of  $\overline{u'v'}$  are about 40% of the measured ones, and have the order of magnitude of the values measured by, for example, Durst and Mckillop (1986).

At the location of maximum shear stress, the correlation coefficient  $R_{uv}$  decreased from 0.54 to 0.47 and the ratio between filtered shear stress and turbulent kinetic energy is 0.31 and, therefore, similar to the value of 0.30 reported by Bradshaw et al (1967) and Harsha and Lee (1970) for turbulent shear flows. Around  $Y/H=1.50$ , where the maximum measured correlation coefficients have reached values close to unity, the maximum filtered coefficients are about 0.50. At these locations the filtered values of  $\overline{u'v'}/k$  are close to 0.30 while the measured values are as high as 0.70.

In summary, these structure parameters show that the values of the filtered shear stress in the present near-wake flow are characteristic of "well-behaved" turbulent shear flows, while the measured values result from the existence of local periodic oscillations. In the zones of maximum velocity oscillations the energy associated with the turbulent fluctuations is about 40% of the total energy. These results imply that the steady-state numerical calculation of the separated flow behind two-dimensional bodies requires modeling of the periodic vortex-shedding motion.

#### 4. CONCLUSIONS

Spectral analysis and digital filtering of LDV data have provided detailed information of the structure of the turbulent flow behind squared obstacles for  $Re=14000$ . The following is a summary of the more important findings and conclusions of this work.

- The shear layer surrounding the recirculation bubble behind the obstacle, for  $Re=14000$ , is a region of intense velocity fluctuations with unusually high values of the Reynolds (normal and shear) stresses, explained as the result of vortex shedding, with a frequency of 4.7 Hz. The analysis of the flow requires consideration

of both turbulent and periodic oscillations.

- In the zones characterized by the highest velocity oscillations the energy associated with the turbulent fluctuations is about 40% of the total energy. The turbulent profiles of  $\overline{u'^2}$ ,  $\overline{v'^2}$  and  $\overline{u'v'}$  exhibit the same trends of the measured quantities with the maximum values located in the same points, but with values respectively about 65%, 30% and 40% of the time-averaged measurements. The levels of turbulence anisotropy are smaller than the measured ones, with maximum values in the centreline about 0.70.
- In general, the experiments reported here quantify the relative importance of the turbulent and non-turbulent motions of the flow around two-dimensional bluff-bodies.

#### ACKNOWLEDGMENTS

We are pleased to record our thanks to Mr. Jorge Martins and colleagues in the Centro de Electronica Aplicada in the Department of Electrical Engineering for help in the frequency analysis and digital filtering techniques used throughout this work. The assistance of Mr. J. Brisson with the laboratory computers is gratefully acknowledge. Thanks are also due to Ms. Susana Valerio for her speedy typing of this report.

The experiments were partially supported by Stiftung Volkswagen Werke and by Nato research grant number 602, and made at the Centro de Termodinamica Aplicada e Mecanica dos Fluidos da Universidade Tecnica de Lisboa.

#### REFERENCES

- Adrian, R.J. and Yao, C.S. (1985). Power spectra of fluid velocities measured by laser Doppler velocimetry. ASME, Winter Annual Meeting, Miami Beach, Florida, November 17-22, 1985.
- Bearman, P.W. (1984). Vortex shedding from oscillating bluff bodies. *Ann. Rev. Fluid Mech.*, 16, pp. 195-222.
- Bendat, J.S. and Piersol, A.G. (1971) Random Data: analysis and measurement procedures. Wiley-Interscience, New York.
- Bradbury, L.J.S. (1976). Measurements with a pulsed-wire and a hot-wire anemometer in the highly turbulent wake of a normal flat plate. *J. Fluid Mech.*, 77, pp.473-497.
- Bradshaw, P., Ferriss, D.H. and Atwell, N.P. (1967). Calculation of boundary layer development using the turbulent energy equation. *J. Fluid Mech.*, 28, pp.593-616.
- Celenligil, M.C. and Mellor, G.L. (1985). Numerical solution of two-dimensional turbulent separated flows using a Reynolds stress closure model. *J. Fluids Engng.*, 107, pp.467-476.

Durão, D.F.G., Durst, F. and Firmino, F. (1984). Velocity characteristics of the flow around cones. Proc. 2nd Int. Symp. on Appl. of LA to Fluid Mech., paper 15.2, Lisbon, July 1984.

Durão, D.F.G., Heitor, M.V. and Pereira, J.C.F. (1986-a). The flow around a squared obstacle. 67th AGARD-PEP Conference, Philadelphia, May 19-23.

Durão, D.F.G., Heitor, M.V. and Pereira J.C.F. (1986-b). A Laser anemometry study of separated flow around a squared obstacle. Proc. of 3rd Int. Symp. on Appl. of LA to Fluid Mech., July 7-9, Lisbon Portugal. Paper 1.4.

Durão, D.F.G. and Whitelaw, J.H. (1978). Velocity characteristics of the flow in the near wake of a disc. J. Fluid Mech., 85, pp.369-385.

Edwards, R.V. and Jensen, A.S. (1983). Particle-sampling statistics in laser anemometers: sample-and-hold and saturable systems. J. Fluid Mech., 133, pp.397-411.

Fujii, S., Gomi, M. and Eguchi, K. (1978). Cold flow tests of a bluff-body flame stabilizer. J. Fluids Engng., 100, pp. 323-332.

Gerrard, J.H. (1966). The mechanism of the formation region of vortices behind bluff bodies. J. Fluid Mech., 25, pp 401-413.

Harsha, P.T. and Lee, S.C. (1970). Correlation between turbulent shear stress and turbulent kinetic energy. AIAA J., 8, pp.1508-1510.

Heitor, M.V., Laker, J.R., Taylor, A.M.K.P. and Vafidis, C. (1984). Instruction Manual for the FS "model 2" Doppler-Frequency Counter. Imperial College, Mech. Eng. Dept., Report FS/84/10.

Lading, I. (1985). Spectral analysis versus counting. ASME, Winter Annual Meeting, Miami Beach, Florida, November 17-22.

Majumdar, S. and Rodi, W. (1985). Numerical calculations of turbulent flow past circular cylinders. 3rd Symp. on Numerical and Physical Aspects of Aerodynamic Flows. Long Beach, California, 21-24 January.

McKillop, A.A. and Durst, F. (1986). A laser anemometry study of separated flow behind a circular cylinder. In: Laser Anemometry in Fluid Mechanics II, ed. Adrian et al, Ladoan.

Okajima, A. (1982), Strouhal numbers of rectangular cylinders. J. Fluid Mech., 123, pp.379-398.

Saxena, V. (1985). Power spectrum estimation from randomly sampled velocity data ASME Winter Annual Meeting, Miami Beach, Florida, November 17-22.

Srikantaiah, D.V. and Coleman, H.W. (1985). Turbulence spectra from individual realization laser velocimetry data. Exp. in Fluids, 3, pp.35-44.

Taylor, A.M.K.P. and Whitelaw, J.H. (1984).

Velocity characteristics in the turbulent near wakes of confined axisymmetric bluff bodies. J. Fluid Mech., 139, pp.391-416.

Yanta, W.J. and Smith, R.A. (1978). Measurements of turbulent-transport properties with a laser Doppler velocimeter. AIAA paper 73-169, 11th Aerospace Science Meeting, Washington.

Yeh, T.T., Robertson, B. and Mattar, W.M. (1982). LDV measurements near a vortex shedding strut mounted in a pipe. ASME Winter Annual Meeting, Phoenix, Arizona, November 14-19.

EVALUATION OF  $k^{-1}$  SPECTRAL LAW  
IN THREE WALL-BOUNDED FLOWS

O. Turan, R. S. Azad  
and S. Z. Kassab

Mechanical Engineering Department,  
University of Manitoba  
Winnipeg, Manitoba,  
Canada R3T 2N2

ABSTRACT

In this paper,  $k^{-1}$  spectral law is examined using the experimental data from fully-developed pipe, boundary layer and diffuser flows (Here,  $k$ , denotes one-dimensional longitudinal wavenumber). The type of pressure gradient present in a wall-bounded-flow has been found to play a controlling role on the presence and extent of  $k^{-1}$  spectral law. Furthermore, it has been observed that the theoretical ideas of Tchen (1953) and Panchev (1969) are not met in all wall-bounded flows. Moreover, the model proposed by Perry and Chong (1982) has been found to be consistent with experimental data in some respects, although further modification of the model is needed to fully corroborate the experimental results.

1. INTRODUCTION

Detailed description of the kinetic energy distribution from low to high wavenumbers of the fluctuating velocity can be obtained from the turbulence kinetic energy equation cast into the spectral form. Among the ranges of the turbulence kinetic energy spectrum in shear flow, the inertial subrange of the universal equilibrium range and the presence of  $k^{-5/3}$  spectral law have been extensively explored. A brief review can be found in Azad and Hummel (1981). In this paper,  $k^{-1}$  spectral law of the longitudinal fluctuating velocity in the mean flow direction,  $u$ , is examined using the data from three wall-bounded shear flows, namely, pipe, boundary layer and diffuser flows. In addition, the ideas of Tchen (1953,1954), Panchev (1969), and Perry and Chong (1982) in modelling and interpreting one-dimensional energy spectrum  $E(k)$ , are evaluated. Here,  $E(k)$  is

defined by the following integral :  $\int_0^{\infty} E(k) dk = \frac{\overline{u^3}}$ .

In spectral formulation of turbulent shear flow, Tchen (1953, 1954) distinguished cases of resonance and no-resonance between the primary and turbulent motions. In the presence of resonance, or strong interaction between the mean and fluctuating flow fields, Tchen reasoned that viscous dissipation was almost balanced by the production of turbulence kinetic energy due to the presence of high mean shear, leading to the following well-known functional form :  $E(k) = k^{-1} \epsilon / (\chi d\bar{U}/dy)$ , where  $\epsilon$  denotes dissipation,  $\bar{U}$  is the mean velocity,  $y$  is the distance from the wall,  $E(k)$  and  $k$  are three-dimensional energy spectrum and wavenumber, respectively, and  $\chi$  is the constant of proportionality. Heisenberg's eddy viscosity formulation has also been used in the previous derivation. On the other hand, if there is no resonance, or interaction between the mean and fluctuating flow fields, Tchen expected viscous dissipation to have the same order of magnitude as the turbulence kinetic energy transfer. The following form is obtained for this case :  $E(k) = [4\epsilon / (3\chi)]^{2/3} k^{-5/3}$ . Hence, Tchen concluded that  $k^{-1}$  and  $k^{-5/3}$  spectral laws governed the non-viscous subrange of the equilibrium range. These laws were present either successively, or either law without the other one, before the viscous subrange began.

By using the eddy viscosity coefficient of Stewart and Townsend (1951), Panchev (1969) obtained parametric solutions of the spectral energy equation in an attempt to connect the asymptotic solutions of Tchen. His solutions

indicated that for small values of the shear parameter  $m$ ,  $(-5/3)$  power law was present without  $(-1)$  power law ( $m = \delta \bar{U}/\delta y / (\epsilon/\nu)^{1/2}$ ,  $\nu =$  kinematic viscosity).  $k_1^{-1}$  spectral law appeared in his solutions as the value of  $m$  increased, and the region of existence of the  $k_1^{-1}$  spectral law increased with increasing  $m$ . Furthermore, his results indicated that the inertial subrange would disappear for large  $m$ . In homogeneous shear flow, Panchev derived the following expression:  $m = (C\nu)^{1/2}/u_*$ , where  $C = d\bar{U}/dy$ ,  $u_*$  is the friction velocity ( $u_*^2 = \tau_w/\rho$ ,  $\tau_w =$  mean shear stress at the wall,  $\rho =$  fluid density). He modified this expression to get  $m = [\nu/(xyu_*)]^{1/2}$ , where  $x = 0.41$ , in the presence of the logarithmic law of the mean velocity (Panchev, 1985).

Another interpretation of the flow in terms of the shear parameter  $m$  can be found in Rotta's work (1962). Rotta concluded that the degree of anisotropy would increase with increasing  $m$  values. Furthermore, for local isotropy, he estimated the condition to be that  $m$  be less than 0.01.

$k_1^{-1}$  spectral law, as well as  $k_1^{-5/3}$  spectral law, can also be obtained through dimensional arguments, as demonstrated by Hinze (1975), Kader and Yaglom (1984), and Abell (1974). From an examination of seven sets of experimental data of different workers, Kader and Yaglom concluded that the following equations should constitute the spectral laws:  $E_1(k_1)/(yu_*^2) = 0.8(k_1y)^{-1}$ , and  $E_1(k_1)/(yu_*^2) = 0.9(k_1y)^{-5/3}$ . The experimental data presented by Kader and Yaglom corresponding to these two lines appear to intersect at about  $k_1y = 1.0$ .

Abell's formulation (1974) of  $k_1^{-1}$  spectral law was based on his observation that his pipe flow spectra were independent of the wall distance in a region defined by the limits  $y^+ > 100$  and  $y/R < 0.1$  where the spectral data collapsed (Here,  $y^+ = yu_* / \nu$  and  $R$  is the inside pipe radius). In addition, Perry and Abell (1975), and Abell (1974) suggested that the region of  $k_1^{-1}$  spectral law coincided with the region of logarithmic law of the mean velocity and constant  $u'/u_*$  ( $u' = [\overline{u^2}]^{1/2}$ ) in the pipe. However, Perry and Abell (1977) later attributed having constant  $u'/u_*$  region to the pipe flow in their experiment not being fully-developed. According to Henbest (1983), the region given by

$140 < y^+$ ,  $y/R < 0.14$  defined the region of  $k_1^{-1}$  spectral law, which is given as the "logarithmic" or "turbulent wall" region by both Abell and Henbest. As can be observed from the respective expressions for  $u'/u_*$ , Perry and Abell (1977) suggested that  $A = 0.8$ , whereas Henbest suggested that  $A = 0.9$  in the following equation for  $k_1^{-1}$  spectral law:  $E_1(k_1)/(yu_*^2) = A/(k_1y)$ . In recent papers, Perry and Chong (1982) and Perry et al. (1986) modelled the  $E_1(k_1)$  spectrum through considering non-viscous vortex formation in potential flow.

## 2. EXPERIMENTAL SET-UP AND PROCEDURE

For the present study, fully-developed pipe flow was obtained in a pipe of inside radius 0.051 m ( $R = 0.051$  m), and length 8.05 m. The first one diameter length,  $D$ , from the inlet to the pipe was used for pasting #16 sand paper for tripping, as recommended by Klebanoff and Diehl (1952). Measurements were taken at one-half diameter from the exit of the pipe, as suggested by Preston (1950). Although any length greater than 70D from the inlet to the pipe is empirically considered to be sufficient for fully-developed pipe flow, an entrance length of 79D was used in the present study, and was found to be adequate for fully-developed condition. As shown by Dang (1986), this conclusion was reached from comparison of up to fourth order moments of all the fluctuating velocity components at 79D with those measured at 90D. For the present study, the pipe Reynolds number was 140,000 based on the mean centerline velocity and pipe diameter. The friction velocity,  $u_*$ , at the measuring station was approximately 0.84 m/sec.

Secondly, a boundary layer of thickness 0.046 m ( $\delta = 46$  mm) was grown on the smooth inner surface of a pipe of inside diameter 0.270 m. The boundary layer tripping and thickening was obtained by pasting the first one pipe diameter length, 0.270 m, of the pipe with #16 sand paper, as in the case of the fully-developed pipe flow set-up. The measurements presented here were made at 2.27 m from the end of the trip. The Reynolds numbers for this flow were 23,000 and 2,730, based respectively on the boundary layer thickness and momentum thickness, and on the local free stream velocity. The friction velocity at the measuring station was

0.32 m/sec.

Thirdly, a conical diffuser was used for the present study, of length 0.72 m and solid angle  $8^\circ$ . This diffuser has an inlet diameter of 0.102 m, and outlet diameter of 0.20 m, thus giving an area ratio of 4:1. The diffuser was fed with fully-developed pipe flow for the measurements presented here. The two locations chosen for the measurements were at  $X_0/D = 0.59$  and 4.13, where  $X_0$  is the distance from the inlet to the diffuser along its wall, and  $D$  is the pipe diameter. As in the case of the fully-developed pipe flow, the Reynolds number of the pipe flow at the inlet to the diffuser was 140,000. The friction velocities at  $X_0/D = 0.59$  and 4.13 were 0.64 and 0.22 m/sec, respectively.

Pressure measurements were obtained with four different manometers: an inclined manometer (Air Flow Developments, Ltd.), a combist micromanometer (Bradshaw, 1965), Hero and Betz micromanometers. For turbulence measurements, boundary layer type hot-wire probes (DISA 55P05) were used that have approximately 1.25 mm sensitive length and 5  $\mu$ m diameter, along with a DISA 55M01 hot-wire anemometer, DISA 55M25 linearizer and DISA 55D35 RMS meter. Spectra of  $u$  were measured using Krohn-Hite 3550 filters. For all hot-wire anemometry measurements, the position of the probe closest to the wall was 0.5 mm from the wall in order to avoid the effect of wall proximity on the hot-wire signal, in accordance with Azad (1983).

The friction velocity was measured using Preston tubes, and cross-log plotting. The Preston tubes were calibrated in fully-developed pipe flow. The values thus obtained were within 3% of those obtained using Patel's calibration (1965). For the diffuser flow, the correction of Frei and Thomann (1980) was used.

### 3. EXPERIMENTAL RESULTS AND DISCUSSION

In the present work, two criteria are used to decide on the presence of  $k_{,y}^{-1}$  spectral law in any one-dimensional spectrum  $E_1(k_1)$  of the velocity fluctuation  $u$  in the direction of the mean flow. First, non-dimensional  $E_1(k_1)$  spectra are expected to vary inversely with non-dimensional wavenumber within the region of validity of  $k_{,y}^{-1}$  spectral law:  $E_1(k_1)/(y u_{\tau}^2) = A/(k_1 y)$ . The second criterion is that the constant of proportionality,  $A$ , must be

the same for different transverse positions, if the above spectral law is valid at those locations. In a given flow, as  $y$  increases, the corresponding spectra peel off from the region of collapse at higher wavenumbers. In contrast with the region of collapse where  $k_{,y}^{-1}$  spectral law exists, the peeling-off is wall distance dependent. Hence, the lower limit of the  $k_{,y}^{-1}$  spectral law range shifts to higher non-dimensional wavenumbers as the distance from the wall increases at a given horizontal (or, equivalently, axial) position in the flow. Consequently, the range of  $k_{,y}^{-1}$  spectral law in terms of non-dimensional wavenumbers decreases with increasing wall distance; whereas the upper limit of the range of  $k_{,y}^{-1}$  spectral law appears to be fixed according to the experimental results ( $k_1 y \approx 1.0$  in pipe and boundary layer flows with favorable and zero pressure gradients, respectively;  $k_1 y \neq 1.0$  in the presence of adverse pressure gradient, however, a fixed upper limit still exists, as will be shown).

In the present work, first, near wall spectral data for  $0.5 \text{ mm} \leq y \leq 15 \text{ mm}$  from the fully-developed pipe, boundary layer and diffuser flows were plotted in the following two forms:  $E_1(k_1)/(y u_{\tau}^2)$  vs.  $k_1 y$ , and  $k_1 E_1(k_1)/u_{\tau}^2$  vs.  $k_1 y$ . Then, these spectral plots were examined using the previously mentioned two criteria. From these plots, only those results that indicate presence of  $k_{,y}^{-1}$  spectral law were chosen to be presented here. Due to page limitation, one example of the second form of spectral plot is given.

As seen in Figure 3 of Azad and Kassab (1984), the extent of logarithmic law for the mean axial velocity,  $\bar{U}$ , in the present pipe flow for  $Re=140,000$  can be taken to be within the following limits:  $30 < y^+ < 500$ . The pipe flow spectra that indicate presence of  $k_{,y}^{-1}$  spectral law are given in Figure 1. The two sets of data presented in this figure correspond to  $y^+ = 183.1$  and 287.7 ( $y/R = 0.07$  and 0.11), respectively. In addition to having the correct slope, these two sets of data collapse to a single configuration where the spectra are proportional to  $(k_1 y)^{-1}$ . Furthermore, in Figure 1, the experimental data given by Kader and Yaglom (1984) in their Figure 1, are represented by the following two lines:  $E_1(k_1)/(y u_{\tau}^2) = 0.8/(k_1 y)$ , and  $E_1(k_1)/(y u_{\tau}^2) =$

$0.9/(k,y)^{0.73}$ . These lines appear in similar plots throughout the present paper. Moreover, as seen in Table 1, the value of the constant of proportionality  $A$  in the spectral equation for  $k^{-1}$  spectral law,  $E_1(k_1)/(y u_{\mu}^2) = A/(k,y)$ , or equivalently,  $k_1 E_1(k_1)/u_{\mu}^2 = A$ , is approximately 0.9 for both sets of spectral data given in Figure 1. The values of  $A$  listed in Table 1 were calculated for each position by first selecting the range of  $k^{-1}$  spectral law from the corresponding  $k_1 E_1(k_1)/u_{\mu}^2$  vs.  $k,y$  plot, and then confirming this range from the plot of  $E_1(k_1)/(y u_{\mu}^2)$  vs.  $k,y$  for that position.

In Figure 2, two sets of spectral data from Abell (1974) are given. These spectra were chosen to be at the same  $y^*$  value of about 150, but at the minimum and maximum Reynolds numbers of 80,000 and 260,000, respectively, that Abell had obtained in his experiments. In spite of the increase in Reynolds number by a factor of about three, the lower end of the  $k^{-1}$  spectral region shifts to lower wavenumber values by only a small amount in the case of the higher Reynolds number. Consequently, the spectrum with the smaller Reynolds number peels off of the line of  $E_1(k_1)/(y u_{\mu}^2) = 0.8/(k,y)$  at a slightly higher value of  $k,y$  than does the spectrum at the higher Reynolds number. Hence, the effect of Reynolds number on the range of  $k^{-1}$  spectral law cannot be concluded from these data, since the observed change is small enough to be within experimental error. It must be noted that all the pipe flow results presented here are for "high Re" pipe flows. By "low Re" in pipe flow, Reynolds numbers in the order of 10,000 are meant, in accordance with Patel and Head (1969). Therefore, a conclusion could be drawn for the effect of Re on the range of  $k^{-1}$  spectral law in pipe flow only if spectral data of low velocity fully-developed turbulent pipe flow were to be compared with the results presented here.

As seen from Figure 1 of Azad and Kassab (1984), the logarithmic region of the mean velocity in the present boundary layer flow extends roughly between  $y^* = 30$  and  $y^* = 200$ . Furthermore, the range given by Abell for the presence of  $k^{-1}$  spectral law, i.e.  $100 \nu / u_{\mu} < y < 0.18$ , corresponds to the following dimensional range in this flow: 4.95 mm <

$y, y < 4.6$  mm. Similarly, the range given by Henbest,  $140 \nu / u_{\mu} < y < 0.148$ , correspond to 6.94 mm <  $y$  as the lower bound, and  $y < 6.44$  mm as the upper bound. Hence, the upper and lower limits of the expected range of  $k^{-1}$  spectral law in the present boundary layer appear to overlap according to both of these predictions. As a result,  $k^{-1}$  spectral law would not be expected to be seen in the spectral plots. However, as seen in Figures 3a and 3b, there is a definite region of  $k^{-1}$  spectral law at  $y = 5.0$  mm ( $y^* = 100.9, y/\delta = 0.11$ ). As given in Table 1, the corresponding value of  $A$  is about 0.9.

In Figures 3a and 3b, one set of spectral data in boundary layer flow obtained by Klebanoff (1955) that is applicable to  $k^{-1}$  spectral law is given along with the previously mentioned set of data. For the present boundary layer, the Reynolds number based on boundary layer thickness,  $Re_{\delta}$ , was 23,000, and the Reynolds number based on momentum thickness,  $Re_{\theta}$ , was 2,730; whereas for the boundary layer reported by Klebanoff, the values of  $Re_{\delta}$  and  $Re_{\theta}$  were 67,742 and 7,400, respectively. Hence, the present boundary layer and corresponding spectral data represent a lower Reynolds number case, in comparison with the boundary layer reported by Klebanoff.

As indicated by Figure 3a, the spectrum of the present boundary layer peels off from the  $k^{-1}$  spectral law region before the higher Reynolds number spectrum of Klebanoff. Hence, the lower end of the  $k^{-1}$  spectral law region of the latter spectrum extends to slightly lower wavenumber values than does the lower end in the former spectrum. As a result, the spectral data of Klebanoff being at higher Reynolds number, have a larger range of  $k^{-1}$  spectral law than do the spectral data from the present boundary layer. It must be noted here that the early peel-off of the spectrum with the lower Reynolds number is actually even more pronounced in Figure 3a than it appears to be. The reason is that the two sets of spectral data compared are not for the same  $y^*$  value. Ordinarily, for the same Reynolds number, the peel-off of the spectra from  $k^{-1}$  spectral law region would be earlier for higher  $y^*$  values. However, in Figure 3a, the spectrum that peels off earlier is at a lower  $y^*$  value than is the spectrum that peels

off later. Hence, the increase in Reynolds number reverses the order of peel-off of these two sets of spectra. Furthermore, it must be noted that the peel-off of the spectra with increasing Reynolds number is consistent with the observation of increased eddy hierarchy in the flow with Reynolds number (Head and Bandyopadhyay 1981, Perry and Chong 1982). Since the peel-off of the spectra has been attributed to increased hierarchy by Perry and Chong, Reynolds number increase must also cause peeling-off of the spectra by causing hierarchy to increase.

The difference between the two types of non-dimensional spectral plots can be observed from Figures 3a and 3b. In Figure 3a, the non-dimensional wavenumber range of  $k_1^{-1}$  spectral law in the boundary layer data of Klebanoff is about 1.3 cycles. However, the same range can be estimated to be less than one cycle from Figure 3b. Hence, an error bar was calculated for the data of Klebanoff through matching these two figures. If the range of  $k_1^{-1}$  spectral law obtained for the spectral data of Klebanoff from Figure 3a,  $0.06 < k_1 y < 1.0$ , is marked in Figure 3b, then the experimental points of the data of Klebanoff that remain within this wavenumber range but are not on the empirical line of  $k_1 E_1(k_1)/u_{*k}^2 = 0.8$ , represent the error in the experiment. Assuming that the error bar has the same width above and below the nominal value, the empirical equation that best represents the spectral data of Klebanoff in the region of  $k_1^{-1}$  spectral law becomes,  $k_1 E_1(k_1)/u_{*k}^2 = 0.8 \pm 0.11$ .

In the diffuser, two axial positions were chosen to test for the presence of  $k_1^{-1}$  spectral law,  $X_0/D = 0.59$  and  $4.13$ . The reason for choosing the first axial position was that the logarithmic profile of the fully-developed pipe flow at the inlet to the diffuser disappears by  $X_0/D = 0.59$  as shown in Figure 5 of Azad and Kassab (1984). The second axial position was chosen because the logarithmic region of the mean flow is recovered by  $X_0/D = 4.13$ , as seen in Figure 7 of Azad and Kassab (1984). The mean flow properties of the present diffuser are discussed in detail in Trupp, et al. (1986). Moreover, at  $X_0/D = 0.59$ , the value of the pressure parameter  $\alpha$ , defined as  $\alpha = \nu dP/dx / (\rho u_{*k}^2)$ , was found to be  $0.03$ ; whereas at  $X_0/D = 4.13$ ,  $\alpha$  was  $0.12$ . Hence, the behavior of the logarithmic law

of the mean velocity observed in the present diffuser is in agreement with Bradshaw and Galea (1967) who expect the logarithmic region to vanish for  $\alpha$  between  $0.01$  and  $0.04$ .

At  $X_0/D = 0.59$ , the range of  $k_1^{-1}$  spectral law predicted according to Abell, gives the following dimensional range:  $2.49 \text{ mm} < y < 5.5 \text{ mm}$ ; whereas the range predicted according to Henbest is as follows:  $3.49 \text{ mm} < y < 7.7 \text{ mm}$ . However, in neither of these ranges could  $k_1^{-1}$  spectral law be observed. Instead, a definite range exists at  $y = 1.0 \text{ mm}$  and  $1.5 \text{ mm}$ , corresponding to  $y^* = 40.13$  and  $60.18$ , respectively, and to  $y/R_0 = 0.02$  and  $0.03$ , respectively, as shown in Figure 4 (Here,  $R_0$  denotes the local radius at a given axial position in the diffuser). In addition, the data appear to be "shifted" with respect to the empirical line defining  $k_1^{-1}$  spectral law,  $E_1(k_1)/(y u_{*k}^2) = 0.8/(k_1 y)$  of Kader and Yaglom. As indicated by the corresponding values given in Table 1, the value of the constant of proportionality  $A$  for these positions is about  $2.0$  instead of  $0.8$ . The resultant spectral equation,  $E_1(k_1)/(y u_{*k}^2) = 2.0/(k_1 y)$ , is given by the solid line in Figure 4.

Along with the spectral data from the previously mentioned two radial positions, one of the four spectral data sets of Samuel and Joubert (1974) is also given in Figure 4. This set of data of Samuel and Joubert had been taken at  $2.38 \text{ m}$  from the first static pressure tap in their boundary layer tunnel and  $y^* = 66.7$  (equivalently,  $y/\delta = 0.025$ ) in an adverse pressure gradient boundary layer. In the corresponding spectrum, a similar "shift" can be observed. In addition to having two-dimensional geometry, the adverse pressure gradient boundary layer of Samuel and Joubert differs from the present diffuser in two more main aspects. First, Samuel and Joubert report much lower pressure parameter values than those encountered in the present diffuser. For the two horizontal locations at which their spectral data had been taken,  $\alpha = 0.0004$  and  $0.0021$  are reported; whereas in the present diffuser,  $\alpha = 0.03$  and  $0.12$  at  $X_0/D = 0.59$  and  $4.13$ , respectively. The higher of these two pressure parameter values reported by Samuel and Joubert,  $\alpha = 0.0021$ , corresponds to the horizontal position at which the spectral data given in Figure 4 had been taken. Hence, the boundary layer reported by Samuel and Joubert represents a case of

"mild" adverse pressure gradient in comparison with the present diffuser. Secondly, whereas the adverse pressure gradient in the present diffuser decreases with axial distance,  $d^2P/dx^2 < 0.0$ , for about 95% of its length from the exit, Samuel and Joubert report an increasing adverse pressure gradient in their boundary layer,  $d^2P/dx^2 > 0.0$ . However, as indicated in Figure 1 of Trupp, et al. (1986),  $X_0/D = 0.59$  in the present diffuser is very close to the increasing adverse pressure gradient region that exits over the first 5% of the diffuser length from the inlet. In other words,  $X_0/D = 0.59$  is located at the beginning of the decreasing adverse pressure gradient region of the present diffuser. Consequently, the spectral data at this axial position which indicate the presence of  $k_{1,1}$  spectral law, and the data presented from Samuel and Joubert appear to be similar. The corresponding constant of proportionality  $A$  for the data of Samuel and Joubert is 3.0, as given in Table 1. Moreover, it must be noted that although there is no logarithmic region present for the mean velocity at  $X_0/D = 0.59$  in the present diffuser, Samuel and Joubert indicate presence of logarithmic law at the transverse position at which their spectral data had been taken.

At  $X_0/D = 4.13$  in the present diffuser,  $k_{1,1}$  spectral law is expected to be present within the following ranges:  $7.27 \text{ mm} < y < 8.02 \text{ mm}$  according to Abell, and  $10.19 \text{ mm} < y < 11.22 \text{ mm}$  according to Henbest. As seen in Figure 5,  $k_{1,1}$  spectral law is present almost within the expected range according to the first of these two regions. For  $y = 6 \text{ mm}$  and  $8 \text{ mm}$  corresponding to  $y^* = 82.5$  and  $110.0$ , respectively, and to  $y/R_0 = 0.08$  and  $0.10$ , respectively, the spectral data show inverse proportionality with non-dimensional wavenumber and collapse. However, at  $X_0/D = 4.13$ , the logarithmic law of the mean velocity is present only for the following  $y^*$  range:  $20 < y^* < 100$ , as seen in Figure 7 of Azad and Kassab (1984). Consequently, the region of logarithmic law appears to have been "pushed" towards the wall. Hence, similar to the "different" nature of the logarithmic law in comparison with the mean velocity profiles in the present pipe and boundary layer flows, both  $k_{1,1}$  and  $k_{1,1/2}$  spectral law regions appear to have been shifted in Figure 5, in comparison with the spectral plots given in Figures 1 and 3a for the

present pipe and boundary layer flows, respectively. This shift in the spectra is similar to the shift observed in the spectral plots given in Figure 4 of the present diffuser at  $X_0/D = 0.59$  and the adverse pressure gradient boundary layer of Samuel and Joubert. However, the shift observed in Figure 5 is more than the shift in the spectra given in Figure 4. The value of the coefficient  $A$  is about 17.0 at  $X_0/D = 4.13$ , as opposed to  $A = 2.0$  at  $X_0/D = 0.59$  and  $A = 3.0$  for the spectrum of Samuel and Joubert, as given in Table 1. This difference must be due to the high adverse pressure gradient at  $X_0/D = 4.13$ ,  $a = 0.12$ , in comparison with the other two cases,  $a = 0.03$  and  $0.0021$ , respectively. The corresponding spectral equation with  $A = 17.0$  is marked with the solid line in Figure 5. In addition, the high adverse pressure gradient at  $X_0/D = 4.13$  has negative second derivative (decreasing adverse pressure gradient), unlike the other two cases where the adverse pressure gradient is increasing.

If Figures 1 and 2 of the plots of pipe flow spectral data are compared with Figure 3a of boundary layer flow, it can be seen that the upper limit of the range of validity of  $k_{1,1}$  spectral law in terms of non-dimensional wavenumber  $k_{1,y}$  is approximately  $k_{1,y} = 1.0$ . Hence, the upper limit of the range of  $k_{1,1}$  spectral law in terms of non-dimensional wavenumbers appears to be  $k_{1,y} \approx 1.0$  for the pipe and boundary layer flows with favorable and zero pressure gradients, respectively. Due to the shift observed in the spectra in the presence of adverse pressure gradient, this upper limit is not valid in Figures 4 and 5. However, there is still a fixed upper limit of the region of  $k_{1,1}$  spectral law for a given group of spectral data at the same Reynolds number. Therefore, the peel-off of the spectra from the line of  $E_v(k_{1,y})/(y u_{\tau}^2) = A/(k_{1,y})$  with increasing distance from the wall can still be observed at  $X_0/D = 0.59$  and  $4.13$  of the present diffuser in Figures 4 and 5, respectively. Consequently, the range of  $k_{1,1}$  spectral law gets reduced with  $y$ .

In relation to the experimental results presented in Figures 4 and 5, two other points must be emphasized. First, although the production and dissipation of turbulence kinetic energy balance each other in the present pipe and boundary layer flows at the locations where  $k_{1,1}$  spectral law is

present, in accordance with the theories of Tchen; the same condition is not met in the present diffuser, according to the measurements of Kassab (1986). Secondly, as can be seen from a comparison of the corresponding  $m$  values given in Table 2 with Figures 4 and 5, low values of the shear parameter  $m$  and dominant nature of  $k, (-5/3)$  spectral law do not appear simultaneously in the diffuser, as would be expected according to Panchev (The dissipation values used in preparing Table 2 were corrected for finite wire length and high turbulence intensity following Azad and Kassab (1986)).

As expected,  $m$  values calculated using  $m = \delta U / \delta y / (\epsilon / \nu)^{1/2}$  and  $m = [\nu / (\chi y u_{\mu}^2)]^{1/2}$  are in close agreement in the present pipe and boundary layer flows where the logarithmic law of the mean velocity is present. However, in the present diffuser, they are quite different. By  $X_0/D = 0.59$ , the logarithmic law disappears despite its presence in the pipe flow at the inlet to the diffuser. On the other hand, although the logarithmic law reappears by  $X_0/D = 4.13$ , the difference between the  $m$  values calculated from these two equalities is even more than it is at  $X_0/D = 0.59$ . This discrepancy can be explained by the fact that according to the measurements of Kassab, the turbulence kinetic energy dissipation at  $X_0/D = 4.13$  is not inversely proportional to the distance from the wall, as assumed in the derivation of Panchev (1985) :  $\epsilon = u_{\mu}^2 (\delta U / \delta y) = u_{\mu}^2 / (\chi y)$ .

Equation (7.9) of Perry and Chong (1982) is plotted in Figure 6 for different number of "observed" hierarchies, up to  $N_0 = 40$ . Following Perry and Chong,  $y_1/y_0 = 10$  was used. In addition, the constant of proportionality, and the value of  $h$  were taken to be unity in the previous equation. Perry and Chong modify this equation with a constant multiplier to obtain a functional form to represent  $k, (-5/3)$  spectral law. The resultant equation, Equation (7.12) of their paper is plotted in Figure 7. As seen in Figures 6 and 7, the previously mentioned functional forms for  $E_i(k, y) / (y u_{\mu}^2)$  have slopes proportional to  $(k, y)^{(-1)}$  and  $(k, y)^{(-5/3)}$ , respectively, for high values of the non-dimensional wavenumber  $(k, y)$ . For lower wavenumbers, both of these functions give constant values. The level of this constant value increases

with increasing hierarchy. Hence, these functional forms are consistent with the experimental data in that they show the slopes expected for the presence of  $k,^{-1}$  and  $k, (-5/3)$  spectral laws. Moreover, the peel-off from the regions with these slopes shifts to lower wavenumbers with increased hierarchy. This behavior would indicate decreasing hierarchy with increasing distance from the wall. However, these functional forms are not applicable to spectral data without further modification. The reason is that, as indicated by Figures 6 and 7, the resulting plots need to be shifted towards higher wavenumbers and lower energy levels to be able to match the experimental data.

#### 4. CONCLUSION

The conclusions drawn from the experimental data presented can be classified in four groups. The first conclusion is regarding the logarithmic law of the mean velocity in relation to the presence of  $k,^{-1}$  spectral law of the velocity fluctuation in the direction of the mean velocity. In the pipe and boundary layer flows, under favorable and zero pressure gradients, respectively, the logarithmic law and  $k,^{-1}$  spectral law appear to exist at the same transverse position simultaneously. However, the presence of adverse pressure gradient modifies this picture. Under mild adverse pressure gradient, the flow shows the same characteristics as the pipe and boundary layer flows regarding the logarithmic law and  $k,^{-1}$  spectral law, except that the value of the coefficient  $A$  is different for this case, as will be pointed out. In the case of high adverse pressure gradient, two distinct cases have been observed. Under increasing adverse pressure gradient, i.e. when the second longitudinal derivative of the mean pressure is positive,  $k,^{-1}$  spectral law has been found to exist without any logarithmic region of the mean velocity. On the other hand, under decreasing adverse pressure gradient, although the logarithmic law exists, the transverse ranges of the logarithmic law and  $k,^{-1}$  spectral law are different.

The second conclusion is that the value of the coefficient  $A$  is also different under favorable, zero and adverse pressure gradients. In the pipe and boundary layer flows, the experiments prior to 1975 indicate  $A$  to be about 0.8; whereas in the more recent experimental results, including the

present ones, the value of  $A$  has been found to be 0.9. On the other hand, under adverse pressure gradient,  $E(k,y)$  spectra have been found to appear "shifted" with respect to spectra under favorable and zero pressure gradients. Hence, higher  $A$  values are found under adverse pressure gradient in general. More specifically, the value of  $A$  is even higher under decreasing adverse pressure gradient than it is under increasing adverse pressure gradient.

The third conclusion is regarding the range of  $k^{-1}$  spectral law in terms of distance from the wall, and the effect of Reynolds number on this range. Most importantly, the ranges defined by Abell and Henbest are strictly for pipe flow. An extension can only be made to include boundary layer flows for the validity of the combined range of these two workers in terms of  $y^+ > 100$ , and  $y/R_f < 0.14$ , defining lower and upper bounds of the range, respectively (Here,  $R_f$  is a reference length, such as the pipe radius, or the boundary layer thickness). Furthermore, in the case of pipe and boundary layer flows, the upper bound of the range can also be expressed in terms of the non-dimensional wavenumber, as  $k,y \approx 1.0$ , as Kader and Yaglom pointed out. However, under adverse pressure gradient, due to the "shift" in the spectra, the same range is not valid, in either of the two previous forms. The lower bound has to be extended to  $y^+ > 50$ , approximately, to be able to include adverse pressure gradient cases. Moreover, the upper bound is no longer  $k,y \approx 1.0$  in the case of adverse pressure gradient.

In the case of boundary layer flows, the lower end of the  $k^{-1}$  spectral law region as a function of non-dimensional wavenumber shifts to lower values of  $k,y$  as Reynolds number increases. As a result of this shift, a spectrum at a lower Reynolds number peels off from the line of  $A/(k,y)$  earlier than another spectrum at a higher Reynolds number, assuming that the same distance from the wall is kept in both cases. Consequently, the spectrum with higher Reynolds number shows a larger region of  $k^{-1}$  spectral law. The same conclusion could also be reached for pipe flow; however, the data presented here are not conclusive.

The fourth conclusion of the present work is that the ideas of Tchen and Panchev are not valid

in all wall-bounded flows. Consequently, this study points out emphatically that certain facts observed in one flow cannot be extrapolated to other flows without thorough examination.

The authors would like to thank Dr. S. W. Greenwood for reading the original manuscript, and K. Tarte for his technical help. The financial support for the work by NSERC Canada is highly appreciated. O. Turan and S. Z. Kassab would like to acknowledge the University of Manitoba Graduate Fellowship.

#### REFERENCES

- Abell, C. J. 1974: Scaling laws for pipe flow turbulence. Ph. D. thesis, University of Melbourne.
- Azad, R. S. 1983: Corrections to measurements by hot wire anemometer in proximity of a wall. Report METR-7, University of Manitoba.
- Azad, R. S.; Hummel, R. H. 1981: Structure functions of turbulence in an adverse pressure gradient. *Phys. Fluids*, 24(10), 1774-1779.
- Azad, R. S.; Kassab, S. Z. 1984: Examination of the  $k^{-1}$  spectrum in wall-bounded shear flow. *Bull. APS*, 29(9), 1521.
- Azad, R. S.; Kassab, S. Z. 1986: A new method of obtaining dissipation. Paper submitted to *J. Fluid Mech.*
- Bradshaw, P. 1965: A compact, null-reading, tilting U-tube micromanometer with a rigid liquid container. *J. Sci. Instrum.* 42, 677-680.
- Bradshaw, P.; Galea, P. V. 1967: Step induced separation of a turbulent boundary layer in incompressible flow. *J. Fluid Mech.* 27(1), 111-130.
- Dang, T. 1986: Experimental investigation of the hot-film anemometry in fully-developed turbulent pipe flow. M. Sc. thesis, University of Manitoba.
- Frei, D.; Thomann, H. 1980: Direct measurement of skin friction in a turbulent boundary layer with a strong adverse pressure gradient. *J. Fluid Mech.* 101, 79-95.
- Head, M. R.; Bandyopadhyay, P. 1981: New aspects of turbulent boundary layer structure. *J. Fluid Mech.* 107, 297-337.
- Henbest, S. 1983: The structure of turbulent pipe flow. Ph. D. thesis, University of Melbourne.
- Hinze, J. O. 1975: *Turbulence*. Second ed., 348-349, McGraw Hill.
- Kader, B. A.; Yaglom, A. M. 1984: Turbulent structure of an unstable atmospheric surface layer. In: *Nonlinear and turbulent processes in physics*. (ed. R. Z. Sagdeev). 2, 829-845, Harwood Academic Publishers.
- Kassab, S. Z. 1986: Turbulence structure in axisymmetrical wall-bounded flows. Ph. D. thesis, University of Manitoba.
- Klebanoff, P. S. 1955: Characteristics of turbulence in a boundary layer with zero pressure gradient. NACA Report 1247.
- Klebanoff, P. S.; Diehl, Z. W. 1952: Some features of artificially thickened fully-developed turbulent boundary layers with zero pressure gradient. NACA Report 1110.
- Panchev, S. 1969: Exact elementary solutions of the spectral equation of non-stratified turbulent shear flow. *Phys. Fluids*, 12, 722-723. Also in: *Random functions and turbulence*. (1971), 219-224, Oxford: Pergamon Press.
- Panchev, S. 1985: Private communication with one of the authors (RSA).
- Patel, V. C. 1965: Calibration of the Preston tube and limitations on its use in pressure gradients. *J. Fluid Mech.* 23, 185-208.
- Patel, V. C.; Head, M. R. 1969: Some observations on skin friction and velocity profiles in fully-

developed pipe and channel flows. *J. Fluid Mech.* 38(1), 181-201.

Perry, A. E.; Abell, C. J. 1975: Scaling laws for pipe flow turbulence. *J. Fluid Mech.* 67(2), 257-271.

Perry, A. E.; Abell, C. J. 1977: Asymptotic similarity of turbulence structures in smooth and rough walled pipes. *J. Fluid Mech.* 79(4), 785-799.

Perry, A. E.; Chong, M. S. 1982: On the mechanism of wall turbulence. *J. Fluid Mech.* 119, 173-217.

Perry, A. E.; Henbest, S.; Chong, M. S. 1986: A theoretical and experimental study of wall turbulence. *J. Fluid Mech.* 165, 163-199.

Preston, J. H. 1950: The three-quarter radius Pitot tube flow meter. *The Engineer*, 190, 400-402.

Rotta, J. C. 1962: Turbulent boundary layers in incompressible flow. In: *Progress in aeronautical sciences*, (ed. A. Ferri, D. Kuchemann; L. H. G. Sterne) 2, 51-52, Oxford: Pergamon Press.

Samuel, A. E.; Joubert, P. N. 1974: A boundary layer developing in an increasingly adverse pressure gradient. *J. Fluid Mech.* 66(3), 481-505

Stewart, R. W.; Townsend, A. A. 1951: Similarity and self-preservation in isotropic turbulence. *Phil. Trans. Roy. Soc.* 243A, 359-386.

Tchen, C. M. 1953: On the spectrum of energy in turbulent shear flow. *J. Research of the National Bureau of Standards*, 50(1), 51-62.

Tchen, C. M. 1954: Transport process as foundations of the Heisenberg and Obukhoff theories of turbulence. *Phys. Rev.* 93(1), 4-14.

Trupp, A. C.; Azad, R. S.; Kassab, S. Z. 1986: Near-wall velocity distributions within a straight conical diffuser. Paper to be published in *Experiments in Fluids*, vol. 4.

Flow	Re	y*	y/R <sub>p</sub>	A
pipe:				
present	140,000	183.09	0.07	0.90
	140,000	287.72	0.11	0.90
Abell (1974)	80,000	150	0.09	0.78
	260,000	148	0.03	0.73
boundary layer:				
present	23,000	100.94	0.11	0.92
Klebanoff (1955)	67,742	125	0.05	0.80
Samuel-Joubert (1974)	79,836	66.7	0.025	3.06
diffuser:				
X <sub>0</sub> /D = 0.59	140,000	40.13	0.02	2.12
	140,000	60.18	0.03	1.85
X <sub>0</sub> /D = 4.13	140,000	82.5	0.08	17.11
	140,000	110.0	0.10	17.65

Table 1. Values of the coefficient A in the spectral equation,  $E_1(k_1)/(y u_0^2) = A/(k_1 y)$ , or equivalently,  $k_1 E_1(k_1)/u_0^2 = A$ , in different flows. R<sub>p</sub> denotes a reference length; namely, pipe radius, boundary layer thickness and local radius in pipe, boundary layer and diffuser flows, respectively.

Flow	y [mm]	m
pipe	0.5	0.78
	1.0	0.34
	2.0	0.19
	3.5	0.14
	5.5	0.11
boundary layer	0.5	1.99
	1.0	0.87
	2.0	0.33
	5.0	0.16
diffuser X <sub>0</sub> /D = 0.59	1.0	0.65
	1.5	0.28
	2.5	0.26
	4.5	0.19
	6.5	0.14
diffuser X <sub>0</sub> /D = 4.13	0.5	0.38
	1.0	0.21
	2.0	0.10
	4.0	0.07
	6.0	0.05
	8.0	0.05

Table 2. Values of the shear parameter,  $m = (\delta U/\delta y)/(u_0/\nu)^{1/2}$ , close to the wall in different flows examined in the present study.

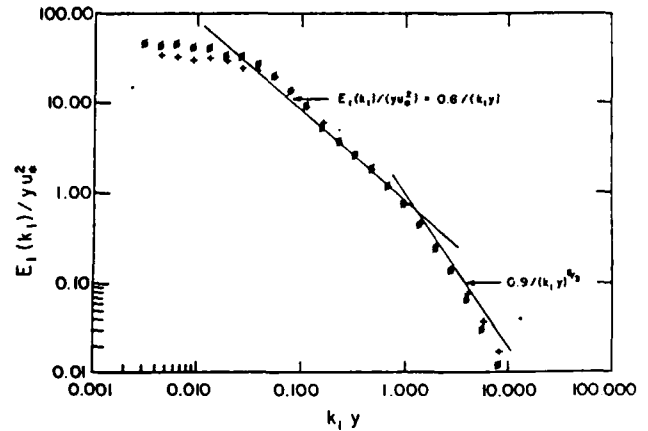


Figure 1. Normalized values of longitudinal spectrum  $E_1(k_1)$  in the fully-developed pipe flow. Only the spectra that indicate the presence of  $k_1^{-1}$  spectral law are given. —, empirical lines of Kader and Yaglom (1984); #,  $y = 3.5$  mm ( $y^* = 183.09$ ,  $y/R = 0.07$ ) and +,  $y = 5.5$  mm ( $y^* = 287.72$ ,  $y/R = 0.11$ ) in the present pipe flow.

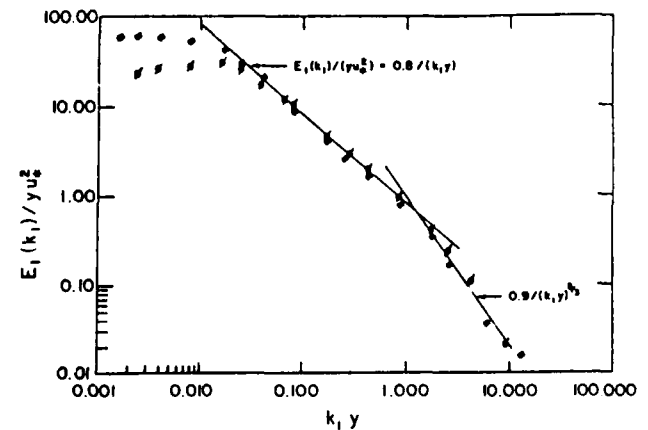


Figure 2. Normalized values of longitudinal spectrum  $E_1(k_1)$  in pipe flow showing the effect of Reynolds number change. Spectral data of Abell (1974): #, Re = 80,000,  $y = 5.2$  mm ( $y^* = 150$ ,  $y/R = 0.09$ ); +, Re = 260,000,  $y = 1.7$  mm ( $y^* = 148$ ,  $y/R = 0.03$ ).

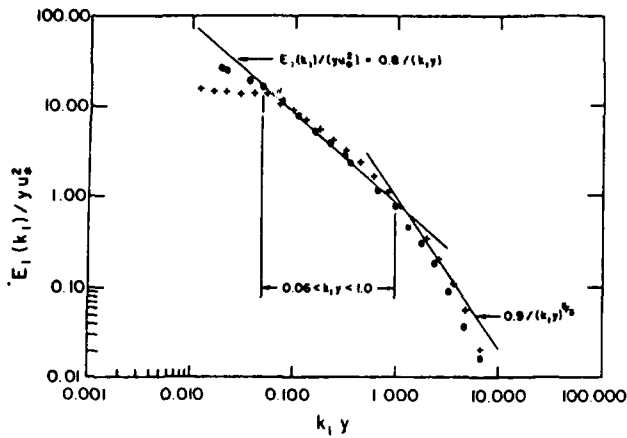


Figure 3a. Comparison of longitudinal spectral data of Klebanoff (1955) with those of the present boundary layer.  $\circ$ , Klebanoff's data,  $y = 3.6$  mm ( $y^* = 125$ ,  $y/\delta = 0.05$ );  $\times$ , data from the present boundary layer,  $y = 5.0$  mm ( $y^* = 100.94$ ,  $y/\delta = 0.11$ ).

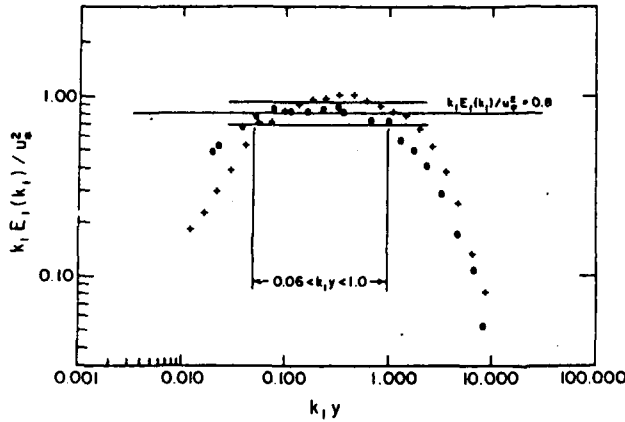


Figure 3b. Longitudinal spectrum  $E_1(k_1)$  normalized to obtain the values the coefficient  $A$  given in Table 1. The data and symbols are the same as in Figure 3a. NB. The error band on Klebanoff's data is based on the variation of the experimental values within the region of  $k_1^{-1}$  spectral law.

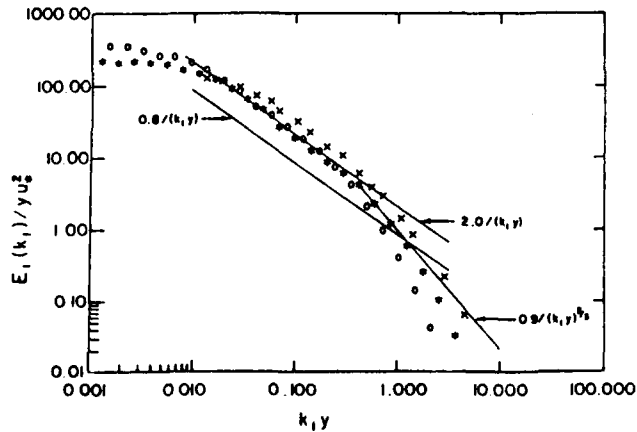


Figure 4. Comparison of longitudinal spectral data of Samuel and Joubert (1974) with those of the present diffuser flow at  $X_0/D = 0.59$ .  $\times$ , data of Samuel and Joubert, taken at 2.38 m from the first static pressure tap in their boundary layer tunnel and  $y = 1.28$  mm ( $y^* = 66.7$ ,  $y/\delta = 0.025$ ); present results,  $\circ$ ,  $y = 1.0$  mm ( $y^* = 40.13$ ,  $y/R_0 = 0.02$ ), and  $\cdot$ ,  $y = 1.5$  mm ( $y^* = 60.18$ ,  $y/R_0 = 0.03$ ).

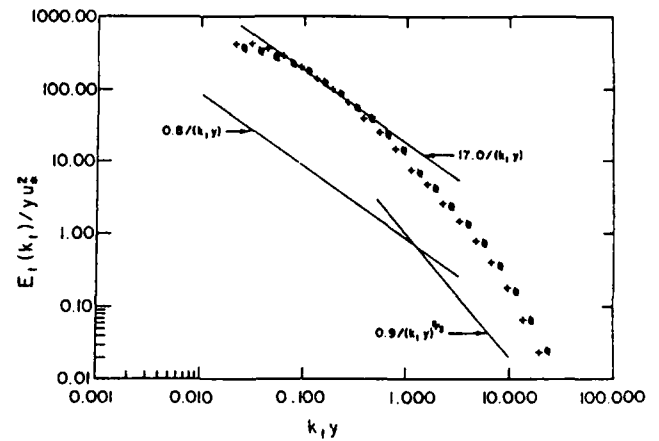


Figure 5. Normalized values of longitudinal spectrum  $E_1(k_1)$  in the present diffuser flow at  $X_0/D = 4.13$ .  $\times$ ,  $y = 6.0$  mm ( $y^* = 82.5$ ,  $y/R_0 = 0.08$ );  $\square$ ,  $y = 8.0$  mm ( $y^* = 110.0$ ,  $y/R_0 = 0.10$ ).

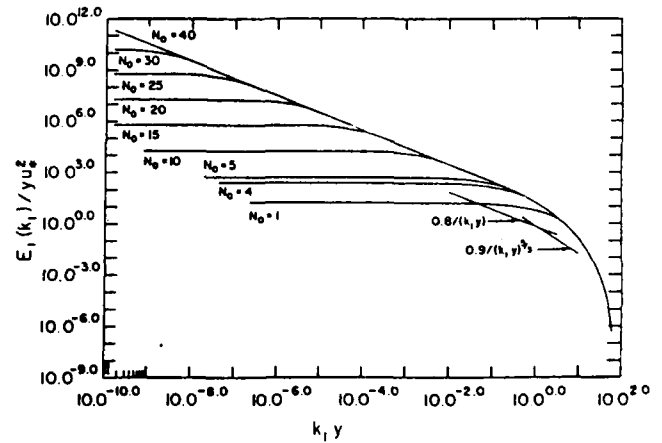


Figure 6. Plot of Equation (7.9) of Perry and Chong (1982) for different values of the hierarchy  $N_0$ . The curves corresponding to  $N_0 = 35$  and  $N_0 = 40$  are indistinguishable within the range of wavenumbers shown in the figure.

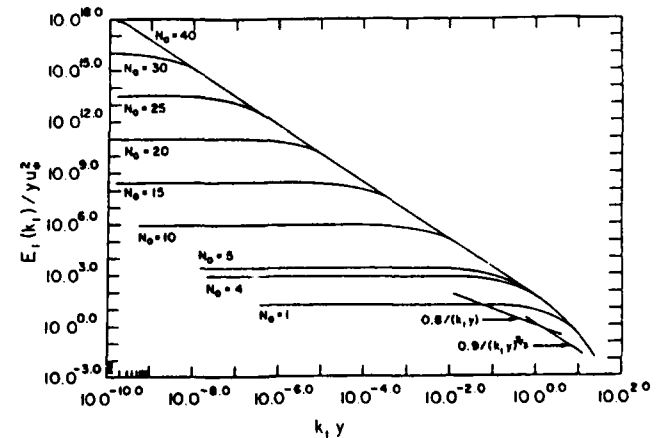


Figure 7. Plot of Equation (7.12) of Perry and Chong (1982) for different values of the hierarchy  $N_0$ . The curves corresponding to  $N_0 = 35$  and  $N_0 = 40$  are indistinguishable within the range of wavenumbers shown in the figure.

CIRCULAR JET: EFFECTS OF SINUSOIDAL  
FORCING AND STROUHAL NUMBER

Carlos A. Thompson  
Military Institute of Engineering.  
Brazil

ABSTRACT

The response of mean fluctuating fields in a circular air jet is obtained using hot-wire technique. Acoustic perturbation is introduced and the induced disturbance is measured and compared with Crow and Champagne [1]. In general the effects of sinusoidal forcing and Strouhal number are more pronounced fluctuating velocity than on mean velocity. Even for strong forcing amplitude the peaks of the fundamental occur at  $x/D \approx 4.0$  on the centerline and the congruence of the mean profiles is achieved using  $\Theta$  as the length scale. Some mean data are also compared with Bouchard and Reynolds [6].

NOMENCLATURE

D : Jet diameter  
f : Frequency of forcing  
H : Shape factor (see [9])  
Q : Mass flow  
 $R_D, R_{\delta^*}, R_\Theta, R_{\delta_w}$  : Reynolds numbers (see [9])  
 $St_D, St_{\delta^*}, St_\Theta, St_{\delta_w}$  : Strouhal numbers (see [9])  
U : Mean velocity component  
u : Fluctuating velocity component  
x : Distance in the direction of streaming  
 $x_o$  : The location of the hypothetical origin from the nozzle (see [9])  
y : Radial coordinate  
 $y_{0.1}$  : The y location at which the mean velocity is 10% of  $U_c$

$y_{0.5}$  : The y location which the mean velocity is 50% of  $U_c$ .  
 $\delta_{0.1}^*$  : Displacement thickness (see [9])  
 $\delta_w$  : Vorticity thickness (see [9])  
 $\Theta_{0.1}$  : Momentum thickness (see [9])

Subscripts

c : centerline  
e : exit  
f : fundamental  
t : forced

1. INTRODUCTION AND MOTIVATION

Turbulent shear flow is one of the least understood subject of the natural sciences. In the past two decades the discovery of large-scale coherent structures caused profound impact in the research about turbulent flow. The presence of coherent structures in circular jet was strongly suggested by Crow and Champagne [1] that imposed a controlled acoustic excitation to study the behavior of the mean and fluctuating velocity distributions near the jet exit. It was found that for low exit excitation amplitude and Strouhal number of 0.30, the fundamental component  $u_f$  reached the largest value at four diameters downstream from the nozzle. According to experimental techniques used the organized motions can appear even at extremely large Reynolds

number. In the fully developed region of a circular jet the incoherent turbulent is not affected by an artificial perturbation. Hussain [2] pointed out that when the excitation amplitude is large, the structure formation, evolution and decay are quite likely to be dependent on  $u_{fe}$ . It is worthwhile to notice that the induced or natural coherent structures are dynamically significant and must be responsible for the transports of mass, momentum and heat. Even though coherent structures related to axisymmetric jet are the objects of intensive contemporary investigations many simple questions about the interaction of the mean flow with the coherent and incoherent structures still remain unanswered. Hussain [2] proposed triple and double decompositions to analyze each variable into the governing equations for incompressible flow. The complexities of the differential equations do not permit an analytic solution although some insight can be obtained from a consideration of the energetics.

Hot-wire and flow visualization techniques have been a helpful tools to study circular jet under controlled excitation. Using these techniques Zaman and Hussain [3] investigated circular air jets subject to pure-tone acoustic excitation. They found that the conditions most favourable to vortex pairing were determined as a function of Strouhal number Reynolds number and the initial shear-layer state, i.e., laminar or turbulent.

Motivated by the studies of Thompson [4] and Hussain and Thompson [5] about plane jet, the present work documents the circular jet response to a sinusoidal acoustic perturbation, and the effects of high and low exit excitation amplitude, Reynolds number and Strouhal number on the natural coherent structures. For the

low forcing case the fundamental component  $u_f$  is compared with Crow and Champagne [1].

## 2. EXPERIMENTAL APPARATUS

Data were obtained by standard hot-wire techniques using DISA equipments. The r.m.s amplitude of the fundamental component was determined by a Lock-in-Analyzer (P.A.R. 5024). Figure 1 displays the schematic diagram of the flow facility and the nozzle was constructed from laminated wood which the internal contour follow a cubic equation. The jet diameter in this study is held constant and equal to 10.0 cm. The contraction ratio 18:1 and the speaker (100 watts) were used such that a high exit excitation amplitude could be obtained in the jet flow.

## 3. RESULTS AND DISCUSSION

### 3.1 Mean Velocity

Figure 2 displays the unforced mean velocity component compared with Bouchard and Reynolds [6] at  $x/D = 0.0$ . It is clear that the effect of Reynolds number is small even for the forced case, as shown in figure 3. The dimensionless mass flux is plotted in figures 4 and 5 in the range  $0.0 \leq x/D \leq 3.0$  for the undisturbed and disturbed flow respectively. Observe that the Reynolds number, the Strouhal number and the amplitude of the imposed oscillations are the same used by Crow and Champagne [1] although these investigators took the mean velocity profiles at only 4 downstream stations (Fig.5). For the unforced case (Fig.4), the present research does not agree with the slope  $dQ/dx = 0.136 Q_e/D$  ( $x/D < 2$ ) calculated by Crow and Champagne [1]. The same discrepancies could be detected in the data  $Q(x)$  presented by Bouchard and Reynolds [6] (see Figs. 4 and 5).

Tables 1 and 2 summarize the local mean parameters at  $x/D = 0.0$ , for

$R_D = 106,000$ ,  $St_D = 0.30$  (for the forced case) and for  $u_{fe}/U_e = 0.0\%$ ;  $2.0\%$ ;  $5.0\%$  and  $8.0\%$ . The numbers in brackets correspond to the results of Crow and Champagne [1].

$u_{fe}/U_e$ (%)	$\delta_{0.1}^*$	$\theta_{0.1}$	$H_{0.1}$	$\delta_w$	$x_0/D$
0	0.41	0.17	2.38	0.63 [0.56]	-0.29
2	0.40	0.18	2.28	0.71	-0.11
5	0.43	0.18	2.35	0.67	0.01
8	0.46	0.19	2.37	0.70	-0.11

Tab.1 - Summary of initially laminar free shear layer data at  $x/D = 0.0$ ;  $R_D = 106,000$ ;  $St_D = 0.30$ ; dimensions in cm.

$u_{fe}/U_e$ (%)	$R_{\delta^*}(St_{\delta^*})$	$R_{\theta}(St_{\theta})$	$R_{\delta_w}(St_{\delta_w})$
0	439( - )	189( - )	666( - ) [1166]
2	426(0.0012)	187(0.001)	754(0.002)
5	452(0.0013)	192(0.001)	702(0.002)
8	486(0.0014)	205(0.001)	741(0.002)

Tab. 2 - Reynolds number and Strouhal number based on the local parameters shown in Tab. 1.

Observe that, there will be initially laminar boundary layers with a shape factor value  $H_{0.1}$  (Tab.1) close to that of the Blasius profile i.e., 2.59 although at  $x/D = 0.0$  large velocity fluctuations were observed in the present data (see also [7]). The discrepancies shown for the Reynolds number  $R_{\delta_w}$  seem to be the high uncertainties to obtain the vorticity thickness  $\delta_w$ . On the other hand the values of the Strouhal numbers  $St_{\theta}$  at different forcing sinusoidal oscillations  $u_{fe}$  (Tab.2) agree with the

"jet column mode" according to Zaman and Hussain [8].

The congruence of the mean velocity profiles for the undisturbed and disturbed cases confirms achievement of self-preservation of the mean flow field (Figs. 6 and 7). Even for strong forcing the momentum thickness  $\theta$  seems to be a good choice for the length scale. Since there are difficulties in measuring the low mean velocities at the outer part of shear layer, the momentum integral scale  $\theta_{0.1}$  is used according to Hussain and Zedan [9].

### 3.2 Fluctuating and Fundamental Velocity Components

Strong forcing amplitude has a significant effect on the fluctuating turbulent velocity (Fig. 8). The forced turbulence  $u_t$  seems to have a high intensity component  $u_f$  along the centerline for  $x/D < 6.0$ ;  $u_{fe}/U_e = 20.0\%$ ;  $St_D = 0.30$  and  $R_D = 61,602$ . For  $x/D > 9.0$  the turbulent field appears to be independent on  $u_{fe}$  and  $St_D$ . The effect of Strouhal number on the axial distributions of  $u$ ,  $u_t$  and  $u_f$  is quite clear when figures 8,9 and 10 are compared. For  $St_D = 0.60$  and  $x/D > 1.0$  the forced turbulence and the fundamental have completely different shapes (Figs. 9 and 10) which means that harmonics and subharmonics (vortex pairing) are generated by sinusoidal forcing ( $u_{fe}/U_e = 5.0\%$ ). On the other hand the peaks of  $u_t$  and  $u_f$  have the same location, i.e.,  $x/D \approx 4.0$  for  $St_D = 0.30$  (Fig.8). The same axial location was reported by Crow and Champagne [1] for  $u_{fe}/U_e = 2.0\%$  and  $St_D = 0.30$ . To investigate more closely the behavior of the forced turbulence near the jet lip, 15 data points are plotted in the range  $0.0 \leq x/D \leq 2.0$  (Fig.9). It is evident the effect of the fundamental  $u_f$  on the turbulence  $u_t$  along  $x/D < 1.0$ . Figures 11 and 12 display the axial

distribution of  $u_f(x)$  for  $St_D = 0.30$  and  $0.60$ ,  $u_{fe}/U_e = 2.0\%$  and  $Re_D = 61,602$ . The peak of  $u_f$  for  $St_D = 0.30$  (preferred mode, [1]) is much higher than that for  $St_D = 0.60$  although near the jet exit, i.e.,  $0.6 < x/D < 2.0$  the fundamental assumes higher values for  $St_D = 0.60$ . Crow and Champagne [1] did not get any conclusion about the behavior of  $u_f$  near the jet lip because only 4 data points were taken along the centerline in the range  $0.0 < x/D < 2.0$ .

In order to compare the influence of the exit excitation amplitude on the fundamental  $u_f(x)$ , the Strouhal number and the Reynolds number were fixed and equal to  $0.30$  and  $61,602$  respectively (Fig. 13). The data show that the peak of  $u_f$  appear to occur at  $x/D = 4.0$  for any value of  $2.0\% \leq u_{fe}/U_e \leq 28.0\%$ . Hence, large changes of  $u_{fe}$  do not alter noticeably the shape of the induced disturbance.

According to Crow and Champagne [1], little change of the forced turbulence  $u_t$  takes place as  $u_{fe}/U_e$  increases from  $2.0$  to  $4.0\%$ . The present work shows that this is not true (Fig. 14) although these discrepancies can probably be attributed to differences in the initial conditions [9].

#### 4. CONCLUDING REMARKS

Hot-wire study shows that controlled acoustic perturbations can remarkably alter the nearfield of a round jet. Small  $x$  intervals near the jet exit reveal that the entrainment  $dQ/dx$  presented by Crow and Champagne [1] should be recalculated. The shape factor  $H_{0.1}$  (Tab.1) used in this work indicates that the initial boundary layer, laminar although were observed large velocity fluctuations at the jet lip. The congruence of the mean velocity profiles for the high forced and unforced

cases was achieved using  $\theta$  as the length scale. In general the effect of Strouhal number, Reynolds number and the exit excitation amplitude on the mean field appears to be marginal as compared with the turbulent field. The value of  $St_D = 0.30$  can still be regarded as the "preferred mode" even for high amplitude forcing and high Reynolds number. Contrarily to Crow and Champagne [1] the axial distributions of  $u_t$  and  $u_f$  are far to reach saturation for high values of  $u_{fe}$ .

#### REFERENCES

1. Crow, S.C. and Champagne, F.H., (1971), "Orderly structure in jet turbulence", J.F.M., 48, part 3, p.p.547-591.
2. Hussain, A.K.M.F., (1983), "Coherent structures-reality and myth", Physics of Fluids, 26, pp.2816-2850.
3. Zaman, K.B.Q. and Hussain, A.K.M.F., (1980), "Vortex pairing in a circular jet under controlled excitation", J.F.M., 101, part 3, pp.449-491.
4. Thompson, C.A., (1975). "Organized motions in plane turbulent jet under controlled excitation", Ph.D dissertation, University of Houston.
5. Hussain, A.K.M.F. and Thompson, C.A., (1980), "Controlled symmetric perturbation of the plane jet: an experimental study in the initial region", J.F.M., 100, part 2, pp.397-431.
6. Bouchard, E.E. and Reynolds, W.C., (1982), "The structure and growth of the mixing layer region of the round jet", report TF17, Stanford University, California.

7. Francesco, S.N., (1986), "Coherent Structures in circular jet", Master Thesis, Military Institute of Engineering, Brazil.
8. Zaman, K.B.M.Q. and Hussain, A.K.M.F., (1980), "The mechanics of vortex pairing in an axisymmetric mixing layer", Turbulent Shear Flows, vol.2, p.p.327-343, Springer-Verlag Berlin Heidelberg, New York.
9. Hussain, A.K.M.F. and Zedan, M.F., (1978), "Effects of the initial condition on the axisymmetric free shear layer: Effect of the initial fluctuation level", The Physics of Fluids, 21, pp.1475-1481

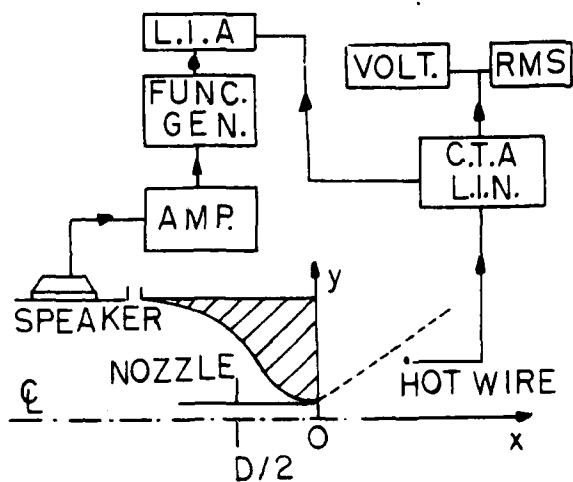


Fig. 1 - Jet flow facility and instrumentation.

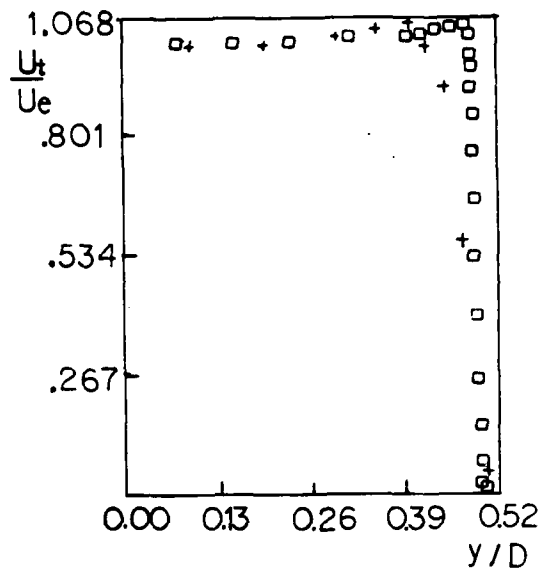


Fig. 2 - Unforced mean velocity at  $x/D = 0.0$ ;  $\square$ , present work ( $R_D = 106,000$ );  $+$ , [6] ( $R_D = 5,700$ ).

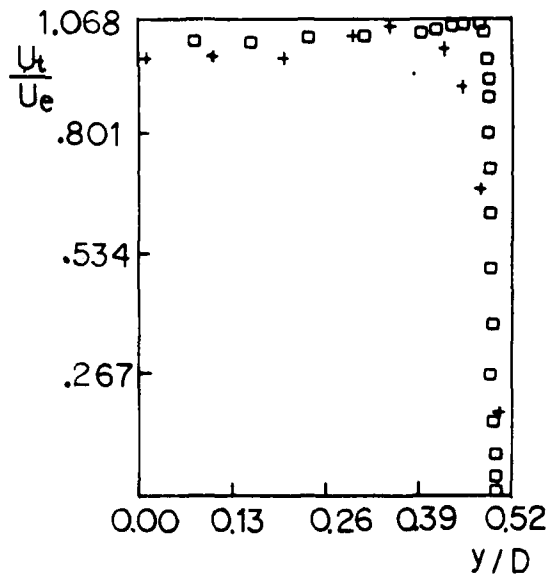


Fig. 3 - Forced mean velocity at  $x/D = 0.0$ ;  $\square$ , present work ( $R_D = 106,000$ ;  $St_D = 0.30$ ;  $u_{fe}/U_e = 8.0\%$ );  $+$ , [6] ( $R_D = 5,700$ ;  $St_D = 0.36$ ;  $u_{fe}/U_e = 33.0\%$ ).

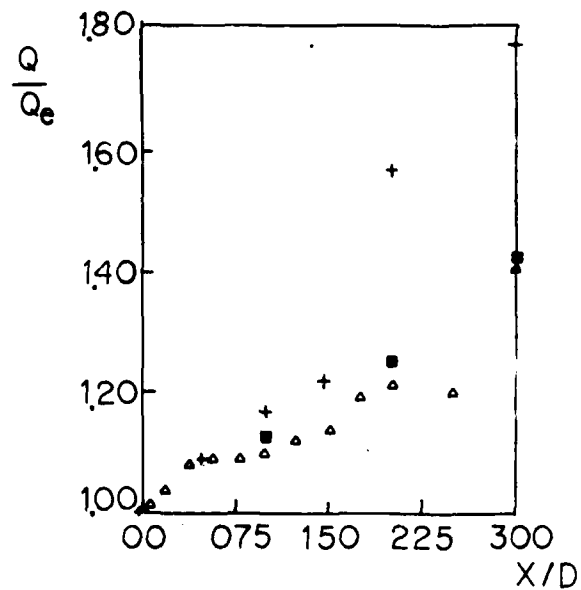


Fig. 4 - Axial variations of mass flux for the unforced case;  $\triangle$ , present work ( $R_D = 106,000$ );  $\blacksquare$ , [1] ( $R_D = 106,000$ );  $+$ , [6] ( $R_D = 5,700$ ).

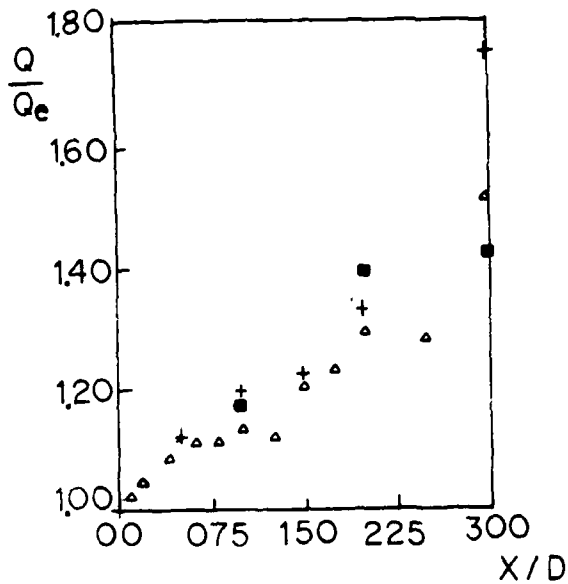


Fig. 5 - Axial variations of mass flux for the forced case;  $\Delta$ , present work ( $R_D = 106,000$ ;  $St_D = 0.30$ ;  $u_{fe}/U_e = 2.0\%$ );  $\blacksquare$ , [1] ( $R_D = 106,000$ ;  $St_D = 0.30$ ;  $u_{fe}/U_e = 2.0\%$ );  $+$  [6] ( $R_D = 5,700$ ;  $St_D = 0.36$ ;  $u_{fe}/U_e = 3.3\%$ ).

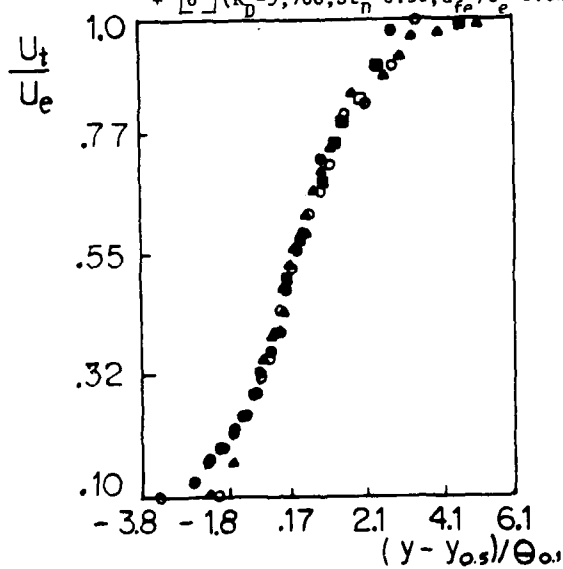


Fig. 7 - Shear layer mean velocity profiles for the forced case ( $R_D = 106,000$ ;  $St_D = 0.30$ ;  $u_{fe}/U_e = 8.0\%$ ) at various axial stations; (see symbols in Fig. 6).

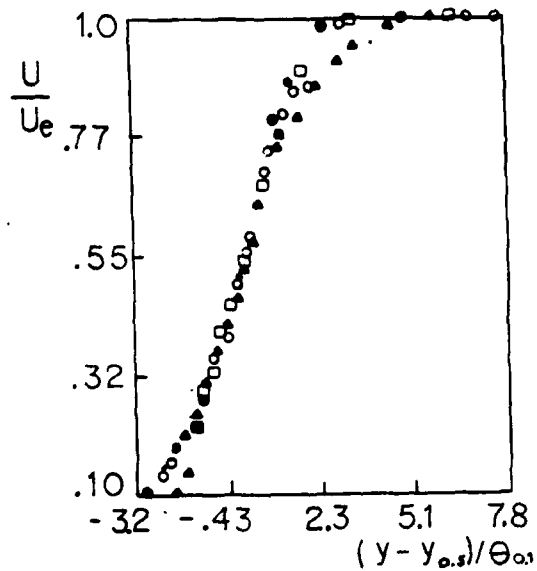


Fig. 6 - Shear layer mean velocity profiles for the unforced case ( $R_D = 106,000$ ) at various axial stations;  $\Delta$ ,  $x/D = 0.0$ ;  $\circ$ ,  $x/D = 0.4$ ;  $\blacksquare$ ,  $x/D = 1.0$ ;  $\diamond$ ,  $x/D = 1.5$ ;  $\bullet$ ,  $x/D = 2.0$ ;  $\circ$ ,  $x/D = 3.0$ .

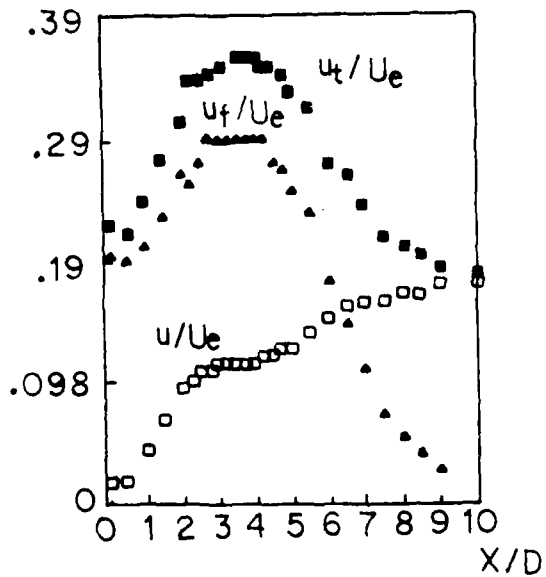


Fig. 8 - Axial variations of  $u$ ,  $u_t$ , and  $u_f$  for  $R_D = 61,602$ ;  $St_D = 0.30$  and  $u_{fe}/U_e = 20.0\%$  (centerline)

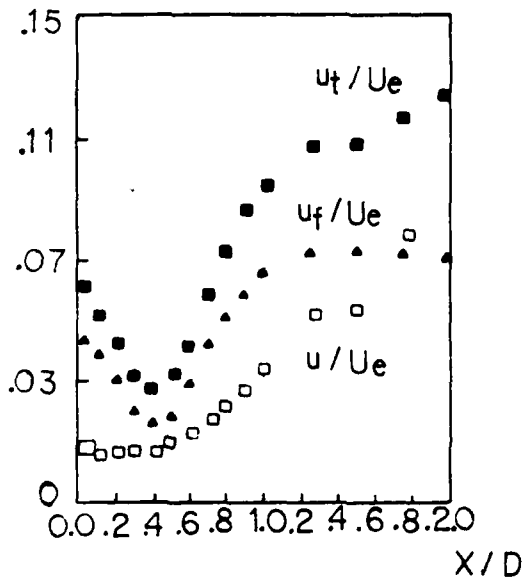


Fig. 9 - Axial variations of  $u$ ,  $u_t$  and  $u_f$  for  $R_D = 61,602$ ;  $St_D = 0.60$ ;  $u_{fe}/U_e = 5.0\%$  in the range  $0.0 < x/D < 2.0$  (centerline)

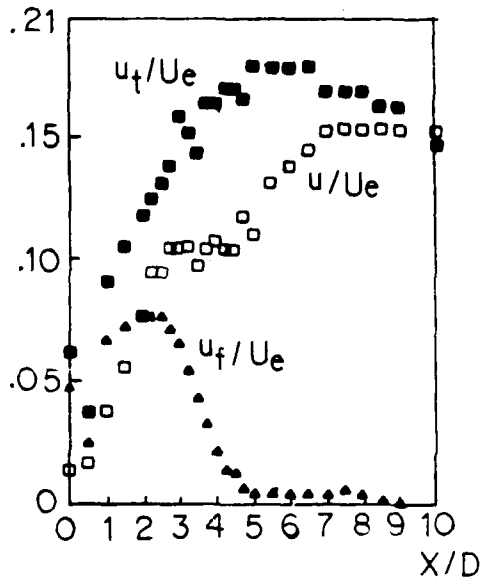


Fig. 10 - Axial variations of  $u$ ,  $u_t$  and  $u_f$  in the range  $0.0 < x/D < 10.0$  (see parameters in Fig. 9)

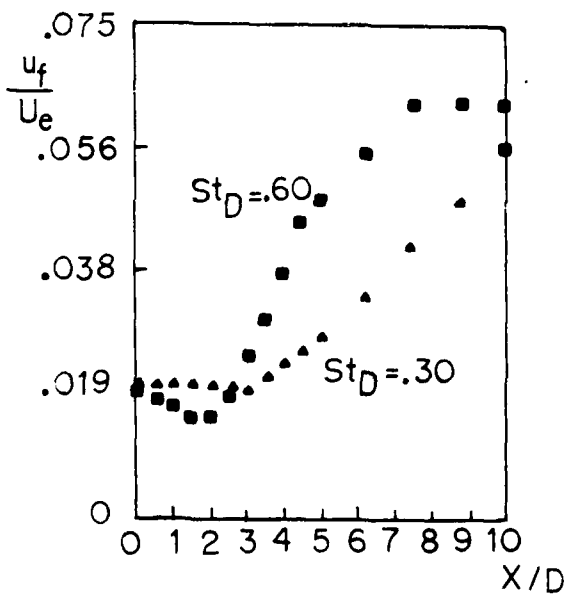


Fig. 11 - Axial variations of  $u_f$  for  $R_D = 61,602$ ;  $u_{fe}/U_e = 2.0\%$  in the range  $0.0 < x/D < 2.0$  (centerline)

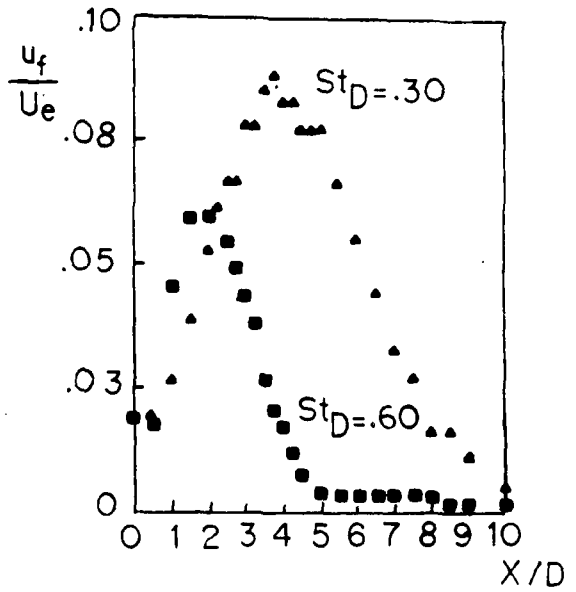


Fig. 12 - Axial variations of  $u_f$  in the range  $0.0 < x/D < 10.0$  (see parameters in Fig. 11)

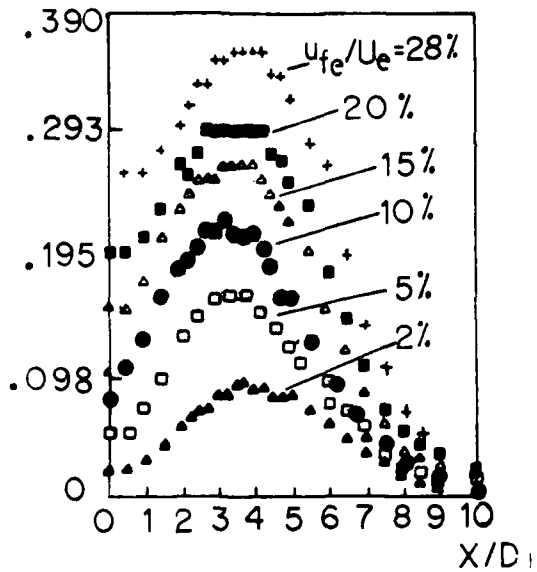


Fig. 13 - Axial variations of  $u_f$  for  $R_D = 61,602$  and  $St_D = 0.30$  (centerline)

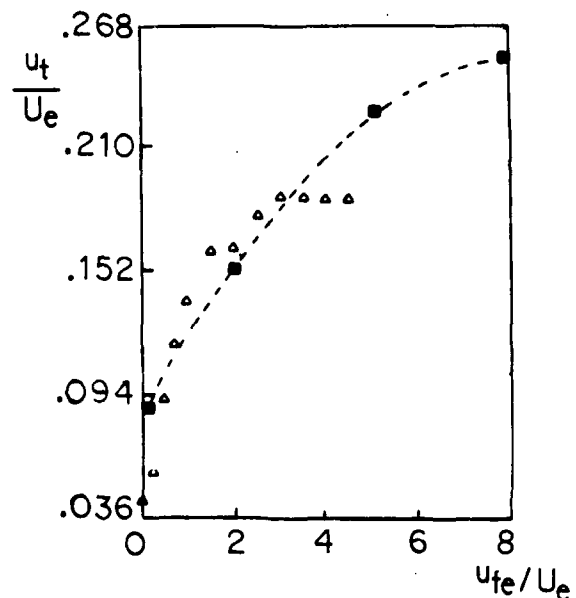


Fig. 14 - Amplitude response functions measured on the centerline at  $x/D = 4.0$  for  $R_D = 106,000$  and  $St_D = 0.30$ ;  $\blacksquare$  present work;  $\blacktriangle$ , [1].

DISTRIBUTION OF CONVECTION VELOCITIES  
AND LIFETIMES OF TURBULENCE STRUCTURES  
IN FULLY-DEVELOPED PIPE FLOW.

J.C.S. LAI<sup>+</sup> and K.J. BULLOCK<sup>++</sup>

<sup>+</sup>University of New South Wales.

<sup>++</sup>University of Queensland.

Australia.

ABSTRACT

The distribution of convection velocities of fully developed turbulence in a smooth pipe has been studied for a Reynolds number of 134,000 by obtaining correlations of the longitudinal component of turbulence with non-zero transverse and longitudinal separations at  $y^+ = 70$  and 200. Three dimensional power spectral density functions were generated by taking Fourier transforms of the correlations. Two estimates for the lifetime of turbulence structures have been derived, one from the spectral sheet thickness data, the other from the phase-shifting effects of shear contained in the relative phase data of the cross-correlations with non-zero transverse and radial separations. The data reported cover a wave size range of about 20 and substantially verify the similarity hypothesis.

1. INTRODUCTION

The understanding of the mechanism of turbulence is fundamental to predicting and improving the performance of heat and momentum transfer in everyday engineering situations. Turbulence consists of random velocity fluctuations and a common approach to studying a turbulent flow using statistical methods is to decompose the instantaneous velocity into a mean velocity component and a turbulent fluctuating velocity component. Following Reynolds (1895), a time averaging process with time scale long compared with the turbulent

fluctuations may be applied to the Navier-Stokes equations, resulting in nine unknown correlations between the various fluctuating velocity components of which six are independent. This is known as the closure problem of turbulence. Consequently, the structure of turbulence can be studied via two-point space-time correlations of the turbulent velocity field which involve three velocity components ( $u, v, w$ ) with six pair combinations. In pipe flow, by assuming stationarity in the space ( $x, z$ ) and the time ( $t$ ) variables (defined in Figure 1), there are still five arguments in the correlation functions:  $\Delta x (=x_1 - x_2)$ ,  $\Delta z (=z_1 - z_2)$ ,  $\Delta t (=t_1 - t_2)$ ,  $y_1$  and  $y_2$ . If  $N$  is the number of points required to define a correlation function in any of the four coordinates (three space and time) then  $6N^5$  data are necessary for a full description of the two-point correlations of three turbulent velocity components at each Reynolds number. For  $N=20$ , the total number of data points required amounts to  $2 \times 10^7$ . It can thus be seen that description of turbulence by multi-point space-time correlations would render the interpretation of these data almost impossible.

Fully-developed flow in smooth pipe, being one of the simplest cases of shear flow turbulence, has received much attention in the past, for example, Favre, Gaviglio & Dumas (1957), Tritton (1967) and Sabot & Comte-Bellot (1973). However, the structural interpretation of time-delayed correlations and data in the

untransformed variables ( $\Delta x, \Delta z, \Delta t, y_1, y_2$ ) is difficult. By performing measurements of the longitudinal  $R_{uu}(\Delta x, \Delta z=0, \omega, y_1=y_2)$  and transverse  $R_{uu}(\Delta x=0, \Delta z, \omega, y_1=y_2)$  correlations of the longitudinal component  $u$  of turbulence in narrow frequency bands and by taking Fourier transforms of the correlation functions so that power spectral densities are formed with frequency,  $\omega$ , and longitudinal or transverse wave-numbers,  $k_x$  or  $k_z$ , as the independent variables, Morrison & Kronauer (1969) successfully demonstrated that their data may be interpreted in the light of a stochastic wave model with coordinates as specified in the wave schematic diagram in Figure 2. By introducing a similarity variable  $k^+y^+$  based on the wave number  $k^+$  and the distance  $y^+$  from the wall, Morrison & Kronauer (1969) were able to collapse their turbulence data in wavenumber space. In particular, the two-dimensional power plots can be written as

$$P(\omega^+, k^+y^+) = f(k^+y^+)A(\omega^+, k_z^+) \quad (1)$$

where  $f$  is the 'wave intensity function'

$A$  is the 'wave strength'

$$k = [k_x^2 + k_z^2]^{\frac{1}{2}} \quad k^+ = kv/u_\tau$$

$$y^+ = yu_\tau/\nu \quad \omega^+ = \omega\nu/u_\tau^2$$

$$\alpha = \tan^{-1} k_x/k_z$$

$\nu$  is the kinematic viscosity of the fluid

$u_\tau$  is the friction velocity

and superscript + refers to normalisation with respect to  $\nu$  and  $u_\tau$ .

With the introduction of a correction procedure which is independent of Reynolds number and applicable to waves of all sizes, Morrison & Kronauer (1969) were also able to extend the similarity concept from the region where the mean velocity profile is logarithmic down to the sublayer regions. More recent work by Perry & Abell (1975) shows that the turbulence intensity correlates well through a similarity variable for the region between  $y^+=100$  and  $y/R=0.1$ . The wall pressure fluctuation data of Bull (1967) and the static pressure and velocity fluctuation data obtained by Elliot (1972) in atmospheric boundary layer are

consistent with the measurements of Morrison & Kronauer (1969). Cross correlations  $R_{uu}(\Delta x=0, \Delta z=0, \omega, y_1, y_2)$  and spectra measured by Bullock et al (1978) demonstrate that low frequency, large scale turbulent fluctuations extend over the majority of the radial region and that these components are highly correlated. By using a similarity variable  $k_x y$ , along with a normalized wall distance  $y/y_{ref}$ , both correlation functions, i.e., the Co and Quad components, are shown to collapse, thus further supporting the similarity hypothesis.

The wave description, if verified to be valid, will therefore, reduce the massive correlation data to one 'wave strength function' as a function of two variables ( $k_x^+$  and  $k_z^+$ ) and a few auxiliary functions of one variable ( $k^+y^+$ ) only. This implies all the properties of turbulence can be summarized in the power distribution over the power sheet and the function of  $k^+y^+$ . The objectives of this study were to extend the measurements of Morrison & Kronauer (1969) by obtaining three-dimensional spectra at  $y^+=70$  and  $y^+=200$ , and cross-correlations  $R_{uu}(\Delta x^+=0, \Delta z^+, \omega^+, y_1^+, y_2^+)$  between  $y_2^+=50, 100, 200, 400$  and  $600$  and  $y_1^+=100$  for a friction velocity  $u_\tau$  of 0.61 m/s. Evidence of structural similarity in the data is examined and two estimates for the lifetime of turbulence structures have been derived and discussed.

## 2. EXPERIMENTAL CONDITIONS

Two experiments have been performed.

### 2.1 3DSPEC EXPERIMENT

In the first experiment, referred hereafter to as 3DSPEC experiment, correlations  $R_{uu}(\Delta x^+, \Delta z^+ | \omega^+)$  of the longitudinal component of turbulence  $u$  in a smooth pipe of diameter 254 mm and length 14.675 m were generated simultaneously in seven narrow frequency bands at two fixed distances from the wall, namely,  $y^+=70$  and 200, by using an automated data acquisition system which jointly varied the longitudinal and transverse separations of two hot-wire probes operated in constant temperature

mode. The pipe flow Reynolds number was 134,000 (based on centre-line velocity and pipe radius  $R$ ) and the centre frequencies of the bandpass filters were 205, 257, 325, 409, 515, 650 and 819 Hz corresponding to non-dimensional circular frequencies  $\omega^+$  of 0.0536, 0.0672, 0.0850, 0.1070, 0.1374, 0.1700, and 0.2142 respectively. The measurement stations were located between 52.75 and 56.75 pipe diameters downstream of the pipe entrance. A total of 1306 and 2551 spatial separations were used for generating the correlations at  $y^+=70$  and 200 respectively. The corresponding maximum longitudinal separations are  $\Delta x^+=6500$  and 10500 and the maximum transverse separations are  $\Delta z^+=572.28(6.65^\circ)$  and  $1381.22(16.5^\circ)$ . The longitudinal resolution  $\Delta x^+$  for both  $y^+=70$  and 200 is 40, corresponding to spatial Nyquist wavenumber  $k_x^+=0.079$  whereas the respective transverse resolutions  $\Delta z^+$  are 30.12 and 25.13, corresponding to  $k_z^+=0.10$  and 0.125. By taking Fourier transforms of the correlations, power spectral density functions  $\phi(k_x^+, k_z^+, \omega^+)$  were obtained with frequency  $\omega^+$  and longitudinal and transverse wavenumbers,  $k_x^+$  and  $k_z^+$ , as independent variables.

## 2.2 Rθ EXPERIMENT

In the second experiment, referred hereafter to as Rθ experiment, cross correlations  $R_{uu}(\Delta\omega^+=0, \Delta\theta, \omega^+, y_1^+, y_2^+)$  between the longitudinal component  $u$  at two points were obtained in a smooth aluminium tube of diameter 133.35 mm at 60 diameters downstream of the tube entrance for the following distances from the wall:  $y^+=50, 100, 200, 400$ , and 600 with 100 taken as the reference position, thus giving a total of 9 pairs of correlations, namely, 50/50, 50/100, 100/100, 200/200, 200/100, 400/400, 400/100, 600/600, 600/100. For each of these pairs of correlations, the following values of angular positions of one probe relative to another were used:  $0^\circ$ - $12^\circ$  in steps of  $1^\circ$ ,  $12^\circ$  to  $28^\circ$  in steps of  $2^\circ$ ,  $28^\circ$  to  $60^\circ$  in steps of  $4^\circ$ . The pipe flow Reynolds number was 69,000 based on the pipe radius and the centre-line velocity. As the correlation function is nonstationary normal to the wall, it is generally

a complex quantity consisting of a Co and Quad component, unless  $y_1^+=y_2^+$ . The Co and Quad correlation functions were obtained directly by applying a heterodyning technique to the hot-wire signals so that a Fourier transformation from time delay to frequency domain was by-passed. The frequencies used were 20, 60, 110, 220, 400, 550 and 700 Hz, corresponding to  $\omega^+=0.00523, 0.01569, 0.02876, 0.0575, 0.1046, 0.1438$  and  $0.183$  respectively. In order to analyse the data in the wavenumber space, the argument of the Co and Quad cross correlations have been first transformed from  $\Delta\theta$  to the transverse coordinate  $\Delta z^+$  through the tube radius  $R$ . The resulting correlations were then Fourier transformed and normalised to give the complex correlation coefficient  $Me^{j\phi}$  with  $k_z^+, y_1^+$  and  $y_2^+$  as the independent variables. Here  $M$  is the magnitude of the correlation coefficient and  $\phi$  is the relative phase between the velocity components  $u$  at  $y_1^+$  and  $y_2^+$ . It is noted that when  $y_1^+=y_2^+$ ,  $M=1.0$  and  $\phi=0$  and when  $y_1^+ \neq y_2^+$ , a value of  $M=1.0$  indicates that the wave components at the two stations are perfectly correlated with  $\phi$  being the phase shift necessary to yield maximum correlation.

## 3. RESULTS

### 3.1 SPECTRAL DENSITY RESULTS

The longitudinal correlation results obtained in the 3DSPEC experiment generally show the same trend as those reported by Morrison & Kronauer (1969). Contours for power spectral density functions are presented in the form  $k_x^+ k_z^+ \phi(k_x^+, k_z^+, \omega^+)$ , with typical plots being shown in Figure 3(a) and (b) for  $y^+=70$  and 200, both being for  $\omega^+=0.2142$ . It is obvious from Figure 3 that the longitudinal wavenumber  $k_x^+$  is constrained by the frequency  $\omega^+$  which has virtually no effect on the transverse wavenumber  $k_z^+$ . In order to illustrate the general effects of frequency  $\omega^+$  and the distance of the wall  $y^+$  on the power spectra, the spectral peaks for various  $\omega^+$  are plotted in Figure 4. Lines of constant wave size  $k^+$  and constant wave angle  $\alpha$  are also indicated. The slopes of the two

lines of best fit to the data, with correlation coefficient better than 0.97, for  $y^+=70$  and 200 are in the ratio of 1.27 which compares well with the ratio  $\log 200/\log 70$ . It is evident that at a given distance from the wall, the spectral peak moves from a smaller wave angle at lower frequency to a larger wave angle at higher frequency. For a given  $\omega^+$ , the spectral peak at  $y^+=200$  is associated with a wave of larger size and larger wave angle than at  $y^+=70$ . Furthermore, for a given  $\omega^+$ , waves of the smaller size that exist at  $y^+=70$  do not extend to  $y^+=200$ .

### 3.2 DISTRIBUTION OF CONVECTION VELOCITIES

The basic principles of the similarity hypothesis are listed as follows:

- (i) There is only one characteristic length scale, that is distance from the wall,  $y^+$ .
- (ii) There is only one characteristic time scale,  $T^+$ , that is  $(du^+/dy^+)^{-1}$ . Because of the logarithmic distribution of the mean velocity  $U^+$ ,  $T^+$  is proportional to  $y^+$ .
- (iii) Absolute velocity is irrelevant and only velocity relative to the local velocity  $U^+$  is relevant.

As a result of principle (iii), the experimental data will be examined for structural similarity in a coordinate system with no relative motion, that is, a coordinate system moving with the average local speed  $U^+(y^+)$ . Consider a two dimensional power spectrum as a function of  $\omega^+$  and  $k_x^+$ . Then  $(\Delta\omega^+)^{-1}$  associated with each  $k_x^+$  can be interpreted as the typical lifetime  $\tau^+$  for a disturbance of that size. In a coordinate system with no relative motion, this is expressed as

$$\Delta\omega^+ = \omega^+ - U^+k_x^+ \quad (2)$$

If  $(\Delta\omega^+)^{-1}$  is normalized by the local time scale  $T^+$ , then from principle (ii) above,  $T^+/\tau^+$  must

be proportional to  $y^+\Delta\omega^+$  and for similarity to be valid, this must be a function of  $k_x^+y^+$  and  $k_z^+y^+$  or alternatively,  $k^+y^+$  and  $\alpha$ , for a three dimensional spectral function  $k_x^+k_z^+\Phi(k_x^+,k_z^+,\omega^+)$ . That is, we must have,

$$y^+\Delta\omega^+ = h(k_x^+y^+,k_z^+y^+) = h(k^+y^+,\alpha) \quad (3)$$

Substituting equation (2) into equation (3), we get,

$$C_x^+-U^+ = g(k^+y^+,\alpha) \quad (4a)$$

$$\text{where } C_x^+ = \omega^+/k_x^+ \quad (4b)$$

Equation (4) indicates that for similarity to be valid, the term  $[C_x^+-U^+]$  for constant wave angle  $\alpha$  must be a function of  $k^+y^+$  only. Convection velocity  $C_x^+$  as a function of  $\alpha$  can be determined from the ridge line of the power spectral density contours as shown in Figure 3 and is plotted as  $[C_x^+-U^+]$  against  $k^+y^+$  for various  $\alpha$  in Figure 5. For small  $\alpha$ , there is some scatter in the data; however, within the limits of experimental accuracy, the results are independent of  $y^+$  and collapse very well for a given  $\alpha$ , thus supporting the similarity hypothesis. According to the geometrically similar wave model of Morrison & Kronauer (1969),  $C_x^+$  matches the mean fluid velocity at a certain  $y^+$  so that

$$C_x^+(k^+y^+)-U^+(y_0^+)=5.756 \log (k^+y_0^+/k^+y^+) \quad (5)$$

Here  $y_0^+$  is the distance to the wall where the data are taken. Equation (5) is a subset of equation (4) and is plotted in Figure 5 for  $k^+y_0^+=0.6$  for comparison with the present data. The model of Morrison & Kronauer (1969) agrees very well with the data for small wave angles such as  $\alpha=10^\circ$  but is not adequate to describe the data for large wave angles.

### 3.3 PHASE CURVES

As shown in Figure 3, frequency filtering constrains the wave sizes in the wavenumber

$k_x^+$ . In order to calculate the wave angle for the data obtained in the R0 experiment, a suitable convection velocity  $C_x^+$  is required to associate with each  $\omega^+$  a particular  $k_x^+$  by equation (4b). The minimum and maximum  $y^+$  used are 50 and 600 respectively, thus giving a geometric mean  $y^+$  of 173. It has been found that the streamwise convection velocity  $C_x^+$  obtained from the power spectral density plots (Figure 3(b)) at  $y^+=200$  is related to  $k^+$  by equation (6)

$$C_x^+ = 5.756 \log(1.28/k^+) + 5.5 \quad (6)$$

Since  $k_x^+ = k^+ \sin \alpha$ , by using equation (4b) and (6), values of  $k^+$  associated with various frequencies and wave angles  $\alpha$  can be calculated. A typical plot of the phase difference  $\phi$  in the complex correlation coefficient  $Me^{j\phi}$  as a function of  $k^+y^+$  is shown in Figure 6(a) for  $\alpha=25^\circ$ . It must be pointed out that since phase reference is arbitrary, Figure 6(a) was obtained by using  $k^+y^+=1$  as the phase reference for  $0^\circ$ . The data obtained at the reference  $y^+$  location of 100 were shown in the figure as flagged symbols to indicate the shift required for the phase curves to have a zero-crossing at  $k^+y^+=1$ . The collapse of the phase curve for various frequencies at  $\alpha=25^\circ$  is good. This is typical of phase curves at other wave angles  $\alpha$ , thus supporting the similarity hypothesis that the phase of the turbulence components is scaled by wave size  $k^+$  and distance from the wall  $y^+$ .

For  $\alpha \leq 60^\circ$ , the phase plots are straight lines for  $3 > k^+y^+ > 0.3$ . The lines of best fit to all the data up to  $\alpha=55^\circ$ , yielding correlation coefficient better than 0.980 in all cases, are shown in Figure 6(b). The phase gradient  $m(\alpha)$  defined by  $d\phi/d(\log k^+y^+)$  can be obtained for various wave angles  $\alpha$  as tabulated in Table 1. In fact, the phase gradient behaves quite closely like  $65^\circ \sec^2 \alpha$ , the values of which are tabulated for comparison with  $m(\alpha)$  in Table 1.

For a fixed size wave,  $k^+$ , the linear dependence of  $\phi$  on  $\log k^+y^+$  implies that  $d\phi/dy^+$

is inversely proportional to  $y^+$ , just as the velocity gradient  $dU^+/dy^+$ . That is, phase gradients are proportional to shear. Consider the fluid motions normal to the wall which tend to make the phases synchronise at different  $y^+$  while the shear processes tend to make the phase of the wave advance at the larger  $y^+$  vis-a-vis the lower  $y^+$ . The equilibrium phase gradient is a balance between the two processes and the phase gradient is largest where the shear is strongest (i.e. near the wall). The fact that the phase gradient is directly proportional to shear implies that the coordinating effect of the motions to and from the wall is the same at all  $y^+$ . For small wave angle  $\alpha$ , the shear becomes oriented toward the lines of constant phase and therefore the component of shear in the direction of the wave vector is reduced, resulting in smaller phase gradients. The  $\sec^2 \alpha$  behaviour of the phase gradient  $m(\alpha)$  may not be fortuitous because since  $\sec^2 \alpha = (k^+/k_z^+)^2 = (C_z^+/C^+)^2$  and  $\hat{w}$  waves are more predominant as the distance  $y^+$  from the wall increases (Fig. 4), the contribution of  $\hat{w}$  waves to the phase shift also increases. Since the shear component behaves like  $\sin \alpha$  (Fig. 2), the  $\sec^2 \alpha$  behaviour of the phase gradient  $m(\alpha)$  suggests that the motions toward the wall behave like  $\sin \alpha \cos^2 \alpha$ . Beyond  $k^+y^+=3$ , the phases jump around (Fig. 6(b)) probably due to the contribution of  $\hat{w}$  component.

Waves with angles between  $60^\circ$  and  $85^\circ$  contain a significant contribution from the  $\hat{w}$  component. For  $\alpha > 60^\circ$ , the  $180^\circ$  jump in the phase data occurs around  $k^+y^+ = 1.3$ , as shown in Fig. 6(c) for  $\alpha=85^\circ$ . This phenomenon of phase jump is also observed in the data of Elliot (1972) taken within the atmospheric boundary layer at heights between 1 and 5m. For  $k^+y^+ < 1$  and  $k^+y^+ > 2$ , that is, outside the region of phase jump, the phase data vary linearly with  $\log k^+y^+$ . In particular, for  $k^+y^+ < 1$ , the phase gradient  $m$  is  $65^\circ$  whereas for  $k^+y^+ > 2$ ,  $m$  has a value of  $-65^\circ$ .

**TABLE 1:**

Variation of parameters  $m(\alpha)$ ,  $p(\alpha)$  and  $g^{-1}(\alpha)$  with  $\alpha$ .

$\alpha$	5°	15°	25°	35°	45°	55°
$m(\alpha)$	58°	73°	80°	99°	130°	195°
$65^{\circ}\text{sec}^{\circ}\alpha$	65°	70°	79°	97°	130°	198°
$g^{-1}(\alpha)$	0.138	0.211	0.244	0.267	0.283	0.296
$p(\alpha)$	0.176	0.197	0.243	0.297	0.394	0.606

**TABLE 2:**

Variation of  $g^{-1}(k^+y^+, \alpha)$  with  $k^+y^+$  and  $\alpha$ .

$k^+y^+$	$\alpha$	15°	20°	30°	50°
0.1		0.179	0.200	0.235	0.283
0.5		0.200	0.220	0.250	0.285
1.		0.211	0.229	0.256	0.290
2.		0.222	0.236	0.263	0.292
5.		0.237	0.252	0.272	0.294

4. LIFETIMES OF TURBULENCE STRUCTURES

By invoking the similarity hypothesis that  $k_x^+$  is inversely proportional to  $y^+$ , equation (3) can be rewritten as

$$\Delta\omega^+ = k_x^+ g(k^+y^+, \alpha) \quad (7a)$$

or  $k_x^+ \tau^+ = g^{-1}(k^+y^+, \alpha) \quad (7b)$

$\Delta\omega^+$  can be determined by measuring the full width between the half-power points in the  $(k_x^+, k_z^+)$  plot of the spectral function  $k_x^+ k_z^+ \Phi(k_x^+, k_z^+, \omega^+)$  in the  $k_x^+$  direction, the half-width being  $k_x^+$ . Assuming the spectral sheet is thin and very closely aligned with the locus  $\omega^+ = k_x^+ l^+$ , we can deduce  $\Delta\omega^+$  from the following relationship:

$$\Delta\omega^+ = \Delta k_x^+ (\omega^+ / k_x^+) = l^+ (y_0^+) \Delta k_x^+ \quad (8)$$

where  $l^+(y_0^+)$  is the local velocity at the measurement station  $y_0^+$ .

From equation (3),  $y_0^+ \Delta\omega^+$  must be a function of  $k^+y^+$  and  $\alpha$  only. The  $y_0^+ \Delta\omega^+$  data extracted using equation (8) from the power spectral density functions (Fig. 3) are plotted against  $k^+y^+$  for three wave angles  $\alpha$  in Fig. 7. For each  $\alpha$ , although there is some scatter, the data for  $y^+=70$  and  $v^+=200$  collapse onto a straight line in the logarithmic plot, with correlation coefficient better than 0.96, as predicted by the similarity hypothesis. It must be pointed out that the data for  $\alpha=15^\circ$  were not shown in Fig. 7 as they tend to be very close to those for  $\alpha=20^\circ$ .

Since from equation (8),  $g^{-1}(k^+y^+, \alpha) = (k_x^+ y_0^+) \tau^+ / y^+ = k^+ y^+ \sin \alpha / (y_0^+ \Delta\omega^+)$ , the values of  $g^{-1}(k^+y^+, \alpha)$  can be obtained from Fig. 7 and are tabulated for various  $k^+y^+$  and  $\alpha$  in Table 2.

From Table 2,  $g^{-1}(k^+y^+, \alpha)$  is a slowly varying function of  $k^+y^+$  and for a first order approximation, can be considered as a function of  $\alpha$  only. The value of  $g^{-1}(k^+y^+, \alpha)$  at  $k^+y^+=1$  is taken as an estimate of the structural lifetime  $k_x^+ \tau^+$  and is tabulated in Table 1 as a function of  $\alpha$ .

There is another time scale  $\tau_\phi^+$  which indicates the period for the effect of the shear to persist in order that the observed phase shift in Fig. 6 can be generated. Let the mean local velocity, frequency, streamwise wavenumber and phase associated with the measured  $v_1^+$  station be  $l^+$ ,  $\omega^+$ ,  $k_x^+$ ,  $\phi$  respectively so that at  $y_2^+$ , the relevant parameters are  $l^+ + \Delta l^+$ ,  $\omega^+ + \Delta\omega^+$ ,  $k_x^+ + \Delta k_x^+$  and  $\phi + \Delta\phi$ . Then

$$\text{Displacement} = \tau_\phi^+ (\Delta l^+) = \Delta\phi / k_x^+ \quad (9)$$

Since from the logarithmic distribution of velocity  $l^+$ ,  $\Delta l^+$  is given by  $5.756 \log (y_2^+ / y_1^+)$  and since at any  $\alpha$ , the phase gradient  $m$  is a constant so that  $\Delta\phi = m \log (y_2^+ / y_1^+)$ , equation (9) can be rewritten as follows:

$$k_x^+ \tau_\phi^+ = \Delta\phi / \Delta l^+ = m / 5.756 = p(\alpha) \quad (10)$$

Results for  $p(\alpha)$  for various wave angles  $\alpha$  are tabulated in Table 1 for comparison with  $g^{-1}(\alpha)$ . For  $\alpha=5^\circ$  to  $35^\circ$ , it appears that  $p(\alpha)$

matches  $g^{-1}(\alpha)$  quite well. However the lifetime  $g^{-1}(\alpha)$  deduced from the three dimensional spectral function  $k_x^+ k_z^+ \phi(k_x^+, k_z^+, \omega^+)$  approaches an asymptote for  $\alpha > 35^\circ$  while the lifetime  $p(\alpha)$  deduced from shear continues to increase. If the structure is moving in  $y^+$ , the lifetime seen at a fixed  $y^+$  will be less than the total lifetime. However, the effect of shear persists with the structure and therefore reflects the total lifetime.

### 5. CONCLUSIONS

Two experiments for studying the structure of turbulence using statistical methods have been described. In the 3DSPEC experiment, three dimensional spectral density contours have been presented from which streamwise convection velocity can be determined. The convection velocity has been shown to be only a function of  $k^+ y^+$  and  $\alpha$  in a coordinate system moving with the average local speed. The geometrically similar wave model of Morrison & Kronauer (1969) is valid for small wave angles only. In the R $\theta$  experiment, phase plots for the complex correlation coefficient have been shown to be a function of  $k^+ y^+$  and  $\alpha$  only. These results substantiate the similarity hypothesis. Furthermore, an estimate of the lifetime of turbulence structure has been obtained as  $p(\alpha)$  from the phase data and as  $g^{-1}(\alpha)$  from the spectral sheet thickness data.

### 6. REFERENCES

Bull, M.K. 1967: Wall pressure fluctuations associated with subsonic turbulent boundary layer flow. *J. Fluid Mech.*, 28, 719.  
 Bullock, K.J., Cooper, R.E. and Abernathy, F.H. 1978: Structural similarity in radial correlations and spectra of longitudinal velocity fluctuations in pipe flow. *J. Fluid Mech.*, 88, 585.  
 Elliott, J.A. 1972: Microscale pressure fluctuations measured within the lower atmospheric boundary layer. *J. Fluid Mech.*, 53, 351.  
 Favre, A.J., Gaviglio, J.J., Dumas, R.J. 1957:

Space time double correlations and spectra in a turbulent boundary layer. *J. Fluid Mech.*, 2, 313.

Morrison, W.R.B. and Kronauer, R.E. 1969: Structural similarity of fully developed turbulence in smooth tubes. *J. Fluid Mech.*, 39, 117.

Perry, A.E. and Abell, C.J. 1975: Scaling laws for pipe-flow turbulence. *J. Fluid Mech.*, 67, 257.

Sabot, J., Renault, J. and Comte-Bellot, G. 1973: Space time correlations of the transverse velocity components in pipe flow. *Phy. of Fluids*, 16, 1403.

Tritton, D.J. 1967: Some new correlation measurements in a turbulent boundary layer. *J. Fluid Mech.*, 28, 439.

Reynolds, O. 1895: On the dynamical theory of incompressible viscous fluids and the determination of the criterion. *Phil. Trans Royal Soc. London, Series A*, 186, 123.

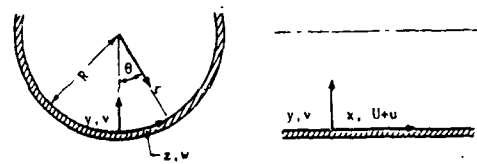


Fig. 1: Pipe coordinates and velocity components.

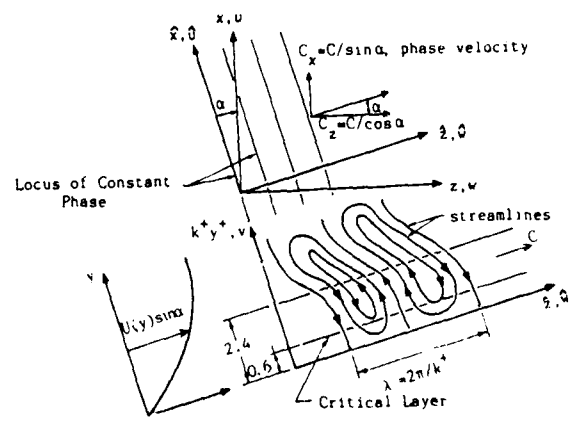


Fig. 2: Wave schematic diagram.

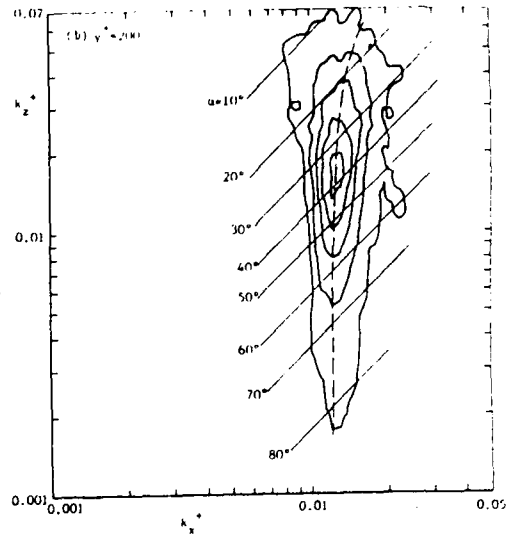
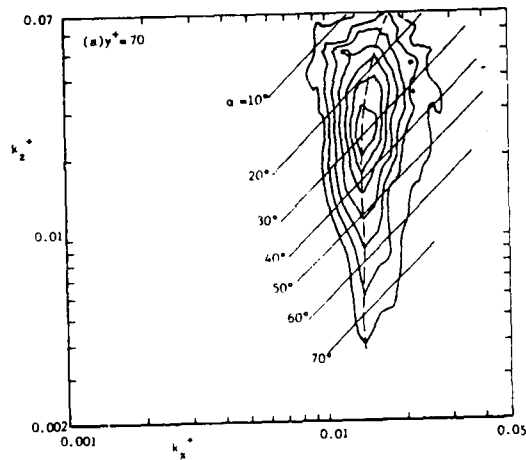


Fig. 3: Power spectral density contours for  $\omega^+ = 0.2142$ .

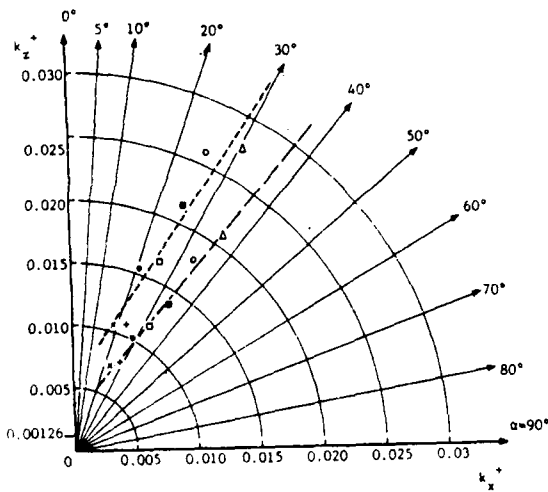


Fig. 4: Locus of spectral peaks  
 $(\omega^+ \times 0.0536, +0.0672, \bullet 0.085, \square 0.107,$   
 $\blacksquare 0.1347, \circ 0.17, \triangle 0.2142).$

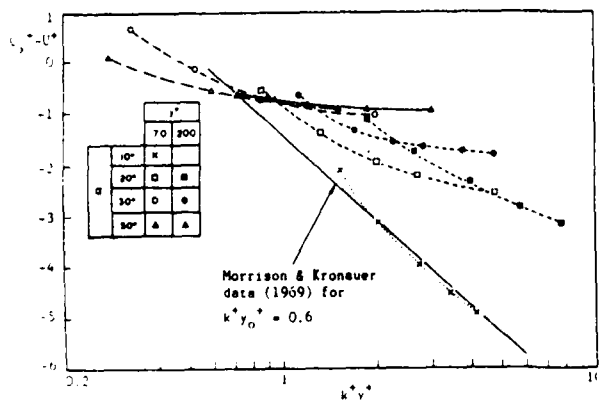


Fig. 5: Variation of  $[C_x^+ - U^+]$  with  $k^+ v^+$ .

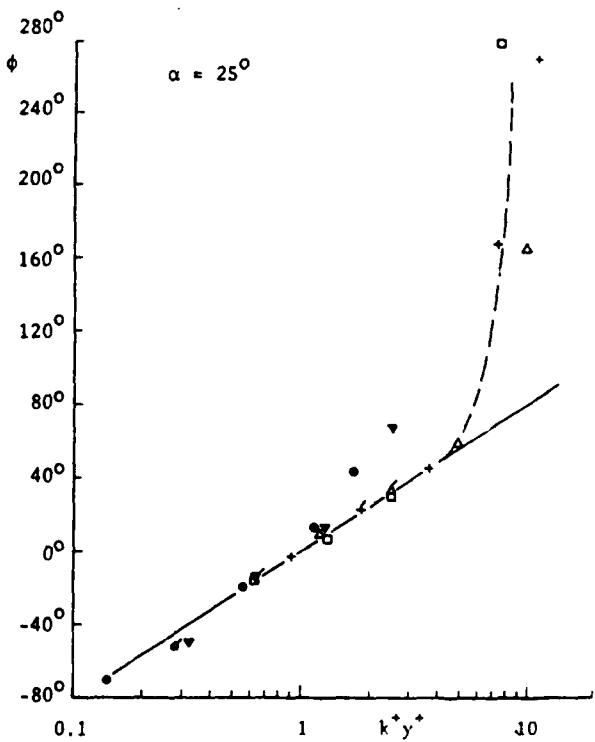
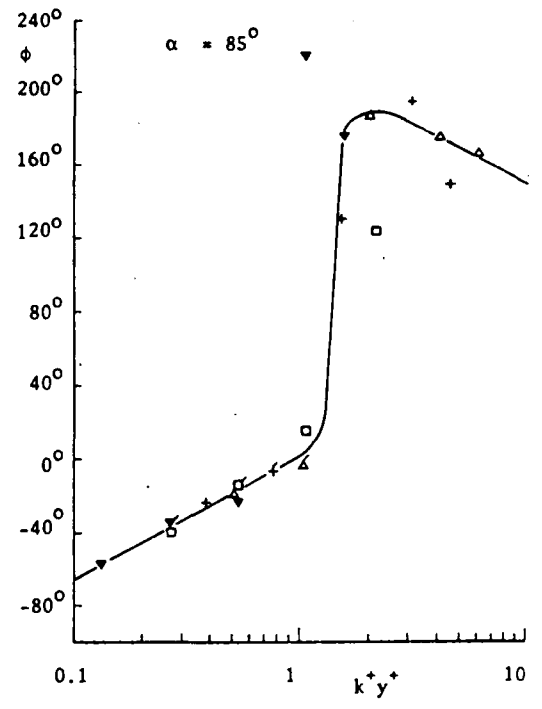
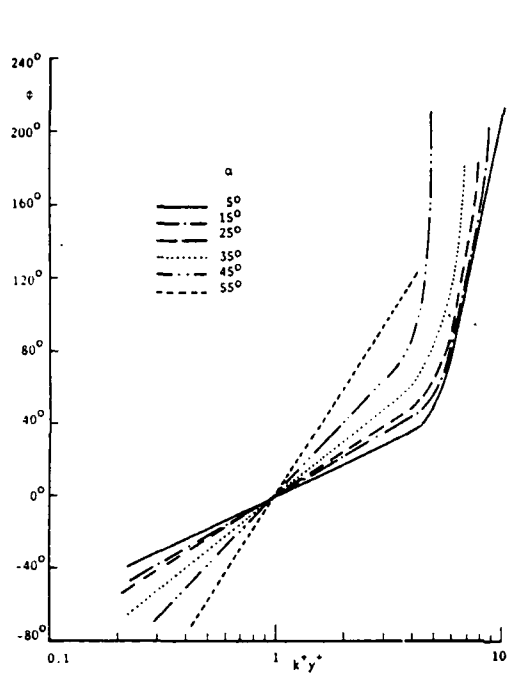


Fig. 6(a): Similarity curves of phase.



Figs. 6(b) & (c): Similarity curves of phase.

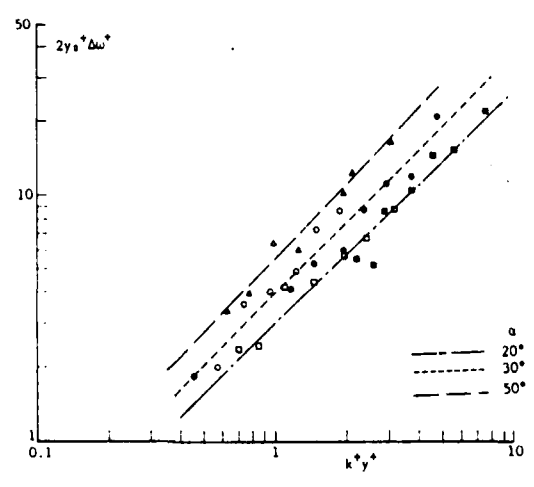


Fig. 7: Variation of  $2y_0^+ \Delta\omega^+$  with  $k^+y^+$ .

HOT-WIRE MEASUREMENTS ON A  
PLANE TURBULENT JET

Carlos A. Thompson  
Military Institute of Engineering  
Brazil

ABSTRACT

Results on the behavior of controlled sinusoidal acoustic disturbances turbulent plane air are presented. Measurements of mean and fluctuating velocity profiles for the forced and unforced cases are obtained through hot-wire technique. For the forced case the fundamental component  $u_f$  is also in the region  $x/H < 10$  for Strouhal number range  $0.15 < St_H < 0.60$ , Reynolds number range  $4,000 < R_H < 50,000$ , and exit excitation amplitude range of  $1.0\% < u_{fe}/U_e < 10.0\%$ . The amplitude profiles of the fundamental as well as the mean and turbulent fields for low values of  $u_{fe}/U_e$  agree quite well with the results reported by Hussain and Thompson [1]. In general the hot-wire data show that the response of the near field of a plane jet is more sensitive to  $St_H$  and  $u_{fe}/U_e$  than to  $R_H$ .

NOMENCLATURE

B slit breadth  
f forcing frequency  
H slit width  
 $R_H = U_e H/\nu$  Reynolds number  
 $St_H = fH/U_e$  Strouhal number  
U longitudinal mean velocity component  
u longitudinal fluctuating velocity component  
x, y cartesian coordinates (see figure 1)

$\nu$  kinematic viscosity

Subscripts

c centerline

e exit (centerline)

f fundamental component

t forced

1. INTRODUCTION AND OBJECTIVE

Although orderly structures have been observed a long time ago in connection with the instability of thin shear layers, the understanding of coherent flows has been subject of great interest over the last few decades. After so many experimental results revealing the existence of large coherent structures in turbulent plane jets, some unanswered basic questions are not universally accepted. Hussain [2] in his work reveals the state of art in this complex field of human knowledge. It would seem premature to call for an theoretical approach towards all the different forms of appearance of organized structures in jet flows. The dynamical significance of coherent structures occurring naturally as well as induced via controlled excitation has been pointed out in the literature in connection with the transports of mass, momentum and heat. In order to get some insight of the interaction between mean, coherent and incoherent flows, more data on turbulent

jet are claimed by many investigators. Comparing with circular jet, less is known about the behavior of a plane jet under an artificial perturbation. Although Hussain and Thompson [1] found no effects of a low controlled acoustic perturbation on the mean and fluctuating velocity fields, Thompson [3] shows through hot-wire data, oscilloscope traces, flow-visualization and one-dimensional frequency spectra the influence of a high amplitude sinusoidal forcing on vortical flow structures in the initial region of a two-dimensional jet. Motivated by these previous studies the present work reports through hot-wire technique the influence of the Strouhal ( $0.15 < St_H = fH/U_e < 0.60$ ) and Reynolds ( $4,000 < R_H = U_e H/\nu < 50,000$ ) numbers as well as the exit amplitude ( $1.0\% < u_{fe}/U_e < 10.0\%$ ) on the mean and fluctuating velocity profiles. The fundamental  $u_f$  is also compared with the forced and unforced longitudinal fluctuating velocities. Because controlled excitation can alter the initial region of a plane jet thirty six data points are located in the region  $x/H < 10.0$ . It is important to notice that in this work the Strouhal number can be fixed while the Reynolds number and the exit excitation amplitude can vary.

## 2. EXPERIMENTAL ARRANGEMENT

The general flow facility and instrumentation are shown schematically in figure 1. Longitudinal velocity data are obtained with a 2 mm long, 4  $\mu$ m diameter tungsten single hot-wire operated by DISA equipment. A function generator provides a sinusoidal signal which is amplified before entering in the speaker. The r.m.s. of the fundamental component  $u_f$  is determined by a Two-phase/Vector Lock-in-Analyzer (P.A.R. 5204). The two-dimensional nozzle is built in a house using the cubic equation contour

according to Thompson [4] such that the internal geometry becomes free of steps and sharp contractions. The plane air jet issues from a rectangular slit ( $H = 0.029$  m,  $B = 0.385$  m). The small aspect ratio ( $B/H = 13$ ) and a 100 watt loudspeaker are used to deliver a high forcing amplitude  $u_{fe}$ .

## 3. RESULTS AND DISCUSSION

Figure 2 displays the one-dimensional frequency spectra of the longitudinal turbulent velocity for the forced and unforced cases. Note that for the location  $x/H = 4.0$  on the centerline,  $St_H = 0.18$  and  $u_{fe}/U_e = 5.0\%$  the second peak (from left) in the spectra corresponds to the frequency of excitation while the subharmonic component is due to the occurrence of pairing. Figures 3 and 4 show respectively the mean and the turbulent velocity distributions on the centerline for  $R_H = 14,700; 25,800; 35,700$  and  $47,600$  where  $H = 0.029$  m. For fixed  $St_H = 0.18$  figures 5 and 6 indicate the effect of low exit excitation amplitude,  $u_{fe}/U_e = 1.0\%$ , on the mean and the turbulent velocities. Comparing figures 4 and 6, it is observed that for  $R_H > 25,000$  the acoustic perturbation affected considerably the turbulent velocity on the centerline of the plane jet. Figure 7 presents the fundamental component  $u_f$  on the centerline for the same parameters mentioned in figures 5 and 6. Observe that since  $St_H = fH/U_e$  is kept constant while  $R_H$  is varying, the excitation frequency  $f$  cannot be fixed. It is clear in figure 7 that for  $R_H > 25,000$  and  $fH/U_e = 0.18$  there is no dramatic change in the  $u_f$  distributions with Reynolds number. Hence, contrarily to Zaman and Hussain [5] the frequencies of excitation can be varied continuously and the amplitude of excitation achievable does not depend on settling chamber resonance

modes. Figures 8 and 9 present  $u_f(x)$  for  $u_{fe}/U_e = 5.0\%$  and  $10.0\%$  respectively for different Reynolds numbers and  $St_H = 0.18$ . Again, the peaks of the fundamental component occur near  $x/H = 4.0$  and depend on the ratio  $f/U_e$  ( $H = 0.029$  m is kept constant). From figures 7, 8 and 9 it is observed that there is no dependence of occurrence of the peak value of  $u_f(x)$  on Reynolds number. The highest peak of  $u_f$  is related to the lowest Reynolds number as the exit excitation amplitude is greater than  $5.0\%$ . Shape of  $u_f$  distributions agrees quite well with the work done by Hussain and Thompson [1]. In their study on plane jet ( $u_{fe}/U_e = 1.4\%$ ) the frequency of excitation is held constant ( $f = 70$  Hz) which implies a unique value of  $R_H = 26,700$  for  $St_H = 0.18$ . The excellent agreement of  $u_f(x)$  for low  $u_{fe}$  can be considered as a strong test of consistency once both researches, studied in different laboratories, had been developed under quite different conditions (eg: nozzle aspect ratio used in [4] was  $B/H = 44$ ). Figure 10 shows that the effect of the acoustic excitation appears to be quite significant on the forced turbulent  $u_t(x)$  for  $x/H < 10$ . Observe that  $u_t(x)$  and  $u_f(x)$  have the same trends which means that the coherent structures on the centerline are dominated by the fundamental component. On the other hand figure 11 compares  $u_t(x)$ ,  $u(x)$  and  $u_f(x)$  distributions in the shear layer region. It is clear that for  $x/H > 3$  the forced turbulence distribution  $u_t$  has different configuration of the fundamental  $u_f$  which means that harmonics and subharmonics dominate the coherent structures. The oscillations downstream from the potential region can be attributed to pairing (or partial pairing), roll-up and breakdown mechanisms of the large structures. Turbulence suppression is evident in the shear layer as the plane jet is pulsated

at large values of  $u_{fe}$ . Figure 11 reveals that the turbulence intensities is reduced in the shear layer ( $3 < x/H < 6$ ) when the plane jet is excited at  $u_{fe}/U_e = 10.0\%$ . The suppression effect, observed and defined by Zaman and Hussain [6], is apparently a consequence of earlier transition of the shear layer vortices, which otherwise naturally grow to larger sizes and survive for large  $x$ , as well as being due to the prevention of successive pairing of these structures. Even for high values of  $u_{fe}$  and for  $0.15 < St_H < 0.60$ , this suppression mechanism on the centerline was not observed in our laboratory.

Figures 12 and 13 are compared in an attempt to show the effect of Reynolds number is less pronounced in the response of a plane jet under acoustic excitation than Strouhal number. These two figures are an "envelope plot" ( $u_{fe}/U_e = 10.0\%$ ) of  $u_t$  and  $u_f$  for  $St_H = 0.18$  and  $0.60$  respectively. Each region shown summarizes all data concerning a Reynolds number ranging from 7,500 to 30,000 (figure 13) and 4,000 to 10,000 (figure 14). The same can be inferred when figures 15 and 16 are compared in the shear layer region, that is, the effect of forcing in  $u_t$  and  $u_f$  is less significant as Reynolds number varies than the Strouhal number. These compact format of organizing the results [7] proved to be a very powerful tool of understanding qualitatively the weak influence of Reynolds number on the  $u_t$  and  $u_f$  distributions. Experimental difficulties, associated with limitations on the instrumentations did not allow data to be taken for  $R_H > 10,000$  when  $St_H = 0.60$  and  $u_{fe}/U_e = 10.0\%$  as shown in figures 14 and 16.

#### 4. CONCLUDING REMARKS

The phenomenon of coherent structures in the near field of a plane air jet (aspect ratio  $B/H = 13.0$ ) under low and high controlled acoustic perturbation has been explored through experimental investigations for several Reynolds numbers and  $St_H = 0.18$  and  $0.60$ . In general the effect of forcing level, Reynolds number and Strouhal number on the mean velocity distribution is negligible as compared with the fluctuating velocity and the fundamental component. The location ( $x/H \approx 4.0$ ) of occurrence of peaks of  $u_f$  and the trend of the distributions appear to be independent on Reynolds number. For the slit width kept constant ( $H = 0.029m$ ) the Strouhal number can be fixed by the ratio  $f/U_e$  and as a consequence, different Reynolds numbers can be used for an unique Strouhal number. It is observed that the nearfield of the plane jet is more sensitive to the Strouhal number than the Reynolds number. On the other hand along the centerline the effect of high forcing excitation on  $u_f$  is more pronounced when the Reynolds number is low. In the shear layer the appearance of harmonics and subharmonics for excited flow is more evident than on the centerline. Turbulence suppression is detected in the shear layer only for high exit excitation amplitude  $u_{fe}$ .

The present results reveal that experimental investigations are a powerful tool to understand the behavior of coherent structures in the nearfield of a plane jet. The peculiarities of this complex phenomenon should encourage others investigators to obtain more experimental information such that theoretical predictions can be pursued.

The author is grateful to Mr. Andrade for his help in various forms.

#### REFERENCES

1. Hussain, A.K.M.F. and Thompson, C.A., 1980, "Controlled symmetric perturbation of the plane jet: an experimental study in the initial region", J.F.M., 100 p.p.100-397.
2. Hussain, A.K.M.F., 1983 "Coherent structure - Reality and myth", The physics of Fluids, 26, p.2816.
3. Thompson, C.A., "An experimental investigation of a forced turbulent plane jet: Strouhal number dependence" - submitted to Physics of Fluids (1985)
4. Thompson, C.A., 1975, "Organized motions in a plane turbulent jet under controlled excitation", Ph.D. dissertation, University of Houston.
5. K.B.M.Q. Zaman and A.K.M.F. Hussain; 1980, "The mechanics of vortex pairing in a axisymmetric mixing layer", Turbulent shear flows, 2, p.p.327-343.
6. K.B.M.Q. Zaman and A.K.M.F. Hussain, 1981, "Turbulence suppression in free shear flows by controlled excitation", J.F.M, 103, p.p.133-159.
7. Costa, F.F., 1985 "The influences of Strouhal and Reynolds numbers on a plane jet", Master Thesis, I.M.E.

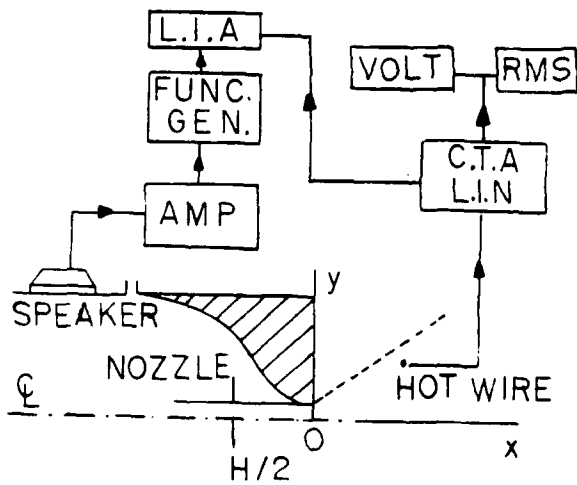


Fig. 1 - Schematic of the plane jet facility and instrumentation.

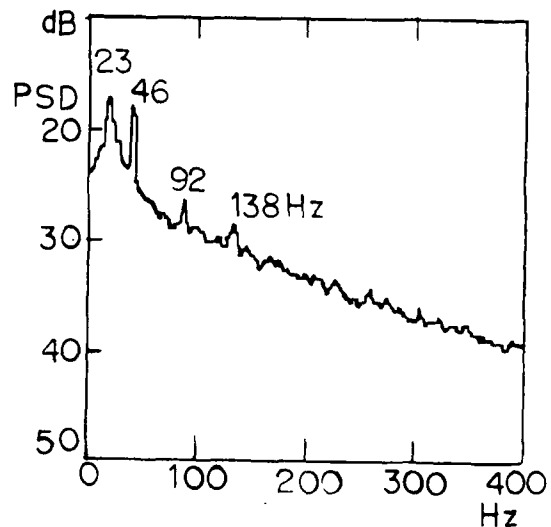


Fig. 2 - Frequency spectra of  $u_t$  on the centerline for  $u_{fe}/U_e = 5.0\%$ ;  $St_H = 0.18$ ;  $x/H = 4.0$ ;  $R_H = 14,700$ .

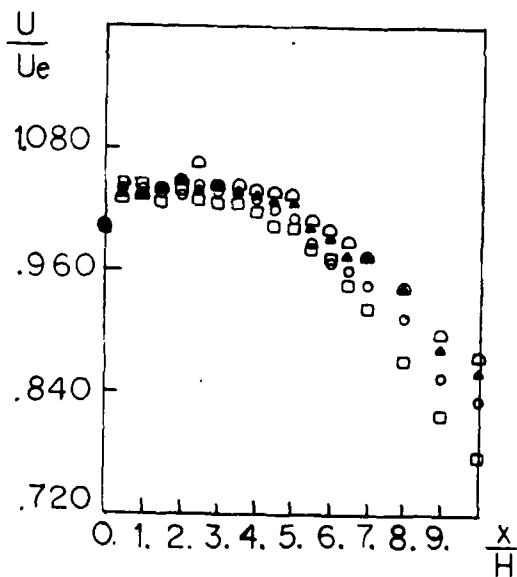


Fig. 3 - Unforced mean velocity on the centerline;  $\square R_H = 14,700$ ;  $\circ R_H = 25,800$ ;  $\blacktriangle R_H = 35,700$ ;  $\square R_H = 47,600$

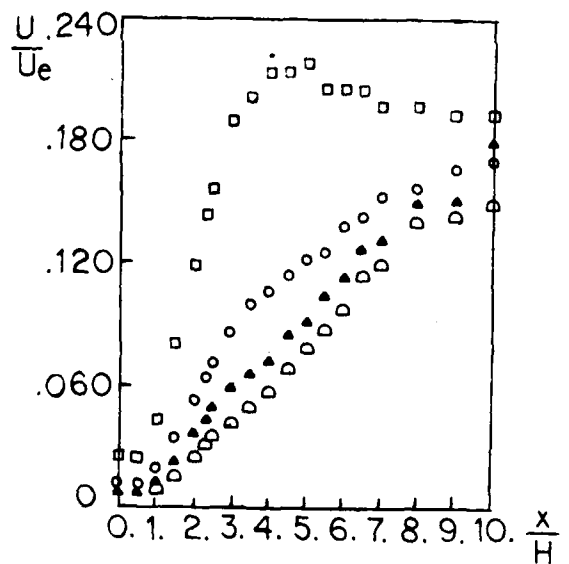


Fig. 4 - Unforced fluctuating velocity on the centerline for the cases in Fig. 3.

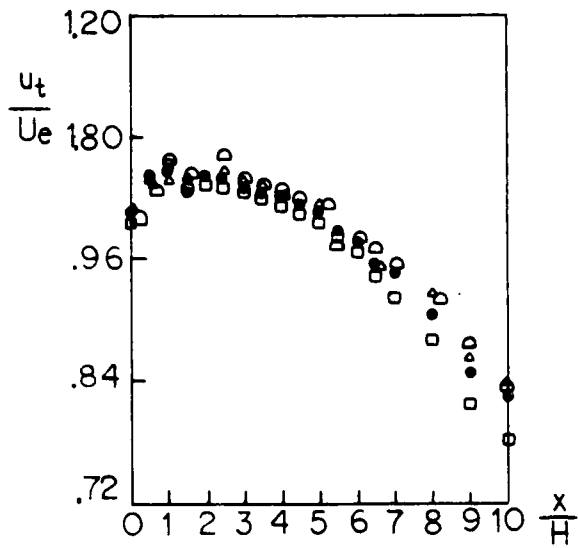


Fig. 5 - Forced mean velocity on the centerline;  $St_H = 0.18$ ;  $u_{fe}/U_e = 1.0\%$ ; for symbols see Fig. 3

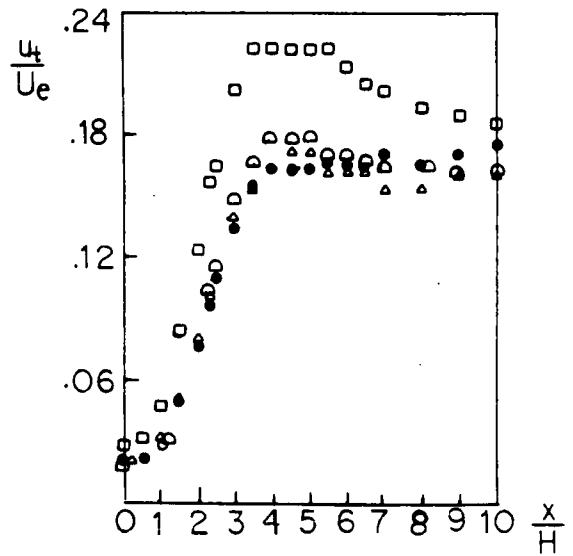


Fig. 6 - Forced fluctuating velocity for the cases in Fig. 5.

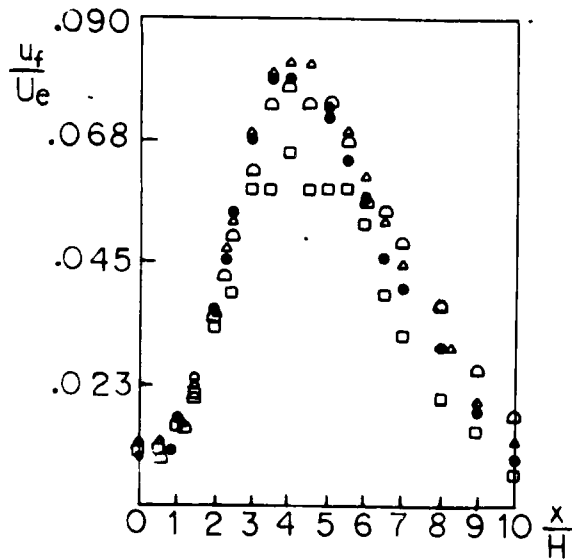


Fig. 7 - Fundamental component for the cases in Fig. 5.

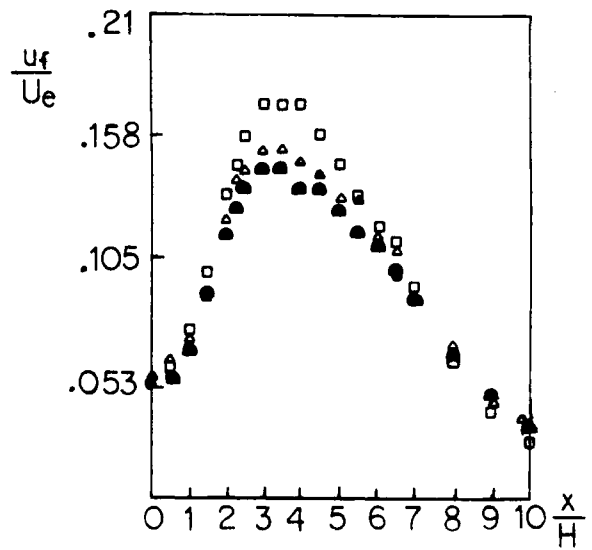


Fig. 8 - Fundamental component on the centerline;  $St_H = 0.18$ ;  $u_{fe}/U_e = 5.0\%$ ;  $\square$   $R_H = 14,700$ ;  $\triangle$   $R_H = 26,800$ ;  $\bullet$   $R_H = 32,700$ .

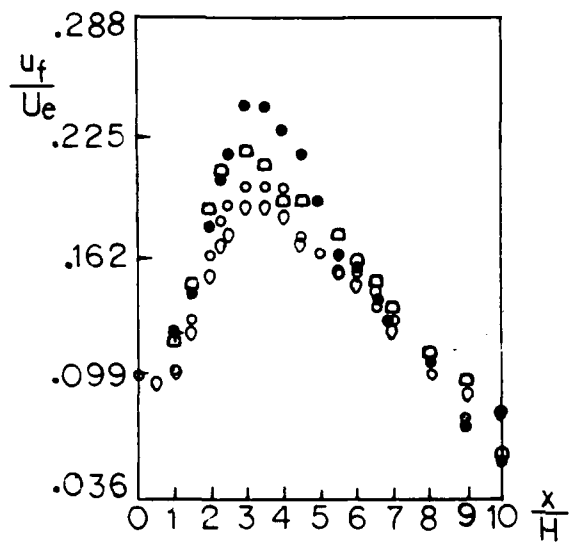


Fig. 9 - Fundamental component on the centerline;  $St_H = 0.18$ ;  $u_{fe}/U_e = 10.0\%$ ;  $\bullet$   $R_H = 7,500$ ;  $\square$   $R_H = 14,700$ ;  $\circ$   $R_H = 22,200$ ;  $\circ$   $R_H = 30,000$ .

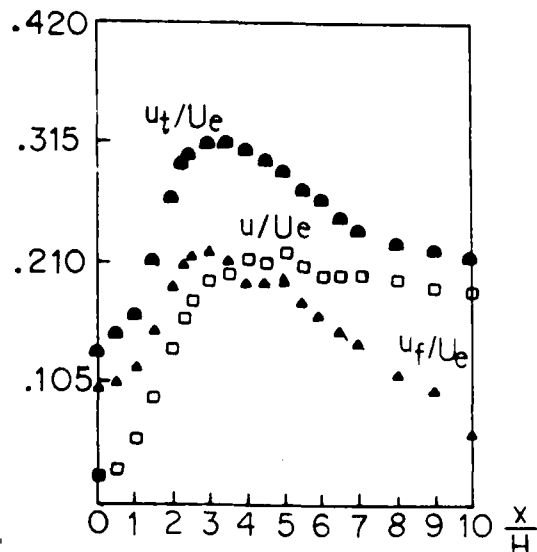


Fig. 10 - Axial variations of  $u$ ,  $u_t$  and  $u_f$  on the centerline;  $St_H = 0.18$ ;  $u_{fe}/U_e = 10.0\%$  and  $R_H = 14,700$ .

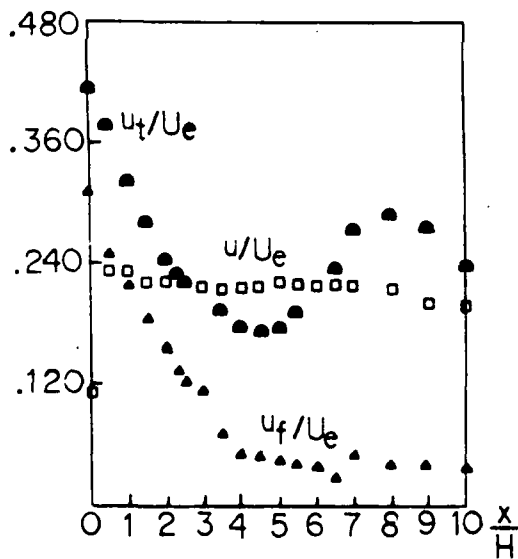


Fig. 11 - Axial variations of  $u$ ,  $u_t$  and  $u_f$  in the shear layer for the cases in Fig. 10.

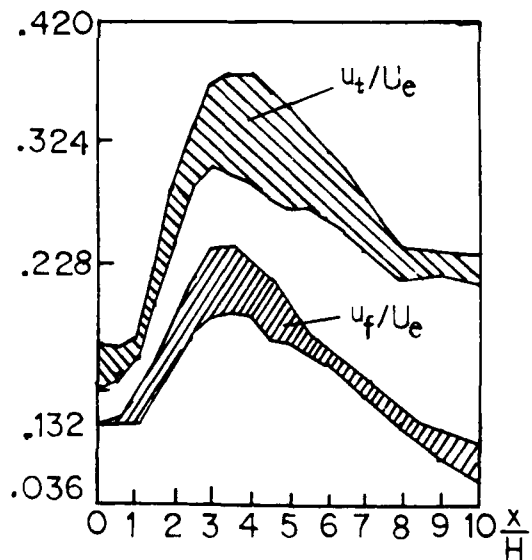


Fig. 12 - Envelope plot of  $u_t$  and  $u_f$  on the centerline for the cases in Fig. 9.

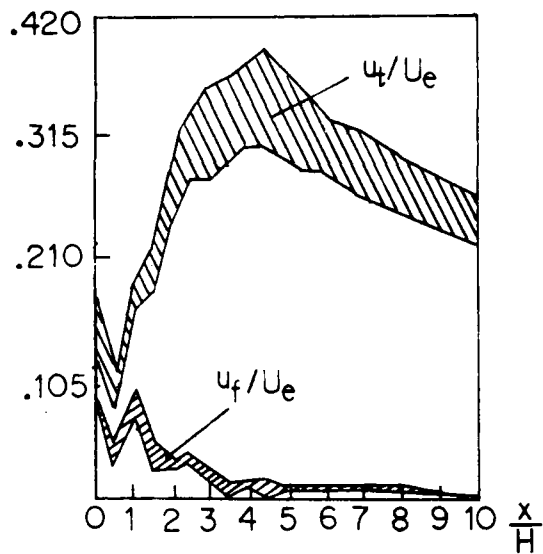


Fig.13 - Envelope plot of  $u_t$  and  $u_f$  on the centerline;  $St_H = 0.60$ ;  $u_{fe}/u_e = 10.0\%$ ;  $4,000 < R_H < 10,000$

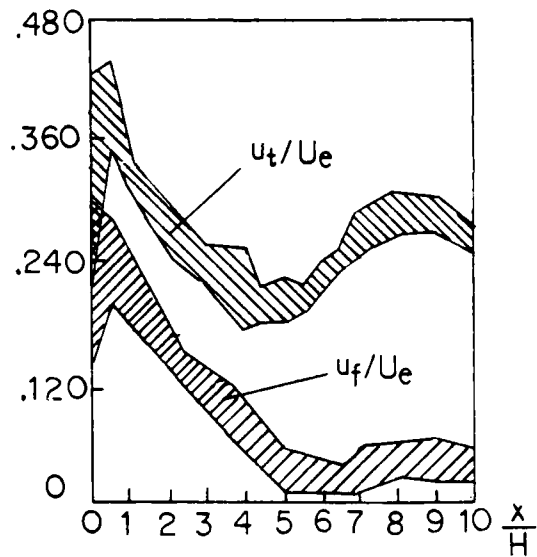


Fig.14 - Envelope plot of  $u_t$  and  $u_f$  in the shear layer for the cases in Fig.9.

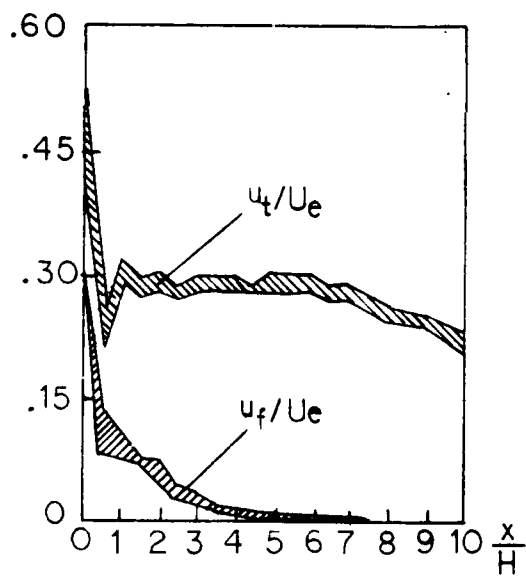


Fig.15 - Envelope plot of  $u_t$  and  $u_f$  in the shear layer for the cases in Fig. 13.

# AN EXPERIMENTAL STUDY OF THE BURST STRUCTURE IN A LEBU- MODIFIED BOUNDARY LAYER

Mark T. Coughran and David G. Bogard  
Mechanical Engineering Department  
University of Texas at Austin  
Austin, Texas 78712

## ABSTRACT

Measurements of the near-wall ejection/burst structure are reported for a LEBU-manipulated boundary layer in a water channel facility. An average skin friction reduction of 11% was measured over  $24 < \xi/\delta_0 < 40$  ( $1650 < Re_\theta < 1950$ ) using the momentum balance technique. The measurements show that the LEBU causes a significant decrease in the ejection frequency, and a lesser decrease in the burst frequency. Normalizing with the inner timescale gives the same nondimensional time between ejections for the standard and LEBU-modified layers. Comparison with polymer flow indicates that the two methods of drag reduction operate by different mechanisms.

## SYMBOLS

b channel half-width  
 $C_f$  skin friction coefficient  
 $F(\tau_E)$  probability distribution of  $\tau_E$   
 $H$  shape factor  
 $L$  threshold parameter for U-level technique  
 LEBU Large Eddy Breakup  
 $N_E$  number of ejections per unit time  
 $R$   $U_{\infty 1}/U_{\infty 2}$ , freestream acceleration parameter  
 $Re_\theta$  momentum-thickness Reynolds number  
 SBL Standard Boundary Layer  
 $\bar{\tau}_B$  mean time between bursts  
 $\bar{\tau}_E$  mean time between ejections  
 $U$  instantaneous streamwise velocity  
 $\bar{U}$  time-mean streamwise velocity  
 $u_{rms}$  root-mean-square streamwise velocity  
 $u_\tau$  shear velocity

$x, y, z$  streamwise, normal, and spanwise coordinates  
 $\delta$  boundary-layer thickness (99% point)  
 $\delta_0$  unmanipulated  $\delta$  at leading edge of LEBU  
 $\delta^*$  displacement thickness  
 $\theta$  momentum thickness  
 $\lambda$  mean streak spacing per unit channel width  
 $\xi$  x distance from leading edge of LEBU  
 $\Pi$  Coles' wake parameter  
 $\tau_{max}$  maximum time between ejections in a burst  
 $\nu$  kinematic viscosity

## Subscripts

$\infty$  freestream condition  
 $a$  averaging time  
 LEBU for LEBU flow  
 SBL for SBL flow  
 $1, 2$  upstream, downstream stations

## Superscripts

$+$  normalized by inner scales  $u_\tau, \nu$   
 $o$  normalized by outer scales  $\bar{U}_\infty, \delta$

## LEBU parameters

$h$  height above wall  
 $s$  streamwise spacing between leading edges  
 $l$  chord length of LEBU element  
 $\alpha$  angle of attack, degrees  
 $Re_l$  chord Reynolds number

## 1. INTRODUCTION

A large-eddy breakup (LEBU) device has been used to modify the outer structure of a turbulent boundary layer, and effects on the inner ejection/burst structures determined. These measurements were made to determine if a

suppression of the large-scale outer structure was accompanied by a suppression of burst and/or ejection activity in the near wall region. Several previous investigators (e.g. Hefner et al., 1979 and Blackwelder and Chang, 1986) have suggested that the reduction of skin friction by a LEBU device could be due to a decrease in bursts at the wall. The argument for this is that bursts might be initiated by the over-lying large scale eddies and consequently the frequency of bursts would be reduced by the suppression of the large scale eddies. However, other investigators such as Mumford and Savill (1984) and Bandyopadhyay (1986) have suggested that LEBU devices would not affect bursts in the near wall region. Therefore, these measurements of the effects on the ejection/burst frequency have direct bearing on determining the dependency of the near-wall structures on outer structures.

The distinction between ejections and bursts made in this study has not generally been accounted for by previous investigators. Bursts have been defined (Kim et al., 1971) as the breakup of a single longitudinal streak structure found in the viscous sublayer. However, the flow visualization studies of Offen and Kline (1975) and Bogard and Tiederman (1986) have shown that the breakup of a single streak may involve the ejection of several discrete elements of low-momentum fluid. Therefore, in general, a burst would comprise either a single ejection or several ejections which are grouped relatively closely together.

There have been several studies of the effects on ejection/burst frequency when polymer solutions are used to induce skin friction reduction. The flow visualization studies of Donohue et al. (1972), Achia and Thompson (1974), and Tiederman et al. (1985) showed that, in general, the time between bursts,  $\bar{T}_B$ , increased for polymer skin friction reduction. Furthermore, when normalized with  $\bar{T}_B$  for a Newtonian fluid at the same wall shear velocity, a net decrease in the frequency of bursts for polymer flows was still indicated. Similar results were obtained by Luchik (1985) using a number of different velocity probe ejection/burst detection techniques. Results of this latter study indicate that the normalized bursting period  $\bar{T}_B^+ = \bar{T}_B u_\tau^2 / \nu$ , increases by 50% for skin friction reduction from 20% to 31%.

Investigations of the effect of polymer on the streak structure show a consistent trend of increased streak spacing,  $\lambda$ , and increased normalized spacing,  $\lambda^+ = \lambda u_\tau / \nu$ . Blanton (1986), using the same facilities as used in the present study, investigated the effect of a LEBU on streak spacing. For a skin friction reduction of approximately 20%, no increase in  $\lambda$  was indicated, with a resulting decrease in  $\lambda^+$ . These results suggest that there are fundamentally different mechanisms by which a LEBU and polymer produce skin friction reduction.

In the extensive study of LEBU devices by Corke et al. (1982),  $\bar{T}_B$  was determined using a "match filter" analysis of velocity signals. These results indicated that  $\bar{T}_B^+$  decreased by approximately 24% when the LEBU induced 40% to 50% skin friction reduction.

The present study was significantly different from previous work in that the LEBU effects were investigated in a water channel facility, and proven ejection/burst detection techniques were used.

The reliability of the burst detection technique was particularly important in this study due to possibilities of changes in both the frequency and structure of the burst. As noted by Bogard and Tiederman (1986), most ejection/burst detection techniques are very sensitive to the thresholds and averaging times used. In their study, sensitivity to changes in the structure of the burst was illustrated by the rapid decrease in  $\bar{T}_E$  from  $y^+=15$  to  $y^+=50$ . However, the technique developed by Bogard & Tiederman for detecting bursts, based on the distribution of  $\bar{T}_E$ , was proven to be insensitive to changes in the burst structure (as well as thresholds used in the detection technique) at various distances from the wall. These techniques for detecting ejections and bursts were used in the present work.

Measurements presented in this paper were made over the range of  $24 < \xi / \delta_0 < 40$ , where  $\xi$  was the distance from the leading edge of the LEBU device, and  $\delta_0$  was the boundary layer thickness at the LEBU device. A momentum balance technique, using velocity profile measurements at several spanwise positions, was used to determine skin friction reduction. Particular attention was placed on obtaining precise measurements of the skin friction coefficient,  $C_f$ . A number of checks were employed

to verify the accuracy of the  $C_f$  measurements, including evaluation of the spanwise variations and a comparison to the "law of the wall" for standard boundary layer cases.

Results presented for  $\bar{\tau}_E$  and  $\bar{\tau}_B$  for both LEBU-modified and standard boundary layer flows show the effects on burst and ejection frequency, and on the burst structure. These results also indicate the effectiveness of different normalizations for  $\bar{\tau}_E$  and  $\bar{\tau}_B$ .

## 2. EXPERIMENTAL FACILITY

### 2.1. Water Channel

The measurements were performed in a recirculating open water channel with a test section 0.5 m wide and 5.0 m long. Figure 1 is a schematic view of the facility. The channel is constructed of clear acrylic to facilitate flow visualization and laser-Doppler velocimeter (LDV) measurements through the side walls. A test plate with a sharp leading edge was installed above the floor of the channel for the measurements described in this paper. The test plate was used to obtain better spanwise uniformity than could be achieved with the bottom-wall boundary layer. Resistance in the form of plastic honeycomb covered by a screen was installed at the end of the test plate in order to shift the stagnation line so that the flow attached smoothly at the leading edge. This was checked by dye flow visualization. Visualization with dye and hydrogen bubbles showed that the flow was laminar up to the

trip rod at  $x = 0.5$  m and turbulent thereafter.

A perforated inlet pipe wrapped with porous foam was used to distribute the flow into the upstream stilling tank. The flow was conditioned in this stilling tank using a 6 mm thick foam section and four plastic screens. These items were carefully selected and positioned to maximize uniformity of downstream conditions. A 3:1 three-dimensional contraction into the channel was used. The channel operated with a freestream velocity of 0.3 m/sec, and had a freestream turbulence intensity of approximately  $u_{rms}/U_\infty = 1\%$ .

### 2.2. Measurement Techniques

Mean velocity profile measurements were performed with a TSI 9100-10 LDV system which was modified to expand the transmitted beams, yielding probe volume dimensions of 70  $\mu\text{m}$  diameter and 500  $\mu\text{m}$  length. The LDV counters were linked to a microcomputer which acquired the data and calculated mean and rms values using a velocity bias correction. For the experiments reported here, only the single streamwise U-velocity component was used.

For the ejection/burst detection, velocity measurements were made with a single-sensor hot-film boundary layer probe (TSI model 1261-10W). The water was filtered to 0.2  $\mu\text{m}$ , and deaerated before being let into the channel. A constant temperature of  $29.5 \pm 0.1$   $^\circ\text{C}$  was maintained by a cooling coil located in the downstream tank. The nonlinear anemometer output was sampled at 200 Hz

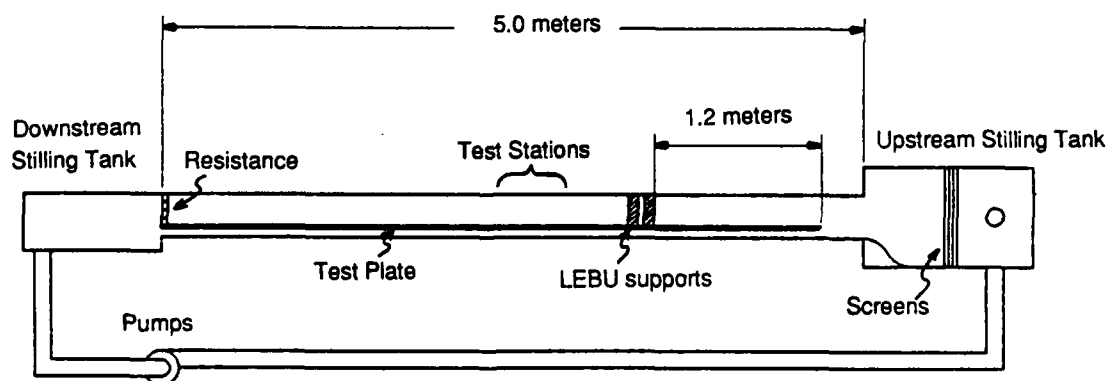


Figure 1: Schematic of water channel.

by an analog-to-digital converter and sent to a second microcomputer which was used to store and process the data. The digitizing rate corresponded to a discretization interval of  $\Delta T^+ = 1.2$ . Calibration data were obtained using the following procedure. The hot-film probe was located in the freestream at the channel centerline with the LDV probe volume positioned slightly upstream and below. The channel velocity was varied using the pump discharge valves and LDV readings were taken while corresponding hot-film voltages were stored on disk. From these data a calibration curve was established using a least squares fit for the following general equation:

$$U = (A + BE^2 + CE^4)^2 \quad (1)$$

This fit was found to give a maximum error of only 0.5% compared to 14% for a King's Law assumption. Following calibration, the hot-film probe was traversed into the boundary layer and records were taken at the various  $x$  and  $y$  positions of interest. After each measurement, the probe was traversed back into the freestream to verify that no significant drift had occurred.

### 2.3. LEBU Installation

The LEBU device was a tandem plate configuration installed at  $x = 1.2$  m, where the unmanipulated boundary layer thickness was  $\delta_0 = 28$  mm. Each LEBU plate consisted of 0.127 mm stainless steel shimstock which was held in tension by the contoured brass supports immersed in the channel. The other pertinent parameters for the LEBU are given in Table I.

$t/\delta_0$	$h/\delta_0$	$s/\delta_0$	$l/\delta_0$	$Re_l$	$\alpha$
0.005	0.60	6.43	1.18	12,600	1.50

Table I. LEBU Parameters

Measurements were taken over  $24.0 < x/\delta_0 < 40.5$  with the LEBU in place and with the LEBU removed (but the supports in place) for the standard boundary layer (SBL) flow. This corresponded to  $1650 < Re_\theta < 1950$  for the SBL. To ensure identical inlet flow conditions for LEBU and SBL, the two sets of

measurements were performed consecutively in one continuous experiment

### 2.4. Momentum Balance

The two-dimensional momentum balance for the boundary layer flow in an open channel yields the following equation in terms of the integral parameters  $\theta$  and  $\delta^*$ :

$$C_f = \tau_w / (\rho U_{\infty 2}^2 / 2) = (1/\Delta x)(\theta_2 - R^2\theta_1 + (1-R)(\delta^*_2 + R\delta^*_1)/2) \quad (2)$$

where  $R = U_{\infty 1} / U_{\infty 2}$ . This equation accounts for the changes in pressure that occur in an open water channel due to the small freestream acceleration from station 1 to station 2.  $C_f$  is the mean skin friction coefficient between the two  $x$  stations. A detailed derivation can be found in the thesis by Blanton (1986).

Since the analysis is two-dimensional, and dependent on small changes in  $\theta$ , it requires that uniform conditions exist across the span. In the present facility, the freestream had spanwise mean velocity uniformity within  $\pm 0.2\%$  over the middle 80% of the span. Despite this, there was considerable variation in the bottom-wall boundary layer thickness across the span. This problem was found to be due to the extreme sensitivity of the boundary layer to conditions in the upstream stilling tank. Hydrogen bubble flow visualization showed that some stilling tank configurations caused vortical structures in the freestream which were not detected by mean velocity measurements. Similar difficulties in obtaining spanwise boundary layer uniformity have been noted in other water channel and wind tunnel facilities.

After these problems were observed in the facility, considerable time was spent establishing an acceptable level of spanwise uniformity. Numerous configurations of screens, honeycomb, foam, and suction were investigated. Also, a test plate was installed 50 mm above the bottom wall. On this test plate spanwise  $\theta$  variations, over the middle 40% of the channel where measurements were taken, were within  $\pm 2\%$  of the mean at all  $x$  positions and flow conditions. This is comparable to the uniformity obtained in the wind tunnel studies by Anders and Watson (1985). As a final check, hydrogen bubble

flow visualization was used to ensure that there were also no vortical structures in the freestream.

Before the experiment, an uncertainty analysis was used to establish the critical parameters in determining  $C_f$ . These included positioning of the probe volume, number of data points and averaging time at each position, and freestream velocity measurement. Based on this analysis a measurement procedure was established to obtain an estimated uncertainty in  $\theta$  of less than  $\pm 1.5\%$  (at 20:1 odds). During the experiment, the precision of the measurement was checked by repeating the first profile for the LEBU-modified boundary layer measurements after profiles at all ten stations had been completed. This repeat of the first profile had a  $\theta$  value within 0.04% of the initial value. Another profile was repeated when temporary changes in channel conditions were suspected. The second value was much more consistent with surrounding conditions, and was used in the subsequent data reduction.

### 3. EJECTION AND BURST DETECTION

As mentioned earlier, the ejection and burst detection techniques used in this study were based on the results of Bogard and Tiederman (1986). Ejection detections were made using  $U$ -velocity (streamwise) measurements from the hot-film probe. Burst detection techniques were based on an analysis of the distribution of  $\tau_E$ .

The  $U$ -level ejection detection technique, which is simply based on the  $U$ -level falling below a threshold set with reference to  $u_{rms}$ , was the technique used. Results from Bogard and Tiederman (1986) showed that  $U$ -level is the most reliable technique for single component  $U$ -velocity measurements. The threshold parameter  $L = 1.3$  suggested by Bogard and Tiederman was used for this technique.

To identify bursts, the maximum time between ejections,  $\tau_{max}$ , from the same burst must be estimated. This was done by using the probability distribution  $F(\tau_E)$  as shown in Figure 2 for a standard boundary layer. The value for  $\tau_{max}$  is estimated as the point where there is a distinct change in the trend of  $F(\tau_E)$ . Following the suggestion of

Barlow and Johnston (1985),  $1-F(\tau_E)$  was plotted on a logarithmic scale and two linear trends within the distribution were identified. As shown in Figure 2,

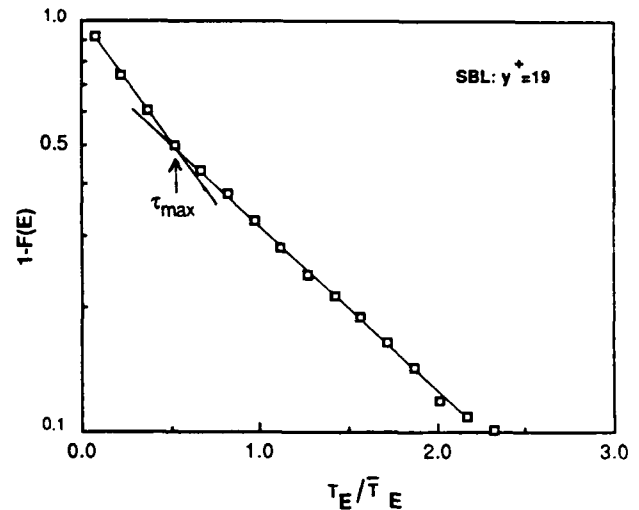
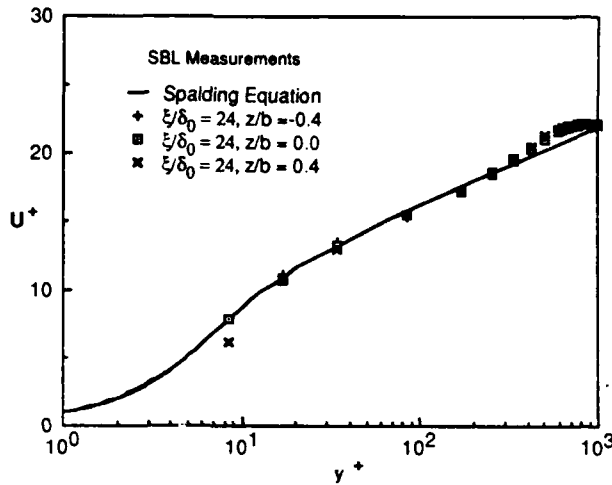
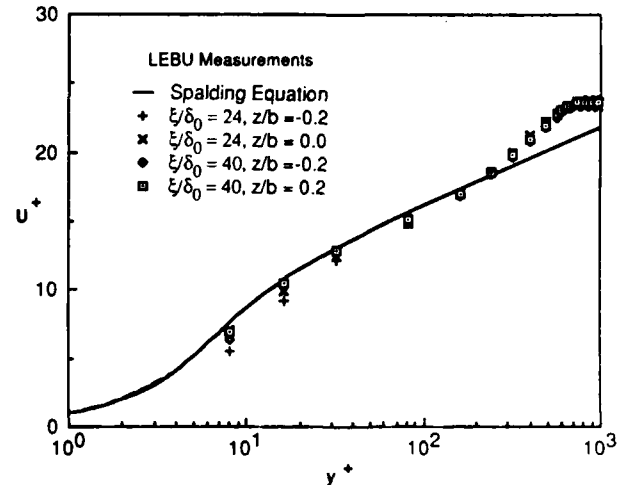


Figure 2: Probability distribution of  $\tau_E$  used to determine  $\tau_{max}$ .

the value for  $\tau_{max}$  was established as the  $\tau_E$  value at which these linear trends intersected. Distributions of  $\tau_E$  were obtained with  $U$ -level and samples, each with 500 to 800 ejections, were analyzed for both the standard and LEBU-modified boundary layer. Three samples for the standard boundary layer, from upstream and downstream stations, and from the station at the maximum height from the wall, were found to have a consistent value of  $\tau_{max} = 175 \pm 15$  msec. Samples at four of the five LEBU-modified boundary layer measurement positions also indicated a value of  $\tau_{max} = 175 \pm 20$  msec. The fifth sample indicated a value of  $\tau_{max} = 225$  msec. However, analysis of subdivisions of this last sample indicated anomalous trends in part of the data; consequently this sample was disregarded. Subsequent analysis of the data to determine  $\bar{T}_B$  for both the standard and LEBU-modified boundary layer was performed using  $\tau_{max} = 175$  msec to discriminate ejections from the same burst.



(a)



(b)

Figure 3: Mean velocity profiles for (a) SBL flow and (b) LEBU flow.

#### 4. RESULTS: MEAN VELOCITY PROFILES AND SKIN FRICTION REDUCTION

##### 4.1. Verification of turbulent boundary layer parameters.

Typical mean velocity profiles for the standard boundary layer at the upstream position are shown in Figure 3(a). These data were normalized using the shear velocity  $u_\tau$  obtained from the momentum balance. Both the precision of the velocity measurements and the spanwise uniformity are evident from the profiles, which essentially coincide at three different spanwise positions. Small discrepancies at near-wall positions, seen on the log scale, are due to the uncertainty in locating the wall. The close correspondence to Spalding's (1961) law of the wall (with parameters  $\kappa=0.41$  and  $B=5.0$ ) also confirms the accuracy of the momentum balance technique for determining  $C_f$  and  $u_\tau$ .

Representative LEBU mean velocity profiles from both upstream and downstream stations (again normalized by  $u_\tau$  from the momentum balance) appear on Figure 3(b). The close correspondence to Spalding's law of the wall shows that these profiles are similar to the standard turbulent boundary layer profiles. This result is consistent with measurements of Lemay et al. (1985) at similar  $\xi/\delta_0$  positions, but is in contrast with the results of Corke et al. (1982).

Corke et al., using a similar tandem plate LEBU, found a definite increase in the slope and intercept of the log-linear region of the profile.

Our measurements did show several distinct changes in the characteristics of the LEBU boundary layer compared to the SBL. These changes are summarized in Table II in terms of ratios of the LEBU parameters to the SBL parameters.

$\xi/\delta_0$	$\delta_L/\delta_S$	$\theta_L/\theta_S$	$H_L/H_S$	$\Pi_L/\Pi_S$
24.0	0.98	1.12	1.07	2.1
40.5	0.98	1.09	1.04	2.0

Table II. Comparison of LEBU and SBL profile parameters

Naturally an increase in the momentum thickness occurs in the near field downstream of the LEBU. However, our results show a definite, albeit small, decrease in the boundary layer thickness for the LEBU boundary layer. This was accompanied by an increase in the shape factor,  $H$ , a characteristic also noted by Anders and Watson (1985). The substantial increase in the wake parameter is clearly noticeable when comparing SBL and LEBU profiles in Figures 3(a) and (b).

The skin friction coefficient calculated by

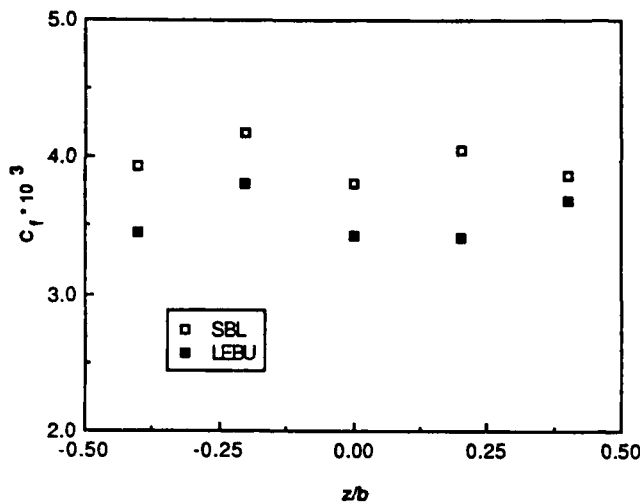


Figure 4:  $C_f$  measurements across the center-span of the channel for both the SBL and LEBU flows.

momentum balance is plotted in Figure 4. Spanwise variations in  $C_f$  are evident in this figure, but the consistent trends for the upstream and downstream stations reflect the accuracy of the measurement. These data indicate an average  $11 \pm 4\%$  skin friction reduction over the streamwise extent of the measurements. The uncertainty of this measurement is based on a standard-error-of-the-mean analysis of the 5 spanwise positions.

The magnitude of the skin friction reduction obtained may be compared with results from similar tandem LEBU configurations in wind tunnel studies. Two studies have been performed with direct drag measurements using drag balances at similar Reynolds numbers. Results of those measurements, averaged over the same positions relative to the LEBU device as used in the present measurements, are presented in Table III.

The results of the present measurements compare favorably with the previous studies using drag balances. Finally, it should be noted that the present measurements were performed without any tuning of the LEBU to maximize the  $C_f$  reduction.

Measurement	$h/\delta_0$	$s/\delta_0$	$Re_\theta$	$C_{fLEBU}/C_{fSBL}$
Lemay et al. (1985)	0.75	5.1	2400 to 6400	0.87
Mumford and Savill (1984)	0.75	$\approx 6$	$\approx 1000$	0.86
Present	0.60	6.4	1650 to 1950	$0.89 \pm 0.04$

Table III. Average  $C_f$  reduction over  $24.0 < \xi/\delta_0 < 40.5$

## 5. RESULTS: EFFECTS OF THE LEBU DEVICE ON EJECTIONS AND BURSTS

The effect of the LEBU device on ejections was deduced by comparing  $\bar{T}_E$  for both SBL and LEBU flows. These results are presented in terms of the ratio  $\bar{T}_{E,LEBU} / \bar{T}_{E,SBL}$  for measurements made at nominally the same point in the flow. Different normalizations of  $\bar{T}_E$  were also evaluated by comparing ratios of  $\bar{T}_E^*$ , based on inner variables, and  $\bar{T}_E^0$ , based on outer variables. Results for different streamwise positions and for different vertical positions are presented in Figure 5.

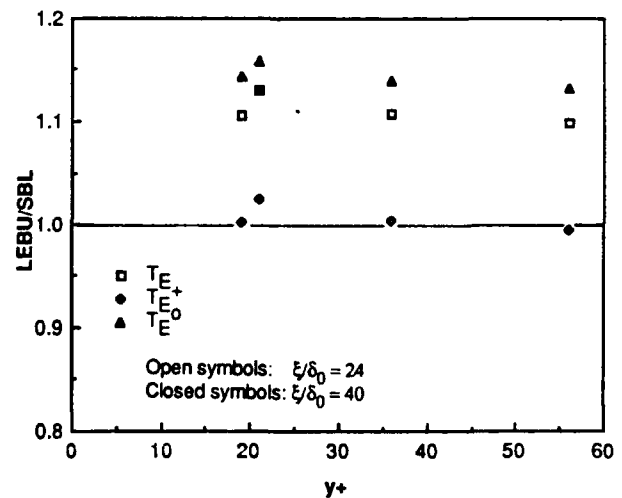


Figure 5: Ratios of  $\bar{T}_E$ ,  $\bar{T}_E^*$ , and  $\bar{T}_E^0$  obtained in the LEBU flow compared to the SBL flow.

Measurements of  $\bar{\tau}_E$  made at  $\xi/\delta_0=32.2$  were not included in Figure 5 because the vertical positions of the probe were inadvertently not matched for the LEBU and SBL flows.

The ratios of the dimensional  $\bar{\tau}_E$  values show a consistent increase in  $\bar{\tau}_E$  for the LEBU flow of approximately 11%, indicating that the LEBU device has decreased the frequency of ejections. Normalizing by the outer timescale  $\delta/U_\infty$  causes a slight upward shift of the ratio. More importantly, normalizing with the inner timescale  $\nu/u_\tau^2$  consistently yields  $\bar{\tau}_E^+_{SBL} = \bar{\tau}_E^+_{LEBU}$  at all positions. In the previous figures the strong variation of  $\bar{\tau}_E$  with distance from the wall was not evident because the  $\bar{\tau}_E$  ratio was used. This variation is shown in Figure 6. This figure also graphically shows the collapse of the LEBU and SBL data when using  $\bar{\tau}_E^+$ .

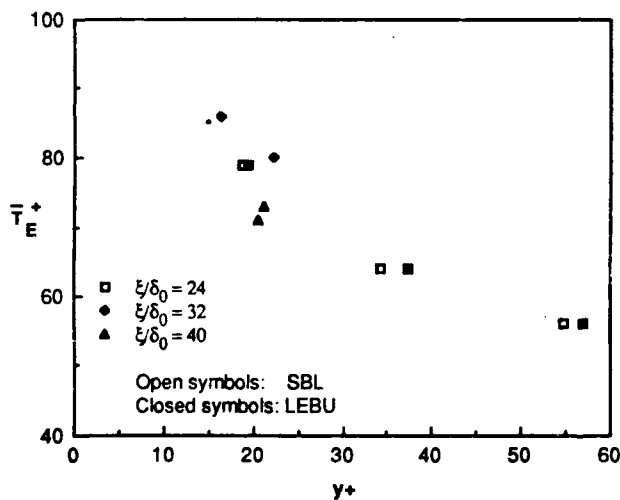


Figure 6: Average time between ejections at increasing distance from the wall.

The normalized average time between bursts,  $\bar{\tau}_B^+$ , for different vertical positions, is shown in Figure 7. These results represent data from the same measurements used to deduce  $\bar{\tau}_E^+$  in Figure 6. In contrast to  $\bar{\tau}_E^+$ ,  $\bar{\tau}_B^+$  was found to be essentially constant over the range of  $y^+$  measurement positions.

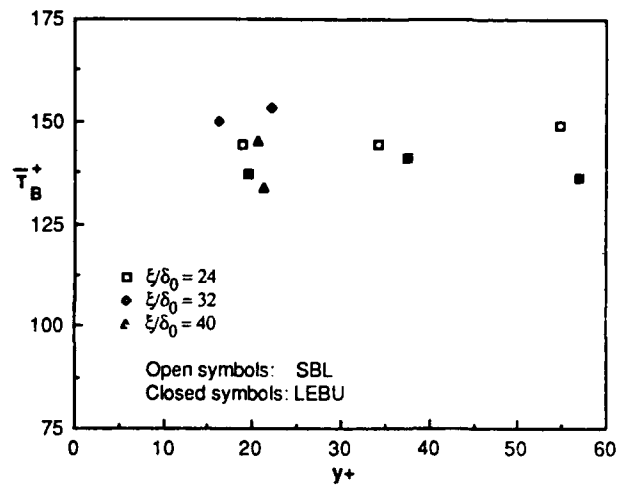


Figure 7: Average time between bursts at increasing distance from the wall.

In Figure 8, ratios of  $\bar{\tau}_B$  and  $\bar{\tau}_B^+$  have been formed. The  $\bar{\tau}_B^+$  ratio shows that normalizing with the inner timescale does not give definitive results as it did for  $\bar{\tau}_E^+$ . In fact, the ratio of dimensional  $\bar{\tau}_B$  values appears to be slightly closer to unity.

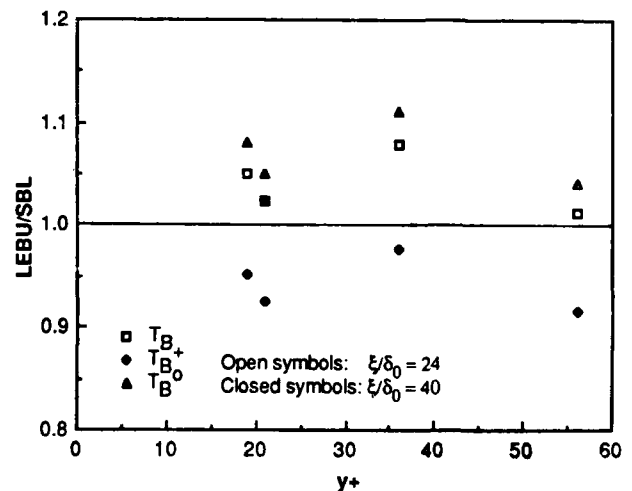


Figure 8: Ratios of  $\bar{\tau}_B$ ,  $\bar{\tau}_B^+$ , and  $\bar{\tau}_B^0$  obtained in the LEBU flow compared to the SBL flow.

A change in the structure of the burst is indicated by a consistent reduction in the number of ejections per burst for the LEBU flow as shown in Figure 9. However, the reduction indicated here is small compared to the rate  $N_E/\text{burst}$  increases moving away from the near wall region.

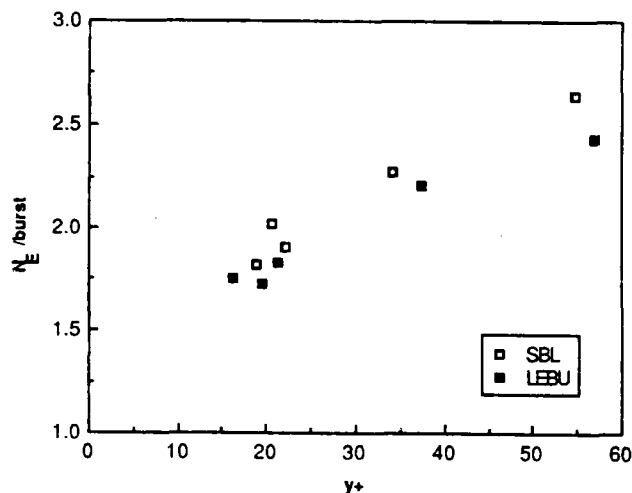


Figure 9: Average number of ejections in a burst for both the LEBU and SBL flows.

## 6. SUMMARY AND CONCLUSIONS

The following effects of a LEBU device on a turbulent boundary layer were found:

- An average skin friction reduction of approximately 11% occurs over the range  $24 < \xi/\delta_0 < 40$ . The magnitude of this reduction is comparable to that obtained in previous wind tunnel studies with similar LEBU parameters.
- The near wall mean velocity profiles, when normalized in the form of  $\bar{U}^+$  vs.  $y^+$ , have the same universal log-law profile as a standard turbulent boundary layer. However, the outer portion of the mean velocity profile is decidedly different, showing a factor of two increase in the wake component.

- There was a clear effect on the ejections, with the LEBU causing a decrease in the ejection frequency. However, the decrease in ejection frequency was proportional to the decrease in wall shear stress such that the normalized  $\bar{\tau}_E^+$  was the same for the LEBU and SBL flows.
- The burst frequency also decreased, but only slightly, and proportionately less than for the ejections. Consequently,  $\bar{\tau}_B^+$  was consistently lower for the LEBU flow compared to the SBL flow.
- As measurements were made at greater distances from the wall,  $\bar{\tau}_E$  decreased approximately 30% for both the SBL and LEBU flows. But  $\bar{\tau}_B$  remained essentially constant,  $\pm 2\%$ , with height variation. As these results suggest, there was a monotonic increase in the average number of ejections per burst at greater distance from the wall. However,  $N_E/\text{burst}$  for the LEBU flow was consistently lower than for the SBL flow.

As noted by Bogard and Tiederman (1986), the increase in the number of ejections at greater distances from the wall can be explained by the continued breakup of a streak element as it moves further from the wall. The decrease in the number of ejections per burst for the LEBU flow suggests that the LEBU causes some suppression of the breakup of a streak. However, bursts are suppressed to a lesser extent than the ejections within a burst.

The effects of the LEBU on both the burst structure and frequency are significantly different than that found in polymer flows. As noted earlier, significant ( $>50\%$ ) increases for both  $\bar{\tau}_B$  and  $\bar{\tau}_B^+$  occur when using polymer. With the LEBU, only a slight increase,  $\approx 4\%$ , in  $\bar{\tau}_B$  and a decrease in  $\bar{\tau}_B^+$  were noted. Furthermore, Luchik (1985) showed that the number of ejections per burst increased by 20% in a polymer flow, whereas the LEBU causes a decrease of  $\approx 7\%$ .

Similar contrasting effects by the LEBU and polymer were found by Blanton (1986) in his study of the effect of a LEBU on streak spacing. As discussed earlier, this study indicated a decrease in  $\lambda^+$

for LEBU flows in contrast to significant increases in  $\lambda^+$  reported by other studies for polymer flow at the same level of drag reduction. Evidently the mechanisms by which LEBU devices and polymer cause reduction in wall shear stress are significantly different.

As a final note, the present results have confirmed the normalization of  $\bar{\tau}_E$  using inner scaling. However, this leads to a somewhat paradoxical situation, since other researchers have suggested that scaling with inner variables would indicate independence of bursting from the outer region. The latter conclusion clearly cannot be drawn for the present experiment, in which manipulation of the outer region by the LEBU device led to changes in the ejections.

#### ACKNOWLEDGEMENTS

This research was supported by the National Science Foundation under Grant #MEA-8404892.

#### REFERENCES

- Anders, J.B.; Watson, R.D. 1985: Airfoil large-eddy breakup devices for turbulent drag reduction. A.I.A.A. Paper 85-0520.
- Achia, B.U.; Thompson, D.W. 1977: Structure of the turbulent boundary layer in drag-reducing pipe flow. *J. Fluid Mech.* 81, 439.
- Bandyopadhyay, P.R. 1986: Review--mean flow in turbulent boundary layers disturbed to alter skin friction. A.I.A.A. Paper 86-1126.
- Barlow, R.S.; Johnston, J.P. 1985: Structure of turbulent boundary layers on a concave surface. Report MD-47, Stanford University.
- Blackwelder, R.F.; Chang, S.I. 1986: Length scales and correlations in a LEBU modified turbulent boundary layer. A.I.A.A. Paper 86-0287.
- Blanton, J.N. 1986: An experimental investigation of large eddy breakup devices in a water channel facility. M.S. Thesis, University of Texas at Austin.
- Bogard, D.G.; Tiederman, W.G. 1986: Burst detection with single point velocity measurements. *J. Fluid Mech.* 162, 389-413.
- Corke, T.C.; Nagib, H.M.; Guezennec, Y.G. 1981: A new view on origin, role and manipulation of large scales in turbulent boundary layers. NASA CR-165881.
- Donohue, G.L.; Tiederman, W.G.; Reischmann, M.M. 1972: Flow visualization of the near-wall region in a drag-reducing channel flow. *J. Fluid Mech.* 56, 559.
- Hefner, J.N.; Weinstein, L.M.; Bushnell, D.M. 1979: Large-eddy breakup scheme for turbulent viscous drag reduction. Symposium on Viscous Drag Reduction, Dallas, Texas.
- Kim, H.T.; Kline, S.J.; Reynolds, W.C. 1971: The production of turbulence near a smooth wall in a turbulent boundary layer. *J. Fluid Mech.* 50, 133-160.
- Lemay, J.; Provencal, D.; Gourdeau, R.; Nguyen, V.D.; Dickinson, J. 1985: More detailed measurements behind turbulence manipulators including tandem devices using servo-controlled balances. A.I.A.A. Paper 85-0521.
- Luchik, T.S. 1985: The effect of drag-reducing additives on the turbulent structure in channel flows. Ph.D. Thesis, Purdue University.
- Mumford, J.C.; Savill, A.M. 1984: Parametric studies of flat plate, turbulence manipulators including direct drag results and laser flow visualization. ASME Symposium on Laminar Turbulent Boundary Layers.
- Offen, G.R.; Kline, S.J. 1975: A proposed model of the bursting process in turbulent boundary layers. *J. Fluid Mech.* 70, 209-228.
- Spalding, D.B. 1961: A single formula for the "law of the wall". *J. Appl. Mech.* 455-458.
- Tiederman, W.G.; Luchik, T.S.; Bogard, D.G. 1985: Wall layer structure and drag reduction. *J. Fluid Mech.* 156, 419-437.

# Heterogeneous Drag Reduction in Turbulent Pipe Flows using Various Injection Techniques

Bodo Frings

Lehrstuhl für Strömungsmechanik, University of Dortmund, F.R.G.

## INTRODUCTION

It is well known that the phenomenon of drag reduction is associated with a modification of the structure of turbulence. Heterogeneous drag reduction obtained by injecting concentrated polymer solutions into a turbulent pipe flow produces different velocity profiles and local drag reduction behaviour than homogeneous drag reduction [1] ; this indicates that a different mechanism is responsible for this type of drag reduction.

The aim of this paper is to analyse the effectiveness of injecting an annular ring of relatively concentrated viscoelastic fluid into the turbulent boundary layer of a pipe flow. In contrast to comparative centre-line injection experiments, the polymer solution was injected into the region where the maximum energy production and dissipation occurs [2] . The presence of such a closed ring of polymer strands should have a significant influence on the larger eddies present in the turbulent pipe flow and enable the processes responsible for drag reduction to be understood more fully.

## EXPERIMENTAL SET-UP

The experimental system is shown schematically in figure 1. Experiments were performed in a straight, smooth-walled acrylic glass pipe 50 mm in diameter. In order to determine the drag reduction from pressure drop measurements the test pipe was provided with 14 pressure taps positioned at 1 m intervals down the pipe. A sufficient entrance pipe length was provided to ensure fully developed flow at the injection point.

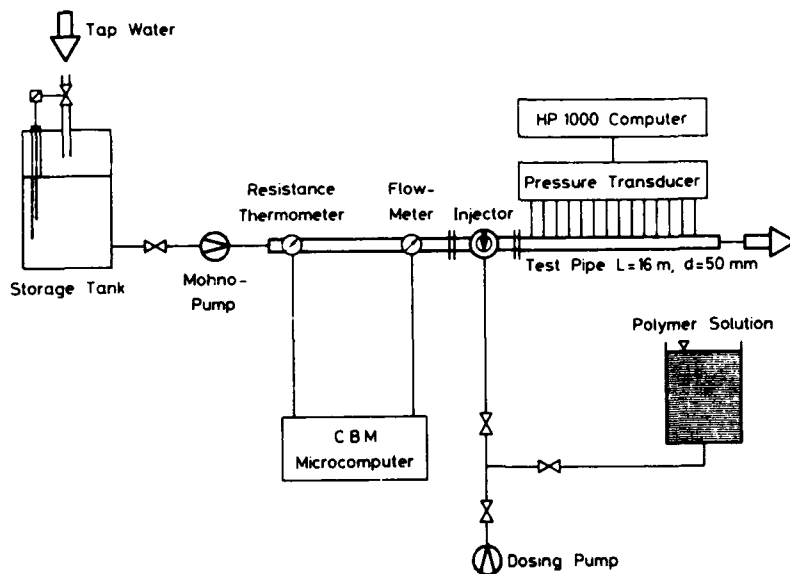


Fig. 1  
Experimental set-up

The water was pumped from a reservoir tank by a Mohno pump, the speed of which was controlled by a microcomputer to maintain a constant Reynolds ( $Re$ ) number during the experiments. The microcomputer continuously measured the temperature of the water with a resistance thermometer and the discharge with a turbine wheel flow meter. The polymer solutions with concentrations between 0.2 and 0.5 weight percent were injected by a dosing pump equipped with a variable speed drive. The polymer used was polyacrylamide SEPARAN AP45 ( $M_w = 4-5 \cdot 10^6$ ). The pressure differences between pressure taps were measured with Philips differential pressure transducers (Model PD2), the outputs of which were connected to a computer (Hewlett Packard 1000) to enable direct analysis of the experimental data.

#### INJECTOR SYSTEM

The design criteria for the injector were that it should be able to inject an annular ring of polymer in the near-wall region at various distances from the wall with various thicknesses (i.e. gap widths). Furthermore, the degradation of the polymer in the injector were to be as small as possible. Figures 2 and 3 of the injector show that the polymer solution was supplied to the injector by an equalizing device 1, which split the polymer feed into four separate streams to ensure a nearly uniform polymer supply around the whole injector slit. In addition, after leaving the annular chamber 2, the polymer solution passed

through a homogenizer 3. At the downstream end of the injector two exchangeable rings 4 were used to create the annular slit with exact dimensions. The gap width was adjustable between 0.1 and 0.5 mm. Varying the distance of the injector slit from wall was accomplished by exchanging the inset 2,3 and 4.

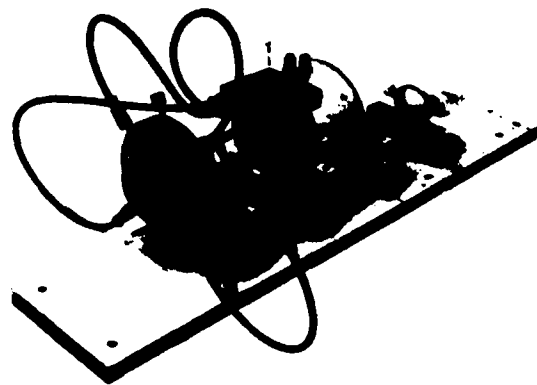


Fig. 2  
Polymer injector

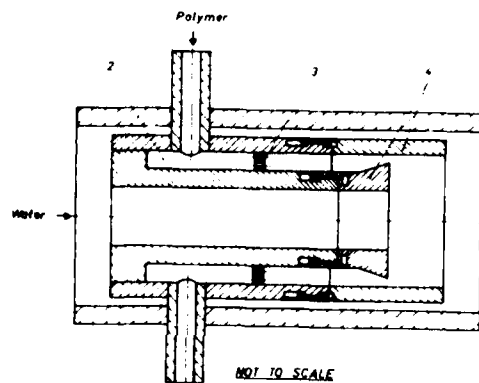


Fig. 3  
Details of the  
polymer injector

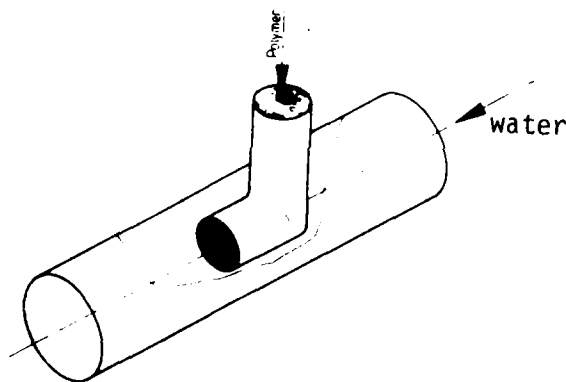


Fig. 4 a  
Centre-Line Injector

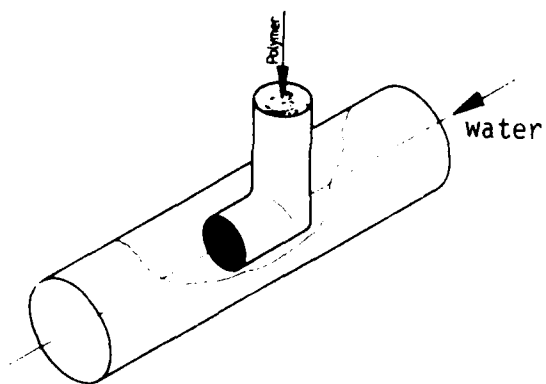


Fig. 4 b  
Perforated Centre-Line Injector

The experiments discussed below were performed using an injector positioned 1.5, 2.5, 3.5 and 9.5 mm from the wall and with a gap width of 0.4 mm.

The centre-line injection of polymer solutions was investigated using bent injection needles as shown by figure 4. The injection velocity was held approximately equal to the bulk flow velocity by varying the diameter of the injection needles.

#### EXPERIMENTAL RESULTS

For investigating the flow behaviour of the injected fluid some of the polymer solutions were dyed with crystal violet, which has been shown not to influence the drag reducing behaviour of polyacrylamide solutions.

Injecting a 0.2% solution equivalent to an average polymer concentration of 50ppm it was evident from our observations that for both investigated injection techniques the injected polymer threads broke up into very short polymer lumps, spreading over the cross-section whilst passing through the pipe; examples are shown by figure 5.

Injecting more highly concentrated solutions, the polymer thread injected at the centre-line remained intact over the entire length of the test section while in the case of ring injection it is believed that the injected polymer solution forms an elastic network ( see figure 6). This conclusion was confirmed by an experiment in which the discharge of water was abruptly stopped. For several metres from the injection point the polymer strands relaxed like stretched rubber bands.

Although no significant mixing of the injected polymer solution was noticed in the visual observations, a large amount of drag reduction was obtained.

It was found to depend on the Re-number, the distance from the injection point, the average polymer concentration  $C_R$ , the concentration of the injected polymer solution  $C_p$  as well as on the type of injector used (i.e. wall distance of injector slit  $w$ ).



Fig. 5 a  
Flow behaviour of the  
injected polymer solution  
 $C_p=0.2\%$  ,  $x/d=0$

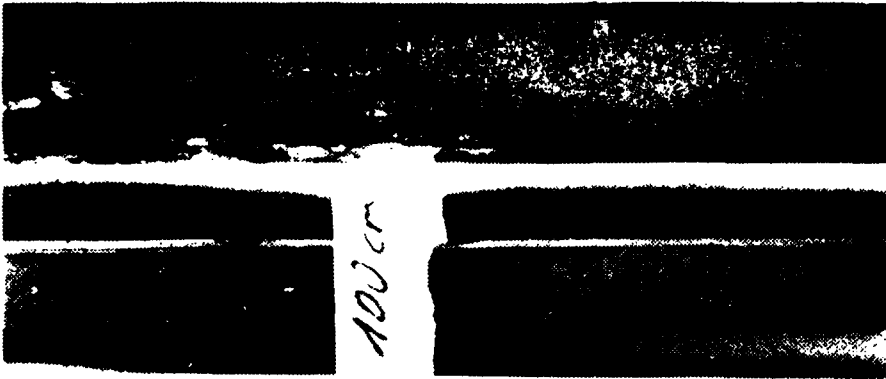


Fig. 5 b  
 $C_p=0.2\%$  ,  $x/d=20$



Fig. 6 a  
Flow behaviour of the  
injected polymer solution  
 $C_p=0.5\%$  ,  $x/d=0$



Fig. 6 b  
 $C_p=0.5\%$  ,  $x/d=20$

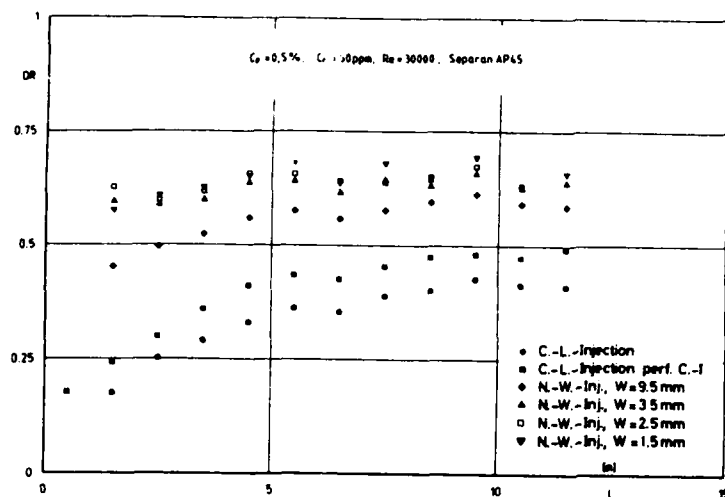


Fig. 7

Local drag reduction  
 $C_p=0.5\%$

Figure 7 shows the local drag reduction behaviour during injection of a 0.5% solution. In the case of near-wall injection with the injector slit up to 3.5 mm from the wall all values of local drag reduction offers the high efficiency of this type of injection technique. Even close to the injector we observed a remarkable drag reducing effect and there was only a weak increase downstream from the injection point.

Furthermore, there were only slight differences for the investigated ring injector types with distances from the wall up to 3.5 mm. Increasing the wall distance of the injector slit to 9.5 mm was found to cause a pronounced decrease in local drag reduction. In the case of centre-line injection the drag reducing effect was much weaker for both the injection of a single polymer thread as well as for the experiments with the perforated centre-line injector.

The same qualitative behaviour was obtained by the injection of the relatively quickly dispersing 0.2% polyacrylamide solution under the same experimental conditions (fig. 8). Probably due to the enhanced mixing process of the polymer solution in the turbulent flow, the differences between the investigated injector systems were much weaker compared to the more concentrated solution.

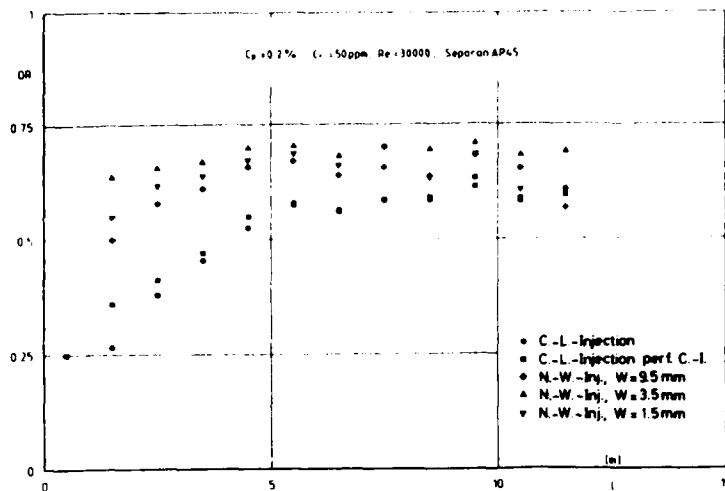


Fig. 8

Local drag reduction  
 $C_p = 0.2\%$

Qualitatively the same behaviour was observed for all investigated parameter combinations of Reynolds number and polymer concentration discussed below. For more details see [3].

Figure 9 shows a friction factor vs. Re-number plot for the injection of a 0.2% solution equivalent to an average polymer concentration  $C_R$  of 20ppm. It is obvious that for all Reynolds numbers the friction factor for the injection experiments were lower than the values obtained for a homogeneous solution of the same average concentration. Even for shear stresses lower than the critical value obtained for the homogeneous solution, both injection techniques exhibited a remarkable drag reducing effect. For increasing Re-numbers all data approach Virk's asymptote of maximum drag reduction for sufficiently high shear stresses.

Increasing  $C_p$  up to 0.5% we obtained a decreasing effectiveness over the whole range of Reynolds numbers investigated.

It should be mentioned that in this case the onset points of the drag reduction for centre-line injection and for the homogeneous solutions are nearly the same.

At the downstream end of the test section velocity profile measurements were made using a DISA two colour Laser-Doppler-Anemometer.

Due to space limitation I will focus on the velocity profiles obtained during the ring injection experiments.

The experiments discussed below were performed using a ring injector system with a wall distance of 3.5 mm and a gap width of 0.4 mm.

At a Reynolds number of 15.000 the core profile of a 20ppm homogeneous polyacrylamide solution was nearly the same as for the solvent, corresponding to the pressure drop measurements which showed no drag reducing effect under these experimental conditions. Injecting a 0.2% solution (fig. 10) using the ring injector, an extended buffer layer was observed. The core profile offers a nearly parallel shift to higher  $U^+$ -values indicating an unchanged turbulent structure in the core region of the pipe flow. The profile is qualitatively the same as for homogeneous solutions under drag reducing conditions. The parallel shift of about 16 dimensionless velocity units can probably be explained by the presence of short polymer lumps seen in the visualisation experiments. These lumps could act like a polymer with a very high molecular weight, decreasing the critical value of wall friction for the onset of drag reduction.

Increasing the Reynolds number up to 35.000 the measured velocity profiles showed the expected increase in drag reduction and also a nearly parallel shift of the core profile as seen by figure 11.

Increasing the average concentration  $C_R$  up to 50ppm (fig. 12) provides no further information, because the profiles are very close to Virk's Maximum Profile.

Injecting a 0.5% solution, which creates a polymer network which remains intact over the entire length of the test section, a different behaviour was observed.

After leaving the ultimate profile a much steeper slope of the core profile in comparison to the Newtonian solvent was observed. The presence of undispersed polymer threads alters the turbulent structure near the wall and also in the core region of the pipe flow. With increasing drag reduction the core profile approaches Virk's asymptote, also corresponding to the pressure drop measurements.

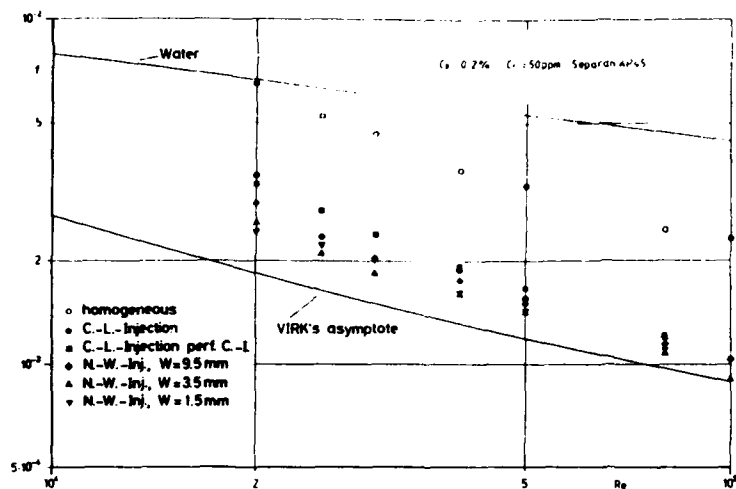


Fig. 9  
Friction behaviour of homogeneous and heterogeneous drag reduction

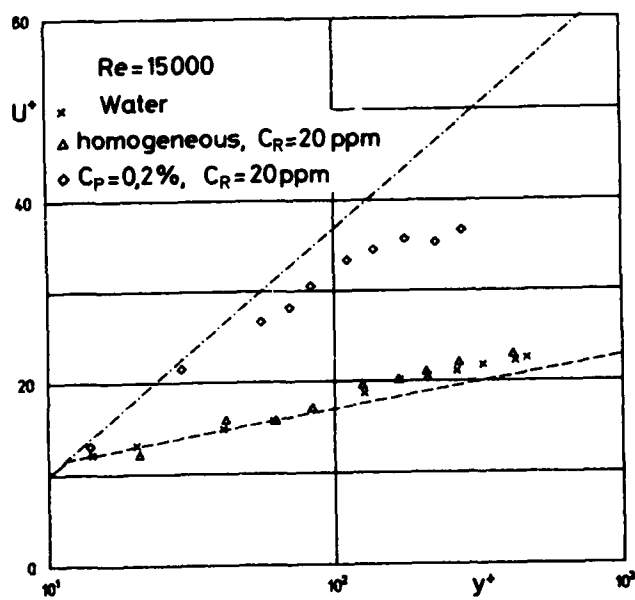


Fig. 10  
Dimensionless velocity profile  
 $C_p = 0.2\%$   
----- : Newtonian Fluid  
- · - · - : Ultimate Profile

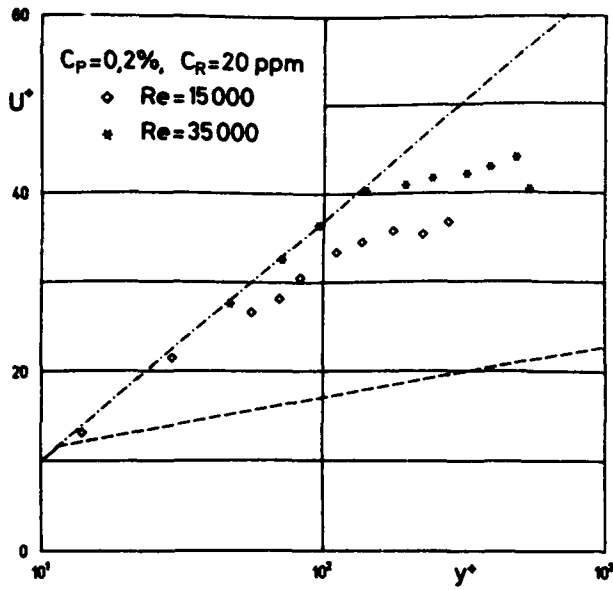


Fig. 11

Dimensionless velocity profile  
 $C_p=0.2\%$

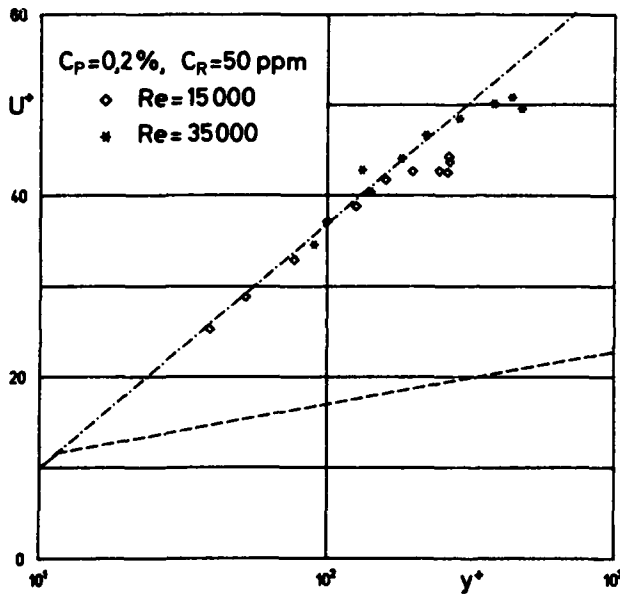


Fig. 12

Dimensionless velocity profile  
 $C_p=0.2\%$

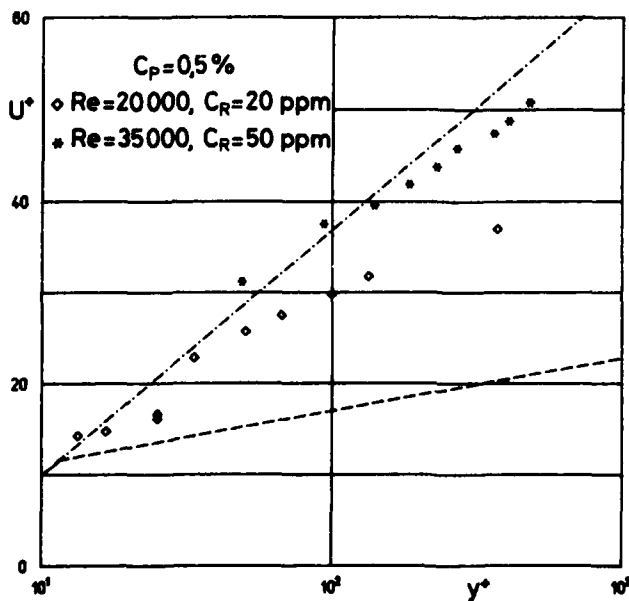


Fig. 13

Dimensionless velocity profile  
 $C_p=0.5\%$

## CONCLUSION

Finally a short summary of the experimental results.

- All experiments described here show drag reduction that was significantly larger than that obtained for homogeneous polymer solutions at the same average concentration.
- The near-wall injection showed much higher effectiveness than the centre-line injection of polymer solutions.
- In case of near-wall injection the turbulent structure was altered in the near-wall and also in the core region of the pipe flow, indicating that the polymer lumps and threads are able to influence a much wider spectrum of turbulent eddies in comparison to centre-line injection or the homogeneous drag reduction where only the small eddies are influenced. This assumption was supported by the fact that the ring injection of a 0.5% solution, which creates a network of polymer threads, exhibited a steeper slope of the core profile than the injection of a relatively quickly dispersing 0.2% solution under the same experimental conditions.

## NOTATION

- $C_p$  : Concentration of the injected polymer solution
- $C_R$  : Average polymer concentration
- $d$  : Tube diameter
- DR : Drag Reduction determined by pressure drop measurements
- $f$  : Fanning friction factor
- $l$  : Distance from the injection point
- Re : Reynolds number based on the solvent viscosity
- $U^+$  : Dimensionless local velocity
- $w$  : Distance of the injector slit from tube wall
- $y^+$  : Dimensionless distance from tube wall

## REFERENCES

- [1] Bewersdorff, H.-W., Rheol. Acta, 23 (1984) 522
- [2] Kowalski, T., Trans. R.I.N.A., 110 (1968) 207
- [3] Frings, B., Thesis, University of Dortmund (1985)  
Shortened version to be published in Rheol. Acta 1987

A MECHANISM FOR DRAG REDUCTION BASED ON  
STRESS RELAXATION

S.M. Penix and C.A. Petty  
Department of Chemical Engineering  
Michigan State University  
East Lansing, MI 48824-1226

ABSTRACT

A theoretical analysis of turbulent drag reduction by polymer additives assumes that dilute polymer solutions are viscoelastic and transport momentum at finite speeds. Transport effects are predicted in terms of known turbulent properties of Newtonian fluids. The Reynolds' stress depends on two distinct physical processes: 1) the space-time relaxation of molecular transport due to viscous and elastic effects; and, 2) the space-time relaxation for velocity fluctuations normal to the wall. Because of the finite memory of turbulent correlations near a rigid boundary, the short-time elastic response of the fluid controls the molecular transport contribution to the Reynolds stress. The theory predicts all the major features of the drag reduction phenomenon.

SYMBOLS

Independent Variables and Geometric Parameters:

$\underline{x}, \hat{\underline{x}}$  distinct position vectors  
 $x_1, x_2, x_3$  components of  $\underline{x}$  relative to the base vectors  $\underline{e}_1, \underline{e}_2,$  and  $\underline{e}_3,$  resp.  
 $t, \hat{t}$  distinct times  
 $\hat{t}$  time difference,  $t - \hat{t}$   
 $D$  diameter of a circular pipe

Physical Properties of the Fluid:

$\rho$  mass density  
 $\mu$  dynamic viscosity  
 $\nu$  kinematic viscosity  
 $\lambda$  stress relaxation time

Dynamic Variables and Turbulent Parameters:

$G(\underline{x}, t | \hat{\underline{x}}, \hat{t})$  Green's Function associated with the differential operator defined by Eq. (14) on the semi-infinite domain  
 $K(x_1, \hat{t})$  viscoelastic memory kernel  
 $T_w$  wall shear stress  
 $\underline{u}(\underline{x}, t)$  instantaneous velocity  
 $\underline{u}'(\underline{x}, \hat{t})$  velocity fluctuations  
 $u_1, u_2, u_3$  components of the velocity field relative to the base vectors  $\underline{e}_1, \underline{e}_2,$  and  $\underline{e}_3,$  resp.  
 $u_b$  bulk average velocity for pipe flow  
 $u_*$  friction velocity,  $(T_w/\rho)^{1/2}$   
 $\langle u_1'^2 \rangle^{1/2}$  root-mean-square of velocity fluctuations normal to the wall  
 $\langle u_3'^2 \rangle^{1/2}$  root-mean-square of velocity fluctuations in the axial direction  
 $\langle u_1' u_3' \rangle$  shear component of the Reynolds' stress  
 $\delta_c$  thickness of the constant stress region near the wall  
 $\nu_e(x_1)$  'eddy' kinematic viscosity  
 $\tau_{M1}, \tau_{H1}$  temporal scales associated with the hydrodynamic autocorrelation  $\langle u_i'(\underline{x}, t) u_j'(\underline{x}, \hat{t}) \rangle$  in a frame of reference moving with the local mean velocity  
 $\tau_{M3}, \tau_{H3}$  temporal scales associated with  $\langle u_i'(\underline{x}, t) u_j'(\underline{x}, \hat{t}) \rangle$  in a frame of reference moving with the local mean velocity  
 $\tau_c(x_1)$  transport time defined by Eq. (17).

Dimensionless Groups:

$\alpha_\lambda$	intrinsic Deborah number defined by Eq. (1); also see Eq. (44)
$\alpha_{M1}, \alpha_\lambda$	dimensionless ratios of characteristic times defined by Eqs. (23) and (24)
f	Fanning friction factor, $T_w / (\frac{1}{2} \rho u_b^2)$
De	gross Deborah number defined as $\lambda \nu / D^2$
$\Lambda$	Karman number, $Re(f)^{1/2}$
$\psi$	correlation coefficient defined by Eq. (2)

1. INTRODUCTION

Trace amounts of certain high molecular weight polymers can have a significant effect on the friction factor for fully developed turbulent pipe flows. Two remarkable, yet unexplained, general features of this phenomenon include the observations that 1) the 'onset' shear stress is approximately independent of the pipe diameter; and, 2) the maximum extent of drag reduction does not depend explicitly on the molecular properties of the polymer (Virk, 1975). The theory discussed here provides some new insights and a physical explanation for these results (also see Lyons and Petty, 1984.

Virk and others have suggested that an intrinsic Deborah number,

$$\alpha_\lambda = \frac{\lambda}{\tau_F} = \frac{(\text{fluid relaxation time})}{(\text{flow relaxation time})} \quad (1)$$

determines the behavior of 'onset'. If  $\alpha_\lambda$  is unique at 'onset' and  $\tau_F$  scales with wall parameters, then it follows that  $T_w^0$ , the 'onset' wall shear stress, is independent of the pipe diameter. Because turbulent flows have many time scales, a relevant characteristic flow time in Virk's criterion remains ambiguous. Virk, however, suggested that  $\tau_F^+ = 1 - 30$ , which corresponds to the duration of a turbulent 'burst' near the wall (Kovaszny, 1970). In what follows,  $\tau_F$  is identified as a characteristic time for the autocorrelation of velocity fluctuations normal to the wall and  $\alpha_\lambda$  is predicted at 'onset'.

Although some exceptions have been noted in the literature (Lee, et al., 1974), a maximum drag reduction asymptote occurs for a wide class of polymer/solvent pairs (Virk, 1975). A related phenomenon, observed indirectly by Seyer and

Metzner (1969a,b) and directly by Logan (1972), is the effect of polymer additives on the correlation coefficient,

$$\psi = \frac{-\langle u_1' u_3' \rangle}{\langle u_1'^2 \rangle^{1/2} \langle u_3'^2 \rangle^{1/2}} \quad (2)$$

in the constant stress region. For Newtonian fluids,  $\psi = 0.44$  (Schlichting, 1968); whereas, for dilute polymer solutions at maximum drag reduction,  $\psi = 0.20-0.30$  (Logan, 1972). As emphasized by Virk, a reduction in  $\psi$  implies that the polymer somehow interferes with the basic connection between radial and axial velocity fluctuations, and that direct dampening of these components may not occur. Because dilute polymer solutions presumably have stress relaxation times as large as  $10^{-2} - 10^{-3}$  sec. (Hershey and Zakin, 1967), momentum transfer from the mean turbulent field by radial velocity fluctuations into axial momentum fluctuations may be delayed enough to cause the decoupling of the Reynolds' stress. Inasmuch as  $\psi > 0$  in the near wall region even at maximum drag reduction, new processes for producing axial momentum fluctuations are apparently excited to counter this decoupling.

Because concentrated solutions of high molecular weight polymers are viscoelastic, it has been generally assumed that dilute solutions also retain some elastic features (Tanner, 1969). Unfortunately, exactly which rheological properties remain significant at concentrations less than 50 wppm is unclear. Consequently, many physical explanations of drag reduction have appeared in the literature based on widely differing, and sometimes incompatible, views. Specific theories emphasize either short-time scale or long-time scale phenomena. For instance, Patterson and Zakin (1968) and many others have developed explanations of drag reduction based on stress relaxation (short-time scale behavior); whereas, Lumley (1973) and others have given arguments for drag reduction based on the existence of high extensional (or elongational) 'viscosities' (long-time scale behavior). Both of these effects are linked to the fundamental property of real fluids that molecular transport of momentum propagates at finite speeds: for water,  $(\nu/\lambda)^{1/2} = 10,000$  cm/sec; but, for dilute polymer solutions,  $(\nu/\lambda)^{1/2} = 1-100$  cm/sec (Denn and Porteous, 1971).

Many researchers have studied drag reduction by examining the direct dynamic response of macromolecules to elemental flow structures thought to control the production of turbulence. Unfortunately, the spatial scales occupied by the polymer for dilute solutions are much smaller than any relevant turbulent scale, and the temporal scales associated with vortex stretching may not be long enough to affect the thermodynamic state of the polymer/solvent solution by 'stretching' the macromolecules. Although the intrinsic fluid properties of concentrated polymer solutions in complex flows are dependent on the invariants of the strain rate field, no direct experimental evidence for this type of behavior has been given for very dilute solutions. Therefore, we assume that polymer additives make the resulting solution viscoelastic and that the stress relaxation time  $\lambda$  and the dynamic viscosity  $\mu$  do not depend on the flow (cf. Hinch, 1977; and, Darby and Chang, 1984). However, because even a dilute viscoelastic fluid is unable to respond instantaneously to sudden changes in the strain rate field (see, esp., Metzner, et al., 1966; and Metzner, 1968), the phenomenon of molecular stress relaxation is retained in the theory.

## 2. MOLECULAR STRESS RELAXATION

For statistically stationary turbulent flows, the mean and fluctuating components of the molecular stress for a Maxwell fluid satisfy the following constitutive equations

$$\langle \underline{T} \rangle + \lambda \langle N(\underline{T}) \rangle = 2\mu \langle \underline{S} \rangle \quad (3)$$

$$\underline{T}' + \lambda \frac{\partial}{\partial t} \underline{T}' + \lambda [ N(\underline{T}) - \langle N(\underline{T}) \rangle ] = 2\mu \underline{S}' \quad (4)$$

The operator  $N(\cdot)$  is the upper convected derivative of Oldroyd (see Astarita and Marrucci, 1974) and makes the classical Maxwell model objective.  $\lambda$  and  $\mu$  are phenomenological coefficients independent of the flow field. Large scale eddies act to stretch fluid elements in the near wall region on a time scale comparable to  $l_c/u_*$ , where  $l_c$  denotes an appropriate length scale for the derivatives in  $N(\cdot)$ . If

$$\lambda \ll l_c/u_*, \quad (5)$$

then Eq. (3) can be approximated by

$$\langle \underline{T} \rangle = 2\mu \langle \underline{S} \rangle. \quad (6)$$

We assume that Eq. (6) holds for dilute polymer solutions and, therefore, that the viscoelastic properties of the fluid affect the mean field only indirectly through the fluctuating field.

Virk's criterion for 'onset',  $\lambda = \tau_F$ , and Ineq. (5) imply that there exist a relevant hydrodynamic time scale important for drag reduction which also satisfies

$$\tau_F \ll l_c/u_*. \quad (7)$$

Ineq. (7) expresses the idea that the short memory of turbulent fluctuations does not allow sufficient time for the development of high normal stresses, so the effect of  $N(\cdot)$  on the fluctuating molecular stress may also be neglected. The result

$$\underline{T}' + \lambda \frac{\partial}{\partial t} \underline{T}' = 2\mu \underline{S}', \quad (8)$$

gives a model which is no longer objective but still retains one of the most essential features of viscoelastic fluids, viz., stress relaxation in its most elemental form. Thus, for short time, Eqs. (6) and (8) imply that the mean field and the fluctuating field are coupled through the equation of motion, not the rheology. Obviously, this constitutive model would be inappropriate for concentrated polymer solutions which clearly show nonlinear behavior not predicted by Eqs. (6) and (8); however, one of the main assumptions here is that for very dilute polymer solutions and for short response times, the phenomenon of stress relaxation, exemplified by Eq. (8), controls the local molecular transport of momentum.

## 3. SCALING HYPOTHESES

The structure of turbulence with and without polymer additives near a rigid interface has been studied intensely for the past several decades. It is noteworthy that many statistical properties of the 'coherent' structures of dilute polymer solutions are apparently similar to their Newtonian counterparts when scaled with wall parameters.

Although these findings are still tentative (see, esp., Berman, 1978, and, Cantwell, 1981), they nevertheless suggest that fluid properties such as  $\mu$  and  $\lambda$  affect some statistical properties of the turbulent flow only indirectly through  $u_*$ . Clearly, the friction factor and the correlation coefficient  $\psi$ , as previously discussed, are two important exceptions.

Some experimental data supports the hypothesis that within the constant stress region,

$$\langle (u'_1)^2 \rangle^{1/2} / u_* = \langle (u'^0_1)^2 \rangle^{1/2} / u_* \quad (9a)$$

(The superscript  $(^0)$  denotes a solvent variable) Although the radial component of the turbulent intensity made dimensionless with the friction velocity shows some minor differences between the solvent and polymer solution, the approximate validity of Eq. (9a) allows estimates of other statistical properties of the flow by using the equation of motion and a rheological constitutive model.

Some temporal and spatial characteristics of 'coherent' structures near the wall also seem to scale with wall parameters (Achia and Thompson, 1977; Blackwelder and Haritonidis, 1983; Cantwell, 1981). For instance, if  $\tau_H$  and  $l_H$  represent integral scales of a space-time correlation between two components of the fluctuating velocity, then

$$\tau_H u_*^2 / \nu = \tau_H^0 u_*^0{}^2 / \nu = \tau_H^+ \quad (9b)$$

and

$$l_H u_* / \nu = l_H^0 u_*^0 / \nu = l_H^+ \quad (9c)$$

Eqs. (9b) and (9c) imply that the 'coherent' structures of dilute polymer solutions have memory times and correlation lengths much larger than their Newtonian counterparts, an indication that the mixing of momentum has been reduced by the presence of the polymer. The idea that  $\tau_H^+$  and  $l_H^+$  are nearly 'universal' is important, but perhaps not unexpected if inertial forces determine these parameters. Thus, once  $u_*$  is set, Eqs. (9b) and (9c) indirectly state that the polymer is unable to alter the underlying mechanism which determines the dynamic behavior of the large scale eddies near the wall.

The theory presented here exploits the experimental observation that some statistical properties of the flow scale with either inner or outer parameters. Hopefully, this strategy will help bridge the gap between basic studies of turbulent structures and estimates of transport effects.

The above scaling hypotheses are assumed to be valid in the constant stress region where

$$-\rho \langle u'_1 u'_3 \rangle + \mu \frac{d \langle u_3 \rangle}{dx_1} = T_w \quad (10)$$

$$x_1 = 0, \quad \langle u_3 \rangle = 0 \quad (10a)$$

$$x_1 = \delta_c, \quad \langle u_3 \rangle = u_b \quad (10b)$$

With  $u_* = (T_w / \rho)^{1/2}$  and  $x_1^+ = x_1 u_* / \nu$ , we also assume that

$$A x_1^{+4}, \quad 0 \leq x_1^+ \leq \delta_v^+ \quad (11a)$$

$$\frac{\langle u_1'^2 \rangle}{u_*^2} = \begin{cases} B x_1^{+3}, & \delta_v^+ \leq x_1^+ \leq \delta_b^+ \\ C x_1^+, & \delta_b^+ \leq x_1^+ \leq \delta_c^+ \end{cases} \quad (11b)$$

$$C x_1^+, \quad \delta_b^+ \leq x_1^+ \leq \delta_c^+ \quad (11c)$$

The parameters  $A$ ,  $B$ ,  $C$ ,  $\delta_v^+$ , and  $\delta_b^+$  are 'universal' (assumption). We assume that the thickness of the constant stress region made dimensionless with wall parameters depends only on the Karman number,  $A = \text{Re}_w^{1/2}$ . An empirical power-law expression will be used for  $\delta_c^+$ :

$$\delta_c^+ = a \Lambda^b \quad (11d)$$

The parameters 'a' and 'b' are also assumed to be independent of polymer/solvent properties. Thus, the foregoing seven parameters appearing in Eqs. (11a)-(11d) can be determined from Newtonian data (see Section 6).

#### 4. A RELAXATION MODEL FOR THE REYNOLDS STRESS

The continuity equation for an incompressible fluid, the equation of motion, and the approximate rheological model, defined by Eqs. (6) and (8), can be combined to obtain an equation for  $u'_3(\mathbf{x}, t)$ , the fluctuating component of the axial velocity. A relaxation model for the Reynolds stress  $\langle u'_i u'_j \rangle$

follows from this equation by using the method of Green's functions to obtain an explicit representation for  $u_j(\mathbf{x}, t)$ , and then ensemble averaging the result with  $u_i(\mathbf{x}, t)$ . The analysis yields

$$\langle u_i u_j \rangle = - \int_{\Omega} dt \int_{\Omega} d\hat{\Omega} G(\mathbf{x}, t | \hat{\mathbf{x}}, \hat{t})$$

$$(1 + \lambda \frac{\partial}{\partial t}) \langle u_i(\mathbf{x}, t) h_j(\hat{\mathbf{x}}, \hat{t}) \rangle \quad (12)$$

where

$$\langle u_i \hat{h}_j \rangle =$$

$$\langle u_i(\mathbf{x}, t) u_j(\hat{\mathbf{x}}, \hat{t}) \rangle \frac{d\langle u_j \rangle}{d x_1}$$

$$+ \langle u_i(\mathbf{x}, t) u'(\hat{\mathbf{x}}, \hat{t}) \cdot \hat{\nabla} u_j(\hat{\mathbf{x}}, \hat{t}) \rangle$$

$$+ \frac{1}{\rho} \langle u_i(\mathbf{x}, t) \frac{\partial p'}{\partial x_3} \rangle \quad (13)$$

In developing Eq. (12), we have assumed that the flow is statistically stationary and statistically homogeneous in the axial and circumferential directions. The Green's function, which has units of reciprocal volume in Eq. (12), is associated with a hyperbolic operator on the semi-infinite domain  $\Omega$ ,

$$L = (1 + \lambda \frac{\partial}{\partial t}) (\frac{\partial}{\partial t} + \langle u_3 \rangle \frac{\partial}{\partial x_3}) - \nu \nabla^2. \quad (14)$$

$L$  is parabolic when  $\lambda = 0$  and hyperbolic for  $\lambda > 0$ . For small values of  $\hat{t} = t - \hat{t}$ ,  $G(\mathbf{x}, t | \hat{\mathbf{x}}, \hat{t})$  is spatially peaked in a frame of reference moving with the local mean velocity and is nonzero over a finite domain which scales with  $\hat{t}(\nu/\lambda)^{1/2} < \infty$ . For  $\lambda = 0$ , Eq. (12) yields an exact, but unclosed, representation for the turbulent flux of the Newtonian solvent.

Two important physical effects involving the mean velocity gradient contribute to the Reynolds' stress. These are (1) an inertial coupling by fluctuations in the radial velocity

$$\langle u_i(\mathbf{x}, t) u_j(\hat{\mathbf{x}}, \hat{t}) \rangle \frac{d\langle u_j \rangle}{d x_1};$$

and, (2) an acceleration coupling because of the elastic nature of the fluid

$$\lambda \langle u_i(\mathbf{x}, t) \frac{\partial}{\partial t} u_j(\hat{\mathbf{x}}, \hat{t}) \rangle \frac{d\langle u_j \rangle}{d x_1}$$

Our previous studies have shown that this latter effect is responsible for the maximum drag reduction asymptote (Lyons and Petty, 1984).

The Green's function in Eq. (12) accounts for the spatial and temporal mixing of axial momentum fluctuations by mean convection and by molecular transport. For  $\lambda > 0$ , a finite propagation velocity due to the elastic nature of the fluid slows down the mixing process. Thus, an apparent 'onset' phenomenon for drag reduction occurs because the local space-time domain over which molecular transport processes affect the Reynolds stress depends simultaneously on the space-time domain over which radial fluctuations in the velocity are statistically correlated. For instance, if the characteristic time scales for  $\langle u_i(\mathbf{x}, t) u_j(\hat{\mathbf{x}}, \hat{t}) \rangle$  are both large compared to  $\lambda$  (see Figure 1), then the viscoelastic Green's function has ample time to relax to the viscous Green's function and no drag reduction occurs. On the other hand, as the wall shear stress increases, the time scales of the turbulence decrease (i.e.,  $\tau_{HI}^+$  and  $\tau_{HI}^+$  remain constant) and, presumably, become comparable to the molecular relaxation time  $\lambda$ . At wall shear stresses above this critical value, the elastic nature of the fluid hinders the mixing of axial momentum so drag reduction results. Thus, the 'onset' phenomenon within this physical framework results because of the interplay between two distinct temporal relaxation processes which govern the Reynolds' stress.

The higher order velocity correlations in Eq. (12), including the pressure fluctuations, make important contributions, but we assume that they influence  $\langle u_i u_j \rangle(x_1)$  indirectly through the space-time structure of  $\langle u_i(\mathbf{x}, t) u_j(\hat{\mathbf{x}}, \hat{t}) \rangle$ . Thus, the scaling hypotheses are fundamental to this study and, hopefully, account for the essential nonlinear aspects of turbulent flows. If the triple velocity correlation approximately balances the pressure correlation, then the above conjecture would be justified with the result that

$$\langle u_i' \hat{h}_j \rangle = \langle u_i'(\mathbf{x}, t) u_j'(\hat{\mathbf{x}}, \hat{t}) \rangle \frac{d \langle u_j' \rangle}{d x_1} \quad (15)$$

Eqs. (12 and 15) define  $\langle u_i' u_j' \rangle(x_1)$  near the wall where the mean gradient is large (cf., Sternberg, and Coles 1978). This approach yields very reasonable predictions for many of the observed features of drag reducing flows.

The space-time correlation and the mean gradient in Eq. (12) vary over distances on the order of  $10 \nu/u_*$ , or larger. In a frame of reference moving with the local mean velocity, the Green's function in Eq. (12) has an "effective" spatial domain of influence comparable to  $(r_{M1} \nu)^{1/2}$ . Therefore, for small values of  $r_{M1}$ , say  $r_{M1}^+ \ll 100$ , a spatial smoothing approximation can be used to estimate  $\langle u_i' u_j' \rangle(x_1)$  for Newtonian and viscoelastic fluids. This yields an "eddy" viscosity type model for the turbulent flux in the near wall region of the form (cf. Poreh and Hassid, 1977; Mizushima and Usui, 1977; Shenoy and Talathi, 1985).

$$\nu_e = \langle u_i'^2 \rangle(x_1) \tau_c(x_1) \quad (16)$$

where the characteristic transport time  $\tau_c(x_1)$  is defined by

$$\tau_c(x_1) = \left[ 1 + \frac{\lambda}{r_{H1}} \right] \int_0^{r_{M1}} K(x_1, \hat{r}) \exp(-\hat{r}/r_{H1}) d\hat{r} \quad (17)$$

The viscoelastic memory kernel  $K(x_1, \hat{r})$  is simply an integral property of the Green's function, viz.,

$$K(x_1, \hat{r}) = \int_0^{+\infty} d\hat{x}_1 \int_{-\infty}^{+\infty} d\hat{x}_2 \int_{-\infty}^{+\infty} d\hat{x}_3 G(\mathbf{x}, t | \hat{\mathbf{x}}, \hat{t}) \quad (18)$$

The parameters  $r_{M1}$  and  $r_{H1}$  in Eq. (17) characterize the hydrodynamic relaxation of the turbulence. As indicated momentarily,  $r_{M1}$  controls the 'onset' of drag reduction, and  $r_{M1}/r_{H1}$  determines the maximum extent of drag reduction.

Because the Green's function is zero on the boundary,  $\tau_c(x_1)$  is also zero for  $x_1 = 0$ ; however, it rapidly approaches its limiting value of  $\tau_c(\infty)$

for  $x_1 \gg (r_{M1} \nu)^{1/2}$ . Inasmuch as  $\nu_e \ll \nu$  deep in the viscous sublayer,  $\tau_c(x_1)$  can be approximated by  $\tau_c(\infty)$  everywhere. Therefore, the resulting relaxation model for the Reynolds' stress in the near wall region is

$$\langle u_i' u_j' \rangle = - \langle u_i'^2 \rangle(x_1) \tau_c(\infty) \frac{d \langle u_j' \rangle}{d x_1} \quad (19)$$

In Eq. (19),  $\tau_c(\infty)$  is defined by Eq. (17) with  $K(x_1, \hat{r})$  replaced by

$$K(\infty, \hat{r}) = 1 - e^{-\hat{r}/\lambda}, \quad \hat{r} \geq 0 \quad (20)$$

If  $\lambda = 0$ , the Green's function is viscous and  $K(\infty, \hat{r}) = 1$  for all  $\hat{r}$ . Thus, as expected, the 'eddy' viscosity for a Newtonian fluid is determined by the hydrodynamic time scales and the intensity of the radial velocity fluctuations (Monin and Yaglom, 1971):

$$\nu_e^0(x_1) = \tau_{H1}^0 (1 - e^{-r_{M1}^0/r_{H1}^0}) \langle u_i'^2 \rangle(x_1) \quad (21)$$

However, for  $\lambda > 0$ , the elastic behavior of the dilute polymer solution reduces the effectiveness of the turbulent transport of momentum with the result that  $\nu_e < \nu_e^0$ . Note that  $K(\infty, \hat{r})$  approaches the Newtonian limit for  $\hat{r} \gg 3\lambda$ . Whence, the 'eddy' viscosity for a Maxwell fluid is the same as for a Newtonian fluid if the hydrodynamic relaxation of the autocorrelation  $\langle u_i'(\mathbf{x}, t) u_j'(\hat{\mathbf{x}}, \hat{t}) \rangle$  is slow relative to the elastic relaxation of

the memory kernel  $K(\infty, \hat{r})$ . Otherwise,  $\nu_e < \nu_e^0$  and drag reduction obtains.

Inserting Eq. (20) into (17) and carrying out the integration gives one of the key results of this approach (Lyons and Petty, 1984)

$$\begin{aligned} \tau_c(\infty) / \tau_{H1} &= \\ &= 1 - \exp(-\alpha_{M1}) \\ &= \alpha_{\lambda 1} \exp(-\alpha_{M1}) \left[ 1 - \exp(-\alpha_{M1}/\alpha_{\lambda 1}) \right] \end{aligned} \quad (22)$$

where

$$\alpha_{M1} = r_{M1}/r_{H1} \quad (23)$$

and

$$\alpha_{\lambda 1} = \lambda / r_{H1} \quad (24)$$

For fixed  $\alpha_{M1}$  and large  $\alpha_{\lambda 1}$ , the characteristic transport time reaches a lower asymptote

$$\begin{aligned} (\tau_c(\infty) / r_{H1})_{MIN} = \\ 1 - (1 + \alpha_{M1}) \exp(-\alpha_{M1}). \end{aligned} \quad (25)$$

Eq. (25) stems from a balance between an increase production of axial momentum due to an elastic coupling of radial velocity fluctuations with the mean gradient and the hindered transport of this momentum due to a finite propagation speed; this phenomenon, as previously mentioned, leads to a maximum drag reduction asymptote. Thus, Eq. (22) may provide a basis for understanding drag reduction in rough pipes (Spangler, 1969; Virk, 1971) or in annular pipes (Tin and Chee, 1979).

Eqs. (16), (21), and (22) combine to give the following result for the eddy viscosity of a viscoelastic fluid

$$\nu_e = R_1 \nu_e^0 \quad (26)$$

where

$$R_1 = 1 - \alpha_{\lambda 1} \frac{(1 - \exp(-\alpha_{M1} / \alpha_{\lambda 1}))}{(\exp(+\alpha_{M1}) - 1)} \quad (27)$$

Figure 2 illustrates the behavior of  $R_1$ . For fixed  $\alpha_{M1}$ , the limiting value of  $R_1$  at maximum drag reduction (i.e.,  $\alpha_{\lambda 1} \rightarrow \infty$ ) is given by

$$(R_1)_{MDR} = 1 - \frac{\alpha_{M1}}{(\exp(\alpha_{M1}) - 1)} \quad (28)$$

Figure 2 and Eq. (27) clearly show that the elastic properties of the fluid begin to dampen the eddy viscosity significantly when  $\alpha_{\lambda 1} = \alpha_{M1}$ . Thus, if the cut-off time for the autocorrelation of velocity fluctuations normal to the wall becomes comparable to the polymer relaxation time  $\lambda$ , then drag reduction occurs.

##### 5. RELAXATION MODELS FOR THE AXIAL INTENSITY AND THE CORRELATION COEFFICIENT

An equation for  $\langle (u_3')^2 \rangle$  can be derived in the same way as Eq. (19) was developed. The result,

reported here for the first time, gives an explicit connection between the underlying temporal structure of the turbulence and the mean field:

$$\begin{aligned} \langle u_3'^2 \rangle(x_1) = \\ R_3 r_{H3} (1 - \exp(-\alpha_{M3})) \langle u_1' u_3' \rangle(x_1) \frac{d\langle u_3 \rangle}{dx_1} \end{aligned} \quad (29)$$

The parameters  $r_{H3}$  and  $r_{M3}$  (i.e.,  $\alpha_{M3} = r_{M3} / r_{H3}$ ) are defined by Figure 1 and  $R_3$  is given by Eq. (27) with  $\alpha_{\lambda 1}$  and  $\alpha_{M1}$  replaced by  $\alpha_{\lambda 3}$  and  $\alpha_{M3}$ , respectively.

Eqs. (16), (19), and (10) can be used to reexpress Eq. (29) as

$$\begin{aligned} \langle (u_3')^2 \rangle / u_*^2 = \\ R_3 r_{H3}^+ (1 - \exp(-\alpha_{M3})) \frac{\nu_e / \nu}{(1 + \nu_e / \nu)^2} \end{aligned} \quad (30)$$

This yields the interesting theoretical conclusion that the peak axial intensity occurs at a distance  $\xi$  from the wall where  $\nu_e(\xi) = \nu$  and, consequently,

$$\frac{\max \langle (u_3')^2 \rangle^{1/2} / u_*}{\max \langle (u_3')^2 \rangle^{1/2} / u_*^0} = \sqrt{R_3} \quad (31)$$

(The superscript (0) denotes a solvent variable.) Moreover, with the model for  $\langle (u_1')^2 \rangle / u_*^2$  defined by Eq. (11), it follows that

$$\frac{\xi_{polymer}^+}{\xi_{solvent}^+} = (R_1)^{-1/3} \quad (32)$$

Because  $0 < R_1 \leq 1$  and  $0 < R_3 \leq 1$  (see Figure 2), we conclude that the peak axial intensity for a Maxwell fluid is less than its Newtonian counterpart and occurs further from the wall.

A relaxation model for the correlation coefficient, defined by Eq. (2), follows by combining Eqs. (16), (19), (10), and (30) with the result that

$$\psi^2 = \frac{R_1 r_{H1}^+ (1 - e^{-\alpha_{M1}})}{R_3 r_{H3}^+ (1 - e^{-\alpha_{M3}})} \quad (33)$$

Eq. (33) is important because it gives a theoretical, albeit approximate, relationship between the assumed 'universal' temporal parameters of the two autocorrelation functions

$\langle u_1'(x, t)u_1'(x, t) \rangle$  and  $\langle u_3'(x, t)u_3'(x, t) \rangle$ . The unexpected result that  $\psi < \psi^0$  provided  $R_3 > R_1$  implies that  $\alpha_{M3} > \alpha_{M1}$  (see Figure 2). It is also noteworthy that Ea. (33) permits  $\psi = \psi^0$  for some turbulent flows, yet drag reduction still obtains. Such a theoretical possibility occurs when

$$\tau_{M1}^+ - \tau_{M3}^+ \ll \tau_{H1}^+ - \tau_{H3}^+ .$$

#### 6. THE FRICTION FACTOR AND PARAMETER ESTIMATES

The parameters in Eq. (21) can be estimated from experimentally determined values of  $\nu_e^0(x_1)$ . The data presented by Virk (1975) implies that

$$\bar{B} = \tau_{H1}^+ (1 - e^{-\alpha_{M1}})_B = .00087 \quad (34)$$

$$\bar{C} = \tau_{H1}^+ (1 - e^{-\alpha_{M1}})_C = .400 \quad (35)$$

and

$$\delta_B^+ = 21.44 \quad (36)$$

Because  $\nu_e^0 \ll \nu$  for  $x_1^+ < \delta_v^+$ , Eq. (11a) does not have a significant effect on any of the calculated quantities; therefore, Eq. (11b) will be applied over the interval  $0 \leq x_1^+ \leq \delta_b^+$ .

A synthesis of the previous results yields an equation for the Fanning friction factor,  $f = 2T_w/\rho u_b^2$ . The expression depends on  $R_1$  and  $\Lambda$  as well as the previously defined 'universal' constants:  $\bar{B}$ ,  $\bar{C}$ ,  $\delta_b^+$ , 'a', and 'b'. With  $R_1 = 1$ , which corresponds to a Newtonian fluid, and with

$$\delta_c^+ = 0.185 \Lambda^{0.988} \quad (37)$$

the derived expression for  $f$  agrees with the Prandtl-Karman law. For a viscoelastic fluid,

$$\begin{aligned} \frac{1}{fE} = X & \left[ 4.584 + 2.528 \ln \left( \frac{(X+1)^3}{X^3+1} \right) \right. \\ & \left. + 8.752 \tan^{-1} \left( \frac{2 \cdot X}{X \sqrt{3}} \right) \right] \\ & + \frac{0.7071}{Y} \ln \left( \frac{1 + \delta_c^+ Y}{1 + 21.44 Y} \right) \quad (38) \end{aligned}$$

where

$$X = 0.4886/(R_1)^{1/3} \quad (39)$$

$$Y = 0.400 R_1 \quad (40)$$

Because  $\psi^0 = 0.44$  and

$$\max \frac{\langle (u_3')^2 \rangle^{1/2}}{u_*} = 2.7,$$

Eqs. (30) and (33) with  $R_1 = 1$  and  $R_3 = 1$  imply that

$$\tau_{H1}^+ (1 - e^{-\alpha_{M1}}) = 5.65 \quad (41)$$

$$\tau_{H3}^+ (1 - e^{-\alpha_{M3}}) = 29.16 \quad (42)$$

These estimates also use the theoretical result that the peak axial intensity occurs when  $\nu_e^0 = \nu$ .

Eq. (38) shows that the friction factor depends on  $\Lambda$ ,  $\alpha_{M1}$ , and an intrinsic Deborah number  $\alpha_{\lambda 1} (= \lambda/\tau_{H1})$ . Because  $\tau_{H1}$  scales with  $u_*$  and  $\nu$  (see Section 3), it is more convenient to introduce a gross Deborah number which depends only on geometry and the physical properties of the fluid. With

$$De = \lambda \nu / D^2 \quad (43)$$

it follows that

$$\alpha_{\lambda 1} = \lambda / \tau_{H1} = De \Lambda^2 / 2 \tau_{H1}^+ = \lambda T_w / \mu \tau_{H1}^+ \quad (44)$$

Once the two 'universal' time scales  $\tau_{H1}^+$  and  $\tau_{M1}^+$  have been estimated, then the reduction in the 'eddy' viscosity can be calculated for different values of the two groups  $De$  and  $\Lambda$ . Eq. (27) defines  $R_1$ . Likewise, once  $\tau_{H3}^+$  and  $\tau_{M3}^+$  have been specified, then  $R_3$  can be calculated in terms of  $De$  and  $\Lambda$ .

Two additional relationships, besides Eqs. (41) and (42), are needed to determine the four dimensionless time constants. Earlier we noted that  $R_1$  depends only on  $\alpha_{M1}$  for large values of  $\alpha_{\lambda 1}$  (see Eq. (28)). Also,  $R_3$  depends only on  $\alpha_{M3}$  for  $\alpha_{\lambda 3} \rightarrow \infty$ . Therefore, for a fixed value of  $\Lambda$ , Eq. (38) can be used to determine  $\alpha_{M1}$  inasmuch as (Virk, 1975)

$$\lim (1/\epsilon) = 43.60, \text{ at } \Lambda = 10,000. \quad (45)$$

$$\alpha_{\lambda 1} \rightarrow \infty$$

Eq. (31) motivates the use of peak axial intensity data at maximum drag reduction ( $\alpha_{\lambda 3} = \infty$ ) to determine  $\alpha_{M3}$ . Although the experimental results are not as compelling as Virk's maximum drag reduction asymptote for the friction factor, an estimate of  $R_3$  at maximum drag reduction can still be made using axial intensity data (See Lumley and Kubo, 1984; and Berman, 1984). Therefore,

$$R_3(\alpha_{M3}, \infty) = 0.49. \quad (46)$$

Finally, Eqs. (41), (42), (45), and (46) fix the values of the hydrodynamic relaxation times as

$$\tau_{H1}^+ = 15, \tau_{M1}^+ = 7 \quad (47)$$

$$\tau_{H3}^+ = 41, \tau_{M3}^+ = 51. \quad (48)$$

## 7. DISCUSSION OF RESULTS AND CONCLUSIONS

Figure 3 shows the predicted behavior of the friction factor given by Eq. (38). Although Eq. (45) was used to estimate  $\alpha_{M1}$ , it is noteworthy that the slope of the maximum drag reduction asymptote closely follows the experimental data summarized by Virk (1975). The dashed line represents Virk's empirical correlation. The lower curve follows from Eq. (38) by setting  $De = 0$ ; the result agrees with the classical Prandtl-Karman 'law' because the two parameters in Eq. (37) were defined so this would occur.

Theoretical calculations presented in Figure 4 give the same qualitative behavior observed experimentally for dilute polymer solutions. A maximum drag reduction asymptote obtains either by increasing  $De$  at constant  $\Lambda$  or by increasing  $\Lambda$  at constant  $De$ . Physically, both of these strategies have the effect of reducing the characteristic transport time  $\tau_c(\infty)$  controlling the 'eddy' viscosity (see Eqs. (22) and (26) as well as Figure 2). Thus, a maximum drag reduction asymptote occurs because the elastic nature of the fluid not only moderates the molecular transport of fluctuating momentum but also enhances the local production of axial fluctuations. Therefore, a

limiting behavior of the friction factor results when these two processes balance.

Because the structure of the turbulence has finite memory and because molecular stress relaxes exponentially (see Eq. (20)), the friction factor in Figure 3 does not deviate significantly from the P-K law until  $\tau_{H1} < \lambda$  (also see Figure 2). If an 'onset' criterion is defined as

$$R_1(\alpha_{M1}, \alpha_{\lambda 1}^0) = 0.90, \quad (49)$$

then for  $\alpha_{M1} = 0.4667$  (see Eq. (47)) it follows that  $\alpha_{\lambda 1}^0 = 0.0595$ . Thus, drag reduction occurs provided the wall shear stress exceeds a certain critical value given by

$$\lambda T_w^0 / \mu = 0.06 \tau_{H1}^+ \quad (50)$$

Eq. (50) depends only on the phenomenological coefficients of the fluid because  $\alpha_{M1}$  is 'universal'. Thus, the ubiquitous observation that the 'onset' wall shear stress is independent of diameter provides a posteriori justification for the temporal scaling hypotheses of Section 3.

Figure 4 shows the effect of polymer additives on the axial intensity. The parameters  $\tau_{H3}^+$  and  $\tau_{M3}^+$  were determined by using experimental measurements of the peak axial intensity for  $De = 0$  and  $De = \infty$ . Other aspects of Figure 4 stem directly from the underlying physical effects contained in Eq. (30). It is noteworthy that the theory predicts the correct location of the peak intensity for the solvent ( $De = 0$ ), but that the results for the polymer ( $De > 0$ ) are closer to the wall than generally observed experimentally. Also, some experimental measurements show peak axial intensities for the dilute polymer solution larger than the solvent. Because  $R_3 \leq 1$ , it follows from Eq. (31) that the theory developed here always predicts

$$\max_{x_1} \frac{\langle (u_3^+)^2 \rangle^{1/2}}{u_*} \leq \max_{x_1} \frac{\langle (u_3^0)^2 \rangle^{1/2}}{u_*}$$

The correlation coefficient  $\psi$  depends on all four turbulent time scales:  $\tau_{H1}^+$ ,  $\tau_{M1}^+$ ,  $\tau_{H3}^+$ , and  $\tau_{M3}^+$ . Eq. (33) implies that

$$\psi/\psi^0 = (R_1/R_3)^{1/2}$$

Figure 5 shows how the polymer affects  $\psi$  and gives the interesting conclusion that for maximum drag reduction

$$\psi_{MDR} = 0.29$$

This theoretical result agrees with earlier experimental findings of Logan (1971).

For small diameter pipes, Figure 6 shows that the stress relaxation theory accurately portrays the effect of diameter on the friction factor for a specific polymer/solvent system. The curve for  $D = 2.92$  mm was used to find the polymer relaxation time  $\lambda$  by using Eq. (38) and the experimental data. The two remaining curves at different diameters were calculated by using Eq. (38) for the same value of  $\lambda$ . The results are encouraging and suggest that this approach may provide a useful methodology for scaling drag reduction data.

**Acknowledgement.** Faith Peterson prepared the final manuscript and H.C. Chen checked our calculations and developed the results shown in Figure 5. We sincerely appreciate these contributions to the manuscript.

#### 8. REFERENCES

- Achia, B.V. and Thompson, D.W., 1977, "Structure of the Turbulent Boundary in Drag-Reducing Pipe Flow," *J. Fluid Mech.*, **81**, 439.
- Astarita, G. and Marrucci, 1974, Principles of Non-Newtonian Fluid Mechanics, McGraw-Hill.
- Berman, N.S., 1978, "Drag Reduction by Polymers," *Ann. Rev. Fluid Mech.*, **10**, 47.
- Berman, N.S., 1984, "A Qualitative Understanding of Drag Reduction by Polymers," IUTAM Symp., Essen, June 26-28.
- Blackwelder, R.F. and J.H. Haritonidis, 1983, "Scaling of the Bursting Frequency in Turbulent Boundary Layers," *J. Fluid Mech.*, **132**, 87.
- Cantwell, B.J., 1981, "Organized Motion in Turbulent Flow," *Ann. Rev. Fluid Mech.*, **13**, 457.
- Coles, D.E., 1978, "A Model for the Flow in the Viscous Sublayer," *Lehigh Workshop on Coherent Structure in Turbulent Boundary Layers*, C.R. Smith and D.E. Abbott (Editors), 462.
- Darby, R. and H.D. Chang, 1984, "Generalized Correlation for Friction Losses in Drag Reducing Polymer Solutions," *AIChE J.*, **30**, 274.
- Denn, M.M. and K.C. Porteous 1971, "Elastic Effects in Flow of Viscoelastic Liquids," *Chem. Eng. J.*, **2**, 280.
- Hershey, H.C. and J.L. Zakin, 1967, "A Molecular Approach to Predicting the Onset of Drag Reduction in the Turbulent Flow of Dilute Polymer Solutions," *Chem. Eng. Sci.*, **22**, 1847.
- Hinch, E.J., 1977, "Mechanical Models of Dilute Polymer Solutions in Strong Flows," *Phys. Fluids*, **20**, S22.
- Kovaszny, L.S.G., 1970, "The Turbulent Boundary Layer," *Ann. Rev. Fluid Mech.*, **2**, 95.
- Lee, W.K., R.C. Vaseleski, and A.B. Metzner, 1974, "Turbulent Drag Reduction in Polymeric Solutions Containing Suspended Fibers," *AIChE J.*, **20**, 128.
- Logan, S.E., 1972, "Laser Velocimeter Measurement of Reynolds' Stress and Turbulence in Dilute Polymer Solutions," *AIAA J.*, **10**, 962.
- Lumley, J.L., 1973, "Drag Reduction in Turbulent Flow by Polymer Additives," *J. Polymer Sci., Macromolecular Reviews*, **7**, 263.
- Lumley, J.L., I. Kubo, 1984, "Turbulent Drag Reduction by Polymer Additives: A Survey," IUTAM Symp. Essen, June 26-28.
- Lyons, S. and C.A. Petty, 1984, "Predictions of Turbulent Drag Reduction for a Linear Viscoelastic Fluid," IUTAM Symp., Essen, June 26-28.
- Mizushima, T. and H. Usui, 1977, "Reduction of Eddy Diffusion for Momentum and Heat in Viscoelastic Fluid Flow in a Circular Tube," *Phys. Fluids*, **20**, S100.
- Metzner, A.B., J.L. White, and M.M. Denn, 1966, "Constitutive Equations for Viscoelastic Fluids for Short Deformation Periods and for Rapidly Changing Flows: Significance of the Deborah Number," *AIChE J.*, **12**, 863.
- Metzner, A.B., 1968, "Sudden Deformation of Viscoelastic Continua," *Trans. Soc. Rheology*, **12**, 57.
- Monin, A.S. and A.M. Yaglom, 1971, Statistical Fluid Mechanics, MIT Press.
- Patterson, G.K. and J.L. Zakin, 1968, "Prediction of Drag Reduction with a Viscoelastic Model," *AIChE J.*, **14**, 434.
- Poreh, M. and S. Hassid, 1977, "Mean Velocity and Turbulent Energy Closures for Flows with Drag Reduction," *Phys. Fluid*, **20**, S193.
- Seyer, F.A. and A.B. Metzner, 1969a, "Drag Reduction in Large Tubes," *Can. J. Chem. Eng.*, **47**, 525.
- Seyer, F.A. and A.B. Metzner, 1969b, "Turbulence Phenomena in Drag Reducing Systems," *AIChE J.*, **15**, 426.
- Shenoy, A.V. and M.M. Talathi, 1985, "Turbulent Pipe Flow Velocity Profile Model for Drag-Reducing Fluids," *AIChE J.*, **31**, 520.
- Spangler, J.G., 1969, "Studies of Viscous Drag Reduction with Polymers Including Turbulence Measurements and Roughness Effects," p. 131 in Viscous Drag Reduction, C.S. Wells (Ed.) Plenum Press.

Sternberg, J., 1962, "A Theory for the Viscous Sublayer of a Turbulent Flow," *J. Fluid Mech.*, **13**, 241.

Tanner, R.I., 1969, "Normal-Stress Effects in Drag-Reducing Fluids," p. in *Viscous Drag Reduction*, C.S. Wells (Ed.), Plenum Press.

Tiu, C. and N.O. Chee, 1979, "Turbulent Flow Behavior of Dilute Polymer Solutions in an Annulus," *Can. J. Chem. Eng.*, **57**, 572.

Virk, P.S., 1971, "Drag Reduction in Rough Pipes," *J. Fluid Mech.*, **45**, 225.

Virk, P.S., 1975, "Drag Reduction Fundamentals," *AICHE J.*, **21**, 625.

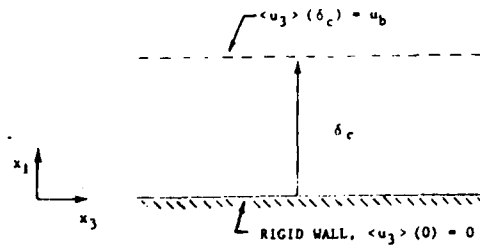


Figure 1a. Constant Stress Region For Fully Developed Pipe Flow.

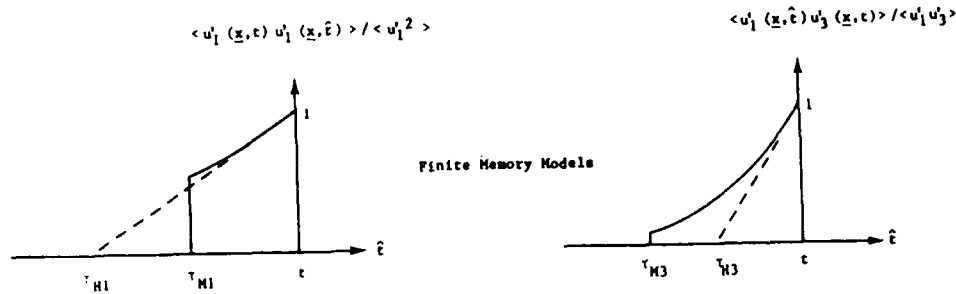


Figure 1b. Turbulent Relaxation Models In The Constant Stress Region.

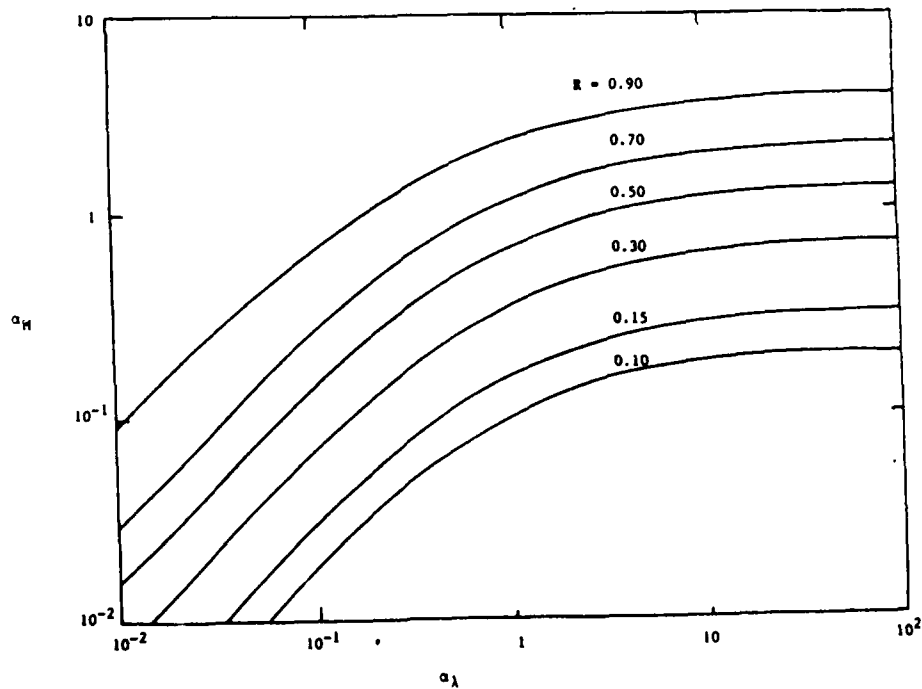


Figure 2. The Effect of Turbulent and Polymer Relaxation Times on the Relative Transport Times for the Stress Relaxation Model (Lyons and Petty, 1984).

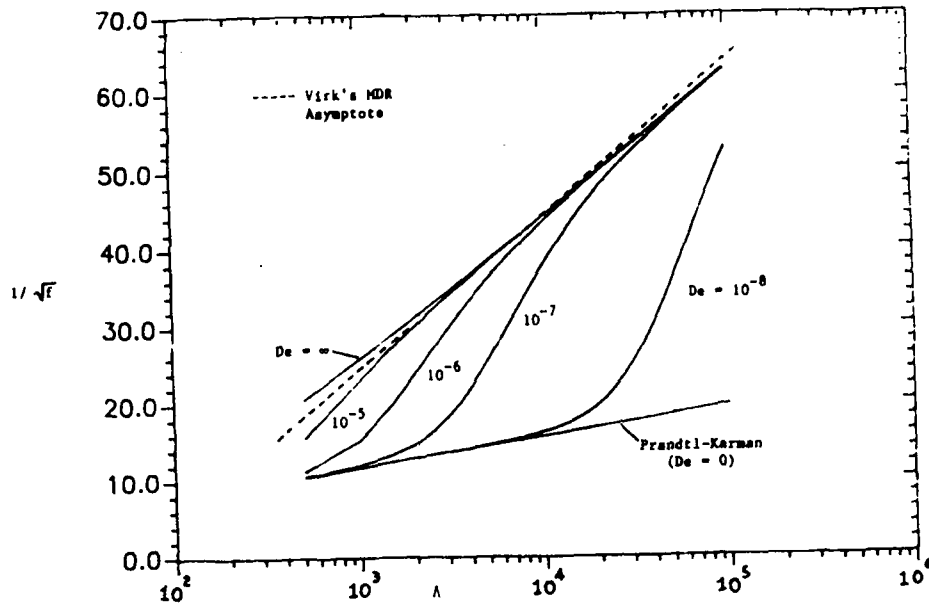


Figure 3. The Turbulent Friction Factor Predicted by The Stress Relaxation Model ( $\tau_{M1}^+ = 15$ ,  $\tau_{M1}^+ = 7$ ).

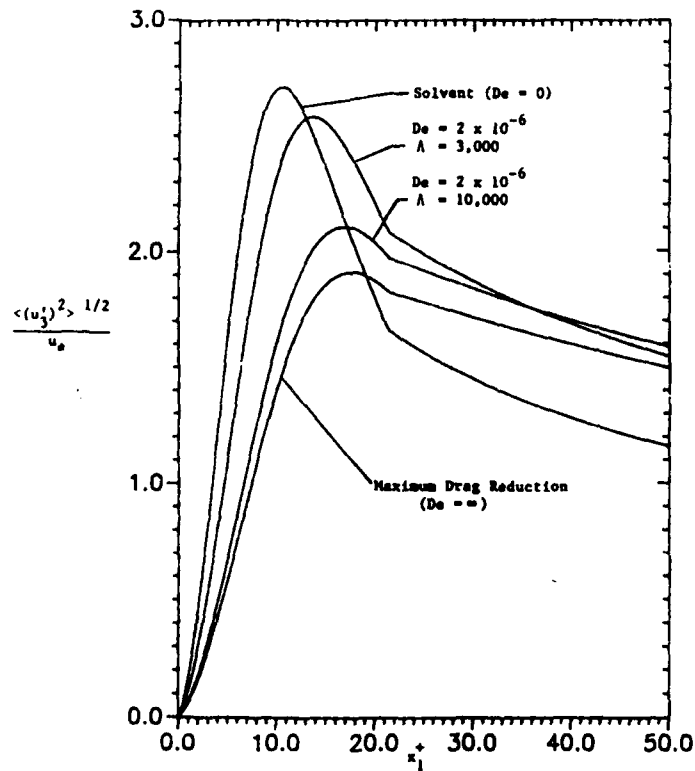


Figure 4. The Axial Turbulent Intensity Predicted by the Stress Relaxation Model ( $\tau_{M1}^+ = 15$ ,  $\tau_{M1}^+ = 7$ ,  $\tau_{M3}^+ = 41$ ,  $\tau_{M3}^+ = 51$ ).

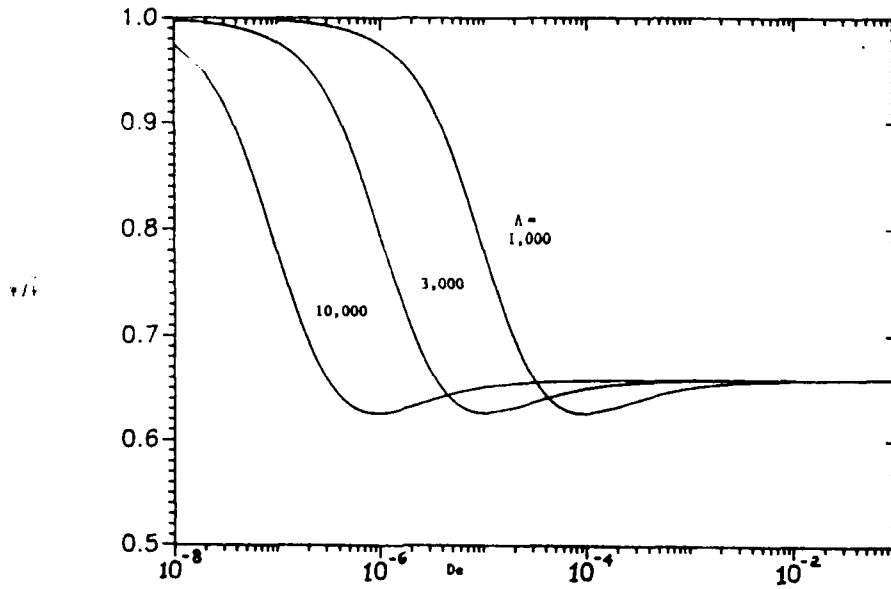


Figure 5. The Correlation Coefficient Predicted by The Stress Relaxation Model ( $\tau_{H1}^+ = 15$ ,  $\tau_{H1}^+ = 7$ ,  $\tau_{H3}^+ = 41$ ,  $\tau_{H3}^+ = 51$ ).

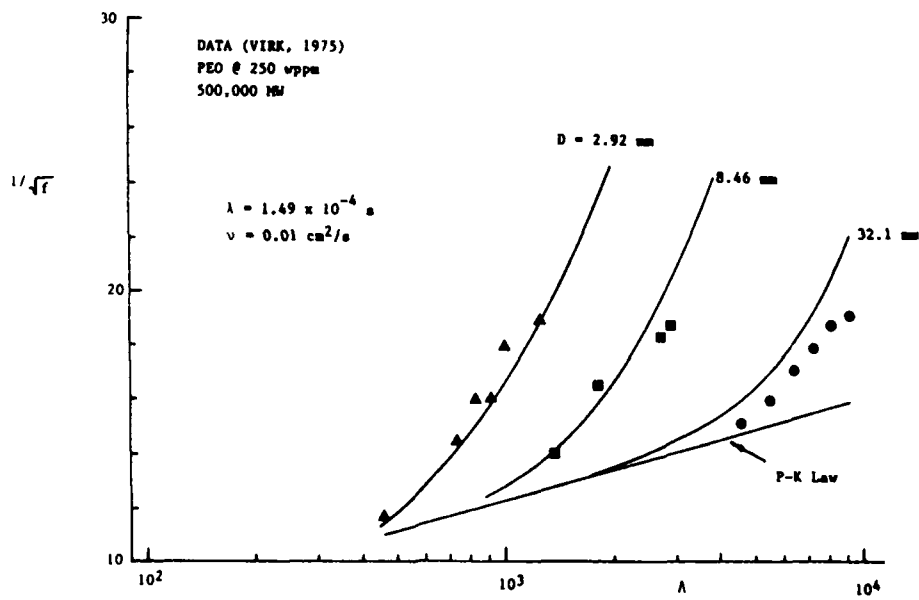


Figure 6. Predicted Scale-Up Behavior For Small Pipes Using the Stress Relaxation Model ( $\tau_{H1}^+ = 15$ ,  $\tau_{H1}^+ = 7$ ).

# TURBULENT MIXING BY THE RATE-OF-STRAIN

Carl H. Gibson

University of California at  
San Diego, La Jolla, CA 92093

## ABSTRACT

Laboratory measurements of turbulent temperature fluctuations in water, air and mercury, with  $Pr = 7, 0.7$  and  $0.018$ , respectively, and 3-D numerical simulations with  $Pr = 1, 0.5$  and  $0.1$  indicate that the small scale structure of scalar fields like temperature mixed by turbulence depend on the local rate-of-strain  $\gamma$  even at small Prandtl numbers  $Pr \equiv \nu/D$ , where  $\nu$  is the kinematic viscosity and  $D$  is the molecular diffusivity of the scalar. Scalar dissipation spectra converge at  $kL_B \approx 0.5$  under Batchelor scaling, and the strain-rate-scalar dissipation correlation coefficient  $\Sigma$  is  $-0.5$  for all  $Pr$  values, with decorrelation length  $1.3L_K$ . Analysis of data from a 2-D numerical simulation of  $Pr < 1$  mixing shows that the mixing process involves at least two interacting rate-of-strain mechanisms: 1. generation, pinching and splitting of extremum points where the scalar gradient magnitude is small or zero; and 2. alignment, pinching and amplification of the gradients where the scalar gradient magnitude is large. Both rate-of-strain mixing mechanisms are Prandtl number independent and together provide a plausible physical basis for the universal scalar similarity hypothesis, and empirical observations, that the turbulent mixing process and smallest scalar structures are determined by  $\gamma$  and  $D$  for all  $Pr$ .

## 1. Introduction

The most important practical property of turbulence is its ability to mix and diffuse momentum and scalar fields such as temperature and chemical species concentration. Such processes as aerodynamic drag, chemical reactions, combustion, heat transfer, mass

transfer and the scattering and propagation of acoustic and electromagnetic waves in turbulent media often depend crucially on turbulent mixing and diffusion. However, no consensus regarding the basic mechanisms of turbulent mixing exists even for the simplest case of dynamically passive, nonreacting scalars. The point of greatest disagreement is whether the rate-of-strain of the turbulence is important to the mixing when the scalar is strongly diffusive; that is, when  $Pr < 1$ .

The first attempts to describe turbulent mixing were intuitive extensions of the Kolmogoroff (1941) universal similarity hypotheses based on dimensional analysis. Obukhov (1949) and Corrsin (1951) independently suggest that the scalar diffusive microscale should be  $L_C = (D^3/\epsilon)^{1/4}$  by analogy with the Kolmogoroff viscous microscale  $L_K = (\nu^3/\epsilon)^{1/4}$ , where  $\epsilon$  is the viscous dissipation rate. No physical mechanisms are proposed to justify  $L_C$  as the diffusive microscale by these papers.

Batchelor (1959) suggests a rate-of-strain regime of mixing by wave-crest-compression should begin at scales smaller than  $L_K$  for weakly diffusive scalars with  $Pr > 1$ , with a diffusive microscale of  $L_B \equiv (D/\gamma)^{1/2}$ . However, because the wave-crest-compression model is non-local and requires that the rate-of-strain be uniform on scales larger than the wavecrest separation, Batchelor et al. (1959) predict that the rate-of-strain should be irrelevant for  $Pr < 1$ . Similar arguments are applied to explain the turbulent mixing of weak magnetic fields with magnetic Prandtl numbers less than unity by Moffatt (1961, 1962), Golitsyn (1960) and Kraichnan and Nagarajan (1967), giving similar predictions for magnetic spectral forms with strong diffusive cutoff  $\phi_\theta \sim k^{-17/3}$  at  $k \approx L_C^{-1}$ .

Gibson (1968a) proposes that the mixing process may actually be local and not require that  $\gamma$  be uniform over scales larger than the scalar wavecrest separation, so that the mixing process is independent of Prandtl number. In the proposed mixing model, extremal points are produced on scales larger than  $L_C$  for  $Pr < 1$  and larger than  $L_K$  for  $Pr > 1$ , and these 'hot-spots' are pinched by the rate-of-strain to maintain a radius of curvature proportional to  $L_B$  for all  $Pr$ . Recent analysis of 2-D numerical simulation experiments of Kerstein and Ashurst (1984) by Gibson et al. (1986) shows that rate-of-strain mixing also occurs by pinching at points where the scalar gradient is very large. Such  $\gamma$ -mixing mechanisms are independent of Prandtl number because they are local, and both support the  $\gamma$ -dependent universal similarity hypotheses proposed by Gibson (1968a), as discussed in the following Section (see Table 2).

Because numerical simulations are most convenient for  $Pr$  values less than 1.0, contrary to the case for laboratory fluids which tend to be poisonous or explosive in this regime, evidence is rapidly accumulating, as large computers become available, which demonstrates the local nature of the small scale turbulent mixing process and the crucial role of the rate-of-strain. The laboratory and numerical simulation evidence are compared to available theories in the following.

## 2. Rate-of-strain in the universal similarity hypotheses of turbulence and scalar mixing

The velocity difference  $d\mathbf{v}$  between two points separated by a small distance  $d\mathbf{x}$  may be decomposed into a rotational component perpendicular to  $d\mathbf{x}$  and a rate-of-strain component parallel to  $d\mathbf{x}$ . That is,

$$d\mathbf{v} = \mathbf{\Omega} \cdot d\mathbf{x} + \mathbf{e} \cdot d\mathbf{x} \quad (1)$$

where  $\mathbf{\Omega}$  is the rotation tensor with components  $\Omega_{ij} \equiv (\partial v_i / \partial x_j - \partial v_j / \partial x_i) / 2$  and  $\mathbf{e}$  is the rate-of-strain tensor with components  $e_{ij} \equiv (\partial v_i / \partial x_j + \partial v_j / \partial x_i) / 2$ . Viscous forces cause  $\mathbf{\Omega}$  and  $\mathbf{e}$  to be uniform at very small scales because the Reynolds number  $dv \cdot dx / \nu$  is proportional to the  $(dx)^2 \times e / \nu$  from (1), where  $e \equiv (e_{ij}^2)^{1/2}$ ,  $\Omega \equiv (\Omega_{ij}^2)^{1/2}$  and  $\Omega \approx e$  in a turbulent flow. Turbulence develops when the Reynolds number exceeds a critical value  $Re_{crit}$ , and this will occur when the separation distance  $dx$  exceeds a critical value

$$dx_{crit} \approx (Re_{crit} \times \nu / e)^{1/2} \quad (2)$$

The viscous dissipation rate  $\epsilon$  is related to  $e$  and  $\gamma$  by

$$\epsilon \equiv 2\nu e_{ij}^2 = 2\nu e^2 = \nu \gamma^2 \quad (3)$$

where  $\gamma \equiv (\epsilon / \nu)^{1/2}$  is the rate-of-strain parameter introduced by Batchelor (1959). Combining (2) and (3) gives

$$dx_{crit} \approx Re_{crit}^{1/2} (\nu^3 / \epsilon)^{1/4} = Re_{crit}^{1/2} \times L_K \quad (4)$$

where

$$L_K \equiv (\nu^3 / \epsilon)^{1/4} \quad (5)$$

is the usual definition of the Kolmogoroff microscale  $L_K$ . From (2) and (3), we see that

$$L_K = (\nu / \gamma)^{1/2} \quad (6)$$

might be a better definition because it shows the dependence of  $L_K$  on  $\gamma$ . The physical significance of  $L_K$  given by (2) is somewhat obscured by its definition in (5).

The assumption of a universal critical Reynolds number for the local transition to turbulence is the physical basis of the universal similarity hypotheses of Kolmogoroff (1941) for high Reynolds number turbulent velocity fields, given in Table 1.

Table 1. Universal Similarity Hypotheses of Kolmogoroff (1941) for Turbulent Velocity

Hypothesis	Length Range
1. $F_n(\epsilon, \nu, y_k)$	$y_k < L_0$
2. $F_n(\epsilon, y_k)$	$L_K < y_k < L_0$

In Table 1,  $F_n$  represents the  $3n$ -joint probability laws for velocity component differences between points with  $n$  separation vectors  $y_k$ , where  $k = 1, \dots, n$ . As part of the hypotheses,  $F_n$  should be homogeneous and isotropic in space and time for small scales. According to the first hypothesis in Table 1, all statistical parameters of turbulent velocity fields on scales smaller than the energy scale  $L_0$ , for example spectra, should collapse to universal curves after a coordinate transformation to length and time scales normalized by the Kolmogoroff length  $L_K$ , from (5), and the Kolmogoroff time  $T_K \equiv (\nu / \epsilon)^{1/2} \approx \gamma^{-1}$ . According to the second hypothesis in Table 1, these universal curves should become independent of the viscosity  $\nu$  for length scales larger than  $L_K$ . By dimensional analysis, it follows from the second hypothesis that, for  $L_0^{-1} < k < L_K^{-1}$ , the energy spectrum  $\phi = \alpha \epsilon^{2/3} k^{-5/3}$ , where  $k$  is the wavenumber and  $\alpha$  is a universal constant.

Universal similarity hypotheses for dynamically passive scalar fields  $\theta$  like temperature mixed by turbulence were proposed by Gibson (1968a), and are summarized in Table 2.

Table 2. Universal Similarity Hypotheses of Gibson (1968a) for Turbulent Mixing

Hypothesis	Length Range	Pr
1a. $F_{\theta n}(\chi, \gamma, D, y_k)$	$y_k < L_B$	all
	$y_k < L_K$	$> 1$
	$y_k < L_C$	$< 1$
1b. $F_{\theta n}(\chi, \epsilon, y_k)$	$L_K < y_k < L_O$	$> 1$
	$L_C < y_k < L_O$	$< 1$
2a. $F_{\theta n}(\chi, \epsilon, D, y_k)$	$L_B < y_k < L_O$	$< 1$
2b. $F_{\theta n}(\chi, D, y_k)$	$L_B < y_k < L_C$	$< 1$
3a. $F_{\theta n}(\chi, \epsilon, \nu, y_k)$	$L_B < y_k < L_O$	$> 1$
3b. $F_{\theta n}(\chi, \gamma, y_k)$	$L_B < y_k < L_K$	$> 1$

In Table 2,  $F_{\theta n}$  are the  $n$ -joint probability laws for scalar differences between points separated by vectors  $\vec{y}_k$ , where  $k = 1, \dots, n$ . Local homogeneity and isotropy are assumed for high Reynolds number flows. Scalar similarity hypothesis 1a. is analogous to velocity similarity hypothesis 1 in Table 1. According to 1a, all statistical parameters describing the turbulent scalar field  $\theta$  should collapse to universal forms after a coordinate transformation to length, time and scalar scales  $L_B$ ,  $T_B$  and  $S_B$  formed from the dimensional parameters  $\chi$ ,  $\gamma$  and  $D$ , where

$$L_B \equiv (D/\gamma)^{1/2} \quad (7)$$

$$T_B \equiv \gamma^{-1} \quad (8)$$

$$S_B \equiv (\chi/\gamma)^{1/2} \quad (9)$$

and

$$\chi \equiv 2D(\nabla \theta)^2. \quad (10)$$

The convergence of scalar statistical parameters to universal forms for length scales smaller than  $L_B$  assumes a rate-of-strain mixing process which is independent of the Prandtl number of the scalar, contrary to the mixing theory of Batchelor et al. (1959) and others.

Universal scalar similarity hypotheses 2a and 2b in Table 2 indicate convergence of scalar statistical parameters to universal forms after coordinate

transformation to length, time and scalar scales  $L_C$ ,  $T_C$  and  $S_C$  formed from dimensional parameters  $\chi$ ,  $\epsilon$  and  $D$  for scalars with  $Pr < 1$ , and hypotheses 3a and 3b indicate convergence after scaling with  $L_K$ ,  $T_K$  and  $S_K$  formed from  $\chi$ ,  $\epsilon$  and  $\nu$ , for  $Pr > 1$ . These scales are defined in Table 3.

Table 3. Scalar Similarity Scales

Scale (parameters)	Batchelor ( $\chi, \gamma, D$ )	Corrsin ( $\chi, \epsilon, D$ )	Kolmogoroff ( $\chi, \epsilon, \nu$ )
Length, $L_{B,C,K}$	$(D/\gamma)^{1/2}$	$(D/\gamma Pr^{1/2})^{1/2}$	$(\nu/\gamma)^{1/2}$
Time, $T_{B,C,K}$	$\gamma^{-1}$	$(\gamma Pr^{1/2})^{-1}$	$\gamma^{-1}$
Scalar, $S_{B,C,K}$	$(\chi/\gamma)^{1/2}$	$(\chi/\gamma Pr^{1/2})^{1/2}$	$(\chi/\gamma)^{1/2}$

Overlapping length scale ranges in Table 2 for the Batchelor, Corrsin and Kolmogoroff similarity spaces require scalar spectral convergence to  $k^{-5/3}$ ,  $k^{-3}$  and  $k^{-1}$  inertial, inertial-diffusive and viscous-convective subranges, respectively, as shown by Gibson (1968b). These subranges also follow by dimensional analysis from scalar similarity hypotheses 1b, 2b and 3b, respectively, in Table 2. From 1b, if the scalar variance spectrum  $\phi_\theta$  depends only on  $\chi$ ,  $\epsilon$  and the wavenumber  $k$ , then

$$\phi_\theta = \beta_K \chi \epsilon^{-1/3} k^{-5/3} \quad (11)$$

is the only dimensionally consistent form, and similarly from 2b,

$$\phi_\theta = \beta_C \chi D^{-1} k^{-3} \quad (12)$$

and from 3b

$$\phi_\theta = \beta_B \chi \gamma^{-1} k^{-1} \quad (13)$$

where  $\beta_K$ ,  $\beta_C$  and  $\beta_B$  are universal constants. Length scale ranges for which these subranges are valid are given in Table 2.

### 3. Kinematics of scalar mixing

Consider a dynamically passive scalar field like temperature mixed by an incompressible Newtonian fluid. Denoting the scalar as  $\theta(\vec{x}, t)$

$$\theta_{,i} + u_j \theta_{,j} = D \theta_{,ij} \quad (14)$$

where commas indicate partial differentiation, repeated space coordinate subscripts  $i, j, k$  are summed (for example,  $\theta_{,i}$  is the partial derivative of  $\theta$  with respect to

time  $t$  and  $\theta_{,ij}$  is  $\nabla^2\theta$ ,  $\bar{x}$  is the position in space and  $\bar{u}$  is the velocity field. Both  $\theta$  and  $\bar{u}$  are assumed to have zero mean values.

The velocity of an isoscalar surface at any point in the fluid is derived by expanding  $\theta(\bar{x},t)$  using the chain rule

$$d\theta = \theta_{,j} dx_j + \theta_{,t} dt. \quad (15)$$

and setting  $d\theta=0$  on an isothermal surface. On such surfaces  $dx_j = u_j^\theta dt$ , so  $u_j^\theta \theta_{,j} = -\theta_{,t}$ . Combining this with (14) gives

$$\theta_{,j}(u_j^\theta - u_j) = -D\theta_{,jj}. \quad (16)$$

The left hand side of (16) equals  $|\theta_{,j}| |u_j^\theta - u_j|$  since the isothermal surface velocity relative to the fluid,  $\bar{u}^\theta - \bar{u}$ , is parallel to the scalar gradient  $\nabla\theta$ . The vector expression for  $\bar{u}^\theta$  is therefore

$$\bar{u}^\theta = \bar{u} - D(\nabla^2\theta/|\nabla\theta|)\bar{g} \quad (17)$$

where  $\bar{g}$  is the unit vector of  $\nabla\theta$ . This equation was first derived by Gibson (1968a) and plays a crucial role in the rate-of-strain mixing theory proposed in that paper. Equation (17) shows the local velocity  $\bar{u}^\theta = \bar{v}_C + \bar{v}_D$  of a scalar field consists of a convective component  $\bar{v}_C = \bar{u}$  and a diffusive component  $\bar{v}_D = -D(\nabla^2\theta/|\nabla\theta|)\bar{g}$ .

For example, when the molecular diffusivity  $D = 0$  the scalar follows the fluid precisely; that is,  $\bar{u}^\theta = \bar{u}$ . When  $D$  is nonzero the diffusion velocity  $\bar{v}_D$  may be larger in magnitude than the fluid velocity, depending on the ratio  $\nabla^2\theta/|\nabla\theta| \approx 1/L$ . For turbulence acting on a uniform gradient scalar field, it follows from (17) and the definition of the Corrsin length scale  $L_C$  that the diffusion velocity

$$v_D \approx D/L \quad (18)$$

is larger than the convective velocity

$$v_C \approx (\epsilon L)^{1/3} \quad (19)$$

for eddies with length scale  $L$  smaller than  $L_C$ , as shown by Gibson (1968a). For  $Pr > 1$ , eddy velocities at all length scales ( $L > L_K > L_B > L_C$ ) are larger than the diffusion velocity  $v_D$ . For  $Pr < 1$ , only eddies with  $L > L_C > L_B > L_K$  have  $v_C > v_D$ .

From (17), when  $|\nabla\theta|$  approaches zero the diffusion velocity  $\bar{u}^\theta$  approaches infinity. Strongly distorted isoscalar surfaces become unstable and then become multiply-connected as new isolated extrema are

formed, as shown by Gibson (1968a).

It also follows from (17) that when the ratio  $\nabla^2\theta/|\nabla\theta|$  is small the diffusion velocity may also be small even though  $D$  is large. This provides a different mechanism by which the local strain-rate may influence the scalar microstructure, termed the 'gradient pinching' mechanism by Gibson et al. (1986). Because the ratio will tend to be small where  $|\nabla\theta|$  is large, compressive pinching of the local scalar gradients can be most effective at aligning and amplifying local scalar gradients just where the mixing is greatest, thus increasing the gradient and further decreasing the ratio in a positive feedback process.

Gibson (1968a) derives the following expression for the velocity of points in the fluid with zero scalar gradient

$$\bar{u}^\theta = \bar{u} - D\{(\theta_{,j1}/\theta_{,11}), (\theta_{,j2}/\theta_{,22}), (\theta_{,j3}/\theta_{,33})\} \quad (20)$$

where the coordinate system is aligned with the principal axes of the tensor  $\theta_{,ij}$  with principal values given by  $\theta_{,11}$  etc.,  $\theta_{,ij}$  represents  $\nabla^2\theta$ , and  $\theta_{,j1}$  etc. are the components of the vector  $\nabla(\theta_{,jj})$ . Equation (20) shows that extrema tend to move toward positions of greater symmetry, where  $\nabla(\theta_{,jj}) = 0$ , by diffusion. The diffusion velocity of zero-gradient points with respect to the fluid velocity  $\bar{u}$  is given by the second term on the right hand side of Eq. (20). When extrema achieve a nearly symmetric shape, or when they are newly created with maximum  $\theta_{,ij}$  principal values, they are convected nearly as fluid particles. When an extremum, or zero-gradient-point, is near the end of its lifetime it tends to diffuse very rapidly because the principal values of  $\theta_{,ij}$  approach zero, and the extremum will find and annihilate with its zero gradient saddle point, which also will have a large diffusion velocity, for the same reason, according to Eq. (20). Zero-gradient-points lie on unique minimal-gradient surfaces which also tend to move with the fluid, and are stretched, pinched and aligned with the local rate-of-strain, as shown by Gibson (1968a). From (17), maximum-gradient-points, and maximal-gradient surfaces, also respond to the local rate-of-strain.

#### 4. Laboratory measurements and numerical simulations

The most extensive laboratory investigation of low  $Pr$  turbulent mixing is the Clay (1973) study of mercury

temperature fluctuations, with  $Pr = 0.018$ , in the flow facility shown in Figure 1. Velocity fluctuations in the wake of the single element, 1 inch mesh grid were made with constant temperature hot film anemometer. Temperature fluctuations were caused by hot and cold water circulated through the 3/16 inch diameter grid tubes, and detected with a microbead thermistor.

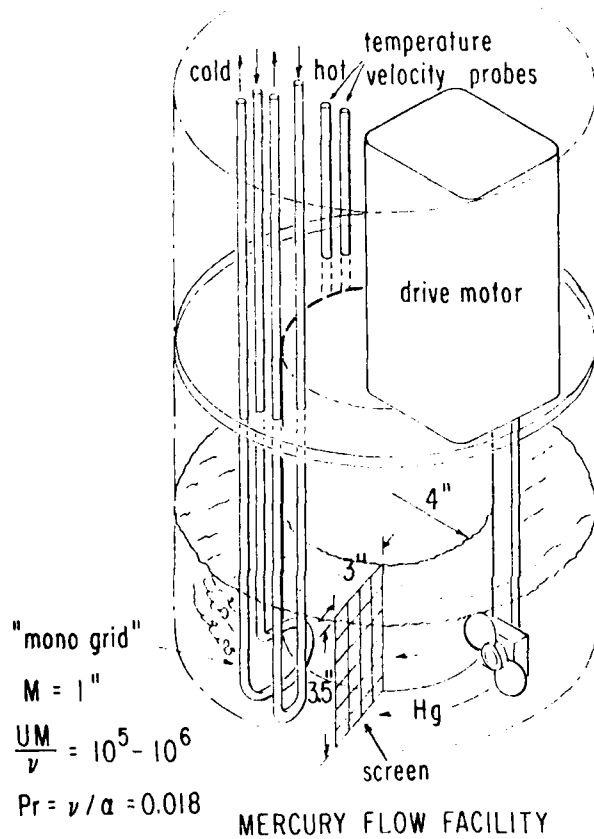


Figure 1. Mercury flow facility of Clay (1973)

Figure 2 shows the measured velocity dissipation spectrum  $k^2\phi$  and temperature dissipation spectrum  $k^2\Gamma = k^2\phi_\theta$ , for the largest grid Reynolds number  $Re_M \equiv MU/\nu = 270,000$ . Spectra and wavenumbers  $k$  are normalized by Kolmogoroff length, time and scalar scales given in Table 3, indicated by K-subscripts. Some degradation of the highest wavenumber velocity spectrum is shown by the droop below the universal form due to spatial resolution limits resulting from the thick thermal boundary layer formed in mercury. The sharp increase in  $k^2\Gamma$  for  $k_k > 0.07$  is due to electronic noise. Universal inertial subrange constants indicated by the spectra are

VELOCITY AND TEMPERATURE POWER SPECTRA OF Hg

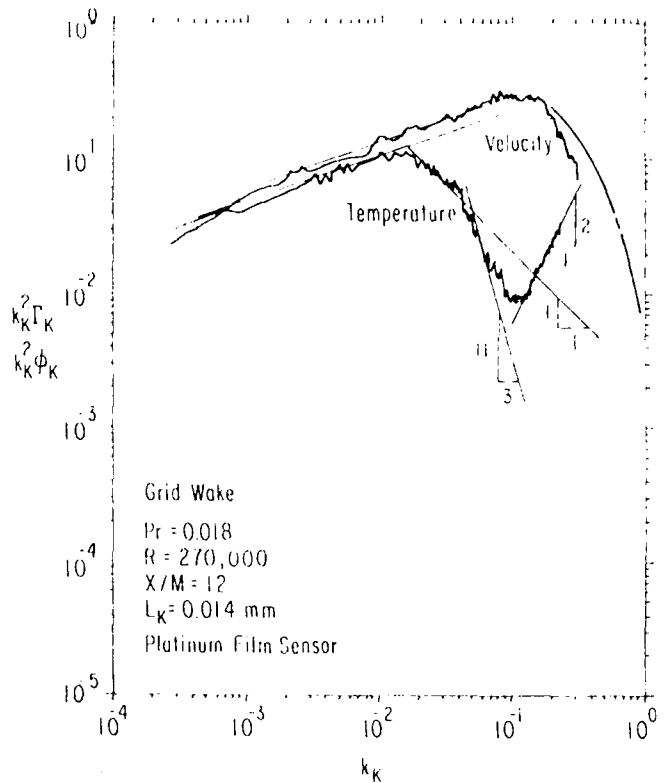


Figure 2. Velocity and temperature dissipation spectra normalized with Kolmogoroff scales for mercury.  $Pr=0.018$ ,  $Re_M=270,000$ ,  $x/M=12$ ,  $L_K=0.014mm$ ,  $0.018mm$  microbead thermistor for temperature and  $0.125mm$  conical platinum film sensor for velocity.

in the generally accepted range of 0.5-0.6, with  $\alpha=0.6$ , where

$$\phi = \alpha \epsilon^{2/3} k^{-5.3} \quad (21)$$

is the velocity inertial subrange implied by the second Kolmogoroff hypothesis in Table 1, and  $\beta_K=0.5$  from (11) for the scalar inertial subrange constant. The universal constant, from (12),  $\beta_c = 0.14$  for the indicated inertial-diffusive subrange in the wavenumber range  $0.014 < k_k < 0.045$ . The factor 3.2 range of wavenumbers covered is close to the  $L_C/L_B = Pr^{1/4} = 2.7$  subrange expected for mercury temperature from Tables 2 and 3.

Figure 3 shows temperature dissipation spectra measured by Clay (1973) in mercury, air and water normalized with Batchelor length, time and scalar scales, as indicated by the B-subscripts. The solid curves are for mercury temperature, with grid Reynolds numbers of

270,000, 61,000 and 21,500. The lower  $Re_M$  spectra have small and nonexistent inertial subranges, respectively, and extend into the diffusive cutoff regime at about  $k_B=0.7$ , before the noise becomes dominant. The noise spike at high wavenumbers for the  $Re_M = 21,500$  data is at the 60 hz line frequency. The dash-dot-dash spectrum is for air temperature fluctuations,  $Pr=0.7$ , on the axis of a heated jet with nozzle Reynolds number of 100,000, and the dash-dot-dot-dash spectrum is for water temperature fluctuation,  $Pr=7$ , in a sphere wake with Reynolds number of 27,600. The air, water and mercury spectra all converge to the same diffusive cutoff spectrum at the highest wavenumbers as predicted by hypothesis 1a in Table 2.

The mercury temperature dissipation spectra of Clay (1973) are compared to numerical simulation spectra of Kerr (1985) in Figure 4, under Batchelor scaling. Circles and triangles are for  $Pr=0.1$ , with  $Re_\lambda=83$  and 56, respectively, and plusses and diamonds are for  $Pr=0.5$  and 1.0, respectively, at the larger  $Re_\lambda=83$ . All spectra show a remarkably precise convergence to the same curve at the highest wavenumbers, within a factor of two. The diffusive cutoff is very close to the  $\phi_\theta \sim k^{-17/3}$  subrange predicted by Batchelor et al. (1959), shown in Fig. 4 as  $-11/3$ , except that the subrange begins at  $k \approx L_B^{-1}$  rather than at  $k \approx L_C^{-1}$  as predicted. However, because wavecrest separations may be nosmaller than about  $2\pi L_B$  from the spectral forms in Fig. 4, the  $-11/3$  subrange must be due to uniform-scalar-gradient wrinkling rather than wavecrest compression.

Figure 5 compares the Clay (1973) measurements of the strain-rate-dissipation correlation coefficient  $\Sigma(r/L_K)$  with numerical simulation values computed by Ashurst et al. (1986) for the Kerr (1985) data, where

$$\Sigma(r) \equiv \langle (u_{x,x})_x (\theta_{,x}^2)_{x+r} \rangle / \langle (u_{x,x}^2)^{1/2} (\theta_{,x}^2) \rangle, \quad (22)$$

$r$  is the separation distance in the streamwise  $x$  direction between sampling points for the strain-rate and dissipation terms shown in parentheses. According to the Batchelor et al. (1959) theory,  $\Sigma(r=0)$  should approach zero as  $Pr \rightarrow 0$ , whereas the Gibson (1968b) spectral theory predicts a nearly constant value of  $-0.5$  independent of  $Pr$ . Kerr (1985) finds  $\Sigma(0) = -0.5$  for 3-D numerical turbulent mixing of scalars with  $Pr = 0.1, 0.5, 1.0$  and 2. The negative sign of the correlation reflects the enhancement of scalar gradients in the direction of

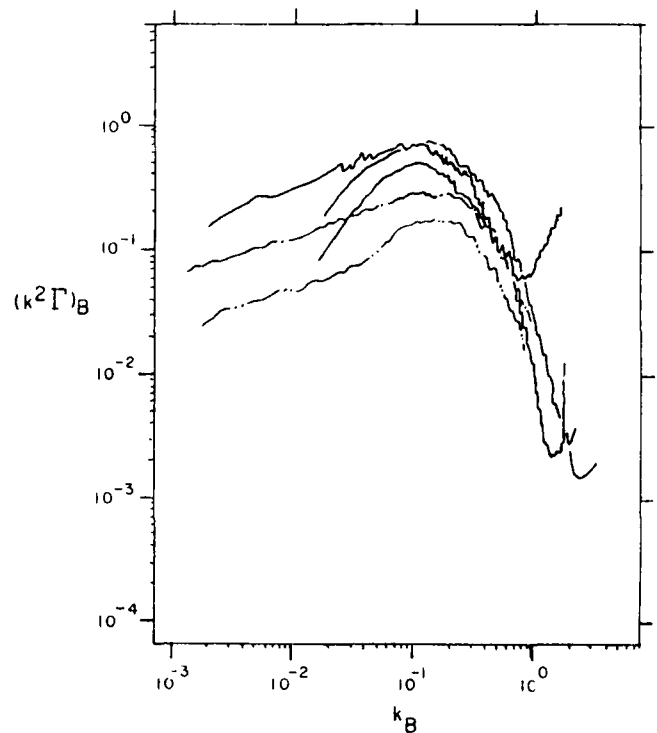
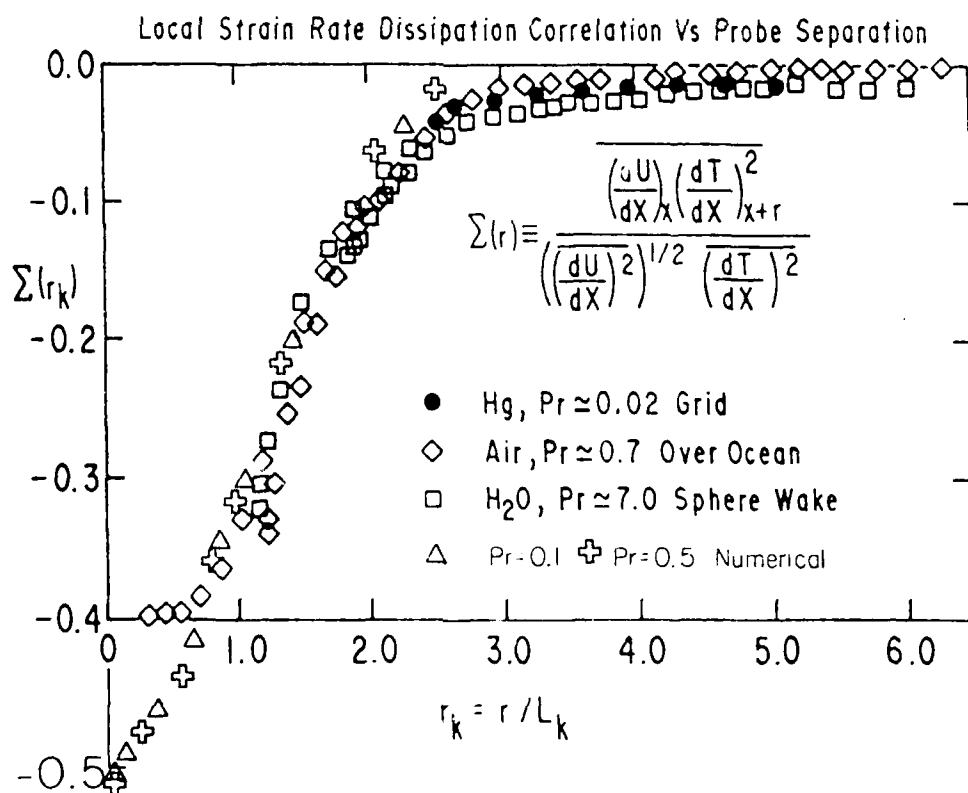
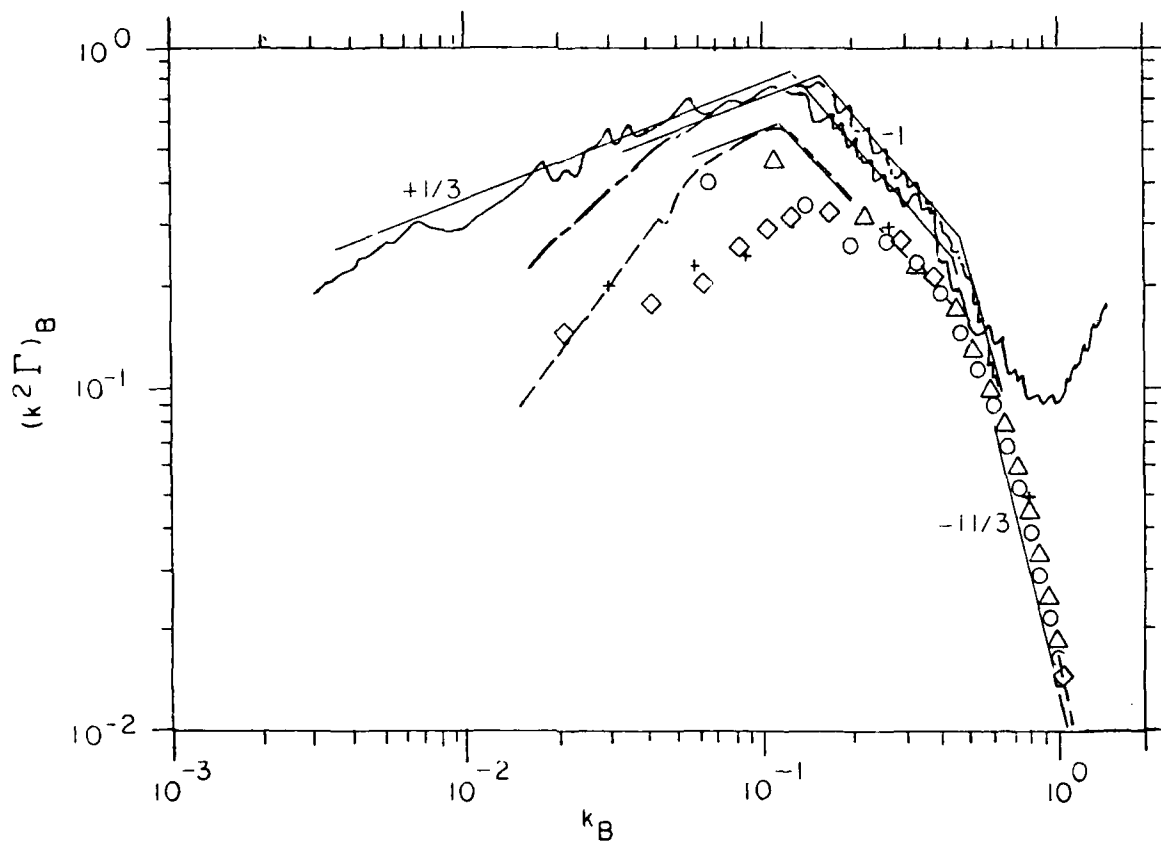


Figure 3. Temperature dissipation spectra for mercury, air and water, from Clay (1973) scaled with Batchelor length, time and scalar scales from Table 3. Solid curves are for mercury with  $Re_M = 270,000, 61,000$  and 21,500. Dash-dot-dash is for a heated air jet ( $Pr = 0.7$ ) in a gymnasium with  $Re_D = 100,000$ , and dash-dot-dot-dash is for a sphere wake in a water tunnel ( $Pr = 7$ ) with  $Re_D = 27,600$ .

Figure 4. Temperature dissipation spectra for mercury (Fig. 3) compared to numerical simulation data of Kerr (1985) using Batchelor scaling. Circles and triangles are for the numerical simulation with  $Pr = 0.1$  with  $Re_\lambda = 83$  and 56, respectively. Plusses and diamonds are for  $Pr = 0.5$  and 1.0, respectively, with  $Re_\lambda = 83$ .

Figure 5. Local strain-rate-scalar-dissipation correlation coefficient versus probe separation for  $\Sigma(r/L_K)$  values measured by Clay (1973) in mercury, air and water by time delay, setting  $r=U't$  based on Taylor's hypothesis, compared to values computed from the Kerr (1985) numerical simulation by Ashurst et al. (1986). Bullets are for mercury, diamonds are for air, squares are for water, triangles are for the numerical simulation with  $Pr = 0.1$ , and open crosses for  $Pr = 0.5$ .



compressive straining, where  $u_{x,x}$  is negative, and a decrease in scalar gradients in the stretching direction, where  $u_{x,x}$  is positive. The agreement between the laboratory and numerical values of  $\Sigma(r/L_K)$  is very good, and indicates a 3 dB decorrelation length scale of only  $r \approx 1.3L_K$ . This is strong evidence that the mixing process is Prandtl number independent, depends on the rate-of-strain, and is highly localized.

Figure 6 shows the result of the analysis of 2-D numerical simulation data of Kerstein and Ashurst (1984) by Gibson et al. (1986). Two hundred random vortices produce a velocity field which mixes a scalar field with  $Pr \approx 0.1$  on an  $80 \times 80$  mesh. At each mesh point a vector

is plotted with direction  $\hat{g}$  and magnitude  $\cos^2\Theta$ , where  $\Theta$  is the angle between the scalar gradient direction  $\hat{g}$  and the compression principle axis of the rate-of-strain tensor  $e$ . Large alignment indicates response of the scalar gradient to the rate-of-strain mixing. The average value of  $\cos^2\Theta$  for Fig. 6 is 0.68, versus 0.5 if the alignment were random. From the scalar contours in Fig. 6, it is clear that the best alignment occurs not only where the gradients are small, but also where the gradients are large. Similar maps in Gibson et al. (1986) show that maximum dissipation rates also occur where the scalar gradients are maximum, supporting the new large gradient strain-mixing mechanism.

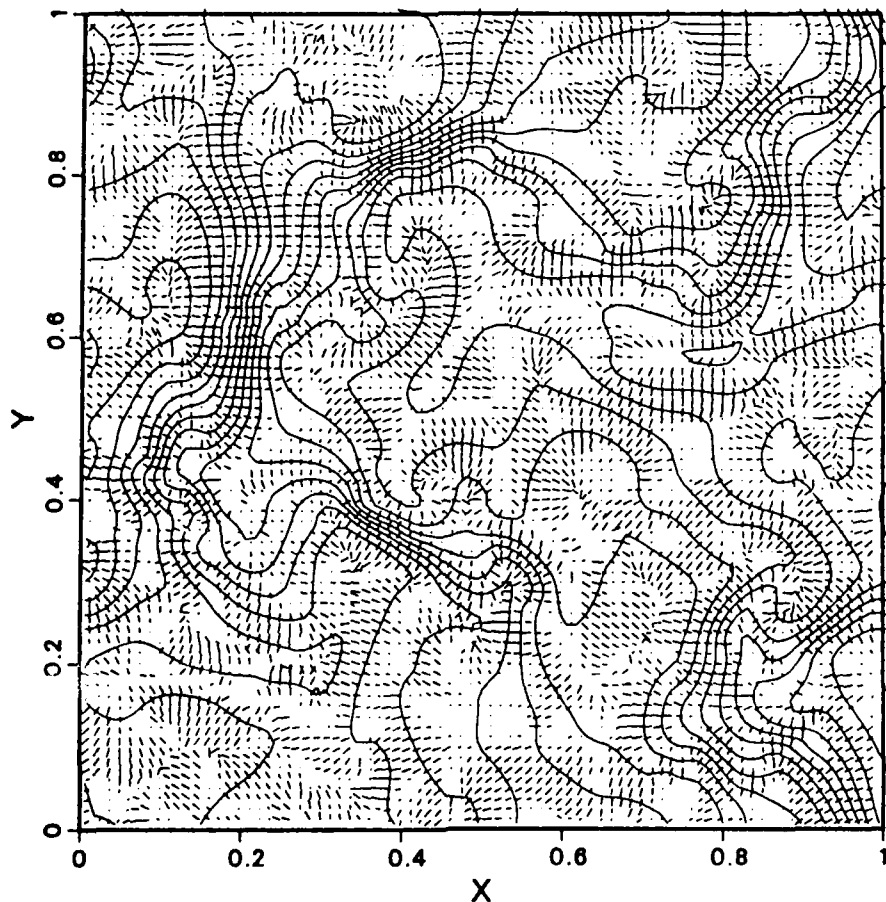


Figure 6. Map of 2-D numerical simulation of  $Pr \approx 0.1$  mixing from Gibson et al. (1986). Scalar contours indicate the direction, magnitude and location of the scalar gradients. Vectors at  $80 \times 80$  mesh points have

scalar gradient directions  $\hat{g}$ , with magnitudes  $\cos^2\Theta$ , where  $\Theta$  is the angle between  $\hat{g}$  and the compression axis of the rate-of-strain tensor  $e$ . The average of  $\cos^2\Theta$  is 0.68, versus 0.5 if the directions were oriented at random.

## 5. Summary and conclusions

Comparison of scalar dissipation spectra from laboratory measurements of Clay (1973) and numerical simulations of Kerr (1985) in Fig.'s 3 and 4 show a remarkable convergence at high wavenumbers under Batchelor scaling for the Prandtl number range 0.02-7. This convergence supports the universal similarity hypothesis of Gibson (1968a) that the small scale structure of passive scalars mixed by turbulence depends only on the rate-of-strain  $\gamma$  and the molecular diffusivity  $D$ . The  $-17/3$  subrange of Batchelor et al. (1959) is indicated by the measurements of Clay (1973), but only for  $kL_K > 0.5$ , so the mechanism must be uniform-scalar-gradient wrinkling by the velocity inertial subrange rather than wavecrest compression.

Strain-rate-dissipation correlation coefficients  $\Sigma(r)$ , defined by (22), also show a remarkable convergence for the Clay (1973) measurements and Kerr (1985) numerical simulations, under Kolmogoroff scaling. From the  $\Sigma(r/L_K)$  values shown in Fig. 5, the correlation occurs at very small separation distances  $r \approx 1.3(\nu/\gamma)^{1/2}$ . This supports the Gibson (1968a) proposal of a highly localized rate-of-strain mixing process independent of  $Pr$ , even for  $Pr > 1$ , because  $1.3L_K$  is much less than the scalar wavecrest separation, which is as large as  $30L_K$ .

The evidence indicating that the rate-of-strain determines small scale mixing for all Prandtl number scalars seems rather strong, if not overwhelming, but much more needs to be done to identify the mechanism, or combination of mechanisms, by which the mixing takes place. Kerr (1985) points out that the maximum scalar gradients and scalar dissipation in his numerical simulation occurs in proximity to vortex tubes. Thus vortex line stretching may enhance the small gradient pinching mechanism of Gibson (1968a,b) and the large gradient pinching mechanism of Gibson et al. (1986) and Ashurst et al. (1986), and may be an essential feature of the turbulent rate-of-strain mixing process.

## 6. Acknowledgements

Support was provided by the Department of Energy, the Office of Naval Research, the Institute of Geophysics and Planetary Physics, Lawrence Livermore Laboratory, and by a summer faculty fellowship provided by Sandia

National Laboratories. Many useful conversations were held with Robert Kerr, William Ashurst and Alan Kerstein on the ideas presented in this paper.

## 7. References

- ASHURST, W. T. (1986). A. R. KERSTEIN, R. M. KERR and C. H. GIBSON (1986). Examination of three-dimensional turbulent flow fields obtained by direct Navier-Stokes simulation. in preparation.
- BATCHELOR, G. K. (1959). Small-scale variation of convected quantities like temperature in turbulent fluid. Part 1. General discussion and the case of small conductivity. *J. Fluid Mech.* **5**, 13-133.
- BATCHELOR, G. K., HOWELLS, I. D. & TOWNSEND, A. A. (1959). Small-scale variation of convected quantities like temperature in turbulent fluid. Part 2. The case of large conductivity. *J. Fluid Mech.* **5**, 134-139.
- CLAY, J. P. (1973). Turbulent mixing of temperature in water, air and mercury. Ph. D. thesis, University of California at San Diego.
- CORRSIN, S. (1951). On the spectrum of isotropic temperature fluctuations in isotropic turbulence. *J. Appl. Phys.* **22**, 469-473.
- GIBSON, C. H. (1968a). Fine structure of scalar fields mixed by turbulence, I. Zero gradient points and minimal gradient surfaces, *Physics of Fluids* **1**, 2305-2315.
- GIBSON, C. H. (1968b). Fine structure of scalar fields mixed by turbulence, II. Spectral theory. *Physics of Fluids* **11**, 2316-2327.
- GIBSON, C. H., W. T. ASHURST and A. R. KERSTEIN (1986). Mixing of strongly diffusive passive scalars like temperature by turbulence. submitted to *J. Fluid Mech.*, also Sandia Report SAND84-8858.
- HILL, R. J. (1978). Models of the scalar spectrum for turbulent advection. *J. Fluid Mech.* **88**, 54-562.
- KERR, R. M. (1985). Higher-order derivative correlations and the alignment of small-scale structures in isotropic numerical turbulence. *J. Fluid Mech.* **153**, 31-58.
- KERSTEIN, A. R. & ASHURST, W. T. (1984). Lognormality of gradients of diffusive scalars in homogeneous, two-dimensional mixing systems. *Physics*

of Fluids 27, 289.

KOLMOGOROFF, A. N. (1941). The local structure of turbulence in incompressible viscous fluid for very large Reynolds number, Dokl. Akad. Nauk SSSR 30, 301.

KRAICHNAN, R. H. & NAGARAJAN, S. (1967). Growth of turbulent magnetic fields. Physics of Fluids 10, 859.

MOFFATT, K. (1961). The amplification of a weakly applied magnetic field by turbulence in fluids of moderate conductivity. J. Fluid Mech. 11, 625.

MOFFATT, K. (1962). Intensification of the earth's magnetic field by turbulence in the ionosphere. J. Geophys. Res. 67, 307.

OBUKHOV, A. M. (1949). Struktura temperaturnovo polia v turbulentnom potoke. Izv. Akad. Nauk SSSR Ser. Geofiz. 3, 59.

## NUMERICAL SIMULATION OF TURBULENT REACTIVE FLOWS

A. Picart and R. Borghi  
Laboratoire de Thermodynamique  
U.A. C.N.R.S. N°230  
Faculté des Sciences et des  
Techniques de Rouen  
76130 Mont-Saint-Aignan, FRANCE.

J.P. Chollet  
Institut de Mécanique de Grenoble  
B.P. 68  
38402 Saint-Martin-d'Heres Cédex  
FRANCE

### ABSTRACT

A direct numerical simulation of a turbulent homogeneous field is used to study the decay of the concentration of a scalar quantity which is advected, diffused and undergoes the effect of a sink term which models the effect of a chemical reaction. The reaction rate and the one-species formulation used herein are oriented towards the simulation of the combustion of a premixed gas in order to study various quantities useful for turbulent combustion models. Computations yield results depending on the "chemical time" under the form of various probability density function (PDF) calculated from the realizations of the reactive scalar fields.

### 1. INTRODUCTION

1.1. The combustion modelling problems are especially difficult to handle because of real shape of chambers with possibly geometrical singularities, chemical reactions with heat release, compressibility effects, very large highly variable characteristics (thickness, stability, ...).

Probably the most important problem is set up by the interaction of turbulence with chemical reactions. The chemical process and their rates are perfectly known, the calculation of global chemical rates needs in addition, the knowledge of exact instantaneous values of species concentrations and temperature within the turbulent medium, including all fluctuations. Indeed, the high non linearity of chemical processes is such that the knowledge of mean values for concentrations and temperature is not sufficient in order to predict even only the mean value of reaction rates. That leads to a closure problem, since there is no possibility to compute all fluctuations...

To overcome this problem, some experimental works are available but always related to a specific geometry, specific type of reactions (usually necessarily simple) and even, at least quite often, particular values of dimensional variables (chamber size, front thickness, ...).

Numerical approaches are also available, but they are necessarily limited to models which are not too much sophisticated since many hydrodynamics and chemical phenomena have to be taken into account. Usually, the turbulent hydrodynamic part of the model is limited to one point closure models (such as  $k-\epsilon$ , mixing length, ...). In addition to turbulence models, a particular turbulent combustion model is needed to compute the mean reaction rates, including the influence of the temperature and concentrations fluctuation. At this time, such models are based on particular assumptions whose validity is difficult to assess in details, Bray (1980), Borghi (1980), Borghi (1985).

1.2. The purpose of this work is just to study in details such closure assumptions. For that, we choose conditions which are liable to a close description of some phenomena, even if it means that such a study-frame seems to be far from industrial prospects.

We focus on the effects of the turbulent velocity field on chemical reactions, so, we turn to full direct numerical simulation of Navier-Stokes and diffusion-reaction equations. Among earlier study dealing with chemical reactants in large eddy simulations we can quote Hamlen (1984) for homogeneous turbulence and Mc Murtry et al. (1985) for mixing layers.

In order to get the right hydrodynamic features, we let the turbulence evolves in by itself without any artificial external energy forcing and we consider idealized boundary conditions, say periodical ones. The computed field is a cubical box which can be viewed as a surrounded by identical box up to infinite distance in the three directions. This homogeneity hypothesis is consistent with description of the flow at smaller scales (and the chemical reaction mentioned later takes place at rather small scales) far from flow singularities such as rigid boundaries. It has proved to be fairly useful in studying basic properties of three dimensional turbulence such as : decay laws of kinetic energy or scalar variance, subgrid scale modelling, ...

Moreover homogeneous flows allow accurate numerical methods such as pseudo-spectral techniques. In a first step, we consider that the turbulence is, in the mean, isotropic ; a zero shear is imposed to the flow. The non zero shear case could be forced later especially as regards to the reaction-front deformations. Anyway, in the present study, we prefer to reduce the number of parameters in order to get only the very basic features of the turbulence.

The combustion or chemical reaction process usually involve many equations with the creation or disparition of many species. Of course, we don't have to necessarily take into explicit account the species whose life time is very short. As being interested in very basic phenomena, we consider a very simple combustion or chemical reaction process as follows.

The A species is transformed by the reaction into B in such a way that we consider only the evolution of the concentration of the species A:  $C_A$  (the concentration of the B species can be derived as  $C_B(\vec{x}, t) = 1 - C_A(\vec{x}, t)$ ).

In the case of combustion reactions, with a large heat release, the species B can be related also a non dimensionalized temperature.

The rate of such a combustion reaction is represented usually by an Arrhenius law :

$$\dot{w} = d - C_A^\alpha \exp\left(-\frac{T_A}{T}\right) \quad (1)$$

where  $T_A$  is an activation temperature, which mainly gives to  $\dot{w}$  its strongly non linear behavior.

In our case, relating  $T$  and  $C_B$  to  $C_A$ , we have adopted a slightly different mathematical form instead of (1) :

$$\dot{w} = -\frac{1}{\tau_c} C_A^\alpha (1 - C_A)^\beta \quad (2)$$

We have chosen  $\alpha = 1$  and  $\beta = 5$ , in order to realistically simulate the usually high activation temperature in (1).

In order to focus on the influence of hydro-dynamical turbulence and also to make computations easier, we assume an isothermal reaction without heat-release. In addition to this isothermal property, we assume extra-properties concerning the A and B species in such a way that the specific mass of the fluid (A and B species included) remains constant, yielding incompressibility.

$\tau_T / \tau_c$ , the Damkhöler number (if  $\tau_T$  is the time which characterizes the turbulence) is the main parameter to be considered in this study. It will define the diffusion rate of the turbulence relatively to the reaction rate.

## 2. EQUATIONS AND NUMERICAL SIMULATIONS

The scalar contaminant, even "chemically reacting" is "passive" as long as the velocity field is concerned.

The evolution of the velocity field is governed by the Navier-Stokes equation :

$$\frac{\partial \vec{u}}{\partial t} + (\vec{u} \cdot \nabla) \vec{u} = -\frac{1}{\rho} \nabla p + \nu \nabla^2 \vec{u} \quad (3)$$

with the incompressibility condition

$$\nabla \cdot \vec{u} = 0 \quad (4)$$

The evolution of the concentration of the species A is governed by

$$\frac{\partial C_A}{\partial t} + (\vec{u} \cdot \nabla) C_A = d \nabla^2 C_A - \frac{C_A (1 - C_A)^\beta}{\tau_c} \quad (5)$$

Two major differences with usual passive scalar calculations (as in Chollet and Lesieur (1982)) can be noticed :

- .  $C_A$  is a bounded variable
- .  $C_A$  is the non dimensionalized value of a real concentration which means that the mean value of  $C_A$  is not zero ; actually it decreases with time, due to the reaction.

As the chemical reaction is supposed to take place also at small scales, we did not try any large eddy simulations (as in Chollet (1985)) and limit ourselves to direct numerical simulations without any subgrid scale modelling. Then in (3) and (5),  $\nu$  and  $d$  are the true molecular viscosity and diffusivity.

The Schmidt number was chosen to be 0.72. Besides any considerations of practical applications, Schmidt numbers smaller than 1 are easier to handle in direct numerical simulations since it can be observed in numerical calculations and even in experimental results (Mestayer et al (1984) that the dissipative scales for the velocity field and the scalar field are identical for values of Prandtl (or Schmidt) number smaller than one.

The initial conditions ( $t = t_0$ ) are obtained as follows : the velocity field is allowed to evolve from an initial field at  $t = 0$  with a random generator and a condition about the energy spectrum which is limited to the large scales only

$$E(k) = k^4 \exp\left(-2 \frac{k^2}{16}\right)$$

The velocity field involves until  $t = t_0$  and the resulting field at this time will be used as the initial velocity field with the advantage of the physical relevance of a field whose energy is not concentrated in a narrow range of large scales and whose spatial and temporal correlations have been built only by the dynamics of the flow.

At  $t = t_0$ , the scalar field is generated by adding a mean value to a randomly generated fluctuation ; nevertheless this fluctuation must correspond to a given variance spectrum which was chosen as

$$E_{C_A}(k) = \exp\left(-2 \frac{k^2}{16}\right) \text{ for } k \geq 1$$

These calculations were carried out from several values of the reaction time  $\tau_c$  ( $\tau_c = 0.5, 2, 8$  sec), the value of  $\tau_T = \frac{\nu}{E}$  being between 2 and 1 sec.

The numerical code derived from Chollet (1985) is based upon a pseudo spectral method. Time stepping uses leapfrog scheme with a Crank Nicholson treatment for the viscous (diffusive) term. The resolution under use is  $32 \times 32 \times 32$ .

### 3. FIRST RESULTS AND DISCUSSIONS

3.1. In order to emphasise the global effect of the turbulent fluctuations on the mean reaction rate, the figure 1 compares  $\langle C_A \rangle$  as a function of time computed by the full simulation and by applying only the (wrong) equation :

$$\frac{d\langle C_A \rangle}{dt} = \frac{-\tau}{\tau_c} \langle C_A \rangle (1 - \langle C_A \rangle)^5$$

The mean value  $\langle C_A \rangle$  has been obtained in the simulation through a spatial average over the whole computation box.

Fig. 1 shows clearly the strong increase of reaction rate (the consumption of the reactant  $C_A$  is faster) due to the turbulent fluctuations ; in fact, caused by the particular form (2), it can be shown that the fluctuations are favourable for the reaction at larger  $\langle C \rangle$ , but unfavourable when  $\langle C \rangle$  approaches zero, at the end of the combustion (see Borghi (1980)) ; fig. 1 allows to quantify this effect, which is here clearly far from negligible.

The purpose of turbulent combustion models is just to allow the right prediction of the differences exemplified fig. 1, as function of  $\tau_c$  and turbulence, when it is not possible, as usual, to perform a full numerical simulation like here.

3.2. A very interesting quantity, which is very useful in models, is the probability density (p.d.f.) of the fluctuations of the reactive species  $C_A$  ; it is used with an approximate shape in some models, or it is calculated with a modelled balance equations in other ones (see Borghi (1980) and Bonniot-Borghi (1979)). In any case, it has been shown that such a p.d.f., in a premixed medium in combustion can displays very large fluctuations, with a strongly non gaussian shape.

Fig. 2a and b show such p.d.f. during full simulations ; two values of  $\tau_c$  have been used, and the p.d.f. are shown at different times during the combustion. We have chosen here to prescribe, at  $t = t_0$ , a very large amount of fluctuations, in such a way that the p.d.f. displays two peaks (one for  $C_A = 1$ , one for  $C_A = 0$ ). The fig. 2 show that, as time goes on, these peaks decreases due to the turbulent mixing, but this decrease is slower when the reaction is faster and faster ( $\tau_c$  decreasing) ; indeed the effect of the reaction is to drive the probability toward  $C_A = 0$ , the effect of the turbulent mixing being to displace it toward the mean value  $\langle C_A \rangle$ , destroying the fluctuations. Of course,  $C_A$  is itself displaced to zero by the reaction, but at a different "velocity" due to the non-linearity. The unsymmetrical shape of the p.d.f. can be explained simply by the unsymmetrical shape of the reaction rate (2).

The shapes of the p.d.f. of Fig. 2 show that the numerical simulation does not violate the property  $0 \leq C_A \leq 1$  ; this is not always the case, due to the numerical errors, and, it is necessary, in order to avoid that, to use very small time steps in the numerical simulation ; in fact, that is the reason why the simulations have been limited up to now to a relatively small time corresponding to a small consumption of  $\langle C_A \rangle$ .

3.3. Another very important quantity in turbulent combustion models, is a time scale of the destruction of the fluctuations of the reactive species, defined by  $\tau_r = \langle C_A'^2 \rangle / E_c$  where  $E_c = d \langle \frac{\partial C_A}{\partial x} \frac{\partial C_A}{\partial x} \rangle$  ; this quantity is similar to the integral time of the velocity fluctuations  $\tau_T = K / E$  and it is very often assumed that  $\tau_r / \tau_T = cte$  is independent of the reaction (see Borghi (1985)) . Since it is also assumed that the velocity spectrum as well than the scalar spectrum are in equilibrium, (with a quasi steady shape depending only on two quantities), it follows that  $\tau_T$  and  $\tau_r$  can be related to an integral length scale of velocity and concentration (respectively) :  $\tau_T = L_T / K^{1/2}$   $\tau_r = L_c / K^{1/2}$  and consequently the proportion  $L_c / L_T = cte$  equally holds.

Fig. 3 shows  $L_c, L_T$  (and  $d\tau$ , the Taylor microscale) computed during the simulation from the velocity and scalar spectra with the formulas  $L_c = \frac{3\pi}{4} \int_0^\infty \frac{E_c(k)}{k} dk / \left( \int_0^\infty E_c(k) dk \right)^{1/2}$  ;  $L_T = \frac{3\pi}{4} \int_0^\infty \frac{E(k)}{k} dk / \left( \int_0^\infty E(k) dk \right)^{1/2}$ . The behavior of such length scale in homogeneous and isotropic equilibrium turbulence must be an increase with time ; the decrease that is displayed here at the beginning of the evolution is due to the relaxation of the shape of the initial spectra to the equilibrium ; after  $t = 1,2$  s the increase is the usual one. The ratio  $L_c / L_T$  is shown Fig. 4 for two values of  $\tau_c$ . We observe first that it is found to vary with time ; it is known that the constancy of  $L_c / L_T$  has not to be perfectly true even without reactions (see Herring et al (1982)) ; in our case, the relaxation of the spectra, in the first period of time, is probably the main cause of that variation. Does the ratio  $L_c / L_T$  plotted figure 4 depend on  $\tau_c$  ? In order to precise that effect, and to quantify it, we need to continue the simulation for a longer time, where the influence of the initial shapes of the spectra will be more forgotten to answer this question.

3.4. The release of the closure assumption  $\tau_r / \tau_T = cte$  needs further studies of  $E_c$  in presence of reaction. In order to do that, we have examined the shape of the joint p.d.f. of  $C_A$  and  $|\nabla C_A \cdot \nabla C_A|$ , which is necessary to compute  $E_c$ . The figures 5(a,b,c) show the isoprobability density lines in the plane  $C_A, |\nabla C_A \cdot \nabla C_A|$  in the case of slow reaction ( $\tau_c = 8$  sec) at different times ; the figures 6(a,b,c) are related to a faster reaction ( $\tau_c = 2$  sec).

In the case of slow reaction, the shape of the joint p.d.f. evolves very slowly ; no particular correlation appears between  $|\nabla C_A|$  and  $C_A$  ; the largest values of  $|\nabla C_A \cdot \nabla C_A|$  is obtained at the beginning for  $C_A = 0.9$ , but, as time goes on, are

displaced toward  $C_A = 0.5$ ; notice that the absolute values of  $|\nabla C_A|$  is decreasing with time, as indicated on the relevant axis.

In the case of faster reaction, the shape of the p.d.f. is clearly modified; more and more probability is found at  $C_A$  close to zero; it appears also that gradients of  $C_A$  are also appearing there. Contrary to the previous case, the absolute values of  $|\nabla C_A|$  are not monotonically decreasing with time: gradients, and consequently  $\epsilon_c$ , are produced by faster reaction. The effect of reaction, however, does not seem to correlate more strongly  $C_A$  and  $|\nabla C_A|$ . In particular, if the turbulent reactive medium would be made with a collection of quasi laminar flamelets, which could evolve almost independently from each other, one would observe, as a result of this structure, the correlation between  $C_A$  and  $\nabla C_A$  that exists in the laminar premixed flame. Such a correlation schematized Fig. 7, is not apparent here.

3.5. Although we have presented, herein, statistical results, the simulations permit a detailed knowledge of the scalar fields. An "animation" of the time evolution of isoconcentration curves through a cross section of the field has been realized on a video tape; the steepening of reaction front when  $\tau_c$  is low, as exhibited by the previous p.d.f., is confirmed. The appearance of pockets of burned gases with larger and larger scales as the combustion proceeds is also clearly put into evidence.

#### 4. CONCLUSION

The numerical results presented here should be considered as preliminary since it appears necessary to explore the phenomena in greater details, for faster reactions and for longer times. Nevertheless, the homogeneous turbulence in a cubical box is confirmed to be a good prototype to study the basic features of natural phenomena which can take place in more complicated flows.

The full simulation presented here gives results on one point mean quantities that are consistent with our previous physical knowledge and the existing turbulent combustion model. More interestingly, the simulation brings new informations on two points statistical quantities like length scales or joint p.d.f. of concentration and gradient of concentration. The results illustrate clearly that, for a given turbulent time, these quantities depend on the chemical time in a way which is difficult to interpret with simplified physical reasoning. A more detailed study by such a simulation will show if there is chance of capturing quasi universal behaviors in order to include them into more simple model for engineering purposes.

Acknowledgements: This work has been supported by the french ministry of Defence (DRET) under contract 84/173. Computing time (on a Cray 1S) was allocated by the Scientific committee of the Centre de Calcul Vectoriel pour la Recherche. Figures have been plotted using the NCAR graphics package

and the "animation" were made at the Centre de Calcul de Rouen with the help of J. CARNET and J. DUJARDIN.

#### REFERENCES

- Bonniot C, Borghi R., 1979 : Joint probability function in turbulent combustion. *Acta astronautica*, 6, 309-327.
- Borghi R., 1980 : Models of turbulent combustion for numerical predictions. In : *Prediction methods for turbulent flows*. (ed. Kollmann W.) A von Karman Institute Book. Hemisphere Pub. Corp.
- Borghi R., 1985 : Critiques sur la modélisation de la combustion turbulente. In : *Numerical simulation of combustion phenomena*. (ed. Glowinski R., Larroturou B., Temam R.). *Lecture notes in Physics*, vol. 241, p. 20, Springer Verlag.
- Bray K.N.C., 1980 : Turbulent Flows with premixed reactants. In : *Turbulent reacting flows*. (ed. Libby P.A., Williams F.A.). *Topics in Applied Physics*. Vol. 44, pp. 115-183. Heidelberg : Springer Verlag.
- Chollet J.P., Lesieur M., 1982 : Modelisation sous maille des flux de quantité de mouvement et de chaleur en turbulence tridimensionnelle isotrope. *La Météorologie*. 29-30, 183-191.
- Chollet J.P., 1985 : Two-point closure used for a subgrid scale model in large eddy simulation. In : *Turbulent Shear Flows 4*. (ed. Bardbury L.J.S., Durst F., Launder B.E., Schmidt F.W., Whitelaw J.H.) Springer-Verlag.
- Hamlen R.C., 1984 : Computer simulation of turbulent scalar transport with applications to chemical reaction. Thesis Iowa State University.
- Herring J.R., Schertzer D., Lesieur M., Newman G.R., Chollet J.P., Larchevêque M., 1982 : A comparative assessment of spectral closures as applied to passive scalar diffusion. *J. Fluid Mech.*, 124, 411-437.
- McMurtry P.A., Jou W.H., Riley J.J., Metcalfe R.W., 1985 : Direct numerical simulations of a reacting mixing layer with chemical heat release. AIAA 23rd Aerospace Sciences Meeting. January 14-17, 1985, Reno, Nevada.
- Mestayer P., Chollet J.P., Lesieur M., 1984 : Inertial subrange of velocity and scalar variance spectra in high Reynolds number three dimensional turbulence. In : *Turbulence and chaotic phenomena in Fluids*. (ed. Tatsumi T.). North-Holland : Elsevier Science Publishers.

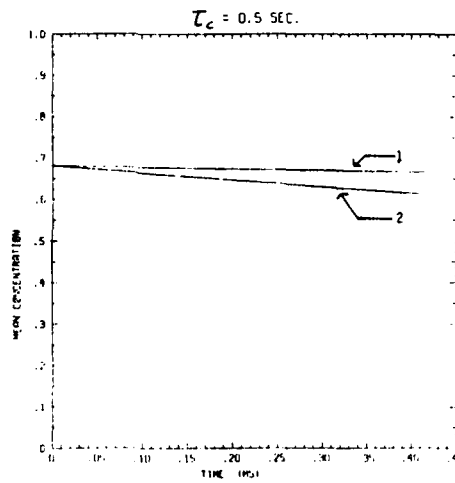


FIGURE 1:  $\langle C_A \rangle$  VERSUS TIME: 1. WITHOUT FLUCTUATIONS OF  $C_A$ . 2. COMPUTED BY THE FULL SIMULATION

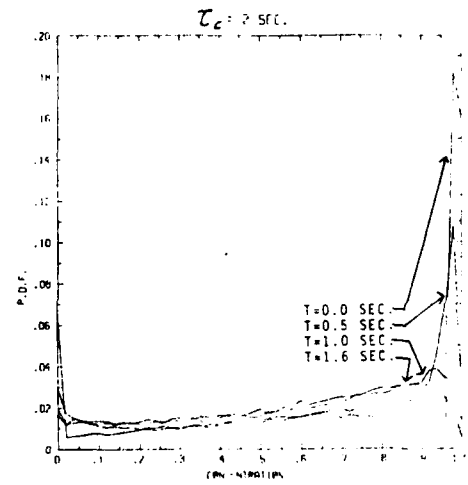
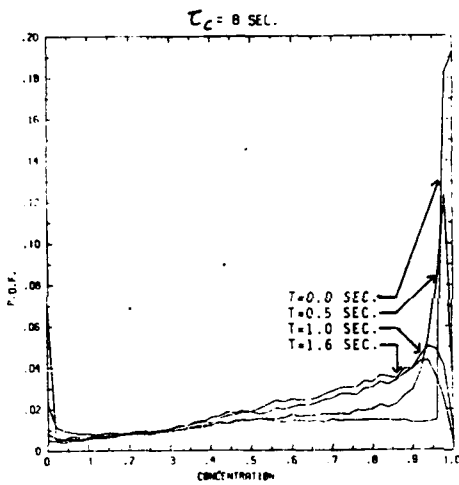


FIGURE 2: EVOLUTION OF THE P.D.F. OF  $C_A$  FOR 4 VALUES OF TIME (0.; 0.5.; 1.0.; 1.6 SEC.). A:  $\tau_c = 8$  SEC. B:  $\tau_c = 2$  SEC.

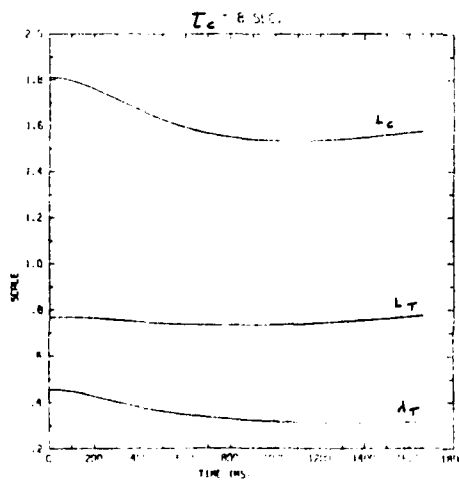


FIGURE 3: EVOLUTION VERSUS TIME OF  $L_c, L_T, A_T$  FOR  $\tau_c = 8$  SEC.

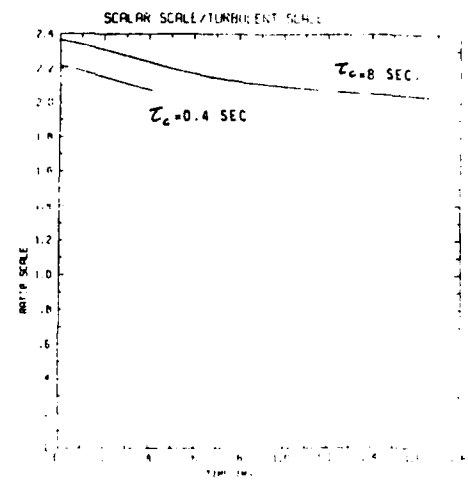


FIGURE 4: EVOLUTION WITH TIME OF THE RATIO  $L_c/L_T$  FOR  $\tau_c = 8$  SEC. AND  $\tau_c = 0.4$  SEC.

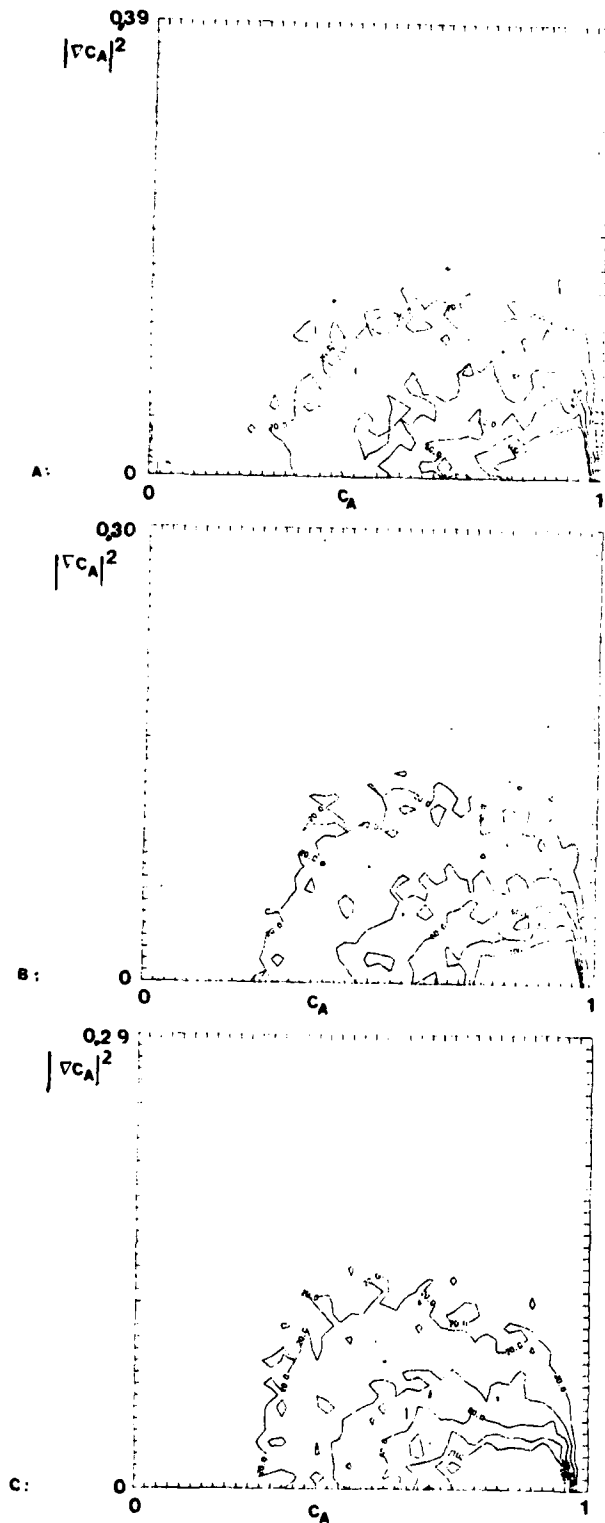


FIGURE 5: EVOLUTION OF JOINT PROBABILITY DENSITY FUNCTION OF  $C_A$  AND  $|v_{CA}|^2$  VERSUS TIME.  $\tau_c = 8$  SEC. A:  $T = 0.8$  SEC. B:  $T = 1.2$  SEC. C:  $T = 1.6$  SEC.

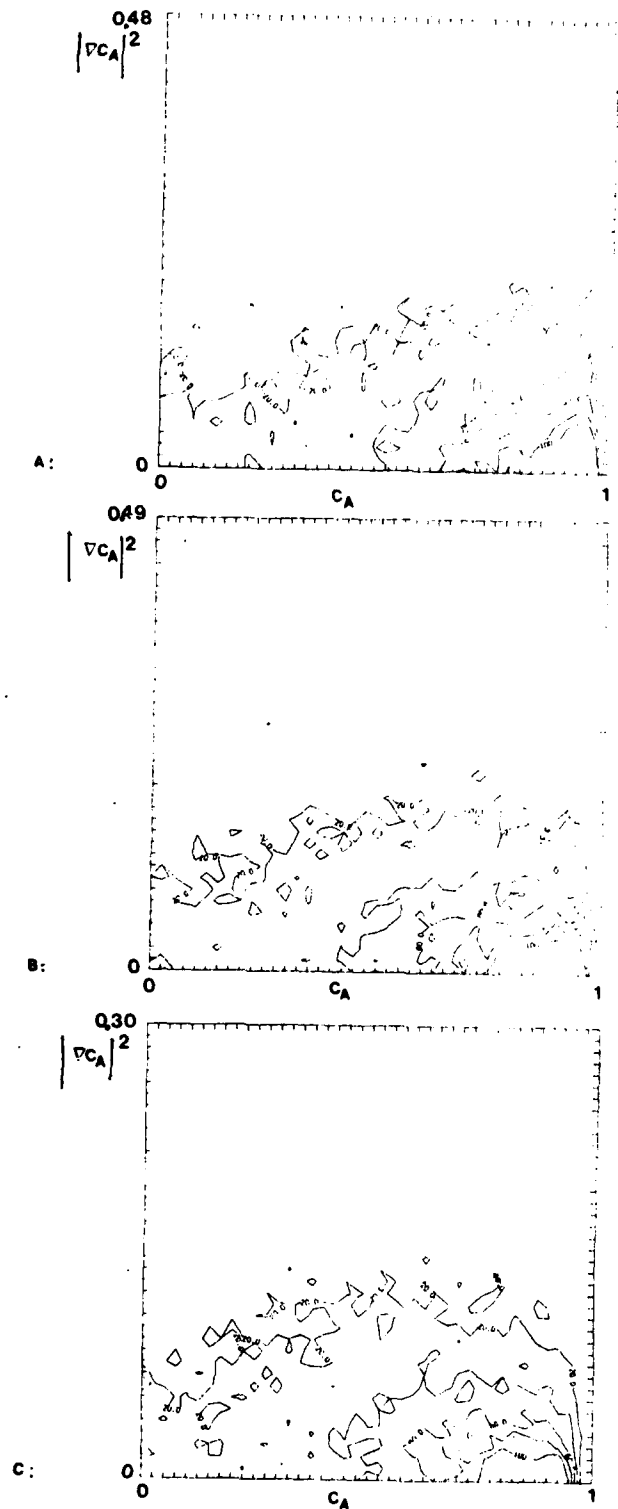


FIGURE 6: EVOLUTION OF JOINT PROBABILITY DENSITY FUNCTION OF  $C_A$  AND  $|v_{CA}|^2$  VERSUS TIME.  $\tau_c = 2$  SEC. A:  $T = 0.8$  SEC. B:  $T = 1.2$  SEC. C:  $T = 1.6$  SEC.

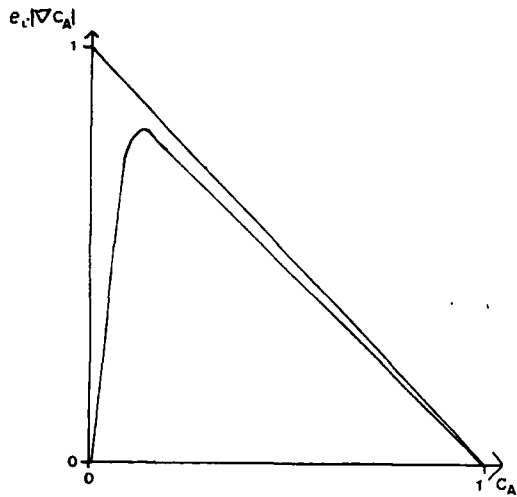


FIGURE 7: STRUCTURE OF A LAMINAR PREMIXED FLAME, IN THE PLANE  $|\nabla c_A|$  -  $c_A$ .  $e_l$  IS THE 'LAMINAR FLAME THICKNESS' -  $(\rho c)^{-1/2}$

A NUMERICAL EXPERIMENT ON THE DILUTION  
OF A CONTAMINANT CLOUD

T. Lookman and P. Sullivan  
Department of Applied Mathematics  
University of Western Ontario

The dilution of a cloud of toxic or flammable contaminant is a problem of real practical consequence, for example in the rupture of storage tanks, and also one of extraordinary theoretical and experimental difficulty. The process is unsteady such that experimentation requires ensemble averaging and hence a very large number of events to compile reliable statistics. The tendency for the turbulent convective motions to stretch contaminant into thin strands of a conduction cut-off thickness presents severe temporal and spatial experimental resolution problems.

The ensemble mean and mean-square values of concentration are not directly related to typical values of instantaneous concentration found in a contaminant cloud because of the spatial reference involved in their definition. In this paper the dilution process is investigated in terms of the cloud surface area in each realization, which is very sensitive to the turbulent convective motions and not dependent on spatial reference, along with a relatively thin transition region over the surface area that contains the predominant effects of molecular diffusivity  $\kappa$ . The surface area (or perimeter in two dimensions) is defined in terms of a cloud with  $\kappa = 0$  and its fractal-like structure. A numerical experiment is conducted on the velocity field generated by a random arrangement of line vortices. For each event a small square region is uniformly filled with contaminant points in sufficient numbers to represent uniform concentration of contaminant. Molecular diffusivity is superimposed on this convective field by using a random walk. This simple construction depends on one

non-dimensional parameter  $\phi = (\xi/\kappa)$  where  $\xi$  is the magnitude of the circulation for each of the line vortices, and allows for a comparison of the evolution of an individual cloud with different values of  $\kappa$  (including  $\kappa = 0$ ) by using an identical sequence of random numbers in the numerical experiment. This model is used to illustrate the concepts outlined above.

INTRODUCTION

When a scalar contaminant of uniform initial concentration  $\theta_0$ , over the volume  $L_0^3$ , is released in a turbulent flow the resulting contaminant cloud is rapidly convected over large distances and significantly distorted by the turbulent motion. Here we consider  $L_0 \ll L$  where  $L$  is the integral length-scale of the turbulent velocity field. The only agency, however, that is responsible for mixing host and contaminant fluid is the molecular diffusivity  $\kappa$ .

The value of the instantaneous concentration  $\Gamma(\underline{x}, t)$  is described, in each realization by,

$$\frac{\partial \Gamma}{\partial t} + \underline{u} \cdot \nabla \Gamma = \kappa \nabla^2 \Gamma \quad (1)$$

where position vector  $\underline{x}$  and velocity are referred in (1) to the centre-of-mass values of the cloud. For some period of time following release the difference between the cloud described by (1) and one described by (1) with  $\kappa = 0$  will be a thin transition-layer straddling the cloud surface area defined by the sharp-edged boundary corresponding to the  $\kappa = 0$  solution of (1). Using  $\theta_0$ ,  $L_0$  and an appropriate velocity scale  $u_0$  the non-dimensional form of (1),

$$\frac{\partial \Gamma'}{\partial t'} + \underline{u}' \cdot \nabla' \Gamma' = \frac{1}{P_e} \nabla'^2 \Gamma' \quad (2)$$

where  $\Gamma' = \Gamma/\theta_0$ ,  $\underline{u}' = \underline{u}/u_0$ ,  $t' = tu_0/L_0$ , suggest that for normally high values of Peclet number  $P_e = u_0 L_0/\kappa$  the right-hand-side of (2) will only be important over the thin boundary-layer on the cloud surface where gradients of  $\Gamma$  are high. When  $\kappa = 0$  the contaminant is contained within the constant initial volume  $L_0^3$  for all time, however, distension of the contiguous contaminant fluid by turbulent motion creates a considerable increase in surface area such that the total amount of mixing through the thin surface layer when  $\kappa \neq 0$  can be quite significant. Ultimately, when the layer thickness becomes comparable with the dimensions of the individual cloud, the above description becomes invalid and in what follows an attempt is made to put the thin-layer epoch in the context of other aspects of the cloud development.

The ensemble-average mean and variance of the concentration are,

$$C(\underline{x}, t) = \int_0^\infty \theta \underline{P}(\theta) d\theta \quad (3)$$

$$\text{and} \quad \overline{c'^2}(\underline{x}, t) = \int_0^\infty (\theta - C)^2 \underline{P}(\theta) d\theta \quad (4)$$

where  $\underline{P}(\theta; \underline{x}, t) d\theta = \{\text{prob. } \theta \leq \Gamma < \theta + d\theta\}$ . As shown in Chatwin and Sullivan (1979),

$$\frac{d}{dt} \int_{\text{all space}} (C^2 + \overline{c'^2}) dV = -\kappa \int_{\text{all space}} (\nabla \Gamma)^2 dV \quad (5)$$

so that when  $\kappa = 0$

$$\int_{\text{all space}} C^2 dV + \int_{\text{all space}} \overline{c'^2} dV = \theta_0^2 L_0^3 \quad (6)$$

and the entire process consists of the transfer of  $\int C^2 dV = \theta_0^2 L_0^3$  at  $t=0$  to  $\int \overline{c'^2} dV = \theta_0^2 L_0^3$  as  $t \rightarrow \infty$ . That is, the only mechanism that takes  $\overline{c'^2}$  out of the system is  $\kappa$  as shown in (5). One notices in (5) that it is the square of the gradients of concentration in individual clouds that gives rise to the dissipation of  $\overline{c'^2}$  and which, at small times, will be significant in a rather thin layer at the cloud surface.

It is of interest to consider  $\underline{P}(\theta)$  for  $\kappa = 0$ , which is

$$\underline{P}(\theta; \underline{x}, t) = (1-\pi)\delta(\theta) + \pi\delta(\theta - \theta_0) \quad (7)$$

where  $\pi(\underline{x}, t)$  is the probability of being in marked fluid with  $\kappa = 0$ . The use of (3) and (4) provides,

$$C(\underline{x}, t) = \pi \theta_0 \quad (8)$$

and

$$\overline{c'^2}(\underline{x}, t) = C(\theta_0 - C) \quad (9)$$

It is apparent from (9) that the distribution of  $\overline{c'^2}(\underline{x}, t)$  will have a minimum value at  $\underline{x} = 0$  and a maximum value on the surface where  $C(\underline{x}, t) = \theta_0/2$  with the constant magnitude  $(\theta_0/2)^2$  until the time when the largest value of mean concentration (here taken to be  $C(0, t)$ ) is equal to  $\theta_0/2$ . Thereafter there will be a unimodal distribution of  $\overline{c'^2}(\underline{x}, t)$  with the maximum value of  $\overline{c'^2}$  at  $\underline{x} = 0$  given by  $C(0, t)(\theta_0 - C(0, t)) = \theta_0 C(0, t)$ . In the methane jet experiments of Birch et al. (1978), with relatively intense mixing, the modal value of  $\overline{c'^2}$  along the jet centre-line is observed at approximately  $C(x, 0) = \theta_0/2$  however the effects of  $\kappa$  are in evidence there in that the maximum value of  $\overline{c'^2}$  is less than  $(\theta_0/2)^2$ . Thus the overall structure of the field does not appear to be very much altered by  $\kappa$  and one can infer that the thin-layer description should be valid at  $C(0, t) = \theta_0/2$ . We note in passing the effects of the size of the initial volume  $L_0^3$  implicit in this prescription of the thin dissipation layer epoch in the cloud evolution.

A further consideration is the cross-over point where the two integrals on the left-hand-side of (6) are equal. Assuming, for simplicity and specificity, a simple uniform distribution of  $C(r, t) = \frac{3}{4\pi R^3(t)} V_0 \theta_0$ ,  $r \leq R(t)$ ;  $C(r, t) = 0$ ,  $r > R(t)$  (10)

then using (9) and (6) one observes the cross-over to take place when  $C = \theta_0/2$ . Thus one expects, in the light of observation on the Birch et al (1978) jet result, that the dominant activity in the cloud for (at least)  $C(0, t) > \theta_0/2$  is the conversion of  $\int C^2 dV$  to  $\int \overline{c'^2} dV$  as per (5). This criterion is relevant to the suggestion of Toompuu (1985) where, in a discussion of the Chatwin and Sullivan (1979) result given in (6), suggested that the conversion to  $\int \overline{c'^2} dV$  occurs explosively at small time and that the overall process is one of decay of  $\int \overline{c'^2} dV$ .

It is useful here to consider the contaminant concentration values that are found within the conserved initial volume when  $\kappa = 0$  (primal fluid) as opposed to the lower concentration values found outside of this volume (amorphous fluid). One can define a joint probability density function

$$M(\theta, \eta; \underline{x}, t) d\theta d\eta = \begin{cases} \text{prob } \theta \leq \Gamma < \theta + d\theta \\ \text{prob } \eta \leq \gamma < \eta + d\eta \end{cases} \quad (11)$$

where the  $\eta$  and  $\theta$  contaminant occupy the same initial volume  $L_0^3$  in uniform concentrations  $\theta_0$  and  $\eta_0$  and for which molecular diffusivity for  $\theta$  is  $\kappa_\theta \neq 0$  and for  $\eta$  is  $\kappa_\eta = 0$ . Then the marginal distribution  $\underline{P}(\theta; \underline{x}, t)$  is found to be

$$\underline{P}(\theta) = (1-\pi)q(\theta) + \pi p(\theta) \quad (12)$$

where  $p(\theta)$  is the probability density function of concentration values found within the conserved volume for the release of contaminant with  $\kappa_\eta = 0$  (primal fluid) and  $q(\theta)$  is that for the contaminant outside of this volume (amorphous fluid). The  $p(\theta)$  will invariably range over higher values of  $\theta$  than will  $q(\theta)$  and there will be some degree of overlapping. In the context of the thin-layer description one would want  $\underline{P}(\theta)$  to be dominated by the primal fluid described by  $p(\theta)$ . This would be generally true for  $\pi \sim \frac{1}{2}$ . We see that the ensemble average of (1)

$$\frac{\partial C}{\partial t} + \nabla \cdot (\underline{u}\bar{C}) = \kappa \nabla^2 C \quad (13)$$

is, to a good approximation, relatively unaffected by  $\kappa$  everywhere (here, by contrast with the thin-layer description,  $C = \bar{C}$  is made smooth in  $\underline{x}$  by ensemble averaging) and the right-hand-side of (13) can be neglected such that (8) is almost always a very good approximation. Thus using (8) when  $C = \theta_0/2$  then  $\pi = \frac{1}{2}$  and one infers that for times for which  $C(\underline{0}, t) \geq \theta_0/2$  the primal fluid described by  $p(\theta)$  in (12) will be a dominant factor and the thin layer approach should be relevant. As  $t \rightarrow \infty$ ,  $\pi \rightarrow 0$  and from (12)  $\underline{P}(\theta) \sim q(\theta)$  such that all of the dominant dilution aspects of the cloud involve previously well mixed contaminant that has diffused out of the conserved volume used in the definition of (11). This range of  $\pi$  is also one in which the 'core-bulk' structure given in Chatwin and Sullivan (1980) will most certainly be applicable even though the value of  $\kappa$  is non-zero.

That is the (diminishing) region surrounding  $C(\underline{0}, t)$  remains the special core region in that (in each realization) these positions are always in primal fluid of relatively high concentration.

During the period for which  $C(\underline{0}, t) \geq \theta_0/2$  one expects  $\Gamma(\underline{0}, t) \sim C(\underline{0}, t)$  with not much variation. Then by defining  $T(t)$  to be the average thickness of the cloud surface layer when  $A(t)$  is the cloud surface area-defined using  $\kappa = 0$  contaminant, and  $V_i(t)$  the volume of fluid interior to the transition layer, conservation of mass provides

$$V_i C(\underline{0}, t) + A(t)T(t) \frac{C(\underline{0}, t)}{2} = L_0^3 \theta_0 \quad (14)$$

where  $\frac{C(\underline{0}, t)}{2}$  has been used to approximate the average of the concentration values found in the transition layer. The ensemble average of (14) can then be solved for this fraction of the original contaminant volume that remains at the (relatively high) value of  $C(\underline{0}, t)$ . That is,

$$\frac{V_i(t)}{L_0^3} = \frac{1}{\pi(\underline{0}, t)} - \frac{A(t)T(t)}{L_0^3} \quad (15)$$

Equation (15) is just the decomposition of contaminant into occupied volumes (in this case two discrete volumes) discussed in Chatwin and Sullivan (1977) in a more general context. A consistency check of (15) should be available using (5) wherein,

$$\frac{d}{dt} \int_{\text{all space}} (C^2 + \overline{C^2}) dV = -\kappa C^2(\underline{0}, t) \frac{A(t)}{T(t)} \quad (16)$$

Direct measurements of  $T(t)$  and  $A(t)$  are not attainable experimentally. A reasonably non-specific, random flow field can be generated using a digital computer and with which the behaviour of quantities like  $A(t)$  and  $T(t)$  can be assessed and in particular as these are related to other, more readily measured, statistics of a diffusing contaminant cloud.

#### A SIMULATED RANDOM FLOW-FIELD

The two-dimensional flow-field for an odd number of line-vortices with circulation  $\xi_i$  of equal magnitude (Lamb 1932, p.229) satisfies

$$\left. \begin{aligned}
 \nabla \cdot \mathbf{v} &= 0 \\
 \nabla \times \mathbf{v} &= 0 \\
 \bar{X} &= B \sum_i X_i \xi_i \\
 \bar{Y} &= B \sum_i Y_i \xi_i \\
 \bar{Z} &= B \sum_i \xi_i (X_i - \bar{X})^2 + \xi_i (Y_i - \bar{Y})^2
 \end{aligned} \right\} \quad (17)$$

with  $B = \sum_i \xi_i$

where  $\bar{X}, \bar{Y}, \bar{Z}$  are constants and  $\mathbf{v}$  is the velocity and  $X_i$  and  $Y_i$  are the co-ordinate locations of the line-vortices in a laboratory frame of reference. Each event of the present experiment consists of a random selection at  $t=0$  of independent vortex-centre locations for the 21 (typically) line vortices in use from a uniform distribution on a 30 unit square domain with the proviso that no two centres could be within 2 units mutual distance. This procedure provides a working section of the central 15 unit square region for which the velocity statistics are, to a good approximation, both homogeneous and stationary. A discrete time step is used to change the location of the vortex centres (due to their mutually induced motion) that is sufficiently small (typically  $\Delta t = .001$  with  $|\xi_i| = 1000$ ) so as to ensure the invariant properties of (17) over the period of experimental runs. More complex configurations of this flow field have been used by others to simulate various aspects of turbulent flows (Base 1981).

A basic experiment consists of following the positions of (up to 50,000) particles released at  $t=0$  on the central 1 unit square within the working section. The working section is subdivided into a square grid and concentration values  $\Gamma_j(X_i, Y_i, t)$  are simulated by counting the number of particles in realization  $\Gamma_j$  on the grid square centered on  $(X_i, Y_i)$  at time  $t$ . The starting procedure is repeated a number of times to determine an ensemble average. Molecular diffusion effects are introduced by the superposition of random-walk motion with a simple  $\pm \Delta X$  and independent  $\pm \Delta Y$  fixed increment to each particle displacement with the sign determined from a random number generator.

The velocity field has an intrinsic length  $L = 1/2\sqrt{n}$  where  $n$  is the number of centers per

unit area, determined to be the average distance-neighbour distance (Chandrasekhar 1954, p. 86). Hence one can non-dimensionalize with  $t' = t\kappa/L^2$ ,  $X' = X\kappa/|\xi|L$ ,  $Y' = LY/|\xi|L$ ,  $\Gamma' = \Gamma/\theta_0$  so that the convective diffusion equation becomes,

$$\frac{\partial \Gamma'}{\partial t'} + u' \frac{\partial \Gamma'}{\partial X'} + v' \frac{\partial \Gamma'}{\partial Y'} = \phi^{-2} \left( \frac{\partial^2 \Gamma'}{\partial X'^2} + \frac{\partial^2 \Gamma'}{\partial Y'^2} \right) \quad (18)$$

and depends on the one parameter  $\phi = |\xi|/\kappa$ . In practice the fixed length used in the random-walk component of the displacement is  $\Delta t' = \pm (\Delta t'/\phi)^{1/2}$ , where  $\Delta t'$  is the small time-increment used in advancing the position of the particles and of the vortex-centres. It is found, for example, that the relevant time for which  $\Gamma' \sim 1/2$  in the Introduction occurs for  $\phi = 10^{+4}$  at  $t' = 6$ .

One of the real advantages of this arrangement is that a cloud can be produced for identical initial conditions and subsequent random motion in each event with  $\kappa = 0$  and  $\kappa \neq 0$  for comparison. It is then more convenient to use arbitrary but consistent dimensional variables. For comparison the above relevant time where  $\Gamma = \theta_0/2$  is  $t = 2$  time units for  $\phi = 10^{+4}$ .

#### PRELIMINARY RESULTS

Two immediate objectives in this study are to define a measure of individual cloud average-thickness  $T(t)$  and of perimeter  $P(t)$ .

The difference between two contaminant clouds; one with  $\kappa = 0$  and the other with  $\kappa \neq 0$  (all else remaining the same) is a region surmounting the sharp-edged perimeter delineating the interior ( $\Gamma = \theta_0$ ) and the exterior ( $\Gamma = 0$ ) of the  $\kappa = 0$  cloud. Consideration of concentration values along a radial line emanating outwards from the cloud centre-of-mass and the use of the parallel axis theorem of moments-of-mass leads to the practical definition

$$T(t) = \frac{\sigma_\kappa^2 - \sigma_0^2}{2\sqrt{3} \sigma_0^2} \quad (19)$$

where  $\sigma_\kappa^2$  and  $\sigma_0^2$  are the second moments-of-mass about the individual cloud centre-of-mass and the subscripts denote a cloud with  $\kappa \neq 0$  and  $\kappa = 0$  respectively. The behaviour of  $T(t)$  is made complex by the dependence on the interaction of effects of molecular diffusivity  $\kappa$  with the convective flow

field. Contaminant is diffused through the cloud surface (with  $\kappa = 0$ ) and hence into regions of different convective velocities than met with by contaminant remaining within the cloud surface. Generally speaking,  $\sigma^2(t)$  in relative diffusion is predominantly governed by convective turbulent motions that have a significant gradient over length-scales comparable with  $\sigma(t)$ . This is an accelerating process in turbulence while  $\sigma(t) \ll L$  and as is found to be the case for the initial release conditions and velocity field outlined in this experiment in §2. One may expect the growth-rate of  $T(t)$  at a particular time in the cloud's evolution to be dominated by the shear effect on the existing layer. That is,

$$\frac{dT}{dt} = T \frac{du}{dy} = T \frac{uL}{L^2} \quad (20)$$

and, replacing the local length-scale  $L$  with  $\sigma_\kappa$  and the product of the local velocity-scale and  $L$  with  $\frac{d\sigma_\kappa^2}{dt}$ , then

$$\frac{1}{T} \frac{dT}{dt} = \frac{1}{\sigma_\kappa^2} \frac{d\sigma_\kappa^2}{dt} \quad (21)$$

that is,

$$\overline{T}(t) = (\overline{\sigma_\kappa(t)})^n$$

where overbars have been used to denote ensemble averaged quantities. Thus (21) suggests that the functional forms of  $T(t)$  and  $\overline{\sigma_\kappa(t)}$  are the same except for the exponent  $n$ . Figure 1 shows the results of a small pilot study where (19) appears to be verified with  $n = 2.7$ . The thickness appears to grow more rapidly than the cloud size but remains reasonably thin (i.e.  $\sim 1\%$  of  $\overline{\sigma_0}$  at  $t = .2$  with  $\phi = 10^4$ ) over the times when  $T(0, t) > \theta_0/2$  discussed in §1.

An individual cloud perimeter can, in principle, be defined for a cloud with  $\kappa = 0$ . In any practical sense the measured perimeter value will depend upon the length-scale of resolution for scales greater than the continuum scale.

Recently there has been much interest in describing fluid flow in terms of fractals which are objects that display self-similarity over a wide range of scales (Lovejoy 1981, Daccord et al. 1986). For example, efforts have been made to determine if the interface between a turbulent and

non-turbulent region is a fractal or not (Sreenivasan 1986).

A fractal object has associated with it a characteristic dimension  $D$  which forms a measure of its roughness or fragmentation. The fractal dimension  $D$  is defined as

$$D = \frac{\log N}{\log(1/\rho)} \quad (22)$$

where the object is thought to be made of  $N$  parts, each of which is obtained from the whole by a reduction of ratio  $\rho$ . Thus a straight line has fractal dimension  $D = 1$  and a plane  $D = 2$ . Departure from these Euclidian values indicate self-similarity over certain length-scales.

It is thus of interest to determine if the boundary of the contaminant cloud ever behaves like a fractal object as it disperses through the field generated by the vortex-centres. The most direct method of determining the fractal dimension of the interface is to cover it with area elements of decreasing size and note how the perimeter changes with the resolution  $\rho$  of these square elements. If the interface is a classical object the perimeter will initially increase with decreasing size of the square elements but will soon asymptote to a fixed value which is the true perimeter. If the interface is self-similar the perimeter will continue to increase, and, although the perimeter increases indefinitely, the ratio of the number  $N$  of perimeter elements required to cover the interface and their size  $\rho$  are related by (22).

Figure 2 shows the number of perimeter elements as a function of resolution  $\rho$  for relatively early times. The straight line with slope almost one indicates that, at least initially, the perimeter of the cloud behaves like a classical object. Of course the length of the perimeter can be directly determined as a function of resolution  $\rho$  from Figure 2. Trials using a number of different initial configurations of centers at time  $t = .02$  were found to be straight lines with the same slope as shown on Figure 2 and with a translation separating the different trials. It remains to be seen whether or not a fractal dimension  $D \neq 1$  will obtain for the perimeter for longer periods in the cloud evolution.

The perimeters for a cloud with  $\kappa \neq 0$  and which are appropriate to the use of (14) are found from the displays given in Figure 2 and from the value of the average cloud thickness. The surface-layer with thickness  $T(t)$  that results from  $\kappa \neq 0$  will eradicate wave-lengths on the perimeter comparable with  $T(t)$ . Thus the value of the perimeter corresponding to the resolution given by  $T(t)$  leads to the operative value of  $P(t)$ . At small times dissipation of  $\overline{c'^2}$  occurs at the high wave-number part of the spectrum (comparable to  $T^{-1}$ ) and physically at the periphery of the individual clouds. The reasonable degree of correlation observed between  $\sigma_0$  and  $P$  for individual clouds suggests that, on average, the same local events in the random velocity field are responsible for increasing  $\sigma_0$  and for increasing the perimeter.

One concludes from these preliminary results that it is worthwhile to undertake a more comprehensive study with more thorough ensemble averaging and with a wide range of  $\phi$  leading to a critical appraisal of (15) and (16).

#### ACKNOWLEDGEMENTS

This work received financial support from the National Science and Engineering Research Council of Canada and the authors would like to acknowledge the contribution of Mr. S. Farazdaghi who was engaged to work on this project.

#### REFERENCES

- Base, T.E. 1981, The behaviour of aerosol particles in a computed turbulent flow model. In: Turbulence in liquids (ed. Patterson and Zakin) p.78. Univ. of Missouri Press, Rolla.
- Birch, A.D., Brown, D.R., Dodson, M.G. and Thomas, J.R., 1978, The turbulent concentration field of a methane jet. *J. Fluid Mec.* 88, 3, 431.
- Chandrasekhar, S. 1954, Stochastic problems in physics and astronomy. In: Selected papers on noise and stochastic processes (ed. Wax) p. 2. Dover, New York.
- Chatwin, P.C. and Sullivan, P.J. 1977, Experiments on the complete mixing of a passive contaminant in turbulent diffusion. In: Proc. 5th Biennial Symposium on Turbulence (ed. Patterson and Zakin) p. 211. Science Press, Princeton.
- Chatwin, P.C. and Sullivan, P.J. 1979, The relative diffusion of a cloud of passive contaminant in incompressible turbulent flows. *J. Fluid Mech.* 91, 2, 337.
- Chatwin, P.C. and Sullivan, P.J. 1980, The core-bulk structure associated with diffusing clouds. In: Turbulent shear flows 2 (ed. Bradbury et al) p. 379, Springer-Verlag.
- Daccord, G., Nittman, J. and Stanley, H.E. 1986, Fractal viscous fingers: experimental results. In: On growth and Form (ed. Stanley and Ostrowsky) p. 203, Martinus Nijhoff Pub., Dordrecht.
- Lamb, Sir Horace, 1932, Hydrodynamics, 6th ed. Dover, New York.
- Lovejoy, S. 1981, Area-perimeter relation for rain and cloud areas. *Science*, 216, 9, 185.
- Sreenivasan, K.R. and Meneveau, C. 1986, The fractal facets of turbulence. *J. Fluid Mech.* (in press).
- Toompuu, A. 1985, A phenomenological model for the passive scalar variance transformation in a turbulent fluid. *Int. J. Heat Mass Transfer*, 28, 9, 1773.

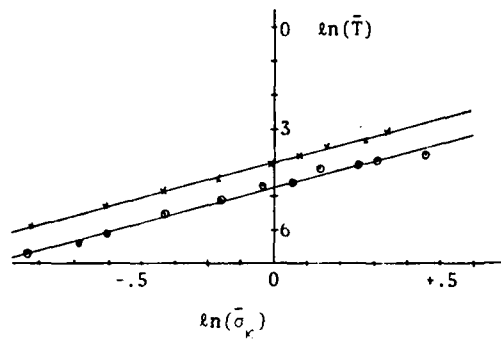


Figure 1. Result of a small pilot study to illustrate the relationship between the average thickness  $\bar{T}(t)$  and the average cloud size  $\bar{\sigma}_\kappa$  as given in (19).

$$\cdot -\phi = 10^4, \quad -\phi = 2 \times 10^4$$

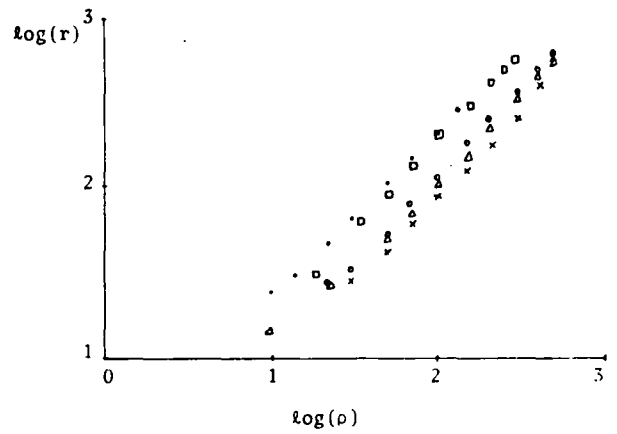


Figure 2. Number of perimeter blocks  $r$  as a function of resolution scale  $\rho$ .

$$t = .05, \quad -t = .10, \quad -t = .15, \quad -t = .2, \\ -t = .25$$

Simultaneous Velocity and Concentration  
Measurements of Turbulent Jet Flows

T. H. Chen  
A. J. Lightman  
P. P. Yaney  
W. J. Schmoll

University of Dayton Research Institute  
Dayton, Ohio 45469

ABSTRACT

An integrated Laser Doppler Anemometry-Laser Raman Spectroscopy (LDA-LRS) System is used to make time- and space-resolved simultaneous velocity and concentration measurements in  $\text{CO}_2$  jet flows. The purpose of this experimental study is to investigate the detailed turbulent transport of mass and momentum in the near-jet region within 20 jet diameters. The results are analyzed to develop better understanding of the role of the large-scale and small-scale structures in the mixing processes.

1.0 INTRODUCTION

Since turbulent mixing and combustion processes are very complicated, the flow geometry chosen for studying these processes must be simple. Jet flow is an ideal choice [Schefer and Dibble, 1986] because it has simple boundary conditions.

To understand the development of the jet flow, the detailed characterization of the initial transport processes near the jet exit must be made. Unfortunately, few research efforts have examined this flow region [List, 1982]. Several researchers [Yule, 1978; Liu, 1974] have found that coherent vortex rings exist in the flow field near the jet nozzle, under certain flow conditions. A recent study [Roquemore, 1986], using a laser-sheet lighting technique for flow visualization, has shown that coherent structures appear in both the reacting

and nonreacting jets. In the nonreacting jet, the coherent structures show up at the interface layer between the jet and annular fluid. In the reacting jet, the structures appear both inside and outside the flame sheet. Inside the flame sheet, where the mixing of fuel and oxidizer takes place, the large structures promote more efficient mixing. Outside the flame sheet, where the hot gases from the thermal plume and the cold gases from the ambient field meet, the coherent structures play an interesting role. These structures, driven by the velocity differences and buoyancy, can couple with the flickering of the jet diffusion flame.

If spatially and temporally resolved scalar measurements cannot be made, the researcher has to study the flow field by the information gained from velocity measurements. The important scalar properties were modeled by assuming values for the Prandtl and Schmidt numbers. However, many researchers have started to question the validity of these assumptions. For example, Chen and Driscoll (1983), proposed that the rotational motion of a vortex transports scalar quantities more efficiently than it transports streamwise momentum. Therefore, the use of closure formulations based upon velocity fluctuation alone to describe turbulent jet flows involving scalars could lead to wrong results.

The flow near the jet nozzle is by no means a fully developed turbulent flow. It consists of a potential-core region and a transitional

region which is formed by a combination of wave-like structures and organized structures. Since the mixing processes near the nozzle tip of the jet influence the behavior of jet diffusion flames [Peters and Williams, 1983], it is important to examine the detailed transport of mass and momentum in that particular flow regime.

## 2.0 EXPERIMENTAL

### 2.1 Flow Apparatus and Test Conditions

A schematic diagram of the flow apparatus designed to study the nonreacting and reacting jet flows is shown in Figure 1. A tapered round nozzle is used to introduce the jet into an annular, co-flowing air stream. The inner diameters of the central and annular jets are 10 mm and 80 mm, respectively. Two electronic flow control units are used to set and regulate the required flow rates. The whole jet-flow apparatus is mounted in a 3-axis transversing base which allows accurate radial and axial scans to be made under computer or manual control.

In this nonreacting jet flow study, CO<sub>2</sub> was chosen for the central jet for two reasons: it has the same molecular weight as propane, the fuel commonly used in reacting flow studies; and the CO<sub>2</sub> molecule provides a strong rotational Raman signal, suitable for species concentration measurements. The N<sub>2</sub> molecule from the co-flowing air stream provides the second probe species for the Raman measurements.

The jet exit velocity chosen, U<sub>j</sub>, is 8.0 m/s; the exit velocity for the annular co-flowing air is 2.0 m/s. This flow condition was selected from the studies of flow visualization at various flow conditions. In this particular flow condition, organized large structures appeared near the jet exit and turbulent small-scale structures developed further downstream. Thus, the contribution of

both large-scale and small-scale structures in the mixing processes can be examined.

In this study, measurements were made at locations within 20 jet diameters, i.e. 20 cm, of the exit. Typically, more than ten axial stations were chosen for the radial scans. For the radial scan at each station there were 30 to 40 spatially chosen measurement locations. At each position 4096 sets of simultaneous CO<sub>2</sub> and air concentrations with axial and radial velocity data are collected.

### 2.2 Integrated LDA-LRS System

A schematic diagram of the integrated LDA-LRS optical diagnostic system, designed to perform the simultaneous velocity and concentration measurements, is shown in Figure 2. Both the LDA and LRS optical techniques are nonintrusive, which is desirable for performing these space- and time-resolved measurements. The two optical probes were focused at the same location. In addition, electronic and software systems have been integrated so that the simultaneous measurements could be made and analyzed. Detailed descriptions of this integrated LDA-LRS system have been published [Lightman et al., 1986].

For the study of a given flow condition, measurements were made at a minimum of 400 different spatial locations across the entire r-z plane. To handle this massive amount of data, sophisticated software was developed which included graphics and file management routines.

## 3.0 RESULTS AND DISCUSSION

### 3.1 Spreading Rate and Decay Law

The contours of axial velocity and CO<sub>2</sub> concentration are shown in Figures 3 and 4. The axial velocity is normalized by the jet velocity, U<sub>j</sub>, and the annular air stream velocity, U<sub>a</sub>, as follows:

$$U_n = (\bar{U} - U_a) / (U_j - U_a)$$

where

- $\bar{U}$  : mean axial velocity to be normalized.
- $U_j$  : exit jet velocity,
- $U_a$  : annular jet velocity,
- $U_n$  : normalized velocity.

After the above normalization, the value of  $U_n$  at the jet exit is one and the value at the annular exit is zero. The concentration of  $CO_2$  is a non-dimensional scalar and also has the value of one at the jet exit and zero at the annular air stream. Direct comparison of velocity and concentration contours immediately shows distinct difference between velocity and concentration distribution. The velocity contours show the well known velocity behavior of a jet flow. The potential core extends five to six jet diameters. The concentration contours show that the potential core defined by the  $CO_2$  concentration extends only 2 to 3 jet diameters and that the concentration decays much faster than the velocity. At the end of the velocity potential core, the  $CO_2$  concentration has been decreased to less than 0.7. That means at least 30% of the co-flowing air has already been entrained into the jet center. One possible cause for this peculiar result is that organized vortex structures exist at the interface of the jet and co-flowing air stream. The rotational motion of these vortices engulfs both the  $CO_2$  and air streams by the roll-up processes. Rolling across the vortex layers, the scalar quantity may retain its identity, whereas the streamwise velocity will lose its axial momentum to the rotational momentum and thereby lose its identity. Due to the effect of vortex motion, the streamwise velocity will not fluctuate as much as radial velocity and concentration. (This observation is further supported by the experimental results to be shown later in Figures 7 and 8.)

Figures 5 and 6 show some of the more relevant information contained in the previous figures. The half-jet width of axial velocity,  $r_{h,u}$ , and  $CO_2$  concentration,  $r_{h,c}$ , are shown in

Figure 5. The half-jet width is defined as the diameter of the boundary where the value of the velocity or that of the concentration is half the value at the jet center. The value of  $r_{h,u}$  increases slowly within the potential core and shows a linear increase downstream of the core. The value  $r_{h,c}$  takes a sudden jump at the end of the potential core defined by concentration, which is 2 to 3 jet diameters. After the jump, the value of  $r_{h,c}$  increases at the same rate as  $r_{h,u}$ . For this particular jet configuration and flow condition, the first coalescence of vortices occurs at around 3 jet diameters downstream from the nozzle tip. The formation of a bigger vortex at that point accelerates the spreading of the  $CO_2$  concentration profile. Figure 6 shows the decay law of the value of velocity and concentration at the jet center. Consistent with the results shown in Figure 5, the decay of  $CO_2$  concentration takes a sudden dip at the same point that the sudden increase of spreading takes place.

Quantitative comparisons of the spreading rate and decay law of velocity and concentration suggest that the velocity and concentration are transported differently by the organized structure that exists at the transitional region near the nozzle tip. Inside the velocity potential core, a substantial amount of the gas entrained from the co-flowing stream has been found. Thus, the conventional assumption, that there is no entrainment inside the potential core for the prediction of a lifted flame, needs to be re-examined.

### 3.2 Velocity and Concentration Fluctuation

For a proper comparison, the root mean square (rms) value of  $u$ ,  $v$ , and  $c$ , as well as covariance,  $\overline{u'v'}$ , need to be normalized. The jet velocity,  $U_j$ , is chosen as the reference velocity. The normalization of  $u'$ ,  $v'$ ,  $c'$ , and  $\overline{u'v'}$  is done as follows:

$$\begin{aligned}u'_n &= u'/U_j \\v'_n &= v'/U_j\end{aligned}$$

$$\overline{u'v'_n} = \text{SIGN}(\overline{u'v'}) \cdot \sqrt{|\overline{u'v'}|} / U_j$$

$$c'_n = c' / 1.0$$

where SIGN is the sign function.

The contour lines of constant  $u'_n$  and  $v'_n$  are plotted in Figures 7 and 8 respectively. The maximum value of  $u'_n$  appears at the location  $z/D = 4$ , near the end of the velocity potential core where the shear layer converged. At this point, the wake effect of the nozzle wall begins to disappear as well. The shape of the  $v'_n$  contours looks very similar to that of the  $u'_n$  contours. The maximum value of  $v'_n$  appears at the same location where the maximum of  $c'_n$  takes place; see Figure 10. The maximum value of  $v'_n$  is measured to be 17.0% and  $u'_n$  to be 15.0%.

The contours of  $\overline{u'v'_n}$  are shown in Figure 9. The maximum magnitude of  $\overline{u'v'_n}$  occurs between the areas where maximum  $u'_n$  and  $v'_n$  are taking place. The higher the value of  $\overline{u'v'}$ , the better  $u$  and  $v$  are correlated. This good correlation between  $u'$  and  $v'$  could be the natural characteristics of the organized structure. At the center of the jet, axisymmetry does bring the magnitude of  $\overline{u'v'}$  to a minimum.

The mixing introduced by the organized motion is considered as macro mixing. This macro mixing process, due to large entrainment of two streams, initiates better mixing which will be completed by the molecular micro mixing following the more complete development of the turbulence. To re-evaluate this well recognized mixing theory, the mixedness,  $M(\phi)$ , of the measure velocity signal is computed as follows [Koop and Browand, 1979]:

$$M(\phi) = \frac{\int_0^T H(\phi - \bar{\phi})(\phi_B - \bar{\phi}) dt + \int_0^T H(\bar{\phi} - \phi)(\phi - \phi_T) dt}{\int_0^T H(\phi - \bar{\phi})(\phi_B - \bar{\phi}) dt + \int_0^T H(\bar{\phi} - \phi)(\phi - \phi_T) dt}$$

The mixedness could be considered as the measure of the completeness of the mixing. A mixedness of one indicates that the mixing is complete.

The contours of  $M(u)$  and  $M(v)$  are compared with the contours of  $u'_n$  and  $v'_n$  respectively, and strong similarity is found. The minimum mixedness occurs at locations where the maximum fluctuation occurs. The shapes of the contour lines of mixedness and fluctuation also look very similar. The direct link between these two quantities should allow us to examine the mixing of the flow using only one of them. Therefore, the contours of the mixedness of velocity  $u$  and  $v$ ,  $M(u)$  and  $M(v)$ , are not shown here. However, the relation between  $M(u)$  and  $u'$  is found to be given by:

$$M(u) = 1.0 - (u' / (U_j - U_a)) * \text{constant.}$$

The rms fluctuation and mixedness of velocity and concentration show that strong entrainment, induced by the organized motion, is taking place in a region between  $Z = 2D$  to  $6D$ . The fact that mixedness reaches its minimum means that the entrained gases do not mix well in a microscopic level.

Figure 10 shows the contour lines of concentration fluctuation,  $(c'_n)$ , of  $\text{CO}_2$  gas. The maximum fluctuation of concentration occurs closer to the nozzle tip than that of the axial velocity fluctuations. This result is consistent with the mean measurement of velocity and concentration. Both the mean velocity and concentration profile spread very slowly upstream of the potential cores defined by velocity and concentration. Near the nozzle tip, the radial gradient of  $\text{CO}_2$  concentration is infinite, whereas the radial gradient of the axial velocity is finite due to the presence of the wall effect from the nozzle. The potential core defined by concentration ends earlier than the potential core defined by velocity, indicating that the  $\text{CO}_2$  concentration mixed more efficiently. Therefore, the vortex motion may transport the scalar concentration across the shear layer more efficiently than it transports velocity.

In this jet study, all the measurements are done within 20 jet diameters. The similarity stage of the flow cannot be reached. It is therefore very interesting to observe how the velocity and concentration fluctuate within the flow region, which includes the transitional regime. Figure 11 shows  $u'_n$ ,  $v'_n$ ,  $c'_n$  and  $u'v'_n$  for  $z = 2D$ ,  $4D$ , and  $12D$ . At  $Z = 2D$ , the value of  $c'_n$  is the largest, followed by  $v'_n$ , and then by  $u'_n$ . At  $z = 4D$ , the value of  $u'_n$ ,  $v'_n$ ,  $c'_n$  are almost the same in the higher shear areas. Further downstream,  $u'_n$  becomes greater, followed by  $c'_n$  and then by  $v'_n$ . In all,  $c'_n$  is greater than  $v'_n$ . The value of  $u'_n$  is the smallest in the beginning, and then surpasses the value of  $c'_n$  and  $v'_n$  later on.

Figure 12 shows more detailed pictures of the values of  $u'$ ,  $v'$  and  $c'$  normalized by their values at the jet center,  $u'_m$ ,  $v'_m$  and  $c'_m$ . The values of  $u'v'$  are normalized by  $u'_m$  since  $u'v'_m$  is zero. The radial positions have been normalized by the half-jet width of the velocity profile. From this figure, the maximum  $u'$  and  $v'$  occur very near the radial location where maximum  $u'v'$  occurs. The maximum  $u'v'$  occurs at the radial position where the radial gradient of the axial velocity is maximum. Since the profile of the concentration spreads wider than that of the velocity, the radial position where the radial gradient of the concentration and  $c'_m$  are maximum is correspondingly further away from the center line.

### 3.3 Joint Velocity and $CO_2$ Concentration Measurements

The  $CO_2$  concentration fluxes due to turbulent fluctuations in the axial and radial direction are defined as:

$$\overline{u'c'} = \frac{1}{N} \sum_{i=1}^N [u_i - \bar{U}] [c_i - \bar{C}]$$

$$\overline{v'c'} = \frac{1}{N} \sum_{i=1}^N [v_i - \bar{V}] [c_i - \bar{C}]$$

where

- $u_i$  : instantaneous axial velocity.
- $\bar{U}$  : mean axial velocity.
- $v_i$  : instantaneous radial velocity.
- $\bar{V}$  : mean radial velocity.
- $c_i$  : instantaneous  $CO_2$  concentration.
- $\bar{C}$  : mean  $CO_2$  concentration.

Figure 13 shows  $\overline{u'c'}$  and  $\overline{v'c'}$  at  $Z = 2D$ , and  $18D$ , respectively. Comparing the profiles of  $\overline{v'c'}$  at these two locations, we find that the value  $\overline{v'c'}$  has dropped by an order of magnitude from  $2D$  to  $18D$ . At  $Z = 2D$ ,  $\overline{v'c'}$  is larger than  $\overline{u'c'}$ , whereas at  $Z = 18D$ , the magnitude of  $\overline{v'c'}$  is smaller than that of  $\overline{u'c'}$ . Similar trends were found by comparison of  $u'_n$  and  $v'_n$  as shown in Section 3.2. In various boundary layer, shear layer, and jet flows,  $u'$  is usually greater than  $v'$  in the relatively well developed turbulent regions. Conversely, the radial velocity fluctuations and the mass flux are generally larger than similar quantities in the axial direction at the transitional flow region near the jet exit.

The radial profile of the ratio of radial and axial mass fluxes at  $Z = 18D$  is depicted in Figure 14. Due to the axisymmetry, the mean mass flux across the center line in the radial direction,  $\overline{v'c'}$  will be zero, as was shown in Figure 13. Since the location of  $Z = 18D$  is not too far away from the jet exit, the correlation between the axial jet velocity and jet species ( $CO_2$  concentration), is still present. The ratio of  $\overline{v'c'}$  to  $\overline{u'c'}$  must be zero at the jet center at this station. It then increases to about 0.5 at the radial position where the maximum  $\overline{v'c'}$  and  $\overline{u'c'}$  take place. The ratio stays fairly constant across a great part of the jet cross section. Further away from the center line, both  $\overline{v'c'}$  and  $\overline{u'c'}$  go to zero and the ratio of these two quantities increases to one.

It can be concluded that in flow regions sufficiently downstream and away from the jet center, the assumption of constant ratio of  $\overline{v'c'}$  and  $\overline{u'c'}$  used in efforts to model the jet flow is probable.

The three-dimensional plot of a turbulence production term.

$$- \overline{v'c'} \delta\bar{C}/\delta r,$$

across the r-z plane is shown in Figure 15. As was pointed out by Launder (1978), the production term is significant only in areas where wall effects or high shears exist. The radial gradient of  $\bar{C}$  is maximum at  $Z = 0$ , but the value of  $\overline{u'c'}$  does not reach its maximum due to the radial suppression of the initial shear layer development near the nozzle tip. As a result, the production peaks up very close to the region where maximum  $c'$  is taking place.

Without considering the radial scale factor  $r$ , we could define turbulence mass and momentum diffusivities  $\sigma_c$  and  $\sigma_v$  by:

$$\sigma_c = - \overline{v'c'}/\delta\bar{C}/\delta r$$

$$\sigma_v = - \overline{v'u'}/\delta\bar{U}/\delta r$$

where

$\overline{v'c'}$ : radial  $\text{CO}_2$  mass flux,

$\delta\bar{C}/\delta r$ : radial gradient of mean  $\text{CO}_2$  concentration,

$\overline{v'u'}$ : radial momentum flux of axial velocity,

$\delta\bar{U}/\delta r$ : radial gradient of mean axial velocity.

Figure 16 shows profiles of  $\sigma_c$  and  $\sigma_v$  at the location of  $Z = 2D$  and  $18D$ , respectively. At both locations, it is clear that even if the values of fluxes and radial gradients have their maxima at the same radial position, their ratios, which were defined as turbulence diffusivities, still peak at that point. In other words, the mass and momentum diffusivity are not constant across the jet as shown in Figure 16. The turbulence Schmidt number which is defined as the ratio of  $\sigma_v$  to  $\sigma_c$ :

$$S_c = \frac{\sigma_v}{\sigma_c}$$

is around 0.7 in the high shear area. At the location  $Z = 18D$ , further downstream from the jet exit, the value of  $\sigma_c$  is actually smaller than the value of  $\sigma_v$  as shown in Figure 16. The turbulence Schmidt number  $S_c$  stays fairly constant across the high shear section. From Figure 17, this value is shown to be around 1.4. Since the radial gradients of  $\bar{U}$  and  $\bar{C}$  go to zero near the jet center, the values of  $\sigma_c$  and  $\sigma_v$  are very uncertain. Therefore, the value of  $S_c$  near the jet center probably is not very significant. Again, across the high shear section of a jet flow, the assumption of constant turbulence Schmidt number is probably justified for the downstream flow region where the principle of similarity is applicable.

#### 4.0 CONCLUSIONS

Studies of turbulent mixing of a  $\text{CO}_2$  axisymmetric jet with a co-flowing air stream were carried out. The emphasis is on the flow field within 20 jet diameters. The transitional flow region, consisting of a potential core, wavelike structures, and organized structures is examined and is compared with the following flow region where small-scale structures develop.

Both the independent and the simultaneous velocity and concentration data were examined to determine the effects on the scalar versus velocity mixing processes due to the presence of the large-scale versus small-scale structure in the jet flow. Many consistent observations presented here deserve emphasis. Due to the presence of the organized structures, the flow region from 2 to 6 jet diameters downstream possesses the following characteristics:

1. Concentration was transported more efficiently across the shear region where mixing between  $\text{CO}_2$  and air occurs. As a result, the potential core of concentration is shorter than that of velocity. Consequently, the concentration profile spreads wider than the

velocity profile by an offset which occurred from location  $Z = 2D$  to  $6D$ .

2. Maximum  $c'$  and  $v'$  occur at the area near  $Z = 2D$ , whereas maximum  $u'$  occurs at the area near  $Z = 4D$ .
3. Relations among rms fluctuations of axial velocity, radial velocity, and concentration were found to be:

$$c'_n > v'_n > u'_n$$

which indicates that significant radial entrainment across the shear layer is taking place at location from  $Z = 2D$  to  $6D$ .

4. Radial mass flow,  $\overline{v'c'}$ , is greater than axial mass flux,  $\overline{u'c'}$ .
5. The turbulence production term,  $-\overline{v'c'}$ ,  $\delta\bar{C}/\delta r$ , is maximum near the location where  $c'$  and  $v'$  are maximum. In the same area,  $\overline{v'c'}$  also reaches its maximum.
6. Turbulence mass diffusivity,  $\sigma_c$ , is greater than turbulence momentum diffusivity,  $\sigma_v$ . Across the high shear section, the turbulence Schmidt number,  $S_c$ , is about 0.7.

The observations that maximum  $c'$  and  $v'$  occur at the same location and that  $\overline{v'c'}$  is greater than  $\overline{u'c'}$  there strongly support the different mechanisms of axial velocity and concentration transport due to the rotational motion, previously observed and explained by Chen and Driscoll (1983).

In the flow region approaching  $Z = 18D$  where small-scale structures are present, different transport characteristics are:

1.  $u'_n > c'_n > v'_n$
2.  $\overline{u'c'} > \overline{v'c'}$
3.  $\sigma_v > \sigma_c$ ,  $S_c = 1.4$  across the high shear section.

As far as the mixing is concerned, large-scale structures are responsible for the global entrainment between jet gas and co-flowing gas, and the small-scale eddies provide mixing at a microscopic or molecular level. Although the radial entrainment is very high in the region from  $2D$  to  $6D$ , the measured

mixedness of velocity and that of concentration are minimum in that region. Premixing between jet fluid and co-flowing fluid takes place in the near jet region at the macroscopic level but not at the microscopic level. Turbulent mixing has not yet approached local and temporal uniformity.

Finally, differences are observed between the spread rate, decay law, fluctuations and mixedness of concentration and of velocity in the jet flow. In the near jet region, radial turbulence passage is significant. To model the flow in the near-jet region correctly, the use of closure formulations based upon velocity fluctuations alone to describe turbulent jet flows involving a scalar must be reconsidered. In addition, the fact that the radial fluctuation is larger than the axial fluctuation, and better correlated with concentration, indicating strong entrainment in the near-jet region, has to be taken into account.

#### ACKNOWLEDGMENT

This work is supported by the U. S. Air Force Wright Aeronautical Laboratories, Aero Propulsion Laboratory, under Contract No. F33615-82-C-2255. The authors are indebted to Drs. W. M. Roquemore, D. R. Ballal, and L. Krishnamurthy for their helpful suggestions concerning this work. Many thanks to M. Spicer, J. Heinrichs and J. Stutrud for their excellent technical assistance.

#### REFERENCES

- Chen, T. H., 1983, "The Stratified Turbulence Mixing Layer," Ph.D. Thesis, University of Michigan, Ann Arbor, MI.
- Koop, C. G. and Browand, F. K., 1979, "Instability and Turbulence in a Stratified Fluid with Shear," *J. of Fluid Mechanics*, Vol. 93, Part 1, pp. 135-159.
- Launder, B. E., 1978, "Heat and Mass Transport," Turbulence - Topics in Applied Physics Vol. 12, ed. P. Bradshaw, Springer-Verlag, New York.
- Lightman, A. J. et al., 1986, "An Integrated LDA/Raman System for Making Measurements of Velocity and Concentration," 5th ICALEO Meeting, Arlington, VA.

List, E. J., 1982, "Turbulent Jets and Plumes," *Annu. Rev. of Fluid Mech.*, Vol. 14, pp. 189-212.

Liu, J. T. C., 1974, "Developing Large-Scale Wavelike Eddies and the Near-Jet Noise Field," *J. of Fluid Mechanics*, Vol. 62, pp. 437-464.

Peters, N. and F. A. Williams, 1983, "Lift-off Characteristics of Turbulent Jet Diffusion Flames," *AIAA*, Vol. 21, No. 3.

Roquemore, W. M., 1986, private communication.

Schefer, R. W. and Dibble, R. W., 1986, "Rayleigh Scattering Measurements of Mixture Fraction in a Turbulent Nonreacting Propane Jet," *AIAA-86-0278*, *AIAA 24th Aerospace Science Meeting*, Reno, NV.

Yule, A. J., 1978, "Large-Scale Structure in the Mixing Layer of a Round Jet," *J. of Fluid Mech.*, Vol. 89, Part 3, pp. 413-432.

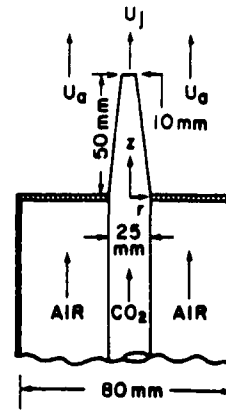


Fig. 1. Sketch of the Jet Flow Geometry.

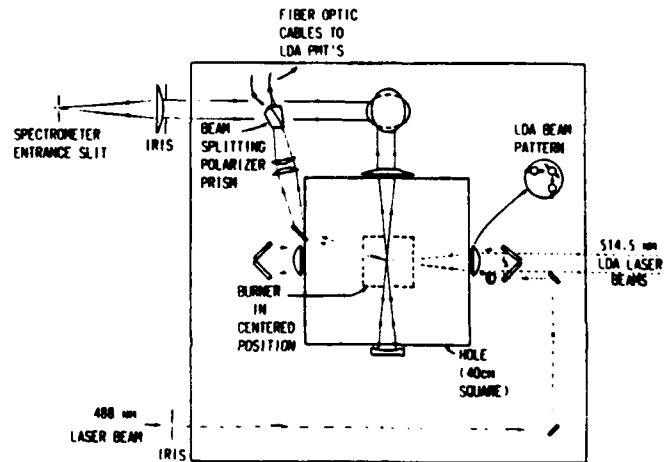


Fig. 2. Schematic of the Integrated LDA/LRS System.

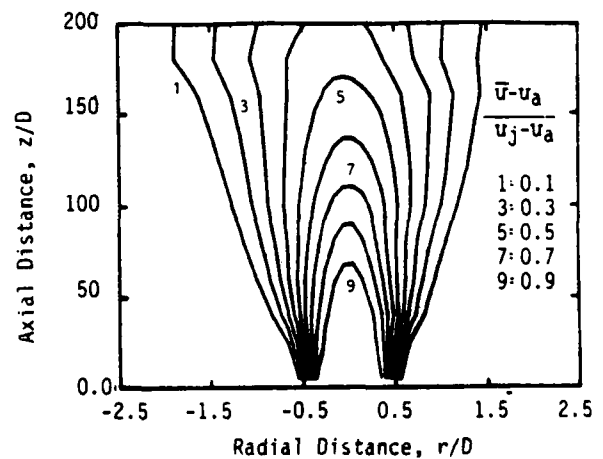


Fig.3. Measured Contours of Mean Axial Velocity,  $\bar{u}$

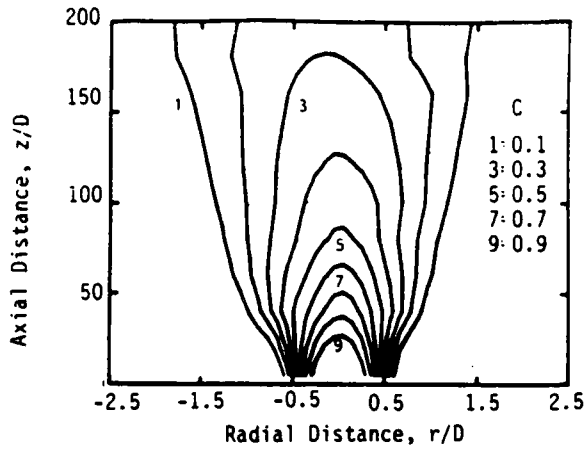


Fig. 4. Measured Contours of Mean  $\text{CO}_2$  Concentration,  $\bar{C}$

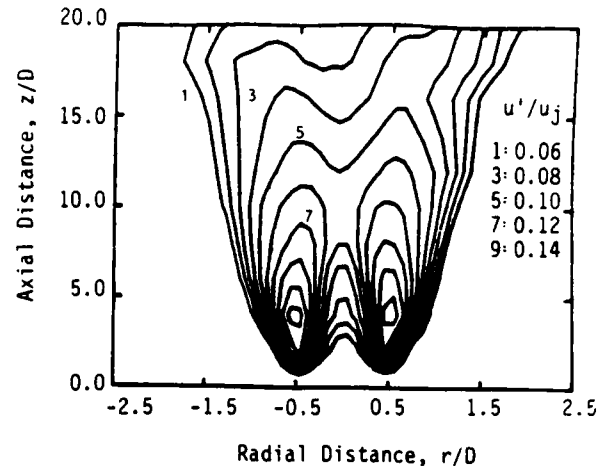


Fig. 7. Measured Contours of  $u'_{\text{rms}} / U_j$

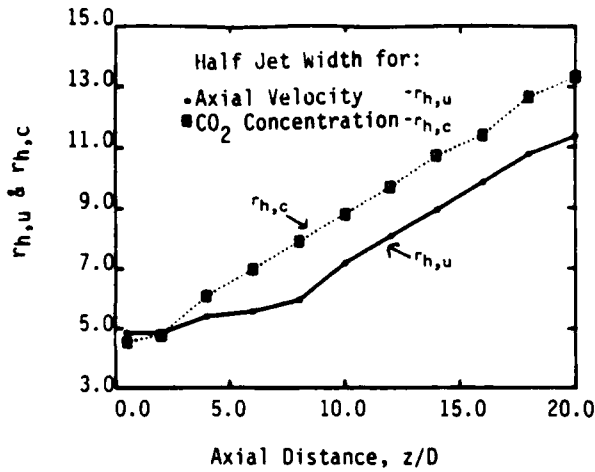


Fig. 5. Measured Half Jet Width for  $\bar{U}$ ,  $r_{h,u}$ , and  $\bar{C}$ ,  $r_{h,c}$

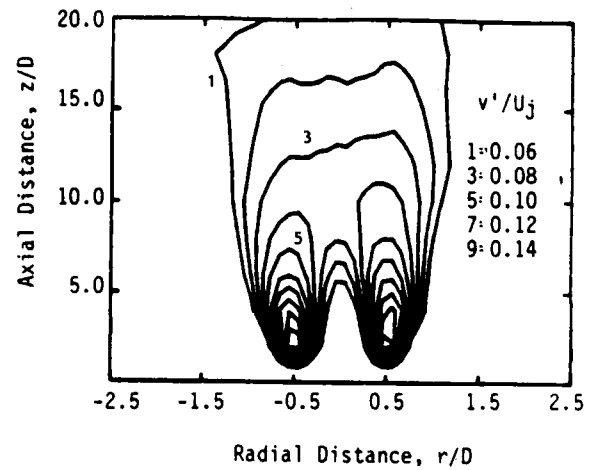


Fig. 8. Measured Contours of  $v'_{\text{rms}} / U_j$

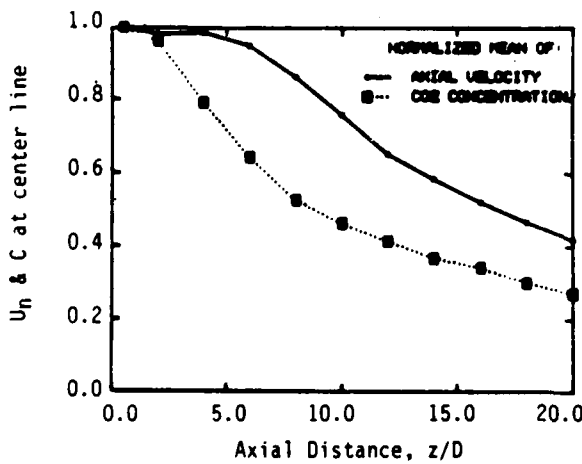


Fig. 6. Decay Law for Axial Velocity and  $\text{CO}_2$  concentration

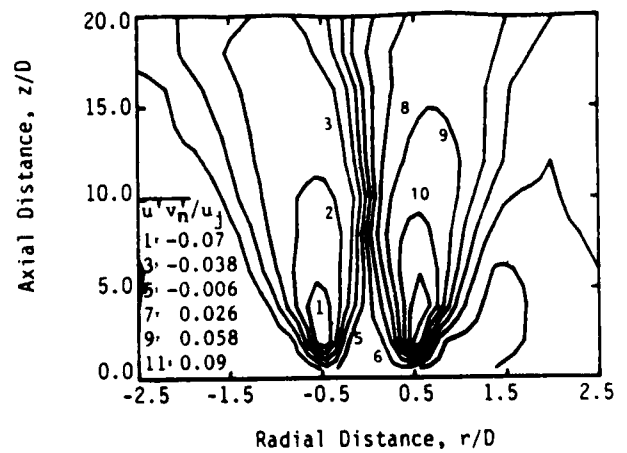


Fig. 9. Measured Contours of  $\overline{u'v'_n} / U_j$

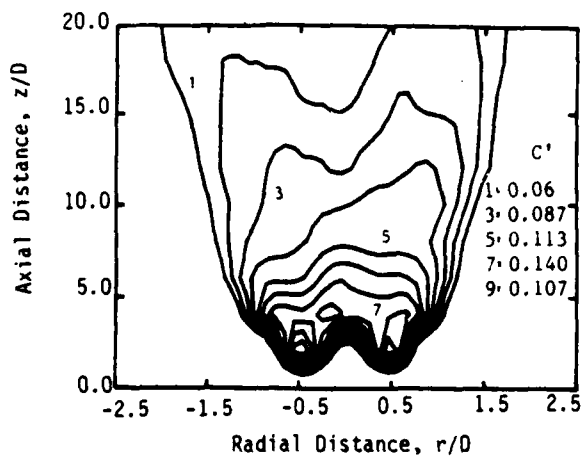


Fig. 10. Measured Contours of  $c'_{rms} / 1.0$

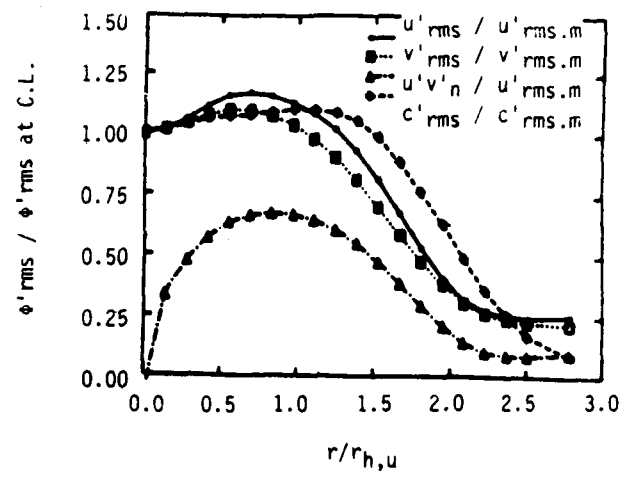


Fig. 12. Velocity and Concentration Fluctuation normalized by Centerline Fluctuation.

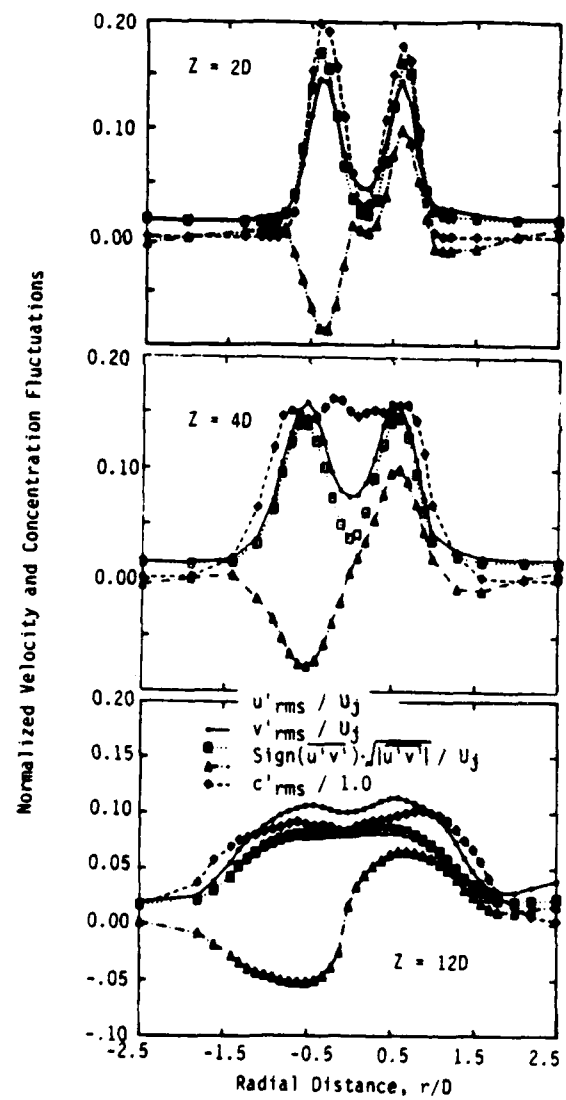


Fig. 11. Measured Velocity and Concentration Fluctuation at  $Z = 2, 4, 12D$ .

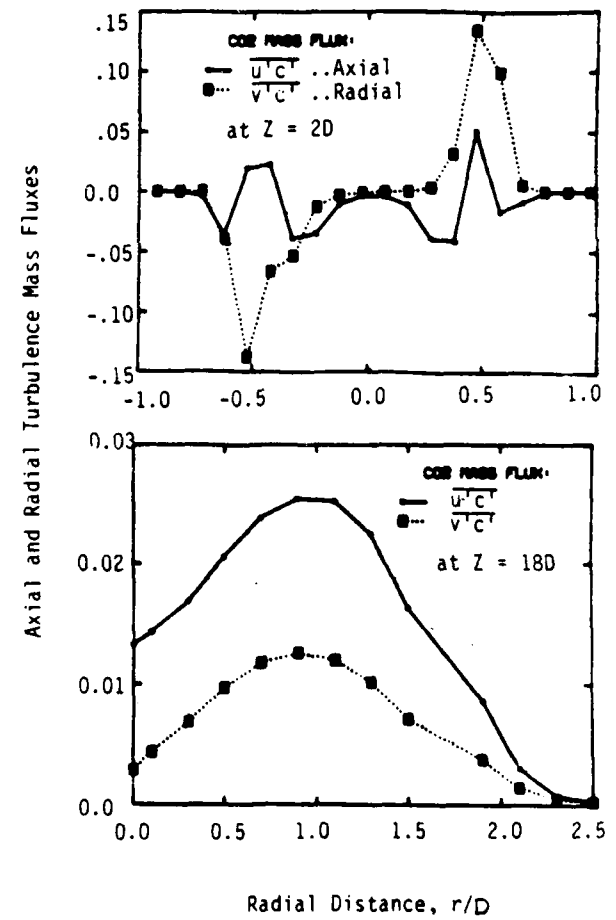


Fig. 13. Measured  $CO_2$  Turbulence Mass Fluxes at  $Z = 20$  and  $180$

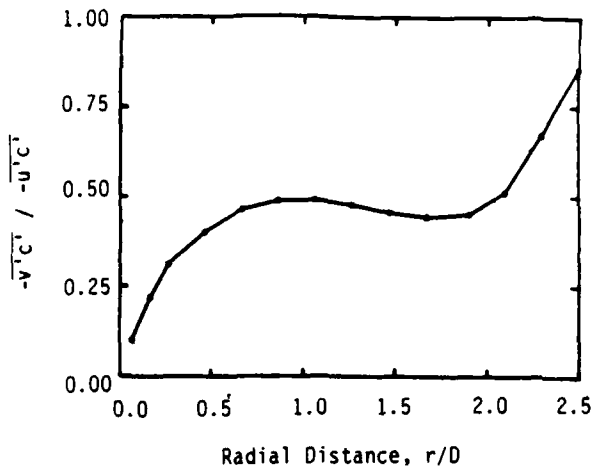


Fig. 14. Ratio of Turbulence Mass Fluxes.

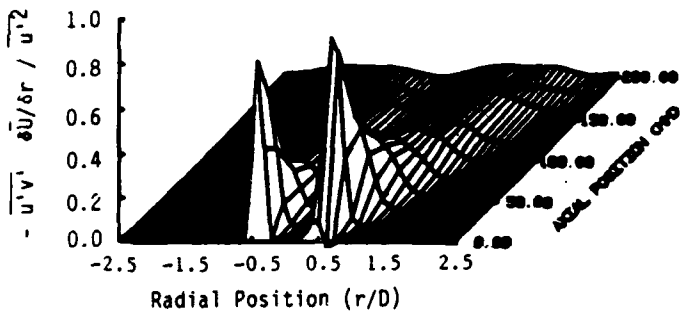


Fig. 15. Measured Turbulence Momentum Production.

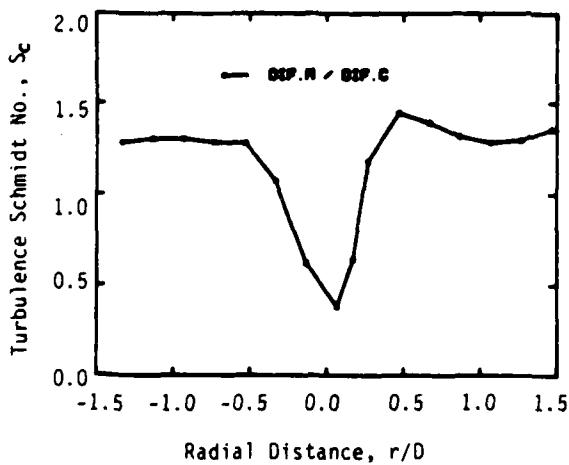


Fig. 17. Measured Turbulence Schmidt Number.  
 $S_c = \sigma_u / \sigma_c$

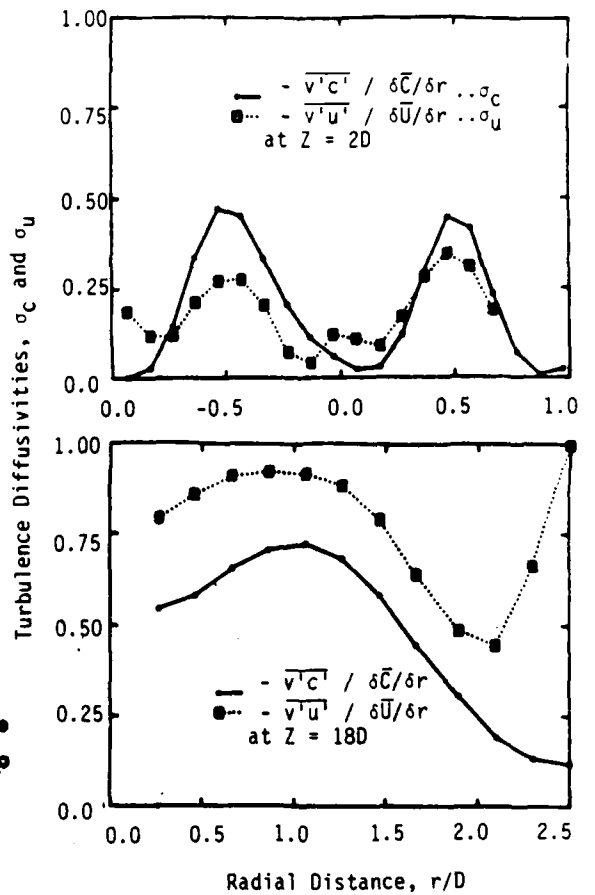


Fig. 16. Measured Turbulence Mass and Momentum Diffusivities at  $Z = 20$  and  $180$ .

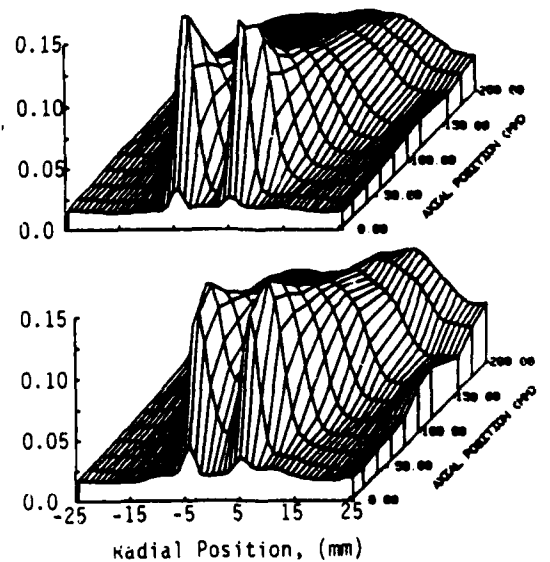


Fig. 7A. 3-D plots of  $v'_n$  and  $u'_n$ .

PHASE AVERAGED MEASUREMENTS USING  
A 3 COMPONENT LDV SYSTEM

Rajan K. Menon  
TSI Incorporated  
St. Paul, MN 55126

ABSTRACT

A flow field is completely defined by the three orthogonal components of velocity. The method used to measure the three components of velocity is important since the introduction of any probing device affects the flow field. The non-invasive LDV approach is ideal for measuring complex flows and measurements of all three components of velocity. It not only provides information on the magnitude and direction of the flow but can also lead to key information on transport mechanisms.

The flow field associated with a periodic phenomenon is studied using an LDV system. The flow field at the exit of a fan is measured to examine the dynamic nature associated with the periodic phenomenon (blade passage).

The purpose of the paper is to outline a method by which the periodic nature of the flow field and its properties are extracted from the simultaneous measurements of three components of velocity, using an LDV system. The software package (RMP) extracts the phase averaged results from the individual measurements.

A three color, three component LDV system (System 9100-12) is used to make measurements of all three components of velocity, simultaneously. These instantaneous velocity measurements are tagged with the phase information of the

phenomenon. This phase information is generated from the once per cycle signal input into the system (Model 1999). The time period of the cycle (360 degrees) is divided into 9000 parts to provide very good angle (phase) resolution. The system is also capable of examining data from the complete cycle or portion of the cycle. Examining data from portions of the cycle, omitting data taking during, etc., can provide insight into the difference between the nature of the phenomenon during various stages of the periodic process. This feature, when selected, can also reduce the experiment duration. The software package provides the ability to control the phase angle resolution (by lumping positions together) to suit periodicity of the phenomenon being studied.

Each velocity measurement - all three components - along with the phase information is collected by a DEC PDP 11/23 computer. The data thus collected is analyzed to obtain various statistical properties. The dynamics of the flow are obtained by phase averaging the input data. Phase-averaged mean, turbulence velocities for each orthogonal component shows the periodic nature of the phenomenon. In addition, cross correlation values, projection of the velocity vector in various cross-sectional planes, higher order statistics, etc., are obtained.

## 1. INTRODUCTION

Fluid flow related aspects influence the performance and design of countless products encountered in everyday life. Power generation, fluid mixing, and rotating machinery are only some of the areas that involve the need to understand the details of fluid flow. Since many of the phenomena of interest are complex, the understanding of the fundamentals as well as the various aspects of fluid-machinery interactions demands information of the three dimensional nature of flow field. Dynamic range, turbulence levels, high temperature, and environmental conditions make flow measurements difficult. Laser Doppler Velocimetry (LDV) technique provides the best opportunity for measuring 3D velocity field in such complex flows. For example, Yanta and Ausherman (1981), Schock et. al. (1983), Weissman (1984), Fry and Kim (1984), Myers and Hepner (1984), and Hoshino et. al. (1985) have used LDV to measure all three components of velocity. In this paper, an LDV system to measure the three components of velocity simultaneously is used.

Some of the flows of practical interest also have periodic or cyclic phenomenon associated with them. Blood flow, flows in rotating machinery, internal combustion engines and similar power generating machinery have a cyclic nature. These flow fields have periodic driving force, strong three dimensionality, turbulence, and environmental complexities.

The characteristics of the flow field could be obtained from the statistical analysis of instantaneous velocity measurement. Simple time averaging of the velocity measurements would dissolve the influence of periodicity. Thus, to understand the influence as well as interaction, if any, the measurements should be "synchronized" with the periodic phenomenon. This would result in preserving, as well as "connecting", the phenomenon with the

measurement. The velocity field in such a situation could be decomposed into

$$u = \bar{u} + \langle u \rangle + u' \quad (1)$$

where  $\bar{u}$  is time averaged value,  $\langle u \rangle$  is the periodic contribution, and  $u'$  is the turbulence contribution. From phase averaging the velocity measurements  $\langle u \rangle$  is obtained. Further details can be found in Reference 4 (Hussain 1977).

In this paper, the simultaneous measurements of the three components of velocity are phase averaged to obtain the periodic nature of the flow. The focus here is more on the method and not so much on the mechanics of the flow.

## 2. SCOPE OF THE WORK

Measurements in the region downstream of the exit plane of a fan are carried out in this study. The velocity measurements were carried out using a three-component Laser Velocimeter system. The fan was operated at constant speed (rpm), and three components of velocity were measured simultaneously.

It can be seen that the blade passage would affect the velocity field at the point of measurement. In this study, one revolution of the fan is taken as one cycle and hence, corresponds to 360 degrees. It follows that the passage of the blades could also be conceived of as cyclic. However, for this to be truly periodic, the blades have to be precisely spaced circumferentially on the shaft. Manufacturing tolerances, twist of the blades, and other practical aspects relating to the shape of the fan blades may indicate that the blades are not symmetrically spaced. Hence, in this case, the freedom to look at the influence of each blade passage during one revolution is preserved. If blades are symmetric, the analysis becomes a simplified special case and the data taken, not assuming

symmetry, can be reduced to correspond to this case.

The purpose of this paper is to outline the procedure and analysis to make detailed measurements in a phase averaged manner. This may be evident by the fact that we have used a simple fan model to demonstrate the method. Further, the desire to measure flow fields in the interblade region in rotating machinery have also influenced this study to approach the flow measurement from the standpoint of rotating machinery. The velocity measurements in the downstream region have been displayed with reference to the position of the blades. This technique could also be used for making measurements in the interblade region of a rotating machine. This study shows the simultaneous measurement of all three components of velocity as a function of the phase angle. The measurements provide mean velocities, turbulence information, cross-correlation values, projections in cross sectional planes, and so on. The aim here is to show that such measurements could be obtained in flows with periodic nature.

Hence, this preliminary study is not oriented towards exploring the aerodynamics of the model. This eliminates the need for mapping the flow field. Instead the focus is on the instrumentation and the technique used.

### 3. EXPERIMENTAL DETAILS

The flow field in the region downstream of the exit of a fan is affected by the periodic passage of the blades. A once per revolution signal is generated by the fan system for synchronizing the data taking with the rotation of the fan. The fan used has five blades with a hub-to-tip ratio of 0.54. The system was typically operated at 4200 rpm.

#### 3.1. LDV SYSTEM

The velocity measurements were made using a three-color, three-component system, Model 9100-12. This system could be considered to be made up of three individual LDV systems, each one using a different color. The system uses the 514.5 nm, 488 nm, and the 476.5 nm lines of the output from the Argon-ion laser operating in the multiline mode. A dispersion prism (Figure 1, Model 9202) color separator is used to obtain clean color separation so that each beam is of a single color. The three beams (green, blue, and violet) with most power are selected and transmitted along two optical paths. The transmitting optics in each axis consists of the necessary modules such as beamsplitters, frequency shift system, beam expanders, and lenses. The green (514.5 nm) and the blue (488 nm) beams are transmitted along the same optical axis, which is at an angle to the optical axis for the violet beams (Figure 2). All three beam pairs are focussed to the same location so that the crossing region overlaps. The system is set up so the green beams and the violet beams are in the horizontal plane and the blue beams are in the vertical plane. The included angle ( $2\theta$ ) between the two optical axes for the set up was 34 degrees. The effective measuring region is the intersection of the individual probe volume generated by the three pairs of beams (Figure 3). Beam expansion ratios of 3.75X provide very good spatial resolution and large scattered light collection aperture. While the blue and green beams are transmitted along one optical train (axis), the blue and green scattered light is collected along the other. This method of collection exploits the advantages of off-axis collection resulting in excellent flare and noise rejection and thus better signal quality. The effective length of the measuring region generated by the

Intersection of the green and violet beams is given by

$$r_{eff} = \frac{d_m}{\sin\theta}$$

where  $d_m$  is the diameter of the measuring region. The measuring volume dimensions are given in Table 1. Further details of the system are given in Reference 8.

$\lambda$ ( $\mu\text{m}$ )	$d_m$ ( $\mu\text{m}$ )	$L_m$ ( $\mu\text{m}$ )	$d_f$ ( $\mu\text{m}$ )
0.5145	89.75	306.97	4.76
0.4765	83.12	284.29	4.41

Table 1

### 3.2. ON AXIS VELOCITY MEASUREMENT

The three measuring volumes generated by the three pairs of beams (green, blue, and violet) are made to overlap so that the region common to all three of them becomes the effective measuring region. A particle going through the effective measuring region will scatter light of all three colors "generating" Doppler signals in all three channels at the same time. The Doppler signal on each channel can be processed to obtain three velocity values. It can be seen from the schematic diagram in Figure 2 that the components of velocity measured by each of these colors are not all orthogonal. The velocity measured by the blue pair of beams will correspond to the velocity component of the particle normal to the plane of the paper. The Doppler signals for the green beams and the violet beams correspond to velocities which are at an angle to each other. In other words, the signals generated by the violet beams and the green beams measure two velocity components, which are not orthogonal to each other in the

horizontal plane. It can be seen that the vector addition of these two signals will provide the two orthogonal components - one along the bisector to the optical axes of the green and violet beams and the other normal to it (Figure 4). Thus, if the individual measurements from the green beams and the violet beams are obtained (for the same particle) then arithmetical calculation would provide the two components of velocity in the horizontal plane which are orthogonal to each other.

The equations for obtaining the orthogonal components of velocity from the individual measurements are given in Figure 4. It can be seen that the signal corresponding to the blue beams directly measures the component of velocity vertical or normal to the plane of the paper. In this experiment, referring to Figure 4

$$\theta_1 = \theta_2 = \theta$$

### 3.3. SIGNAL PROCESSING

Since the LDV system uses three distinct colors and the system has three separate photomultipliers corresponding to each one of these colors, three signal processors are used to process the output of these photodetectors. Frequency shift systems are provided for each of the components so that frequency shift values can be selected independently for each of the channels. The output from the signal processor will be used for obtaining the three orthogonal components of velocity. TSI Model 1990B Signal Processors are used to process the output of the photomultiplier signal. The range of the signal processor is from 1 MHz to 150 MHz. The counter processor measures the time for a certain number (e.g., eight) of Doppler cycles with a clock resolution of 1 nanosecond. The input signal to the signal processor (after downmixing the photomultiplier signal) is bandpass filtered (roll-off 100 dB/decade) and amplified before processing. The signal processor for this

application was operated in the continuous mode where time for eight cycles was determined by the signal processor. A 5/8 comparison was used for eliminating noise contributions and the comparison accuracy was selected to be 1%. The digital output of the processor is a 16 bit digital word with 12 bit mantissa. Thus, the time for 8 cycles obtained with 12 bit resolution is sent to the Model TSI Model 1998A interface unit. This master interface unit "receives" data from all three channels. A PDP 11/23 minicomputer, which is linked to the TSI Model 1998A master interface, was used for data collection and analysis. To ensure the measurements on all three channels are obtained from the same particle, data was taken in the coincidence mode. Thus, the output from the three signal processors are used to compute the three orthogonal components of velocity. Further details on the signal processors and interfaces are given in Reference 12.

The signal processor outputs from the green beams and violet beams are used to compute the two orthogonal velocity components in that plane. Since  $\theta_1 = \theta_2 = \theta$ , the equations for  $u_x$  and  $u_y$  are

$$u_x = \frac{u_A + u_B}{2 \cos\theta} \quad (2)$$

$$u_y = \frac{u_A - u_B}{2 \sin\theta} \quad (3)$$

where  $u_A$  and  $u_B$  are the velocity measurements obtained from green beams and violet beams.  $u_y$  is referenced as the on-axis (radial) component of velocity and is the component along the bisector of the angle between the two optical axes. The more generalized expression could be used in a situation where the optical axis is not equally inclined to the on-axis component of velocity direction. Thus, for each particle crossing the measuring volume, the three orthogonal components of velocity are calculated from

the output of the signal processors. The process of obtaining the orthogonal components from the measurements of non-orthogonal components is done using software. It can be found that in almost all situations where direct measurement of the on-axis or the third component is not possible such an approach is used. The measurement resolution of the on-axis component is a function of the included angle. Orloff and Snyder (1982) have looked at this aspect in detail. Fingerson and Adrian (1985) have shown that the resolution is inversely proportional to  $\sin\theta$  where  $2\theta$  is the angle between the optical axes. Generally, this angle is set up to be more than 30 degrees.

#### 3.4. PHASE AVERAGING

In this paper, we are dealing with a flow field where the measuring point of the LDV system is fixed in space but the velocity field at that point is periodically influenced by the passage of the blade. This results in having a velocity field which is influenced by the periodic blade passage. If the interest is to relate the measurements to the passage of the blade, then it is important to synchronize the data taking with the passage of the blade. The once per revolution signal from the fan system is used for synchronizing the data taking. This once per revolution signal is fed into the TSI Model 1999 Encoder System. The duration of one cycle corresponds to 360 degrees or one complete revolution, and the Model 1999 is locked onto the once per revolution signal.

The 360 degrees corresponding to one period of revolution is divided into a large number of points (9,000) resulting in an angular resolution of 0.04 degrees. The output of the 1999 Encoder System is also sent to the Model 1998A Interface. Thus, every time a velocity measurement is made (all three components simultaneously) the phase information corresponding to that

measurement is also obtained from the encoder system. The angular position for any measurement will correspond to a number between 1 and 9,000. This number generated in the 1999 is passed on to the 1998A interface as a digital word (16 bit). Thus, the velocity measurement along with the phase measurement, is passed on to the computer. Hence, every data point is tagged along with its phase or angle information. The data is stored such that during measurement, velocity information corresponding to the same phase information is put into the same location (bin) in the computer. In other words, the same phase angle corresponds to the same fixed phase position in the periodic phenomenon. This results in the fact that for each phase angle, a large number of data points are collected; and from this data, the various statistical properties are calculated.

### 3.5. SOFTWARE PACKAGE FOR DATA ANALYSIS

The periodic phenomenon takes place rapidly and the data which is obtained along with the phase information needs to be transferred for storage and data analysis. In this case, for the three-component velocity measurements, each data point corresponds to seven 16 bit words. Of the seven 16 bit words, one of the words corresponds to the phase angle information, and for each of the components of velocity, two 16 bit words of information are used to obtain the velocity. In order to obtain high speed data transfer so that no data is omitted because of the limitations on data transfer, DMA transfer was used in this case. This results in data being transferred at the fastest rate possible into the computer. Once the information is stored in the computer, a software package (RMP Analysis Program) is used to obtain the various statistical properties. This package allows one to do various things such as window averaging, adjusting the angle resolution of

the measurements, etc. As pointed out earlier, one period is divided into a very large number of points. In an event where such a large resolution is not needed, the resolution could be readjusted by lumping the data from different locations into one location. However, this could be done after the data has been taken. In other words, the raw data information is kept the same, and the analysis allows one to select the "resolution" that is required so that data displayed is suitable to the type of information that is required. The resolution of the phase angle could be readjusted by lumping the information from various phase locations to one particular point. Obviously, this results in having more data at every location when the resolution is reduced. The interesting point here is the fact that since the raw data is not tampered with, one can recalculate or reevaluate the statistics based on various values of resolution. The thing to remember is that if the resolution value is very low (lumping of too many number of data points), then one can have the statistical results essentially being smoothed out so that characteristic features of the flow field may not be visible. On the other hand, if the resolution is very high, then one may have to run the experiment for an extremely long duration in order to get a statistically good sample at each one of these phase angle locations. The encoder system could be used to selectively look at a portion of the revolution, to omit data taking during blade passage, etc., (Figure 6). Once a large enough sample is obtained, the various statistical properties (from mean velocity to skewness and flatness coefficients, as well as Reynolds stress, correlation coefficients, etc.) could be estimated. The experimental setup with the LDV system, signal processors, and the encoder system with the computer is shown in Figure 5.

The flow field was seeded using PSL particles of nominal diameter of 0.5 microns. The particles were generated by using a TSI Model 9306 atomizer. A dilute solution, with PSL suspended in it, was atomized using the six jet atomizer and introduced into the flow upstream of the fan.

#### 4.0 RESULTS

To check the setup, the three-component system was first used to measure the velocities in a circular jet. The center line velocity at the exit of the jet was compared with the values from the measured  $\Delta P$  values. The measured mean velocity values agree to within less than 0.2% of computed values.

Next, the velocity measurements were made downstream of the exit plane of the fan. The encoder system was used to divide 360 degrees, corresponding to one cycle, into 9,000 locations, thus giving a resolution of 0.04 degrees. For these measurements, data from 100 such stations were lumped together giving us phase angle position or stations every four degrees. As pointed out earlier, this results in having more data points per station. The typical number of data points per phase angle position is about 1,000. Although this may not be sufficient from a statistical standpoint for some applications, for a three-component LDV system, this would correspond to collecting approximately  $10^6$  sixteen-bit words!

Collecting data only during the desired portion of the complete revolution would result in getting a larger amount of data in the region of interest. The encoder system (Model 1999) allows one to take data during a portion of, different segments of, or the complete revolution.

The RMP data analysis package was used to obtain the statistical properties of the data stored. Various statistical properties such as mean, rms, skewness, flatness, cross correlation values, projections in

cross-sectional planes, etc., are obtained. These properties are displayed as a function of the phase angle position. The angle is measured with respect to the position on the shaft corresponding to the generation of the once per revolution signal. However, for simplicity, the blade locations (at the exit plane) are also referenced. Hence, the display of the results as a function of the angle also indicate the position of the blades (vertical lines) at the exit plane of the fan. It can be seen that the data display covers one cycle (360 degrees) or one revolution of the fan. The results indicate the values obtained by averaging over many revolutions of the fan.

Figure 7 shows the display of the mean velocity values of the streamwise component ( $u_x$ ) as a function of the angle. The range shown from 24 degrees to 20 degrees covers one cycle (one revolution). The vertical lines correspond to the position of the blades at the exit plane of the fan and 6.4 cms from the axis of rotation. The measurement location is 0.8 cms downstream of the exit plane of the fan. The region shown by the vertical line corresponds to the region behind the blades. Since the entire flow field was not seeded, it was not surprising to see that the data rate in the region "behind the blades" is very low. Since we were not focussing our study in this region, it was decided not to collect data large enough to obtain a large number of measurements in this region. Hence, in this preliminary study, we have omitted the data obtained in the region indicated by the two vertical lines, corresponding to an "effective thickness" of the blade. Referring to Figure 6, when the window signal is high, the data is taken, and when it is low, data is not taken. Thus, the effective thickness here will correspond to the time when the window signal is low.

The velocity variations of the other two components  $u_y$  and  $u_z$  are shown in Figures 8

and 9. Channel 1 corresponds to the streamwise component of velocity, Channel 2 corresponds to the radial component, with respect to the fan, and Channel 3 corresponds to the circumferential (vertical) component of velocity. It can be seen that the phase averaging process shows the variation of the properties during one revolution (cycle). No property values are indicated in the figures in regions where the number of data points was zero.

Samples of other statistical properties of the flow are shown in Figures 9 through 12. They include turbulence intensities, cross correlation values, and flow direction and magnitudes in cross-sectional planes. It can be seen that detailed properties of the flow field are obtained as a function of the rotation of the fan.

#### 5.0 CONCLUSIONS

The measurements show that the phase angle averaged statistics indicate the influence of the periodic blade passing at the measuring point. A simple time averaging approach would have smeared out the details of this interaction. The method of data collection allows the user to go back and change the angular resolution so that details, if any, can be examined. In addition, the system can lock into portions of the revolution to examine details, explore the similarities during various portions of the revolutions, etc. The system, thus could be used to explore any type of periodic flow, including the flow in the interblade region of a compressor, turbine, fan, etc. The instantaneous three-component measurements can also provide the flow properties in different cross-sectional planes (Figure 11 & 12).

This preliminary work is being supplemented by measurements in the interblade regions of the fan.

#### REFERENCES

1. Fingerson, L. M., Adrian, R. J., and Kaufman, S. L. 1985: "Laser Doppler Velocimetry: Theory, Application, and Techniques," TSI LDV Short Course Notes.
2. Fry, D. J., and Kim Y. H. 1984: "Bow Flow Field of Surface Ships," Fifteenth Symposium on Naval Hydrodynamics.
3. Hoshino, T., Matsuo, H., Sasajima, T., and Oashima A. 1985: "Application of Three-Component Laser Doppler Velocimeter to Flow Measurement in Cavitation Tunnel." International Symposium on Fluid Control and Measurement, Tokyo, Japan.
4. Hussain, A. K. M. F. 1977: "Mechanics of Pulsatile Flows of Relevance to The Cardiovascular System," Cardiovascular Flow Dynamics and Measurements., (ed. H. H. C. Hwang and N. A. Normann) Chapter 15, University Park Press, Baltimore.
5. Meyers, J. F. and Hepner, T. E. 1984: "Velocity Vector Analysis in a Juncture Flow Using a Three-Component Laser Velocimeter," Second International Symposium on Applications of Laser Anemometry to Fluid Mechanics, Lisbon, Portugal.
6. Orloff, K. L., and Snyder, P. K., 1982: "Laser Doppler Anemometer Measurements Using Nonorthogonal Velocity Components: Error Estimates." Applied Optics, 21, pp. 339-344.
7. Scheck, H. J., Rice, W. J., and Chlebecek, R. A. 1983: "Multicomponent Velocity Measurement in a Piston-Cylinder Configuration Using Laser Velocimetry," TSI Quarterly, Volume IX.
8. TSI Incorporated, 1984: System 9100-12 Brochure.
9. Weissman, C. B. 1984: "Three-Component Laser Velocimeter Developments with a Unique Method of Data Presentation," AIAA 17th Fluid Dynamics, Plasma Dynamics, and Lasers Conference, Snowmass, Colorado.

10. Yanta, W. J. and Ausherman, D. W. 1981:  
"A 3D Laser Doppler Velocimeter for Use  
in High Speed Flows, " Symposium on  
Turbulence, Kolla.
11. TSI Incorporated, 1985: Rotating  
Machinery Program (RMP), User's Manual.
12. TSI Incorporated, 1984: Laser Doppler  
Velocimeter Systems Catalog.

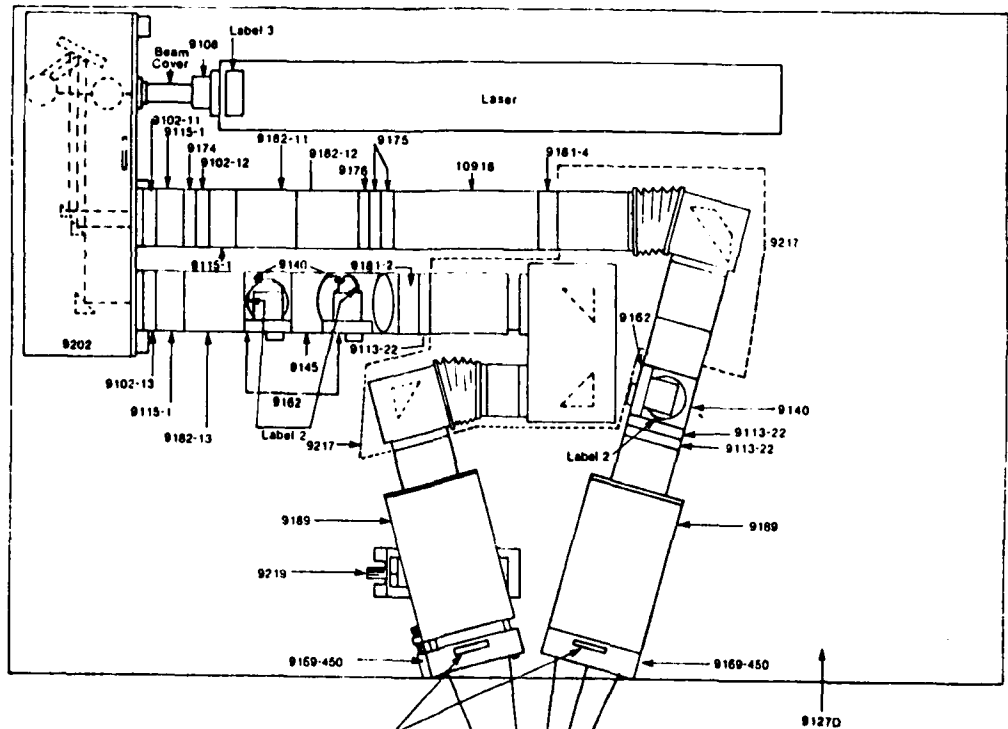


Figure 1. Schematic of Model 9100-12 LDV System

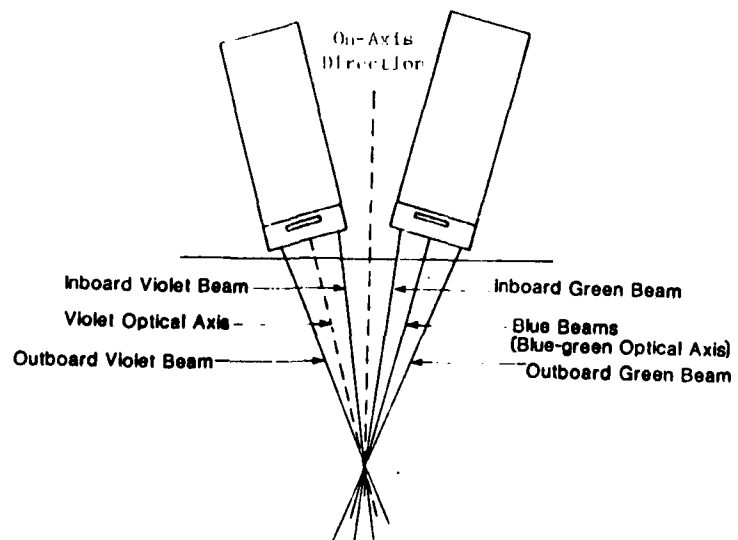


Figure 2. Beam Crossing - 3 Color Arrangement

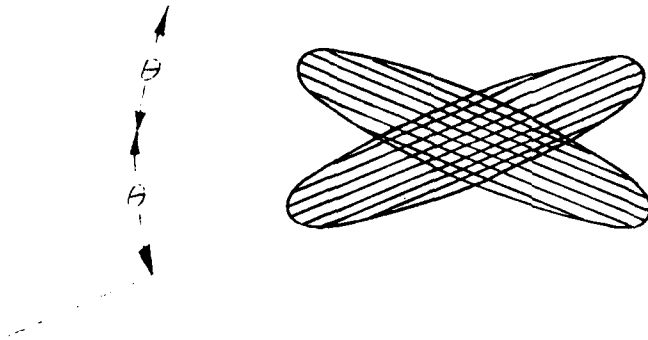
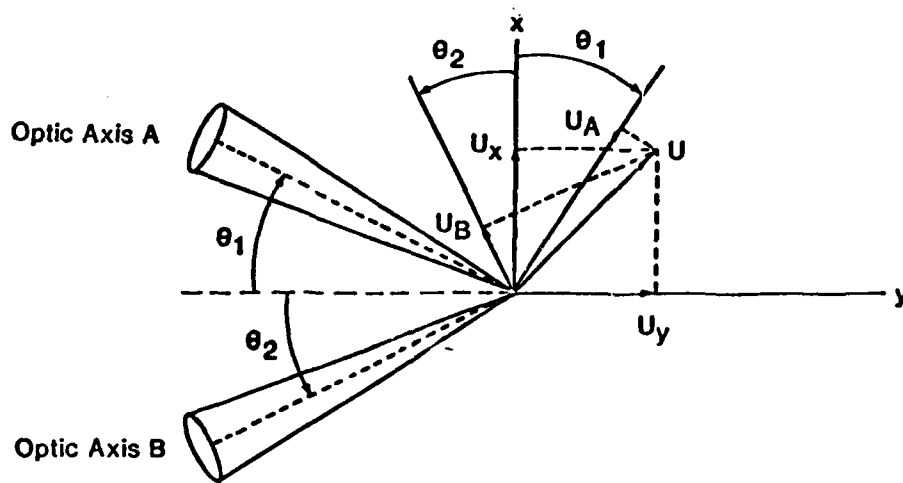


Figure 3. Effective Measuring Volume: From Green and Violet Pairs of Beams



$$U_x = \frac{U_B \sin \theta_1 + U_A \sin \theta_2}{\sin(\theta_1 + \theta_2)}$$

$$U_y = \frac{U_A \cos \theta_2 - U_B \cos \theta_1}{\sin(\theta_1 + \theta_2)}$$

Figure 4. Calculation of Streamwise and On-Axis Components of Velocity

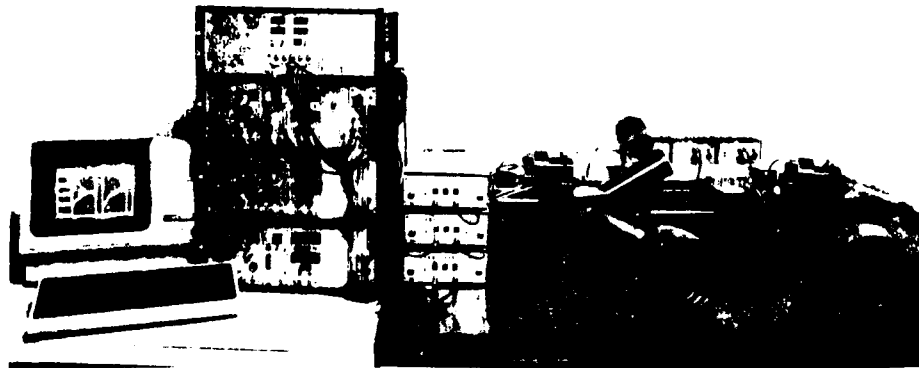


Figure 5. LDV System With Signal Processors, Encoder System and Computer

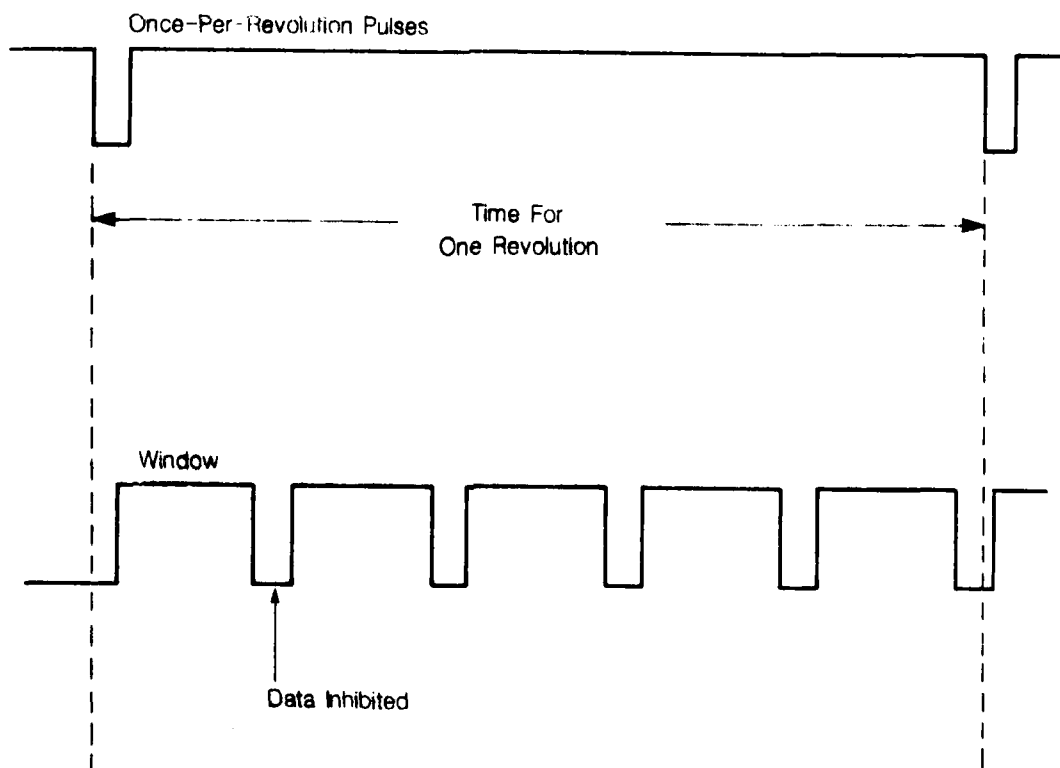


FIGURE 6. Model 1999 Encoder System Window Generation For Data Taking

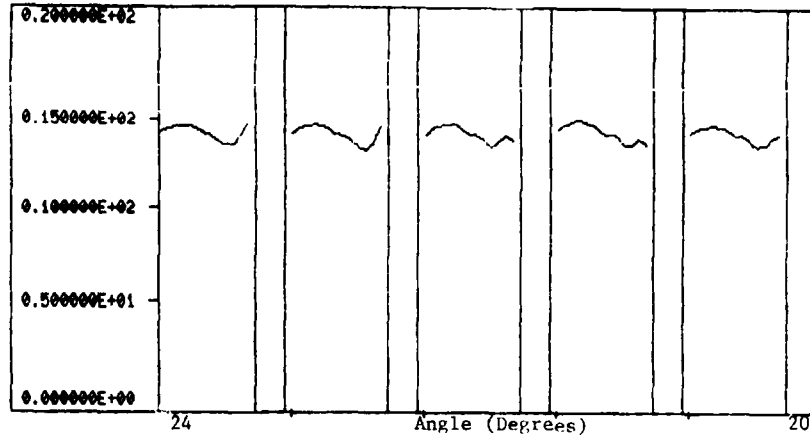


Figure 7. Mean Velocity vs Angle x Component

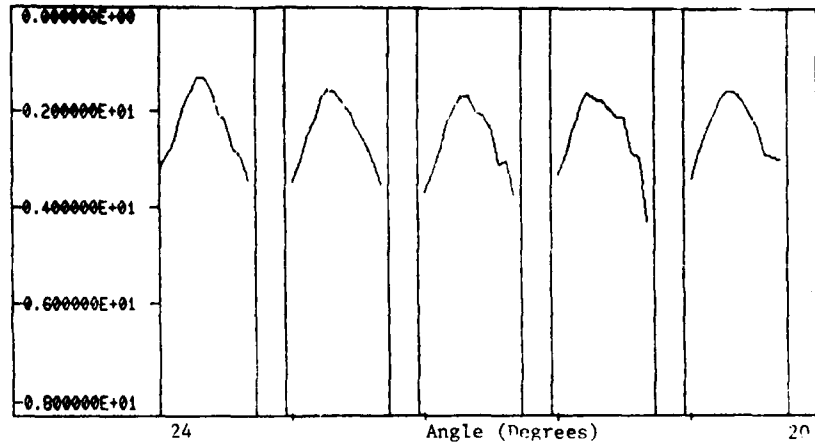


Figure 8. Mean Velocity vs Angle y Component

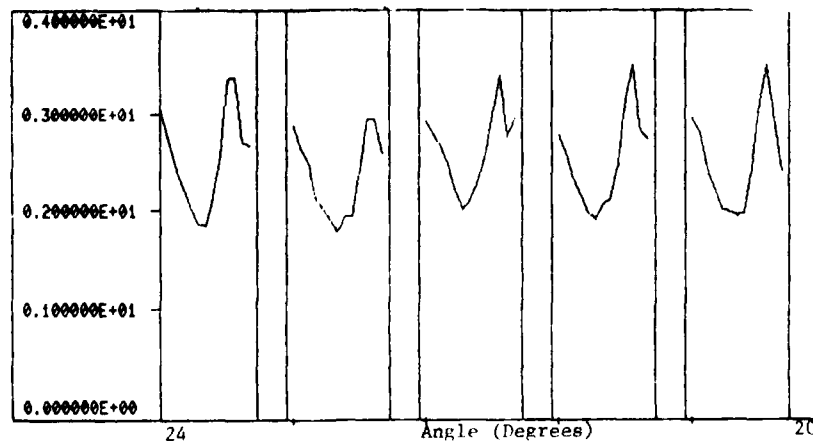


Figure 9. Mean Velocity vs Angle z Component

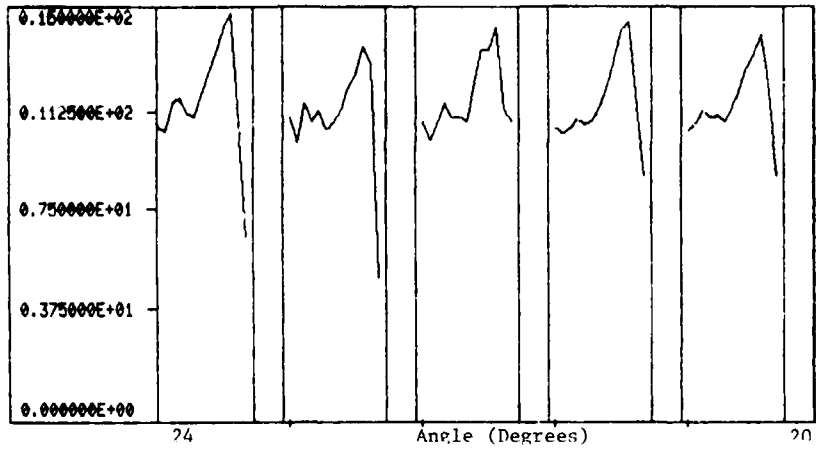


Figure 10. Turbulence Intensity vs Angle x Component

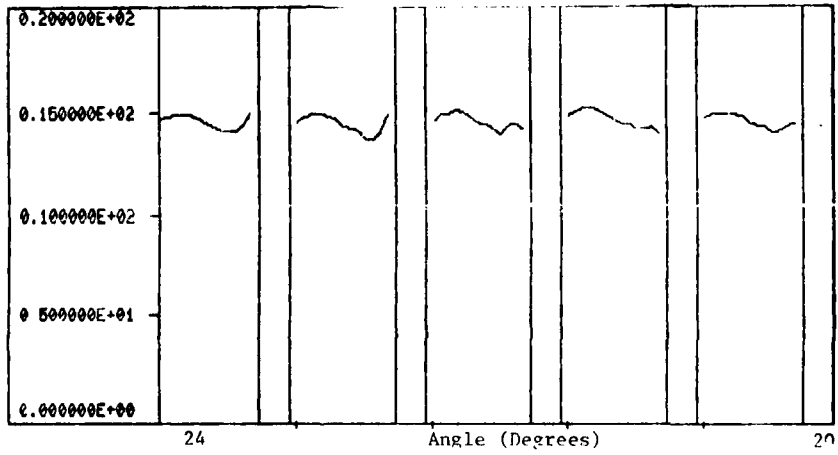


Figure 11. Projection in x-z Plane Velocity Magnitude vs Angle

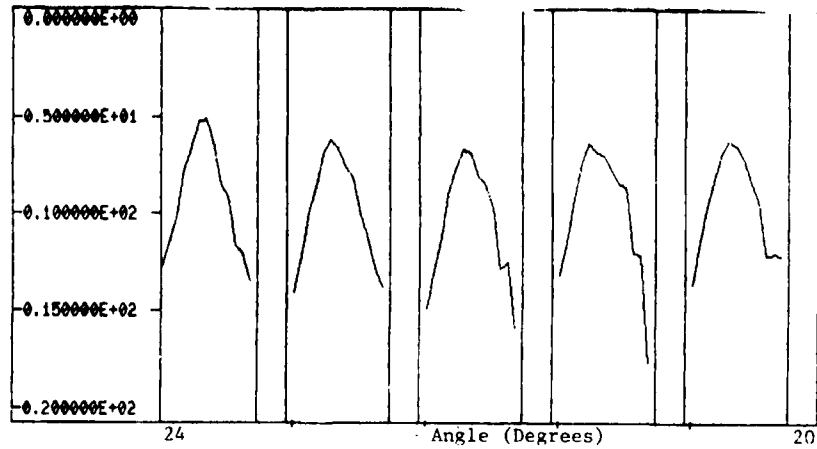


Figure 12. Mean Flow Angle vs Angle x-y Plane

CYCLE-TO-CYCLE VARIATION EFFECTS ON  
TURBULENT SHEAR STRESS MEASUREMENTS IN  
PULSATILE FLOWS

W.G. Tiederman, R.M. Privette\*, and  
W.M. Phillips

School of Mechanical Engineering  
Purdue University  
West Lafayette, IN 47907

ABSTRACT

Accurate evaluation of turbulent velocity statistics in pulsatile flows is important in estimating potential damage to blood constituents from prosthetic heart valves. Variations in the mean flow from one cycle to the next can result in artificially high estimates. Here we demonstrate a procedure using a digital, low-pass filter to remove the cycle-to-cycle variation from turbulence statistics. The results show that cycle-to-cycle variations can significantly affect estimates of turbulent Reynolds stress and should be either eliminated or demonstrated to be small when reporting pulsatile flow results.

LIST OF SYMBOLS

D	Inside diameter of aortic valve
R	Radius of model aorta
$\Delta t$	Time window
t	Time
T	Period of cycle
$T'$	Duration of outflow pulse from ventricle
U	Instantaneous axial velocity
$U_L$	Low-pass axial velocity
$U_P$	Mean periodic axial velocity
$\langle U \rangle$	Ensemble averaged axial velocity
$\langle uv \rangle$	Ensemble-average turbulent velocity product

\* Current address: Goodyear Aerospace Corp.,  
Akron, Ohio

$\langle u^2 \rangle$	Root-mean-square of turbulent axial velocity
$\langle U_{\max} \rangle$	Maximum, ensemble-averaged axial velocity
V	Instantaneous radial velocity
y	Vertical distance from aorta centerline
z	Axial distance downstream of prosthetic heart valve

1. INTRODUCTION

Elevated levels of fluid stress which may result in damage to red blood cells and platelets (National Institutes of Health, 1985) have been observed in the thin shear layers downstream of prosthetic aortic valves (Tiederman et al., 1986; Woo and Yoganathan, 1985; Walburn et al., 1985). Numerous in vitro studies of heart valve and cardiovascular flows have been conducted in an attempt to quantify fluid stress levels present in such flows. However, accurate evaluation of turbulent stress in pulsatile flows is complicated by cycle-to-cycle variation in the mean periodic flow such as that shown in Fig. 1.

Several methods which account for cycle-to-cycle variation have been used to calculate the mean periodic velocity (Rask, 1981; Walburn et al., 1983; Liou and Santavicca, 1985). In each case, some technique is used to identify the mean pulse. Rask used a cubic-spline technique to smooth the time-resolved measurements while Walburn used a non-recursive, low-pass, digital filter. Liou and Santavicca used a spectral

technique. A method based on conditional sampling was used by Witze et al. (1984) to eliminate cycle-to-cycle variations from turbulence measurements immediately ahead of the flame front in a spark ignition engine. These techniques work well when the mean periodic velocity has frequency content that is distinct and separable from the frequency content of the turbulence.

In this study, the mean periodic velocity and turbulence statistics were calculated with both a simple ensemble method and a filter method. In the latter, a digital low-pass filter was used to separate the mean periodic signal of each cycle from the turbulent fluctuations. This filter technique is similar to that of Walburn et al. (1983) for determining the mean periodic signal. However, Walburn et al. reported turbulent statistics that were averaged over the entire outflow portion of the cycle. In this study, the data was reduced to yield ensemble averaged quantities for specified times in the cycle. This approach is a unique attempt to assess the influence of cycle to cycle variation on turbulent statistics.

## 2. APPARATUS AND PROCEDURE

All experimental measurements were made in the mock circulation system shown schematically in Fig. 2 (see Rosenberg et al., 1981). Capacitors with adjustable springs and a variable resistance element allowed good simulation of the physiological pressures and flows in the region near the ventricle.

A prototype left ventricle and pneumatic drive unit were used to produce a 75 beat/min. pulsatile flow. In the model aorta, the beat period was made up of a 267 ms outflow pulse followed by a 533 ms quiescent period. A straight, quartz-tube model aorta was attached to the ventricle outlet. The aortic valve was positioned between the ventricle body and the quartz tube. All velocity measurements were made within the 25 mm ID quartz tube downstream from the valve.

Difficulties involved in making velocity measurements with an optical instrument in a

circular tube are well known and were circumvented by eliminating the quartz-tube optical interface through the use of a tube-in-box arrangement with index matching fluid on both sides of the tube. The fluid was a mixture of potassium thiocyanate, water, and glycerin with a viscosity of 3.3 cp and a density of 1290 kg/m<sup>3</sup>. The average flow rate was 6 liters/min.

The 24 mm ID, tilting disc valve and its orientation with respect to the Cartesian coordinate system are shown in Fig. 3. A Cartesian coordinate system was used because the valve was not axisymmetric. The valve flow area was divided by the cupped-disc surface into major and minor orifices shown above and below the disc respectively. The origin of the laboratory coordinate system was located at the center of the valve rim. The z-axis was aligned with the mean flow direction and the positive y-axis extended through the major orifice.

Velocity measurements were made with a 2-color, 4-beam, 2-component laser velocimeter. TSI optics were configured for dual beam, forward scatter operation. Counter-type processors were operated in the N-cycle mode with 8 cycles required for a valid measurement. Each processor was equipped with an analog output module.

A 500 mW Argon-ion laser supplied pairs of blue and green beams that were frequency shifted using Bragg cells. Electronic downmixers were used to achieve effective shift frequencies of 1 MHz. A 2.27x beam expander and 250 mm focal length lens produced a probe volume with diameter of 47  $\mu$ m and length of 703  $\mu$ m. The flow was seeded with milk at a concentration of 15 parts per million by volume. Data was recorded at several y locations for each of three axial locations corresponding to z/D = 0.71, 1.21, 1.71 and x = 0. The probe volume was positioned with tolerances of  $\pm 0.0127$  mm along the y and z axes by translating the model aorta with a three-dimensional traverse.

Analog velocity signals from the processors were digitized, buffered, and transferred to a D.E.C. VAX 11/780 computer using a Norland

Waveform Analyzer. The Norland was equipped with two input modules which digitized the velocity signals at 5 kHz. The equal-time sampling process and the average particle arrival rate of  $> 12$  kHz eliminated velocity bias.

Velocity data were recorded beginning 51 ms prior to the pulse and ending 92 ms after the end of the pulse. Fifty-five cycles of two-component velocity data were recorded at each spatial location to ensure that the ensembles would yield statistics with small uncertainties. The data transfer rate between the Norland and the VAX was such that one out of every ten cycles of velocity data was stored on the VAX.

The instantaneous velocity was decomposed into the sum of a mean periodic component and a turbulent component as shown in Fig. 4. Flow statistics were calculated in 15 ms windows positioned throughout the mean pulse and were based upon ensembles of 4000 points.

The simple ensemble analysis is based on the assumption that the mean periodic velocity is exactly repeatable from one cycle to the next. The mean periodic velocity at time  $t_o$  was approximated by an ensemble-average of the total velocity within a window,  $\Delta t$ , centered around  $t_o$  as given below.

$$U_p(t_o) = \langle U(t_o) \rangle = \frac{1}{N} \sum_{i=1}^N U_i(t_o \pm \frac{\Delta t}{2} + nT) \quad (1)$$

where  $N$  is the number of points in the ensemble,  $n$  is the index for the cycle,  $T$  is the period of the cycle, and  $0 < t_o < T$ .

The turbulent velocity component was obtained by subtracting the mean periodic velocity in a window from the instantaneous velocity in that window as shown in Eq. (2).

$$u_i = U_i(t_o \pm \frac{\Delta t}{2} + nT) - \langle U(t_o) \rangle \quad (2)$$

Root-mean-square (RMS) values of turbulent velocity and average turbulent velocity products were calculated as follows:

$$\langle u^2(t_o) \rangle = \left[ \frac{1}{N-1} \sum_{i=1}^N (u_i^2) \right]^{1/2} \quad (3)$$

$$\langle uv(t_o) \rangle = \frac{1}{N} \sum_{i=1}^N u_i v_i \quad (4)$$

To eliminate non-valid velocity data from the statistics, all data that were more than three standard deviations from the mean were excluded from the calculation.

The filter method is based on the assumption that the mean periodic velocity can be isolated by passing each cycle of instantaneous total velocity through a low-pass filter. That is:

$$U_p(t) = U_L(t). \quad (5)$$

The mean periodic velocity generally varied from one cycle to the next. A standard deviation of the mean periodic velocity during the window corresponding to time  $t_o$  was calculated as follows:

$$\langle U^2(t_o) \rangle = \left[ \frac{1}{N-1} \sum_{i=1}^N [U_{L,i}(t_o \pm \frac{\Delta t}{2} + nT) - \langle U_L(t_o) \rangle]^2 \right]^{1/2} \quad (6)$$

where

$$\langle U_L(t_o) \rangle = \frac{1}{N} \sum_{i=1}^N U_{L,i}(t_o \pm \frac{\Delta t}{2} + nT) \quad (7)$$

This standard deviation is a measure of the cyclic variation in the mean periodic velocity at time  $t_o$ . The turbulent velocity component was obtained by subtracting the mean periodic velocity from the total velocity.

$$u_H(t) = U(t) - U_L(t) \quad (8)$$

RMS levels of turbulent velocity and average turbulent velocity products were calculated in the manner given previously with

$$u_i = u_{H,i}(t_o \pm \frac{\Delta t}{2} + nT) - \langle u_H(t_o) \rangle \quad (9)$$

The cutoff frequency of the digital filter was chosen based upon estimates of the frequency content of the mean periodic and turbulent velocity components. The frequency content of the mean periodic velocity was estimated from one-dimensional power spectral density (PSD) measurements where the instantaneous velocity was sampled at 100 Hz for 10.24 seconds yielding a

Nyquist frequency of 50 Hz with resolution of 0.1 Hz. Fig. 5 shows the PSD function for the point  $y/R = 0.25$ ,  $z/D = 0.71$ . A large spike can be seen at the beat rate of 1.3 Hz, with several smaller spikes at higher frequencies. These components, which were highest at this location, were attributed to the mean periodic velocity. Based on Fig. 5 the upper frequency limit of the mean periodic velocity was estimated to be 25 Hz.

An estimate of the lower bound on the turbulence frequency content was obtained by assuming the lowest frequencies associated with turbulence result from eddies with the diameter of the model aorta that are connected with the mass-averaged velocity during the pulse. This mass-averaged velocity is defined by

$$\bar{v} = \frac{Q T}{T' A} \quad (10)$$

where  $Q$  is the average volumetric flow rate,  $T$  is the cycle period,  $T'$  is the period of the mean pulse and  $A$  is the cross-sectional area of the model aorta. A lower frequency limit of 25 Hz for the turbulence was estimated from these length and velocity scales.

Filtering was accomplished by passing each cycle of instantaneous velocity data through a 2<sup>nd</sup> order, 0.1 dB Chebychev low-pass digital filter four times (Walraven, 1980). This procedure yielded 8<sup>th</sup> order filter cutoff characteristics while avoiding the instabilities common in high order recursive filters. Phase shift was eliminated by passing the data through the filter twice in the direction of increasing time, followed by two passes in the direction of decreasing time. Data filtering, sorting and statistical analyses were carried out on a VAX 11/780. For the filter method, these processes required approximately 433 seconds of central processing unit (CPU) time for seven time windows at one location. The simple ensemble method does not require as much sorting and any filtering and therefore the CPU time for seven time windows at one location was about 137 seconds. Since the filter method required more computer time, the simple ensemble method was used for mapping the mean flow field and the filter method was used

only at locations where high turbulent shear stress estimates from the simple ensemble method indicated that cycle-to-cycle variations would be important.

## 5. RESULTS AND DISCUSSION

Radial profiles of the mean periodic velocity at the three axial locations are shown in Fig. 6 for several times during the cycle. Solid lines have been drawn through the data to illustrate profile development. The maximum axial velocity was 1.58 m/s and occurred 0.71D downstream from the major orifice at  $t = 155$  ms. This maximum velocity was used to normalize all velocity statistics.

A jet formed downstream of the major orifice early during the cycle. Flow through the minor orifice developed more slowly. Both a sharp velocity gradient in the thin shear layer behind the valve disc and a recirculation region below the disc persisted throughout the duration of the mean pulse. The shear layers at  $z/D = 1.21$  and 1.71 developed later in the mean pulse with the gradients decreasing with increasing downstream distance. The data points taken during maximum flow for the axial location closest to the valve are shown in Fig. 7 to illustrate the good spatial resolution in regions of sharp velocity gradients.

As the flow accelerated through the tilting-disc valve, a starting vortex was shed from the downstream edge of the cupped disc. This was apparent from both flow visualization and analog velocity traces. Velocity traces from three radial locations 0.71D downstream from the valve are shown in Fig. 8. Large spikes in both velocity components occurred at approximately  $t = 50$  ms. At  $y/R = 0.4$ , the axial velocity change indicates a transient velocity increase. A transient axial velocity decrease, indicated by the negative spike, is seen in the trace from  $y/R = 0.25$ . Axial velocity traces from  $y/R = 0.25$  and 0.28 reflect the recirculating flow behind the disc for times greater than 80 ms.

Spikes in the radial velocity traces indicate that the flow on the leading edge of the vortex was directed toward  $y/R = -1.0$  while the flow on

the trailing edge of the vortex was directed toward  $y/R = +1.0$ . A major spike occurred in the radial velocity trace from  $y/R = 0.28$  corresponding to the sharp velocity gradient across the core of the vortex.

The starting vortex was repeatable from cycle to cycle as determined from both flow visualization and analog velocity traces. However, the frequency content of the convecting vortex was higher than 25 Hz and therefore the vortex motion was not included in the mean periodic flow. Instead, the rapid velocity variations of the vortex were treated as turbulence and extremely high turbulence levels are reported during the passage of the vortex through the probe volume.

Profiles of the axial, root-mean-square turbulent velocity are shown in Fig. 9. Peaks in the profiles of both  $\langle u' \rangle$  and  $\langle v' \rangle$  at  $z/D = 0.71$ ,  $t = 50$  ms occurred at the radial location corresponding to the core of the vortex. As expected, peaks in  $\langle u' \rangle$  also occurred in the region of the sharp shear layer shown in Fig. 8. Elevated RMS velocities also were observed behind the monostrut. Since the wake behind the monostrut was aligned with the diameter across which measurements were taken, elevated RMS velocities were seen along the entire minor orifice side of the profiles.

Radial profiles of the fluctuating velocity product shown in Fig. 10 also indicate that the axial and radial turbulent velocity fluctuations were uncorrelated in the shear layer at  $z/D = 0.71$  after passage of the starting vortex. This result suggests that the shear layer at  $z/D = 0.71$  was not yet fully turbulent, but rather was still "laminar" with little turbulent mixing. The upstream measurement location was the location closest to the valve that allowed optical access across the entire diameter and was approximately 2 mm from the disc edge. At  $z/D = 1.21$ , the fluctuating velocity product profiles show significantly more mixing across the shear layer.

The thickness of the shear layer was estimated in an attempt to quantify shear layer

development. At  $z/D = 0.71$  the shear layer was approximately 0.9 mm wide and at  $z/D = 1.21$  the thickness had grown to 3.8 mm. The width at  $z/D = 0.71$  was less than 1/3 the thickness of the shear layer measured by Alchas et al. (1980) 0.7D downstream from a cupped-disc valve. The early stage of development indicated by the narrow shear layer resulted in axial turbulence intensities which were 50 percent lower than those found by Alchas. The results of this study indicate that peak turbulence activity does not always occur at downstream locations closest to the valve. The shear layer resulting from the disc obstruction requires some distance to become unstable before peak turbulent mixing occurs. Since shear layer development begins at the disc edge, an axial coordinate measured from this point might lead to a better understanding of the flow behind tilting disc valves. However, few investigators have reported the valve dimensions required for such an evaluation.

At  $z/D = 1.21$  increased turbulence activity associated with the more fully developed shear layer resulted in  $\rho\langle uv \rangle$  levels as high as  $-538$  dynes/cm<sup>2</sup>. Peak  $\rho\langle uv \rangle$  levels in the current study were significantly lower than the  $1200$  dynes/cm<sup>2</sup> level measured by Woo and Yoganathan (1985) downstream from a cupped-disc valve. An important difference is that the shear layer thickness was more than 3 times as wide at the point of peak  $\rho\langle uv \rangle$  in Woo and Yoganathan's study. Similarly, Tiederman et al. (1986) measured peak  $\rho\langle uv \rangle$  levels as high as  $-2021$  dynes/cm<sup>2</sup> in a 2 mm wide shear layer downstream from a flat-disc valve. The more fully developed shear layers observed by Woo and Yoganathan and Steinle resulted in higher turbulent shear stress levels. It is, however, entirely possible that all three valves produced flows with similar maximum  $\rho\langle uv \rangle$  levels at equivalent stages in their shear layer development. Differences in measurement locations and times preclude quantitative comparisons.

The degree of cyclic variation changed with time in the cycle, and position in the flow. Table 1 lists both RMS level for the mean velocity

normalized with the local velocity and a measure of the filter's ability to isolate the turbulence, each based on data from the shear layer at  $z/D = 0.71$ . The ratio  $\langle U_L' \rangle / \langle U_L \rangle$  shows that the amount of cycle-to-cycle variation increased late in the cycle. The largest standard deviations in the low-pass velocity were found in the shear layer, indicating slightly different jet boundaries from one cycle to the next. Small changes in the disc opening sequence resulted in variations in the position of the shear layer. Since the velocity gradient in the shear layer was large, small changes in position had large effects on the local velocity.

The quantity  $\langle U_L \rangle / \langle U \rangle$  is a measure of the ability to isolate the turbulence from the mean flow by filtering at 25 Hz. An ensemble averaged high-pass velocity of zero (represented by a ratio of 100 percent) indicates that the high-pass velocity has the same zero mean behavior as turbulence.

Profiles of  $\langle uv \rangle$ ,  $\langle u' \rangle$  and  $\langle v' \rangle$ , calculated by both simple ensemble and filter methods, are shown in Figs. 11 and 12 at peak  $\langle uv \rangle$  for  $z/D = 0.71$  and 1.21, respectively. The profiles are similar. Peak  $\langle uv \rangle$  levels differed by 22 percent and 12 percent at  $z/D = 0.71$  and 1.21, respectively. Maximum levels of  $\langle u' \rangle$  varied by less than 13 percent at both  $z/D$  locations. Peak levels of  $\langle v' \rangle$  varied by 16 percent and 3 percent at  $z/D = 0.71$  and 1.21.

Comparisons of root-mean-square axial and radial velocities calculated by the simple ensemble and filter methods at  $z/D = 0.71$  are shown at several times in the cycle in Fig. 13. The effects of cycle-to-cycle variation on the axial RMS velocities in the shear layer increased during the cycle and at  $t = 230$  ms the peak axial RMS velocity was nearly 52 percent lower with cycle-to-cycle variation effects removed. Estimates of the radial RMS velocities in the shear layer at  $z/D = 0.71$  show similar trends with differences between filtered and unfiltered data as high as 36 percent at  $t = 230$  ms. These results indicate that, in the shear layer,

variations in the velocity from one cycle to the next artificially inflate the estimated RMS velocities calculated by the simple ensemble method. The shear layer was particularly susceptible to this due to the large variations in velocity across short radial distances.

Fig. 14 shows a comparison of the fluctuating velocity products calculated by the simple ensemble method and the filter method at  $z/D = 0.71$  for several times in the cycle. The simple ensemble method predicted levels of  $\langle uv \rangle$  in the shear layer that were as much as 10 times the filtered values. This strong influence of cycle-to-cycle variation on estimates of  $\langle uv \rangle$  could result in large errors due to inaccurate flow statistics. That is, cycle-to-cycle variation could lead one to believe that a laminar flow was turbulent based on a simple ensemble analysis.

#### 4. CONCLUSIONS

This study demonstrated that cycle-to-cycle variations in the mean flow were significant near the valve. Standard deviations in the low-pass velocity components were largest in the shear layer. At locations of peak turbulence, removal of cycle-to-cycle effects from the turbulent shear stress estimates resulted in a 12 percent decrease. Closest to the valve, where cycle-to-cycle variations were greatest, removal of cycle-to-cycle effects resulted in estimates of turbulent shear stress that were 10 times lower than the simple ensemble estimates. Cycle-to-cycle variation can significantly affect turbulence statistics in pulsatile flows, and should be removed or shown to be small when reporting such statistics.

The results also show that the development stage of shear layers in pulsatile flows play an important role in the amount of turbulent mixing across the layer. The findings suggest that an appropriate method for nondimensionalizing distance for flows downstream of prosthetic disc valves should be based on a local fluid length scale such as shear layer width, and that distances measured from the disc edge may be more closely related to the physics of the shear layer.

5. REFERENCES

Alchas, P.G., Snyder, A.J., and Phillips, W.M. 1980: Pulsatile Prosthetic Valve Flows: Laser-Doppler Studies. In Biofluid Dynamics (ed. Schneck, D.J.). Vol. 2, pp. 243-265. New York: Plenum.

Liou, T.M., Santavicca, D.A. 1985: Cycle Resolved LDV Measurements in a Motored IC Engine. J. Fluids Engng. Vol. 107, pp. 232-240.

National Institutes of Health. 1985: Guidelines for Blood-Material Interactions. U.S. Department of Health and Human Services, Public Health Service, NIH Publication No. 85-2185.

Rask, R.B. 1981: Comparison of Window, Smoothed-Ensemble, and Cycle-by-Cycle Data Reduction Techniques for Laser Doppler Anemometer Measurements of In-Cylinder Velocity. In: Fluid Mechanics of Combustion Systems (eds. T. Morrel, R.P. Lohmann, and J.M. Rackley) pp. 11-20 ASME.

Rosenberg, G., Phillips, W.M., Landis, D.L., Pierce, W.S. 1981: Design and Evaluation of the Pennsylvania State University Mock Circulatory System. J. Am. Soc. for Artif. Intern. Organs. Vol. 4, pp. 41-45.

Tiederman, W.G., Steinle, M.J., Phillips, W.M. 1986: Two-Component Laser Velocimeter Measurements Downstream of Heart Valve Prostheses in Pulsatile Flow. J. of Biomechanical Engineering. Vol. 108, pp. 59-64.

Walburn, F.J., Sabbah, H.N., Stein, P.D. 1983: An Experimental Evaluation of the Use of an Ensemble Average for the Calculation of Turbulence in Pulsatile Flow. Annals of Biomedical Engineering. Vol. 11, pp. 385-399.

Walburn, F.J., Sabbah, H.N., Stein, P.D. 1985: Turbulent Stresses in the Region of a Hancock Porcine Bioprosthetic Aortic Valve. J. Fluids Engng. Vol. 107, pp. 200-205.

Walraven, R. 1980: Digital Filters. Proc. of the Digital Equip. Computer Users Society, pp. 827-834.

Witze, P.O., Martin, J.K., Borgnakke, C. 1984: Conditionally-Sampled Velocity and Turbulence Measurements in a Spark Ignition Engine. Combustion Science and Technology. Vol. 56, pp. 301-317.

Woo, Y.K., Yoganathan, A.P. 1985: In Vitro Pulsatile Flow Velocity and Turbulent Shear Stress Measurements in the Vicinity of Mechanical Aortic Heart Valve Prostheses. Life Support Systems, Vol. 3, pp. 283-312.

Table 1 RMS levels for the mean velocity and a measure of the ability to isolate the turbulence by filtering for  $y/R = 0.35$ ,  $z/D = 0.71$ .

time (ms)	$\frac{\langle U_L^2 \rangle}{\langle U_L \rangle^2}$	$\frac{\langle U_L \rangle}{\langle U \rangle}$
110	8%	99%
140	10%	99%
170	18%	100%
200	16%	101%

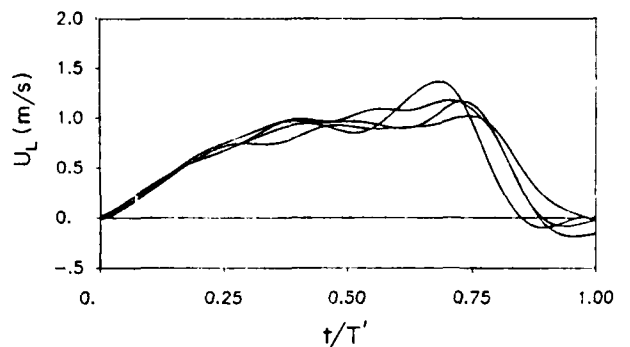


Fig. 1 Mean periodic axial velocity of simulated cardiovascular (Aortic) flow at  $z/D = 0.71$ ,  $y/R = 0.35$  during several pulses.

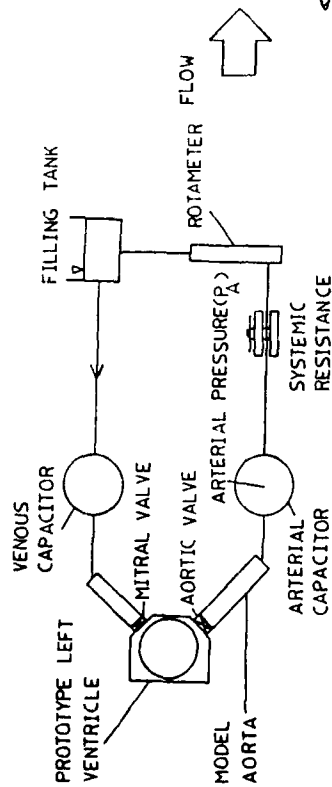


Fig. 2 Schematic of the mock circulation system.

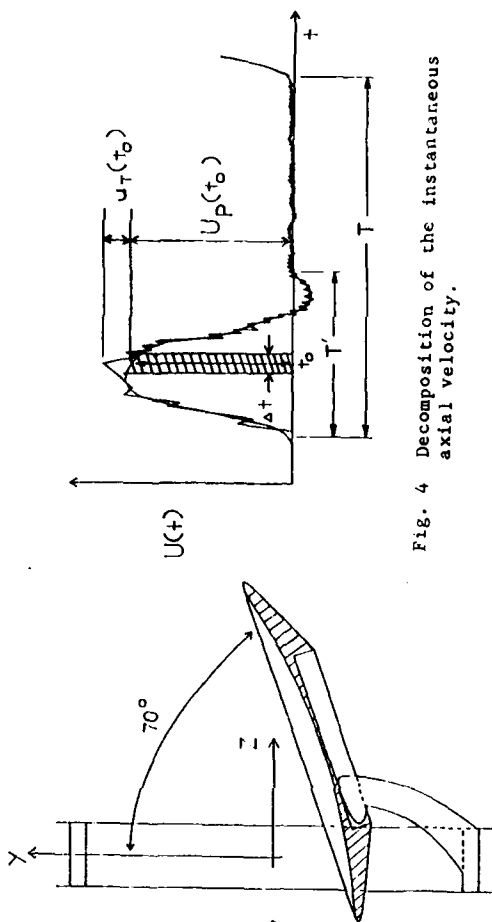


Fig. 4 Decomposition of the instantaneous axial velocity.

Fig. 3 Open configuration of a tilting disc monostitut valve in laboratory coordinate system.

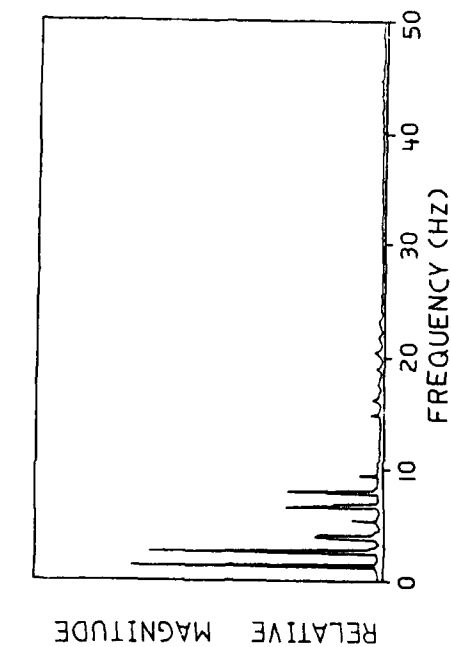


Fig. 5 Ensemble-averaged power spectral density function for the location  $y/R = 0.25$ ,  $z/D = 0.71$ .

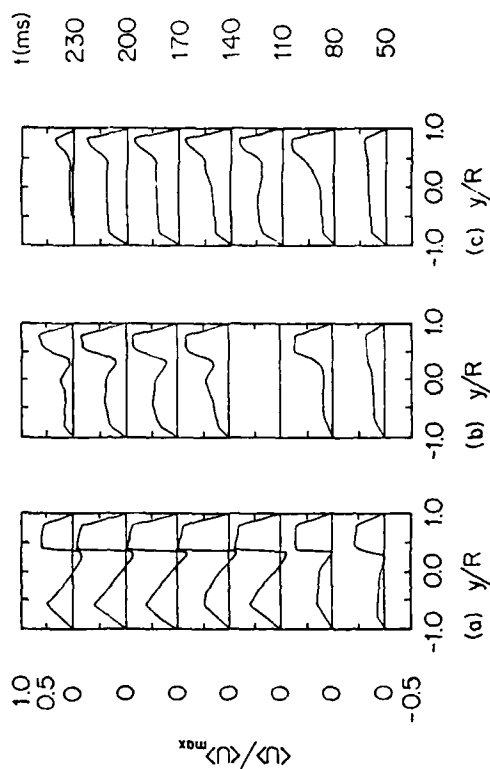


Fig. 6 Radial profiles of the mean periodic axial velocity at (a)  $z/D = 0.71$ , (b)  $z/D = 1.21$ , (c)  $z/D = 1.71$  for several times during the mean pulse; simple ensemble method.

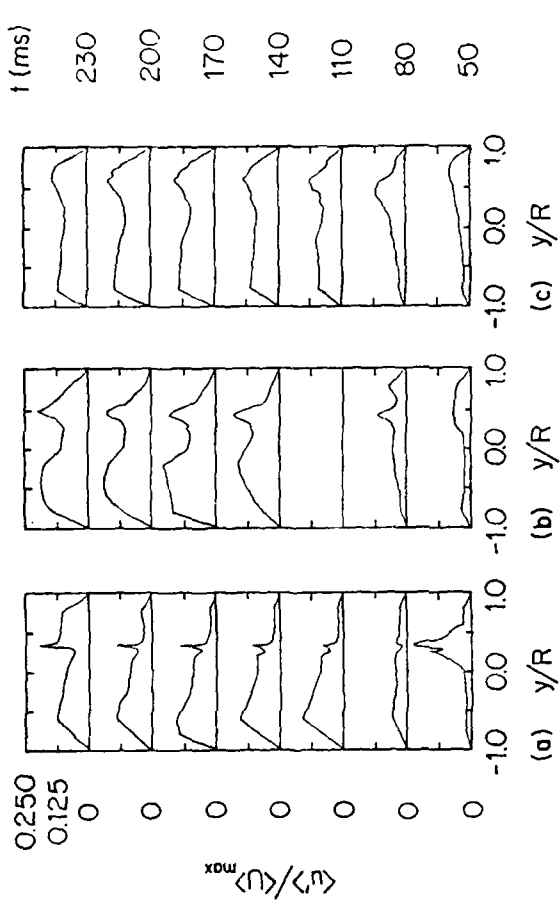


Fig. 7 Radial profiles of the mean periodic axial velocity at  $z/D = 0.71$  during maximum flow; simple ensemble method.

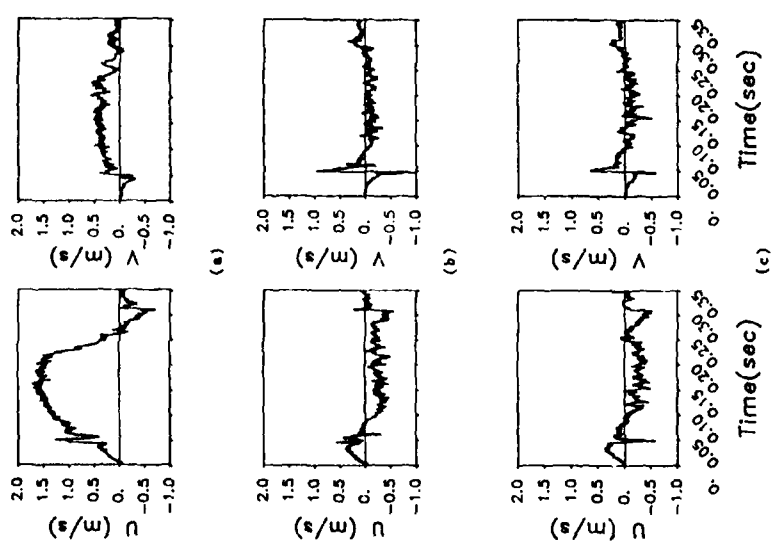


Fig. 8 Typical analog axial and radial velocity traces recorded at  $z/D = 0.71$  and  $y/R = 0.4$ , (b)  $y/R = 0.28$ , (c)  $y/R = 0.25$ .

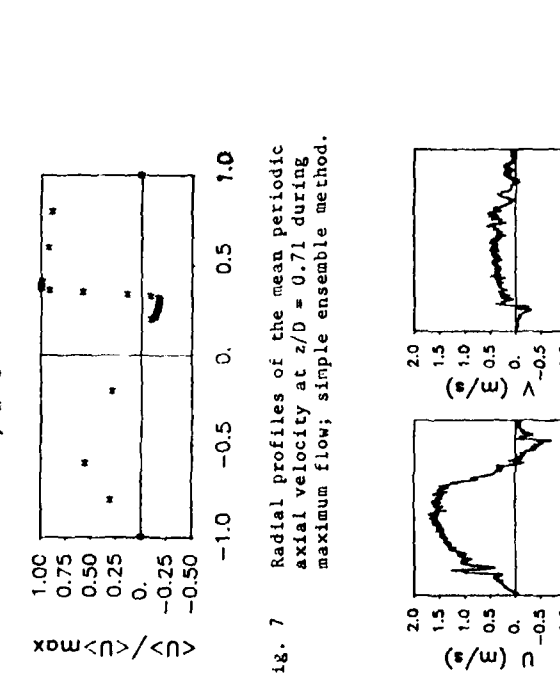


Fig. 9 Radial profiles of root-mean-square axial velocity fluctuations at (a)  $z/D = 0.71$ , (b)  $z/d = 1.21$ , (c)  $z/D = 1.71$  for several times during the mean pulse; simple ensemble method.

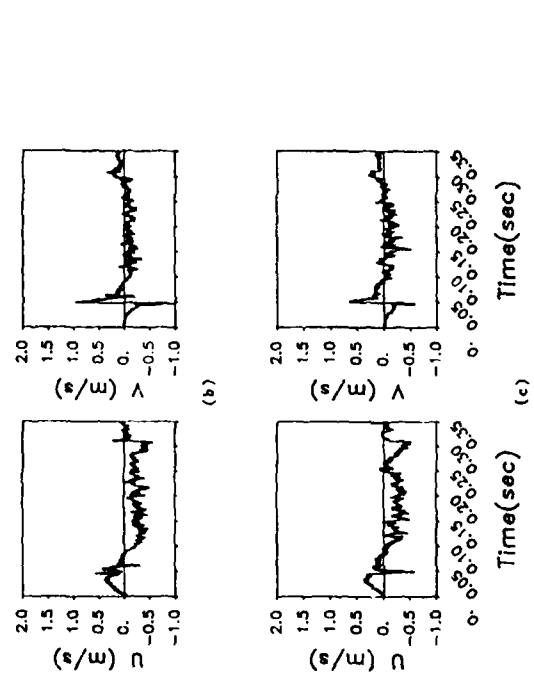


Fig. 10 Radial profiles of average fluctuating velocity products at (a)  $z/D = 0.71$ , (b)  $z/d = 1.21$ , (c)  $z/D = 1.71$  for several times during the mean pulse; simple ensemble method.

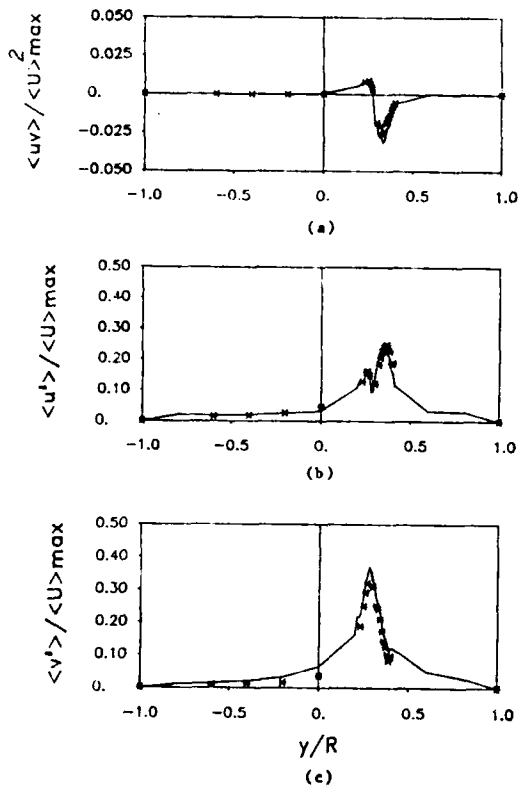


Fig. 11 Comparison of radial profiles of the (a) average fluctuating velocity product, (b) RMS axial fluctuating velocity, (c) RMS radial fluctuating velocity, with (—) and without ( \* ) cycle-to-cycle variation influence at  $t = 50\text{ ms}$ ,  $z/D = 0.71$ .

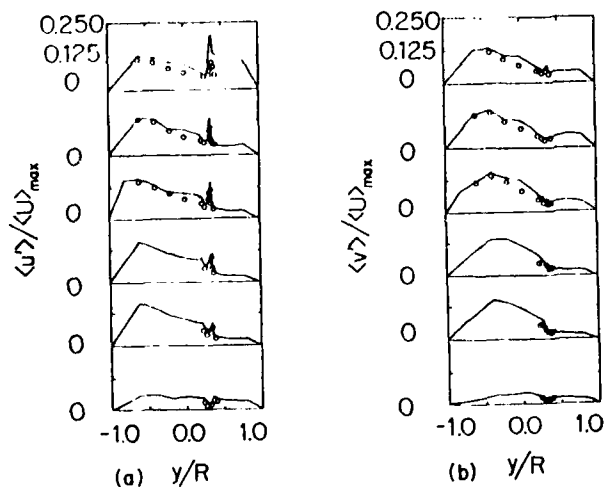


Fig. 13 Comparison of the estimated RMS (a) axial and (b) radial velocity fluctuations calculated by the (—) simple ensemble method, and ( o ) the filter method at  $z/D = 0.71$ .

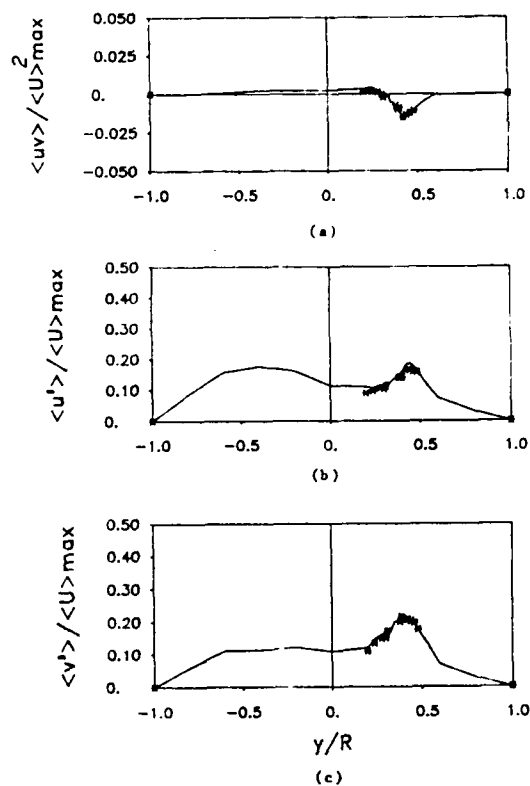


Fig. 12 Comparison of radial profiles of the (a) average fluctuating velocity product, (b) RMS axial fluctuating velocity, (c) RMS radial fluctuating velocity, with (—) and without ( \* ) cycle-to-cycle variation influence at  $t = 155\text{ ms}$ ,  $z/D = 1.21$ .

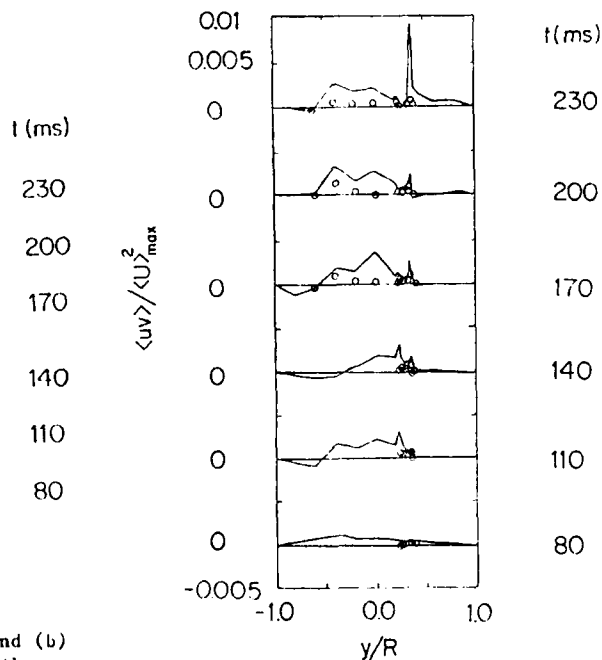


Fig. 14 Comparison of the fluctuating velocity product calculated by the (—) the simple ensemble method, and ( o ) the filter method at  $z/D = 0.71$ .

EXPERIMENTAL STUDY OF A PERIODIC REVERSE CURRENT IN A PULSED TURBULENT FLOW

R. CREFF and P. ANDRE  
 J.E. CNRS 034 936  
 Laboratoire de Mécanique et Energétique - Université d'Orléans - BP 6749  
 45067 ORLEANS Cedex 2 - France

ABSTRACT

The present study is devoted to the experimental investigation of the dynamic fluid field of a pulsed turbulent flow in a circular duct. The emphasis is placed on that situation where the oscillating velocity amplitude is larger than the steady velocity component. It has been experimentally shown [1] that the time-averaged effect of the resulting periodic reverse flow would consist in a large improvement for the convective heat transfer rate, up to 50 %, between the heated wall and the fluid. This confirms the analysis made by KAIPING [2]. Therefore, a study of the dynamic fluid field was carried out to explain that important feature. Using hot-wire anemometry with split-film probes, the behaviour of the reverse flow is described. A specific investigation of the main and reverse velocities has been made by means of a frequency spectrum analysis. The coherence and phase functions of the two velocity signals are also presented.

The experimental arrangement is already described elsewhere [1] and is shortly reminded here: the air flow is generated by a vacuum pump through a circular tube, 10 cm in diameter, 9,30 m in length. Mean Reynolds numbers extend from  $8.10^5$  to  $1.5.10^5$ . A sonic nozzle provides a time modulation for the mass flow rate with the sonic section alternatively closed up by a solid body moved along the nozzle axis. Flow modulation frequencies are then obtained up to 35 c/s.

In each section, the instantaneous velocity can be written as :

$$u(r,t) = U_0(r) + U_p(r) \cos [ t + \psi(r) ] + u'$$

Two conditions can lead to a periodic reverse flow, i.e.  $U_p > U_0$  : a sonic section variation rate and then a mass flow rate greater than 100 % or an acoustic resonance. From some mechanical consideration, the former situation was not available. The latter arises for some specific frequencies, a fundamental mode and subsequent harmonics of  $k$  - order, depending on the tube length  $L$ , the sound velocity  $a_0$ , such as :

$$F_{0k} = \frac{2k + 1}{4L a_0} \cdot (a_0^2 - U_0^2)$$

which here leads to a fundamental frequency and its first harmonic equal to 9.3 and 27.7 c/s respectively. A standing wave is then set up in the tube. The unsteady velocity vanishes in a node whereas in an antinode section it exceeds the steady velocity  $U_0$ .

Two consecutive node and antinode are separated by an axial distance equal to a quarter of the corresponding standing wave length (Fig.1). Then, between those two sections, a longitudinal variation of the reverse flow intensity can be depicted.

The interest is now focused on the antinode section, called herein the  $C_0$  section where the periodic reverse flow occurs for the second acoustic frequency  $F_{02}$  (27.7 c/s). In that section, the steady flow is already fully developed.

Because of the non-sensitivity of classical hot wire or hot film probes to reverse flows, dual probes designed as split-film probes, DISA 55 R 55, have been used : two semi-cylindrical hot films separated by a diametrical insulating plane are deposited on a quartz fiber. For a transversal investigation of the flow field two situations have been considered :

i) the insulating plane is perpendicular to the main flow axis ; then, the upstream film detects the main flow velocity component whereas the downstream film placed on the rear face of the probe body can measure any reverse velocity (Probe 1).

ii) the insulating plane is parallel to the main flow axis ; because of the probe symmetry any radial component can be pointed out (Probe 2).

Specific calibrations and cares have been used to adjust the output signals of the anemometer because of the possible probe sensitivity to the main flow direction alignment and to the non symmetry in film resistance overheating.

Thereafter, using probe 1, radial profiles of the main and reverse velocities have been worked out. As an interesting result, it has been shown that the maximum intensity in the reverse velocity was obtained near the wall ( $r/R \approx 0.975$ ) contrary to the main velocity which, as the steady one, reaches its maximum value on the center axis. Between two consecutive node and antinode sections referred to  $B_0$  and  $C_0$  respectively on figure 2 the longitudinal variation of the reverse velocity is shown for different radial positions.

By means of probe 2, it was pointed out that the reverse velocity component has a time variable orientation depending on the radial position ; the maximum angle value being obtained in the vicinity of the wall. On the other hand, the main flow velocity is clearly parallel to the duct axis.

The frequency spectrum analysis was made for the two hot film signals of Probe 1 and comparisons have been made with the no reversing flow si-

tuation (i.e. : a pulsed flow for a modulation frequency far from the resonance mode). Among the different results, the frequency spectra obtained for the two hot film signals (figure 3) show a fundamental corresponding to the flow pulsation frequency (27.7 c/s) and harmonics 1 and 2 in the studied frequency range (0 to 100 c/s). For the upstream film (case 1) the fundamental level decreases regularly from the axis to the wall whereas for the downstream film, a maximum is reached near the wall.

The coherence function defined as the squared correlation coefficient of the two signals is equal to 1 for the fundamental and harmonics and goes down to zero elsewhere. On the other hand, the 180° phase-lag between the main flow velocity and the reverse current is clearly shown for the fundamental frequency, no phase-lag being obtained for the harmonics.

As a complement to that study, turbulent intensity profiles have been performed in different low frequency ranges over 100 c/s. From these, it appears that, if compared to the no-reverse flow situation, the deviation from the steady flow decreases as the fluctuation frequency increases. This is in agreement with other results obtained along a flat plate [3] and it tends to confirm that the mean flow is largely decoupled from the large amplitude oscillations.

As a concluding remark, the different results brought up by the study confirm and explain the important role played by the periodic reverse flow in convective heat transfer improvement previously shown.

1. ANDRE P., CREFF R., CRABOL J., Int.J.Heat Mass Transfer, vol.24 n° 7, pp. 1211-1219 (1981)
2. KAIPING P., Int. J. Heat Mass Transfer, vol.26, n° 4, pp. 545-557 (1983)
3. BINDER G., TAROU S., BLACKWELDER R.F., KUENY J.L., Proceedings of Turbulent Shear Flows - 5, 16-1, 16-7, Cornell University (N.Y.), 7-9 Août 85.

This note is provided to attendees at the Tenth Symposium on Turbulence, University of Missouri Rolla, 22-24 Septembre 1986, as a support for the oral presentation. An extended paper will be sent to organizers shortly after the Symposium. Any enquiry may be made directly to authors.

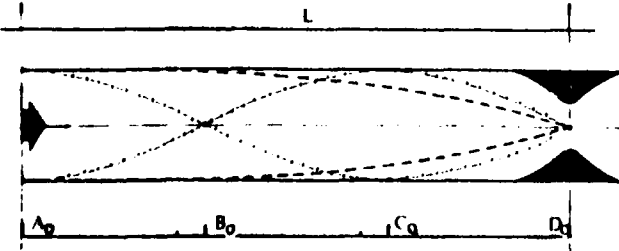


Fig.1 Longitudinal evolution of the unsteady velocity amplitude for the two resonance modes  $F_{01}$  --- ;  $F_{02}$  - - -

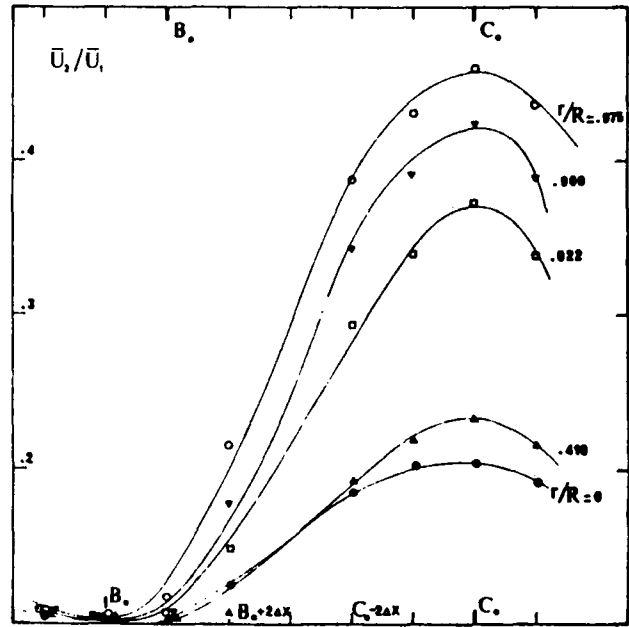


Fig.2 Longitudinal evolution of the reverse flow velocity for different radial positions.

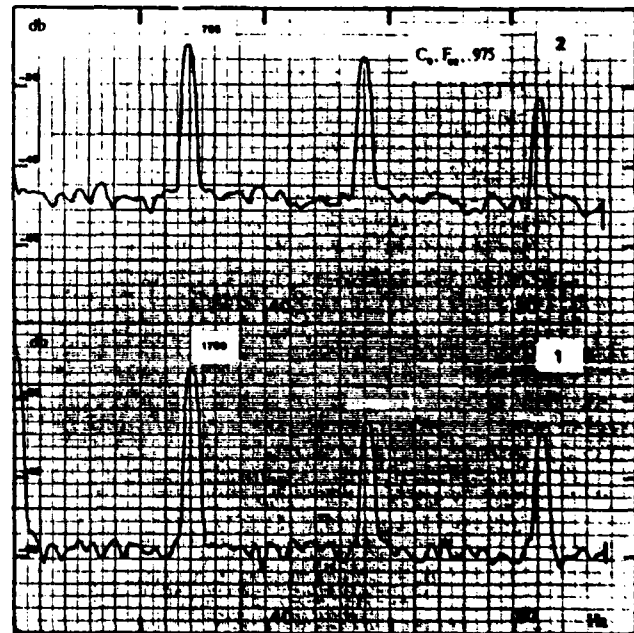


Fig.3 Amplitude spectra for the two velocities : 1 : main velocity ; 2 : reverse velocity at radial position  $r/R = .975$

DISTRIBUTION OF TURBULENCE ENERGY DISSIPATION  
RATES IN A RUSHTON TURBINE STIRRED MIXER

by

H. Wu, G.K. Patterson, and M. Van Doorn  
University of Arizona

ABSTRACT

An approximate method of measuring the turbulence energy dissipation rate ( $\epsilon$ ) in mixers by use of laser-Doppler measurements of the velocity autocorrelation and turbulence energy was successful in yielding remarkably consistent values.

The necessary corrections for periodic, non-dissipative velocity fluctuations were made by an autocorrelation method. Two modes of periodic fluctuation were found to be significant. Transformation of the corrected autocorrelations yielded completely normal turbulence energy spectra.

INTRODUCTION

There are various reasons to have a better knowledge about the flow characteristics in a stirred tank. The general purpose is a better understanding of the apparent phenomena in order to make better predictions for full-scale behavior. It might also lead to improved impeller and tank design. On the other hand turbulence plays an important role, not only for the fluid flow itself, but also for mixing and, eventually, chemical reactions. Here results are presented concerning the impeller flow in a baffled stirred tank equipped with a 6-blade disk turbine.

The mean radial velocity distributions are a measure of the large scale circulation. For large Reynolds numbers these large scale motions depend

partly on the geometry of the vessel and the rotational speed and partly on the turbulence produced by the flow.

The interaction between mean and fluctuating velocities is still a poorly understood phenomenon but kinetic turbulent energy and energy dissipation rate are key variables. For example, the "k- $\epsilon$  model" of turbulence uses the kinetic energy and the dissipation rate to overcome the so-called "closure problem" of turbulence. The turbulent kinetic energy can be used to characterize the flow at a scale small compared to that of the mean motion. The energy dissipation rate,  $\epsilon$ , is an important characteristic of the flow and mixing at a scale where the molecular transport processes become dominant. Therefore, the root-mean-square of the velocity fluctuations has been measured and also an attempt was made to quantify the dissipation rate of turbulent kinetic energy per unit mass. The accuracy of the measured quantities and the short-comings and possible improvements of the experimental technique will be discussed.

The results presented here cover only the impeller flow in one plane relative to the baffles and are, therefore, far from complete. The object of this paper is to discuss the theoretical background, the experimental method and the accuracy. It must be emphasized that the determination of the energy dissipation rate still needs more analysis.

#### THEORETICAL BACKGROUND FOR THE DETERMINATION OF $\epsilon$

The question arises as to how the energy dissipation rate  $\epsilon$  can be measured. In the first instant the idea arises to differentiate the analogue output of the frequency tracker used with the laser-Doppler velocimeter<sup>1</sup> (LDV)

---

<sup>1</sup>"Velocimetry" must be preferred to "Anemometry" because the latter is literally intended to measure air velocities.

technique. For isotropic turbulence the general expression for the dissipation of turbulence energy reads (see for example Hinze, (1975)):

$$\epsilon = 15 \nu \overline{\left(\frac{\partial u'}{\partial x}\right)^2} \quad (1)$$

In general the determination of the space derivative of the velocity fluctuation  $u'$  is rather difficult and requires more than one velocimeter. An alternative may be found in relating the time derivative to this space derivative using the so-called convective velocity  $U_c$  of the turbulent pattern.

By definition let

$$U_c^2 \overline{\left(\frac{\partial u'}{\partial x}\right)^2} = \overline{\left(\frac{\partial u'}{\partial t}\right)^2} \quad (2)$$

Then the following results

$$\epsilon = \frac{15\nu}{U_c^2} \overline{\left(\frac{\partial u'}{\partial t}\right)^2} \quad (3)$$

Measuring the time derivative is rather simple when the output voltage of the velocimeter is proportional to the instantaneous velocity. It requires a good differentiating network whose characteristics cover the whole frequency range of the voltage fluctuations. However, in the use of this method the convective velocity causes problems. For one-dimensional (1-D) flows with a low turbulence level  $U_c$  reads, according to Taylor (1938),

$$U_c = \bar{U}_1 \quad (4)$$

where  $\bar{U}_1$  is the mean main flow velocity.

For highly turbulent shear flows this relation needs some modification. Heskestad (1965) found for high Reynolds number shear flow in the 1 direction that:

$$U_c^2 = \bar{U}_1^2 + u_1'^2 + 2u_2'^2 + 2u_3'^2 \quad (3)$$

where  $u_1'$  denotes the RMS of the velocity fluctuations in the 1 direction. Van Doorn (1981) extended this result to 3-D shear flow and found that it still holds approximately for a given component direction:

$$U_{c1}^2 = \bar{U}_1^2 + u_1'^2 + 2u_2'^2 + 2u_3'^2 \quad (4)$$

where  $U_{c1}$  couples time and space derivatives in the 1-direction. These results indicate that measurements of turbulence in three principal directions are necessary in order to determine the energy dissipation rate from the averaged time-derivative squared of the velocity fluctuations. Some simplifications might be made when the turbulence is geometrically similar in the flow field of interest.

Unfortunately, an LDV is not suitable for using Equation 3. The problem is that the size of the measuring volume is large compared to the small scale eddies responsible for the energy dissipation. The size also allows more than one scattering particle flowing at the same time through the interference pattern. The result of this relatively large size is the so-called ambiguity noise with a frequency range wider than the turbulence power spectrum. George (1975) and Durst et al. (1976) have described this phenomenon extensively. Especially in the high frequency range of the power spectrum where the energy dissipation occurs this noise is relatively large. George described a way to subtract this ambiguity noise from the turbulent power spectrum, but the method

is very laborious. Van Haaver et al. (1973) succeeded in removing this noise experimentally. It requires a LDV with two photodetectors whose signals are cross correlated. However, the time differentiating technique still cannot be used, and the energy dissipation rate can only be determined by an integration in the frequency domain. This requires a Fourier transformation of each cross correlation function. Using this method requires extensive equipment to include an on-line computer.

Without removing the ambiguity noise, measurements in a stirred tank using Equation 3 resulted in dissipation rates approximately 2 orders of magnitude larger than the estimated power input per unit mass.

Since the isotropic approximation does not seem to be practical for the LDV, other approaches for measuring  $\epsilon$  must be considered. The classical approach by Laufer (1954) was to measure all the correlation terms in the turbulence energy balance equation, then properly sum them to determine  $\epsilon$ . This measurement intensive approach is what the authors wished to avoid.

Previous measurements of  $\epsilon$  have been reported by Cutter (1966), Rao and Brodkey (1972), Antonia, Sarraptakash, and Hussain (1980), Sato et al. (1970), and Sato and Yamamoto (1984). Cutter's measurements were based on velocities inferred from streak lengths on photographs of suspended particles. He then computed  $\epsilon$  as follows using a simplified version of Laufer's approach:

$$\epsilon = \frac{1}{2r} \frac{\partial}{\partial r} \left[ (2q + U^2 + V^2 + W^2 + 2\overline{Ww})r \right] \quad (7)$$

where  $q = \frac{1}{2} (\overline{u^2} + \overline{v^2} + \overline{w^2})$ .

Cutter found that most of the power was dissipated in the impeller stream for a disk turbine stirred vessel. The method is still measurement and calculational intensive.

Rao and Brodkey computed  $\epsilon$  as follows:

$$\epsilon = 15 \nu \overline{u^2} / \lambda^2 \quad (8)$$

where  $\lambda = \overline{u^2} / (\overline{du/dr})^2$

$\lambda$  is the microscale of turbulence. They made their velocity measurements in the impeller stream with a hot-film anemometer aligned with the direction of the resultant vector. The hot-film anemometer does not suffer from ambiguity noise to the same degree as the LDV, but the probe interferes with the flow affecting the measurements.

Complexities of previous methods made it necessary to look for another way to measure  $\epsilon$ . According to Batchelor (1953) large (small wave number) eddies carry energy subtracted from the main motion. These eddies break up into smaller ones due to shear and this process repeats until finally very small eddies have been formed. In this so-called energy cascade process the kinetic energy is mainly transferred from the large eddies into smaller ones without significant dissipation. The smaller the scale, the more important molecular viscosity becomes. At the so-called microscale, these molecular forces are dominant and govern the process, resulting in the dissipation of turbulent energy.

The above analysis is a typical example of a Lagrangian approach where individual eddies are followed. For practical purposes, however, an Eulerian approach makes more sense. In that situation the energy cascade model can only

be applied when the local production of turbulence kinetic energy equals the local turbulence dissipation. For example, near walls or obstacles where no large eddies can exist there must be convection of turbulence energy; a physical picture is that turbulence energy containing eddies move from the turbulence production regions to other parts of the turbulent boundary layer. Fortunately the smaller eddies are generally in mechanical energy equilibrium (i.e. production = dissipation), which means that the energy cascade process as described in the foregoing can be applied to eddies having a size  $l \leq l_e$  the largest size in the equilibrium range.

The important result is that the dissipation rate can be calculated from the turbulence kinetic energy of the eddies with size  $l_e$ . Batchelor suggested on dimensional grounds that:

$$\epsilon = \frac{A u'^3}{l_e}$$

with  $l_e$  on the order of the integral scale  $\Lambda$ . For isotropic turbulence Batchelor found that  $A = O(1)$ . Tennekes (1977) suggested a slightly different relation:

$$\epsilon \sim \frac{q^3}{l} \quad (10)$$

with  $q = \frac{1}{2} \sqrt{u'_1{}^2 + u'_2{}^2 + u'_3{}^2}$  and called this the first law of turbulence in order to emphasize its importance.

The question is how this result can be applied to shear flows. Townsend (1976) stated that in self-preserving shear flows the energy dissipation reads:

$$\epsilon = q^3/L_e \quad (11)$$

where

with  $L_{1,2,3}$  the integral scales measured in three principal directions.

It is important to realize that the turbulence kinetic energy measured with an LDV is also influenced by ambiguity noise, systematically resulting in too large values. The error, however, is small compared with that of the differentiating technique. Another important remark is that the spatial structure of turbulence is still needed in order to calculate  $\epsilon$ .

The simpler to measure integral time scale  $\tau$  might be coupled to the space scale using an appropriate convective velocity:

$$\tau = L_c / U_c \quad (13)$$

The convective velocity  $U_c$  in Equation 13 is especially defined in order to couple the time and space derivatives squared and there is no proof that the result may also be applied to Equation 12. Goldschmidt et al. (1995) found for plane turbulent jets that the convective velocity tends to increase for increasing wave numbers. This suggests

$$U_c \propto k \quad (14)$$

Generally, more analysis is needed to relate  $U_c$  to measurable quantities and, especially for this specific application, those expressed in a cylindrical coordinate system.

Antonia, Satyaprakash, and Hussain used the method suggested by Batchelor, Tennekes (1977), and Townsend to measure  $\epsilon$  in jets. They used the following equation:

$$\epsilon = Au'^3/L_0 \quad (15)$$

More generally

$$\epsilon = Aq^{3/2}/L, \quad (15a)$$

where

$$q = \frac{1}{2} (\overline{u^2} + \overline{v^2} + \overline{w^2}),$$

$$L = (L_x^2 + L_y^2 + L_z^2)^{1/2}$$

and

A = adjustable constant of O(1).

Antonia, et al. obtained the scale  $L_0$  from the jet width, but for non-similar flows the integral scales apply as follows:

$$L_x = \frac{U_c}{u^2} \int_0^\infty \overline{u(t)u(t+\tau)} d\tau, \text{ where } U_c \approx (\overline{U^2} + u'^2)^{1/2} \quad (16)$$

In practice an upper limit of  $\infty$  is impractical, so the point of zero crossing must be used.

The basis for the method of Equations 15a and 16 is as follows:

1. Energy cascade from large to small eddies exists.
2. Local equilibrium exists between turbulence production (at the large, measurable scales) and dissipation (at the small, unmeasurable scales).
3. Local isotropy of small scales exists even through large scales are very anisotropic.

Antonia, Satyaprakash, and Hussain made measurements of  $\overline{u^2}$  and  $L_x$  in round and plane jets, then computed  $\epsilon$  using Equations 15 and 16. They found that A should be approximately 1.0 for both a round jet and for a plane jet.

## EXPERIMENTAL WORK

The apparatus used in this work consisted of a stirred tank mixer and a laser-Doppler velocimeter with computer data acquisition. A schematic drawing of the stirred tank is shown in Figure 1. The tank was 27 cm inside diameter and 27 cm high. The top surface of the fluid, which was water, was open. The 4 baffles were 2.7 cm wide. The 6-bladed disk turbine used was of standard design, of diameter approximately equal to one-third the tank diameter. The shaft ran the full length of the tank and the impeller disk was 9 cm above the tank bottom. Measurements were made at a 45° angle to the baffle planes.

The laser-Doppler velocimeter used was a standard one-direction model by DISA with coaxial optics operating in the dual-beam differential mode. The velocimeter was used to measure velocities in all three directions in all portions of the tank. The highest density of measurement points was near the impeller tip where the radial jet was formed. Corrections were made for the periodic non-turbulent velocity pulsations produced by the turbine blades. The turbulence intensity near the blade tips was reduced by about 10%. The correction diminished rapidly away from the impeller. Tracking particles were 6 micron polystyrene spheres.

The length scales were measured by integrating autocorrelations, then multiplying by average velocity, as in Equation 16. Only small effects of measurements in different directions were noticed, since turbulence in most locations was not strongly anisotropic. Measurements reported here were made at 200 rpm which corresponds to an impeller Reynolds number  $(ND^2/\nu)$  of 27,000.

## REMOVAL OF PERIODIC FLUCTUATIONS

It is well known that periodic pulsations in velocity, primarily in the radial direction, are produced by the rotating impeller in a disk turbine stirred vessel. Since these pulsations are non-dissipative, do not contribute to production of shear stresses, they must be subtracted from the measured total velocity fluctuations in order to calculate  $q$ . Determine  $q$ .

Methods for removing the periodic component may rely on spectral corrections of course times to the autocorrelation function. Although the methods would seem to be equivalent, the autocorrelation basis has two advantages. First, at long delay times the periodic portion of any autocorrelation function is retained, even though the random fluctuation portion has become zero. This can be used to determine the random portion of the autocorrelation back to zero time. Second, the autocorrelation yields a good estimate of the integral scale, if the convection velocity is known. Thus, the random contribution to the value of  $q$  and the value of  $L$  may be both ascertained from the corrected autocorrelation function.

Figures 2-3 show measured and corrected autocorrelation at two different locations relative to the impeller. These locations and all others used for measurements reported here are shown in Figure 8. The exact numerical methods for matching a periodic wave to the long time portions of the autocorrelations will be described in the Ph.D. thesis of Wu (1986) and a later publication. It should be noticed that the correction is large (60 to 75% on  $q$ ) near the impeller tip and becomes negligible (see Figure 4) further away. Also at the disk plane (Figure 2) the periodic part of the autocorrelation function consists of only the fundamental frequency ( $6N$ ), but near the blade edges

(Figure 3) at least two frequencies (6N and 12N) are evident. Both these frequencies were fit to the autocorrelation function to correct it.

Figures 5-7 show energy spectra obtained from Fourier transformations of the first three autocorrelations ( $r/R = 1.07$ ,  $z/R = 0$ ;  $r/R = 1.07$ ,  $z/R = 0.22$ ;  $r/R = 1.66$ ,  $z/R = 0$ ) for both uncorrected and corrected cases. The remarkable result is how nearly free the corrected spectra are of periodic contributions (peaks). The spectrum for ( $r/R = 1.07$ ,  $z/R = 0.22$ ) has a slight remaining hump, but that may be because a second harmonic (18N) is evident which was not corrected for.

#### VELOCITY, TURBULENCE AND DISSIPATION RESULTS

In order to meet the objective of measuring  $\epsilon$  at various locations in the stirred vessel, it was necessary to have accurate measurements of velocity and turbulence at each point. Part of the data obtained is reported here in order to indicate magnitudes of these values. More details are given in the thesis by Wu and will be reported in a later publication.

Locations of measurements are shown in Figure 8. They are concentrated in the region of the radial impeller stream, since it was found that very little energy dissipation occurs outside this region. This is in contrast to findings by Gunkel and Weber (1975) and by Rao and Brodkey (1972), but in agreement with findings by Cutter (1966) and Laufhutte and Mersmann (1985). It is also qualitatively in agreement with observations that most mixing seems to take place in the impeller stream (see Patterson, 1981).

The mean radial velocity component at 200 rpm and various radial distances is shown in Figures 9-13. The influence of the free top surface is seen in the tendency for the velocity peak to move upward as the wall is approached.

Figures 14-18 show the values of the root-mean-square radial fluctuating velocity component ( $u'$ ) at the same radial locations as before. Approximately the same trend is observed as the wall is approached. Of particular note is the degree of correction for periodic fluctuation near the impeller ( $r/R = 1.0$  and  $1.29$ ) and the final double peaked shape of the curves. The spread of the peaks are much narrower than the impeller blades as shown, but must be related to the trailing vortex pattern behind each blade edge. The corrections and the double peaks both become negligible at  $r/R = 1.50$  ( $r=7.0$  cm), which is 2.4 cm from the blade tip.

The profiles of  $\epsilon$  shown here were calculated with the approximation as follows:

$$\epsilon = Au_r'^3 / (\tau \sqrt{\bar{U}_r^2 + u_r'^2}) \quad (1)$$

where  $\tau = L_r / \bar{U}_c$ ;  $\bar{U}_c = \sqrt{\bar{U}^2 + u'^2}$ ,  $A = 1$ .

This was justified by the observation that little difference existed between the values of turbulence intensity in the three directions, so the effect of the other components ( $u'_\theta$  and  $u'_z$ ) would be small.

Figures 19-23 show the profiles of  $\epsilon$  at various distances from the impeller tip. Of particular significance is that the  $\epsilon$ -values are effectively zero at the impeller stream edges. This condition holds throughout the remainder of the tank. Also of note is the non-symmetry of the double peaks. This again seems to be a result of the influence of the free surface of the liquid. Various measurements show these peaks to be reproducible.

The values of  $\bar{U}_r$ ,  $u_r'$ , and  $\epsilon$  are shown normalized as  $\bar{U}_r/ND$ ,  $u_r'/ND$ , and  $\epsilon/N^3D^2$  since these values maintain reasonable similarity for various impeller

sizes as long as the flow is turbulent. The flow scale is set by the distance from the tank walls are baffled and the free surface is maintained.

#### VALUE OF CONSTANT A

In order to evaluate the constant A for comparison with Antonia et al.'s values for the present study, the total power (P) dissipated in the vessel was computed with the spatial integration of the measured  $\epsilon$  values. This calculation yields

$$P/\rho = \int_0^R 2\pi r \int_0^L \epsilon(z) dz = 0.005$$
 This value is less than those reported by Antonia et al. were the Antonia, et al. values for A.

A previous paper (Patterson and Wu, 1977) indicated that the data reported for the Rushton turbine impeller had three measurements that had been found to be in error. The corrections for the particle velocity fluctuations were inadequate, leaving the  $\epsilon$  values much too high in the vicinity of the impeller.

Figure 10 shows a comparison of this data for  $\epsilon$  with that of Lauffhutte and Mersmann at the radial location of  $r/R = 1/2$ . The differences between the two sets of data probably stem mainly from the differences in integral scale. Lauffhutte and Mersmann assumed a constant scale equal to impeller diameter rather measure it through use of an autocorrelation. It is felt that the values from autocorrelation used here are more representative of the correct values. Because the much lower scales in the impeller vortex region were not accounted for when a constant scale was assumed, the double peak did not appear in Lauffhutte and Mersmann's data.

## CONCLUSION

The methods used seem to provide a valid way to quickly measure values of  $\epsilon$ . The rather close correspondence between constants (A) for the impeller stream and for jet measurements lends confidence in its use.

## REFERENCES

- Antonia, R.A., B.R. Satyaprakash, and A.K.M.F. Hussain, "Measurements of Dissipation Rate and Some Other Characteristics of Turbulent Plane and Circular Jets", Phys. Fluids, 23, 695 (1980).
- Batchelor, G.K., "The Theory of Homogeneous Turbulence", Cambridge Univ. Press, 1953.
- Cutter, L., "Flow and Turbulence in a Stirred Tank", AIChE Journal, 12, (1966), p. 35.
- Durst, F.A., Melling and J.M. Whitelaw, "Principles and Practice of LDT", Academic Press, London, (1976).
- George, W.K., Jr., "Limitations to Measuring Accuracy Inherent in the Laser Doppler Signal", Proceedings of the LDA - Symposium Copenhagen (1975), pp. 20-64.
- Goldschmidt, V.W., M.F. Young, and E.S. Ott, "Turbulent Convective Velocities in a Plane Jet", J. Fluid Mech., 105 (1981), pp.327-345.
- Günkel, A.A., and M.E. Weber, "Flow Phenomena in Stirred Tanks", AIChE Journal, 21, (1975), pp.931-948.
- Heskestad, G., "A Generalized Taylor Hypothesis with Application for High Reynolds Number Turbulent Shear Flows", Trans. ASME, Journal of Applied Mechanics 32, 4, (1965), pp. 735-739.
- Hinze, J.O., "Turbulence, Second Edition", McGraw Hill, 1975.
- Laufer, J., NACA Technical Report 1174, 1954.
- Laufhütte, H D., and Mersmann, A.B., "Dissipation of Power in Stirred Vessels", 5th European Conference on Mixing, Würzburg, West Germany, June 1985.
- Patterson, G.K., and Wu, H., "Distribution of Turbulence Energy Dissipation Rates in Mixers", 5th European Conference on Mixing, Würzburg, West Germany, June 1985.
- Patterson, G.K., "Application of Turbulence Fundamentals to Mixed Chemical Reactors", Chemical Engineering Comm., 8, 25 (1981).
- Rao, M.A., and R.S. Brodkey, "Continuous Flow Stirred Tank Turbulence Parameters in the Impeller Stream", Chem. Eng. Sci., 27, 137 (1972).
- Sato, Y., and K. Yamamoto, "Two-Equation Model of W.C. Reynolds for Isotropic Turbulence", AIChE Journal, 30, 831 (1984).
- Sato, Y., M. Kamiwano, and K. Yamamoto, "Turbulent Flow in a Stirred Vessel-Effects of Impeller Types", Kagaku Kogaku, 34, 104 (1970).

Taylor, G. I., "The Spectrum of Turbulence", Proceedings of the Royal Society, A. 164, (1938), pp 476-490

Tennekes, H., "Turbulence: Diffusion, Statistics, Special Dynamics", Handbook of Turbulence, Vol. 1, 127, Ed. by Frost and Moulden, Plenum Press, 1977

Townsend, A.A., "The Structure of Shear Turbulent flow" 2nd Edition, Cambridge Univ. Press, 1976.

Van Maanen, H.R.E., K. Van der Molen and J. Blom "Reduction of Ambiguity Noise in Laser-Doppler Velocimetry by a Cross Correlation Technique", Proceedings of the LDA-Symposium Copenhagen, (1975), pp 81-89

Van Doorn, Maarten, "On Taylor's Hypothesis in Turbulent Shear flows", Internal note 811123, University of Missouri-Rolla, 1981

Wu, H., "Measurements of turbulence Energy Dissipation Rates in a Rushton Turbine Stirred Tank", Ph.D. Thesis, University of Arizona, 1986.

## NOMENCLATURE

$c$	fluctuating concentration, $C - \bar{C}$
$D$	impeller diameter
$D$	molecular diffusivity
$f(\tau)$	autocorrelation function
$E_1(n)$	one-dimensional energy spectrum function
$k$	turbulence energy (= $q$ )
$L_s$	macroscale of segregation
$L_x$	integral velocity scale
$N$	impeller rotation rate
$N_{Sc}$	Schmidt number ( $\nu/D$ )
$q$	turbulence energy (= $k$ )
$r$	radial distance from impeller shaft
$R$	impeller radius
$T$	tank diameter
$U, V, W$	velocity in x, y, z directions
$u, v, w$	velocity fluctuations
$u_r, u_\theta, u_z$	fluctuating velocities in radial, tangential, and axial (shaft) directions
$U_r, U_\theta, U_z$	velocities
$z$	axial distance from impeller disk
$Z$	tank height
$\epsilon$	turbulence energy dissipation rate
$\mu$	viscosity
$\tau$	time delay

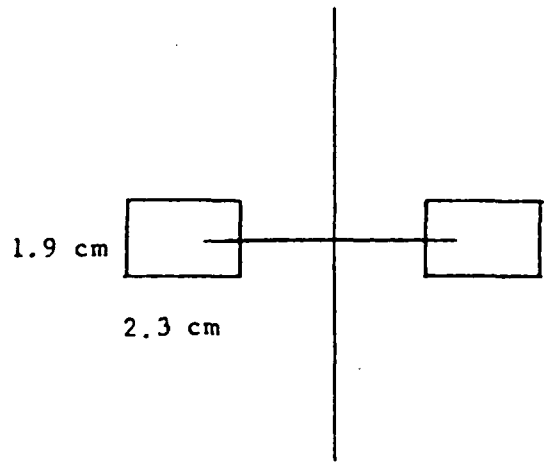
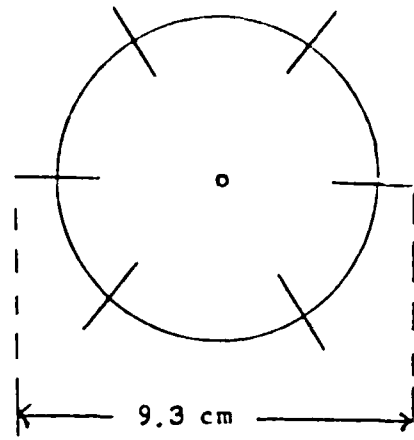
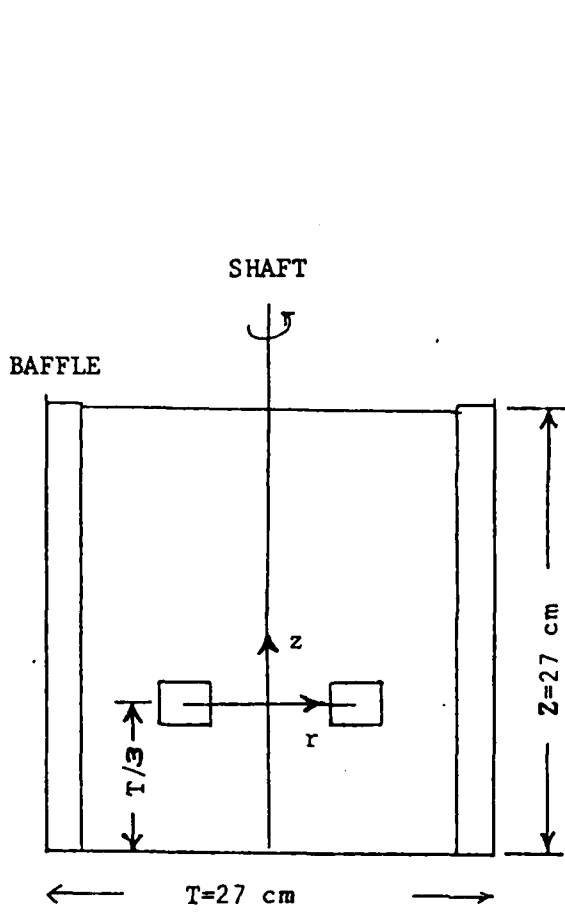


Figure 1. Schematic drawing of stirred tank.

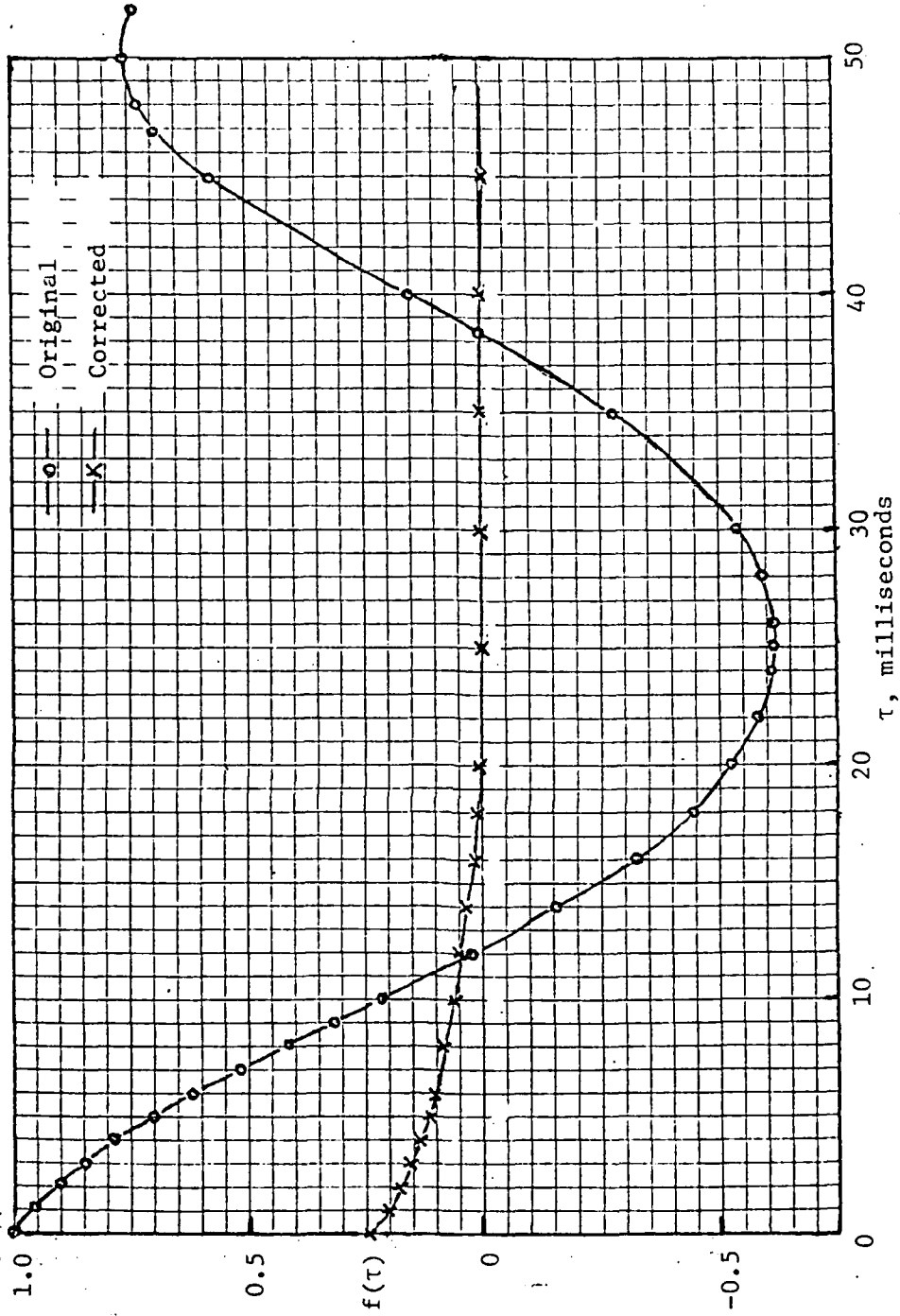


Figure 2. Original and corrected autocorrelation coefficients at  $r/R = 1.07$ ,  $z/R = 0$ ,  $N = 200$  rpm.

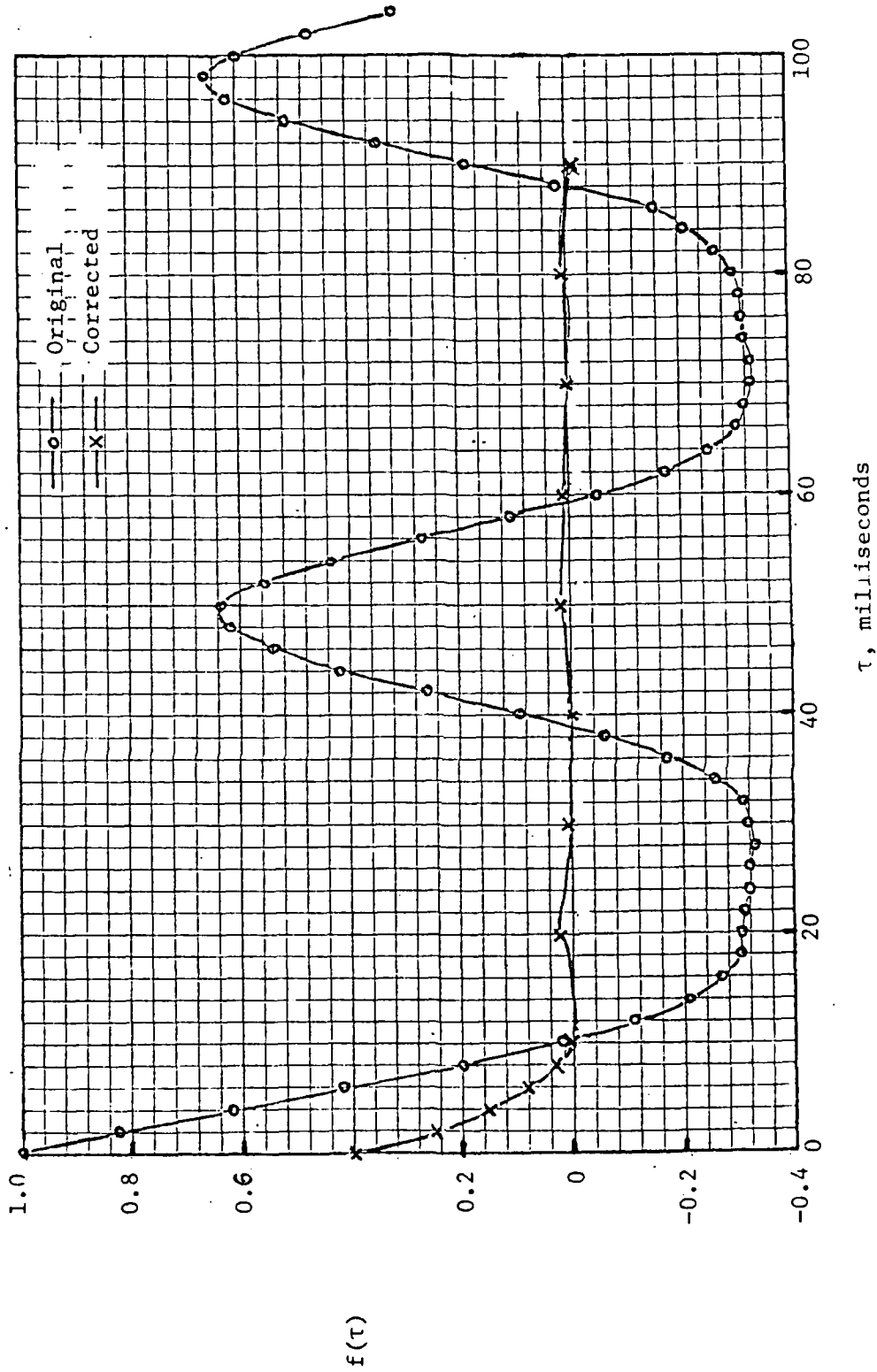


Figure 3. Original and corrected autocorrelation coefficients at  $r/R = 1.07$ ,  $z/R = 0.22$ ,  $N = 200$  rpm.

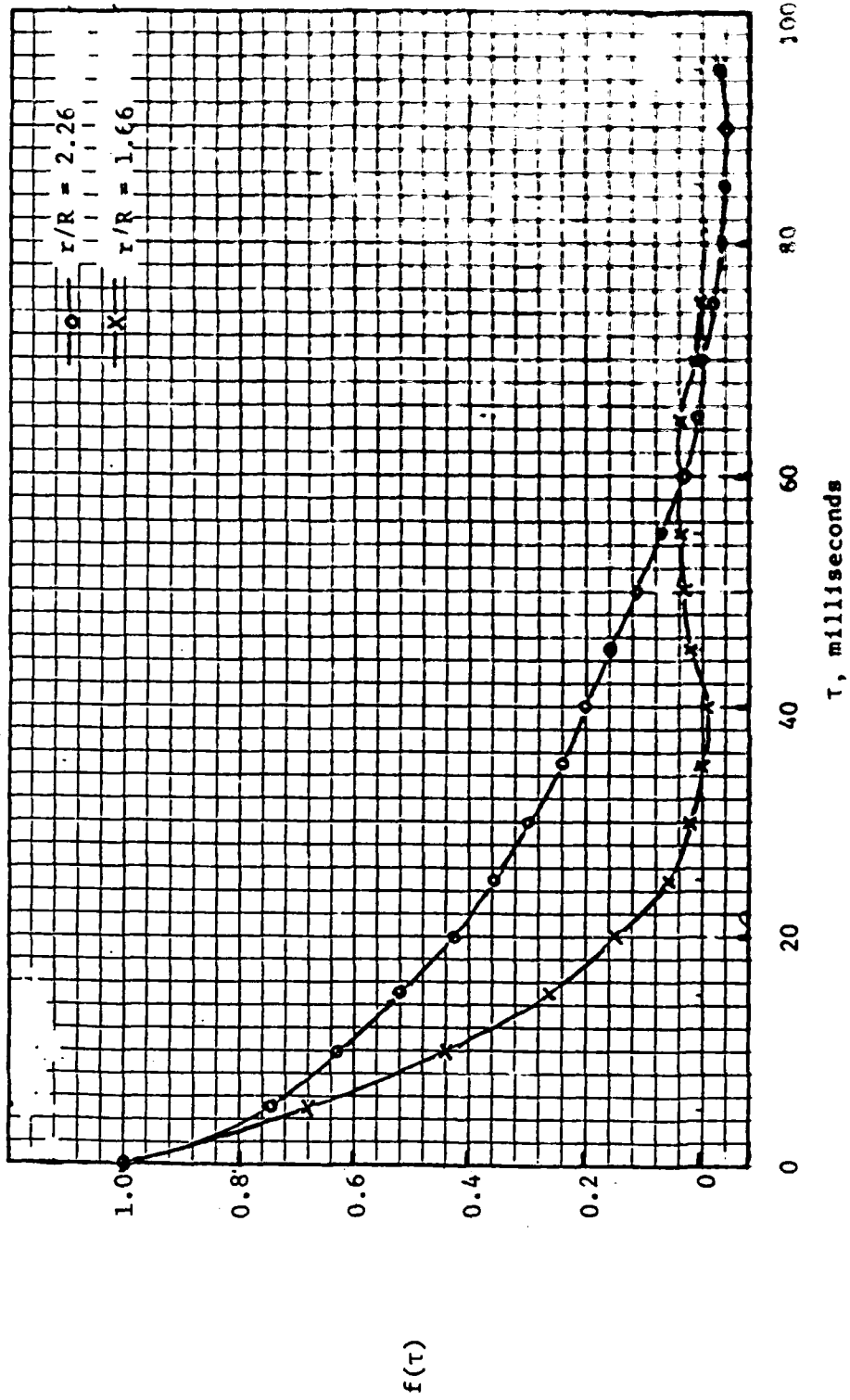


Figure 4. Autocorrelation coefficients at  $N = 200$  rpm,  $z/R = 0$ .

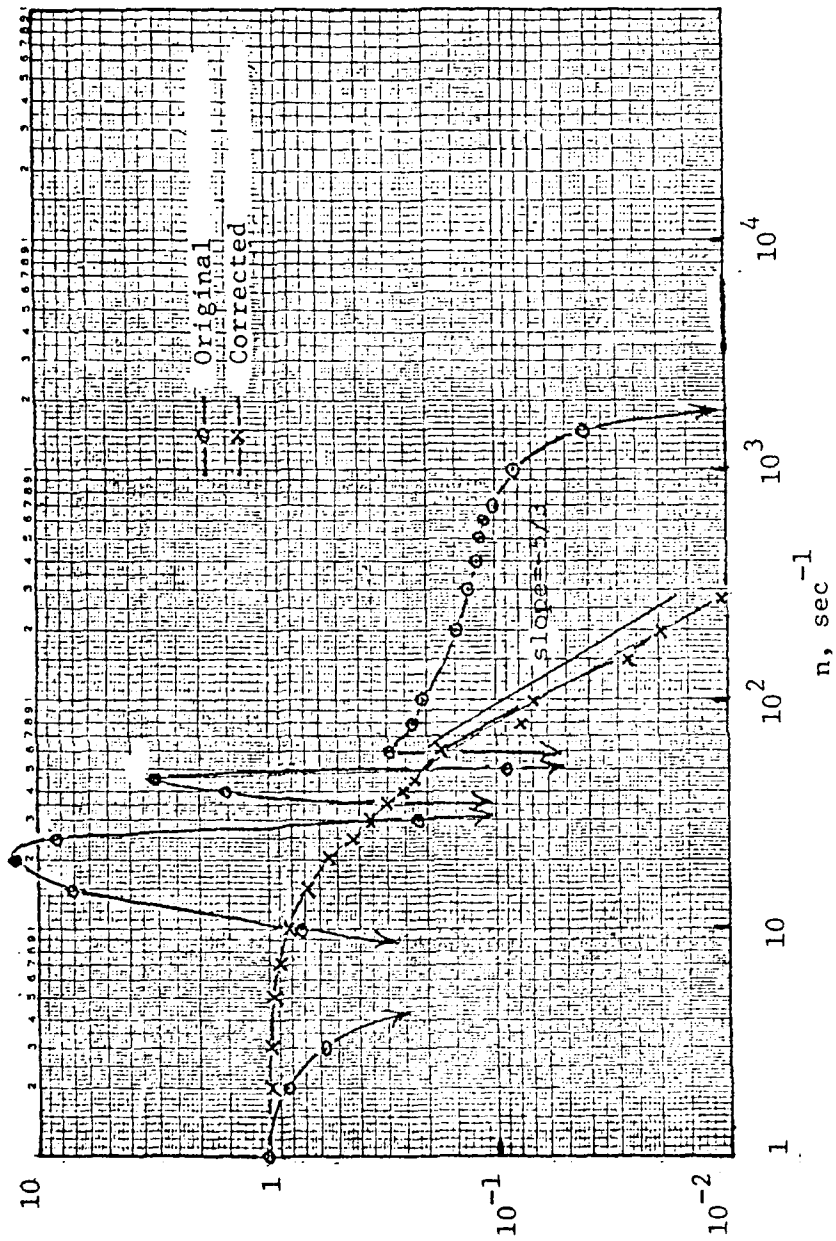


Figure 5. One-dimensional energy spectrum function at  $r/R = 1.07$ ,  
 $z/R = 0$ ,  $N = 200$  rpm.

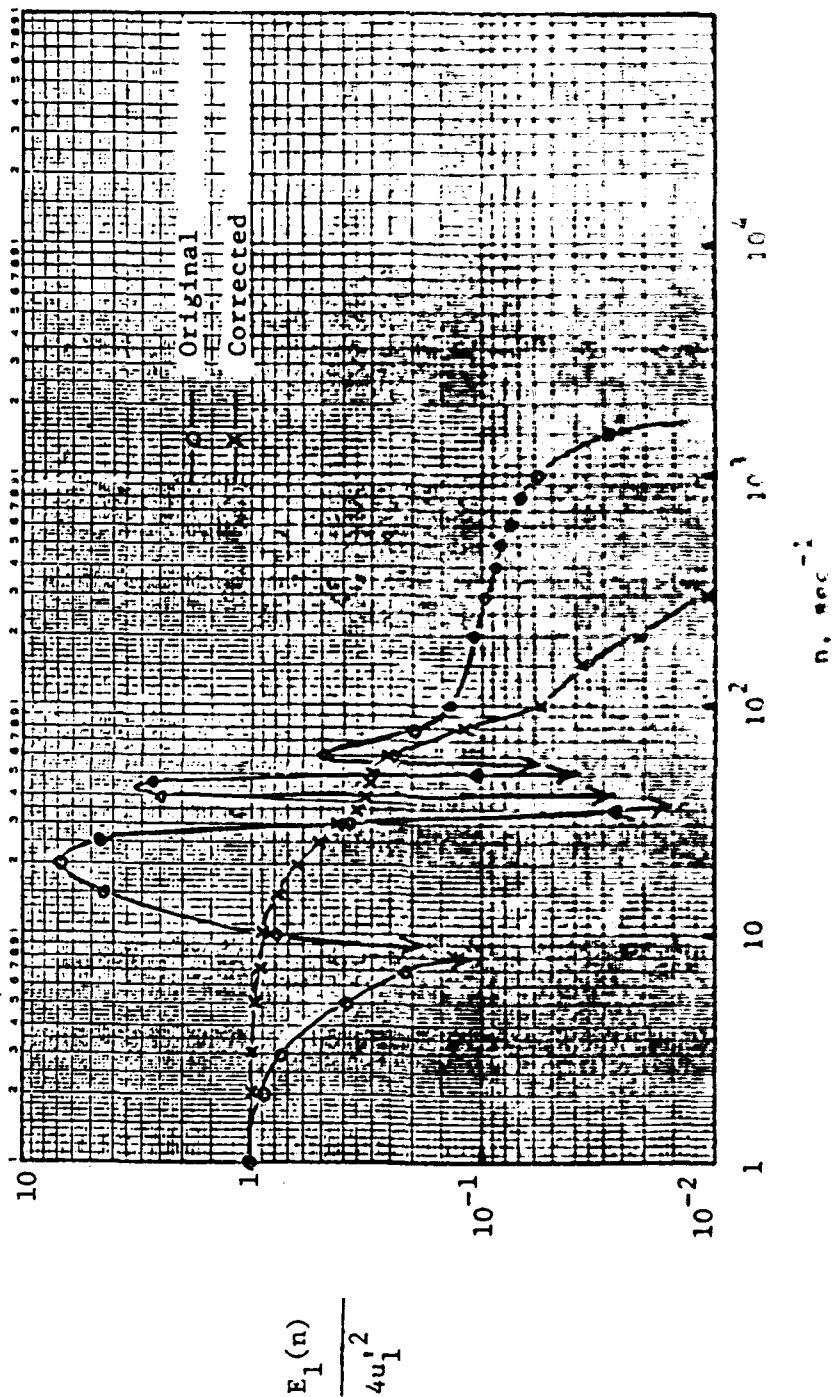


Figure 6. One-dimensional energy spectrum function at  $r/P = 3.07$ .  
 $z/R = 0.22$ ,  $N = 200$  rpm.

$$\frac{E_1(n)}{4u_1^2}$$

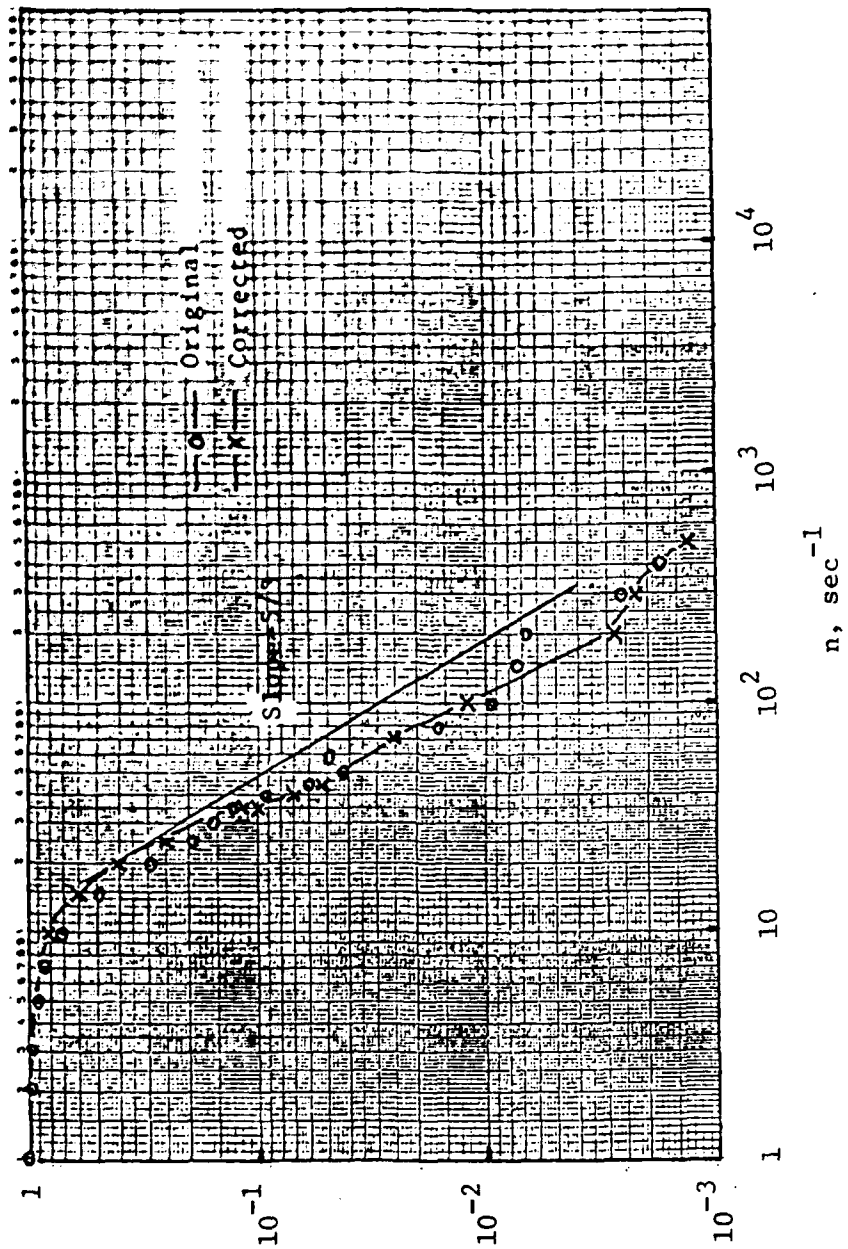


Figure 7. One-dimensional energy spectrum function at  $r/R = 1.66$ ,  $z/R = 0$ ,  $N = 200$  rpm.

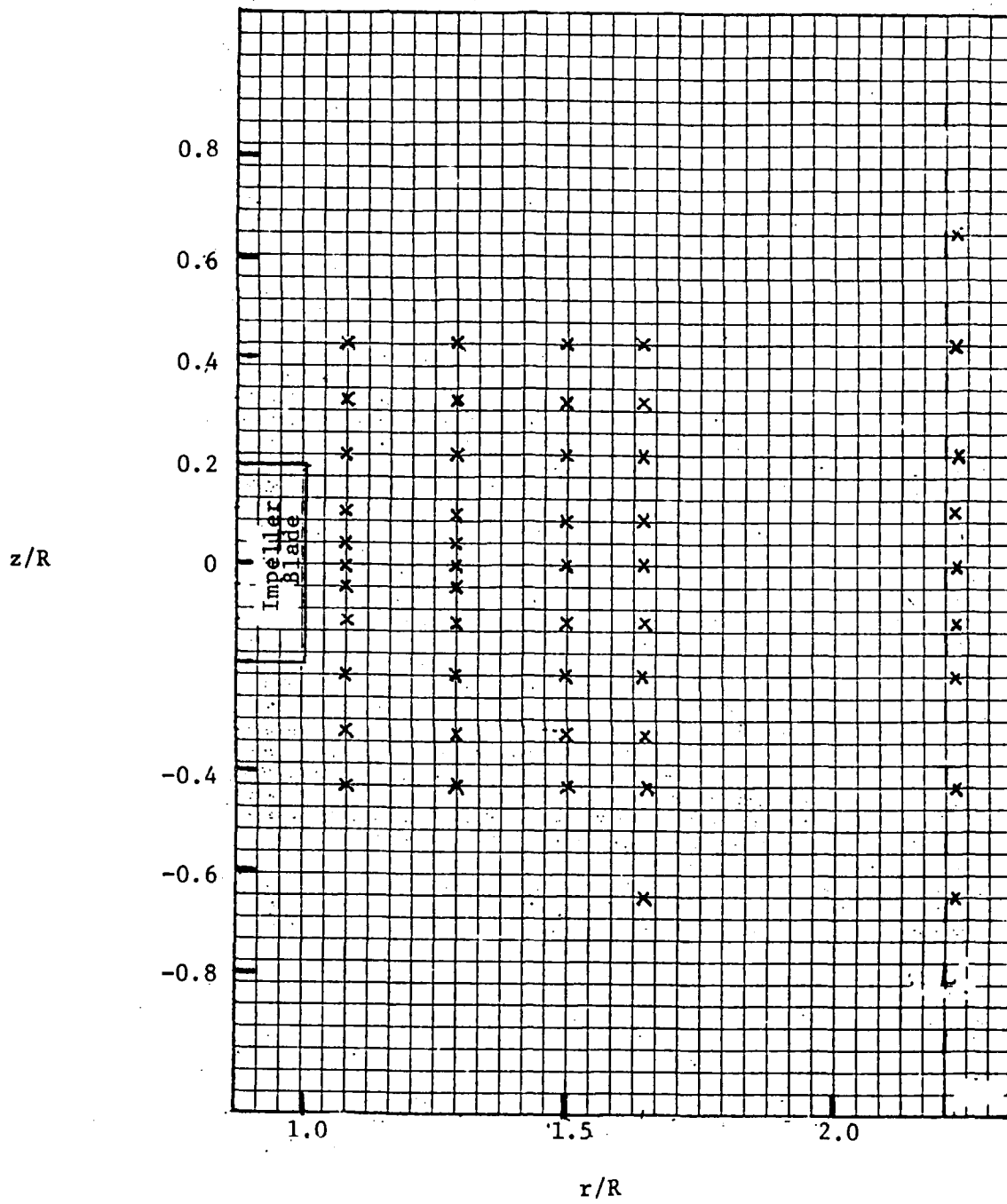


Figure 8. Locations of measurement points in and near the impeller stream.

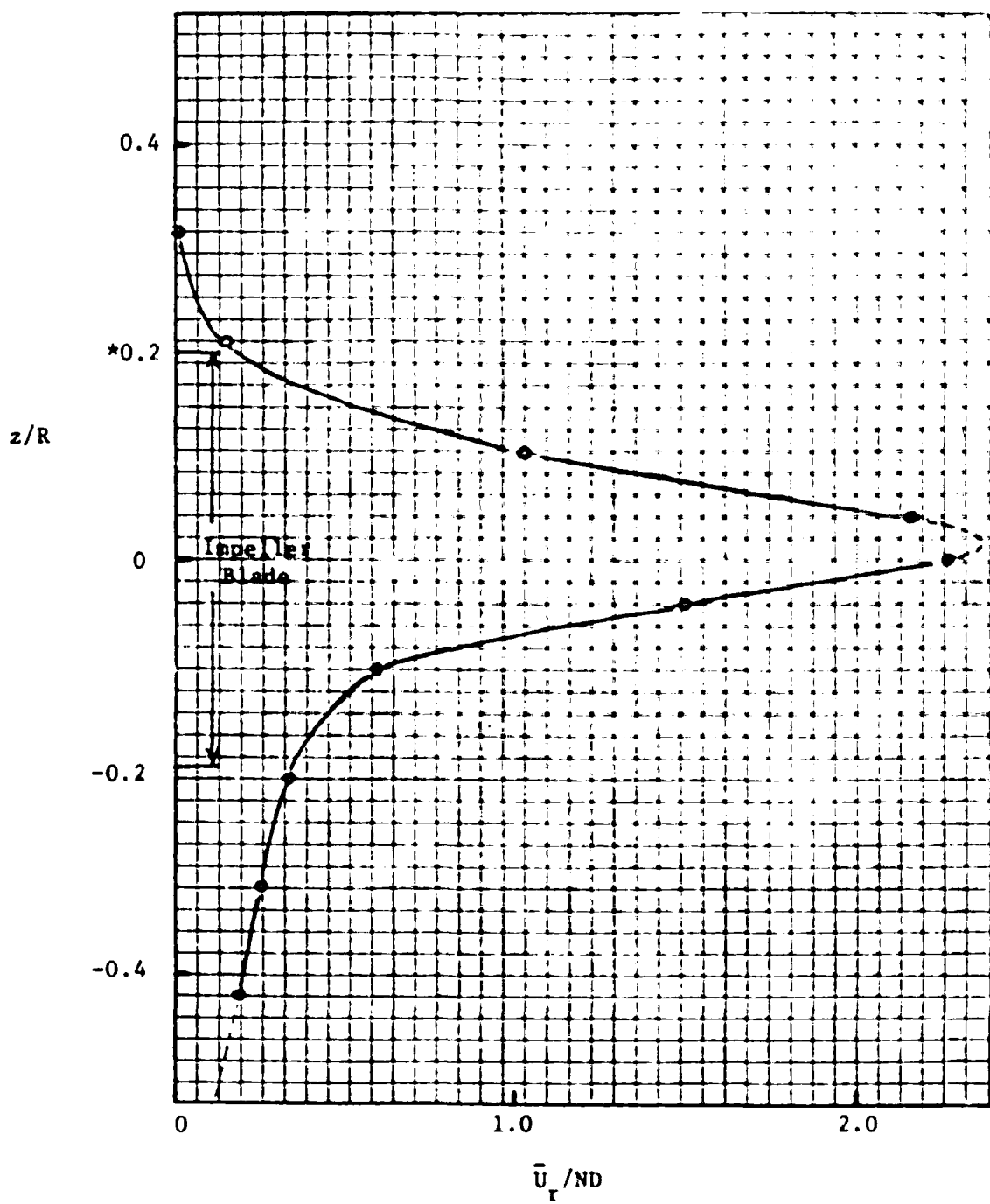


Figure 9. Mean radial velocity profile at  $r/R = 1.07$ ,  $N = 200$  rpm.

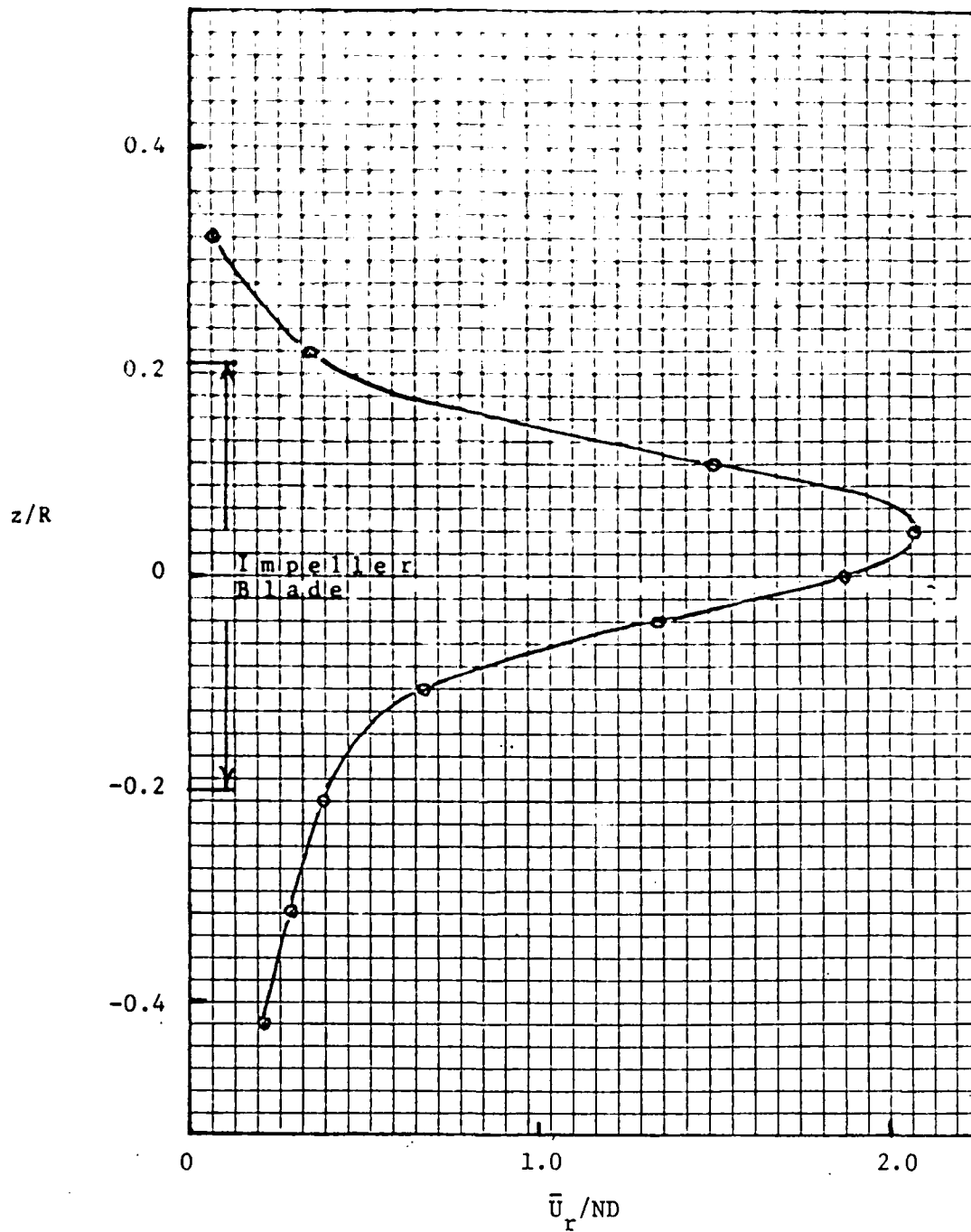


Figure 10. Mean radial velocity profile at  $r/R = 1.29$ ,  
 $N = 200$  rpm.

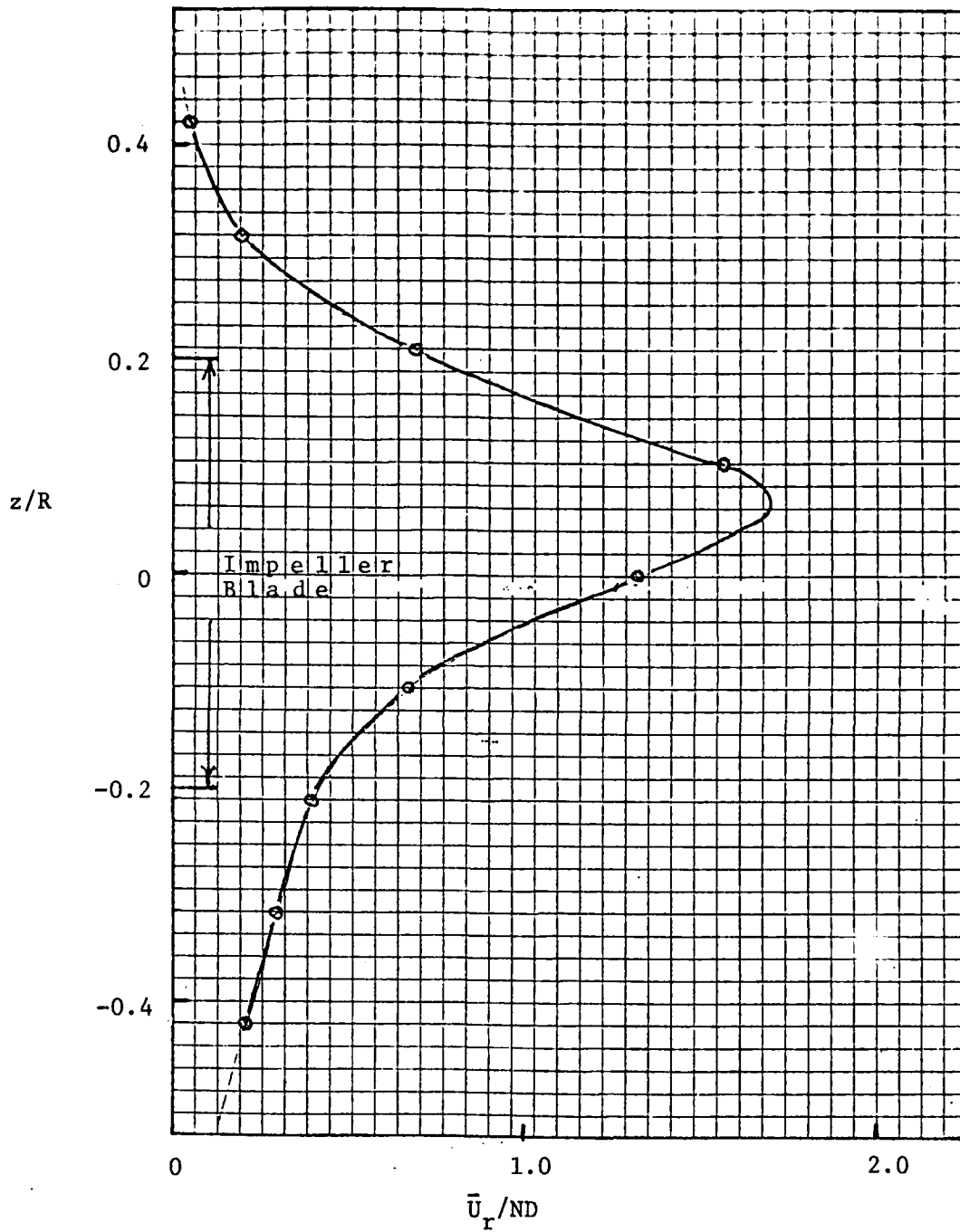


Figure 11. Mean radial velocity profile at  $r/R = 1.50$ ,  
 $N = 200$  rpm.

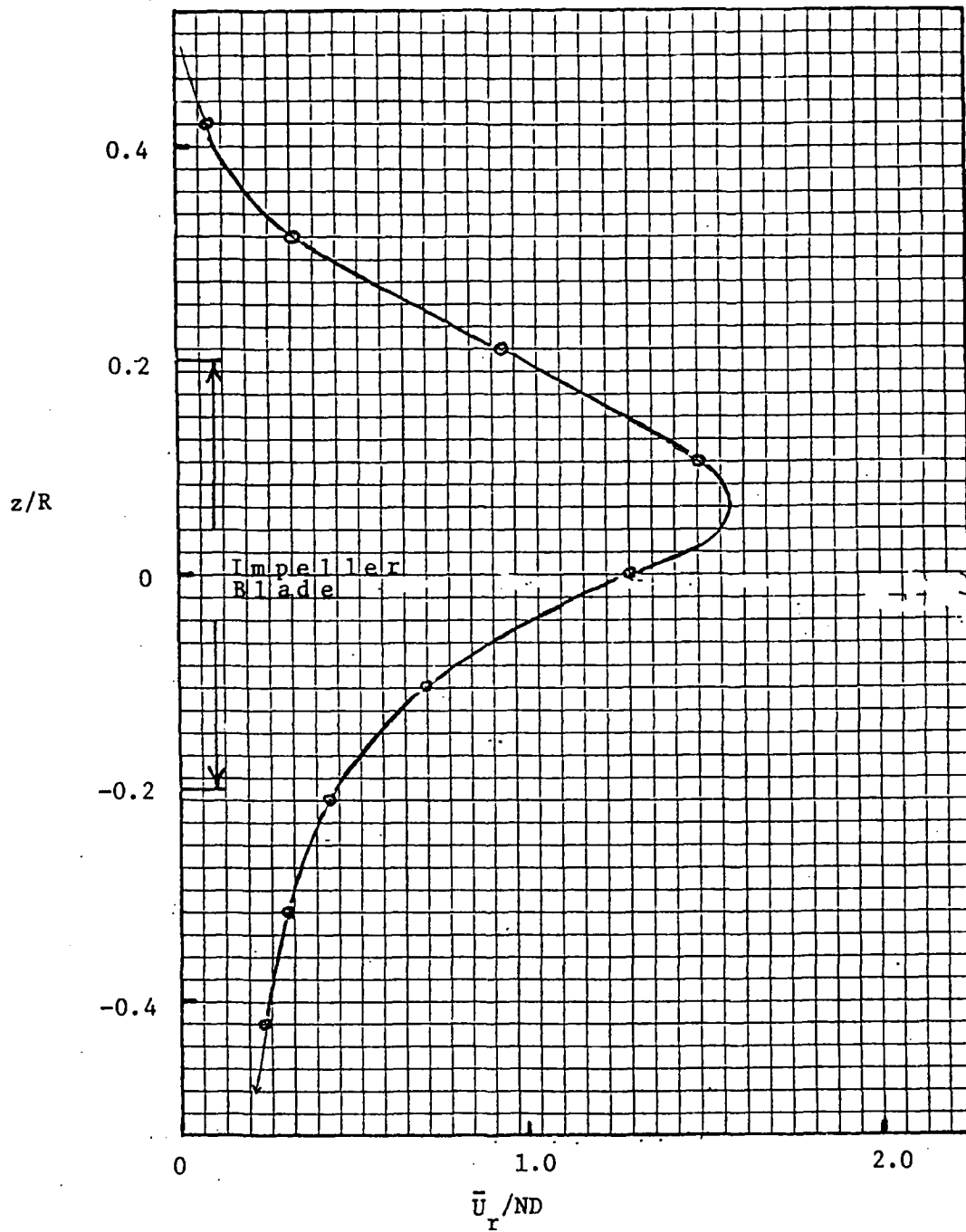


Figure 12. Mean radial velocity profile at  $r/R = 1.66$ ,  
 $N = 200$  rpm.

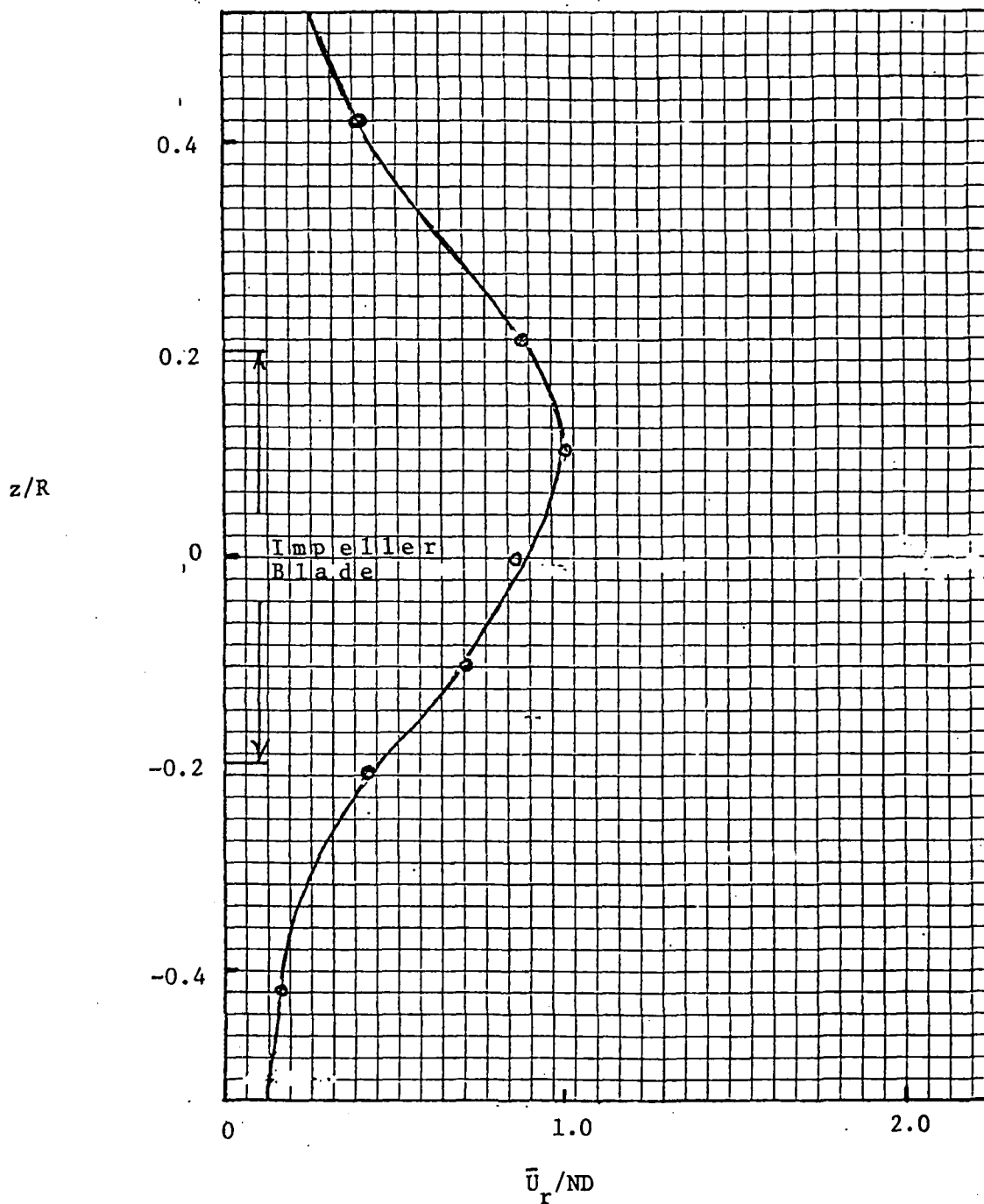


Figure 13. Mean radial velocity profile at  $r/R = 2.26$ ,  
 $N = 200$  rpm.

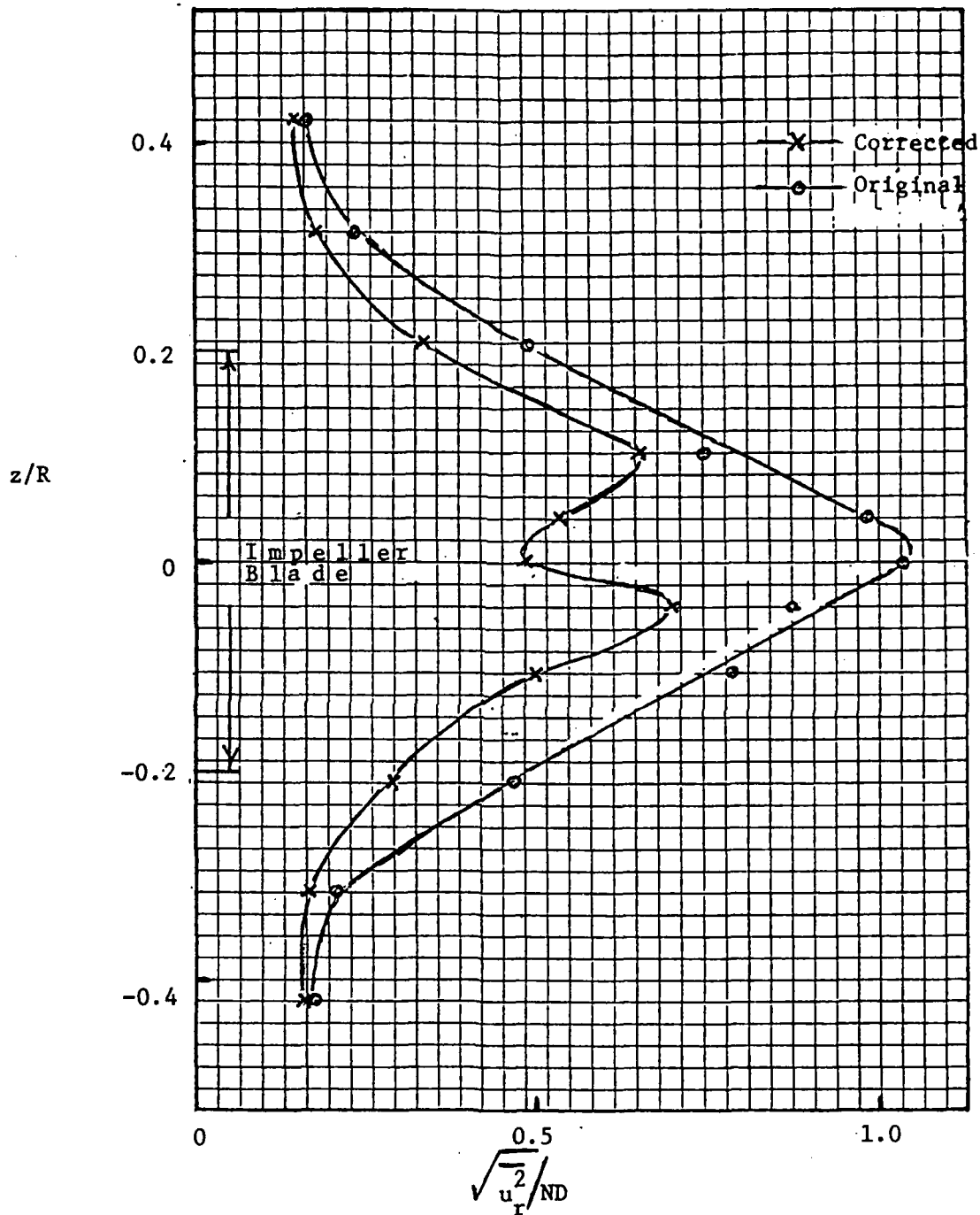


Figure 14. Radial turbulence intensity profile at  $r/R = 1.07$ ,  $N = 200$  rpm.

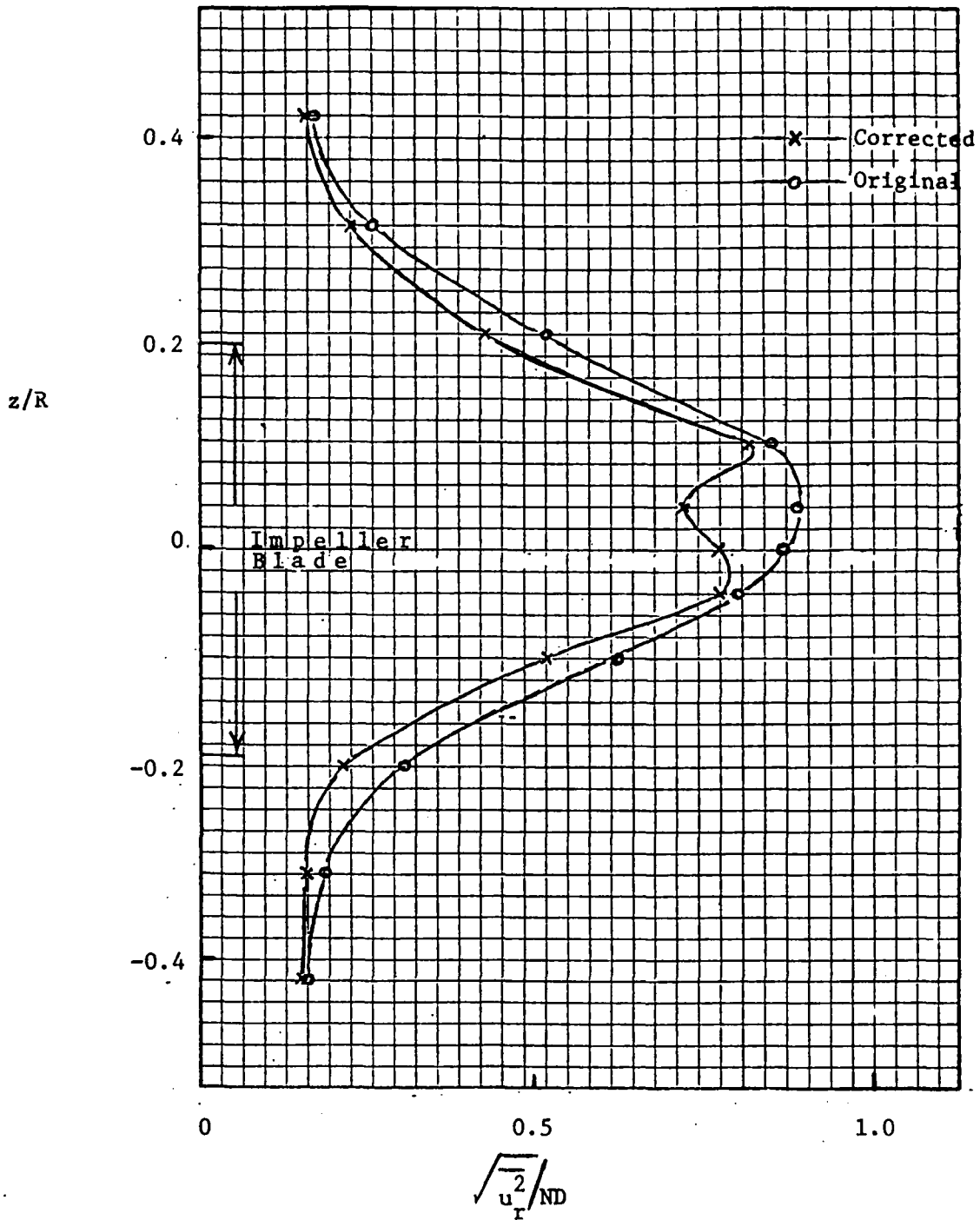


Figure 15. Radial turbulence intensity profile at  $r/R = 1.29$ ,  $N = 200$  rpm.

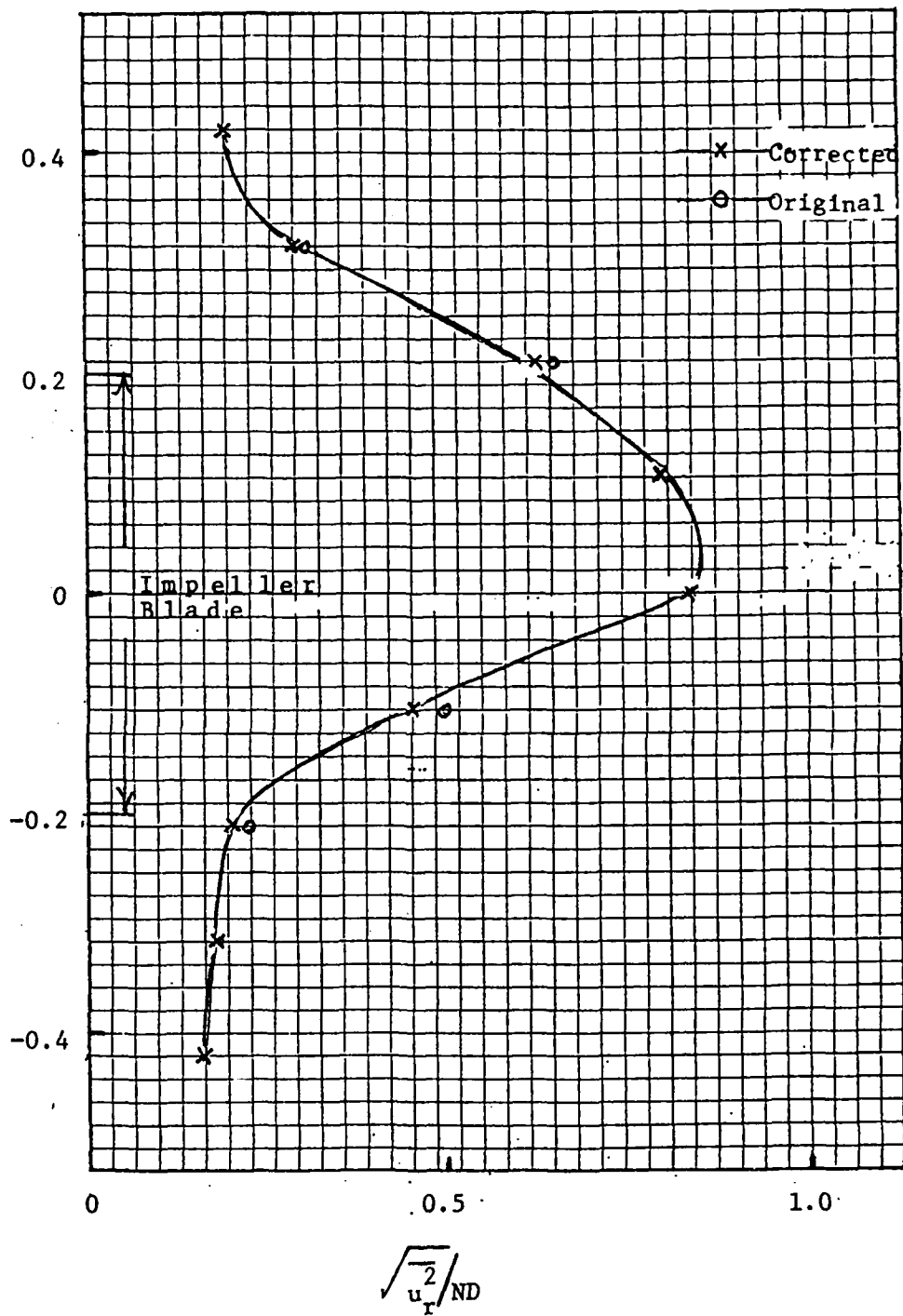


Figure 16. Radial turbulence intensity profile at  $r/R = 1.50$ ,  $N = 200$  rpm.

$z/R$

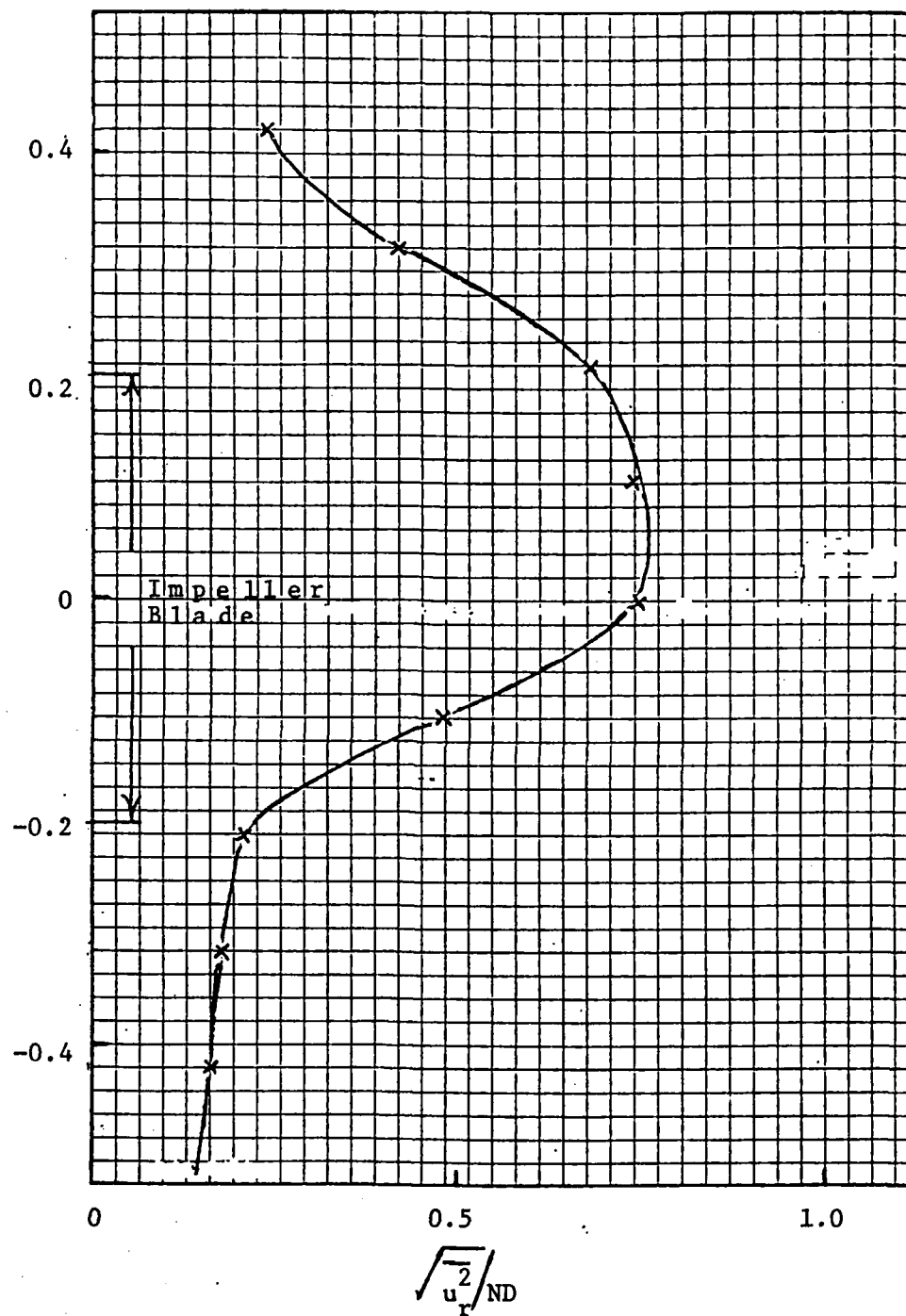


Figure 17. Radial turbulence intensity profile at  $r/R = 1.66$ ,  $N = 200$  rpm.

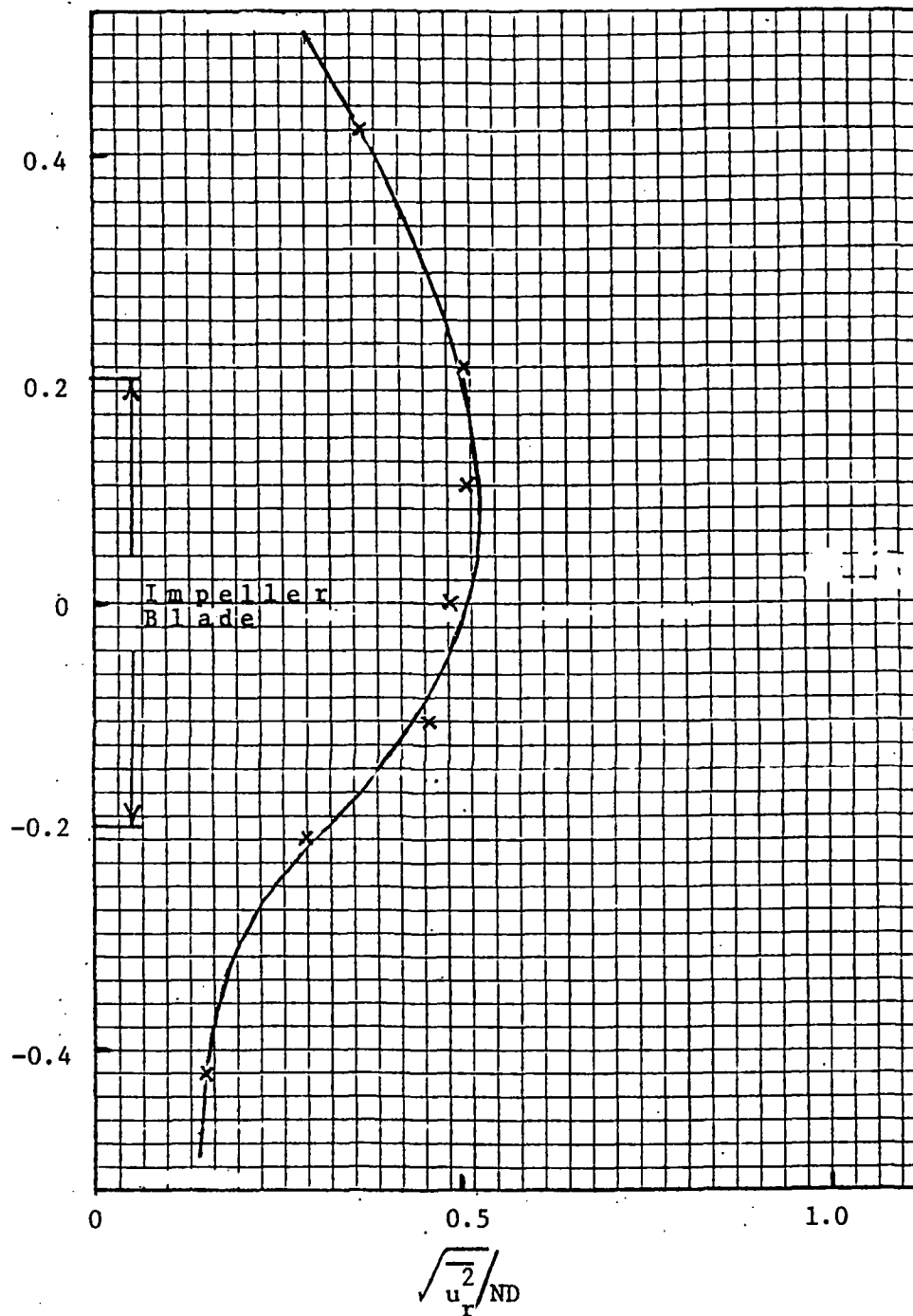


Figure 18. Radial turbulence intensity profile at  $r/R = 2.26$ ,  $N = 200$  rpm.

$z/R$

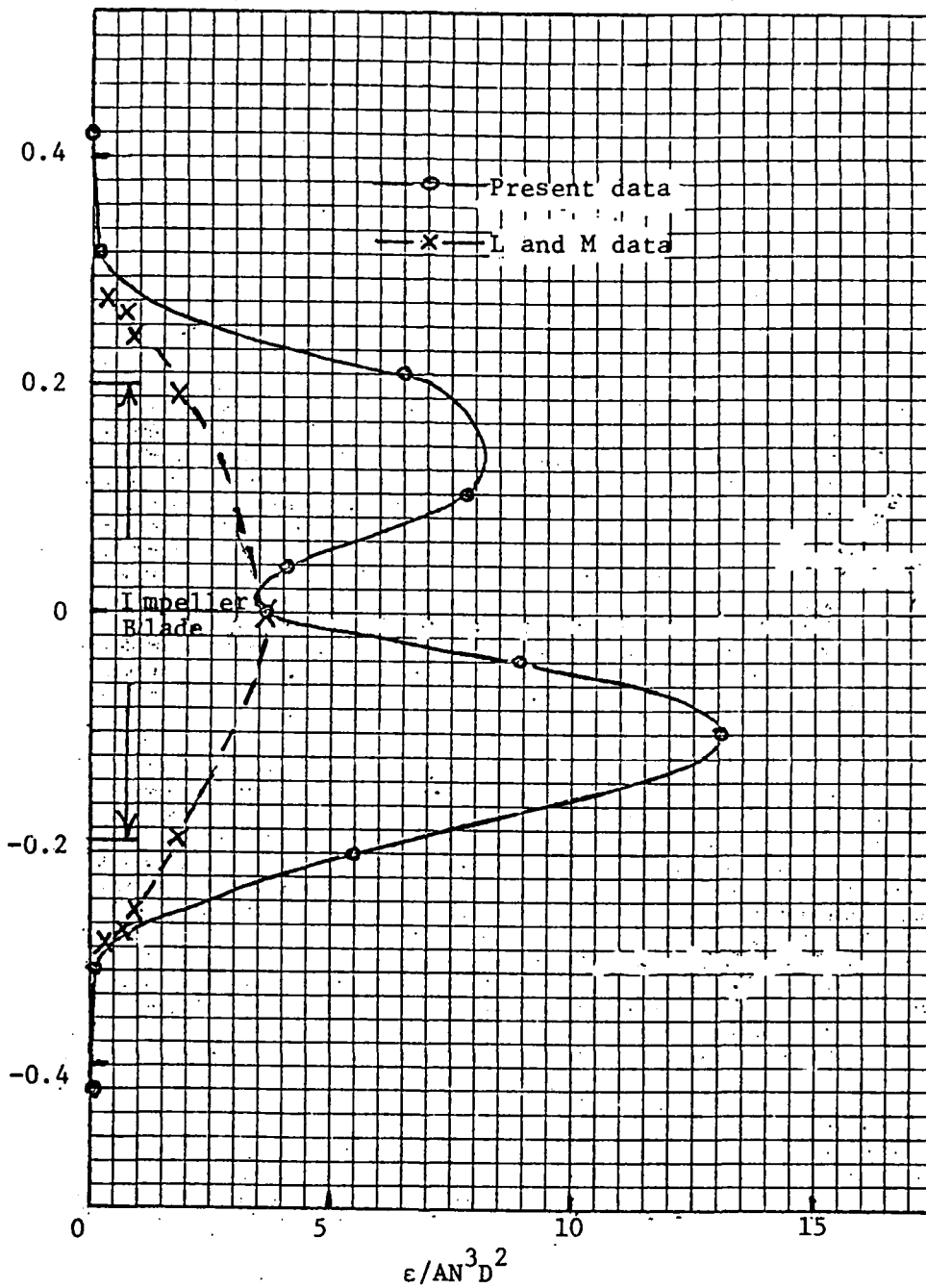


Figure 19. Energy dissipation rate profile at  $r/R = 1.07$ ,  $N = 200$  rpm.

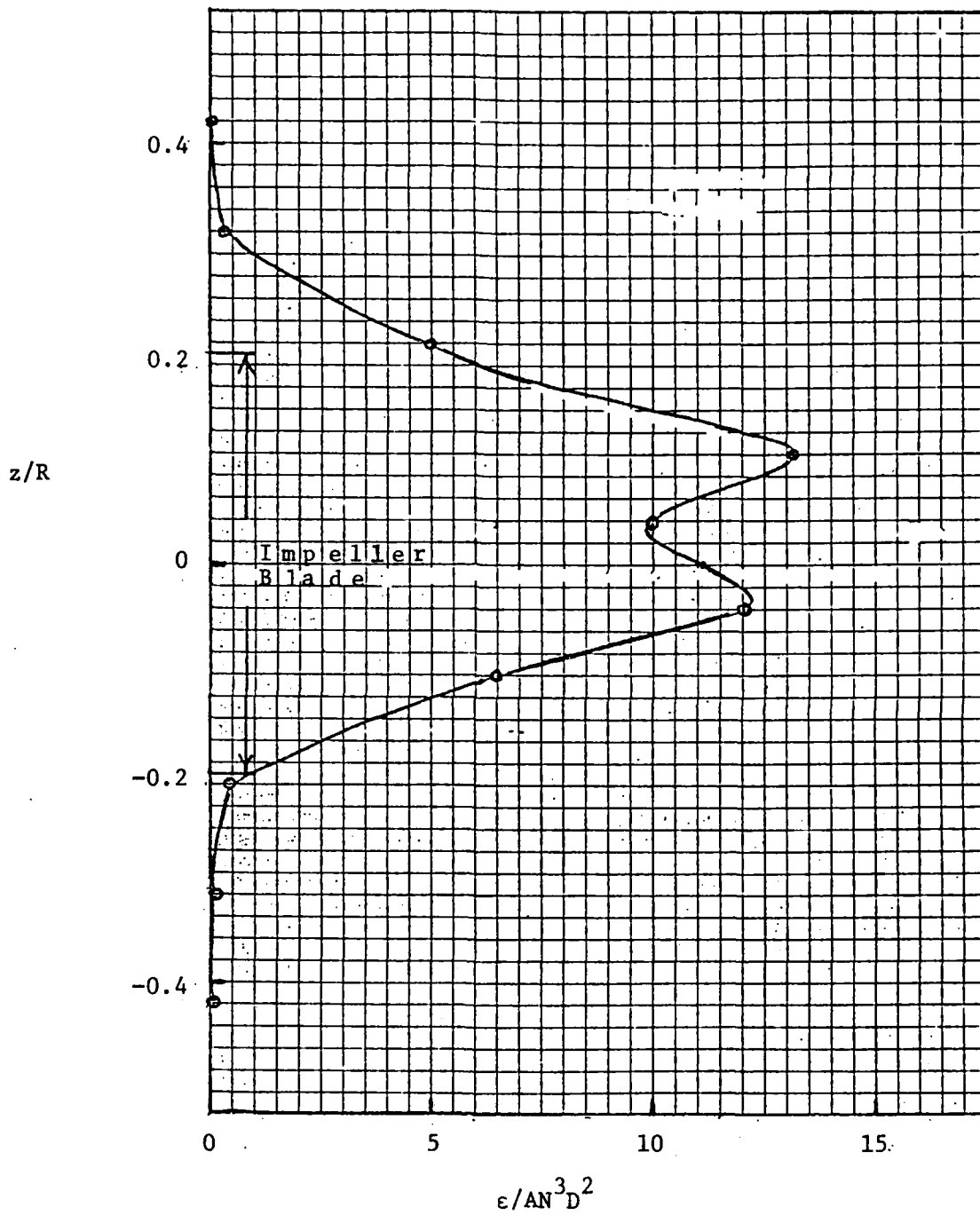


Figure 20. Energy dissipation rate profile at  $r/R = 1.29$ ,  $N = 200$  rpm.

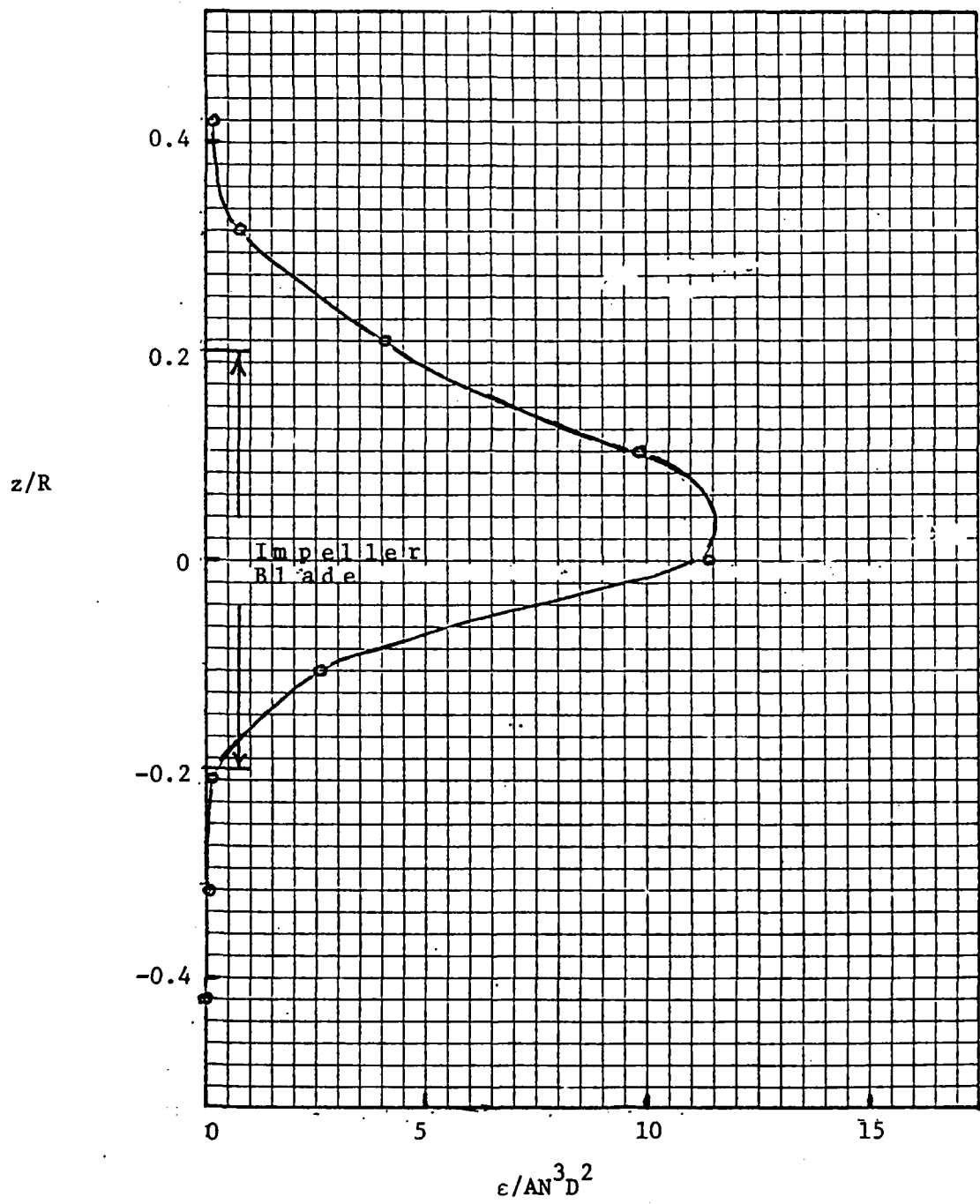


Figure 21. Energy dissipation rate profile at  $r/R = 1.50$ ,  $N = 200$  rpm.

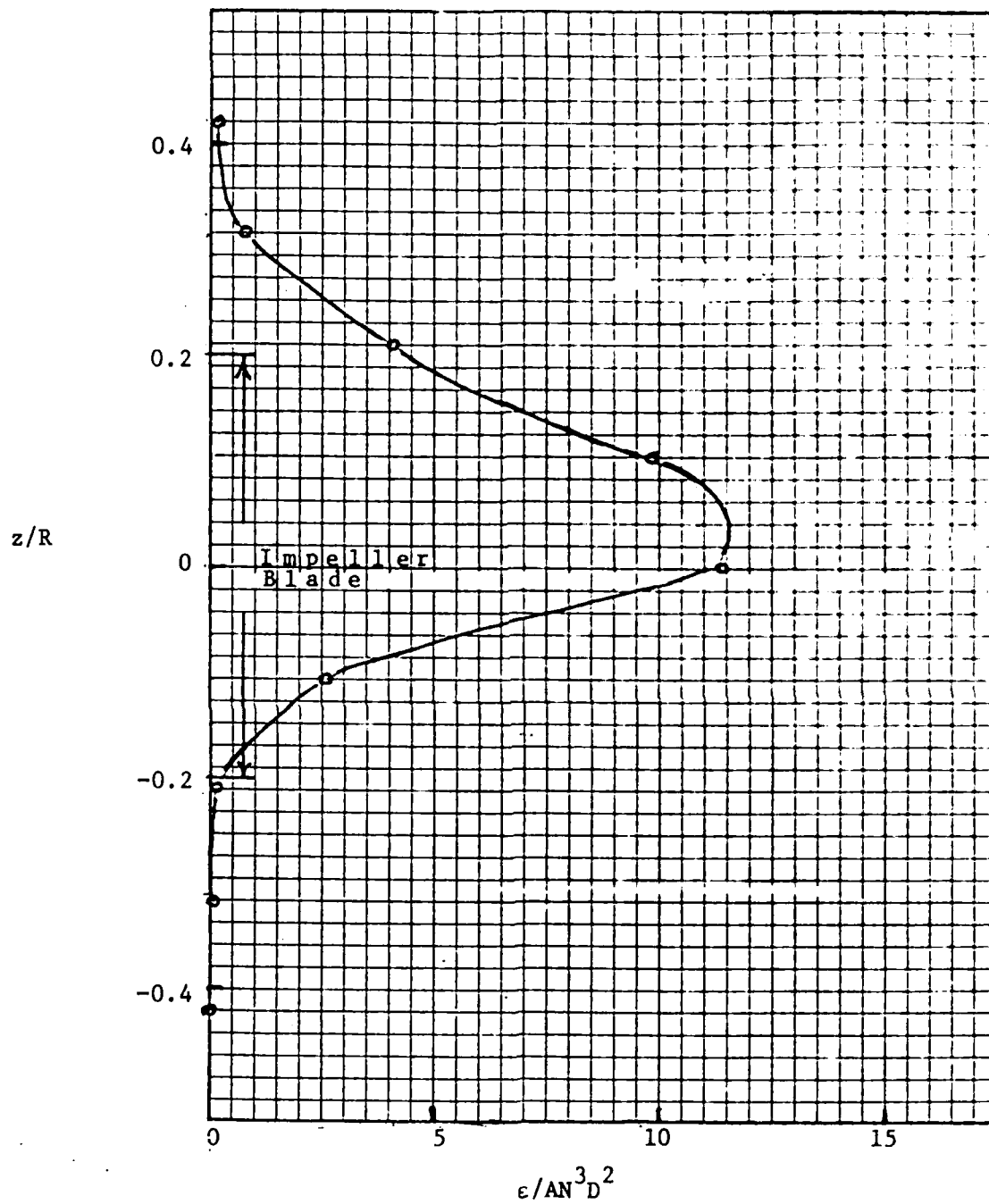


Figure 22. Energy dissipation rate profile at  $r/R = 1.66$ ,  $N = 200$  rpm.

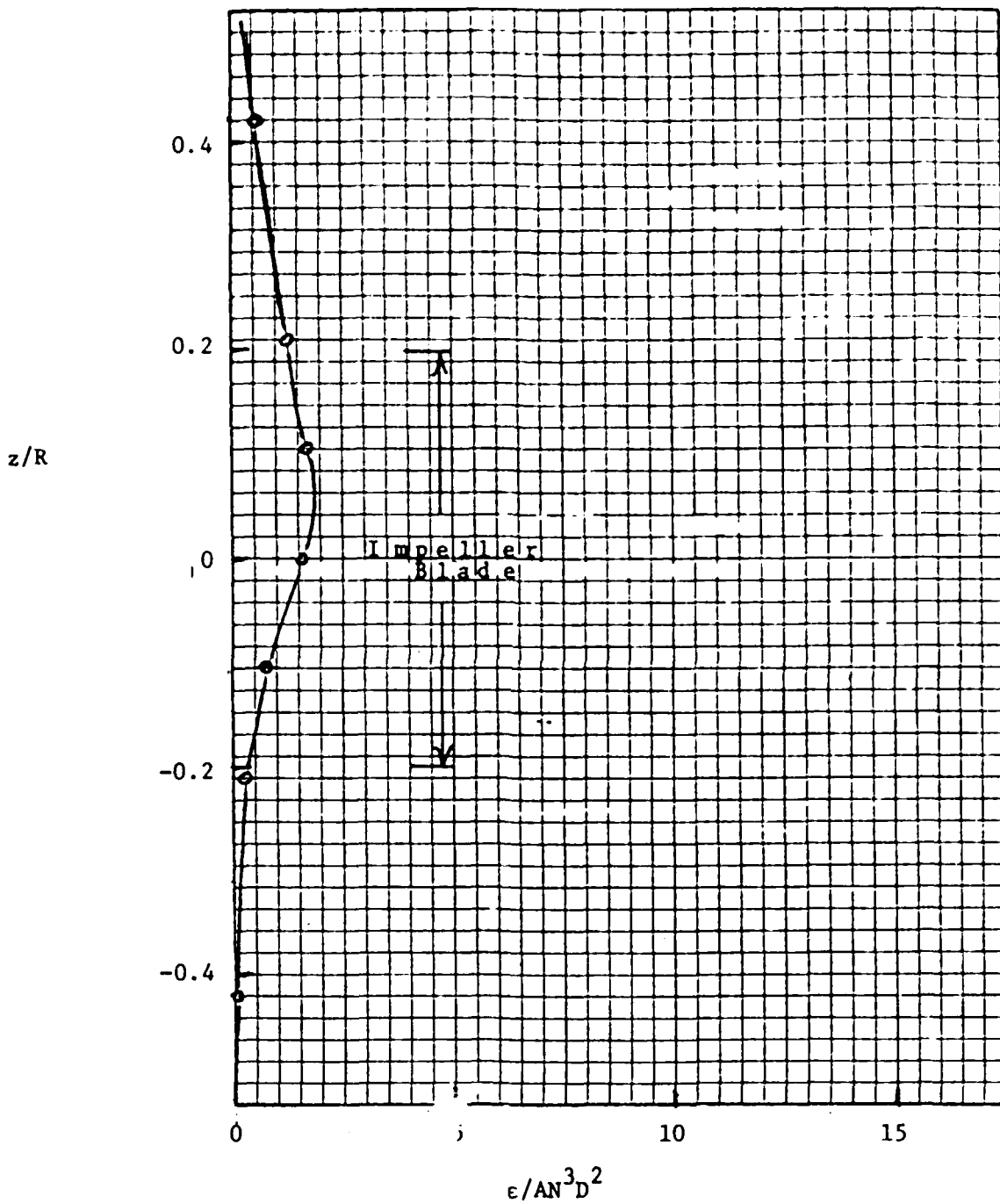


Figure 23. Energy dissipation rate profile at  $r/R = 2.26$ ,  
 $N = 200$  rpm.